Deliverable D6.8.

Barrier integrity: gas-induced impacts and model-based interpretation.

Task 3. Final technical report

Work Package GAS

The project leading to this application has received funding from the European Union's Horizon 2020 research and innovation programme under grant agreement No 847593.

Document information

Project Acronym	**EURAD**
Project Title	**European Joint Programme on Radioactive Waste Management**
Project Type	**European Joint Programme (EJP)**
EC grant agreement No.	**847593**
Project starting / end date	**1st June 2019 – 30 May 2024**
Work Package No.	**6**
Work Package Title	**Mechanistic understanding of gas transport in clay materials**
Work Package Acronym	**EURAD-GAS**
Deliverable No.	**6.8**
Deliverable Title	**Barrier integrity: gas-induced impacts and model-based interpretation. Task 3. Final technical report**
Lead Beneficiary	**Nagra**
Contractual Delivery Date	**29 February 2024**
Actual Delivery Date	**31 May 2024**
Type	**Report**
Dissemination level	**PU**
Editors	MARSCHALL Paul **(Nagra),** TALANDIER Jean **(Andra)** and KOLDITZ Olaf **(UFZ)**
Contributors	**PART 1**: MARSCHALL Paul **(Nagra),** TALANDIER Jean **(Andra),** KOLDITZ Olaf **(UFZ),** KUCEROVA Marketa **(CTU),** MOKNI Nadia **(IRSN),** GRGIC Dragan **(CNRS-U Lorraine),** AGBOLI Mensan **(CNRS-U Lorraine),** ZHANG Chun-Liang **(GRS),** CUSS Robert **(UKRI-BGS),** WISEALL Andrew **(formerly UKRI-BGS),** GONZALES-BLANCO Laura **(CIMNE),** ROMERO Enrique **(CIMNE),** LLABJANI Qazim **(EPFL),** FERRARI Alessio **(EPFL)** **PART 2:** KOLDITZ Olaf **(UFZ)**, TALANDIER Jean **(Andra)**, MARSCHALL Paul **(Nagra),** AMROFEL Nathan **(CNRS-U Lorraine)**, BURLAKA Victoria **(BGE)**, COLLIN Frédéric **(U Liège)**, CORMAN Gilles **(U Liège)**, DIEUDONNÉ Anne-Catherine **(TU Delft)**, DYMITROVSKA Magdalena **(IRSN)**, FAIVRE Maxime **(CNRS-U Poitiers)**, GIOT Richard **(CNRS-U Poitiers)**, GOLFIER Fabrice **(CNRS-U Lorraine)**, GRANET Sylvie **(EDF)**, GRUNWALD Norbert **(UFZ)**, HASSANZADEGAN Alireza **(BGE)**, HUANG Zhaojiang **(TU Delft)**, LIAUDAT Joaquín **(TU Delft)**, MÜLLER Christian **(BGE)**, OLIVELLA Sebastia **(UPC)**, PITZ Michael **(BGR)**, OWUSU Jerry-Peprah **(PSI)**, QUACQUARELLI Adriana **(U Liège)**, SIMO Eric **(BGE)**, TATOMIR Alexandru **(BGE)**, TINET Anne-Julie **(CNRS-U Lorraine)**, TOPRAK Erdem **(UPC)**, VARDON Philip J. **(TU Delft)**, ZIEFLE Gesa **(BGR)**

To be cited as:

Marschall P., Talandier J. and Kolditz O. (editors) (2024). Barrier integrity: gas-induced impacts and model-based interpretation. EURAD-GAS: Work Package GAS (Mechanical understanding of gas transport in clay-based materials) of the HORIZON 2020 project EURAD. EC Grant agreement N°847593. Task 3. Final Technical Report. Deliverable 6.8 (D6.8).

Disclaimer

Acknowledgment

This document is a deliverable of the European Joint Programme on Radioactive Waste Management (EURAD). EURAD has received funding from the European Union's Horizon 2020 research and innovation programme under grant agreement No 847593.

Status of deliverable		
	By	Date
Delivered (Lead Beneficiary)	Part 1 Paul Marschall (Nagra) Part 2: Olaf Kolditz (UFZ)	5 March 2024 25 March 2024
Verified (WP Leader)	Séverine Levasseur (ONDRAF/NIRAS)	27 March 2024
Reviewed (Reviewers)	Part 1: Jon Harrington and Elena Tamayo-Mas (UKRI-BGS) and Xavier Sillen (ONDRAF/NIRAS) Part 2: Jacques Wendling (Andra)	1 May 2024 22 April 2024
Verifier (WP Leader)	Séverine Levasseur (ONDRAF/NIRAS)	21 May 2024
Approved (PMO)	Bharti Reddy (Nuclear Waste Services)	31 May 2024
Submitted to EC (Coordinator)	Coordinator (Andra)	31 May 2024

The authors express their sincere gratitude to all participants of EURAD-GAS, whose dedicated contributions played a pivotal role in the success of the work package. In particular, special thanks are extended to the following individuals for their contributions to and/or review of this document: Elena Tamayo-Mas and Jon Harrington from British Geological Survey for the detailed and knowledgeable technical review of the Part 1 of this report, Jacques Wendling from Andra for the review of the Part 2 and Séverine Levasseur, Xavier Sillen and Véronique Pirot from ONDRAF/NIRAS for professional leadership and tireless support.

Executive summary

Work Package 6 of the EURAD European Joint Programme (WP 6 – EURAD-GAS – “Mechanistic understanding of gas transport in clay materials”) was aimed at improving the mechanistic understanding of gas transport processes in natural and engineered clay materials, their couplings with the mechanical behavior and their impact on the properties of these materials. Task 3 of Work Package EURAD-GAS was dedicated to the hydro-mechanical phenomena and processes, associated with the gas-induced failure of clay barriers (Subtask T3.1) and to the effectiveness of self-sealing processes along gas-induced pathways in the clay barriers of a geological repository (Subtask T3.2). The evaluation of achievements has been accomplished by model-supported data analyses, predictive modelling and the application of newly developed modelling tools on in-situ experiments (Subtask T3.3). The final documentation of the achievements of EURAD- GAS requires a thematic report on barrier integrity (Deliverable D6.8), which consists of 2 parts:

- Part 1: Final Report on gas induced impacts comprising the experimental results of Subtasks T3.1 and T3.2.
- Part 2: Model-based interpretation by Subtask T3.3).

The first part of this report (Part 1) summarises the experimental results associated with gas induced failure of clayey materials and the effectiveness of self-sealing processes along gas-induced pathways in the clay barriers. Two project partners (CTU, IRSN) concentrated their experimental activities on combined gas / water transport in engineered barrier materials (Czech Ca-Mg bentonite, Na-smectite-based Wyoming bentonite). Five teams (GRS, CNRS / Uni Lorraine, BGS/UKRI, EPFL and CIMNE) performed gas invasion and self-sealing experiments on samples of clayey host rocks (Boom Clay, Callovo-Oxfordian, Opalinus Clay). Last, but not least, a dedicated research activity (ZHAW) was aimed at developing new workflows for the analysis of digital pore models, bridging the interface between experimental work and numerical modelling.

In the course of Task 3 a wealth of new experimental results has been collected, which is evaluated in the final chapter of the first part of this report, both from the end-users side and from a more general geoscientific perspective. Major achievements are summarized here:

- Consolidation and confirmation of the gas-related processes and the corresponding data bases, both for EBS and clayey rocks. From the end-users perspective, this may be considered the most important achievement, because trust is built in existing concepts of gas transport in clay-rich media.
- New μ-CT techniques provide a better mechanistic understanding of gas transport and self-sealing processes at pore scale and provide a new source of data for the validation of process models in the context of digital rock physics.
- Combined water/gas injection experiments were conducted in oedometric cells, triaxial cells and in a shear box apparatus, designed for accurate measurement of the volumetric / deviatoric behaviour of the clayey material during the entire test sequence. The close interactions of the experimentalist with the modelling teams of Task 3.3 during the EURAD-GAS progress meetings facilitated a traceable and transparent hand-over of data to the modellers as input for the development of gas-related process models, for model benchmarking and for back calculation of experimental data (see the second part of the report – Part 2).

The second part of this report (Part 2) summarises the activities carried out in the Subtask 3.3 of the WP GAS by each partner involved in this subtask. Their activities mainly focused on the development of conceptual process models of gas-induced damage evolution and self-sealing processes for damaged or intact host rocks and EBS clay barriers. These models were then validated in a series of configurations of relevance for geological disposal in clays. Close interactions of the experimentalists of Subtasks 3.1 and 3.2 with the modelling teams of Subtask 3.3 during the EURAD-GAS facilitated a traceable and transparent hand-over of data to the modellers as input for the development of gas-related process models, for model benchmarking and for back calculation of experimental data.

Important model developments were performed during EURAD-GAS concerning the process chain and code implementations, e.g.,

- In CODE_ASTER (EDF): Coupling of two-phase flow model (liquid and gas phases)[1] with elasto-viscoplastic mechanical law with second gradient. Development of couplings between permeability and plastic deformation.
- In CODE_BRIGHT (UPC): 3D heterogeneous, coupled HM-G, BBM + cubic law for permeability, comprehensive protocol of hydration intervals and gas injection intervals (Toprak et al., 2023).
- In LAGAMINE (ULiège): Extension of the second gradient method to two-phase flow hydro-mechanically coupled conditions including strong couplings between transfer properties and the deformations (Corman et al., 2022, Corman, 2024). Development of a hydro-mechanical interface constitutive model to reproduce the self-sealing process in an artificially fractured sample (Quacquarelli et al., 2024).
- In LAGAMINE (TU Delft): Development of a pneumo-hydro-mechanical (PHM) framework to model gas-induced crack initiation and propagation in clays (Liaudat et al., 2023).
- In OpenGeoSys (OGS-6; UFZ, BGR, BGE): Development of a hierarchical thermo-hydro-(two-phase-flow)-mechanical TH2M models (Grunwald et al., 2022, 2023, Pitz et al., 2023a,c) and fracture mechanics based on phase-field method (Mollaali et al., 2023) and various applications to laboratory and field experiments.

Compared with the FORGE EC project, EURAD-GAS has made huge progress in the development of (T-)HM process models, including model calibration and back-calculation of experimental data. The model portfolio obtained in EURAD-GAS provides new tools for systematic model abstraction (geometric, process abstraction, scaling/homogenisation) in performance assessment.

[1] We use the term H2M to denote two-phase flow in a deformable porous medium, where the fluid phases include liquid and gaseous ones.

Contents

Part 1. Gas induced impacts comprising the experimental results of Subtasks T 3.1 and 3.2

Contributors

PART 1: MARSCHALL Paul **(Nagra),** TALANDIER Jean **(Andra),** KOLDITZ Olaf **(UFZ),** KUCEROVA Marketa **(CTU),** MOKNI Nadia **(IRSN),** GRGIC, Dragan **(CNRS-U Lorraine),** AGBOLI Mensan **(CNRS-U Lorraine),** ZHANG Chun-Liang **(GRS),** CUSS Robert **(UKRI-BGS),** WISEALL Andrew **(formerly UKRI-BGS),** GONZALES-BLANCO, Laura **(CIMNE),** ROMERO, Enrique **(CIMNE),** LLABJANI Qazim **(EPFL),** FERRARI Alessio **(EPFL)**

Contents

List of figures

List of tables

Acronyms

BC	Boom Clay (Belgium and the Netherlands) (a poorly indurated clay rock)
BCV	Czech bentonite
Andra	National Agency for Radioactive Waste Management (*Agence Nationale pour la Gestion des Déchets Radioactifs*) (France)
BGS	British Geological Survey (UKRI) (United Kingdom)
CIMNE	International Centre for Numerical Methods in Engineering (Spain)
COx	Callovo-Oxfordian claystone (France) (an indurated clay rock)
CTU	Czech Technical University (Czech Republic)
EBS	Engineered barrier system
EC	European Commission
EDZ	Excavation damaged zone
EPFL	*Ecole Polytechnique Fédérale de Lausanne* (Switzerland)
EURAD	European joint programme on radioactive waste management – EC funded (2019–2024)
FORGE	Fate of repository gases. Investigation of process of gas generation and transport and their potential impact on a disposal system – *EC project (2009–2013)*
GRS	*Gesellschaft für Anlagen- und Reaktorsicherheit* (Germany)
HADES URL	High-activity disposal experimental site – underground research laboratory in Mol (Belgium)
HITEC	RD&D work package of EURAD devoted to the study of the influence of temperature on clay-based material behaviour
HLW	High-level waste
IRSN	Institute for radiation protection and nuclear safety (*Institut de radioprotection et de sûreté nucléaire*) (France)
IUPAC	International Union of Pure and Applied Chemistry
MEGAS	Modelling and experiments on gas migration in repository host rocks (under the umbrella of the PEGASUS EC project) – *EC project (1992–1997)*
Mont Terri URL	Underground research laboratory in Switzerland
MX-80 type	Wyoming bentonite (USA)
Nagra	National Cooperative for the Disposal of Radioactive Waste (*Nationale Genossenschaft für die Lagerung radioaktiver Abfälle*) (Switzerland)
ONDRAF/NIRAS	Belgian Agency for Radioactive Waste and Enriched Fissile Materials (*Organisme national des déchets radioactifs et des matières fissiles enrichies / Nationale instelling voor radioactief afval en verrijkte Splijtstoffen)* (Belgium)
OPA	Opalinus clay (Switzerland) (an indurated clay rock)
PEGASUS	Project on the effects of gas in underground storage facilities for radioactive waste – *EC umbrella project (1991–1998)*
RD&D	Research, development and demonstration

SCK CEN	Belgian Nuclear Research Centre (*Studiecentrum voor Kernenergie / Centre d'Étude de l'énergie Nucléaire*) (Belgium)
SOTA 1 / 2	State-of-the-art report (Initial / Update)
THM	Thermo-hydro-mechanical
UFZ	Helmholtz Centre for Environmental Research (*Helmholtz Zentrum für Umweltforschung*) (Germany)
ULiège	University of Liège (Belgium)
UPC	Technical University of Catalonia (*Universitat Politècnica de Catalunya*) (Spain)
URL	Underground research laboratory
WMO	Waste management organization

1. Background and scope

The European Joint Programme on Radioactive Waste Management (EURAD) has been implemented as part of the EU Research and Innovation Programme Horizon 2020 to coordinate activities on agreed priorities of common interest between European Waste Management Organisations (WMOs), Technical Support Organisations (TSOs) and Research Entities (REs). The EURAD Grant Agreement No. 47593 between the European Union and 51 awarded beneficiaries sets out the rights and obligations and the terms and conditions for the implementation of the action with duration of 60 months (2019-2024). The EURAD programme is organized into 13 Work Packages. WP 6 – GAS ("Mechanistic understanding of gas transport in clay materials") is aimed at:

- Improving the mechanistic understanding of gas transport processes in natural and engineered clay materials, their couplings with the mechanical behavior and their impact on the properties of these materials;
- Evaluating the gas transport regimes that can be active at the scale of a geological disposal system and their potential impact on barrier integrity and repository performance.

The work package WP6 – GAS encompasses 20 beneficiaries and a total of 18 participating organisations; ONDRAF/NIRAS acts as WP-leader. The work package is subdivided into 4 tasks:

- Task 1 – S/T coordination, State-of-the-art and training material
- Task 2 – Transport mechanisms
- Task 3 – Barrier integrity
- Task 4 – Repository performance aspects

Task 3 is aimed at gaining a mechanistic understanding of the hydro-mechanical phenomena and processes, associated with the gas-induced failure of clay barriers (Subtask 3-1) and with the effectiveness of self-sealing processes along gas-induced pathways in the clay barriers of a geological repository (Subtask 3-2). The evaluation of achievements is accomplished by model-supported data analyses, predictive modelling and the application of newly developed modelling tools on in-situ experiments (Subtask 3-3).

According to the EURAD Grant Agreement, Task 3 of WP 6 – GAS has to deliver a final experimental report comprising a complete documentation of the experimental results and a synopsis of the main achievements of subtasks 3-1 and 3-2. Reporting of technical activities is based on the detailed work programme (Marschall et al. 2021) which was completed in May 2021 and subsequently approved by the board of the EURAD project. The Task 3 final experimental report contains:

- A brief review of the unresolved issues reported in the SOTA1 report (Levasseur et al. 2021) at the start of the EURAD-GAS project. Emphasis is on as-induced failure of clay barriers and the effectiveness of self-sealing processes in the clay barriers of a geological repository.
- A comprehensive description of the technical activities of each partner contributing to Subtasks 3-1 and 3-2.
- A detailed discussion of the experimental results and an evaluation of the achievements from the perspective of the project partners.
- An overall evaluation of the achievements in Task 3 from the end-user perspective.

2. EURAD-GAS / Task 3 – Experimental programme

The detailed work programme of EURAD-Gas / Task 3 was completed and reported in May 2021 (Marschall et al. 2021). The experimental programme was elaborated in close coordination with the EURAD-Gas / Initial State-of-the-Art Report (Levasseur et al. 2021), which summarizes among other aspects the state of knowledge, shared understanding and unresolved issues in the following research areas:

- Gas induced failure of clayey materials (Chapter 3.1 in Levasseur et al. 2021)
- Self-sealing mechanisms in clay barriers (Chapter 3.2 in Levasseur et al. 2021)

In chapter 2.1 of this final Task Report, a brief synopsis of the state of knowledge associated with gas induced failure of clayey materials and corresponding self-sealing mechanisms is given. Chapter 2.2 discusses the experimental programme of Task 3 and chapter 2.3 describes the assessment procedure pursued in this report for the evaluation of achievements from the perspective of the project partners and from the viewpoint of the end-users, respectively.

2.1 State of knowledge and unresolved issues

The state of knowledge is extracted with slight modifications from Levasseur et al. (2021).

2.1.1 Gas induced failure of clayey materials (Subtask 3-1)

2.1.1.1 Shared understanding

The mechanical characteristics of clay-rich materials cover a wide property range in terms of strength and stiffness in the transition between soft soils and weak rocks. Despite the marked differences, these materials have in common a relatively low strength together with high gas entry pressures which makes them prone to failure when subjected to high gas pressures. When an initially water saturated clay-barrier with high water retention capacity is invaded by a gas phase, failure initiation is linked to debonding of the solid aggregates at the locus of gas entry. Microfabric of the material (i.e. geometric arrangement of the solid aggregates) contributes to its strength as it determines the geometric characteristics of the water-filled inter-aggregate pore space and establishes the contact forces between the solid aggregates.

Gas invasion experiments with *engineered clay barriers* such as bentonite and sand/bentonite mixtures have been conducted by many geotechnical laboratories worldwide. When bentonite content of the barrier material is ≥ 40%wt, the experiments show consistently that high gas pressures are required to invade the fully saturated material, typically in the range of the applied confining pressure. The typical deformation behaviour of the material in response to gas invasion exhibits first a continuous volume expansion as long as the gas front propagates through the test specimen, followed by contraction when gas breakthrough at the downstream end of the sample is reached. At the end of the gas invasion phase, when pore pressure recovers to the initial state, a minor component of irreversible strain may be observed. Several experimentalists performed post-mortem analyses of clay samples after gas invasion, indicating moderate changes in pore structure. Recent international research activities seem to reveal a strong impact of compaction and hydration procedures on the gas transport behaviour and the associated deformation behaviour of engineered clay barriers.

In *hard clays*, strength may be controlled by the degree of cementation of the mineral aggregates. It is generally agreed that the microstructure of natural clay barriers is a result of diagenetic evolution. After deposition as a clay-rich soil and depending on the tectonic evolution at large scale, the geomaterial undergoes diagenetic processes, forming its peculiar structure and affecting its hydro-mechanical

behaviour. Indurated clays such as claystone and shales are characterised by well-marked bedding-plane fissility and low plasticity, i.e. they do not form a plastic mass when wet, although they may disintegrate when immersed with water. With increasing depth, effects of compaction and diagenesis cause the shale to deviate more and more from the abovementioned typical properties and behaviour of a clay-rich soil. The impact of porewater chemistry on the deformation behaviour of the material reduces gradually with decreasing porosity, because the capacity of the swelling clay aggregates to expand in contact with external water is locked-in as a consequence of partial cementation of the solid grains.

Gas invasion experiments on hard clays have been conducted not only in the field of radioactive waste disposal but also in other geoscientific disciplines like oil and gas industry, geothermal exploration and CO_2 sequestration. Similar to the experience with clay-rich soils, high gas pressures are required to invade the fully saturated material, which are close to the applied confining pressure. Experiments in triaxial cells under well-controlled mechanical boundary conditions indicated, that gas-induced failure of the material is not only controlled by the plasticity and bedding fissility of the material but depends also on the evolution of gas pressure build-up (loading history) and on the applied mechanical boundary conditions. Depending on the speed of pressure build-up, both gradual and sudden propagation of the damage front has been observed. Gradual damage evolution was predominantly observed at low pressure build-up rates and high confining stresses. This phenomenon may be attributed to the process of subcritical crack growth ("pathway dilatancy"), where the gas production rate is balanced steadily by the newly created pore volume at the crack tip. Sudden fracture initiation was observed only in a few cases; it seems to be related to high gas pressure build-up rates or it was triggered by sudden changes of the confining pressure. From a fracture mechanics perspective, this phenomenon can referred to the process of supercritical crack growth ("gas fracturing"), where the propagation of the crack tip is driven by high uniform gas pressure.

2.1.1.2 Knowledge gaps

Phenomena and features associated with gas induced damage evolution in clay materials are difficult to predict. This is an inherent issue with many localisation phenomena in geoscience and structural mechanics. The limited predictability of localisation phenomena in geomechanics concerns the locus of damage initiation as well as the propagation of damage in space and time. The uncertainties in predicting damage evolution have various causes, including a lack of microstructural information (e.g. small-scale variability of stiffness and strength or undetected microfractures), incomplete description of the prevailing boundary and initial conditions (e.g. disequilibrium in initial state) and immature mechanistic understanding of the involved hydro-mechanical processes. It is also a challenge to upscale laboratory scale results to behavior at in-situ scale. While comprehensive theoretical frameworks for modelling damage propagation in partially saturated geomaterials have been developed in soil mechanics and to lesser extent in rock mechanics, the validation of such models is a challenge due to the lack of integrated validation workflows.

For this, dedicated experimental workflows are required, which interact closely with model-supported test designs and traceable calibration procedures. Complementary information such as microstructural imaging and high-resolution measurements of stress and strain behavior of the tested material shall be integrated in the calibration process for constraining the uncertainties of model predictions for a wide range of relevant gas invasion scenarios. Concerning gas induced damage in engineered clay barriers special issues to address are:

- The impact of the compaction and hydration procedure as well as porewater chemistry on the on-set of damage
- The impact of loading history on the on-set of damage

- The evolution of gas transport paths when subjected to very long-term gas injections (including the aspect of colloid mobilisation)
- Safety relevant knowledge gaps associated with gas induced damage in geological barrier materials concern:
- Damage evolution under fast / slow gas pressure build-up (sub-critical vs. super-critical crack growth).
- The impact of the stress path (from tensile fracturing towards shear compaction) on damage evolution.
- The evolution of gas transport paths when subjected to very long-term gas injections (including desaturation of the intact rock matrix).
- The impact of microstructural variability on damage initiation (including the role of bedding and tectonic overprint).

2.1.2 Self-sealing mechanisms in clay barriers (Subtask 3-2)

2.1.2.1 Shared understanding

Self-sealing depends on (thermo-) hydro-mechanical and chemical processes, the mineral composition of the material in link with its swelling capacity and controlled by the prevailing state conditions. Mechanical closure of fractures (e.g., crack closure, fracture sliding), hydro-chemical interactions of the pore water with the clay-bearing solid phase of the geomaterial (e.g., swelling, dis-aggregation) and colloidal transport processes (e.g. sedimentation, clogging) have been identified as typical self-sealing mechanisms in clay-rich materials. Self-sealing mechanisms are well identified for both host rock (Boom Clay, Opalinus Clay and Callovo-Oxfordian claystone) and bentonite based materials used for engineered barriers. A summary of these mechanisms is given in Levasseur et al. 2021. A large number of experiments at different scales on all the materials of interest and performed under several conditions THMC give confidence on the exhaustivity in the identification of these processes.

The contribution of small-scale imaging techniques complementary to macroscopic tests is important in confirming the physico-chemical processes relevant for self-sealing. By this means, it has been possible to visualise the closure of fractures of multiple origin and to show the rearrangements of clays in and around the fractures. For clay rocks, it highlights a difference in the microstructure of the material formed inside the fracture zone.

Gas tests in host rocks have shown that after the creation of dilatant pathways or gas fracturing, the rock always keep a capacity for self-sealing. In contrast, changes in the structure of the material in the clogged zone usually lead to changes in gas transfer properties, in particular lower gas entry pressures than in the intact rock.

2.1.2.2 Knowledge gaps

If basic understanding and identification of the phenomena and processes that contribute to the self-sealing after gas breakthrough or gas fracturing has been acquired, a certain amount of knowledge still needs to be consolidated. An improvement of conceptualization of self-sealing mechanisms at process level is needed to be able to model and predict the self-sealing capacity of clay barriers and the host rocks under the THM-C conditions that prevail in a deep geological repository.

Several situations have to be explored to demonstrate that self-sealing capacity is not lost due to gas breakthrough such as:

- successive opening/closing of gas pathways in particular for engineered barriers or at the interfaces between clay materials and other components of the repository.
- long-term gas flow in a fracture and possible transformations or microstructural reorganisations at the fracture wall.

2.2 Experimental programme – Issues addressed in Task 3

A comprehensive description of the detailed work programme of Task 3 of WP 6 – GAS is given in Milestone MS 58 (2021). The subsequent paragraphs provide brief descriptions of the research activities at the level of Subtasks 3-1 and 3-2.

2.2.1 Research activities related to the engineered barriers

The favorable barrier properties of clayey materials (low permeability, high swelling capacity, contaminant retention capacity, mineralogical stability in the conditions of geological disposal systems) suggest their use as sealing elements in engineered barrier systems. Most geological disposal concepts worldwide use bentonite as sealing material, a naturally occurring absorbent swelling clayey material with a low permeability (see Levasseur et al. 2021). Depending on the intended safety functions and the corresponding design specifications of the engineered barrier system, bentonite is processed in different forms and compacted to various densities.

In this context, another issue to consider is the type and the quality of the bentonite. A broad range of different qualities with respect to exchangeable ion, accessory minerals and production techniques are used by the waste management organisations, depending on the intended application. Comprehensive geotechnical data bases exist for Wyoming sodium bentonite, encompassing not only the basic geotechnical characteristics of the material but also dedicated investigations on gas induced failure and its self-sealing capacity.

Two experimental activities were conducted in Task 3 with focus on gas induced failure and self-sealing capacity of bentonite (chapter 3):

- **CTU - Cyclical water and gas injection experiments with Czech Ca-Mg bentonite** (called *BCV bentonite*). Phenomenological studies were carried out with constant volume cells, comprising cyclic hydration / gas invasion tests on BCV bentonite samples of different dry densities. Tests were conducted both on homogeneous samples and on samples with an artificial joint. The experimental programme complements previous studies on gas transport in bentonite, which were carried out with Wyoming sodium bentonite MX-80.
- **IRSN - Gas migration processes in initially heterogeneous bentonite mixtures**. The evolution of microfabric of a mixture of MX-80 pellets with bentonite powder was investigated in response to hydration and gas invasion processes. An X-ray CT scanner was used for monitoring of hydration / gas invasion processes of the pellet/powder mixture in a constant volume cell. Data analyses included the evolution of porosity, gas/water permeability and local displacements of the solid skeleton, highlighting the paramount relevance of microfabric for a mechanistic understanding of gas transport processes in bentonite.

2.2.2 Research activities related to the geological barriers

When subjected to excessive gas pressures, clayey rocks are particularly prone to failure due to their low mechanical strength. The impacts of gas accumulation, gas pressure build-up and gas transport processes on the performance of the clay barriers depend not only on the hydro-mechanical properties of the barrier materials but also on the environmental conditions at repository level, on the repository design and on various other aspects such as waste-related source terms. Consequently, an in-depth understanding of the gas-related failure mechanisms is required for a balanced assessment of the safety-related impacts on barrier performance (see also Levasseur et al. 2021).

The mechanical characteristics of geological clay barriers cover a wide property range in terms of strength and stiffness, representing the full spectrum of deformation behaviour in the transition between hard soils and soft rocks (see also Gens 2013). Three geomaterials were investigated in Task 3, namely Boom Clay (BC), a slightly overconsolidated stiff soil, Callovo Oxfordian (COx), a overconsolidated soft rock and Opalinus Clay, a moderately overconsolidated soft rock.

Five laboratory experiments were conducted in Task 3 with focus on gas induced failure and self-sealing capacity of clayey host rocks (chapter 4):

- **GRS – Gas transport along fractures in clayey rocks and impact of self-sealing**. The experimental programme consisted of long-term self-sealing and gas injection tests in triaxial cells on artificially fractured claystones (COx, OPA). Exceptional data bases were acquired by monitoring the evolution of hydraulic conductivity, axial and radial strains over a period of up to 700 days. Gas injection tests on the resealed material were aimed at exploring the gas pressure needed to invade the resealed material under a given confining stress. Resealing tests after completion of gas injection sequences and post-mortem investigations of the dismantled test samples complemented the experimental programme.
- **CNRS (Uni Lorraine) – Visualisation of gas transport in fractures and impact on their self-sealing capacity.** Water and gas permeability tests with flow direction parallel and perpendicular to bedding were conducted in triaxial cells on intact and artificially fractured claystone (COx). The innovative aspect in the experimental programme was the use of a µ-CT-equipment for the visualization of gas transport processes during gas invasion phase and, subsequently, the self-sealing processes in response to re-hydration of the sample. Evolution of permeability, volumetric strain and fracture volume was monitored in the gas invasion phase and during re-hydration.
- **BGS (UKRI) – Effects of gas transport on fracture transmissivity and self-sealing.** A novel test concept for fracture transmissivity measurements under well-defined shearing conditions was pursued using a highly instrumented (normal stress, shear stress, shear displacement, normal displacement, porewater pressure/flow, etc) bespoke direct shear apparatus. The experiments were conducted with indurated claystones (COx, OPA). The test results encompassed not only the transients of ga/water flow, stresses and shear strains but also scans of the fracture surfaces before and after testing. Such complementary spatial information about the evolution of the fracture surface in response to gas injections and re-hydrations provides invaluable insights in the gas transport and self-sealing mechanisms.
- **EPFL – Gas transport in intact and remoulded / recompacted claystone.** Combined water/gas injection experiments were conducted on indurated clay samples (OPA) using a high-pressure oedometric cell, specifically designed for testing at high confining stresses. Special focus was on accurate measurement of the volumetric behaviour of the material during the entire test sequence, comprising the initial sample equilibration phase, water permeability tests, gas injection tests, rehydration tests and a final pressure recovery phase. The experiments were carried out on intact material and on material, which had been remolded and recompacted

for mimicking the microfabric of fault gouge material. The impact of gas transport on the microfabric of the test samples was studied as part of a post mortem investigation programme.

- **CIMNE (UPC) – Hydromechanical response of claystones during gas injections.** Combined water/gas injection experiments were conducted with a clayey material in transition between a stiff soil and a soft rock (BC). For this, a new oedometric cell was designed and tested, allowing for highly accurate measurements of the volumetric behaviour of the material and for monitoring of the lateral stress acting on the test sample. Outstanding experimental results were achieved with the new cell, indicating a distinct dependence of the gas transport capacity of the BC samples on the gas injection rate. Post mortem studies indicated a measurable impact of the gas injections on the microfabric of the material.

2.2.3 Two-phase flow properties derived from pore-scale imaging

Methods of Digital Rock Physics (DRP) such as µ-CT or SEM imaging are emerging as a complementary part of the geotechnical characterization of clayey materials. The digital outputs can be used to create a digital twin of the material under investigation. IRSN and CNRS-UNI Lorraine used such techniques successfully to visualize the evolution pore space of bentonite mixtures (chapter 3.2) and of fractured COx (chapter 4.2) in response to hydration, gas injections and subsequent re-hydration phases. BGS-UKRI developed a method, which allows to scan fracture surfaces and to reconstruct fracture aperture in 3 dimensions. Imaging and reconstruction of the pore networks of intact claystones with dominant pore sizes in the order of 10 nm is a topic of ongoing research, even though pioneering work has been carried out in this field during the last decade (e.g. Keller et al. 2013).

A dedicated research activity (ZHAW) in Task 3 was aimed at developing new workflows for the analysis of digital pore models (chapter 5):

- Development of workflows for statistical analysis of 3-D images of pore size distribution as input for water retention behavior and relative permeability – saturation relationships
- Development of workflows for statistical analysis of fracture roughness as input for mechanistic models for damage evolution and self-sealing (e.g. shear box experiments described in chapter 4.2).

2.3 Evaluation of achievements – Assessment procedure

The experimental programme of Task 3 (“Barrier integrity”) of the WP EURAD-Gas comprises the *gas induced failure of clayey materials* (Subtask 3-1) and *self-sealing mechanisms in clay barriers* (Subtask 3-2). The final experimental results of Task 3 are reported in chapter 3 (engineered barriers), chapter 4 (geological barriers) and chapter 5 (workflows for the analysis of digital pore models) of this report. The bulk of experimental results will feed in Task 3.3 (Model based interpretation of experimental results), which is documented in a separate report (Milestone Report 230).

The overall evaluation of the achievements associated with the experimental programme of Task 3 is presented in chapter 6. Evaluations were conducted on two levels:

- **Evaluation from the viewpoint of the experimentalists:** each project partner was requested to conclude their own contributions with a short section with “key learning points”
- **Evaluation from the viewpoint of the end users:** the task leaders were requested by the WP leaders to provide an evaluation of the achievements with focus on the interests and needs of the end users

The subsequent paragraphs provide further insight in the assessment workflow.

2.3.1 Evaluation from the viewpoint of the experimentists

The task leaders of the WP EURAD-Gas decided in June 2023 to elaborate a joint report outline, applicable to all partner contributions to the Task 2 and Task 3 Final Reports. In this context, the partners of Task 2 and 3 were requested to highlight the key achievements of their own technical contributions in a short section "key learning points", addressing the following aspects:

- New knowledge acquired
- Impact of the acquired knowledge
- Recommendations for the future

The statements of the partner contributions reported in chapters 3 – 5 reflect the viewpoints of the experimentalists in the context of their national research programmes; they remain uncommented by Task 3 - Task Leader Team.

2.3.2 Evaluation from the viewpoint of the end users

The SOTA1-report (Levasseur et al. 2021) formulates the motivation of WP EURAD-GAS *"to provide results that are applicable to a wide range of National Programmes. This is possible because the results of previous efforts on the identification and characterisation of the possible gas transport processes suggest that the mechanisms at play in different clays are generally similar, while the conditions (gas pressure, stresses/deformations, saturations, …) for the transition from one transport regime (diffusion, two-phase flow, pathway dilation and fracturing) to another strongly depend on the specific properties of a given clayey material."* In this sense, the scientific expectations of EURAD-GAS / Task 3 are concentrating on the confirmation of existing understanding with particular focus on an improved quantitative description of gas-related failure mechanisms in clay barriers. From the side of the end-users, as important are new qualitative and quantitative insights in the self-sealing capacity of these materials. The following key questions from the end-user side are posed in the SOTA1 report:

- How could gas be transported within the repository and which water soluble and volatile radionuclide transport could be associated with it?
- How and to what extent could the hydro-mechanical perturbations induced by gas affect barrier integrity and long-term repository performance?

The SOTA-Report-Update 2024 (Levasseur et al. 2024) reflects the interests and needs of the end-users regarding the impact of gas on repository safety, drawing on the latest results of the EURAD-GAS research programme. In Levasseur et al. (2024) / chapter 2.2 the shared needs of the end-users are formulated regarding *gas evacuation* and *gas impacts on barrier performance*. A refined questionnaire summarises the needs of the end-users:

- How do the gas transport mechanisms in the clayey barrier materials of a geological repository depend on the conditions to which these materials are subjected, primarily mechanical stresses and fluid pressures?
- What are the relevant material and fluid properties controlling these mechanisms?
- How to characterise the material properties, accounting for the fact that some of these might well be affected by the passage of gas?
- Which gas-related processes could impair repository performance with respect to the intended safety functions *radionuclide retention* and *waste confinement*?
- What are the safety-related consequences on the barrier properties during and after the passage of gas to be considered?

Multiple lines of convincing evidence are required to build confidence towards a robust safety case, demonstrating the resilience of clay barriers and the efficiency of self-sealing mechanisms for the conditions that could arise in a repository. This involves performing experiments at different scales in the laboratory and in-situ in underground research laboratories, looking at natural analog examples and also developing and validating conceptual models that might then be used to extrapolate to the time and spatial scales of relevance to the post-closure performance of a repository.

Chapter 6 of this report reviews the wealth of evidence gained during the execution of Task 3 to build confidence in the robustness of clay barriers and the efficiency of self-sealing mechanisms for a wide spectrum of gas release scenarios.

2.4 References

Keller L. M., Schuetz P., Gasser P., Holzer, L. (2013) Pore-space relevant for gas-permeability in Opalinus Clay: Statistical analysis of homogeneity, percolation and representative volume element. Journal of Geophysical Research: Solid Earth 118, 2799–2812 https://doi.org/10.1002/jgrb.50228.

Levasseur S., Collin F., Daniels K., Dymitrowska M., Harrington J., Jacops E., Kolditz O., Marschall P., Norris S., Sillen X., Talandier J., Truche L. and Wendling J. (2021). Initial state-of-the-art on gas transport in clayey materials. European Commission, Work Package GAS: Mechanical understanding of gas transport in clay-based materials of the HORIZON 2020 project EURAD. Deliverable 6.1.

Levasseur S., Collin F., Dymitrowska M., Harrington J., Jacops E., Kolditz O., Marschall P., Norris S., Sillen X., Talandier J., Truche L. and Wendling J. (2024). State of the Art on Gas Transport in Clayey Materials – Update 2023. Deliverable D6.2 of the HORIZON 2020 project EURAD, Work Package Gas. EC Grant agreement no: 847593.

Marschall P., Horseman S. and Gimmi T. (2005). Characterisation of gas transport properties of the Opalinus Clay, a potential host rock formation for radioactive waste disposal. Oil and Gas Science and Technology - Revue de l'IFP 60 (1), 121–139.

Milestone MS 58: Interim Experimental Design Report comprising a revised detailed work programme of SubT 3.1, 3.2 and 3.3 Work Package Gas. European Commission, Work Package GAS: Mechanical understanding of gas transport in clay-based materials of the HORIZON 2020 project EURAD.

3. Clayey materials for Engineered Barrier Systems

Two experimental activities were conducted in Task 3 with focus on gas induced failure and self-sealing capacity of bentonite:

- CTU carried out cyclical water and gas injection experiments with Czech BCV bentonite, a Ca-Mg-type of bentonite. The experimental programme complements and extends previous studies on gas transport in bentonite, which were carried out with Wyoming sodium bentonite MX-80 (chapter 3.1).
- IRSN investigated gas migration processes in initially heterogeneous bentonite mixtures using an X-ray CT scanner, highlighting the paramount relevance of microfabric for a mechanistic understanding of gas transport processes in bentonite (chapter 3.2).

3.1 Cyclical water and gas injection experiments with Czech Ca-Mg bentonite (CTU)

The main objectives of the WP GAS are to improve the understanding of the mechanisms of gas transport processes in clay materials, to interrelate gas transport processes with the mechanical behaviour of clays, and to determine their influence on the various properties of clays. A further objective comprises the evaluation of the gas transport modes that may occur in the deep geological repository environment and their potential impacts on the integrity of the barrier and the overall reliability of the deep geological repository system.

Laboratory experiments represent the main tool for obtaining the necessary knowledge and for fulfilling the various objectives. Furthermore, it will be necessary to transfer the knowledge obtained from the experiments to address the questions that remain in terms of currently considered repository designs and concepts.

The CTU experimental programme prioritises the performance of the bentonite buffer when exposed to processes that may impair the mechanical integrity of the buffer and the study of the consequences of buffer failure. The proposed experiments comprise cyclical water and gas injection experiments using constant volume cells.

In order to address the various research issues, a series of cyclical experimental tests were planned involving the “rapid” injection of gas into samples subjected to a constant volume boundary condition with the intention of attaining a breakthrough event. The 'rapid' buildup of pressure allowed observation of the whole spectrum of processes involved in the impact of the initial state (compaction) on the gas transport behaviour and the impact of gas-induced failure on the transport properties; moreover, the cyclical loading approach allowed observation of the impact of intermittent gas flow / repeat gas events. A specially designed constant volume cell, which allowed for the total saturation of the sample and the subsequent determination of the swelling pressure, was used for testing purposes that involved the injection of the gas medium from the bottom of the sample. The high constant value of the gas pressure allowed for the observation of the time required for the occurrence of a breakthrough event and the flow of gas from the sample during/after the breakthrough event via the monitoring of the outflow of gas at the top of the cell. Monitoring total pressure helped to monitor the evolution of stress inside the sample. The tested material comprised powdered BCV (Ca-Mg) bentonite compacted to various dry densities (1300-1500 kg/m^3). The execution of the experimental programme was divided in two phases, related to the subtasks Subtasks T3-1 (“gas-induced impacts on barrier integrity”) and T 3-2 (“Pathway closure and sealing processes”):

- Subtask T3-1: Investigation of the material, preparation, and saturation of homogeneous samples (6 months), 5 gas injection and resaturation cycles (3 months per cycle).
- Subtask T3-2: Investigation of nonhomogeneous samples (with discontinuities), the same testing procedure after completion of T 3-1.

3.1.1 Experimental setup

3.1.1.1 Description of the apparatus

The testing procedure involved the use of specially designed permeameter cells, which comprised a cylindrical steel chamber (ring) for the housing of the samples (diameter: 30 mm, height: 20 mm). The constant volume of the sample was ensured by the rigid structure of the experimental cells while allowing for the monitoring of total pressure. The top and bottom of the samples have been fitted with sintered steel permeable plates to prevent the leaching ("mobilisation") of the material. The piston and pressure sensor for the measurement of the total (or swelling) pressure of the bentonite was positioned between the upper flange of the chamber and the upper surface of the sample. A pressure sensor was connected to a central data logger. The high-pressure constant volume cell has been designed for the investigation of the flow of both water and gas through the bentonite samples.

The cells were used in two different experimental setups:

- Setup A – the measurement of water permeability and total pressure (Figure 3-1)
- Setup C – the measurement of the "rapid" gas breakthrough tests with total pressure (Figure 3-2)

The gas testing procedure involved the temporary disconnection of the cell from the permeameter (set-up A) and its connection to the gas injection set-up (set-up C).

Czech Ca-Mg bentonite (BCV) was subjected to testing via the uniaxial compaction of the material in the powdered form (initial water content of approximately 10%) in the rings of the cells. Distilled water was used as the saturation medium.

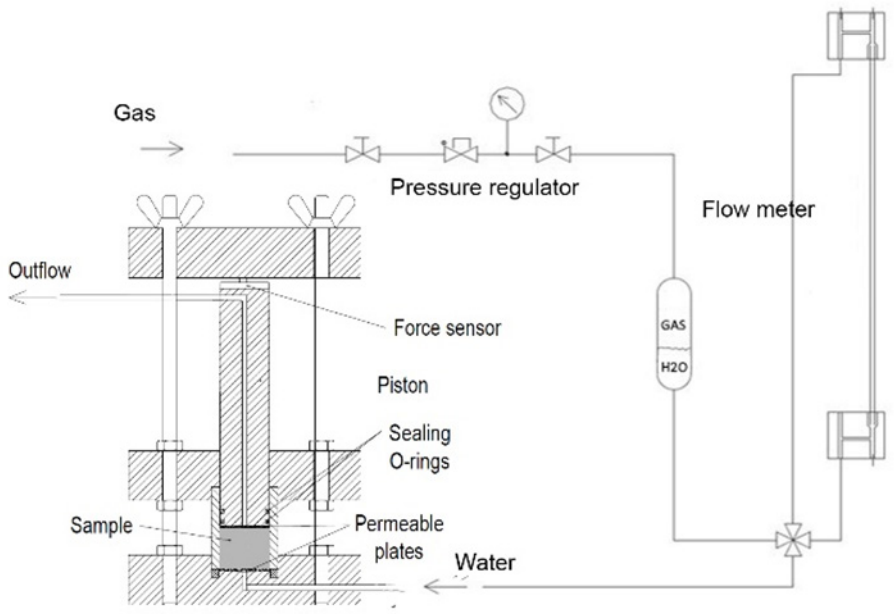

Figure 3-1 – Experimental setup A – water permeability testing and the measurement of total pressure.

Setup A: The apparatus setup as illustrated in Figure 3-1 was used to investigate water permeability and total pressure during the saturation phases. Distilled water was used as the saturation medium, which was pushed into the material using compressed argon. The water flow was determined manually using a graded capillary tube-based flow meter in the inflow part.

The test was conducted up to the point at which the flow and the total pressure were observed to stabilise. The final water flow values were used for the determination of permeability. The water pressure source was subsequently disconnected to allow for the determination of swelling pressure.

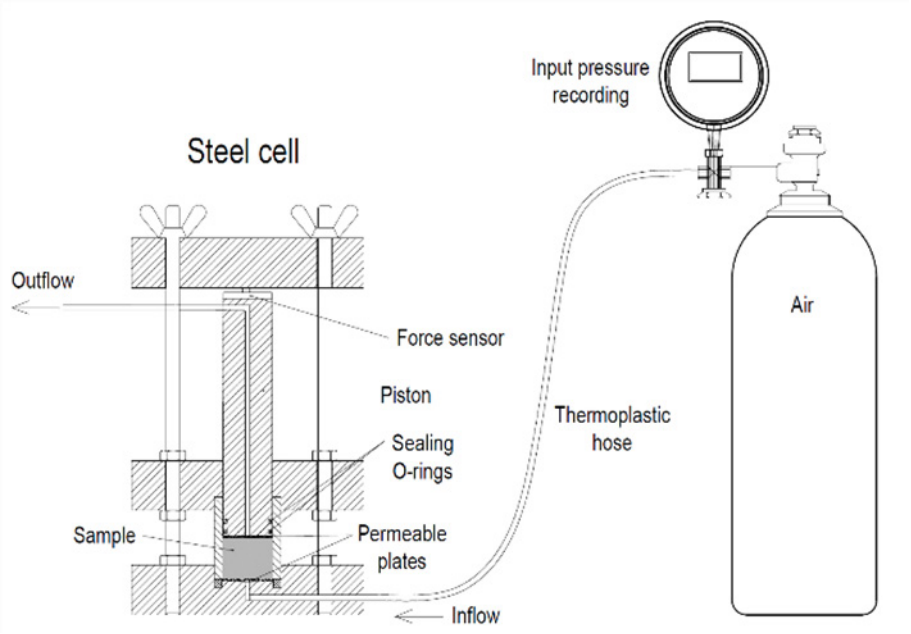

Figure 3-2 – Experimental setup C – "fast" gas breakthrough testing and the measurement of total pressure.

Setup C: The apparatus illustrated in Figure 3-2 was used for the conducting of gas pressure testing. The principle of the test procedure was to subject the sample to a high gas injection pressure until breakthrough occurs. The testing procedure allowed for the monitoring of the injection pressure at the inlet to the sample, the total pressure, as measured by pressure sensors positioned on the pistons (i.e. the total pressure that was influenced by the injection pressure) and the gas flow at the outlet of the sample.

3.1.1.2 Testing fluids

The gas used for the breakthrough experiments was compressed dry air. Compressed air was chosen for safety reasons and simplicity of handling. Air was compressed using a high-pressure compressor in air cylinders with a capacity of 2 litres. The cylinders were then used in the experiments.

3.1.2 Material properties (pre-test and post-test characteristics)

The calcium-magnesium BCV bentonite used in this project was extracted in 2017 from the Černý vrch deposit (KERAMOST a.s., Czech Republic).

The specific density is around 2758 kg m^{-3}. The bulk chemical analysis of the BCV bentonite was performed in the laboratories of Gematest spol. s.r.o. The results are shown in Table 3-1.

The semi-quantitative phase analysis of the BCV bentonite was conducted by Červinka et al. (2018). X-ray analyses were performed by three different institutions, i.e. the Institute of Inorganic Chemistry of the Czech Academy of Sciences (Řež), the Czech Geological Survey (Barrandov, Prague), and the Institute of Geology of the Czech Academy of Sciences (Suchdol). An overview of the results is presented in Table 3-2.

Table 3-1 – Bulk chemical analysis of Czech BCV bentonite (Červinka, 2018).

Component	% dry wt.	Component	% dry wt.
SiO_2	49.75	Na2O	0.34
Al_2O_3	14.80	K2O	1.15
Fe_2O_3	11.11	P2O5	0.86
TiO_2	3.04	CO2	2.29
FeO	<0.10	SO3 sulphate	0.30
MnO	0.21	SO3 total	0.34
MgO	2.50	H2O+	9.71
CaO	3.10	Total	97.21

Table 3-2 – Semiquantitative X-ray powder diffraction results for BCV bentonite: c: the estimate of the amount of goethite was not included in the calculation, N.A: not analysed, N.D: not detected in the bentonite (Červinka et al., 2018).

Component	IICCAS, Řež	CGS, Barrandov	IGCAS, Suchdol
Smectite	58.3	86	53,5
K-micas	4.4	N.A.	4
Kaolinite	2.3	1	2.5
SiO_2 phase	8.9	9.5	26.5
Calcite	2.1	2	N.D.
Anatase	4.3	1.5	5.5

Component	IICCAS, Řež	CGS, Barrandov	IGCAS, Suchdol
Fe oxides, Goethite	10.1	(1-2) [c]	4
Mg-siderite	N.A.	N.D.	2
Ankerite	0.4	N.D.	2
Analcime	0.4	N.D.	N.D.
Amorphous phase	8.8	N.A.	N.A.
Total	100.0	100.0	100.0

Červinka et al. (2018) stated that the hydraulic conductivity and swelling pressure of the BCV bentonite was determined at the CEG CTU. The samples were saturated with distilled water at a constant pressure of 1 MPa. Table 3-3 presents the hydraulic conductivity values depending on the dry density of the samples.

Table 3-3 – Hydraulic conductivity of BCV bentonite 2017 (Červinka et al., 2018)

Dry density ρ_d [g.cm^{-3}]	Hydraulic conductivity K [m s^{-1}]
1.391	5.02E^{-13}
1.471	2.26E^{-13}
1.567	1.44E^{-13}
1.633	1.45E^{-13}
1.803	4.55E^{-14}

Figure 3-3 shows the swelling pressures obtained in the Czech Republic and published in various reports including (Červinka et al., 2018) and (Laurel, 2021).

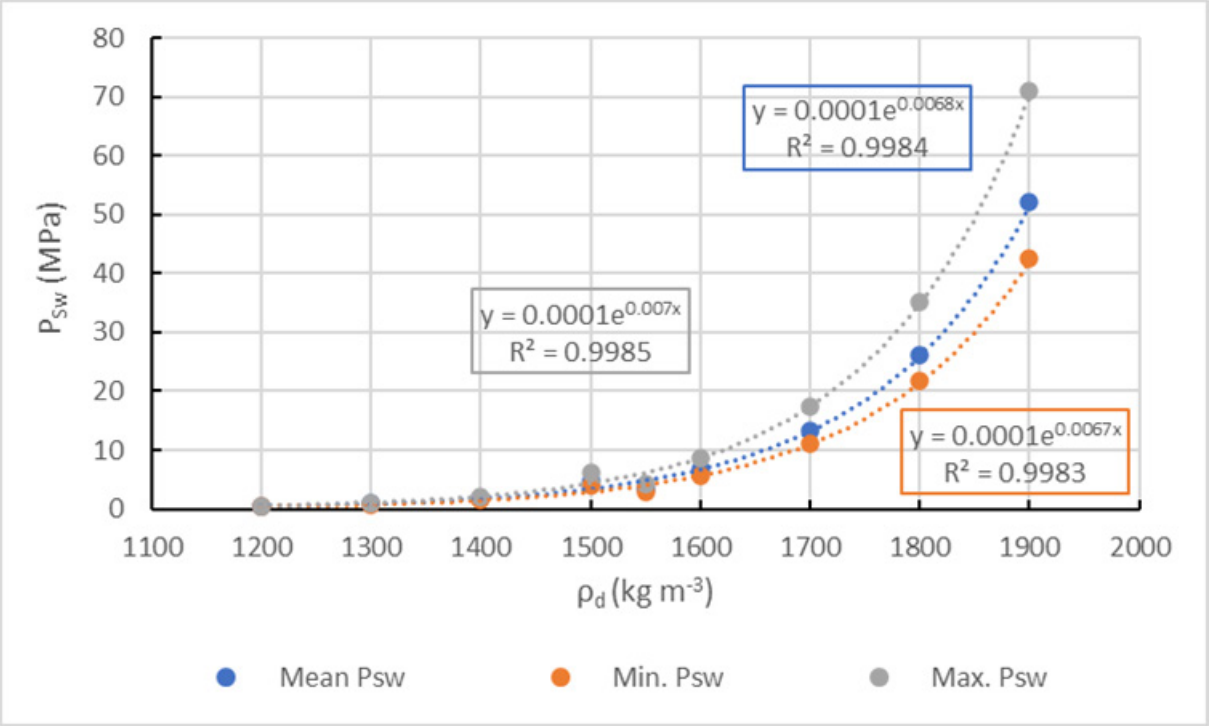

Figure 3-3 – Swelling pressures of BCV bentonite.

3.1.3 Testing protocol

3.1.3.1 Preparation of the bentonite sample

Homogeneous samples (Subtask 3-1)

The sample was compacted directly into the cell using a piston (uniaxial compaction) to the desired dry density. Powder material with an initial water content of approximately 10% was used as the sample material.

Samples with artificial joint (Subtask 3-2)

The sample was compacted into the cell as in the case of a homogeneous sample. Two samples of the same dry density were always compacted and then displaced. Each sample was cut longitudinally by a saw so that a “perfect” half was produced without a cutting through. This 'perfect' half from both samples was used to create one sample with a joint. The two halves were placed into the cell and the cell was connected to the testing apparatus. This specimen preparation procedure was chosen to minimize the loss of material due to cutting.

3.1.3.2 Experimental procedure

The experimental procedure comprises two consecutive phases – A & C (Note: Set-up B is used in Task 2.2). Setup A is used for Phase A (Figure 3-1) and setup C is used for Phase C (Figure 3-2).

Phase A – the investigation of saturation, water permeability and swelling pressure

The samples were firstly saturated, and their permeability and swelling pressure were measured to establish a baseline prior to the gas injection phase. Water was pushed from the bottom part of the cell under a pressure of 1 MPa. The hydraulic gradient corresponded to the difference between the input injection pressure and the output pressure. Once the flow had stabilised, the permeability was determined, and the water pressure was switched off to allow for the equilibration of the pore pressure in the sample. The swelling pressure was then measured. Once the baseline conditions have been established, gas injection commenced at the bottom of the sample (Phase C).

Phase C – Gas injection

Gas (air) was injected via a high constant injection pressure up to the occurrence of a breakthrough event (Figure 3-4). The injected pressure value had to exceed the swelling pressure limit value determined in the saturation phase. A value of 13 MPa was selected as the testing injection pressure for set-up C. The time required to attain the breakthrough event was measured accompanied by the monitoring of the injection pressure at the inlet of the sample and the gas flow at the outlet of the sample. The total sample stress was measured by a pressure sensor positioned on the piston (i.e. the total/swelling pressure that is influenced by the injection pressure). Once the test was completed, the cell was connected to set-up A and the sample was subjected to resaturation. The cyclical testing involved the initial or resaturation of the sample (including the determination of the hydraulic conductivity and the swelling pressure) followed by the gas breakthrough test.

Once the testing procedure was completed (several cycles for each sample), the cell was dismantled and the water content, bulk density and dry density of the samples were determined using the gravimetric method.

The standard development of the breakthrough test is shown in Figure 3-5 via the graphical presentation of the data recorded from part C (setup C) of the test procedure. Initially, the cell was connected to set-up C without the application of injection pressure (the blue line in Figure 3-5); the total pressure (the black line) was equal to the swelling pressure and the gas flow (the purple line) was zero. Once injection pressure was applied (1) (part C.ii of the test procedure), the total pressure increased and remained constant up to the occurrence of the breakthrough event (2). Moreover, the gas flow remained zero until the breakthrough event occurred. Once breakthrough was achieved, the flow initially increased sharply then decreased as the gas was gradually depleted from the tank, which led to a drop in the gas pressure. As soon as breakthrough occurred, the injection pressure and the total stress began to decrease. The measuring range of the flow meter used in this test was from 0 to 20 nl/min. If a value of 20 nl/min was exceeded during the test, the data was clipped, i.e. the exact flow rate could not be determined.

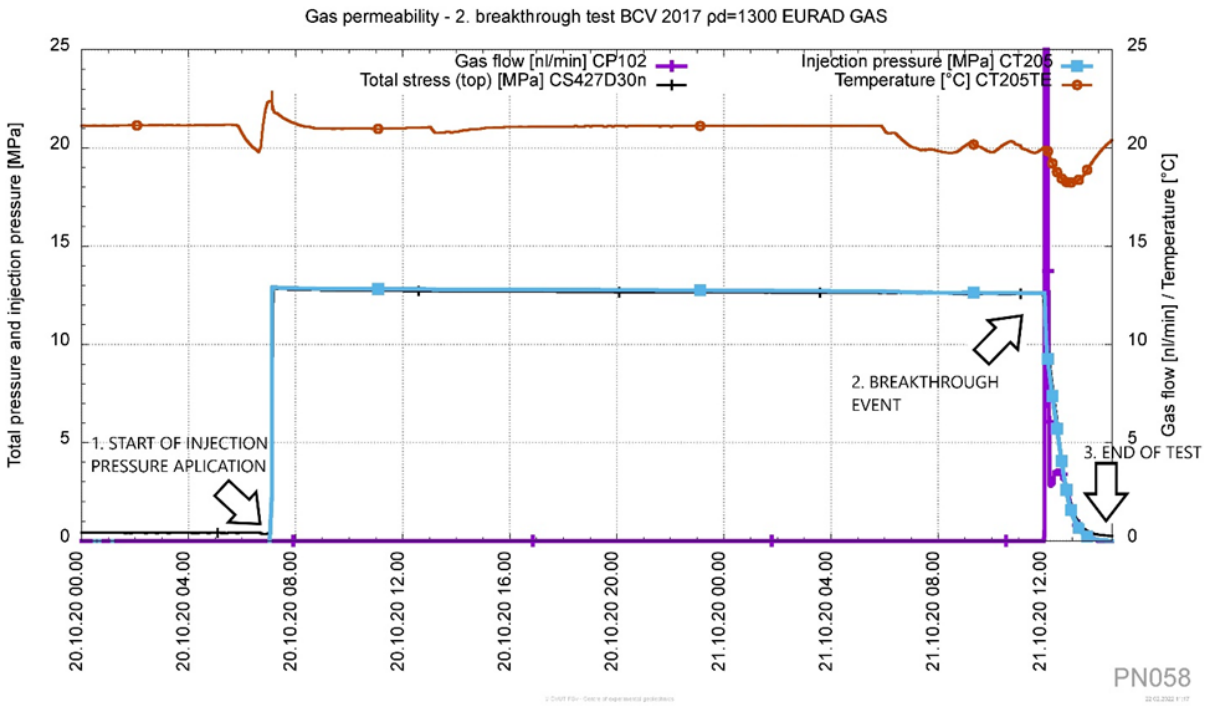

Figure 3-4 – Setup of fast gas breakthrough test (P739 - the second breakthrough test).

The most interesting part of the process concerns the breakthrough event itself (a so-called episode), at which point the flow of gas increased rapidly (usually exceeding a value of 20 nl/min), followed by a decrease in the gas flow. The gas injection pressure gradually fell to a value of zero due to the emptying of the gas cylinder. While the gas flow decrease curve was unique to each sample and test, certain patterns were identified. Some tests exhibited a fluctuation of the gas flow after the breakthrough event and the curve featured a “wave”. The decrease/re-increase of the gas flow at the outlet of the sample indicate the closing of the preferential path through which the injected gas flows.

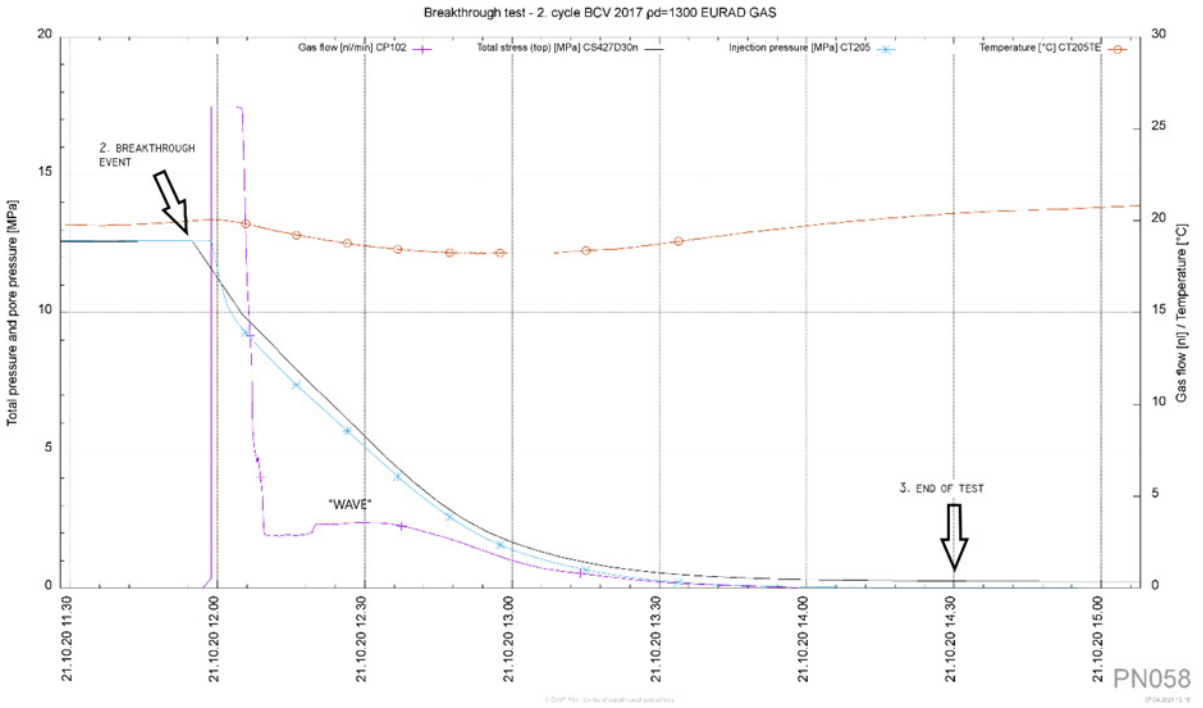

Figure 3-5 – Graph of the breakthrough test results (episode) for sample P739 (the second breakthrough

Test procedure (one or more cycles):

A) Sample (re)saturation (Set-up A)

i. Compaction of the sample in the cell (ring)
ii. Connection to the permeameter set-up (Figure 3-1, Set-up A)
iii. Saturation, monitoring of water flow and total pressure
iv. Permeability measurement (water)
v. Switching off of the saturation pressure
vi. Swelling pressure measurement

C) Gas injection test (Set-up C)

i. Connection of the cell to the gas injection set-up (Figure 3-2)
ii. Application of a gas injection pressure equal to 12 MPa
iii. Monitoring of the time to the breakthrough event, the injection pressure and the gas flow at the outlet of the sample
iv. Once breakthrough occurs, connection of the cell to the permeameter set-up (Set-up A) and repetition of the testing cycle

Expected results

Set-up A

- Material water content prior to saturation
- Water permeability
- Swelling pressure

Set-up C

- Injection pressure
- Total pressure
- Gas flow at the outlet of the sample
- Breakthrough character

After dismantling

- Water content of the sample
- Bulk density and dry density

Two sets of specimens were produced for testing purposes: homogeneous specimens that were directly compacted into the test cells and specimens with an artificially created longitudinal joint. For each set, 5 samples with a different dry density were produced. The set of specimens with the joint had to have a higher dry density than the homogeneous specimens due to the requirement for material integrity during the cutting process. A description of the tests and specimens is given in Table 3-4 and Table 3-5.

Table 3-4 – Overview of the experimental tests on the BCV bentonite homogeneous samples.

sample no	saturation phase	number of BT	dry density determination after dismantling	degree of saturation determination after dismantling
P739	completed	5	completed	completed
P738	completed	5	completed	completed
P737	completed	5	completed	completed
P736	completed	5	completed	completed
P735	completed	5	completed	completed

Table 3-5 – Overview of the experimental tests on the BCV bentonite homogeneous samples with an artificial joint.

sample no.	saturation phase	number of BT	dry density determination after dismantling	degree of saturation determination after dismantling
P824	completed	1	completed	completed
P846	completed	4	completed	completed
P830	completed	5	completed	completed
P831	completed	5	completed	completed
P832	completed	5	completed	completed

3.1.4 Results

3.1.4.1 Experimental testing on homogeneous samples

The first set of samples contained five homogeneous samples with a dry density ranging from 1290 to 1510 kg/m^3. All samples were placed in the test cells and saturation (Phase A) was initiated. From Phase A, the hydraulic conductivity was determined and the swelling pressure for each sample was estimated. These readings were taken as initial values. A description of the initial state of the homogeneous samples is summarized in Table 3-6.

Table 3-6 – An initial state of the homogeneous samples.

sample no.	ρ_d [kg/m^3]	initial water content [%]	first saturation duration [days]	k [m/s]	σ_{sw} [MPa]	void ratio [-]	porosity	compaction stress [MPa]	initial degree of saturation
P739	1295	12.3	167	9.58E-13	0.84	1.13	0.531	0,5 - 40	0.30
P738	1373		174	4.73E-13	2.24	0.99	0.497		0.33
P737	1434		178	3.21E-13	3.07	0.83	0.452		0.36
P736	1457		188	2.65E-13	3.41	0.81	0.447		0.37
P735	1512		202	2.09E-13	4.83	0.72	0.418		0.40

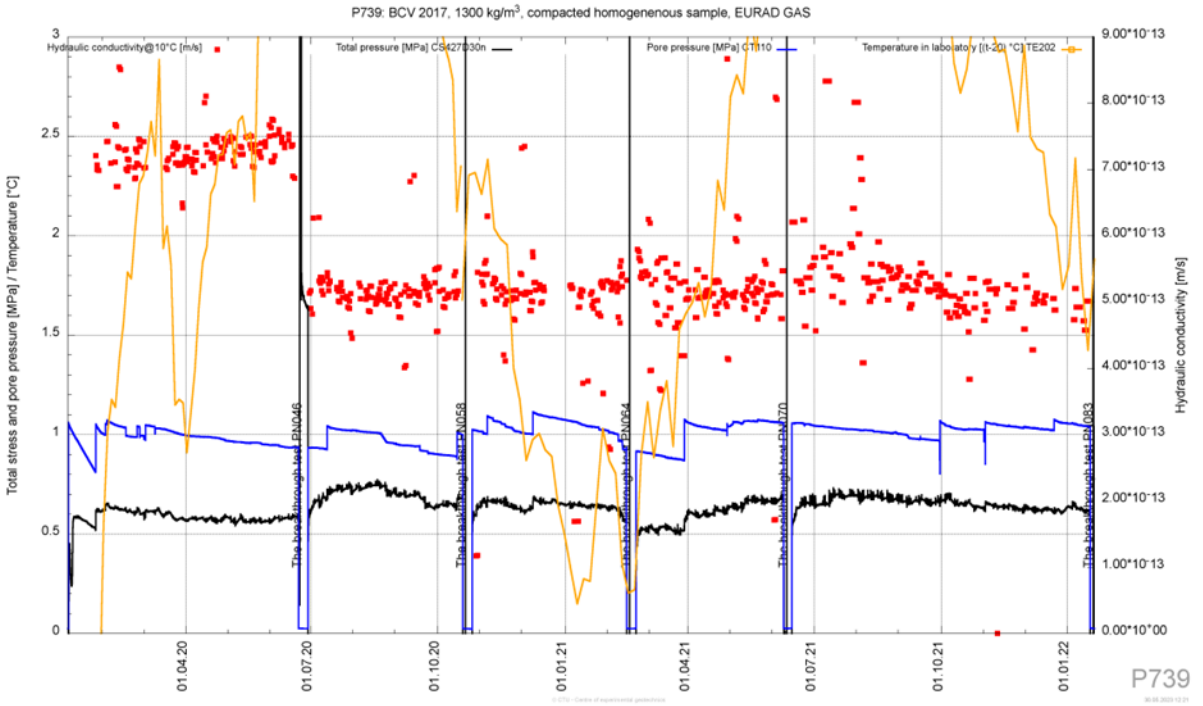

Figure 3-6 – Evolution of total pressure, hydraulic conductivity, pore pressure and temperature during the test of the sample with a dry density of 1295 kg/m³ (P739).

The testing of sample P738 with a bulk density of 1370 kg/m³ lasted over a year (Figure 3-7). A total of five rapid gas breakthrough tests were performed on the sample, and the resaturation phase between each gas test was 3 months, except for a semisedentary resaturation phase between the fourth and fifth gas tests, where the resaturation time was 6 months. The prolongation of the last resaturation phase was chosen to determine the effect of the duration of the saturation on the self-sealing of the bentonite (specifically, the time required for the breakthrough). The testing process and all measured parameters are depicted in Figure 3-7. The red points are the determined hydraulic conductivity for temperatures of 10°C, the black line shows the evolution of the total stress. The horizontal lines represent the individual fast gas breakthrough tests. The hydraulic conductivity decreased again after the first fast gas test. Compared to the previous test, the decrease is more moderate (approx. 20%). The influence of the high gas injection pressure, which exceeded the value of the compressive force for the sample, is visible here again. In this case, the bulk density of the sample was higher and consequently the compaction rate at 13 MPa of injection gas pressure was lower. With a lower dry density, the hydraulic conductivity increased, and hence the hydraulic conductivity decreased after the first fast gas test. Following the next fast gas tests, no further compaction of the sample occurred, and the hydraulic conductivity did not change significantly during the testing. The development of hydraulic conductivity and its moderate decrease during testing were not affected by the fast gas tests. Comparing the evolution of hydraulic conductivity on the reference sample that was not loaded with gas tests, the same evolution of hydraulic conductivity was observed. Long-term decrease in hydraulic conductivity during long-term testing is a property of the material. The evolution of the total stress (black line in Figure 3-7) was less affected by the evolution of the water injection pressure during Phase A than in the case of the previous sample (Figure 3-6). The decreases and increases in total stress between the fast gas tests are probably due to the different effects of the sample during the fast gas tests. It is clear from the response of the pressure sensor for the total stress measurement that the sample was shearing off (overcoming the friction on the test cell walls) and being stressed by the injection gas pressure. After the breakthrough event and the drop in gas injection pressure, the measured total stress always drops to a different constant value. It is not possible to clearly say what causes the different evolution of the total stress during Phase A between the fast gas tests. At the end of the test period of sample P738 (mid-November 2021) an error was made in following the test protocol.

The test cell was unloaded and this caused the sample to "breathe" causing a sharp drop in the total stress measurement and an increase in the hydraulic conductivity.

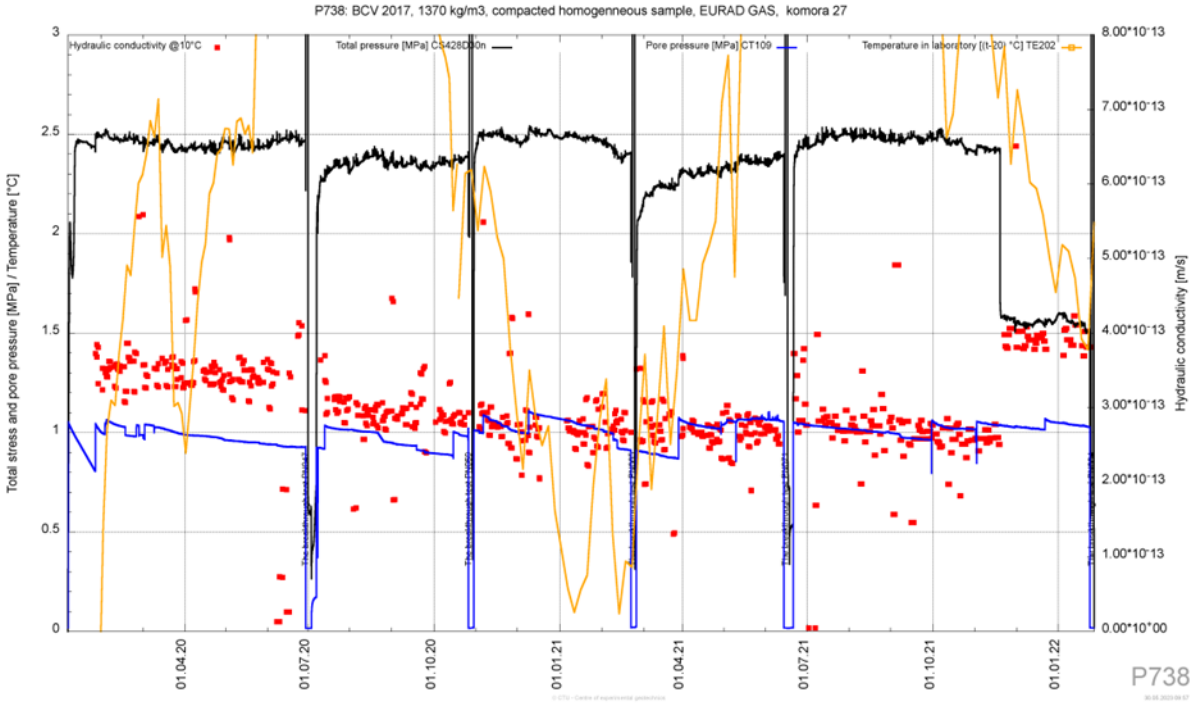

Figure 3-7 – Evolution of total pressure, hydraulic conductivity, pore pressure and temperature during the test of the sample with a dry density of 1370 kg/m³ (P738).

Figure 3-8 shows the progress of testing in sample P737 with a dry density of 1430 kg/m³, on which a total of 5 fast gas tests were performed with a resaturation interval of 3 months. In the test progress, the minimal effect of the fast gas breakthrough test on the development of hydraulic conductivity was observed. Again, a moderate decrease in hydraulic conductivity can be observed during the entire testing period. The evolution of the total stress was steadier than in the previous sample and the variation of the total stress (swelling pressure) after each fast gas test was minimal.

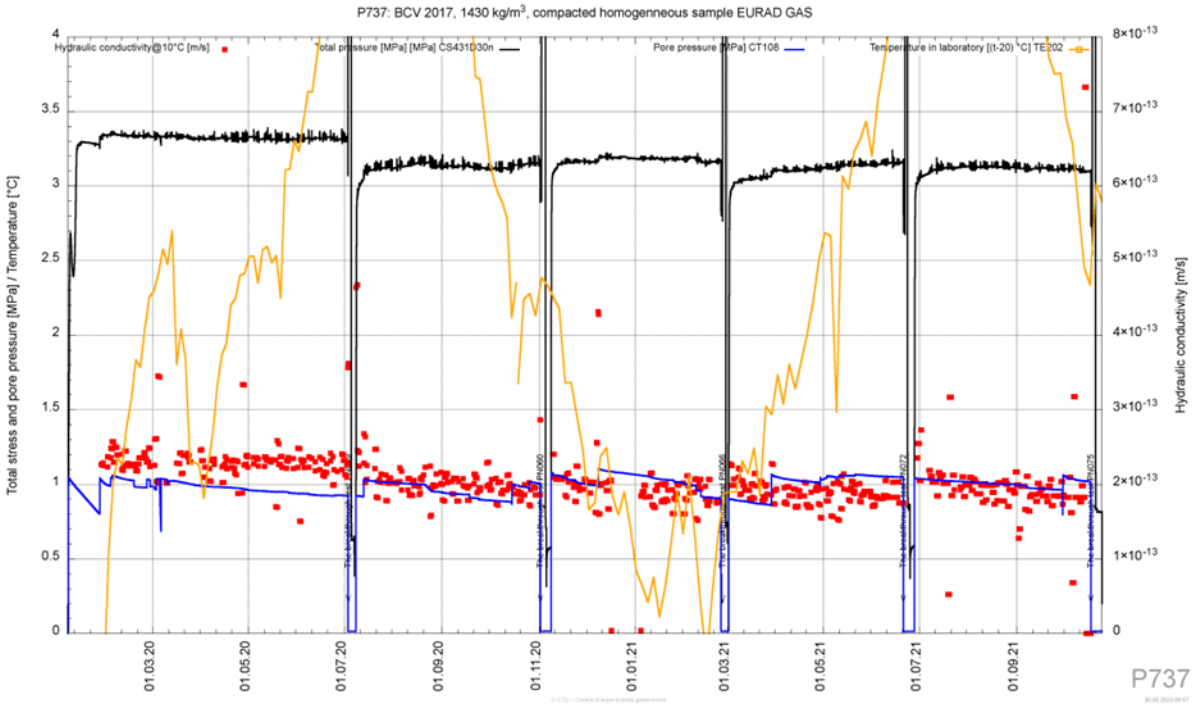

Figure 3-8 – The evolution of total pressure, hydraulic conductivity, pore pressure and temperature during the testing of the sample with a dry density of 1430 kg/m³ (P737).

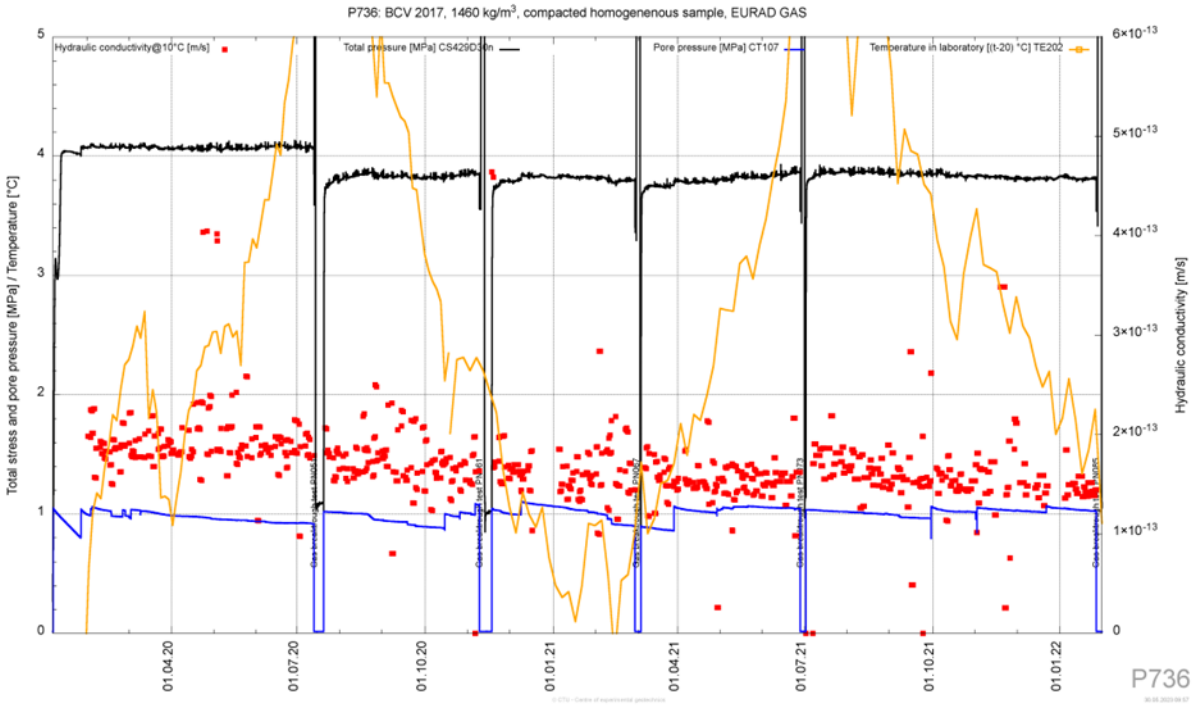

Figure 3-9 – Evolution of total pressure, hydraulic conductivity, pore pressure, and temperature during the test of the sample with a dry density of 1457 kg/m³ (P736).

Testing of sample P736 with a dry mass of 1457 kg/m^3 is shown in Figure 3-9. The resaturation phase between the first four fast gas breakthrough tests was about 3 months, the last resaturation phase lasted twice as long (6 months), in order to verify the effect of saturation time on the self-sealing process. Total stress decreased by 3.5% after the first fast gas test and there was no significant decrease after the following fast gas tests. No significant changes in the hydraulic conductivity were observed after fast gas tests. Only a moderate long-term decrease in hydraulic conductivity can be observed again during the entire testing period (over 1 year).

For the last sample P735 with the highest dry mass (1512 kg/m^3) - Figure 3-10 -, a systematic decrease in total stress was observed after each fast gas test. The decrease is 1-4% compared to the previous measured value. In terms of geotechnical test evaluation, this change was still within the range of values for the determination of swelling pressure. However, a long-term trend can be observed. The hydraulic conductivity was more fluctuating compared to the previous samples. The sharper and significant increases in hydraulic conductivity were due to technical complications with the measuring equipment. When filtering out these data, it can be said that there are no significant changes in hydraulic conductivity after each fast gas test.

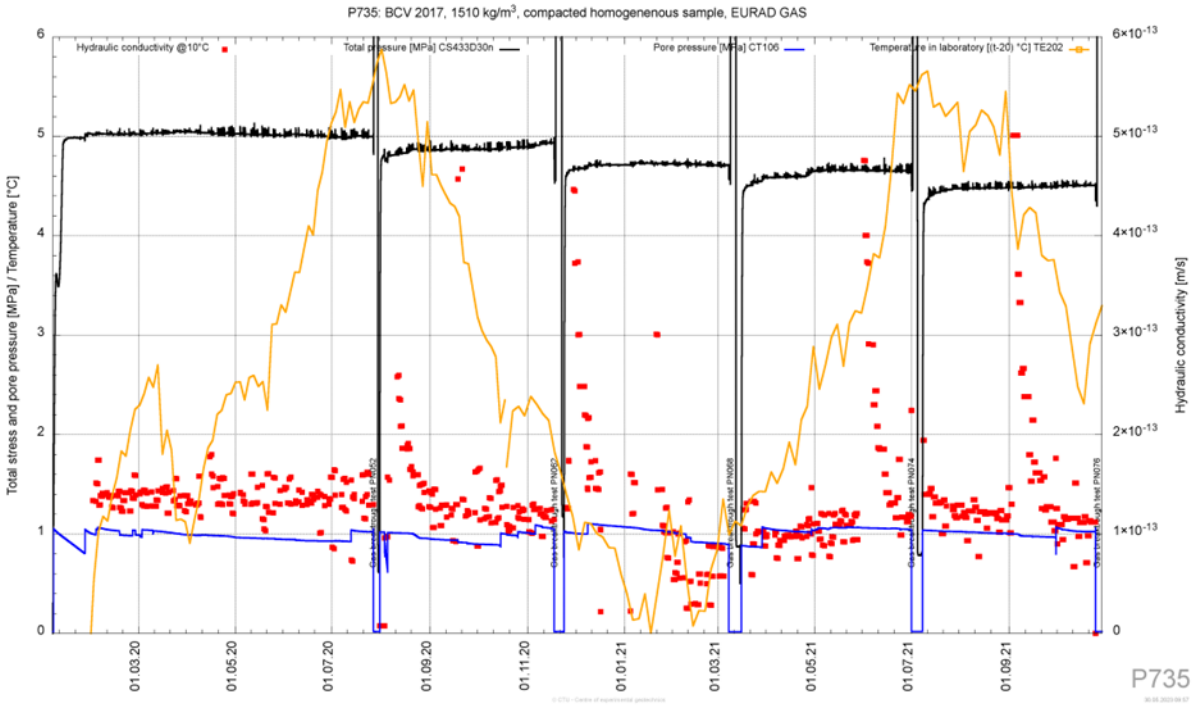

Figure 3-10 – Evolution of total pressure, hydraulic conductivity, pore pressure, and temperature during the test of the sample with a dry density of 1510 kg/m^3 (P735).

For all samples, a minor change in the evolution of total stress during testing can be seen. For the low dry density samples (P739 1295 kg/m^3 and P738 1370 kg/m^3) the evolution of the total stress was unsystematic, after some fast gas tests there was a decrease of the total stress after others there was even an increase of the total stress above the measured initial value. As this is unsystematic behaviour, it was not possible to generalise what may be the cause. A likely explanation is the occurrence of local inhomogeneities in the sample and their occurrence after the formation of the dilatation pathway during the fast gas test. For a deeper interpretation of the processes leading to the observed total stress development, visualisation of the sample (CT scanning) before and after the fast gas test could help.

The hydraulic conductivity for all samples was not affected by the fast gas break tests or their frequency. During the test, a moderate long-term decrease was observed. This is most likely a material property.

A summary of the results from all samples is shown in Figure 3-11 and Figure 3-12. Specifically, the change in hydraulic conductivity after gas breakthrough events and resaturation (Figure 3-11) and the change in swelling pressure (Figure 3-12) after fast gas breakthrough tests were monitored.

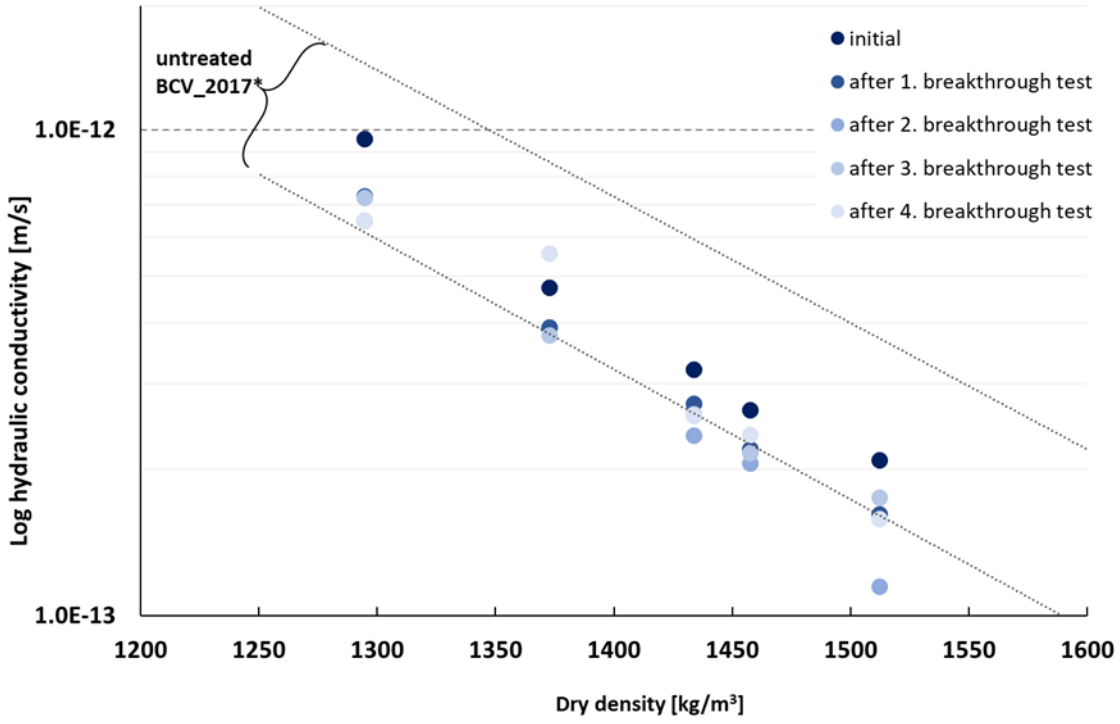

*Figure 3-11 – Hydraulic conductivity (at 10°C) after the fast gas breakthrough tests and resaturation phase for the homogeneous samples of BCV bentonite in comparison with an initial values (*data from Šachlová, 2022).*

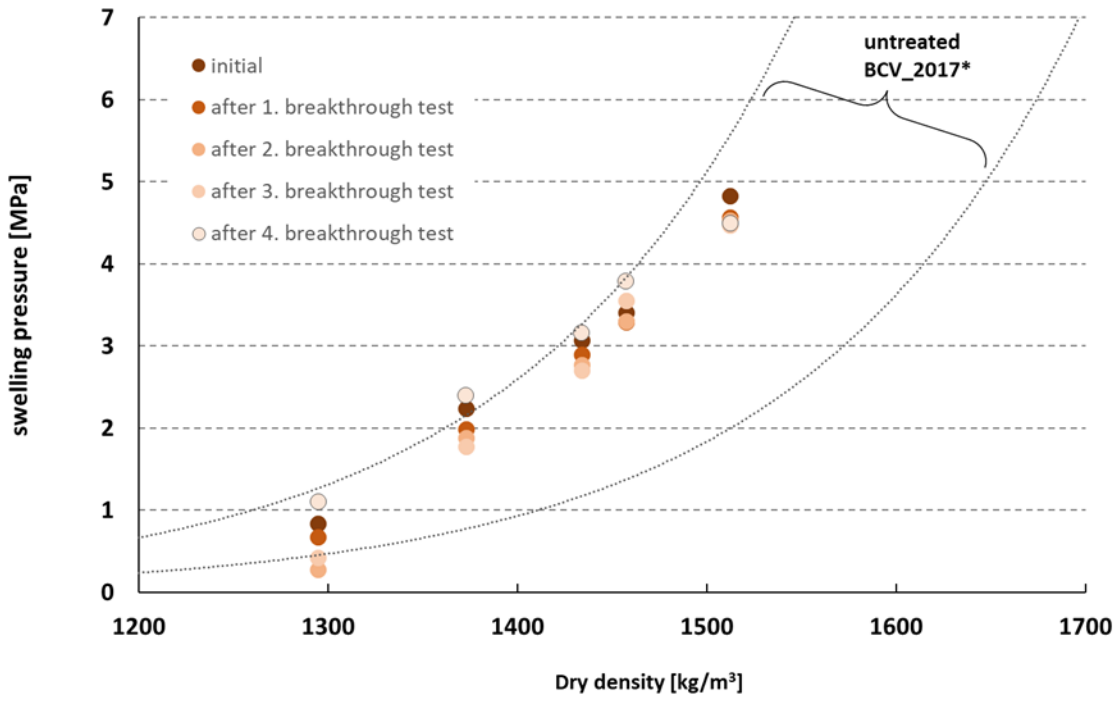

*Figure 3-12 – Swelling pressure after fast gas breakthrough tests and resaturation phase for the homogeneous samples of BCV bentonite (*data from Šachlová, 2022).*

Endurance of samples

On the basis of the findings obtained from the fast gas tests, where one of the monitored parameters was the time required to obtain the breakthrough event (endurance), it was decided to deal with this property in more detail, as it can help us to clarify the behaviour of bentonite under gas pressure loading.

The following graph (Figure 3-13) shows the endurance values for each homogeneous sample and each fast gas breakthrough test.

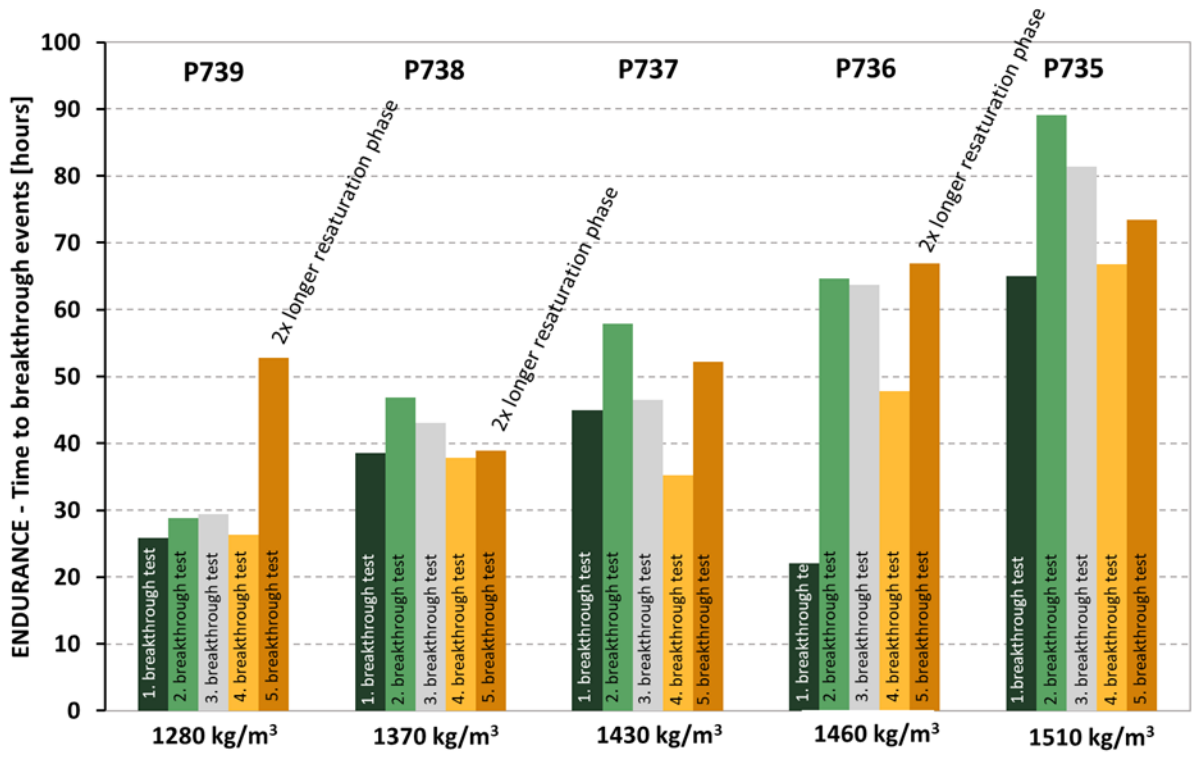

Figure 3-13 – Time to required to a breakthrough event occurring during homogeneous samples testing.

From the measured data, the time required for the breakthrough increases with increasing dry density of the sample. The gas pressure has to overcome more resistance (swelling pressure) in higher dry density samples. It is possible that the preferential dilatation pathway created by gas pressure is more complex for high dry density samples than for low dry density samples. The higher dry density samples (from 1430 kg/m^3) display significant changes in endurance in each fast gas test. The behaviour is not fully systematic, only an increase in endurance at the second fast gas test can be noticed for all samples.

Likely a new preferential pathway is formed at each breakthrough test and the more complex the pathway the more time variations in its formation occur. In sample P739 with the lowest bulk density (1280 kg/m^3), the preference path generated is simpler and more direct and consequently no significant differences in endurance are observed for each fast gas breakthrough test. Interesting information was also provided by the doubling of the resaturation time between the fast gas tests for 3 samples (P739, P738 and P736), i.e. from the original 3 months of Phase A to 6 months. After 6 months of saturation of sample P739, there was a 100% increase in endurance during the fifth fast gas test. For sample P738, the sample unloading was incorrectly performed at the end of the testing (see Figure 3-7) and the endurance result of the fifth fast gas test could have been significantly affected. Accordingly, it is not included in the evaluation of the effect of saturation time on the breakthrough time. The third sample with a 6 month resaturation time prior to the fifth fast gas test was P736. An increase in endurance can be observed during the fifth fast gas test of 30% compared to the previous test. However, compared to the second and third fast gas test no significant change occurred. The effect of saturation time on endurance for sample P736 was not easily determined. The effect of saturation time on the self-sealing ability of bentonite deserves further testing. The endurance value from the fast gas tests appears to be a useful parameter for estimating the degree of self-sealing of bentonite samples.

Episodes of the fast gas breakthrough tests

This chapter evaluates the individual fast gas breakthrough tests and their progression, especially the so-called episodes. The episodes of fast gas breakthrough tests are the part after the breakthrough, i.e. when the gas starts to flow out of the sample. During an episode, gas escapes through the sample and the injection pressure of the gas at the sample inlet declines. The monitored parameters are the gas injection pressure drop rate and the fluctuation of the gas flow rate at the sample outlet. The following graph (Figure 3-14) presents an overview of all gas break test episodes in homogeneous samples. The blue line represents the injection pressure, and the magenta line represents the gas flow rate. To simplify the evaluation of the fast gas test episodes, the episodes were divided into instantaneous episodes, where the injection pressure decreases to zero in two hours, and gradual episodes, where the time required to empty the cylinder is longer than two hours.

The instantaneous episodes can be observed for all samples with a dry density below 1460 kg/m^3 for the first three breakthroughs, except P735 respectively (Table 3-7). After that (4th and 5th breakthrough tests), the gradual episode was observed for all samples. For the P735 sample with the highest dry density (1510 kg/m^3), all episodes are gradual, except for the last 5th breakthrough test, where, conversely, an instantaneous episode occurred. When instantaneous episodes had a sharp pressure decline at the sample input and hence a high gas flow at the sample outlet, the dilatant pathway for instantaneous episodes was larger (wider dilatant pathway or more paths) than for gradual episodes, where the gas injection pressure decreased more slowly. Therefore, instantaneous episodes would indicate a lower material integrity than in the case of gradual episodes. This statement contradicts (Gutiérrez-Rodrigo, 2021) who writes that instantaneous episodes signify higher material integrity than slow gradual episodes of breakthroughs. This can be explained by the fact that during the gradual episodes, there was more drying of the sample along the dilatation path, and during the second breakthrough test (which in the case of (Gutiérrez-Rodrigo, 2021) followed immediately after the first breakthrough test without resaturation of the sample and from the opposite side of the sample), the breakthrough pressure was lower than in the first case. It could be said that in the case of Gutiérrez-Rodrigo (2021), the issue was not the integrity of the material but the degree of drying of the sample.

Based on the finding that after the third breakthrough test, in almost all homogeneous samples the episode changed from instantaneous to gradual (Table 3-7) the integrity of the material is not affected by the increasing number of breakthrough events.

Table 3-7 – Evaluation of fast gas breakthrough test episodes for homogeneous samples

sample no.	1. breakthrough test	2. breakthrough test	3. breakthrough test	4. breakthrough test	5. breakthrough test
P739	instant	instant	instant	gradual	gradual
P738	instant	instant	instant	gradual	gradual
P737	instant	instant	instant	instant	
P736	instant	instant	instant	instant	gradual
P735	gradual	gradual	gradual	gradual	instant

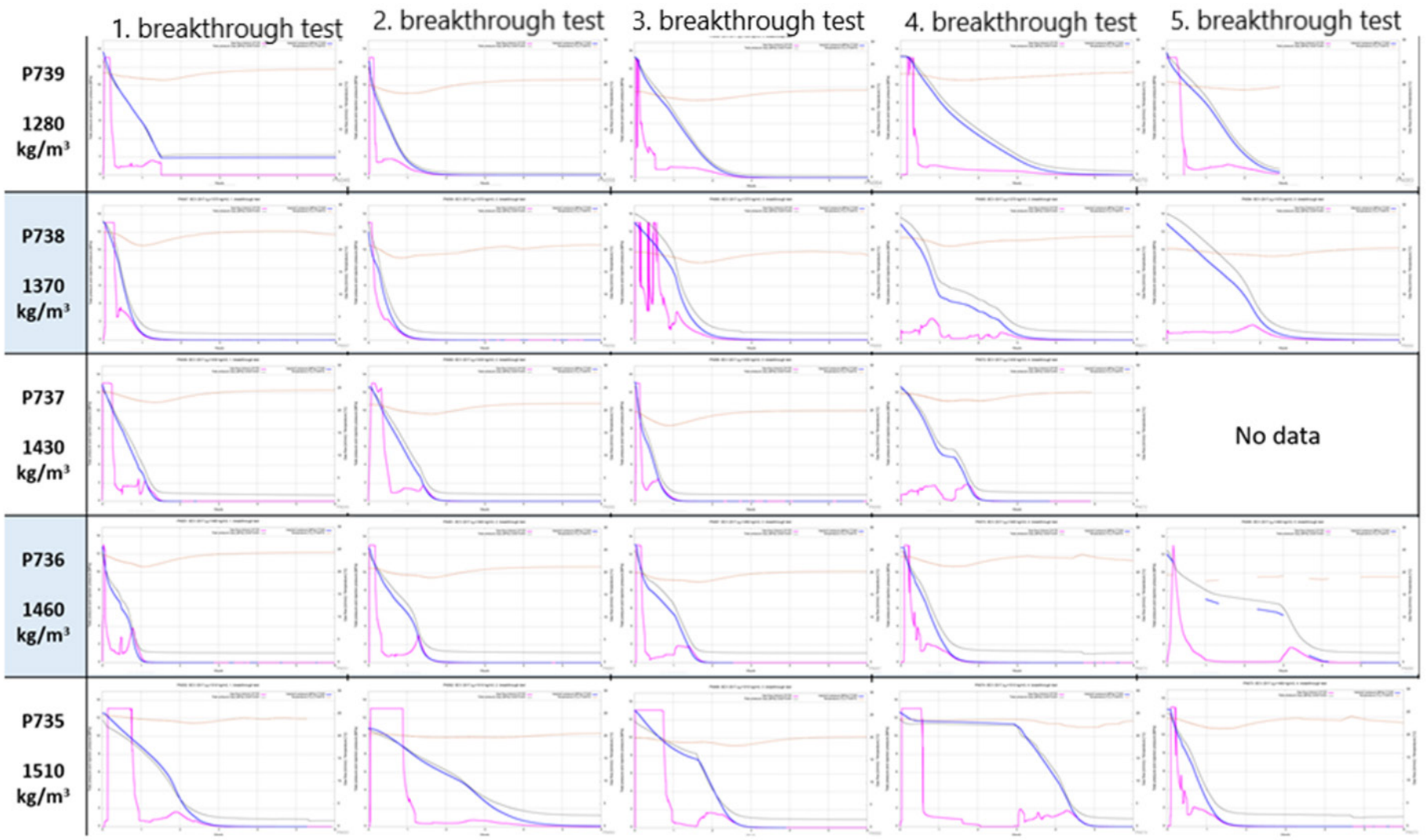

Figure 3-14 – Fast gas breakthrough episodes for homogeneous samples (blue line = gas injection pressure at the input of the sample, magenta line = gas flow rate at the outlet of the samples, black line = total pressure, red line = temperature).

3.1.4.2 Experimental testing of samples with artificial joint

The second set of samples contained five samples with an artificial longitudinal joint with dry densities ranging from 1318 to 1585 kg/m^3. All samples were placed in the testing cells and saturation (Phase A) was initiated. From Phase A, the hydraulic conductivity was evaluated and the swelling pressure for each sample was determined. These values were taken as initial values. Table 3-8 provides a summary of the initial state of the samples with artificial joint.

Table 3-8 – Overview of initial state of the samples with an artificial joint

sample no.	ρ_d [kg/m^3]	initial water content [%]	first saturation duration [days]	k [m/s]	σ_{sw} [MPa]	void ratio	porosity	compaction stress [MPa]	initial degree of saturation	degree of saturation after last breakthrough test
P824	1318	12.3	181	8.07E-13	1.72	1.09	0.523	0.5 - 40	0.32	0.66
P846	1360		188	7.56E-13	1.56	1.03	0.507		0.33	0.90
P830	1502		195	2.42E-13	2.20	0.84	0.456		0.41	1.00
P831	1540		190	2.00E-13	4.24	0.79	0.442		0.43	1.02
P832	1585		214	1.35E-13	6.70	0.74	0.426		0.46	1.04

Following the saturation phase, which lasted approximately 6 months for each sample, cyclic loading was initiated. The measuring apparatus was connected to Setup C and a fast gas breakthrough test was performed. During the resaturation phase after the fast gas test, the hydraulic conductivity and the evolution of the swelling pressure were evaluated. The progress of the general testing on each sample is shown in the following figures (Figure 3-15 - Figure 3-19).

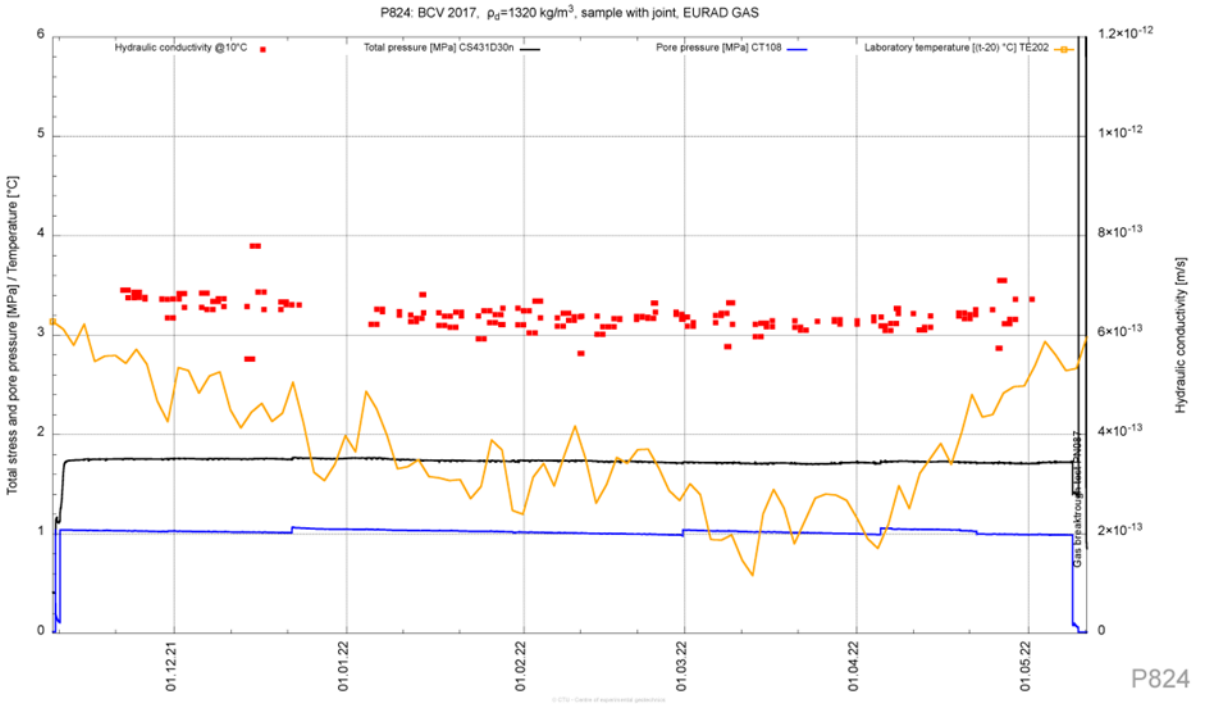

Figure 3-15 – Evolution of total pressure, hydraulic conductivity, pore pressure and temperature during the test of the sample with an artificial joint with a dry density of 1320 kg/m^3 (P824).

Testing of sample P824 with a dry density of 1318 kg/m^3 took 6 months. Only one fast gas test was performed. The reason for stopping the testing was to test the CT scan of the bentonite samples. Therefore, the sample was disassembled and taken for CT scanning and to determine the possibility of using this method to analyse the experiment. The sample was replaced with a new sample P846 of similar dry density. The saturation phase (Phase A) for sample P824 lasted 6 months, followed by a fast gas breakthrough test. The progress of the testing is shown in Figure 3-15. The sample was not cyclically loaded, and it was not possible to evaluate the impact of the breakthrough event on the sealing ability of bentonite and self-sealing properties. Only the evolution of the hydraulic conductivity and total stress during the saturation phase could be observed, since no changes in these properties occurred during the testing and the parameters were in steady state. Progress in the fast gas breakthrough test is evaluated in the following chapters.

The progress of testing on sample P846 with a dry density of 1360 kg/m^3 is shown in Figure 3-16. The testing lasted approximately 16 months and a total of 4 load cycles were performed. The resaturation phase between fast gas tests was 3 months. Following the fourth fast gas test, the cell containing the sample was disassembled and the dry density and degree of saturation of the sample were determined. The effect of the first fast gas test on the hydraulic conductivity value can be observed in the progress of the testing, where the hydraulic conductivity value decreased by 35% compared to the initial value. This decrease in hydraulic conductivity was due to the compaction of the sample during the first fast gas test, since the injection pressure value (13 MPa) exceeded the compaction pressure value of the sample and the bulk density was low. The evolution of the total stress was not affected by the fast gas tests and the total stress rises to the initial value during the resaturation phase (Phase A) after every fast gas test.

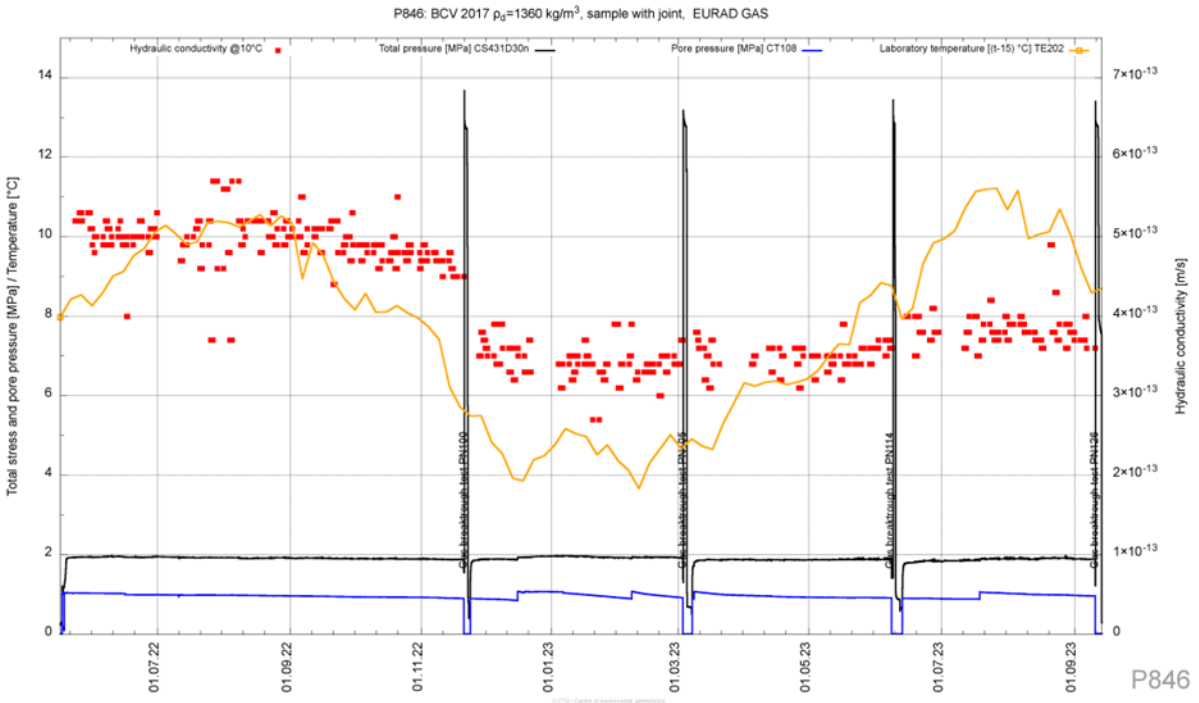

Figure 3-16 – Evolution of total pressure, hydraulic conductivity, pore pressure and temperature during the test of the sample with an artificial joint with a dry density of 1360 kg/m^3 (P846).

Figure 3-17 shows the progress of testing on a P830 sample with a dry density of 1502 kg/m^3. The testing lasted almost 21 months and the sample was loaded for a total of 5 cycles. The evolution of the hydraulic conductivity indicates a moderate decrease after the first and second fast gas tests, whereas after the third and fourth tests the hydraulic conductivity value was constant and did not change significantly. This may be due to the long-term development of the hydraulic conductivity during the testing and sealing of the artificial joint. In a sample with this dry density, significant compression of the sample was no longer expected to be present during the fast gas test due to high injection pressure. The effect of fast gas tests on the development of hydraulic conductivity was not evident. The total stress measured during the testing was more or less at the stated value of 2.2 MPa and during the resaturation phase (Phase A) following each fast gas test the total stress rises to the initial value. This means that the evolution of total stress was not affected by cyclic loading and repeated breakthrough events.

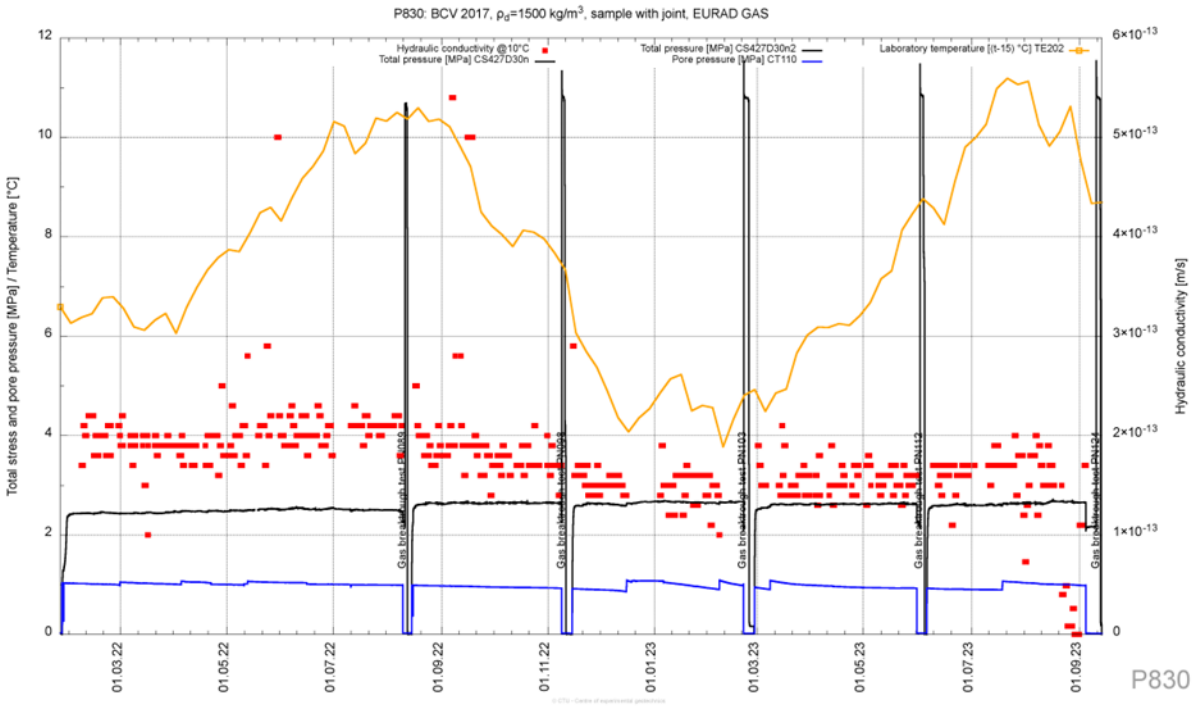

Figure 3-17 – The evolution of total pressure, hydraulic conductivity, pore pressure, and temperature during the testing of the sample with an artificial joint with a dry density of 1500 kg/m^3 (P830).

Testing of sample P831 with a dry density of 1540 kg/m^3 is shown in Figure 3-18. The loading was again performed for 5 cycles and the resaturation phase between each fast gas test lasted about 3 months. The hydraulic conductivity was not affected by the repeated loading, again there was a moderate long-term decrease in its value over the testing period. This is likely to be a material property. The total stress was not affected by cyclic loading and during the resaturation phase its value rises to the initial value.

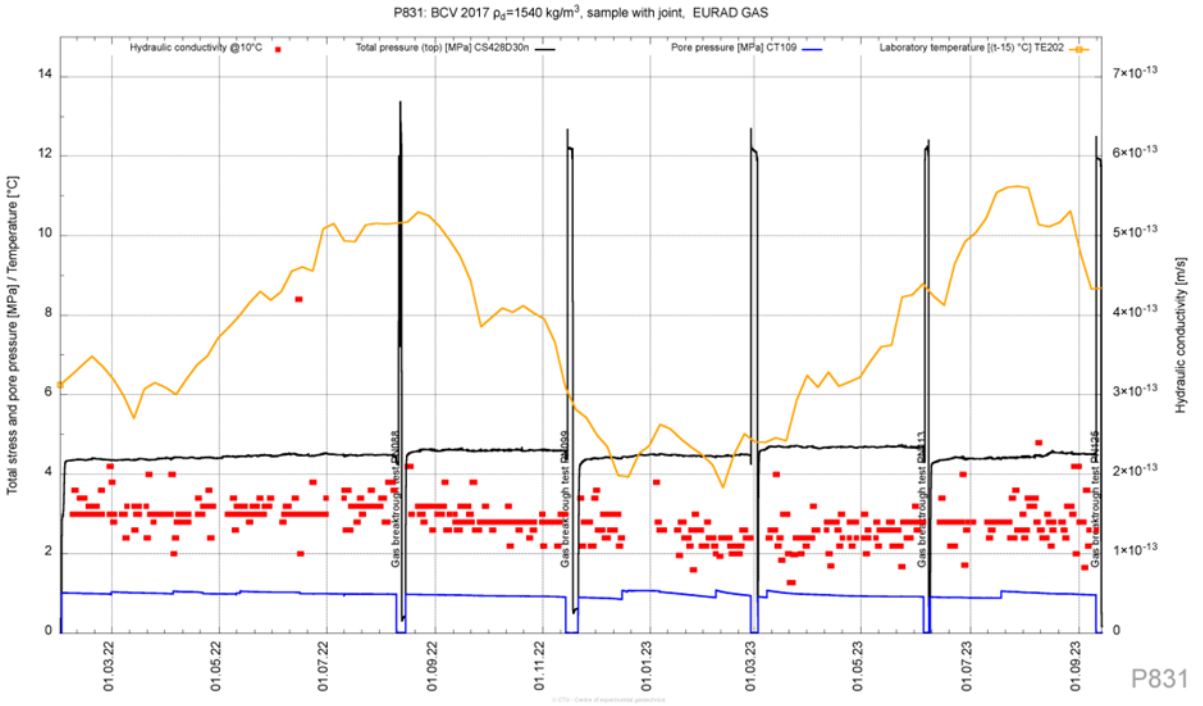

Figure 3-18 – Evolution of total pressure, hydraulic conductivity, pore pressure, and temperature during the test of the sample with an artificial joint with a dry density of 1540 kg/m³ (P831).

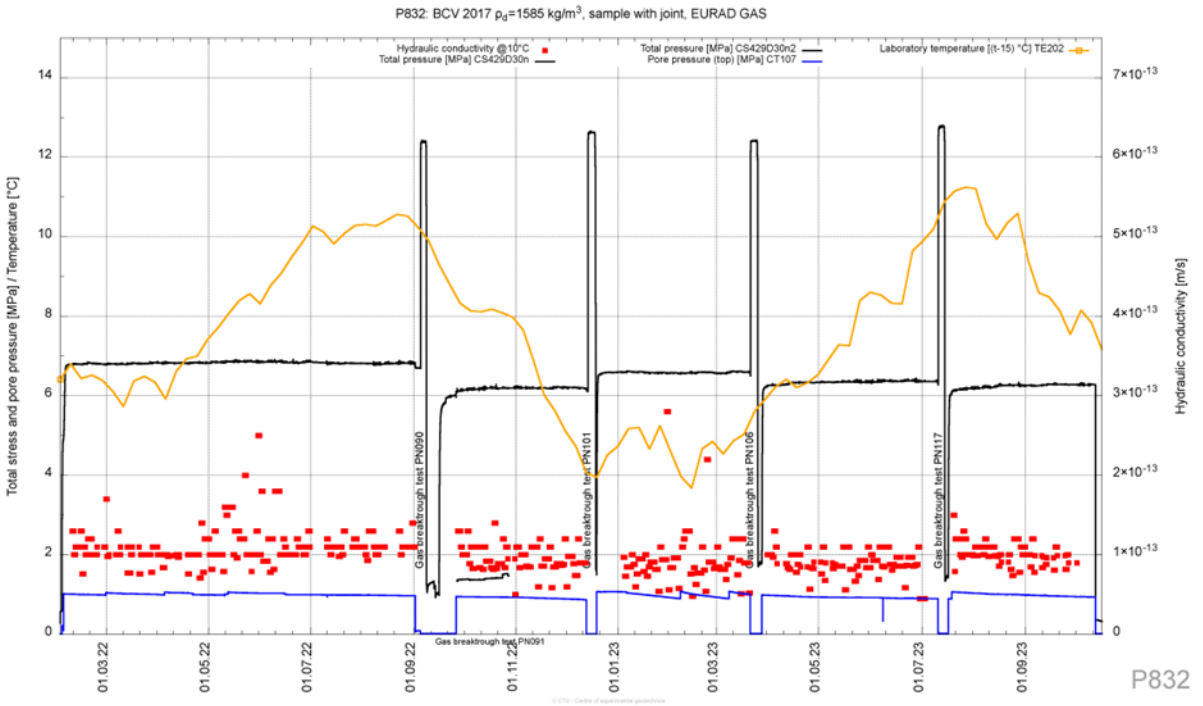

Figure 3-19 – Evolution of total pressure, hydraulic conductivity, pore pressure, and temperature during the test of the sample with an artificial joint with a dry density of 1585 kg/m³ (P832).

Sample P832 with a dry density of 1585 kg/m^3 was loaded for 5 cycles and the resaturation phase between each fast gas test lasted approximately 3 months (Figure 3-19). The hydraulic conductivity was not affected by repeated loading, there was observed a moderate long-term decrease in its value during the whole testing. The total stress was slightly affected by cyclic loading and during the resaturation phase its value rose to a value lower (by 3-6 %) than the initial value.

The unsystematic decrease in total stress after fast gas tests on sample P832 (dry density of 1585 kg/m^3) could be due to the major "breakage" of the sample experienced during the fast gas test and the formation of local inhomogeneities in the material leading to a different evolution of the axial total stress. In the case of lower dry-density samples, no changes in total stress were observed following the fast gas tests. Presumably, the longitudinal artificial joint served as a preset preferential pathway for gas to pass through the sample, and no local inhomogeneities were formed in the samples. For the sample with the highest dry density (P832 1585 kg/m^3), a higher degree of joint self-sealing occurred during the first saturation phase and the gas injection pressure created a dilatant pathway outside the artificial joint. This theory could be supported by evaluating visualisation methods (CT scanning) after individual gas fast breakthrough tests. Hydraulic conductivity was affected by gas fast tests only for the low dry density sample (P846 1360 kg/m^3) and this was due to the compaction pressure being overcome by the injection pressure of the gas. For the other samples, no influence of the fast gas tests and the following resaturation phase on the evolution of the hydraulic conductivity was observed.

A summary of the results of all samples with the artificial joint is shown in Figure 3-20 and Figure 3-21. Specifically, hydraulic conductivity after breakthrough events (Figure 3-20) and swelling pressure (Figure 3-21) after fast gas breakthrough tests were observed.

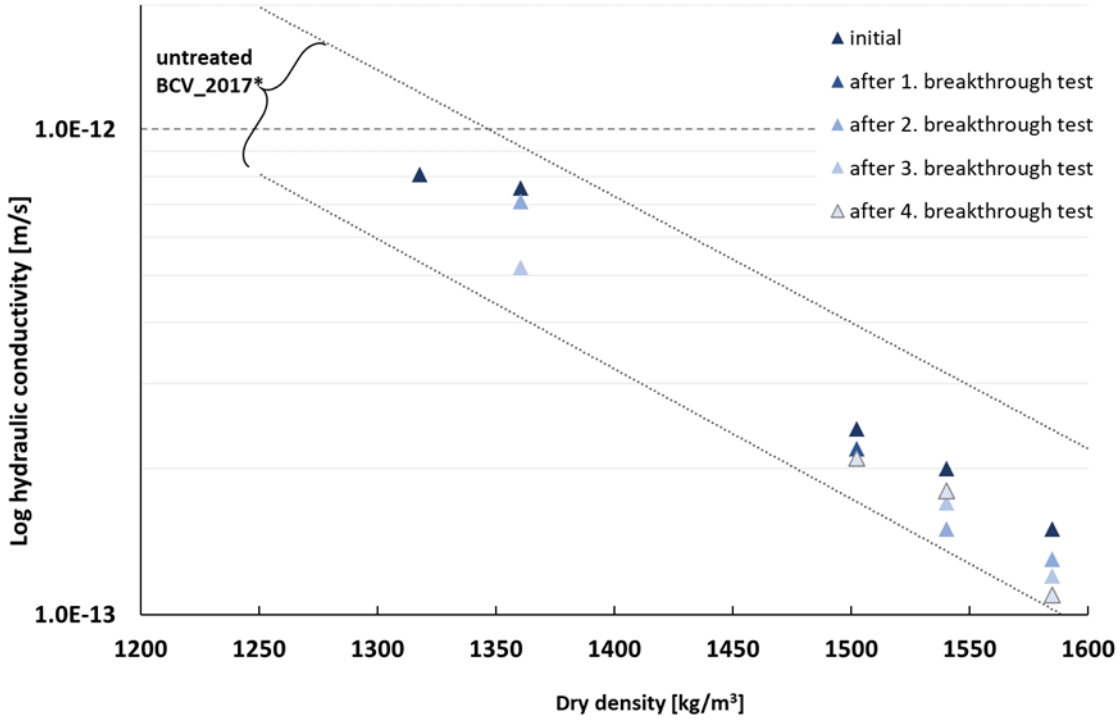

*Figure 3-20 – Hydraulic conductivity (at 10°C) after the fast gas breakthrough tests and resaturation phase for samples of BCV bentonite with the artificial joint in comparison with an initial values (*data from Šachlová, 2022).*

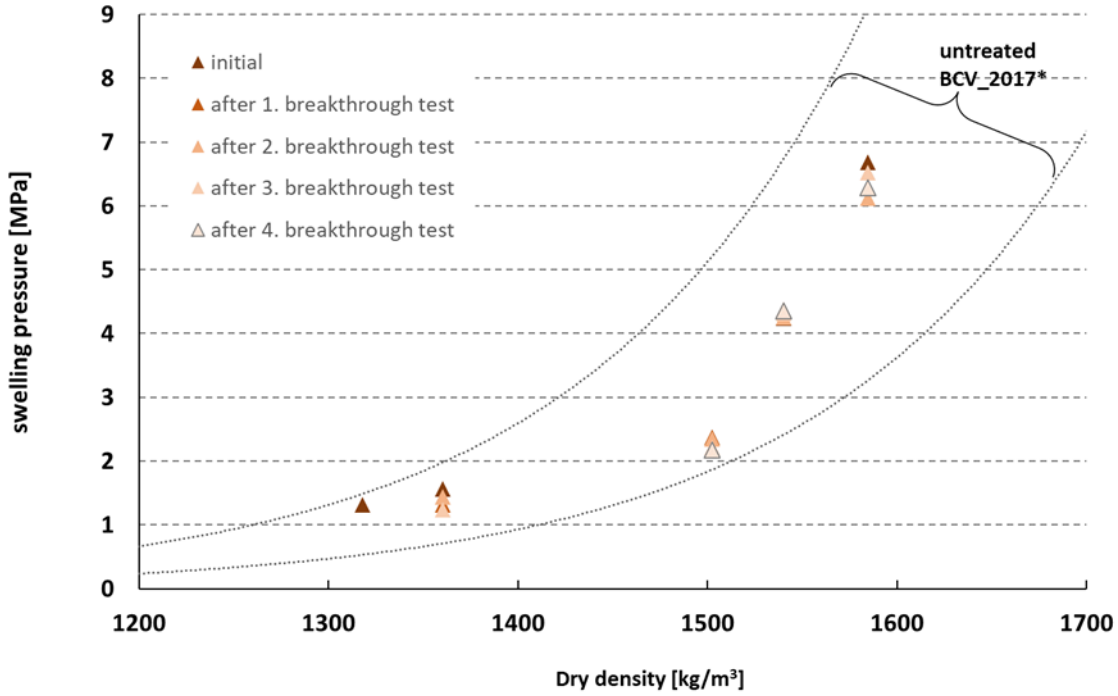

*Figure 3-21 – Swelling pressure after fast gas breakthrough tests and resaturation phase for the samples of BCV bentonite with the artificial joint (*data from Šachlová, 2022).*

Endurance of samples with an artificial joint

The other parameter evaluated in the fast gas tests is endurance (the time needed to complete the event). This parameter can be used to clarify the behaviour of bentonite under gas pressure loading and to evaluate the degree of self-sealing of bentonite.

Figure 3-22 shows the endurance value for each of the samples with artificially formed joints and each of the fast gas breakthrough tests. The measured data shows that the time required for the breakthrough event increased with increasing dry density of the sample. The low dry density sample (P846 - 1360 kg/m^3) did not show a significant change in endurance, except for the third fast gas test, which showed a 40% decrease in endurance compared to the other fast gas tests. Similar results were obtained for homogeneous samples. Presumably, the preferential pathway formed was simpler and more direct for the low-dry density samples than for the high-dry density samples, and thus no significant change in endurance was observed. For samples with higher dry density (1500 kg/m^3 and above), a significant change in endurance was observed in each fast gas test. The behaviour was not perfectly systematic; only an increase in endurance could be observed in the second and third fast gas tests for all samples.

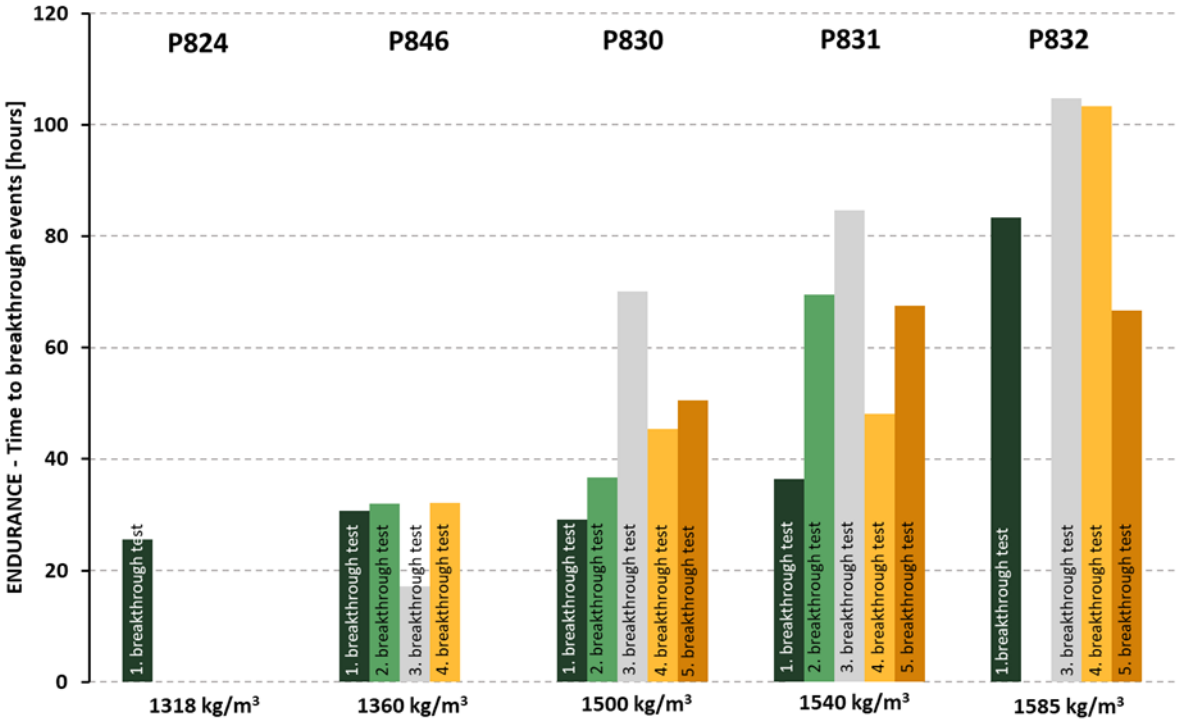

Figure 3-22 – Time required for a breakthrough event occurring during testing of the samples with the artificial joint.

Episodes of the fast gas breakthrough tests

In this chapter, the individual fast gas breakthrough tests and their progress on samples with artificial longitudinal joints, especially the so-called episodes, are evaluated. The parameters monitored during the episodes are the injection gas pressure and the gas flow rate at the sample outlet. Figure 3-23 provides an overview of all episodes of gas breakthrough tests in samples with an artificial joint. The blue line represents the injection pressure and the magenta line represents the gas flow rate. To simplify the evaluation of fast gas test episodes, the episodes were divided into instantaneous episodes, where the injection pressure decreases to zero in two hours, and gradual episodes, where the time required to empty the cylinder is more than two hours.

A summary of all the episodes shows that the progression of the test was completely variable in the comparison of the samples and between the fast gas test sequence. Since the behaviour of the samples during the episodes is completely unsystematic, the episodes were not able to be quantified and evaluated in any meaningful sense. Table 3-9 indicates that most of the episodes are gradual and they last for more than two hours. The homogeneous samples had more instantaneous episodes than gradual ones. This observation was quite surprising, as it would suggest that the preferential pathway created in the homogeneous samples was more extensive than that created by gas pressure in the samples with a joint. However, since we do not know where the gas passes through the bentonite sample, we are not able to confidently say what this difference might be due to. It is possible that the artificial joint in the samples was a predetermined preferential dilatant pathway for the gas, the sample was not significantly disrupted as in the case where the gas had to create a completely new dilatant pathway in the homogeneous material.

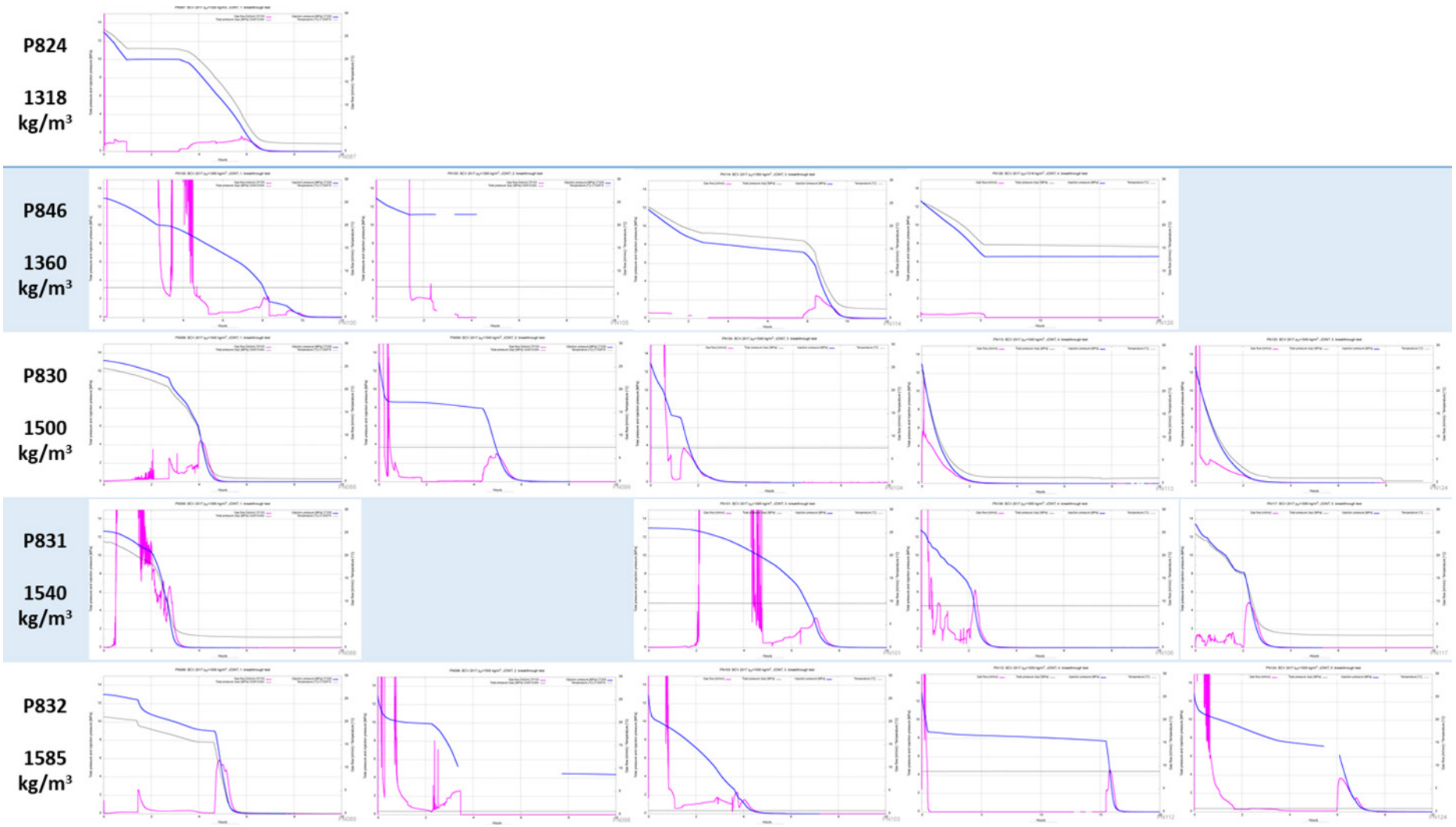

Figure 3-23 – Fast gas breakthrough episodes for the samples with the artificial joint (blue line = gas injection pressure at the inlet of the sample, magenta line = gas flow rate at the outlet of the samples, black line = total pressure, red line = temperature).

Table 3-9 – Evaluation of the fast gas breakthrough test episodes for the samples with the artificial joint

sample no.	1. breakthrough test	2. breakthrough test	3. breakthrough test	4. breakthrough test	5. breakthrough test
P824	gradual				
P846	gradual	gradual	gradual	gradual	
P830	gradual	gradual	gradual	instant	instant
P831	gradual		gradual	gradual	gradual
P832	gradual	gradual	gradual	gradual	gradual

3.1.5 Summary

Constant volume cells were used to conduct these experiments, allowing fully saturation of the sample and measurement of swelling pressure and hydraulic conductivity. The experiments used powdered Czech Ca-Mg bentonite compacted to different dry densities. The experimental programme Task 3 involved two subtasks / phases:

- Subtask T 3-1: Investigation of homogeneous samples, sample preparation, and saturation, followed by 5 gas injection and resaturation cycles.
- Subtask T 3-2: Investigation of nonhomogeneous samples with an artificial joint, employing the same testing procedure as in T3.1.

During testing, the total axial pressure was monitored using force sensors placed on the upper piston. The sintered steel permeable plates on the top and bottom of the samples prevent material leaching. The gas used for breakthrough experiments is compressed dry air, chosen for safety and ease of handling. The details of the properties of the Czech Ca-Mg bentonite used in the experiments, including its chemical composition and semiquantitative phase analysis, are described in a chapter 3.1.2. This information is crucial for understanding the behaviour of the material during experiments. The testing protocol involved two phases: Phase A focusses on saturation, hydraulic conductivity, and swelling pressure determination, while Phase C is dedicated to a fast gas injection test.

The experimental process included multiple cycles of sample (re)saturation, hydraulic conductivity measurement, and gas breakthrough testing. After the testing was completed, the cells were dismantled and various sample characteristics, such as water content, density, and dry density, were determined. The report summarises the experimental tests performed on two sets of specimens: homogeneous samples and samples with artificial joints. Batches of samples with varying dry densities were tested for each set.

A series of tests were conducted on homogeneous BCV bentonite samples with varying dry densities, ranging from 1290 to 1510 kg/m³. The primary focus was on the evaluation of the hydraulic conductivity, swelling pressure, and endurance of the samples during and after the fast gas breakthrough tests. The experiments lasted over a year for each sample, with five fast gas breakthrough tests, and resaturation phases lasting three or six months. Research began with the saturation phase, where hydraulic conductivity and swelling pressure were measured and recorded as initial values for each sample. Cyclic loading was initiated after the saturation phase, involving a series of fast gas breakthrough tests to evaluate the self-sealing ability of the bentonite samples.

Sample P739, with a dry density of 1295 kg/m³, showed that hydraulic conductivity decreased significantly after the first gas test due to compaction during the test. Subsequent gas tests did not further compress the sample and the hydraulic conductivity remained constant.

Sample P738, with a dry density of 1370 kg/m³, exhibited a moderate decrease in hydraulic conductivity after the first gas test. Similar to P739, subsequent gas tests did not have a significant impact on hydraulic conductivity. Sample P737, with a dry density of 1430 kg/m³, displayed minimal changes in hydraulic conductivity after fast gas tests. The evolution of total stress was steadier compared to previous samples. Sample P736, with a dry mass of 1457 kg/m³, showed a 3.5% decrease in total stress after the first gas test and no significant changes in hydraulic conductivity. A minor and moderate long-term decrease in hydraulic conductivity occurred during the testing period. Sample P735, with the highest dry mass (1512 kg/m³), exhibited a systematic decrease in total stress after each gas test. Overall, hydraulic conductivity showed a moderate long-term decrease, likely a material property.

Endurance values, which represent the time to gas breakthrough, increased with the higher dry density, indicating greater resistance.

The prolongation of the resaturation time had varying effects on endurance, suggesting the need for further testing.

The fast gas test episodes, both instantaneous and gradual, provided insights into material integrity.

The second set of experiments involved five samples with an artificial longitudinal joint made of BCV bentonite, with dry densities ranging from 1318 to 1585 kg/m³. These samples were subjected to a series of tests to assess hydraulic conductivity, swelling pressure, and endurance during and after fast gas breakthrough tests. After an initial saturation phase lasting about 6 months for each sample, cyclic loading was initiated, and a fast gas breakthrough test was performed.

Sample P824, with a dry density of 1318 kg/m³, was tested for 6 months, but only one fast gas test was conducted. The experiment was halted for CT scanning analysis of the sample. The hydraulic conductivity and total stress remained relatively constant throughout the test for this sample. Sample P846, with a dry density of 1360 kg / m^3, was tested for approximately 16 months, involving four load cycles. After the first gas test, the hydraulic conductivity decreased by 35% due to sample compaction, while total stress remained consistent. Sample P830, with a dry density of 1502 kg/m^3, was tested for almost 21 months, with five load cycles. Hydraulic conductivity experienced a moderate decrease after the first and second fast gas tests, while the values stabilised afterward. Total stress was not significantly affected by cyclic loading and returned to its initial value during the resaturation phases. Sample P831, with a dry density of 1540 kg/m³, was also tested for almost 21 months, and hydraulic conductivity exhibited a similar pattern as P830. The total stress remained stable throughout the test, unaffected by cyclic loading. Sample P832, with the highest dry density of 1585 kg/m³, underwent testing for 5 cycles over a similar time frame. The hydraulic conductivity displayed a moderate long-term decrease, while the total stress experienced unsystematic changes after fast gas tests.

Higher dry-density samples with the artificial joint showed significant changes in endurance during each fast gas test, while low-density samples did not. The endurance increased with higher dry density, suggesting that the gas had to overcome greater resistance to break through the sample. For low-density samples, the preferential dilatation pathway formed during fast gas tests was simpler and more direct, resulting in no significant change in endurance.

The fast gas tests of the samples with the artificial joint, both instantaneous and gradual, did not show a clear pattern of behaviour across the samples. Most episodes were gradual and lasted over two hours, with homogeneous samples displaying more instantaneous episodes than those with artificial joints.

The artificial joint in the samples may have served as a predetermined preferential pathway for gas, leading to less disruption compared to homogeneous samples. Therefore, for samples with an artificial joint, episodes were usually gradual (longer than 2 hours). The exact reason for the difference in episode behaviour between artificial joint and homogeneous samples remains uncertain, and further analysis is needed. The progression of test episodes of samples with artificial joint was variable and unsystematic, making it difficult to quantify and evaluate.

The results of these experiments provide valuable insights into the behaviour of BCV bentonite samples (in homogeneous condition and with artificial joint) under the fast gas breakthrough conditions, emphasising hydraulic conductivity, swelling pressure, endurance, and episode as key parameters. Further research is recommended to delve into the self-sealing capacity of the material and the factors that affect the test outcomes.

3.1.6 Key learning points

3.1.6.1 New knowledge acquired

No significant changes in the key parameters for verifying the sealing ability of the material (hydraulic conductivity and swelling pressure) were observed after one year of cyclic loading with fast gas tests on BCV bentonite. Three months of sample resaturation after a breakthrough event was sufficient to allow the sample to seal and not affect the previously mentioned parameters. The minor observed changes in hydraulic conductivity, especially the gradual long-term decrease throughout the testing is probably a characteristic feature of the material associated with microstructural changes. The conclusion that there is no effect on the sealing properties of BCV bentonite after repeated breakthrough events is the same for the homogeneous material and the artificially formed joint samples.

An important finding from the evaluation of the endurance parameter measured during the fast gas tests is that this parameter and the whole testing procedure (fast gas breakthrough test) can serve as a laboratory verification of bentonite integrity for the evaluation of self-sealing processes. Although the sealing of the joints and dilatant preferential pathway in terms of the sealing parameters of bentonite is short-term (on the order of months), we know that the developed discontinuities do not show relevant self-healing on a long-term scale (on the order of years). These unhealed discontinuities in bentonite represent a preset preferential pathway for gas to penetrate through the sealing material. The fast gas test can be one of the methods to verify the self-healing process.

3.1.6.2 Impact of acquired knowledge

The results obtained from the experiments met the objectives set at the beginning of the project. The aim was to determine whether the sealing properties of a bentonite barrier loaded with the high gas pressure that will be generated in a deep geological repository will be negatively affected. Under high gas pressure loading, a dilatant pathway is formed in the bentonite, which may be a preferential pathway for radionuclide leakage. The self-sealing ability of bentonite is absolutely essential for the safe design of a deep geological repository. We now know that after three months of saturation following a breakthrough event, the sealing properties of bentonite are not compromised by breakthroughs caused by high gas pressure in key parameters (hydraulic conductivity and swelling pressure).

3.1.6.3 Remaining knowledge gaps

In the testing process, we reached several unanswerable questions based on the measurements and findings. Knowing how and where the dilatant pathway is formed seems to be crucial in evaluating the breakthrough episodes themselves. The gas passes through the sample or passes through the interface between the sample and the cell wall. A valuable knowledge would be to know the complexity of the dilatant pathway formed and whether a new pathway is formed at each fast gas test or whether the

original pathway is recreated. In this context, a visualisation method to show inhomogeneities in the sample (CT scanning) should be useful.

Knowledge obtained from laboratory experiments is the first step in obtaining knowledge about the influence of a gas breakthrough event on bentonite. However, already in the testing process we have encountered the limits of the laboratory scale. For example, the evolution of total stress development during testing is probably influenced by the design of the test cell. The applicability of the obtained knowledge for the safe design of a deep repository should be verified by medium-scale experiments and further by experiments under in-situ conditions.

3.1.6.4 Recommendations for the future

The application of visual methods to image processes inside the material seems to be essential for moving experimental work forward. More detailed visual analyses will contribute significantly to the evaluation of experimental data and a better understanding of the mechanism of dilatant pathway formation during gas breakthrough tests and the bentonite self-sealing process. Therefore, the next experiment should include a visual CT scan evaluation of the samples.

As mentioned in the previous chapter, the most significant challenge and the next proposed work should be the up-scaling of small-scale laboratory experiments. Up-scaling to medium scale is proposed, and subsequently the knowledge generated should be used to design and perform experiments in in-situ conditions and at large scale.

3.1.7 References

ČERVINKA, Radek, Radek VAŠÍČEK, Petr VEČERNÍK a Vlastislav KAŠPAR. 2018. Kompletní charakterizace bentonitu BCV 2017: Technical Report 419/2019. Prague: SÚRAO Prague.

GUTIÉRREZ-RODRIGO, Vanesa, Pedro MARTÍN a María VILLAR. 2021. Effect of interfaces on gas breaktrough pressure in compacted bentonite used as engineered barrier for radioactive waste disposal. Process Safety and Environmental Protection. 149: 244-257. DOI: 10.1016/j.psep.2020.10.053. ISSN 09575820. Dostupné na internete: https://linkinghub.elsevier.com/retrieve/pii/S0957582020318565

LAUFEK, František, Irena HANUSOVÁ, Jiří SVOBODA et al. 2021. Mineralogical, Geochemical and Geotechnical Study of BCV 2017 Bentonite—The Initial State and the State following Thermal Treatment at 200 °C. Minerals. 11(8). DOI: 10.3390/min11080871. ISSN 2075-163X. Dostupné na internete: https://www.mdpi.com/2075-163X/11/8/871

ŠACHLOVÁ, Šárka, Kateřina ČERNOCHOVÁ, Kateřina ČERNÁ et al. 2022. Analýza českých bentonitů – Vyhodnocení dat z databáze (podkladová zpráva): Zpráva SÚRAO 624/2022. Praha. Technical report.

3.2 Gas migration processes in initially heterogeneous bentonite mixtures (IRSN)

Bentonite materials are commonly considered for composing the Engineered Barriers (EB) in deep geological repository, due to their advantageous hydromechanical properties, including low permeability and high swelling ability. In geological repositories, several processes are expected, including anaerobic corrosion of metals (e.g., waste containers), microbial decomposition of organic waste and radiolysis of water. These processes will result in the production of gases such as H_2, O_2, CH_4, and CO_2 within the repository. The presence of this gaseous phase can potentially alter the flow paths and hydro-mechanical conditions of the host rock and bentonite plugs used as engineered barriers. When the pressure of the accumulated gas reaches the breakthrough value, it can affect the integrity of the repository's structure and properties, and therefore potentially impact the transport of radionuclides. Thus, understanding the movement of gases through the sealing materials is required to accurately assess the magnitude of these effects and take them into account in repository design and safety assessments.

Mixtures of bentonite powder and pellets (MX80) is one of the materials envisaged for EB and sealing systems. It has been identified that these mixtures exhibit a highly complex hydromechanical behaviour, which is primarily influenced by the significant initial heterogeneity of the mixture. These initial variations in dry density may act as preferential gas pathways. This research focuses on the characterization of the microstructural heterogeneities and gas migration processes in initially heterogenous powder/pellets bentonite mixtures.

To achieve this objective, laboratory experiments involving water and gas injections were conducted in an X-ray transparent constant volume cell. 3D X-ray CT scans were taken during hydration and gas injection phases. High-contrast images were analysed to track changes in porosities, flow paths, and local displacements. Water and gas permeability were continuously measured throughout all the tests.

3.2.1 Experimental set-up

The layout of the experimental setup for small-scale constant volume infiltration/gas injection cell is presented in Figure 3-24. The designed experiment comprises: (1) a constant-volume cell; (2) two pressure/volume controllers (PVCs); (3) a nitrogen gas cylinder; (4) a water pre-charged cylinder; (5) a pressure regulator; and (6) a computer-based data acquisition system.

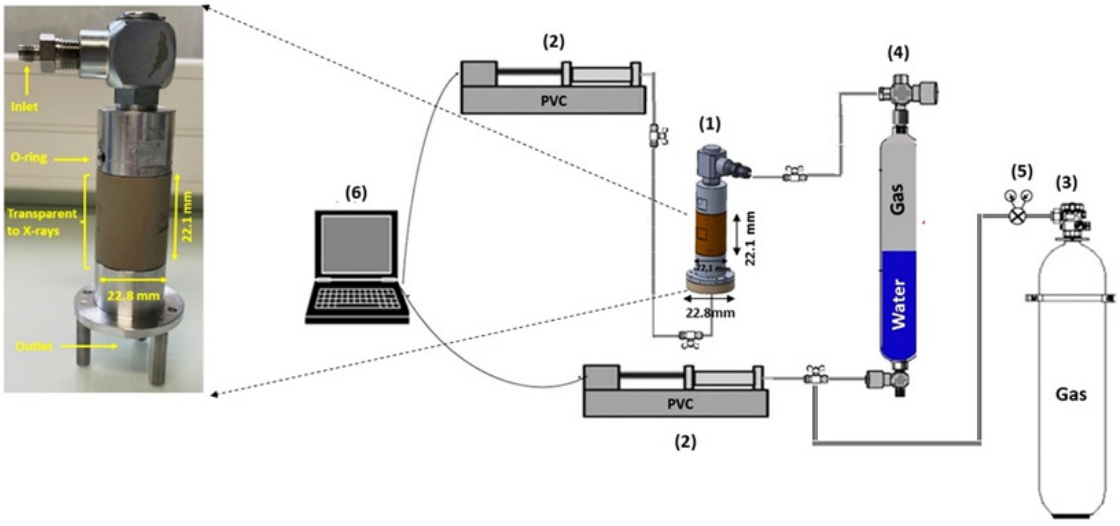

Figure 3-24 – Schematic view of the experimental set up.

The experimental constant-volume cell has a volume of 9 cm^3 (22.8 mm in diameter and 22.1 mm in height). The cell's is composed of a high-performance semi-crystalline thermoplastic transparent to X-rays, which also prevents possible chemical interactions between saturated bentonite and the cell walls. The cell allows water/gas injection from the top and bottom ends of each sample.

The two volume/pressure controllers (PVCs) with a capacity of 200 ml (with an accuracy of ± 1 mm^3 in volume and ± 1 kPa in pressure) are used to inject compressed gas (Nitrogen) and water at the inlet (with a maximum pressure of 4 MPa) and maintain a back pressure at the sample outlet.

The pre-charged cylinder is used to ensure nitrogen saturation to prevent bentonite desiccation.

3.2.2 Material properties

The investigated material (Figure 3-25) is a mixture of pellets and powder of MX80 bentonite (Wyoming, USA) with a proportion of 80 pellets/20 powder in dry mass prepared at a dry density, ρd=1.47 Mg/m^3. The material has a high smectite content (80%) with some inclusions of non-clayey minerals (quartz – 4% of the total mass; muscovite – 4% of the total mass; pyrite – less than 1% of the total mass; and some elements of calcite). The cation exchange capacity (CEC) is 98 meq/100 g, with Na+ as the major exchangeable cation. The liquid limit is 560%, the plastic limit is 62% and the unit mass is 2.77 Mg/m^3 (Molinero et al., 2017). Pellets were industrially produced in Laviosa-MPC company by instantaneously compacting a powder of MX80 bentonite in a mould of 0.07 m diameter and 0.07 m of height (Laviosa Minerals). The fabrication was done at water content w = 5% - 7% and at dry unit mass ρd =1.998 Mg/m^3 - 2.12 Mg/m^3. The average measured water content of the pellets after a long storage period is 4.38 %. The MX80 bentonite powder constituting the mixture was produced by crushing pellets. The produced powder grains present a diameter between 0·0008 m and 0.002 m (Molinero et al. 2017). Compared to the fabrication value of water content (between 5% and 7%), a value of 4.36 % was found in the laboratory.

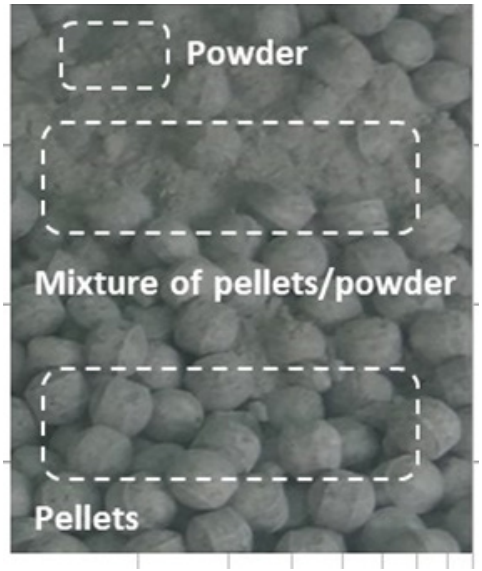

Figure 3-25 – View of the MX80 pellets and powder mixture.

3.2.3 Testing protocol

3.2.3.1 Stage 1. Sample preparation

A special preparation protocol, consisting in placing manually the mixture layer-by-layer was adopted. Molinero et al. (2017) tested three protocols to prepare MX80 bentonite pellet and powder mixture (80/20 in dry mass) samples. The homogeneity of the specimens obtained by using each of the three protocols was examined by using X-ray computed microtomography. The results have shown that the layer-by-layer construction protocol provided a reasonably good homogeneity of the mixture, with regular scattering of the powder grains within the pores located between the pellets. The sample preparation comprised the emplacement of 21 pellets (three layers of 7 pellets). For each layer, the bentonite were arranged according the an ideal concentric arrangement and then gaps were filled by pouring manually the corresponding bentonite powder mass (20 % in dry mass) (Figure 3-26). The total heigh of the sample was 21 mm, and an upper technological void of 1.1 mm remained between the upper face of the sample and the porous filter.

Additionally, spherical bed glasses (of 1 mm in diameter) were placed between the pellets and between the layers at different positions to allow quantification of local displacement within the mixture during hydration and gas injection. Once the sample is prepared, it was placed in the X-ray CT scanner for imaging the specimen at initial state before hydration.

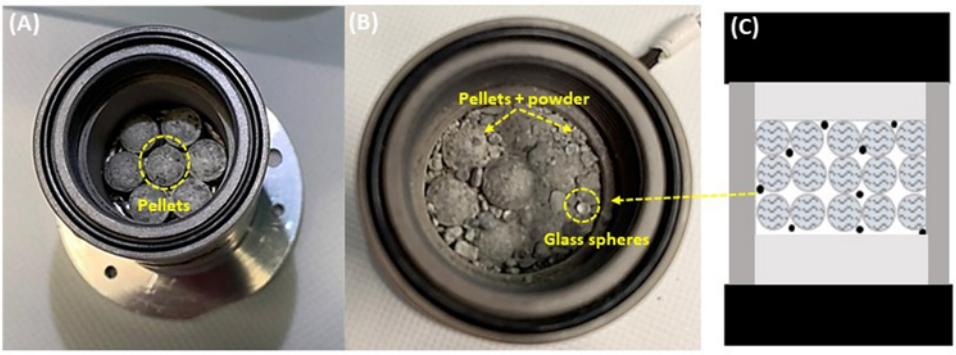

Figure 3-26 – Mixture preparation. (A) view of a layer of pellets, (B) pellets and powder mixture (MX80) layer, and (C) arrangement of the glass spheres within the cell.

3.2.3.2 Stage 2. Hydration stage

A long-term hydration stage lasted 355 days. The test was started by opening the water inlet valves. At the beginning of the test, air was evacuated by opening the air outlet valve until no air bubble was observed in the pipes. Distilled water was injected by the top of the sample. The volume of injected water was also controlled during hydration by the PVC connected to the hydration system. No water pressure was applied during the saturation process. During this stage, the sample underwent some swelling due to the top technological void.

3.2.3.3 Stage 3 Water permeability determination

The water permeability of the sample was determined under steady state at a pressure gradient of 0.9 MPa (bottom and top water pressures were kept at 0.1 and 1 MPa, respectively).

During this stage and at different hydration times, the specimen was scanned using X-ray tomograph to track microstructural changes occurring during saturation (Figure 3-27).

3.2.3.4 Stage 3. Gas injection stage

Two gas injection stages were performed by increasing gradually the gas pressure at the top of the cell. Gas injection was applied through eleven injection pressure ramps. During gas testing water pressure was decreased to 0.5 MPa. It is worth noting that for the second stage, a water pre-charged cylinder was used to saturate the nitrogen with vapor.

To visualize the evolution of pore networks and the formation of gas preferential pathways X-ray CT observations were performed before and after each gas injection stage using a Skyscan 1172 micro-tomograph (Figure 3-27). The X-ray tube was operated at 122 kV and 65 µA, and a brass filter of 0.25 mm filter was selected. The data acquisition system recorded a total of 1117 projections, evenly distributed over a 360° rotation along the vertical axis of the sample. To obtain the 3D reconstructions, the recorded projections were processed using NRecon 1.6 software (Skyscan Bruker). Image analysis was performed using ImageJ (Fiji) and Avizo software.

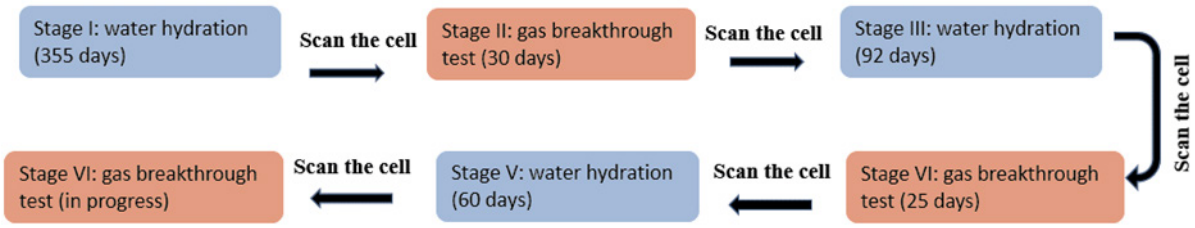

Figure 3-27 – Schematic diagram of hydration and gas injection stages, and X-ray CT scans.

3.2.4 Results

3.2.4.1 Hydration phase

Qualitative analysis of the swelling behaviour

The behavior of the pellet/powder mixture was firstly investigated by carrying out a qualitative analysis of the µ-CT observations. Figure 3-28 shows 3D reconstructions of the mixture at initial state and at different hydration times. At the initial state, the top of the mixture is characterised by the presence of larger inter-pellets voids between the pellet and the porous stone, most probably due to segregation in the fabrication process. After 1 day of hydration, these voids are completely sealed together with the top technological gap due to their vicinity to the hydration front, so the material at this level swells quickly. Progressively, the initial structure loses its granular nature while wetting; air-filled inter-pellet voids are still visible after 7 days of hydration at the bottom layer. Finally, an apparently global homogeneous sample is observed after 23 days of hydration. At this time, almost all the air-filled inter-pellet voids have been completely sealed.

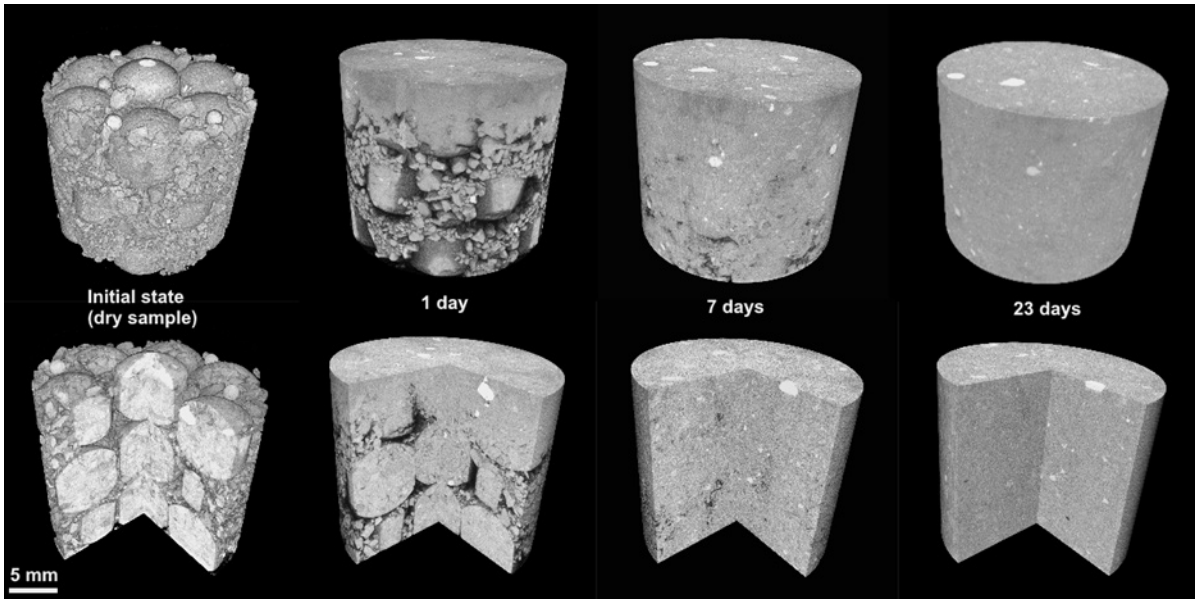

Figure 3-28 – X-ray CT visualization of the temporal evolution of the wetting front in the bentonite MX80 mixture during the first hydration stage (voxel size: 16 µm).

Density evolution

In order to explore the long-term homogenisation of the mixture during hydration, an analysis of the bulk density distribution from X-ray CT images was performed. A calibration process was applied to convert CT gray-scale values into material density (Van Geet et al., 2005; Molinero, 2018). To this end, various regions of different materials in the MX80 sample were examined to determine grey-scale values (GVs), as shown in Table 3-10. A linear relationship was established between normalized grey levels and material bulk density, as shown in Figure 3-29.

Table 3-10 – Density of material and the correspondent grey value

	Air	Body cell	Glass spheres	Quartz
Density (kg/m^3)	1.22	1490	2000	2700
Grey value (for 8 bit)	0	115	210	254

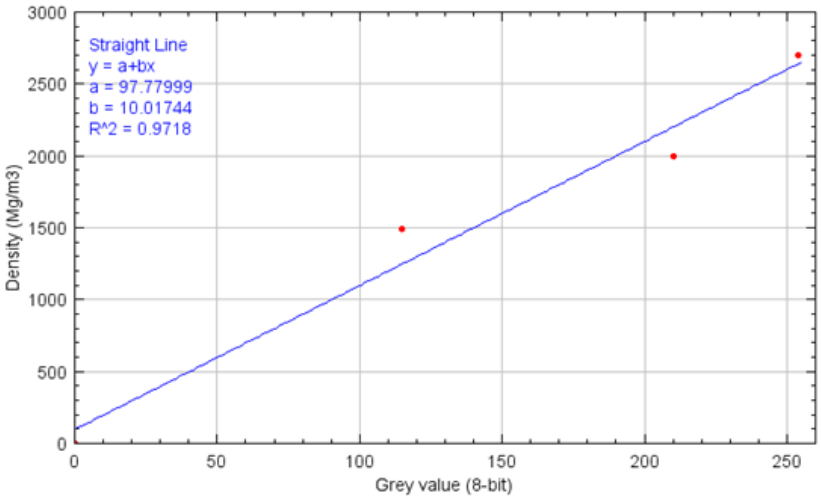

Figure 3-29 – Calibration function of the density.

Figure 3-30 illustrates the bulk density distribution calculated using the calibration function throughout the hydration process. At the initial state, a heterogeneous distribution of dry density is observed. The density curve exhibits fluctuations marked by low density, due the presence of the discontinuities (inter-limits) between the three layers of pellets. As the hydration front progresses, these oscillations gradually disappear, as shown from 3D images in Figure 3-28. After the 23 days of hydration, the density gradient decreases significantly, indicating homogenization of the saturated sample.

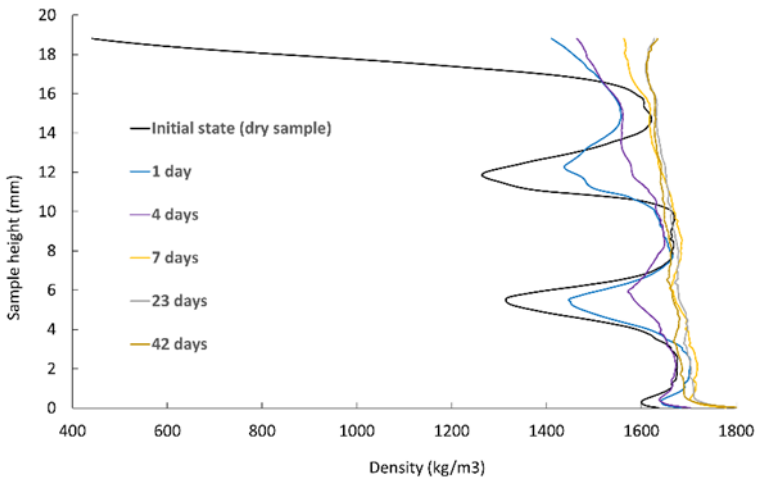

Figure 3-30 – Density distribution obtained from image analysis.

Porosity evolution

Figure 3-31 presents the evolution of the macroporosity versus the hydration time. The total porosity was obtained from X-ray CT images with a 16 µm voxel size. For clarity, in the initial dry state, the calculated average porosity corresponds to 20 % of the specimen's total volume. As can be observed, the porosity distribution was not uniform along the specimen's height. The local porosity at the top and between layers of the sample is higher due to the presence of larger voids. As the hydration front progresses and swelling increases, porosity decreases significantly near the upper part of the specimen, close to the water inlet. While the reduction is minimal in the middle and bottom sections of the specimen, it gives rise to a gradient in porosity between these areas. After one day of hydration, the average porosity decreased to 6.52 %. And after the 7th day, this distribution became uniform, and the average detected macroporosity dropped below 1%. Beyond this hydration time, the porosity was lower than 0.1%. It should be noted that the reported porosity values do not represent the effective porosity, which is likely higher, as they are limited by the voxel size used for scanning the entire cell.

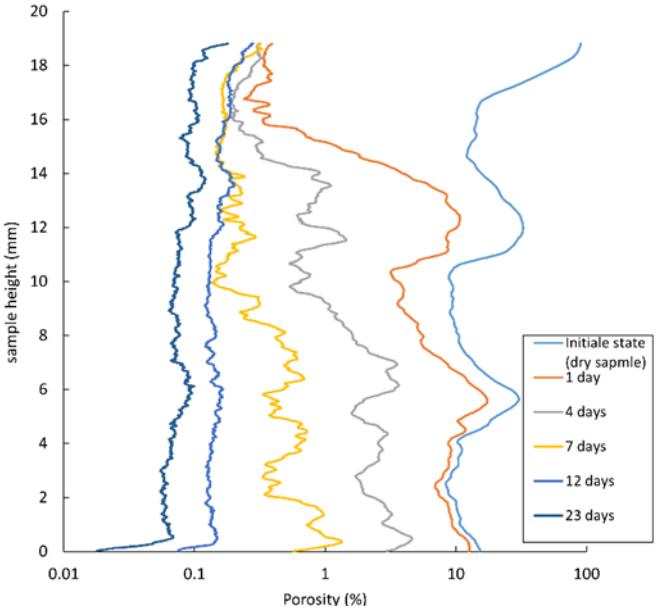

Figure 3-31 – Evolution of the porosity of the MX80 bentonite (voxel size: 16 µm).

Water Permeability Measurements

The first permeability test on the mixture was carried out after 4 months of hydration. Darcy's law was applied. The intrinsic permeability K was calculated considering a water dynamic viscosity of μ_w = 1.0016x10^{-3} Pa.s (at 20°C) and water density of ρ_w = 998.2 kg/m^3. The obtained average value is 8.28 x 10^{-21} m^2. This value corresponds to the swollen mixture at a bulk density of 1.40 Mg/m^3, reached after filling the technological gap. The intrinsic permeability value is shown in Figure 3-32 as a function of porosity together with data reported by different authors (Villar, 2005; Karnland et al., 2008 and Alcantara et al., 2020) on the MX80 bentonite.

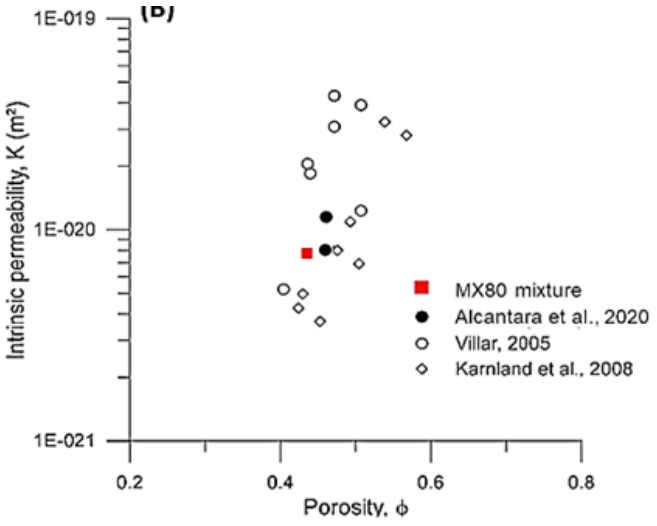

Figure 3-32 – MX80 bentonite pellet mixture permeability evolution with porosity.

3.2.4.2 Gas injection phases

Gas breakthrough tests

At the end of the hydration phase, which lasted for 355 days, the cell inlet was connected to the PVC pre-charged with gas, while the outlet was connected to the second PVC. The water trapped in the porous stone was evacuated, and gas injection started. As mentioned in the testing protocols section, two type of gas injection experiments were conducted to assess the effect of vapor-saturated gas on the mechanism of gas migration in the MX80 bentonite mixture. The first test involved injecting dry gas (nitrogen), while the second test used a water pre-charged cylinder to saturate the gas. The inlet gas pressure started at 500 kPa and was increased every 48h by 250 kPa and the outlet pressure was recorded by the PVC at the bottom. Note that in some stages the injection pressure slightly exceeded 48h which is due to calendar events (Figure 3-33).

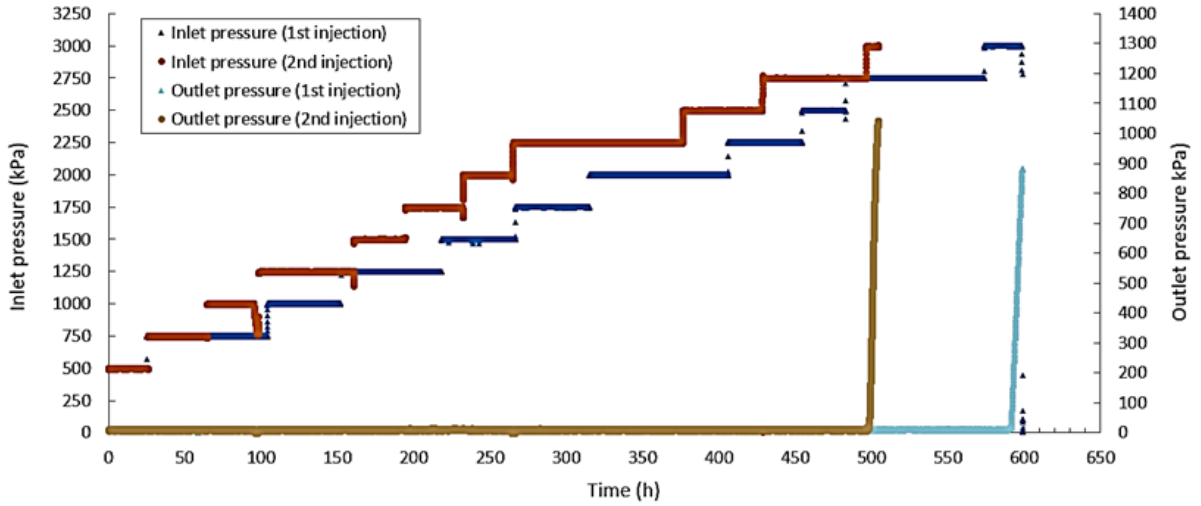

Figure 3-33 – Evolution of gas pressures in injection and receiving PVC with time.

Figure 3-33 shows the evolution of gas outlet pressure. For both gas injection tests, gas breakthrough was observed at 3 MPa. For both cases, the breakthrough pressure was slightly higher than the material's swelling pressure (2.9 MPa).

Gas and water permeability measurements

After gas breakthrough, a continuous flow of gas evolves from the high-pressure (cell inlet) to the low-pressure PVC (cell outlet). Effective gas permeability is calculated using Darcy's law for compressible media ans outflow data. Figure 3-34 shows the evolution of gas permeability for the two-gas tests. The average gas permeabilities are 9.74×10^{-20} m^2 and 1.12×10^{-19} m^2 respectively, for the first and the seconds stages. The increase in gas permeability, observed after 35 min for the first injection and 10 min for the second, suggests a reduction in flow resistance resulting from the expansion of microcracks at the interface between the sample and the cell.

It is also observed that the gas permeability is slightly higher than when water is flowing (K_w = 8.28 x 10^{-21} m^2). This difference can be attributed to the fact that gas flows through preferential pathways different from those followed by water. However, some differences in water/gas permeability could also be explained due to the pore pressure dependence on gas permeability of the Klinkenberg slippage effect (Klinkenberg, 1941). This phenomenon becomes significant when the intrinsic permeability is low (< 10^{-18} m^2) or when the average pore pressure is low (Zimmerman, 2018; Alcantara, 2021).

After gas injection stage, a second hydration stage was started. Water permeability (K_w) measured after 2 days was 5.06 x 10^{-20} m^2. Kw then decreased to 1.88 x 10^{-20} m^2 after 2 weeks of hydration. The obtained value is notably close to the water permeability of the MX80 bentonite pellet mixture obtained by Alcantara (2021) (17 x 10^{-20} m^2) after 200 days at a dry density of 1.49 Mg/m^3.

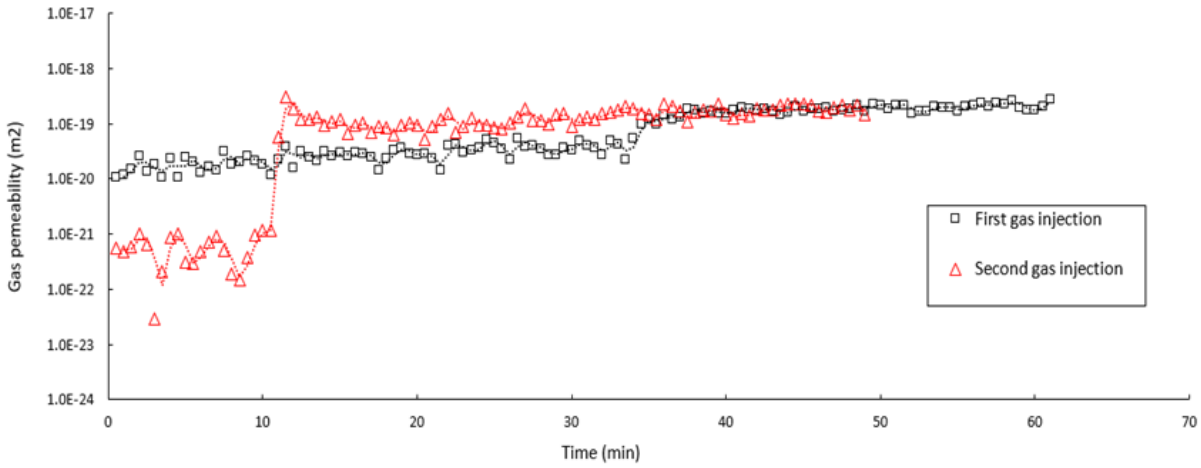

Figure 3-34 – Evolution of gas permeability during breakthrough tests.

3.2.4.3 Microstructural Analysis

Macroporosity and microcracks network

Figure 3-34 shows the pore network of the MX80 bentonite, segmented from X-ray CT images acquired after gas breakthrough at 3 MPa. Images from both gas injection phases reveal a network of pores and

microcracks concentrated at the top of the specimen (Figure 3-35 and Figure 3-36). The microcracks appear to propagate from the outside of the sample inwards. The observed interface gas pathway is covering 25% of the height (Figure 3-35C). The 16 µm voxel size used to scan the sample made it challenging to identify a continuous preferential path for the gas migration. In addition, desiccation was observed at the bottom part of sample. Note that when the cell was scanned at a pressure of 2 MPa prior to gas breakthrough, no desiccation was observed at the edges of the specimen. However, it is likely that desiccation occurred between 2 and 3 MPa, allowing the gas to cross along the sample/wall cell interface at 3 MPa.

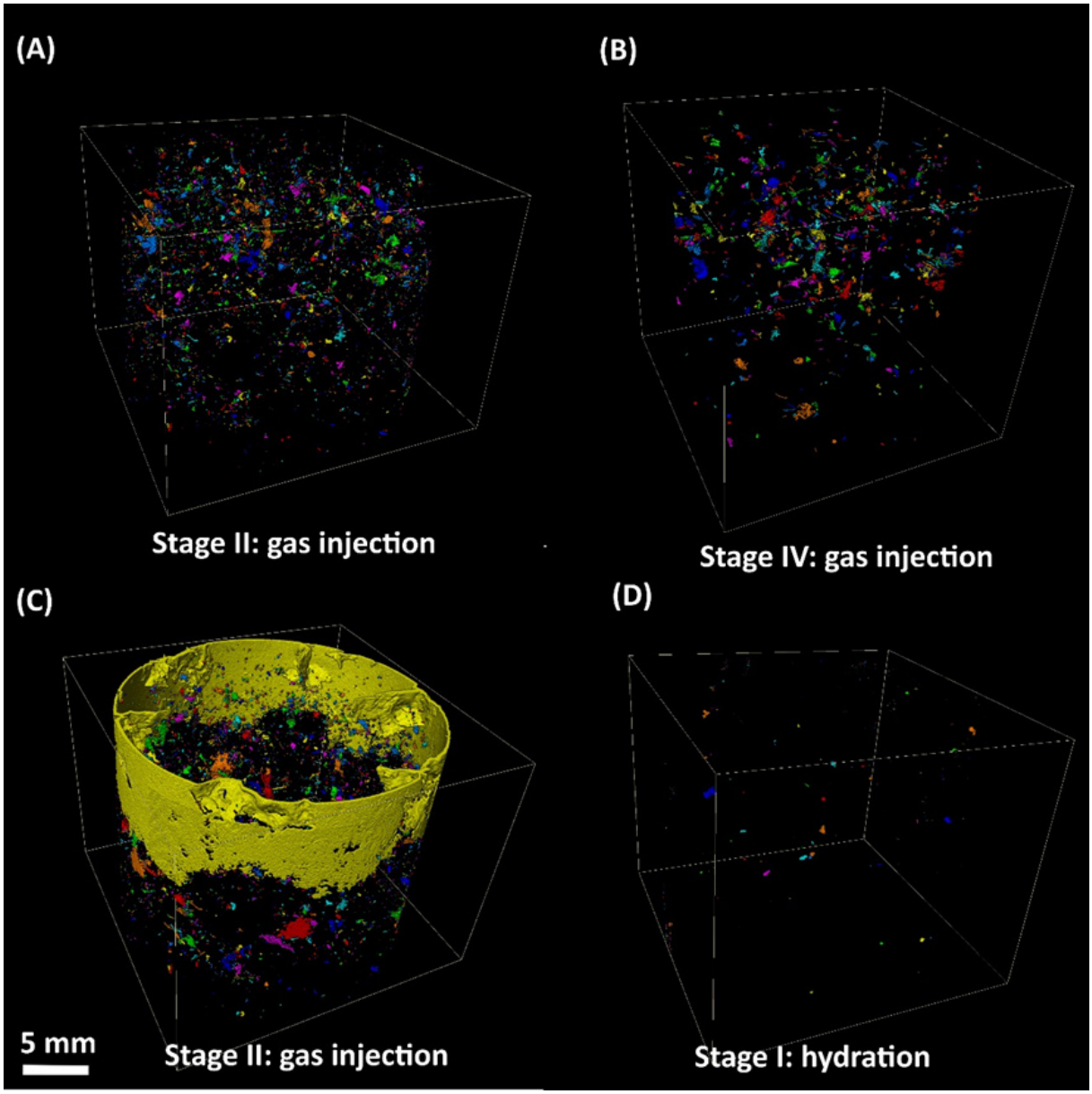

Figure 3-35 – X-ray CT images of MX80 bentonite pores and crack network. (A) For the first breakthrough test and (B) for the second breakthrough test. (C) Pore network with desiccation, and (D) pores detected after the second re-saturation stage. Colors refer to different macropores sizes.

After each gas injection phase, the MX80 bentonite mixture was X-ray scanned and subjected to further hydration by injecting at 1 MPa de-ionized water. The water pressure remained constant for 3 and 2 months during the second and third hydration stages, respectively. The water pressure imposed at the

cell bottom was 100 kPa. As shown in Figure 3-35D and Figure 3-36, the X-ray CT images revealed a rapid swelling of the specimen after just one day of hydration. The desiccation along the specimen/cell interface was sealed, and the macropores developed during gas injection were closed.

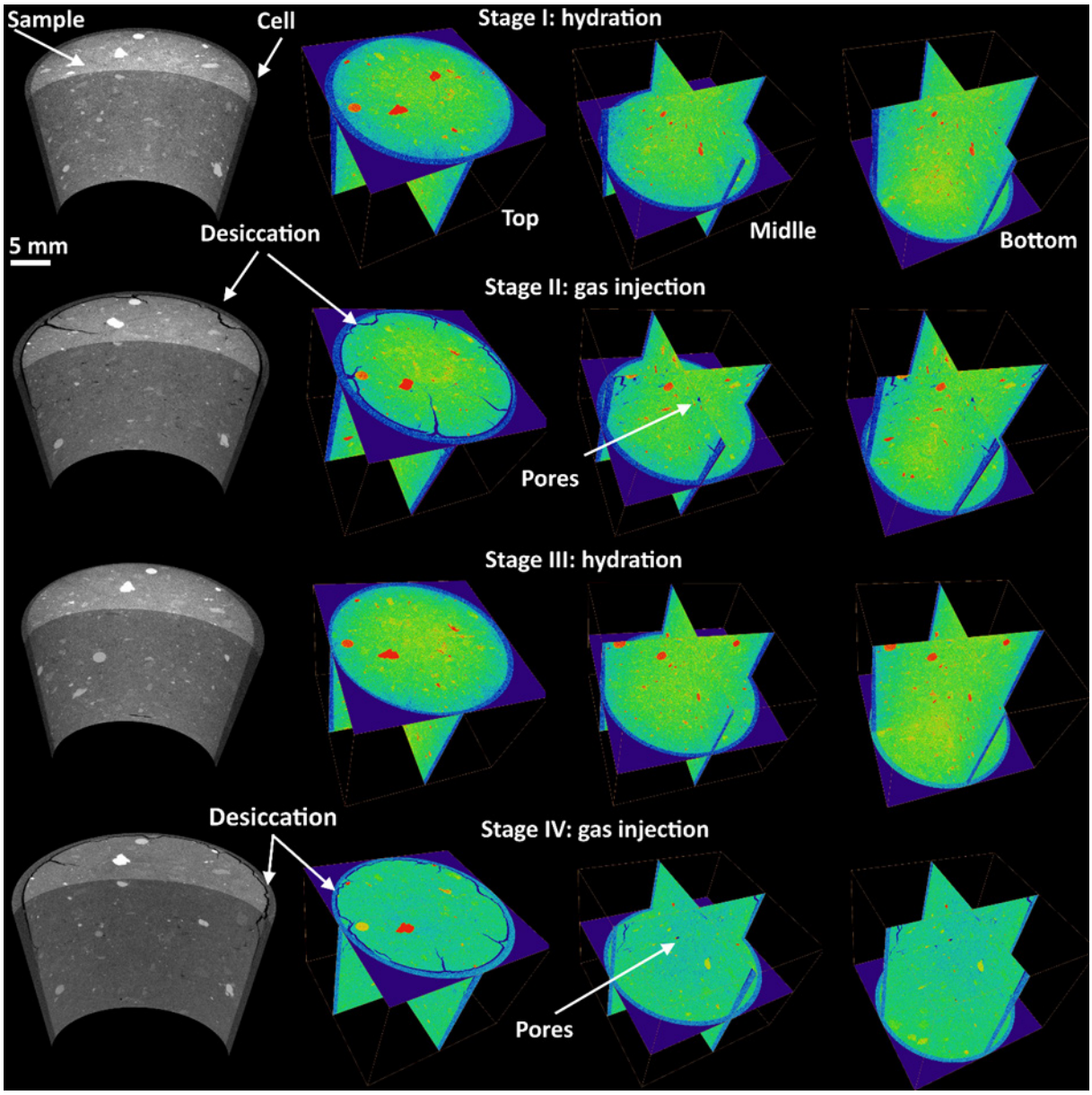

Figure 3-36 – X-ray CT visualizations of the MX80 bentonite sample after gas breakthrough and during hydration stages. The coloured images represent the cross-section at the top cell, at 50% height, and at the bottom (voxel size: 16 µm).

Local displacements

The local displacements of the MX80 pellets and powder at different locations were calculated during the hydration and gas injection stages by measuring the movement of the glass spheres randomly placed within the mixture at various locations during the fabrication process. In total, 15 spheres with a diameter of 1 mm at different locations were identified and marked as GS1 to GS15 (Figure 3-37) through image analysis. The coordinates of the mass center were extracted for displacement-related

analysis. The Digital Image Correlation (DIC) technique was applied to calculate the distance in millimeters covered by the spheres as a function of the X, Y and Z coordinates of the image edges.

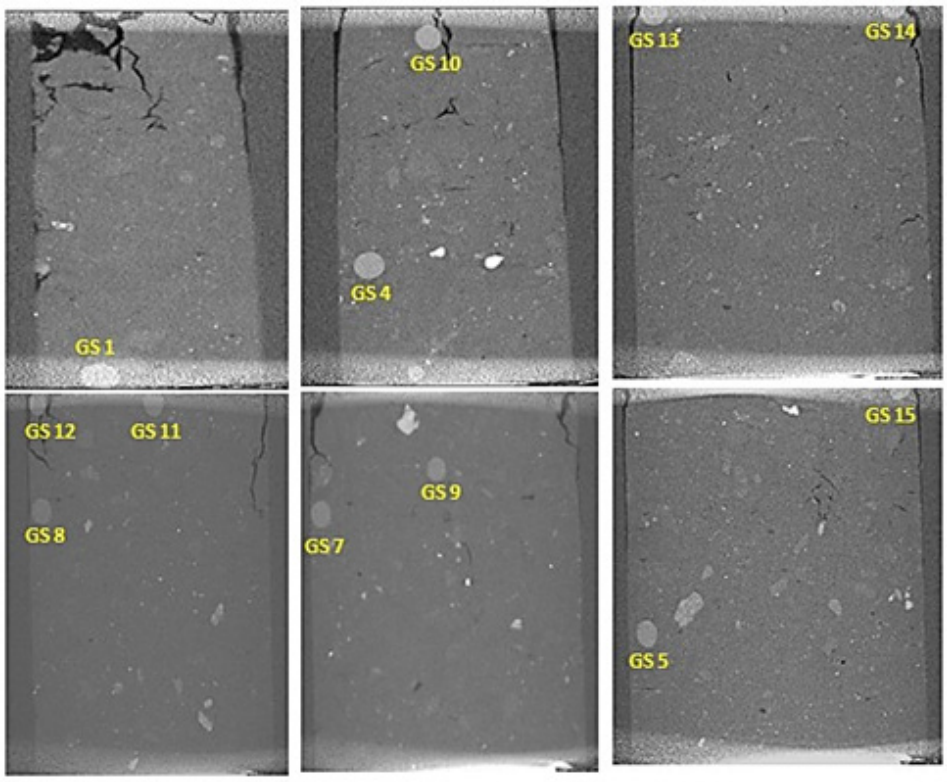

Figure 3-37 – Positions of glass spheres (GSs) in the specimen cross-sections.

In the axial direction, a positive sign indicates upward movement. The results from the initial hydration stage (orange part), illustrated in Figure 3-38(A), reveal a vertical displacement of glass spheres ranging from -0.1 to 3.2 mm. As the sample swelled, the three spheres (GS 1, 2, and 3) placed at the bottom on the bentonite powder were slightly displaced downward after 26 days of hydration. However, the GSs situated in the upper layer (GS 10-13) moved upward from 2.6 to 3.2 mm, except for GSs 14 and 15, which were displaced by 2 mm. This movement can be attributed to their initial placement within the air-void between the pellets and the wall cell/sample interface. Following the hydration stage, the sample continued to swell, and the GSs kept moving upwards until 75th days, were GSs stabilized, particularly at the top surface. The glass spheres at the lower part of the cell exhibited a minor downward shift. After gas injection (grey part), most of the glass spheres went slightly upward (Figure 3-38B). After re-saturation, the sample swelled rapidly. This is clearly demonstrated by the fact that all the spheres moved upwards after just one week of water reinjection. The last points of the curves show a stabilization of sphere movement after 15 days of re-saturation.

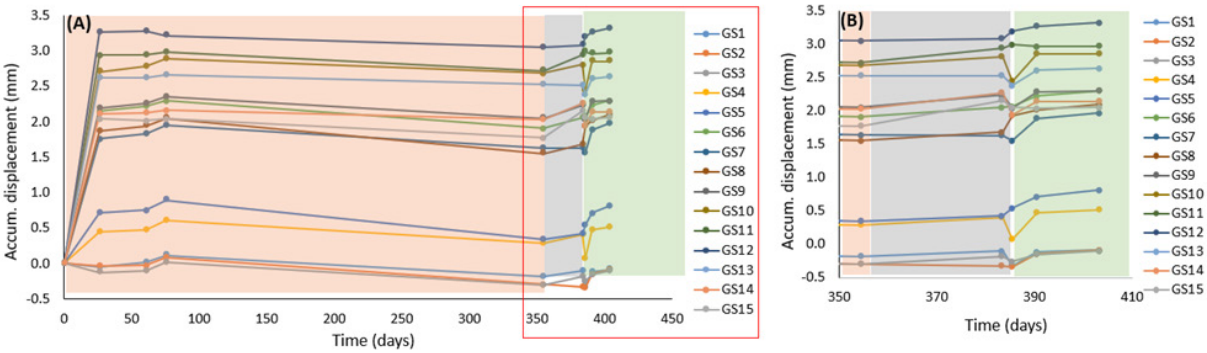

Figure 3-38 – Axial displacements of the glass spheres (GSs) over time (A). Zoom on the gas and re-saturation stages (B).

Figure 3-39A illustrated the radial displacements occurred during the three first stages of hydration and gas injection. The results indicate an initial displacement ranging from 0.2 and 1.2 mm for all GSs, except the GS 13, which moved substantially further (compared to the other spheres) by 4.7 mm after about 26 days of hydration. This significant displacement is due to the position of GS 13 (within large macrovoid and away from the cell wall), as shown in Figure 3-37. Upon hydration, the mixture swelling induces the movement toward the cell interface. Similarly, GS's 15, 14, 12 and 11, initially placed in the first layer of the powder/pellets, moved toward the interface by about 1 mm, and then was blocked when touching the porous filter. As hydration progressed, all these spheres did not move. GS's from 1-10 in the second and third layers moved slightly during hydration. Indeed, hydration causes the material to swell, increasing the swelling pressure and leading to the rearrangement of the pellets. The movement of the pellets then induces the displacement of the bentonite powder and the spheres located in the voids between the pellets. The pellets at the top of the cell, as well as the spheres between the pellets and between the sample and the wall cell, moved significantly because of their location close to the hydration front. Figure 3-39(B) shows that the spheres at the top (except for GS 11) of the sample have moved towards the centre. This displacement is mainly due to sample desiccation, as shown in the X-ray CT images. GS 11 has not moved too much, as it is located in the centre of the sample. The spheres positioned in the 2nd and 3rd layers are slightly displaced. The positive displacement of certain spheres (in the direction of the wall cell) is likely due to the cracks adjacent to them (GS 10), causing them to move toward the interface.

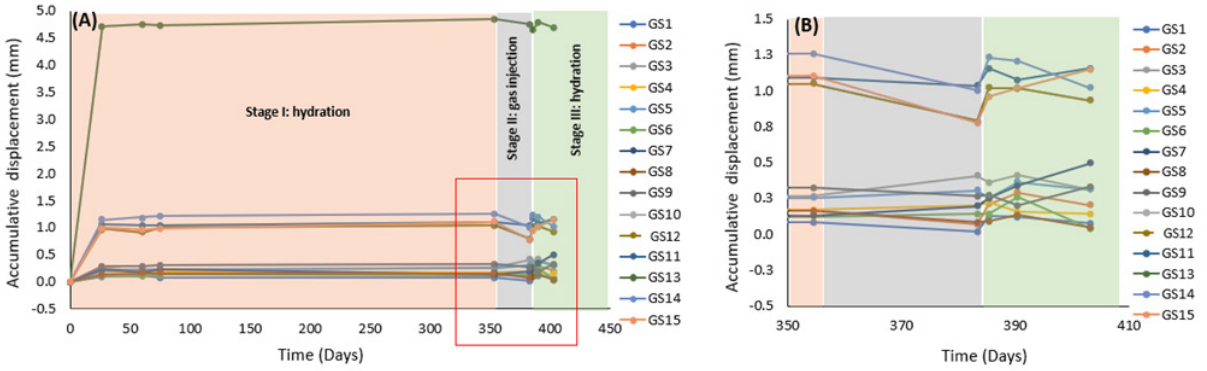

Figure 3-39 – Radial displacements of the glass spheres (GSs) over time (A). Zoom on the gas and re-saturation stages (B).

3.2.5 Summary

In this study, the hydro-mechanical behaviour, and the microstructure of the MX80 bentonite mixture with 80/20 ratio in dry mass was investigated at different scales.

The first part of this work focused on microstructural characterization of the mixture at initial state and during hydration. To this end, several experiments of hydration and X-ray CT imagining were carried out to analyse the changes in microstructure and density during the hydration process. The X-ray images showed a rapid progression of the humidification front leading to homogenisation of the mixture after about 1 month of hydration. The water permeability measured after long-term saturation (K_w=8.28 x 10^{-21} m^2) aligns with values reported in the literature.

The second part of the study involved gas injection experiments after 355 days of long-term hydration. Two types of injections were performed: one with water saturated gas and another without i.e. dry gas. The gas inlet pressure began at 500 kPa and increased in steps of 250 kPa every 48 h. High-contrast images were analysed to track changes in porosities, flow paths, and material displacements inside the mixture.

The results revealed that gas breakthrough occurred at 3 MPa close to the swelling pressure (2.9 MPa) for both types of injection. Saturating gas with water vapor did not influence the gas pressure value at breakthrough. The outlet pressure curves showed a continuous gas flow. X-ray CT images obtained immediately after breakthrough revealed the development of new macropore and microcrack networks compared with the hydration phase. The pore network was concentrated in the upper quarter of the sample, indicating local development of gas pathways. As the pressure increased, the gas migrated along the wall cell/sample interface.

Analysis of the glass spheres' movements in radial and axial directions revealed non-uniform swelling of the material. During the hydration phase, the sample continued to swell, causing the glass spheres to move upwards until the 75th day, after which they stabilized, particularly at the upper surface. In the lower part of the sample, the glass spheres moved slightly downwards, probably due to sample densification and/or pressure applied by the upper layers. During gas injection, most of the glass spheres displaced slightly upwards. Compressive strain may be responsible for this upward movement. After re-saturation, the sample swelled rapidly.

3.2.6 Key learning points

3.2.6.1 New knowledge acquired

- CT µ-tomography clearly showed preferential gas paths occur along the cell/material interface at gas pressure of 3 MPa (swelling pressure 2.9 MPa)
- Diffused porosity desaturation is observed inside the sample after breakthrough.
- Saturating gas with water vapor did not influence the gas pressure at breakthrough.

3.2.6.2 Impact of acquired knowledge

The aim of the work was to investigate the impact of the initial structural heterogeneities of MX80 bentonite pellets mixture on gas migration processes. The tested pellet/powder mixture with an 80/20 proportion in dry mass, was prepared following a specific protocol designed to minimize initial structural heterogeneity. During the long-term hydration stage, a progressive apparent homogenization of the tested mixture was observed., the gas testing, under constant volume conditions, clearly demonstrate that preferential gas paths occur along the cell/material interface.

3.2.6.3 Recommendations for the future

- Testing of a highly heterogeneous sample.
- Testing of localized gas injection within the mixture.
- Restrain the passage of gas through the interface (e.g. use of rough cell walls).

3.2.7 References

Van Geet, M., Volckaert, G., & Roels, S. (2005). The use of microfocus X-ray computed tomography in characterising the hydration of a clay pellet/powder mixture. Applied Clay Science, 29(2), 73-87.

Molinero Guerra, A. (2018). Caractérisations expérimentale et numérique du comportement hydro-mécanique d'un matériau hétérogène: mélange de poudre/pellets de bentonite (Doctoral dissertation, Paris Est).

Villar, M.V. (2002). Thermo-hydro-mechanical characterisation of a bentonite from Cabo de Gata. A study applied to the use of bentonite assealing material in high level radioactive waste repositories. ENRESA Technical Publishing 01/2002. Madrid, Spain.

Karnland, O., Nilsson, U., Weber, H., & Wersin, P. (2008). Sealing ability of Wyoming bentonite pellets foreseen as buffer material – Laboratory results. Physics and Chemistry of the Earth, Parts A/B/C, 33, S472–S475. https://doi.org/10.1016/J.PCE.2008.10.024

Alcantara, A. M., Romero, E., Mokni, N., & Olivella, S. (2020). Microstructural and hydro-mechanical behaviour of bentonite pellets and powder mixtures. In E3S Web of Conferences (Vol. 195, p. 04003). EDP Sciences.

Klinkenberg, L. J. (1941). The permeability of porous media to liquids and gases. Drilling and Production Practice. American Petroleum Inst., 200–213.

Zimmerman, R. W. (2018). Imperial College Lectures In Petroleum Engineering, The- Volume 5: Fluid Flow In Porous Media. World Scientific.

Mesa Alcantara, A. (2021). Hydro-mechanical behaviour of pellet/powder mixture of bentonite and impact of gas migration.

4. Gas Transport and Impact on Self-sealing of Fractures

Five laboratory studies were conducted in Task 3 with focus on gas induced failure and self-sealing capacity of clayey rocks:

- GRS dedicated a comprehensive experimental programme to gas transport along fractures in clayey rocks and its impact on self-sealing. Exceptional new databases were acquired as input to constitutive modelling (Task 3.3) by monitoring the evolution of hydraulic conductivity, axial and radial strains over a period of up to 700 days (chapter 4.1).
- CNRS (Uni Lorraine) developed a workflow for the visualisation of gas transport processes in fractures and their self-sealing capacity. The evolution of permeability, volumetric strain and fracture volume was monitored in the gas invasion phase and during re-hydration as input for constitutive modelling (Chapter 4.2).
- BGS (UKRI) investigated the effects of gas transport on fracture transmissivity and self-sealing using a highly instrumented, bespoke direct shear apparatus. The test results encompassed not only the transients of gas/water flow, stresses and shear strains but also scans of the fracture surfaces before and after testing (Chapter 4.3).
- EPFL conducted gas transport experiments in intact and remoulded/recompacted claystone. Special focus was on accurate measurement of the volumetric behaviour of the material in response to gas transfer (chapter 4.4).
- CIMNE (UPC) studied the hydromechanical response of claystones on gas injections. Outstanding experimental results were achieved with a new test cell, indicating a distinct dependence of the gas transport capacity of the clay samples on the gas injection rate (chapter 4.5).

4.1 Experimental Study of Gas Transport and Impact on Self-sealing of Fractures in Indurated Claystones (GRS)

GRS performed an experimental study of gas transport and impact on self-sealing of fractures in indurated claystones. Originally, large hollow cylinder tests were designed to investigate self-sealing of fractures with water and gas transport under mechanical load (EURAD Milestone 58, 2020). Unfortunately, the testing apparatus was damaged in the beginning and the necessary reparation could not be done in time by the manufacturer due to the coronavirus crisis. As a consequence, the work programme had to be modified (EURAD Milestone 124, 2021) to test normally sized samples with artificial fractures under various load conditions. Core samples were extracted from the indurated Callovo-Oxfordian (COx) and Opalinus (OPA) claystones with different mineralogical compositions. Long-term consolidation, water and gas flow experiments were undertaken on the fractured samples with different sizes and fracture intensities. Self-sealing performance of fractures was characterised by fracture closure, water permeability change, gas breakthrough pressure, and recovery of gas-induced pathways, respectively. The experimental work and results are presented in this final report.

4.1.1 Material properties

Core samples were extracted from the three units (i.e., clay-rich unit, transition unit, and silty-carbonated unit) of COx (Figure 4-1) and sandy facies of OPA in the URLs at Bure, and Mont-Terri, respectively. They have different mineralogical compositions, petrophysical and hydro-mechanical properties. Table 4-1 summarises the main mineralogical components of the claystones: clay mineral, carbonate and quartz. Compared to the COx clay-rich unit and OPA shaly facies, the COx carbonate-rich unit and OPA sandy facies have less clay minerals but more carbonates and quartz. The mineralogical composition

of each facies displays a spatial variability. Kaufhold et al. (2013) and Houben et al. (2014) demonstrated that the OPA sandy facies is more heterogeneous on millimetre- to centimetre-scale than the shaly facies. For instance, the samples taken from the OPA sandy facies for the present tests showed a large mineralogical variability within a short interval of 5 m with clay contents of 24%-39%, quartz of 34%-39%, carbonate of 15%-33%, and feldspar of 8%-9% (Table 4-2). Similarly, a mineralogical heterogeneity appears in the COx carbonate-rich unit on centimetre- to decimetre-scale as observed at a drift front at the −445 m level of the URL at Bure (Figure 4-2). A sample from this area showed a large carbonate content of 50%, quartz of 25%, and a small clay content of 21% (Table 4-2).

The mineralogical heterogeneity can lead to local differences in deformability, swelling capacity, and thus self-sealing capacity of rock mass. Generally, the swelling capacity of a claystone is determined by the fraction of clay mineral. The previous swelling experiments (Zhang et al., 2010, 2019; Zhang, 2017) showed that the studied claystones possess certain swelling capacities with free volumetric expansion up to 10% at the COx clay-rich unit and OPA shaly facies and to 5% at the OPA sandy facies. The swelling with water uptake leads to degradation of the inner structure and reductions of stiffness and strength.

For testing, four samples were taken from OPA sandy facies, two from COx clay-rich and four from COx carbonate-rich. They were prepared to different sizes of diameter / length (D/L) = 50 / (75-100) and 79 / (280-300) in mm. Their characteristics determined before testing are summarized in Table 4-3. All the OPA and COx samples have similar solid grain densities of 2.69 – 2.70 g/cm^3 (Zhang et al. 2019; Zhang and Laurich, 2020). The data in Table 4-2 show that the OPA sandy samples have relatively high dry densities or lower porosities compared to the COx carbonate- and clay-rich samples. The physical properties of each facies vary from a sample to another, indicating the heterogeneity of the clay facies, particularly the OPA sandy and COx carbonate-rich facies. Due to sampling and long storage durations of 1-2 years, the samples were desaturated to 43-50% degrees at OPA samples, ~70% degree at COx clay-rich ones and 27-54% at COx carbonate-rich ones.

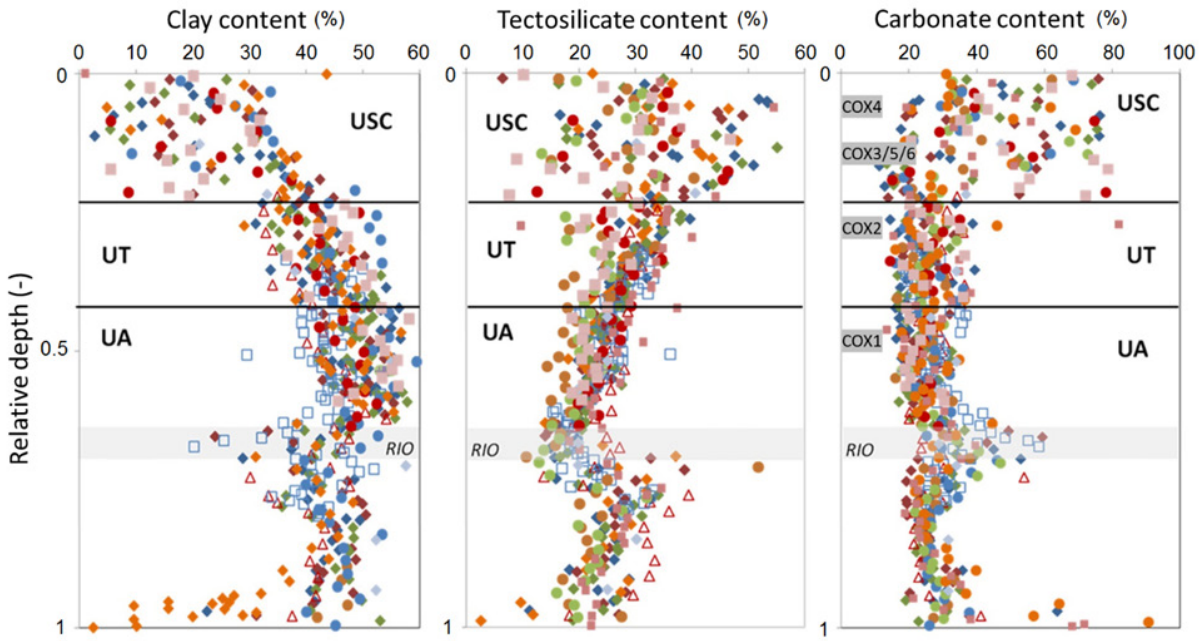

Figure 4-40 – Variation in mineralogical composition across the thickness of the COx formation. Data come from different boreholes and the relative depth is between the top of silty-carbonated unit and the bottom of clay-rich unit. UA represents the clay-rich unit at the base; UT denotes the transition unit; USC is the silty-carbonated unit; RIO is a small oolitic limestone layer (Andra)

Figure 4-41 – Heterogeneous distribution of carbonates (light grey) in the COx carbonate-rich unit observed in a drift at the -445 m level of the URL Bure (Andra)

Table 4-11 – Main mineralogical components of the sandy and shaly facies of OPA formation and the carbonate- and clay-rich facies of COx formation.

Main component	OPA[1] sandy facies	OPA[1] shaly facies	COx[2] carbonate-rich facies	COx[2] clay-rich facies
Clay minerals	20 – 40	55 – 75	15 – 40	40 – 55
Carbonates	15 – 40	5 – 30	25 – 50	20 – 35
Quartz	30 – 45	5 – 25	20 – 40	17 - 27

1: after Mazurek et al. (2008), Bock et al. (2010), Kaufhold et al. (2011) and Zhang et al. (2019)
2: after Andra (2005), Robinet et al. (2015) and Conil et al. (2018)

Table 4-12 – Main mineralogical components of the test samples from the OPA sandy facies.

Sample	Hole depth (m)	Clay (%)	Quartz (%)	Carbonates (%)	Feldspar (%)	Others (%)
BDM-B9-9	8.2	24	34	33	9	<1
DBM-B9-18	10.2	36	39	15	9	< 1
DBM-B9-29	12.8	39	38	15	8	< 1

Table 4-13 – Initial characteristics of the claystone samples before testing.

Lithological facies	Drilled core	Depth/ orientation	Sample number	Size D/L (mm)	Bulk density (g/cm^3)	Dry density (g/cm^3)	Poro-sity (%)	Water content (%)	Degree of saturation (%)
OPA sandy facies	BLT-A10		OPA1	50/75	2.487	2.445	9.4	1.72	44
	BDM-B9-9		OPA2	50/90	2.515	2.478	8.2	1.49	45
	DBM-B9-18		OPA3	50/90	2.563	2.532	6.2	1.22	50
	DBM-B9-29		OPA4	50/90	2.559	2.527	6.4	1.27	50
COx clay-rich unit	EST49093	-482m/V	COx1	50/100	2.383	2.262	16.2	5.35	75
COx transition unit	EST57262	-456m/V	COx2	80/298	2.400	2.291	15.1	4.76	72
COx carbonate-rich unit	EST51223	-444m/H	COx3	50/80	2.437	2.369	12.2	2.87	56
	EST52318	-437m/V	COx4	80/283	2.584	2.553	5.4	1.21	56
	EST52335	-445m/H	COx5	80/300	2.425	2.397	11.2	1.14	25
	EST52337	-445m/H	COx6	80/280	2.434	2.405	10.9	1.21	27

As observed in-situ at the Mont-Terri and Bure URLs (Bossart et al. 2017; Armand et al. 2014; De La Vaissiere et al. 2015), tensile fractures are mostly generated in the near-field close to the opening walls, which are responsible for highly increased hydraulic conductivity. For laboratory testing, such fractures were artificially created across the sample length by tensile loading or direct splitting. Figure 4-3 shows photos of the fractured samples with different fracture patterns in three groups.

Group 1: Three samples normal to bedding COx1, COx2 and OPA1 (D = 50 mm; L = 75-100 mm) were inserted in rubber jackets and then loaded along the sample axis up to create single major fracture parallel or subparallel to the length with a few minor fissures. The fracture aperture reached to 1-2 mm.

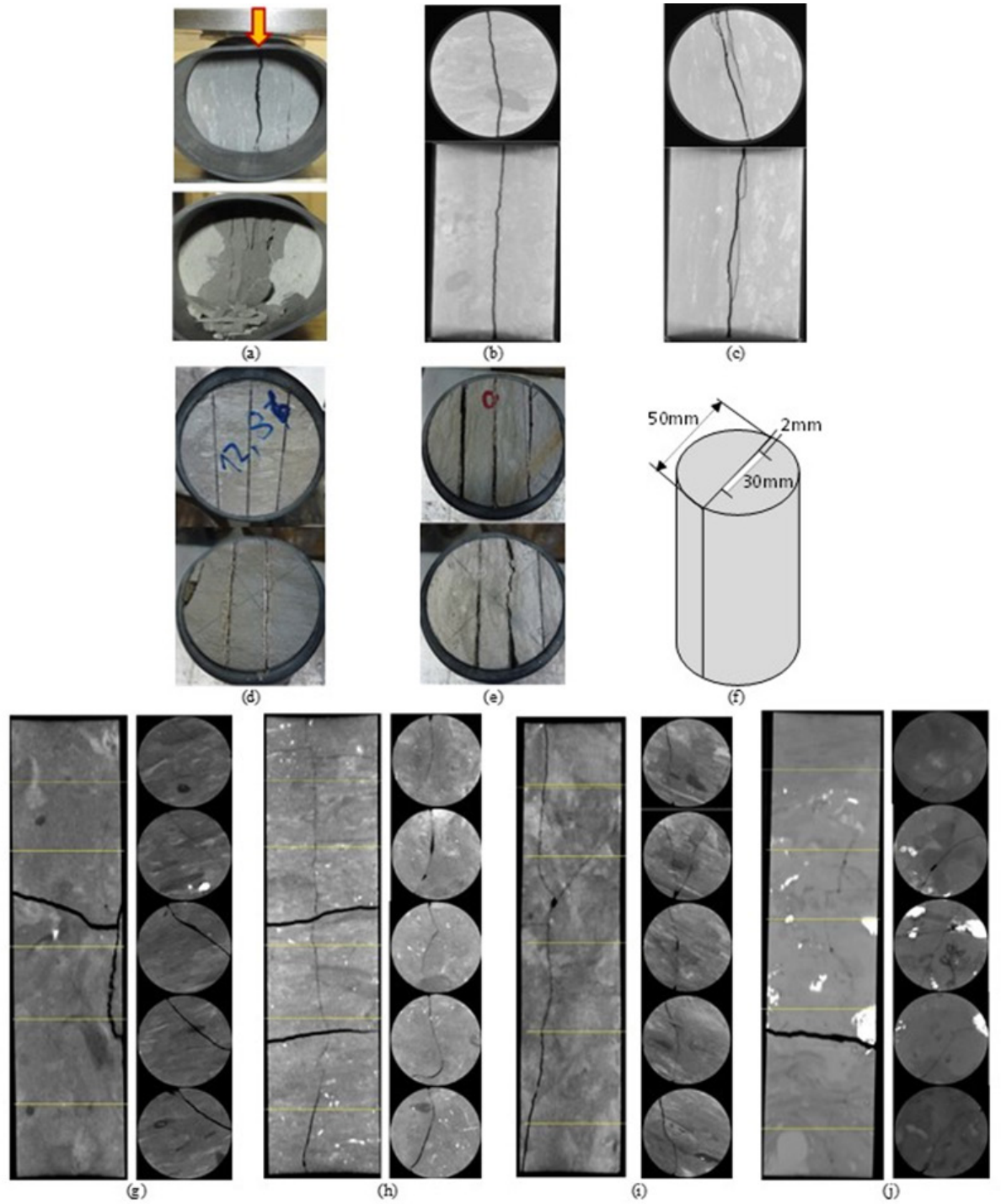

Figure 4-42 – Fracture patterns in the claystone samples illustrated with photos made before testing and CT images (Group 3) after testing: Group 1: (a) COx1, (b) COx3, and (c) OPA1; Group 2: (d) OPA2, (e) OPA3, and (f) OPA4; Group 3: (g) COx2 (D/L = 80/298 mm), (h) COx4 (D/L = 80/283 mm), (i) COx5 (D/L = 80/300 mm), and (j) COx6 (D/L = 80/280 mm).

Group 2: Three major fractures were generated in two samples normal to bedding OPA2 and OPA3 (D = 50 mm; L = 90 mm) subparallel to the length in distance of ~15 mm. The fracture aperture reached to 1-2 mm. However, a fracture in OPA2 was largely inclined and did not fully cross another end face. In another sample OPA4, a regular fracture was produced in a half-part by milling to a width of 30 mm and an aperture opening of 2 mm at the middle along the length.

Group 3: Four large samples COx2/4/5/6 (D = 79 mm; L = 280-300 mm) were used for examining scale effect on hydraulic conductivity of fractures. Fractures were created in each sample by pressing a steel wedge along the length to failure. Each of the samples was separated into several pieces with irregular shapes. The fracture surfaces are rough and nonplanar. The separated pieces were then assembled in rubber jackets but not matched well together. Note that the colour of sample COx4 with a higher density appeared light grey and might be dominated by carbonates.

Generally, most of the generated fractures with a wide aperture of 1–2 mm and high fracture density exhibited a similar scale of the in-situ macro-fractures near the rock walls but much larger micro-fractures than those in the deep areas of the EDZ as observed in the ULRs at Bure and Mont Terri (Armand et al., 2014; Hale et al., 2021). Furthermore, the artificially generated fractures in the samples are more intensively interconnected than the real fractures within the EDZ.

4.1.2 Experimental setups

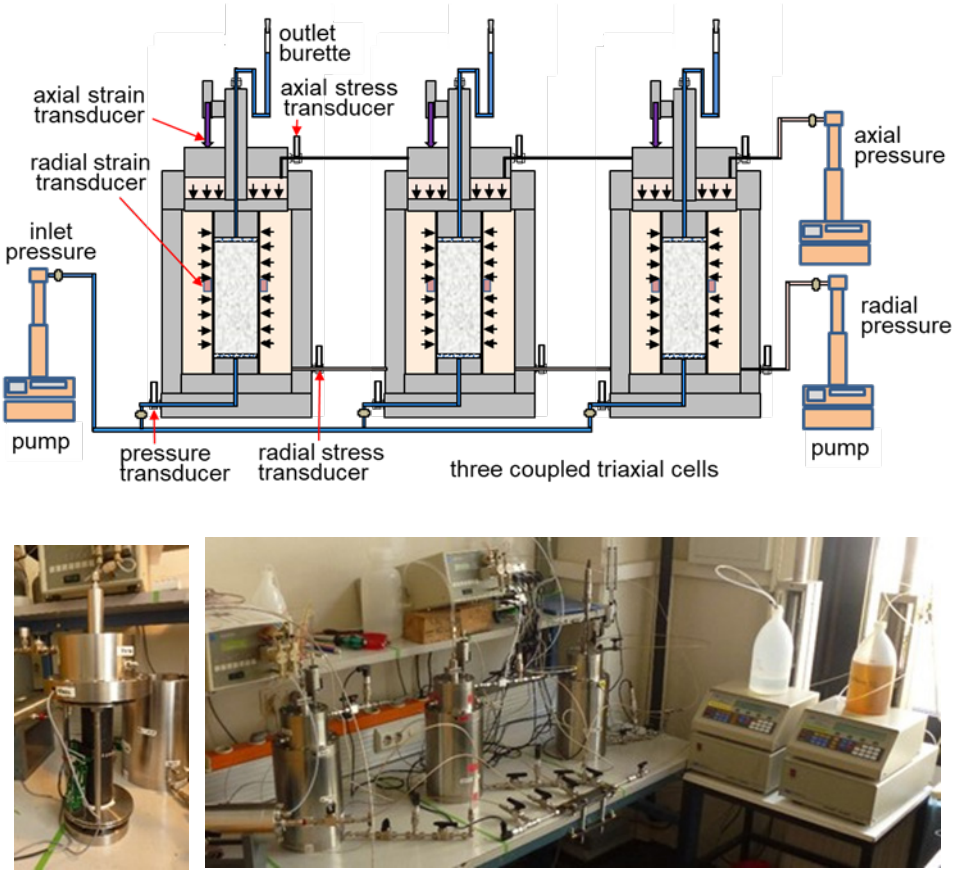

Figure 4-43 – Setups for testing of water and gas transport in fractured claystone samples under identical hydro-mechanical conditions: A setup with three triaxial cells for hydro-mechanical testing of three samples in parallel.

Two GRS designed setups were used for self-sealing tests on the fractured claystone samples. Figure 4-4 and Figure 4-5 illustrate the schematic assemblies of both setups. The first setup (Figure 4-4) consists of three triaxial cells and three samples can be tested simultaneously under identical conditions. The triaxial cells allow cylindrical samples of a diameter of 50 mm and different lengths of 70-120 mm. The samples were inserted in rubber jackets and loaded in individual cells at identical axial and radial stresses, which were controlled by two respective syringe pumps (Model 260D) with a maximum pressure limit of 50 MPa with accuracy of ±0.1% of readings. Another pump was installed for

injecting water or gas to the samples via inlet lines and sintered porous discs at bottom. A pressure sensor was installed for monitoring the inlet pressure of each sample. In order to avoid possible elution of fine-grained clay particles with water flow, specific filter papers are inserted in both interfaces between sample and porous discs. The fluid outflow is individually recorded at the top of each sample by means of burettes (with resolution accuracy of ±0.05 cm^3) at atmospheric pressure. During mechanical loading and fluid flow, axial deformation is recorded by a linear variable differential transducer (LVDT) installed outside at the top of each cell, while radial strain is measured by a circumferential extensometer mounted around the sample outside the jacket in the cell. The samples in group 1 and 2 (Figure 4-3a and Figure 4-3b) were tested using this setup.

Four large samples in group 3 (Figure 4-3c) were tested in a pressure vessel (Figure 4-5), which allows hydraulic testing of four samples in parallel under identical conditions. Each sample was inserted in a rubber jacket and between two sintered porous discs and two platens Filter papers were inserted in the end interfaces between sample and porous discs to avoid elution of fine clay particles with water flow. The assembled samples were compressed by a pressure/volume GDS-controller allowing a maximum pressure of 25 MPa. The fluid injection was controlled by using an syringe pump (Model 260D), while the fluid outflow is individually recorded at the opposite side of each sample by means of burettes (with resolution accuracy of ±0.05 cm^3) at atmospheric pressure.

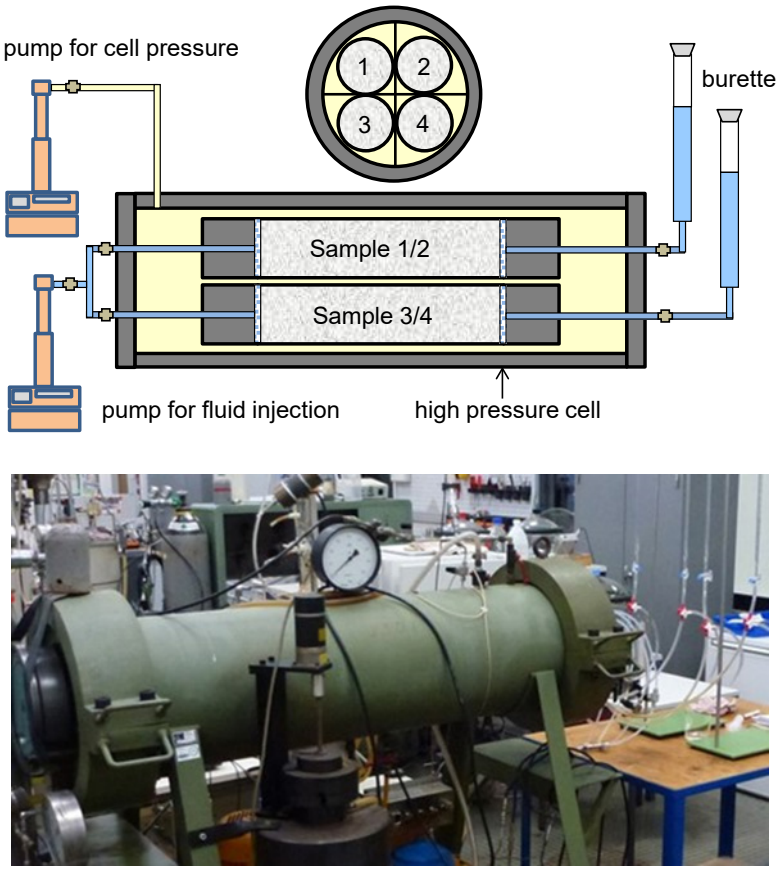

Figure 4-44 – Setups for testing of water and gas transport in fractured claystone samples under identical hydro-mechanical conditions: A pressure vessel for hydraulic testing of four samples in parallel

4.1.3 Testing protocol

Under consideration of the prevailing hydro-mechanical processes in the EDZ and the objectives of the present study, a general test procedure was performed on the fractured claystone samples in each group in three phases:

i. **Self-sealing:** The self-sealing of fractures created in the samples was measured by water permeability and fracture closure (partly in group 2) under confining stresses. Synthetic COx and OPA water were injected to the respective COx and OPA samples. The chemical compositions of the synthetic waters are summarized in Table 4-4, which were derived from the data of COx porewater (Andra 2005) and OPA porewater (Pearson 1999). The confining stress was stepwise increased up to 10 MPa (group 1), 8 MPa (group 2), and 4 MPa (group 3), during which the synthetic water was continuously injected to the samples at pressures of 0.1 – 1.0 MPa. Each load step lasted for a long period of 1 – 4 months. During steady-state water flow, apparent water permeability can be determined by Darcy's law:

$$K_w = \frac{Q_w \cdot \mu_w \cdot L}{A \cdot (P_i - P_o)} \qquad (4\text{-}1\text{-}1)$$

where K_w is the water permeability (m^2), Q_w is the water flow rate (m^3/s), μ_w is the dynamic viscosity of the synthetic water (a same value of 0.95×10^{-3} Pa·s for both COx and OPA waters), L is the sample length (m), A is the cross section of the sample (m^2), P_i and P_o are the inlet and outlet pressure (Pa) respectively.

ii. **Gas testing:** Following the water flow at the last load step, gas penetration testing was then undertaken. Firstly, an attempt was made to remove the water in the inlet and outlet reservoirs, but some water remained in very small pores of the sintered plates. Helium gas was injected into the inlet by stepwise increasing pressure with small increments of 0.1 – 0.2 MPa at time intervals of 1 – 3 days. As first gas bubbles were detected at the outlet side at atmospheric pressure, the gas pressure in the inlet was considered as the gas breakthrough pressure Pb. Beyond the breakthrough, the gas injection continued for determination of apparent gas permeability by Darcy's law:

$$K_g = \frac{2 \cdot Q_g \cdot \mu_g \cdot P_o \cdot L}{(P_i^2 - P_o^2) \cdot A} \qquad (4\text{-}1\text{-}2)$$

where K_g is the gas permeability (m^2), Q_g is the outflow rate of the gas (m^3/s), and μ_g is the dynamic viscosity of the helium gas (1.66×10^{-5} Pa·s), P_i and P_o are the inlet and outlet pressure (Pa) respectively.

iii. **Resealing**: In order to examine resealing capacity of gas-induced pathways, synthetic porewater was reinjected to the samples again. Water permeabilities before and after the gas flow were compared to highlight the gas impact on the self-sealing of fractures in the claystones.

iv. **Post-testing:** The samples was loaded down and dismantled. They were then confined in the rubber jackets and fixed in PVC tubes. The confined samples were scanned by μ-CT for visualization of the resealed fractures.

Table 4-14 – Main chemical components of the synthetic COx and OPA water in mmol/L

Component	Na	Cl	Mg	Ca	SO_4	K	Derived from
COx water	27.7	31.1	11.0	13.3	25.0	6.8	Andra (2005)
OPA water	24.0	30.0	16.9	25.8	14.1	1.6	Pearson (1999)

4.1.4 Experimental results

4.1.4.1 Self-sealing of fractures

Fracture closure

The fracture closure was measured by radial strain ε_r (sub)normal to the fracture planes along the sample axis. Figure 4-6 shows the typical process of fracture closure obtained on two fractured samples, OPA2 and OPA4, during water flow under multistep increased stresses, together with axial strain ε_a parallel to the fracture planes and water permeability K_w. As already shown in Figure 4-3d and f, OPA2 consisted of three axially (sub)parallel fractures with apertures of around 1 mm and around 15 mm apart of each other; and OPA4 had a regular fracture geometry with a length of 30 mm and a wide aperture of 2 mm along the axis.

Firstly, a low hydrostatic stress of 0.5 MPa was applied without water injection to stabilize the fracture structure. Over a month, the fractures gradually closed with time to ε_r = 0.1% at OPA2 and ε_r = 0.04% at OPA4, respectively. The closure of the regular fracture in OPA4 is limited because of the strong resistance of the wide pillars on both end sides. In contrast, the closure of the irregular fractures in OPA2 is larger due to effect of high stress concentration on smaller contacting areas between the rough fracture walls.

As the synthetic water was injected into the fractures, a rapid swelling took place in all directions to strains of $\varepsilon_a \approx \varepsilon_r \approx 0.2\%$ at OPA2 and 0.3% at OPA4, respectively. The radial swelling observed externally indicates high local swelling pressures acting in contact areas between rough fracture surfaces, which exceed the external stress. Furthermore, the fracture walls expanded into the non-stressed interstices. This was demonstrated by submerging a fractured disc in the synthetic water without mechanical loading (Figure 4-7a and b). The initial fracture opening of 2 mm was quickly filled by the swelling claystone in contact with water. The filling material became mud with low density and could be easily compacted under stress (Figure 4-7c). The subsequent increase of the hydrostatic stress to 2 MPa, 3 MPa, 4 MPa, 6 MPa, and 10 MPa resulted in higher normal compaction compared to the parallel one, $\varepsilon_r \approx 2\varepsilon_a$. Under each constant stress, the strains evolved gradually with decreased rates until stabilization occurred. In response to the longterm compaction over 1.7 years, the water permeability decreased by 3-4 orders of magnitude to low values of 9×10^{-20} m^2 at OPA2 and 1×10^{-17} m^2 at OPA4, respectively.

In order to examine shearing effect on the fracture sealing, a deviatoric stress was applied by decreasing the radial stress to zero and increasing the axial stress to 13 MPa, $\sigma_a - \sigma_r$ = 13 MPa. This caused shear fractures inclined to the axis at angles of 30°–35° (Figure 4-7d and e). The relative shear movements of the separated matrix blocks partly disconnected the gouge-filled fractures. The combined effects of local normal compaction to close fracture aperture, shear deformation to disconnect fracture network, and clay swelling/slaking to seal fracture void are illustrated in Figure 4-7f.

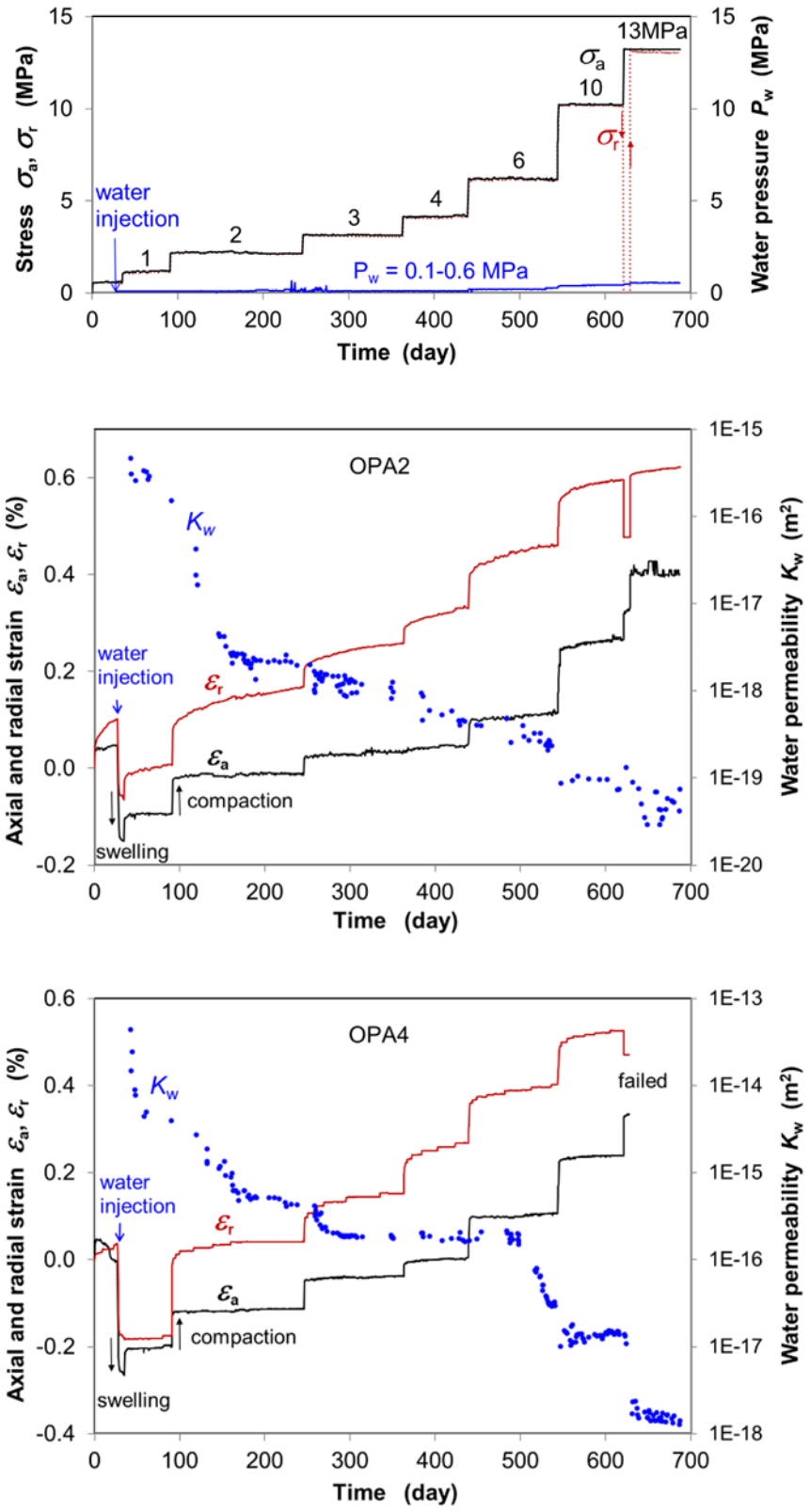

Figure 4-45 – Evolution of axial/radial strains and water permeability obtained on the sandy claystone samples OPA2 and OPA4 during water flow under stresses: (a) Applied confining stress and water injection pressure; (b) Resulted deformation and permeability change of OPA2; and (c) Resulted deformation and permeability change of OPA4.

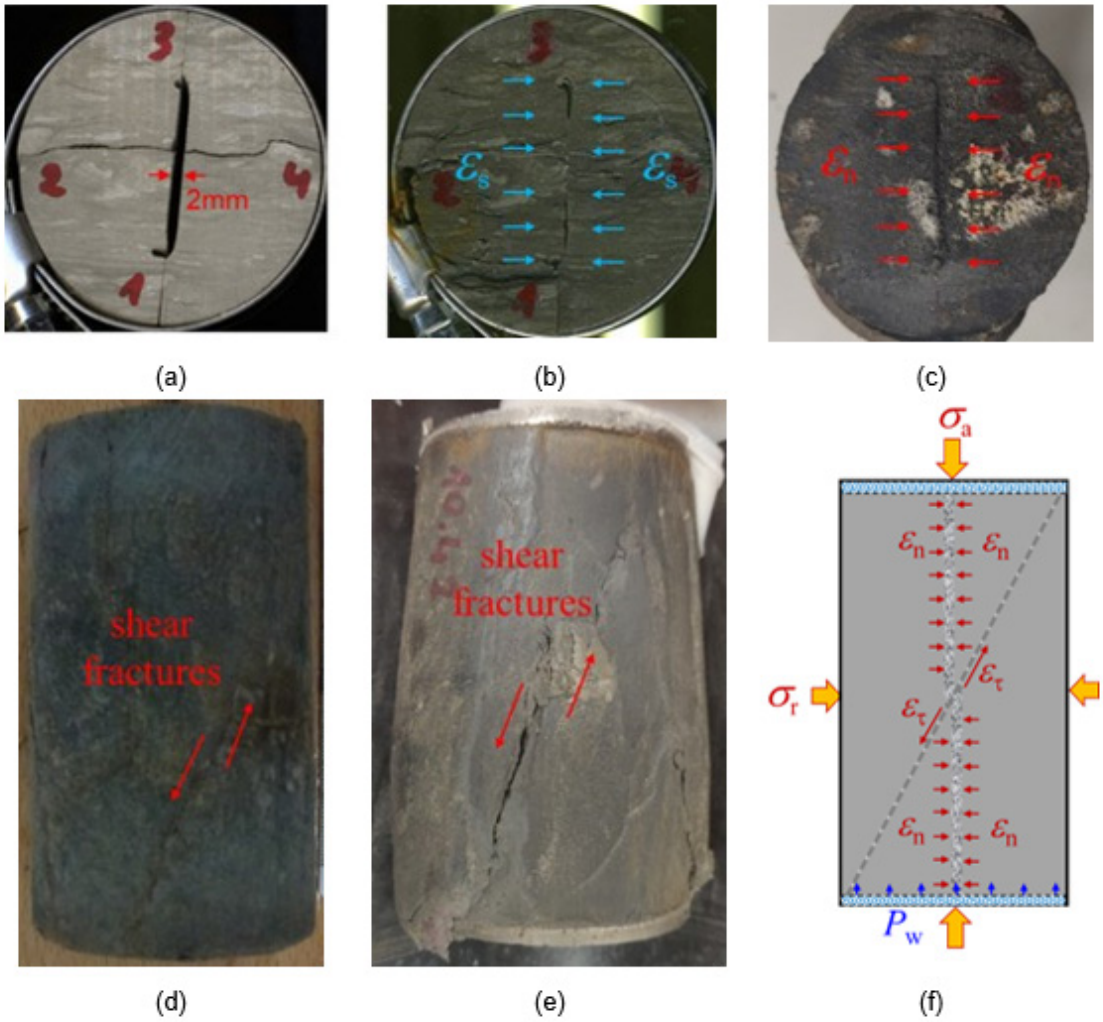

Figure 4-46 – Fracture sealing observed in the OPA sandy claystone samples under combined effects of water-induced swelling/slaking (ε_s), local normal and shear deformation (ε_n, ε_t) under hydrostatic and shear stresses: (a) A fracture of 2 mm opening in a sandy claystone sample OPA4; (b) Filling of the fracture by water-induced swelling/ slaking of fracture walls; (c) Normal compaction of the fracture under hydrostatic stress; (d) Shear fractures in (d) OPA2 and (e) OPA4 generated at a deviatoric stress of 13 MPa; and (e) Effects of normal and shear deformations and clay swelling on fracture sealing.

Water permeability

As a key parameter of fracture sealing, the water permeability of each fractured sample was measured during water injection under increased stresses. The results are depicted for selected samples in Figure 4-8.

Initially, the permeabilities of fractured samples were determined by gas injection at a pressure of 0.03 MPa and under the low stresses of 1 MPa for Groups 2 and 3 and 2 MPa for Group 1, respectively. High gas permeabilities were obtained (10^{-13}–10^{-12} m^2) for all samples. As soon as the water was supplied, the fracture walls were wetted and expanded into the interstices and clogged the pathways (Figure 4-7b). This significantly decreased the permeability by several orders of magnitude to low values of 10^{-18}–10^{-17} m^2 at the clay-rich facies of COx1 and COx2, 10^{-16}–10^{-14} m^2 at the sandy ones of OPA1-4, and 10^{-15}–10^{-13} m^2 at the carbonate-rich ones of COx3-6. The permeability reduction continued with

time to lower values of 10^{-18}–10^{-17} m^2 within 1-2 months for most samples. However, the carbonate-rich sample COx3 with a low clay content of 21% and two sandy ones OPA3 and OPA4 with high fracture intensities exhibited a limited permeability reduction to 10^{-15}–10^{-14} m^2. During further consolidation at higher stresses, COx3 and OPA3 showed some permeability fluctuations. The dropping might reflect local collapse of fracture walls and clogging of the pathway, and on the contrary, the rising might be caused by widening of some narrower pores due to possible erosion and movement of fine particles from the surfaces under relatively high injection pressures (P_w = 0.1–1 MPa). As mentioned earlier, the deviatoric stress applied to OPA2-4 in Group 2, sheared the matrix, disconnected the pathways locally, and hence decreased the permeability. Furthermore, by comparing the results from the different samples, more effects can be identified as follows.

- (1) Effect of mineralogical composition

The samples in Group 1 with similar initial fractures (Figure 4-3a-c) and under the same load conditions (Figure 4-8a) showed large differences in water permeability. K_w values of the COx1 are one and four orders of magnitude lower than those of the sandy OPA1 and the carbonate-rich COx3, respectively. This is also true for the large samples with high fracture intensities in Group 3 (Figure 4-8c), i.e., K_w values of the clay-rich COx2 being one order lower than those of the carbonate-rich COx4-6. As discussed above, the fracture sealing is determined mainly by the swelling capacity of the claystone, which is in turn determined by its clay content. The more clay content present the more water it can take up, leading to more swelling and slaking of the fracture walls and clogging the interstices more effectively.

- (2) Effect of fracture intensity

The OPA sandy samples in Groups 1 and 2 had been fractured to different geometries or intensities (Figure 4-3a-f). The water permeabilities of samples OPA3 with three parallel fractures and OPA4 with a wide aperture of 2 mm (Figure 4-8b) are 2-3 orders higher than those of the relatively less fractured ones, i.e., OPA1 with a single fracture (Figure 4-8a) and OPA2 with three, but one inclined to a dead end (Figure 4-8b). This demonstrates the significance of fracture intensity (density, aperture, connectivity, etc.) for the fracture permeability, particularly for the initial value. With water flow, the initial sharp fracture patterns tend to disappear to mud with more homogeneously redistributed micropores (Figure 4-7b). Further variation of the permeability with load is then more dominated by the consolidation of the mud and the stiffness of the surrounding claystone matrix.

- (3) Scale effect

A scale effect can be recognised by comparing the water permeabilities of the large samples COx4-6 with lengths (L) of 280-300 mm (Figure 4-8c) and the small one COx3 with L = 80 mm (Figure 4-8a) from the same borehole in the carbonate-rich unit. The large samples, even though more intensively fractured (Figure 4-3g-j), showed low Kw values of approximately 3×10^{-19} m^2 at a stress of 4 MPa, being four orders of magnitude lower than that of the small sample even at high stress up to 10 MPa. As mentioned earlier, the distribution of carbonates is heterogeneous, and appears in the form of bands on centimetre- to decimetre-scale (Figure 4-2). If a fracture network is distributed through both carbonate-rich and clay-rich regions, the self-sealing performance of the entire network is determined mainly by the clay-rich part of the network. Therefore, it is important to take representative sample sizes for laboratory tests and sufficiently large areas for field experiments to provide reliable data for the rock regions of interest, for instance, where seals will be constructed.

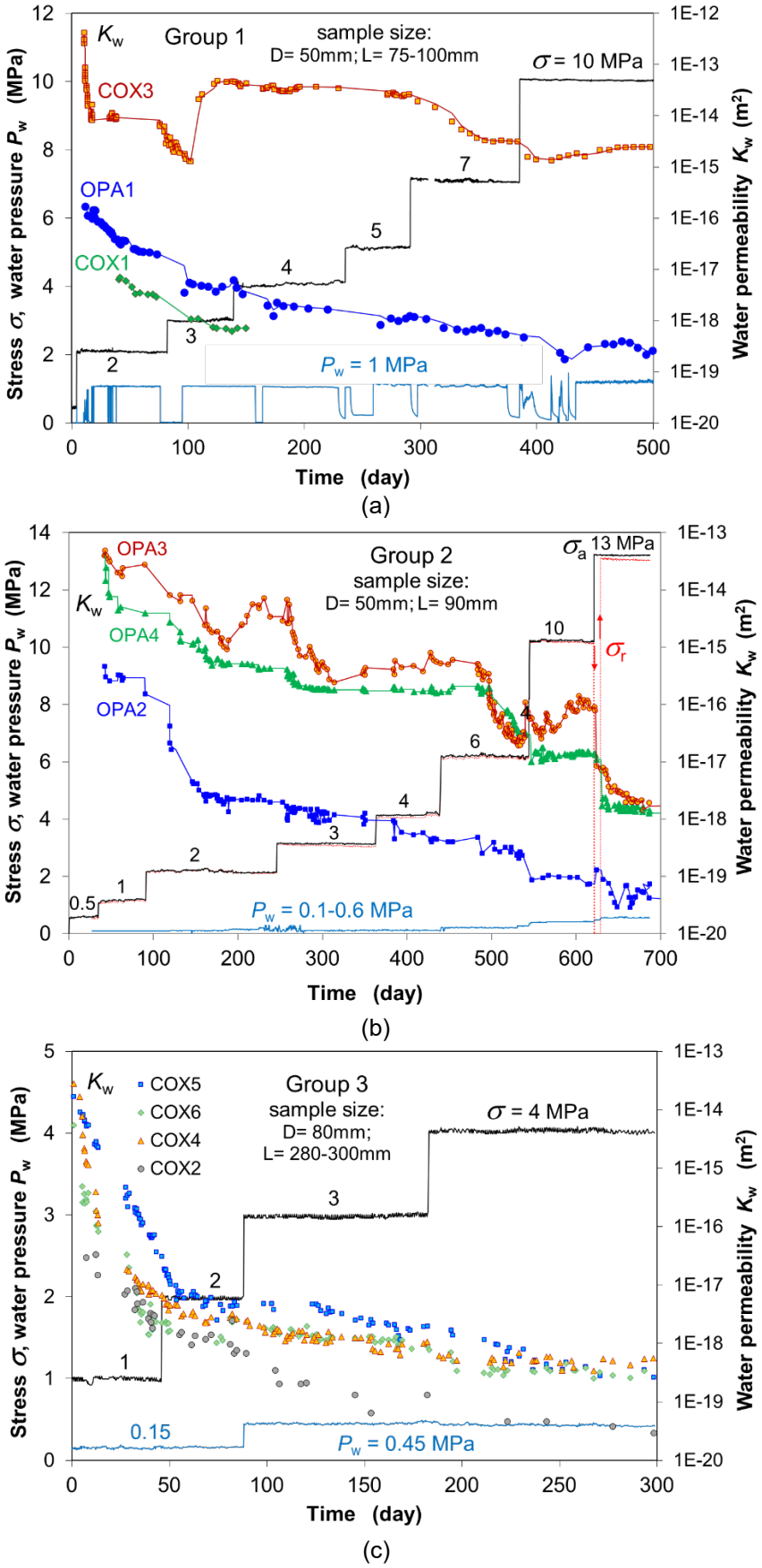

Figure 4-47 – Evolution of the water permeability measured on the fractured COx and OPA claystones during water injection under increased confining stresses: (a) group 1, (b) group 2, (c) group 3.

Stress dependence of fracture sealing

Two key parameters of the fracture sealing, i.e., fracture closure (or compaction) and water permeability, are strongly dependent on the applied stress. As a typical example, the radial and volumetric strains (ε_r, ε_v) and water permeabilities Kw obtained on samples OPA2 and OPA4 at the end of each load step (Figure 4-6) are depicted in Figure 4-9 as a function of effective hydrostatic stress ($\sigma_{eff} = \sigma - P_w/2$, where σ is the total stress). As mentioned earlier, the radial strain reflects the closure of fractures parallel to the sample axis. In the case of these tests, there were also some micro-fractures randomly distributed and connected to the fracture network. Therefore, the volumetric strain is also needed for characterizing the sealing of the fracture network. The measured data in Figure 4-9a and b show that the fracture closure (ε_r, ε_v) increases non-linearly and the associated water permeability decreases non-linearly with increasing effective stress. In fact, the water permeability is directly related to the fracture closure, which can be approximately approached by

$$K_w = K_{wi} \exp(-\alpha\, \varepsilon_r) \qquad (4\text{-}1\text{-}3)$$

where K_{wi} is the initial water permeability and α is a fitting parameter. The K_w–ε_r data in Figure 4-9c can be reasonably fitted by an empirical model with α = 8 and $K_{wi} = 8 \times 10^{-18}$ m^2 for OPA2 and α = 12 and $K_{wi} = 2 \times 10^{-14}$ m^2 for OPA4. The underestimation of the initial value for OPA2 is due to the lack of swelling/slaking effect at the beginning. A similar modelling result is also provided for the relation between water permeability and volumetric strain (K_w–ε_v) with α = 3 for OPA2 and α = 4.5 for OPA4 (Figure 4-9d).

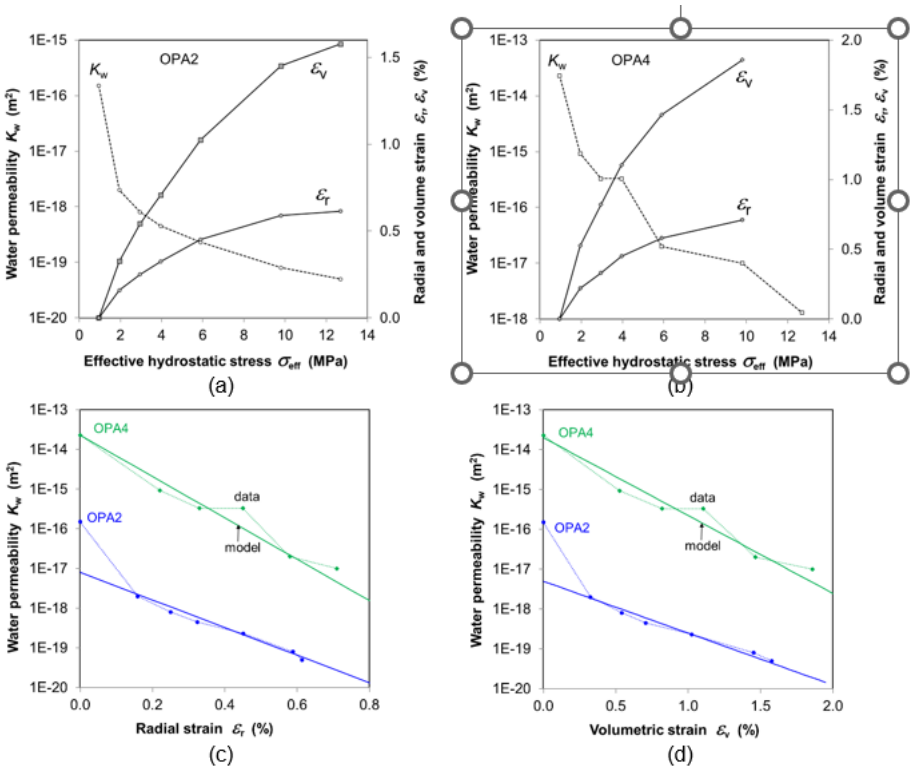

Figure 4-48 – Dependences of fracture closure (radial and volumetric compressions) and water permeability on effective hydrostatic stress: (a) OPA2 with a high initial fracture density and (b) OPA4 with a regular fracture aperture of 2 mm; water permeability in relation with (c) radial and (d) volumetric strain.

For purpose of comparison, the Kw data are summarised in Figure 4-10 as a function of the effective stress for most samples including the previous results from the clay-rich samples COx7-10 (Zhang, 2013). The data from samples COx3, OPA3 and OPA4 are not included because of the unrepresentative sample sizes and fracture intensities. The dependence of water permeability on effective stress can be approximated by

$$K_{\mathrm{w}} = K_{\mathrm{wo}} \exp(-\beta\, \sigma_{\mathrm{eff}}) \qquad (4\text{-}1\text{-}4)$$

where K_{wo} is the initial water permeability at zero effective hydrostatic stress (σ_{eff} = 0) and β is a parameter characterising the compressibility of the pathways.

As discussed above, the water-induced sealing of fractures and associated permeability reduction are strongly dependent on the clay content. As shown in Figure 4-10, the clay-rich COx samples exhibited low initial permeabilities of K_{wo} = 10^{-19}–10^{-17} m^2, lower than K_{wo} = 10^{-17}-10^{-16} m^2 of the carbonate-rich COx and the sandy OPA ones. The permeability values are consistent with the in-situ values of the EDZ observed in URLs at Bure and Mont-Terri (Bossart et al., 2004; de La Vaissiere et al., 2015). The slope of the $\log_{10} K_w$–σ_{eff} curve varies with mineralogical composition and fracture intensity, which is reflected by the parameter β ranging from 0.15 MPa^{-1} to 0.8 MPa^{-1} for the samples. A high value of β implies a high significance of the mechanical impact on the fracture sealing.

Generally, the test results from the representative samples showed significant self-sealing of fractures in the clay-, carbonate- and sand-rich claystones. Most of the fractured samples reached low water permeabilities of 10^{-18}-10^{-20} m^2 even at relative low stresses of 2-4 MPa. These values are relatively close to that of the intact claystone, determined to 4 × 10^{-21} m^2 on an intact clay-rich COx sample at a hydrostatic stress of 14 MPa and a pore pressure of 4.5 MPa, equivalent to the in-situ conditions expected for the potential repository in the COx formation. By extrapolation of the test data to the in-situ conditions, a complete recovery of the EDZ can be expected during a long-term consolidation phase of tens of thousands of years. This important conclusion needs to be further confirmed with more representative samples in size and fracture intensity like the EDZ.

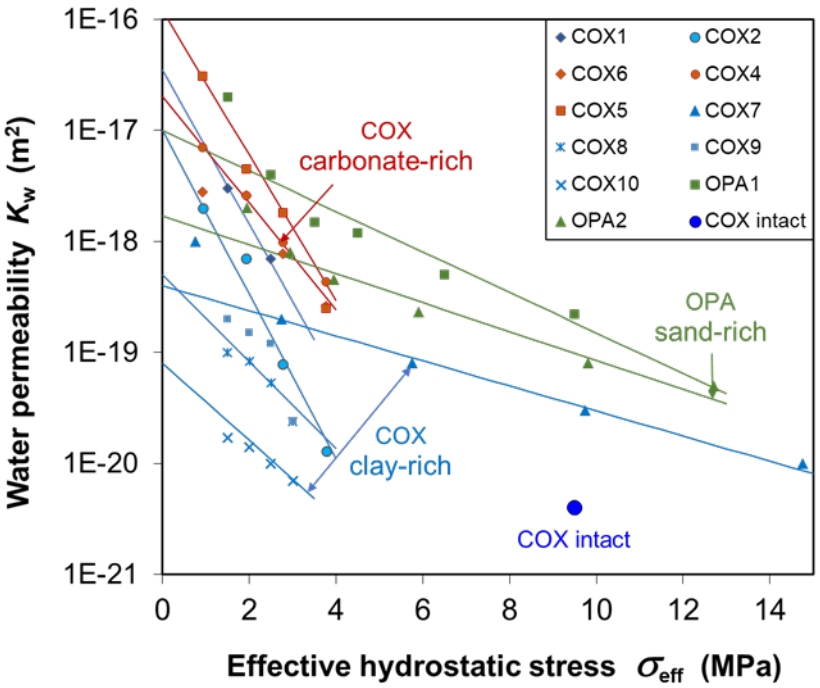

Figure 4-49 – Water permeabilities of the fractured claystone samples as a function of effective hydrostatic stress (blue colour for clay-rich COx, red for carbonate-rich COx, green for sandy OPA).

4.1.4.2 Gas penetration and impact

Gas testing followed the last consolidation stage at respective constant stress of 10 MPa, 13 MPa, and 4 MPa for the samples in groups 1-3 respectively, to investigate gas penetration through sealed fractures and recovery of gas-induced pathways. Results are illustrated in Figure 4-11-Figure 4-13.

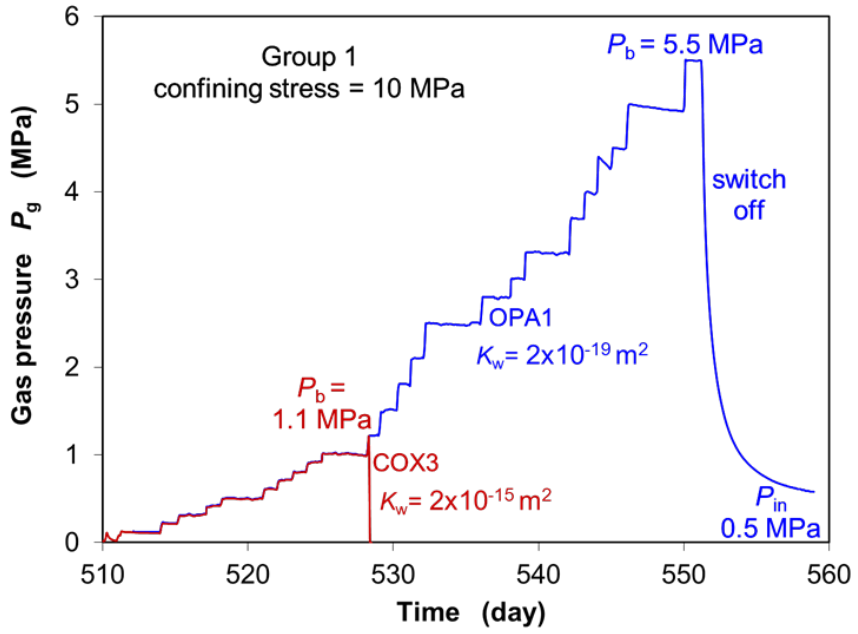

Figure 4-50 – Variation of gas breakthrough pressure of the samples in Group 1 at a hydrostatic stress of 10 MPa with time.

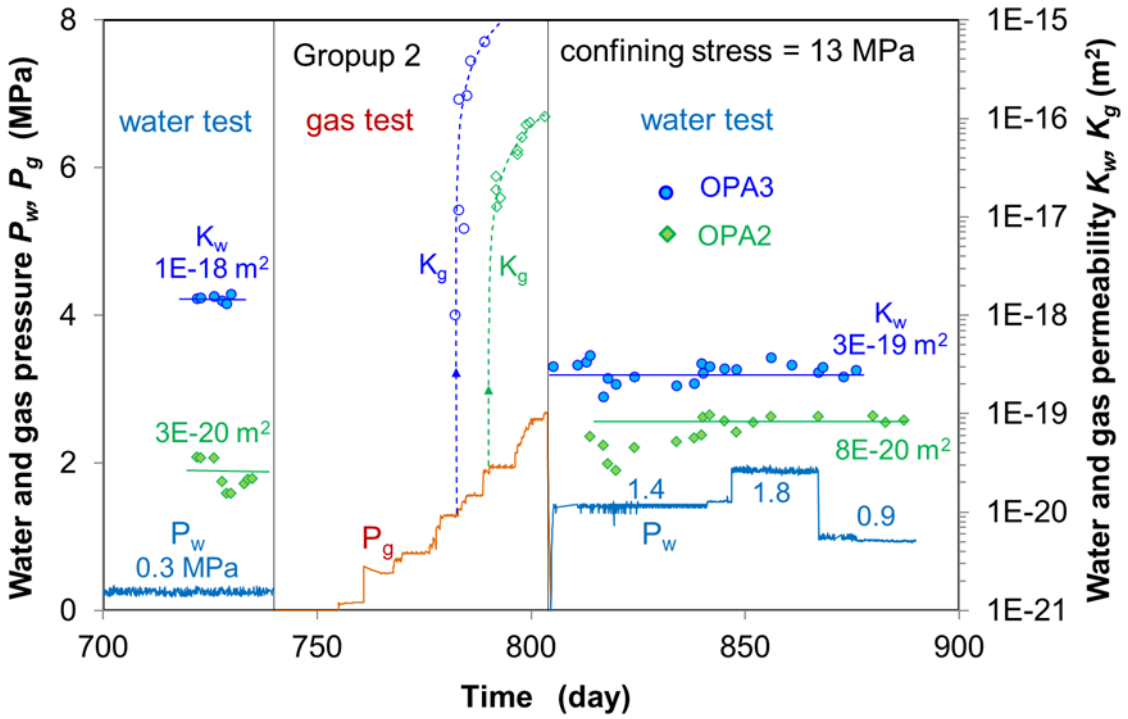

Figure 4-51 – Gas breakthrough pressures and permeability variations of the samples in Group 2 and resealing of gas pathways by water flow at a hydrostatic stress of 13 MPa.

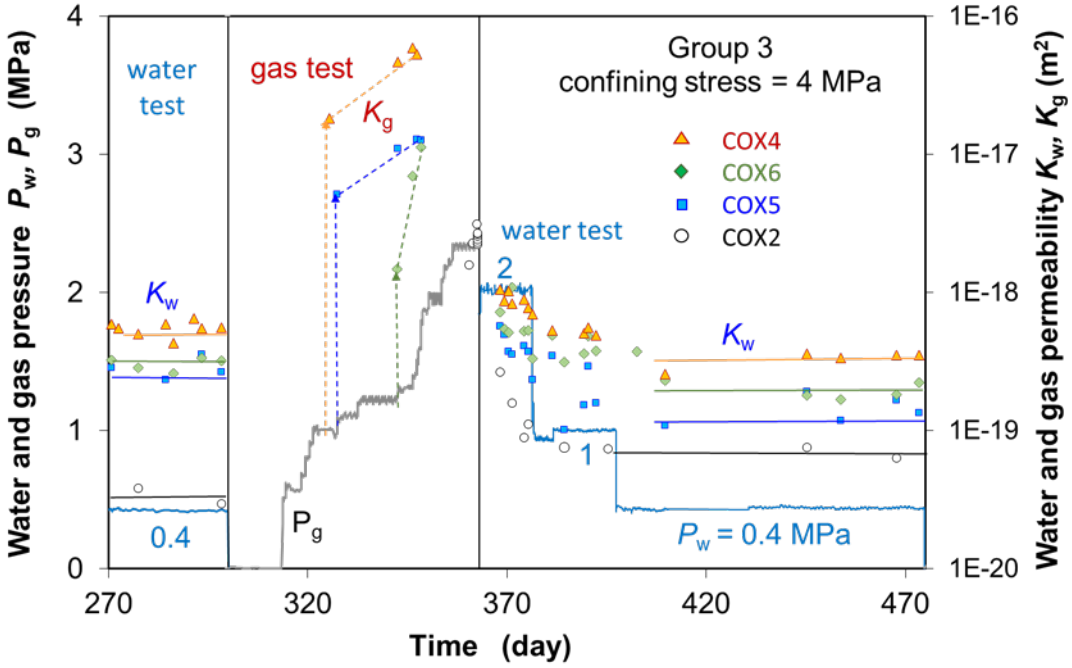

Figure 4-52 – Gas breakthrough pressures and permeability variations of the samples in Group 3 and resealing of gas pathways by water flow at a hydrostatic stress of 4 MPa.

Gas breakthrough pressure

The measured gas breakthrough pressures are summarised in Table 4-5. As mentioned above, the gas breakthrough pressure depends on the sealing intensity of the fractures, which can be represented by the intrinsic (water) permeability. Theoretical studies and experimental measurements on rock samples in laboratory and in different rock masses, such as plastic clay, indurated shale, limestone, anhydrite, and bedded salt (Volckaert et al., 1995; Horseman et al., 1996; Rodwell et al., 1999), suggest that P_b is reciprocally dependent on the cube root of water permeability K_w:

$$P_{\mathrm{b}} = B\ (K_{\mathrm{w}})^{-1/n} \qquad (4\text{-}1\text{-}5)$$

where B is a parameter; and n is a constant equal to 3. This relationship is also confirmed by previous experiments on the COx and OPA claystone samples with sealed fractures (Zhang, 2015). The gas breakthrough pressure is also related to the minimum principal stress σ_{min}:

$$P_{\mathrm{b}} = B\ (K_{\mathrm{wo}})^{-1/n} \exp(\lambda\ \sigma_{\mathrm{min}}) \qquad (4\text{-}1\text{-}6)$$

By fitting the present data in Table 4-4 and previous data in Zhang (2015), the parameters are obtained to be B = 3.5 × 10^{-7} MPa $m^{2/3}$, n = 3, λ = 0.2 MPa^{-1}, and K_{wo} varying from 8 × 10^{-20} m^2 to 1 × 10^{-17} m^2 (Figure 4-10). Figure 4-14 shows a reasonable agreement between the model curves and test data. Obviously, the gas breakthrough pressure increases with decreasing initial water permeability and increasing stress. This model can also capture the high gas breakthrough pressures of 10–12 MPa measured both on intact COx and OPA samples (Romero and Gómez, 2013; Harrington et al., 2017) and in the rock mass (de La Vaissiere et al., 2015). However, all the gas breakthrough pressures observed do not reach the gas fracturing threshold P_{fr} of the rocks:

$$P_{\mathrm{b}} < P_{\mathrm{fr}} = \sigma_{\mathrm{min}} + \sigma_{\mathrm{T}} \qquad (7)$$

where σ_T is the tensile strength of 1–2 MPa for the intact claystones (Bock et al., 2010). Because the gas breakthrough pressures of the sealed claystones are always lower than the intact ones, the EDZ, even when highly sealed, can still act as preferable pathways for gas release without compromising the integrity and barrier functions of the host COx and OPA formations.

Table 4-15 – Results of measured gas breakthrough pressure P_b, water permeability before (K_{wa}) and after (K_{wb}) gas penetration through the resealed claystone samples under various confining stresses σ.

Group No.	Sample	σ (MPa)	P_b (MPa)	K_{wa} (m^2)	K_{wb} (m^2)
1	COx3	10	1.1	2 × 10^{-15}	-
	OPA1	10	5.5	2 × 10^{-19}	-
2	OPA2	13	2	3 × 10^{-20}	8 × 10^{-20}
	OPA3	13	1.3	1 × 10^{-18}	3 × 10^{-19}
3	COx2	4	2.3	3 × 10^{-20}	6 × 10^{-20}
	COx4	4	1	6 × 10^{-19}	3 × 10^{-19}
	COx5	4	1.1	3 × 10^{-19}	1 × 10^{-19}
	COx6	4	1.2	3 × 10^{-19}	2 × 10^{-19}

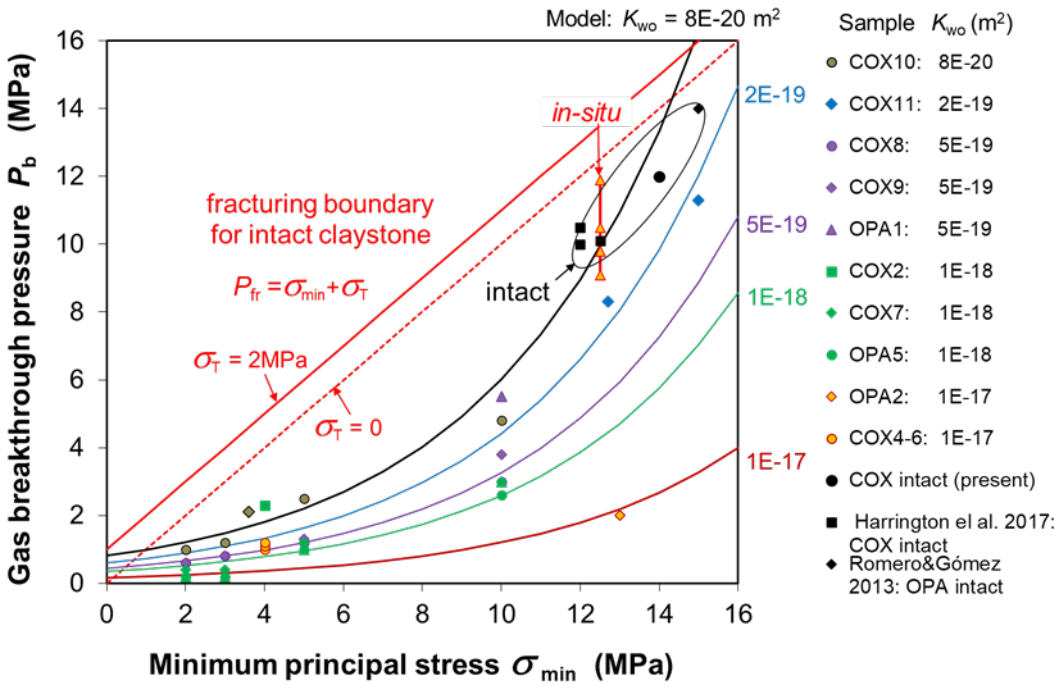

Figure 4-53 – Gas breakthrough pressures of the resealed and intact claystones as a function of minimum principal stress and initial water permeability.

Recovery of gas-induced pathways

Recovery of gas-induced pathways was examined by measuring water permeability and comparing with to before gas penetration. The measurements were carried out at different injection pressures: P_w = 1.4 MPa, 1.8 MPa, and 0.9 MPa for OPA2 and OPA3 (Figure 4-12); and P_w = 2 MPa, 1 MPa, and 0.4 MPa for COx2 and COx4-6 (Figure 4-13). The injection pressures applied are significantly higher than the previous ones (0.3–0.4 MPa) before gas penetration. All samples exhibited low values of $K_w = 5 \times 10^{-19}$–3×10^{-20} m². Most samples (OPA3, COx4-6) showed some reduction of water permeability after gas penetration than before. This suggests that the gas-induced pathways were more consolidated with time or residual gas blocks the pores, entailed by a reduced effective water permeability. Only the strongly resealed samples (OPA2, COx2) showed a slight increase of K_w after gas penetration. This can be attributed to dilatancy effect induced by the applied high injection pressures. The dilatancy effect decreases with decreasing injection or pore pressure (Figure 4-13). Generally, the results indicate a significant recovery of gas-induced pathways in the studied claystones.

Long-term gas migration

In order to understand long-term gas migration through the resealed pathways, gas was injected simultaneously into the resealed gas pathways in the four large samples COx2 and COx4-6 for longer time periods. Figure 4-15 and Figure 4-16 show the evolution of the inlet gas pressure and outflow rates of the samples as “a whole resealed EDZ” during the first and second injection phases of more than two months each, respectively. The confining stress was kept at 4 MPa.

During the first phase, the gas pressure P_{gi} was stepwise increased with a controlled gas inflow rate of 0.04 ml/min. At P_{gi} = 1.3 MPa, gas outflow was firstly detected on samples COx2 and COx 5-6 (point A in Figure 4-15a). With gas escape, the pressure dropped down slightly. The pressure rising/dropping repeated sequentially to the next higher peaks of 1.5 and 1.8 MPa. From the maximum, the pressure

dropped down to approximetaley 0.9 MPa due to a quicker release of gas. After a subsequent slight pressure increase, a breakthrough occurred at the last sample COx4 (point D in Figure 4-15b) with very quick gas release. This resulted in a further reduction of the gas pressure to a low level of 0.23 MPa over ~5 days. After shutting off the inlet, the gas pressure decreased to a low constant shut-in pressure of 0.14 MPa.

The second gas injection followed in the same way (Figure 4-16), yielding a maximum breakthrough pressure of 1.1 MPa, at which a rapid gas outflow was recorded at COx2. During the relaxation of the gas pressure, gas outflow was sequentially detected at COx6 at P_{gi} = 0.7 MPa, COx5 at P_{gi} = 0.4 MPa and COx4 at P_{gi} = 0.3 MPa. As the pressure reached at the minimum of 0.23 MPa, it increased slowly again to a constant at 0.25 MPa. The following shut-off led to a pressure decrease to 0.16 MPa.

The test data indicate that the advective movement of gas through the resealed samples varies temporally and spatially, reflecting unstable pathways with multiple opening/sealing processes. The question if a steady gas flow will be reached over the much longer time periods and repository conditions, still needs to be answered in the future.

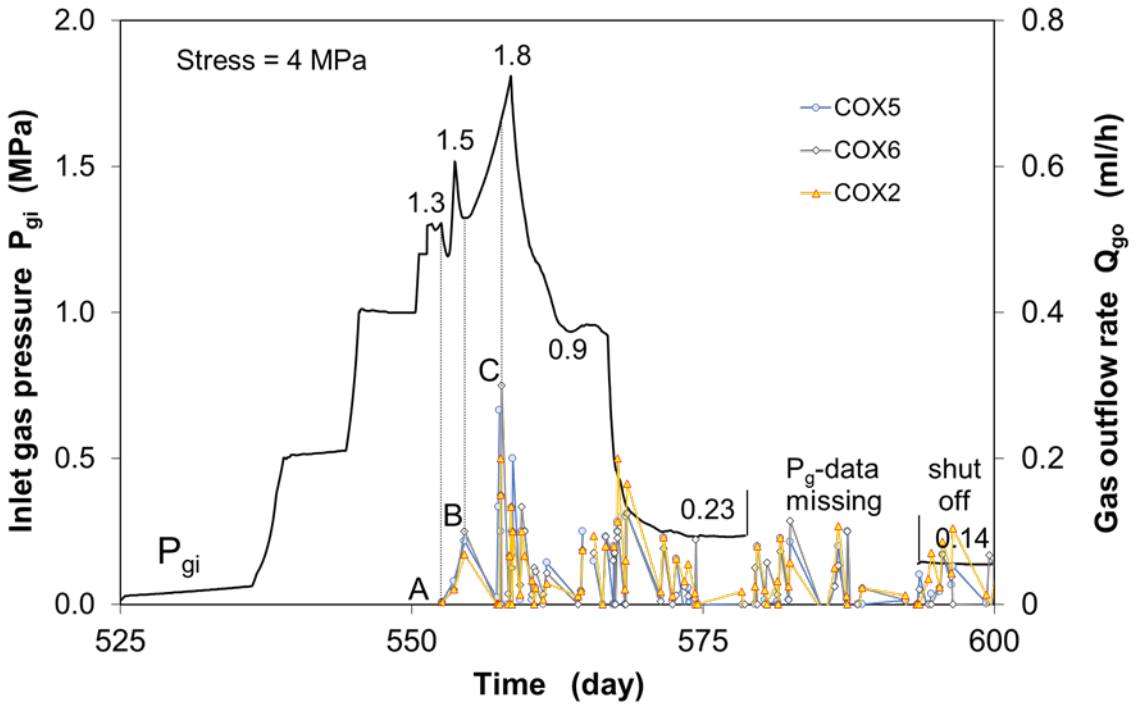

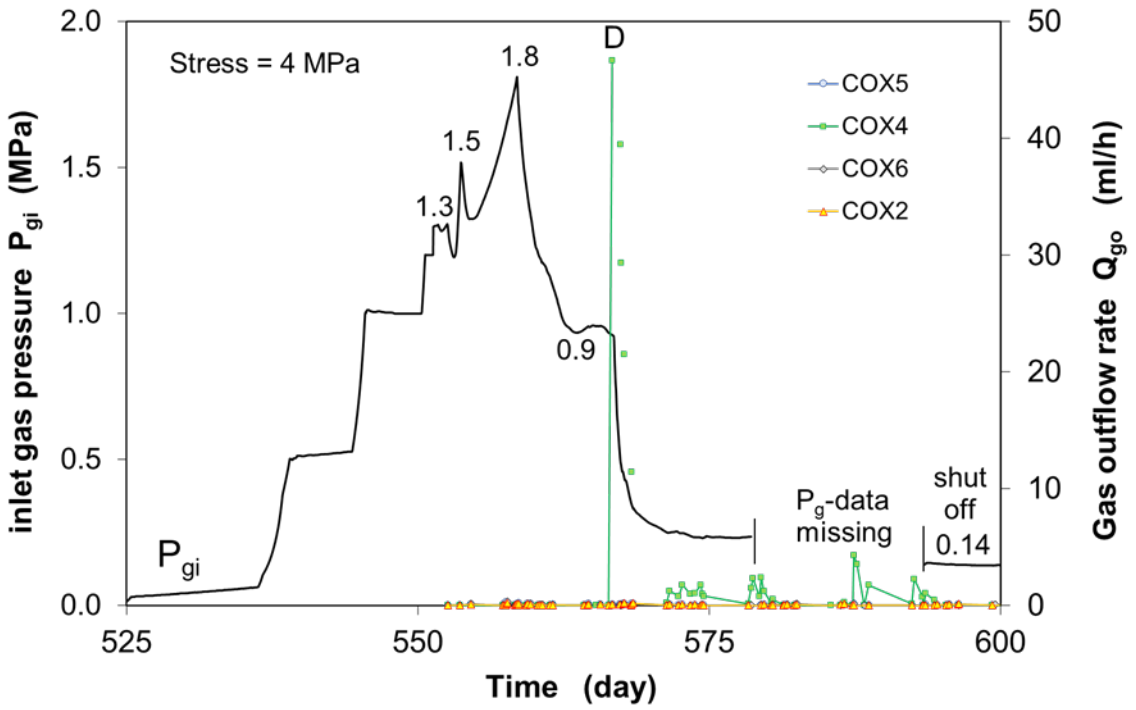

Figure 4-54 – Long-term evolution of the inlet gas pressure and outflow rates obtained on the fractured resealed COx samples during the first phase.

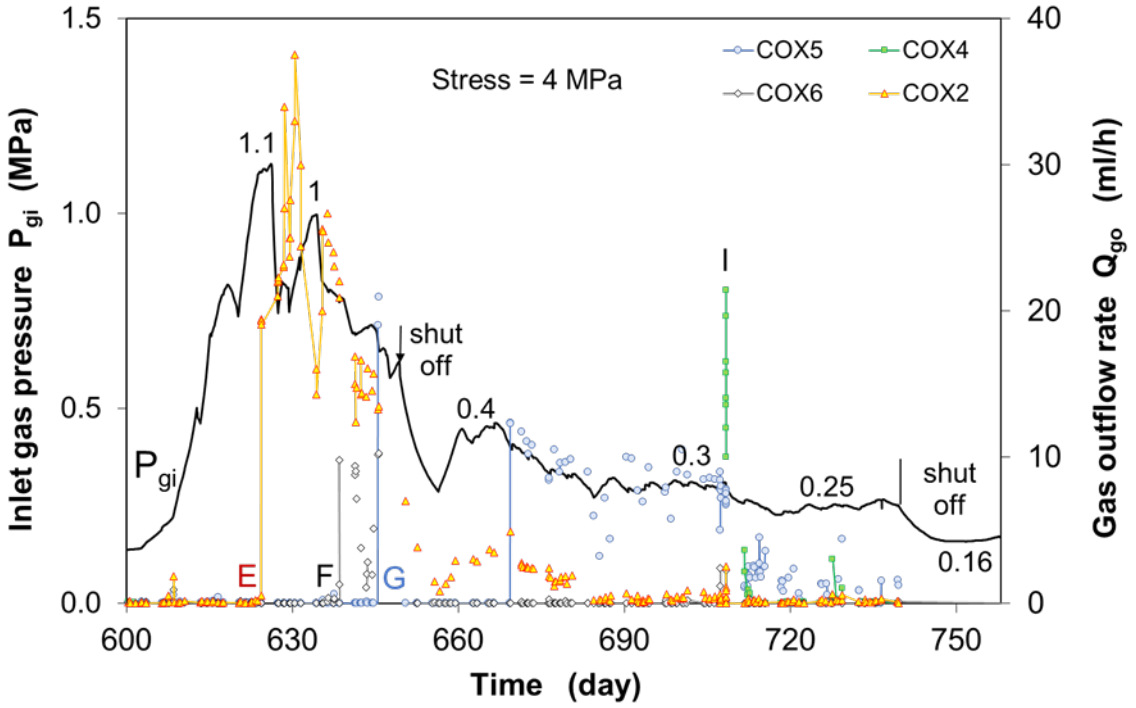

Figure 4-55 – Long-term evolution of the inlet gas pressure and outflow rates obtained on the fractured resealed COx samples during the second phase.

4.1.5 Summary

The experiments aimed to investigate a) self-sealing of fractures in the indurated COx and OPA claystones under the prevailing repository conditions, b) gas transport in water-saturated/compacted fractures, and c) resealing of gas-induced pathways. The samples were extracted from four lithological facies with different mineralogical compositions and petrophysical properties: COx clay-rich, transition and silty-carbonated units, and OPA sandy facies. Fractures were artificially created by tensile loading or direct splitting along the sample length to different intensities, including single and multiple subparallel fractures in six normal samples (D = 50 mm; L = 75-100 mm); and irregularly distributed fractures in four large samples (D = 80 mm; L = 280-300 mm). The artificially created fractures with high interconnectivity represent the realistic EDZ-fractures near the rock walls. The large samples were used for the examination of scale effects due to the heterogeneous distribution of the mineralogical components in the formations.

Two specific setups were developed and used for parallel testing on the samples under identical boundary conditions. One consists of three coupled triaxial cells for the normal samples, whereas another one is a pressure vessel for the four large samples. Long-term tests were undertaken following a common procedure with four sequential phases to examine: 1) self-sealing of fractures by injection of synthetic COx and OPA water under stepwise increased confining stresses over 1–2 years; 2) gas transport process along the water-saturated/compacted fractures; 3) resealing of gas-induced pathways under stress and water flow; and 4) visualisation of the resealed fractures by CT scanning the dismantled samples.

The self-sealing of fractures was measured by fracture closure, water permeability, and gas breakthrough pressure. Test results were analyzed concerning different influence factors such as mineralogical composition, sample size, fracture intensity, water or gas injection pressure, and confining stress. Some important phenomena were observed during the tests.

The studied COx and OPA claystones have sufficient self-sealing capacities, which increase with content of clay minerals. Under combined impact of mechanical compression and clay swelling, the fractures tend to seal to low water permeabilities of 10^{-18} – 10^{-20} m^2 being close to that of the intact rock. The fracture sealing intensity that is characterised by water permeability is dependent on the mineralogical composition, initial fracture intensity, effective confining stress, and load duration. A significant scale effect was also observed. The large samples of the COx carbonate-rich unit showed about four orders lower water permeabilities than that of the small sample. This is because the sealing of the fracture network is dominated by the clayey matrix and not by the carbonate bands distributed in the large samples.

The sealed fractures become gas-tight at certain pressures. Gas flow requires excessive pressures. The gas breakthrough pressure depends on the fracture sealing intensity (water permeability) and the effective confining stress. The more sealed fractures, the higher the gas breakthrough pressure. The gas breakthrough pressures of the sealed fractures are lower than that of the intact samples. This implies that the EDZ, even highly consolidated, can still act a preferable route for gas release without compromising the integrity of the host rock. No macro-fractures were observed by the gas injection tests. The gas flow process recorded varies temporally and spatially, reflecting unstable pathways with multiple opening/sealing cycles. When water is injected again, the gas-induced pathways tend to reseal.

4.1.6 Key learning points

4.1.6.1 New knowledge acquired

The studied COx and OPA claystones with the different mineralogical compositions and properties have favourable self-sealing capacities for the long-term isolation of radioactive waste. The self-sealing

capacity of the clay-rich claystone is higher than that of the carbonate-rich and sandy ones. Based on the test data, a relationship of fracture water permeability to confining stress is derived. A significant scale effect is observed due to the heterogeneous distribution of the mineralogical components, particularly clay minerals.

Based on the test data obtained on the fracture-sealed and intact samples, a relationship is established for the gas breakthrough pressure with the fracture sealing intensity (water permeability) and the effective confining stress. All the gas breakthrough pressures observed are lower than the applied confining stresses. The gas transport in the sealed fractures is a dynamic process with unstable flow due to pathway opening/sealing effects. Water injection can seal the gas-induced pathways to the same low water permeability as before gas injection.

4.1.6.2 Impact of acquired knowledge

The self-sealing tests provide meaningful evidence of favourable self-sealing potential of the studied claystones (COx clay-rich, transition and silty-carbonated units, and OPA sandy facies). The excavation generated fractures in the clay rocks can self-seal under the combined impacts of mechanical consolidation and clay swelling resulting in low water permeabilities close to that of intact material.

The gas injection tests indicate that a) no macro-fractures will be created in the host rocks by gas pressures generated in the repositories, b) the EDZ can still act a preferable route for gas release, and c) the gas-induced pathways can reseal again when water flows through.

4.1.6.3 Remaining knowledge gaps

While the high self-sealing capacity of the claystones with high clay contents is largely documented, knowledge about the self-sealing behavior of fractures in carbonate and quartz-rich claystones is still limited.

The durations of the gas injection tests performed are still not long enough to observe and understand the long-term gas transport process in the fracture-sealed and intact claystones.

The transferability of the test results at laboratory scale to in-situ conditions (EDZ around underground structures, fractured rock mass) is a pending issue.

4.1.6.4 Recommendations for the future

More precise experiments are needed to confirm the obtained results and to consolidate the established data base. Aspects to address are (i) the self-sealing of the fractures (fracture water permeability) related to the confining stress, (ii) the gas breakthrough pressure related to the fracture water permeability and confining stress.

Because of the influences of mineralogical composition, distribution and fracture intensity on the self-sealing and gas transport properties, the hydraulic properties of the EDZ may vary locally. To date, it is also not well understood how the fractures in the EDZ are interconnected, particularly in direction along the tunnel. If the fractures in some regions are not or less interconnected, the hydraulic conductivity may be lower than elsewhere. Therefore, upscaling tests to large scale EDZ experiments typical of locations around and along a gallery need to be performed to verify this and to evaluate the barrier effects of the EDZ in a repository.

4.1.7 References

Andra, DOSSIER 2005, Synthesis–Evaluation of the feasibility of a geological repository in an argillaceous formation, https://international.andra.fr/sites/international/files/

Armand, G., Leveau, F., Nussbaum, C., de La Vaissiere, R., Noiret, A., Jaeggi, D., Landrein, P., Righini C., 2014. Geometry and properties of the excavation-induced fractures at the Meuse/Haute-Marne URL drifts. Rock Mech. Rock Eng. 47 (1), 21-41.

Bock, H., Dehandschutter, B., Martin, C.D., Mazurek, M., de Haller, A., Skoczylas, F., Davy, C., 2010. Self-sealing of fractures in argillaceous formations in the context of geological disposal of radioactive waste–Review and synthesis. NEA Report No. 6184. OECD.

Bossart, P., Trick, T., Meier, P.M., Mayor, J.C., 2004. Structural and hydrogeological characterisation of the excavation-disturbed zone in the Opalinus Clay (Mont Terri Project, Switzerland). Appl. Clay Sci. 26 (1-4), 429-48.

Bossart, P., Jaeggi, D., Nussbaum, C., 2017. Experiments on thermo-hydro-mechanical behaviour of Opalinus Clay at Mont Terri rock laboratory, Switzerland, J. Rock Mech. Geotech. Eng. 9 (2017), 502-510.

Conil, N., Talandier, J., Djizanne, H., de La Vaissière, R., Righini-Waz, C., Auvray, C., Morlot, C., Armand, C., 2018. How rock samples can be representative of in-situ condition: a case study of Callovo-Oxfordian claystones, J. Rock Mech. Geotech. Eng. 10 (2018), 613-623.

De La Vaissiere, R., Armand, G., Talandier, J., 2015. Gas and water flow in an excavation-induced fracture network around an underground drift: A case study for a radioactive waste repository in clay rock, Journal of Hydrology 521 (2015), 141–156.

EURAD Milestone 58, 2020. Interim Experimental Design Report comprising a revised detailed work programme of SubT 3.1, 3.2 and 3.3.

EURAD Milestone MS 124, 2021. Progress Report of Experimental Design comprising a revised detailed work programme of SubT 3.1 and 3.2.

Harrington, J.F., Cuss, R.J, Talandier, J., 2017. Gas transport properties through intact and fractured Callovo-Oxfordian mudstones. Geol. Soc. Spec. Publ. 454 (1), 131–154.

Horseman, S.T., Higgo, J.W., Alexander, J., Harrington, J.F., 1996. Water, Gas and Solute Movement through Argillaceous Media. Report CC-96/1. Nuclear Energy Agency.

Houben, M.E., Desbois, G., Urai, J., 2014. A comparative study of representative 2D microstructures in Shaly and Sandy facies of Opalinus Clay (Mont Terri, Switzerland) inferred form BIB-SEM and MIP methods. Mar. Pet. Geol. 49 (2014) 143-161.

Kaufhold, A., Gräsle, W., Plischke, I., Dohrmann, R., Siegesmund, S., 2013. Influence of carbonate content and micro fabrics on the failure strength of the sandy facies of the Opalinus Clay from Mont-Terri (Underground Rock Laboratory). Eng. Geol. 156, 111-118.

Mazurek, M., Gautschi, A., Marschall, P., Vigneron, G., Lebon, P., Delay, J., 2008. Transferability of geoscientific information from various sources (study sites, underground rock laboratories, natural analogues) to support safety cases for radioactive waste repositories in argillaceous formations. Phys. Chem. Earth 33, 95-105.

Pearson, F.J., Arcos, D., Bath, A., Boisson, J.Y., Fernandez, A.M., Gäbler, H.E., Gaucher, E., Grifault, L., Hernan, P., Waber, H.N., 2003. Mont Terri Project–Geochemistry of Water in the Opalinus Clay formation at the Mont Terri Rock Laboratory, Reports of the FOWG, No. 5, Bern.

Rodwell, W.R., Harris, A.W., Horseman, S.T., Lalieux, P., Müller, W., Ortiz, A.L., Pruess, K., 1999. Gas Migration and Two-Phase Flow through Engineered and Geological Barriers for a Deep Repository for Radioactive Waste. A Joint EC/NEA Status Report, European Commission, EUR 19122 EN.

Robinet, J.C., Sardini, P., Siitara-Kauppi, M., Pret, D., Yven, B., 2015. Upscaling the porosity of the Callovo-Oxfordian mudstone from the pore scale to the formation scale; insights from the 3H-PMMA autoradiography technique and SEM BSE imaging. Sediment. Geol. 321, 1–10.

Romero, E. and Gómez, R., 2013. Water and air permeability tests on deep core samples from Schlattingen SLA-1 borehole. Nagra Arb. Ber. NAB 13-51. Nagra, Wettingen, Switzerland.

Volckaert, G., Ortiz, L., de Canniere, P., Put, M., Horseman, S.T., Harrington, J.F., Fioravante, V., Impey, M.D., 1995. MEGAS–Modelling and Experiments on Gas Migration in Repository Rocks, Final Report Phase 1, European Commission Report EUR 16235 EN.

Zhang 2010, C.L., Wieczorek, K., Xie, M.L., 2010. Swelling experiments on mudstones, J. Rock Mech. Geotech. Eng. 2 (1), 41-47.

Zhang, C.L., 2013. Sealing of Fractures in Claystone. J. Rock Mech. Geotech. Eng. 5, 214-220.

Zhang, C.L., 2015. Investigation of gas migration in damaged and resealed claystone. In: Shaw, R.P. (Ed.), Gas Generation and Migration in Deep Geological Radioactive Waste Repositories, pp. 75-93.

Zhang, C.L., 2017. Response of clay rock to moisture change. In: Ferrari, A., Laloui, L. (Eds.), Advances in Laboratory Testing and Modelling of Soils and Shales (ATMSS). Springer Nature, New York City, NY, USA.

Zhang, C.L., Komischke, M., Kröhn, M., Rogalski, A., Zehle, B., 2019. Experimental Study of the Mechanical Behaviour of the Sandy Facies of Opalinus Clay at Mont Terri, LT-A Program within the Mont-Terri-Project, Gesellschaft für Anlagen- und Reaktorsicherheit (GRS), Braunschweig, GRS-555.

Zhang, C.L. and Laurich, B. 2020. Mechanical behavior of sandy facies of Opalinus Clay under different load conditions. Journal of Rock Mechanics and Geotechnical Engineering 12.

Zhang, C.L. and Talandier, J., 2022. Self-sealing of fractures in indurated laystones measured by water and gas flow, J. Rock Mech. Geotech. Eng., https://doi.org/10.1016/j.jrmge.2022.01.014.

4.2 Visualisation of gas transport in fractures and impact on their self-sealing capacity – (CNRS - ULorraine)

The Callovo-Oxfordian (COx) Claystone in Meuse/Haute-Marne is the selected host rock for the underground disposal of radioactive waste by Andra, due to its radionuclide retention properties, its low permeability (Grgic et al. 2023; Escoffier et al. 2005; Homand et al. 2004), and its self-sealing properties (Agboli et al. 2023; Giot et al. 2019). In the current design of the disposal project of Andra (Cigéo), the high-level waste will be emplaced in horizontal micro-tunnels excavated in the rock located at a depth of 500 m. The excavation of galleries or micro-tunnels in the rock creates a fractured zone around them in the near field called Excavation Damaged Zone (EDZ). This network of cracks leads to desaturation of the claystone and causes it to lose its mechanical and hydraulic (i.e., sealing) properties. But it was noted that during the resaturation of structures, the fractures generated during the excavation can self-seal and caused both a significant decrease in water permeability in the EDZ and a partial restoration of the mechanical properties of the rock (Bock et al. 2010). This phenomenon was called self-sealing. In addition, through the process of the radioactive waste storage, large amounts of gas will be generated from corrosion of the waste canisters. In the context of radioactive waste disposal, knowing the long-term self-sealing phenomenon in the COx claystone is of great importance. In addition, the evolution of the gas permeability with the increase of damage is also worth investigating.

Many scholars have investigated the occurrence of self-sealing fractures in claystone caused by water percolation. Self-sealing is induced by a rearrangement of minerals and pores inside the fracture region, according to Auvray et al. (2015). Hence, these structural changes are expected to ameliorate mechanical and transfer properties of the fractured zone. Bastiaens et al. (2007) defined self-sealing as the lowering of permeability in the EDZ by any hydro-mechanical-bio-chemical mechanism. Furthermore, Bastiaens et al. (2007) and Van Geet et al. (2008) investigated in-situ studies on Opalinus clay and Boom clay presenting their capabilities to self-sealing rather than self-healing. De La Vaissière et al. (2015) have shown the partial restoration of the permeability of the COx claystone during in-situ resaturation experiments. Over a year, the hydraulic conductivity in the boreholes reduced by up to four orders of magnitude, nearing the value of healthy claystone, demonstrating the COx claystone's potential to self-seal. At the laboratory scale, many experiments have already been performed to demonstrate claystone's capacity to self-seal. Auvray et al. (2015) performed self-sealing tests on the COx argillite in a PEEK triaxial cell with only 2D X-ray scans. Giot et al. (2019) performed comparable studies but with 3D X-ray scans with basic voxel data analysis. In these studies, only the clayey facies of COx claystone were tested. Zhang and Talandier (2023) investigated the self-sealing capacities of different claystones (i.e. relatively rich in clay minerals, carbonates and quartz) on artificially fractured samples under various hydro-mechanical conditions by measuring fracture closure, water permeability, gas breakthrough pressure and permeability, and recovery of gas-induced pathways. They found that under the combined impact of mechanical compression and water-induced clay swelling, the fractures in the (COx and OPA) claystones tend to seal to low water permeabilities that are close to that of the intact rock, due to their mineralogical composition, fracture intensity, confining stress, and load duration. In addition, they concluded that the EDZ is a preferable route for gas release without compromising the integrity of the host rock and that the gas-induced pathways can reseal to hinder water transport.

Within the framework of the Task 2 of HITEC WP, CNTS - ULorraine investigated the impact of different parameters on the self-sealing process of artificially fractured core samples of COx claystone (Agboli et al. 2023). These parameters are: calcite content, initial crack aperture and sample orientation (parallel or perpendicular to the bedding plane). Here, we have focussed on the impact of gas injection on the self-sealing process. Self-sealing experiments have been performed in a triaxial compression cell under X-ray tomography on artificially fractured (parallel and perpendicularly oriented) samples of the COx claystone. 3D X-ray scans have been performed on all tested samples before, during and after the experiments. The voxel data has been analyzed with a specific software for the visualization and analysis of computed tomography (CT) data in order to assess the evolution of the crack volume.

Fracture permeability (to water and gas) have been measured continuously during all tests. In addition, the impact of damage-induced cracks on gas permeability of COx claystone (clay host rock) has been studied. The experiments consist of triaxial compression tests with and without X-ray tomography scans on samples oriented both parallel and perpendicular to the bedding plane. The issues that have been addressed are: (i) the impact of the deviatoric stress on gas permeability, (ii) the impact of confining pressure and (iii) the influence of cracks geometry and distribution on gas permeability.

4.2.1 Experimental set-up

4.2.1.1 Description of apparatus

The triaxial compression tests with gas permeability measurements are carried out on cylindrical samples in two types of triaxial compression cell. The first is a classic steel triaxial compression cell (Figure 4-17) where the samples are equipped with strain gauges to measure the material deformation during the mechanical test. Water and gas permeability can be measured with this triaxial cell.

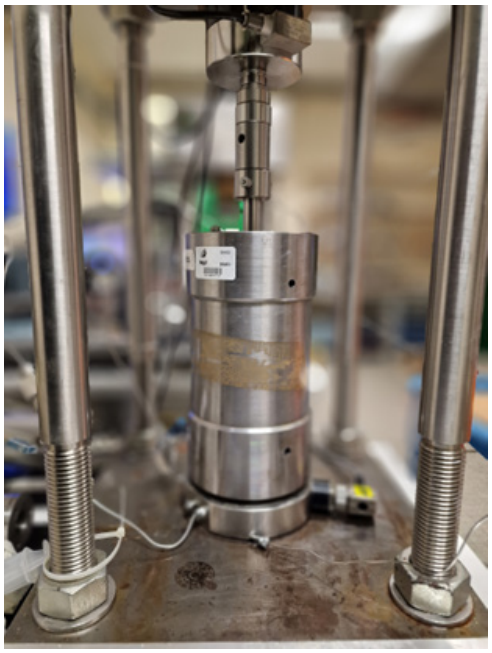

Figure 4-56 Steel triaxial compression cell.

The second is a triaxial compression cell developed for the EURAD project. The body of this cell is made of PEEK CF30 (PolyEtherEtherKetone, 30% carbon fibers) and is therefore transparent to X-rays, thus allowing 3D scans in an X-ray computed tomography scanner (GE Phoenix Nanotom S CT scanner) with a voxel resolution of approximately 24 µm to be made. It enables high isotropic and deviatoric stresses to be applied to cylindrical samples of 20 mm diameter and 40 mm height. The cell is placed in an X-ray tomograph, as shown in Figure 4-18. Since this triaxial cell was scanned with X-rays, it was not possible to use strain gages to measure the material deformation during the mechanical test. Water and gas permeability were also be measured with this triaxial cell.

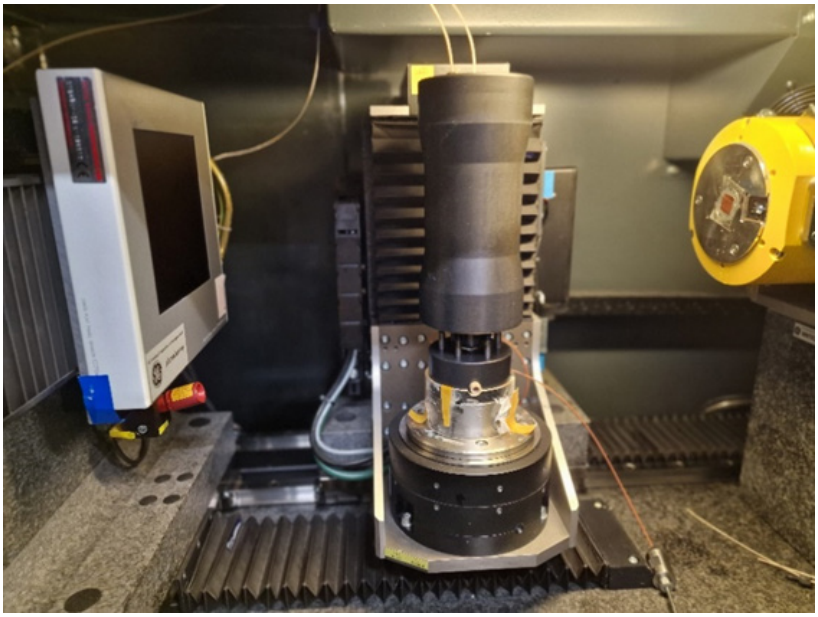

Figure 4-57 – PEEK triaxial compression cell in an X-ray nano-tomograph (Agboli et al., 2023).

During the mechanical loading, gas was injected into the samples and permeability is continuously measured. Injection of gas at different pressures into the sample was carried out through drain holes at both ends (outlets) of the triaxial cell. Gas is injected using pressure generators (high-precision syringe pumps) connected to flexible fittings and injection circuit connectors made of PEEK material (Figure 4-19). This system allows 360° rotation of the sample during X-ray tomography, facilitating 3D scans of the sample before, during and after the self-sealing test. This PEEK triaxial cell was also used to perform self-sealing tests with water and gas injections.

Figure 4-58 – Fluid injection pumps and acquisition devices.

Visualization and analysis of CT voxel data were performed using VGStudio MAX software (Volume Graphics GmbH). The volume of damage-induced cracks during triaxial compression tests is thus determined by image analysis. In addition, this tool allows isolation and visualization of the initial fracture and the quantification of its volume during self-sealing tests.

4.2.1.2 Testing fluids

The gas used for the triaxial compression tests with gas permeability measurements is nitrogen because it is inert and therefore will not react significantly with rock forming minerals.

The synthetic water of ANDRA, whose chemical composition is close to in-situ porewater at the ANDRA URL, was used in the self-sealing experiments. Its chemical composition is presented in the Table 4-6. The gas used for these self-sealing tests is also nitrogen.

Table 4-16 – Mineralogical composition of Andra's synthetic water (Andra, 2015).

Chemical element	Content (g/l)
NaCl	1.950
NaHCO3	0.130
KCl	0.035
CaSO4,2H2O	0.630
MgSO4,7H2O	1.020
CaCl2,2H2O	0.080
Na2SO4	0.700

4.2.2 Material properties (pre-test and post-test characteristics)

The Callovo-Oxfordian (COx) claystone was used for the purpose of this study. The material comes from Andra's Meuse/Haute Marne underground research laboratory located at Bure which is excavated at two levels (445 m and 490 m) below the surface, in the middle of the sub-horizontal layer of COx claystone that is 160 million years old, with a thickness of about 130 meters under Bure. The mineral composition of the COx argillite has been widely studied in the past by many researchers (e.g., Robinet et al. 2015; Montes et al. 2004; Bauer-Plaindoux et al. 1998; Wright 2001). It consists of: 20-60% of phyllosilicates (illite, interstratified illite/smectite, kaolinite, mica, chlorite), 10-40% of tectosilicates (quartz, feldspars), 15-80% of carbonates (calcite, dolomite), 0-3% of pyrite, iron oxides and a small proportion of organic components. To simplify, the three main mineral phases are clays, quartz, and calcite, with a high content of swelling clay minerals (smectites). The clay minerals content is approximately anti-correlated with the carbonates content and the relative proportions of clay and carbonates phases vary with depth. This study used the clayey facies of the COx claystone with a very low calcite content (around 20-25%). From a simplified microstructural point of view, the COx claystone is composed of a homogeneous clay matrix surrounding solid inclusions/grains of silicates and carbonates (mainly quartz and calcite) of diameter lower than 200 µm (Gasc-Barbier 2002). The porosity

of this clayey facies of the COx claystone is about 18% and the water permeability ranges from 10^{-20} m^2 to 10^{-21} m^2.

Cylindrical samples of the Callovo-Oxfordian claystone with a diameter of 20 mm and a height of 40 mm were used for the triaxial compression tests with gas permeability measurements. These samples were taken from boreholes drilled by Andra. For these tests, two orientations of the sample axis were considered: parallel and perpendicular to the bedding plane (Figure 4-20), in order to take into account the effect of claystone anisotropy. The references of the various samples, together with their characteristics and experimental conditions, are presented in the Table 4-7. The mechanical properties of the COx claystone have been shown to be very sensitive to water saturation. Indeed, the microstructure can be damaged during the water desaturation or resaturation processes (Auvray et al. 2015; Liu et al. 2018; Bemer et al. 2004; Montes et al. 2004; Conil et al. 2018; Grgic et al. 2023). Therefore, special attention was taken in this study to minimize samples damage due to variation in water saturation. First, the samples were carefully stored after core drilling and preparation to avoid a significant decrease in water content during the waiting time before the mechanical test and keep the water saturation degree of the samples as close as possible to that of the original drill core (i.e., close to 100%). Second, according to the recommendations of Andra, the samples were not resaturated before the mechanical tests to avoid a significant damage of the material (decrease of the peak strength up to 50% according to Grgic et al. 2023), which would complicate the interpretation of the experimental results presented here. The initial degree of liquid saturation of all tested samples was above 90%. This little desaturation, due to core drilling and sample preparation, is within an acceptable limit fixed at ~90% by Andra for mechanical testing (Conil et al. 2018).

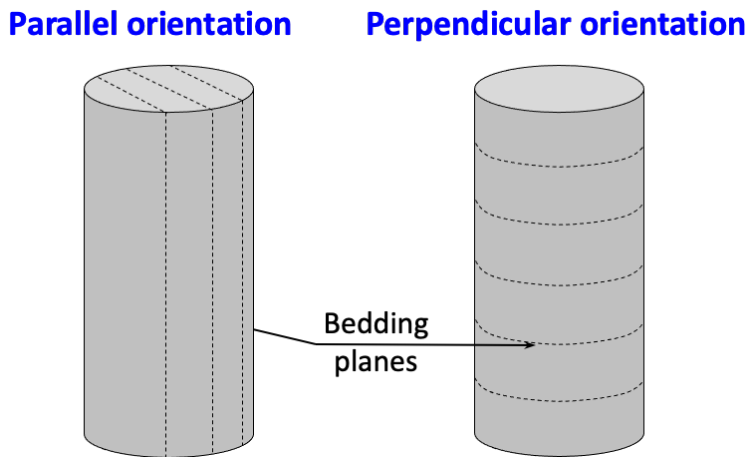

Figure 4-59 – Geometry of COx cylindrical sample Ø=20mm / L=40mm.

Table 4-17 – References of the various samples with the corresponding characteristics and experimental conditions.

Sample	Borehole	Orientation	%CaCO3	Solid grain density (g/cm3)	Initial saturation degree (%)	Injected fluid
EST66721-01	PGZ3004 19.08 – 19.38 m	Parallel	22.27	2.67	90.2	Nitrogen
EST66721-18	PGZ3004 19.08 – 19.38 m	Perpendicular	22.27	2.67	90.8	Nitrogen

ANDRA boreholes were also used to core cylindrical samples of 20 mm diameter and 40 mm height for the self-sealing tests. Two sample orientations were also considered, namely parallel and perpendicular to the bedding plane, in order to take into account the effect of argillite anisotropy. These core samples were purposely fractured. First, samples were sawn in two along a plane containing the axis of the cylinder. Second, one of the faces was machined by milling with a high precision tool in order to obtain an artificial crack on a one-third of the diameter with an opening of 400 µm (Figure 4-21). This regular milling method creates an artificial space without causing significant damage to the matrix. In fact, only a small number of particles were extracted until the desired depth was reached. It is important to note that creating this artificial crack does cause some drying of the crack ends, but this is likely to remain moderate given that this process is relatively quick (around half an hour). In addition, the crack is rapidly resaturated during the first stage of the self-sealing test. We chose an aperture of 400 µm for the initial crack according to previous works (Auvray et al. 2015 and Giot et al. 2019) and ANDRA's recommendations. Therefore, the initial crack has a theoretical initial volume equal to 106.5 mm^3. The references of the various samples, together with their characteristics and experimental conditions, are presented in Table 4-8.

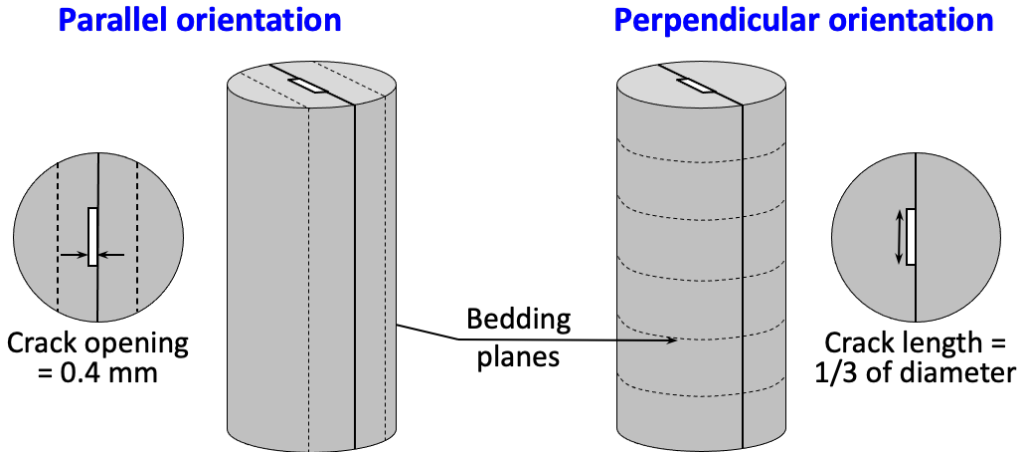

Figure 4-60 – Artificial crack geometry of cylindrical samples (Ø = 20 mm; h = 40 mm) for self-sealing tests. (Agboli et al., 2023).

Table 4-18 – References of the various samples with the corresponding characteristics and experimental conditions.

Sample	Borehole	Orientation	%$CaCO_3$	Solid grain density (g/cm3)	Fracture opening (µm)	Injected fluid	Temperature (°C)
EST66418-5 //	OHZ3010 12.50 – 12.80 m	Parallel	25.4	2.6911	400	Water/ Nitrogen	20
EST66723-11 ⊥	PGZ3004 19.96 – 20.34 m	Perpendicular	20.8	2.66	400	Water/ Nitrogen	20

4.2.3 Testing protocol

4.2.3.1 Triaxial compression tests with gas injection

Triaxial compression tests with gas injection (at room temperature) without X-ray tomography scanning were carried out as follows:

- (1) Cylindrical specimens were equipped with strain gauges according to the following procedure:

Due to the presence of bedding planes, the COx claystone exhibits structural anisotropy (transverse isotropy). The mechanical behaviour depends then on the loading direction with respect to the bedding plane. Two orientations of the cylindrical sample axis were then considered, namely perpendicular and parallel to the bedding plane. During the mechanical tests, samples deformations (ε_{11}, ε_{22} and ε_{33}) were measured with strain gages. Considering that the COx claystone is a transversely isotropic material, the reference frame (1, 2, 3) is defined in Figure 4-22 for a cylindrical sample, (1, 2) being the bedding plane. For each main deformation, two strain gages, facing each other on the cylindrical sample, were glued (with an epoxy resin) on the sample surface at half height. For samples cored perpendicularly to the bedding plane (θ = 0°), one axial deformation and one lateral deformation were measured, while one axial deformation and two lateral deformations were measured for samples cored parallel to the bedding plane (θ = 90°), as illustrated in Figure 4-22. The convention of positive compressions for stresses and strains will be used.

- (2) Once the strain gages had been glued, cylindrical samples were inserted into a Viton© membrane and placed in the steel triaxial cell.
- (3) The hydrostatic stress (confining pressure) was then increased to 12 MPa. This confining pressure is kept constant throughout the test.
- (4) After stabilization of the confining pressure, the gas breakthrough pressure was determined using an imposed pressure (step-by-step method).

    a. A gas pressure (5 MPa) was imposed upstream (downstream left at atmospheric pressure) with an injection rate limit of 1 ml/min.

    b. This pressure was maintained for 7 days.

c. If there was no increase in gas injection volume during this period, the upstream pressure was increased by 1 MPa.

d. This operation was repeated every 7 days until an increase in the volume of gas injected during the pressure step was observed, and gas is released downstream.

- (5) Once the gas breakthrough pressure had been determined, it was imposed at the upstream end of the sample while the downstream was left at atmospheric pressure during the deviatoric loading (triaxial compression test).
- (6) The deviatoric stress was then increased until failure under controlled displacement ($40x10^{-6}$ mm/s) and the gas permeability was measured continuously. Each 5 MPa, the deviatoric stress was kept constant during 2 hours in order to measure properly the gas permeability.

During the test, the volumes of injected gas, displacements (LVDT's sensors between the mechanical press platens) and sample deformations (with strain gages) were measured continuously.

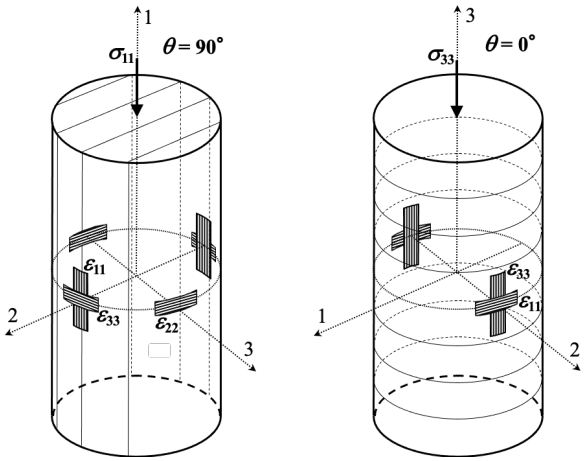

Figure 4-61 – Strains gauges and coordinate system oriented with respect to the bedding plane of the (transverse isotropic) COx claystone cylindrical sample for both sample orientations (parallel to the bedding plane at the left, perpendicular to the bedding plane at the right).

Triaxial compression tests with gas injection (at room temperature) with X-ray tomography scanning were carried out using the following procedure:

- (1) Cylindrical samples was inserted into a Viton© membrane and placed in the PEEK® triaxial cell.
- (2) The hydrostatic stress (confining pressure) was then increased to 12 MPa. This confining pressure is kept constant throughout the test.
- (3) Once the confining pressure had stabilized, an initial 3D X-ray scan was performed to record the initial state of the sample.
- (4) After this first scan, the gas breakthrough pressure was determined using an imposed pressure (step-by-step method) as describe previously.
- (5) Once the gas breakthrough pressure had been determined, it was imposed at the upstream and the downstream was left at atmospheric pressure during the deviatoric loading (triaxial compression test).

- (6) The deviatoric stress was then increased without going until failure and the gas permeability was measured continuously. Each 5 MPa, the deviatoric stress was kept constant during 2 hours in order to measure properly the gas permeability and perform the 3D X-ray scans to study the evolution of cracks.

During the test, the volumes of injected gas were measured continuously and the permeability was calculated with the steady state method.

The gas permeability k_g was calculated at equilibrium using Darcy's equation for compressible gas flow:

$$k_g = \frac{2\mu QLP_u}{S(P_u^2 - P_d^2)} \quad (4\text{-}2\text{-}1)$$

Where k_g is the gas permeability (m^2), Q the volumetric flow rate ($m^3 \cdot s^{-1}$), μ the liquid (water or gas) dynamic viscosity (Pa·s), S the injection surface of the sample (m^2), L the length of the sample (m), and P_u and P_d the upstream and downstream gas pressure (Pa).

4.2.3.2 Self-sealing tests

Self-sealing tests with gas injection were carried out in accordance with the following stages, defined in agreement with Andra:

(1) Initially artificially fractured cylindrical specimens were fitted with a Viton© membrane, which isolates the sample from the confining oil, and placed in the PEEK triaxial cell.

(2) A hydrostatic stress (confining pressure) of 4 MPa was then applied. This confining pressure was kept constant throughout the test.

(3) A first 3D X-ray scan was performed to record the initial shape of the crack.

(4) Synthetic water was then injected from the bottom (upstream) of the sample at a constant rate of 0.05 ml/min to saturate the crack.

(5) When the water begun to exit the cell from the top (downstream), the injection was stopped and a second 3D X-ray scan was performed to analyze the crack after water saturation.

(6) Next, water circulation was imposed in the fractured sample with a water pressure gradient of 0.2 MPa (upstream pressure = 1 MPa; downstream pressure = 0.8 MPa), maintaining a limiting flow rate of 0.02 ml/min to avoid crack damage due to too rapid water circulation. The triaxial cell and experimental conditions are shown in Figure 4-23.

(7) Once steady state flow was achieved at a constant pressure gradient of 0.2 MPa, the water permeability is measured.

Self-sealing tests were carried out at room temperature (20°C) and lasted at least one month. After step 7, gas was injected into the sample (through the baseplate) at different times, with upstream pressure varying according to the level of crack sealing, while the downstream was maintained at atmospheric pressure. During these gas injection stages, gas removed first the water filling the crack and the tubing and, next, could flow continuously through the sample. Once the gas flow had stabilized, we measured the gas permeability. Following the gas injection phase, which lasted an average 24 hours, procedure from step 4 was repeated, without necessarily performing a 3D X-ray scan.

The water permeability k_w of the cracked samples was calculated from the volumes measured at both upstream and downstream sides of the sample. It is based on a steady-flow approach taking into consideration Darcy's law. The gas permeability k_g is calculated at equilibrium using Darcy's equation for compressible gas flow. Both permeabilities are given by the equation (1) below:

$$k_w = \frac{Q\mu L}{S(P_u - P_d)} \qquad k_g = \frac{2\mu Q L P_u}{S(P_u^2 - P_d^2)} \tag{4-3-1}$$

where k_w and k_g are the intrinsic permeabilities (m^2), Q is the volumetric flow rate ($m^3.s^{-1}$), μ is the liquid (water or gas) dynamic viscosity (Pa·s), S is the injection surface of the sample (m^2), L is the length of the sample (m), and P_u and P_d are the upstream and downstream fluid (water or gas) pressures (Pa).

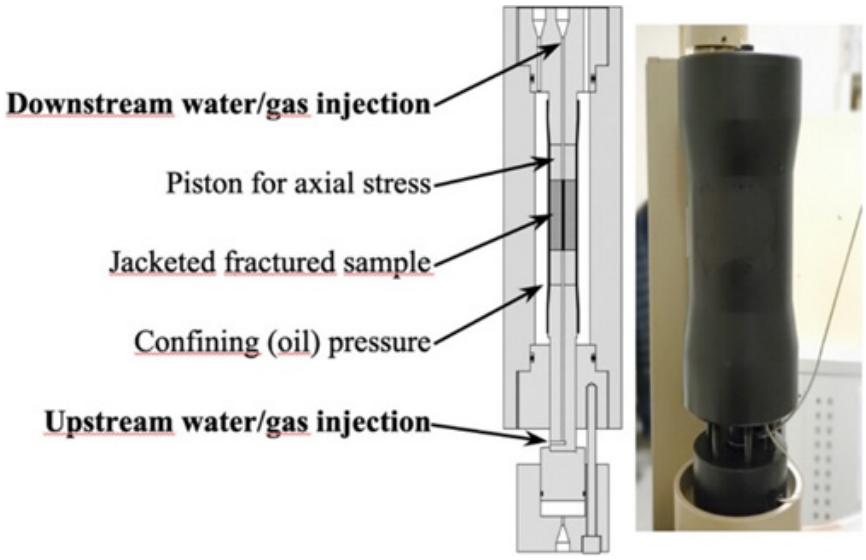

Figure 4-62 – Schematic of PEEK triaxial cell with COx argillite sample inside. (Agboli et al., 2023).

4.2.4 Results

4.2.4.1 Triaxial compression tests with gas injection

We carried out several trials to define the experimental protocol. In this report, we present the latest results obtained with the recent protocol. One test was carried out for each sample orientation (parallel and perpendicular to the bedding plane). These tests were performed without X-ray tomography. Triaxial compression tests with gas injection with X-ray tomography have not been performed.

Sample parallel to the bedding plane

At a pressure around 7 MPa, gas began to flow through the parallel sample (EST66721-01//) with a confining pressure of 12 MPa. We therefore decided to carry out the test with a gas pressure of 8 MPa. This gas pressure was maintained constant and enabled us to measure the gas permeability of the sample during the triaxial compression test. The stress-strain curves of this triaxial compression test are represented in Figure 4-24: axial (ε_{11}), lateral (ε_{22} and ε_{33}) and volumetric (ε_v) strains measured by the strain gages. Figure 4-25 shows the evolution of the axial displacement curve (measured with LVDT's sensors between the mechanical press platens) as a function of the deviatoric stress. On this sample, oriented parallel to the bedding plane, we obtained a deviatoric stress at failure (peak strength) equal to 30.4 MPa.

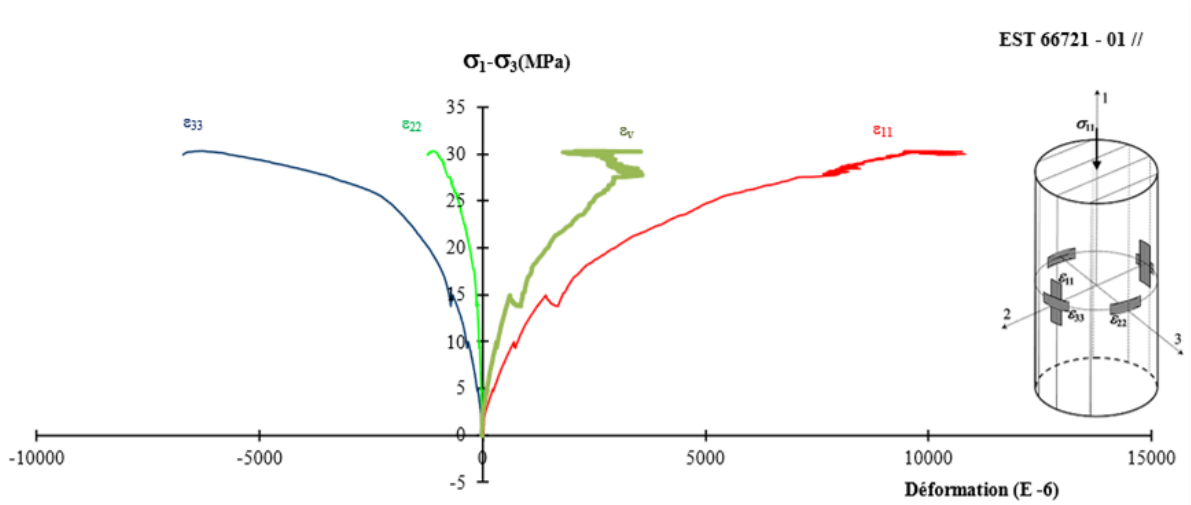

Figure 4-63 – Deviatoric stress-strain curves of parallel sample (EST 66721 – 01).

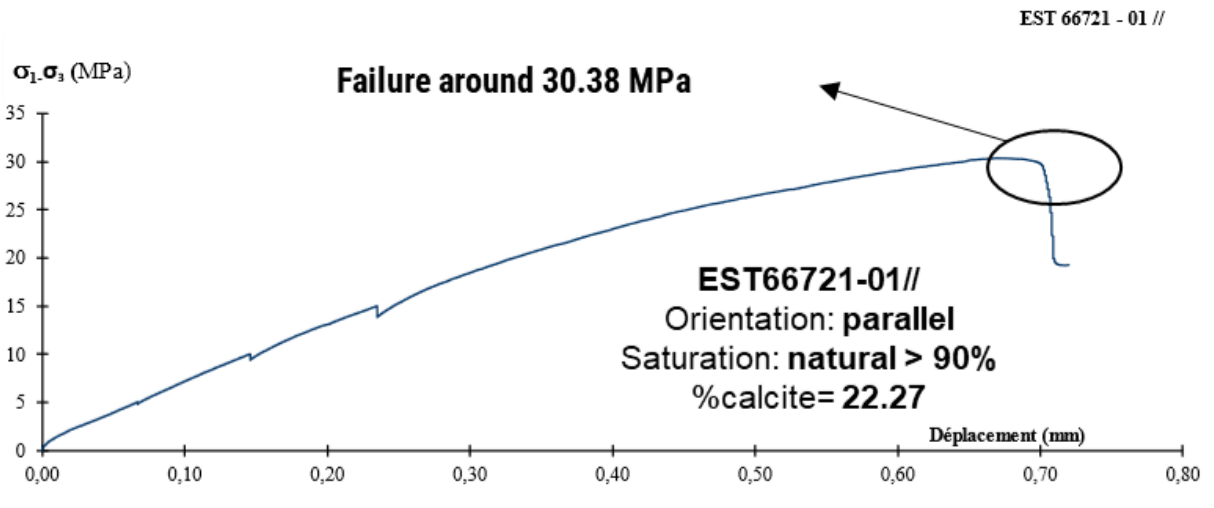

Figure 4-64 – Deviatoric stress-axial displacement curve of parallel sample (EST 66721 – 01).

Figure 4-26 represents the evolution of the gas permeability and the deviatoric stress as a function of time, while Figure 4-27 represents the evolution of the gas permeability and the volumetric strain as a function of time. At the start of the test, gas permeability was equal to approximately 10^{-19} m^2. As the deviatoric stress increases, gas permeability gradually decreases to around 10^{-20} m^2, which is probably due to the closure of initial cracks because of the axial compression of the sample. During this permeability decrease, the volumetric deformation is contractant.

Close to the failure and the dilatancy threshold (volumetric strain curve), there is a very significant increase in the gas permeability, which is about $5 \cdot 10^{-18}$ m^2, due to the material damage. The volumetric dilatancy is due to opening of microcracks. The deformation ε_{33} increases systematically much more than ε_{22} during the deviatoric loading. Therefore, an anisotropic micro-cracking damage develops during the deviatoric loading and this damage corresponds probably to the opening of microcracks mainly axial (vertical) and oriented in parallel to the bedding plane and to the applied axial stress, with opening direction mainly parallel to the axis 3 and thus perpendicular to the bedding plane (Figure 4-22). For the parallel orientation, microcracking damage therefore induced the opening of the bedding planes, which

has already been proposed by Grgic et al. (2019) from uniaxial compression tests on another claystone with strains and ultrasonic wave velocities measurements.

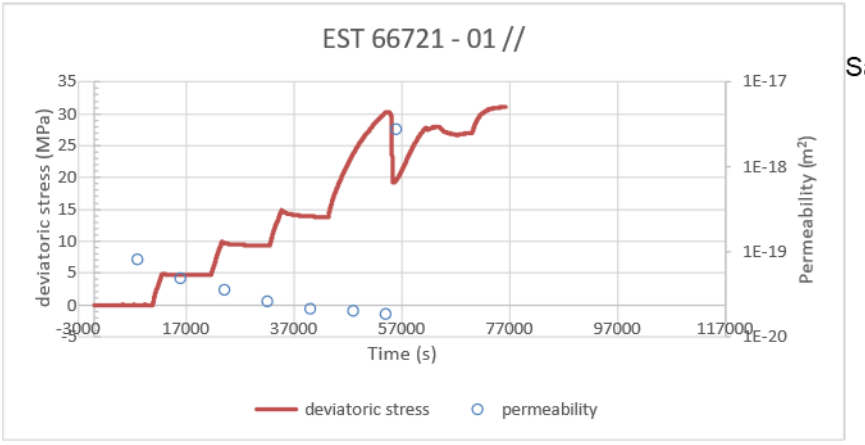

Figure 4-65 – Evolution of gas permeability and deviatoric stress as a function of time of a parallel sample (EST 66721 – 01).

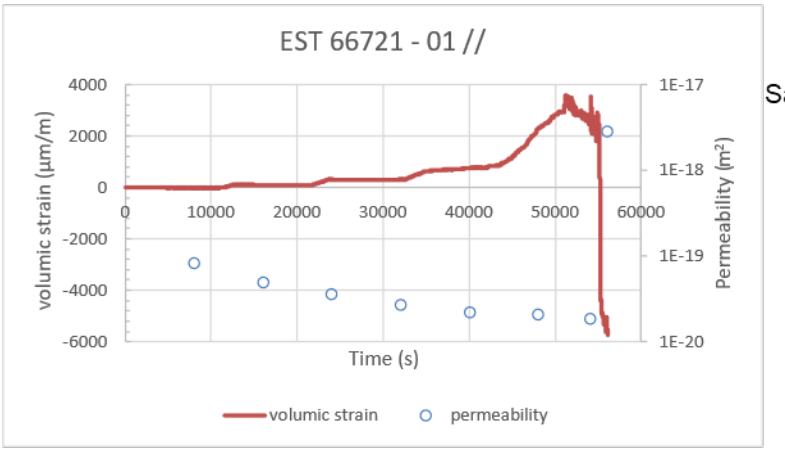

Figure 4-66 – Evolution of gas permeability and volumetric strain as a function of time of a parallel sample (EST 66721 – 01).

Sample perpendicular to the bedding plane

At a pressure of around 5 MPa, gas began to flow through the perpendicular sample (EST66721-18 ⊥) with a confining pressure of 12MPa. We therefore decided to carry out the test with a gas pressure of 7 MPa. This gas pressure was maintained constant and enabled us to measure the gas permeability of the sample during the triaxial compression test. The stress-strain curves of this triaxial compression test are represented in Figure 4-28: axial (ε_{11}), lateral (ε_{22} and ε_{33}) and volumetric (ε_v) strains measured by the strain gages. The Figure 4-29 represents the evolution of the axial displacement curve (measured with LVDT's sensors between the mechanical press platens) as a function of the deviatoric stress. On this sample, oriented perpendicular to the bedding plane, we obtained a deviatoric stress at failure (peak strength) equal to 34.9 MPa.

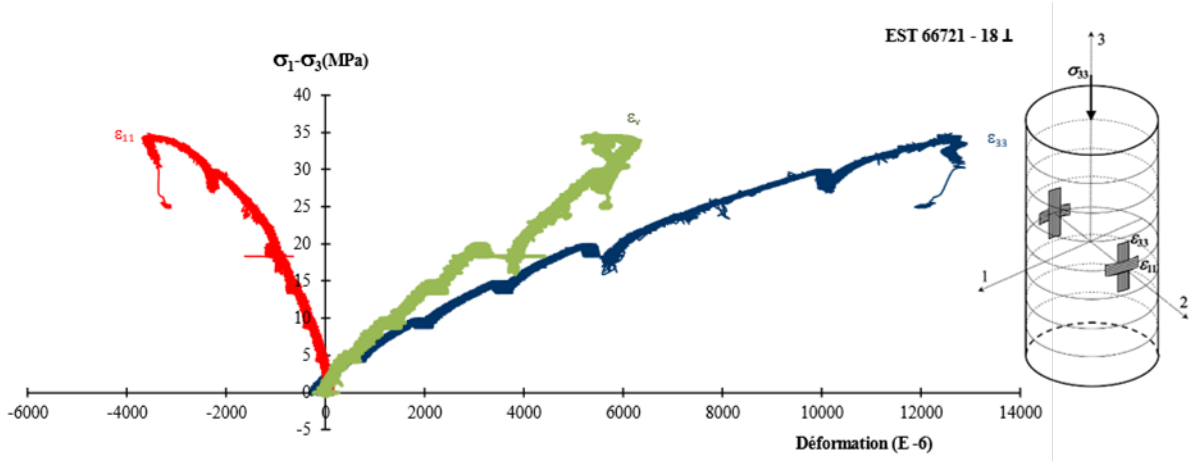

Figure 4-67 – Deviatoric stress-strain curves of perpendicular sample (EST 66721 – 18).

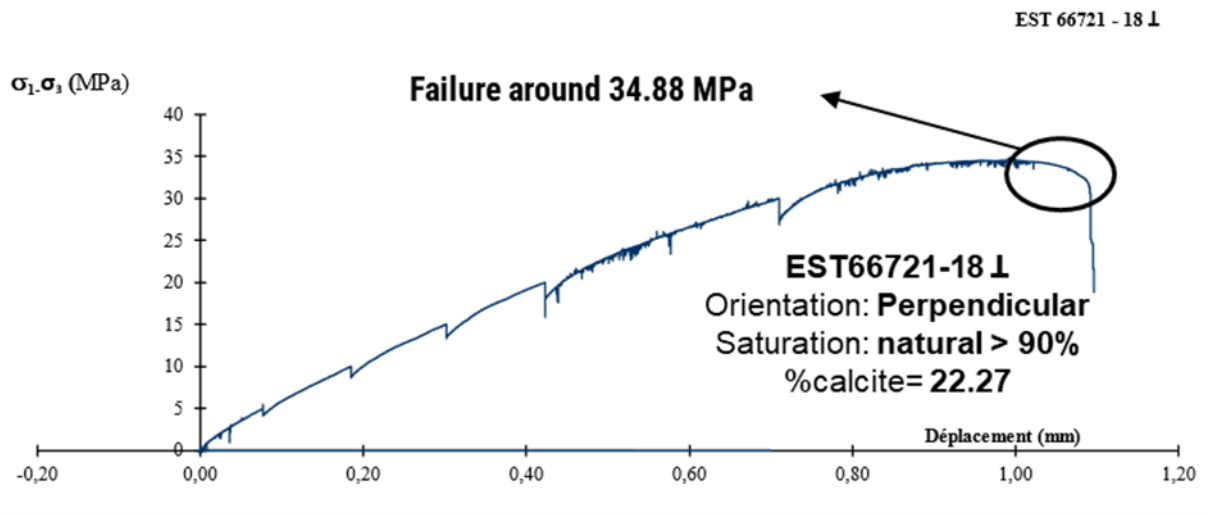

Figure 4-68 – Deviatoric stress-axial displacement curve of perpendicular sample (EST 66721 – 18).

Figure 4-30 represents the evolution of the gas permeability and the deviatoric stress as a function of time, while Figure 4-31 represents the evolution of the gas permeability and the volumetric strain as a function of time. At the start of the test, gas permeability was equal to approximately 10^{-20} m^2, which is one order of magnitude lower than the initial permeability of the parallel sample EST66721-01. Usually for transverse isotropic clay rocks, the permeability measured perpendicularly to the bedding plane is lower than the permeability measured parallel to the bedding plane. These gas permeability values are similar to the work of Zhang & Rothfuchs (2004) obtained with slightly higher confining pressures. As the deviatoric stress increases, gas permeability gradually decreases overall until almost 10^{-21} m^2, which is probably due to the closure of initial cracks because of the axial compression of the sample, as already shown by Zhang & Rothfuchs (2008). During this permeability decrease, the volumetric deformation is contractant.

Close to the failure and the dilatancy threshold (volumetric strain curve), there is a significant increase in the gas permeability, which is about $5 \cdot 10^{-20}$ m^2, due to the material damage. The volumetric dilatancy is due to opening of microcracks. Therefore, an anisotropic micro-cracking damage develops during the deviatoric loading and this damage corresponds probably to the opening of axial (vertical) microcracks

perpendicular to the direction of the bedding plane. This interpretation has already been proposed by Grgic et al. (2019) from uniaxial compression tests on another claystone and by Sarout et al. (2007) from triaxial compression tests on the COx claystone, both with strains and ultrasonic wave velocities measurements.

The data demonstrates there is therefore a relationship between the evolution of gas permeability and material damage. The dilatancy threshold is the turning point from which the cracks opening induces a significant increase in the gas permeability. This increase is greater when the applied axial stress is parallel to the bedding planes because microcracks, which are mainly oriented in parallel to the applied axial stress, induces the opening of the bedding planes.

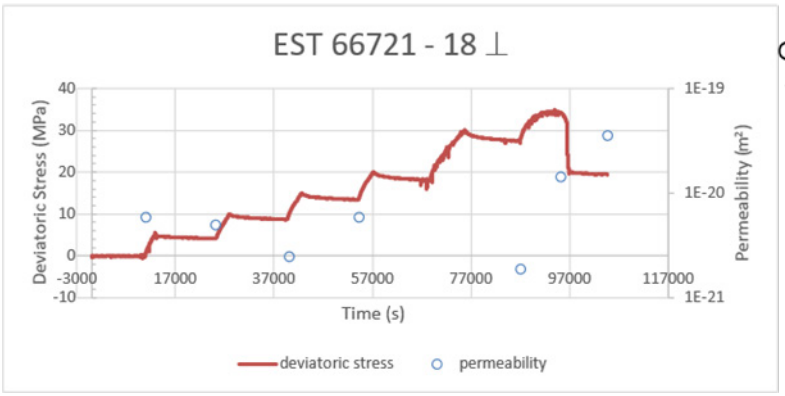

Figure 4-69 – Evolution of gas permeability and deviatoric stress as a function of time of a perpendicular sample (EST 66721 – 18).

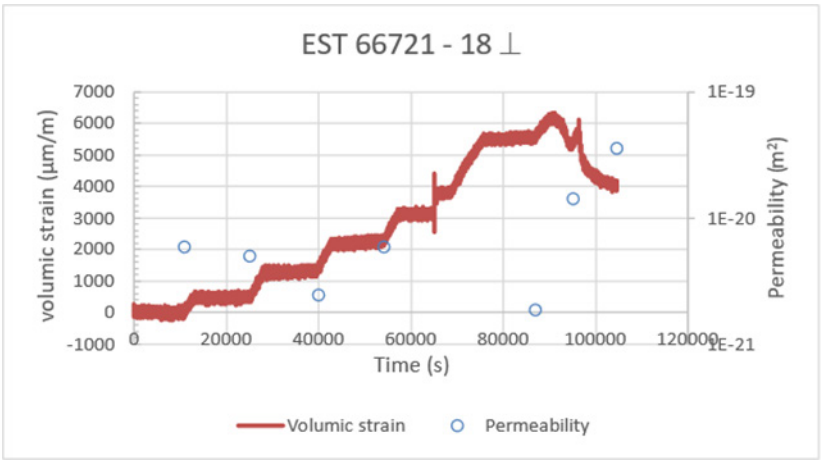

Figure 4-70 – Evolution of gas permeability and volumetric strain as a function of time of a perpendicular sample (EST 66721 – 18).

4.2.4.2 Self-sealing tests

We compare here the results obtained from 2 self-sealing tests (a parallel sample EST66418-5 with %CaCO3 = 25.4 and a perpendicular sample EST66723-11 with %CaCO3 = 20.8) with water and gas injection with the results of 5 self-sealing tests (parallel sample EST60766-3 with %CaCO3 = 21, parallel sample EST63744-7 with %CaCO3 = 32, perpendicular sample EST63744-11 with %CaCO3 = 32, perpendicular sample EST60007-71 with %CaCO3 = 53 and perpendicular sample EST59996-71 with %CaCO3 = 68) performed with only water injection. These 5 self-sealing tests were performed within the Task 2 of HITEC WP (Agboli et al. 2023). The initial crack opening is the same for all these samples (0.4 mm). The evolution of the water permeability is presented in Figure 4-32, Figure 4-33 and Figure 4-34. Only the downstream curves were represented (the upstream curves are almost identical). Concerning the very carbonated samples (EST60007-71 and EST59996-71), self-sealing was very moderate and the fracture remained globally open. Therefore, no water permeability measurements could be performed since the flow rate was too fast.

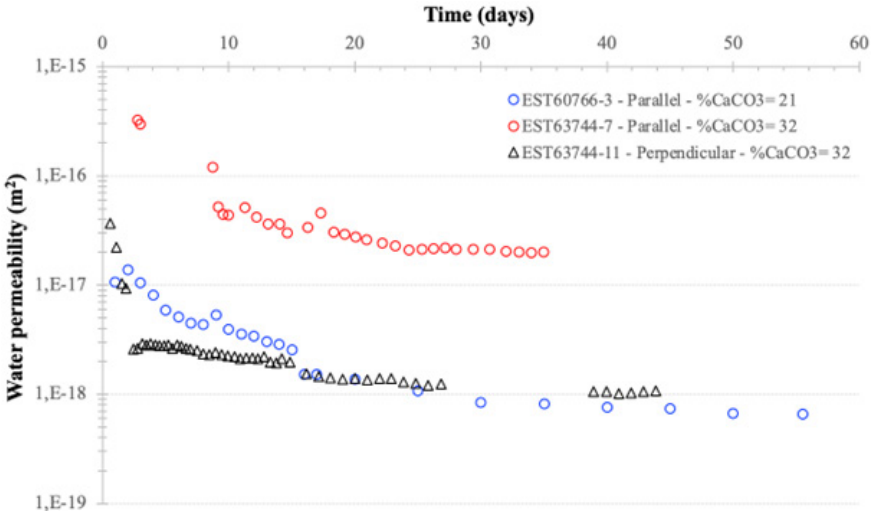

Figure 4-71 – Evolution of crack water permeability during self-sealing tests with only water on samples EST60766-3, EST63744-7 and EST63744-11 (performed within the Task 2 of HITEC WP).

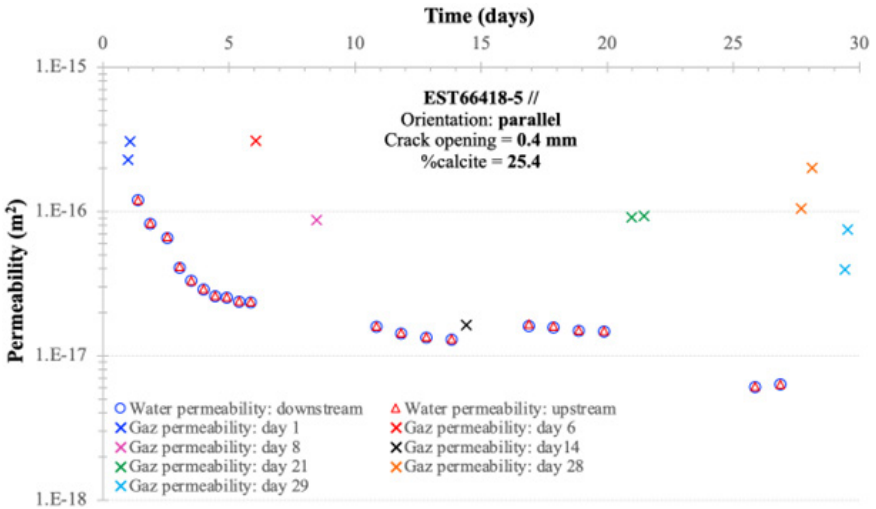

Figure 4-72 – Evolution of crack water permeability during the self-sealing test with both water and gas on parallel sample EST66418-5.

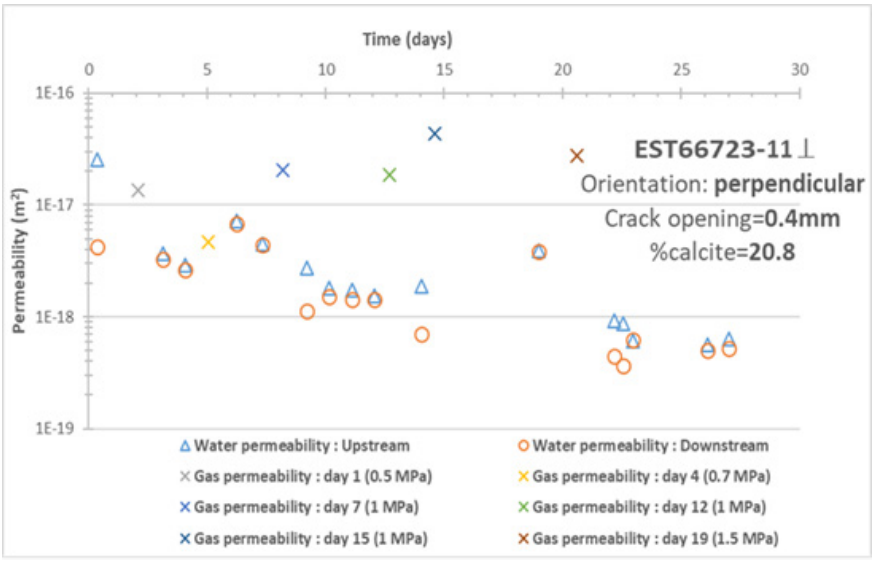

Figure 4-73 – Evolution of crack water permeability during the self-sealing test with both water and gas on perpendicular sample EST66723-11.

X-ray 3D tomography images of parallel sample EST60766-3 showing the evolution of the crack volume with time during the self-sealing test with only water are represented in Figure 4-35. Figure 4-36 represents X-ray 3D tomography image of parallel sample EST66418-5 showing the crack volume at the end of the self-sealing test with water and gas. Figure 4-37 represents X-ray 3D tomography image of perpendicular sample EST66723-11 showing the evolution of the crack volume with time during the self-sealing test with water and gas.

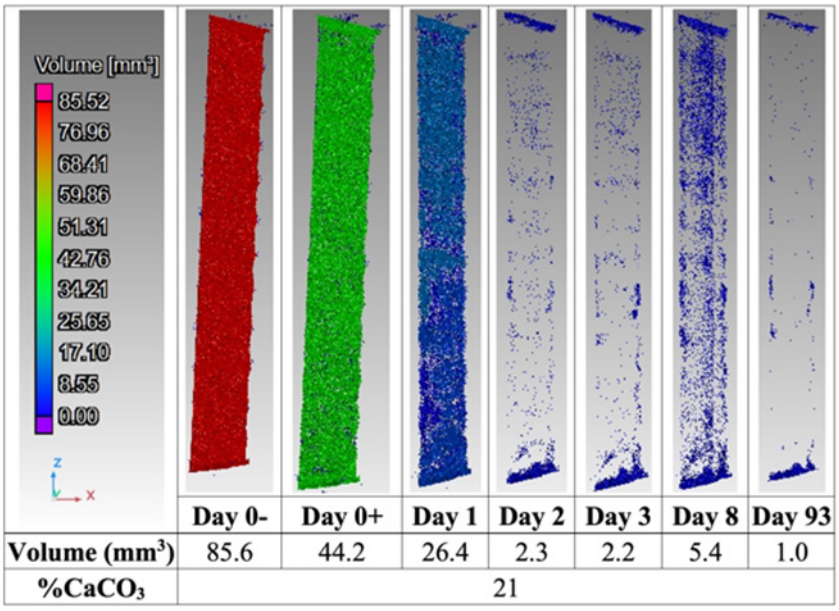

	Day 0-	Day 0+	Day 1	Day 2	Day 3	Day 8	Day 93
Volume (mm³)	85.6	44.2	26.4	2.3	2.2	5.4	1.0
%$CaCO_3$	21						

Figure 4-74 – X-ray 3D tomography images of parallel sample EST60766-3 showing the evolution of the crack volume with time during the self-sealing test with only water (Day 0-: after hydrostatic loading; Day 0+: after crack saturation).

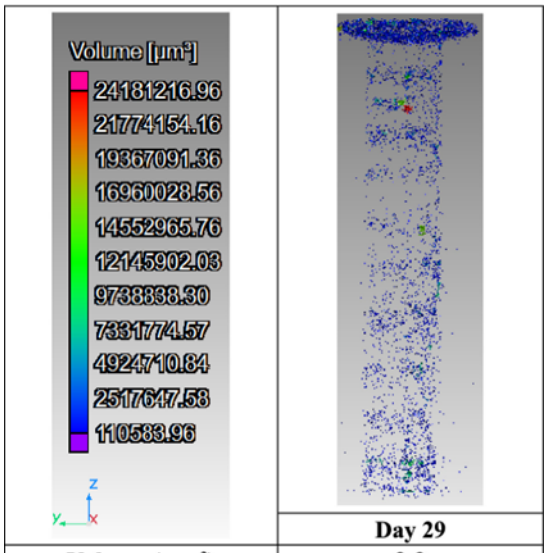

	Day 29
Volume (mm³)	3.3
%$CaCO_3$	25.4

Figure 4-75 – X-ray 3D tomography image of parallel sample EST66418-5 showing the crack volume at the end of the self-sealing test with water and gas.

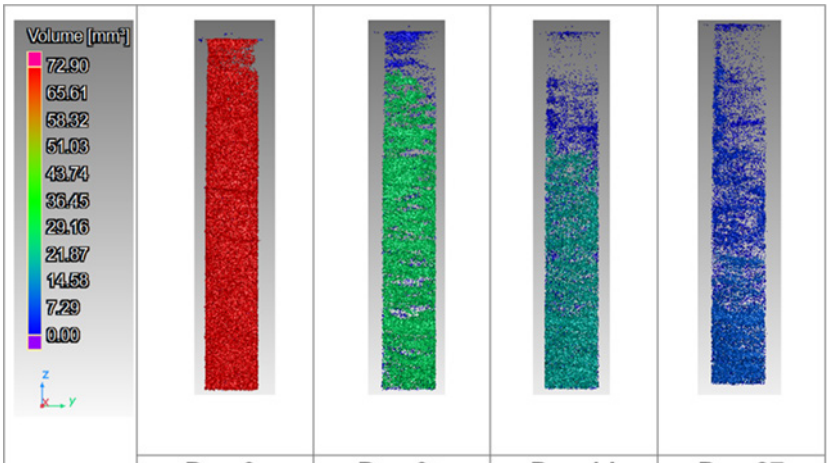

	Day 0-	Day 0+	Day 14	Day 27
Volume (mm³)	73.01	28.99	22.69	18
%$CaCO_3$	20.8			

Figure 4-76 – X-ray 3D tomography images of perpendicular sample EST66723-11 showing the evolution of the crack volume with time during the self-sealing test with water and gas (Day 0-: after hydrostatic loading; Day 0+: after crack saturation).

Figure 4-38 represents the percentage volume variation of the initial crack (normalized with the volume after hydrostatic loading) obtained from X-ray tomography 3D images during all self-sealing tests. Only sample EST66418-5 was not represented in this Figure because only one scan was performed at the end of the test. The hydrostatic loading at a confining pressure of 4 MPa and the sample saturation induced a partial closure of the initial crack in all cases.

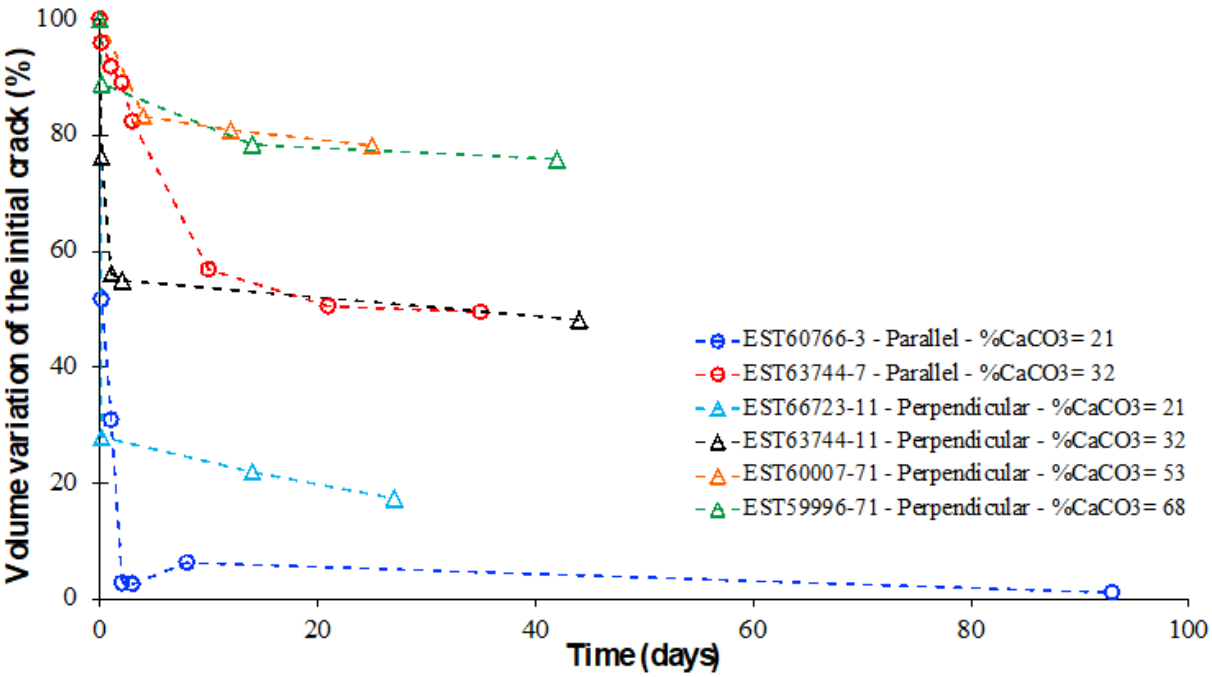

Figure 4-77 – Volume variation percentage of the initial crack (normalized with the volume after applying confining pressure) obtained from X-ray tomography 3D images during all self-sealing tests.

For Auvray et al. (2015) and Giot et al. (2019), there are three main processes implied in self-sealing. The first is swelling between smectite sheets (intra-particle or crystalline swelling) due to adsorption of water since the samples are a little desaturated initially. The second is inter-particle swelling due to osmotic effects by absorption of water between clay particles at higher water saturation (i.e., during self-sealing experiment). The last is plugging of the fractures by particle aggregation. Water penetrates more easily between the clay sheets in samples oriented in parallel to the bedding plane, thus initiating the self-sealing process more quickly. During these quick phases, there is a rapid decrease of the water permeability and the crack volume (Figure 4-32). Then, there is a moderate and progressive decrease in water permeability and crack volume (Figure 4-35 and Figure 4-38) due to the progressive swelling of smectite clay minerals in the whole sample and the expansion and densification of clay plugs in the central crack. For parallel samples, clay minerals can freely swell laterally towards the inside of the fracture without any constraint whereas for perpendicular samples, the axial contraction (due to the 4 MPa confining pressure) prevents probably a free swelling of the clay minerals surfaces in the axial direction. From these first results, it seems surprisingly that the self-sealing process is not more efficient for the parallel sample (i.e., when the bedding plane is parallel to the fracture surface). The (crystalline and osmotic) swelling mechanisms are certainly more efficient for the parallel samples, but the final phases of clogging, expansion and densification, which are maybe less dependent on the sample orientation, are possibly much more efficient to seal cracks.

The water permeability of clayey facies samples decreased significantly during self-sealing tests: from 10^{-17} to 7×10^{-19} m^2 in 55 days for sample EST60766-3, from 3×10^{-16} to 2×10^{-17} m^2 in 35 days for sample EST63744-7, and from 4×10^{-17} to 1×10^{-18} m^2 in 44 days for sample EST63744-11. However, the initial permeability of the healthy (i.e., initial) claystone, which is almost 2 orders of magnitude lower (10^{-20} m^2 to 10^{-21} m^2) according to previous works (Escoffier 2002 and Homand et al. 2004), is never recovered. Moreover, the self-sealing process induces a significant reduction of the crack volume (Figure 4-35 and Figure 4-38). Concerning the samples with high calcium carbonate content (EST60007-71 and EST59996-71), self-sealing was very moderate and the fracture remained globally open (Figure 4-38). In these tests, the calcite content, which is roughly anti-correlated with the clay content, has a strong

impact on the physico-chemical sealing process in claystone. The higher the carbonate content is, the slower the self-sealing process, whatever the sample orientation. Our results support the work of Giot et al. (2019) where it is indicated that the threshold regarding the carbonate content to observe an effective self-sealing is around 40%. This result highlights the importance of the mineralogy of the clay host rock to allow a good sealing of fractures in the EDZ during the resaturation of the underground structures for radioactive waste storage in clayey rocks.

Self-sealing tests were performed with gas injections on the parallel sample EST66418-5 and the perpendicular sample EST66723-11 to determine the influence of an inert gas on the self-sealing process. The water and gas permeability of this specimen are presented in Figure 4-33 and Figure 4-34. The scattering of gas permeability measurements may be explained by: (i) the difficulty to obtain a measurable steady state gas flow (the time interval is not the same for all gas permeability measurements), (ii) the difficulty to apply and measure precisely low gas pressures at the bottom/upstream of the triaxial cell and (iii) the residual water inside the crack that can disturb the gas flow.

At the end of the self-sealing test on the parallel sample EST66418-5, the water permeability is equal to 6×10^{-18} m^2, whereas the gas permeability is about 10^{-16} m^2. At the end of the self-sealing test on the perpendicular sample EST66723-11, the water permeability is equal to 6×10^{-19} m^2, whereas the gas permeability is about 10^{-17} m^2. In both cases, the water permeability decreases quite rapidly at the beginning similar to other tests (Figure 4-23) but the decrease is slower thereafter. In addition, for both orientations, there is a very significant closure of the crack (Figure 4-36, Figure 4-37 and Figure 4-38). Gas injections induce each time the desaturation of the crack but there is no evidence for a significant slow-down of the decrease in the water permeability and a significant reduction of the self-sealing process. This result has obviously to be confirmed by additional similar experiments and, more importantly, with longer experimental run times and longer gas injection durations. Indeed, in that case, the long-term injection of an inert gas could have a retarding effect on the self-sealing process.

4.2.5 Summary

The aim of the triaxial compression tests with gas injection was to analyze the impact of damage-induced cracks on gas permeability of COx claystone (clay host rock). The experiments consisted of a series of triaxial compression tests on samples oriented both parallel and perpendicular to the bedding plane with permeability measurements made using the steady state method. The initial gas permeability was about 10^{-19} m^2 for the parallel orientation and about 10^{-20} m^2 for the perpendicular orientation with a total confining pressure of 12 MPa. During the triaxial compression testing, the gas permeability first decreases for both orientations by one order of magnitude due to the closure of initial cracks because of the axial compression of the samples. During this permeability decrease, the volumetric deformation is contractant. As the axial stress increases, the material becomes progressively dilatant because of the opening of axially oriented microcracks. From the volumetric dilatancy threshold and till the macroscopic failure, there is a very significant increase in the gas permeability, which is about 5.10^{-18} m^2 for the parallel orientation and about 5×10^{-20} m^2 for the perpendicular orientation, due to the large opening of these microcracks. There is therefore a relationship between the evolution of gas permeability and material damage. The dilatancy threshold is the turning point from which the cracks opening induces a significant increase in the gas permeability. This increase is greater when the main principal stress is parallel to the bedding planes because microcracks, which are mainly oriented in parallel to the main stress, induces the opening of the bedding planes. These first results have to be confirmed with additional similar tests. Triaxial compression tests with gas injection with X-ray tomography have also to be performed to analyze the influence of cracks geometry and distribution on gas permeability. Finally, the impact of confining pressure has also to be investigated in the future.

Self-sealing experiments have been performed in a triaxial compression tests under X-ray tomography on two artificially fractured (parallel and perpendicularly oriented) samples of the COx claystone. 3D X-

ray scans have been performed on all tested samples before, during and after the experiments. The voxel data have been analyzed with a specific software for the visualization and analysis of computed tomography (CT) data in order to assess the evolution of the crack volume. Fracture permeability (to water and gas) was measured continuously during all tests. The focus was to study the impact of gas injections on the self-sealing process. We compared the results from these two self-sealing tests with water and gas injection with those obtained from five self-sealing tests (with both orientations and different calcite contents) performed within the Task 2 of HITEC WP with only water injection. Self-sealing tests were carried out at room temperature (20°C) and lasted at least one month. Generally speaking, the higher the calcite content, the less effective the self-sealing process, whatever the sample orientation (parallel or perpendicular). An effective sealing requires a carbonate content lower than 40%. Moreover, it seems that the self-sealing process is equally efficient for both parallel and perpendicular orientations. Generally, the self-sealing process is faster at the beginning of the test and then the rate of reduction stabilizes after one month. The permeability of the COx claystone samples is partially restored compared to the initial permeability of the intact claystone and the initial crack is very significantly closed at the end of the self-sealing experiment. These first results are very promising and give confidence to the positive impact of the self-sealing process on the restoration of the initial mechanical and hydraulic (i.e., sealing) properties of the COx claystone. It is all the more promising that the duration of our experiments is much shorter than the in-situ time scale. The physico-chemical mechanisms examined in this study demonstrate a good sealing of fractures in the EDZ during the resaturation of the underground structures for radioactive waste storage, which will guarantee the safety of the site. Gas injections induce each time the desaturation of the crack but there is no evidence for a significant slow-down of the decrease in the water permeability and a significant reduction of the self-sealing process. These first results are also very promising and give confidence to the positive impact of the self-sealing process even if there is a gas flow. However, they have obviously to be confirmed by additional similar experiments and, more importantly, with longer experimental run times and longer gas injection durations. Indeed, in the latter case, the long-term injection of an inert gas could have a retarding effect on the self-sealing process.

4.2.6 Key learning points

4.2.6.1 New knowledge acquired

There is a relationship between the evolution of gas permeability and microcracking damage within the COx claystone. The dilatancy threshold is the turning point from which the cracks opening induces a significant increase in the gas permeability. This increase is greater when the main principal stress is parallel to the bedding planes because microcracks, which are mainly oriented in parallel to the main stress, induces the opening of the bedding planes.

During self-sealing tests, gas injections induce each time the desaturation of the crack but there is no evidence for a significant slow-down of the decrease in the water permeability and a significant reduction of the self-sealing process.

4.2.6.2 Impact of acquired knowledge

In the near field of the excavation, the gas leakage will be more significant in the direction parallel to the bedding plane according to the orientation of the in-situ stress state.

First, self-sealing tests give confidence to the positive impact of the self-sealing process, even if there is a gas flow, on the restoration of the initial mechanical and hydraulic (i.e., sealing) properties of the COx claystone. It is all the more promising that the duration of our experiments is much shorter than the in-situ time scale.

4.2.6.3 Remaining knowledge gaps

These first results obtained from triaxial compression tests with gas injection need to be confirmed with additional similar tests. Also, triaxial compression tests with gas injection with X-ray tomography have also to be performed to analyze the influence of cracks geometry and distribution on gas permeability. Finally, the impact of confining pressure has also to be investigated in the future.

The first self-sealing tests with water and gas injections have to be confirmed by additional similar experiments and, more important, with longer experimental run times and longer gas injection durations. The focus would be to verify if the long-term injection of an inert gas could have a retarding effect on the self-sealing process.

4.2.6.4 Recommendations for the future

Only 2 triaxial compression tests with gas permeability measurements (one for each orientation) have been performed up to now. Similar tests are necessary to confirm the identified tendencies. In addition, these tests should be performed at different confining pressures to analyze the impact of this parameter on the breakthrough pressure and the gas permeability evolution during the deviatoric loading.

Only 2 self-sealing tests with water and gas injections (one for each orientation) have been performed up to now. Similar tests with longer durations are necessary to confirm the identified tendencies. In addition, self-sealing tests with natural cracks (i.e., induced by a deviatoric loading) should also be performed because in that case the self-sealing process would probably be faster and would induce a better recovery of the initial mechanical and hydraulic (i.e., sealing) properties of the COx claystone.

4.2.7 References

Agboli, M., Grgic, D., Moumni, M., & Giraud, A. (2023). Study Under X-Ray Tomography of the Impact of Self-Sealing Process on the Permeability of the Callovo-Oxfordian Claystone. Rock Mechanics and Rock Engineering. https://doi.org/10.1007/s00603-023-03350-y

Andra. (2005). Dossier Argile 2005.

Andra. (2015). Protocoles expérimentaux pour des essais sur l'argilite.

Auvray, C., Grgic, D., Morlot, C., Fourreau, E., & Talandier, J. (2015). X-Ray Tomography Applied to Self-Healing Experiments on Argillites. 13th ISRM International Congress of Rock Mechanics, Montréal, (Québec, Canada).

Bastiaens, W., Bernier, F., & Li, X. L. (2007). SELFRAC: Experiments and conclusions on fracturing, self-healing and self-sealing processes in clays. Physics and Chemistry of the Earth, Parts A/B/C, 32(8–14), pp. 600-615. DOI: 10.1016/j.pce.2006.04.026.

Bauer-Plaindoux, C., Tessier, D. & Ghoreychi, M. (1998). Propriétés mécaniques des roches argileuses carbonatées : Importance de la relation calcite-argile. Comptes Rendus de l'Académie des Sciences - Series IIA - Earth and Planetary Science, 326 (4) : 231-37.

Bemer, E., Longuemare, P., & Vincké, O. (2004). Poroelastic parameters of Meuse/Haute Marne argillites: Effect of loading and saturation states. Applied Clay Science - APPL CLAY SCI, 26, 359–366. https://doi.org/10.1016/j.clay.2003.12.012

Bock H, Dehandschutter B, Derek Martin C, Mazurek M, de Haller A, Skoczylas F, Davy C (2010) Selfsealing of fractures in argillaceous formations in the context of geological disposal of radioactive waste – Review and synthesis. OECD Publications, Paris. ISBN 978-92-64-99096-1.

Conil, N., Talandier, J., Djizanne, H., de La Vaissière, R., Righini-Waz, C., Auvray, C., Morlot, C., & Armand, G. (2018). How rock samples can be representative of in-situ condition: A case study of Callovo-Oxfordian claystones. Journal of Rock Mechanics and Geotechnical Engineering, 10. https://doi.org/10.1016/j.jrmge.2018.02.004

De La Vaissière, R., Armand, G., & Talandier, J. 2015. Gas and water flow in an excavation-induced fracture network around an underground drift: A case study for a radioactive waste repository in clay rock. Journal of Hydrology, 521, pp. 141–156. DOI: 10.1016/j.jhydrol.2014.11.067.

Escoffier, S. (2002). Caractérisation expérimentale du comportement hydromécanique des argilites de Meuse/Haute-Marne [PhD Thesis]. Institut National Polytechnique de Lorraine.

Escoffier, S., Homand ,F., Giraud, A., Hoteit, N. & Su, K. (2005). Under stress permeability determination of the Meuse/Haute-Marne argillite. Eng. Geol., 81(3):329–340.

Gasc-Barbier, M. (2002). Étude des mécanismes de déformation de roches argileuses profondes : apport de la microstructure et des analyses pétrophysiques. Phd Thesis, Paris (France).

Giot, R., Auvray, C., & Talandier, J. (2019). Self-sealing of claystone under X-ray nanotomography. Geological Society, London, Special Publications, 482(1), 213–223. https://doi.org/10.1144/SP482.4

Giot, R., Giraud, A., & Auvray, C. (2014). Assessing the Permeability in Anisotropic and Weakly Permeable Porous Rocks Using Radial Pulse Tests. Oil & Gas Science and Technology – Revue d'IFP Energies Nouvelles, 69(7), 1171–1189. https://doi.org/10.2516/ogst/2013146

Giot, R., Giraud, A., Auvray, C., Homand, F., & Guillon, T. (2011). Fully coupled poromechanical back analysis of the pulse test by inverse method. International Journal for Numerical and Analytical Methods in Geomechanics, 35(3), 329–359. https://doi.org/10.1002/nag.897

Giot, R., Giraud, A., Guillon, T., & Auvray, C. (2012). Three-dimensional poromechanical back analysis of the pulse test accounting for transverse isotropy. Acta Geotechnica, 7(3), 151–165. https://doi.org/10.1007/s11440-012-0158-7

Grgic, D., Giraud, A. & Schoumacker, L. (2019). Dynamic anisotropic elastic properties of a claystone under variable loading direction and saturation. Geophysical Journal International, Vol. 216: 148-163.

Grgic, D., Moumni, M., Giraud, A., de La Vaissière, R., & Talandier, J. (2023). Water Permeability Measurements by Steady-State and Pulse Decay Methods on the Callovo-Oxfordian Claystone and Impact on its Mechanical Properties. Rock Mechanics and Rock Engineering, 1–20. https://doi.org/10.1007/s00603-023-03340-0

Homand, F., Giraud, A., Escoffier, S., Koriche, A., & Hoxha, D. (2004). Permeability determination of a deep argillite in saturated and partially saturated conditions. International Journal of Heat and Mass Transfer, 47(14), 3517–3531. https://doi.org/10.1016/j.ijheatmasstransfer.2004.02.012

Liu, Z., Shao, J., Xie, S., Conil, N., & Zha, W. (2018). Effects of relative humidity and mineral compositions on creep deformation and failure of a claystone under compression. International Journal of Rock Mechanics and Mining Sciences, 103, 68–76. https://doi.org/10.1016/j.ijrmms.2018.01.015

Montes, H. G., Duplay, J., Martinez, L., Escoffier, S., & Rousset, D. (2004). Structural modifications of Callovo-Oxfordian argillite under hydration/dehydration conditions. Applied Clay Science, 25(3), 187–194. https://doi.org/10.1016/j.clay.2003.10.004

Robinet, J.C., Sardini, P., Siitara-Kauppi, M., Prêt, D., Yven, B. (2015). Upscaling the porosity of the Callovo-Oxfordian mudstone from the pore scale to the formation scale; insights from the 3H-PMMA autoradiography technique and SEM BSE imaging. Sediment Geol 321:1–10.

Sarout, J., Molez, L., Gu´eguen, Y. & Hoteit, N. (2007). Shale dynamic properties and anisotropy under triaxial loading: experimental and theoretical investigations, Phys. Chem. Earth, 32(8-14), 896–906.

Van Geet, M., Bastiaens, W., & Ortiz, L. 2008. Self-sealing capacity of argillaceous rocks: Review of laboratory results obtained from the SELFRAC project. Physics and Chemistry of the Earth, Parts A/B/C, 33, pp. S396–S406. DOI: 10.1016/j.pce.2008.10.063.

Wright, Hervé (2001). Rôle de la minéralogie, de la texture et de la structure dans la déformation et la rupture des argilites de l'Est, Phd Thesis, ENPC (France).

Zhang, C.-L., & Rothfuchs, T. (2004). Experimental Study of the Hydro-Mechanical Behaviour of the Callovo-Oxfordian Argillite. Applied Clay Science - APPL CLAY SCI, 26, 325–336. https://doi.org/10.1016/j.clay.2003.12.025

Zhang, C.-L., & Rothfuchs, T. (2008). Damage and sealing of clay rocks detected by measurements of gas permeability. Physics and Chemistry of the Earth, Parts A/B/C, 33, S363–S373. https://doi.org/10.1016/j.pce.2008.10.013

Zhang, C.-L., & Talandier, J. (2023). Self-sealing of fractures in indurated claystones measured by water and gas flow. Journal of Rock Mechanics and Geotechnical Engineering, 15(1): 227-238.

4.3 Effects of gas transport on fracture transmissivity and self-sealing (UKRI-BGS)

Fractures are likely to form around the repository as it is constructed. The stress that was supported by the material removed during construction must be taken up by the remaining rock, leading to stress concentrations. Depending on the strength of the host-rock, this stress concentration is likely to result in fracturing and the formation of an Excavation Damaged Zone (EDZ). It is difficult to construct any form of opening at depth without the formation of an EDZ. If tunnel supports are added, the wall rock can deform/converge to close the gap between the support and the face of the excavation. This further develops the EDZ. Gaining an understanding of the hydro-mechanical behavior of the Excavation Damaged Zone and the movement of gas is a vital area of meeting the Performance Assessment criteria for the disposal of radioactive waste. Questions are raised to whether the fractures are conduits of flow over the lifetime of the repository or whether they seal with time. Over the lifetime of the repository the saturation around the repository will evolve. The interaction of the fractures and the re-saturation of the host rock is an important area of research and is a current focus of effort. The re-saturation of clay-rich host rocks, such as shales, may result in the swelling of clay surrounding the fractures around the EDZ. The swelling of clays on a fracture surface thus may influence the fracture permeability. To investigate the self-sealing potential of fractures within the EDZ a series of direct shear experiments were conducted by BGS.

The properties of fractures in clay-rich rocks shows that self-sealing and shear can have a marked influence on the hydraulic and gas properties of the EDZ, near-field fractures, far-field faults, and joints. Limited experiments have been conducted on gas transport within fractured rocks of interest. These data suggest that fractures act as foci for gas flow and the presence of gas can perturb hydraulic transmissivity. Understanding the interaction between re-saturation, gas flow, and mechanical behaviour therefore requires further quantification.

To directly address these issues, BGS performed a series of novel experiments using a highly instrumented (normal stress, shear stress, shear displacement, normal displacement, porewater pressure/flow, etc) bespoke direct shear apparatus. Previous experiments at BGS have looked at the fracture transmissivity in Opalinus Clay along an idealised fracture (Cuss et al., 2009; Cuss et al., 2011). A follow-on study investigated hydraulic flow along a realistic fracture (Cuss et al., 2012). This work showed that hydration alone reduced fracture transmissivity by one order of magnitude, while shear displacement reduced it by a second order of magnitude. Continued shear then resulted in increased flow, eventually increasing by five orders of magnitude, three orders of magnitude greater than the starting transmissivity. The injection of fluorescein showed that only around 25% of the fracture surface was conductive. Two later studies on Callovo-Oxfordian claystone (COx) looked at the flow properties of the COx (Cuss et al., 2017) and the interface between COx and concrete (Cuss et al., 2019; 2018; 2023). However, none of these studies looked at gas flow along fractures. Other work at BGS has looked at gas flow along clay pastes at angle to the shear direction (analogue fractures/faults), e.g. Cuss et al. (2016), and the potential for fault reactivation, e.g. Cuss & Harrington (2016).

The current experimental programme was designed to answer the following research questions:

- What is the mechanical strength of intact rock during direct shear and the variability of this data?
- What is the topology/texture of the fracture formed and the variability found with repeat testing?
- What is the starting gas transmissivity of the fractures?
  - Is the variation in gas transmissivity related to the texture of the formed fracture?

- What is the hydraulic flow of the fracture following gas injection?
  o Is the variation in hydraulic transmissivity related to the texture of the formed fracture?
- What is the self-sealing potential of gas flow following hydration of the fracture?
- What is the self-sealing potential of gas flow following shear of the fracture?
- What is the influence of gas and hydraulic flow on the texture of the fracture after re-shear?

The study aimed to investigate these questions in Boom Clay, Callovo-Oxfordian claystone, Opalinus Clay, and synthetic rock made up of a mixture of clay, silt, and sand.

4.3.1 Experimental set-up

4.3.1.1 Description of apparatus

The Direct Shear Rig (DSR)

The experiments were performed using two bespoke Direct Shear Rigs (DSR), a schematic is shown in Figure 4-39. This apparatus was designed to fracture intact, cylindrical cores with the added capability of being able to directly inject water or gas onto the fracture surface to observe the fracture transmissivity over time. The apparatus and experimental approach have been proven in a number of fracturing studies which have been applied to both radioactive waste disposal research and the field of carbon capture and storage (Cuss et al., 2019; 20181,2; 2017; 2016; 2015; 2011; Harrington et al., 2017; Wiseall et al., 2018).

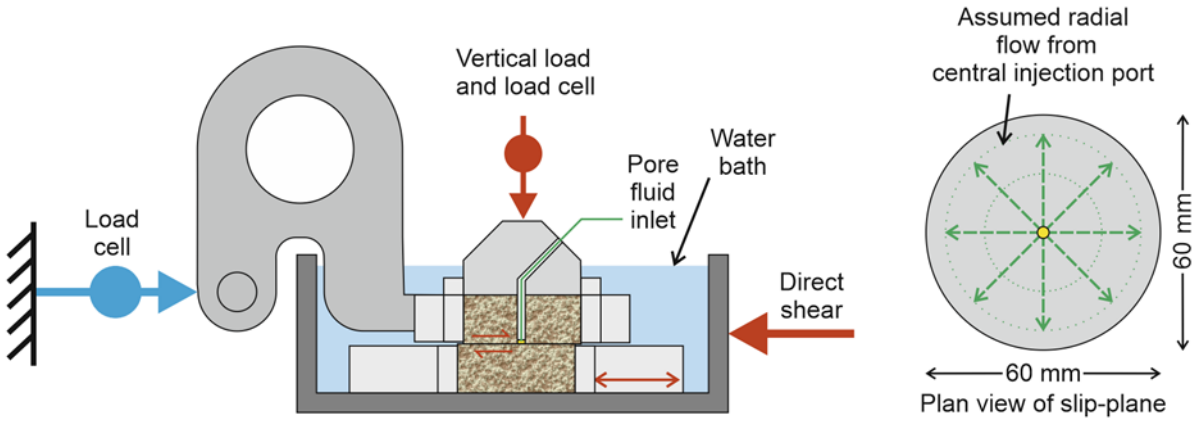

Figure 4-78 – Schematic of the Direct Shear Rig (DSR).

The custom-made Direct Shear Rig (Figure 4-39, Figure 4-40) comprises the following components:

1. Rigid steel frame that had been designed with a bulk modulus of compressibility and shear modulus approximately 2 orders of magnitude greater than the rock tested, resulting in minimal deformation of the apparatus compared to the test sample;
2. Vertical load system comprising an Enerpac hydraulic ram controlled by a Teledyne/ISCO 260D syringe pump, a rigid loading frame and an upper thrust block (up to 72 kN force). Vertical travel

of the thrust block was measured by a high precision non-contact capacitance displacement transducer, which had a full range of ± 0.5 mm and an accuracy of 0.06 µm;

3. Shear force actuator comprised of a modified and horizontally mounted Teledyne/ISCO 500D syringe pump designed to drive shear as slow as 14 µm a day at a constant rate (equivalent to 1 mm in 69 days) or as fast as 0.5 mm per second along a low friction bearing. The movement of the bottom-block was measured using a linear variable differential transformer (LVDT), which had a full range of ± 25 mm and an accuracy of 0.5 µm;
4. Fluid injection system comprising a Teledyne/ISCO 500D syringe pump that could deliver water or gas to a pressure of up to 25.8 MPa;
5. A custom designed data acquisition system using National Instruments LabVIEW™ software facilitating the remote monitoring and control of all experimental parameters;
6. A sample assembly comprising two sample holders, where the bottom block was actively sheared, and the top block was connected through a linkage system to a force gauge measuring the shear stress along the slip plane. Vertical load was applied to the rock samples by means of a steel thrust block.

Cylindrical samples of 60 ± 0.01 mm diameter and 53 ± 1 mm height (Figure 4-41) were rigidly housed within two steel collars. The sample was loaded vertically by means of a hydraulic ram, which was actuated using an ISCO/Teledyne 260D syringe pump. The capacity of the pump and ram meant a maximum of 34.7 MPa could be achieved, although in practice vertical stress was lower. Load was measured by two Applied Measurements Limited load cells (DBBW-5T) with an accuracy of ± 0.01 MPa and vertical displacement by a MicroSense 4810/2810 induction sensor with a full range of ±0.5 mm and an accuracy of ±0.06 µm. Horizontal stress was created by the Poisson's effect in response to vertical loading in a K0 geometry. The sample was sheared by means of a second (500D) syringe pump, which had been modified to directly shear the sample along a low-friction track. Shear stress transmitted through the sample/fracture was measured by a 50 kN rated load cell (17.6 MPa) with an accuracy of 0.01 MPa. Horizontal movement of the shear water bath was measured by either a Mitutoyo Digimatic Indicator with a full range of 25 mm and an accuracy of 1 µm, or a linear variable differential transformer (LVDT), which had a full range of ±25 mm and an accuracy of 0.5 µm; dependant on which DSR was used. Fluid was injected directly to the fracture through a 4 mm bore drilled to the fracture plane, which had a porous plastic filter at the end. Injection pressure was controlled by a third (500D) syringe pump. For the injection of gas, a 1,000 ml water/gas interface vessel was used. Injection pressure was measured using a Gems 3100 series pressure transducer with a maximum range of 10 MPa and an accuracy of ±0.025 MPa. All three syringe pumps recorded pressure (±0.003 MPa), flow rate (±0.25 µl/h), and volume (±1 µl).

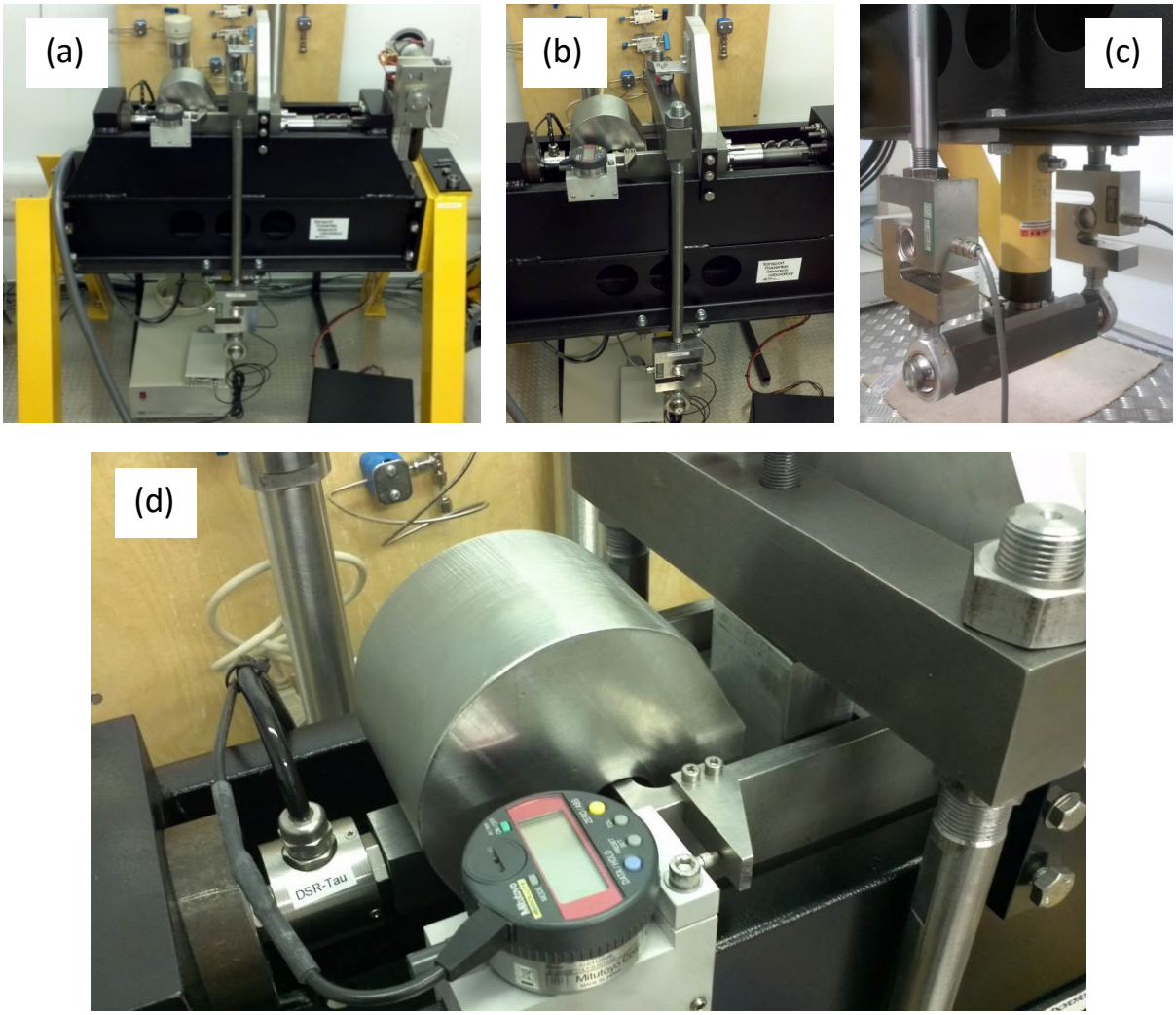

Figure 4-79 – Components of the Direct Shear Rig. a) Photo of the complete apparatus; b) Loading frame with normal load cells at the bottom; c) normal load ram (yellow); d) sample assembly, shear load cell and Mitutoyo Digimatic Indicator.

The original DSR used square samples, meaning that as a sample sheared, the contact area between the top and bottom sample changed, and as a result normal stress increased if normal load was maintained constant. The use of a cubic arrangement meant that the change in contact area was simple and experience showed that it was not necessary to correct if strain was limited to a maximum of 0.1 (10 %). Subsequent studies required the apparatus to be modified to accommodate cylindrical samples (Figure 4-41a). Holders were designed with two semi-circular collars that were bolted together to create a complete circular sample holder (Figure 4-41b). These were held in blocks that had been machined to hold the circular holders (Figure 4-41d). These were manufactured to give a close fit, with a grub screw securing the holders. This arrangement meant that samples could be stored between experimental stages and that batch testing could occur as multiple sets of collars were available.

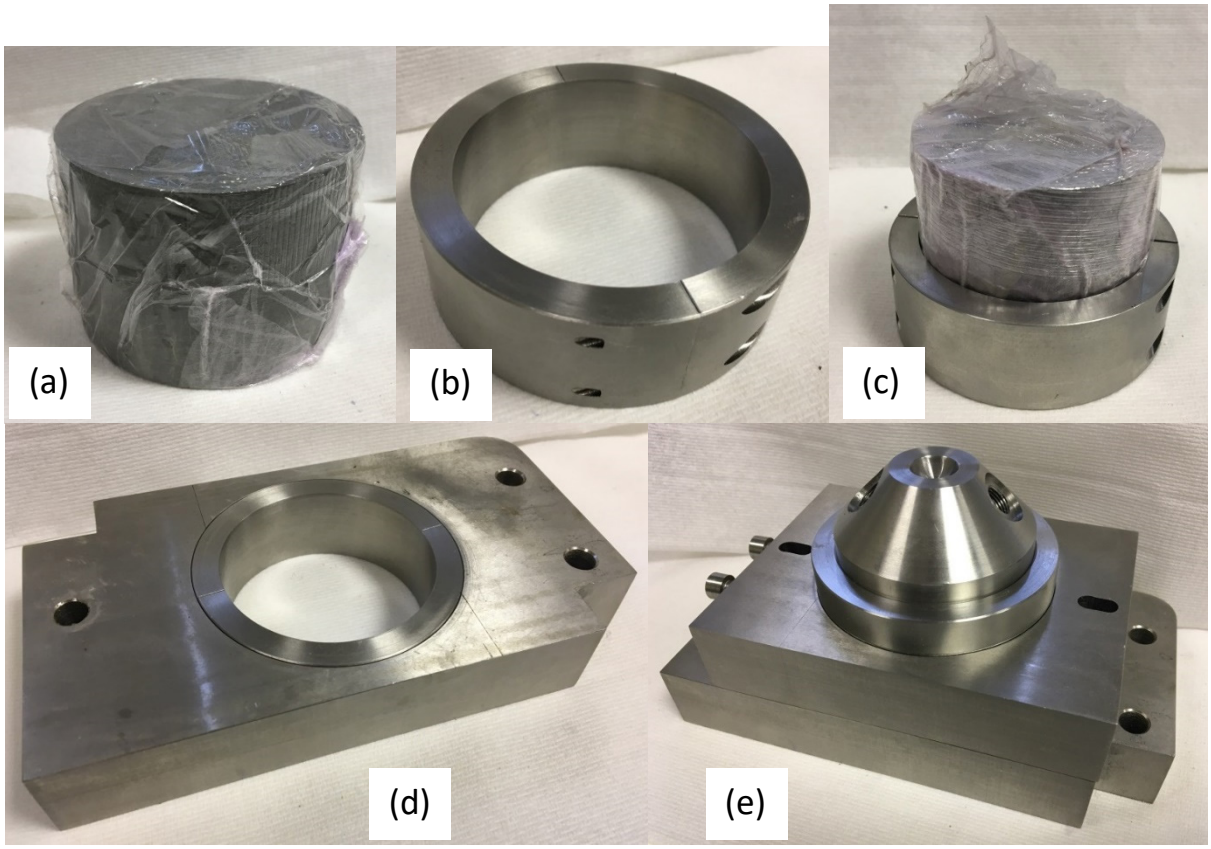

Figure 4-80 – Sample holder arrangement. a) cylindrical sample of rock; b) sample holder; c) sample holder and sample; d) sample holder and lower block arrangement; e) complete sample holder arrangement.

Fracture surface scanner

Understanding the topography of fracture surfaces (fracture roughness) is important in estimating the hydro-mechanical behaviour of discontinuities within a rock mass or along interfaces. Flow properties and mechanical strength will be affected by the spatial distribution of contact areas, which in turn affect the stress distribution and ensuing asperity damage during normal and shear loading.

Fracture surfaces were measured using laser triangulation, whereby the fracture surfaces were scanned to produce a 3D mesh model of the fracture surface. A NextEngine 3D Scanner HD, or latterly a Revopoint MINI 3D Scanner was used (Figure 4-42). The NextEngine scanner had an accuracy within an error of ± 65 microns, whereas the Revopoint MINI had an accuracy of ± 20 microns. The reason for changing scanners mid-experimental programme was the Revopoint MINI allowed the fractures to be scanned whilst still in the apparatus and did not require for the surface to be oriented vertically for scanning, which resulted in some loss of material. Both scanners output surface data that were processed using TrueMap 5.0 surface topography software.

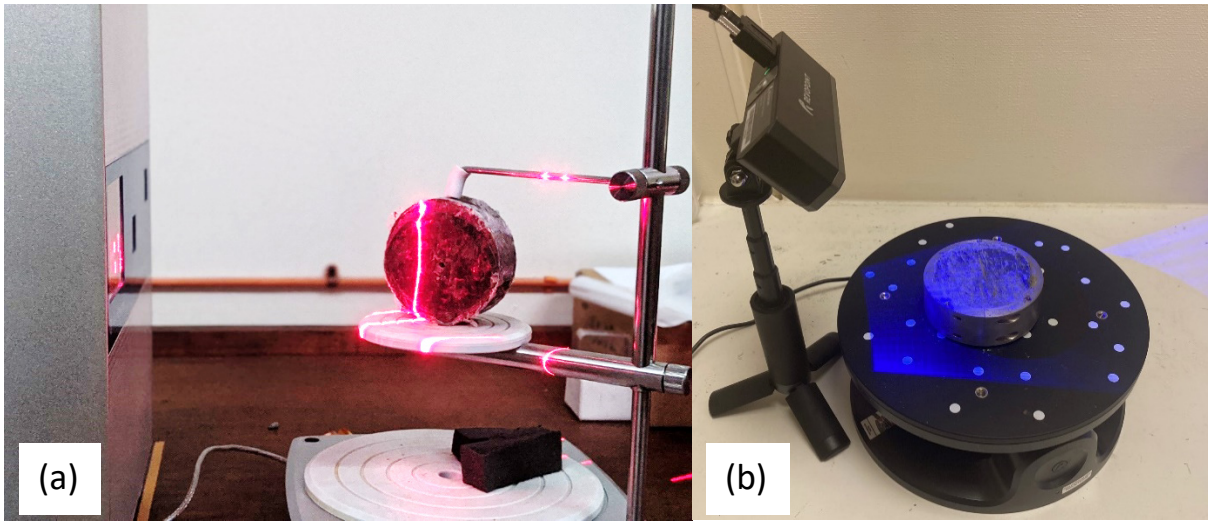

Figure 4-81 – Laser scanning of fracture surfaces. a) NextEngine 3D Scanner HD; b) Revopoint MINI 3D Scanner.

4.3.1.2 Calibration

The apparatus comprised three syringe pumps, three load cells, one pore pressure sensor, one sensor for measuring displacement, and one induction sensor for measuring vertical displacement. Each type of device had a different calibration routine and/or cycle between repeat measurements.

Only two of the syringe pumps could be calibrated as the third was modified to give direct drive to system and as such didn't need calibration. The syringe pumps were calibrated at regular intervals by pressurising at 0 (atmospheric), 2.5, 5, 7.5, 10, 7.5, 5, 2.5, and 0 MPa. At each stage the pressure reading of a Fluke pressure calibrator was noted to give precise pressure measurement. The Fluke calibrator was itself re-calibrated by the manufacturer on an annual basis to industry standards. A similar approach was used for the pore pressure transducer; however, it was pressurised at 0, 0.8, 1.6, 2.4, 3.2, 4, 3.2, 2.4, 1.6, 0.8, and 0 MPa.

The three displacement devices were only re-calibrated at the end of the experimental programme. For all three devices the manufacturer supplied calibration was initially assumed. Re-calibration was performed using calibration blocks, which were manufactured to high standard and allowed the devises to be displaced by known distances. By using multiple calibration blocks over a range of lengths, it was possible to confirm calibration of all three devices.

The load cells were not easily accessible and re-calibration was not straightforward. Therefore, manufacturer supplied calibrations were adopted and at the end of the experimental programme, the calibration was confirmed. To calibrate the load cells, the device was removed from the apparatus and placed within a small hydraulic load-frame. Each load cell was placed one at a time in series with a calibration load cell device. The load cells were loaded over a range of steps and the electrical output was noted against the load reading of the calibration device. The latter was re-calibrated annually by the manufacturer to industry standards.

For all calibration data the slope, intercept, and R2 were calculated, the latter being used to ascertain whether the calibration had been of sufficient quality, with R2 expected to be close to unity. As well as R2, graphs of the calibration were also inspected. Where necessary, calibration was repeated if R2 was not acceptable. During the experimental programme, no device showed significant deviation from the initial calibration.

4.3.1.3 Testing fluids

All tests were conducted with helium as the gas permeant. Given the importance of fluid chemistry on the behaviour of clay-rich materials, it was crucial that transport and mechanical testing was conducted using water in equilibrium with the test material. For the hydraulic stage of the experiment, synthetic pore water was manufactured to ensure the water was chemically balanced with the test samples.

Boom Clay synthetic pore fluid

A detailed analysis of pore fluid data for the Boom Clay formation was conducted by De Craen et al. (2004) and a reference pore water composition defined for the HADES underground research laboratory (Table 4-9). Synthetic solutions were mixed in batches approximately every 6 months, depending on the amount of testing being conducted. The recipe for making the pore fluid is described in Table 4-10.

Table 4-19 – Reference Boom Clay pore water after De Craen et al. (2004).

Ion	mg/l	mmol/l	Ion	mg/l	mmol/l
Ca	2.0	0.05	**Al**	0.6×10^{-3}	2.4×10^{-5}
Fe	0.2	0.003	**Total S**	0.77	0.02
Mg	1.6	0.06	**Cl -**	26	0.7
K	7.2	0.2	**SO_4^{2-}**	2.2	0.02
Si	3.4	0.1	**HCO_3 -**	878.9	14.4
Na	359	15.6			

Table 4-20 – Recipe for making Boom Clay synthetic pore water.

Chemical	mg/l	Chemical	mg/l	Chemical	mg/l
$NaHCO_3$	1209	**$FeSO_4$**	0.456	**KCl**	14.91
Na_2SiO_3	12.2	**$MgSO_4$**	2.046	**NaCl**	18.35
$CaCl_2$	5.55	**$MgCl_2$**	4.094	**NaOH**	27.44

Callovo-Oxfordian claystone synthetic pore fluid

The hydrochemistry of the interstitial fluid was provided by Andra (Table 4-11). A stock solution was used when mixing all clay pastes.

Opalinus Clay synthetic pore fluid

A detailed analysis of the pore fluid chemistry of the Opalinus Clay was reported by Pearson et al. (2003), the so-called Pearson Water. Table 4-12 shows the recipe of the pore fluids used in the current study.

Table 4-21 – Recipe for making Callovo-Oxfordian claystone synthetic pore water.

Ion	mg/l	Ion	mg/l	Ion	mg/l
$CaSO_4,2H_2O$	930	**NaCl**	1724	**$NaHCO_3$**	344
$MgCl_2,6H_2O$	915	**$SrCl_2,6H_2O$**	53		
KCl	45	**Na_2SO_4**	1023		

Table 4-22 – Pore-water chemistry used as test fluid on all samples, from Pearson et al. (2003).

Ion	mg/l	Ion	mg/l
NaCl	7598	CaCl2,2H20	816
KCl	231	Na2SO4	1420
MgCl2,6H20	511	Na2CO3	33

4.3.2 Material properties (pre-test and post-test characteristics)

Boom Clay

The geological and hydrogeological setting of the Boom Clay in northern Belgium has been summarised by Beerten & Leterme (2012) and in the Netherlands by Vis & Verweij (2014). The Boom Clay (usually referred to as the Rupel Clay in the Netherlands) is of lower Oligocene (ca 28 to 34 Ma) age and forms part of the Rupel Formation. In the Netherlands the Rupel Formation has been subdivided into the Vessem, Rupel Clay, and Steensel members (Wong et al., 2007). These members are diachronous, with both the basal Vessem and the overlying Steensel members being sandy marine deposits (Vis & Verweij; 2014) laid down close to the palaeo-shorelines. The Boom Clay is a pyritic, grey to dark brown marine clay with septarian (carbonate rich) concretions. Towards the basin margins the clays grade into sands. The formation reaches a maximum thickness of up to 250 m, with a mean thickness of around 65 m, and dips gently towards the north-east at between 1 and 2°.

The core material used in the current study was taken from the HADES underground research laboratory at Mol in Belgium. Here, the Boom Clay consists mainly of mixed clay and silt, with additional minor sand (Bernier, 2007). Mineralogical composition of the Boom Clay is widely reported, predominantly assessed using XRD. The clay content is generally reported to vary from between 23 and 60 % of the bulk material composition and is predominantly made up of illite, smectite and kaolinite, which is often seen in interlaminated zones (Blanchart et al., 2012; Dehandschutter et al., 2004; Wemaere et al., 2008; Yu et al., 2012). The non-clay fraction of the Boom Clay primarily consists of quartz, again widely reported to vary between 23 and 60 %. The remaining percentage of the non-clay fraction consists of feldspars, calcite, and pyrite. Honty & De Craen (2011) report the composition to be 22-77 % quartz, 0-6.3% albite, 0.4-17.3% k-feldspar, 0-1.5% siderite, 0-4.6% calcite, 0-2% apatite, 0.3-5% pyrite, 5-37% illite/muscovite, 6.8-35% smectite + illite/smectite, 2-16% kaolinite, and 14-4% chlorite. This demonstrates the variability of Boom Clay. Cores of Boom Clay were acquired from SCK-CEN (Belgium) from the HADES URL from a depth of 220m.

Callovo-Oxfordian claystone

The Callovo-Oxfordian claystone (COx; 150-160 Ma) was deposited under marine basin conditions during a period in which the Paris Basin, France, was variously linked to the Atlantic and Tethyan Oceans, as well as to the London Basin and North Sea (Rousset & Clauer, 2003). Clay sedimentation is therefore considered to have two primary inputs: continental and oceanic. The claystone is over- and underlain by Oxfordian and Bathonian shelf limestones. It is primarily clayey at its base, then becomes increasingly silty and then increasingly calcareous at its top (Gaucher et al., 2004). A maximum clay content zone within the clayey base has been identified; this is interpreted to mark the inflection point (and interval of maximum flooding) from a lower transgressive sequence to an upper regressive sequence (Gaucher et al., 2004).

The UA variety of the COx occurs at repository depth and can be considered to be the clay-rich part of the unit. The samples used came from the Meuse/Haute-Marne underground research laboratory at Bure in France. Yven et al. (2007) report three main mineral phases; clay minerals, quartz and calcite. Secondary mineral phases include dolomite, feldspar, pyrite, hematite and traces of siderite. Calcite and quartz represent 40 – 55 % of the rock. Clay represents 20 – 55 %, with secondary minerals forming less than 5 %. Clay minerals include illite and illite-smectite with subordinate kaolinite and chlorite. Wenk et al. (2008) reports clay 25-55 wt%, 23-44% carbonates and 20-31% silt (essentially quartz + feldspar). Clay minerals are reported to include illite and illite-smectite with subordinate kaolinite and chlorite. In the upper half of the formation the illite-smectite is disordered and contains 50-70% smectite interlayers, whilst in the lower half the illite-smectite is ordered (R=1 type) with lower contents (20-40%) of smectite interlayers (Wenk et al., 2008). Beds can contain common organic matter. Other authors report compositions similar to these. Wileveau & Bernier (2008) quote values for quartz (18%), calcite (25%), clay minerals (55%; illite-smectite ~65%, illite 30%) and kaolinite and chlorite (2%) with subordinate feldspars, pyrite and iron oxides (2%). Esteban et al. (2006) report 35-60% clay minerals with the remaining shared by calcite and silt. Armand et al. (2017) report that the UA unit makes up two-thirds of the total geological layer thickness.

Upon receipt of preserved T-cell core barrels from Andra, the material was catalogued and stored under refrigerated conditions of 4 °C to minimize biological and chemical degradation. The preserved core barrels consisted of a multi-layered arrangement designed to re-stress the core to in-situ stress and to environmentally seal it to reduce chemical, biological and drying effects. Samples were tested within 12 months of the core being extracted from the Meuse/Haute-Marne URL.

Opalinus Clay

The Opalinus Clay (OPA) is a Jurassic (Aalenian, ~180 Ma) shallow marine clayshale found in Switzerland. The formation, named after the ammonite Leioceras opalinum, consists of indurated dark grey micaceous claystones (shales) that are subdivided into several lithostratigraphic units. Some of them contain thin sandy lenses, limestone concretions, or siderite nodules. The clay-mineral content ranges from 40 – 80 wt% (9 – 29 % illite, 3 – 10 % chlorite, 6 – 20% kaolinite, and 4 – 12 % illite/smectite mixed layers in the ratio 70/30). Other minerals are quartz (15 – 30 %), calcite (6 – 40 %), siderite (2 – 3 %), ankerite (0 – 3 %), feldspars (1 – 7 %), pyrite (1 – 3 %), and organic carbon (<1 %). The total water content ranges from 4 – 19 % (Gautschi, 2001). At the Mont Terri underground research laboratory, three facies can be distinguished; a shaly facies in the lower half of the sequence, a 15 metre thick sandy, carbonate-rich facies in the middle of the sequence and a sandy facies interstratified with the shaly facies in the upper part. For the current study, samples from the shaly facies were used. The OPA at Mont Terri is an over-consolidated shale with a maximum burial depth of 1,200m and is presently around 280m depth. All core material used in the current study came from the shaly facies at the Mont Terri underground research laboratory. Core material derived from two drilling campaigns. For samples with bedding oriented perpendicular with the shear direction, the core was drilled for the Eurad project from borehole BFI-4. For samples oriented with bedding parallel with the shear direction, core from BFI-3 or BGT-1 was used. The latter was drilled for the Gas Transfer (GT) project of the Mont Terri Consortium and was agree for use in the current study by GT project partners.

Sample Preparation

Callovo-Oxfordian claystone arrived at BGS in a pre-stressed state in a T-cell. The Opalinus Clay samples were taken by BGS or contractors at the Mont Terri underground research laboratory and were stored in clamped arrangements similar to a T-cell. The Boom Clay samples were stored in vacuum packed foil. Once extracted from the storage arrangement, lengths of approximately 300mm of core were supplied, which were subsampled for testing. During the sub-sampling process a section of core approximately 60 mm in length was cut using a diamond saw. This cut length of core was then trimmed on the lathe (Figure 4-43) to the sample dimensions of 60 mm in diameter and 53 mm in length; during this process care was taken to ensure the faces of the sample were perpendicular to the length of the sample. This process was done as quickly as possible to reduce the time the sample was exposed to the atmosphere and therefore maintain, as much as possible, the in-situ properties of the core. Both the cut sample for testing, as well as the remains of the large core were then wrapped in cling film and vacuum packed for storage.

Figure 4-82 – Callovo-Oxfordian Claystone sample being cut on a lathe during the careful sample preparation process.

4.3.3 Testing protocol

Cylindrical samples were prepared by machine lathing with dimensions of 60 mm diameter and 53 mm height. The height of the sample can vary between 52 and 54 mm without affecting the experiment, whereas the diameter of the sample must be as close to 60 mm as possible to fit closely within the steel collars, with a maximum of 60 mm. Tests were conducted using Boom Clay, Callovo-Oxfordian Claystone, and Opalinus Clay, with further testing being conducted using rock simulant (precompacted quartz, clay, and silt). Each test consisted of eight distinct steps as outlined below and summarized in Table 4-13 and Figure 4-44:

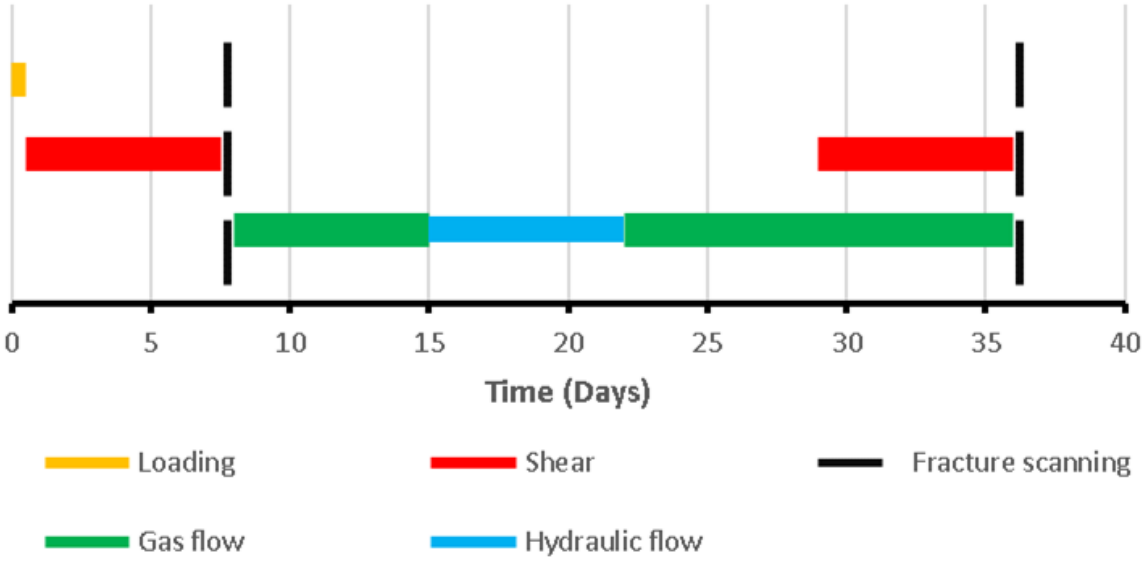

Figure 4-83 – Graphical summary of the test stages.

Stage 1: Sample loading. Each sample was weighed and measured, and then wrapped in cling film to reduce the de-saturation of the sample during testing. Two stainless steel collars were attached, with the sample/collar arrangement loaded into the apparatus. Vertical load was placed upon the sample slowly in steps, taking a few minutes to reach the desired load. Once the sample was fully loaded, the evenness of the load across the load frame was noted and adjusted, if necessary, with the two normal load cells reading the same load within 2 or 3%.

Stage 2: Intact Shear. The "intact" sample was sheared to create a fracture at the mid-plane of the sample and to determine baseline mechanical properties. The shear rate was set to achieve 5 % shear strain over a period of one week. This data determined the shear modulus, peak shear stress, and residual shear stress. In addition, data on dilation/contraction of the sample during shear was recorded.

Table 4-23 – Description of test stages.

Stage	Detail	Duration (days)
Sample loading	Sample weighed and measured, wrapped in cling film, and loaded into two steel rings. Sample loaded into the DSR, and normal load increased in a series of steps to target stress.	1
Intact shear	Intact sample sheared at constant rate to create a realistic fracture.	7
Fracture scanning	Both fracture surfaces were laser scanned to determine fracture topology. Top fracture had a 4mm hole drilled to allow the addition of an injection bore directly to the fracture plane.	1
Initial gas flow	Constant gas pressure of 1 MPa created, and flow monitored	7
Hydraulic flow	Injection of synthetic pore water at a constant pressure of 1 MPa	7
Repeat gas flow	Constant gas pressure of 1 MPa created, and flow monitored	7
Repeat shear	Sample re-sheared at a constant rate and gas flow monitored	7
Repeat fracture scanning	Both fracture surfaces were laser scanned to determine fracture topology.	1

Stage 3: Fracture Scanning. The normal load on the fracture was removed and the apparatus taken apart so that the sample could be extracted. Photographs were taken of the fracture during disassembly to note any features of interest and to reorient the samples correctly after scanning had been completed. The two fracture surfaces were scanned using either a NextEngine or a Revopoint Mini scanner. The top sample had a 4 mm hole drilled through it using a masonry drill. Care was taken to not heat the drill, which was centrally located by means of a former. The hole was drilled from the fracture face so as not to damage the fracture surface when drilling all the way through the sample. This hole allowed an injection bore to be added. This 4mm diameter pipe had a porous plastic filter at the end and was inserted into the hole to a depth flush with the fracture surface. A small quantity of silicone sealant was smeared on the bore prior to insertion, additional silicone was also smeared on the top-block to seal between this component and the top of the sample. The complete sample assembly was then carefully re-loaded into the apparatus so that re-shearing would occur in the same direction. A small degree of

mismatch between the upper and lower fracture faces was likely. However, this was deemed more representative of fractures within the EDZ. Normal load was then re-established to restart testing. Note: Stage 3 lasted less than one hour and whenever necessary, the sample was stored in sealed plastic boxes to reduce drying effects.

Stage 4: Initial Gas Flow. The first flow stage saw gas pressure increased to 1 MPa (an initial helium volume of around 100 ml at 1 MPa). The flow rate was monitored from the volume of the injection syringe pump. The initial flow in establishing 1 MPa was often high as there was void space created by the asperities on the fracture surface and within the injection bore. Gas flow was then monitored for one week. This stage determined the fracture gas transmissivity and the stability of transmissivity over a period of one week.

It should be noted that some tests had considerable flow, with the full volume of gas draining through the fracture in less than an hour. When this occurred, flow was determined from the syringe pump when 1 MPa pressure was achieved. Two to three repeat flows were then conducted over the course of a few days to see if flow was changing. In some tests, high initial flow meant that Stage 4 was abandoned.

Stage 5: Hydraulic Flow. Synthetic pore fluid was injected into the fracture to re-saturate the fracture and to encourage self-sealing. Injection pressure was set to 1 MPa with the pump volume determining the flow rate. Initial flow was relatively high as the gas filled asperities meant the system was compressible. However, flow quickly settled and was not seen to be high enough (<100 µl/h) to be concerned about erosion of the fracture. Pore fluid was injected for one week, or shorter if flow averaged 0 µl/h for a prolonged period. This stage determined the hydraulic flow properties of the fracture, as well as swelling behaviour.

Stage 6: Repeat Gas Flow. Following the hydraulic test, the injection system was flushed of water in readiness for a repeat gas injection stage. Gas pressure was increased to 1 MPa (an initial helium volume of around 100 ml at 1 MPa), with the flow rate monitored from the volume of the injection syringe pump. Gas flow was then monitored for one week. This stage determined the fracture gas transmissivity following re-hydration of the fracture and the stability of transmissivity over a period of one week. Comparing Stage 4 with Stage 6 determined the self-sealing capacity of the fracture to hydraulic flow.

Stage 7: Flow During Shear. The sample underwent shear for a period of one-week, continuing gas injection. This investigated the effect of shearing on gas transmissivity. The shear rate was set to achieve ~10 % strain (6mm). This stage determined the shear modulus, yield shear stress, peak shear stress, and residual shear stress of the fracture on re-shear. In addition, data on dilation/contraction of the sample during shear was recorded. Comparing the gas flow rate of Stage 6 with Stage 7 determined the self-sealing capacity of the fracture to shear displacement.

Stage 8: Test decommissioning. The experiment was dismantled, and the fractures was scanned once more to determine whether repeat shearing had created a new failure surface or exploited the existing fracture. This would show whether any self-healing had occurred or whether only self-sealing had been seen. The sample was photographed and stored in sealed boxes that had holes drilled into them so that the sample could be stored in vacuum sealed bags. The use of the plastic boxes meant that the vacuum sealing bag did not contact the fracture surface.

All tests were conducted as near-identical as possible to allow comparison.

Experimental programme

Table 4-14 summarises the planned test programme. For Boom Clay (BC), two test conditions were investigated, with two different normal loads to investigate the differences expected at the different depths of the proposed disposal concepts in Belgium and the Netherlands. For both Callovo-Oxfordian

claystone (COx) and Opalinus Clay (OPA), tests were conducted with bedding either parallel or perpendicular to the shear direction. Finally, a suite of six experiments were planned to be conducted in synthetic rocks, as used by BGS in other experimental components of EURAD-GAS. This meant 24 experiments were planned. At the time of reporting, most experiments had been completed in BC, COx, and OPA, with no tests conducted in the synthetic rocks. All test conditions in BC, COx, and OPA had at least two tests completed in time for reporting, as summarised in Table 4-14.

Table 4-24 – Experimental programme.

Rock	Normal load (MPa)	Fluid injection pressure (MPa)	Shear orientation
Boom Clay	5.1	1	Parallel
	3	1	Parallel
Callovo-Oxfordian claystone	7.1	1	Parallel
	7.1	1	Perpendicular
Opalinus Clay	4	1	Parallel
	4	1	Perpendicular
Synthetics#	4	1	Parallel

Fracture Roughness Measurements

Fracture roughness can influence the mechanical, hydraulic, and gas properties of a fracture and therefore influence the overall hydro-mechanical properties of the rock mass. On a fracture surface there may be areas both in contact and not in contact with the opposing fracture wall, this will create a non-uniform stress distribution on the fracture surface. In turn this will influence the formation of asperities on the fracture surface. The degree to which these asperities form can influence the connectivity of flow pathways on the surface, therefore influencing the transmissivity of fluids along or across a fracture surface.

In the present study, laser triangulation method was adopted, whereby the fracture surfaces were scanned using either a NextEngine 3D Scanner HD or a RevoPoint MINI 3D scanner. This produced a 3D mesh model of the fracture surface accurate within an error of ± 65 microns. Algorithms inbuilt within the data acquisition ScanStudio HD or RevoScan software produced clean surface data, which were used in subsequent empirical and statistical analysis.

The measured surface data was composed of three components: form, waviness, and roughness. The form corresponds to the underlying shape and tilt of the surfaces with respect to the measuring platform. A “corrected” profile obtained by removing form from the surface data can be used to obtain a 2-D profile that describes the surface texture. This profile after removal of form is usually referred to as the “primary profile”. The stages are depicted in Figure 4-45.

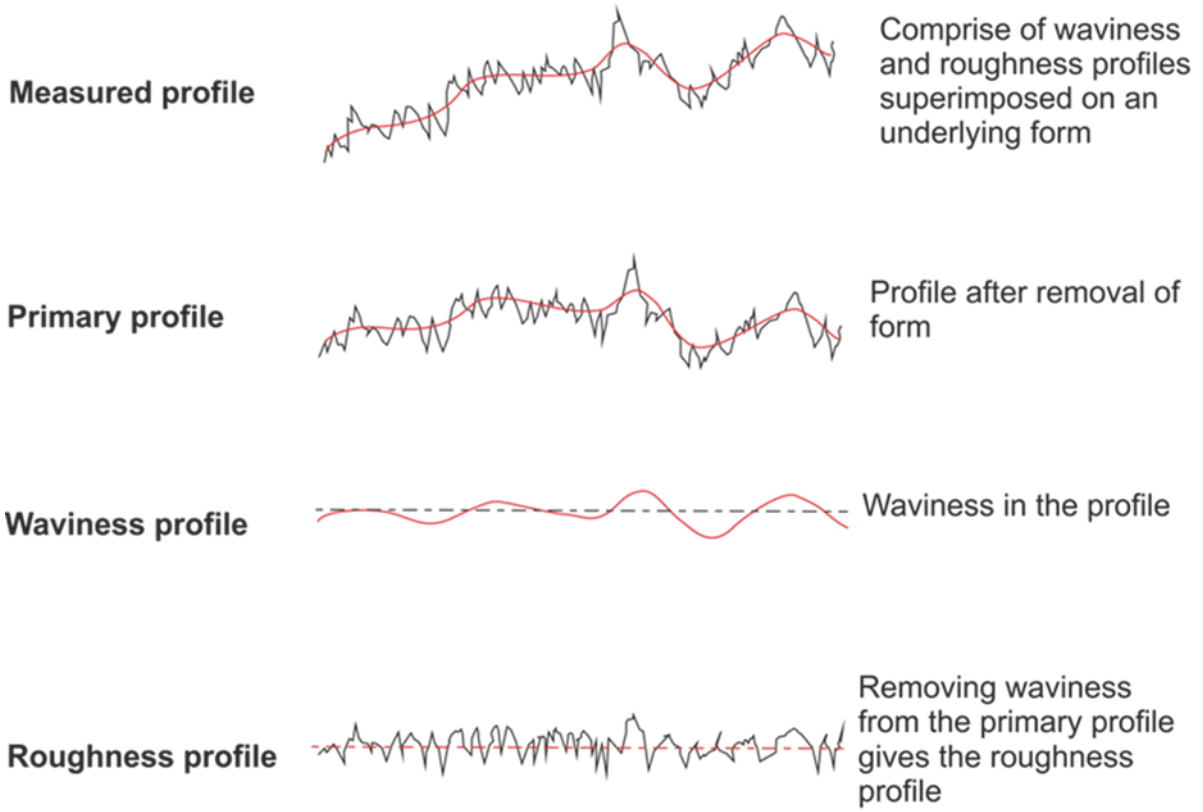

Figure 4-84 – Summary of stages involved in analysis of measured profile to obtain a roughness profile (From ASTM standard, 2009).

From the primary profile, the waviness profile is removed by applying a band-pass filter. In theory, difference between the primary and waviness profile gives the roughness profile. However, in the present study no band-pass filters were applied due to lack of uniform waviness in the dataset. Hence, surface roughness calculations were performed on "primary profile" datasets spanning the entire fracture surface. All the data processing and surface parameter calculations were performed in TrueMap 5.0 surface topography software. This software package was able to calculate surface or profile parameters using SI methods. Table 4-15 lists the common parameters calculated for describing the fracture surfaces.

Table 4-25 – List of parameters calculated to describe surface characteristics of a test fracture.

Parameter	Symbol	Description
Roughness average	R_a ; S_a	Arithmetic mean of the absolute distances of the surface points from the mean plane/profile
Root Mean Square (RMS) Roughness	R_q; S_q	Square root of average squared absolute height values of the surface profile from the mean line
Peak Height	R_p; S_p	Maximum height above the mean line/plane
Valley Depth	R_v; S_v	Maximum depth below the mean line/plane
Peak to Valley Height	R_t; S_t	Maximum peak to valley distance
Kurtosis	R_{ku}; S_{ku}	Measure of the sharpness of the surface/profile
Skewness	R_{sk}; S_{sk}	Measures the symmetry of the variation of a profile/surface about its mean line/plane
Texture Direction	S_{td}	Direction of the texture of a surface with respect to the y axis
Texture Direction Index	S_{tdi}	Measure of how dominant the predominant direction is relative to the rest of the surface

Calculation of fracture transmissivity

Fracture transmissivity was calculated assuming radial flow from the injection hole given the steady state fluid flow rate Q and the pressure head H at the injection point. Steady flow in a cylindrical geometry can be given by:

$$Q = \frac{2\pi T\left(h_i - h_0\right)}{\ln\left(r_o\right) - \ln\left(r_i\right)} \qquad 4\text{-}4\text{-}1$$

where T is the transmissivity, h_i is the head on the inner surface with radius r_i, and h_o is the head on the outer surface at radius r_o. Therefore fracture transmissivity is given by:

$$T = \frac{Q\ln\left(r_o\right) - \ln\left(r_i\right)}{2\pi\left(h_i - h_0\right)} \qquad 4\text{-}4\text{-}2$$

For the experimental setup r_o = 30 mm, r_i = 1.96 mm, h_o = 0.05 m and h_i ~ 100 m, transmissivity can simply be calculated from:

$$T = 1.183 \times 10^{-12}\,\frac{Q}{P_p} \qquad 4\text{-}4\text{-}3$$

if the fluid flux (Q in $\mu l.hr^{-1}$) and pore pressure (P_p in kPa) are known. This relationship was used to calculate the transmissivity of the fracture throughout the experiment. A correction could be made for the change in contact area between the blocks, and hence the outer radius of the fracture, however scoping calculations demonstrated this had only a negligible effect on the overall calculation compared with the uncertainty of how the fracture contact area changed with time.

Calculation of self-sealing potential (SSP)

Experience has shown that there is considerable variation in flow in repeat experiments. For example, in the current study the initial gas flow stage for samples that were sheared perpendicular to bedding gave variation between 3.3 µl/h and 1.5 × 10^6 µl/h. Of the four experiments, one showed very high variation, even discounting this test, flow varied between 3.3 and 276 µl/h; three orders of magnitude variation. The hydraulic flow stages in these tests also showed variation between 0.4 and 152 µl/h, a variation of more than three orders of magnitude. The fracture topology was measured to ascertain whether variation in flow is related to the surface characteristics of the fracture. However, flow is likely to be associated with asperities and fracture roughness is not a measure of mismatch between the top and bottom fracture surface and therefore not an estimate of the properties of asperities.

The experiment was designed to determine four different flow magnitudes; initial gas flow, hydraulic flow, repeat gas flow, and gas flow during shearing. From these four parameters it was aimed to determine the change in flow as a result of (1) hydration of the fracture and (2) shear along the fracture. The change in flow determines the self-sealing potential of the rock. Therefore, self-sealing potential is defined as:

$$SSP_{H2O} = \frac{Flow\ of\ gas_{initial}}{Flow\ of\ gas_{repeat}} \quad \text{and} \quad SSP_{\tau} = \frac{Flow\ of\ gas_{repeat}}{Flow\ of\ gas_{shear}}$$

This measure of self-sealing potential removes the variation in flow and defines a proportional variation. It is still expected that variation will exist but that this approach removes a large part of the variation. It should be noted that that SSP > 1 means that gas flow is reduced. Therefore, a SSP_{H2O} of 2 means that hydration of the fracture has resulted in a halving of the gas flow. Conversely, SSP < 1 means that flow has increased. Therefore, a SSP_{τ} of 0.5 means that flow has doubled because of shearing.

4.3.4 Results

At the time of reporting, a total of 20 shear experiments had been completed (Table 4-16). For all of the natural rock types, this meant that at least two experiments had been completed for each condition, with most having all three planned tests. At the time of reporting, none of the experiments using synthetic material had been conducted.

It is not necessary to report the detail of every test. Therefore, one test is described in detail to describe the features seen and the method used to calculate parameters. Following this description, the results will concentrate on comparisons between tests.

Table 4-26 – References of the various samples with the corresponding characteristics and experimental conditions.

Rock type	Normal load (MPa)	Luid injection pressure (MPa)	Shear orientation	Status
Boom Clay	5.1	1	Parallel	1 2 3
	3	1	Parallel	1 2 3
Callovo-Oxfordian	7.1	1	Parallel	1 2 3
	7.1	1	Perpendicular	1 2 3
Opalinus	4	1	Parallel	1 2 3
	4	1	Perpendicular	1 2 3
Synthetics	4	1	Parallel	1 2 3 4 5 6

4.3.4.1 Example test: FPR_21_047 – Callovo-Oxfordian ⊥

Test FPR_21_047 was started on the 25th November 2021 and was completed on the 14th January 2023, a total of 50 days duration. The test was the first conducted in Callovo-Oxfordian claystone with the shear direction perpendicular to bedding.

Initial shear

The first stage of the experiment takes the intact cylindrical sample of around 53 mm height and 60 mm diameter and creates a shear fracture at the midplane, creating two halves of the sample around 26 mm in height. Figure 4-46 shows the results of the initial shear stage. Figure 4-46a shows the stress result. A normal load of 7 MPa was placed on the sample, but this can be seen to have increased as the sample was sheared. This is commonly seen in the Direct Shear Rig. As the sample begins to move it results in the loading beam to slightly move from vertical, resulting in an increase in the load recorded by the two normal load cells. It is believed that the change seen was not problematic and did not require correction. The shear stress response is relatively complex. It is common to see different stages within the initial loading phase. Three distinct near-linear responses are seen, from Day 0 – 0.7, 0.7 to 1.3, and 1.3 up to peak stress. These derive from the apparatus and the non-perfect fit of the steel collar in the apparatus, and looseness and backlash seen in the shear stress linkage and shear drive. During the second linear phase between day 0.7 and 1.3 a series of stress reductions are seen. These are not believed to represent sample deformation. The final linear region is representative of the shear modulus of the sample and saw stress increase quickly. The shear modulus was 217 MPa. As shear stress approached normal stress there was a change in modulus as the sample began to deform, this is seen by an acceleration in normal displacement of the sample (Figure 4-46b). The peak in shear stress can be seen at 7.76 MPa, marginally above the normal stress at this time of 7.46 MPa. This was followed by two events of reduction in shear stress, the second of which occurred shortly before shear was stopped and saw a reduction of around 3 MPa. The remainder of the stage saw stress relaxation as the fracture continued to slide in response to the shear stress giving a residual shear strength of 3.54 MPa.

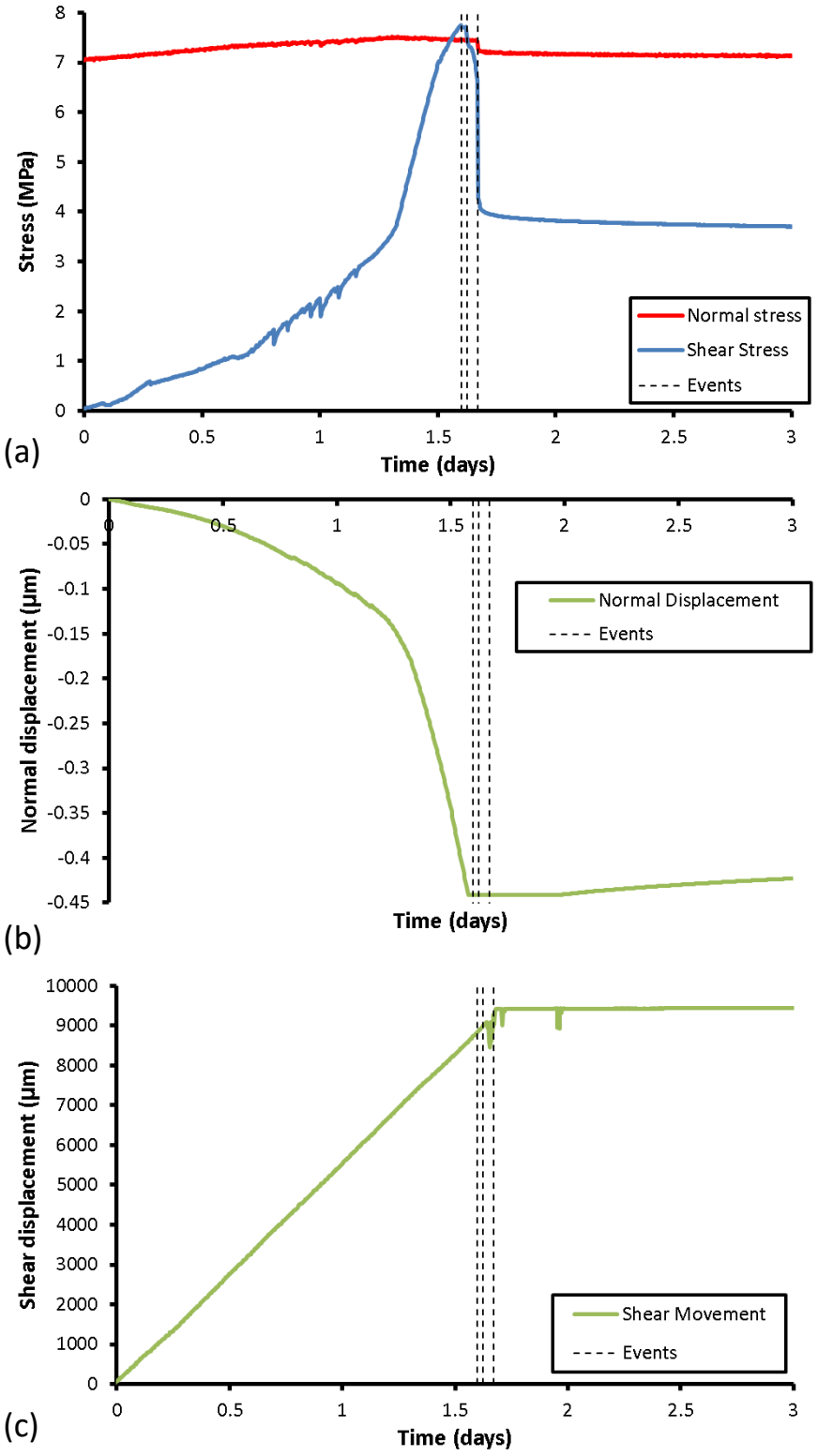

Figure 4-85 – Initial shear stage of test FPR_21_047. a) Stress response; b) normal displacement; c) shear displacement.

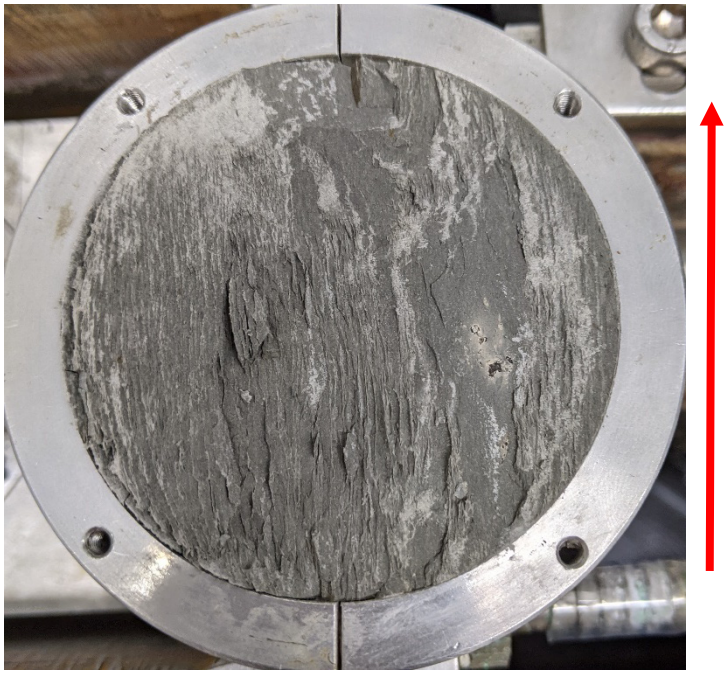

Figure 4-86 – Photograph of the fracture surface formed in the top sample. Shear direction as indicated.

Figure 4-47 shows a photograph of the top fracture surface. As can be seen, a rough fracture was formed as a result of shearing perpendicular to bedding, i.e., the bedding of the sample was into and out of the plane of the photo. A series of ridges were formed in the direction of shear with some polishing seen. On some of the ridge tops the colour of the rock lightened because of shearing. Figure 4-48 shows the topology of the fracture as determined by laser scanning. Only one of the fracture surfaces was scanned successfully and this was the opposite face as shown in Figure 4-47. After “form” had been removed from the fracture topology, the direction of the fabric is apparent in Figure 4-48. This can be seen in profile, plan, and 3D surface results. The average roughness of the fracture was determined to be 0.698 mm, with an RMS roughness of 0.861 mm, and a peak to valley height of 5.138 mm. The latter is quite high for a shear sample from the apparatus because of shear.

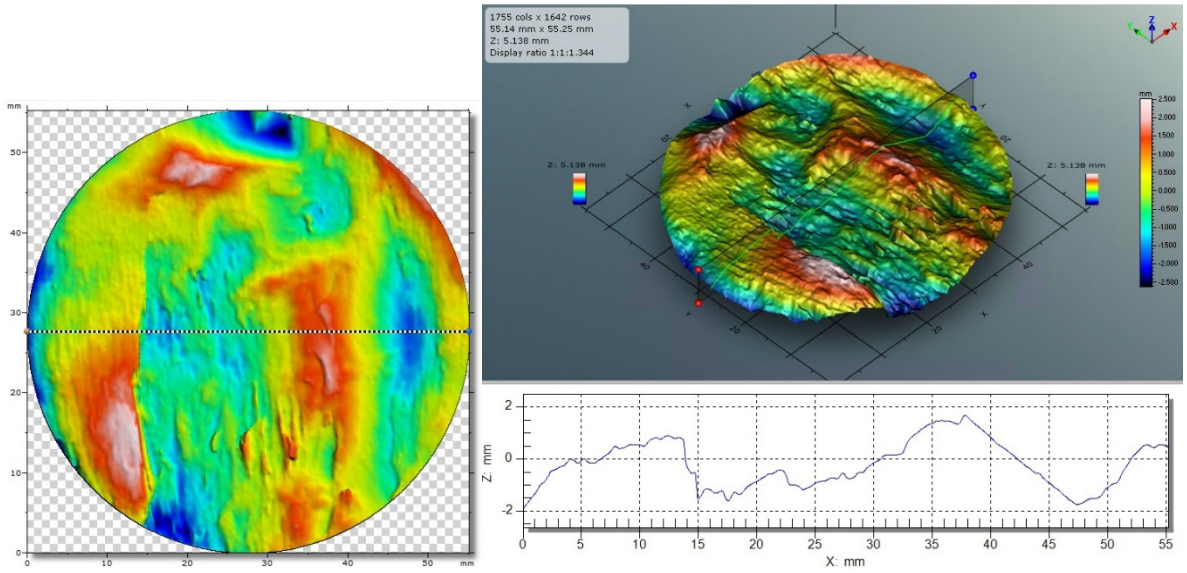

Figure 4-87 – Topology of the fracture of test FPR_21_047 after initial shearing.

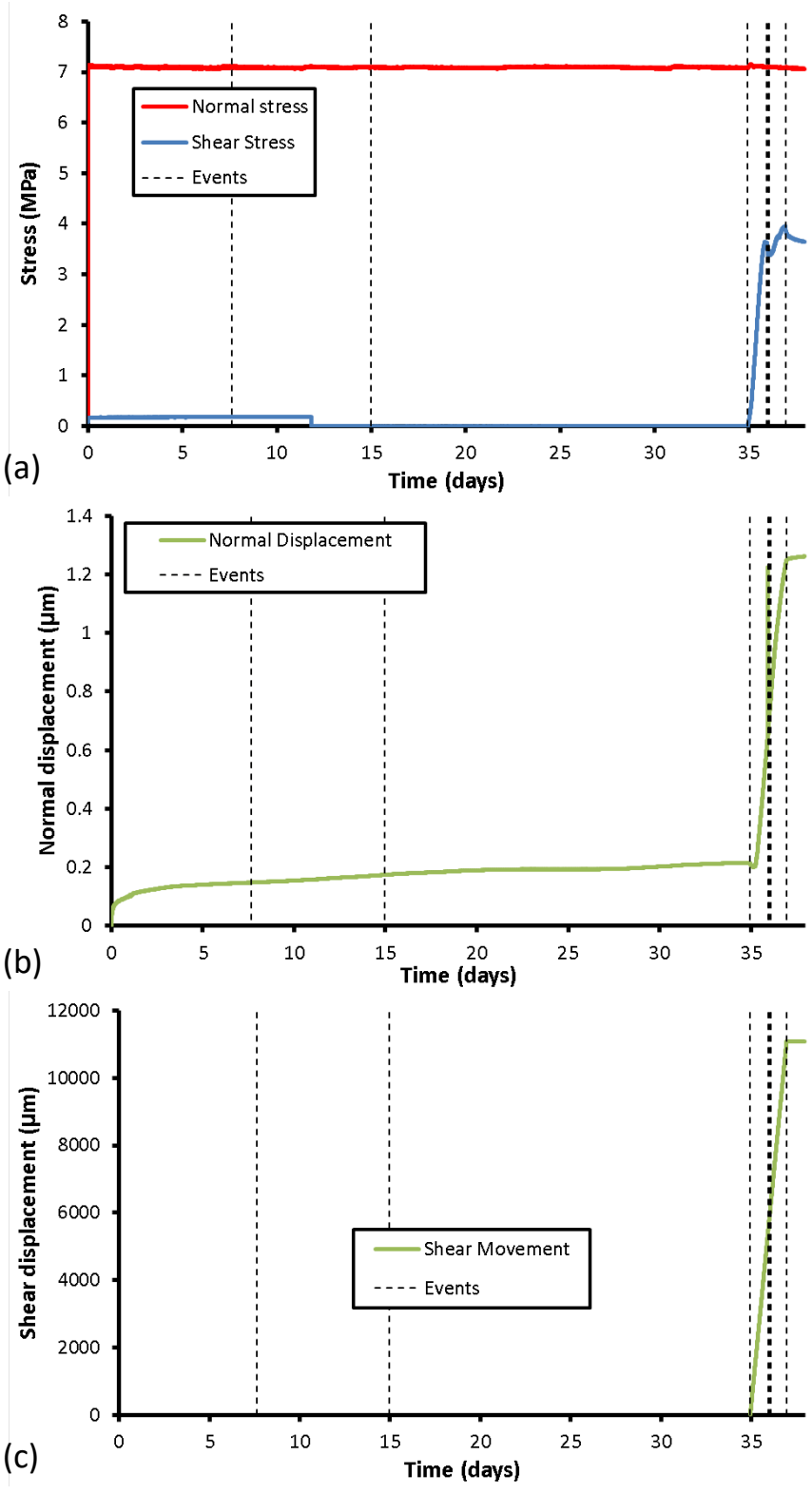

Figure 4-88 – Flow stage of test FPR_21_047. a) Stress response; b) normal displacement; c) shear displacement.

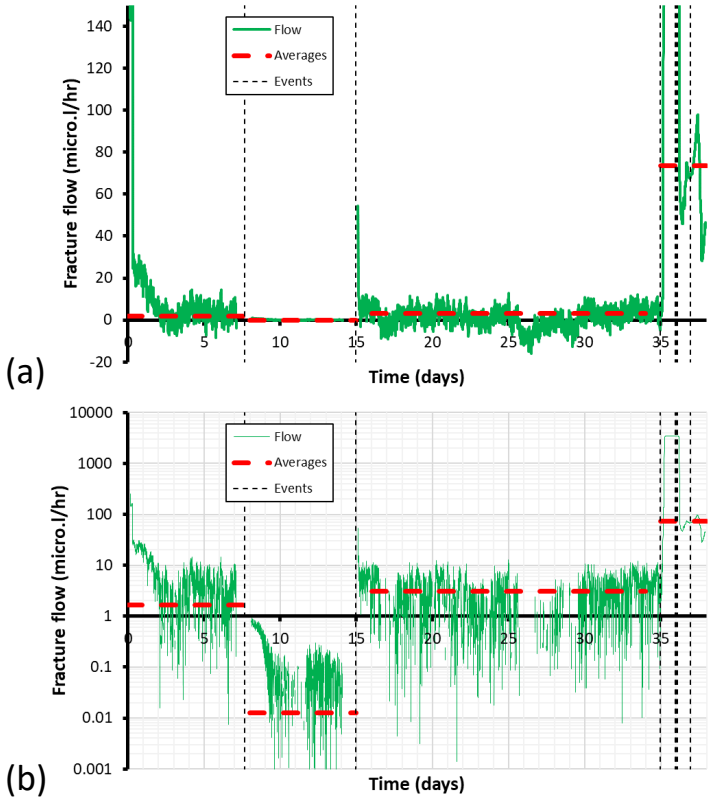

Figure 4-89 – Flow during test FPR_21_047. a) Flow; b) Log of flow.

Flow stage

After the shear fracture had been formed and scanned, a 4mm hole was drilled in the top fracture surface to add an injection bore. The fracture surfaces were re-aligned during re-assembly of the apparatus and normal load was created once more. Figure 4-49 summarises the results for the flow stage of the experiment. As shown, little of significance happened in stress (Figure 4-49 a) prior to the repeat shear (Figure 4-49c; described later). The sample underwent a small amount of compression (Figure 4-49b).

Figure 4-50 shows the flow of gas and water into the fracture during the flow stage. In the first flow stage from Day 0 to 7.64 gas was injected into the fracture. Initially the flow was high and quickly reduced to around 40 µl/h, this slowly reduced over around 2 days to a steady flow of below 10 µl/h. The flow behaviour was complex with periods of flow reduction and increase. An average flow during this stage was 7.34 µl/h and for the final 24 hours averaged 1.68 µl/h. The reduction in gas flow over a period of days was not seen in all shear tests. At Day 7.64, the permeant changed, and synthetic pore water was injected. As seen in Figure 4-50 b the initial flow rate was 1 µl/h, reducing by an order of magnitude over a period of two days. This reduction was the result of re-hydration of the clay on the fracture surface. Hydraulic flow then became steady with an average of 0.01 µl/h. Note: hydraulic flow showed considerably less noise than gas flow, as seen in Figure 4-50a. At Day 14.97 the water from the injection bore was flushed and helium injection restarted. Flow quickly stabilized to an average of 3.06 µl/h. This showed that the injection of water on the fracture resulted in an increase in gas flow from 1.68 to 2.42 µl/h, equivalent to an increase by a factor of 1.4. Shear was started at Day 34.93 and quickly flow increased; this is described in more detail later. However, average flow during the shear period was 543 µl/h, with a steady flow of 73.4 µl/h achieved, the equivalent of an increase in flow of

×24, greater than one order of magnitude increase. Therefore, hydration was seen to marginally increase the gas flow of the fracture, with shear increasing gas flow significantly.

Repeat shear

Figure 4-51 shows the repeat shear stage of the experiment in detail. Shear was started at Day 34.93 (Figure 4-51c). This resulted in shear stress increasing quickly (Figure 4-51a) and initially a small reduction in normal displacement (dilation). This quickly developed into a compression of the sample. Normal load (Figure 4-51a) did not vary during the repeat shear in contrast to the initial shear stage. This shows that movement was occurring along the fracture surface. Shear stress increased to give a near-linear response representing the shear modulus, giving an average modulus of 181 MPa. Shear stress peaked at 3.85 MPa, followed by reduction of around 0.2 MPa. This reduction corresponded with a short-lived displacement of the sample (Figure 4-51b) and flow into the clay started to increase (Figure 4-51d). This resulted in a peak in flow of 12,000 µl/h (note the data in Figure 4-51d has been time-averaged). This increase in flow was very short-lived and flow rapidly reduced. However, shear stress saw a minor-peak at Day 36.08 with a second short-lived peak in flow of 190,000 µl/h. Both events were short-lived and did not result in the establishment of a pathway to the sample outer diameter. As the fracture continued to shear, stress continued to increase, reaching a maximum of 3.95 MPa when shear movement was stopped.

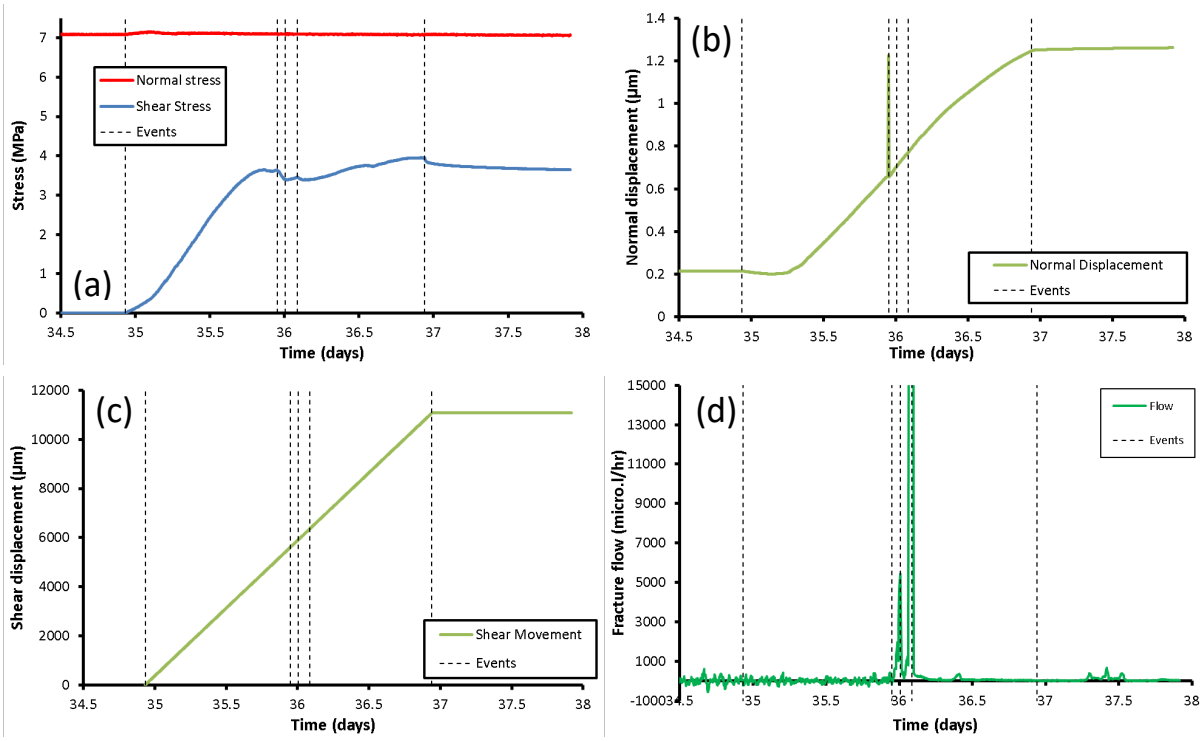

Figure 4-90 – Repeat shear stage of test FPR_21_047. a) Stress response; b) normal displacement; c) shear displacement; d) flow.

Figure 4-52 shows the result of the laser scan of the top and bottom fracture surfaces following the re-shearing of the fracture. Note that the scans have not been oriented the same. Similar features can be seen on the top and bottom sample in profile, plan, and 3D surface. While there are some features oriented in the shear direction (left to right in Figure 4-52a), the clear fabric seen in the initial shear is largely absent on re-shear. There are also features apparent that were not seen previously, most

notably the sharp linear seen in Figure 4-52a at a Y axis height of 23 mm and an X distance of 35 mm. The lack of fabric and formation of new features shows that the re-shearing of the fracture was not a simple slip along the existing fracture. It is likely that re-shear has resulted in the formation of a shear zone. The bottom fracture surface had an average roughness of 0.457 mm, and RMS roughness of 0.625, and a peak to valley height of 4.673 mm, while the top surface had 0.694 mm, 0.956 mm, and 7.108 mm respectively. While parameters have changed between the initial and re-sheared fracture, the most notable is an increase in peak-to-valley height.

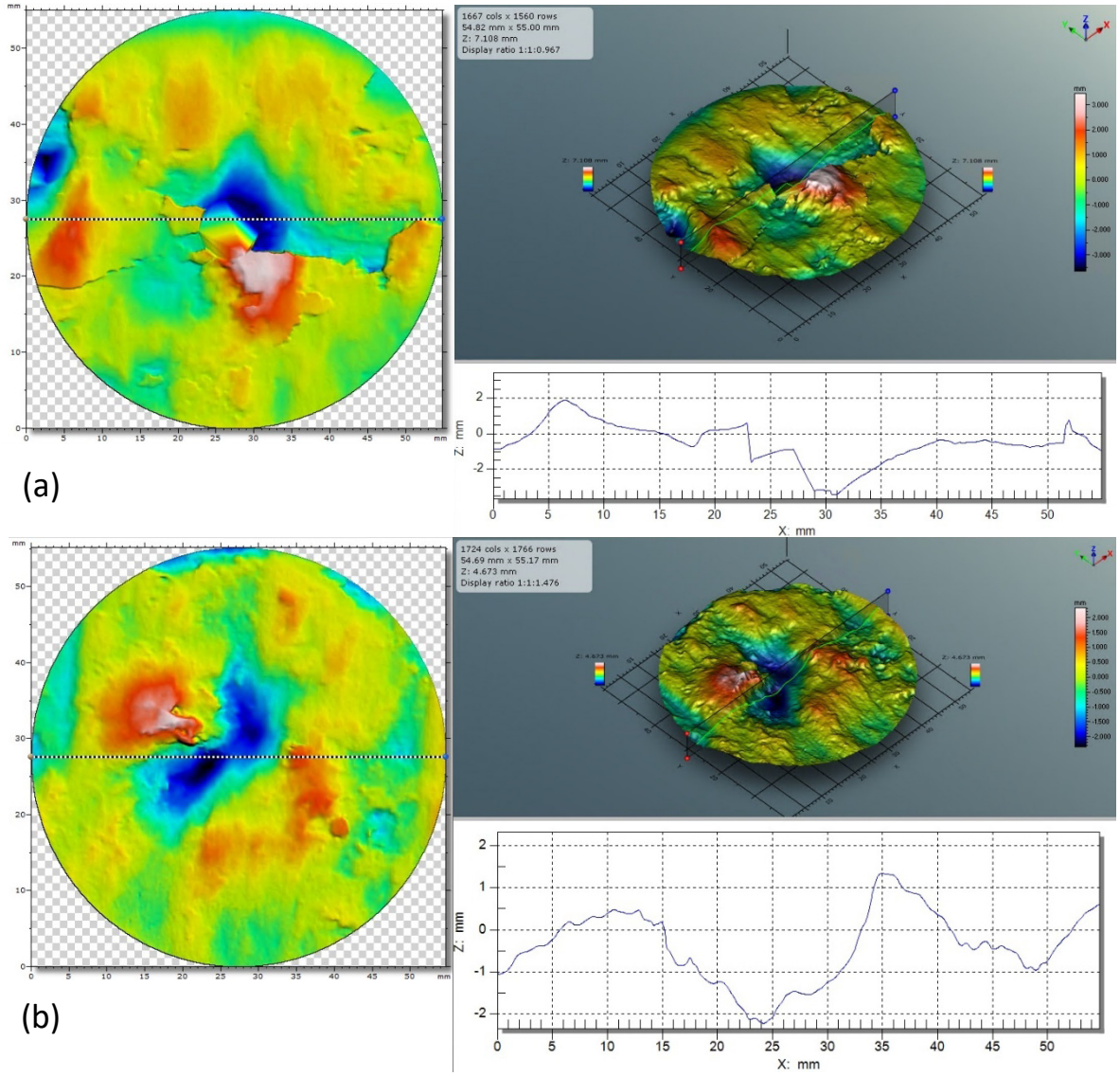

Figure 4-91 – Topology of the fracture following repeat shearing. a) Top fracture surface; b) Bottom fracture surface.

Shear comparison

Figure 4-53 shows a comparison of the two shear stages of the test. The initial shear stress response matches in both, until something changes in the initial shear stage. As described earlier, this is likely to be related with the apparatus. The shear stress response is as expected. As a result, Figure 4-53b

shows the repeat shear test transposed about the X-axis so that the linear regions of the two tests correspond with one another. The intact sample shows an elastic – brittle response with a clear residual stress level. The repeat shear shows an elastic – plastic response with the peak in shear stress corresponding to the residual strength in the intact sample. Therefore, the fracture showed no strength on reloading and the fracture was sliding along the existing fracture plane. The two tests show a similar shear modulus, although the repeat shear test did have a lower modulus indicating that the fractured sample was weaker than the intact.

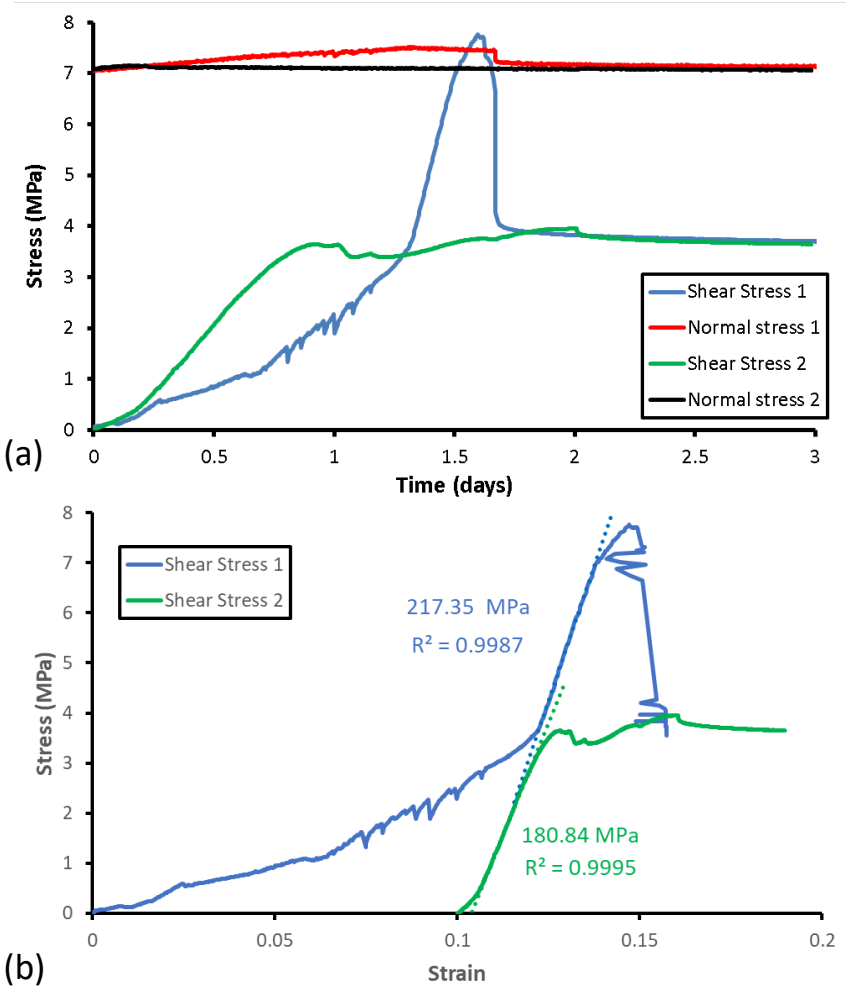

Figure 4-92 – Comparison of shear stages of test FPR_21_047. a) Stress versus time; b) Stress versus strain.

4.3.4.2 Results from test FPR_21_047

Table 4-17 summarises the complete results of test FPR_21_047.

Table 4-27 – References of the various samples with the corresponding characteristics and experimental conditions.

Test	**FPR_21_047**	
Date start	25/11/2021	
Date end	14/01/2022	
Quality	Good	
Rock	COx	
Orientation	Parallel	
Diameter	60.04 mm	
Height	53.21 mm	
Weight	361.68 g	
Density	2.401 g/cc	
	Initial	Re-shear
Average normal stress	7.12 MPa	7.09 MPa
Peak strength	7.76 MPa	3.85 MPa
Shear modulus	217.35	180.84 MPa
Maximum strain	0.16	0.03
Residual strength	3.54 MPa	3.55 MPa
Average roughness	0.698	0.576
RMS roughness	0.861	0.791
Peak to Valley height	5.138	5.891
Flow of gas 1	1.68 µL/hr	
Flow of Water	0.01 µL/hr	
Flow of gas 2	3.06 µL/hr	
Flow of gas during shear	73.48 µL/hr	
SSP_{H2O}	0.55	
SSP_{τ}	24.00	

Table 4-28 – Results for all tests. Note: BC – Boom Clay; OPA – Opalinus Clay; COx – Callovo-Oxfordian claystone; NL – Depth relevant to the Netherlands; BE – Depth of HADES URL; Bure – Depth of URL at Bure; MT – Mont Terri; // - sheared parallel to bedding; ⊥ - sheared perpendicular to bedding; + good test; - incomplete test.

												Initial shear					Re-shear					Flow					
Number	Rock type	Orientation	FPR No.	Date start	Date end	Stress condition	Quality	Sample diameter	Sample height	Sample Weight	Average density	Normal stress	Peak strength	Stiffness	Maximum strain	Residual strength	Normal stress	Peak strength	Stiffness	Maximum strain	Residual strength	Flow of gas 1	Flow of water	Flow of gas 2	Flow during shear	SSP_{H2O}	SSP_x
								mm	mm	g	g/cc	MPa	MPa	MPa		MPa	MPa	MPa	MPa		MPa	µL/hr	µL/hr	µL/hr	µL/hr		
1	BC	//	FPR_19_020	06/12/2019	24/03/2020	NL	+	59.61	52.51	293.75	2.005	4.09	1.71	78.25	0.16	1.62	4.42	1.86	199.8	0.10	1.77	3.05	1.12	1.98	3302	1.54	1670
2	OPA	//	FPR_19_018	31/07/2020	03/09/2020	MT	+	59.85	52.81	362.85	2.442	3.97	3.44	94.80	0.08	1.60	-	-	-	-	-	10.75	6.88	9.01	13.92	1.19	1.54
3	OPA	//	FPR_20_021	15/10/2020	22/11/2020	MT	+	59.86	53.45	365.64	2.431	4.01	4.34	147.1	0.12	2.25	3.99	2.14	56.11	0.10	1.96	3959	64.21	52.64	50.65	75.21	0.96
4	BC	//	FPR_20_020	20/10/2020	27/11/2020	NL	+	59.66	52.83	296.14	2.006	4.87	1.74	57.85	0.10	1.56	4.67	1.33	164.3	0.12	1.32	15.26	6.77	10.51	11.76	1.45	1.12
5	BC	//	FPR_20_036	15/12/2020	08/02/2021	NL	-	59.96	53.18	302.23	2.013	4.82	1.42	33.87	0.10	1.00	4.83	1.09	18.09	0.02	-	-	-	-	-	-	-
6	OPA	//	FPR_20_037	15/12/2020	04/01/2021	MT	-	58.57	53.42	345.47	2.400	4.19	2.62	48.68	0.13	1.08	-	-	-	-	-	-	-	-	-	-	-
7	BC	//	FPR_21_005	22/02/2021	06/04/2021	BE	+	59.19	52.09	293.94	2.051	2.11	1.01	23.21	0.11	0.68	2.13	0.55	31.62	0.11	0.54	14.83	21.56	18.39	2476	0.81	134.6
8	BC	//	FPR_21_016	13/04/2021	24/05/2021	BE	+	59.48	53.61	298.47	2.004	2.11	1.26	63.51	0.09	0.95	2.06	1.22	44.36	0.03	0.89	3.78	6.03	9.21	14.37	0.41	1.56
9	BC	//	FPR_21_039	10/08/2021	01/10/2021	BE	-	59.86	53.46	307.72	2.045	2.20	1.03	72.12	0.08	0.61	-	-	-	-	-	-	-	-	-	-	-
10	COx	//	FPR_21_047	25/11/2021	14/01/2022	Bure	+	60.04	53.21	361.68	2.401	7.12	7.76	217.4	0.16	3.54	7.09	3.85	180.8	0.03	3.55	1.68	0.01	3.06	73.48	0.55	24.00
11	COx	⊥	FPR_22_040	11/07/2022	23/09/2022	Bure	+	59.85	53.20	359.31	2.401	7.11	7.47	169.2	0.14	3.25	7.37	4.27	72.23	0.13	2.40	1.40	0.78	0.87	1817	1.60	2080
12	COx	//	FPR_22_075	06/10/2022	08/11/2022	Bure	+	59.87	53.12	364.34	2.436	7.05	7.13	170.4	0.12	3.28	6.99	3.86	127.7	0.13	3.50	18.16	1.71	2.58	69.26	7.03	26.81
13	OPA	⊥	FPR_22_066	20/10/2022	28/11/2022	MT	+	60.00	53.30	367.46	2.438	4.07	4.44	359.2	0.04	0.90	3.99	0.75	72.67	0.02	0.53	8.83	4.35	8.05	8.96	1.10	1.11
14	BC	//	FPR_23_003	17/01/2023	20/02/2023	NL	-	59.00	52.84	294.28	2.037	1.97	0.76	54.37	0.05	-	-	-	-	-	-	-	-	-	-	-	-
15	OPA	⊥	FPR_23_004	19/01/2023	13/03/2023	MT	+	59.84	53.30	361.03	2.408	4.09	5.28	117.7	0.13	2.40	3.85	2.44	32.70	0.15	2.22	3.30	0.41	2.22	6.81	1.48	3.06
16	OPA	⊥	FPR_23_005	21/03/2023	02/05/2023	MT	+	59.91	53.49	362.90	2.41	4.05	5.67	135.6	0.13	2.10	4.08	3.11	114.1	0.10	2.70	276.3	0.54	0.75	13.12	367.65	17.46
17	BC	//	FPR_23_048	15/05/2023	20/06/2023		+	59.58	53.59	299.92	2.01	1.83	0.67	7.41	0.14	-	1.85	0.66	25.68	0.11	-	2939	0.12	0.05	0.10	63037	2.14
18	OPA	⊥	FPR_23_050	22/06/2023	26/07/2023	MT	+	59.66	53.43	365.20	2.445	4.00	3.60	239.3	0.12	2.00	3.97	2.09	97.99	0.12	1.75	1537351	152.3	9608	450734	159.9	46.91
19	COx	⊥	FPR_23_059	01/08/2023	05/09/2023	Bure	+	59.87	52.96	358.72	2.406	7.00	7.36	384.7	0.08	4.05	7.01	6.64	134.3	0.12	-	891.79	21.17	1489	10534	0.60	7.07
20	COx	⊥	FPR_23_063	07/08/2023	11/09/2023	Bure	+	59.30	53.01	357.43	2.442	7.00	7.08	228.0	0.11	3.70	6.90	3.55	186.0	0.11	-	83250	61.26	7676	341741	10.84	44.52

4.3.4.3 Comparison of all tests

At the time of reporting, twenty tests had been completed, two tests were on-going, with at least another eight shear tests to be completed before the end of the project. Of the twenty completed tests, 8 were conducted using Boom Clay, 5 using Callovo-Oxfordian Claystone, and 7 tests using Opalinus Clay. The primary aim of the experimental programme was determining self-sealing potential, and four of the twenty tests did not record flow data (three in Boom Clay and one in Opalinus Clay). These are reported as they all include shear data for the intact rock and expand the dataset for mechanical data. Table 4-18 shows all the achieved data for the twenty experiments reported. Note, the ten non-reported experiments include Opalinus Clay parallel to bedding, Callovo-Oxfordian Claystone parallel and perpendicular to bedding, Boom Clay at the depth of the Netherlands, and six different compositions of synthetic rock.

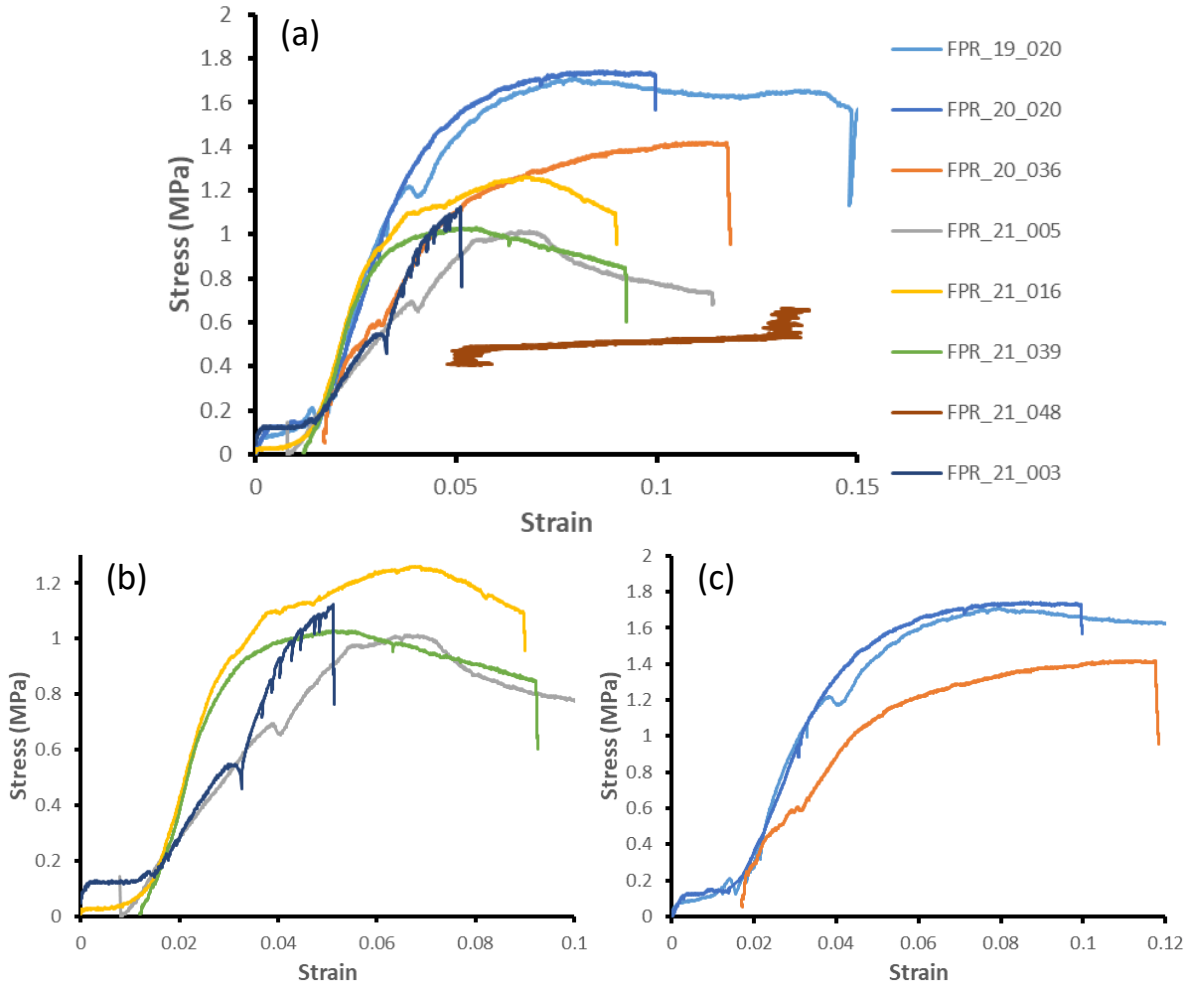

Figure 4-93 – Comparison of shear stress for Boom Clay (BC). a) All tests; b) BC tests conducted at a depth representative of Belgium; c) BC tests conducted at a depth representative of the Netherlands.

Shear results

Boom Clay (BC): Figure 4-54 summarises the shear results for intact Boom Clay; note that data have been transposed along the x-axis for comparison reasons. As shown, eight tests have been conducted, although because of a logging error, test FPR_21_048 does not contribute reliable shear data. Considerable variation can be seen in terms of shear modulus, peak strength, and the amount of shear strain. Figure 4-54b shows the results for the tests conducted at a depth representative of the Belgian disposal case. These tests were conducted as identical as possible but still show notable variation. The average peak strength was 1.02 MPa, although the complete story is a range of 0.76 to 1.26 MPa. There was also variation seen the shear modulus, ranging between 23.2 and 72.1 MPa with an average of 53.3 MPa. Figure 4-54b appears to show that three of the tests may correspond well, although test FPR_21_003 appears to terminate early, which may have been the result of an issue with the apparatus. Figure 4-54c shows the results for the conditioned sample at a depth representative of the Netherlands. Two of the samples (FPR_19_020 and FPR_20_020) show very good comparison, while FPR_20_036 shows a slightly lower strength, but similar form. The conditioned samples show better comparison than the non-conditioned ones. The three tests show an average peak strength of 1.63 MPa, varying between 1.42 and 1.74 MPa. The shear modulus showed an average of 56.7 MPa but varied considerably between 33.9 and 78.2 MPa. The visual inspection of Figure 4-54 shows a similar slope for all three experiments. Figure 4-54 and Table 4-18 show that Boom Clay shows marked variation even in tests conducted as identical as possible.

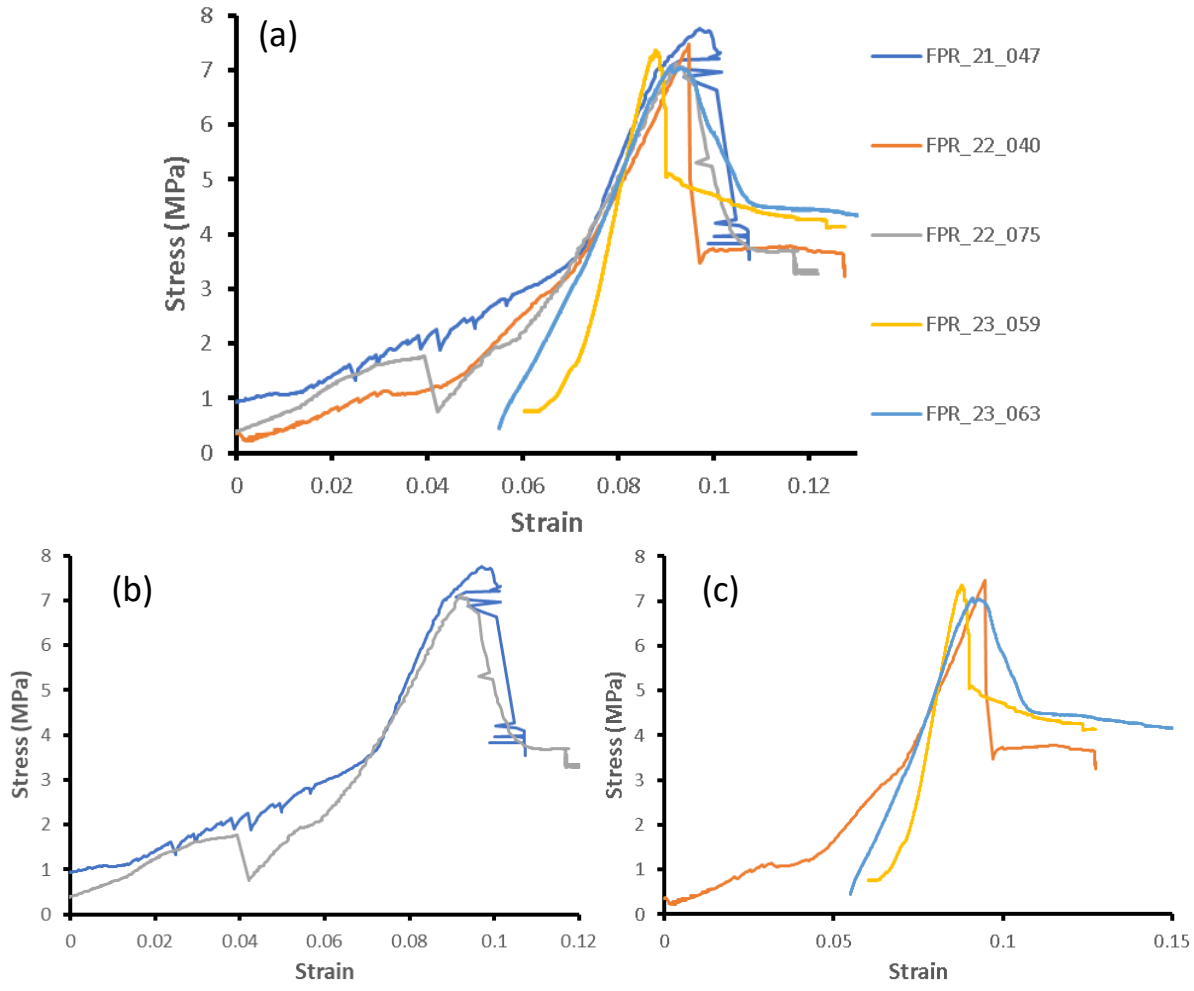

Figure 4-94 – Comparison of shear stress for Callovo-Oxfordian Claystone (COx). a) All tests; b) COx tests conducted parallel with bedding; c) COx tests conducted perpendicular with bedding.

Callovo-Oxfordian claystone (COx): Figure 4-54 and Table 4-18 summarises the shear results for intact Callovo-Oxfordian Claystone; note that data have been transposed along the x-axis for comparison reasons. As shown, five tests have been conducted. Considerable variation can be seen in terms of shear modulus, peak strength, and the amount of shear strain. Of note is the variation in the early stress-strain response, with three tests showing at least 6% strain at a low shear modulus. This is likely to derive from the characteristics of the shear apparatus and the "bedding in" of the experimental components and sample. Figure 4-54b shows the results for the tests conducted with the shear direction parallel with bedding. The two tests correspond well, with an average peak shear strength of 7.44 MPa (7.1 – 7.8 MPa) and an average shear modulus of 194 MPa (170 – 217 MPa). Differences are seen in the experiments where the shear direction was perpendicular to bedding (Figure 4-54c). Peak shear strength averaged 7.3 MPa (7.1 – 7.5 MPa) and shear modulus averaged 260 MPa (169 – 385 MPa). While peak shear stress corresponded quite well, differences were seen in shear modulus. There wasn't significant difference seen in the shear properties of COx with reference to the shear direction. Shear stress had an average of 7.36 MPa (7.1 – 7.8 MPa) and shear modulus averaged 224 MPa (169 – 385 MPa). Therefore, it is concluded that the direction of shear movement does not play a significant role on the shear properties of COx.

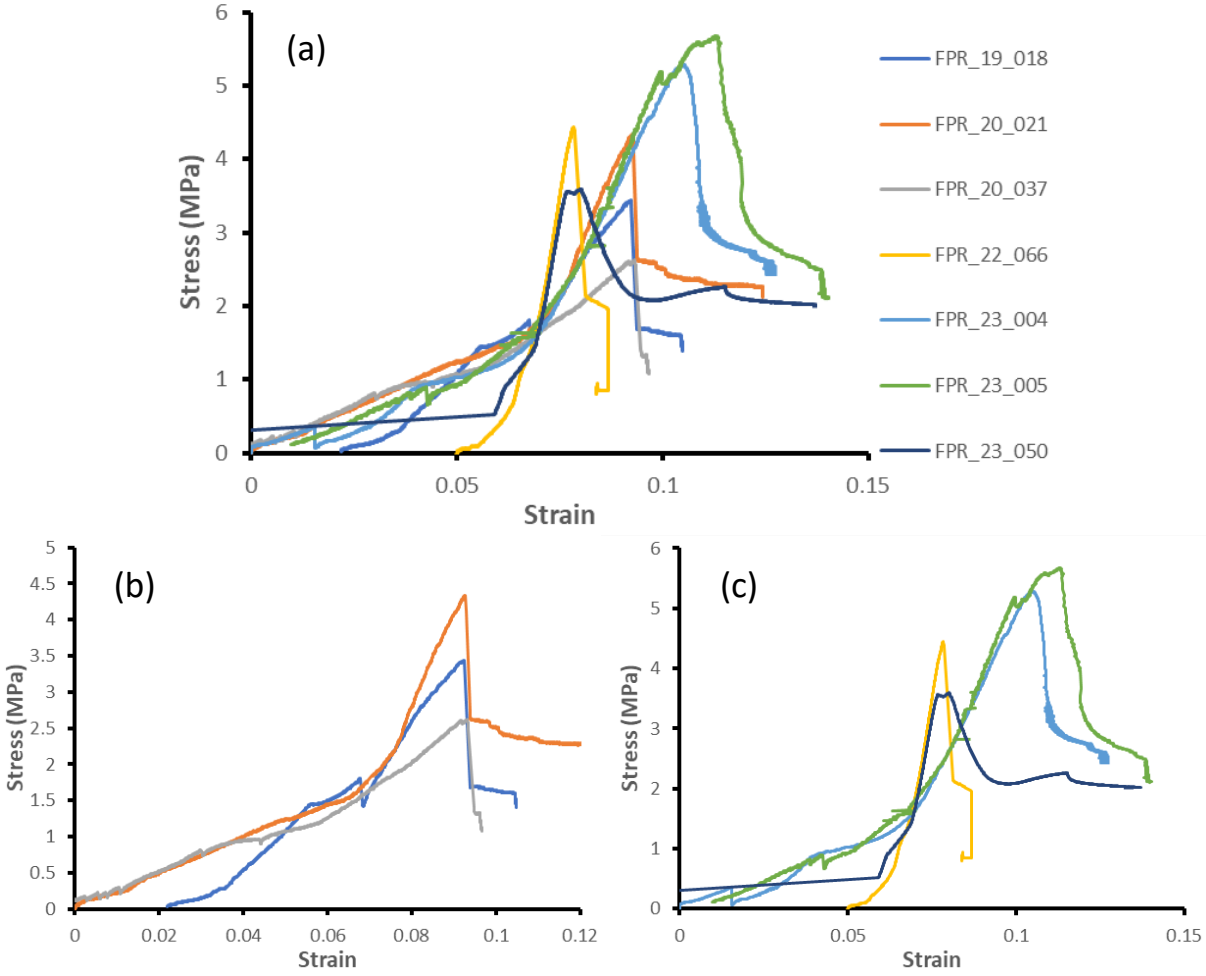

Figure 4-95 – Comparison of shear stress for Opalinus Clay (OPA). a) All tests; b) OPA tests conducted parallel with bedding; c) OPA tests conducted perpendicular with bedding.

Opalinus Clay (OPA): Figure 4-56 and Table 4-18 summarises the shear results for intact Opalinus Clay; note that data has been transposed along the x-axis for comparison reasons. As shown, seven tests have been conducted. Considerable variation can be seen in terms of shear modulus, peak strength, and the amount of shear strain. Of note is the variation in the early stress-strain response, with three tests showing at least 6% strain at a low shear modulus. This is likely to derive from the characteristics of the shear apparatus and the "bedding in" of the experimental components and sample. Figure 4-56b shows the results for the tests conducted with the shear direction parallel with bedding. The three tests show a similar form (elastic-brittle response) but show considerable variation. Peak stress shows an average of 3.47 MPa, with a considerable range of 2.62 to 4.34 MPa. The shear modulus had an average of 96.9 MPa, with a range of 48.7 to 147.1 MPa. It should be noted that the weakest sample had the lowest shear modulus and the strongest had the highest modulus. This relationship suggests a real variation in strength of the samples. Considerable differences are also seen in the experiments where the shear direction was perpendicular to bedding (Figure 4-56c). Peak shear strength averaged 4.75 MPa (4.4 – 5.7 MPa) and shear modulus averaged 213 MPa (118 – 359 MPa). Figure 4-56c suggests two populations of test result with a weaker stiffer pair of tests and a stronger but less compliant pair of tests. Variation within these populations is less marked. Overall, all tests showed an average peak shear strength of 4.2 MPa with a considerable range of 2.6 to 5.7 MPa. Shear modulus also showed considerable spread, with an average of 163 MPa with a range of 48.7 to 359 MPa, nearly one order of magnitude variation. No clear difference is seen between shear fractures formed at different directions primarily as the variance in the data is so large.

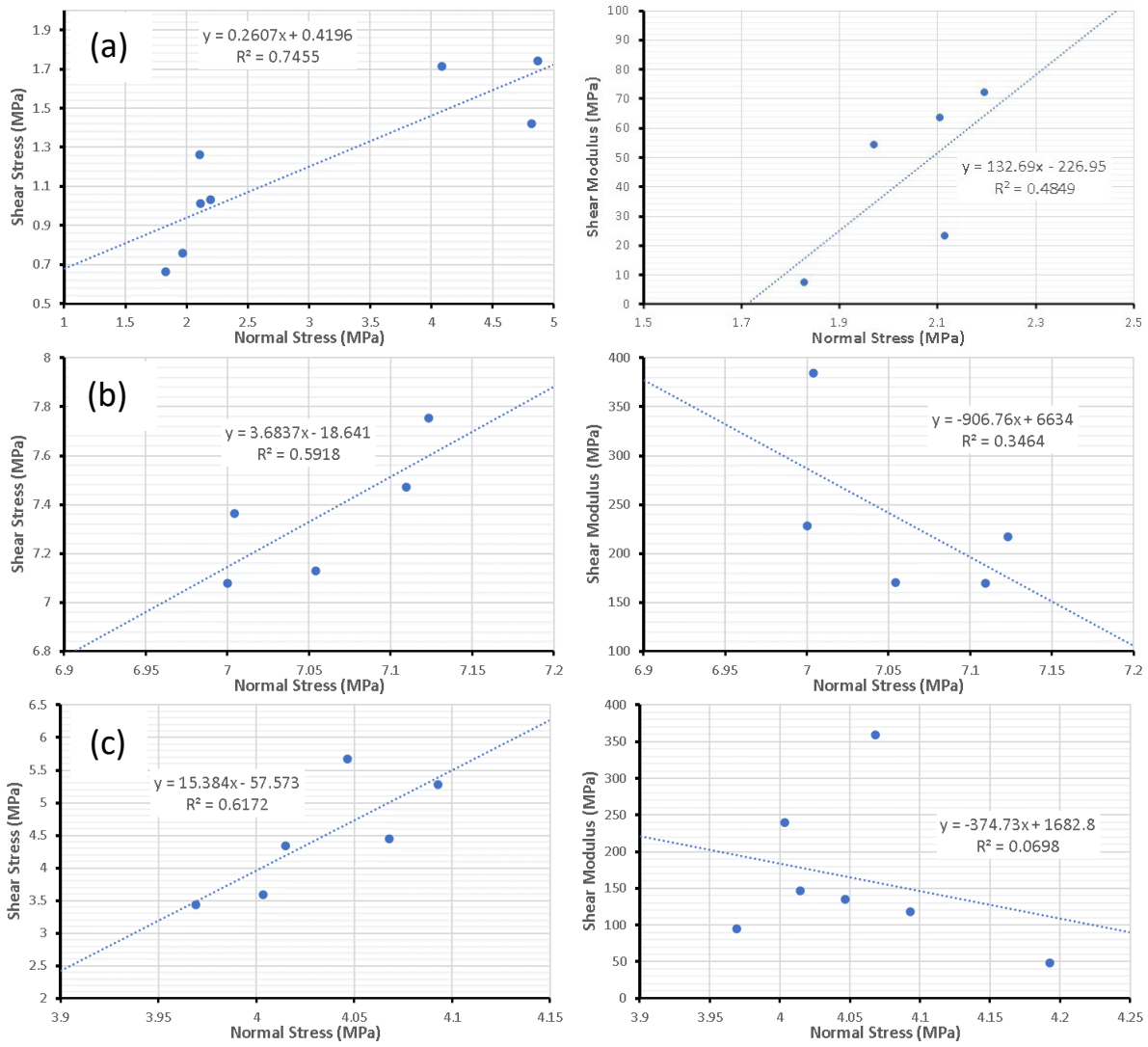

Figure 4-96 – The relationship between normal stress and shear properties. a) Boom Clay; b) Callovo-Oxfordian claystone; c) Opalinus Clay.

Figure 4-57 shows the relationship between normal stress and shear stress, and normal stress and shear modulus for the three rock types tested. All three rock types show a positive linear relationship between normal stress and peak shear stress. Therefore, it is suggested that increasing normal stress results in a higher peak shear strength. The relationship between normal stress and shear modulus is less well defined for all three rock types. In Boom Clay, a linear positive relation is seen, although the R2 is poor. In both Callovo-Oxfordian claystone and Opalinus Clay a negative relationship is seen between normal stress and shear modulus. Therefore, at higher normal loads the samples appear less compliant, although the spread in the data is considerable.

Flow results

Table 4-19 summarises the flow results from the 20 shear experiments conducted, with 17 tests yielding reliable flow data.

Table 4-29 – Results for Self-Sealing Potential (SSP).

Rock	Condition	FPR No.	Test No.	SSP_{H2O}		SSP_{τ}	
Boom Clay	BC BE	FPR_21_005	1	0.806	333.7	0.007	0.371
		FPR_21_016	2	0.411		0.641	
		FPR_23_048	3	63037		0.466	
	BC NL	FPR_19_020	4	1.541	1.496	0.001	0.447
		FPR_20_020	5	1.452		0.893	
		-	-	-		-	
Callovo-Oxfordian claystone	COx Perp	FPR_22_040	1	1.601	4.348	0.001	0.055
		FPR_23_059	2	0.599		0.141	
		FPR_23_063	3	10.84		0.022	
	COx Para	FPR_21_047	4	0.547	3.788	0.042	0.039
		FPR_22_075	5	7.028		0.037	
		-	-	-		-	
Opalinus Clay	OPA Para	FPR_19_018	1	1.19	38.20	0.648	0.844
		FPR_20_021	2	75.21		1.039	
		-	3	-		-	
	OPA Perp	FPR_22_066	4	1.10	132.6	0.898	0.326
		FPR_23_004	5	1.48		0.326	
		FPR_23_005	6	367.7		0.057	
		FPR_23_050	7	160.0		0.021	

Boom Clay: Figure 4-58 shows the flow test results for Boom Clay. Figure 4-58a shows the raw flow results with the arrows showing whether flow reduced or increased because of hydration of the fracture, while Figure 4-58b shows the results when converted to Self-Sealing Potential (SSP_{H2O}). At a depth representative of the Belgian disposal concept (220m), two of the tests showed a small increase in flow, whereas one test showed a considerable decrease in flow of over four orders of magnitude. This latter test represents a test where initial gas flow could not hold a prolonged gas pressure in the fracture, this was sealed by hydraulic injection and repeat gas injection could sustain a gas pressure of 1 MPa. When these data are converted to SSP_{H2O} (Figure 4-58b) the average result is dominated by the one test that showed sealing, giving an SSP_{H2O} of 334. The full picture is hydration showed an increase in flow for

two tests and a reduction in a third. For the case where stress was representative of that of the Netherlands disposal concept (500m), the two tests showed a decrease in flow as a result of hydration (Figure 4-58a), showing a small decrease in flow as an average (Figure 4-58b). This average is just outside of the condition displayed where a minor change would be considered no change in flow with SSP_{H2O} of 1.5. Figure 4-58c shows that the raw flow result showed an increase in gas flow for all five tests because of re-shearing along the fracture. There was considerable variation in this result, ranging from minor increase up to over two orders of magnitude increase. The later, seen in two tests, represents a fracture that shear resulted in a condition where gas pressure could no longer be sustained. There appears no significant difference between tests conducted at a stress representative of 220m and 500m. Figure 4-58d shows that both stress conditions tested showed a small average increase in flow because of active shearing with SSP_{τ} of 0.4 for both stress conditions investigated. This was not expected.

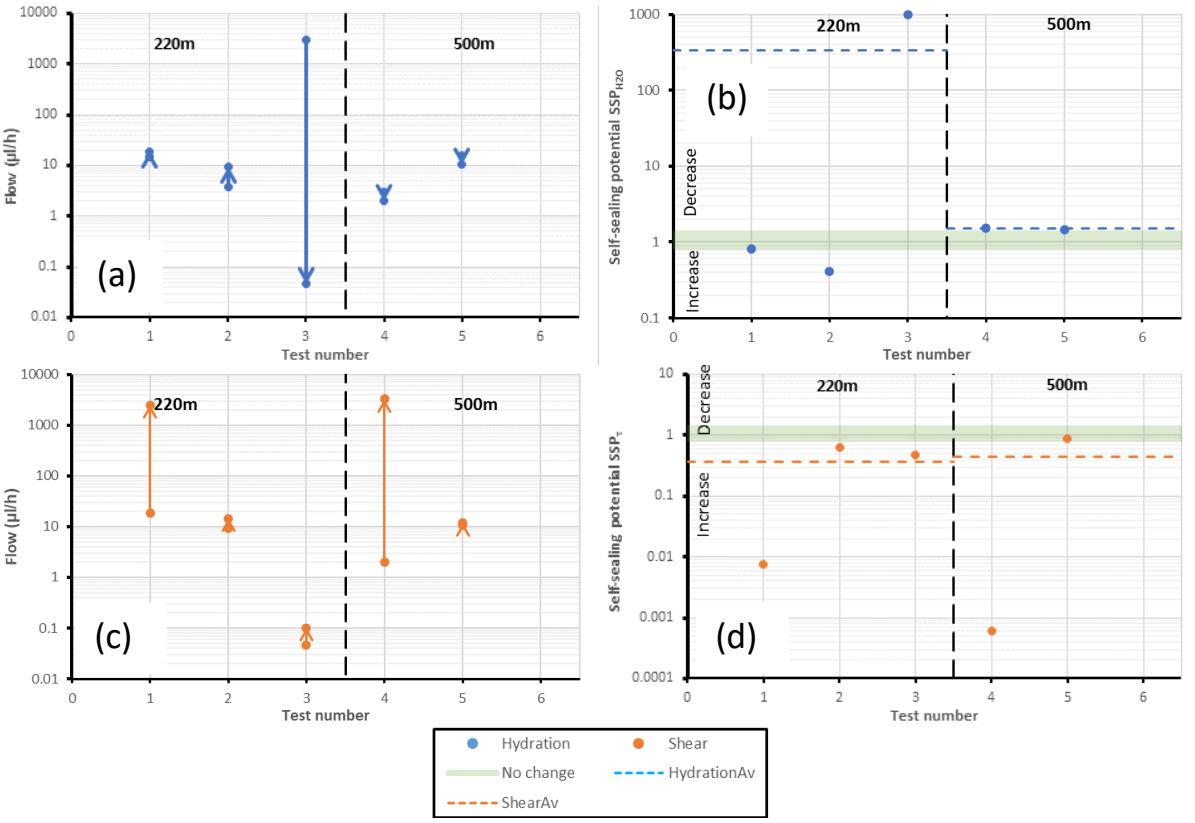

Figure 4-97 – Flow test results for Boom Clay (BC). a) Variation in gas flow as a result of hydration of the fracture; b) Self-Sealing Potential as a result of hydration of the fracture (SSPH2O); c) Variation in gas flow as a result of shear of the fracture; b) Self-Sealing Potential as a result of shear of the fracture (SSP_{τ}).

Callovo-Oxfordian Claystone: Figure 4-59 shows the flow test results for Callovo-Oxfordian claystone (COx). Figure 4-59a shows the raw flow results with the arrows showing whether flow reduced or increased as a result of hydration of the fracture, while Figure 4-59b shows the results when converted to Self-Sealing Potential (SSPH2O). For tests that were sheared perpendicular to the bedding direction (Figure 4-59a), two tests showed a decrease in flow because of hydration, while one test showed a small increase. The average of the three results shows a SSP_{H20} of 4.3. For the tests conducted where shear direction was parallel to bedding, one test showed a small increase in flow, whereas one test showed a decrease of nearly one order of magnitude. These two experiments gave an average SSP_{H20}

of 3.8. The five experiments do not show a systematic variation in behaviour based on shear direction, with both conditions either showing a small increase in flow or a marked decrease. Figure 4-59c shows that the raw flow result showed an increase in gas flow for all five tests as a result of re-shearing along the fracture. There was considerable variation in this result, ranging from one order of magnitude up to three orders of magnitude. This results in an average SSP_τ of ~0.05 for both directions of shear (Figure 4-59d). As with hydration, the five experiments do not show a systematic variation in behaviour based on shear direction, with both conditions showing a marked increase in flow. This was not expected, with shear predicted to result in a better seal (i.e. $SSP_\tau > 1$).

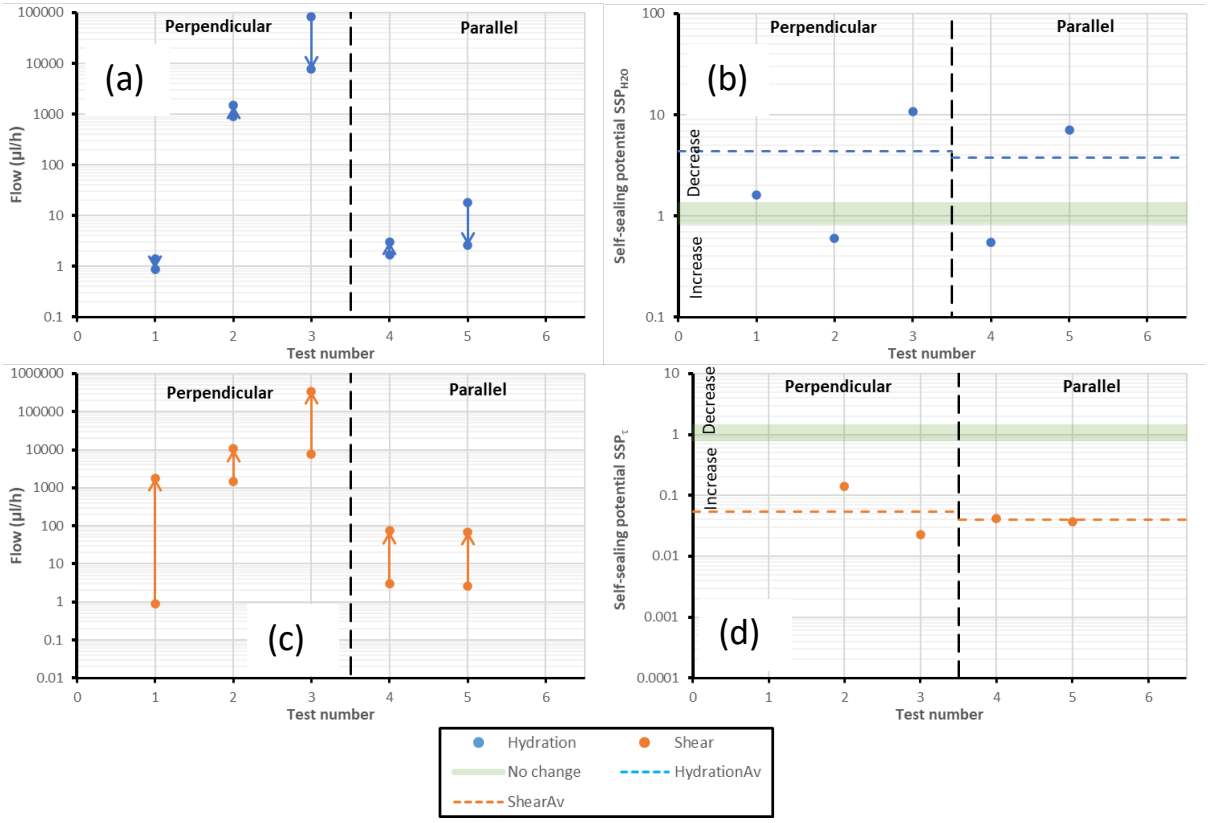

Figure 4-98 – Flow test results for Callovo-Oxfordian claystone (COx). a) Variation in gas flow as a result of hydration of the fracture; b) Self-Sealing Potential as a result of hydration of the fracture (SSPH2O); c) Variation in gas flow as a result of shear of the fracture; b) Self-Sealing Potential as a result of shear of the fracture (SSP_τ).

Opalinus Clay: Figure 4-60 shows the flow test results for Opalinus Clay (OPA). Figure 4-60a shows the raw flow results with the arrows showing whether flow reduced or increased as a result of hydration of the fracture, while Figure 4-60b shows the results when converted to Self-Sealing Potential (SSP_{H2O}). For tests that were sheared parallel to the bedding direction (Figure 4-60a), both tests showed a decrease in flow because of hydration. The average of the results shows a SSP_{H20} of 38. For the tests conducted where shear direction was perpendicular to bedding, all four tests showed a decrease in flow, ranging between a minor decrease to over two orders of magnitude. These experiments gave an average SSP_{H20} of 133. Figure 4-60c shows that the raw flow result showed an increase in gas flow for five of the six tests because of re-shearing along the fracture, with one test showing a marginal decrease. There was considerable variation in this result, ranging from minor variation to over one order of magnitude increase. This results in an average SSP_τ of 0.84 for shearing parallel to bedding and 0.33 for tests conducted perpendicular to bedding. It should be noted that much greater variation is seen in SSP_τ perpendicular to bedding. Difference is therefore seen in SSP_τ based on shear direction

with respect to bedding, with SSP_τ perpendicular to bedding showing a much greater increase in flow as a result of shearing. Both orientations show an increase in flow with shear, which was not expected, with shear predicted to result in a better seal (i.e. $SSP_\tau > 1$).

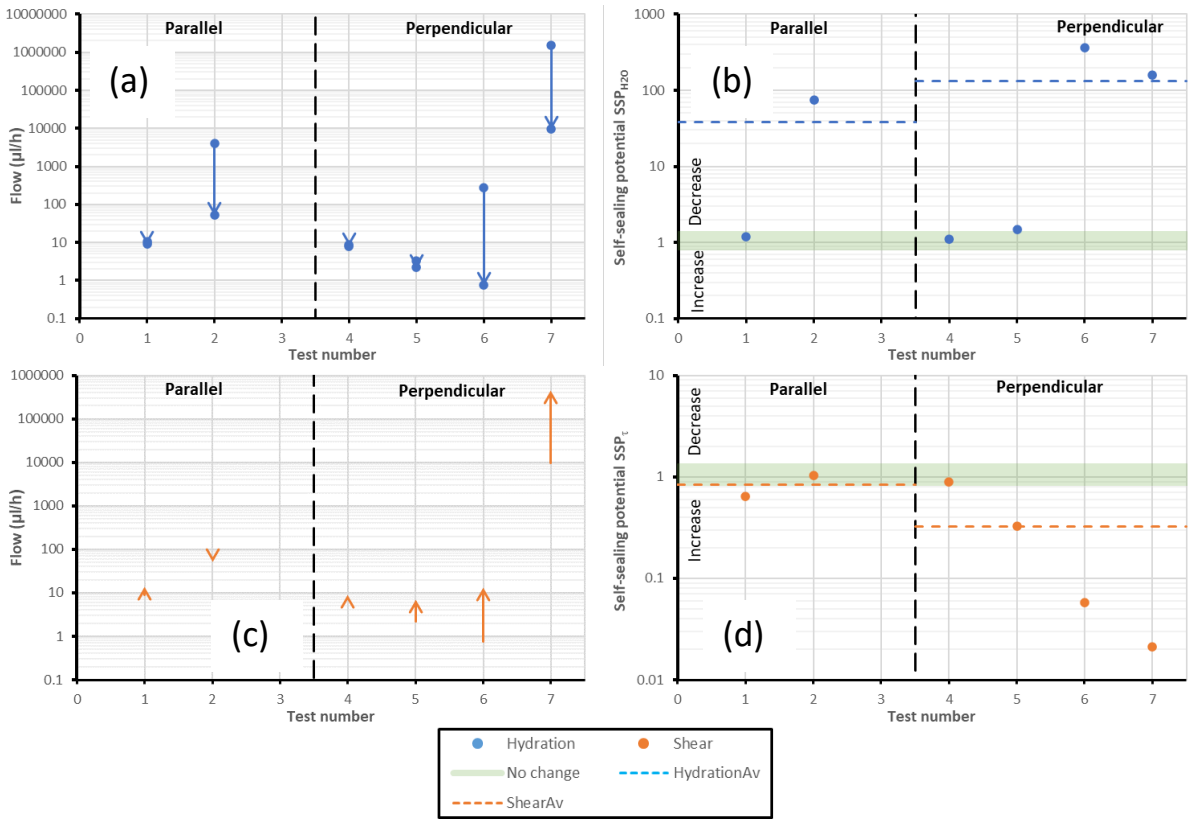

Figure 4-99 – Flow test results for Opalinus Clay (OPA). a) Variation in gas flow as a result of hydration of the fracture; b) Self-Sealing Potential as a result of hydration of the fracture (SSP_{H2O}); c) Variation in gas flow as a result of shear of the fracture; b) Self-Sealing Potential as a result of shear of the fracture (SSP_τ).

Figure 4-61 compares the results for all three rock-types, showing Self-Sealing Potential (SSP) on the same y-axis scale. All tested conditions showed either a reduction or no change in gas flow because of hydration of the fracture. The influence of water on gas flow was greatest for Opalinus Clay, with over one order of magnitude greater SSP than Callovo-Oxfordian claystone, the latter only having a moderate decrease in flow as a result of hydration. Opalinus Clay had nearly two-orders of magnitude reduction in flow as a result of injection of water on the fracture. In Boom Clay, the full story is more complex. Discounting the one test that showed considerable SSPH20 after the fracture would initially not hold gas pressure, the two other tests at the Belgian depth range showed a modest increase in gas flow. Therefore, small volumes of excess water on the fracture plane enhances gas flow. Figure 4-61 shows that there is considerable difference in SSP_{H20} between rock types, but there is limited variation within the rock types that were sheared at different directions. Shearing showed either no change, or an increase in flow. In Opalinus Clay no change in flow was seen for shearing parallel with bedding, with a modest increase for samples oriented perpendicular to bedding. In Boom Clay, only a modest increase was seen, with little variation based on the depth of study. Almost all the five tests conducted in Callovo-Oxfordian claystone showed an increase in flow of around one order of magnitude. Table 4-20 summarises the conclusions of the flow results, with entries shown in red indicating an increase in

flow (SSP < 1) and entries in green showing a decrease in flow (SSP > 1). If sealing is desired, SSP > 1 is preferable.

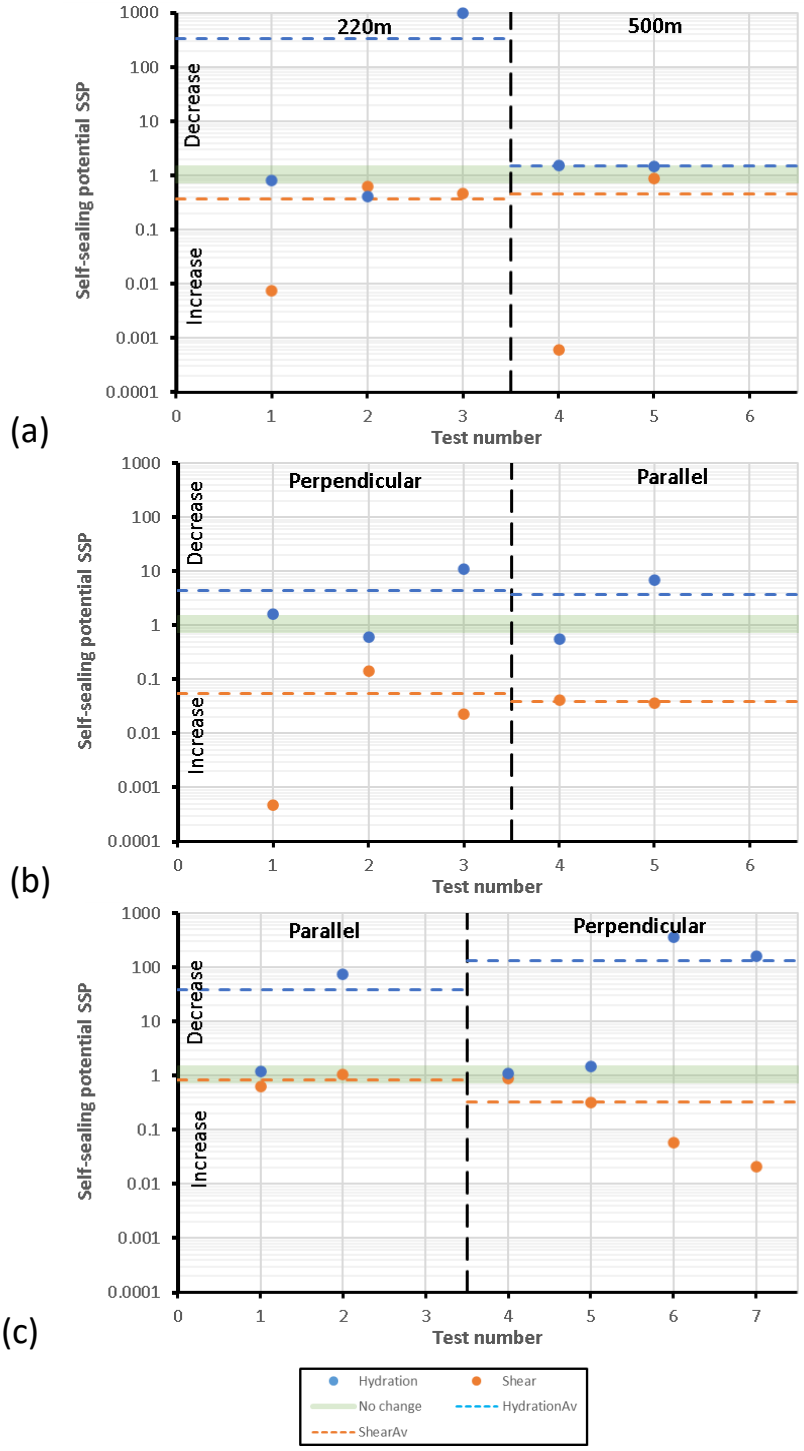

Figure 4-100 – Self-Sealing Potential (SSP). a) Boom Clay; b) Callovo-Oxfordian claystone; c) Opalinus Clay.

Table 4-30 – Self-Sealing Potential (SSP) conclusion. Note # - increase seen when one test with high degree of sealing is discounted.

Rock Type	Condition	Hydration		Shear	
Boom Clay	220m	Increase#	0.6	Increase	0.4
	500m	No change	1.5	Increase	0.4
Callovo-Oxfordian claystone	Parallel	Decrease	3.8	Increase	0.06
	Perpendicular	Decrease	4.3	Increase	0.04
Opalinus Clay	Parallel	Decrease	38	No Change	0.8
	Perpendicular	Decrease	133	Increase	0.3

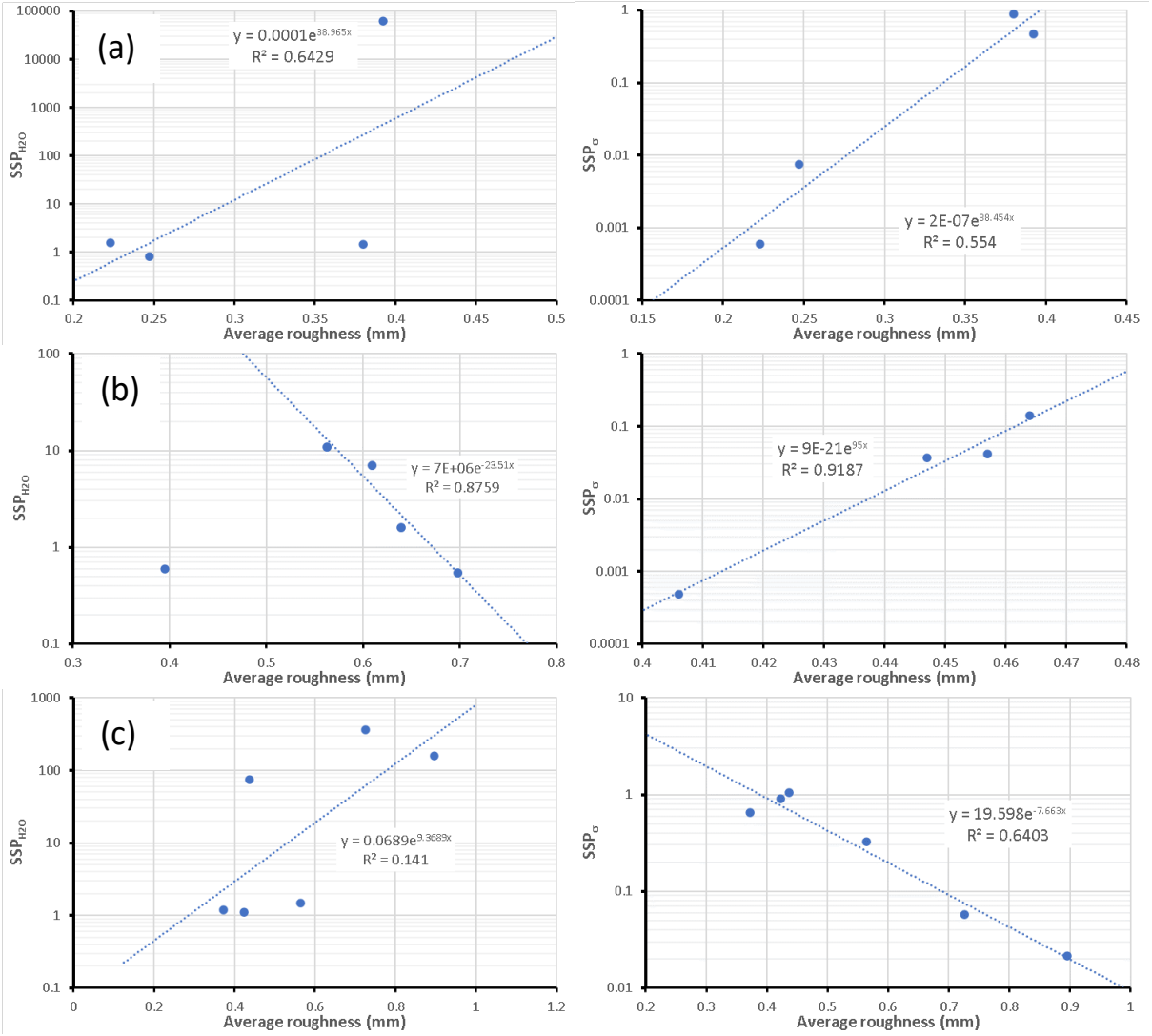

Figure 4-101 – The relationship between Self-Sealing Potential (SSP) and fracture roughness. a) Boom Clay; b) Callovo-Oxfordian claystone; c) Opalinus Clay.

The influence of fracture characteristics on self-sealing potential

As noted earlier, considerable spread was seen in many of the datasets even though tests were attempted to be performed as identical as possible. To ascertain whether there was a connection between physical properties (shear strength and fracture characteristics) and self-sealing potential or flow properties, an Excel routine was written to plot all data against one another. From this complete result, it was apparent that a correlation could be seen between average fracture roughness and self-sealing potential (Figure 4-62). Boom Clay shows a general relationship with SSP_{H2O} increasing with average roughness, as shown by an exponential fit in Figure 4-62a. This is because a rougher fracture will have a greater surface area, and this will result in more Boom Clay accessing water and swelling. The result is dominated by the test with the high value of SSP_{H2O}. A trend is seen with higher average roughness resulting in less SSP_{τ}. Therefore, a smooth fracture results in more enhanced gas flow. In Callovo-Oxfordian claystone, the relationship between roughness and SSP_{H2O} is more difficult to define. Figure 4-62b shows a negative trend fitted to the data excluding the test with a low SSP_{H2O} for a low roughness. The fit to the remaining four data points is good but is opposite to the trend seen in Boom Clay. In COx, an increase in roughness reduces the effectiveness of hydraulic self-sealing. This may be because very rough fractures have considerable mismatch between the two faces of the fracture. The roughness of COx fractures is considerably greater to that seen in Boom Clay. A strong trend is seen between average roughness and SSP_{τ} in COx. As with BC, this shows that a smoother fracture results in greater enhanced flow. This will be related to mismatch between the two surfaces of the fracture. In Opalinus Clay (Figure 4-62c), a positive relationship is seen between SSPH2O and average roughness, and a negative trend between SSP_{τ} and average roughness. However, the spread of data for SSP_{H2O} is considerable, whereas the trend with SSP_{τ} gives a good R^2. Therefore, in OPA, a rougher fracture results in greater enhanced gas flow.

No correlation was found to explain the difference in flow seen. This can be explained by considering what will cause variation in flow. Gas is likely to move along the asperities created between the two fracture surfaces. Fracture roughness is not a measure of mismatch, although it can suggest how likely mismatch is. If we consider a fracture where both surfaces are made up of perfect sinusoidal ridges, a single roughness can be defined. If the two surfaces are oriented so that the peaks of the bottom fracture lie perfectly in the troughs of the upper fracture, there will be no mismatch and no asperities. If the same fracture is oriented so that the peaks of the bottom surface align with the peaks of the top surface, there will be considerable mismatch and large asperities between the two sinusoidal surfaces. Both scenarios have the same roughness, but different mismatch. Without x-ray CT, it is impossible to define mismatch and asperity geometry, and that is outside of the scope of the current research. Even with x-ray CT, the size of the asperities are likely to be too small to be detected.

Additional comments

One test that produced an interesting result was FPR_23_063, as shown in Figure 4-63. In this test, the second stage of gas injection resulted in a steady flow up until Day 16.9, when gas flow started to increase. By Day 17.1 gas flow had reached 1000 µl/h, reaching 10,000 µl/h by Day 18.8 and reaching a maximum of 16,500 µl/h at Day 19.2. At this latter time, the gas volume in the interface vessel ran out and the pressure on the fracture rapidly decayed. This test was the only one that had this characteristic. It is interpreted that a small conductive pathway had reached the outside of the fracture plane and as gas started to “leak” from the system, the pathway grew, allowing increasing amounts of gas to reach breakthrough. Alternatively, more individual pathways may have reached the outside of the fracture, increasing the volume of gas able to be transmitted along the fracture. On retrieval of the sample after the test had been completed, a small patch of broken-up clay was apparent (Figure 4-63b). It is suggested that gas had reached a conductive feature in the sample and had exploited this, creating an area of different texture on the fracture surface.

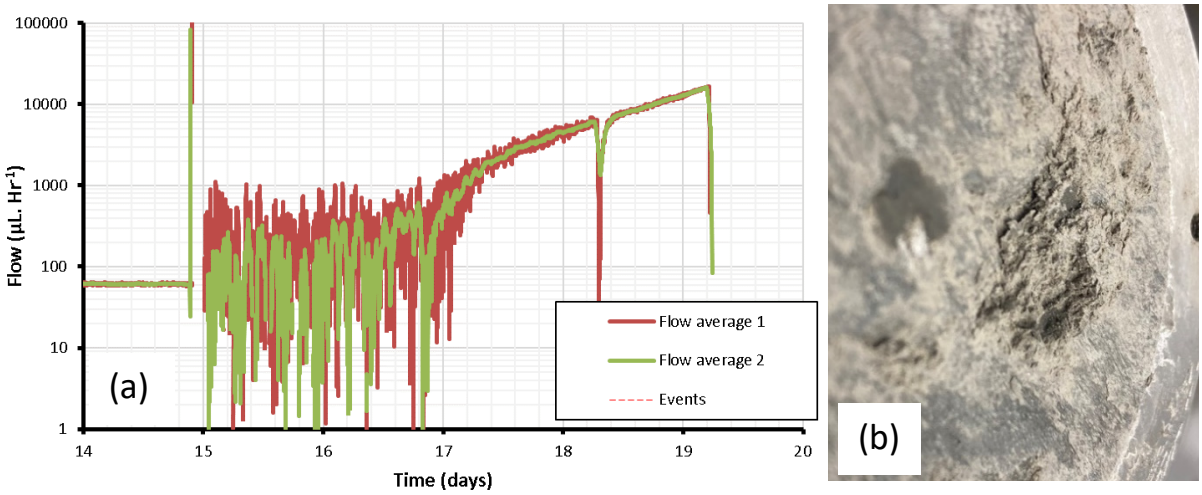

Figure 4-102 – Increasing gas flow seen in test FPR_23_063. a) Flow data; b) Photograph of the fracture surface.

4.3.5 Summary

This package of work conducted twenty shear experiments on Boom Clay, Callovo-Oxfordian claystone, and Opalinus Clay examining gas flow properties. Each test was conducted in an identical way, with five stage; 1) An intact cylindrical sample was sheared to create a realistic shear fracture at the centre of the sample. This stage lasted around one week; 2) Gas was injected into the centre of the fracture to determine the gas flow properties. This stage lasted around one week; 3) Synthetic pore fluid was injected into the centre of the fracture to re-hydrate the fracture surfaces. This stage lasted around one week. 4) Gas was injected into the centre of the fracture to determine gas flow following re-hydration. This stage lasted around one week; 5) Gas flow was monitored during re-shearing of the sample. This stage lasted around one week. By comparing the steady gas flow of stages (2) and (4) determined the self-sealing potential of hydration (SSP_{H2O}). Comparing gas flow of stages (4) and (5) determined the self-sealing potential of shear movement (SSP_{τ}). An SSP greater than unity represented a reduction in flow and therefore advantageous changes in flow. An SSP less than unity represented an increase in gas flow, which may be considered deleterious. At the end of stages (1) and (5) the fracture surfaces were laser scanned to measure the topology of the fractures. This was analysed to determine fracture roughness and peak to valley height. It should be noted that a further ten shear experiments are planned to complete the experimental programme. For each rock type two conditions were investigated. In Boom Clay this was a depth representative of the Belgian disposal concept (220m) and a depth representative of the Netherlands (500m). In both Callovo-Oxfordian claystone and Opalinus Clay the two conditions investigated were shearing in the direction parallel and perpendicular of the bedding direction.

Mechanical results

Stage (1) of the experiment determined the shear characteristics of the intact sample, notably the peak shear stress and shear modulus. These parameters describe the strength and compliance of the sample under direct shear. In **Boom Clay**, Considerable variation was seen in terms of shear modulus, peak strength, and the amount of shear strain. At a depth of 220m the average peak shear strength was 1.02 MPa (0.76 to 1.26 MPa) and average shear modulus of 53.3 MPa (23.2 to 72.1 MPa). Three of the tests corresponded well, with one test terminating early. At a depth of 500m the average peak shear strength was 1.63 MPa (1.42 to 1.74 MPa) and average shear modulus of 56.7 MPa (33.9 to 78.2 MPa). The repeatability of test results was much better in the conditioned samples representative of 500m. Comparing the two conditions showed increased depth resulted in a stronger sample but with only a

marginal increase in compliance. A positive linear relationship was seen between normal stress and peak shear stress. A positive linear relationship was also seen between normal stress and shear modulus.

Considerable variation in shear modulus, peak strength, and the amount of shear strain was also seen in **Callovo-Oxfordian claystone**. Variation was seen in the early stress-strain response, likely because of the characteristics of the shear apparatus and the "bedding in" of the experimental components and sample. For tests conducted with the shear direction parallel to bedding, the average peak shear strength was 7.44 MPa (7.1 – 7.8 MPa) and the average shear modulus was 194 MPa (170 – 217 MPa). In tests conducted perpendicular to bedding, peak shear strength averaged 7.3 MPa (7.1 – 7.5 MPa) and shear modulus averaged 260 MPa (169 – 385 MPa). Peak shear stress corresponded quite well but differences were seen in shear modulus. No significant difference was seen in shear properties in the two orthogonal directions. Therefore, the direction of shear movement did not play a significant role on the shear properties of COx. A positive linear relationship was seen between normal stress and peak shear stress but a negative relationship was seen between normal stress and shear modulus. Therefore, the sample was stronger at increasing normal stress but less compliant. It should be noted that the range of normal loads tested was limited.

Opalinus Clay showed considerable variation in shear modulus, peak strength, and the amount of shear strain. As with COx, variation was seen in the initial strain response that probably derived from bedding in of the sample and apparatus components. Shearing parallel to the bedding direction gave an average peak shear stress of 3.47 MPa (2.62 to 4.34 MPa) and an average shear modulus of 96.9 MPa (48.7 to 147.1 MPa). The weakest sample had the lowest shear modulus and the strongest had the highest modulus, suggesting a real variation in strength of the samples. In samples sheared in a direction perpendicular to bedding, the average peak stress was 4.75 MPa (4.4 – 5.7 MPa) and shear modulus averaged 213 MPa (118 – 359 MPa). Two populations of result may exist with a weaker stiffer pair of tests and a stronger but less compliant pair. Variation within these populations is less marked. No clear difference was seen between shear fractures formed at different directions. A positive linear relationship was seen between normal stress and peak shear stress, but a negative relationship was seen between normal stress and shear modulus. Therefore, the sample was stronger at increasing normal stress but less compliant. It should be noted that the range of normal loads tested was limited.

Gas flow results

At a depth representative of the Belgian disposal concept (220m) in Boom Clay, two tests showed a small increase in flow after hydration, with one test showing a considerable decrease in flow of over four orders of magnitude. The average SSP_{H2O} was 334, although the full picture was complex, with hydration showing an increase in flow for two tests and a reduction in a third. Active shearing of the fracture was seen to increase flow along the fracture with an average SSP_{τ} of 0.4. At a depth representative of 500m depth, hydration was seen to reduce gas flow, this gave an average SSP_{H2O} of 1.5. Active shear was seen to increase flow in all five tests, ranging from minor increase up to two orders of magnitude increase. This gave an average SSP_{τ} of 0.4. Differences and similarities were seen between the two stress conditions. Both depths showed the same self-sealing potential result because of shear. In response to hydration, discounting the sample that showed considerable sealing, no test showed a significant change in flow. However, the data suggests at the lower stress condition flow increased, whereas at the higher stress condition flow decreased. It was concluded that both hydration and shear resulted in small increased gas flow in Boom Clay or no change in flow properties. Therefore, hydration and shear were not effective self-sealing processes for gas flow.

Boom Clay showed a general exponential relationship with SSP_{H2O} increasing with average roughness. This is because a rougher fracture will have a greater surface area, and this will result in more Boom

Clay accessing water and swelling. A trend was seen with higher average roughness resulting in less SSP_{τ}. Therefore, a smooth fracture results in more enhanced gas flow.

Callovo-Oxfordian claystone sheared in the direction parallel to bedding showed one test with a small increase in gas flow following hydration of the fracture and one test showed nearly one order of magnitude decrease in flow. These gave an average SSP_{H20} of 3.8. As a result of active shear, gas flow considerably increased, giving an average SSP_{τ} of ~0.05. For samples sheared in the direction perpendicular to bedding, two tests showed a decrease in flow as a result of hydration, while one test showed a small increase. The average of the three results showed a SSP_{H20} of 4.3. As a result of active shear, gas flow considerably increased, giving an average SSP_{τ} of ~0.05. No systematic variation was seen between the two orthogonal test directions. Hydration was seen to decrease gas flow, while shearing was seen to increase flow. This was not expected, with shear predicted to result in a better seal (i.e. $SSP_{\tau} > 1$) as seen in hydraulic testing.

In one test of COx steady gas flow was established after hydration of the fracture. However, gas flow started to increase over a period of two days, reaching a maximum of 16,500 µl/h when the gas interface vessel ran out of gas and the pressure was relieved on the fracture. It is interpreted that a small conductive pathway had reached the outside of the fracture plane and as gas started to “leak” from the system, the pathway grew, allowing increasing amounts of gas to reach breakthrough. On retrieval of the sample after the test had been completed, a small patch of broken-up clay was apparent, suggesting that a structural feature of the sample had resulted in gas breakthrough.

In Callovo-Oxfordian claystone a negative exponential trend was seen with SSP_{H2O} decreasing with average roughness. Therefore, an increase in roughness reduces the effectiveness of hydraulic self-sealing. This may be because very rough fractures have considerable mismatch between the two faces of the fracture. A strong trend was seen between average roughness and SSP_{τ}. Therefore, a smoother fracture results in greater enhanced flow. This will be related to mismatch between the two surfaces of the fracture.

In Opalinus Clay sheared in a direction parallel to bedding, a decrease in flow of one order of magnitude was seen as a result of hydration, with an average SSP_{H20} of 38. However, no significant change was seen as a result of shear, with a small average increase of SSP_{τ} of 0.84. In tests sheared perpendicular to bedding, hydration of the fracture significantly decreased gas flow, with an average SSP_{H20} of 133 (Over two-orders of magnitude reduction in gas flow). However, active shearing resulted in an increase in gas flow with an average SSP_{τ} of 0.33. It should be noted that much greater variation is seen in SSP_{τ} perpendicular to bedding. There was systematic difference between the two orthogonal directions, with both orientations showing an increase in gas flow because of shear movement. In Opalinus Clay, a positive relationship was seen between SSP_{H2O} and average roughness, and a negative trend between SSP_{τ} and average roughness. Therefore, in OPA, a rougher fracture results in greater enhanced gas flow.

Comparing the three rock types, considerable difference is seen in the self-sealing potential of hydration and shear. Opalinus Clay saw the most sealing caused by hydration, with Boom Clay seeing the least. As a result of shear, Callovo-Oxfordian claystone saw the most increase in flow, with Boom Clay seeing the least. Generally, no variation was seen in Callovo-Oxfordian claystone and Opalinus Clay with respect to shear direction, with only minor variation seen in self-sealing potential in Boom Clay with depth. In all three rock types, no correlation was found to explain the difference in flow seen.

4.3.6 Key learning points

4.3.6.1 New knowledge acquired

Previous experiments of fracture flow have concentrated on the transmissivity of water. These experiments have shown that water flow along a fracture can reduce fracture transmissivity by up to one order of magnitude. Active shear of the fracture can result in a further order of magnitude reduction in flow, although prolonged flow can result in increases of transmissivity. This had been interpretated as showing hydraulic flow and shear are effective self-sealing mechanisms in clay-rich rocks. This was assumed to also apply to gas flow. The current study has shown that the assumption that hydration and shear are effective self-sealing mechanism for gas flow is over simplified.

Considerable variation was noted in initial gas flow for all three rock types tested. No systematic correlation was found between fracture properties (roughness, peak to valley height etc) and initial gas (or water) flow properties. This has been attributed to fracture roughness not being a direct proxy for fracture mismatch, with the latter being a measure of asperities within the fracture plane that are conductive to gas.

The current study has defined a new parameter, called Self-Sealing Potential (SSP), to remove the variation in flow rates seen. Self-Sealing Potential as a result of hydration (SSP_{H2O}) is a measure of the proportional change in gas flow seen before and after hydraulic flow along the fracture. Self-Sealing Potential as a result of shear (SSP_{τ}) is a measure of the proportional change in gas flow as a result of active shear movement. For both parameters, SSP > 1 indicates a decrease in flow, SSP < 1 indicating an increase in flow. An SSP > 1 therefore therefore indicates self-sealing. The current study suggests that 0.9 < SSP < 1.25 means that no change in flow has been seen, although this could be extended to 0.8 < SSP < 1.5 to include only minor changes in self-sealing.

SSP in Boom Clay: Neither hydration nor shear were effective self-sealing processes for gas flow. It was concluded that both hydration and shear resulted in small increases in gas flow in Boom Clay or no change in flow properties. Data suggested that excess water on the fracture plane resulted in increased gas flow. At the two stress conditions investigated, both showed the same self-sealing potential result because of shear. In response to hydration, discounting one sample that showed considerable sealing, no test showed a significant change in flow. However, the data suggests at the lower stress condition flow increased, whereas at the higher stress condition flow decreased.

A rougher fracture was seen to have a better self-sealing potential (SSP_{H2O}) as it will result in greater surface area being accessed by water for swelling. However, a smoother fracture resulted in more enhanced gas flow and a smaller SSP_{τ}.

SSP in Callovo-Oxfordian claystone: No systematic variation was seen between the two orthogonal test directions, perpendicular and parallel to bedding. Hydration was seen to decrease gas flow (SSP ~4), while shearing was seen to significantly increase flow (SSP ~0.05). In COx, an increase in roughness reduces the effectiveness of hydraulic self-sealing, as rough fractures have considerable mismatch between the two faces of the fracture. A strong trend was seen between average roughness and SSP□. Therefore, a smoother fracture results in greater enhanced flow. This will be related to mismatch between the two surfaces of the fracture.

SSP in Opalinus Clay: Systematic difference was seen between the two orthogonal directions. Hydration was seen to be an effective self-sealing mechanism with SSP_{H20} of 38 and 133 for parallel and perpendicular shearing respectively, with the latter representing an average reduction in flow of over two orders of magnitude. Shear was seen to enhance gas flow, with a small increase when sheared parallel to bedding and a significant increase perpendicular to bedding. A positive relationship was seen between SSP_{H2O} and average roughness, and a negative relationship between SSP□ and average

roughness. Therefore, in OPA, a rougher fracture results in a better gas seal following hydration, but a worse seal because of shear.

Comparison: considerable difference is seen in the self-sealing potential of hydration and shear. Opalinus Clay saw the most sealing caused by hydration, with Boom Clay seeing the least. As a result of shear, Callovo-Oxfordian claystone saw the most increase in flow, with Boom Clay seeing the least. Generally, no variation was seen in Callovo-Oxfordian claystone and Opalinus Clay with respect to shear direction, with only minor variation seen in self-sealing potential in Boom Clay with depth. In all three rock types, no correlation was found to explain the difference in flow seen.

Mechanical data: Considerable variation was seen in terms of shear modulus, peak strength, and the amount of shear strain for all three rock types. In Boom Clay, increased depth resulted in a stronger sample but with only a marginal increase in compliance. A positive linear relationship was seen between normal stress and peak shear stress. A positive linear relationship was also seen between normal stress and shear modulus. In Callovo-Oxfordian claystone, no significant difference was seen in shear properties in the two orthogonal directions. A positive linear relationship was seen between normal stress and peak shear stress, but a negative relationship was seen between normal stress and shear modulus. Therefore, the sample was stronger at increasing normal stress but less compliant over the limited range of normal stress applied. In Opalinus Clay, the weakest sample had the lowest shear modulus and the strongest had the highest modulus, suggesting a real variation in strength of the samples. No clear difference was seen between shear fractures formed at different directions. A positive linear relationship was seen between normal stress and peak shear stress, but a negative relationship was seen between normal stress and shear modulus. Therefore, the sample was stronger at increasing normal stress but less compliant over the limited range of normal stress applied.

4.3.6.2 Impact of acquired knowledge

The current study has shown that self-sealing processes are not as strong when considering gas flow. Hydration is an effective self-sealing process in Callovo-Oxfordian claystone and Opalinus Clay, with the latter showing orders of magnitude decrease in flow. However, no change in flow was seen in Boom Clay, with some samples seeing an increase in gas flow properties. This was not expected and has not been previously reported. All rock types showed that active shear had a detrimental impact on sealing to gas, most significantly in Callovo-Oxfordian claystone. Therefore, the self-sealing potential must be better consider in Performance Assessment when considering gas transport and not to assume that fractures will seal sufficiently with time, as seen for hydraulic properties. Therefore, certainly fractures will keep favourable properties to gas migration even if water transfer is reduced. Shearing in these fractures increasing this gas flow capacity. The current study does impact Performance Assessment and will require careful consideration in long term modelling of gas flow along the engineered damaged zone.

4.3.6.3 Remaining knowledge gaps

The role of fracture mismatch has not been investigated and requires better understanding. Fracture roughness has not been found to be a good proxy of mismatch, and therefore on the quantification of asperities in the fracture plane. Longer-term hydration of the fracture has also not been investigated.

4.3.6.4 Recommendations for the future

Only three repeat experiments were conducted at each condition considered. Considerable spread was seen in mechanical data, flow, and self-sealing potential. A greater body of experimental results will lead to more robust statements about self-sealing in fractures.

The experimental results require modelling to elicit the full understanding of the dataset. The impact on the EDZ also requires modelling to understand the impact on long-term sealing.

Hydraulic flow was limited to one week in duration. A study is required to see how longer periods of hydration change self-sealing potential.

4.3.7 References

Armand, G., Conil, N., Talandier, J. and Seyedi, D.M. (2017) Fundamental aspects of the hydromechanical behaviour of Callovo-Oxfordian claystone: from experimental studies to model calibration and validation. Computers and Geotechnics, 85, pp.277-286.

ASTM Standard (2009) Standard guide for assessment of surface texture of non-porous biomaterials in two dimensions. F2791-09.

Beerten, K, Leterme, B (2012) Physical geography of north-eastern Belgium – the Boom Clay outcrop and sub-crop zone SCK-CEN report ER-202 12/Kbe/P-2 60p.

Bernier, F, Li, XL, and Bastiaens, W (2007) Twenty-five years' geotechnical observation and testing in the Tertiary Boom Clay formation, Géotechnique 57(2) 229–237.

Blanchart, P, Faure, P, De Craen, M, Bruggeman, C, and Michels, R (2012) Experimental investigation on the role of kerogen and clay minerals in the formation of bitumen during the oxidation of Boom Clay, Fuel 97, 344–351.

Cuss, R.J., and Harrington, J.F. (2016) An experimental study of the potential for fault reactivation during changes in gas and porewater pressure. International Journal of Greenhouse Gas Control, 53, pp.41-55. DOI: 10.1016/j.ijggc.2016.07.028

Cuss, R.J., Harrington, J.F., Sathar, S., and Norris, S. (2015) An experimental study of the flow of gas along faults of varying orientation to the stress-field; Implications for performance assessment of radioactive waste disposal. Journal of Geophysical Research – Solid Earth. 120, pp.3932-3945, doi:10.1002/2014JB011333

Cuss, R.J., Harrington, J.F., Sathar, S., Norris, S., and Talandier, J. (2017) The role of the stress-path and importance of stress history on the flow of water along faults; an experimental study. Applied Clay Science, 150, pp.282-292, https://dx.doi.org/10.1016/j.clay.2017.09.029

Cuss, R.J., Milodowski, A., and Harrington, J.F. (2011) Fracture transmissivity as a function of normal and shear stress: first results in Opalinus clay. Physics and Chemistry of the Earth. 36, pp.1960-1971. DOI: 10.1016/j.pce.2011.07.080

Cuss, R.J., Wiseall, A.C., Dobbs, M.R., Parkes, D., Harrington, J.F., Talandier, J., and Bourbon, X. (2018) Experiments on interface processes at the cement/Callovo-Oxfordian Claystone interface and the impact on physical properties; Mechanical and flow properties of fresh interfaces. Proceedings of the 3rd Annual Workshop of the CEBAMA Project, Nantes, France, 17th-18th April, 2018. 10pp.

Cuss, R.J., Wiseall, A.C., Harrington, J.F., Talandier, J., and Bourbon, X. (2019) Experiments on interface processes at the cement/Callovo-Oxfordian claystone interface and the impact on physical properties; mechanical results from the Callovo-Oxfordian claystone. In Proceedings of the Second Workshop of the HORIZON 2020 CEBAMA Project (KIT Scientific Reports; 7752) (Vol. 7752, p. 41). KIT Scientific Publishing.

Cuss, R.J., Wiseall, A.C., Tamayo-Mas, E., and Harrington, J.F. (2018) An experimental study of the influence of stress history on fault slip during injection of supercritical CO2. Journal of Structural Geology, 109, pp.86-98. https://doi.org/10.1016/j.jsg.2018.01.006

De Craen, M, Wang, L, Van Geet, M, Moors, H (2004) Geochemistry of Boom Clay pore water at the Mol site, SCK-CEN-BL-990 04/MDC/P-48, SCK-CEN.

Dehandschutter, B, Vandycke, S, Sintubin, M, Vandenberghe, N, Gaviglio, P, Sizun, JP Wouters, L, (2004) Microfabric of fractured Boom Clay at depth: a case study of brittle-ductile transitional clay behaviour, Applied Clay Science, 26(1-4) pp.389-401.

Esteban, L., Bouchez, J.L. and Trouiller, A., 2006. The Callovo-Oxfordian argillites from the eastern Paris Basin: Magnetic data and petrofabrics. Comptes Rendus Géoscience, 338(12-13), pp.867-881.

Gaucher, E., Robelin, C., Matray, J.-M., Négrel, G., Gros, Y., Heitz, J.-F., Vinsot, A., Rebours, H., Cassagnabère, A. and Bouche, A.T. (2004) ANDRA underground research laboratory: interpretation of the mineralogical and geochemical data acquired in the Callovo-Oxfordian formation by investigative drilling, Phys. Chem. Earth 29, pp. 55–77.

Gautschi, A. (2001) Hydrogeology of a fractured shale (Opalinus Clay): Implications for deep geological disposal of radioactive wastes. Hydrogeology Journal, 9, pp.97–107

Graham, C.C., Cuss, R.J., Wiseall, A.C., (2014). Progress report with data on processes, constitutive relations and parameters for modelling work. ULTimate CO2 Project no 281196, Deliverable 4.5.

Harrington, J.F., Cuss, R.J., and Talandier, J. (2017) Gas transport properties through intact and fractured Callovo-Oxfordian mudstones. In Rutter, E.H., Mecklenburgh, J. & Taylor, K.G. (eds) Geomechanical and Petrophysical Properties of Mudrocks. Geological Society, London, Special Publications, 454, https://doi.org/10.1144/SP454.7

Harrington, J.F., Cuss, R.J., Wiseall, A.C., Daniels, K.A., Graham, C.C. and Tamayo-Mas, E. (2017). Scoping study examining the behaviour of Boom Clay at disposal depths investigated in OPERA. OPERA-PU-BGS523&616.

Honty, M, and De Craen, M. (2011) Boom Clay mineralogy – qualitative and quantitative aspects, SCK CEN contract: CO-90-08-2214-00 NIRAS/ONDRAF contract: CCHO 2009-0940000, Research Plan Geosynthesis.

Pearson, F.J., Arcos, D., Bath, A., Boisson, J.Y., Fernandez, A.M., Gabler, H.E., Gaucher, E., Gautschi, A., Griffault, L., Hernan, P., Waber, H.N. (2003) Geochemistry of Water in the Opalinus Clay Formation at the Mont Terri Laboratory. Mont Terri Project Technical Report 2003-03

Rousset, D. and Clauer, N. (2003) Discrete clay diagenesis in a very low-permeable sequence constrained by an isotopic (K–Ar and Rb–Sr) study. Contributions to Mineralogy and Petrology, 145(2), pp.182-198.

Vis, GJ, and Verweij, JM. (2014) Geological and geohydrological characterization of the Boom Clay and its overburden, OPERA-TNO 411 Technical Report.

Wemaere, I, Marivoet, J, and Labat, S (2008) Hydraulic conductivity variability of the Boom Clay in north-east Belgium based on four core drilled boreholes, Physics and Chemistry of the Earth, Parts A/B/C 33 24-36.

Wenk, H.-R., Voltolini, M., Mazurek, M., Van Loon, L.R. and Vinsot, A. (2008) Preferred Orientations and Anisotropy in Shales: Callovo-Oxfordian Shale (France) and Opalinus Caly (Switzerland), Clays and Clay Minerals, 56, pp 285-306.

Wileveau, Y. and Bernier, F. (2008) Similarities in the hydromechanical response of Callovo-Oxfordian clay and Boom Clay during gallery excavation. Physics and Chemistry of the Earth, Parts A/B/C, 33, pp.S343-S349.

Wiseall, A., Cuss, R. and Hough, E. (2019) September. Visualising Hydraulic Fractures in Bedded and Fractured Shales: A Series of Analogue Experiments. In Fifth International Conference on Fault and Top Seals (Vol. 2019, No. 1, pp. 1-5). European Association of Geoscientists & Engineers.

Wiseall, A.C., Cuss, R.J., Graham, C.C. and Harrington, J.F. (2015) The visualization of flow paths in experimental studies of clay-rich materials. Mineralogical Magazine, 79(6), pp.1335-1342.

Wiseall, A.C., Cuss, R.J., Hough, E, and Kemp, S.J. (2018) The role of fault gouge properties on fault reactivation during hydraulic stimulation; an experimental study using analogue faults. Journal of Natural Gas Science and Engineering, 59, pp.21-34 https://doi.org/10.1016/j.jngse.2018.08.021

Wong, T, Batjes, DAJ, and de Jager, J, (Eds.; 2007) Geology of the Netherlands. Herent: Royal Netherlands Academy of Arts and Sciences.

Yu, HD, Chen, WZ, Jia, SP, Cao, JJ, and Li, XL (2012), Experimental study on the hydro-mechanical behaviour of Boom clay, International Journal of Rock Mechanics and Mining Sciences 53 159-165.

Yven, B., Sammartino, S., Géraud, Y., Homand, F., and Villiéras, F. (2007) Mineralogy, texture and porosity of Callovo-Oxfordian argillites of the Meuse/Haute-Marne region (eastern Paris Basin). Mémoires de la Société géologique de France, 178, pp.73–90.

4.4 Gas transport in intact and remoulded/recompacted claystone (EPFL)

In the scope of European Joint Programme on Radioactive Waste Management (EURAD) for the Work Package 6 – "Mechanistic understanding of gas transport in clay materials" (WP6-GAS), this report presents the contribution of the Laboratory of Soil Mechanics (LMS) of the Swiss Federal Institute of Technology in Lausanne (EPFL) to Milestone 229 "Task 3.1 / 3.2 Experimental report" (MS 229). EPFL's experimental program on Opalinus Clay addresses three major aspects, namely (i) the phenomena and processes related to the initiation and propagation of rock failure in response to gas pressure build-up, (ii) the characterization of gas transport processes in remoulded and recompacted OPA, mimicking the gas transport behaviour of fault gouge material and (iii) the phenomena and processes that contribute to the self-sealing of OPA after gas invasion. The proposed experiments are combined water/gas injection experiments with an oedometer cell, allowing for assessment of axial strain.

The main objectives for the subtask 3.1 are the following:

- Derivation of constitutive relationships of the water retention behaviour, relative permeabilities and stress-strain relationships in response to gas invasion processes.
- Validation of existing concepts of effective stress (e.g. Bishop's formulation) for their applicability on gas invasion processes.
- Gas transport properties of remoulded and recompacted OPA (mimicking fault gouge material): empirical relationships between porosity, permeability and gas entry pressure; water retention behaviour; particle mobilization in response to long-term gas transfer. Quantification of the role of mineralogy and grain size distribution.
- Fracture re-activation of faulted rock samples: on-set of dilatancy / rupture; gas transport characteristics of fractured material.

The main objectives for the subtask 3.2 are the following

- Constitutive relationships of the geomaterials in response to the re-saturation process ("imbibition of the wetting fluid") after long-term gas invasion (hysteresis of water retention behaviour, stress-strain behaviour).
- Determination of the evolution of hydraulic conductivity after long-term gas invasion.

The experimental set-ups used in the gas injection tests are presented in section 4.4.1. Section 4.4.2 presents the tested materials and their relevant parameters related to water/gas injection tests. Section 4.4.3 presents the tests procedures including the hydro-mechanical stress path prior to gas testing. The main results and a summary of the findings are presented in sections 4.4.4 and 4.4.5, respectively. The key learning points are finally highlighted in section 4.4.6.

4.4.1 Experimental set-up

This section presents the high-pressure oedometer set-up used in the water and gas injection tests.

4.4.1.1 Description of apparatus

The experimental work used a high-pressure oedometer cell specifically developed to analyse the hydro mechanical behaviour of geomaterials at high-confining stresses (Ferrari et al., 2013). The layout of the apparatus is depicted in Figure 4-64. The cell is designed to hold cylindrical specimens with a height and diameter of 12 mm and 35 mm, respectively. The specimens are placed in a stainless steel oedometer ring with a thickness of 15 mm. The bottom and top parts of the specimen in the oedometric

ring are in contact with metallic plates equipped with a drainage system. The latter is composed of vertical holes which are connected by a spiral path. The spiral path is then connected to the water/gas injection systems as shown in Figure 4-65. Pre-compressed filter paper disks are placed between the specimen and the plates. The interfaces between each element are sealed using O-rings.

The vertical load is applied by a hydraulic jack connected to a volume/pressure controller (VPC), enabling it to reach a vertical total stress up to 100 MPa. Different VPCs can be connected to the oedometer cell to perform water and gas injections from the bottom and top side of the specimen with a fluid pressure up to 16 MPa (water) and 20 MPa (gas). All the VPCs have a resolution of 1 kPa for the pressure and 1 mm^3 for the volume; the accuracy is <0.1% and 0.25% respectively. The assessment of the vertical deformation was done using three Linear Variable Differential Transformers (LVDTs) which measure the relative displacement of the cell with respect to the piston. The resolution of the LVDTs used for the tests on natural OPA was 0.2 μm, while it was 1 μm for the tests on remoulded and recompacted OPA with an accuracy of 0.1%. The natural specimens were tested with the vertical mechanical load and fluid injection perpendicular to bedding plane (S sample).

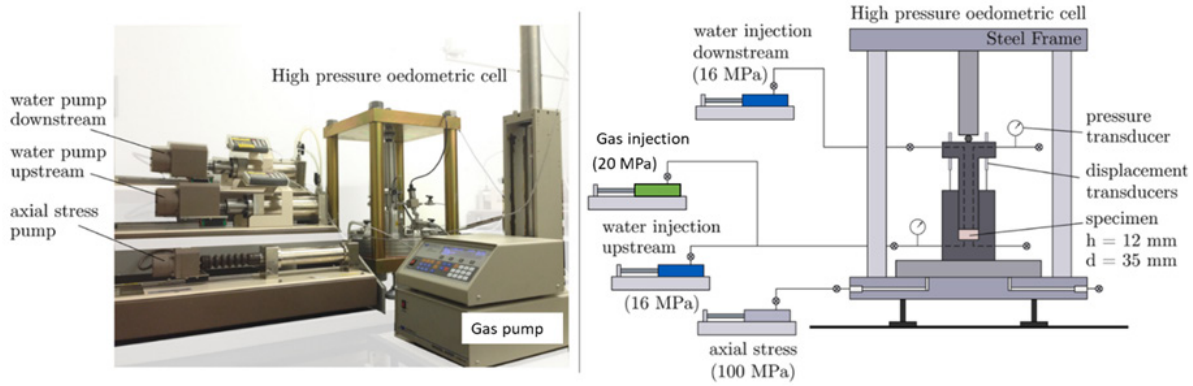

Figure 4-103 – High pressure oedometer test set-up.

Figure 4-104 – Oedometer ring with the metallic base

4.4.1.2 Calibration

The compliance of the oedometer apparatus was quantified by testing a metallic dummy sample of known mechanical properties for both configurations: mechanical loading (vertical stress) and fluid injection. The measured deformation during the experiments with OPA were corrected accordingly.

4.4.1.3 Testing fluids

For the oedometric and hydraulic conductivity tests on natural OPA, synthetic porewater was used in order to reproduce the chemical composition of the in-situ porewater, which may affect the hydro mechanical response of clayey geomaterials. The recipe of the synthetic porewater (SW) was adopted considering the reference porewater composition of the Zürich Northeast (ZNO) siting area (Ammen and Palten, 2021). Distilled water (DW) was used to prepare remoulded and recompacted specimens for the water retention measurements. Compressed nitrogen was used for the gas injection tests.

4.4.2 Material properties (pre-test and post-test characteristics)

4.4.2.1 Geotechnical characterization of natural and remoulded OPA

The core samples used in this experimental campaign were retrieved from the deep borehole in Trüllikon (TRU1-1) in the Zürich Northeast siting region in Switzerland (Ammen and Palten, 2021) and were sourced from a depth of about 850 m. A complete geotechnical characterization of the cores samples was presented in Llabjani et al. (2021) according to EURAD deliverables. Therefore, only the relevant properties of the tested specimens are presented in this report.

A complete geotechnical characterization has been performed on the tested specimens, as shown in Table 4-21 (natural OPA) and Table 4-22 (remoulded and recompacted OPA).

Table 4-31 – Material properties of tested specimens – Natural OPA; GW = gas/water injection tests, WRC = water retention curves.

Material	OPA_848	OPA_848
Test	GW	WRC
Depth (m)	848.7	848.7
Bulk density, ρ *(g/cm³)*	2.50	2.48
Density of solid particles, ρ_s (g/cm³)	2.78*	2.78*
Void ratio, e (-)	0.15	0.17
Degree of saturation, *Sr* (-)	0.63	0.66
Initial total suction, ψ (MPa)	66	104
* grain density measurements according to ASTM D854-14. In Trüllikon, samples extracted from a depth of 845, 848 and 899 m with grain densities of 2.76, 2.78 and 2.72 g/cm³,.		

The following procedure was adopted for the characterization of the natural specimens. The volume of the specimen used for the computation of the bulk density (ρ) was obtained from independent measurements of the height and diameter with a digital calliper with a resolution of 1 μm and an accuracy of 2 μm. The water content (w) was measured on a different piece of material that was obtained from the same slice of the core used to prepare the specimen. Another piece was used for the measurement of the total suction (ψ) with the dew-point psychrometer (WP4C, e.g., Leong et al., 2003; Cardoso et al., 2007). The particle density was measured on material preliminarily crushed and passing a 0.5 mm sieve. Average values on three determinations are reported. The void ratio and degree of saturation were then computed accordingly. The values of degree of saturation (S_r) and initial total suction (ψ) highlight a desaturation of the specimens induced by the exposure to free air during its preparation.

The geotechnical characterization of the remoulded and recompacted specimens were performed after the consolidation of the material in the oedometer apparatus at the target vertical effective stress. More details on the specimens' preparation are presented in section 4.5.4.

Table 4-32 – Material properties of tested specimens – Remoulded and recompacted OPA; GW = gas/water injection tests, WRC = water retention curves

Material	OPA_R14	OPA_R5	OPA_R14	OPA_R50
Test	GW	WRC	WRC	WRC
Depth (m)	848.6-848.7	848.6-848.7	848.6-848.7	848.6-848.7
Bulk density, ρ *(g/cm³)*	2.28	2.20	2.29	2.39
Density of solid particles, ρ_s (g/cm³)	2.78	2.78	2.78	2.78
Void ratio, e (-)	0.37	0.47	0.38	0.28
Degree of saturation, *Sr* (-)	1	0.95	1	0.89
Compaction vertical effective stress (MPa)	14	5	14	50
Preparation fluid	SW	DW	DW	DW

4.4.2.2 Microstructural characterization of natural and remoulded OPA

The pore structure of Opalinus Clay was studied with the Mercury Intrusion Porosimetry (MIP) test, where a freeze-drying technique was adopted for the preparation of each sample. To overcome the conformance effect and the compressibility of the sample below the entry pressure of mercury, a correction was applied to the MIP results (Comisky et al., 2011). Limitations of the MIP test can be found in Delage et al. (1996).

As shown in Figure 4-66 (left) the maximum void ratio detected by MIP (e_{Hg} = 0.07) on natural OPA is lower compared to the void ratio of the specimens obtained in the identification tests (e = ~0.15). The

differences can be attributed to the limitations of the MIP technique, such as the presence of non-connected pores and/or pore throats smaller than 4 nm which is the smaller pore size detectable with the apparatus. Figure 4-66 (right) shows a unimodal distribution with a peak value at about 10 nm. The detected pore diameter is from 4 nm to 60 nm. The results of the MIP test agree with the literature (e.g., Crisci et al., 2019; Minardi et al., 2021).

Regarding the remoulded and recompacted OPA, the material has been first compacted in the oedometric apparatus at a vertical effective stress of 14 MPa (similar to the in-situ conditions of the retrieved core) before being unloaded and freeze-dried for the MIP test. The maximum void ratio detected by MIP (e_{Hg} = 0.35) is much closer to the void ratio obtained by the identification tests (e = 0.37). This indicates that the remoulding process has almost removed the presence of non-connected and/or smaller pores (<4 nm). The diameter of the larger detected pores (600 nm) is one order of magnitude bigger than for natural OPA.

Using the Young-Laplace equation from the larger detected pores, assuming cylindrical shape, air is expected to enter the pore space of an initially saturated material at a capillary pressure of about 5 MPa and 0.5 MPa for natural and remoulded OPA, respectively. The low air entry value estimated for the remoulded and recompacted OPA may indicate that the procedure for the MIP test (e.g., freeze-drying) has induced some damage to the material. Such low air entry value was not observed in the gas injection tests on remoulded and recompacted OPA.

Additionally, according to Romero and Simms (2008), the mercury intrusion process is similar to air intrusion during the drying path of the water retention curve. Thus, the injection of non-wetting mercury is equivalent to the ejection of water by the non-wetting front advance of air. The remaining pore volume that is not intruded by mercury can be used to evaluate the degree of saturation corresponding to the equivalent applied matric suction s. The water retention curves for the main drying path obtained from the MIP analyses are shown in Figure 4-67.

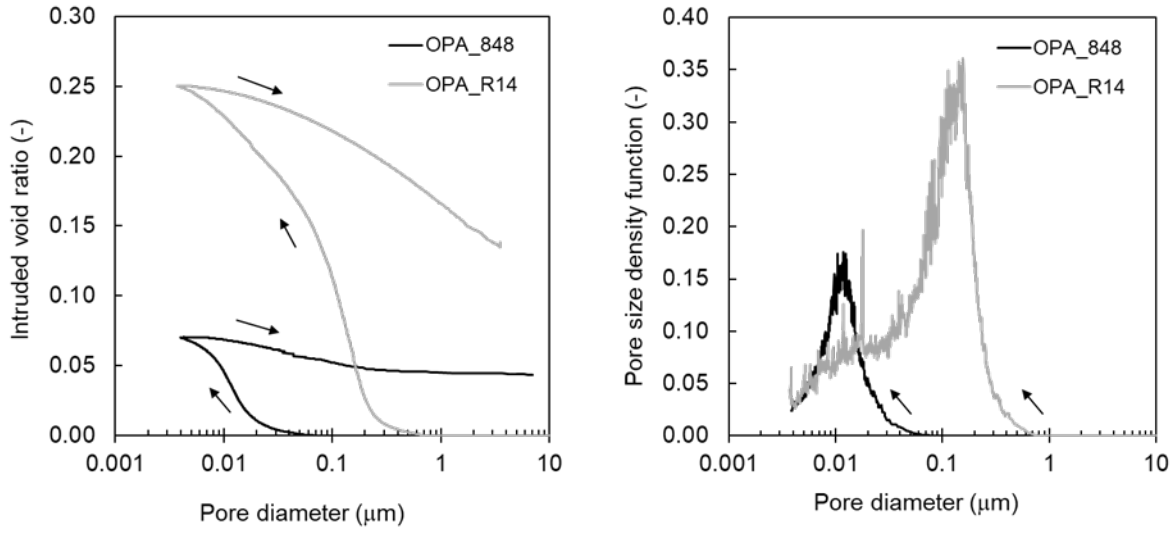

Figure 4-105 – MIP test result: intruded void ratio (left) and pore size density function (right).

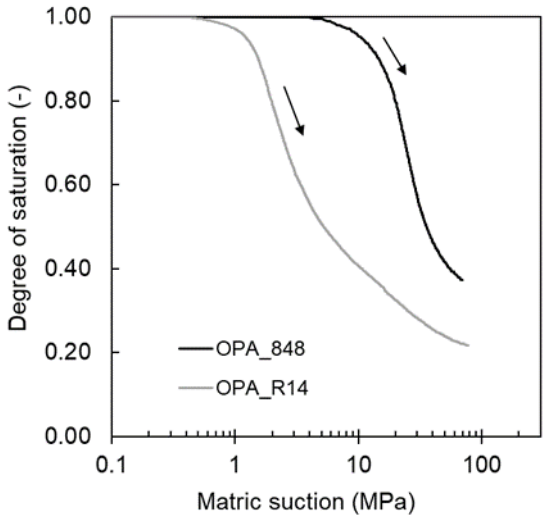

Figure 4-106 – Water retention curves derived from the MIP tests.

4.4.3 Testing protocol

In this section, the procedures followed in this experimental campaign are described, including the specimen preparation for both intact and remoulded material, the water retention measurements and the water/gas injection tests in the high-pressure oedometer apparatus.

4.4.3.1 Natural specimens preparation

First, the location of the specimen was selected on the core sample using X-ray images to prevent from choosing initially cracked or heterogeneous portions. A slice with a thickness of approximately 30 mm was sawn from the core without unpacking it, in order to minimize the disturbance to the specimen. For the water/gas injection test in the oedometer apparatus, a cylinder with a diameter slightly larger than the final confining ring was obtained using a lathe machine; final re-coring using the confining ring was performed using a hydraulic press. Lastly, the lower and upper faces were smoothed using sandpaper in order to obtain parallel and plane surfaces. For the water retention measurements, twin cylindrical specimens (h = 25 mm, d = 20 mm) were shaped using a lathe machine.

No fluid was used during the specimen preparation phase in order to preserve the original water content/composition as much as possible and to reduce the disturbance of the material due to swelling.

4.4.3.2 Remoulded and recompacted specimens preparation

The remoulded and recompacted specimens were prepared with material that has been carefully mixed with water at a water content 1.2-1.5 times the liquid limit (w_L), without air drying or oven drying, and then consolidated under one-dimensional conditions. The intact Opalinus Clay was crushed by means of a grinder, and the fraction passing through a 0.5 mm sieve was selected. The slurry, having water content 1.2-1.5 times w_L, was prepared by mixing the powdered shale with distilled water (water retention measurements) or synthetic water (water/gas injection tests) and by vigorously working with a metal spatula in a container. After 24 h of equalisation in a closed environment, the slurry was placed in the oedometric ring with the aid of the metal spatula, and small portions of material were progressively added to avoid trapping any air; the upper and lower bases were finally smoothed. The specimens were then loaded up to the target vertical effective stress in multiple steps using the high-pressure oedometer apparatus. The water and gas injection tests were performed directly after the consolidation was

complete. To proceed to the water retention measurements, the specimens were carefully extruded from the oedometric ring.

4.4.3.3 Water retention measurements

To analyse the water retention behaviour upon suction changes, the employed methodology combines total suction control with an accurate assessment of the deformations in two orthogonal directions and is briefly recalled in the following.

The vapor equilibrium technique (VET) was used for the application of wetting/drying processes and the definition of the water retention behaviour. The technique allows for the control of the relative humidity inside a closed desiccator with saturated saline solutions. Through the application of the psychrometric law (Fredlund and Rahardjo, 1993), relative humidity can be converted to total suction.

$$\psi = -\frac{RT\rho_w}{M_w}\ln(RH) \qquad (4\text{-}4\text{-}1)$$

with ψ the total suction (Pa), R the constant for ideal gas constant (8.314J/K·mol), T the temperature (K), ρ_w and M_w the water density (kg/m^3) and molecular mass (kg/mol) respectively, and RH the relative humidity..

By using several types of salt, different total suction values can be imposed inside the desiccator. Table 4-23 summarizes the salts used for the investigation and the corresponding reference values of total suction at 25°C as measured using a dew-point chilled mirror psychrometer (WP4C, e.g., Leong et al., 2003, Cardoso et al., 2007). The tests were performed at a reference temperature of 24°C; the temperature fluctuation during the entire test period was in the range of ± 1°C; the consequent variations of total suction were within 2% of the target values and could be considered negligible compared with the whole range of total suction values applied during the experiment.

Table 4-33 – Salts used for the preparation of the saline solutions and corresponding values of total suction (at 25 °C)

Salt	**LiCl**	**$MgCl_2$**	**$Mg(NO_3)_2$**	**KCl**	**KNO_3**	**K_2SO_4**	**SW**	**DW**
Total suction (MPa)	300	125	85	30	10	3.5	1.2	~0.2

To assess the volumetric response upon suction variations, the deformations were measured in both axial and radial directions using a calliper with a micrometre resolution.

The natural OPA specimens were prepared from slices cut from the cores using a mechanical saw without cooling fluid (Figure 4-68a). The final cylindrical shape was obtained by the mean of a lathe (Figure 4-68b & c). Cylindrical specimens were placed inside the desiccator (Figure 4-68e). During each step of imposed total suction, both deformation(Figure 4-68d) and weight evolution were monitored. The first suction step was close to the initial condition of the specimen and assessed using the WP4C on a fragment from the same slice used to prepare the specimen. The tested specimens were then wetted in steps up to ~100% relative humidity (≈0.2 MPa of total suction). Then, a complete drying path was performed up to a total suction of 300 MPa (RH = 11%). At each suction step, the achievement of the equilibrium condition was assessed from the stabilization of both the strains and the mass of the specimens.

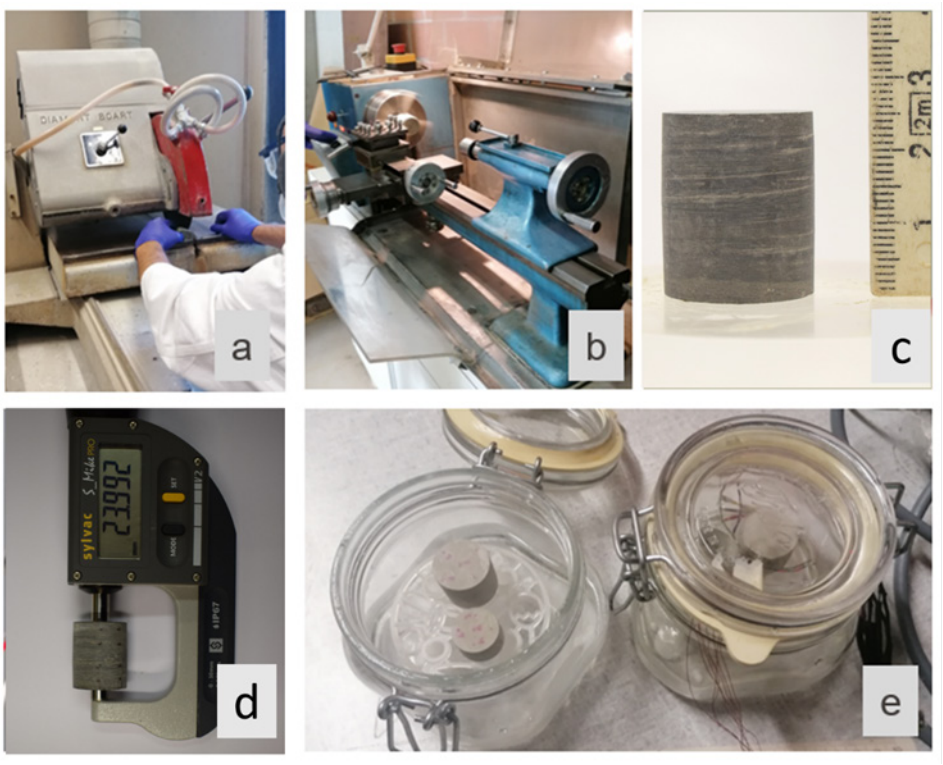

Figure 4-107 – Specimen preparation for the water retention measurements: a) Slice cut using a saw in dry conditions; b) cylindrical shape obtained with a lathe; c) prepared specimen; d) measurement of the specimen size with the caliper; e) tested specimens in a closed container with saline solution.

Remoulded and recompacted OPA specimens were already close to saturation as the specimens were prepared from slurry that was compacted up to the target vertical effective stresses. To proceed to the water retention measurements, the specimens were carefully extruded from the oedometric ring. The first suction step was performed at 100% relative humidity (≈0.2 MPa of total suction). Then, a complete drying path was performed up to a total suction of 300 MPa (RH = 11%), followed by a wetting path.

4.4.3.4 Injection tests on natural OPA

This section presents the protocol followed for the injection tests on natural OPA, namely the specimen OPA_848 (S sample).

Initial water resaturation

As previously described, no fluid was used during the specimen preparation phase in order to preserve the original water content/composition as much as possible and to reduce the disturbance of the material due to swelling. However, a slight drying of the material was expected during the preparation. Therefore, the test started first with a water resaturation in isochoric conditions using synthetic water mimicking the in-situ porewater (Aschwanden et al., 2021). The motivations for performing resaturation in isochoric conditions are described below.

The disturbance that the coring, the preparation and the reconditioning cause to the material may affect the sample response upon hydro-mechanical loading. Although a perfect sampling of shales is rarely feasible, efforts are devoted to the minimisation of sample disturbance. Because of sample extraction, the total stress is released, and negative porewater pressure is generated. Under the assumption of Bishop's effective stress formulation (Bishop, 1959) and a Skempton's B coefficient equal to 1

(Skempton, 1953), if the process is quick enough to occur in undrained condition, the effective stress remains constant. It results in the development of suction inside the sample, without changes in volume. Afterwards, samples are trimmed from the core. Depending on the technique adopted for the sample preparation, the exposure to the atmosphere and the mechanical load, the sample may be partially desaturated, and therefore subjected to an increase in mean effective stress, due to the increase of the suction. Testing without a proper resaturation would yield the behaviour of a partially saturated material, that is widely known to differ from the saturated (as in-situ) state (Wild et al., 2015; Minardi et al., 2018). Various ways to resaturate samples have been presented in the literature:

a) Resaturation in free-swelling conditions, e.g., by the use of vapour transfer technique or by the direct flooding with water;

b) by applying a total stress level corresponding to the in-situ condition, and then putting the sample in contact with water;

c) in isochoric conditions, i.e., putting the sample in contact with water, and preventing the swelling deformation that would occur by progressively increasing the radial and vertical stress.

In the first case (a) the effective stress is brought to zero by reducing the suction without any confinement, resulting in the swelling of the sample. The free swelling phenomenon is known to be non elastic, and damage occurs as presented in section 4.4.3.1. At the end of the saturation, the sample is cracked and may behave differently from the original material. In the second case (b), the final condition is similar to the in-situ condition. However, during its stress path, the sample is subjected to an increase in effective stress, which is higher than the initial and the in-situ condition, and may cause yielding of the sample. In the third case (c) the sample volume is kept constant, and, in the isotropic elastic hypothesis, the mean effective stress stays constant. The maximum stress experienced during this conditioning process is constrained, while it is not in case (b). For the mentioned reasons, it was decided to adopt the third methodology to recondition all the samples, namely resaturation in isochoric conditions.

Those conditions were ensured by progressively increasing the vertical total stress as swelling occurs. The displacements were maintained within a value corresponding to a vertical strain of ±0.1% in order to preserve as much as possible the initial porosity. Once the deformation and water uptake were stabilized, the saturation phase was considered complete and the total vertical stress corresponds to the swelling pressure.

Water and gas injection tests

Regarding the water and gas injection tests, once the resaturation (sequence (i) in Figure 4-69) was performed in isochoric conditions as described above, (ii) a mechanical loading up to the target vertical effective stress was performed to simulate in-situ stress conditions. To do so, constant water pressure at the bottom ($u_{w,bot}$) and top ($u_{w,top}$) of the specimen was applied ($u_{w,bot} = u_{w,top} = 1$ MPa) and the vertical total stress σ_v was increased in steps up to σ_v = 15 MPa. (iii) Constant head water permeability tests were performed at different vertical effective stresses by applying a differential water pressure of 1 MPa between the top and bottom side of the specimen. (iv) Then, in order to perform the first gas injection test, the water VPC connected at the bottom side of the specimen was replaced by the gas VPC. Nitrogen (N_2) was used in the experiments. At first, water in the bottom drainage line was flushed out and replaced by gas at an initial pressure of $u_{g,bot}$ = 3 MPa. The sequence comprised then a constant rate gas injection period (0.2 ml/min for an initial gas volume of 500 ml in the reservoir) during which gas pressure was increased from 3 MPa to 10 MPa. Gas pressure was then kept constant until quasi steady state conditions were observed for both gas flow and volumetric response of the tested specimen. Finally, the gas VPC was stopped, ensuring constant gas volume at the inlet, and the resulting gas pressure decay was monitored (so-called shut-in phase). Water back-pressure at the top

of the specimen was kept constant during the entire sequence at $u_{w,top}$ = 1 MPa. The maximum gas pressure always remained at least 5 MPa below the total vertical stress in order to avoid preferential flow paths at the interface between the specimen and the oedometer ring. (v) After the gas injection phase, water resaturation was performed under constant vertical total stress, followed by a water permeability test in order to assess the evolution of the intrinsic permeability due to gas transport. This was followed by a second gas injection phase (vi) with a different rate of gas injection period (0.05 ml/min for an initial gas volume of 500 ml in the reservoir) with the aim to observe the response of the specimen under different loading conditions. Finally, the specimen was rapidly unloaded and followed by post mortem analyses to determine the final degree of saturation and to characterise the microstructure of the tested material (vii). The test sequences and the generic boundary conditions are illustrated in Figure 4-69 and Figure 4-69, respectively.

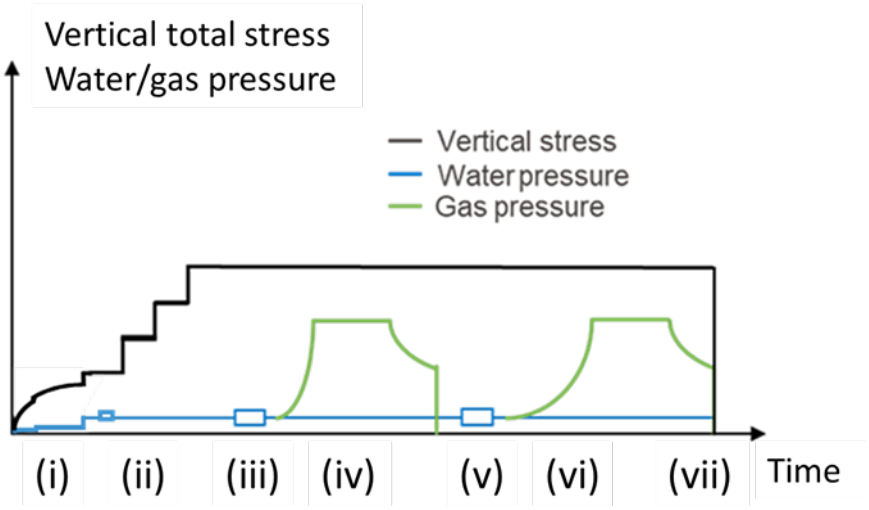

Figure 4-108 – Sequences for the water and gas injection tests.

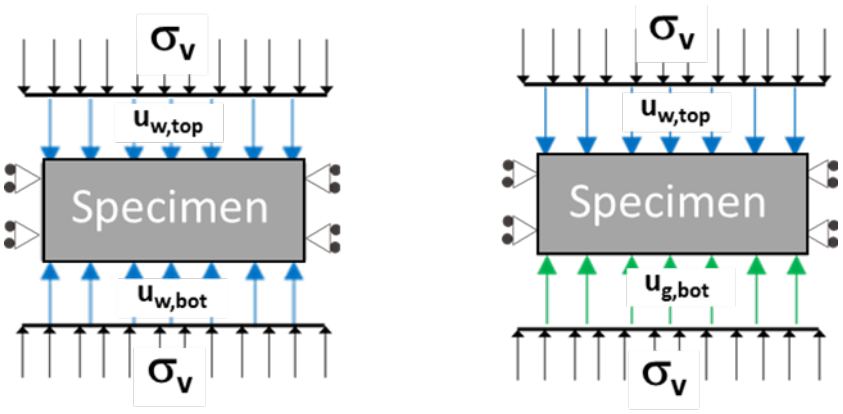

Figure 4-109 – Generic boundary conditions for the injection tests: water (left) and gas (right) injection phases.

4.4.3.5 Injection tests on remoulded and recompacted OPA

The slurry obtained from the remoulding procedure described above was placed in the oedometer ring and was loaded up to the target vertical effective stress in multiple steps using the high-pressure oedometer apparatus (sequence (ii) in Figure 4-69). (iii) The evolution of the water permeability upon loading was assessed by a constant head permeability test. Then, in order to perform a first gas injection test (iv), the water VPC connected at the bottom side of the specimen was replaced by the gas VPC. Nitrogen (N2) was used in the experiments. At first, water in the bottom drainage line was flushed out and replaced by gas at an initial pressure of $u_{g,bot}$ = 3 MPa. The sequence comprised then a constant rate gas injection period (1 ml/min for an initial gas volume of 500 ml in the reservoir) during which gas pressure was increased first from 3 MPa to 5.8 MPa as a slight outflow was already observed at this gas pressure. Once both outflow and volumetric deformation were stabilized, gas pressure was increased up to 7.5 MPa. Again, gas pressure was kept constant until quasi steady state conditions were observed for both gas flow and volumetric response. Finally, gas pressure was increased up to 10 MPa, but the large amount of gas outflow was not sustainable by the recovery system, and it was decided to stop the gas VPC, ensuring constant gas volume at the inlet, and the resulting gas pressure decay was monitored (so-called shut-in phase). Water back-pressure at the top of the specimen was kept constant during the entire sequence at $u_{w,top}$ = 1 MPa. The maximum gas pressure always remained at least 5 MPa below the total vertical stress in order to avoid preferential flow paths at the interface between the specimen and the oedometer ring. (v) After the gas injection phase, water resaturation was performed under constant vertical total stress, followed by a water permeability test in order to assess the evolution of the intrinsic permeability due to gas transport. This was followed by a second gas injection phase (vi) at a different constant rate gas injection (10 ml/min for an initial gas volume of 500 ml in the reservoir) with the aim to observe the response of the specimens under different loading conditions. With the experience gained during the first gas injection test, it was decided to increase the gas pressure from 3 to 7.5 MPa. Finally, the specimen was unloaded and followed by post mortem analyses to determine the final degree of saturation (vii).

4.4.4 Results

4.4.4.1 Water retention behaviour

Water retention behaviour of natural OPA

The results obtained in the determination of the water retention behaviour of natural OPA are shown in Figure 4-71. A wetting path was first applied starting from the initial condition, during which the applied total suction started from 85 MPa down to 0.2 MPa. A drying path was then imposed by increasing the applied total suction up to 300 MPa. The water content, initially determined at 2.9%, increased up to 9.1% during the wetting phase, while it decreased down to 1.1% during the drying phase. A hysteretic behaviour is also observed on the evolution of the water content upon wetting and drying.

The material experienced significant swelling and shrinkage upon suction changes. The monitoring of the strain evolution in both directions allowed to differentiate between the axial and radial strains. Results indicate that significant swelling occurred in the axial direction (perpendicular to bedding), while significantly less strain occurred in the radial direction (parallel to bedding). This significant anisotropy can be the result of opening/closure of the bedding planes upon suction changes. Furthermore, it can be noted that some irreversible strain is accumulated upon wetting. For both water content and strains evolution with suction, non-linear responses can be observed.

From the measured quantities (water content and strains), the evolution of the void ratio and degree of saturation can be computed. A notable increase in the void ratio was observed upon wetting, while it decreased close to the initial value upon drying, but still not wholly reversible. The evolution of the

degree of saturation (S_r) in main drying path is fitted according to Van Genuchten model (Van Genuchten, 1980).

$$S_r = \left(1 + \left(\frac{\Psi}{P}\right)^n\right)^{\left(\frac{1}{n}-1\right)} \quad (4\text{-}4\text{-}2)$$

where P = 11.38 MPa and n=1.39 are the fitting parameters, obtained by the least square method.

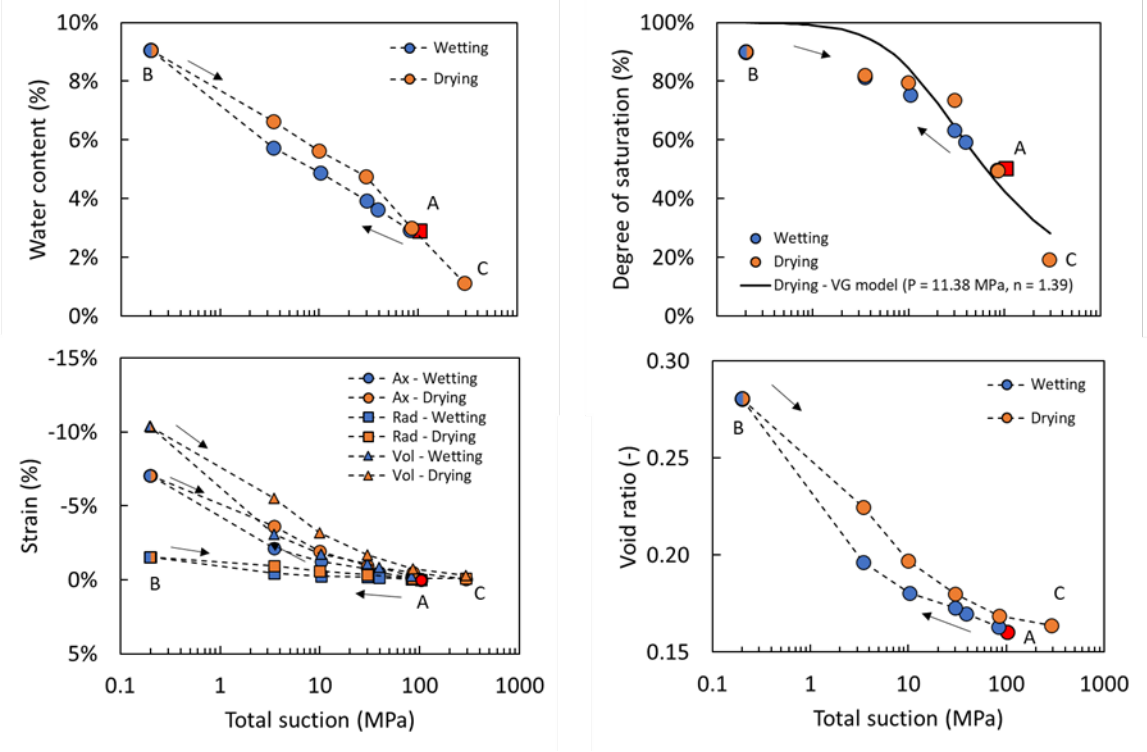

Figure 4-110 – Water retention behaviour of natural OPA (OPA_848): first wetting and drying paths.

The results obtained in the determination of the water retention behaviour of remoulded and recompacted OPA specimens are shown in Figure 4-72, Figure 4-73 and Figure 4-74. Figure 4-75 compare the results of all three remoulded and recompacted specimens. A drying path was first applied starting from the initial conditions, during which the applied total suction increased up to 300 MPa. A wetting path was then imposed.

Upon drying, a decrease in water content and shrinkage of the specimens was consistently observed. Upon wetting, the specimens were subjected to an increase of the water content increased coupled with swelling. The evolution of the water content was characterised by a hysteresis. An isotropic and reversible deformation was observed for all three specimens that can be attributed to the effect of the remoulded process on the fabric configuration of natural OPA.

From the measured quantities (water content and strains), the evolution of the void ratio and degree of saturation can be computed. Table 4-24 shows the best fitting parameters for the evolution of the degree of saturation according to the Van Genuchten model. The results showed higher water retention properties (in terms of degree of saturation versus suction) for higher compaction stress. These

observations are consistent with the lower initial porosity of the material, which may affect the capillary mechanisms.

Table 4-34 – Best fitting parameters for the Van Genuchten model for remoulded and recompacted OPA.

Suction path	Drying		Wetting	
Specimen	P (MPa)	n (-)	P (MPa)	n (-)
OPA_R5	4.31	1.57	1.08	1.44
OPA_R14	6.10	1.51	2.93	1.44
OPA_R50	7.27	1.52	1.68	1.38

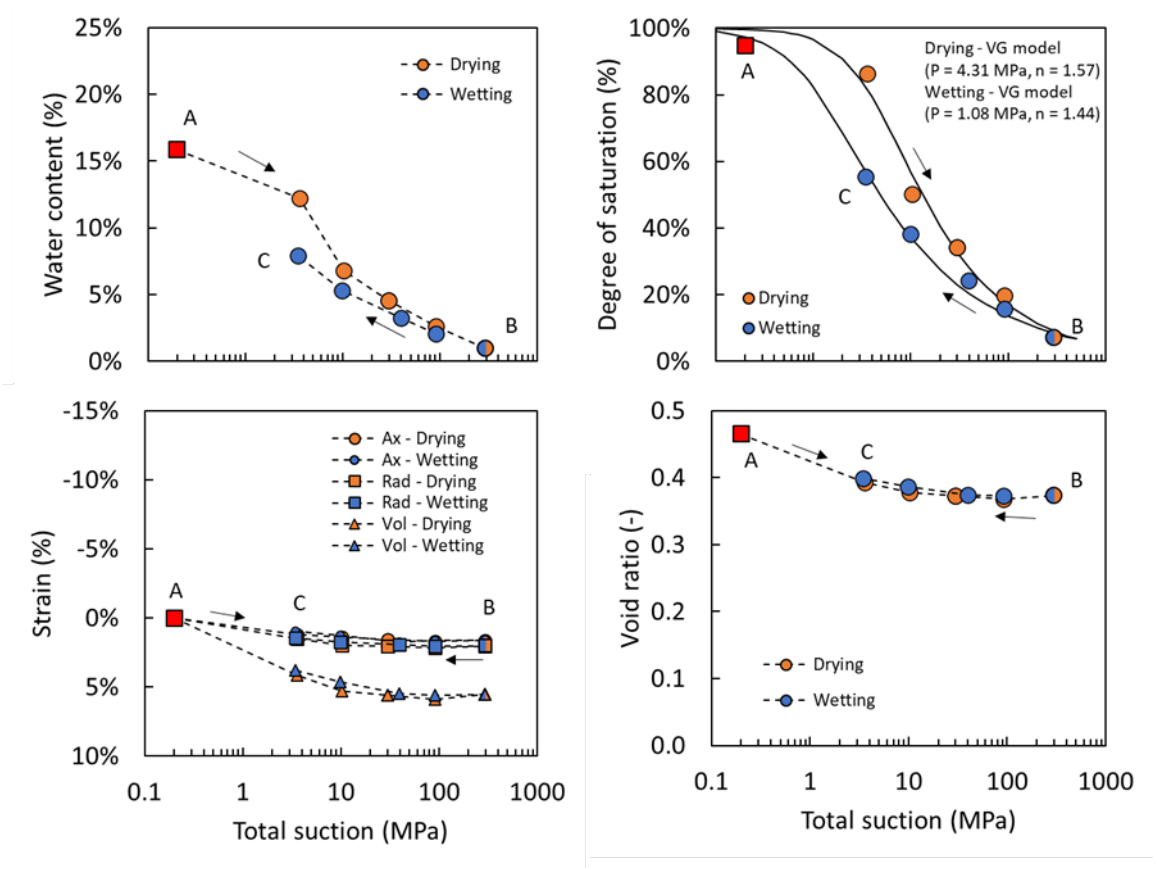

Figure 4-111 – Water retention behaviour of remoulded and recompacted OPA (OPA_R5): Drying and wetting paths.

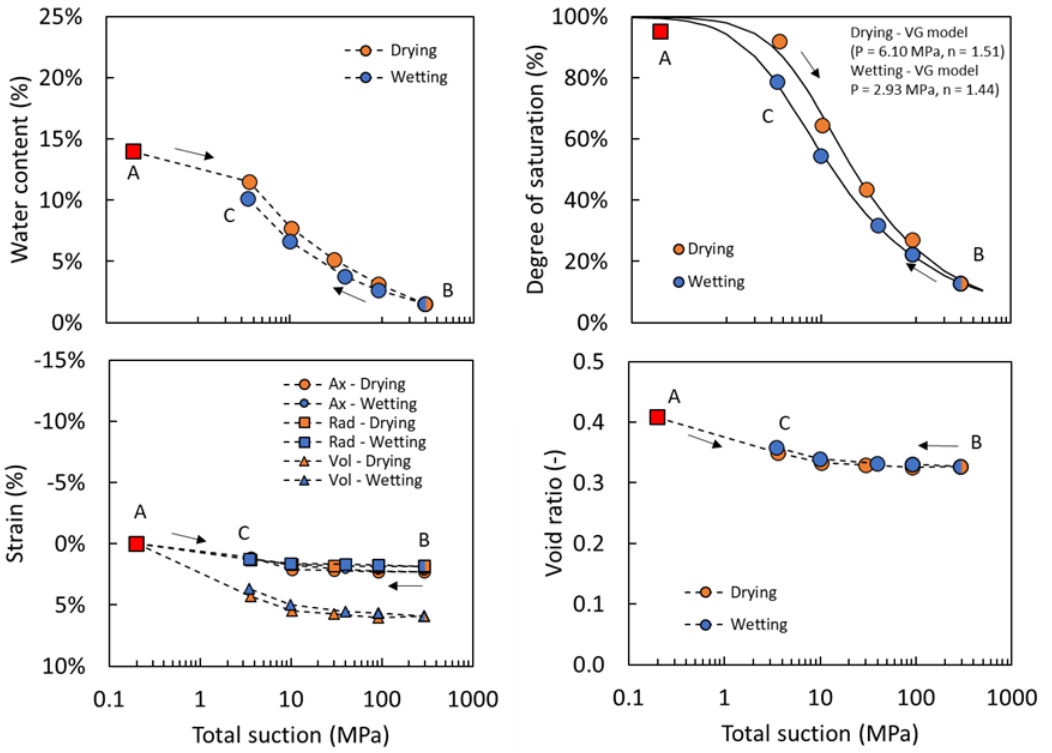

Figure 4-112 – Water retention behaviour of remoulded and recompacted OPA (OPA_R14): Drying and wetting paths.

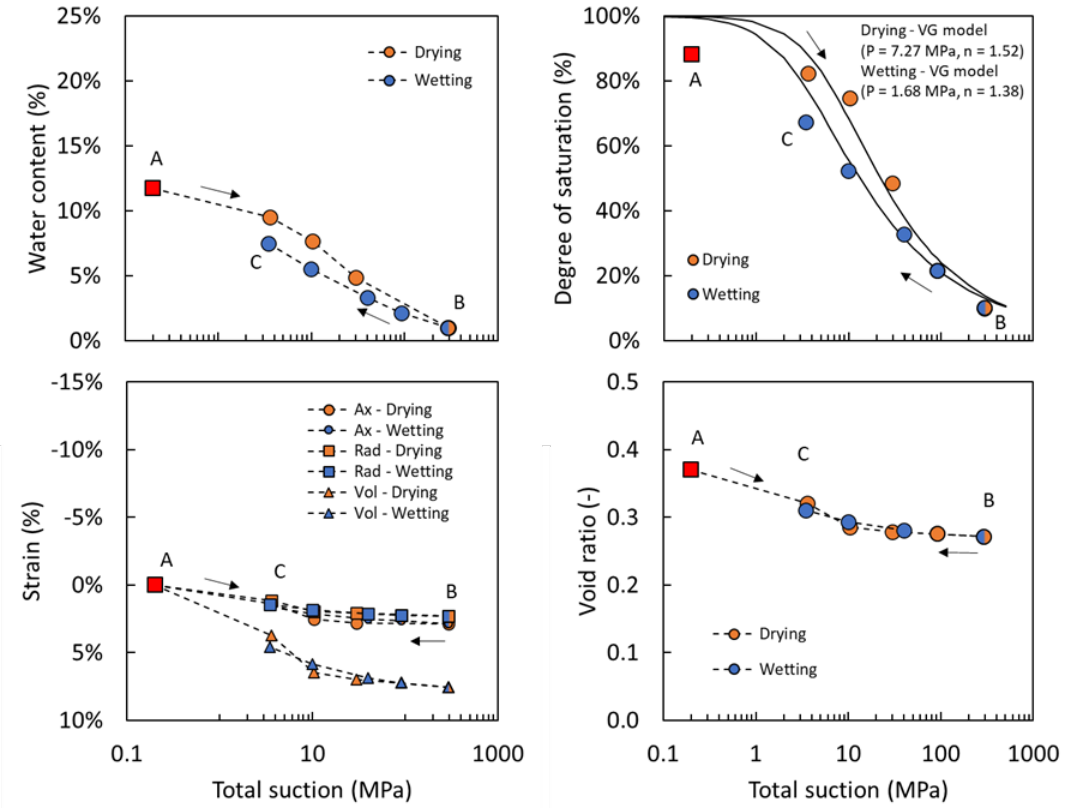

Figure 4-113 – Water retention behaviour of remoulded and recompacted OPA (OPA_R50): Drying and wetting paths.

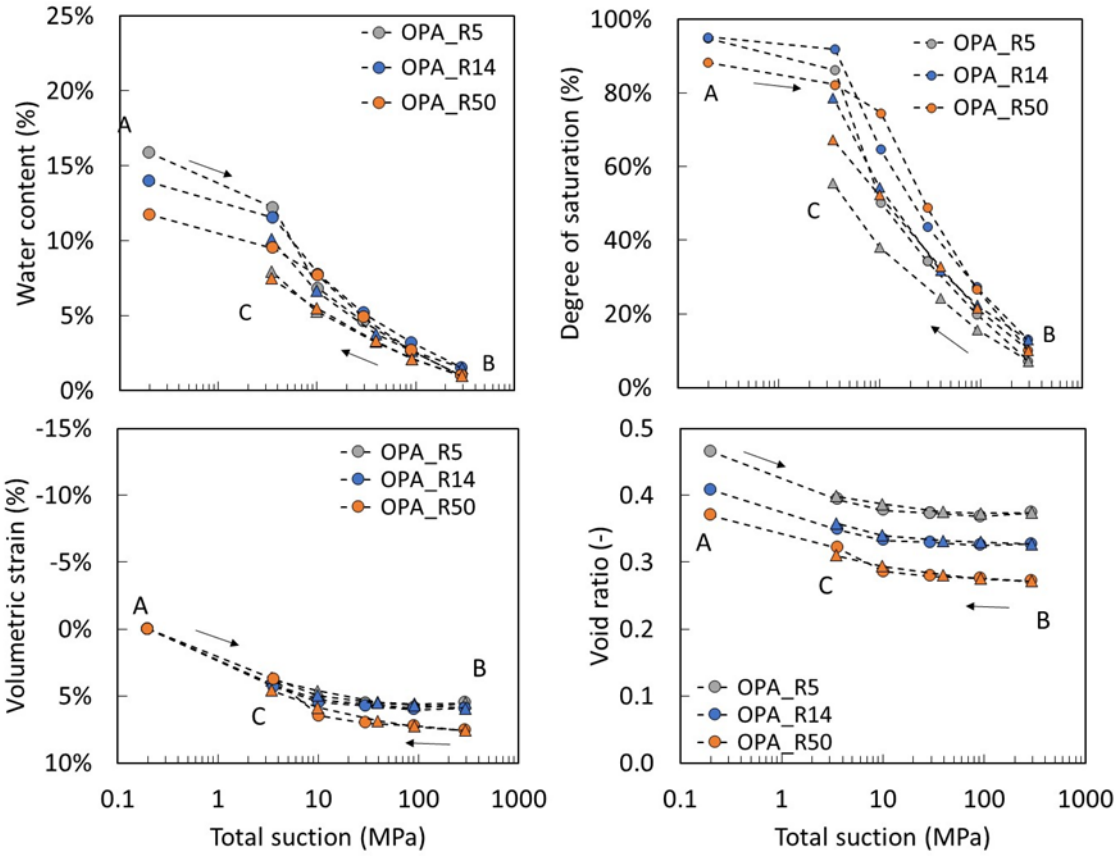

Figure 4-114 – Water retention behaviour of remoulded and recompacted OPA specimens.

4.4.4.2 Injection tests on natural OPA

This section presents the results of laboratory tests performed on natural OPA. It includes the injection tests on specimen OPA_848, as well as the one-dimensional compression results on a twin specimen from the same core that was used to perform a full oedometer test with a vertical stress up to 100 MPa.

Initial resaturation and swelling pressure

During resaturation, the tested specimen was put in contact with water at low pressure (50 kPa). During water uptake, as the specimen had the tendency to swell, vertical total stress was progressively increased to ensure isochoric conditions and minimize damage due to swelling as discussed in section 4.4.3.4. To enhance saturation, the water pressure was increased up to 1 MPa and a differential water pressure was applied between the bottom and the top of the specimen so that water could flow and flush the trapped gas within the pore space. The stress value when equalization conditions were achieved is called the swelling pressure of the tested material; a value of S_p = 3 MPa is obtained consistently on both specimens as shown in Figure 4-76.

One-dimensional compression and water permeability

The one-dimensional compression allowed to assess the relationship between deformation, expressed in terms of void ratio, and the applied stress. Additionally, the water permeability was computed from the one-dimensional consolidation theory for shales (Ferrari et al., 2016). Figure 4-76 shows the compaction of the specimens up to the target vertical effective stress (σ'_v = 14 MPa) and the full

compression curve on Opalinus Clay on the same core as OPA_848. Results suggest a stiffer response of the specimen used in the injection tests. Furthermore, it can be observed that the state of the specimen used in the injection tests belonged to the normal compression line. Figure 4-77 shows a decrease of the computed water permeability from the consolidation theory (empty dots) with decreasing void ratio. These results are in line with those obtained from the constant head water permeability tests and computed form Darcy's law (filled dots), neglecting the elevation terms:

$$k_w = \frac{dV_w}{dt}\frac{H}{A}\frac{\mu_w}{\Delta u_w} \qquad (4.5.3)$$

where k_w is the water intrinsic permeability, dV_w/dt the water flow across the specimen, H and A are the height and the cross-section of the specimen, respectively, μ_w is the water dynamic viscosity and Δu_w the water pressure difference applied between the bottom and top of the specimen. The water intrinsic permeability was obtained in the range of $2.7 \cdot 10^{-21}$ m^2, and is in agreement with values reported in the literature [e.g., Marschall et al., 2005; Crisci et al., 2019, Minardi et al., 2021].

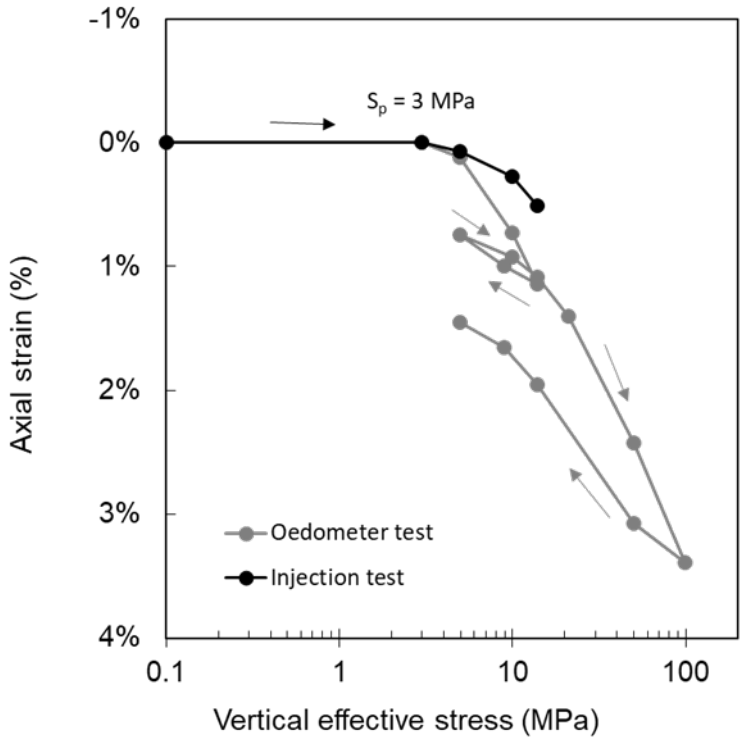

Figure 4-115 – Oedometric compression curve (OPA_848).

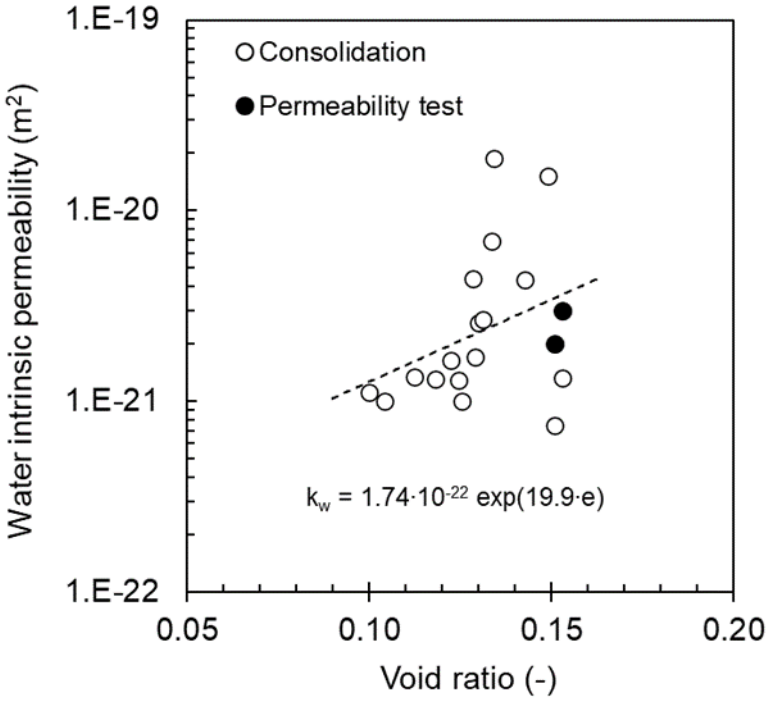

Figure 4-116 – Water intrinsic permeability obtained from constant head permeability tests and from consolidation analyses.

Gas injection test 1 (sequence iv)

As mentioned in section 4.4.3.1, a first gas injection test was performed at a fast gas injection rate with the intention to favour an undrained response of the tested specimen. The controlled boundary conditions, such as vertical stress and fluids pressure/flow rate (gas injection rate and pressure and water back-pressure), as well as the gas pressure decay in constant volume conditions during the shut in are shown in Figure 4-78 (top).

The global axial strain of the specimen computed from the measurement of the vertical deformation, shown in Figure 4-78 (middle), indicates that almost no deformation was observed at the early phase as gas pressure was likely below the gas entry pressure and had not yet invaded the pore space. Once gas reached a pressure of about 5 MPa (t = 17 h), expansion of the specimen was observed, indicating that gas likely entered the pore space, started to displace water and capillary pressure developed. The air entry value was very consistent to the one estimated from the MIP test and supports the above observations.

After t = 17 h, expansion continues as gas pressure continued to increase. Once gas pressure was kept constant at 10 MPa (from t = 30.5 h), expansion continued to slightly increase and reached a value of 0.14%, and was followed by a slow reduction and stabilization at about -0.07% (t = 193 h). As gas pressure decreased during the shut-in phase (t > 193 h), the specimen experienced compression. Gas pressure after shut-in was measured at 5.7 MPa.

Those observations on the mechanical response are consistent with the measured outflow from the specimen. Gas breakthrough, which was assessed from the detection of a significant increase of the outflow, was detected only after the maximum gas pressure was reached. This suggests that gas flow was impaired by the low permeability of the specimen, leading to the delayed observation of gas

breakthrough (t = 50 h). With time, gas outflow was increasing until quasi-steady state conditions were observed at about t = 193 h. The gas outflow at standard temperature and pressure (STP) conditions was about 2·10 9 m^3/s. During the shut-in phase, gas outflow decreased until almost no flow was observed anymore.

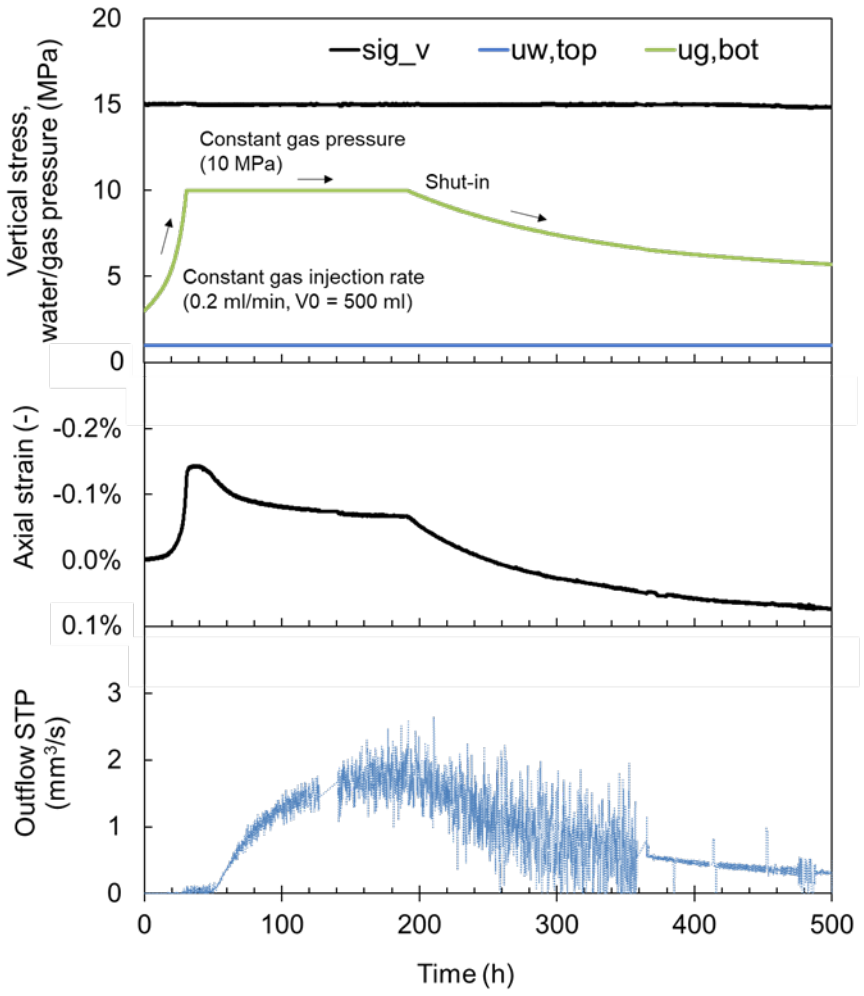

Figure 4-117 – Gas injection test 1 (fast gas injection).

Resaturation after gas invasion (sequence v)

The water resaturation at constant vertical stress has not shown any significant strain upon water uptake (less than 0.01 %). The water intrinsic permeability computed after resaturation was very similar to the one obtained prior to the gas injection (2.1×10^{-21} m^2) and suggests that the permeability of the specimen was not impaired by the gas transport.

Gas injection test 2 (sequence vi)

The second gas injection test was performed at a much slower rate in order to observe the response of the specimen under slower loading conditions.

As shown in Figure 4-79, no excessive expansion of the specimen was observed upon gas injection compared to the fast gas injection test. Rather, the strain evolved in a much stable manner and remained almost constant once the maximum gas pressure was reached (t = 136 h). During the shut-in phase (t > 390 h), the specimen experienced compression as a result of gas pressure decay. Consistent observation was made regarding the measured outflow as gas breakthrough was detected at lower pressure (5 MPa) compared to the first gas injection, and was in line with the estimation from MIP. The gas outflow rate at a late time (t = 390 h) was very similar to what was observed in the first gas injection. As expected, gas outflow decreased during the shut-in phase. Gas pressure after shut-in was measured at 5.4 MPa.

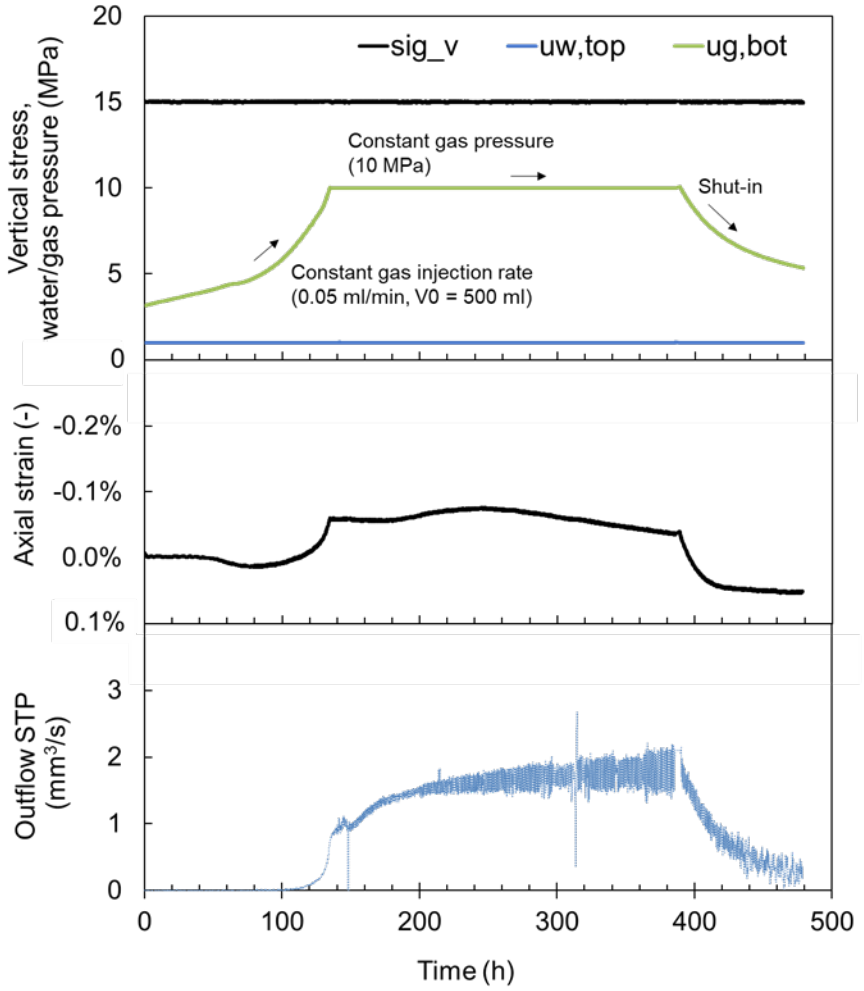

Figure 4-118 – Gas injection test 2 (slow gas injection).

Dismantling and post-mortem analysis (sequence vii)

The tested specimen was finally unloaded and weighted. Half of the specimen was oven-dried (at 105 °C) allowing to compute the final degree of saturation at about 97%, respectively. The high value of the final degree of saturation is consistent with the high retention properties of Opalinus Clay which required a significant capillary pressure to drain the water out of the pore space.

To assess the evolution of the microstructure due to the gas invasion processes, MIP tests was performed on the remaining half of the tested specimen. Figure 4-80 depicts the pore size density (PSD) function of natural OPA before and after gas invasion. The PSD functions are shown without the correction of the conformance effect in order to compare the results on the whole range of the obtained data. The MIP results showed no marked differences in the pore size distribution on specimens tested before and after gas invasion, indicating no significant modification of the microstructure after gas invasion.

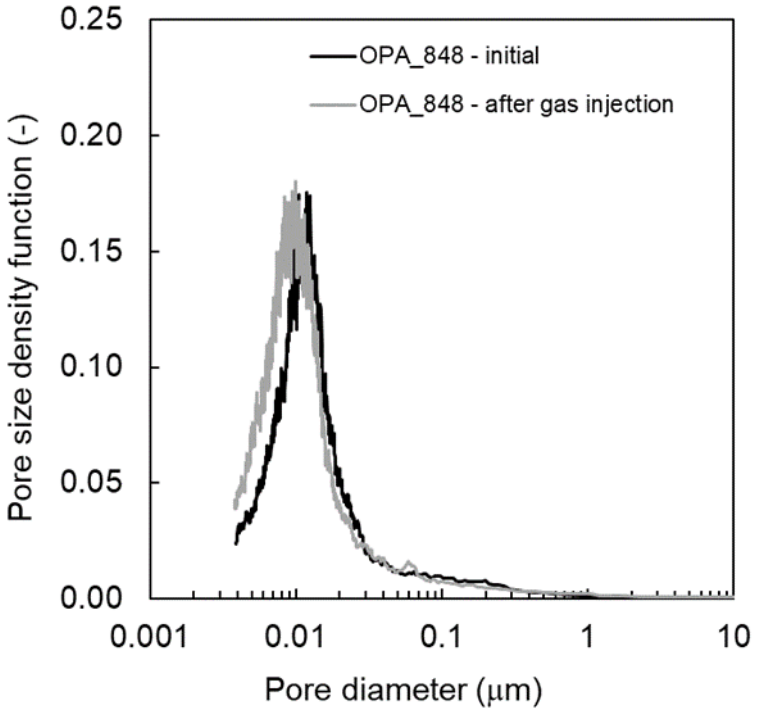

Figure 4-119 – PSD function of natural OPA before and after gas invasion.

Discussion

The mechanical and hydraulic response on slow/fast gas injection exhibit similar characteristics as the gas injection tests by Gonzales-Blanco et al (2022). The interpretation of the results in terms of drained/undrained behaviour is consistent with the general deformation behaviour of clayey geomaterials. In the undrained case with fast gas pressure build-up, it is more likely that gas transfer is associated with larger deformation due to generation of excess porewater pressure during the transient phase. The comparison between the slow and fast gas injection tests suggest that gas-induced porewater displacement is a key feature during gas invasion processes in clay-rich host rock, namely the visco-capillary two-phase flow regime. On the other hand, preliminary quantitative analyses have shown an enhanced gas phase mobility in both tests, suggesting the development of preferential flow paths, leading to greater permeability and measured gas flow that visco-capillary two-phase flow would predict.

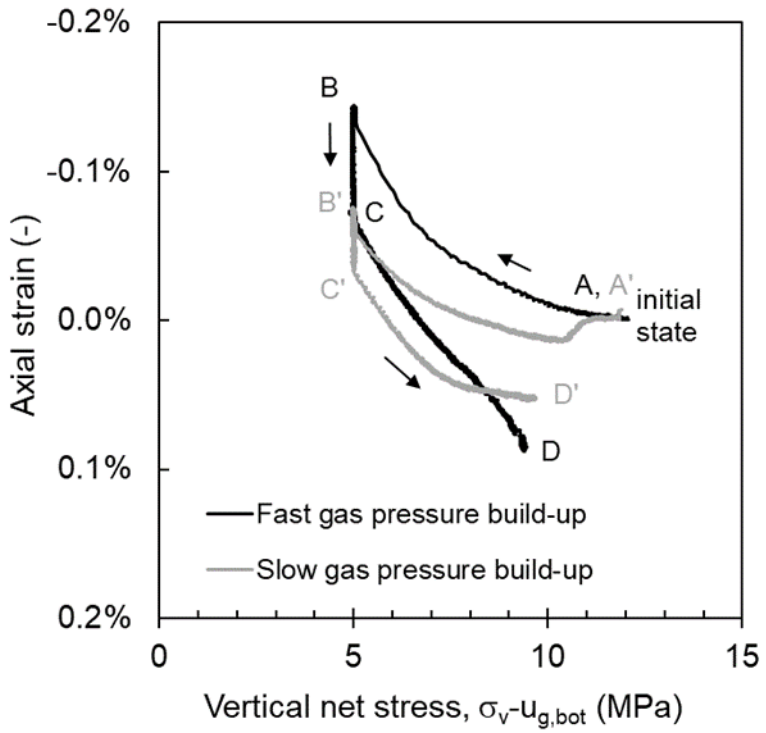

Figure 4-120 – Vertical net stress versus axial strain – Natural OPA.

The generation of excess porewater pressure, due to an undrained response of OPA upon gas invasion, can be further highlighted by analysing the evolution of axial strain as function of vertical net stress expressed as the difference between the applied vertical total stress and the gas pressure at the bottom of the specimen, as depicted in Figure 4-81. In the fast injection test, the specimen showed expansion upon gas build-up pressure (path A-B) in Figure 4-81, and compression at constant gas pressure (B-C). This compression at constant gas pressure indicates that the excess water pressure that built-up during the injection phase is dissipating. Finally, after shut-in, the specimen experienced further compression as a result of gas pressure decay, thus increase in effective stress (C-D). The final compressive strain (point D) could be the result of two phenomena: (i) a higher effective stress as a result of remaining suction within the material and (ii) the applied total stress at the bottom of the specimen increased due to the applied gas pressure. This latter aspect could also explain the observed initial compression during the slow gas injection test (A'-B'). The compression was followed by expansion as gas entered the pore space and reduced the effective stress. As the gas pressure build-up rate was slower, less excess porewater pressure is expected to build-up, therefore, the compression at constant gas pressure is less significant (B'-C') with respect to the fast gas injection test. Finally, after shut-in, the specimen experienced further compression as a result of gas pressure decay (C'-D').

These observations suggest that similar mechanisms control the hydro-mechanical response of OPA during gas invasion processes in both tests, such as porewater displacement by gas and change in effective stress that can induce differential deformation in the porous media and the development of preferential pathways as a consequence. In other words, both mechanisms, namely visco-capillary two-phase flow and dilatancy-controlled gas flow, are relevant and necessary to describe the hydro mechanical response of OPA to gas invasion.

Comparison of the water intrinsic permeability and the PSD function before and after gas invasion suggest no significant differences. Therefore, the present results suggest that the barrier function of the host rock is not impaired by the gas invasion processes.

4.4.4.3 Injection tests on remoulded and recompacted OPA

One-dimensional compression and water permeability

The one-dimensional compression allowed to assess the relationship between deformation, expressed in terms of void ratio, and the applied stress. Additionally, the water permeability was computed from the one-dimensional consolidation theory for shales (Ferrari et al., 2016). Figure 4-82 compares the compaction of remoulded OPA with respect to natural OPA. When the compression behaviour of a remoulded clay is compared to that of the same clay in the natural state, the compression lines display a tendency to become parallel at high vertical stresses as a result of fabric orientation (Burland, 1990). At the maximum effective stress level, the void ratio of the remoulded material is still far from that of the intact OPA leading to the conclusion that the porosity of the natural Opalinus Clay shale is related not only to the mechanical compaction and fabric configuration but also to diagenesis. Consistent results have been observed in the literature (Favero et al., 2016; Crisci et al., 2019). Figure 4-83 highlights a decrease of the computed water permeability from the consolidation theory (empty dots) with decreasing void ratio. Those results are in line with those obtained from the constant head water permeability tests and computed form Darcy's law (filled dots), neglecting the elevation terms:

$$k_w = \frac{dV_w}{dt}\frac{H}{A}\frac{\mu_w}{\Delta u_w} \qquad (4\text{-}4\text{-}4)$$

where k_w is the water intrinsic permeability, dV_w/dt the water flow across the specimen, H and A are the height and the cross-section of the specimen, respectively, μ_w is the water dynamic viscosity and Δu_w the water pressure difference applied between the bottom and top of the specimen. The water intrinsic permeability showed significant decrease upon compaction, and is in agreement with values reported in the literature (Favero et al., 2016). The results were fitted according to an exponential law.

Despite a significantly higher void ratio of the remoulded OPA, permeability values close to natural OPA are observed with increased compaction. Those aspects have been already discussed in Favero et al. (2016), in which the processes associated with diagenesis are likely to reduce the overall porosity of the material and, therefore, the storage capacity, while the permeability would be less affected compared to the porosity.

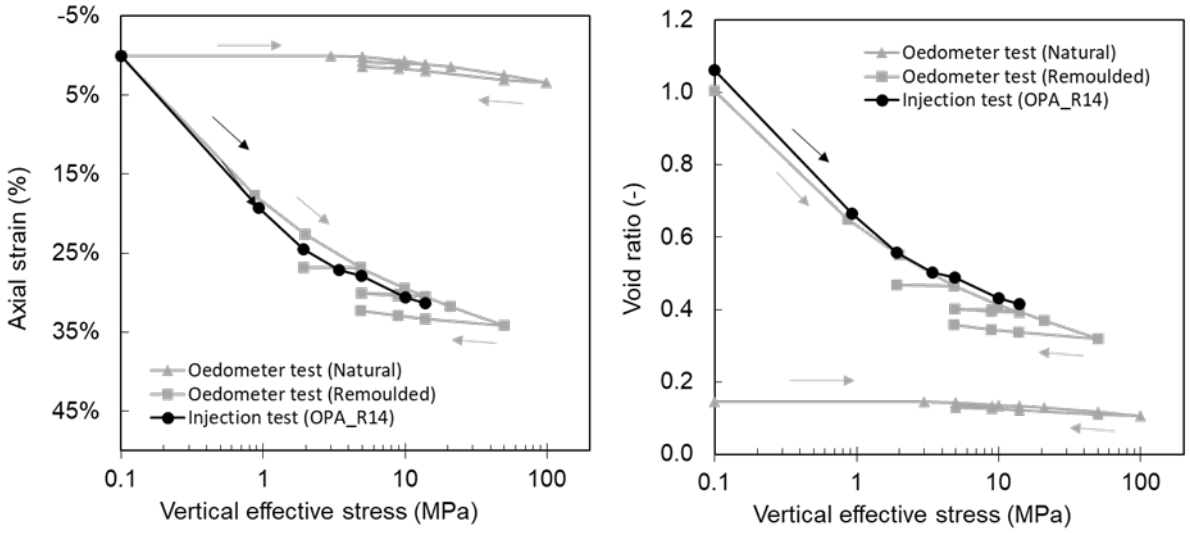

Figure 4-121 – Oedometric compression curves of natural and remoulded OPA: (left) axial strain versus vertical effective stress; (right) void ratio versus vertical effective stress.

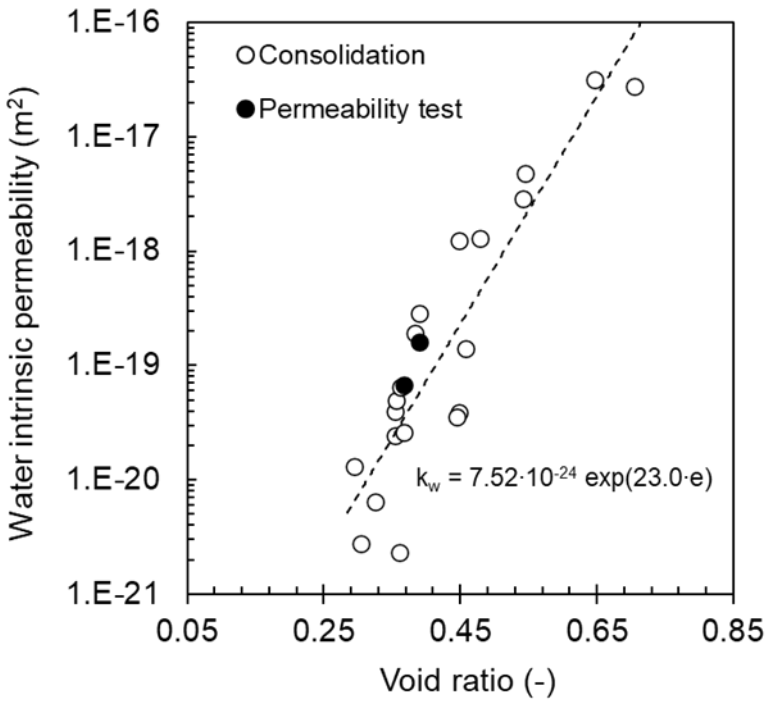

Figure 4-122 – Water intrinsic permeability of remoulded and recompacted OPA obtained from constant head permeability tests and from consolidation analyses.

Gas injection test 1 (1ml/min)

A first gas injection test was performed at a gas injection rate of 1 ml/min (for an initial gas reservoir of 500 ml). The controlled boundary conditions, such as vertical stress and fluids pressure/flow rate (gas injection rate and pressure and water back-pressure), as well as the gas pressure decay in constant volume conditions during the shut-in are shown in Figure 4-84 (top).

The global axial strain of the specimen, computed from the measurement of the vertical deformation, shown in Figure 4-84 (middle), indicates a compression of the material upon gas injection during the first phases of the gas injection. Extension was observed during the last phase of the gas pressure build-up (t = 163 h). As gas pressure decreased during the shut-in phase (t = 174 h), the specimen experienced further compression. Gas pressure after shut-in was measured at 3.75 MPa. Additional investigations are required to fully understand these results, but preliminary considerations suggest that gas pressure induced an increase in the applied total stress.

Regarding the measured flow, little outflow (0.3 mm^3/s at STP conditions) was detected in the first phase ($u_{g,bot}$ = 5.8 MPa). It is not clear whether this was mainly as a result of gas diffusion or advection. A significant increase of the gas outflow was detected once gas pressure reached 6.5 MPa (t = 73 h). At constant gas pressure ($u_{g,bot}$ = 7.5 MPa), the outflow further increased until reaching steady-state conditions (45 mm^3/s in STP conditions). A further increase in gas pressure (10 MPa) led to unsustainable gas outflow (250 mm^3/s in STP conditions). During the shut-in phase, gas outflow decreased until almost no flow was observed anymore.

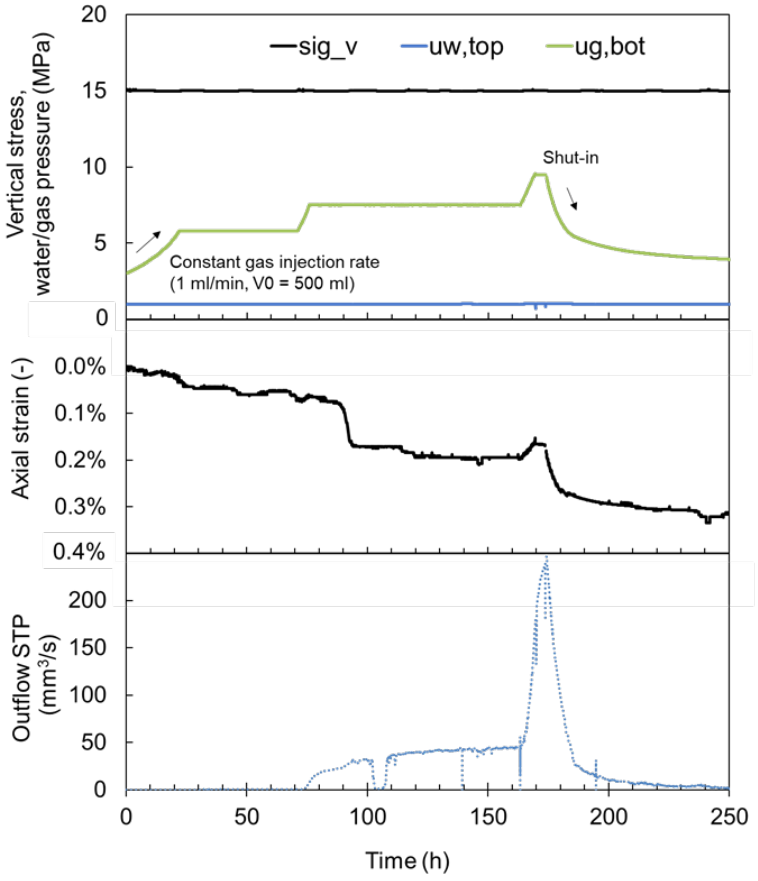

Figure 4-123 – Gas injection test 1 (1 ml/min).

Resaturation after gas invasion

During the water resaturation at constant vertical stress the specimen experienced slight compression strain (0.26%) which was most probably the result of creeping phenomena. The water intrinsic permeability computed after resaturation was slightly lower than the initial one ($4 \cdot 10^{-20}$ m^2) which is consistent with the measured compressive strain of the specimen during the gas injection phase.

Gas injection test 2 (10 ml/min)

The second gas injection test was performed at a much faster rate in order to observe the response of the specimen under faster loading conditions.

As shown in Figure 4-85, gas pressure was increased quickly from 3 to 7.5 MPa. This let to swelling of the material, followed by a slight compression. These results are consistent with the fast gas injection test on natural OPA, and indicates the generation of excess porewater pressure in the transient phase. However, these processes occurred at a faster rate with remoulded OPA due to the higher permeability of the specimen. During the shut-in phase (t > 145 h), the specimen experienced compression as a result of gas pressure decay. Regarding the outflow, breakthrough was detected after maximum gas pressure was reached. Once steady-state conditions were achieved, measured gas outflow was significantly lower than in the previous gas injection (8.5 mm^3/min, instead of 45 mm^3/s in STP conditions at $u_{g,bot}$ = 7.5 MPa). Gas pressure after shut-in was measured at 3.5 MPa.

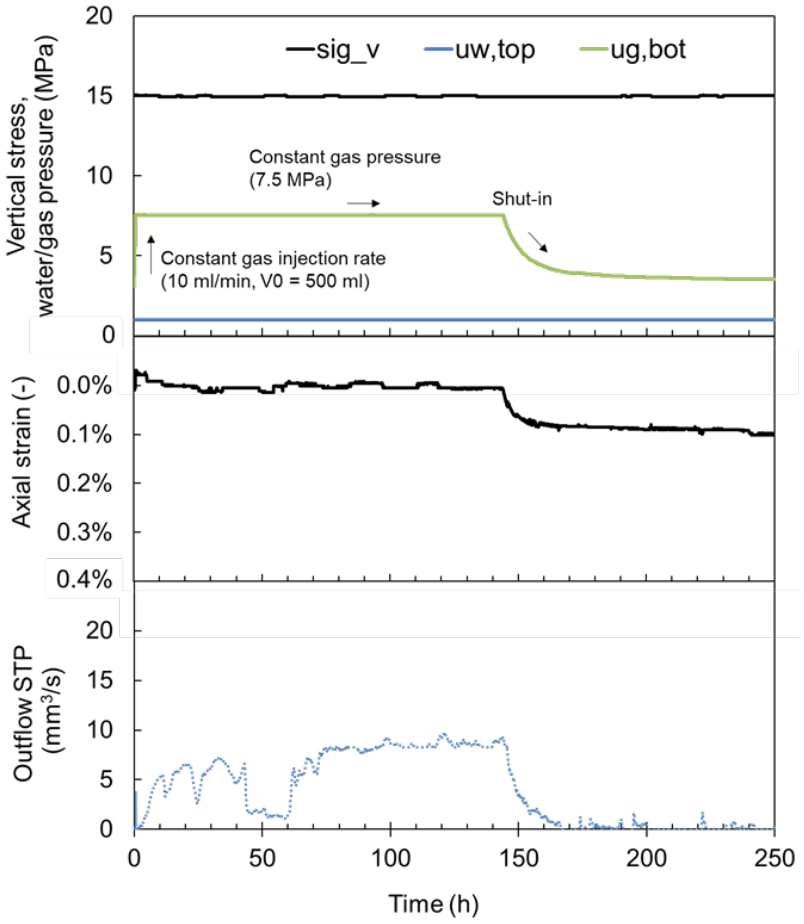

Figure 4-124 – Gas injection test 2 (10 ml/min).

Dismantling and post-mortem analysis (sequence vii)

The tested specimen was finally unloaded, weighted and oven-dried (at 105 °C) allowing to compute the final degree of saturation at about 88%. The high value of the final degree of saturation is consistent with the high retention properties of remoulded Opalinus Clay presented in section 4.4.4.1.

Discussion

The mechanical and hydraulic response on remoulded OPA subjected to gas injection suggests that the gas injection process induced an increase in the applied total stress on the specimen. As a result, compression and decrease of permeability was observed. Further investigation is required to better understand these results. This behaviour can be further observed in Figure 4-86, which depicts the evolution of the axial strain as a function of the vertical net stress expressed as the difference between the applied vertical total stress and the gas pressure at the bottom of the specimen. During the first gas injection test (rate of 1 ml/min), the specimen experienced significant compression. During the second gas injection test (rate of 10 ml/min), slight expansion was measured (A'-B'), followed by compression (B'-C'), indicating the dissipation of the excess water pressure that built-up during the injection phase. Further compression was observed during the shut-in phase (C'-D').

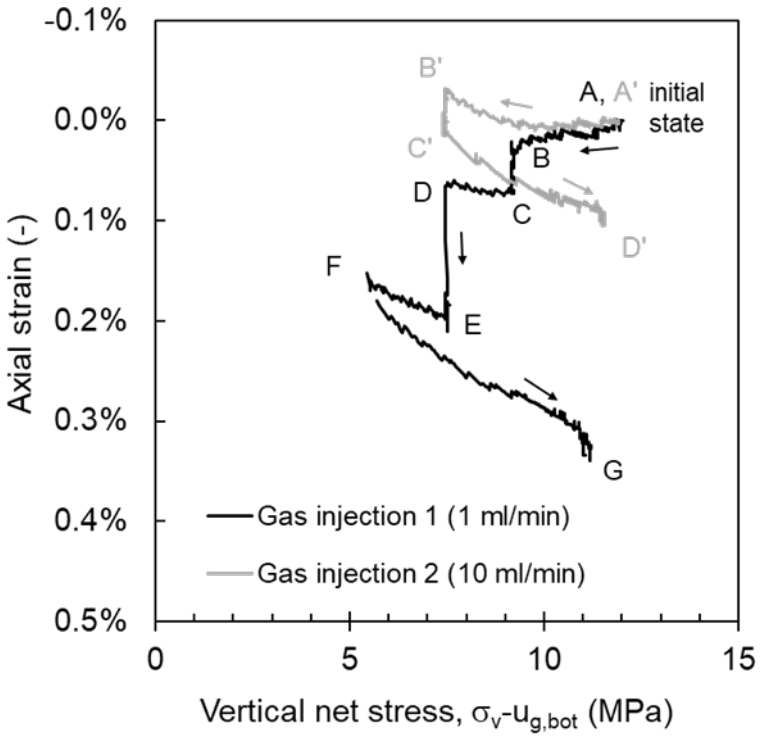

Figure 4-125 – Vertical net stress versus axial strain – Remoulded and recompacted OPA.

4.4.5 Summary

This report presented the experimental campaign performed on natural and remoulded and recompacted OPA in order to characterise three major aspects in the context of EURAD-GAS, namely (i) the phenomena and processes related to the initiation and propagation of rock failure in response to gas pressure build-up, (ii) the characterization of gas transport processes in remoulded and recompacted OPA, mimicking the gas transport behaviour of fault gouge material and (iii) the phenomena and processes that contribute to the self-sealing of OPA after gas invasion.

The experimental work used a high-pressure oedometer cell specifically developed to analyse the hydro mechanical behaviour of geomaterials at high-confining stresses. The apparatus allowed to apply a vertical stress up to 100 MPa, to inject fluids (water, gas) from both sides of the specimen (top and bottom) to a pressure up to 20 MPa for gas, and 16 MPa for water. The assessment of the vertical deformation was done using three LVDTs. When considering laboratory testing of shales, rigorous experimental procedure and test set-up is required due to its low permeability and porosity, high water retention properties, as well as the dependency of the material's behaviour on the saturation state. In this regard, a systematic procedure was adopted to obtain intact specimens for the injection tests.

Regarding the water retention properties of both natural and remoulded and recompacted OPA, a coupling between water content and strains was observed. Remoulded and recompacted OPA showed an isotropic and reversible behaviour upon suction changes, while natural OPA was characterised by an anisotropic and irreversible behaviour. Larger deformation was observed in the axial direction, as a results of opening/closure of the bedding planes and irreversible strain was accumulated upon wetting.

The interpretation of the gas injection results in terms of drained/undrained behaviour is consistent with the general deformation behaviour of clayey geomaterials. In the undrained case with fast gas pressure build-up, it is more likely that gas transfer is associated with larger deformation due to generation of excess porewater pressure during the transient phase. The comparison between the slow and fast gas injection tests suggest that gas-induced porewater displacement is a key feature during gas invasion processes in clay-rich host rock, namely the visco-capillary two-phase flow regime. On the other hand, preliminary quantitative analyses have shown an enhanced gas phase mobility in both tests, suggesting the development of preferential flow paths, leading to greater permeability and measured gas flow that visco-capillary two-phase flow would predict. Those observations suggest that similar mechanisms control the hydro-mechanical response of OPA during gas invasion processes in both tests, such as porewater displacement by gas and change in effective stress that can induce differential deformation in the porous media and the development of preferential pathways as a consequence. In other words, the results suggest that both mechanisms, namely visco-capillary two-phase flow and dilatancy-controlled gas flow, are relevant and necessary to describe the hydro mechanical response of OPA to gas invasion. This interpretation is mainly based on indirect observations, and more research is required to further understand the involved processes. An experimental configuration with distributed strain measurement is currently in development in our group. This technique, allowing for more than 1'000 strain measurements points, is aimed to fully couple the gas/water migration with strain evolution in time and space, to detect strain localization and/or micro-fissures and to pose a robust foundation for model development and calibration.

Comparison of the water intrinsic permeability and the PSD function before and after gas invasion of natural OPA suggest no significant differences. Therefore, the results suggest that the barrier function of the host rock is not impaired by the gas invasion processes.

4.4.6 Key learning points

4.4.6.1 New knowledge acquired

When considering laboratory testing of shales, rigorous experimental procedure and test set-up is required due to its low permeability and porosity, high water retention properties, as well as the dependency of the material's behaviour on the saturation state. In this regard, a systematic procedure was developed and adopted to obtain as closely as possible intact specimens for the injection tests.

The impact of both porosity and fabric configuration on the water retention properties of OPA was presented.

The interpretation of the gas injection results in terms of drained/undrained behaviour is consistent with the general deformation behaviour of clayey geomaterials. The gas injection tests suggest that gas induced porewater displacement is a key feature during gas invasion processes in clay-rich host rock.

Comparison of the water intrinsic permeability and the PSD function before and after the gas injection tests suggest no significant differences. Therefore, the present results suggest that the barrier function of the host rock is not impaired by the gas invasion processes.

4.4.6.2 Impact of acquired knowledge

A well-defined experimental procedure is a key aspect when considering hydro-mechanical testing of shales, especially for the gas injection tests. The developed knowledge can serve as a base on the design of future experiments.

Acquired knowledge on the water retention properties of both natural and remoulded and recompacted OPA allowed to determine the constitutive relationships of those material when subject to wetting and drying processes. This will help to further understand the role of the material variability on the water retention properties at the repository and how this may impact the barrier function of the host rock in the long term.

The interpretation of the hydro-mechanical response of OPA upon gas injection allowed to identify the occurrence and the relevance of visco-capillary two-phase flow as well as dilatancy-controlled gas flow. The acquired knowledge will help on the development of comprehensive conceptualization of the gas transport processes as well as of accurate numerical models to safely design the repository concept.

Lastly, the results suggest that the long-term barrier function of the host rock is not impaired by the gas invasion processes.

4.4.6.3 Remaining knowledge gaps

To better understand the impact of wetting and drying cycles on the host rock barrier function, further investigation is required on the evolution of the fluid transport properties upon wetting and drying processes.

Identification of the role of the microstructure and the stress history on the gas transport properties of remoulded and recompacted OPA is required to better understand the role of fault gouge material on the repository.

To increase the confidence on the repository concept, further configurations (gas injection test in triaxial configuration) have to be tested to address the conditions which may favour gas-induced failure of natural OPA .

4.4.6.4 Recommendations for the future

Given the low permeability and porosity, high water retention properties, and the dependence of material behavior on saturation state, shale testing requires comprehensive experimental procedures and setups. To achieve this, a systematic approach must be developed and implemented for a thorough characterization of relevant properties related to gas transport in these materials. This includes the characterization of water retention properties, stress-strain relationship, and permeability of the material, coupled with a well-designed and controlled hydro-mechanical path before gas injection, ensuring the quality of the tested specimens.

Moreover, the observed disparities in experimental results among different teams underscore the need for an experimental benchmark exercise to identify and gain a deeper understanding of the origins of these differences, ultimately establishing fundamental requirements for the gas testing of clay-rich materials.

4.4.7 References

Ammen, M., Palten, P.-J., (2021). TBO Trüllikon-1-1: Drilling. Nagra, NAB 20 09.

Aschwanden, L., Camesi, L., Gimmi, T., Jenni, A., Kiczka, M., Mäder, U., Mazurek, M., Rufer, D., Waber, H.N., Wersin, P., Zwahlen, C., and Traber D., (2021). TBO Trüllikon-1-1: Rock Properties, Porewater Characterisation and Natural Tracer Profiles. Nagra, NAB 20 09.

Bishop, A.W., 1959. The principle of effective stress. Tecnisk Ukeblad 39, 869–863.

Burland, J.B., 1990. On the compressibility and shear strength of natural clays. Géotechnique 40, 329–378.

Cardoso, R., Romero, E., Lima, A., and Ferrari, A., (2007). A comparative study of soil suction measurement using two different high range psychrometers. In: Experimental unsaturated soil mechanics. Springer Berlin Heidelberg, pp. 79-93.

Comisky JT, Santiago M, McCollom B, Buddhala A, Newsham KE. (2011) Sample size effects on the application of mercury injection capillary pressure for determining the storage capacity of tight gas and oil shales. In Canadian unconventional resources conference. Society of Petroleum Engineers.

Crisci, E., Ferrari A., Giger S. B. and Laloui, L., (2019). Hydro-mechanical behaviour of shallow Opalinus Clay shale. Engineering Geology (251), pp.214-227

Delage, P., Audiguier, M., Cui, Y.-J., & Howat, M. D. (1996). Microstructure of a compacted silt. In Canadian Geotechnical Journal (Vol. 33, Issue 1, pp. 150–158). Canadian Science Publishing.

Favero, V., Ferrari, A. and Laloui, L. On the hydro-mechanical behaviour of remoulded and natural Opalinus Clay shale. Engineering Geology (2016) 208: 128-135.

Ferrari, A. and Laloui, L. (2013). Advances in the testing of the hydro-mechanical behaviour of shales. In: Multiphysical Testing of Soils and Shales, Springer: 57-68.

Ferrari, A., Favero, V. and Laloui, L. (2016) One-dimensional compression and consolidation of shales. International Journal of Rock Mechanics and Mining Sciences 88: 286-300.

Fredlund, D.G., Rahardjo, H., 1993. Frontmatter, in: Soil Mechanics for Unsaturated Soils. John Wiley & Sons, Inc., pp. i–xxiv.

Leong, E.-C., Tripathy, S., Rahardjo, H., 2003. Total suction measurement of unsaturated soils with a device using the chilled-mirror dew-point technique. Géotechnique 53, 173–182.

Llabjani Q., Ferrari A., Laloui L. (2021). Basic characterisation of the Opalinus Clay shale from the deep borehole of Trüllikon (ZH-CH). EURAD deliverables.

Marschall P, Gimmi T, Horseman S, et al (2005) Characterisation of Gas Transport Properties of the Opalinus Clay. Sci Technol 60:121–139

Minardi, A., Ferrari, A., Ewy, R., Laloui, L., 2018. Nonlinear Elastic Response of Partially Saturated Gas Shales in Uniaxial Compression. Rock Mech Rock Eng 51, 1967–1978.

Minardi A., Stavropoulou E., Kim T., Ferrari A. and Laloui L., 2021. Experimental assessment of the hydro-mechanical behaviour of a shale caprock during CO2 injection. International Journal of Greenhouse Gas Control. 106. 103225.

Minardi A., (2018). Hydro-mechanical characterization of gas shales and Opalinus Clay shale in partially saturated conditions. PhD Thesis No. 8315, École Polytechnique Fédérale de Lausanne, Switzerland.

Romero, E. and Simms, P.H., (2008). Microstructure investigation in unsaturated soils: a review with special attention to contribution of mercury intrusion porosimetry and environmental scanning electron microscopy. In Laboratory and Field Testing of Unsaturated Soils (pp. 93-115). Springer Netherlands.

Skempton, A., (1953). The colloidal activity of clays. Selected Papers on Soil Mechanics, pp.106-118.

Van Genuchten, M.T.: A closed-form equation for predicting the hydraulic conductivity of unsaturated soils. Soil Sci. Soc. Am. J. 44, 892–898 (1980).

Wild, K.M., Wymann, L.P., Zimmer, S., Thoeny, R., Amann, F., 2015. Water Retention Characteristics and State-Dependent Mechanical and Petro-Physical Properties of a Clay Shale. Rock Mechanics and Rock Engineering 48, 427–439. https://doi.org/10.1007/s00603-014- 0565-1

4.5 Hydromechanical response of claystones on gas injections (CIMNE)

The European Joint Programme on Radioactive Waste Management (EURAD) was implemented as part of the EU Research and Innovation Programme Horizon 2020 (EURAD, 2019). The work package EURAD-WP 6 – GAS ("Mechanistic understanding of gas transport in clay materials") aimed at (i) improving the mechanistic understanding of gas transport processes in natural and engineered clay materials; (ii) evaluating the gas transport regimes that can be active at the scale of a geological disposal system and their potential impact on barrier integrity and repository performance. Within this WP, the CIMNE group (International Centre for Numerical Methods in Engineering) is participating in Task 3 ("Barrier Integrity") whose purpose is to gain a mechanistic understanding of the hydro-mechanical phenomena and processes, associated with:

- Gas-induced failure of clay barriers, including the engineered barrier system, the EDZ and the argillaceous host rock.
- Effectiveness of self-sealing processes along gas-induced pathways in the clay barriers of a geological repository.

Task 3 is divided into three sub-tasks, Sub-Task 3.1 and Sub-Task 3.2 devoted to experimental research, while Sub-Task 3.3 is dedicated to numerical simulations. CIMNE is involved in the first two performing the laboratory work in the Geotechnical Lab of UPC (Universitat Politècnica de Catalunya).

4.5.1 Experimental set-up

Two different apparatus were used during the project to perform gas tests. The first was an oedometer cell that was available in the Geotechnical Laboratory of UPC, while the second one was specifically designed and built for this project.

4.5.1.1 Description of apparatus

High-capacity oedometer cell

This cell was developed for previous research in gas migration in Boom Clay (Gonzalez-Blanco et al., 2016; Gonzalez-Blanco, 2017) and was updated for this project. The apparatus is an unconventional oedometer cell that along with the boundary condition controllers and the data acquisition system forms the set-up illustrated in Figure 4-87.

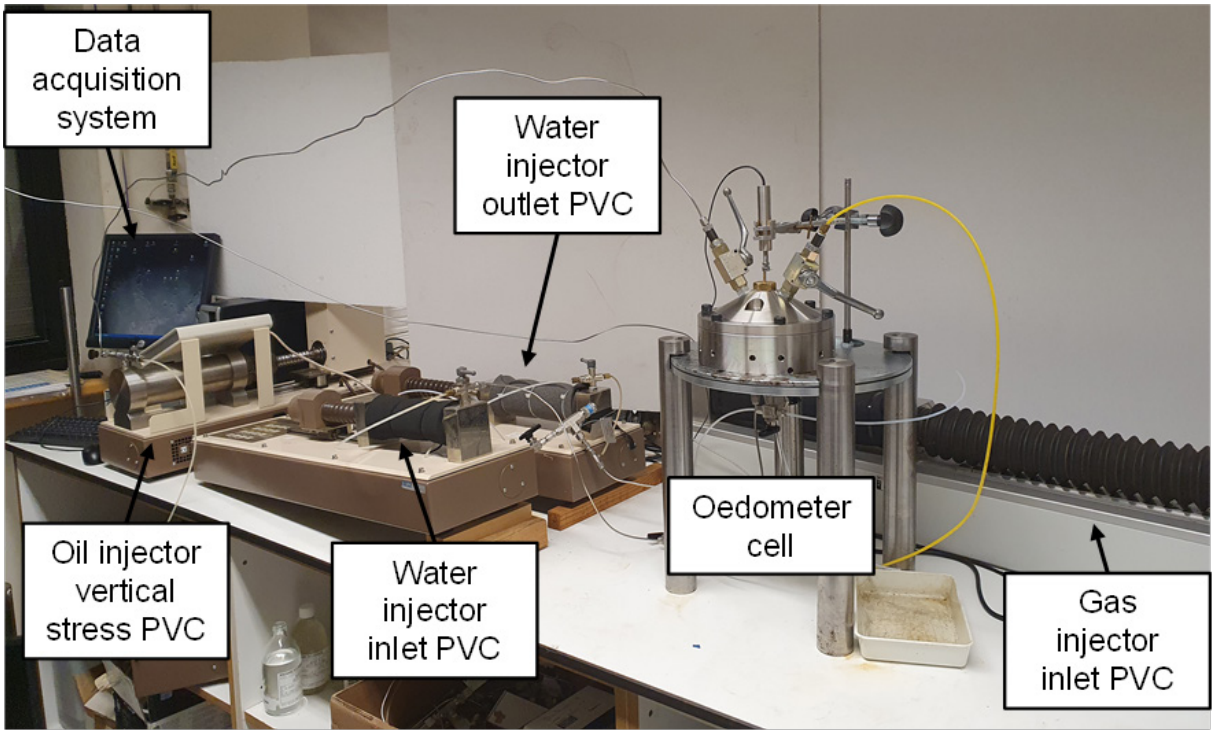

Figure 4-126 – Set-up of the oedometer.

The soil samples (height of 20 mm in a 50 mm diameter ring) are placed between the top and bottom caps made of concentric stainless-steel rings (number 2 in Figure 4-88), which operate as coarse porous stones allowing the injection and recovery, as well as the proper distribution of the injected fluids (water and gas). At both boundaries of the sample, there are two connections for flushing the fluids contained in the porous stone, when needed. The bottom boundary corresponds to upstream while the top to downstream. A pneumatic axial loading piston (blocking system – number 3 in Figure 4-88), which supports a vertical stress capacity of more than 20 MPa, is used to apply the vertical load.

Silicone oil (WACKER AK5) was chosen to apply vertical load through an automatic pressure/volume controller (PVC) from GDS Instruments. This controller (number 4 in Figure 4-88) has a maximum range of 64 MPa (volume 1000 ml) with a resolution of 16 kPa and 0.01 ml (pressure and volume accuracy were 0.10% and 0.20% respectively). It is connected to the axial piston with a high-strength steel tube to ensure proper transmission of the load and to prevent leakages.

The equipment uses three additional automatic PVCs, two for water (injection and recovery at the downstream point), and one for gas (injection at the upstream point). PVCs can be used in combination (for example, gas injection and water pressure at downstream or water pressure at both sides). The gas injector PVC from Wille Geotechnik (number 5a in Figure 4-88) has a maximum range of 20 MPa (volume 500 ml) and can control volume rates between 10^{-4} ml/min and 100 ml/min (volume resolution 1 mm^3) (pressure and volume accuracy were 0.15% and 0.20% respectively). It is connected to a compressed gas cylinder to achieve high pressures. The other two controllers (numbers 5b and 6 in Figure 4-88) are from GDS Instruments, with a maximum range of 2 MPa (volume 200 ml) and a resolution of 1 kPa (1 mm^3) (pressure and volume accuracy were 0.15% and 0.25% respectively). The controller located downstream is protected with a safety valve. All these controllers have volume change gauges for the precise regulation and measurement of fluid pressure and volume changes.

Vertical displacements are measured with a calibrated external linear variable differential transformer (LVDT) from Solartron Metrology with a range of measurement of ±0.5 mm and a resolution of 0.001 mm (number 7 in Figure 4-88).

The data acquisition software was developed in Visual Basic (Microsoft) to monitor the pressures and volumes of controllers and the vertical displacements using an electronic box with a National Instrument Card.

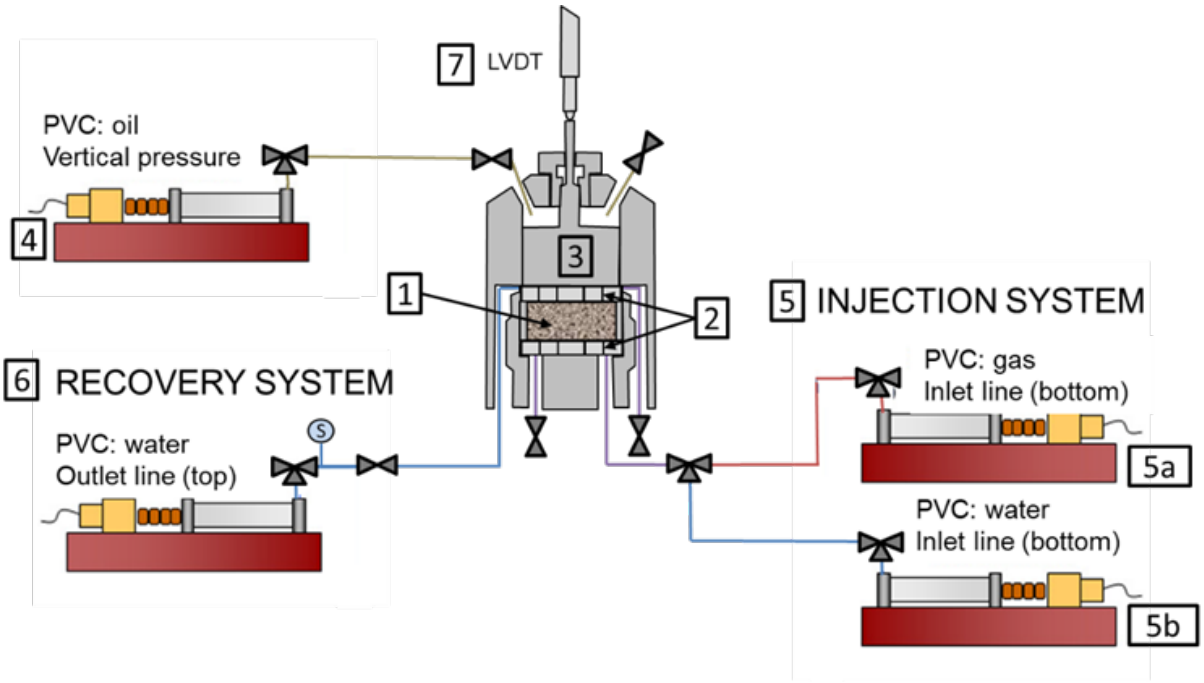

Figure 4-127 – Scheme of oedometer setup: 1) Sample; 2) Coarse porous rings; 3) Hydraulic piston; 4) Oil PVC; 5) Injection system: a) water PVC, b) air PVC; 6) Recovery system: water PVC; 7) LVDT.

Oedometer cell with lateral stress measurements

A new apparatus was designed and built to evaluate the gas migration processes. It has a double modality and can work as an oedometer cell or an isochoric cell, thanks to a blocking system of the pneumatic piston with a load cell, although during this work, oedometer conditions were used. Moreover, the equipment includes a deformable ring that allows the estimation of the radial stresses through the measurement of the radial displacement.

The instrumentation of the set-up has been greatly improved with respect to the high-capacity oedometer cell described above. It includes a pore-pressure transducer, a gas trap system and several sensors to maximise the recorded information during the tests. Figure 4-89 shows the complete setup.

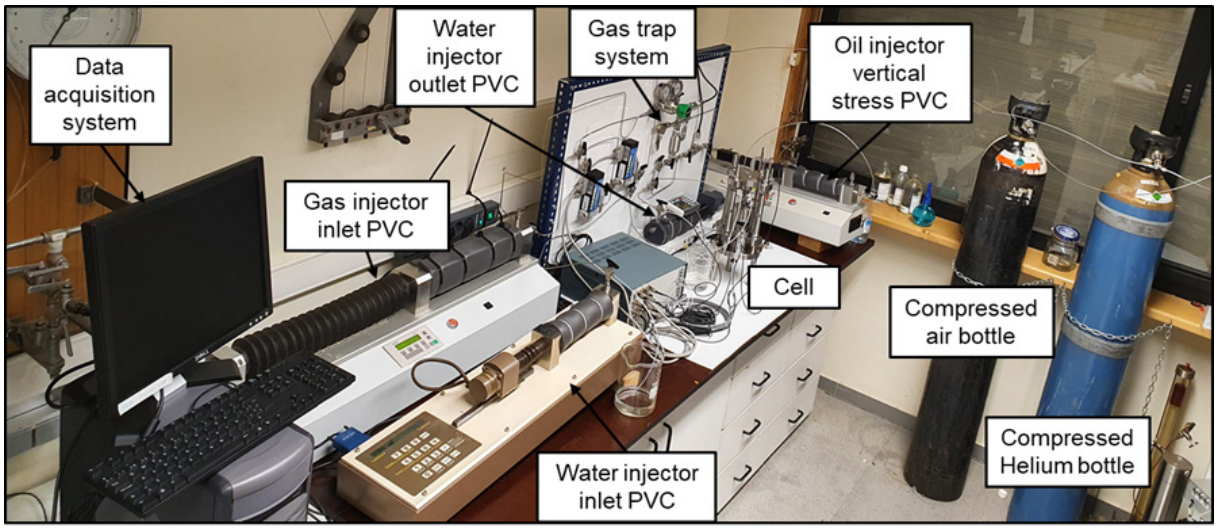

Figure 4-128 – Set-up of the new oedometer / isochoric cell.

The sample (height of 25 mm in a 50 mm diameter ring) (number 1 in Figure 4-90) is placed in the oedometer ring (number 2 in Figure 4-90) between the top and bottom caps made of concentric stainless-steel discs acting as porous stones (number 3 in Figure 4-90), which are placed together with a fluid distributor to properly distribute the injected fluids (water and gas). At the bottom cap, the three connections are standing at 120º-angle which improves the flushing of the fluids contained in the porous stones when it is needed. The bottom cap also hosted a small sintered stainless-steel disc (8 mm in diameter and 2 mm in height) acting as a separator thanks to an O-ring to isolate the chamber where a pore-pressure transducer is located (bottom of the sample) (number 4 in Figure 4-90). The top cap counts with two connections at 180º-angle (number 5 in Figure 4-90).

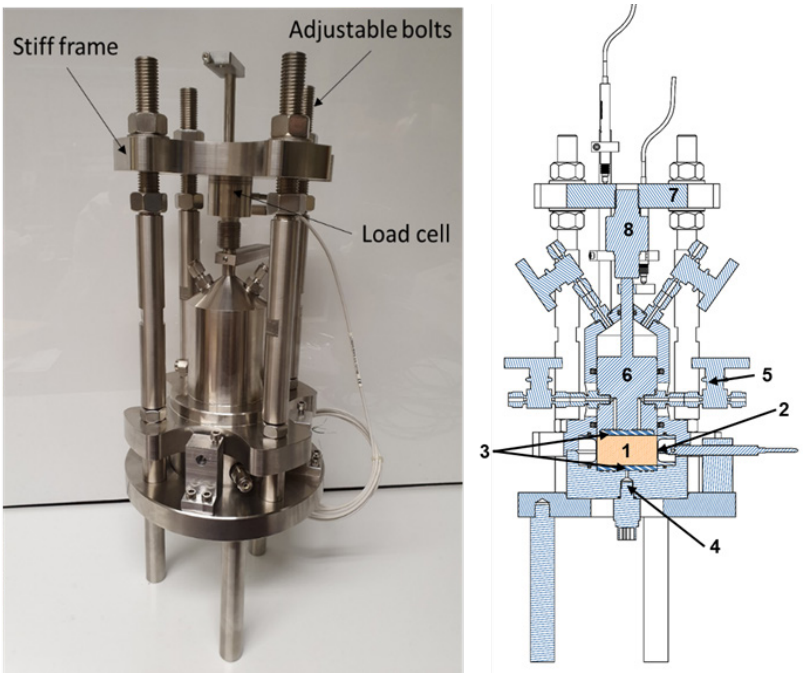

Figure 4-129 – Schematic of the cell: 1) sample; 2) oedometer ring; 3) concentric stainless-steel discs; 4) pore-pressure transducer; 5).valves; 6) piston; 7) frame; 8) load cell.

The ring was designed to be slightly deformable without losing the K_o-condition in order to measure the radial displacements and estimate the lateral stresses (Figure 4-91). It has a U-profile with a very thin central part (t = 0.5 mm; ϕ = 50 mm; H = 25 mm) allowing the deformation. The calculation of ring deformation was carried out with the finite element software PTC Creo Parametric (3.0) using materials properties of the steel SS304 and Boom Clay. The worst scenario of the simulations gave a maximum lateral displacement of 35 µm, which constitutes 0.14% of lateral deformation. This implies some small loss of K_o-condition, although between values of 0.02% and 0.15% are considered for semi-rigid systems.

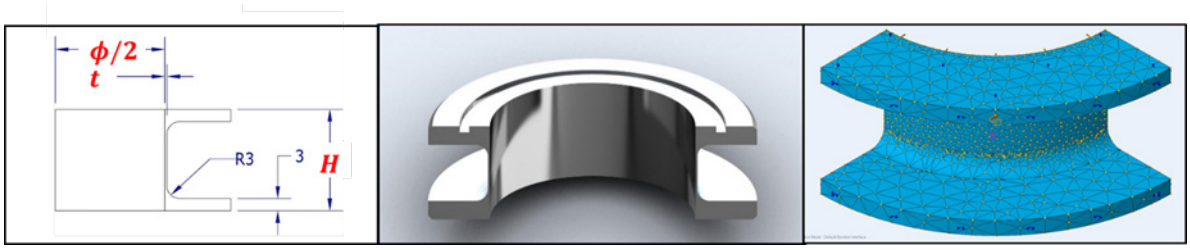

Figure 4-130 – Deformable ring size (left), 3D section (middle) and 3D element mesh (right).

The cell was designed for maximum vertical and lateral stress of 8 MPa that is applied through a pneumatic piston (number 6 in Figure 4-90), which allows a maximum vertical displacement of ±5.74 mm from its neutral position, which implies a maximum deformation of the sample of 23%.

The piston can be blocked by a stiff frame (number 7 in Figure 4-90) that includes a load cell (number 8 in Figure 4-90), enabling the possibility of working at constant volume conditions, either since the beginning of the experiment or at a given stress stage. In the latter case, the tightening of the bolts allows achieving the stress level previously imposed by the PVC and then it will be measured with the load cell (Figure 4-90).

The set-up includes several devices to increase the recorded information during the tests. Figure 4-92 shows a simplified scheme of the set-up under oedometer conditions. The blue lines in the figures are those that transport water, red lines correspond to gas flow and purple means that can transport both fluids mixed or separated.

Silicone oil (WACKER AK5) was chosen to apply vertical load through an automatic pressure/volume controller (PVC) from Wille Geotechnik. This controller (number 1 in Figure 4-92) has a maximum range of 10 MPa (volume 250 ml) with a resolution of 0.1 kPa and 0.05 ml (pressure and volume accuracy were 0.15% and 0.20% respectively). It is connected to the axial piston with a high-strength steel tube to ensure proper transmission of the load and to prevent leakages.

The equipment uses three other automatic PVCs, two for water (injection and recovery at the downstream point), and one for gas (injection at the upstream point), which can be used in combination (for example, air injection and water pressure at downstream or water pressure at both sides). The gas injector PVC from Wille Geotechnik (number 2 in Figure 4-92) has a maximum range of 20 MPa (volume 500 ml) and can control volume rates between 10^{-4} ml/min and 100 ml/min (volume resolution 1 mm^3). It is connected to a compressed gas cylinder to achieve high pressures (number 3 in Figure 4-92). The other two controllers (numbers 4 and 5 in Figure 4-92) are from GDS Instruments, with a maximum range of 2 MPa and 4 MPa respectively (volume 200 ml) and a resolution of 1 kPa (1 mm^3) (pressure and volume accuracy were 0.15% and 0.25% respectively). All of these controllers have volume change gauges for the precise regulation and measurement of fluid pressure and volume changes.

A flush diaphragm pressure transducer from Honeywell is placed at the bottom of the cell just below the small porous stone to work as a pore-pressure transducer (number 6 in Figure 4-92). The dead volume between the sample and the transducer was minimized as much as possible. Its pressure range was between 0 and 5.2 MPa, with an accuracy of 0.5% of the full scale, which means a resolution of 26 kPa. The porous stone linked to the transducer is placed 2 mm inside the sample.

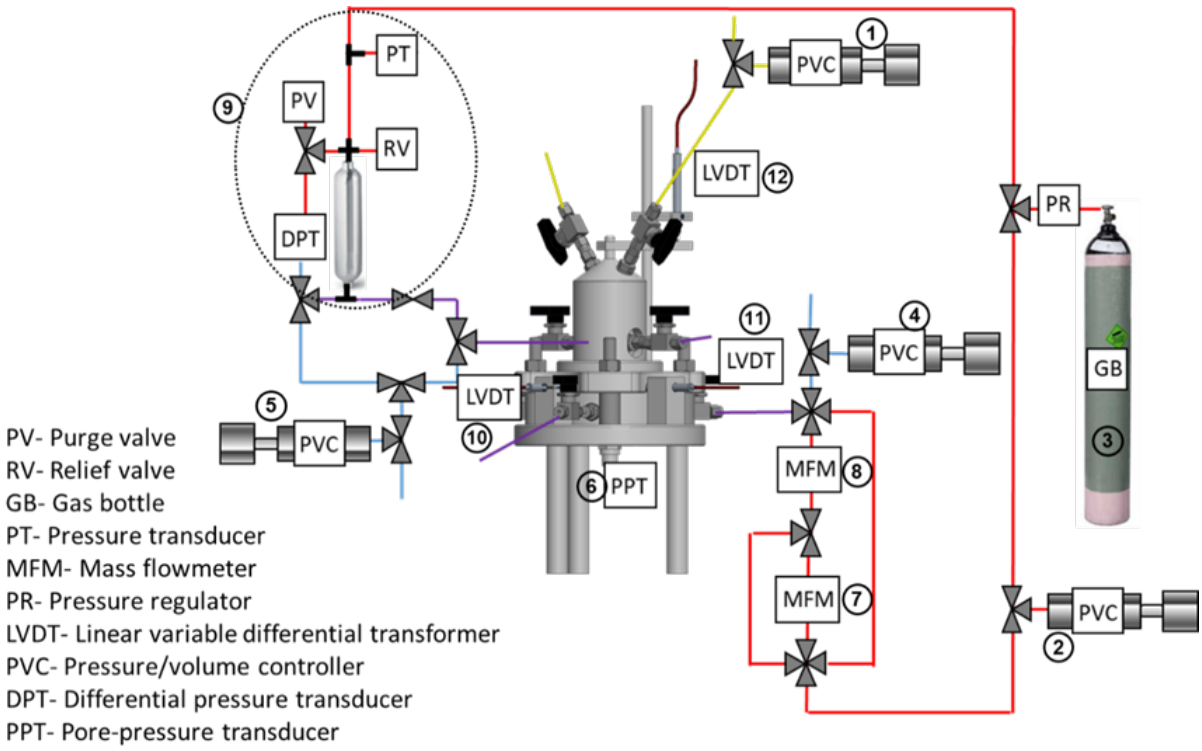

Figure 4-131 – Set-up scheme working under oedometer conditions.

A gas-trap system (number 9 in Figure 4-92) was introduced to separate the gas from the water on the downstream side. It consists of a stainless-steel cylinder of 50 ml of volume that is almost full of water at a known height. The change of the water level, when the outflow occurs, is measured by a wet/wet differential pressure transducer (DPT) from Omega Engineering located at the bottom of the cylinder. This transducer has a pressure range of 2.5 kPa (accuracy 0.5% of the full scale) and can withstand a static pressure of 3500 kPa. Moreover, it has a digital dynamic thermal compensation across the temperature and pressure range. At the top of the cylinder, gas pressure was applied through a pressure regulator (PR) directly from the gas bottle. A pressure transducer (PT) from Omega Engineering with a pressure range of 3.45 MPa and accuracy of 0.5% of the full range (17 kPa of resolution) measures the possible increase of gas pressure when the outflow occurs. The system also has a relief valve from Swagelok with a factory setting of 2 MPa for protecting the DPT and a purge valve.

Four LVDTs from Micro-Epsilon have been acquired for this set-up. Two of them are used for measuring the lateral displacement of the oedometer ring (numbers 10 and 11 in Figure 4-92). They are located orthogonally at half the height of the ring. Their displacement range is ±1 mm with an accuracy of 0.3% of the full scale, given a resolution of 0.15 µm. As explained above, the maximum displacement of the ring is expected to be 35 µm when the lateral stress is 4 MPa, which means that each LVDT measures 233 steps. Therefore, the resolution in terms of lateral stress is 20 kPa. The unit for measuring the

vertical displacement of the piston (number 12 in Figure 4-92) has a larger displacement range (±5 mm) with an accuracy of 0.01% of the full scale, given a resolution of 1 µm.

The data acquisition software was developed in Visual Basic (Microsoft) to monitor and/or control all the devices described above using an electronic box with a National Instrument Card.

4.5.1.2 Calibration

Sensors and cells' deformation

All the sensors used in both set-ups were properly calibrated. Additionally, the vertical deformation of the structures of the oedometer cells was carefully calibrated for loading and unloading paths. To this aim, a solid steel disc that simulated the samples and the oedometer rings was placed inside both cells. These metallic discs were considered non-deformable. The calibrations were used to correct the displacements at different stress levels.

Dead volume of the high-capacity oedometer

To determine the dead volume of the inlet and outlet lines, the equipment was mounted with a fake steel sample and loaded to ensure proper contact between the porous disc and the steel piece.

The inlet line consists of: the gas controller; three high-pressure ball valves; approximately 0.50 m of metal tubing of 1.4 mm of inner diameter; and, the gaps inside the cell. Its volume (Figure 4-93), including the porous disc at the bottom, was measured using the air pressure decay method in each stretch, assuming that P·V=const. The gas PVC was filled with gas at the beginning of every injection test (Stretch 1 in the figure). The results are shown in Table 4-25.

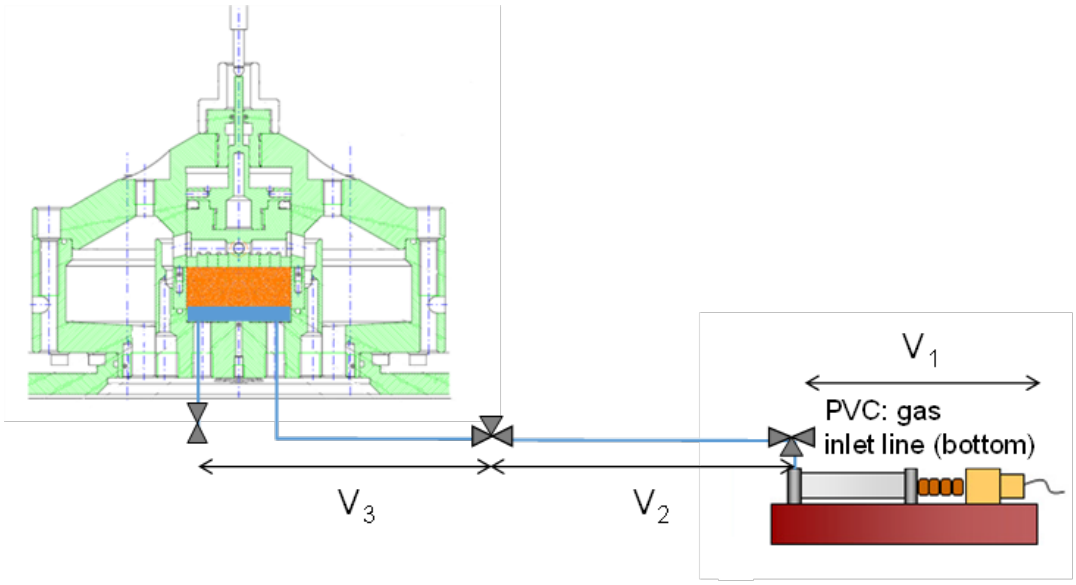

Figure 4-132 – Scheme of inlet line in the oedometer cell.

Table 4-35 – Volume of each stretch in the inlet line in the oedometer cell.

Stretch	Pressure (kPa)	Accumulated volume (ml)	Volume (ml)
0 (PVC)	3030.25	500.001	
1	3020.25	501.656	1.655
2	2989.72	506.779	5.123
Total volume of inlet lines			6.778

The outlet line consists of: the water controller; two high-pressure ball valves; one low-pressure valve; a safety valve to protect the controller; approximately 0.5 m of metal tubing of 1.4 mm of inner diameter; and, the gaps inside the cell. Its volume (Figure 4-94) was determined with direct measurement of water volume to the first stretch and using the air pressure decay method in the second and third stretches, including the porous disc at the top. The water PVC in the outflow line was partially filled with water during the injection tests (around 10 ml of initial volume). The approximate volume of the outlet lines is 39.64 ml. The results are shown in Table 4-26.

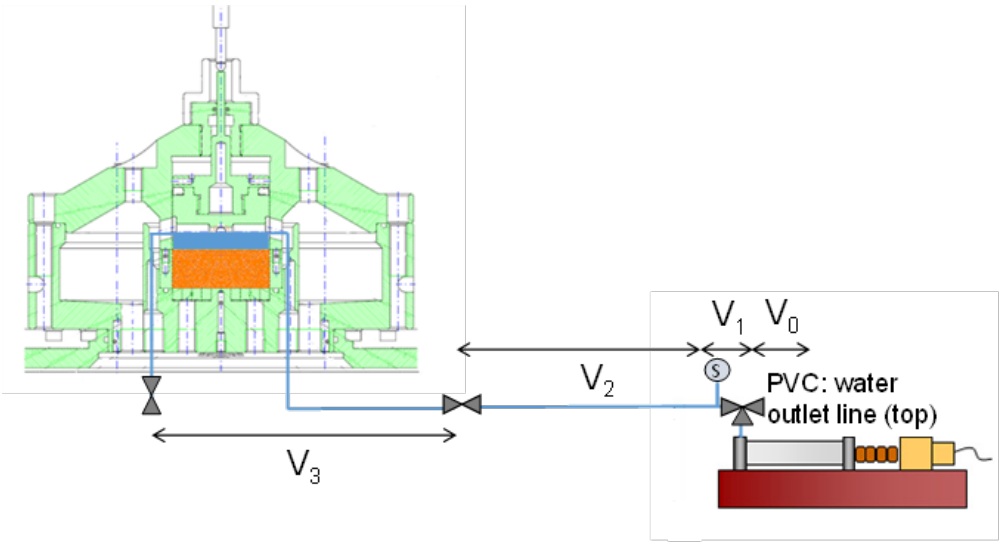

Figure 4-133 – Scheme of outlet line in the oedometer cell.

Table 4-36 – Volume of each stretch in the outlet line in the oedometer cell.

Stretch	Accumulated volume (ml)	Volume (ml)
0 (PVC)	10.000	
1	10.068	0.068
2	12.293	2.225
3	39.636	27.343
Total volume of inlet lines		29.636

Dead volume of the oedometer cell with lateral stress measurement

To determine the dead volume of the inlet and outlet lines, the equipment was mounted with a fake steel sample and loaded to ensure proper contact between the porous discs and the steel pieces. Both the inlet and outlet lines present diverse paths for using all the devices and sensors or only the PVCs, and hence, the dead volumes will depend on the selected path. Connections of the different elements are schematically represented in Figure 4-93.

Dead volume of the inlet lines

Option A: Bottom of the cell directly connected to the gas PVC

This inlet line consists of: the gas controller; seven high-pressure ball valves; approximately 0.75 m of metal tubing of 1.4 mm of inner diameter; and, the gaps inside the bottom part of the cell (including the porous stone). Its volume was measured using the air pressure decay method in each stretch, assuming that P·V=const. resulting in 7.927 mL.

Option B: Using the mass flow meter (MFM) of 100 mL/min

This inlet line consists of: the gas controller; nine high-pressure ball valves; approximately 0.70 m of metal tubing of 1.4 mm of inner diameter; and, the gaps inside the bottom part of the cell (including the porous stone). It also includes the volume inside a mass flowmeter. The total volume, measured using the air pressure decay, is 16.439 mL.

Option C: Using both MFM (10 and 100 mL/min)

This inlet line consists of: the gas controller; nine high-pressure ball valves; approximately 0.60 m of metal tubing of 1.4 mm of inner diameter; and, the gaps inside the bottom part of the cell (including the porous stone). It also includes the volumes inside the two mass flowmeters. The total volume, measured using the air pressure decay, results in 21.278 mL.

Dead volume of outlet lines

Option A: Top of the sample directly connected to the water PVC

This outlet line consists of: the water controller; six high-pressure ball valves; approximately 0.40 m of metal tubing of 1.4 mm of inner diameter; and, the gaps inside the top part of the cell (including the porous stone). The total volume, measured using the air pressure decay, is 6.753 mL.

Option B: Using the gas trap system

This outlet line consists of: the water controller; eight high-pressure ball valves; approximately 0.80 m of metal tubing of 1.4 mm of inner diameter; and, the gaps inside the top part of the cell (including the porous stone). It also includes the gas trap system (stainless steel cylinder of 50 mL, the DPT sensor, and the PT sensor). The total volume, measured directly with water, is 60.740 mL.

Calibration of the deformable ring

The deformable ring, used to indirectly measure the lateral stresses, was calibrated by filling it with water. Water pressure was varied (increased and decreased) in steps and measured with the pore-pressure transducer. The hydrostatic pressure of water was then equal to the lateral stress applied to the ring. By recording the lateral displacement with the two LVDTs, a linear fitting was obtained and used for estimating the lateral stresses (Figure 4-95).

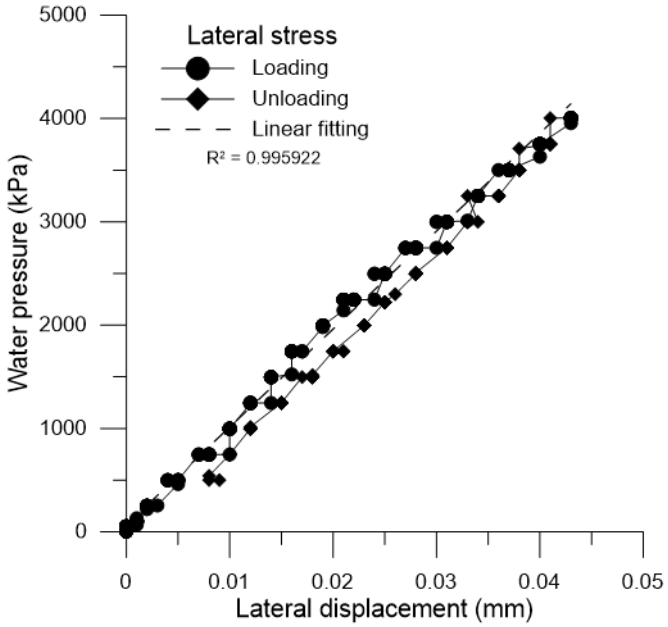

Figure 4-134 – Curve obtained from one of the LVDT used for the calibration of the deformable ring.

4.5.2 Material properties (pre-test and post-test characteristics)

4.5.2.1 Geological origin, core references, initial and geotechnical properties

Boom Clay samples were retrieved at the HADES underground research facility URL (Mol, Belgium). Figure 4-96 shows a scheme of the URL in the Boom Clay formation and the location of the retrieved samples. Afterwards, the cores were vacuum-packed using reinforced aluminium foil and thermo-welded plastic. They were stored at room temperature ranging between 15 and 20°C and at an average relative humidity of 45% before being sent. The core samples used in this research were received at the UPC Geotechnical Laboratory in May 2014. The first was also used in the previous research agreement: Core 8 (ID: CGR66-67W_Core 8_Sectiona) and was horizontally drilled from Ring 66-67 of the borehole 2012/6 at the HADES (horizontal borehole towards the West) at a depth of 223 m. The second is identified as Core 12 (ID: CGR74/75D Core 12 11.30-12.08 m) and was vertically drilled from

Ring 74-75 of the borehole 2014/1 twelve meters below HADES. This core presented the central part very degraded when it was opened in the UPC (Figure 4-97).

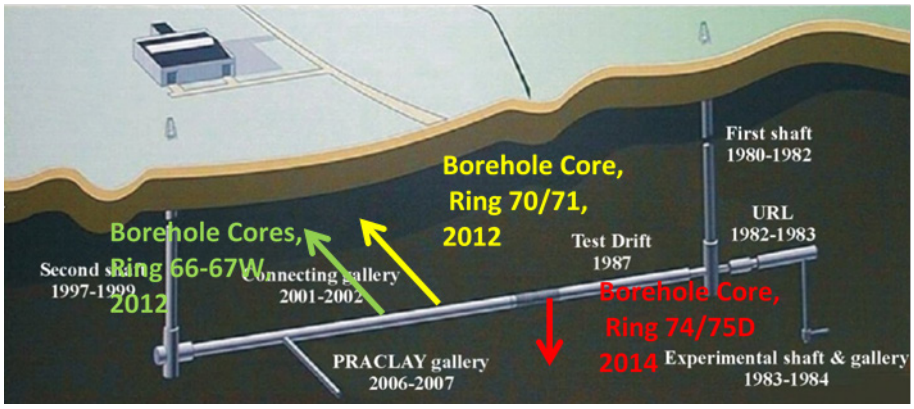

Figure 4-135 – Scheme of the URL in the Boom Clay formation at Mol and locations of sample retrieval.

Figure 4-136 – At the top Core 8 (ID: CGR66-67W_Core 8_Sectiona), at the middle Core 12 (ID: CGR74/75D Core 12 11.30-12.08 m) at HADES, at the bottom Core 12 (ID: CGR74/75D Core 12 11.30-12.08 m) when it was opened at UPC.

A part of each core was used for determining the geotechnical and initial properties which are summarised in Table 4-27 together with results of previous studies (Gonzalez-Blanco, 2017; Gonzalez-Blanco et al., 2022; Gonzalez-Blanco & Romero, 2022). The air entry value (AEV) indicated in the table, corresponds to the dominant pore mode detected from MIP data and was determined using Laplace's equation.

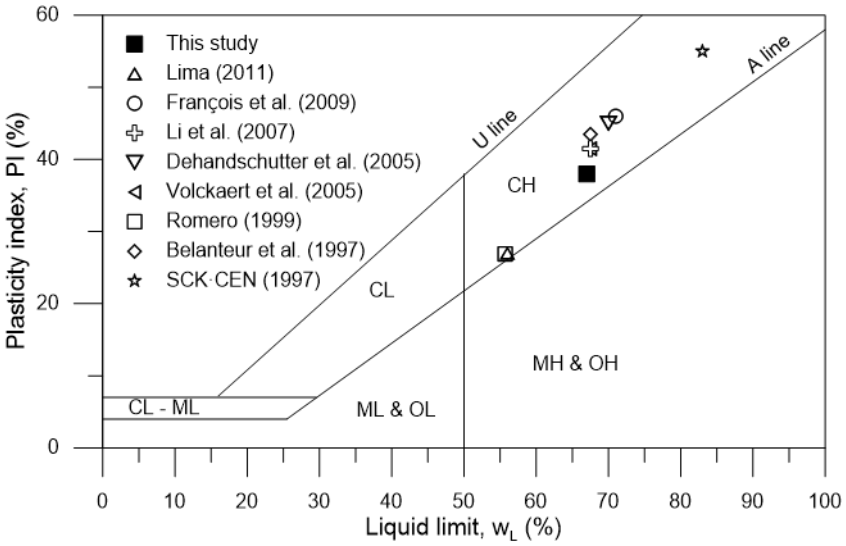

Figure 4-137 – Plasticity chart (after (Lima, 2011)).

The specific gravity of the soil grains (G_s) at 20 ºC is 2.67 for Boom Clay, determined according to ASTM D854. Other values reported in the literature varied between 2.65 and 2.70 (Coll, 2005; Horseman et al., 1987; Romero, 1999).

Consistency limits were also investigated for Boom Clay (ASTM D4318). A limit liquid (w_L) of 67% and a plastic limit (w_P) of 29% were measured, resulting in a value of plasticity index of 38%. Figure 4-98 shows the plasticity chart, which also includes consistent results reported by different authors. Boom Clay can be classified according to the plasticity chart as high-medium plastic inorganic clay (CH) (Unified Soil Classification System, ASTM D2487).

Table 4-37 – Initial conditions and properties.

Parameter	Previous results (Gonzalez-Blanco, 2017)	New results	
		Core 8	Core 12
Geotechnical properties			
Density of soils, ρ_s (Mg/m^3)	2.67		
Liquid limit w_L (%)	67		
Plasticity index, I_P (%)	38		
Initial conditions			
Density, ρ (Mg/m^3)	2.02-2.06	2.04-2.05	2.01
Dry density, ρ_d (Mg/m^3)	1.63-1.69	1.67-1.69	1.61
Porosity, n	0.37-0.39	0.37	0.398
Void ratio, e	0.58-0.63	0.58-0.59	0.66
Water content, w (%)	22.6-24.0	19.0-20.2	24.18
Degree of saturation	1	0.93-0.96	0.99
Total suction after retrieval, Ψ (MPa)	2.45	3.2-4.4	3.47
Osmotic suction, π (MPa)	0.5		
Increase in matric suction, s (MPa)	0.20	0.95-2.15	1.22
Air-entry value from MIP (MPa)	4.8		
Dominant pore mode from MIP (nm)	65-70		

Table 4-28 contains the initial conditions of samples used in each test and Figure 4-99 shows the zone of sample extraction (in blue) together with samples used in previous works (in green). The nomenclature used in the reference consists of: Set of tests (SET1, SET2, SET3 or SET4) - Protocol (A, B, HM, GAS or DAM) – Orientation of bedding planes (N: normal to flow; P: parallel to flow).

Table 4-38 – Sample reference, core and initial conditions for samples used in each test.

Reference	Core	Density	Porosity	Void ratio	Water content
SET1_A_P	CGR66-67W_Core8_Section_a	2.05	0.37	0.59	19.02
SET1_A_N	CGR66-67W_Core8_Section_a	2.05	0.37	0.59	19.27
SET1_B_N	CGR66-67W_Core8_Section_a	2.05	0.37	0.58	20.21
SET2_HM_N	CGR74/75D_Core 12	2.05	0.37	0.58	24.18
SET2_HM_P	CGR74/75D_Core 12	2.07	0.36	0.56	23.70
SET3_GAS_N	CGR74/75D_Core 12	2.06	0.37	0.58	21.64
SET3_GAS_P	CGR74/75D_Core 12	2.06	0.36	0.57	22.40
SET4_DAM_N	CGR74/75D_Core 12	2.07	0.36	0.57	19.66
SET4_DAM_P	CGR74/75D_Core 12	2.07	0.36	0.57	19.66

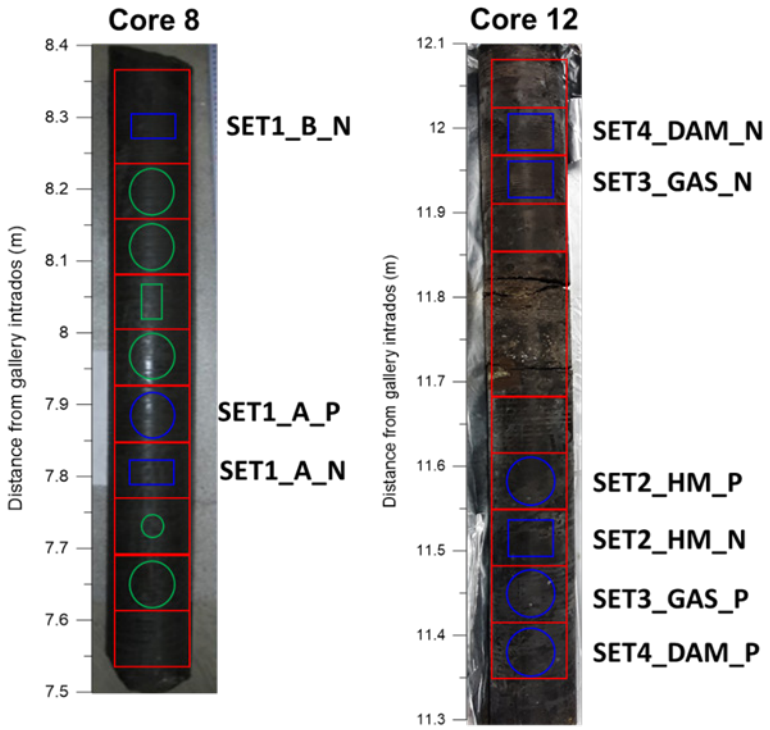

Figure 4-138 – Location of the tested samples in Core 8 and Core 12.

4.5.2.2 Water retention behaviour

A dew point psychrometer (Cardoso et al., 2007) was used to obtain the water retention curve in the total suction range from 1 to 150 MPa and volume change was assessed by using a high-precision calliper. The specimens were dried in steps starting from the initial total suction, stored for one day for equalization, weighed and then, total suction was measured. Afterwards, from the dry state, samples were wetted in steps following an identical procedure until saturation.

Suction (s) and degree of saturation (S_r) data in the drying and wetting branch were fitted to van Genuchten's equation:

$$S_r = \left[1 + (s/p_0)^{(1/(1-\lambda))}\right]^{-\lambda} \quad (4\text{-}5\text{-}1)$$

Figure 4-100 shows the estimated water retention curve, which includes the fitted van Genuchten's parameters λ and p_o, the latter associated with the air entry value.

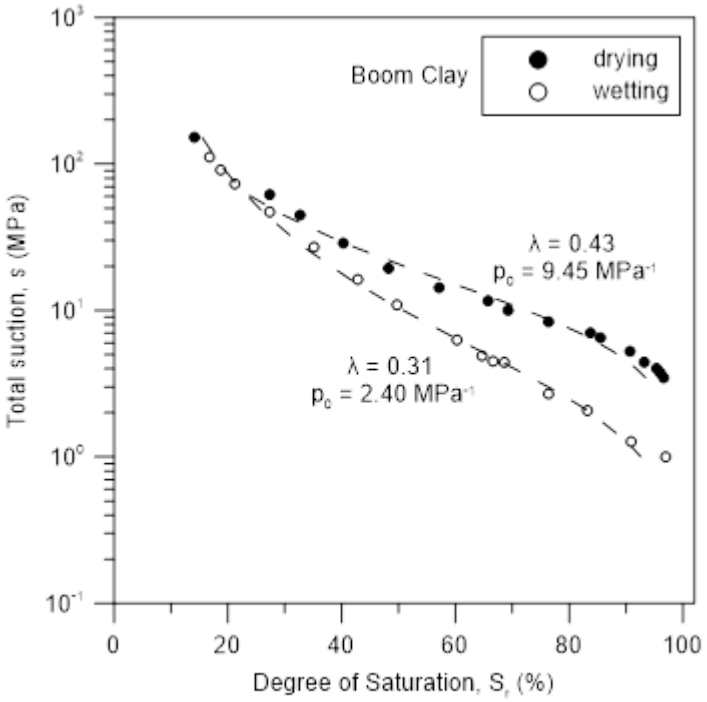

Figure 4-139 – Water retention curve of Boom Clay

4.5.2.3 Microstructural analysis at the initial state

MIP tests

Mercury Intrusion Porosimetry (MIP) tests were performed to characterise the porosity network on an 'AutoPore IV 9500 – Micrometrics Instrument Corp' porosimeter. Cubical samples of Boom Clay were trimmed by 10 mm in dimension and freeze-dried before the MIP tests.

The pore network description of Core 8 was complemented by nitrogen adsorption tests carried out on 'ASAP 2020 – Micrometrics Instrument Corp' equipment. The pore size distribution was estimated

following the Barrett, Joyner and Halenda (BJH) method using the desorption information (Webb and Orr, 1997). A wider range of pore sizes is covered when using this complementary information.

Figure 4-101 shows the cumulative intruded pore volume normalised by solid volume (intruded void ratio) plotted against the entrance pore size for Boom Clay samples. There is some deviation from the initial void ratio in MIP data (refer to Table 4-28), which is higher for the Core 12 sample due to the limited capacity of the porosimeter to enter the smallest pores (non-intruded porosity with pores size below 6 nm). This deviation was covered by data from the nitrogen adsorption method and the initial void ratio of Core 8 was almost reached. Information on MIP limitations can be found in Romero & Simms (2008).

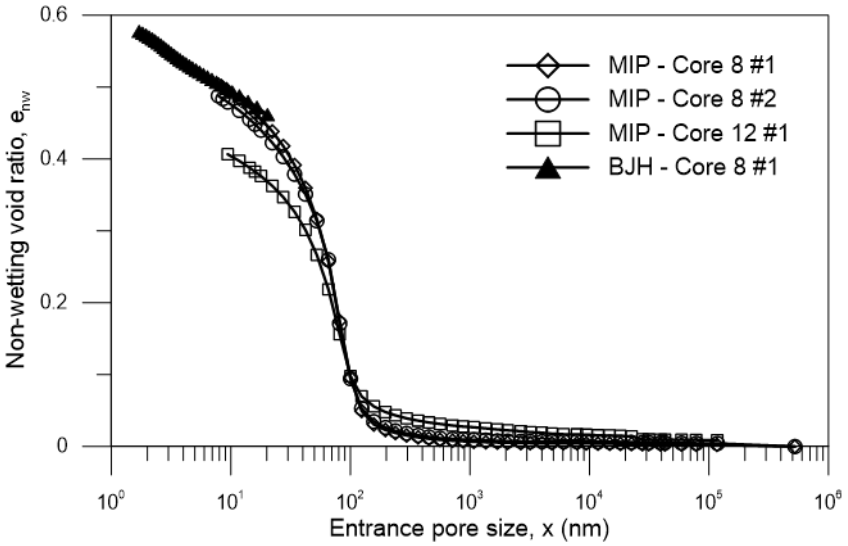

Figure 4-140 – Cumulated intruded void ratio obtained with MIP and BJH techniques.

The PSD function (see section 4.5.5.6 for more details) obtained from MIP displays one dominant pore size at an intra-aggregate scale, as expected for a matrix-type microstructure, being around 70 nm for both cores. Regarding BJH data, a less important smaller peak is observed around 3 nm (Figure 4-102).

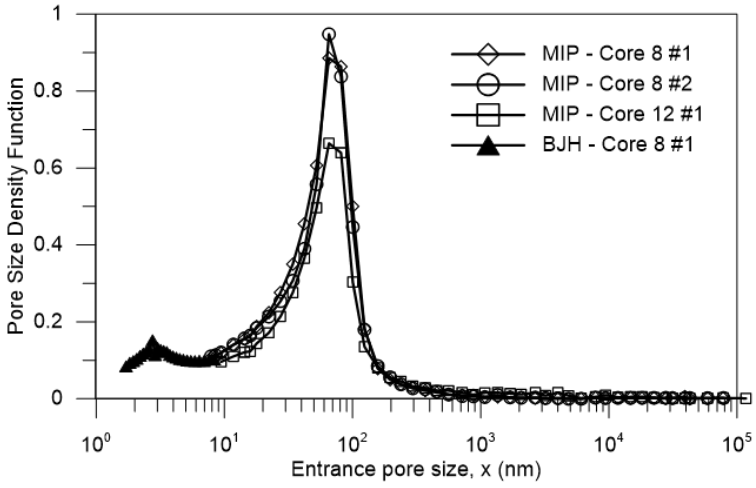

Figure 4-141 – PSD function of intact Boom Clay.

Microstructural images

Samples of intact Boom Clay were directly trimmed from undisturbed cores (Core 8 CGR66-67_Core_8_Section_a) in both directions, bedding parallel and orthogonal to the axis using a fine saw.

Although µ-CT does not need any samples pre-treatment (freeze-drying), in this study, it was decided to subject the sample to the same process as in the MIP tests to allow further comparison. After trimming, all samples were freeze-dried by plunging the samples into liquid nitrogen and then applying vacuum to remove the pore water from microstructure. Afterwards, samples were preserved and vacuum packed until they were scanned.

Volume rendering was performed with the 3D Viewer plugin of Image J software using a trilinear interpolation. Figure 4-103 shows the volume reconstruction for the intact sample at both orientations of bedding planes. Neither bedding planes nor fissures are visible in the natural samples which indicates that, even though these natural discontinuities exist, they are initially closed or cannot be observed with the used techniques.

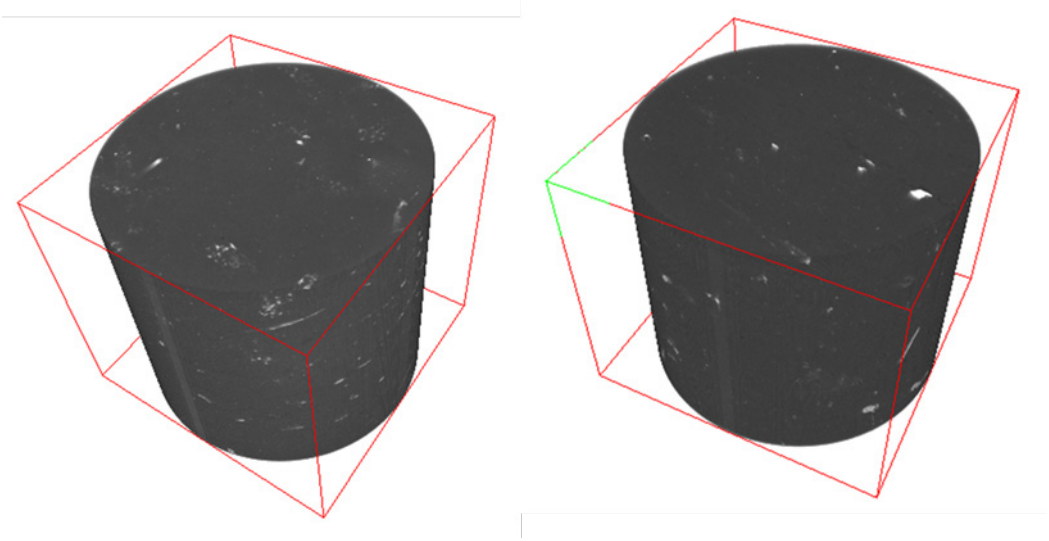

Figure 4-142 – Volume reconstruction of Boom Clay samples: with bedding planes normal to the sample axis (left); with bedding planes parallel to the sample axis (right).

4.5.3 Testing fluids

4.5.3.1 Liquid

Synthetic Boom Clay water (SBCW or just water hereafter) was prepared according to De Craen et al. (2004) as a solution of approximately 15 mM NaHCO3 (84.007 kg/kmol). The solution presented an electrical conductivity of around 2400 µS/cm, associated with an osmotic suction < 0.5 MPa. To prepare it, a specified amount of NaHCO3 (1170 mg/L) was dissolved per litre of solution (solvent distilled water), followed by thorough stirring.

4.5.3.2 Gas

During the research, Air (21% O2 and 79% N2) and Helium (purity >99.999%) have been used as testing gases.

4.5.4 Testing protocols

During EURAD WP6 GAS, CIMNE is participating in Task 3 'Barrier integrity'. The test program is divided into Sub-Task 3.1 'Gas induced impacts on barrier integrity' and Sub-Task 3.2 'Pathway closure and sealing processes'.

CIMNE's experimental programme on Boom Clay addressed the basic phenomena and processes related to gas transport when gas pressure is below confining pressure and contributed to gaining knowledge of the self-sealing mechanisms at the process level. Odeometer conditions were selected since the control and measurements of the strains is more precise than under other conditions. The protocols were developed to assess the following issues:

- Derivation of constitutive relationships of the water retention behaviour and stress-strain relationships in response to gas invasion processes.
- Validation of existing concepts of constitutive stress (e.g. net stress, Bishop's formulation) for their applicability to gas invasion processes.
- The investigation of the re-saturation process ("imbibition of the wetting fluid") after the gas invasion.
- Studying the possible loss of hydraulic integrity by comparing water permeability before and after gas injection.
- Evaluating the effect of a second injection after re-saturation.
- Determining the self-sealing capacity on previously damaged samples (by loading/unloading) and possible fissure re-activation upon gas injection.

Table 4-29 gathers the main stages of each protocol which are explained in detail in the subsequent sub-sections.

Table 4-39 – Stages of the different protocols.

Stage	SET 1-A	SET1-B	SET 2	SET 3	SET 4
1	Pre-conditioning	Pre-conditioning	Pre-conditioning	Pre-conditioning	Pre-conditioning
2	Drained loading	Drained loading	Water permeability	Drained loading	Drained loading
3	Water permeability	Water permeability	Drained loading	Water permeability	Water permeability
4	Gas injection	Gas injection	Drained unloading	Gas injection	Drained unloading
5	Re-saturation	Re-saturation	Drained reloading	Re-saturation	Drained reloading
6	Water permeability	Water permeability	Water permeability	Water permeability	Water permeability
7	Undrained unloading	Gas injection	Undrained unloading	Gas injection	Gas injection
8	Post-mortem analyses	Undrained unloading		Undrained unloading	Re-saturation
9		Post-mortem analyses		Post-mortem analyses	Water permeability
10					Gas injection
11					Undrained unloading

4.5.4.1 Test Protocols for SET 1

SET 1 of experiments dealt with the self-sealing capacity of Boom Clay. The samples were tested with the high-capacity oedometer cell at different orientations of bedding planes to study its effect (bedding parallel and orthogonal to the axis). This protocol presented two variations, sub-protocol A in which the post-mortem samples were analysed after the re-saturation, and sub-protocol B, in which a second gas injection was performed and post-mortem samples were analysed subsequently.

Protocol SET 1-A

The main stages for Protocol SET 1-A were:

- Stage 1: Pre-conditioning

Initially, samples were loaded to reach a stress state representative of in-situ conditions. The pre-conditioning paths are mandatory to reach the geostatic conditions of the material in the in-situ state, which were the starting point of any test, ensuring the most similar stress state. These paths consisted mainly of loading the samples up to a pre-defined stress level at constant water content reducing the initial matric suction and afterwards, flooding the sample with synthetic water. The samples could undergo expansion and degradation as a clear consequence of suction reduction effects due to water contact at low stress levels. To minimise these effects, the samples were always loaded to a target total stress of 3 MPa and only then put in contact with water under atmospheric pressure to avoid any damage. After reaching steady-state conditions, water pressure at the downstream and upstream boundaries was increased from 0 (atmospheric pressure) to 0.5 MPa and hence, once the pore pressure was equalized, the effective stresses were equivalent to the in-situ ones.

- Stage 2: Drained loading

The samples were loaded at drained conditions (the absence of pore water pressure increase was checked by stopping the load and recording the displacements, which were negligible) at a rate of 0.5 kPa/min up to a maximum total vertical stress of 6 MPa. This vertical stress was kept constant. This vertical stress was selected to enable injecting gas at large pressure (4 MPa) without exceeding the minor effective stress.

- Stage 3: Water permeability determination

After ensuring full saturation, water permeability was measured by applying a hydraulic gradient. Water pressure at the bottom side was increased from 0.5 to 0.6 MPa to induce the flow of water through the sample. Downstream pressure remained constant (0.5 MPa, this pressure applied at the top of the sample was maintained constant along the different stages of the test). Axial deformation was monitored along this hydraulic process. Water permeability was measured under steady-state conditions using the water volume information at the inflow and the outflow. After that, the backpressure was reduced to 0.5 MPa again until stabilization.

- Stage 4: Gas injection

Firstly, water pressure in the upstream vessel was reduced to atmospheric conditions to allow for its fast replacement by gas. Gas pressure at the upstream point was rapidly increased from atmospheric conditions to a value of 0.5 MPa.

Gas injection from an initial pressure of 0.5 MPa to a maximum gas pressure below the lateral stress was applied at different constant flow rates (2 ml/min or 100 ml/min). These rates were large enough to ensure that gas flow through preferential pathways was the main gas transport mechanism. Once reaching the maximum gas pressure, the injection system was stopped (shut-off) and a recovery phase at constant gas volume started until gas dissipation. In the case of using the oedometer with lateral stress measurement, the lateral stress variations were estimated from the thin wall of the ring movement. Information on gas volume at the inflow was recorded. At the outflow, the gas trap accounted for the volume of gas and displaced water (if any).

- Stage 5: Re-saturation

After gas injection, a re-saturation stage was carried out. The top and bottom caps were firstly filled with water at atmospheric pressure. A small hydraulic gradient was applied to displace the gas that might be stored in the sample. This process lasted until stabilization.

- Stage 6: Water permeability determination

After ensuring full saturation, the hydraulic gradient was increased to impose a water flux. Axial deformation was monitored along this hydraulic process. Water permeability was measured under steady-state conditions using the water volume information at the inflow and the outflow.

- Stage 7: Undrained unloading

Gas pressure in the upstream vessel was reduced instantaneously to atmospheric conditions as well as the fluid pressure in the downstream vessel. Simultaneously, vertical stress was decreased under undrained conditions to preserve the samples and track possible microstructural changes due to gas passage.

- Stage 8: Post-mortem analyses

A microstructural study of the samples after the tests was carried out, with two different techniques: Mercury Intrusion Porosimetry (MIP) and Micro-Focus X-ray Computed Tomography (µ-CT). Freeze-drying of the sub-samples is mandatory for the two first techniques, while µ-CT is performed on sub-samples with the final water content.

Protocol SET 1-B

The stages for Protocol SET 1-B were the same as the Protocol SET 1-A but an additional gas injection stage was added after Stage 5. During this stage, the same conditions described above for Stage 4 were applied.

4.5.4.2 Test protocols for SET 2 - HM

SET 2 aimed at checking the functionality of the oedometer cell with lateral stress measurements while studying Boom Clay hydro-mechanical performance under oedometer conditions with a complete picture in terms of stresses. Two samples were tested using this protocol at different bedding orientations (parallel and orthogonal to the axis).

The main stages of Protocol 2 were:

- Stage 1: Pre-conditioning

Equal to Stage 1 described in Section 4.5.4.1

- Stage 2: Water permeability determination

Equal to Stage 3 described in Section 4.5.4.1

- Stage 3: Drained loading

The samples were loaded under drained conditions (absence of pore water pressure increase was checked by stopping the load and recording the displacements, which were negligible) at a rate of 0.5 kPa/min up to a maximum total vertical stress of 8 MPa to study the post-yield behaviour.

- Stage 4: Water permeability

Equal to Stage 3 described in Section 4.5.4.1

Stage 5: Drained unloading

The samples were unloaded under drained conditions (the absence of pore water pressure increase was checked by stopping the load and recording the displacements, which were negligible) at a rate of 0.5 kPa/min up to a minimum total vertical stress of 3 MPa to study the evolution of the K_o with the OCR.

- Stage 6: Drained reloading

The samples were reloaded under drained conditions (the absence of pore water pressure increase was checked by stopping the load and recording the displacements, which were negligible) at a rate of 0.5 kPa/min up to a total vertical stress of 8 MPa.

- Stage 7: Water permeability

Equal to Stage 3 described in Section 4.5.4.1.

- Stage 8: Undrained unloading

The samples were finally unloaded under undrained conditions following the steps explained in Section 1.4.1.

4.5.4.3 Test protocols for SET 3 – GAS

SET 3 of the experiments were launched to study the gas transport properties and the self-sealing behaviour of the samples measuring the lateral stresses under oedometer conditions. Additionally, a second injection stage was applied to investigate the possible fissure re-opening after self-sealing. Two samples with bedding orientated parallel and orthogonal to the flux were tested.

The main stages of this protocol were:

- Stage 1: Pre-conditioning

Equal to Stage 1 described in Section 4.5.4.1

- Stage 2: Drained loading

Equal to Stage 2 described in Section 4.5.4.1.

- Stage 3: Gas injection

Equal to Stage 4 described in Section 4.5.4.1

- Stage 4: Re-saturation

Equal to Stage 5 described in Section 4.5.4.1.

- Stage 5: Water permeability determination

Equal to Stage 6described in Section 4.5.4.1

- Stage 6: Second gas injection

Equal to Stage 4 described in Section 4.5.4.1

- Stage 7: Undrained unloading

Equal to Stage 7 described in Section 4.5.4.1

- Stage 8: Post-mortem analyses

Equal to Stage 8 described in Section 4.5.4.1

4.5.4.4 Test protocols for SET 4 - DAM

SET 4 of tests were carried out to examine the gas transport behaviour of BC samples previously disturbed (damaged) by unloading/reloading cycles. Two samples with bedding orientated parallel and orthogonal to the flux were tested, however, the test on the sample with the bedding planes parallel to the flow (SET4_DAM_P) was running at the time of writing this document and the results are not reported here.

The protocol followed for this SET was:

- Stage 1: Pre-conditioning

Equal to Stage 1 described in Section 4.5.4.1

- Stage 2: Water permeability determination

Equal to Stage 3 described in Section 4.5.4.1

- Stage 3: Drained loading

Equal to Stage 3 described in Section 4.5.4.2

- Stage 4: Drained unloading

Equal to Stage 5 described in Section 4.5.4.2

- Stage 5: Drained reloading

The samples were reloaded at drained conditions (the absence of pore water pressure increase was checked by stopping the load and recording the displacements, which were negligible) at a rate of 0.5 kPa/min up to a total vertical stress of 8 MPa.

- Stage 6: Gas injection

Equal to Stage 4 described in Section 4.5.4.1

- Stage 7: Gas injection

Equal to Stage 4 described in Section 4.5.4.1

- Stage 8: Re-saturation

Equal to Stage 5 described in Section 4.5.4.1

- Stage 9: Water permeability determination

Equal to Stage 6 described in Section 4.5.4.1

- Stage 10: Second gas injection

Equal to Stage 4 described in Section 4.5.4.1

- Stage 11: Undrained unloading

Equal to Stage 7 described in Section 4.5.4.1

4.5.5 Results

4.5.5.1 Compressibility behaviour

Figure 4-104 displays the continuous loading outcomes for SET 1 under a controlled stress rate, presented in terms of axial strain (positive in compression) and total vertical stress. The samples were tested with bedding planes arranged both normally (depicted by green lines and square symbols) and parallel (illustrated by blue lines and round symbols) to the loading axis during stage 1. The plot also incorporates results from earlier studies by Gonzalez-Blanco (2017), Gonzalez-Blanco et al. (2022) and Gonzalez-Blanco & Romero (2022). The observed compressibility arises from matric suction and stress variations. Samples with bedding planes aligned parallel to the axis of revolution exhibited higher stiffness. This behaviour was attributed to the elastic regime's anisotropy, coupled with a potential closure of discontinuities and/or bedding planes. Notably, the samples from Core 8, utilized in this study, showed greater stiffness compared to those from previous campaigns, possibly attributable to a slight loss of water content during storage (refer to Table 4-27).

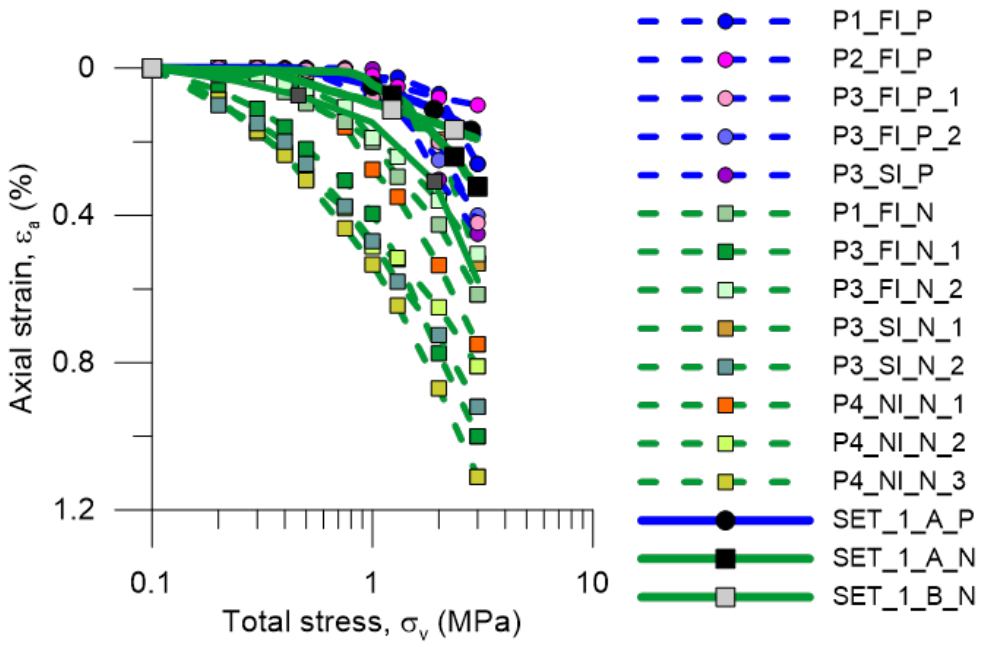

Figure 4-143 – Compressibility of the samples from Core 8 during the initial load of the pre-conditioning stage together with samples reported in Gonzalez-Blanco (2017).

Figure 4-105 shows the same stage but for samples extracted from Core 12 and tested with the oedometer cell with lateral stress measurement. Additionally, the figure also includes the evolution of the lateral stress during the vertical loading.

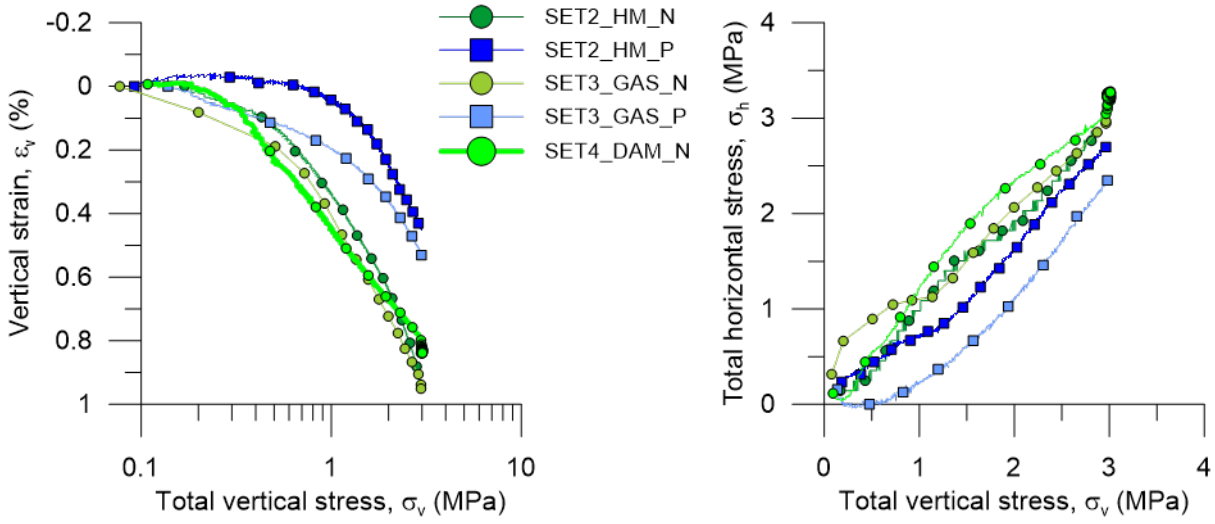

Figure 4-144 – Compressibility of samples from Core 12 during the initial load of the pre-conditioning stage.

After achieving total stress of 3 MPa, the samples were brought into contact with SBCW at atmospheric pressure on both the top and bottom sides to try to ensure null matric suction. During this process, all samples experienced some degree of swelling. The expansion was less pronounced in samples with bedding planes parallel to the axis, as they were constrained from expanding due to oedometer conditions. The observed swelling was a consequence of residual matric suction. An additional test measured a small matric suction of 0.15 MPa, which was predicted using a hydro-mechanical simulation (as detailed in Gonzalez-Blanco et al., 2016). Figure 4-106 illustrates the swelling deformation of the samples during the flooding process until stabilization over time (negative values indicate expansion), alongside results from previous studies (Gonzalez-Blanco, 2017).

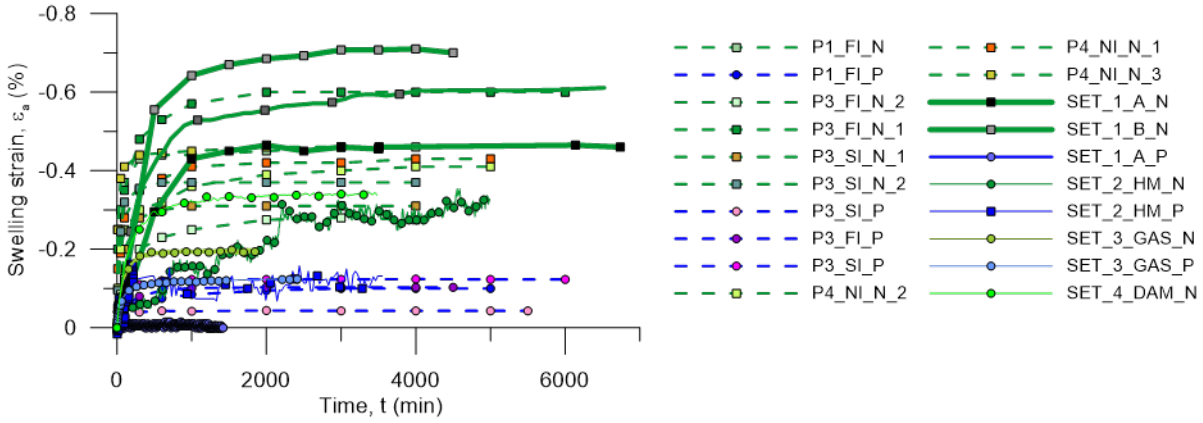

Figure 4-145 – Swelling strains during soaking at constant total stress of samples at both orientations.

After full saturation (null matric suction) of the samples, a continuous loading was carried out in all the oedometer tests at a slow stress rate of 0.5 kPa/min to ensure drained conditions. This rate allowed water to be expelled during the process resulting in the absence of excess pore water pressure. Deformation measurements could then be plotted in terms of effective vertical stress, calculated as the total stress minus the pore water pressure. Figure 4-107 shows the compressibility curves for samples from SET 1 with bedding planes normal and parallel to the axis together with previous results (Gonzalez-Blanco & Romero 2022). Even though these are natural samples, a level of consistency was maintained throughout the hydro-mechanical loading process. A subtle anisotropic behaviour was still visible during this stage, as evidenced by the fact that samples with bedding planes oriented normal to the axis exhibited slightly higher compressibility.

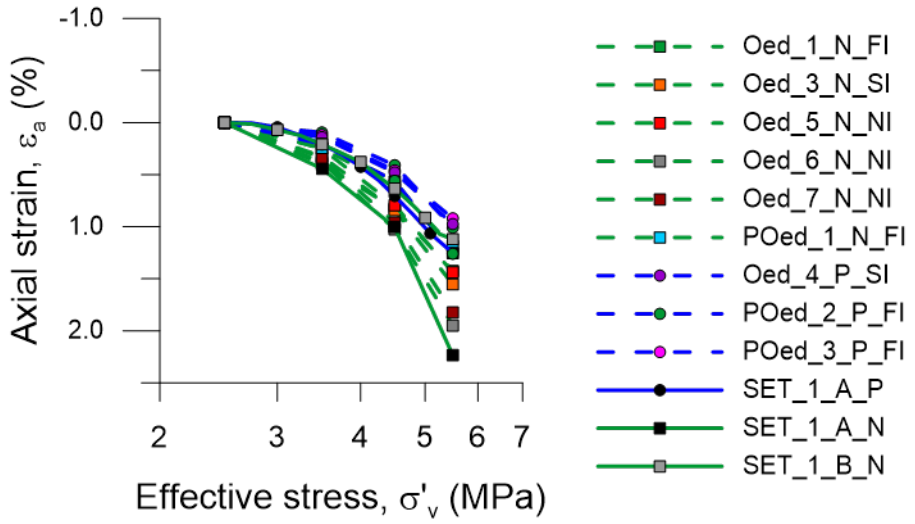

Figure 4-146 – Compressibility curves after soaking under continuous loading at drained conditions for samples of SET 1 at both orientations.

The same hydro-mechanical path was carried out for SET 3 in the oedometer cell with lateral stress measurement. However, samples from SET 2 and SET 4, tested with the same device, were subjected to different loading/unloading/reloading paths. The paths are presented in Figure 4-108 in terms of effective vertical stress versus axial strain, but also the evolution of K_o where the vertical stress level was computed. For the first loading stage, the yield stress was 5.5 MPa, whereas for the unloading/reloading stage it corresponds to the maximum stress underwent (8 MPa).

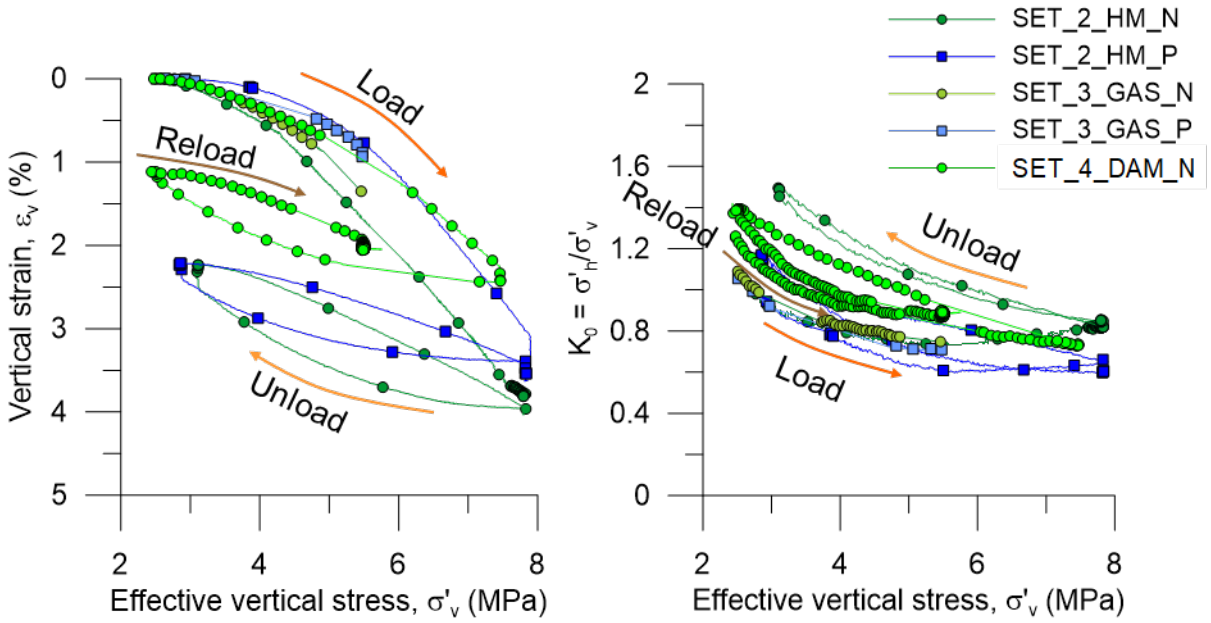

Figure 4-147 – Compressibility curves after soaking under continuous loading/unloading/reloading at drained conditions for samples of SET 2, SET 3 and SET 4 at both orientations.

The measurement of the lateral stress made it possible to examine the evolution of the K_0 with the OCR during the drained unloading. Anisotropy of the samples was observed. The experimental data were fitted with the equation illustrated in Figure 4-109 and are in good agreement with the values reported by Dao (2015) for normally consolidated conditions, which ranged between 0.65 and 0.70 for samples with bedding planes parallel to the axis and between 0.78-0.86 for samples with bedding planes normal to the axis.

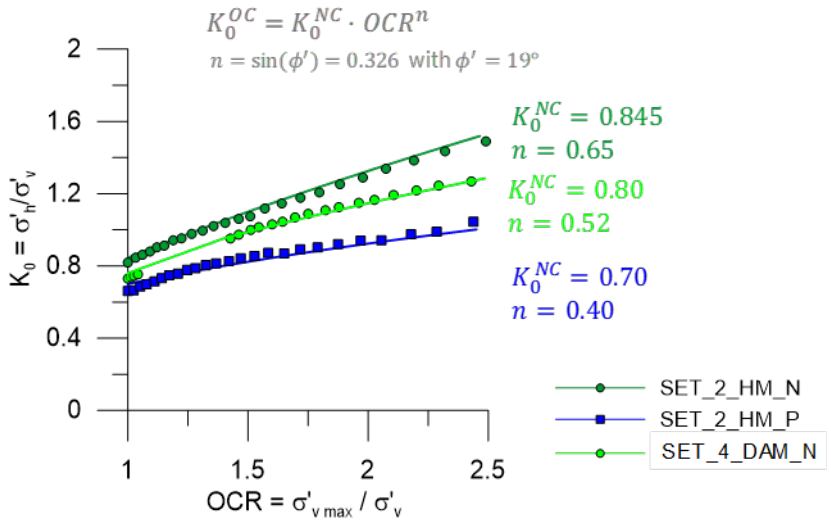

Figure 4-148 – Evolution of K_o with the OCR for both orientations for the different unloading stages.

4.5.5.2 Water permeability before gas injection

Figure 4-110 shows the water permeability estimated at the equivalent to in-situ effective stress (2.5 MPa) and after the drained loading (effective stress of 5.5 MPa as a function of the average void ratio for each sample. The results, are in good concordance with the previous data (unfilled marks in the figure) (Gonzalez-Blanco & Romero 2022), and highlight the clear dependence of the water permeability on the porosity. Furthermore, as expected, higher water permeability was observed with flow parallel to bedding planes, indicating a marked anisotropic feature with an average anisotropic ratio $k_{w//}/k_{w\perp} = 2.3$.

.

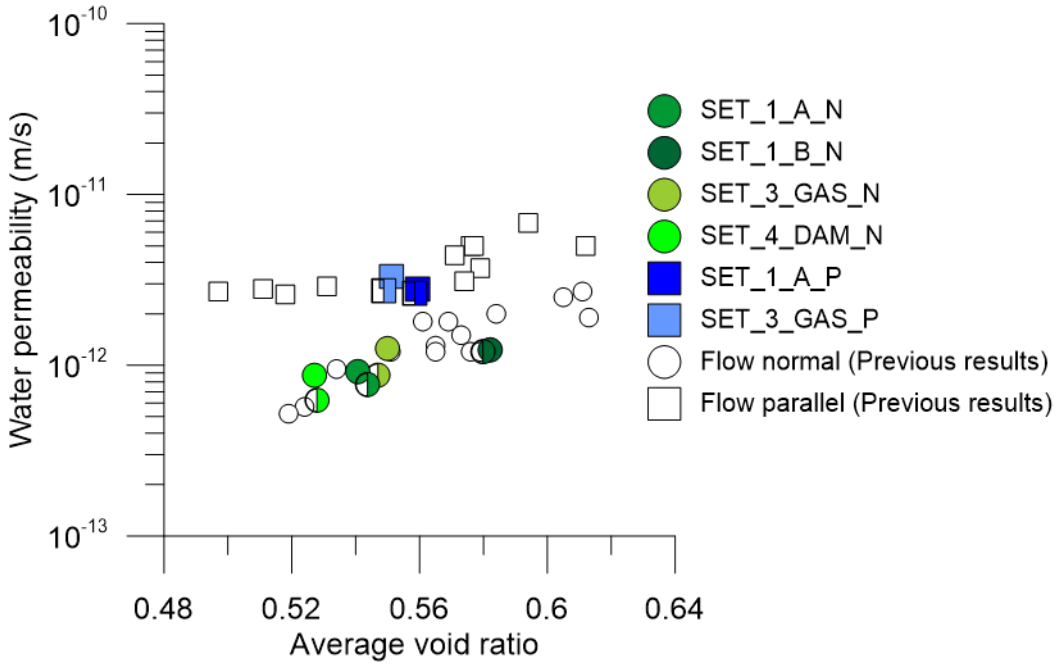

Figure 4-149 – Water permeability results as a function of the void ratio.

For SET 2 and SET 4 of experiments, water permeability was measured at various stress levels before and after the loading/unloading cycle. It can be observed (Figure 4-111) that water permeability at the stress level equivalent to in-situ and after the first loading to 6 MPa was equivalent for both bedding orientations, keeping the anisotropy feature. In contrast, the loading/unloading cycle caused a significant decrease in water permeability.

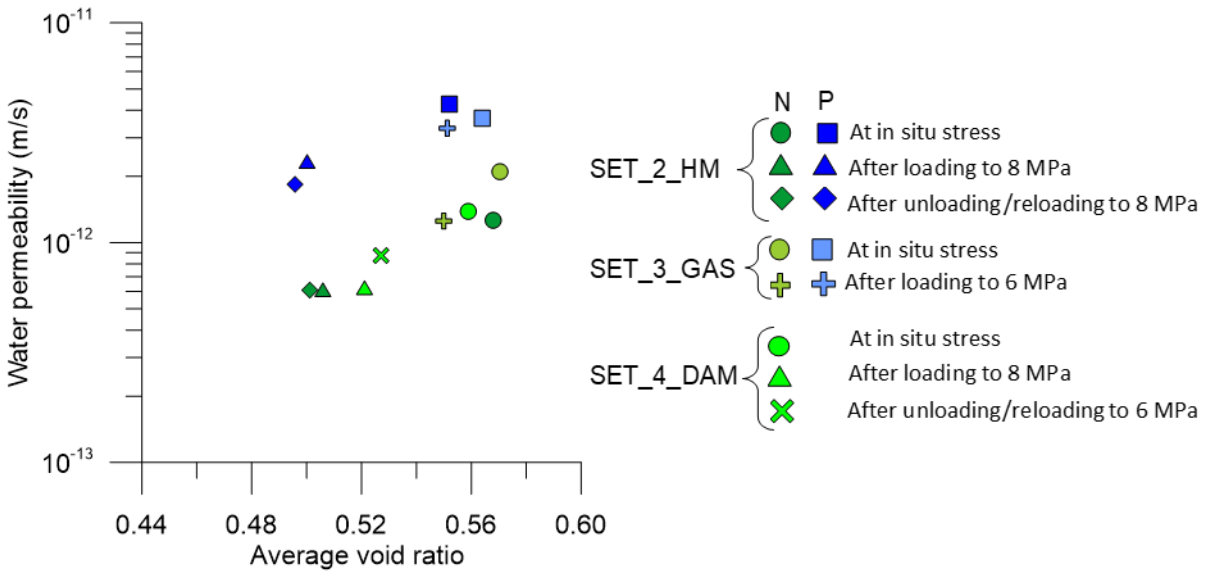

Figure 4-150 – Water permeability after different hydro-mechanical paths for samples at both orientations.

4.5.5.3 Gas injection and dissipation

The gas injection was performed at two constant volumetric injection rates. SET 1 of tests were carried out at a relatively fast rate of 100 ml/min, aiming to compare the macro-phenomenological behaviour and microstructural changes of the tested samples with the ones reported in Gonzalez-Blanco & Romero (2022). In this case, air was used as gas. For the rest of the experiments, Helium was used in order to compare the response of Boom Clay to different gas molecules and a slower injection rate of 2 ml/min was selected.

In any case, the injection pressure was increased until a maximum of 4 MPa (shut-off), and then, the injection system was stopped, while the total vertical stress was kept constant during the whole process (6 MPa). Throughout this entire process, the total vertical stress was maintained at a constant level of 6 MPa. Detection of gas passage through the samples was accomplished by observing a decrease in the inlet pressure and an increase in the outflow volume in the downstream PVC. This approach diverges from what is conventionally referred to as 'breakthrough tests' (Volckaert et al. 1995; Harrington & Horseman 1999; Rodwell 2003; Hildenbrand et al. 2004; Harrington et al. 2012; Wiseall et al. 2015; J. F. Liu et al. 2016), where in gas pressure is steadily increased until a recorded outflow volume indicates the breakthrough pressure. The utilization of the oedometer cell with lateral stress measurement in SET 3 and SET 4 helped in discarding gas flow through the ring-sample interface since maximum gas pressure was consistently below the minor lateral stress.

Figure 4-112 and Figure 4-113 depict the temporal progression of the air inflow pressure at the upstream boundary, the outflow volume (maintained a constant downstream water pressure of 0.5 MPa), and the axial strain during gas injection and dissipation for SET 1 (Gonzalez-Blanco et al., 2023). These figures also include data from previous tests on samples at both orientations (Gonzalez-Blanco & Romero, 2022). In all cases, the gas pressure at the upstream boundary increased from 0.5 to 4 MPa ('A' to 'B' in the figures), followed by a shut-off at point 'B' and dissipation at a constant inflow volume.

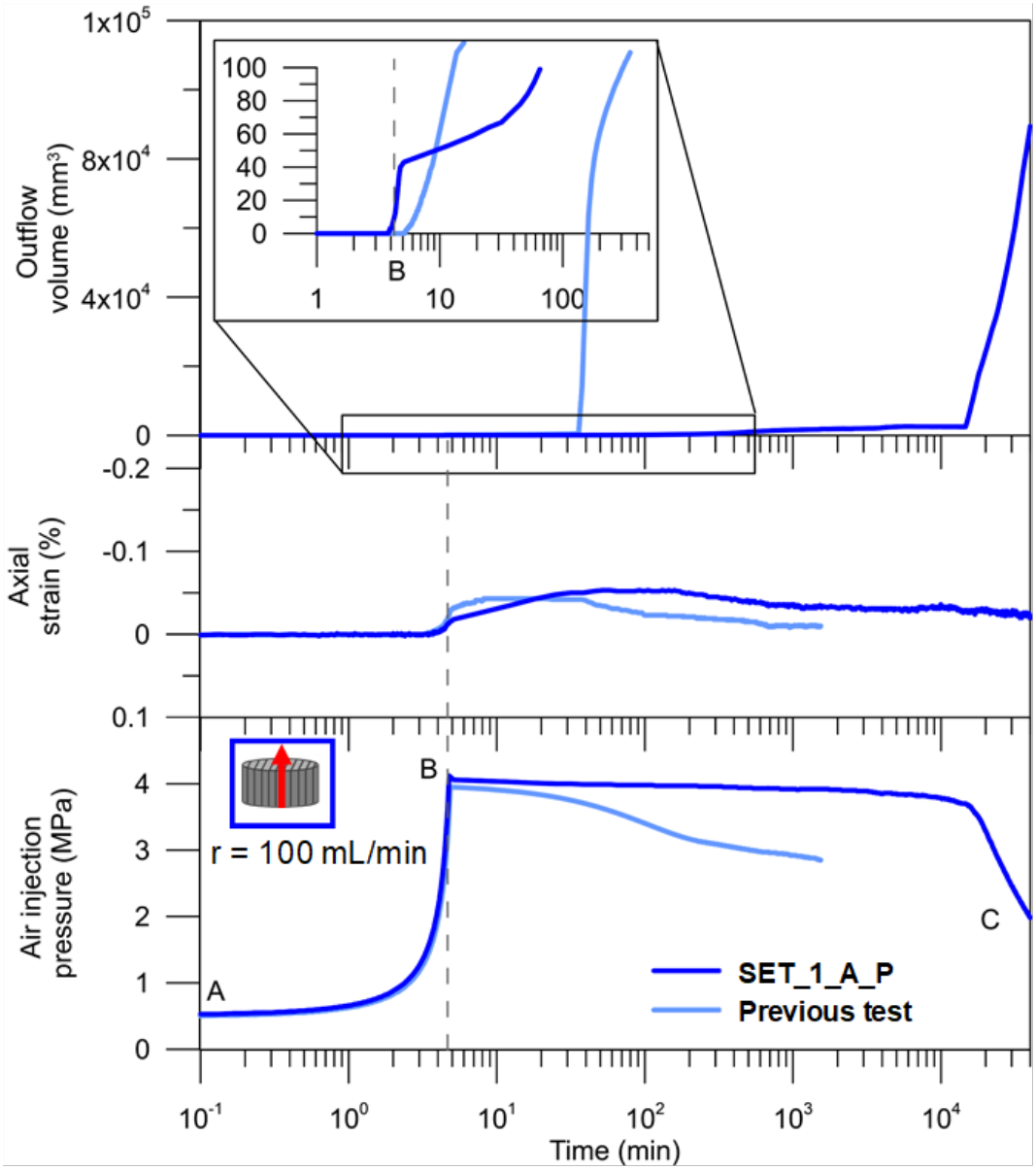

Figure 4-151 – Time evolution of the recorded data during gas injection/dissipation stage for samples with bedding planes parallel to flow: air injection pressure (bottom); axial (middle); outflow volume (top). Zoomed area in the upper graph from 1 to 500 min to observe the initial outflow volume.

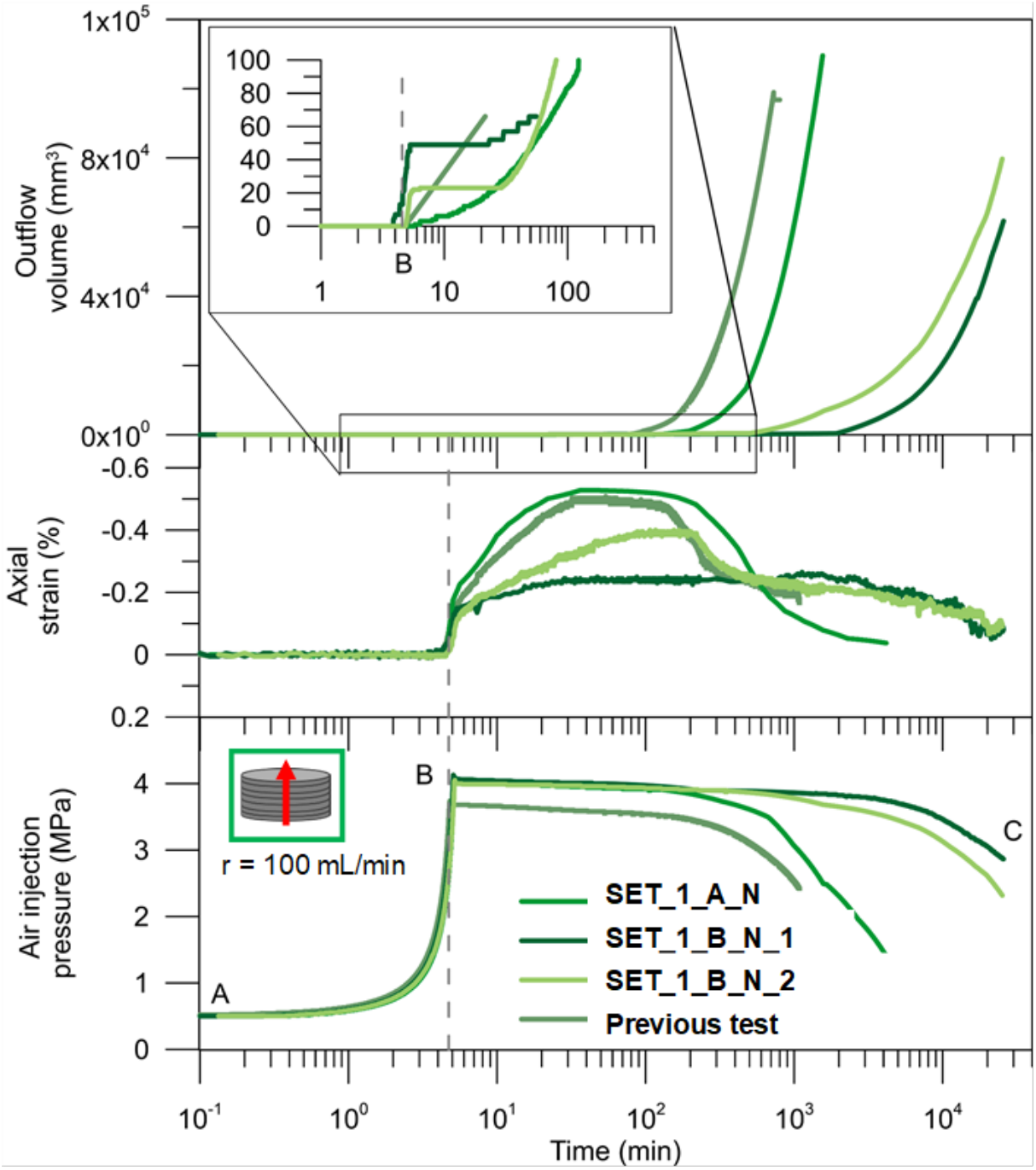

Figure 4-152 – Time evolution of the recorded data during gas injection/dissipation stage for samples with bedding planes normal to flow: air injection pressure (bottom); axial strain (middle); outflow volume (top). Zoomed area in the upper graph from 1 to 500 min to observe the initial outflow volume.

A consistent pattern emerged across all tests: as gas pressure increased, effective stress decreased, prompting sample expansion until outflow occurred. At that point, the upstream pressure decreased, leading to an increase in effective stress, causing the samples to undergo compression. This indicates a highly coupled process in gas migration.

These findings align with trends observed in earlier tests. Samples with bedding oriented normal to flow consistently exhibited greater expansion. This behaviour is consistent with the anisotropic deformation observed during loading and soaking, where samples with bedding planes parallel to the flow are more

constrained from expanding due to oedometer restrictions. Notably, at the fast injection rate, there is an observable delay in response to the gas pressure front propagation, as most of the expansion occurs after shut-off. The initial outflow was detected during the dissipation stage, with the outflow volume rapidly increasing, signifying the breakthrough time. Although the samples used came from different boreholes, these results generally align with and reinforce trends observed in previous tests.

In analysing the outflow volume collected during gas dissipation in SET 1, two distinct procedures were employed to distinguish between gas and water volumes. The initial quantity of pressurized water in the outflow line, encompassing tubes and the PVC piston, was known. Initially, the volume of gas was estimated by applying the ideal gas law to pressurize the fluids in the closed outflow line. Subsequently, the volume of water was calculated by emptying the outflow line and comparing the initial and final volumes. It is worth noting that these procedures may be influenced by the dead volumes of the outflow line, despite rigorous calibration efforts.

Throughout all tests, the volume of displaced water represented a negligible portion of the total outflow, accounting for only around 1%. This suggests that the global degree of saturation after the injection stage remained close to 1.

The observed expansion during gas pressurization and the very slight desaturation during the gas injection/dissipation stage suggest that the primary transport mechanism is gas flow through pressure-dilatant preferential pathways. The consideration of diffusion of dissolved gas through pore water was dismissed due to the rapid nature of the process, and the reported diffusion coefficients for Boom Claywhether measured (Jacops et al., 2013; Jacops et al., 2015) or numerically computed (Gonzalez-Blanco et al., 2016) are low. Confirmation of the development of preferential gas paths was obtained through the analysis of microstructure evolution.

Gas injection/dissipation tests for experiments of SET 3 and SET 4 displayed similar behaviour. During these tests, several aspects were considered.

Figure 4-114 shows the comparison between gas injection using air or Helium in two different samples orientated with the bedding orthogonal to the flow. Results indicate that the gas type did not have a significant influence on the gas transport, although slightly faster dissipation and higher expansion were recorded when using Helium. However, these differences are within the expected range of variability found in other tests.

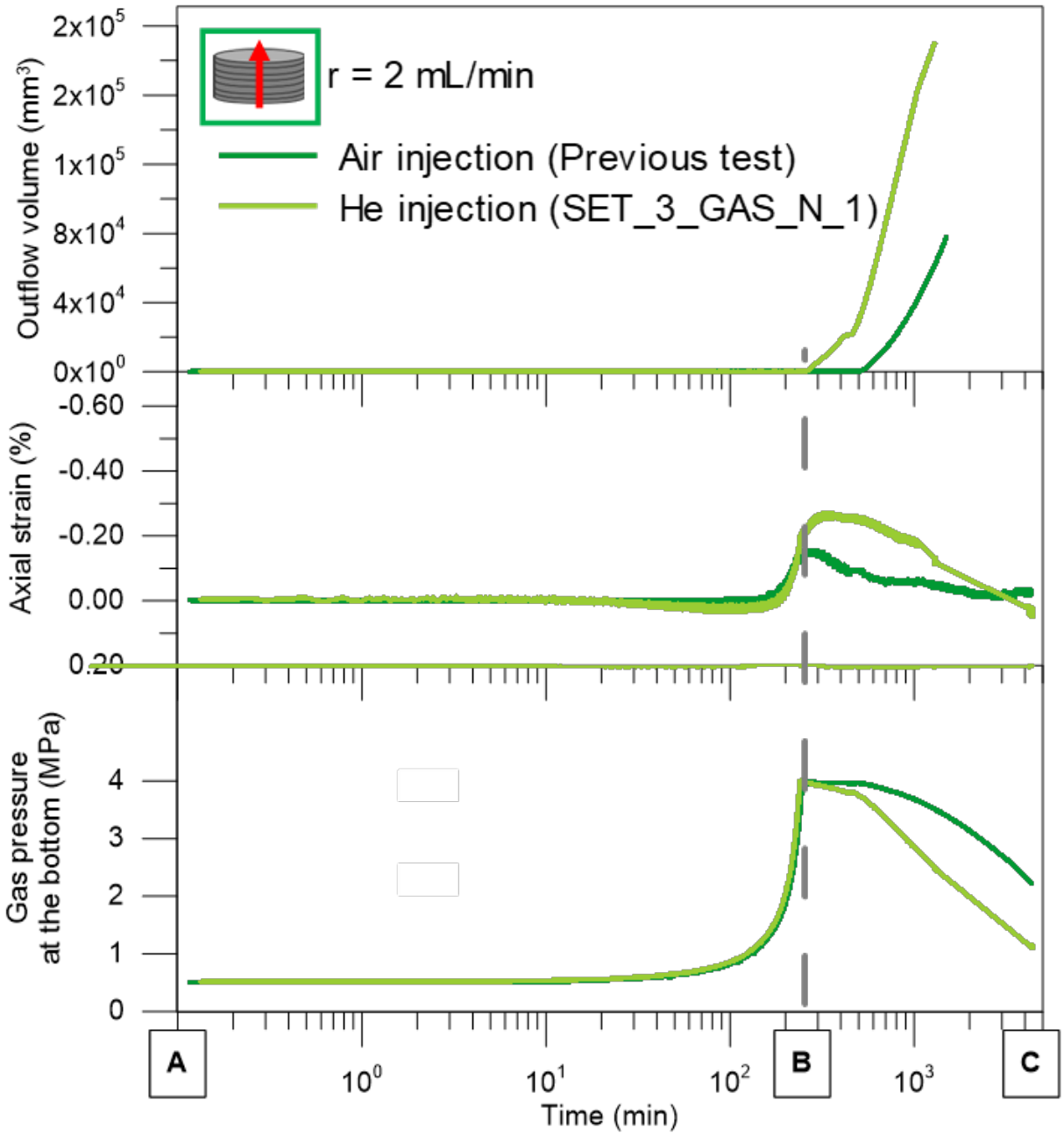

Figure 4-153 – Time evolution of gas injection pressure (bottom), axial strain (middle), and outflow volume (top) for two samples tested with the bedding planes orthogonal to the flow using air and Helium.

To study the possible fissure reactivation after self-sealing (see section 4.5.5.4), a second gas injection stage was conducted on sample SET_1_B_N once it was re-saturated. The results of the second injection are shown in Figure 4-115. Despite the similar behaviour, it can be noticed that for this second injection stage, the pressure dissipation was faster and the expansion larger. Moreover, although the time at which the first outflow occurred was equivalent, in the second, the outflow rate was more rapid, meaning that gas flow experienced less restrictions along the sample, suggesting the reopening of some of the preferential paths formed during the first injection, even if sealed during the re-saturation, still not completely healed. The microstructural analyses will support this hypothesis.

Additionally, a second gas injection was performed after the re-saturation stage for the test of SET 3 (Figure 4-115) and SET4 (Figure 4-116). The response during the second injection with respect to the first one was rather similar in both cases. However, the final expansion strain was larger after the second injection, which also could imply more connectivity of the gas pathways resulting in larger effective gas permeability, as was observed (detailed in section 4.5.5.5).

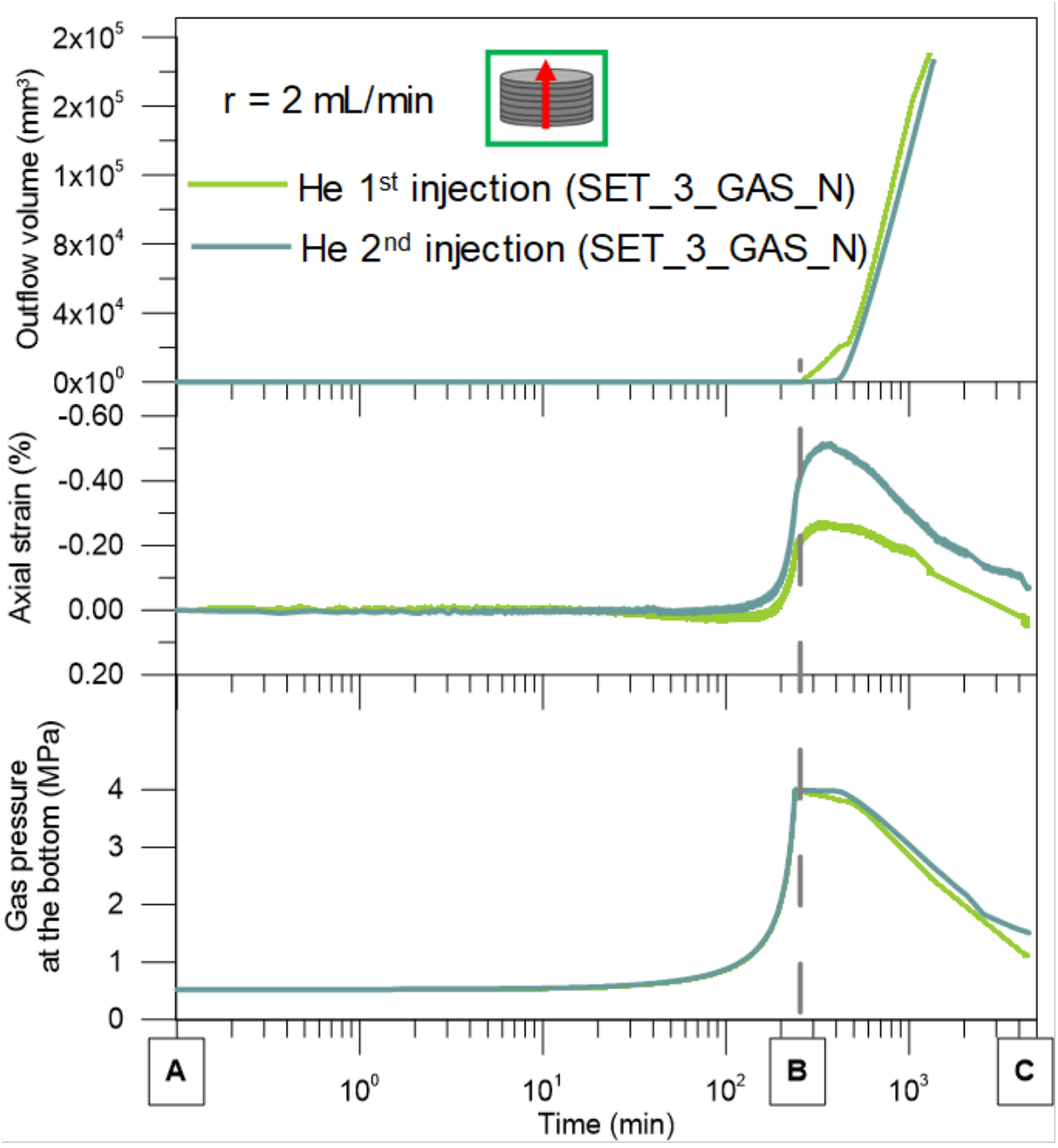

Figure 4-154 – Comparison of two injection stages (before and after re-saturation) in terms of the time evolution of gas injection pressure (bottom), axial strain (middle), and outflow volume (top) for a sample with the bedding planes orthogonal to the flow.

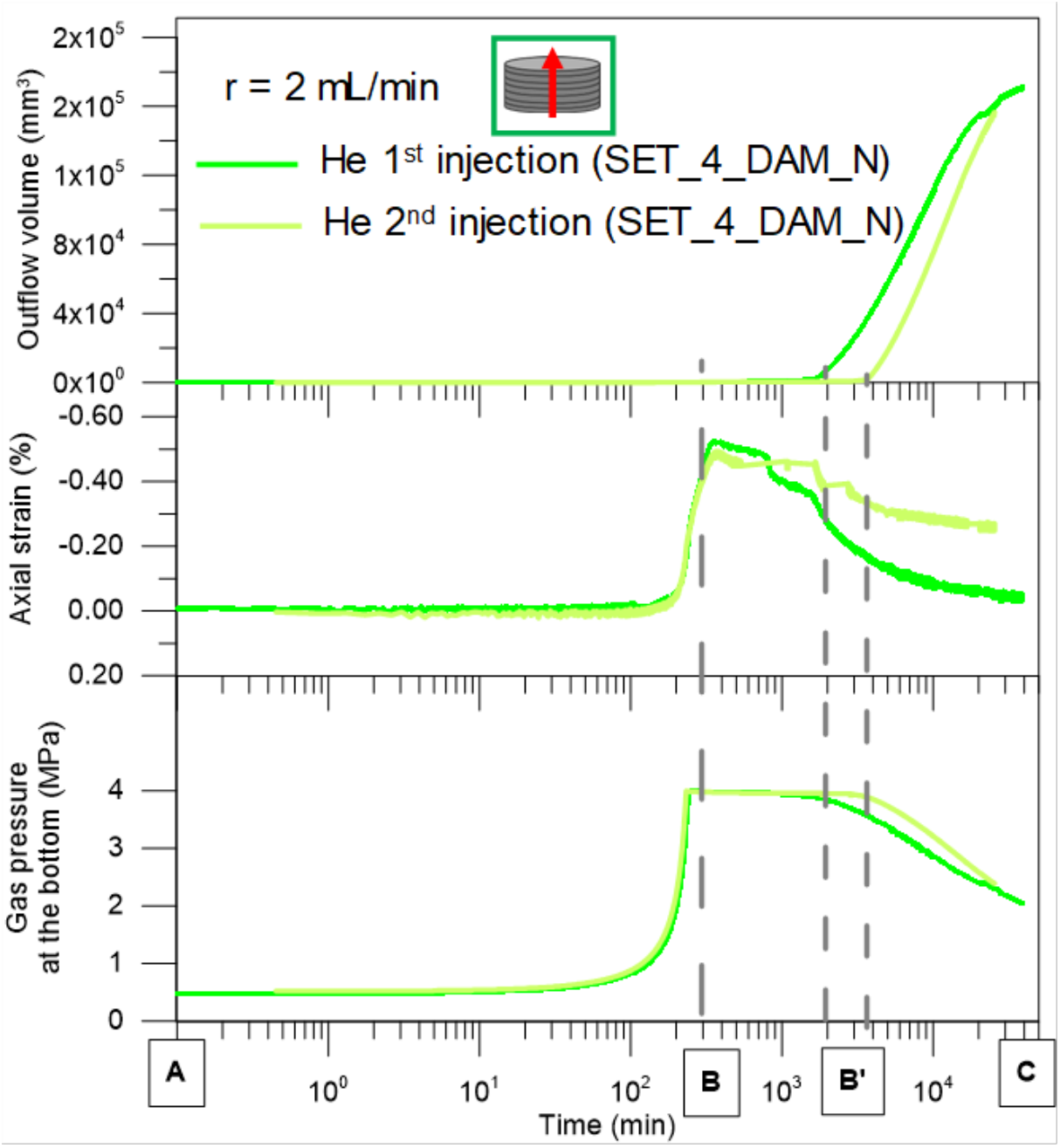

Figure 4-155 – Comparison of two injection stages (before and after re-saturation) in terms of the time evolution of gas injection pressure (bottom), axial strain (middle), and outflow volume (top) for a sample with the bedding planes orthogonal to the flow subjected to previously hydro-mechanical damage.

During the tests presented in Figure 4-115 and Figure 4-116, total vertical and lateral stress were recorded. The lateral stress increased as the gas pressure increased (Figure 4-117) keeping a higher value during all the tests. Consequently, the gas passage in between the oedometer ring and the sample was discarded. The lateral stress at the beginning of the injection stage for the sample SET_4_DAM_N was larger due the previous hydro-mechanical, which resulted in some damage and a reduction of the porosity. It also impacted the slower gas dissipation, given a smaller gas permeability (see section 4.5.5.5)

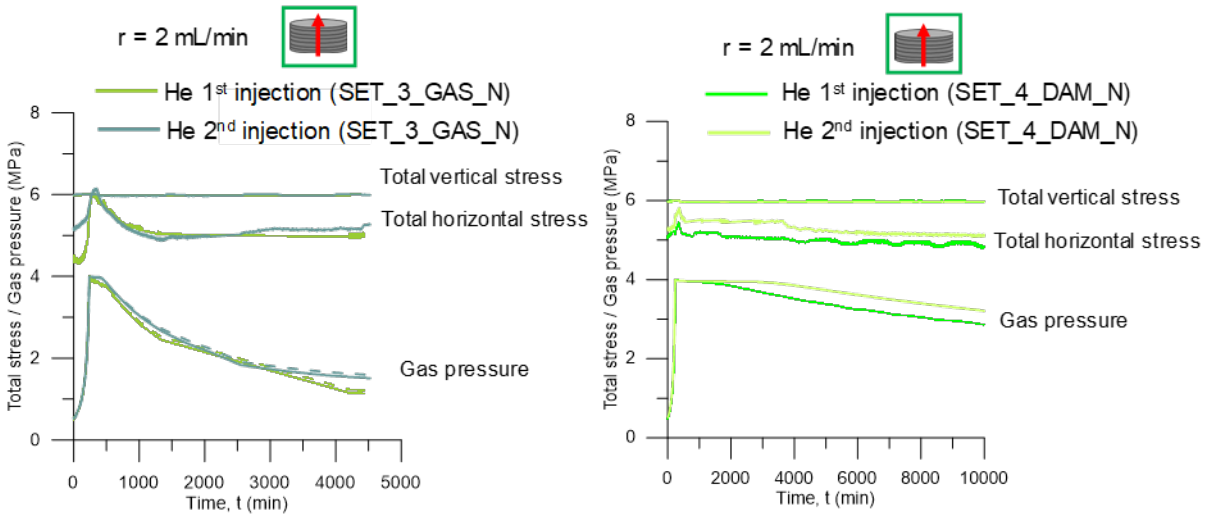

Figure 4-156 – Time evolution of gas pressure and total vertical and lateral stresses during the two gas injection/dissipation stages for samples with bedding planes orthogonal to the flow.

Samples with the bedding planes parallel to the flow were also tested following protocols of SET 3 and SET 4. However, at the time of writing this report, sample SET_4_DAM_P was still running and the results have not been includedhere. Figure 4-118 presents the gas injection data using Helium in the oedometer with lateral stress measurement in comparison with those corresponding to another injection using air in the rigid oedometer ring (Gonzalez-Blanco & Romero, 2022). It can be noticed that the behaviour of the former followed the typical one, but at a certain moment, there was a sharp increase in the outflow volume coupled with a decrease in the gas pressure. This behaviour could be due to the gas passage through the flexible ring-sample interface. This phenomenon can be better explained by looking at the lateral stress evolution (Figure 4-119). The sample with the bedding planes in parallel to the flow developed anisotropic lateral stress and caused an ovality in the ring, that produced lower lateral stress in one of the directions. It seems that at the end of the injection, the lateral stress measured with one of the sensors was equal to the gas pressure, and therefore, the sample could detach from the ring. However, the sharp pressure decrease was delayed, probably affected by the elapsed time taken by the pressure front propagation, since the gas pressure was measured at the bottom of the sample, while the lateral stresses were measured at the mid-height. Even though, after this event of gas passage, the gas pressure dissipation followed the same trend observed in previous tests, pointing that the interface closed and the gas at the end of the stage was transported through the sample.

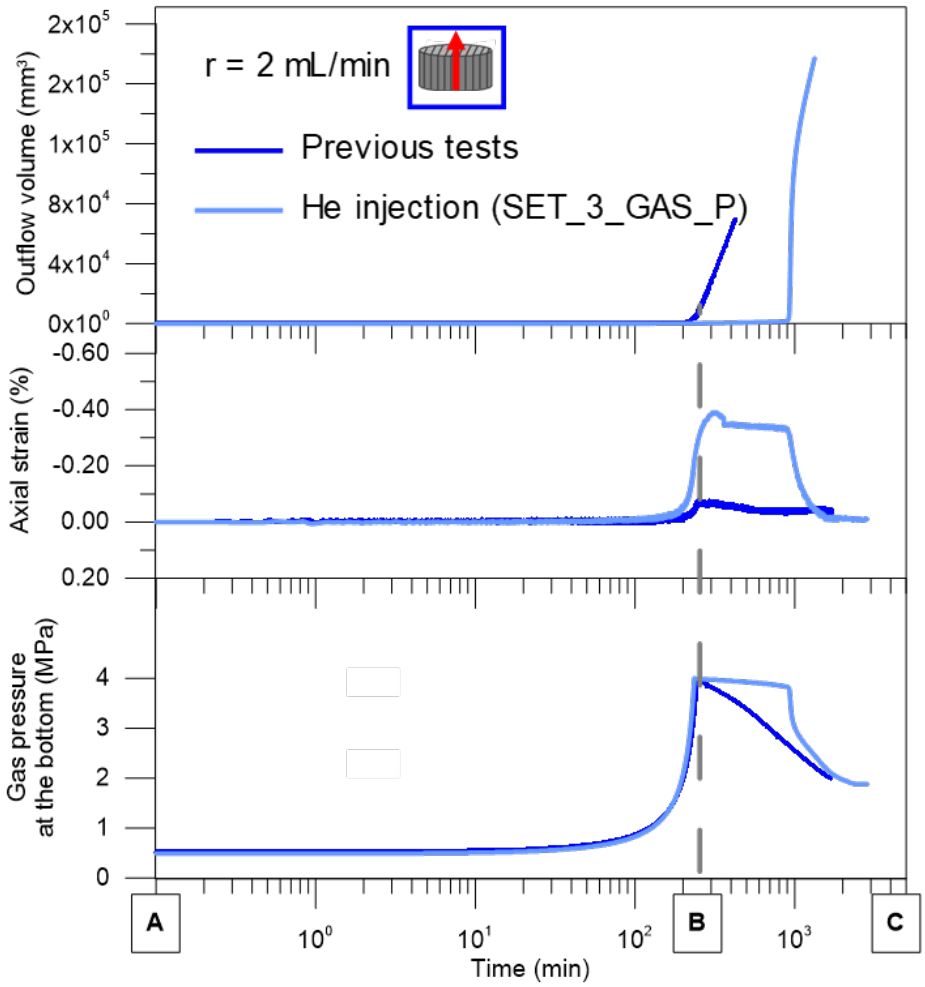

Figure 4-157 – Time evolution of gas injection pressure (bottom), axial strain (middle), and outflow volume (top) for samples tested with the bedding planes parallel to the flow using air and Helium.

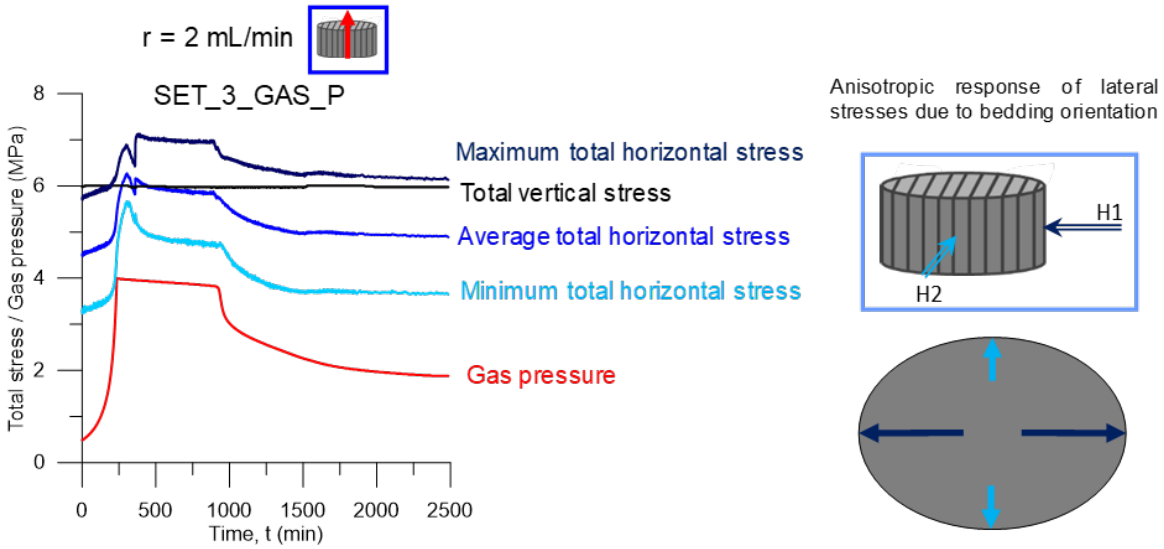

Figure 4-158 – Time evolution of gas pressure and total vertical and lateral stresses during the gas injection/dissipation stages for the sample with bedding planes parallel to the flow. Anisotropic response of the lateral stress development.

The water displaced by the gas during the injection was measured with the developed gas trap system for tests performed in the oedometer cell with lateral stress measurement (Table 4-30). However, these volumes should have been taken with caution since even the dead volumes of the system were considered for the calculations, the accuracy was limited.

Table 4-40 – Volume of water expelled during gas injection and final degree of saturation.

Test	Bedding orientation	Injection stage	Volume of water expelled (mL)	S_r at the end of the injection
SET_3_GAS_N	Orthogonal to the flow	First injection	2.22	0.87
		Second injection	2.6	0.85
SET_4_DAM_N	Orthogonal to the flow	First injection	2.82	0.83
		Second injection	2.75	0.83
SET_3_GAS_P	Parallel to the flow	First injection	1.92	0.89

4.5.5.4 Re-saturation and water permeability

After the gas injection and dissipation stage, the samples from SET 1, 3 and 4 were put in contact with water under atmospheric pressure until they reached steady-state conditions. During this stage, the deformation was very small (less than 0.05%), confirming that no significant desaturation occurred during the gas transport (Figure 4-120).

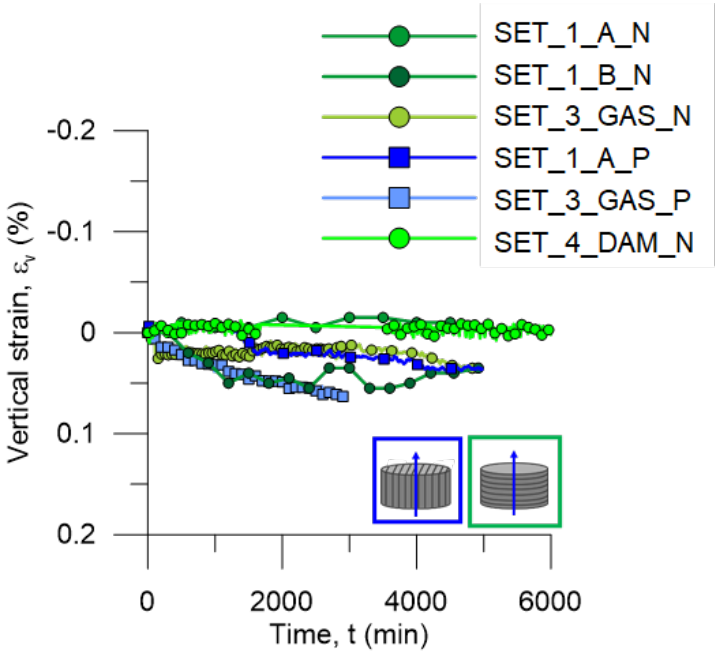

Figure 4-159 – Strain evolution during the re-saturation stage.

After stabilisation, water permeability was measured again by applying a hydraulic gradient at constant vertical stress (downstream and upstream water pressures were increased up to 0.6 MPa and 0.5 MPa, respectively). Figure 4-121 shows the results of this stage in comparison with the results obtained before the gas injection. For each sample, the water permeability values did not present significant changes, which might entail an excellent self-sealing of the fissures that formed during gas injection due to the re-saturation process. As the re-saturation was done under constant vertical stress, the driving mechanism of self-sealing is the swelling of clay minerals, although some creep could also contribute to the closure of the fissures. From these results, it can be concluded that Boom Clay's self-sealing capacity is significant in recovering the hydraulic barrier function.

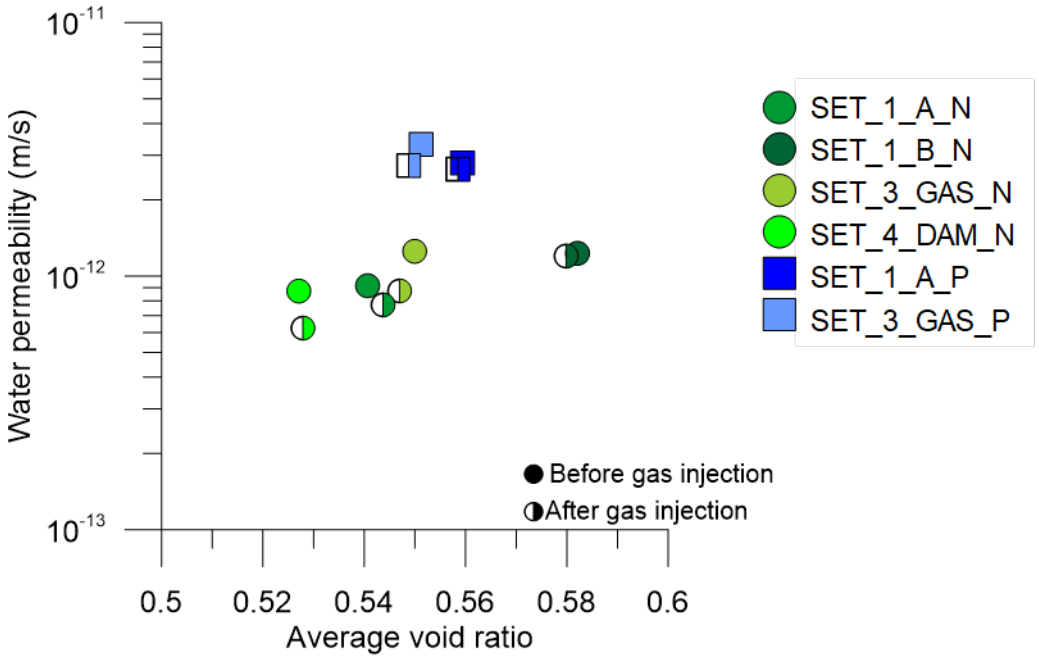

Figure 4-160 – Water permeability before and after gas injection.

4.5.5.5 Gas permeability

The computation of gas permeability was calculated under steady-state conditions during the dissipation stage. Although gas flow was anticipated to occur along localized pathways, for the determination of global gas permeability (k_g), the entire area of the sample was considered. The pressure decay method (Arnedo et al. 2013; Pineda et al. 2014) and the generalized Darcy's law for compressible fluids were employed. The recorded evolution of the absolute pressure decay ($d\bar{u}_g/dt$) from 4.1 MPa to around 2.1 MPa was utilized to estimate the mass of gas, assuming the perfect gas law, with a constant volume of the upstream reservoir (V) and a constant downstream pressure at the top cap ($\bar{u}_{gt}$):

$$k_g = \frac{k_i k_r \rho_g g}{\mu_g} = -\frac{2 L V \rho_g g}{A(\bar{u}_g{}^2 - \bar{u}_{gt}{}^2)} \frac{d\bar{u}_g}{dt} \qquad (4.5.2)$$

where k_i is the intrinsic permeability, k_r the relative permeability to gas, $k_i\,k_r$ represents the effective permeability to gas, independent of fluid properties, as a measure of the ability of this phase to flow in the presence of water, A and L are the cross-sectional area and length of the sample, μ_g the air or Helium dynamic viscosity at standard temperature and pressure, ρ_g the air or Helium density at standard temperature and pressure, and g the acceleration of gravity. $k_i\,k_r$ was used since the degree of saturation of the material was not precisely known during the steady-state dissipation stage.

The effective gas permeability is compared with intrinsic water permeability, measured in fully saturated conditions before and after the injection stage. Figure 4-122 shows it as a function of the void ratio for the two bedding orientations. Three key observations can be clearly made from the figure:

i. Gas permeability consistently exhibits larger values than water permeability regardless of the bedding orientation:

ii. A distinct anisotropy effect is evident in the case of water permeability (as seen in Figure 4-110, Figure 4-111 and Figure 4-121), which is not replicated when gas flow is established;

iii. A second stage of gas injection slightly increases the gas permeability.

The first two points align with the findings reported by Gonzalez-Blanco and Romero (2022). Consequently, gas flows through the fissures generated during gas pressurization, increasing the permeability for both orientations. This is substantiated by microstructure analyses in the following section. Additionally, in the previously damaged sample (SET 4) subjected to a loading path that overpassed the yield stress, both gas and water permeability consistently exhibited lower values, in line with the decrease in porosity.

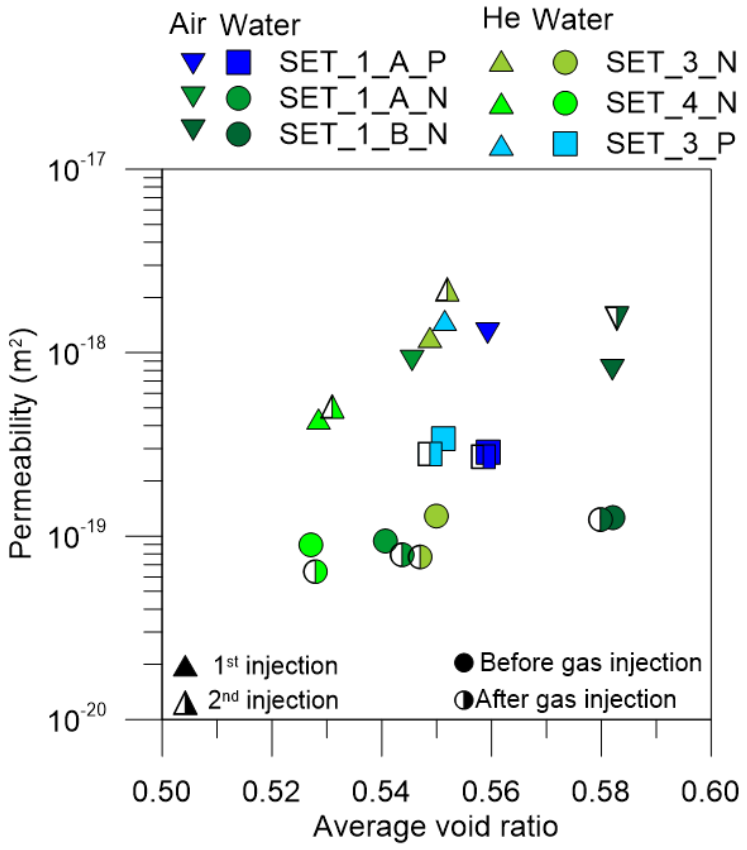

Figure 4-161 – Permeability to water and gas against void ratio.

4.5.5.6 Microstructural analyses

The microstructure of the samples was analysed through Mercury Intrusion Porosimetry (MIP) and micro-computed tomography (μ-CT), and the findings were compared with those presented in Gonzalez-Blanco and Romero (2022) for the initial state and after the gas injection tests. Representative sub-samples were meticulously trimmed from oedometer specimens after tests and under unstressed conditions. Two distinct shapes were considered for the analyses: a cubical shape of 1000 mm³ for MIP and a cylindrical shape measuring 10 mm in height and 10 mm in diameter for μ-CT tests to avoid corner artefacts. In both cases, the samples underwent a freeze-drying process, essential for MIP, to facilitate results' comparison.

The Pore Size Density curves (PSDs) obtained with MIP for the intact state exhibited a monomodal distribution with a dominant size of 70 nm and a low volume at the macro-scale. In contrast, samples after gas injection tests in previous research campaigns (Gonzalez-Blanco et al., 2017; Gonzalez-Blanco & Romero, 2022) consistently revealed a new family of large pores. These larger pore sizes, exceeding 2 μm, were linked to the expansion experienced by Boom Clay samples during gas injection and early shut-off stages, as well as the dilation of gas pathways. These PSDs are now compared with the ones obtained after re-saturation (SET_1_A) and after the second gas injection stage (SET_1_B and SET_3) (Gonzalez-Blanco et al., 2023). In Figure 4-123, the PSD curves are presented in a log-log plane to highlight the larger pore sizes. After re-saturation, lower volumes at the macro-scale were observed compared to samples after gas injection for both bedding orientations. However, these volumes were still slightly higher than those corresponding to the intact sample, suggesting that there was no complete healing of the material during re-saturation, and some pores or fissures did not completely close. On the other hand, the PSD of the samples after the second gas injection revealed the highest volume at the macro-scale. The analysis of μ-CT images allows for a better understanding of these results.

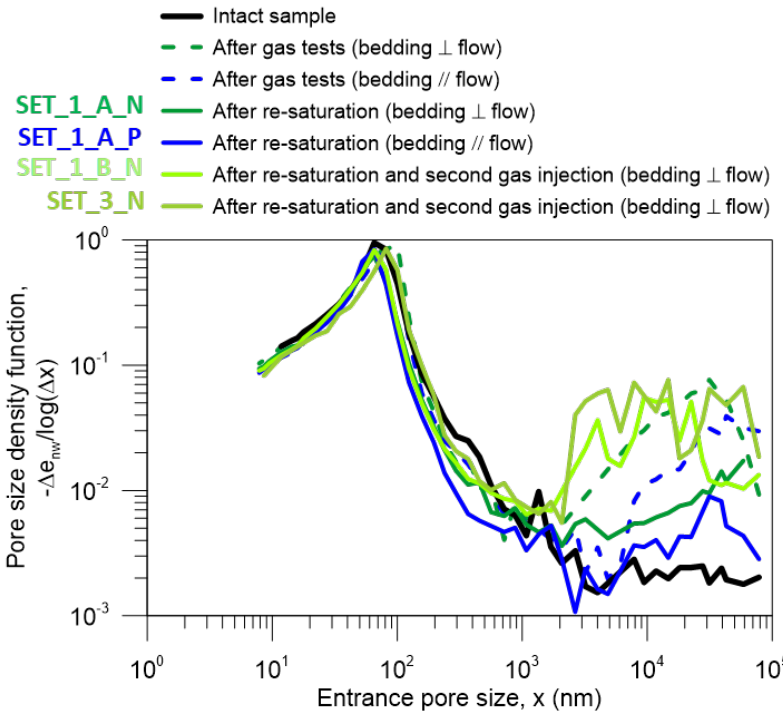

Figure 4-162 – Pore size density curves from MIP on the intact sample, samples after gas injection tests, samples after re-saturation and samples after second gas injection.

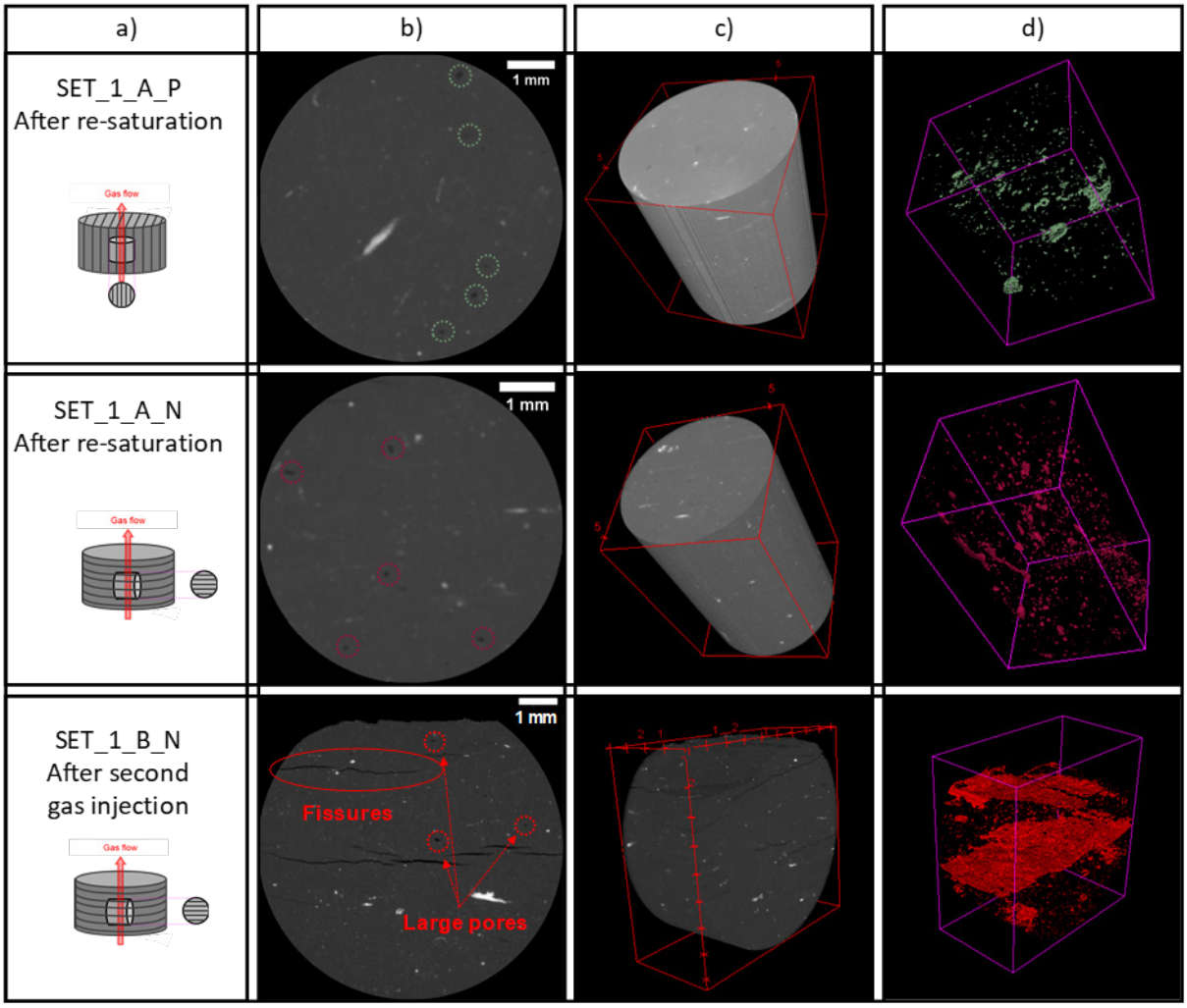

Figure 4-163 – a) Sub-sampling scheme; b) cross-section at the mid-height; c) 3D volume reconstruction of μ-CT images; and d) porosity segmentation of the samples S1_P after re-saturation (top) and S2_N after re-saturation (middle) and S3_N after second gas injection (bottom).

μ-CTs were conducted on cylindrical samples with 720 projections over 360º and a voxel size of 20 µm. The sub-samples were trimmed so that the bedding planes were in the cross-section of the cylinder. For one sample (SET_1_B_N), two sub-samples were trimmed at different orientations to visualize the fissures that might develop due to gas passage between the bedding planes, with an improved resolution of 10 µm. The sub-sampling orientations are sketched in Figure 4-124 and Figure 4-125. The figures also present cross-section images at the mid-plane and the 3D volume reconstructed using ImageJ software (Schneider et al. 2012).

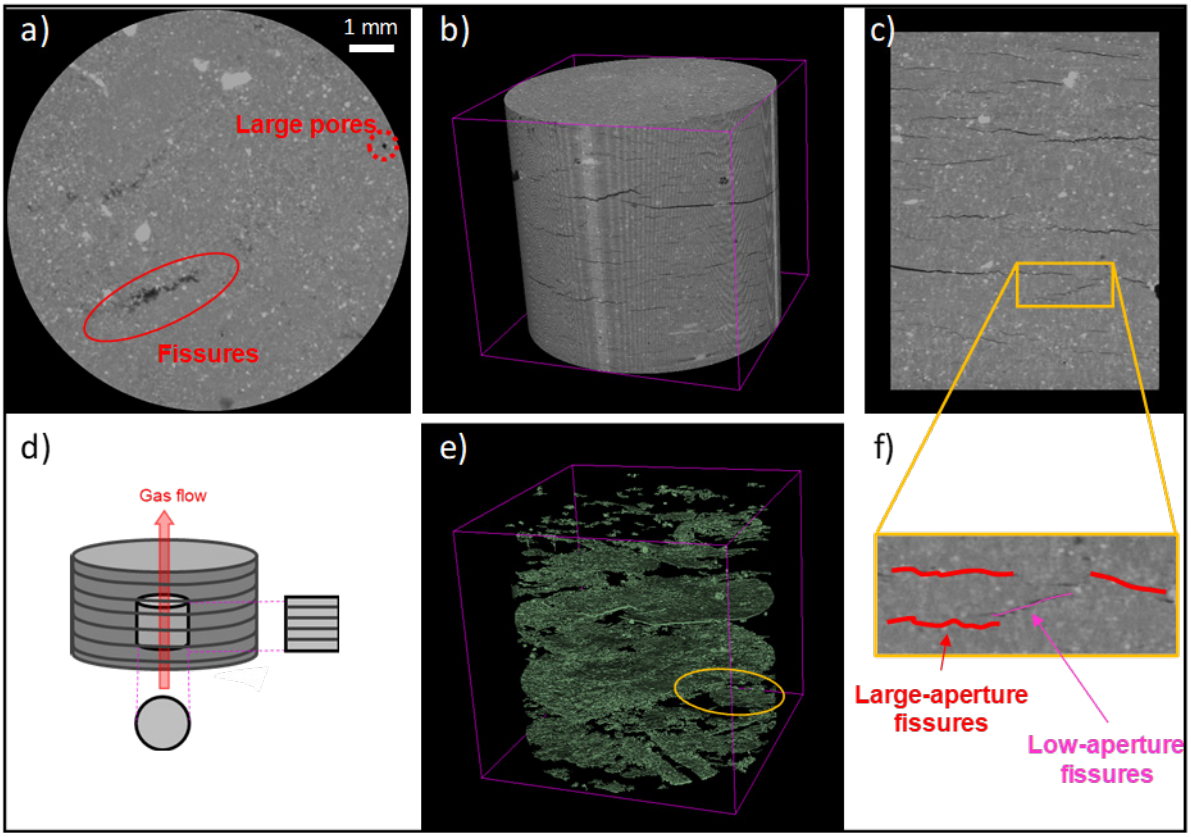

Figure 4-164 – μ-CT data of sample SET_1_B_N after second gas injection with improved resolution. a) Cross-section at the mid-height; b) 3D volume reconstruction of μ-CT images; c) longitudinal-section at the middle; d) sub-sampling scheme; e) porosity segmentation and f) zoom showing a low-aperture fissure bridging large-aperture fissures.

As depicted in Figure 4-124, μ-CT did not identify large-aperture fissures (larger than 40 μm, double the scanner resolution) in either orientation after the re-saturation process. This is in contrast to systematic detection after gas injection tests in previous research (Gonzalez-Blanco & Romero, 2022), which suggests excellent self-sealing of the fissures formed during gas injection. However, some large pores, that were not observed previously, were detected in both orientations. These are associated with gas entrapped in macro-pores that were not completely closed during re-saturation and magnified during undrained unloading (Gonzalez-Blanco et al., 2023). These pores, highlighted in the cross-section images (Figure 4-124b) and isolated in Figure 4-124d after a segmentation process, did not show connectivity at the current resolution. This is consistent with the recovery of the initial water permeability after re-saturation.

In contrast, large-aperture fissures acting as gas pathways were detected in the sample after the second injection stage (Figure 4-124 at the bottom), along with some large pores likely caused by gas entrapment during the first injection. In this configuration, the fissures coincided with the direction of the bedding planes, as reported by Gonzalez-Blanco and Romero (2022). However, to establish a flow normal to the bedding, the development of low-aperture fissures bridging the bedding planes is required, which is not evident in the images in Figure 4-124. To attempt to detect these fissures, sample SET1_B_N was also trimmed with the bedding orthogonal to the axis of revolution, as indicated in Figure 4-125d. With the sub-sample in this position and an improved scanner resolution of 10 μm, it became possible to discern some low-aperture fissures. However, these fissures were unconnected (Figure 4-125f) due to closure during gas dissipation (compression of the sample in the last stage). Only

a few fissures with apertures between 20 and 40 µm were detected obliquely to the bedding planes (Figure 4-125). Therefore, the majority of these fissures connecting bedding planes should have apertures between 2 and 20 µm, as detected in the PSD curves determined by MIP.

To provide a comprehensive overview that facilitates the understanding of microstructural evolution due to different processes, Figure 4-126 compares µ-CT images for samples with bedding planes parallel and normal to the flow at the initial state, after gas injection, and after re-saturation. It also includes an image of the sample with bedding planes normal to the flow after a second injection.

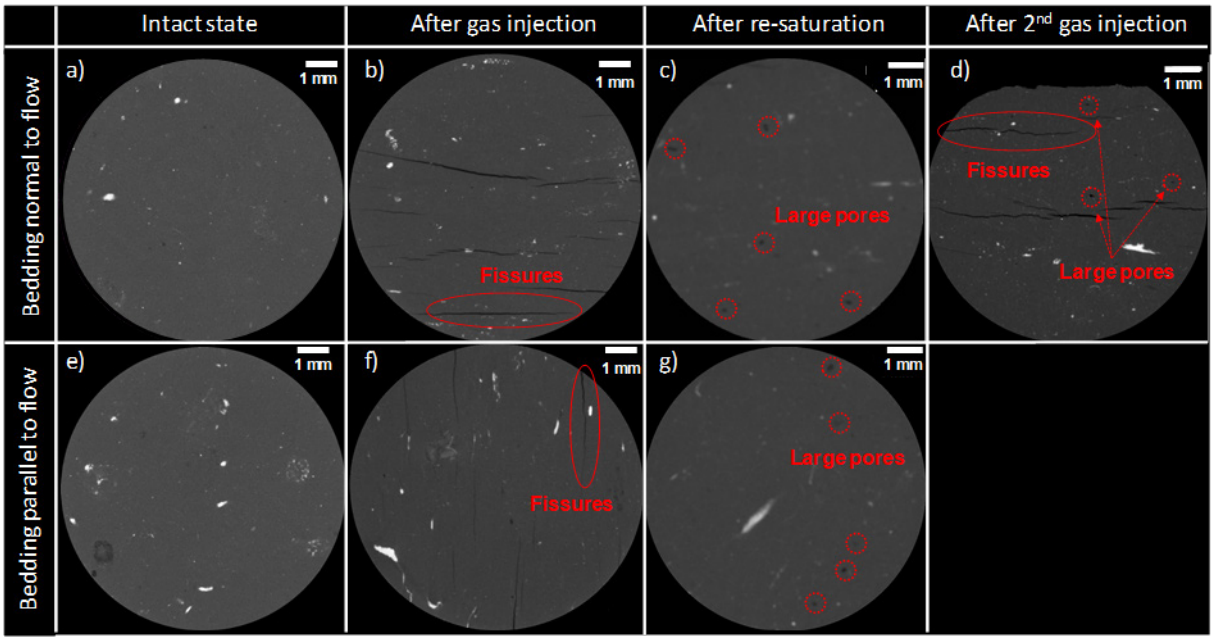

Figure 4-165 – Cross-section µ-CT images of Boom Clay samples. Top: sample with bedding planes normal to flow a) at the intact state (Gonzalez-Blanco & Romero 2022); b) after gas injection (Gonzalez-Blanco & Romero 2022); c) after re-saturation; d) after second gas injection (Gonzalez-Blanco et al 2023). Bottom: sample with bedding planes parallel to flow: e) at the intact state (Gonzalez-Blanco & Romero 2022); f) after gas injection (Gonzalez-Blanco & Romero 2022); g) after re-saturation (Gonzalez-Blanco et al 2023).

For the intact state, only a very small volume of pores is identifiable, and bedding planes are not visible at the current resolution. After gas injection, samples in both orientations exhibit fissures in the direction of the bedding planes. The analysis of the fissure network (Gonzalez-Blanco & Romero, 2022) revealed that in the sample with bedding planes parallel to flow, the fissures are closer and have a lower mean aperture than in the opposite orientation. This is because radial deformation was restricted by the oedometer conditions. However, the fissure density was remarkably similar for both orientations, indicating no significant orientation effects during gas transport, consistent with the results on effective gas permeability that did not show anisotropy.

After re-saturation, the fissures self-sealed in both orientations, but as mentioned earlier, some large pores remained after this process. Again, the volume detected is quantitatively similar for both orientations.

In the case of the sample subjected to a second injection, the mean aperture of the fissures is slightly higher than after the first gas injection, consistent with the higher gas permeability. This is a

consequence of some memory of the fissure network developed during the initial gas injection, which involved mechanical damage to the material (Gonzalez-Blanco et al., 2023). Additionally, the pores with entrapped gas could have formed due to the non-uniform closure of the pathways during re-saturation. It is essential to note that the microstructural analyses were performed after an undrained loading, and as a result, these air-filled macro-pores could be enlarged during this phase, as the volume of entrapped gas under stress conditions might not be significant.

4.5.5.7 Interpretation of the results

The differences between gas and water permeability are linked to the evolution of the microstructure in Boom Clay. To account for it, a simple model was developed, using the volume of fissures and pores at the macro-scale detected after the tests and related them to the permeability measured at the last stage of each test (Gonzalez-Blanco et al. 2023).

A macro-fissure fraction was defined to consider the changes in the microstructure:

$$f = \frac{e_f + e_M}{e} \tag{4.5.3}$$

where the e_f is the fissured void ratio (volume of fissures to the volume of solids V_f/V_s), e_M is the macro void ratio (volume of macropores to the volume of solids V_M/V_s) and e represents the void ratio at the end of the tests. The threshold value chosen to define the macro-scale was 2 µm (Gonzalez-Blanco & Romero, 2022; Gonzalez-Blanco et al., 2023) since it marked the discrepancy in between the PSDs of intact sample and samples after testing.

The volumes to define f were calculated from µ-CT images after the filtering process and from MIP for all the tests including those after gas injection of previous research (Gonzalez-Blanco & Romero, 2022). However, due to the resolution, only pores and fissures larger than 40 µm can be detected with this technique. Consequently, MIP data was finally considered for the analysis since it provided data of a wider range of pore sizes than µ-CT. The values of e_f and e_M from MIP data were determined by calculating the area below the PSD curves after the tests for pore sizes x larger than e.

The self-sealing capacity was studied by comparing the water permeability before and after gas injection, and the initial anisotropy (water permeability of samples with bedding planes parallel to the flow was systematically larger) should be taken into account (Figure 4-110) since it was recovered after the re-saturation (Figure 4-121). Therefore, a permeability ratio was defined as $k/k_{initial}$, being k the permeability measured during the last stage of the tests (whether during gas or water flow) and normalised with the initial permeability to water before any injection.

The permeability ratio was then calculated for all the samples to correlate it with the macro-fissure fraction f:

$$\frac{k}{k_{initial}} = [\alpha_i(f - f_0) + 1] \tag{4.5.4}$$

where f_0 represents the volume of the macro-pores at the intact state, which is independent of the bedding orientation and can be obtained from MIP data. Considering pore sizes larger than 2 µm for the calculation, $f_0 = 0.02$. Conversely, the value of α_i is a constant parameter that depends on the orientation of the bedding concerning the flow and was fitted with the experimental data.

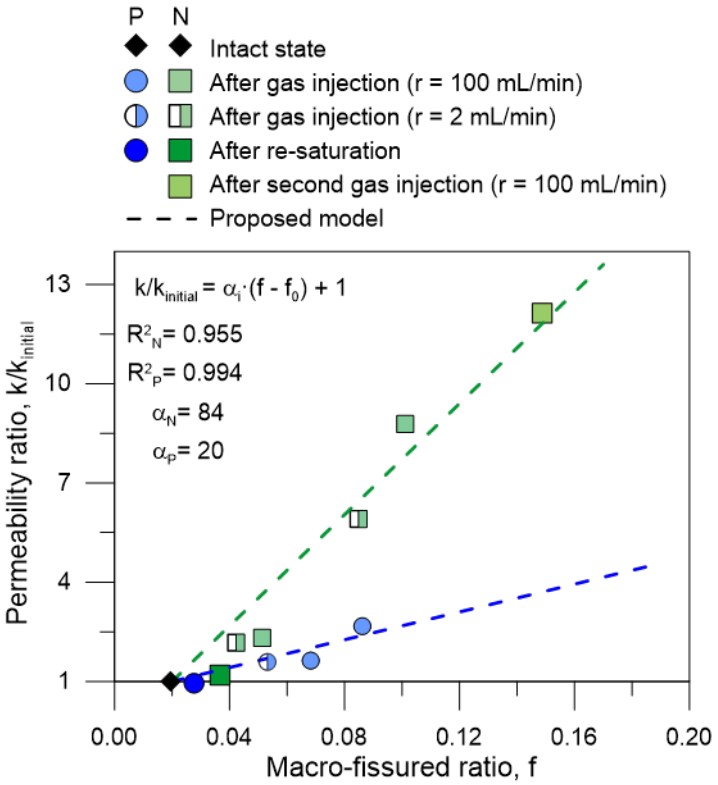

Figure 4-166 – Proposed linear model relating the macro-fissured ratio with the permeability ratio for both bedding orientations (P: samples with bedding planes parallel to flow; N: samples with bedding planes normal to flow).

The suggested model (Figure 4-127) accounted for several phenomena: (i) the formation of fissures during gas injection, leading to an increase in effective permeability; (ii) the subsequent closure of these fissures upon re-saturation, resulting in the restoration of initial permeability, encompassing the unconnected macro-pores filled with occluded gas; and (iii) the enlargement of the macro-fissure ratio upon successive injections, illustrating the simultaneous development of fissures and macro-pores, ultimately leading to largest gas permeability.

However, it was required to calibrate the slope parameter individually for each orientation. Samples with bedding planes perpendicular to the flow exhibited a more pronounced increase in permeability ratio for equivalent damage during gas injection. Specifically, a value of $\alpha_P = 20$ was derived for samples with bedding planes parallel to the flow, whereas $\alpha_N = 84$ was determined for the opposite orientation. This discrepancy is a result of the inherent anisotropy in Boom Clay and the influence of oedometer conditions. The initial permeability was greater in samples with bedding planes parallel to the flow due to the favourable alignment of these initially closed gaps. Gas flow needed the opening of bedding, coupled with the development of bridging planes. During this process, samples with bedding normal to the flow encounter fewer restrictions due to oedometer conditions, resulting in a greater expansion during gas pressurization and dissipation. Despite comparable gas permeability values for both orientations, the increase in permeability relative to the initial state was more pronounced for samples with bedding planes normal to the flow. This disparity is captured in the model through a larger α_i parameter.

After re-saturation and fissure closure, the initial permeability was nearly restored for both orientations, returning to the initial anisotropy. Figure 4-128 provides a schematic compilation of the key parameters involved in each process. Despite the model's simplicity, it effectively describes complex macroscopic

hydro-mechanical response, including gas transport in initially saturated Boom Clay and its self-sealing capability, by examining changes in the microstructure at key stages of the tests.

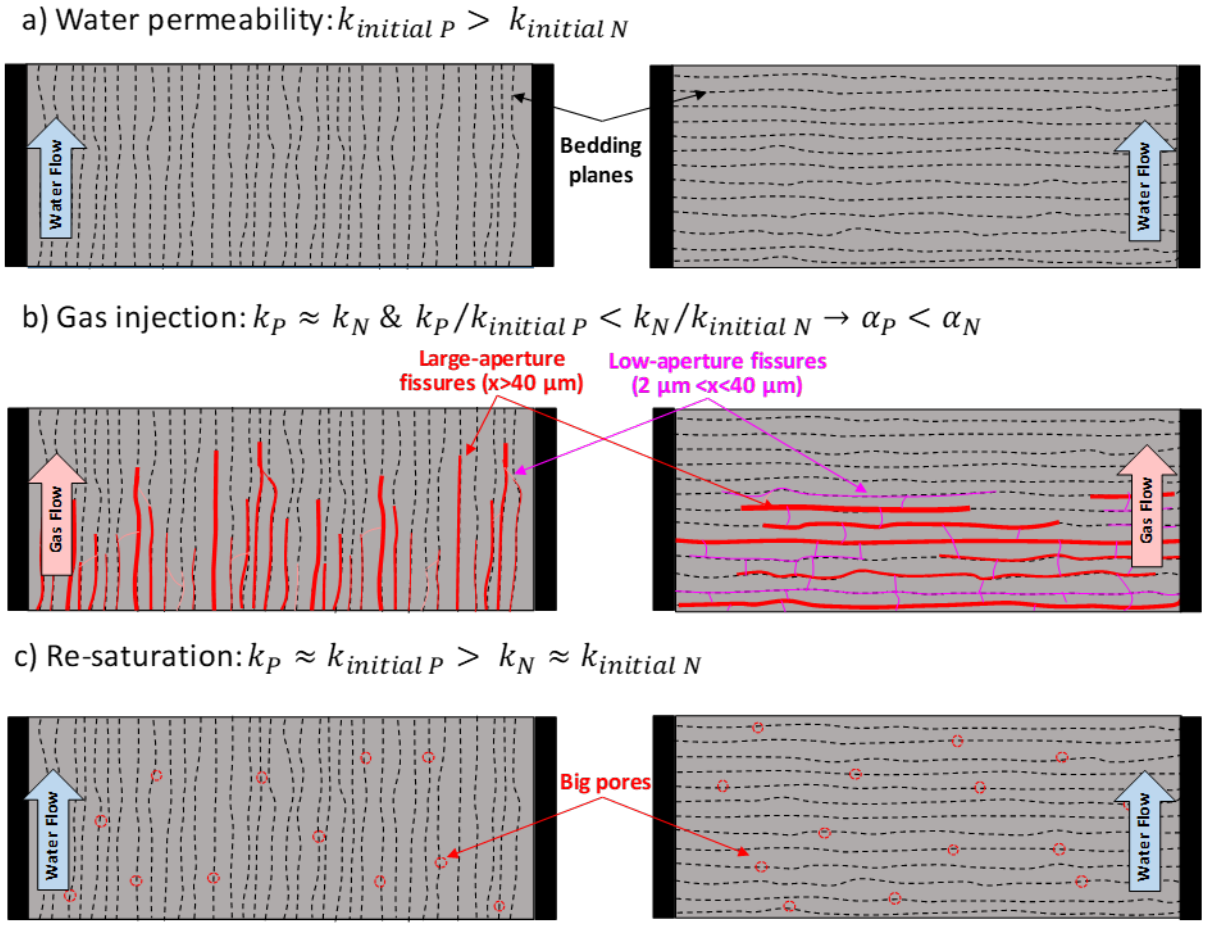

Figure 4-167 – Illustration of fluid transport during each process outlined by the model, highlighting key variables and parameters. Dashed lines denote bedding planes, continuous lines depict gas pathways, and circles symbolize pores containing entrapped gas.

4.5.6 Summary

Initially, the transport of gases, which is crucial to ensure the long-term feasibility of argillaceous formations for the deep disposal of radioactive waste, was studied. For that, an experimental campaign was launched using a multi-scale and hydro-mechanical coupled methodology. Gas injection and dissipation tests under oedometer conditions in saturated deep Boom Clay were carried out. Relatively fast controlled-volume rate (100 and 2 ml/min) gas injection tests (gas pulse tests) were performed in order to study gas flow mechanisms associated with the opening of stress-dependent pathways, rather than on slower displacement flow (displacement of the wetting fluid by the invading non-wetting fluid) and gas diffusion mechanisms through the clay matrix. The tests were conducted on samples with oriented bedding planes (parallel and orthogonal to the flow), varying gas injection rates and stress states, with the aim of investigating their impact on the coupled hydro-mechanical mechanisms that govern gas transfer. The experimental setups permitted volume changes, and the deformation response was studied throughout the stages of gas pressure increase and dissipation.

As gas pressure increased, effective stress decreased, prompting sample expansion until outflow occurred. At that point, the upstream pressure decreased, leading to an increase in effective stress, causing the samples to undergo compression. In all the tests, the rapid increase in gas outflow volume at maximum expansion during gas pressurization and the higher effective permeability to gas during the gas dissipation stage (compared to water permeability results before the gas tests) indicated the development of preferential pathways (fissures) across the specimen. Furthermore, the effective gas permeability did not significantly depend on the orientation of the sample.

The gas injection rate had a significant influence on the stress-strain response observed during both the gas injection and dissipation stages. At slower rates, expansions occurred during the injection stage, given the nearly equilibrated pore pressure. In contrast, at faster rates, this expansion response was temporally delayed. The occurrence and timing of these distinct behavioural features are contingent on the porosity of the rock. For Boom Clay samples, an injection rate of 2 ml/min can be categorized as slow. However, for the low-porosity indurated clays, the 2 mL/min rate yielded results comparable to the faster rate of 100 mL/min (Gonzalez-Blanco et al., 2022). Additionally, the orientation of bedding planes was investigated and proved to be key in the volume change behaviour during gas migration. Samples with bedding planes orthogonal to gas flow experienced less constraint to expand and consistently exhibited higher deformations than samples with bedding planes parallel to the flow.

In addition, the effect of gas type on the gas transport properties was analysed finding no significant differences between the response of Boom Clay against air and Helium injection. Moreover, the quantity of water displaced by gas during the gas injection/dissipation stages was measured using an advanced gas trap system. The results reflected that the majority of the fluid collected upstream was gas together with a residual amount of water that only meant a small desaturation of the clay matrix. This fact reinforced the idea of gas transport through preferential pathways.

The microstructural study after gas tests by using complementary techniques confirmed the opening of fissures with varying apertures and separations. Additionally, MIP results identified a new family of fissures larger than 2 μm that did not depend on the orientation and aligned with the isotropic response of effective gas permeability. Image processing using μ-CT confirmed the opening of fissures with large apertures (> 40 μm), primarily developing along weaker bedding planes. With this technique, lower mean apertures and closer mean separations were detected with bedding planes parallel to axial flow. However, the density of fissures was similar in both orientations, in agreement with the observations from MIP results.

The mechanism for gas transport with bedding planes orthogonal to flow appeared to be driven by low-aperture fissures with narrower separations connecting non-perfectly parallel bedding planes. Therefore, it was considered that these inter-bedding and low-aperture pathways were also very efficient in gas transport, as indicated by the effective permeability to gas showing no clear anisotropy.

In the second stage of the work, the ability to self-seal of Boom Clay was assessed since it is a property that impacts the hydraulic barrier function of radioactive waste disposal systems. The effectiveness of the self-sealing was evaluated by comparing water permeability before and after the gas invasion. The initial water permeability was determined under oedometer conditions for samples with two bedding orientations: parallel and normal to the flow, displaying a distinct anisotropic behaviour. Notably, samples with bedding planes favourably oriented to the flow (parallel) exhibited higher initial water permeability. Following this, the samples underwent a gas injection and dissipation stage at constant vertical stress. As explained above, this gas invasion led to the development of pressure-induced fissures. During re-saturation, very small deformations were recorded pointing out to the closure of the localised gas paths. The re-saturation of the samples at constant vertical stress resulted in the restoration of the initial permeability for both orientations, replicating the original anisotropy. This was considered evidence of the Boom Clay's effective self-sealing capacity. However, complete self-healing was not conspicuous, as microstructural analyses revealed higher volumes at the macro-scale than in

the initial state. This could be attributed to potential gas entrapment or occlusion in large pores, which were not entirely closed during re-saturation. Nevertheless, these pores did not exhibit connectivity, aligning with the restoration of the initial permeability.

In a further step, the effect of a subsequent gas injection stage was addressed in order to study possible fissure reactivation during gas transport after self-sealing. The effective gas permeability measured in this stage was the highest, aligning with the largest volume of pores at the macro-scale as detected by MIP. Analyses of μ-CT images revealed the opening of large-aperture fissures in the direction of the bedding planes, and with improved resolution, low-aperture fissures bridging the bedding planes were also identified. Furthermore, some large pores were discerned in the images, likely associated with gas entrapment during the initial injection and subsequently enlarged during undrained unloading. These observations suggest that the second episode of gas invasion could reopen the fissures, facilitating the flow of gas with greater ease.

Finally, a model was put forward to account for the multi-scale information gathered during the experiments. The model can explain the macroscopic response of permeability evolution (both gas and water) by introducing a microstructural damage variable. A macro-fissured void ratio was defined by using MIP data, that captured the evolution of the Boom Clay's pore network from its initial state to the condition following various transport processes; while the permeability ratio described the permeability changes with respect to the initial one. Despite its simplicity (the model only used two parameters, one from the microstructural experimental data of the initial state, and the other as a fitting parameter), the model demonstrates the capability to reflect complex hydro-mechanical behaviours, encompassing gas injection, self-sealing and fissure reactivation on a subsequent gas injection.

Additionally, during this work, complementary aspects were assessed. All tests followed robust and comparable protocols, giving priority to restoring in-situ conditions and full saturation. The hydro-mechanical response was studied during the initial stages. Furthermore, the construction of a new experimental oedometer cell, specially designed to measure the lateral stress made it possible to have a more detailed picture of the stress state during the different hydro-mechanical paths, including gas injection and dissipation. This was particularly important since allowed to dismiss the gas flow through the sample-cell interface, ensuring that gas was transported throughout the sample.

4.5.7 Key learning points

4.5.7.1 New knowledge acquired

During this project, an extensive experimental campaign in Boom Clay, a plastic argillaceous rock potential for hosting nuclear waste in Belgium was developed. The new knowledge acquired can be summarized in the following points:

- Gas transport under oedometer conditions is a highly coupled process: as gas pressure increased, effective stress decreased, prompting sample expansion until outflow occurred, followed by the upstream pressure decreased, which led to an increase in effective stress, causing the samples to undergo compression.
- The gas injection rate had a significant influence on the stress-strain response observed during the gas injection and dissipation phases. At slower rate (2 ml/min), expansions occurred during the injection stage, given the nearly equilibrated pore pressure. In contrast, at faster rate (100 ml/min), this expansion response was temporally delayed.
- The bedding planes' orientation affects the volume change behaviour. Samples with bedding oriented normal to flow consistently exhibited greater expansion, consistent with the anisotropic deformation observed during loading and soaking, whereas samples with bedding planes parallel to the flow are more constrained to expand due to oedometer restrictions.

- Higher effective permeability to gas, compared to water permeability results, indicated the development of preferential pathways (fissures) across the specimen.
- Effective gas permeability did not significantly depend on the orientation of the sample.
- Gas type (air vs Helium) does not have a significant influence on gas transport properties.
- During gas transport, the displaced water was residual, meaning that only a small desaturation of the clay matrix occurred, reinforcing the idea of gas transport through preferential pathways.
- A new family of fissures larger than 2 µm were identified using the MIP technique. They did not depend on the sample orientation, in agreement with the isotropic response of effective gas permeability.
- Image processing using µ-CT confirmed the opening of fissures with large apertures (> 40 µm), primarily developing along weaker bedding planes.
- Gas transport with bedding planes orthogonal to flow appeared to be driven by low-aperture fissures with narrower separations connecting non-perfectly parallel bedding planes.
- The effectiveness of the self-sealing was evaluated by comparing water permeability before and after the gas invasion. The re-saturation of the samples at constant vertical stress resulted in the restoration of the initial water permeability for both orientations, replicating the original anisotropy.
- During the re-saturation, very small deformations were recorded pointing out to the closure of the localised gas paths, but complete self-healing was achieved since microstructural analyses revealed higher volumes at the macro-scale than in the initial state, attributed to potential gas entrapment or occlusion in large pores, which were not entirely closed during re-saturation. Nevertheless, these pores did not exhibit connectivity, in agreement with the restoration of the initial permeability.
- The possible fissure reactivation during gas transport after self-sealing was envisaged. The effective gas permeability measured during the second gas injection presented largest values during the first one.
- The microstructure study after the second gas injection reflected the largest volume of pores at the macro-scale as detected by MIP. Analyses of µ-CT images revealed the opening of large-aperture fissures in the direction of the bedding planes, also identifying low-aperture fissures bridging the bedding planes and some large, likely associated with gas entrapment during the initial injection and subsequently enlarged during undrained unloading.
- These observations suggested that the second episode of gas invasion could reopen some of the fissures developed during the first injection, facilitating the flow of gas.
- A multi-scale model was proposed to account for the changes in permeability due to the evolution of the microstructure. The model can properly represent the increase in permeability during gas injection due to the development of fissures, the recovery of the initial permeability thanks to self-sealing and the subsequent re-opening of preferential pathways increasing again the permeability.

4.5.7.2 Impact of acquired knowledge

The tests were performed following robust and consistent experimental protocols equivalent to those used in Gonzalez-Blanco (2017), which allows comparison and creates confidence in the results. Therefore, they can serve as a guide for future gas experiments in argillaceous rocks.

The experimental results, regarding gas transport under relatively high gas pressures and gas injection rates, point out that the main transport mechanism is through preferential paths, which leads to an

increase in the effective permeability. Nevertheless, the subsequent re-saturation enables the closure of the gas pathways restoring the initial intrinsic permeability, which is crucial for the safety assessment of the repositories.

Combining macroscopic parameters such as permeability with microstructural analyses of the pore network is key for a correct understanding of these very coupled processes. Therefore, a multi-scale approach is necessary to evaluate the behaviour of these materials on gas transport and self-sealing and develop numerical models able to simulate and predict them correctly.

4.5.7.3 Remaining knowledge gaps

The effect of long-term gas injection and its effect on the self-sealing capacity was not assessed during this study. If the gas pathways and the material surrounding them exhibit major desaturation due to a long period of gas passage, the behaviour might change.

Additionally, the microstructural evaluation was performed on post-mortem samples, which may impair in the quantification of the gas pathways due to the unloading process. Therefore, the realization of gas injection tests under stress conditions while scanning the sample using a tomography would avoid these artefacts.

Finally, to gain confidence in the gas transport mechanisms, new experimental configurations (gas injection test in triaxial/isotropic cells) must be proven.

4.5.7.4 Recommendations for the future

The experiments carried out during this research were time-consuming consuming (between 4 and 8 months for each test) and it was decided to perform the tests under different conditions, thus, the repeatability of the results was not addressed. Additionally, the disparity of experimental configurations and test protocols hinders the possibility of a direct comparison of the results between different experimental teams. Therefore, a previous definition of hydro-mechanical paths before gas injection and gas injection features (pressures, rates, etc) will allow better integration of the information and provide more confidence in it.

4.5.8 References

Arnedo, D., Alonso, E.E., & Olivella, S., 2013. Gas flow in anisotropic claystone: modelling triaxial experiments. International Journal for Numerical and Analytical Methods in Geomechanics, 37, pp.2239–2256.

Cardoso, R., Romero, E., Lima, A., & Ferrari, A., 2007. A Comparative Study of Soil Suction Measurement Using Two Different High-Range Psychrometers. Experimental Unsaturated Soil Mechanics, 112, pp.79–93.

De Craen, M., Wang, L., Van Geet, M., & Moors, H., 2004. Geochemistry of Boom Clay pore water at the Mol site. SCK·CEN Technical Report

Coll, C., 2005. Endommagement des roches argileuses et perméabilité induite au voisinage d ' ouvrages souterrains. PhD Thesis, Universite Joseph Fourier–Grenoble I, France.Dao 2015

EURAD, 2019. EURAD Deployment plan 2019-2024. HORIZON 2020 project EURAD. EC Grant agreement no: 847593, p.25.

Gonzalez-Blanco, L., Romero, E. & Levasseur, S., 2023. Self-Sealing of Boom Clay After Gas Transport. Rock Mechanics and Rock Engineering. Available at: https://doi.org/10.1007/s00603-023-03529-3

Gonzalez-Blanco, L., Romero, E., Jommi, C., Li, X., & Sillen, X., 2016. Gas migration in a Cenozoic clay: Experimental results and numerical modelling. Geomechanics for Energy and the Environment, 6, pp.81–100. Available at: http://linkinghub.elsevier.com/retrieve/pii/S2352380816300260.

Gonzalez-Blanco, L., Romero, E. & Levasseur, S., 2023. Self-Sealing of Boom Clay After Gas Transport. Rock Mechanics and Rock Engineering. Available at: https://doi.org/10.1007/s00603-023-03529-3

Gonzalez-Blanco, L., Romero, E., Marschall, P., & Levasseur, S., 2022. Hydro-mechanical Response to Gas Transfer of Deep Argillaceous Host Rocks for Radioactive Waste Disposal. Rock Mechanics and Rock Engineering, 55(3), pp.1159–1177. Available at: https://doi.org/10.1007/s00603-021-02717-3.

Gonzalez-Blanco, L. & Romero, E., 2022. A multi-scale insight into gas migration in a deep Cenozoic clay. Géotechnique, (Ahead of Print), pp.1–18. Available at: https://doi.org/10.1680/jgeot.21.00208.

Harrington, J.F., de la Vaissière, R., Noy, D.J., Cuss, R.J., & Talandier, J., 2012. Gas flow in Callovo-Oxfordian claystone (COx): results from laboratory and field-scale measurements. Mineralogical Magazine, 76(8), pp.3303–3318.

Harrington, J.F. & Horseman, S.T., 1999. Gas transport properties of clays and mudrocks. Geological Society, London, Special Publications, 158(1), pp.107–124. Available at: http://sp.lyellcollection.org/lookup/doi/10.1144/GSL.SP.1999.158.01.09 [Accessed December 1, 2016].

Hildenbrand, A., Schlömer, S., Krooss, B.M., & Littke, R., 2004. Gas breakthrough experiments on pelitic rocks: comparative study with N2, CO2 and CH4. Geofluids, 4, pp.61–80.

Horseman, S.T., Winter, M.G., & Entwistle, D.C., 1987. Geotechnical characterization of Boom Clay in relation to the disposal of radioactive waste. Final report EUR 10987, p.100

Jacops, E., Volckaert, G., Maes, N., Weetjens, E., & Govaerts, J., 2013. Determination of gas diffusion coefficients in saturated porous media: He and CH4 diffusion in Boom Clay. Applied Clay Science, 83–84, pp.217–223.

Jacops, E., Wouters, K., Volckaert, G., Moors, H., Maes, N., Bruggeman, C., Swennen, R., & Littke, R., 2015. Measuring the effective diffusion coefficient of dissolved hydrogen in saturated Boom Clay. Applied Geochemistry, 61, pp.175–184.

Lima, A., 2011. Thermo-Hydro-Mechanical Behaviour of two deep Belgian clay Formations: Boom and Ypresian clays. PhD Thesis, Universitat Politècnica de Catalunya, Barcelona, Spain.

Liu, Z.B., Shao, J.F., Liu, T.G., Xie, S.Y., & Conil, N., 2016. Gas permeability evolution mechanism during creep of a low permeable claystone. Applied Clay Science, 129(July), pp.47–53.

Pineda, J., Romero, E., Alonso, E.E., & Pérez, T., 2014. A new high-pressure triaxial apparatus for inducing and tracking hydro-mechanical degradation of clayey rocks. Geotechnical Testing Journal, 37(6), pp.1–15.

Rodwell, W., Norris, S., Cool, W., Cuñado, M., Johnson, L., Mäntynen, M., Müller, W., Sellin, P., Snellman, M., Talandier, J., Vieno, T., & Vines, S., 2003. A thematic network on gas issues in safety assessment of deep repositories for radioactive waste (Gasnet). Final Report EUR 20620, p.61.

Romero, E., 1999. Characterisation and Thermo-Hydro-Mechanical behaviour of unsaturated Boom Clay: an experimental study. PhD Thesis, Universitat Politècnica de Catalunya, Barcelona, Spain.

Schneider, C.A., Rasband, W.S., & Eliceiri, K.W., 2012. NIH Image to ImageJ: 25 years of image analysis. Nature Methods, 9(7), pp.671–675.

Volckaert, G., Ortiz, L., De Canniere, P., Put, M., Horseman, S.T., Harrington, J.F., Fioravante, V., & Impey, M., 1995. MEGAS Modelling and experiments on gas migration in repository host rocks. EUR 16235 MEGAS Final Report Phase 1, p.464.

Webb, P.A. & Orr, C., 1997. Analytical methods in fine particle technology. Micromeritics Instrument Corp., Norcross, GA, USA, p.301.

Wiseall, A.C., Cuss, R.J., Graham, C.C., & Harrington, J.F., 2015. The visualization of flow paths in experimental studies of clay-rich materials. Mineralogical Magazine, 79(6), pp.1335–1342.

5. Two-phase flow properties derived from pore-scale imaging (ZHAW)

5.1 Background and literature review

5.1.1 Transport in porous clay rocks

In the present work, model pore structures of Opalinus Clay were used to predict critical material properties related to gas transport. This topic is important, for example, because rocks such as Opalinus Clay are considered as potential host rocks for the disposal of radioactive waste (Andra, 2005; Nagra, 2002, 2004). Thereby, these transport properties are of interest in connection with the production of gas, for example through corrosion of the waste containers, and its subsequent transport through the rock material surrounding the radioactive waste. The produced gas can be transported from the place of formation through the rock by various transport processes (e.g. diffusion, advection, two-phase flow etc.). Here, the focus is on the so-called two-phase transport where the produced gas displaces the water in the pores as a separate phase. This process is known as drainage. Two-phase flow is controlled by the microstructure of the porous medium, in particular by the characteristic pore throat radius and its distribution.

During drainage, the water in the pores is successively replaced by gas. This reduces the volume fraction of connected water bodies, which extend over the whole sample. As a consequence, the effective permeability of water is thereby continuously reduced and the effective gas permeability increases continuously as soon as a connected gas transport path is formed across the sample. Furthermore, there is a pressure difference between the phases, the capillary pressure that a gas must exceed in order to be transported into a water-saturated material. Transport of gas by two-phase flow depends on the following material properties of the porous medium: i) the permeability, ii) the porosity, iii) the effective permeability and iv) capillary pressure as functions of saturation.

These properties are controlled on the pore scale but estimates of the suitability of a potential host rock require evaluations of gas transport on a larger length scale, where micropores cannot be considered as physical objects. Large-scale numerical simulations are often used to evaluate a potential host rock, which in turn require the aforementioned gas transport properties as input. These properties can be determined by laboratory experiments, but the available data related to Opalinus Clay are sparse. For example, water retention curves were determined to evaluate relationship between capillary pressure and saturation (Zhang and Rothfuchs, 20017; Munoz et al. 2003; Romero and Gomez, 2013; Ferrari and Laloui, 2012; Nagra, 2013). Despite these laboratory data, it remains unclear to what extend anisotropy affects the relationship between saturation and capillary pressure. In addition, data availability is poor in case of effective permeabilities and it is also unclear to what extent anisotropy affects effective permeability (Nagra, 2013). The aim of this study is the prediction of gas transport properties based on pore microstructures, which were reconstructed from 3D image data and in combination with numerical simulations. The predicted gas transport properties will be compared with experimental data. For those properties for which no experimental data are available (i.e. effective permeability during drainage, effect of anisotropy), the study makes predictions that hopefully will ignite further experimental work.

On the microscale, pores can be observed within the clay-rich parts of Opalinus Clay. There, pores are formed due to geometric incompatibilities between the grain boundaries of small clay platelets. These pores are commonly referred as to intergranular pores and the radii associated with these pores range are from about 2 nm to around 100 nm. In 3D, these pores were imaged using Focused Ion Beam nano tomography (FIB), which allowed reconstructing pore microstructures on the tens of micrometer scale (Keller et al. 2013). Unfortunately, FIB cannot resolve the whole pore space (Keller et al. 2011). With a typical voxel size of 5-10 nm about 30 % of the pores can be imaged (Keller et al. 2011). In relation to

the objectives of this study, this has the consequence that material properties can only be calculated incompletely. To overcome this problem, we assume that the pore morphology in Opalinus Clay is approximately similar for the whole pore size spectrum, which spans over two orders of magnitude. This allowed the construction of a digital pore structure, which covers almost the complete pore size spectrum. Regarding upscaling of transport properties, it should be noted that the pores are in the clay matrix and consequently it is the volume fraction of the clay matrix that controls the transport properties on a larger scale.

5.1.2 Hydromechanical behaviour of shear fractures

In connection with the storage of hazardous materials in rock units, the presence of fractures is of special interest because they can fundamentally change the transport properties of the rock (Evans and Rasmussen, 1991; Braester, 1999). In the project of radioactive waste storage in clay rocks (Nagra, 2002), fracture zones are formed due to the construction activity; however, it is also possible that during the long storage, shear zones are formed, which modify the transport properties locally. It is therefore fundamental to understand the material transport in fractures formed in clay rocks.

Transport along fractures is mostly studied for either single fractures or fracture networks. Thereby, one difficulty is how to take into account the complex geometrical properties of real fractures in mathematical transport models and transport simulations (e.g. Ge, 1997; Oron and Berkowitz, 1998; Wang et al., 2015). A simplification is the so-called cubic law (e.g. Zimmerman and Bodvarsson, 1996), which is often used for geological applications. The cubic law states that the flow rate in single fractures is proportional to the square of the aperture and is valid for fractures with smooth and parallel interfaces separated by a local aperture. Deviations from this simplification to real conditions were and are the subject of discussions (e.g. Witherspoon et al., 1980; Raven and Gale, 1985; Oron and Berkowitz, 1998; Wang et al., 2015; Lee and Babadagli, 2021). Attempts to contribute to this discussion require models for realistic fractures to study how transport is affected by fracture roughness, which ultimately determines the complex aperture distribution. Previous studies used natural fractures, mechanically induced fractures in rock samples (Raven and Gale, 1985; Witherspoon et al., 1980), casts of fractures (Develi and Babadagli, 2015; Li et al., 2018), and combinations of these methods. Apart from laboratory-based experimental work computer generated fractures were produced by the SynFrac method (Ogilvie et al., 2006; Briggs et al., 2017) and other methods (Oron and Berkowitz, 1998) and were then used for parameter studies to quantify the influence of the different variables characterizing the fractures (e.g. fractal dimension, root mean square height etc.) on the transport properties (e.g. Briggs et al., 2017). Results of these efforts result in, for example, modified formulations of the cubic law (Wang et al., 2015), which must first be confirmed in their applicability, since they also contain quantities that cannot be easily extracted from given natural fractures. According to the comprehensive review of Lee and Babadagli (2021), the most studied rock types are granites, sandstones and dolomites.

This study investigates the wall roughness of natural shear fractures formed in Opalinus Clay, which is a Jurassic shale designated as host rock for radioactive waste in Switzerland. Because clay rocks have not often been studied in this respect this study increases the variability of examined lithologies. It also addresses the question of whether fracture surfaces have similar fractal properties that are independent of the type of fracture generation and mineralogy as suggested by Berkowitz (2002). For this reason, two different types of fracture surfaces are examined here. These are a slickenside fracture surface with striations and a glassy naturally polished fracture surface. The height distribution of the fracture surfaces was optically measured and characteristic quantities such as the root mean square height and fractal dimension were determined from the roughness power spectrum. The measured roughness power spectra were then used as input for the generation of artificial fracture models, which in turn were used for virtual compression experiments and numerical flow simulations to predict hydromechanical properties in single fractures of Opalinus Clay. In the past the interrelation between contact formation during compression and permeability were controversially discussed (Brown and Scholz, 1986; Unger

and Mase, 1993; Oron and Berkowitz, 1998; Pyrak-Nolte and Morris, 2000). This is the reason why we are looking into this question and trying to shed light on it, at least in the case of Opalinus Clay.

5.2 Methods of Digital Rock Physics (DRP)

5.2.1 Derivation of two-phase flow properties with DRP workflows

5.2.1.1 Image Data

Only published image data were used in this study (Keller et al. 2013). Data from a sample of the shaley facies of Opalinus Clay (BDR sample) were used. The sample was taken from Opalinus Clay unit at the Mont Terri rock laboratory, Switzerland (Figure 5-1, Table 5-1). For the BDR sample, also pore size data, which were determined by using the nitrogen gas-adsorption technique in combination with the BET theory (BET), are available (Keller et al. 2013, Table 5-1).

All used methods (e.g., imaging methods, image processing and characterization) are described in detail in our previous publications. Here, only a short summary is given. For electron microscopy analysis clay samples need to be dried prior to analysis. Conventional air-drying causes artifacts such as the frequently observed desiccation cracks, which can lead to misleading conclusions in terms of transport paths in clay rocks. In addition, freeze-drying of moist materials may cause preparation artifacts such as ice formation or surface roughness during mechanical polishing. Special methods such as high-pressure freezing and subsequent freeze- drying were used in order to avoid these artifacts (Bachmann and Mayer, 1987; Keller et al. 2011). The porosity that can be resolved by FIB corresponds to about 20-30% of the total pore space (Table 5-1, Keller et al. 2011). With a typical voxel size of 5-10 nm only pores > 5-10 nm can be imaged. These comparatively larger pores control the gas entry pressure and the capillary pressure at the beginning of the drainage of water from the pores. Hence, the capillary pressure curve determined on the base of FIB image data is largely incomplete because a large part of the present pore sizes is not considered.

Table 5-41 – Information on samples used in this report.

Sample	Locality	Characteristics of sample location	Method	Sample size [μm^3]	Voxel size [nm]	Porosity [vol. %]	Pore radii range [nm]
BDR_OC 1	Mont Terri Opalinus Clay	Shaley facies	FIB	303	10	2.8 clay matrix	10-80
			BET	-	-	11.5	1.4-60.8

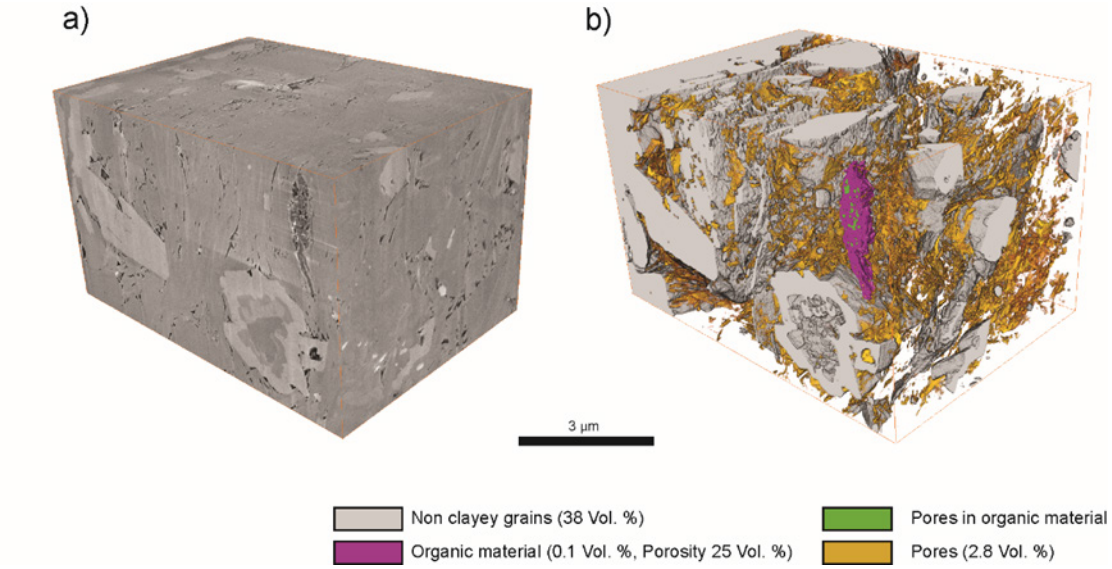

Figure 5-168 – Reconstructed microstructures based on FIB. See Table 1 for voxel resolution and porosity. (a) The 3-D reconstruction of the analyzed volume of OPA from the shaley facies based on SE (secondary electron) images. (b) The 3-D reconstruction of the analyzed volume of OPA from the sandy facies based on SE (secondary electron) images.

5.2.1.2 Building digital pore structures

The calculation of the capillary pressure curve and related permeabilities requires as input a pore structure representing a large part of the pore size spectrum. In order to construct such a digital pore structure, we used a partial volume of the 3D image data as a starting point. This volume had a size of 300x300x300 voxels at a voxel size of 10 nm and a porosity of 2.72 vol.%. BET pore size data show that the investigated sample from the shaley facies had a porosity of about 12.0 vol.%. Therefore, the porosity of the starting pore structure was increased in order to account for the resolution limitation of FIB (see above). This has been achieved by the following procedure:

- Argue that the pore structure is self-similar.
- If the condition that the pore structure is self-similar would be satisfied, this would justify the superposition of a finer pore structure with coarser pore structures, where the pore structures are topologically identical (see also Wang et al. 2014).

In order to provide evidence that the clay pore structure is self-similar we follow the approach of Katz and Thompson (1985), who correctlypredicted porosity from fractal dimensions and used it as an argument that the pore structure is therefore a fractal. Yu and Li (2001) analytically derived an expression between fractal dimension and porosity as:

$$\phi = \left(\frac{\lambda_{min}}{\lambda_{max}} \right)^{d-D_f} \qquad (5\text{-}1)$$

where d is the Euclidian dimension (d = 3 in 3D), D_f is the fractal dimension and λ is the pore size scale (from smallest (λ_{min}) to the largest diameter (λ_{max})) and the statistical self-similarity exists for a set of fractal pores in this range. In addition, Kou et al. (2009) pointed out that the relation $\lambda_{min} << \lambda_{max}$ must

be satisfied for a media to be considered as fractal. Regarding the pore structure of sample BDR we have from BET measurements λ_{min} = 1.4 nm and λ_{max} = 60.8 nm, which yields λ_{min} / λ_{max} = 0.02, which according to Yu and Cheng (2002) satisfies the previous relation.

In this study the fractal dimension was calculated by using the box counting method. Thereby, the volume that was analyzed by FIB (Figure 5-1) is covered with an orthogonal cubic lattice with increasing lattice constant r. For each box size r the number n of boxes containing any part of the pore structure is counted. To obtain a uniformly distributed data density in a logarithmic plot, it was ensured that the box size grows exponentially, resulting in equidistant data points in a logarithmic plot (Dathe et al. 2001). Regarding fractal objects the relation

$$\log n(r) = -D_f \cdot \log(r) + c \qquad (5\text{-}2)$$

is represented by a straight line, where D_f is the slope of that line and c is the intercept. D_f was determined by a linear fit and by considering all data points, which yielded D_f = 2.41 (Figure 5-2).

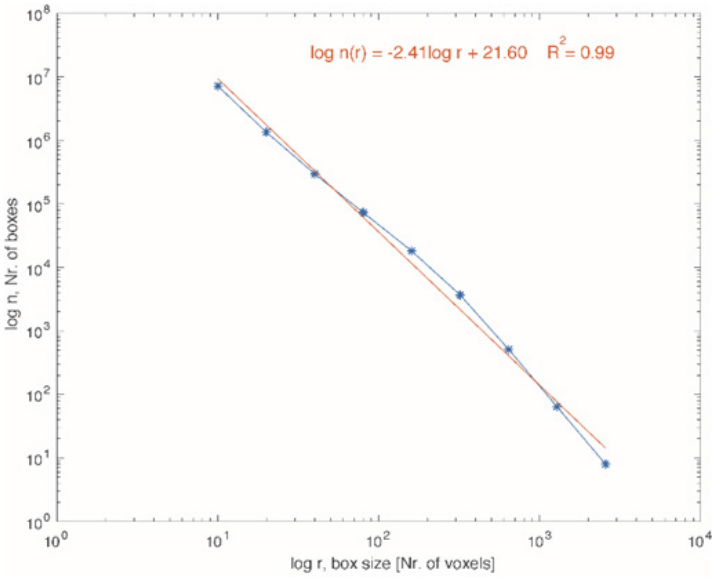

Figure 5-169 – A graph of log n (number of boxes) against log r (box sizes). The data were obtained by the box counting method (see text).

Using the determined value of Df in equation (5-2) a porosity of 12.4 vol. %. was predicted. This value is about 1 vol.% higher when compared to the value that was determined by BET (Table 5-1). This prediction is a reasonable consideration and is therefore used as further (in addition to the above relation) evidence that the pore structure of sample BDR is approximately self-similar.

Now that evidence has been presented that pore space in OPA is self-similar, we used the same pore structure at different levels of details or resolutions. The procedure for the construction of a pore structure in Opalinus Clay, which contains a large part of the pore-size spectrum is outlined in Figure 5-3. We used an original and self-similar pore structure (see above) as well as FIB derived pore structure with the size of 300x300x300 voxels with a voxel size of 10 nm as a starting point.

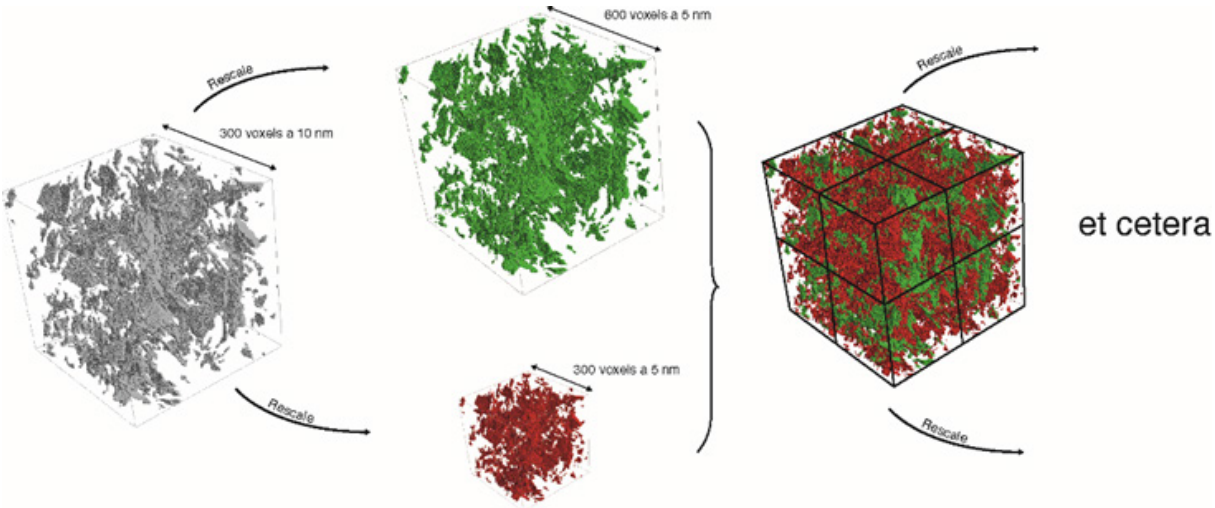

Figure 5-170 – Illustration of the process for creating the pore structure in the Opalinus Clay.

First, this image stack was converted into one with a size of 600x600x600 voxels and a voxel size of 5 nm. Second, the original image stack was converted into a 300x300x300 voxel image stack with a voxel size of 5 nm. From the latter, eight pieces were combined into a cubic image stack. To ensure continuity across the image boundaries, the cubes were arranged so that all boundaries are mirror planes. This compiled image stack was combined with the former image stack (green pores in Figure 5-3). This can also be described as a superposition of a finer pore structure with coarser pore structures, where the pore structures are topologically identical. This step is supported by the evidence that the pore structure is self-similar. This procedure was continued up to a voxel size of 1.25 nm and an image stack size of 2400x2400x2400 voxels. The final pore model is large with regard to the size of the image stack and is therefore only of limited use for the calculation of petrophysical properties. With respect to pore size distribution (PSD) and capillary pressure curve, the calculations were performed for four different sub-volumes with the size of 2400x2400x640 voxels. Two of each of these sub-volumes were used to calculate the properties parallel and perpendicular to the bedding plane, while the squares of the cuboids are either perpendicular or parallel to the bedding plane. Figure 5-4(a) shows the calculated continuous pore size distributions (CPSD) (Muench and Holzer, 2008), which were compared to the ones that were determined by BET. The CPSD indicates the pore volume fraction that can be filled with spheres of a certain radius. For the calculation it is irrelevant whether the pore space is connected or whether the pore bodies are isolated. Therefore the CPSD indicates nothing about the interconnectedness of the pores. It can be assumed that the nitrogen gas penetrates almost the entire pore space of the dried sample during the absorption analysis. Furthermore, the absorption process, as far as we know, is not affected by the ink-bottle effect (see next section). Therefore, we compare the BET pore size distribution with the CPSD to see if the model structure in terms of pore size distribution is consistent with the reality. It turned out that the model PSD and the BET target PSD (green lines in Figure 5-4(a)) are similar in terms of the pore-size spectrum and porosity (Figure 5-4(a)).

The capillary pressure behavior related to drainage or imbibition cannot be inferred from the CPSD and BET pore size distribution because these processes are related to a pressure-driven intrusion process that has its beginning at an entry surface into the material. Such a process depends on the pore geometry, which follows the entrance surface. In addition, this process is affected by the ink-bottle effect that occurs after a material (e.g. water, air, mercury) is pressed into the pore space. The pore size distribution related to an intrusion process is the so-called MIP-PSD. Thereby, in a laboratory experiment mercury is gradually pressed into the material with increasing pressure. Because the narrowest pore passages control the applied pressure, the resulting MIP-PSD corresponds rather to a bottleneck size distribution than to the real PSD (see Muench and Holzer, 2008). Here, the MIP process

was simulated for the model pore structures (Muench and Holzer, 2008) to calculate their MIP-PSD (Figure 5-4). The orientation of the intrusion surface was either parallel or perpendicular to the bedding plane. It must be noted that the MIP intrusion process does not affect the whole pore space but only the part connected to the entrance surface. The same applies to the drainage process (see below). Furthermore, the MIP-PSD underestimates the volume fraction of larger pores because the volume of larger pores located downstream of a narrow pore bottleneck is added to the radius of the bottleneck. In Figure 5-4 it can be seen that this effect is more pronounced when the direction of intrusion is perpendicular to bedding compared to intrusion parallel to bedding. Consequently, the bottlenecks connecting larger pore bodies in the direction perpendicular to the bedding have smaller radii than those parallel to the bedding. Based on the MIP-PSD the corresponding capillary pressure can be estimated. Based on the MIP-PSD, the capillary pressure P_c can be estimated using the relationship between capillary pressure and pore radius r given as $P_c = 2\gamma\cos\theta/r$, where γ is the interfacial (surface) tension between water and air (72.8 mN/m) and θ is the contact angle. As for the material constants, there are uncertainties regarding this contact angle. Based on the reported values of capillary pressures in OPA (see below), it can be assumed that this clay-rich rock is hydrophilic. In such a case, the contact angle is small (10°-30°) (Borysenko et al. 2009). Thus, we have used 30° for the contact angle in the above equation. A consistent picture emerges that the capillary pressure to be overcome increases more for an intrusion perpendicular to bedding after the entry than for an intrusion parallel to the bedding (Figure 5-4(b)). This is related to the constrictivity anisotropy described above. The largest pores in the entry surfaces vary in the partial volumes, resulting in some variation in the entry pressure (2-5 MPa).

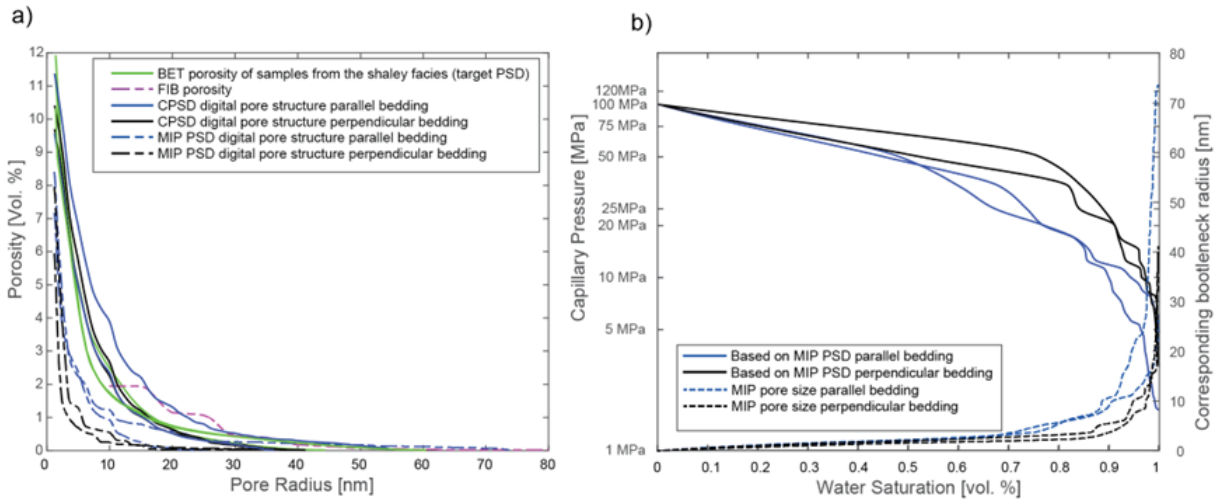

Figure 5-171 – a) Different types of pore size distributions (PSD) of samples and model pore structures as indicated. b) The MIP-PSD was converted to a capillary pressure curve using the relationship between capillary pressure and pore radii. The corresponding pore radii are also shown.

5.2.2 Methods: Hydromechanical behaviour of shear fractures

5.2.2.1 Surface roughness measurements and roughness properties

Samples containing visible shear planes were taken from the Opalinus Clay Unit at the Mont Terri Rock Laboratory in Switzerland (Bosshard and Thury, 2008). In this study, single fractures were analyzed but it cannot be simply assumed that below the fracture surface of the samples taken, the material is intact or whether it has also been affected by the deformation. Therefore, the material below the fracture surface was examined with a dual beam instrument. A cross-section was prepared with the focus ion beam, which was then imaged with the scanning electron microscope integrated in the instrument (Holzer et al., 2004; Keller at al., 2011). Figure 5-5 shows scanning electron images of the two fracture surfaces where the different topographies are clearly visible. Slickensides (Figure 5-5(A)) clearly show the grooving while the glassy surface (Figure 5-5(B)) appears rather smooth. The cross sections show that the rock below the fracture surface is intact (Figure 5-5(C,D)). Deformation has therefore occurred locally along these shear fractures and increased transport was controlled by the fracture geometry and not by a diffuse zone where deformation has led to increased porosity.

In order to obtain a better resolution of the microstructure just below the shear surface, two additional cross-sections were prepared at the specimen edge. The material at this location may have been somewhat affected by the mechanical sample processing but based on visual inspection in the SEM the condition of the shear surface does not differ from that inside the sample (Figure 5-6). The orientation of the platy clay minerals with respect to the shear surface varies, ranging from parallel to nearly vertical.

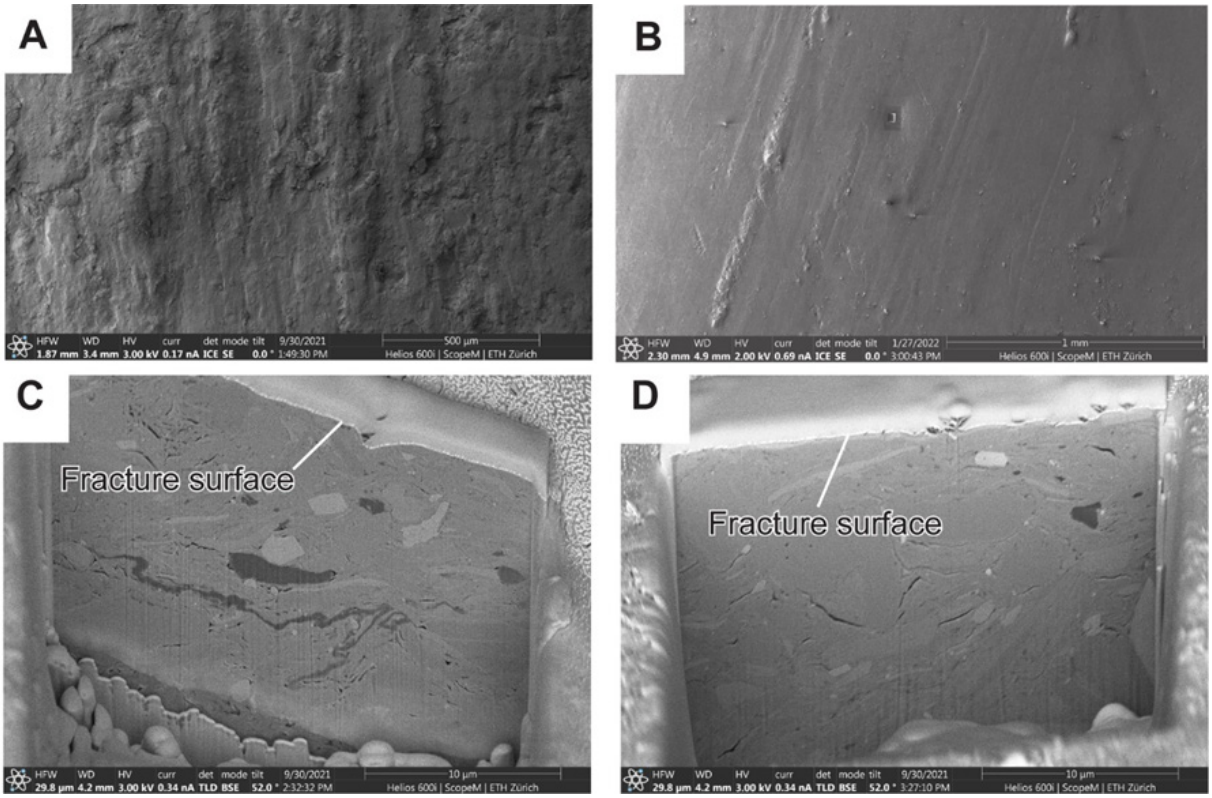

Figure 5-172 – Focused Ion Beam investigations on Opalinus Clay samples. (A) Secondary electron image (SEM) image showing the surface of the slickensides fracture surface. (B) Same as (A) but for the glassy fracture surface. (C) Back scatter electron (BSE) image sowing a cross-section perpendicular to the slickenside fracture surface. (D) Same as (C) but for the glassy fracture surface.

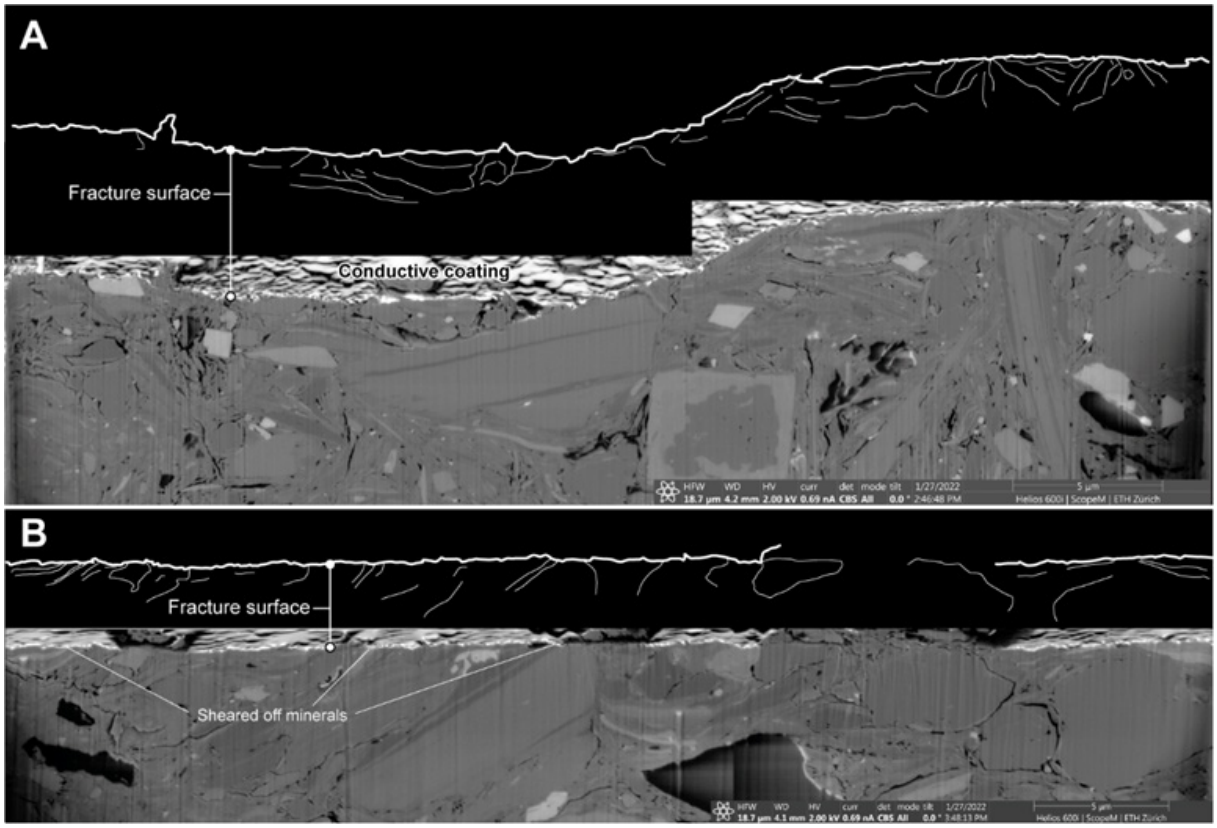

Figure 5-173 – Focused Ion Beam investigations on Opalinus Clay samples. (A) Back scatter electron (BSE) image sowing a cross-section perpendicular to the slickenside fracture surface. (B) Same as a) but for the glassy fracture surface. In the upper black part of the figure, one can see the drawn height profile of the shear plane with the traces of the visible grain boundaries in the area of the shear plane.

Some minerals were sheared off, indicating that the present microstructure was already present before deformation. The short-wavelength roughness elements with wavelengths in the range of 100 nanometers are similar for both surfaces. The differences in the longer wavelength roughness elements, however, can already be seen on the length scale of the cross section examined.

An Alicona InfiniteFocus optical microscope was used in this study, which operates according to the principles of focus variation (Helmli, 2011). This instrument was used to measure the topography h(x,y) of the fracture surfaces (Figure 5-7). The topography was measured at two different magnifications to account for structures with different scales. For example, it was assumed that the striations of the slickensides were larger scale structures, which loses its significance at higher magnifications. Measurements were made with an objective magnification of 2.5x and 20x which corresponds to a vertical resolution of approximately 2300 nm and 50 nm. The elevations of the striation at low magnification were in the range of 200-300 micrometers and were elongated but not continuous in the direction of movement. At higher resolutions the analyzed area decreased, which reduced the captured roughness spectrum and roughness anisotropy. On the length scale studied, the glassy surface was flat with small-scale asperities.

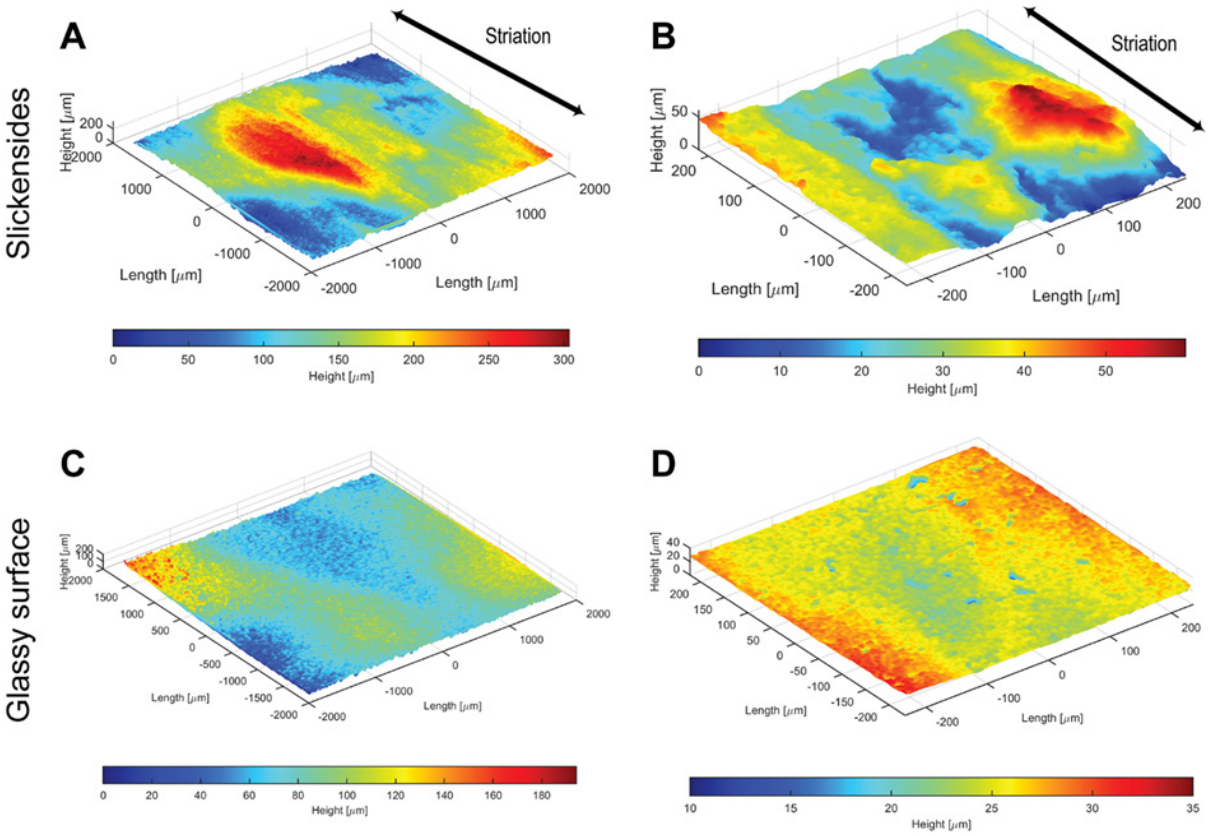

Figure 5-174 – Measured topography of the fracture surfaces at different magnifications. (A) Slickenside topography measured with an optical lens at 2.5x magnification. (B) Slickenside topography measured with an optical lens at 20x magnification. (C) Same as (A) but for the glassy fracture surface. (D) Same as (B) but for the glassy fracture surface. Note, that the range of the colorbars, which refers to the surface height, is different in the illustrations.

In addition to visual inspection, the properties of the surface topography were quantified by means of power spectral density function (PSD) of the surfaces (Nayak, 1971; Persson et al. 2004; Jacobs et al. 2019). The 2D surface roughness power spectrum C2D was calculated with the Matlab code provided by M. Kanafi (Kanafi et al. 2015; Kanafi and Tuonoen, 2017), which is based on the following definition

$$C^{2D}_{qx,qy} = \frac{\Delta x \times \Delta y}{m \times n \times 2\pi^2} |FFT^{2D}|^2 \qquad (5\text{-}3)$$

where q_x and q_y are the wavevectors, $\Delta x \times \Delta y$ defining the pixel size and m × n are the number of pixels of the topography image h(x,y). FFT^{2D} stands for the fast Fourier transform of the surface topography h(x,y). The parameters presented in the following part were all calculated based on C^{2D} related to the measured surface topographies. These parameters include the root mean square height h_{rms} that was calculated based on the following relationship

$$h_{rms} = \sqrt{\frac{2\pi^2}{m \times n \times \Delta x \times \Delta y} \sum_1^n \sum_1^m C^{2D}_{qx,qy}} \qquad (5\text{-}4)$$

where $m \times n \times \Delta x \times \Delta y$ is the area of the topographic image.

It can be seen in Figure 5-8(A,B) that for q <~0.2e+5 m^{-1}, $C^{2D}(q)$ related to slickensides is not radially symmetric with respect to the origin $q_x=q_y=0$, indicating that surface roughness elements with the

longest wavelength (small wavevector q) are anisotropic. However, most of the wavelengths and related roughness elements related to slickensides are isotropic and the corresponding part of C^{2D} is radially symmetric. At least for the size of the investigated areas, $C^{2D}(q)$ related to the glassy fracture surface appear to be radially symmetric which indicates that the surface roughness elements are isotropic (Figure 5-8(C,D)). Therefore, a radially averaged C was calculated from C^{2D} with respect to the origin for both fracture types (Figure 5-8E). This procedure allows the calculation of the Hurst exponent H from the C and the related fractal dimension D_f (Figure 5-8E). The Hurst exponent H can be calculated from the slope of $\log_{10}C$-$\log_{10}q$ relation of the radially averaged power spectrum (Figure 5-8E).

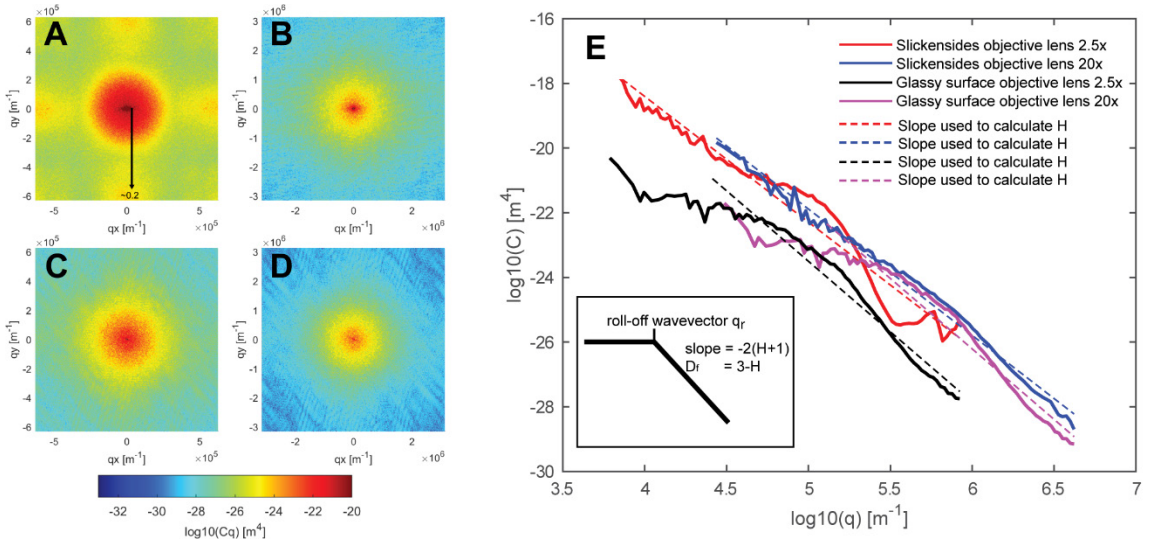

Figure 5-175 – Power spectral densities C2D related to the measured surface topographies depicted in Figure 5-7. (A), (B), (C), and (D) have the same meanings as in Figure 5-7. (E) Radially averaged 2D power spectral densities related to the C2Ds depicted in Figure 5-7. The sketch shows the important quantities that can be determined from the curves.

Since the slope is dominated by the short wavelengths of the isotropic topographic components, the long wavelength anisotropic components are not expected to have a substantial effect on the result in case of the slickensides. However, the calculated fractal properties may not be valid on a larger length scale. In addition, Figure 5-8E shows that the $\log_{10}C$-$\log_{10}q$ relation is not perfectly linear, which shows that the fracture surfaces cannot be described exactly as self-affine fractals. The average slopes of the curves indicate a fractal dimension $D_f \sim 2.1$ in the case of the slickensides and $D_f \sim 2.0$ in the case of the glassy fracture surface. It is interesting to note that in the case of the glassy surface the $\log_{10}C$-$\log_{10}q$ relation tends to become approximately constant below a roll-off wavevector region q_r. In such a case the Hurst exponent H is calculated from the slope defined by the wavevectors > q_r. Depending on the magnification, the roll-off wavevector q_r varies between $\sim 10^{4.4}$ and $\sim 10^{4.9}$ (m^{-1}). Regarding slickensides, the lack of a roll-off area has the consequence that the value of h_{rms} depends on the size of the measured area (Persson et al. 2005, Table 5-2).

Table 5-42 – Parameters which characterise the roughness of the fracture surfaces.

	Slickenside		Glassy		
Objective lens	h_{rms}	D_f	h_{rms}	D_f	q_r
	[µm]	[–]	[µm]	[–]	[m^{-1}]
2.5x	63.97	2.07	2.04	2.00	$10^{+4.9}$
20x	9.80	2.08	2.03	2.00	$10^{+4.6}$

5.2.2.2 Artificial fracture generation and fracture characterization

In the following, C^{2D} that were determined based on real fracture surfaces will be used as input for artificial fracture formation. These in turn have been used to investigate the influence of fracture surface roughness on the hydromechanical behavior of different fracture types. A fundamental problem is the definition of the aperture of fractures based on the measured surface roughness when the two coexisting surfaces were separated. The degree of geometric congruence of the two fracture surfaces determines the aperture distribution along a fracture. In the case of complete correspondence, the open fracture volume approaches zero and no through transport path exists. The geometric relationship between two fracture surfaces in this study is the same as suggested in previous studies: on a larger scale they are well mated, but on a smaller, local scale they were not (Oron and Berkowitz, 1998 and references therein). In the following, fracture models were generated with different levels of geometrical agreement between fracture halves.

In the following it is outlined how the artificial fractures were generated. Four slickensides and four glassy fracture models were constructed with the models differing in their congruence. The procedure is illustrated in Figure 5-9 for two slickenside models with different congruence, but the same applies to the glassy models. In a first step, a synthetic slickenside and glassy fracture surface (Figure 5-9(B)) was generated from the C^{2D} (Figure 5-9(A)), which was determined from the measured topography of fracture surfaces (Figure 5-7). These two surfaces are equal in all slickensides and glassy models and were combined surfaces generated from the part of C^{2D} corresponding to the roughness elements with shorter wavelengths. This objective was achieved with the introduction of a roll-off wave vector q_r, which removed the long wavelength components (Figure 5-9(C)). The effect of this introduction is documented in Figure 5-9D.

The initially produced fracture surfaces (Figure 5-9B) were combined with two different modified (i.e. with roll-off wave vector) surface realizations (Figure 5-9E), resulting in two surfaces that complement each other well on a longer scale, but are slightly worse on a shorter scale. The heights of one of these surfaces were then shifted so that its minimum value was zero. Then the other surface was shifted onto the first surface until they touched (see Oron and Berkowitz, 1998). The procedure was performed for four different roll-off wave vectors q_r (= 10e+6 m^{-1}, $0.5 \cdot 10^{+6}$ m^{-1}, $0.25 \cdot 10^{+6}$ m^{-1}, $0.1 \cdot 10^{+6}$ m^{-1}) resulting in different fracture models with variable congruence of the fracture surfaces. Regarding slickensides models, Figure 5-9F shows cross-sections through two slickenside models with different congruence between the upper and lower fracture surface. In order to use the fracture models as input for

simulations, the height values have been discretized (Figure 5-9G). The resulting fracture models have voxel size of 500 nm.

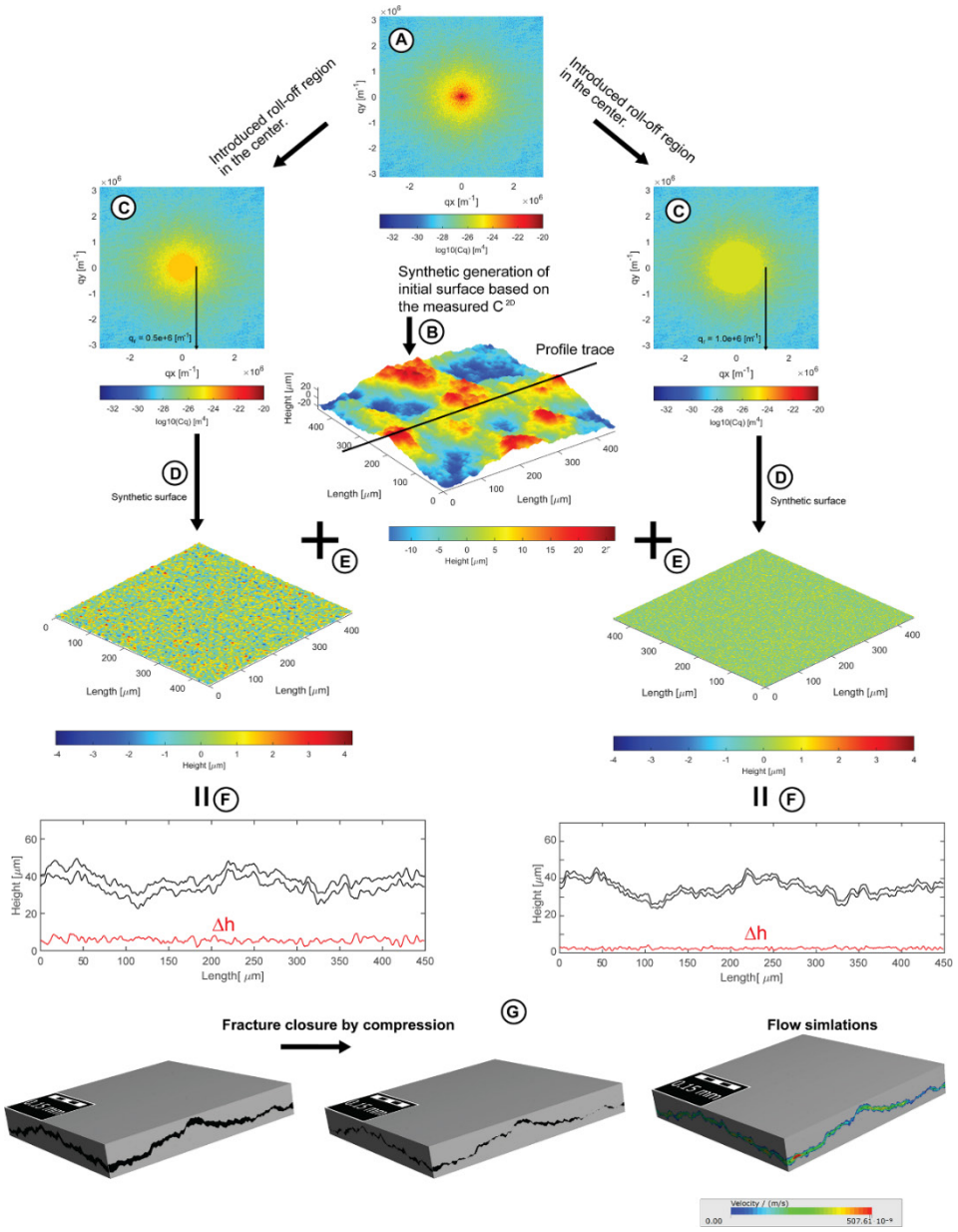

Figure 5-176 – Procedure of artificial fracture generation by taking the slickensides fracture type as example. The initial surfaces were generated (B) using the measured C^{2D} (A) (see also Figure 5-3 and Figure 5-4). For all fracture models, the lower and upper fracture surfaces consist of these initial surfaces. The short wavelength roughness elements in the initial surfaces (A) were modified so that the misfit between the two fracture surfaces is defined by different short wavelength roughness elements in the lower and upper fracture surfaces. Thereby, the initial fracture surface was combined (E) with random surfaces (D) which were generated from the measured but modified C^{2D} (C), where a roll-off region was introduced. The congruence between the two fracture surfaces is controlled by different values of roll-off wave vectors q_r (C,D). After generating the lower and upper fracture surfaces, these were brought into contact. (F) shows profiles through the resulting fractures along with the related aperture Δh which documents the influence of the procedure on the congruence. (G) In order to simulate fracture closure mechanism and transport, the fracture models were discretized.

The root mean square value $aper_{rms}$ of the aperture distribution $\Delta h(x,y) = h(x,y)^u - h(x,y)^l$ was considered as a measure of the congruence between the upper $h(x,y)^u$ and lower $h(x,y)^l$ fracture surface and was calculated according to equation (5-4) where $aper_{rms}$ replaces h_{rms}. Thereby, the power spectral densities C^{2D} that are required as input in equation (5-4) was calculated for the aperture distribution $\Delta h(x,y)$ according to equation (5-3).

5.3 Results

5.3.1 Results: transport in porous media

5.3.1.1 Calculated two-phase flow properties

The GeoDict software was used to calculate numbers of these properties (Wiegmann et al. 2010). This software uses 3D pore microstructures in voxel representation as input and calculates a variety of flow characteristics by solving flow partial differential equations. GeoDict determines the capillary pressure curve (Figure 5-5) on the basis of the pore morphology method (Hilpert and Miller, 2001). For the calculation of the relative permeabilities of water and air, the required phase distribution (Figure 5-6) was taken from the previously simulated drainage or imbition process related to the capillary pressure curve calculation. After the saturation steps, flow direction and boundary condition had been set, the flow partial differential equations were solved by the software for values of flow properties (Figure 5-6) and permeability by using an iterative solver (Wiegmann et al. 2010). On the nanoscale there are physical phenomena, which may influence material transport in clay rocks and which are not included in the classical transport equations, for example gas slip. An evaluation of these phenomena in terms of their impact on gas transport is complicated because they depend also on other parameters such as for example pore wall roughness, velocity and pore geometry. A discussion of these phenomena therefore beyond the scope of this work and must be dealt with in a subsequent study. However, if for example gas slip plays a role, the gas permeability may be underestimated in this study but the basic results such as the anisotropy of the relative permeabilities are not affected. Furthermore, gas transport can be hampered by the lack of gas transport paths connecting pores with comparatively large radii. In such a case dilatancy may be involved in the gas transport process. Whether gas transport can take place with or without dilatancy in the case of the present pore geometry is discussed at the end of this work.

The larger pores of the size spectrum within the gas entrance plane control gas entry pressure. For this pore size spectrum there is coincidence between the PSD determined from BET measurements and the PSD related to digital pore structures. Gas entry occurs for gas pressures >~ 2.4 MPa (see also discussion). Figure 5-5 shows the capillary pressure curves related to the model pore structures.

In Figure 5-10, the simulated curves were compared with laboratory data. The relationship between capillary pressure and water saturation can be derived from the water retention curves (WRC) measured in the laboratory (Munoz et al. 2003; Ferrari and Laloui, 2012; Nagra, 2013; Romero and Gomez, 2013; Ferrari et al., 2014; Zhang and Rothfuchs, 2017). The capillary pressure curve was also evaluated based on data acquired by mercury intrusion porosimetry (MIP) (Romero and Gomez, 2013). The laboratory data were divided into data points referring to samples taken at shallow depths (~ 300 m) and data points referring to samples taken at greater depths (~ 800-900 m). Simulations reasonably agree with the laboratory data for flow parallel to bedding and for samples taken from shallower depths. The laboratory data determined for rocks from greater depth show slightly higher capillary pressures. The simulations predict that especially at the beginning of drainage, the capillary pressures are higher for a flow perpendicular to the bedding than for a flow parallel to the bedding. This must have to do with the fact that the larger pores are connected by narrow bottlenecks in direction perpendicular to bedding.

Therefore, for a given gas pressure the residual saturation depends on the direction in which the gas pressure is applied.

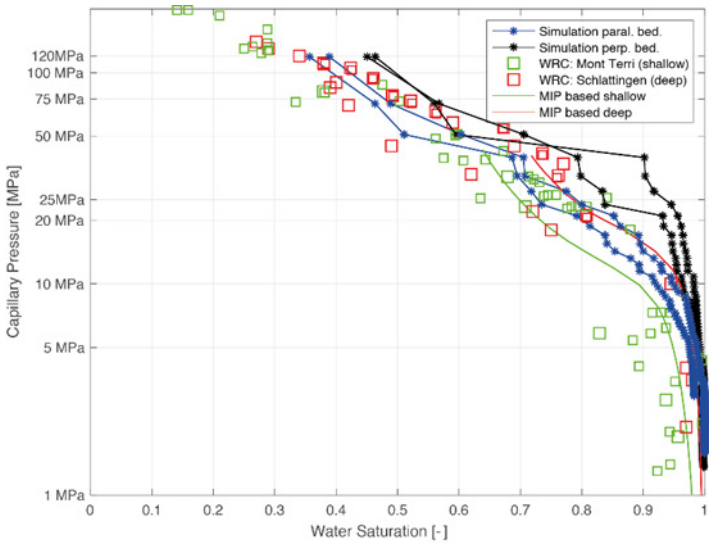

Figure 5-177 – Capillary pressure curves related to four digital pore structures as indicated (simulations). These curves are compared with laboratory data (WRC, MIP). The latter were subdivided according to depth (see text).

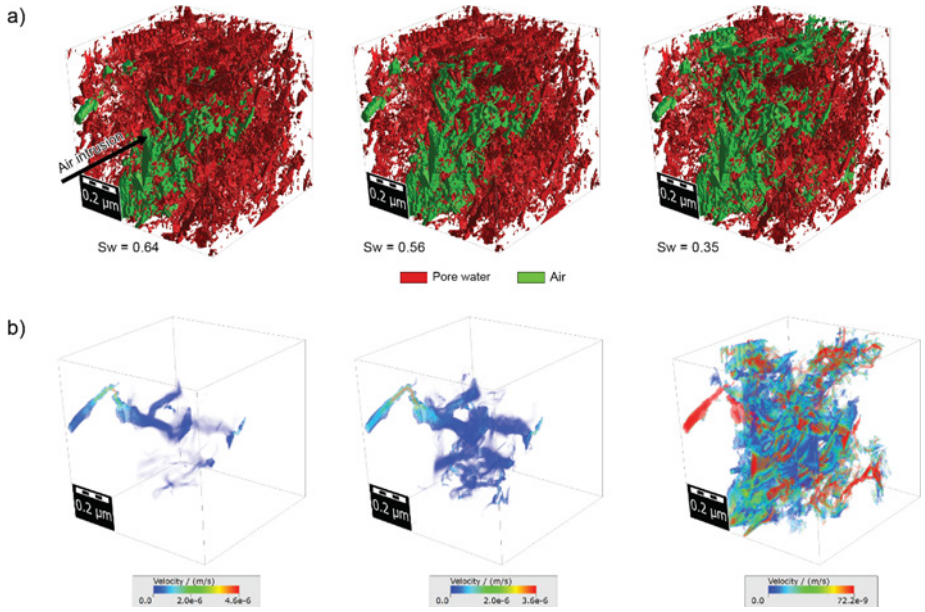

Figure 5-178 – a) a) Stages during drainage of water from the pore structure related to Figure (5-13a,c) showing the distribution of water and air related to different water saturations. b) Visualization of air-flow properties showing the distribution of air flow velocities at different water saturation stages.

Due to the long calculation time, effective permeabilities related to the drainage and imbibition cycles were calculated only for two partial volumes of the size of 600x600x600 voxels (Figure 5-11, Figure 5-12, Figure 5-13). Figure 5-12 shows the corresponding PSD. The pore structure model related to Figure 5-13(b,d) has the larger pores, which as a consequence leads to a lower air entry pressure at the beginning of the intrusion process. Thereafter, the structural model related to Figure 5-13(a,c) has

about the same capillary pressure because the comparatively smaller pores in the entrance area are connected to the rest of the pore space with similarly large pore constrictions. This shows that not only the bulk constriction distribution determined from the MIP-PSD, where the mercury enters the sample from all sides, but also the directional constriction connectivity plays a role.

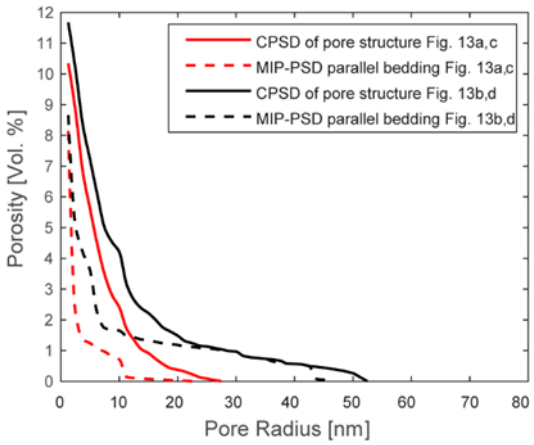

Figure 5-179 – Pore size distributions related to the two partial volumes that were used to calculated the relative permeability shown in Figure 5-13.

Drainage with subsequent imbibition was calculated for flow parallel to the bedding (Figure 5-13). The influence of the anisotropy of the rock on the capillary pressures and the associated permeabilities was studied by calculating drainage with flow parallel and perpendicular to the bedding (Figure 5-14).

Using the model pore structures as input for simulations a residual saturation of around 0.35 along the drainage curve at P_c ~ 120 MPa was predicted (Figure 5-10, Figure 5-13). At this point on the drainage curve water permeability drops to zero and no more water can be displaced. A continuous path of air through the sample starts to form at P_c ~ 21-25 MPa (gas emergence pressure) in case of the smaller pore models (see also discussion). The related water saturation at gas emergence pressure ranges between 0.8-0.93. According to Figure 5-13(c,d) the formation of continuous gas transport paths in the shaley facies of Opalinus Clay requires the displacement of around 10-20% of the pore water (Figure 5-13(c,d)). Afterwards, air permeability increases from zero along the drainage curve to the final air permeability at an air saturation of around 0.65 (Figure 5-13c). After that and along the imbibition air permeability curve, air permeability drops to zero at a water saturation in the range of 0.53-0.60. Hence, the volume fraction of trapped air after imbibition is around 0.40-0.47 (Figure 5-13(c,d)). The volume fraction of free air during subsequent imbibition is around 0.15-0.25 (Figure 5-13(c,d)).

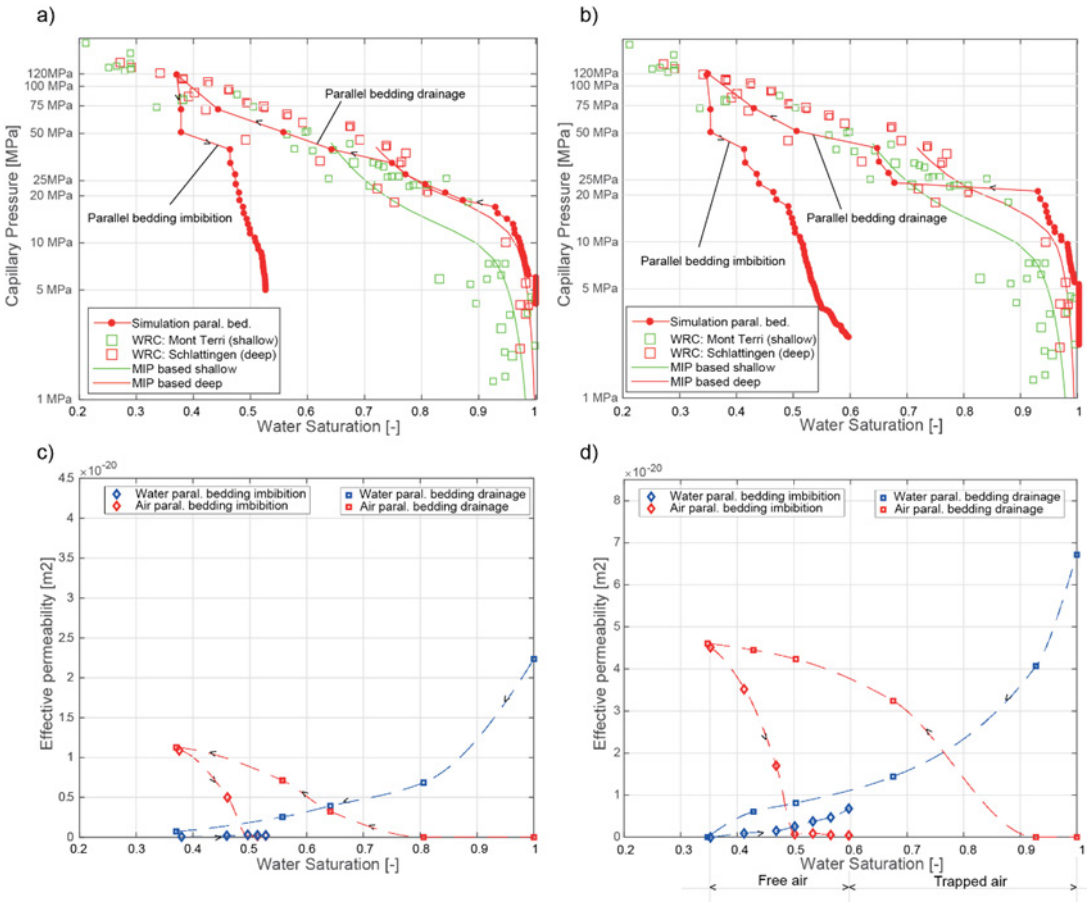

Figure 5-180 – Capillary pressure curves and related effective permeabilities calculated for two different pore structures: a) and c) drainage with subsequent imbibition for the pore structure with lower permeability. b) and d) drainage with subsequent imbibition for the pore structure with somewhat higher permeability.

Initial water permeability parallel to the bedding is about a factor of 10 higher than water permeability perpendicular to bedding (Figure 5-14(b)). The same applies to final air permeability at the point on the drainage curve that corresponds to residual water saturation, where no further water is displaced. In Figure 5-15, a continuous path of air through the samples starts to form at water saturation of around 0.80 regardless whether flow occurs parallel or perpendicular to bedding. However, the corresponding gas emergence pressure is considerably different for the two flow directions. Parallel to bedding gas emergence occurs at around 25 MPa whereas perpendicular to bedding gas emergence occurs at 75 MPa (see also discussion). In summary, water and air permeability behavior during drainage are strongly affected by the anisotropy of the rock.

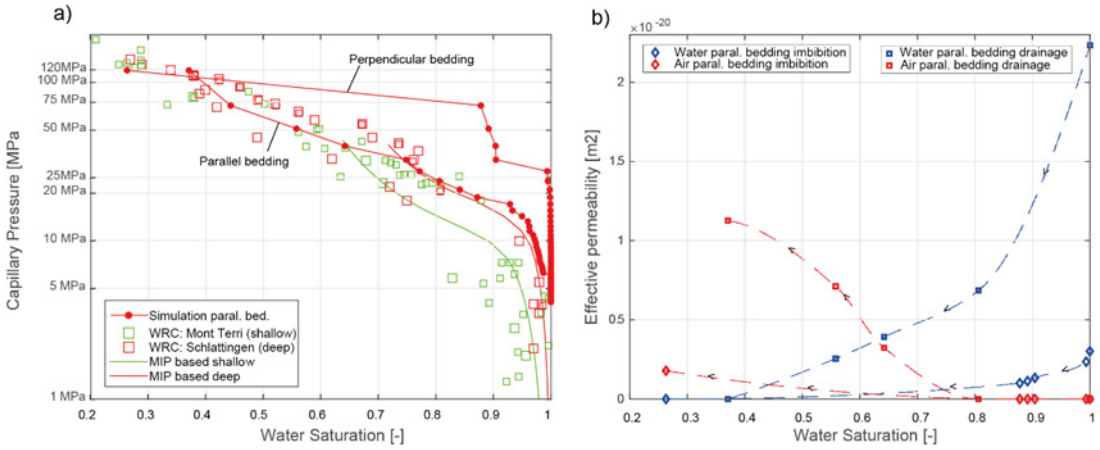

Figure 5-181 – a) Capillary pressure curves and b) related effective permeabilities for drainage parallel and perpendicular to bedding.

5.3.2 Results: Hydromechanical behaviour of shear fractures

5.3.2.1 The influence of fracture congruence (matedness) on transport properties

To determine the influence of the degree of congruence between the two fracture surfaces on the transport properties, the mean aperture D_{50} (50% of the fracture volume has smaller apertures than D_{50} and 50 vol. % has a larger aperture) was calculated for each fracture model. This procedure was also chosen to compare the results with the parallel plate fracture model (Witherspoon et al. 1980). GeoDict calculates the flow velocity in each voxel of the domain (i.e. fracture and solid in Figure 5-9) and computes an average flow velocity, which is then used to determine the permeability of the whole domain via the Darcy law (Versteeg and Malalasekera, 2007). Therefore, the averaged velocity in the volume (black volume in Figure 5-9) of the fracture was used to calculate the permeability of the fracture. The permeabilities were calculated in x and y directions to account for a potential anisotropy. Figure 5-15 summarizes the results of these calculations. The statement is that for the same mean aperture, the type of shear surfaces has only a marginally effect on permeability.

The calculated permeabilities were compared with those based on the cubic law $k = 1/12D^2$, where D is the aperture. It turns out that surface roughness plays a role. The difference is in the range of half an order of magnitude. Based on these results, it can be concluded that the long wavelength structural elements have little influence on the permeability, in contrast to the short wavelength elements with $q>10^5$ (m^{-1}), which are approximately the same for both surfaces (Figure 5-8).

Permeability anisotropy in slickensides is not very pronounced, but permeability parallel to the striations (Y direction) is slightly higher than perpendicular to it. The structural anisotropy of the slickensides nevertheless has a pronounced influence on the flow velocity field. Along the grooves, flow channeling occurs where the flow velocity is enhanced along the channels. In shear direction, the transport in fractures with slickensides is therefore enhanced when compared to transport perpendicular to shear direction.

For geological applications, knowledge of single fracture permeability is only of secondary interest. Based on the flow velocity field, the permeability was converted to a permeability for multiple parallel fractures where the fractures are separated by a regular spacing (Figure 5-15b). A permeability model was fitted to the calculated permeabilities. Based on the parallel plate model, the permeability for parallel multi fractures is given as $k = 1/(12s)D^3$, where s is the mean fracture spacing. Using this formula, the following relationship was fitted to the data $k = f/sD^3$, where f is a factor, which takes into

account the structural properties of the fractures. Rounded to 2 decimal places factor f = 0.03, which allows the reader an estimation of the permeability for an arbitrary mean spacing, which was for example estimated from mapping fractures.

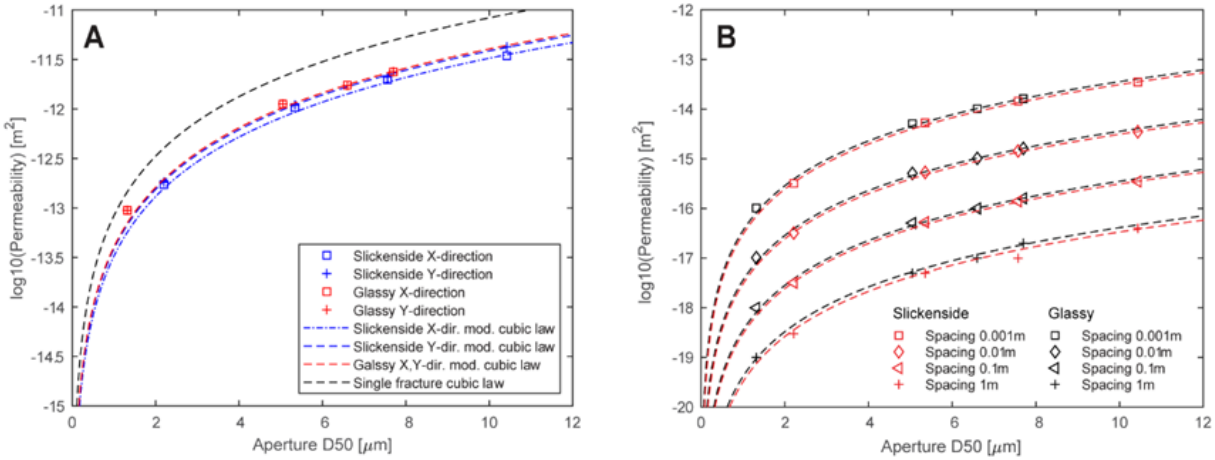

Figure 5-182 – (A) Single fracture permeability as a function of mean fracture opening D50 for the two fracture types and with a comparison to single fracture permeability calculated based on the cubic law. (B) The single fracture permeabilities were converted to a bulk permeability depending on the mean spacing between the fractures.

5.3.2.2 Contact behavior during fracture closure by compression

When fractures are closed by compression, the contact behavior plays a major role in regard of the hydromechanical behavior as the two fracture surfaces approach each other. This behavior can be estimated by analyzing the aperture distribution $\Delta h(x,y)$ between fracture surfaces. For this purpose, the cumulated area fraction corresponding to an increasing aperture range was calculated. This range can also be considered as displacement during compression and thus Figure 5-16 shows the expected evolution of the contact area fraction and the evolution of the number of contact regions with increasing closure of the fracture.

The curves in Figure 5-16A were calculated from the aperture distribution $\Delta h(x,y)$, which has the properties of an image with an aperture Δh assigned to each pixel. Then, for a given aperture Δh^{given} the number of pixels N with apertures smaller than Δh^{given} was determined. By converting the number of pixels N into area units, the contact area was calculated that is formed when the two fracture surfaces approach each other by a distance = Δh^{given}. This calculation was done for all unique values of Δh, which yielded the curves. The area corresponds to the projected area that is perpendicular to the compression direction and thus largely controls closure by compression. In addition, for all unique values of Δh, the connected contact regions were determined using the bwlable function of Matlab in combination with the given contact pattern. This resulted in the number of contact regions with increasing convergence Δh of the two fracture surfaces (Figure 5-16B). Figure 5-16 shows that for slickensides and glassy fracture surfaces with different initial congruence between the fracture surfaces, the contact behavior does not depend on the roughness of the individual fracture surface, but on $aper_{rms}$. This is obvious since the order of the curves in Figure 5-7A does not depend on the roughness of the respective fracture surface. Contact area formation is controlled by $aper_{rms}$ and the smaller $aper_{rms}$, the larger is the formed contact area for a given displacement. Note, the smaller $aper_{rms}$, the better the congruence between the two fracture halves. Because fracture stiffness depends on the total contact area, fractures with a comparatively small $aper_{rms}$ are expected to be stiffer. The evolution of the number of contact regions

also depends on $aper_{rms}$. At the beginning of fracture closure, the rate of contact area formation and the total number of contacts formed is higher for fractures with comparable low $aper_{rms}$ (Figure 5-16B). At a certain point, a coalescence of contacts occurs, and the number of contacts decreases with increasing fracture closure (Figure 5-16B).

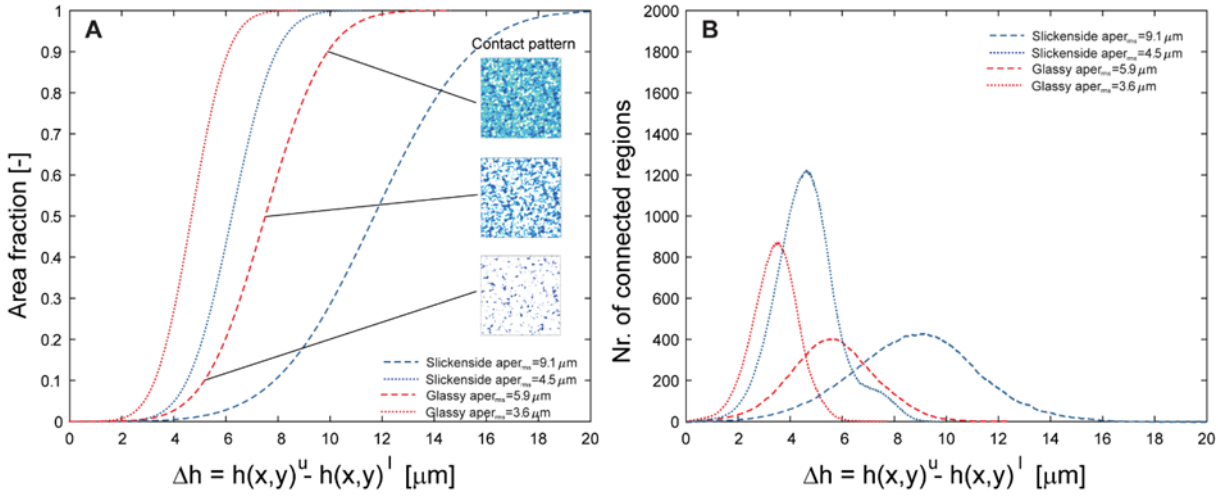

Figure 5-183 – (A) Area fraction as a function of the aperture ⊿h between the upper and lower fracture surfaces for slickenside and glassy fracture types with different congruence aperrms. The area fraction corresponds approximately to the area formed by successive fracture closure where the aperture corresponds to the displacement. The inserted images correspond to the expected contact pattern at different stages during fracture closure. (B) Number of contact regions as a function of aperture ⊿h between the upper and lower fracture surface for slickenside and glassy fracture types with different congruency aperrms.

5.3.2.3 Fracture closure by compression and related transport behaviour

The FeelMath-LD module of the GeoDict software simulates non-linear large deformation (Moulinec and Suquet, 1998; Kabel et al. 2015). It allows the set-up of a compression experiment in arbitrary directions. Here it was used to compress the generated fracture models (Figure 5-9) and the simulation tool can detect new material contacts when the fracture surfaces increasingly touch each other as the compression increases. The fractures were compressed in steps normal to the fracture surface. After each step, the deformed structure was used as input for the next deformation step. The respective strain per step was 2 % and a total of 5 steps were calculated. An isotropic behavior was assumed and for this case the Young Modulus and Poisson's ratio of clay rock matrix was set to 6 GPa and 0.27 respectively (Bock, 2001). Experimental data for normal stress/fracture closure curves show the influence of plastic deformation on fracture closure (Zhang, 2011). In order to address the influence of plastic deformation, the calculations were performed for i) pure elastic deformation and for ii) elastic-plastic deformation. The experimentally determined compressive strength of Opalinus Clay depends on various parameters, such as the confining pressure, water content, specimen orientation, and also specimen size. The macroscopic uniaxial strength ranges up to 40 MPa, while for the microscopic strength of the porous clay matrix higher values of > 100 MPa where obtained (Giger and Marschall, 2014; Keller et al. 2017). To account for the variation in the available strength data the yield stress related to elastic-plastic deformation was set to 40 MPa and 100 MPa in two different calculations. If these values are exceeded locally at a specific contact between the fracture surfaces, the deformation proceeds purely plastically during ongoing closure. The simulations were performed for a slickenside model with $aper_{rms}$ = 9.1 μm and for a glassy model with $aper_{rms}$ = 5.9 μm. For these two fracture models the contact behavior was also analyzed (Figure 5-16).

At the beginning of the compression experiment both fracture types had a similar contact area and number of contact regions, but slickensides with $aper_{rms}$ = 9.1 μm are more compliant than glassy fractures with $aper_{rms}$ = 5.9 μm and therefore the aperture in the slickenside model decreases more with increasing load (Figure 5-17A). For the present case, this behavior is largely controlled by the rate of contact area formation and rate of contact region formation during fracture closure, which in turn are controlled by $aper_{rms}$.

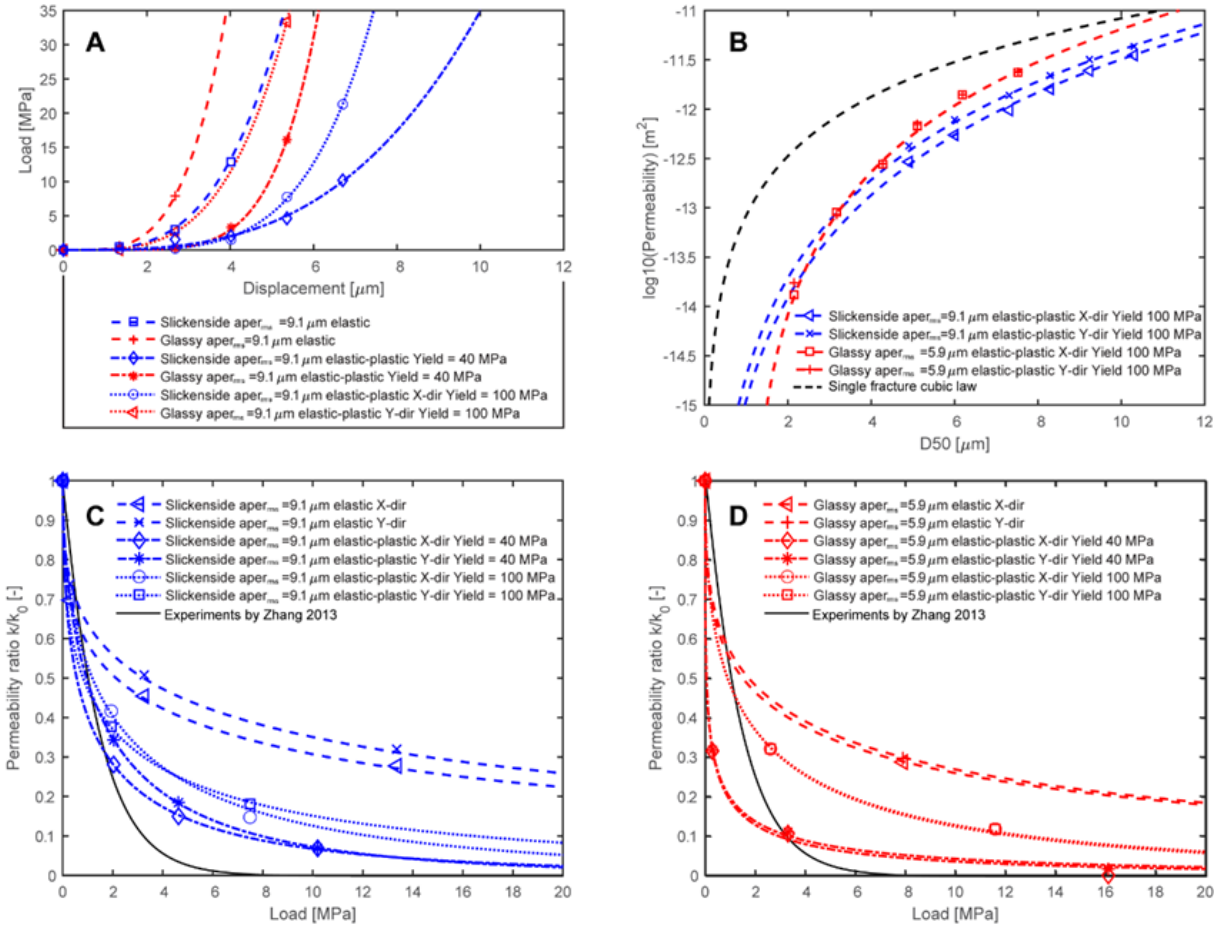

Figure 5-184 – (A) Relationship between vertical load and vertical displacement during the virtual compression experiment in the case of a slickenside or glassy fracture surface. (B) Permeability in relation to the mean aperture D50 related to fracture closure by compression and for elastic-plastic deformation. (C) Ratio between reduced and initial permeability as a function of applied normal load for slickensides under elastic and elastic-plastic deformation. (D) Same as (C) but for glassy fractures.

Figure 5-17C,D show that with increasing normal load, the permeability of the glassy model decreases more than that of the slickenside fracture model particularly at low yield strengths. At a normal load of about 5 MPa and at the used material laws, the permeability is reduced by ~60 % in case of elastic deformation and by ~85-95 % in case of elastic-plastic deformation at a yield strength of 40 MPa. Figure 5-8(C,D) also show the experimental data of Zhang (2013), which are related to fractures in drill cores of Opalinus Clay that were closed by compression. The data imply that the permeability during the first load increment of 5 MPa decreases below a value of 10 % of the initial value. In this respect, the glassy fracture model behaves similarly in case the yield-strength is set to 40 MPa. What the comparison between experiments and simulation shows, however, is the importance of plastic deformation and also of the characteristics of the aperture distribution $aper_{rms}$ both controlling fracture closure by compression (see also Zhang, 2013).

In case congruence controls the aperture and also in the case of the parallel plates fracture model, permeability is proportional to the second power of the aperture. Under compression, permeability of the two fracture types deviates from this relation and the permeability-mean aperture relationship of the two fracture models differs not only by a different proportionality factor (Figure 5-17(B)). Figure 5-18 ((A,B,C,D,E,F) shows the flow fields along the y-direction for the two fracture models at three different normal loads. With an increasing normal load, both the number of contact regions and their area increase. This gradually divides the fluid flow into a series of channels which increases the tortuosity. This, along with the decreasing aperture, is the reason for the decreasing flow with increasing normal load. The shape of the contact points varies. In slickensides they are elongated and tend to be arranged in rows. In glassy fractures, no directional dependence is apparent. This results in a permeability anisotropy for slickensides and a permeability isotropy for glassy fractures.

We also simulated (using the SatuDict module of GeoDict) the draining of water from the fracture at different stages of compression to study effects of the contact area formation on the presence of residual water. Figure 5-18(G,H,I,J,K,L) shows the phase distribution at a capillary pressure when most of the mobile water has been drained and in case air pressure is applied in the y-direction. Figure 5-18 also shows the contact areas between the fracture surfaces in red. The residual water is bound to the constrictions which are in the vicinity of contact regions or future contact regions. Larger connected water bodies form where the distance between the contact regions is small, i.e., where many contacts form in a certain displacement increment. If draining occurs simultaneously with compression, the residual water will be displaced into regions with larger apertures, but then the air pressure must be further increased to drain this water as the aperture further decreases. As expected, the gas entry pressure P_c^{entry} (the pressure of gas starting to enter the fracture) and the gas emergence pressure $P_c^{emerg.}$ (the pressure of gas starting to emerge the fracture) increase with increasing compression since the aperture becomes smaller (Figure 5-18). However, the calculate pressure values in Figure 5-18 are imprecise because the drainage is discontinuous due to the discretization.

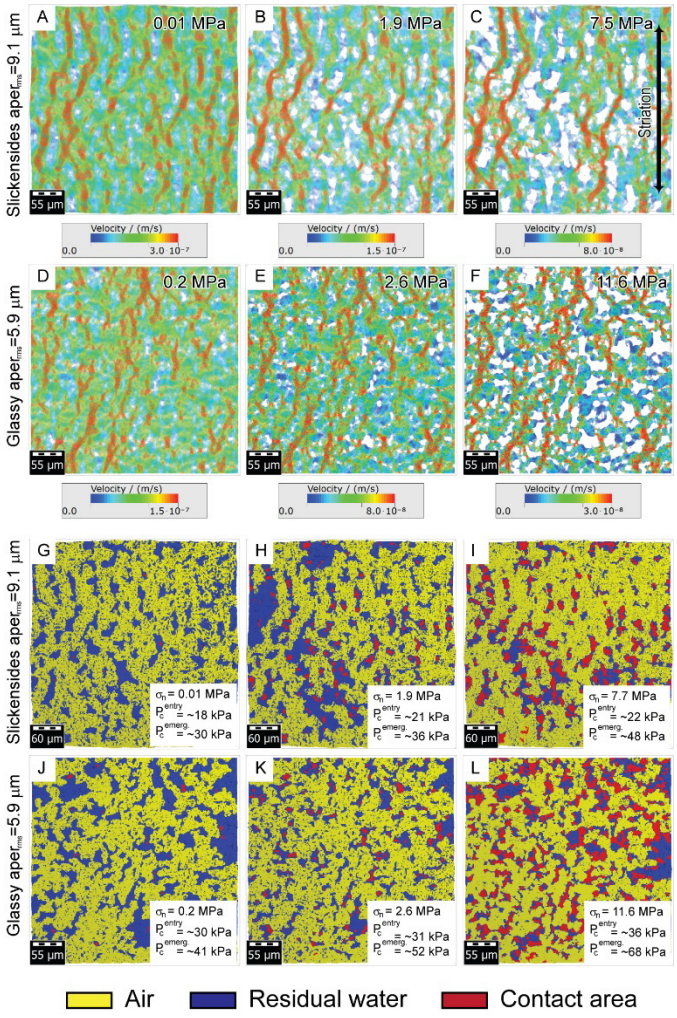

Figure 5-185 – (A,B,C,D,E,F): flow velocity distribution for the flow in y-direction in slickensides of a glassy fracture type. (G,H,I,J,K,L) top view into the fracture interior shows the influence of compression and different types of fractures on the formation of contact areas (red) and the residual water (blue) during the drainage of water from the fracture. The vertical load increases from left to right.

5.3.2.4 Fracture closure by swelling

Fracture closure by swelling is considered effective in clay rocks. Swelling is controlled on the nano to micro scale and is related to the incorporation of water in the crystal lattice, adsorption of water on mineral surfaces and osmotic processes. Depending on how the rock is restricted in its expansion, swelling manifests itself in the form of swelling pressure or volumetric expansion, the latter being important in the closure of fractures. In a study analyzing published data on experimentally determined swelling volume, it was found that confining pressure is the dominant parameter (Lyu et al. 2015). Clay content and initial water content have a minor influence, but of course cannot be neglected. Furthermore, it was found that water penetrates clayey material only in the immediate vicinity of the fracture surface (Davy et al., 2007) and thus swelling is most likely limited to the fracture zone (Davy et al., 2007). Since swelling volume is affected by confining pressure, this study investigates possible effects of local stress variations along the fracture surfaces, which is controlled by roughness, on fracture closure by swelling. Swelling depends strongly on the confining pressure and at pressures > 1 MPa, according to the data of Lyu et al. (2015), the effectiveness of swelling to close fractures in clay rock is limited. This is especially true when the rock is already saturated with water (Figure 5-20).

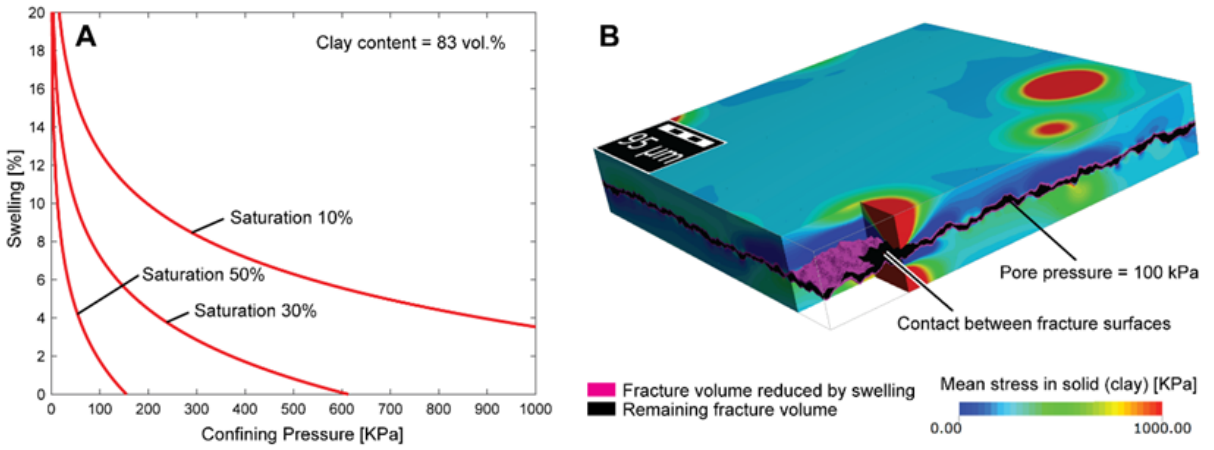

Figure 5-186 – (A) Swelling as a function of confining pressure at a clay content of 83 vol. % and at different water saturations according to Lyu et al. (2015). (B) Example of a mean pressure distribution. Also visualized is the volume in pink by which the fracture has been reduced. Note that no swelling occurs in the vicinity of the contact region due to the high pressure.

This is supported by the experiments of Zhang et al. (2010) where the swelling strain under confined conditions is less than 0.1%. To investigate how the fracture models are closed by swelling, the mean pressure distribution was calculated for a vertical strain of 1 % and by variating the pore pressure, which results in different confining pressures (Figure 5-19). These pressure distributions were then used together with swelling data from Lyu et al. (2015). Thereby, clay content was set to 83 vol. % (according to Figure 5-6) and the water saturation to 10 %. The swelling volume was then calculated for each voxel. Then the total volume change in each voxel column below and above the fracture was calculated. This volume change is then considered as the volume that contributes to the closure of the fracture (Figure 5-20(B)). Figure 5-20(A) shows the influence of swelling on permeability. Swelling is more effective for fractures with comparatively low $aper_{rms}$ such as glassy fractures. However, the effectiveness depends strongly on the hydrostatic pressure. For the selected parameters, an increase in hydrostatic pressure of about 0.5 MPa substantially reduces the swelling effect. In addition, Figure 5-20(A) shows that the contact area fraction between the fracture surfaces increases non-linearly with decreasing hydrostatic pressure and that at a contact area fraction of 30-40 % the fractures become impermeable. It should be noted that the closure efficiency depends on the relative volume fraction of the rock that is penetrated by water. For the fracture models, this is between 85-90 vol. %. As under compression, for fracture closure by swelling, permeability is not proportional to the second power of the mean aperture (Figure 5-20(B)).

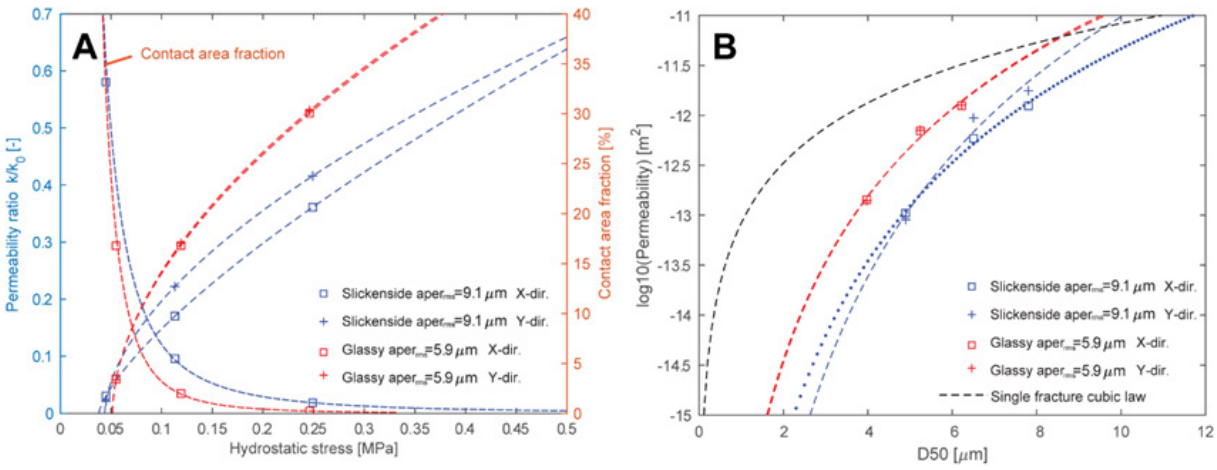

Figure 5-187 – (A) Ratio between permeability reduced by swelling and initial permeability as a function of hydrostatic pressure. Also plotted is the contact area fraction as a function of hydrostatic pressure. (B) Permeability in relation to the mean aperture D50 related to fracture closure by swelling.

5.4 Summary

5.4.1 Transport in porous media

The 3D reconstruction of the pore space in Opalinus Clay is faced with the difficulty that high-resolution imaging methods reach their limits at the nanometer-sized pores in this material. Until now it has not been possible to image the whole pore space with pore sizes that span two orders of magnitude. Therefore, it has not been possible to predict the transport properties of this material with the help of computer simulations that require 3D pore structures as input. Following the concept of self-similarity, a digital pore microstructure was constructed from a real but incomplete pore microstructure. The constructed pore structure has the same pore size spectrum as the one measured in the laboratory. Computer simulations were used to predict capillary pressure curves during drainage, which also agree with laboratory data. It is predicted, that two-phase transport properties such as the evolution of effective permeability as well as capillary pressures during drainage depend both on transport directions, which should be considered for Opalinus Clay when assessing its suitability as host rock for nuclear waste. This directional dependence is controlled on the pore scale by a geometric anisotropy in the pore space.

5.4.2 Hydromechanical behaviour of shear fractures

The role of surface roughness of fractures in Opalinus Clay and in rocks in general is relevant in understanding the hydromechanical behavior of fractures. Two different fracture surfaces of shear fractures in the Opalinus Clay were investigated. The fracture surfaces were characterised based on their roughness power spectrum. It was found that slickensides fracture surfaces are near fractal-like up to the longest scale with a fractal dimension $D_f \sim 2.1$ and in the absence of a roll-off region at long wavelengths. In contrast, the glassy fracture surfaces show a roll-off region, which is characteristic of a flat surface with rather small and local topographic height variations. The glassy fracture surface is near fractal like with $D_f \sim 2.0$. The measured roughness power spectra were used to create fracture models to study the behavior of different fracture closure mechanism: i) increasing congruence (matedness), ii) closure by compression and iii) closure by swelling. It turned out that the relationship between permeability and mean aperture depends on the fracture closure mechanism. Concerning closure by compression, the root mean square (rms) value of the aperture (aper) distribution $aper_{rms}$ influences the contact formation behavior, which in turn controls the hydromechanical properties. The lower the $aper_{rms}$ is, the lower the fracture compliance. Apart from $aper_{rms}$, the simulations predicted that in clay rocks, plastic deformation plays an important role in the closure of fractures by compression. In agreement

with the experiments, the simulations predict that the permeability falls below 10 % of the initial value at a compressive stress of 5 MPa. The simulations predict that fracture closure by swelling is rather ineffective for confining pressures exceeding ~1 MPa.

5.5 Key learning points

5.5.1 New knowledge acquired

- The capillary pressure curves calculated from the realistic pore microstructures agree with the curves obtained in the laboratory, corroborating that the gas transport processes are indeed controlled at the pore scale, as generally assumed by laboratory experimenters at the macroscale.
- Anisotropy effects related to two-phase transport properties can be expected also in Opalinus Clay. Permeabilities related to drainage and imbibition must be given as effective values and the concept of relative permeabilities is not applicable.
- Gas transport might be possible without mechanical response parallel to bedding, while a transport perpendicular to bedding is hardly possible.
- The root mean square (rms) value of the aperture (aper) distribution $aper_{rms}$ influences the contact formation behavior, which in turn controls the hydromechanical properties.
- Apart from $aper_{rms}$, the simulations show that in clay rocks, plastic deformation plays an important role in the closure of fractures by compression.
- It turned out that the relationship between permeability and mean aperture depends on the fracture closure mechanism.
- The simulations predict that fracture closure by swelling is rather ineffective for confining pressures exceeding ~1 MPa.

5.5.2 Impact of acquired knowledge

The present work is based on a combination of microstructural analysis and computer simulations, which predicted that in case of Opalinus Clay the development of the effective permeability during drainage and the corresponding development of the capillary pressure depend on the transport direction. This material behavior is controlled on the pore scale and in particular by the geometric anisotropy of the pore space. Regarding the suitability of Opalinus Clay for safe containment of nuclear waste, the anisotropic behavior of the effective permeability and capillary pressure during drainage and associated two-phase flow has been neglected until now. Here we show that this negligence is not appropriate because the results of this study show that the two-phase transport in Opalinus Clay and the related material properties such as capillary pressure and effective permeability are anisotropic during drainage.

The study of natural fracture surfaces with different roughness characteristics gives an insight into how different roughness components control the hydromechanical properties of fractures. Relying on the roughness power spectrum, the fracture roughness largely controls the contact behavior during fracture recompression. The higher the root mean square value of the aperture $aper_{rms}$ is, the higher is the fracture compliance, which is related to the contact formation behavior. Comparatively smaller values of $aper_{rms}$ increase the rate of contact area and contact region formation during fracture closure, which results in a higher fracture stiffness and reduced permeability when compared to fractures with a higher $aper_{rms}$. In addition, contact formation affects the distribution of the residual water during the drainage of water from fractures. In clay rocks the relationships between mean aperture and permeability depend on the fracture closure mechanism.

5.5.3 Remaining knowledge gaps

Regarding the prediction of two-phase transport properties from 3D images and reconstructed pore microstructures, the open issues lie in the approach to construct realistic pore microstructures that cover the entire pore size spectrum and match the morphological characteristics of the pore space in clay rocks. The reconstruction approach used here is pragmatic, yet accurate, because it uses copies of real 3D pore structures at different length scales. Clay rocks, on the other hand, exhibit a spectrum of pore space geometries that is closely related to the local mineralogical composition. However, it is unrealistic to investigate all of these pore geometries using high-resolution imaging techniques. A pore structure reconstruction modeling approach, using as input specific morphological data extracted from real pore structures, generates different realizations of potential 3D pore geometries in clay rocks and thus provides a range of expected transport properties. This provides a deeper insight into the local transport properties and possible transport pathways for gas, including those requiring larger pore throats.

What was not addressed here are physical phenomena on the nanoscale, which may influence gas transport in clay rocks and that are not included in the classical transport equations, for example gas slip as well as dilatancy. Because these factors depend also on other parameters (e.g. roughness, velocity, pore geometry, locale micromechanical properties etc.) it would be worthwhile to study the impact of these phenomena on gas transport in a subsequent study.

The aperture distribution and related fracture roughness $aper_{rms}$ is the fundamental parameter that controls the contact behavior and the hydromechanical behavior of fractures. Unfortunately, relatively little is known about the aperture distribution in clay rock fractures because it is methodologically difficult to determine. Therefore, the primary focus should be on determining the aperture distribution in natural fractures. For example, by mapping the surface of separated fracture halves. In order to extrapolate the results of these laboratory-scale investigations of natural fractures to field-scale predictions, the scaling effects on rock properties and their relationships must be clarified. This can be done by modeling synthetic fractures using the fractal properties of real rock fractures and the scaling law of surface roughness.

5.6 References

Andra, 2005. Dossier (2005) Argile – evaluation de la faisabilité du stockage géologique en formation argileuse profonde – Rapport de synthèse. Juin 2005. Andra, France. Available at: http.//www.Andra.fr.

Bachmann L., E. Mayer (1987) Physics of water and ice: implications for cryofixations. In: Steinbrecht, R.A., and Zierold, K. (Eds.), Cryotechniques in biological electron microscopy. Springer, Berlin.

Bakhshian S., Hosseini S. A., Lake L. W. (2020) CO2-brine relative permeability and capillary pressure of Tuscaloosa sandstone: Effect of anisotropy. Advances in Water Resources 135, 103464.

Bear J., Breaster C. (1987) Effective and Relative Permeability of Anistropic Porous Media. Transport in Porous Media 2, 301-316.

Borysenko A., Clennell B., Sedev R., Burgar I., Ralston J., Raven M., Dewhurst D., Liu K. (2009) Experimental investigation of the wettability of clays and shales. Journal of Geophysical Research 114, B07202.

Dathe A., Eins S., Niemeyer J., Gerold G. (2001) The surface fractal dimension of the soil-pore interface as measured by image analysis. Geodema 103, 203-229.

Davies P. B. (1991) Evaluation of the role of threshold pressure in controlling flow of waste-generated gas into bedded salt at the Waste Isolation Pilot Plant (WIPP). Sandia Rep. SAND 90-3246, Sandia National Laboratories, Albuquerque, New Mexico.

Ferrari A., Laloui L. (2012) Advances in testing the hydro-mechanical behaviour of shales, in: L. Laloui and A. Ferrari editors. Multiphysical Testing of Soils and Shales, pp. 57-68, Springer, 2012.

Ferrari A., Favero V., Marschall P., Laloui L. (2014) Experimental analysis of the water retention behaviour of shales. International Journal of Rock Mechanics & Mining Science 72, 61 – 70.

Hipert M., Miller C. (2001) Pore-morphology-based simulation of drainage in totally wetting porous media. Adv. Water Resources 24, 243-255.

Katz A. J., Thompson A. H. (1985) Fractal Sandstone Pores: Implications for Conductivity and Formation. Physical Review Letters 54, 1325-1328.

Keller L. M., Holzer L., Wepf R., Gasser P. (2011) 3D Geometry and topology of pore pathways in Opalinus clay: Implications for mass transport, Appl. Clay Sci. 52, 85-95.

Keller L. M., Schuetz P., Gasser P., Holzer, L. (2013) Pore-space relevant for gas-permeability in Opalinus Clay: Statistical analysis of homogeneity, percolation and representative volume element. Journal of Geophysical Research: Solid Earth 118, 2799–2812 https://doi.org/10.1002/jgrb.50228

Kou J., Wu F., Lu H., Xu Y., Song F. (2009) The effective thermal conductivity of porous media based on statistical self-similarity. Physics Letters A 374, 62-65.

Marschall P., Horseman S., Gimmi T. (2005) Characterisation of Gas Transport Properties of the Opalinus Clay, a Potential Host Rock Formation for Radioactive Waste Disposal. Oil & Gas Science and Technology – Rev. IFP 60, 1, 121-139.

Münch B., Holzer L. (2008) Contraticting geometrical concepts in pore size analyzes attained with electron microscopy and mercury intrusion. Journal of American Ceramic Society 91, 4059-4067.

Nagra (2002) Projekt Opalinuston–Synthese der geowissenschafftlichen Untersuchungsergebnisse. Entsorgungsnachweis für abgebrannte Brennelemente, verglaste hochaktive sowie langlebige mittelaktive Abfälle. Nagra technical report NTB 02–03. Nagra Weinfelden, Switzerland.

Nagra (2004) Effects of post-disposal gas generation in a repository for spent fuel, highlevel waste and long-lives intermediate waste sited in the Opalinus Clay. Nagra Technical report NTB 04–06. Nagra, Wettingen, Switzerland.

Nagra (2013) Gas related property distributions in the proposed host rock formations of the candidate siting regions in Northern Switzerland and in the Helvetic Zone. Nagra Arbeitsbericht NAB 13-83. Nagra Weinfelden, Switzerland.

Romero E., Gómez R. (2013) Water and air permeability tests on deep core samples from Schlattingen SLA-1 borehole. Nagra Arb. Ber. NAB 13-51. Nagra, Wettingen, Switzerland.

Wang C., Yao J., Wu K., Ren G., Sun H., Yang Y., Gao Y., Chen Z. (2014) Organic and Inorganic Pore Structure Analysis in Shale Matrix with Superposition Method. Unconventional Resources Technology Conference (URTeC) DOI 10.15530/urtec-2014-1922283.

Wiegmann A., Iliev O., Schindelin A. (2010) Computer aided engineering of filter materials and pleated filters, in: Global Guide of the Filtration and Separation Industry. Roedermark, Germany: E. von der Luehe. VDL Verlag, pp. 191–198.

Yu B., Li J. (2001) Some fractal characters of porous media. Fractals 9, 365-372.

Yu B. M., Cheng P. (2002) A Fractal Permeability Model for Bi-Dispersed Porous Media. Int. J. Heat Mass Transfer 45, 14, 2983.

Zhang C.-L., Rothfuchs T. (2007) Moisture Effects on Argillaceous Rocks, in: Proceedings 2nd International Conference of Mechanics of Unsaturated Soils (editor T. Schanz), Springer Proceedings in Physics 112, pp. 319-326.

References: Hydromechanical behaviour of shear fractures

Berkowitz, B. (2002). Characterizing flow and transport in fractured geological media: A review. Adv. in Water Res. 25, 861-884.

Bock, H. (2001). RA experiment. Rock mechanics analysis and synthesis: Data report on rock mechanics. Technical Report 2000-02. Mont Terri Project.

Bossart, P., and Thury, M. (2008). Mont Terri Rock Laboratory: Project, Programme 1996–

2007 and Results. Reports of the Swiss Geological Survey, No. 3.

Braester, C. (1999). Radioactive waste repositories in fractured rocks formations: hydrodynamic aspects, in Energy and the Environment, eds A. Bejan, P. Vadasz, D.G. Kröger (Springer Netherlands), 15, 229–238, https://doi.org/10.1007/978-94-011-4593-0_20.

Brown, S. R., and Scholz, C. H. (1986). Closure of rock joints. J. Geophys. Res. 91, 4939.

Briggs, S., Karney, B., and Sleep, B. (2017). Numerical modeling of the effects of roughness on flow and eddy formation in fractures. J. Rock Mech. Geotech. Eng. 9, 105–115. doi.org/ 10.1016/j.jrmge.2016.08.004.

Davy, C.A., Skoczylas, F., Barnichon, J.-D., and Lebon, P. (2007). Permeability of macro-cracked argillite under confinement: Gas and water testing. Phys. Chem. Earth. 32, 667-680.

Develi, K., and Babadagli, T. (2015). Experimental and visual analysis of single-phase flow through rough fracture replicas. Int. J. Rock Mech. Min. Sci. 73, 139–155. doi.org/10.1016/j.ijrmms.2014.11.002.

Evans, D., and Rasmussen, T. (1991). Unsaturated Flow and Transport through Fractured Rock Related to High-Level Waste Repositories. Final Report, Phase 3. Nuclear Regulatory Commission, Washington, DC (United States). Div. Of Engineering; Arizona Univ. Dept. of Hydrology and Water Resources, Tucson, AZ (United States). doi. org/10.2172/137966.

Ge, S. (1997). A governing equation for fluid flow in rough fractures. Water Resour, Res. 33, 53-61.

Giger, S., and Marschall, P. (2014). Geomechanical properties, rock models and in-situ stress conditions for Opalinus Clay in Northern Switzerland. Arbeitsbericht NAB 14-01, Nagra Wettingen, Switzerland.

Helmli, F. (2011). Focus Variation Instruments, in Optical Measurement of Surface Topography, ed. R. Leach (Springer, Berlin), 131-166.

Holzer, L., Indutnyi, F., Gasser, Ph., Münch, B., and Wegmann, M. (2004). Three-dimensional analysis of porous BaTiO3 ceramics using FIB nanotomography. J. Microsc. 216, 84–95.

Kabel M., Merkert D., and Schneider M. (2015). Use of composite voxels in FFT-based homogenization. Comput. Methods Appl. Mech. Eng. 294, 168-188.

Kanafi, M. M., Kuosmanen, A., Pellinen, T. K., and Tuononen, A. J. (2015). Macro- and micro-texture evolution of road pavements and correlation with friction. Int. J. Pavement Eng. 16, 168-179.

Kanafi, M. M., and Tuononen, A. J. (2017). Top topography surface roughness power spectrum for pavement friction evalution. Tribology Int. 107, 240-249.

Keller, L.M., Holzer, L., Wepf, R., and Gasser, P. (2011). 3D Geometry and topology of pore pathways in Opalinus clay: implications for mass transport. Appl. Clay Sci. 52, 85–95.

Keller, L. M., Schwiedrzik, J. J., Gasser, P., and Michler, J. (2017). Understanding anisotropic mechanical properties of shales at different length scales: In-situ micropillar compression combined with finite element calculations. J. Geophys. Res. Solid Earth, 122, doi:10.1002/2017JB014240.

Lee, J., and Babadagli, T. (2021). Effect of roughness on fluid flow and solute transport in a single fracture: A review of recent developments, current trends, and future research. J. Nat. Gas Sci. 91, 10371.

Li, B., Zhou, F., Li, H., Tian, Y., Yang, X., Zhang, Y., and Feng, Y. (2018). Experimental investigation on the fracture conductivity of ultra-deep tight gas reservoirs: especially focus on the unpropped fractures. Seattle, Washington. In: 52nd U.S. Rock Mechanics/Geomechanics Symposium, pp. 17–20. June. ARMA-2018-1273.

Lyu, Q., Ranjith, P.G., Long, X., Kang, Y., and Huang, M. (2015). A review of shale swelling by water adsorption. J. Nat. Gas Sci. Eng. 27, 1421-1431.

Moulinec H., and Suquet P. (1998). A numerical method for computing the overall response of nonlinear composites with complex microstructure. Comput. Methods Appl. Mech. Eng. 157, 69-94

Nagra, 2002, Projekt Opalinuston-Synthese der geowissenschafftlichen Untersuchungsergebnisse. Entsorgungsnachweis für abgebrannte Brennelemente, verglaste hochaktive sowie langlebige mittelaktive Abfälle. Nagra Technical Report, NTB 02–03.

Nayak, P.R. (1971). Random process model of rough surfaces. J. Lubr. Technol. 93, 398–407.

Oron, A.P., and Berkowitz, B. (1998). Flow in rock fractures: the local cubic law assumption reexamined. Water Resour. Res. 34, doi.org/10.1029/98WR02285.

Ogilvie, S., Isakov, E., and Glover, P. (2006). Fluid flow through rough fractures in rocks. II: a new matching model for rough rock fractures. Earth Planet Sci. Lett. 241, 454–465. doi.org/10.1016/j.epsl.2005.11.041.

Persson, B.N.J., Albohr, O., Tartaglino, U., Volokitin, A.I., and Tosatti, E. (2005) On the nature of surface roughness with application to contact mechanics, sealing, rubber and adhesion. J. Phys.: Condens. Matter, 17, R1-R62.

Pyrak-Nolte, L.J., and Morris, J.P. (2000). Single fracture under normal stress: The relation between fracture stiffness and fluid flow. Int. J. Rock Mech. Min. Sci. 37, 245-262.

Raven, K., and Gale, J. (1985). Water flow in a natural rock fracture as a function of stress and sample size. Int. J. Rock Mech. Min. Sci. Geomech. Abstr. 22, 251–261. Doi.org/10.1016/0148-9062(85)92952-3.

Unger, A. J. A., and Mase, C. W. (1993). Numerical study of the hydromechanical behavior of two rough fracture surfaces in contact. Water Resour. Res. 29, 2101-2114.

Versteeg, H.K., and Malalasekera, W. (2007). An Introduction to Computational Fluid Dynamics: The Finite Volume Method, (Pearson, Prentice Hall, 2nd Edition).

Voltoloni, M., and Ajo-Franklin J.B. (2020). The sealing mechanism of a fracture in Oplinus Clay as revealed by in-situ synchrotron X-ray micro-tomography. Front. Earth Sci. 8:207. doi:10.3389/feart.2020.00207.

Wang, L., Cardenas, M., Slottke, D., and Ketcham, R. (2015). Modification of the local cubic law of fracture flow for weak inertia, tortuosity, and roughness. Water Resour. Res. 51, 2064–2080. doi.org/10.1002/2014WR015815.

Wiegmann A., Iliev O., and Schindelin A. (2010) Computer aided engineering of filter materials and pleated filters, in Global guide of the filtration and separation industry, ed. E. von der Luehe. (VDL Verlag, Roedermark, Germany), pp. 191–198.

Witherspoon, P., Wang, J., Iwai, K., and Gale, J.E. (1980). Validity of cubic law for fluid flow in a deformable rock fracture. Water Resour. Res. 16, 1016–1024. doi.org/ 10.1029/WR016i006p01016.

Zhang, C.-L., Wieczorek, K., and Xie, M.L. (2010). Swelling experiments on mudstones. J. Rock Mech. Geotech. Eng. 2, 44-51.

Zhang, C.-L. (2011). Experimental evidence for self-sealing of fractures in claystone. Phys. Chem. Earth. 36, 1972-1980.

Zhang, C.-L. (2013). Sealing of fractures in claystone. J. Rock Mech. Geotech. Eng. 5, 213-220.

Zhang, C.-L. (2016). The stress-strain-permeability behavior of clay rock during damage and recompaction. J. Rock Mech. Geotech. Eng. 8, 16-26.

Zimmerman, R., and Bodvarsson, G. (1996). Hydraulic conductivity of rock fractures. Transp. Porous Media. 23, 1–30. doi.org/10.1007/BF00145263.

6. Evaluation of achievements

6.1 The end-users perspective

According to the SOTA1-report (Levasseur et al. 2021) *"… the results of previous efforts on the identification and characterisation of the possible gas transport processes suggest that the mechanisms at play in different clays are generally similar"*. In other words, in the recent years a fundamental level of trust has been developed regarding the effective gas transport regimes and the gas-related failure mechanisms, which is complemented by a mutual understanding of the efficiency of self-sealing mechanisms. On the other hand, the report revealed honestly a deficiency of quantitative approaches and modelling tools, which are needed to implement such basic knowledge in quantitative performance assessment workflows for a sufficiently wide range of relevant repository settings.

Significant further achievements have been made in the course of the EURAD-GAS project, both on the experimental and the modelling side. Their evaluation is carried out in the subsequent sections with reference to the questionaires, which were compiled in the SOTA1 and SOTA2 reports (see chapter 2.3) to formulate the end-user needs according to the general mission of the project.

How could gas be transported within the repository and which water soluble and volatile radionuclide transport could be associated with it?

Innovative visualization techniques at pore scale provide new insights in gas/liquid flow and transport of dissolved / volatile radionuclides in clay barriers. In Task 3 of the EURAD-GAS project, visualisation of gas transport paths has been the subject of several laboratory experiments. IRSN's experimental programme (chapter 3.2) was dedicated to the visualization of hydration and gas invasion processes in initially heterogeneous bentonite mixtures. Hydration processes and gas injections were imaged in an X-ray transparent constant volume cell with a 3D μ-CT scanner. Hydration of the initially heterogeneous bentonite mixture ended in a rather quick homogenization of the material with little residual variability in bentonite density. During the subsequent gas invasion phase, clear evidence was found for preferential gas flow along grain boundaries and interfacial flow along the wall of the constant volume cell. This indicates that the gas transport paths in saturated bentonite are still affected by the initial distribution of bentonite density ("memory effect"), even though the hydration process reduces the density variations significantly. Future modelling strategies for seal design can make use of such insights to optimize the gas transport capacity of bentonite seals by adapting the grain size distribution of the bentonite mixtures.

CNRS-Uni Lorraine performed visualization experiments on gas transport and self-sealing in artificially fractured COx in a triaxial cell (chapter 4.2). Emphasis was on the fracture mechanisms, gas permeability and fracture closure for a wide range of stress conditions parallel and perpendicular to bedding. For different flow configurations a systematical determination of the dilatancy threshold was carried out, representing the turning point from which the cracks opening induces a significant increase in the gas permeability. This increase was greater when the main principal stress was parallel to the bedding planes due to the development of bedding parallel microcracks. Visualisation of fracture closure during the self-sealing tests was not restricted to the qualitative description of the associated self-sealing mechanisms but included a quantitative estimation of the evolution of the crack volume with time. This is a new category of information that can be used in the context of digital rock physics for the development of pore scale models and the validation of process models associated with the gas transport in fractured rock and self-sealing of gas induced fractures.

Broad consensus has been gained among the experimentalists, confirming that gas transport through clayey materials is barely associated with any displacement of porewater from the clay matrix. Corresponding evidence is not only based on the gas injection experiments by EPFL (chapter 4.4) and

UPC/CIMNE (chapter 4.5), but can be deduced indirectly from the huge existing data bases, that have been compiled in recent years to characterise the water retention behaviour of clayey barrier materials (e.g., Levasseur et al. 2021). Mercury intrusion porosimetry and water retention measurements on all sorts of clays indicate that a high mass fraction of typically 80 to 90 % of the porewater occupies the meso- and micropores of the saturated clay matrix. This porewater can be hardly displaced by an invading gas phase; this is of high relevance for the gas-induced transport of dissolved radionuclides in clay barriers. It can be concluded, that the expulsion dissolved radionuclides by gas is not a relevant transport mechanism.

How and to what extent could the hydro-mechanical perturbations induced by gas affect barrier integrity and long-term repository performance?

The gas-induced failure mechanisms of potential relevance are well-established (Levasseur et al. 2021) and have been largely confirmed within the EURAD-Gas project. Pathway dilation (terminology after Horseman et al. 1996) / dilatancy-controlled gas flow (preferred term in Marschall et al. 2005) is a plausible failure mechanism of special importance for clayey media with low tensile strength. Due to the expected micro-scale variability of the microfabric of the clayey material, it is conceivable that gas-induced microfractures will form before yielding (ductile fracturing; e.g., Gross & Seelig 2007). The process of gas-driven microfracturing leads to an increase of the void space, which is accompanied by a detectable increase in intrinsic permeability and a change in the capillary pressure-saturation relationship.

Evidence for dilatancy-controlled gas transport in clay-rich host rocks has been reported by CNRS-Uni Lorraine (chapter 4.2), EPFL (Chapter 4.4) and UPC/CIMNE (chapter 4.5), which builds confidence in the existing conceptual frameworks as described in the SOTA1 report. Beyond that, new insights were gained about the volumetric behaviour of soft and hard clays in response to water/gas injections. UPC/CIMNE conducted water/gas injection tests on Boom Clay samples and EPFL did similar tests on Opalinus Clay in a high-pressure oedometric cell, allowing for highly accurate measurements of the volumetric behaviour of the tested material. Both teams could demonstrate independently with their experimental set-ups, that clayey media exhibit a distinct drained / undrained volumetric response depending on the applied gas pressure build-up rates. This observation is of great significance for the assessment of repository performance, because gas pressure build-up in a real repository will take place at time scales in the order of 10^3 to 10^4 years, whereas a typical laboratory experiment on gas transport is conducted typically within a few months. The experiments of EPFL and UPC/CIMNE reveal that gas invasion under drained conditions is associated with less expansion of the rock, and thus with a lower risk for gas-induced microfracturing.

Several tests performed on bentonite by CTU (Chapter 3.1) showed no significant change in hydraulic conductivity and swelling pressure after one year of cyclic loading with fast gas tests. The integrity of the EBS appears to be preserved despite extreme stresses. The integrity of the EBS appears to be preserved despite extreme stresses.

CNRS-Uni Lorraine (chapter 4.2) and GRS (chapter 4.1) developed an experimental set up showing that the gas migration through the fracture clay does not limit the self-sealing ability of the material. This ability was observed on large fractures that could be associated with the initial excavation damaged.

How do the gas transport mechanisms in the clayey barrier materials of a geological repository depend on the conditions to which these materials are subjected, primarily mechanical stresses and fluid pressures?

Multiple experimental evidence has been provided in Task 3 to point out the impact of the in-situ state conditions (in particular pore pressure and stress) on the gas transport mechanisms in clay-rich host

rock. GRS (chapter 4.1) developed empirical relationships between the gas breakthrough pressure, water permeability and the effective confining stress. Further relationships were aimed at establishing new fracture closure laws. The correlation between clay mineral content and self-sealing capacity was demonstrated for COx and Opalinus Clay.

CNRS-Uni Lorraine (chapter 4.2) carried out systematic determinations of the dilatancy threshold for different flow configurations and different loading paths. A significant increase in the gas permeability was observed close to failure during triaxial test and deviatoric loading. The experiments can serve as input for model-based assessments, which allow to extrapolate the findings to a wider range of environmental conditions.

The shear-box experiments by BGS-UKRI (chapter 4.3) were aimed at analysing the impact of the stress state and the prevailing tectonic regime on water / gas transport in fractured Boom Clay, COx and OPA. Considerable variation was noted in initial gas flow and in the self-sealing capacity for all three rock types tested. The origin of these differences is not yet understood; further model-supported analyses are required to interpret the experimental results in the context of the prevailing hydro-mechanical state conditions. It is worth mentioning that the acquired experimental data base will serve as indispensable input for model development.

Gas transport in clayey barrier materials is strongly controlled by heterogeneities at various scales, ranging from microfabric to large scale heterogeneities such as sedimentological or tectonic features. EPFL carried out gas injection tests on remolded and recompacted OPA, aimed at mimicking the gas transport characteristics of fault gouge material (chapter 4.4). The experiments indicate a low gas entry pressure and a high gas permeability of the remolded material, whereas the water permeability remained low. This demonstrates that natural and excavation induced fractures in clayey rocks act as distinct preferential gas transport paths, whereas the hydraulic barrier function of the fractured rock is maintained due to its self-sealing capacity.

What are the relevant material and fluid properties controlling these mechanisms?

Gas transport in natural and engineered clay barriers is largely controlled by the mineralogical composition and the microstructure of the materials. Clay mineral content is typically above 40% with significant amount of swelling clay minerals such as smectites or illite-smectite mixed layers. The pore space is formed by a network of micro/meso- and macropores with typical pore sizes in the range of 1 - 100 nm. Water permeability of clays is generally low, the water retention curves display high gas entry pressures. Geomechanically, clays are characterised by low strength, low stiffness and distinct swelling pressures. Comprehensive geotechnical data bases were compiled in the SOTA1 report (Levasseur et al. 2021), which have been in the EURAD-GAS project. All experimental teams of Task 3 contributed to the existing data bases with new geotechnical characterisations of the tested material.

How to characterise the material properties, accounting for the fact that some of these might well be affected by the passage of gas?

Reliable test protocols have been developed to characterise the basic geotechnical properties of clay barriers. The consistency of the collected data from different geotechnical laboratories builds confidence in the quality of the existing gas-related data bases for a wide range of clay material.

Water / gas permeability testing under well-constrained hydro-mechanical conditions may represent the most challenging type of geotechnical laboratory tests on clay materials. In the past, the comparison of experimental results from different geotechnical laboratories has shown discrepancies. Often the origin of such discrepancies could not be explained unequivocally. Further efforts are required in this context to benchmark the test protocols and test equipment. The integrated experimental procedures for water

/ gas injection testing, developed by EPFL and UPC/CIMNE in the context of Task 3 may serve as a basis for launching new international benchmark exercises.

Which gas-related processes could impair repository performance with respect to the intended safety functions radionuclide retention and waste confinement?

The SOTA2 report (Levasseur et al. 2024) summarises the detrimental effects of gas produced within a geological repository after closure that could impair the long-term repository performance:

- The potential for over pressurization and damage if gas would be produced at a faster rate than it can diffuse out of the multi-barrier system.
- The potential for release of volatile radionuclides to the biosphere.
- The potential for accelerated gas-driven expulsion of water containing dissolved radionuclides to the biosphere.
- The risk associated to the accumulation and/or sudden release of flammable gas.

In the light of the new experimental results gained in Task 3 of the EURAD-GAS project, it is particularly the potential for accelerated gas-driven expulsion of dissolved radionuclides which can be downgraded in terms of its safety relevance. The recent gas injection experiments by UPC/CIMNE, CNRS-Uni Lorraine and EPFL on Boom Clay, COx and OPA provide clear evidence for negligible pore water expulsion in response to gas invasion, which is expressed in the two-phase flow formulation of gas transport processes by a marginal phase interference (distinct separation of the relative permeability curves for gas/water).

The feature of drained / undrained behaviour of clayey rocks (Boom Clay and OPA, respectively) observed by UPC/CIMNE and EPFL may be considered as new evidence to consider in the evaluation of the potential for gas-induced over pressurization and damage. It can be assumed that gas transport in the clayey host rock of a real repository will happen at under drained conditions due to the because pressure build-up in the backfilled repository structures. The recent experiments have shown that the observed strains in response to slow gas invasion (i.e. undrained conditions) are less pronounced than in the case of fast pressure build up. However, further confirmation of the experimental results is needed to build a reliable line of arguments on this observation.

Another source of potential bias is associated with the choice of the test material. It is common practice to chose “intact” rock samples for gas testing, which means that test material is selected with low variability of the fabric at the sample scale. Such a sample bias may lead to an overestimation of the effective gas entry pressure and the water retention curves at the in-situ scale. At the decameter to hectometer scale of gas accumulation in the backfilled repository structures, lithostratigraphic variability of the host rock and tectonic features are expected to form a more heterogeneous host rock. In essence, increasing heterogeneity of the rock mass corresponds to lower gas entry pressure and less distinct water retention behaviour, which is mainly controlled by the “flaws” in the rock fabric. Geostatistical analyses of the microfabric of Opalinus Clay samples from different lithostratigraphic units provide clear evidence for the scale dependency of pore size distributions and the corresponding water retention behaviour (ZHAW; see chapter 5.2). From a safety assessment perspective, two phase flow parameters derived from “intact” rock samples may represent an upper limit of gas entry pressures and water retention curves. The influence of the natural variability of clay microstructure on gas properties needs to be verified on the different clay host rocks such as Boom clay or COx.

What are the safety-related consequences on the barrier properties during and after the passage of gas to be considered?

During gas passage, the transport of dissolved radionuclides by advection and diffusion is limited, because the gas phase occupies preferentially the macropores of the clay matrix and blocks the most transmissive transport paths for dissolved radionuclides. Diffusion and advection of dissolved radionuclides is restricted to the connected pore space constituted by the meso-and micropores. The observed low phase interference is a clear indication for the insignificant role of porewater expulsion during gas passage. Even in the case of dilatancy controlled gas transport, there is no evidence for major desaturation of the clay matrix.

The investigation of self-sealing of gas induced (micro-)fractures has been the subject of all experimental teams (CTU, IRSN, GRS, CNRS-Uni Lorraine, BGS-UKRI, EPFL and UPC/CIMNE). All teams report an efficient self-sealing of the tested clay materials (engineered barriers, natural barriers). Visualization of gas-induced fractures during the rehydration process provides convincing evidence for the efficient self-sealing of clay-rich materials.

6.2 Further achievements of general scientific interest

In the course of Task 3 a wealth of new experimental results has been collected, which is of general scientific interest from the viewpoint of the RWMO. The questionnaire in chapter 6.1 addresses only a little fraction of relevant achievements in the field of gas induced impacts on barrier integrity.

In this context the confirmation and extension of the comprehensive gas-related data bases for a wide range of clay barriers are of invaluable relevance for building a mechanistic understanding of gas transport in engineered and geological clay barriers. From a performance assessment perspective, it is not the new unresolved scientific issues of gas-induced impacts that build confidence in the performance of the repository system, but the confirmation of a sound understanding of the basic phenomena and processes. On the other hand, a rigorous and honest evaluation of newly discovered phenomena and processes of potential safety relevance is an indispensable step to build trust in current future PA workflows.

CTU's comprehensive laboratory programme (chapter 3.1) consisting of cyclical water and gas injection experiments with Czech Ca-Mg bentonite BVC is a typical example for the extension of existing data bases which is of value for other RWMCs. The experimental programme complements previous studies in bentonite barriers, which were mostly carried out with Wyoming sodium bentonite MX-80. A long-lasting laboratory programme was executed by CTU using oedometric cells and consisting of a series of cyclic gas injection and resaturation phases. Water and gas injections were conducted with homogeneous bentonite samples of different dry density and with samples, which included a discontinuity. In good agreement with other types of bentonites, the experiments did not reveal significant changes in the sealing performance of the material (hydraulic conductivity and swelling pressure) after one year of cyclic loading. An interesting detail of the results with the heterogeneous test samples was the formation of distinct preferential gas paths even after long resaturation times. A similar behaviour has been observed in IRSN's experiments, where gas transport paths in saturated bentonite were still affected by the initial distribution of bentonite density, even though the hydration process had reduced the density variations significantly. Imaging of the hydration processes and gas injections with a 3D µ-CT scanner may provide further mechanistic insights in the saturation processes during hydration and flow localization during the gas injection phases. The experimental results of CTU demonstrate that the BVC bentonite may represent a reliable alternative to the expensive MX-80 which is used in other repository programs.

From the end-user side the remarkable experimental data bases for model development may be seen as the most important achievements. The close interactions of the experimentalist with the modelling teams of Task 3.3 during the EURAD-GAS progress meetings facilitated a traceable and transparent documentation and hand-over of data to the modellers. Innovative new visualization techniques allowed

to test state-of-the-art methods of digital rock physics. ZHAW used 3-D visualization data to reconstruct digital pore structures and fracture surfaces. These digital structures are applicable for multiphase flow and transport simulations and, in a longer perspective, to build digital twins of the geological and engineered barrier systems at spatial scales from micro to macro. The use of the experimental data bases of Tasks 3.1 and 3.2 by the modelling teams of Task 3.3 is essentially documented in the Milestone Report MS 230.

6.3 References

Gross, D., Seelig, Th. (2007): Bruchmechanik. Springer Verlag.

Horseman, S.T., Higgo, J.J.W., Alexander, J. & Harrington, J.F. (1996): Water, gas and solute movement through argillaceous media. Nuclear Energy Agency Rep. CC-96/1, Paris, OECD.

Levasseur S., Collin F., Daniels K., Dymitrowska M., Harrington J., Jacops E., Kolditz O., Marschall P., Norris S., Sillen X., Talandier J., Truche L. and Wendling J. (2021). Initial state-of-the-art on gas transport in clayey materials. European Commission, Work Package GAS: Mechanical understanding of gas transport in clay-based materials of the HORIZON 2020 project EURAD. Deliverable 6.1.

Levasseur S., Collin F., Dymitrowska M., Harrington J., Jacops E., Kolditz O., Marschall P., Norris S., Sillen X., Talandier J., Truche L. and Wendling J. (2024). State of the Art on Gas Transport in Clayey Materials – Update 2023. Deliverable D6.2 of the HORIZON 2020 project EURAD, Work Package Gas. EC Grant agreement no: 847593.

Marschall P., Horseman S. and Gimmi T. (2005). Characterisation of gas transport properties of the Opalinus Clay, a potential host rock formation for radioactive waste disposal. Oil and Gas Science and Technology - Revue de l'IFP 60 (1), 121–139.

Part 2. Barrier integrity: model-based interpretation by Subtask T 3.3

Contributors **Part 2. Olaf Kolditz, Jean Talandier, Paul Marschall; Nathan Amrofel, Victoria Burlaka, Frédéric Collin, Gilles Corman, Anne-Catherine Dieudonné, Magdalena Dymitrovska, Maxime Faivre, Richard Giot, Fabrice Golfier, Sylvie Granet, Norbert Grunwald, Alireza Hassanzadegan, Zhaojiang Huang, Joaquín Liaudat, Christian Müller, Sebastia Olivella, Michael Pitz, Jerry-Peprah Owusu, Adriana Quacquarelli, Eric Simo, Alexandru Tatomir, Anne-Julie Tinet, Erdem Toprak, Philip J. Vardon, Gesa Ziefle**

Table of content

List of figures

List of tables

.

Introduction

1. Introduction

This part of the report summarises the model developments and applications in the EURAD work package GAS. It continues the previous progress reports of Task 3 produced during the duration of the EURAD-GAS project (MS125, MS216+217) and aims to improve the mechanistic understanding of gas transport processes in clay-rich materials, addressing both engineered barrier systems and the host rock as geological barriers.

The main objectives of this work package, as stated in the original proposal, are

- to enhance the mechanistic understanding of gas transport processes in natural and engineered clay materials, including their couplings with mechanical behaviour and their impact on material properties.
- Additionally, the aim is to assess the gas transport regimes that may be active at the scale of a geological disposal system and their potential impact on barrier integrity and repository performance.

The program aimed to produce results that are relevant to a broad range of national programs. The possibility of gas transport in different clays is supported by previous research on the identification and characterisation of gas transport processes. The mechanisms involved are generally similar, but the conditions for the transition from one transport regime to another (diffusion, two-phase flow, pathway dilation and fracturing) strongly depend on the specific properties of the clay material, such as gas pressure, stresses/deformations, and saturation.

This work package aimed to transfer knowledge gained from laboratory and in-situ experiments to configurations commonly found in current repository designs.

- It addresses key questions from end-users, such as how gas could migrate within the repository and which water-soluble and volatile radionuclides could be associated with it.
- It also examines how hydro-mechanical perturbations induced by gas could affect barrier integrity and long-term repository performance.

This work package GAS relied on the experience feedback and conclusions from the previous EC Project FORGE. The experimental investigation of gas transport in FORGE revealed complex mechanisms, such as the development of discrete, unstable pathways controlled by the mechanical behaviour of the porous media. However, it has been suggested that this complexity can be addressed by bounding the effects of these mechanisms using simpler and more robust descriptions for evaluation purposes. This work package aims to increase confidence in the overall understanding of gas behaviour in clay materials gained from the FORGE EC project and improve its integration into the conceptualisation process for the different components of a repository system. This statement should support and justify the use of rigorous evaluation methods and confirm the expert judgment at the end of FORGE that gas does not prevent geological disposal, but rather requires managing uncertainties.

The GAS models address both Task 2 transport mechanisms, including gas diffusion, advection, and retardation processes, and Task 3 barrier integrity. Task 2 also covers hydromechanical processes related to multiphase flow phenomena, such as fluid displacement versus dilatant gas flow, which directly affect

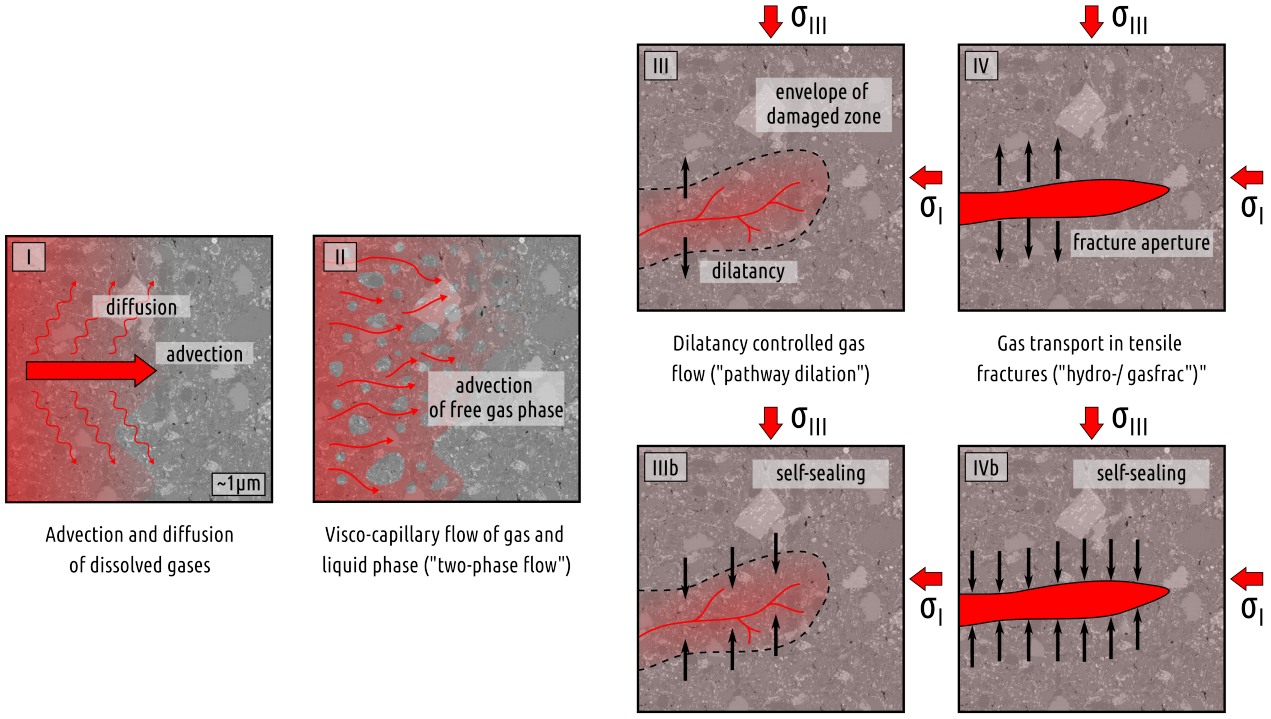

Figure 1.1: Modified version of an overview of gas transport regimes in low-permeable clay rock after Marschall et al. (2005a), Figure 2. and Cuss et al. (2014b), Figure 1.

the integrity of barrier functions in Task 3. In our model, we examine the entire process chain, as shown in Fig 1.1. Therefore, throughout the WP GAS course, we did not separate Task 2 or 3 activities but instead combined them in our conceptual, holistic approach.

In MS216+217 report (Chapter 4) results on the modelling of laboratory experiments on gas transport in clay materials carried out in EURAD WP had been presented. During the EURAD-GAS Workshop in October 2022 the experimentalists and modeler have discussed their joint strategy for the analyses of the EURAD-GAS experiments. As a results the work program as illustrated in Fig. 1.2 has been drafted along the process chain concerning the barrier integrity for both buffer materials and host rock (various clay rocks). Gas diffusion, triax gas injection and swelling experiments in boxes with solid frame lines have been analyzed and are described in the following. Experiments in boxes with dashed frame lines are under debate currently.

This deliverable D6.8 - Part 2 summarises activities carried out in the subtask 3.3 of the WP GAS by each partners involved in this subtask. Their activities, detailed in chapter 2, mainly focused on the development of conceptual process models of gas-induced damage evolution and self-sealing processes for damaged or intact host rocks and EBS materials. These models were then validated in a series of configurations of relevance for geological disposal in clays.

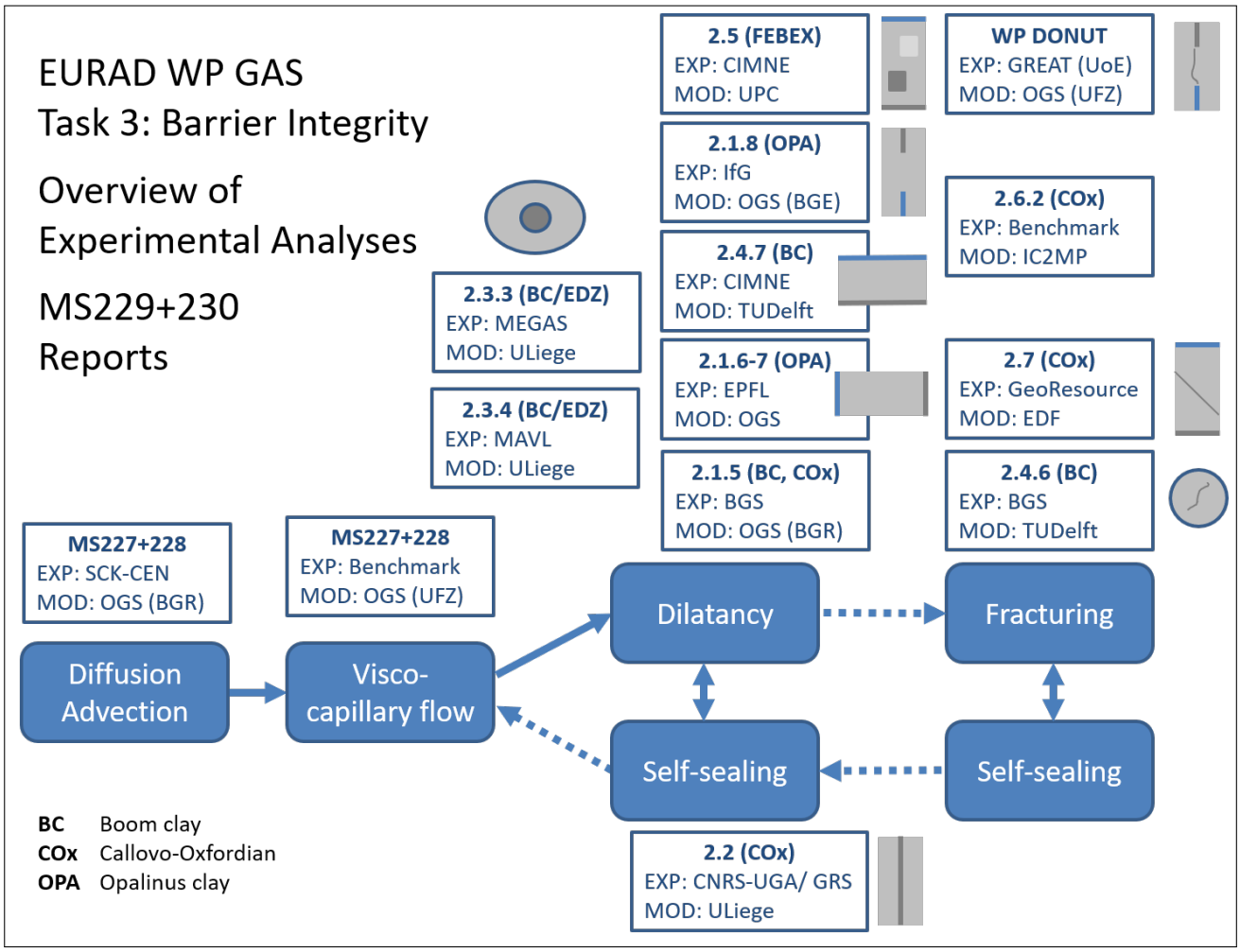

Figure 1.2: This is the current status (24.02.2024) and will serve as an overview/guide through the report MS230

.

Team Reports

2. Team Reports

.

OpenGeoSys Team
(UFZ, BGE, BGR)

2.1. Triax gas injection tests (OGS Team)

2.1.1. Introduction

Clays, known for their low hydraulic conductivity, low molecular diffusion, and significant radionuclide retention capacity, are viewed as prospective host rocks for geological disposal across numerous European nations. Due to the natural water content of porous clays, it is anticipated that after the closure of the final repository, there will be an influx of solution from the host rock into the backfilled mine cavities. Over time, this could at least partially fill the mine cavity with the solution. The contact of the inflow solution with the steel disposal canisters will eventually lead to anaerobic corrosion in the absence of oxygen. This process transforms the iron into magnetite and produces hydrogen. Depending on the repository design, the volume of gas produced can lead to a significant gas pressure in the repository that can potentially affect the confinement properties of the clay. Thus, the generation and transport of gas through clay materials is a crucial concern for the geologic disposal of radioactive waste.

Marschall et al. (2005b) identified four fundamental gas transport mechanisms in clay-based materials. These mechanisms are discerned based on phenomenological observations and include: the advection and diffusion of gas dissolved in pore water, the visco-capillary two-phase flow, the gas flow controlled by dilatancy and gas movement along prominent tensile fractures, termed as gas fracturing. Despite extensive research on the subject, there remains a notable lack of clarity regarding the factors that influence the activation, progression, and stability of the different gas transport mechanisms. In this context, extensive research activities, development and implementation of cutting edge numerical methods have been carried out in the numerical framework OpenGeoSys. The ultimate goal pursued by the OpenGeoSys team is to encapsulate all four gas transport mechanisms within one unified framework, tailored to analyse gas transport processes from the microscale up to the repository scale. The different methods and concepts developed was validated in the work package GAS through modelling of different laboratory experiments.

2.1.2. OpenGeoSys platform

OpenGeoSys (OGS)[1] is a scientific open-source initiative for the numerical simulation of thermo-hydro-mechanical/chemical (THMC) processes in porous and fractured media. The basic concept of OGS consist on providing a flexible numerical framework, using primarily the Finite Element Method (FEM) for solving multi-field coupled processes with application in different scientific and technical disciplines. The development history of OGS with its roots in ROCKFLOW and FEFLOW started in the 1980ties (a more detailed description can be found in Kolditz et al. (2012)). Provided years are indicating starting points of related software developments.

OGS has been successfully applied in the fields of regional, contaminant and coastal hydrology, technical and geothermal energy systems, geotechnical engineering, energy storage, CO2 sequestration/storage and nuclear waste management and disposal. The current version OGS-6 is providing complete workflows starting from data integration, High Performance Computing (HPC) for coupled process simulation and using virtual reality (VR) concepts for data analytics. OGS-6 is developed and maintained platform-independently using professional software engineering tools such as version management (GitHub) and containerization (e.g. Docker, Singularity). A strict code review is conducted for quality assurance completed by unit testing and comprehensive benchmarking. OGS provides open interfaces for combining with other simulators (e.g. GEMS, iPhreeqc for geochemical processes) including Python bindings. A recent overview of OGS software engineering can be found in Bilke et al. (2019).

A new OGS-6 model has been recently developed (Grunwald et al., 2022) in order to address the TH2M

[1] www.opengeosys.org

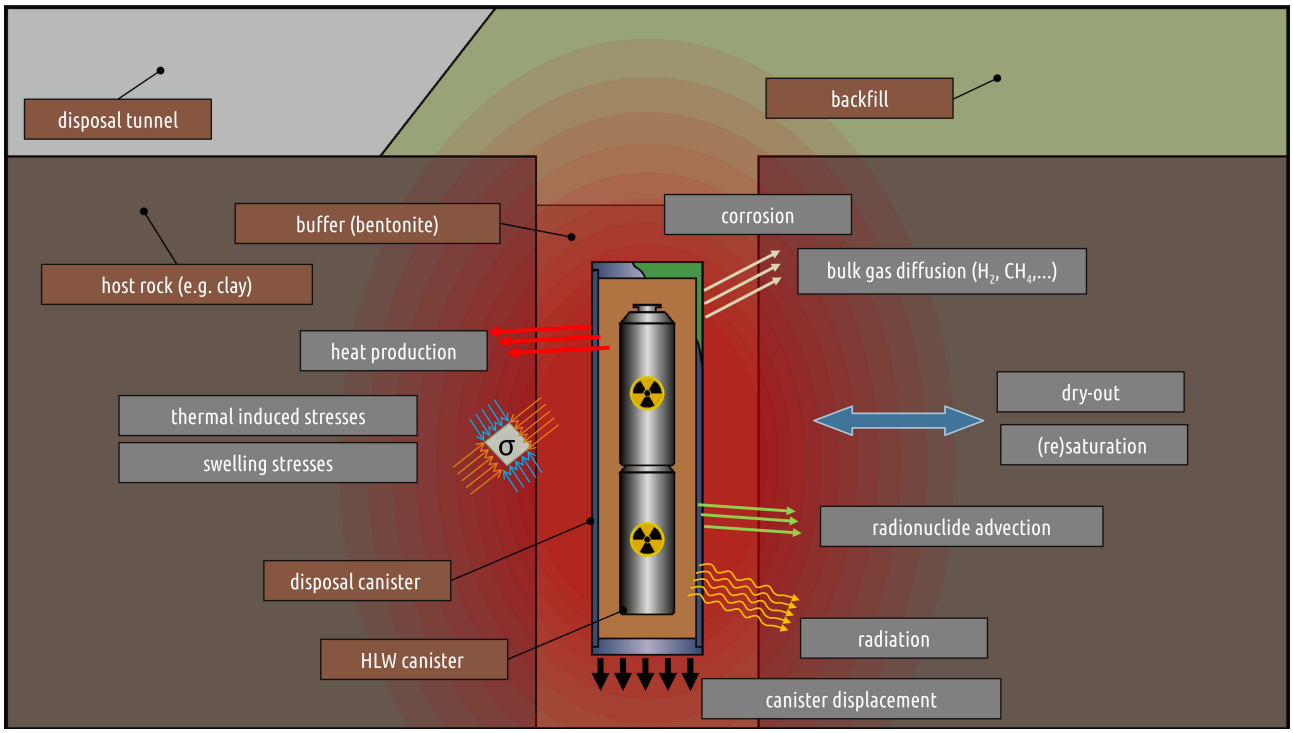

Figure 2.1: TH2M processes in the near-field of heat emitting radioactive waste (Grunwald et al., 2022)

processes in the near-field of heat emitting radioactive waste in full complexity (Fig. 2.1). We briefly list some recent developments in THM modeling the such as: Error-controlled elasto-visco-plastic constitutive models for clay rock (Zhang and Nagel, 2020), multi-scale approaches for fluid inclusions in salt rock (Shao et al., 2019), brittle-ductile transitions and related processes in volcanic systems (Parisio et al., 2019b,c), variational phase field methods for fracture mechanics (Yoshioka et al., 2019; Miao et al., 2019), non-local integral plastic-damage constitutive theory (Parisio et al., 2019a, 2018), pressure solution and stress corrosion processes in crystalline rocks (Lu et al., 2018), two-phase flow reactive transport processes (Huang et al., 2018), and introducing novel visualization concepts for THM analyses (Blecha et al., 2019).

The current OGS-6.5.0[2] release contains several feature supporting the modelling of TH2M and reactive transport processes. The reactive transport process and its Phreeqc interface were enhanced, e.g. by an extended porosity interface and providing two ways of calculating solid/liquid ratio. A new process, the non-isothermal Richards mechanics (OGS-TRM) was implemented completing abilities for complex thermo-hydro-mechanical simulations under unsaturated conditions. The TH2M and TRM allow a direct comparison of two-phase and unsaturated flow processes under full THM conditions.

Concerning the verification procedure for the new OGS-6 TH2M model, a comprehensive benchmark suite has been developed (Fig. 2.2). The basic concept is to test the complete hierarchy of process couplings from individual T, H (gas and liquid flows), M via binary and ternary to the full TH2M processes. The benchmark suite contains also classic test cases as the heat pipe problem, the Liakopoulos experiment and an analytical solution for the point heat source.

2.1.3. Conceptual model

Concerning model development, we briefly recall the governing equations of the continuum mechanical TH2M concept (sec. 2.1.3.1) and provide a link to related activities in WP DONUT regarding the development of variational phase field methods for modeling discontinuities over several scales.

[2]https://discourse.opengeosys.org/t/opengeosys-6-5-0-released/1339

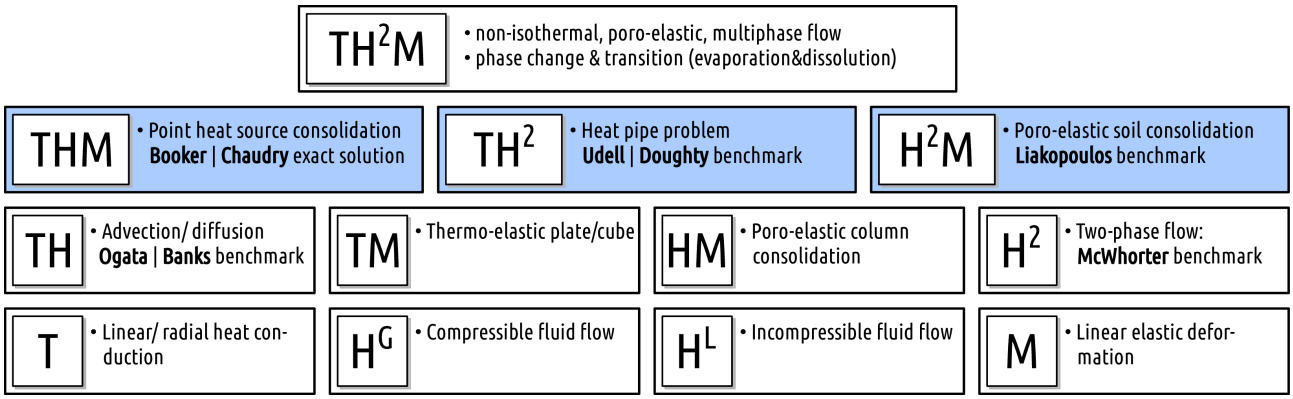

Figure 2.2: TH2M benchmarking concept Grunwald et al. (2022)

2.1.3.1. Governing equations for the TH2M process model

We provide an overview of the governing equations for OGS-TH^{2}M problems Grunwald et al. (2022). The equation system given below shows an example formulation for non-isothermal two-phase flow in porous media. All of the partial differential equations are developed from basic balance equations of mass, linear momentum and energy. For the hydraulic part, gas pressure p_{GR} and capillary pressure p_{cap} have been chosen to be primary variables. Temperature T and displacement u_S serve as primary variables for the thermodynamic and mechanical parts.

Mass balance governing equations are given by

$$\underbrace{s_G\left(\phi\beta_{p,GR}+\frac{\alpha_B-\phi}{K_{SR}}\right)\frac{d_S p_{GR}}{dt}}_{\text{storage term (gas pressure)}}-\underbrace{s_G\left(\phi\beta_{T,GR}+(\alpha_B-\phi)\,\beta_{T,SR}\right)\frac{d_S T}{dt}}_{\text{thermal expansion}}+\underbrace{s_G\alpha_B\,\mathrm{div}\,\frac{d_S u_S}{dt}}_{\text{deformation}}$$
$$-\underbrace{\left(s_G\,(\alpha_B-\phi)\,\beta_{p,SR}\left[s_L+p_{cap}\frac{\partial s_L}{\partial p_{cap}}\right]+\phi\frac{\partial s_L}{\partial p_{cap}}\right)\frac{d_S p_{cap}}{dt}}_{\text{storage term (capillary effects)}}+\underbrace{\mathrm{div}\,(\tilde{w}_{GS})}_{\text{gas flow}}=0 \tag{2.1}$$

for the gas phase and

$$\underbrace{s_L\left(\phi\beta_{p,LR}+\frac{\alpha_B-\phi}{K_{SR}}\right)\frac{d_S p_{GR}}{dt}}_{\text{storage term (gas pressure)}}-\underbrace{s_L\left(\phi\beta_{T,LR}+(\alpha_B-\phi)\,\beta_{T,SR}\right)\frac{d_S T}{dt}}_{\text{thermal expansion}}+\underbrace{s_L\alpha_B\,\mathrm{div}\,\frac{d_S u_S}{dt}}_{\text{deformation}}$$
$$-\underbrace{\left(s_L\,(\alpha_B-\phi)\,\beta_{p,SR}\left[s_L+p_{cap}\frac{\partial s_L}{\partial p_{cap}}\right]+\phi\left[s_L\beta_{p,LR}-\frac{\partial s_L}{\partial p_{cap}}\right]\right)\frac{d_S p_{cap}}{dt}}_{\text{storage term (capillary effects)}}+\underbrace{\mathrm{div}\,(\tilde{w}_{LS})}_{\text{liquid flow}}=0 \tag{2.2}$$

for the liquid phase. Phase saturation s_α is the ratio of phase volume fraction ϕ_α (for $\alpha = L, G$) to porosity ϕ, with $s_G = 1 - s_L$ and where s_L is usually a function of capillary pressure. The volume fraction ϕ_α is the ratio of the volume occupied by phase α over the total volume ($d\Omega_\alpha\,(d\Omega^{-1})$). The *Darcy*-velocities $\tilde{w}_{\alpha S}$ given by

$$\phi_\alpha \boldsymbol{w}_{\alpha S}=\tilde{\boldsymbol{w}}_{\alpha S}=-\frac{k_\alpha^{Rel}\boldsymbol{k}_S}{\mu_{\alpha R}}\left(\mathrm{grad}\,p_{\alpha R}+\rho_{\alpha R}\boldsymbol{a}_\alpha-\rho_{\alpha R}\boldsymbol{b}_\alpha\right) \tag{2.3}$$

are velocities of the fluid phases relative to the deforming solid phase. The remaining symbols are defined

Symbol	Description
$\beta_{p,GR}$	gas phase compressibility
$\beta_{p,LR}$	liquid phase compressibility
$\beta_{T,GR}$	gas phase thermal expansivity
$\beta_{T,LR}$	liquid phase thermal expansivity
$\beta_{T,SR}$	solid phase thermal expansivity
K_{SR}	compression modulus of solid phase
$\frac{d_S(\bullet)}{dt}$	material time derivative of $\bullet$ w.r.t. solid phase

Table 2.1: Symbols

in table 2.1. The Energy equation for the overall multiphase aggregate can be written as

$$\underbrace{\left(\rho c_p\right)_{eff}\frac{d_S T}{dt}}_{\text{thermal energy storage}} \underbrace{-\left(\phi_L\beta_{T,LR}+\phi_G\beta_{T,GR}+\phi_S\beta_{T,SR}\right)T\frac{d_S p_{GR}}{dt}}_{\text{pressure work storage (gas phase)}} \underbrace{+\beta_{T,LR}T\tilde{w}_{LS}\cdot \operatorname{grad} p_{cap}}_{\text{advection}}$$
$$\underbrace{+\left(\phi_L\beta_{T,LR}T+\phi_S\beta_{T,SR}T\left(s_L+p_{cap}\frac{\partial s_L}{\partial p_{cap}}\right)+\phi p_{cap}\frac{\partial s_L}{\partial p_{cap}}\right)\frac{d_S p_{cap}}{dt}}_{\text{pressure work storage (gas and liquid phase)}} + \underbrace{\operatorname{div} q}_{\text{heat conduction}}$$
$$\underbrace{-\left(\beta_{T,LR}\tilde{w}_{LS}+\beta_{T,GR}\tilde{w}_{GS}\right)T\cdot \operatorname{grad} p_{GR}+\left(\rho_{LR}c_{pL}\tilde{w}_{LS}+\rho_{GR}c_{pG}\tilde{w}_{GS}\right)\cdot \operatorname{grad} T}_{\text{advection}} = 0$$

where the assumption of local thermal equilibrium was made. This assumption follows the idea that heat transfer among the phases occurs very fast such that all phases share the same temperature at a certain point. The effective heat capacity of the overall aggregate $\left(\rho c_p\right)_{eff}$ is defined as $\left(\rho c_p\right)_{eff} = \sum_\alpha \phi_\alpha \rho_{\alpha R} c_{p,\alpha}$ for $\alpha = G, L, S$ with intrinsic phase mass densities $\rho_{\alpha R}$. Similarly, the combined heat conductive flux $q = q_{GLS}$ is defined as $q = \sum_\alpha q_\alpha$.

The mechanical part of the equation system is governed by the displacement equation given by

$$0 = \rho \boldsymbol{b} + \operatorname{div}\left(\boldsymbol{\sigma}_S^E - \alpha_B p_{FR}\mathbf{I}\right) \tag{2.4}$$

where ρ is the bulk density of the overall multiphase aggregate defined as $\rho = \sum_\alpha \phi_\alpha \rho_{\alpha R}$ for $\alpha = G, L, S$ and b are body force accelerations acting equally on all phases. The total stress $\boldsymbol{\sigma}$ is given by the effective stress $\boldsymbol{\sigma}_S^E$, which is governed by constitutive laws, attenuated by the pore fluid pressure p_{FR}, which is given by $p_{FR} = \sum_\alpha s_\alpha p_{\alpha R}$. To close the above equation system, constitutive laws or material property relations are required.

2.1.3.2. Variational phase fields extension

Within the Work Package DONUT the OGS team is focusing on the Variational Phase Field (VPF) method for multiscale simulation of fracture propagation processes. The VPF method has two advantages, first, it can be smoothly embedded into the finite element method for multiphysics simulations namely thermo-hydro-mechanical-chemical (THMC) processes and, second, it is fracture propagation processes do not depend on meshing effects, however mesh density is important for the sake of accuracy. The present work described in this report is dealing with calculation of fracture aperture. To this purpose two methods have been evaluated, line integral and level-set approaches with certain pros and cons. Fracture aperture is the most important factor for fracture permeability and, therefore, affecting flow and transport processes in both near and far fields. Precise estimations of discontinuities concerning fracture size and crack openings are of essential importance of multi-scale processes in subsurface systems Lepillier et al. (2020); Yoshioka et al. (2019); Chukwudozie et al. (2019); Cajuhi et al. (2023).

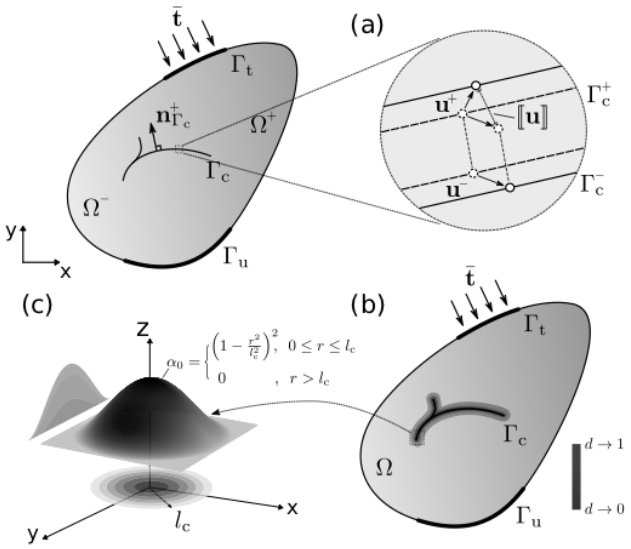

Figure 2.3: Various modelling concepts for fracture mechanics as introduced in Yoshioka et al. (2019)

2.1.3.3. Gas permeability models

Numerous laboratory and in-situ studies were conducted in FORGE on gas transport within clay systems, as cited by researchers such as Birgersson and Karnland (2013) and Zhang et al. (2013). A shared conclusion from these studies is that free gas transport in low-permeability water-saturated or near-saturated porous media happens via the formation of specific gas pathways. This leads to either sample dilatancy or the emergence/reactivation of discontinuities in the tested material. Laboratory experiments, like those of Harrington et al. (2013), have distinctly observed this dilation. Yet, according to Nosek et (2013), no experiment could evidence the two-phase flow transport in FORGE on low-permeability clay media nearing water saturation.

Traditional models based on a continuum two-phase flow approach couldn't accurately mimic these preferential pathways formed during gas transport in clay. To better represent the influence of pathway dilation on gas transport on a relevant scale, FORGE introduced several strategies. Some involve pressure-dependent porosity and permeability to better simulate a swift gas flow increase post a certain injection pressure threshold. Others, like suggestions from Arnedo et al. (2013) and Yamamoto et al. (2013), proposed a more explicit coupling of two-phase flow transport models with poro-mechanics models. This was to more adequately consider the evolving stress field and its potential impact on pathway dilation during gas transport.

In many instances, the FORGE models reasonably mirrored experimental results. Nonetheless, their predictive accuracy remains unconfirmed. Under WP GAS, we revisited and applied some of these models to experiments from EURAD to evaluate their predictive reliability.

In Task 2.2 of WP GAS, BGE and its partners UFZ and BGR implemented different gas permeability models aiming at modelling the dilatancy controlled gas flow in clay materials. The first model put forward by Xu et al. (2013b,a) provides a functional relationship between the permeability of the material and the local gas pressure. The model assumes based on in situ observations that permeability changes increase significantly when a specific gas pressure threshold is exceeded. When the critical gas pressure threshold is exceeded, micro-cracks are formed which significantly increase permeability through the development of a percolation network.

$$k(p) = \begin{cases} (1 + a_1 p)k_0, & \text{if } p < p_{th}. \\ [1 + a_1 p_{th} + (p - p_{th})a_2]k_0, & \text{otherwise.} \end{cases} \tag{2.5}$$

a_1 and a_2 are empirical parameters.

In the second model, the change of permeability is expressed as function of changes in deformation. The deformation considers the volumetric strain (ε_{vol}) and the equivalent plastic strain (ε_p) Xu et al. (2013b,a). It describes an increase of permeability as soon as a plastic failure occurs. It is expressed by

$$k(\varepsilon) = \begin{cases} (10^{b_2 \Delta\varepsilon} e^{b_1 \varepsilon^p} k_0, & \text{compression.} \\ (10^{b_3 \Delta\varepsilon} e^{b_1 \varepsilon^p} k_0, & \text{tension.} \end{cases} \tag{2.6}$$

where b_1, b_2 and b_3 are empirical parameters.

The third model has been developed in the scope of the DECOVALEX project and implemented in OpenGeoSys. It is based on the Mohr-Coulomb Failure Index Wang et al. (2021). The failure index dependent permeability model according to Wang et al. (2020) is defined as

$$k = k_0 + H(f - 1)\, k_r\, e^{bf}\, I \tag{2.7}$$

where k_0 is the intrinsic permeability of the undamaged material, H is the Heaviside step function, f is the failure index, k_r is a reference permeability, b is a fitting parameter. k_r and b can be calibrated by experimental data.

The failure index f is calculated from the Mohr-Coulomb failure criterion comparing an acting shear stress. With the conventional mechanics notations, which mean that tensile stress is positive, the Mohr-Coulomb failure criterion Labuz and Zang (2012) takes the form

$$\tau_f(\sigma) = c - \sigma \tan\phi \tag{2.8}$$

with τ the shear strength, c the cohesion, σ the normal stress, and ϕ the internal friction angle. We further introduce the maximum shear stress $\tau_m = (\sigma_3 - \sigma_1)/2$ and the mean stress $\sigma_m = (\sigma_1 + \sigma_3)/2$, where σ_1 and σ_3 are the minimum and maximum principal stress, respectively. The criterion varies depending on whether it is below or above a specific threshold value, denoted as $\sigma_m^{max} \in (0, c/\tan\phi)$, which falls within the range $(0, c/\tan\phi)$. This threshold is related to, but not equivalent to, the material's tensile strength.

Then, the failure index is determined by

$$f = \begin{cases} \dfrac{|\tau_m|}{\cos(\phi)\tau_f(\sigma_m)} & \text{if } \sigma_m \le \sigma_m^{max} \\ \max\left\{ \dfrac{|\tau_m|}{\cos(\phi)\tau_f(\sigma_m)}, \dfrac{\sigma_m}{\sigma_m^{max}} \right\} & \text{if } \sigma_m > \sigma_m^{max} \end{cases} \tag{2.9}$$

The computed permeability components are restricted with an upper bound, i.e. $k := k_{ij} < k_{max}$.

A fourth model originally put forward by Alonso et al. (2006) and applied to model gas transport in clay barriers by Olivella and Alonso (2008c) has been recently further developed and introduced in OpenGeoSys

by Zill et al. (2021). The proposed approach is based on a homogenizing sets of parallel fractures on the micro-scale, as illustrated in Figure 2.4. The geometry of these fractures can be characterized by several parameters. The mean fracture distance a represents the average distance between adjacent fractures, while the fracture aperture b represents the opening of each fracture. The fracture normal vector n describes the orientation of the fractures. Additionally, the height of the volume element in the fracture normal direction s is required for the derivation of the permeability equation. These parameters are crucial in determining the flow behavior of fluids through fractured porous media, making them essential for developing accurate models and predictions Zill et al. (2021). Assuming the tensor notation $M = n \cdot n$ the equation for the permeability tensor can be written as

$$k = k_{\perp} M + k_{||} (I - M) \tag{2.10}$$

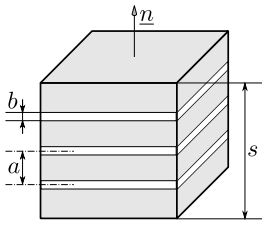

Figure 2.4: Volume element with embedded fractures.

Here, we have the permeability perpendicular to the fracture plane denoted by $k_{\perp}$, which is typically assumed to be equal to the matrix permeability k_m. On the other hand, the permeability parallel to the fracture plane $k_{||}$ is a combination of k_m and the fracture permeability k_f. The contribution of k_m and k_f to $k_{||}$ is weighted based on the combined height of the fractures in the volume element. This height is determined by the product of the number of fractures per element n and the mean fracture aperture b Zill et al. (2021).

$$k = k_m M + \left(\frac{s - nb}{s} k_m + \frac{nb}{s} k_f \right) (I - M) \tag{2.11}$$

$$k = k_m I + \frac{nb}{s} (k_f - k_m) (I - M) \tag{2.12}$$

By using the parallel plate approximation (Witherspoon et al., 1980), the fracture permeability can be derived as $k_f = \frac{b^2}{12}$. By also considering the geometry of the fracture network, we can express the number of fractures per volume element as $n = \frac{s}{a}$. Substituting these expressions into the equation allows us to eliminate the dependence on n and s, resulting in a simplified equation Zill et al. (2021).

$$k = k_m I + \frac{b}{a} \left(\frac{b^2}{12} - k_m \right) (I - M) \tag{2.13}$$

The models outlined above have been employed to simulate laboratory experiments. These experiments aimed to explore and enhance the impact of gas on the integrity of clay barriers.

2.1.4. Model verification

OGS is participating in several benchmarking initiatives. BenVaSim (section 2.1.4.2) is dedicated to verify TH2M models. DECOVALEX is a long-term international benchmarking initiative for validation of THMC models against experiments (section 2.1.4.3).

2.1.4.1. TH^{2}M benchmark gallery

An extensive suite of test examples was created for the development of the OGS-TH2M model Grunwald et al. (2022). A hierarchical concept was developed and implemented that systematically checks all (reasonable) process couplings based on the individual processes (Figure 2.2). The extensive collection of benchmarks (>100 tested test examples) from OGS is directly available via the portal and offers users an ideal introduction to THM/CB modelling. Some of the OGS benchmarks are already available as Jupyter notebooks (see section 2.1.4.4) and can thus be integrated into other Python applications with the corresponding advantages of user-specific data analysis.

2.1.4.2. TH^{2}M Model Verification

Before the application of the non-isothermal two-phase flow implementation in deformable porous media (TH^{2}M model), an extensive verification of the implementation was conducted. While the TH^{2}M reference paper Grunwald et al. (2022) features a set of benchmarks already, some further testing and documenting took place in the scope of the EURAD WP GAS modelling activities. The suite of benchmarks used for this purpose originates from the international BenVaSim benchmarking initiative Lux and Rutenberg (2018); Lux et al. (2021). The focus of these benchmarks are two-phase flow phenomena coupled to mechanical medium deformation as well as temperature-driven processes as introduced in section 2.1.3.1. The layout of each modelling test is motivated with TH^{2}M processes in deep geological nuclear waste repositories in mind Pitz et al. (2023b). A variety of well established codes and teams from international institutions participated in the BenVaSim project Lux et al. (2021), modelling and comparing in detail the results for different benchmark cases. The verification of the numerical implementation and results is achieved via the comparison with analytical results and –where analytical results are not available due to the high complexity of a benchmark – the systematic comparison of results obtained by the different codes. In Pitz et al. (2023b), all test cases were revisited using the new TH^{2}M implementation in OGS-6, and a comparison of the newly obtained results with other codes (like COMSOL, CodeBright, ToughFlac) and/or analytical solutions is conducted and documented. Thus, the verification/validation basis for the application of OGS-6 for the experimental modelling of the EURAD WP Gas experiment is provided.

2.1.4.3. DECOVALEX benchmarking project

The DECOVALEX project is an international research and model comparison collaboration, initiated in 1992, for advancing the understanding and modeling of coupled thermo-hydro-mechanical-chemical (THMC) processes in geological systems [3]. Regarding the model validation process, the DECOVALEX project plays an extraordinary role since three decades. In the current phase D2023, Tasks A, B and G are also related to fluid transport and barrier integrity aspects due to gas migration processes in clay rocks. Another focus in D2023 are thermally induced THM processes (Tasks C, D, E) which are not in the focus of this report. In Task A gas migration processes due to container corrosion, microbial degradation and radiolysis of water are in the focus of model analyses based on experimental data from the Meuse/Haute-Marne Underground Research Laboratory (MHM URL) located in Callovo-Oxfordian claystone (COx), e.g. gas injection tests with low and high rates in the PGZ experiment. Task B, based on the Lasgit experiment in Äspö HRL, is investigating possible development of dilatant pathways, permeability changes associated to this pathway

[3] https://decovalex.org/

development, and the coupling between permeability and stress in bentonite buffer systems. Task G is a more fundamental exercise on fracture evolution resulting from pressure and thermally induced effects and comparing various conceptual and numerical approaches of fracture mechanics for HM and TM coupled processes. The experimental basis stems from laboratory experiments. EURAD GAS also benefits from DECOVALEX progress in model verification and in turn already provides ideas for the next DECOVALEX phase D2027.

2.1.4.4. Benchmarking workflows

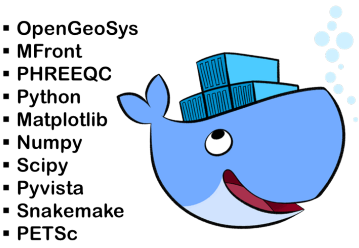

Figure 2.5: Illustration of the OGS-Container concept (Docker) for Jupyter applications (figures source: Docker).

Benchmarks and Jupyter notebooks A new technical development in OGS is the provision of container applications for Jupyter Notebooks Kolditz et al. (2023)[4]. In addition to the OGS core and external modules / libraries (e.g. MFront, PHREEQC, PETSc), these containers also contain the Jupyter Notebook server application and a number of Python packages which can be added as needed (Figure 2.5). After starting the container, the Jupyter Notebook can be accessed as a browser application as usual and OGS can be executed using notebooks. Jupyter Notebooks also forming a new basis for OGS benchmark presentation and integration. New test cases are formulated and explained in Python-based Jupyter notebooks which can intermix script logic with explanatory text and images. Moreover, the large variety of existing Python tools can be used for pre- and postprocessing of OGS simulation results. Figure 2.7 shows the OGS benchmark gallery page[5] which is organized the according to the THMC process coupling hierarchy (Figure 2.6).

Benchmark gallery The OpenGeoSys benchmark gallery (Fig. 2.7) is organized according to the THM/RTP process hierarchy, thermo-hydro-mechanical and reactive transport processes. A specific process class is represented by a tile showing a simulation result of the related process class. After clicking a tile, the available benchmarks of a process class become visible and can be further selected. Typically, an OGS benchmark starts with a short description of the problem description and showing most important results for the benchmark test. All benchmarks are linked with the OGS project file (prj-file), therefore, the benchmark settings are directly available through the gallery. All benchmarks are part of the OGS quality assurance workflow which is continuously running all tests (benchmarks and so-called unit-tests for basic functionalities) after any code changes, automatically. For new benchmarks Jupyter notebooks are available for user convenience and user-specific pre- and postprocessing operations. New process classes and/or those with new benchmarks are highlighted as featured processes on top of the benchmark gallery.

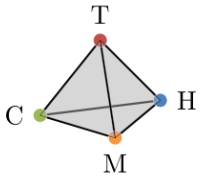

Figure 2.6: THMC processes.

[4] https://www.opengeosys.org/docs/userguide/basics/jupyter-notebooks/
[5] https://www.opengeosys.org/docs/benchmarks/

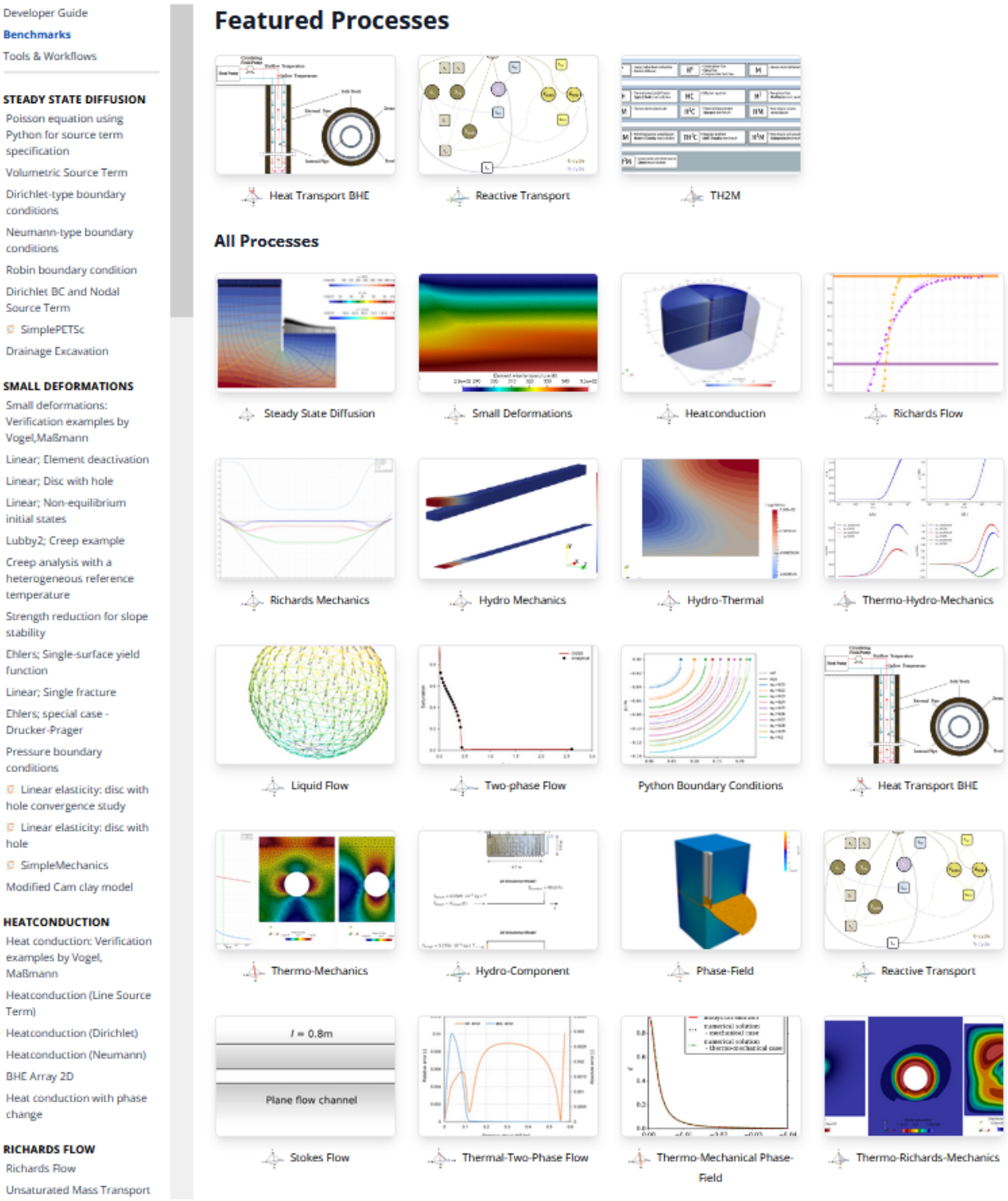

Figure 2.7: OGS Benchmark Gallery organized by process classes. Benchmarks of a specific process class are behind the tiles.

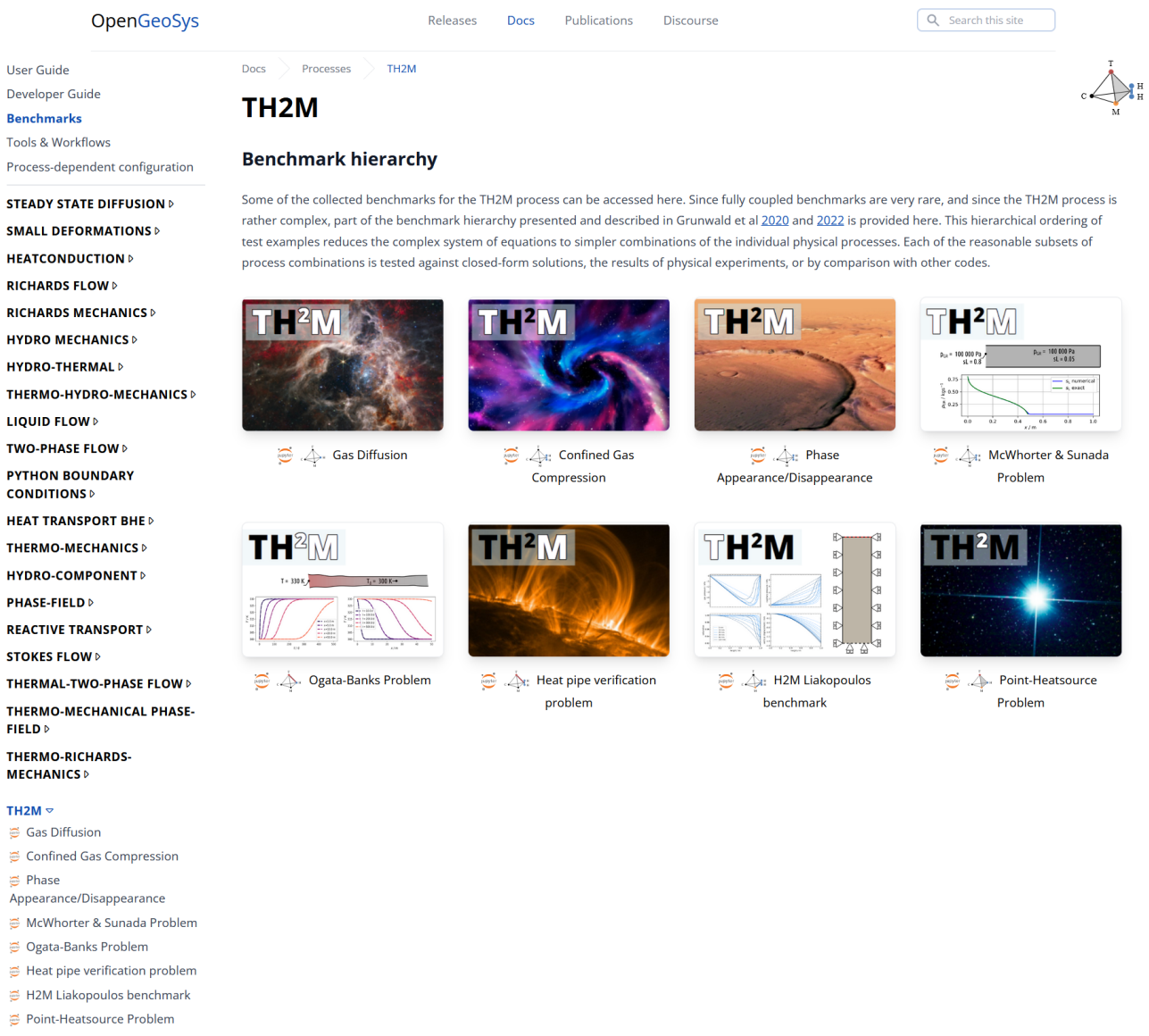

Figure 2.8: Benchmark collection of the OGS-TH2M model class with increasing complexity.

2.1.5. BGS experiment modelled by BGR

In the scope of Task 2 of work package GAS, the British Geological Survey (BGS) is performing a series of triaxial gas injection tests in samples of Boom and COx clay samples. The experimental setup and test description is given in the EURAD Mile Stone 20 'experimental design' report. Therein, a detailed description of the test cycle is given including some pre-tests to define Young's modulus of the sample, the hydration phase to reach in-situ conditions prior to conducting the gas injection tests and some flushing of the injection filters. The test cycle which is numerically modelled features a constant flow gas ramp which will increase gas pressure to a value close to the axial stress. Then, the gas injection rates remain constant until the end of the test. Based on this description, a numerical model has been implemented in OGS 6 featuring a structured mesh with a rotational symmetry to reflect the cylindrical shape of the test samples.

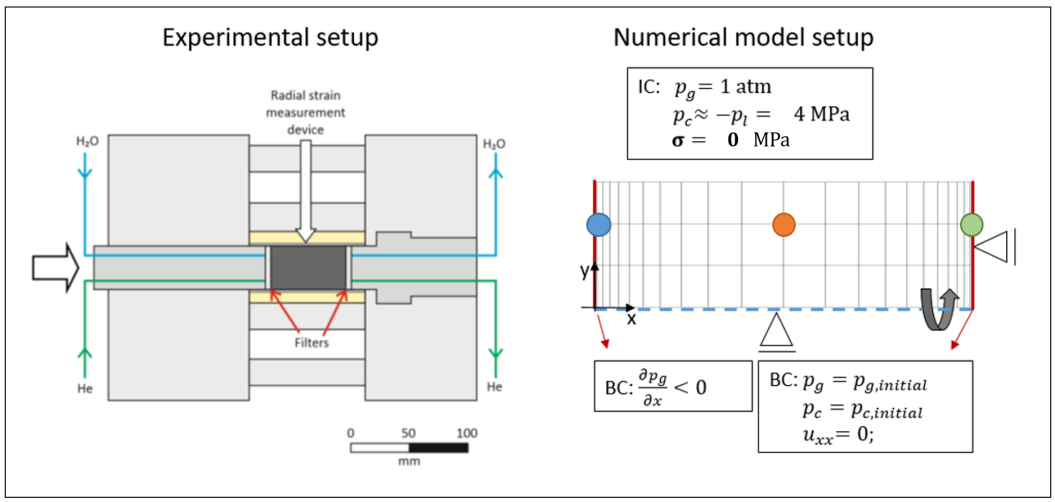

Figure 2.9: Left: Experimental sketch (from EURAD MS20 experimental design report) of the Task 2 experiment 'displacement vs dilatant gas flow (natural material)', BGS. Right: Sketch of the numerical mesh with initial conditions and boundary conditions. Gas is injected from the left side through a constant flow boundary condition and exits the sample at the right side, where gas pressure is kept at constant atmospheric pressure.

As a general basis, a set of generic parameters was chosen to characterise a generic clay rock sample for this simulation. A specific set of parameters was yet to be determined in the laboratory when numerical modelling was conducted. For this H2M simulation, the following initial conditions as illustrated in Fig. 2.9 were applied: Initial gas pressure in the sample was defined as atmospheric pressure and the initial capillary pressure was set to -4 MPa which corresponds to an initial saturation of 0.9 [-]. Initial stresses and displacements were all set to zero. Boundary conditions comprise zero flux Neumann BCs on all sides for the capillary pressure, whereas the gas pressure is fixed to atmospheric conditions (and initial condition) on the right hand side of the sample (down stream side) and at the left hand side, a time dependent Neumann BC is imposed to reflect the constant flow gas injection ramp. At the top and bottom boundary, no gas flow is allowed. X-displacements are set to zero at the right side and Y-displacements are set to zero at the bottom of the sample. The top and left side of the sample are free movement boundaries.

The results of this OGS 6 simulation are illustrated in Fig. 2.10 and reflect the increasing gas pressures in the sample following the gas injection. After each step-wise increase of the gas injection rate, a steady state gas flow is achieved in the sample after about 5000 s. The temporal evolution of the saturation at the inlet, the middle and the outlet of the sample shows that water is displaced by the gas injection at the inlet. Saturation increases at the outlet since water is not allowed to cross the outlet boundary due to the imposed boundary condition. The displacement plot shows that the sample expands as a response to the

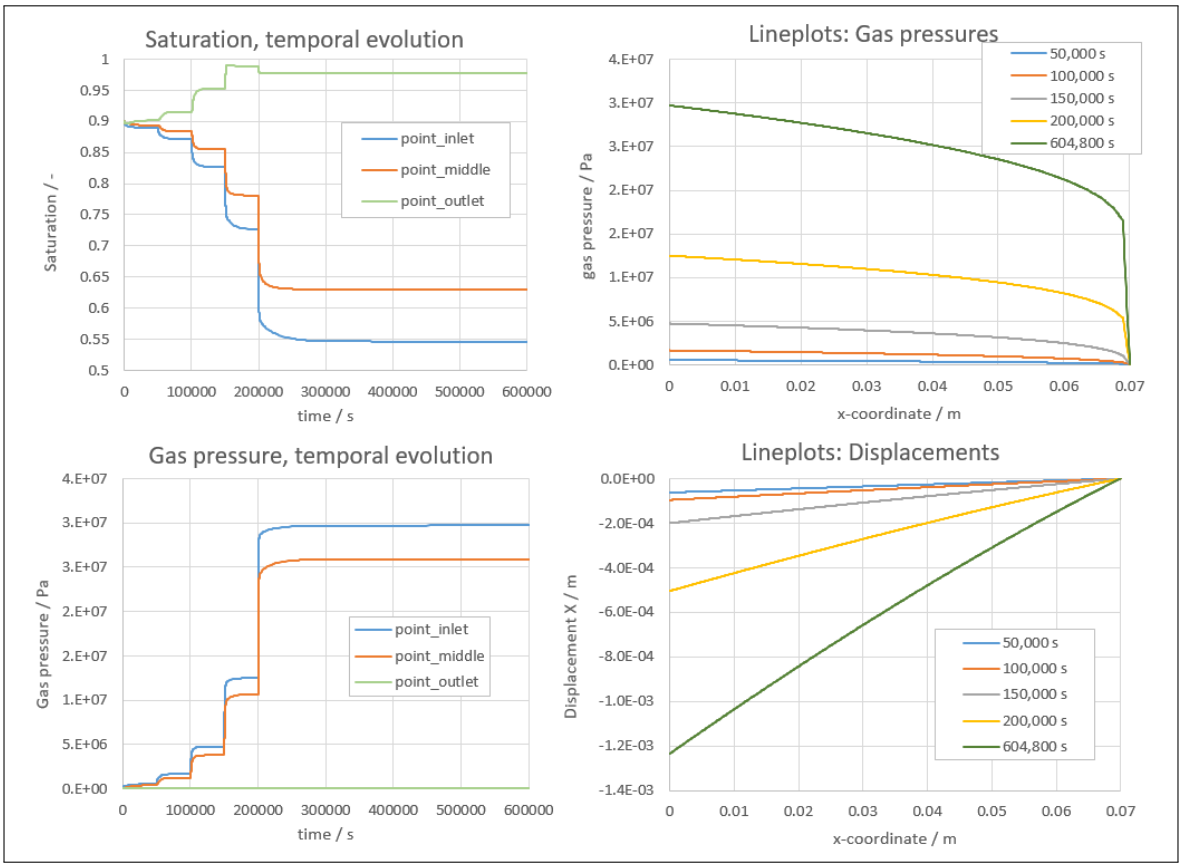

Figure 2.10: Results of BGRs numerical simulation of the BGS gas injection experiment. The material was given a generic parameter set similar to the one used in the IfG-Experiment described below. The two plots on the left side show the temporal evolution of the water saturation and gas pressure at three points marked in green, blue and red in Fig. 2.9. The displacement of pore water near the gas injection side is visible as well as the increase of gas pressures following the gas injection. On the right side, gas pressures and x displacements are plotted at selected points in time along the line in the center of the sample parallel to the x-axis. The increasing gas pressures are visible as well as the expansion of the sample as a HM-response to the gas injection.

gas injection which is the poro-mechanically expected behaviour of a porous medium.

2.1.6. EPFL experiment modelled by BGR

In the scope of work package GAS, Task 3, the École Polytechnique Fédérale de Lausanne (EPFL) is performing a series of triaxial gas injection experiments which are described in the EURAD Mile Stone 58 report (interim experimental design report comprising a revised detailed work programme of subtasks 3.1, 3.2 and 3.3). Therein, the objectives of EPFL's work are to investigate '(i) the initiation and propagation of rock failure in response to gas pressure build-up and (ii) the characterization of gas transport processes in remoulded and recompacted OPA.' The experiments feature an injection of gas or water into the sample with continuous measurements of axial and volumetric strains. Gas transport in fractured media is investigated as the test continues after the onset of dilatancy of the sample post-rupture.

Numerical simulations of this experiment were performed using a generic set of parameters to characterise the porous medium as the exact material parameters are yet to be determined in the laboratory. The results show an increased gas pressure and the gas pressure distribution in the sample after each stepwise increase of the gas pressure at the inlet/bottom boundary. The distribution of the saturation shows

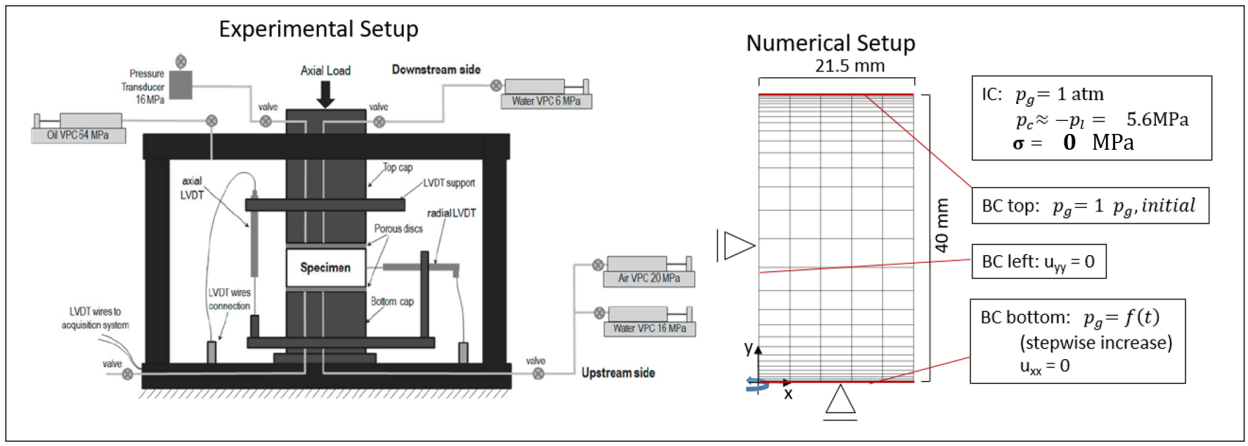

Figure 2.11: Left: Experimental set up with sample in the triaxial test cell and multiple measurement devices (EPFL, EURAD MS58 report. Right side: Structured mesh with dimensions and axisymmetry. Boundary conditions comprise zero displacement at the top and left boundary and zero flux Neumann boundary conditions at all boundaries for the capillary pressure. At the top boundary, gas pressure is kept constant at initial conditions, whereas at the bottom boundary, the gas pressure is step-wise increased.

that the numerical results indicate that pore water is displaced by the gas injection and a water outflow at the outlet of the sample is predicted by this model. It is possible to apply other numerical models which assume immobile water or which could predict less water displacement. This would allow to test whether water displacement plays an important role, especially if experimental findings show little water outflow downstream.

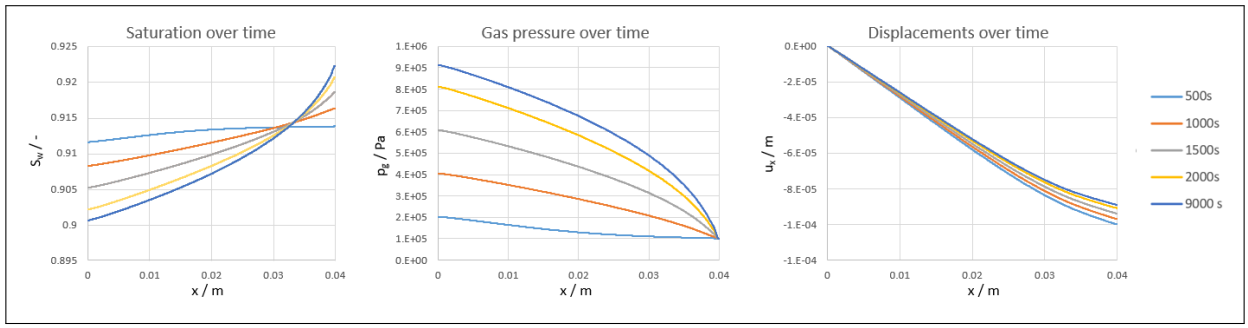

Figure 2.12: First numerical results of a simulation of the EPFL triaxial experiment. All line plots are plotted over the central, vertical line across the sample in Fig. 2.11 where X = 0 m corresponds to the bottom of the sample and X = 0.04 corresponds to the top of the sample. The increasing gas pressure distribution is visible in the central plot. In the left plot, water is displaced by the gas injection at the left hand side and saturation increases at the right hand side (outlet) due to the zero flux Neumann boundary for capillary pressure. The displacements show an expansion of the sample as a poroelastic reponse to the gas injection.

2.1.7. EPFL experiment: Triaxial gas injection test (BGE)

Understanding the conditions that govern gas flow mechanisms in clay materials is a pivotal area of research. This is particularly true when distinguishing between the transition from viscous-capillary flow to dilatancy-controlled gas flow within clay porous media. In our current study, we undertook numerical evaluations of gas injection into a clay sample. Our goal was to determine which of the aforementioned mechanisms (viscous-capillary flow or dilatancy-controlled gas flow) is the driving force behind the observed outflow during the experimental investigations on gas injection in clay at low gas pressure, i.e. below the level where tensile failure occurs.

To achieve this, we referenced an experiment performed at EPFL by Minardi (2018). This research explored the hydro-mechanical behavior of water-saturated samples subjected to gas injection at different gas pressures. Notably, a significant mechanical interplay between the sample's hydraulic and mechanical behaviors was observed. The data demonstrated that rising gas pressures directly instigated a swelling (in the sense of dilation) deformation in the sample, as confirmed by strain measurements. Remarkably, this volumetric strain was found to be entirely reversible upon gas injection.

Minardi (2018) interpreted these findings as evidence of the sample's elastic behaviour during gas injection. This reversible nature also implies that the sample remained undamaged throughout the gas injection process. Based on these insights, it's inferred that the predominant gas transport mechanism in Minardi's experiment was the viscous-capillary flow. Our numerical analysis aims to validate these conclusions.

2.1.7.1. Experimental design

The sample of Opalinus Clay shale was obtained from the Mont-Terri underground research laboratory. The tested specimen has a diameter of 43.2 mm and a height of 23.8 mm. The experimental set-up was developed by EPFL in order to investigate the gas flow mechanisms in shales considering the volumetric response of the cylindrical tested sample during gas injection (Figure 2.13). The axial and radial stress can be applied to the specimen. At the same moment water and air can be injected on the downstream and upstream sides of the sample. To analyse volumetric response of the tested specimen, an internal system of Linear Variable Differential Transformers (LVDTs) was implemented in the device. For a detailed description of the experimental set-up, please refer to the works of Minardi (2018).

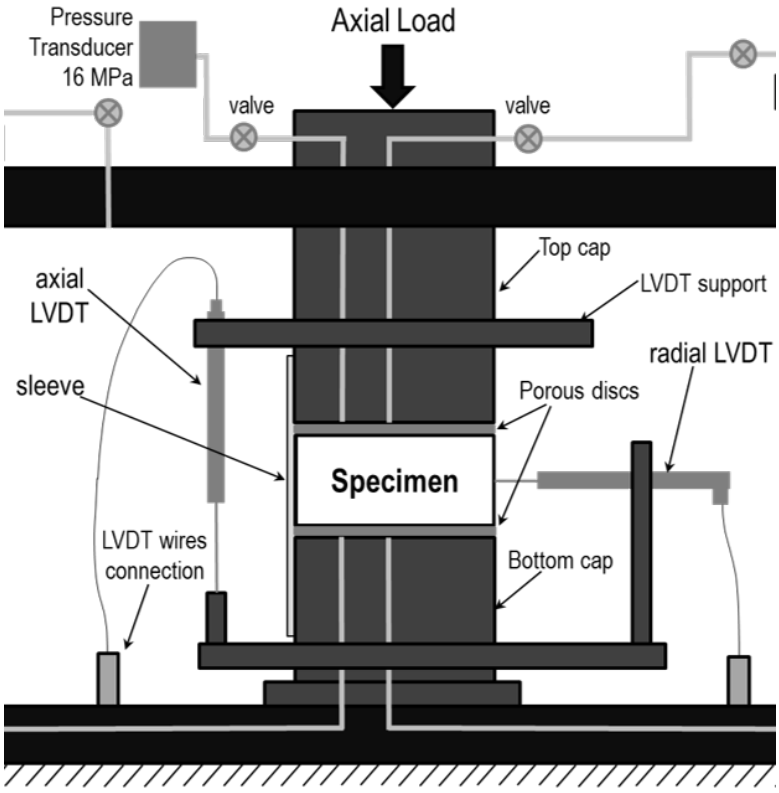

Figure 2.13: Schematic layout of the testing set-up used by EPFL (Minardi, 2018)

The experiment was divided into two phases. Starting from an initial saturation of the sample was 62 %, the sample was resaturated in the first phase of the experiment as a precondition for water permeability measurement. After the water saturation, a water pressure gradient was applied across the sample, with

3.5 MPa on the upstream side and 2.5 MPa on the downstream side of the sample (see Figure 2.14, left). Hydraulic conductivity was estimated to $1 - 2 \cdot 10^{-13}$ m s^{-1} according to Darcy's law after the steady state was reached.

In the second phase of the experiment, the water pressure at the upstream side of the sample was decreased to 0 MPa and gas (air) injection was applied, Figure 2.14, right. At the downstream side of the sample, water pressure was reduced to 1 MPa and was kept constant. Radial and axial stress of 20 MPa were applied on the sample and kept constant during the gas injection phase. The outflow volume was measured at the downstream side.

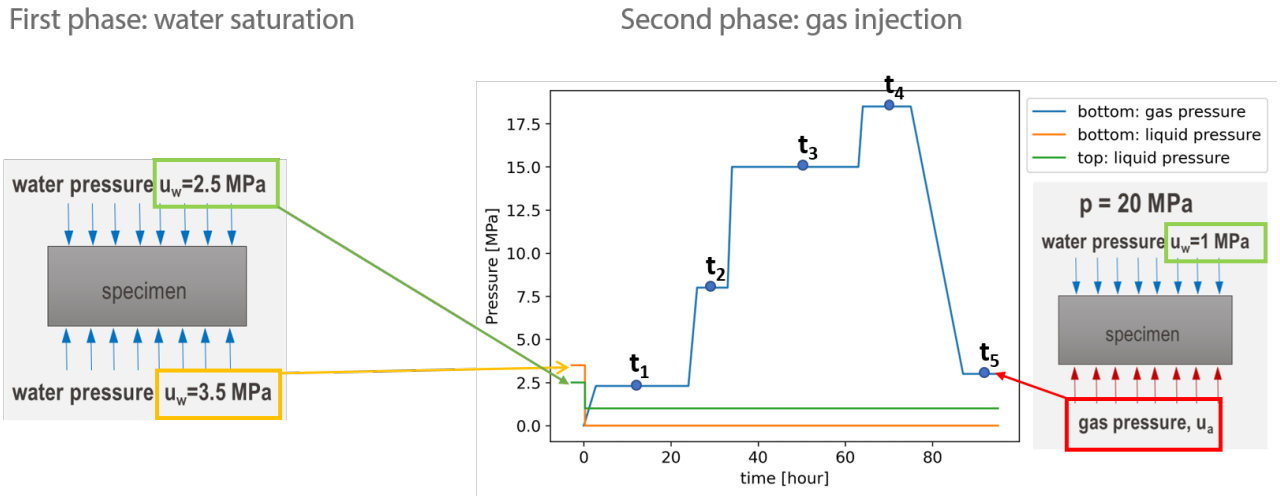

Figure 2.14: First phase of the experiment (left): water pressure at upstream and downstream sides of the sample during the water saturation phase; Second phase of the experiment (right): evolution in time of the gas pressure during the gas injection phase (Minardi, 2018).

2.1.7.2. Modelling design

Numerical model

The simulation model for the Minardi experiment operates under the assumption of axial symmetry. As such, only the rotational plane of the sample is considered for the analysis. This leads to a rectangular domain representation where the width is equal to the sample's radius, and the height is equivalent to the sample's own height. A depiction of this domain can be found in Figure 2.15.

For computational accuracy, a mesh of 10,000 elements has been employed. This mesh is subdivided into 50 elements in the horizontal direction and 200 elements vertically. In the vertical direction, the mesh highly densified.

The model employs a quadratic shape function for displacements, while linear shape functions are used for both the liquid and gaseous phases. Given the axial symmetry assumption, displacements normal to the symmetrical axis are restricted. To mimic the triaxial conditions of the experiment, the top boundary of the domain is constrained. Simultaneously, normal stresses of 20 MPa are applied to both the bottom and right boundaries, resulting in an isotropic initial stress of 20 MPa. It's worth noting that the entire simulation is executed under isothermal conditions, see Figure 2.15.

The EPFL experiment was modelled in OpenGeoSys. The TH2M process class described in section 2.1.3.1 was employed to analyse the two phase flow gas transport mechanism in the sample.

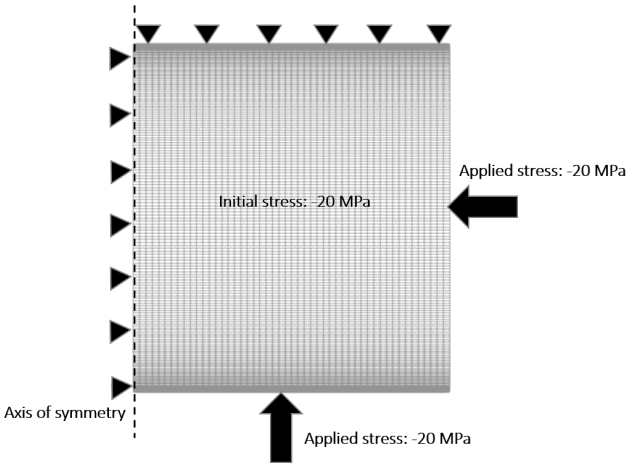

Figure 2.15: Numerical domain with mechanical boundary initial and boundary conditions.

Initial and boundary conditions

In the first step of the modelling, the initial water saturation in the sample was assumed to be 100 %. At the downstream and at the upstream side of the model water pressure of 2 MPa and 3.5 MPa were applied (as at the end of the first phase of the experiment), respectively. Once steady state was reached, the boundary conditions were changed as shown in Figure 2.14 in order to simulate the second phase of the experiment.

In the second phase of the experiment, careful consideration must be given to the hydraulic boundary conditions established at the upstream and downstream sides of the model. Water and gas are injected into the sample via porous discs, complicating the assessment of capillary conditions at these interfaces. Consequently, two scenarios have been devised to encompass the range of potential capillary pressure values. In the first scenario, we assume the capillary pressure to be zero which is the case in the sample after saturation. Since the capillary pressure is defined as the difference between the gas and liquid pressure, it follows from this assumption that the liquid pressure at the upstream side of the sample should be in equilibrium with the gas pressure. The same assumption at the top of the sample means that the applied liquid pressure will increase the gas pressure in the pores located at the vicinities of the sample and thus leading to an equilibrium between water and gas. In the second scenario, We just follow the conditions of the experiment by assuming that the liquid pressure on the upstream surface should be zero as no liquid pressure has been applied on that surface in the second phase of the experiment. The same assumption implies that since there were no gas injection at the top, the gas pressure there should be zero. From the definition of capillary pressure, boundary conditions of capillary pressure can be determined. The two scenarios are displayed in Figure 2.16.

Mechanical, hydraulic model and material parameters

Table 2.2 summarizes the material properties of the tested sample. The water retention curve was obtained from the mercury intrusion porosimetry test and the gas entry-pressure was defined for the specimen (Minardi, 2018). In the simulations, van Genuchten capillary pressure function was used to describe relation between capillary pressure and water saturation, Mualem approach was employed to characterize relative permeabilities for gas and water phase. A constant intrinsic permeability is assumed in the present analysis. Two-phase flow properties of the sample are listed in Table 2.3. OpenGeoSys formulation of van Genuchten water retention model is given by:

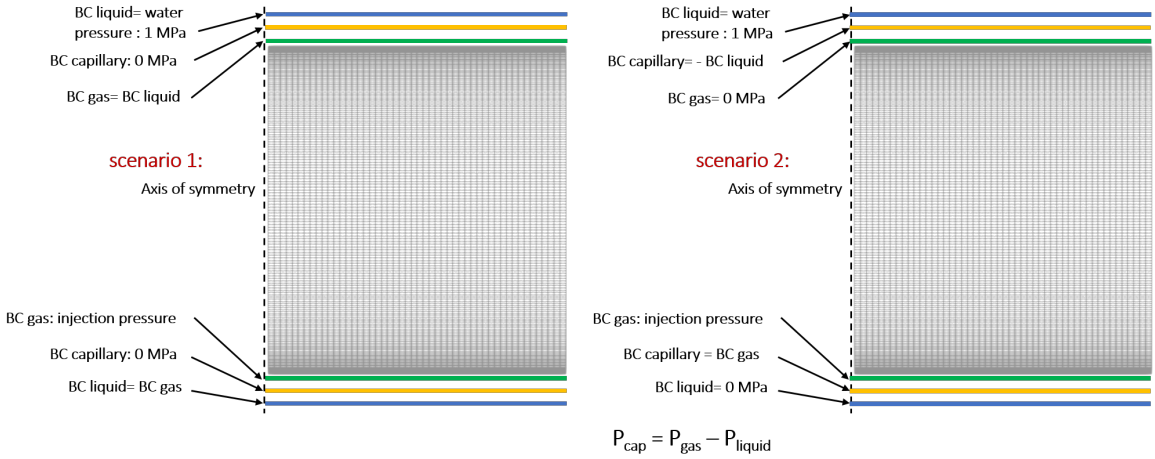

Figure 2.16: Two-phase-flow hydraulic boundary conditions for scenarios 1 and 2.

$$p_c = p_b(S_e^{-1/m} - 1)^{1-m} \tag{2.14}$$

with

$$S_e = (S - S_r)/(S_{max} - S_r) \tag{2.15}$$

where p_b entry pressure S_r residual saturation S_{max} maximum saturation m exponent

Material properties	Values
Density, kg m^{-3}	2,750
Porosity, –	0.17
Permeability, m^2	6.25×10^{-21}
Young's modulus, MPa	2,500
Poisson ratio, –	0.27

Table 2.2: Material properties used in the simulation.

Two-phase flow properties	Relative Permeability function (water) Mualem approach	Relative permeability function (gas) Mualem approach	Capillary pressure function van Genuchten
Residual water saturation, –	0.01	0.01	0.01
Residual gas saturation, –	0.01	0.01	0.01
m exponent, –	0.5	0.5	0.5
Gas entry pressure, MPa	–	–	8

Table 2.3: Two-phase flow properties for the OPA sample assumed in the simulation.

2.1.7.3. Numerical results

The gas injection test was divided into five steps (Figure 2.14, right) in order to investigate various gas flow mechanisms in the sample with a entry pressure of 8 MPa. This value was experimentally obtained by Minardi (2018) for the OPA clay used for the gas injection. The gas pressure was increased step-wise from 2.3 MPa to 18.5 MPa and hence exceeds the gas entry pressure. Hydraulic flow rates and outflow volume during gas injection phase were computed at the downstream side of the model for the two defined boundary conditions scenarios. Simulation results of the scenario 1 were compared with experimental data (Figure 2.17, left and Figure 2.18). They show that the computed flow rate and the outflow volume are in a good agreement with the results obtained experimentally. These results were obtained for a permeability of $6.5 \cdot 10^{-21}$ m^2 which is still close to the measured value in the range of $1 - 2 \cdot 10^{-20}$ m^2. From the modelling, it was observed that only water is expelled from the sample at the downstream side of the model (Figure 2.19). The volumetric expansion of the sample was determined during the gas injection. It appears that only the bottom part of the sample dilates and the computed strains in that location are in line with the experimental data, see Figure 2.18). The compaction of the sample during the decreasing gas pressure highlights the reversible hydro-mechanical response of the sample. The computed strains in the middle and the top part of the sample remain constant and nearly zero during the experiment.

The numerical outcomes from the scenario 2 model (refer to Figure 2.17, right) revealed occurrences of both gas and water outflows. However, the computed gas outflow rates were nearly three orders of magnitude greater than those observed experimentally. This discrepancy suggests that if gas had indeed flowed from the sample, it would have been detectable during the experimental. Since this was not observed, it can be inferred that capillary two-phase flow does not account for the outflow results recorded by Minardi (2018). The computed water flow is in the same order of magnitude as the experimental data, but the kinetics of the numerical and experimental outflow curve are different. The water starts to flow out of the sample only after the gas entry pressure is exceeds. Few hours later, a gas outflow is observed. This shows that the gas has displaced the water out of the sample and clearly evidences that the capillary two-phase flow is the ruling mechanism in the second scenario. Thus, one can conclude that the results of the two-phase flow modelling are completely different than those observed experimentally. This adds another doubt in the conclusion of Minardi (2018). More detailed analysis of the results is necessary to identify the primary mechanism at play in this experiment.

A detailed analysis of the evolution of the primary and secondary variables of the H2M analysis is presented in Figure 2.19. It shows the evolution of gas, liquid and capillary pressure (top, from left to right); horizontal displacement, saturation and vertical stress (middle: left to right); vertical displacement, gas and liquid velocity (bottom: left to right). The evolution of these variables were captured at five time points during the experiment that are depicted in Figure 2.13, right. In this figure, one can see that the effect of gas is limited at the upstream side of the model where some variations of gas pressure and gas velocity are observed. From this, one derives that no gas has penetrated in the sample during the experiment. The results shows that the applied gas pressure leads to an increase of the liquid pressure at the upstream side subsequently causing a higher hydraulic water gradient. This higher gradient leads to an increase of liquid velocity in the sample from which the liquid outflow results. This scenario means that during the experiment, a liquid film was formed at the bottom of the experiment probably in the porous disc prior to gas injection. This is probably the case if some liquid remained trapped in the porous disc at the end of the saturation phase. This phenomenon can occur when the water conduits on the downstream side are removed, leading to a loss of water pressure at the bottom of the sample prior to the gas injection. During this period, the inner portion of the sample remains under overpressure. This creates a hydraulic pressure gradient, which can cause water to drain towards the downstream surface. Consequently, this can lead to water accumulation within the disc just before the gas is injected. During the gas injection, the pressure in this liquid film was in equilibrium with the applied gas injection pressure. This film therefore first prevented the gas to enter into the sample and second changed the acting liquid pressure at the bottom surface of

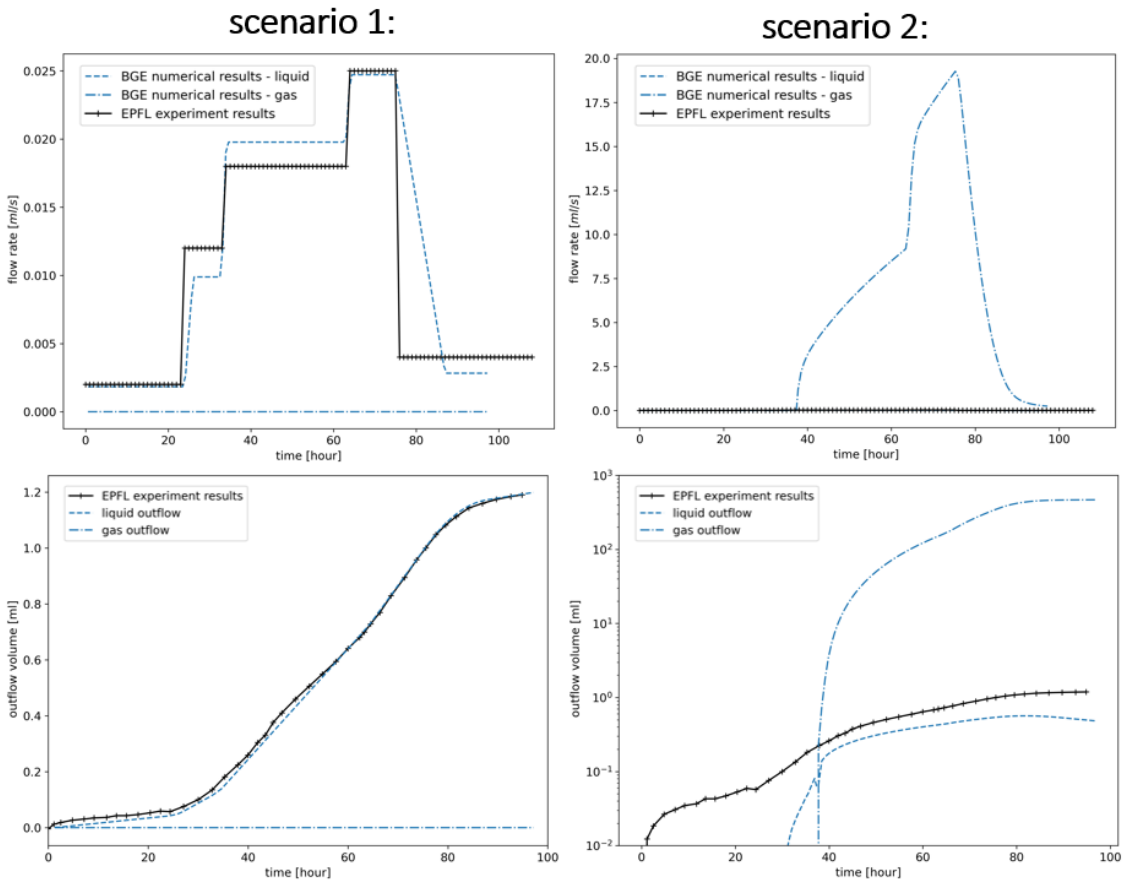

Figure 2.17: Evolution of outflow rates of gas and water in the model and measured outflow rate in the specimen in time.

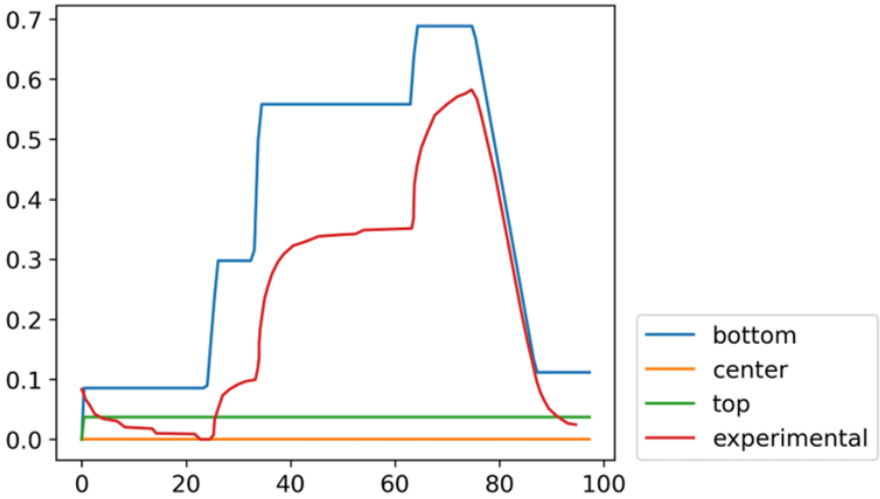

Figure 2.18: Evolution of volumetric strain: numerical and experimental results.

the sample. Therefore, one can derive from this hypothesis that a single water phase flow similar to the first saturation phase of the experiment took place also during the gas injection phase of the experiment. This is in contradiction with the conclusions of Minardi that identified the capillary two-phase flow as the ruling mechanism during the experiment. Our conclusions are in line with those of the project FORGE where there were no experimental evidences of two-phase flow that could be identified in the FORGE experiments on low permeability porous media such as clays and bentonite close to saturation with water

(Shaw, 2013).

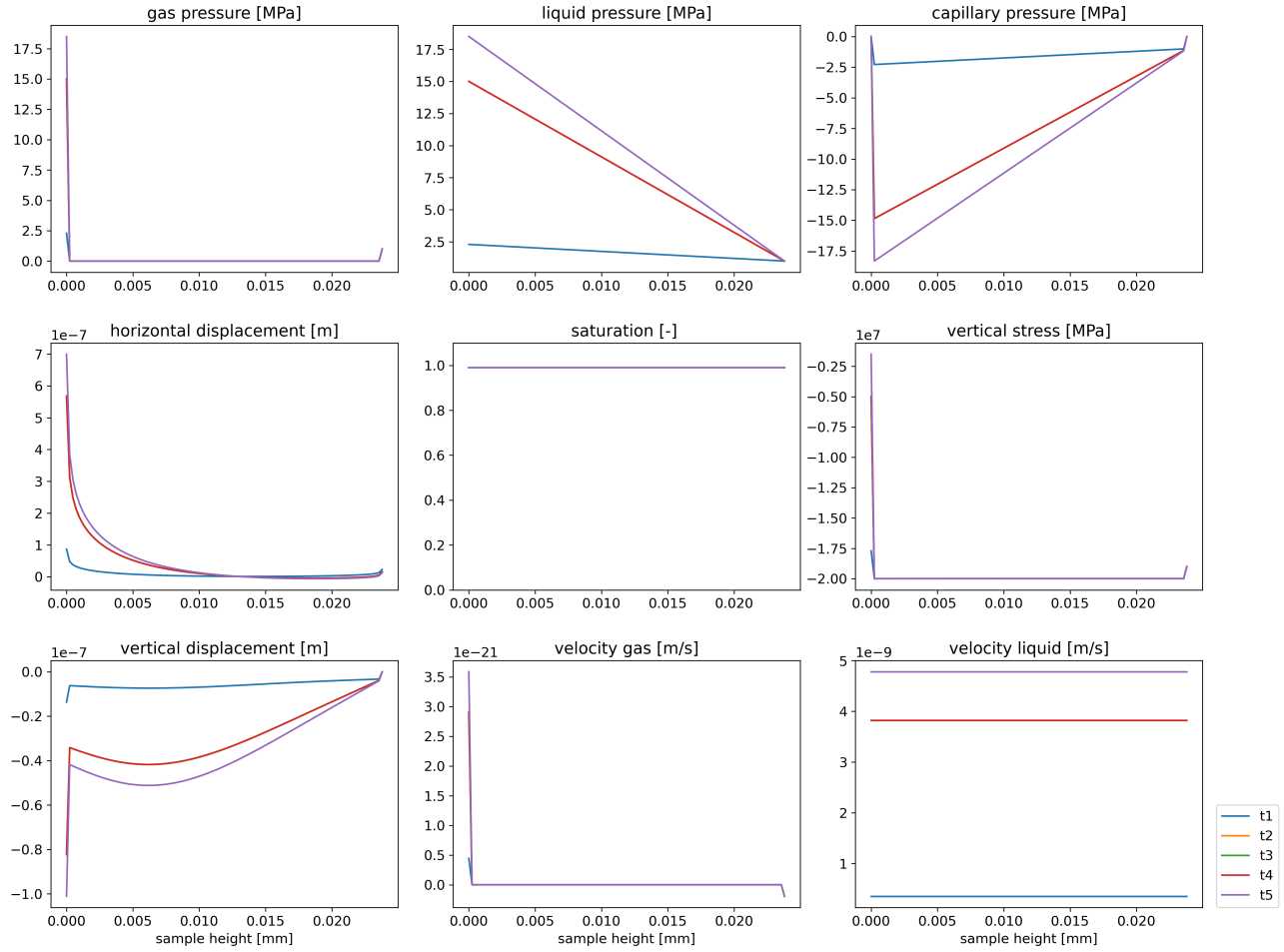

Figure 2.19: Evolution of variables: numerical results of the scenario 1 model.

Furthermore, the displacements and strains observed and computed in the sample can also be explained by the presence of a liquid film at the bottom side of the sample. In Figure 2.19 one can clearly see that dilation occur in the sample from the volumetric strain results. This dilation is maximum at the bottom and decreases over the height of the sample. At the upper one third of the sample, almost no dilation or a little compaction is observed. The plot of vertical displacement shows that compaction occurs in axial direction. These two observations can be explained by the gas injection pressure acting as an axial and external load at the bottom surface. Such a load will cause a vertical compaction and a radial dilation in triaxial conditions as observed in the modelling results.

In the case of scenario 2, the evolution of the primary and secondary variables are summarised in Figure 2.20. The evolution of gas pressure along the sample clearly evidences that in this scenario, the gas is propagating in the pores of the clay sample. During the gas pressure, the liquid pressure increases in the middle of the sample but the extremities remains equal to the boundary conditions. The capillary pressure increases significantly starting from the bottom surface and reaches rapidly a constant value around 5 MPa at the different time points. From this gas propagation, it follows a desaturation of the sample of up to 0.4 at the bottom and 0.8 at the top. The volumetric strain shows that the sample dilates progressively over time from the bottom to the top. The effective stress, strain and gas pressure show the same kinetic because of the elasticity and the effective stress concept assumed. Finally, the evolution of gas and liquid velocities shows that gas starts to flow out between time t2 and t3. At the outlet of the sample, the gas velocity is increased. The liquid velocity shows for this scenario that liquid flows out from the bottom and from top. The outflow from the bottom is expressed by negative velocity in the corresponding plot. This

observation is in line with the liquid pressure distribution in the sample. The maximum of liquid pressure in the sample occurs at around 5 mm from the bottom of the sample. This same location corresponds to the point where the velocity is zero or changes the direction. At this location, the hydraulic gradient goes in both direction which explains a flow towards the upstream and towards the downstream side of the sample. From this surprising but explanable effect one can derive a new hypothesis that helps to understand the experimental results: When the gas injection starts, liquid begins to flow out of the bottom surface. A liquid film covers the surface and interrupts the gas penetration into the sample. Here, the mechanisms described in scenario 1 takes place and the regime changes from a two-phase to a single phase flow.

In summary, one can conclude that it is unlikely that viscous capillary two-phase flow took place in the Minardi's experiment. Due to the reversibility of strain and the little volume of outflow collected in the experiment, the dilatancy controlled pathway can also be eliminated as possible phenomenon. Thus we propose a new hypothesis that can explain the experimental results. This hypothesis states that during the experiment, the bottom surface probably became covered by a liquid layer due to some water trapped in the apparatus after the saturation phase or due to the early propagation of gas in the sample leading to an outflow from the downstream surface. This liquid film changes the flow regime in the sample by allowing a higher hydraulic gradient that eventually leads to the observed outflow of water. Further experimental investigations are necessary to confirm this hypothesis. A first evidence can be found in the post mortem analysis of saturation of the sample. If the hypothesis is true, the sample should remain saturated after the gas injection experiment.

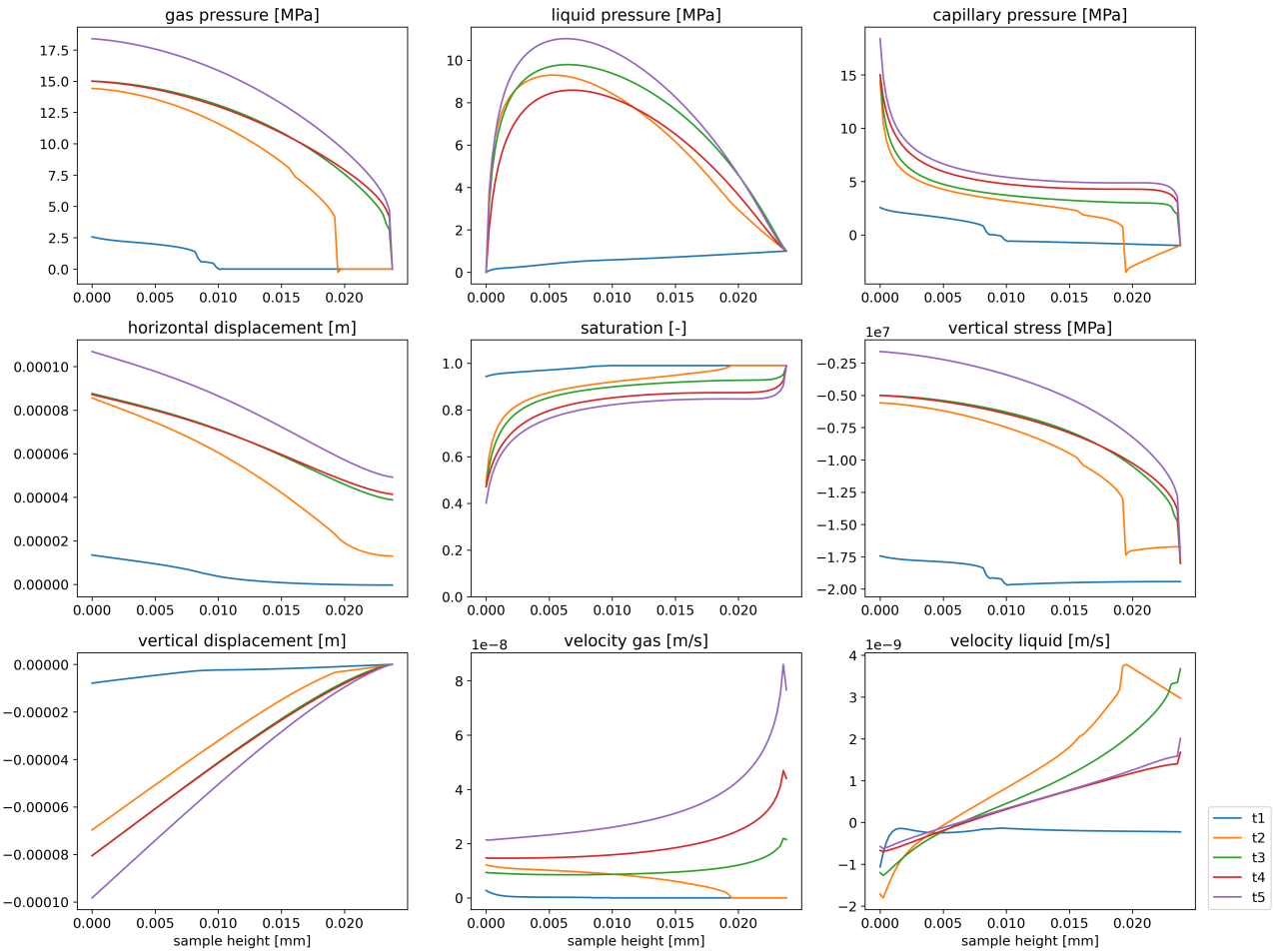

Figure 2.20: Evolution of variables: numerical results of the scenario 2 model.

2.1.8. IfG experiment: Triax gas injection test with dilation (BGE, BGR)

The IfG triaxial gas injection experiment has been analysed by BGE and BGR using latest OGS model development by UFZ (section 2.1.3.1). The laboratory experiment carried out by Popp et al. (2007) has been considered in WP GAS as one of the candidate experiments to be modelled by the involved modelling teams because it clearly highlights the gas transport through Opalinus Clay subjected to high gas pressure. The predominant gas transport mode in this experiment according to Figure 1.1 is between the dilatancy gas flow and the gas transport in tensile fracture. The IfG experiment consists of two different laboratory gas injection tests (gas loading cycle test and gas breakthrough test). These tests were analysed by BGE and BGR using different modelling approaches. The results of these two organisations are discussed in this section.

2.1.8.1. Experimental design and observations

The IfG experiment consists of two different laboratory gas injection tests that were performed on cylindrical specimens with a length of 150.45 mm and a diameter of 73.59 mm. The first test investigates the behaviour of a Opalinus sample during a gas injection loading cycle. In the second test, a gas breakthrough is provoked in the sample due to high gas pressure. A borehole was drilled at the lower side of the specimens where the gas was injected. In a second borehole prepared at the upper side the outflow of gas was collected. In the experiment, nitrogen was used as test gas. A rubber jacket prevented any leakages at the outer surface of the cylindrical specimens. The sample is subjected to a confining isotropic stress applied through a piston that evolves during the test. The experimental setup is presented in Figure 2.21, left.

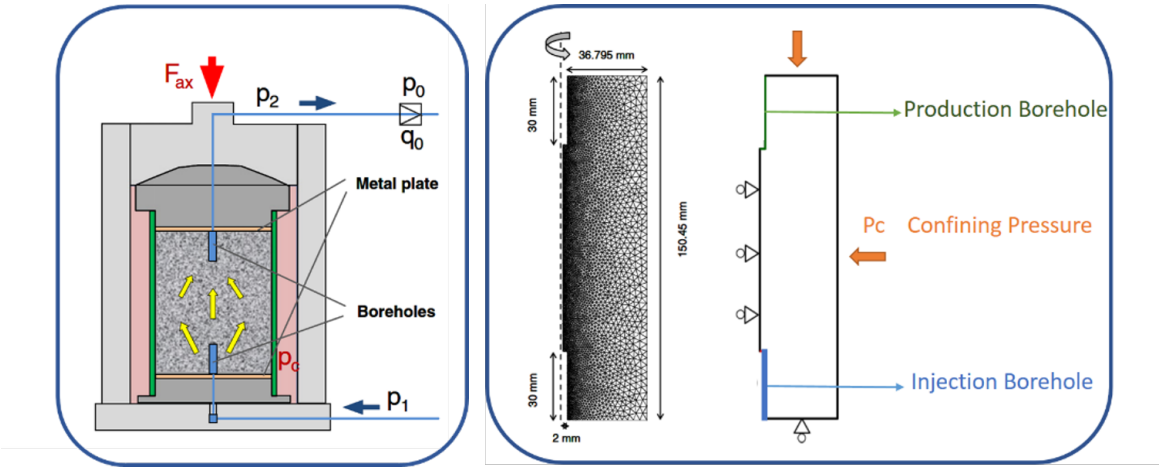

Figure 2.21: Sketch of laboratory experiment (left) and mesh of numerical model (right).

In the loading cycle test, the gas pressure and confining pressure both were increased step-wise, but the gas pressure was always lower than the confining pressure. Beginning with a pressure restraint of 1 MPa and a relatively high gas permeability, approximately $10{\cdot}10^{-17}$ m^2, the gas pressure was initially raised from 0.1 MPa to around 0.95 MPa. Here, the gas outflow increases steadily, see Figure 2.22, left. Longer holding times with constant injection pressure result in fluctuations in the gas outflow rate, indicating discontinuous gas transport. With an increase of the confining pressure, the permeability decreases progressively with a significant time-dependent reaction effect (Popp et al., 2007). In this test, the hydromechanical response of the sample is reversible upon gas injection. This clearly evidences that the dilatancy-controlled gas flow is the main gas transport mechanism in this experiment.

During the gas fracture cycle test, the confining pressure was kept constant at 3 MPa and the gas injection pressure increased step-wise and finally exceeded the confining pressure, see Figure 2.22, right.

Here, a different gas transport behaviour occurs compared to the loading cycle test. The specimen has a lower permeability as a result of the higher confining pressure. The gas outflow rate increases from zero smoothly until a quasi-plateau is reached around 0.5 and 1 ml/min. Shortly after the gas injection pressure exceeded the confining pressure, a gas breakthrough event occurred which was characterized by a sharp increase of the outflow rate. In this case, the gas transport in tensile fractures (gas-frac) can be seen as the main gas transport mechanism. This event was immediately followed by a sharp decrease to less than 0.5 ml/min after reduction of the injection pressure to a value of 1 MPa, which is below the confining pressure again (Popp et al., 2007).

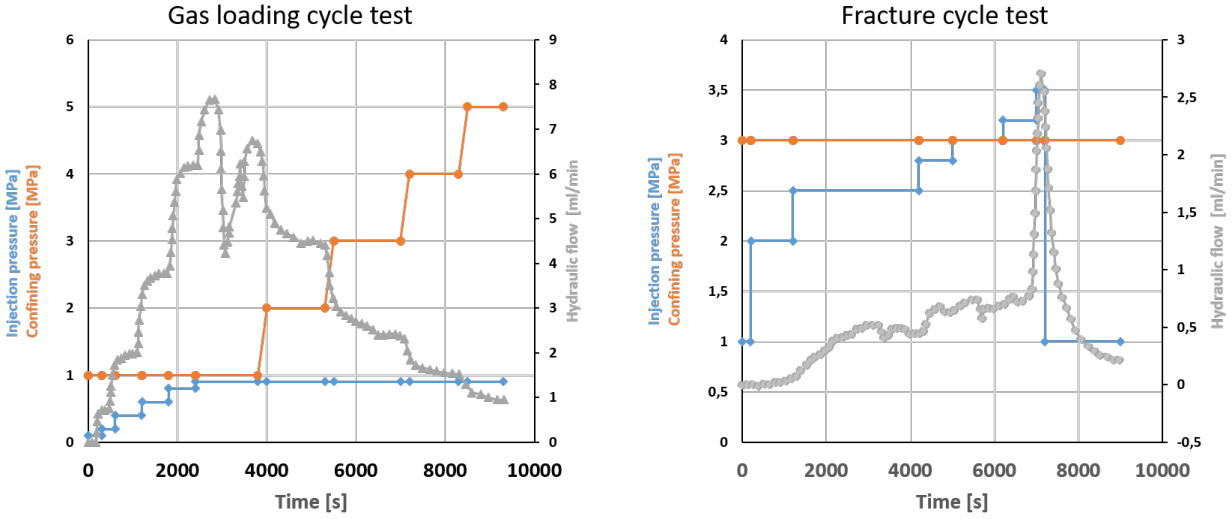

Figure 2.22: Experimental plan and results for the loading cycle test (left) and gas fracture test (right).

2.1.8.2. Modelling design

BGE and BGR parallely carried out the modelling of the IfG experiments using OpenGeoSys. Simulations by BGE focus on the hydromechanical response of the clay sample during the gas injection tests. Thus the two phase flow process is neglected. BGR on the other hand performed simulation in the TH2M process class with the aim at capturing the effect of the two phase flow in these experiment.

Both teams use the same numerical model to simulate the laboratory experiments. The numerical model is shown in Figure 2.21, right. It consists of a second order triangular elements model with an axisymmetric geometry. As it can be observed, a hydrostatic boundary condition was applied and the model is assumed to be hydraulically sealed except from injection and production boreholes. The injection pressure and confining pressure are time dependent and varied according to experimental plan on the boundaries. An initial injection pressure of 0.1 MPa was applied. The four permeability models described in 2.1.3.3 were used to model the gas transport in the sample during the two gas injection tests. The material parameters assumed for the simulation are summarized in Table 2.4.

2.1.8.3. Numerical results

The modelling of the first gas injection show that the dilation of the rock due to gas transport could be satisfactorily captured using the gas permeability models (see equations 2.7, 2.5 and 2.6) implemented in OpenGeoSys. The failure index permeability model (equation 2.7) gives similar results than the gas dependent model (equation 2.5). Both models predict the production behaviour associated with pore pressure changes appropriately but are not sensitive to changes in confining pressure. The best results were obtained using the strain dependent permeability model (equation 2.6), where gas production behaviour is

Parameters	Description	Value	Unit
P_0	Initial pressure	1×10^5	Pa
α	Biot coefficient	1	–
Φ	Porosity	0.16	–
μ	Gas viscosity	1.6×10^{-5}	Pa
E	Young's modulus	2.5×10^9	Pa
ν	Poisson ratio	0.27	–
c	Cohesion	4.5×10^5	Pa
ϕ	Friction angle	30	°
T	Tension strength	2.33×10^5	Pa
K_0	Intrinsic permeability	$\perp$: 2.1×10^{-16}, $\parallel$: 2.1×10^{-17}	m^2

Table 2.4: Material parameter assumed for the simulation of the IfG experiment

sensitive to both changes in the pore pressure and confining pressure, see Figure 2.23.

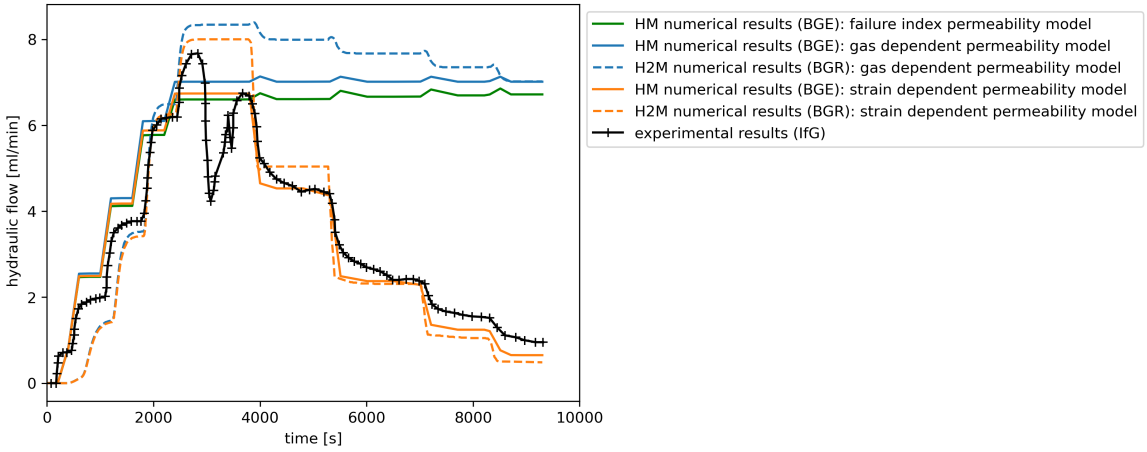

Figure 2.23: Comparison of experimental and numerical results for the IfG gas loading test with and without two-phase flow.

The numerical results obtained by BGR using a two-phase flow model and the gas dependent and strain dependent permeability model (see Figure 2.23) show similar result as BGE, which assumes only a single-phase hydromechanical behaviour. This suggests that the effect of two phase flow seems to be negligible in this test. The observed discrepancies between BGE and BGR results in Figure 2.23 can be explained by the desaturation of the sample that occurs during the gas injection when a two-phase flow model is used.

The second gas injection test was modelled by BGE using three of the four permeability models (see equations 2.6, 2.5 and 2.13) assuming a single-phase flow. All models were able to qualitatively reproduce the gas transport occurring in the sample during the test. After a parameter calibration, it was also possible to meet the magnitude of the gas flow from the beginning to the end of the test, see Figure 2.24. The maximum of gas flow rate during the gas breakthrough event could be satisfactorily captured with the three permeability models.

For the gas fracture test, the distributions of gas velocity, permeability and strain in the model using the different permeability models was further processed, see Figures 2.25,2.26. The aim was to understand how exactly the permeability model affect the gas transport. For the embedded permeability model, the isolines of gas velocity along the sample are nonuniform. One can clearly see that the gas flows through preferential pathways concentrated in the center of the sample. The magnitude of gas velocity in this region is maximum. The same observations can also be made in the permeability distribution in the sample right

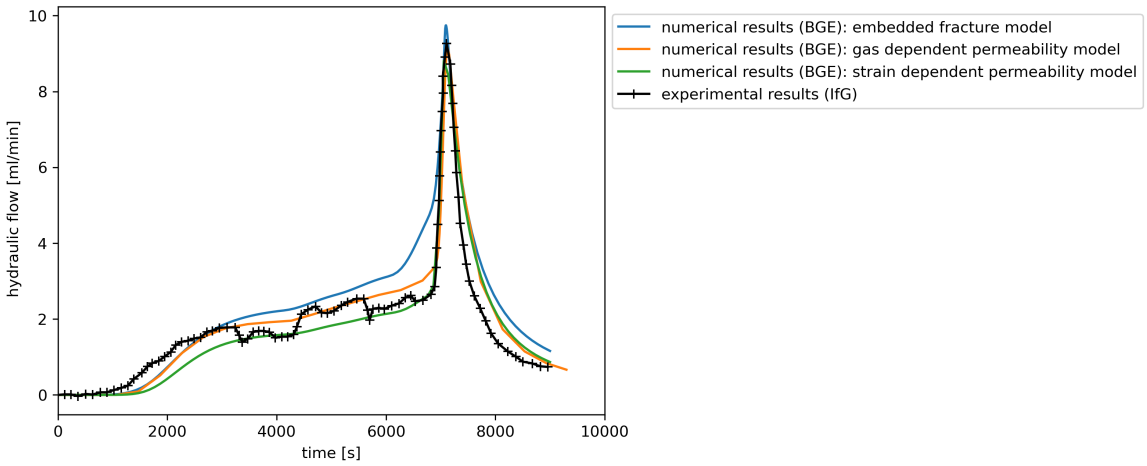

Figure 2.24: Comparison of experimental and numerical results by BGE for the IfG gas fracture test.

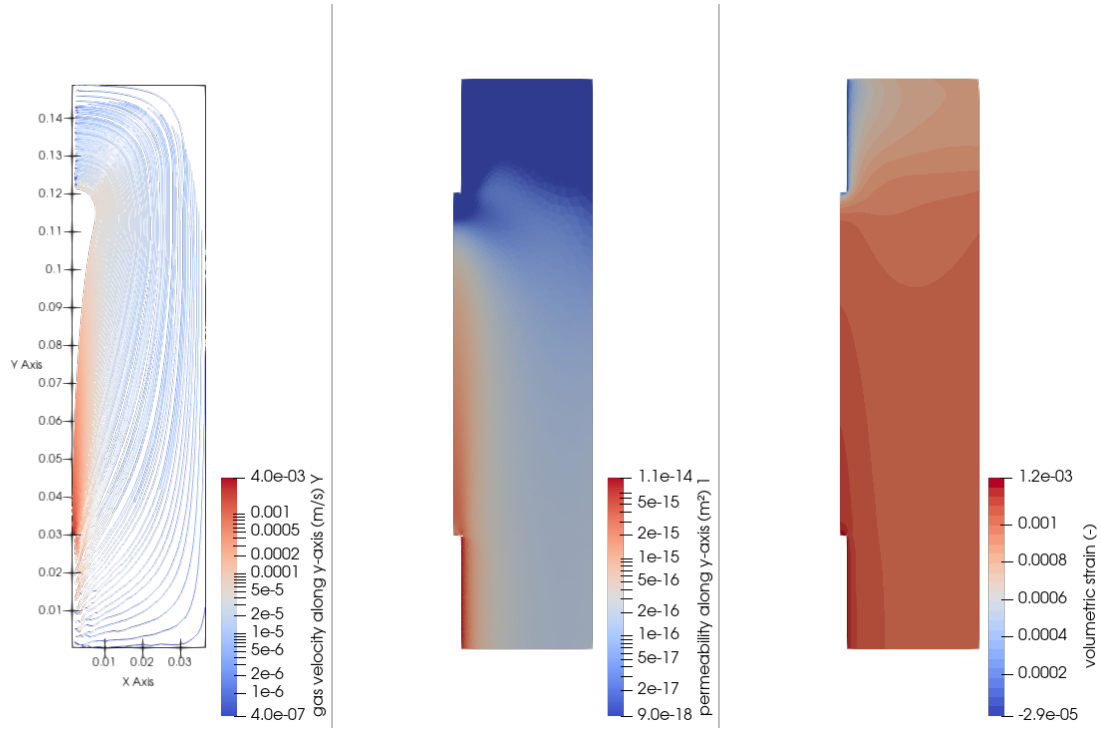

Figure 2.25: Gas velocity, permeability and volumetric strain distribution in the sample at the breakthrough event of the gas fracture test using the embedded fracture permeability model.

after the breakthrough event. One can observe an increase of permeability in the main axis of the sample between the upstream and downstream boreholes. The region of increased permeability is also correlated to the region with the highest volumetric strains. This means that the gas injection leads to dilation of the clay matrix that results in an increase of permeability. This observation is in line with the experimental evidences showing the formation of discrete tensile fracture at the breakthrough event.

The same analysis for the strain dependent permeability and the gas pressure dependent permeability shows a more uniform distribution of the isolines of gas velocity. The increase of permeability is also uniform across the sample without showing preferential pathways for the gas transport. The permeability increase is concentrated in the two third lower part of the sample. At the upper part, the permeability remains unchanged. This behaviour is not observed experimentally. However these models are able

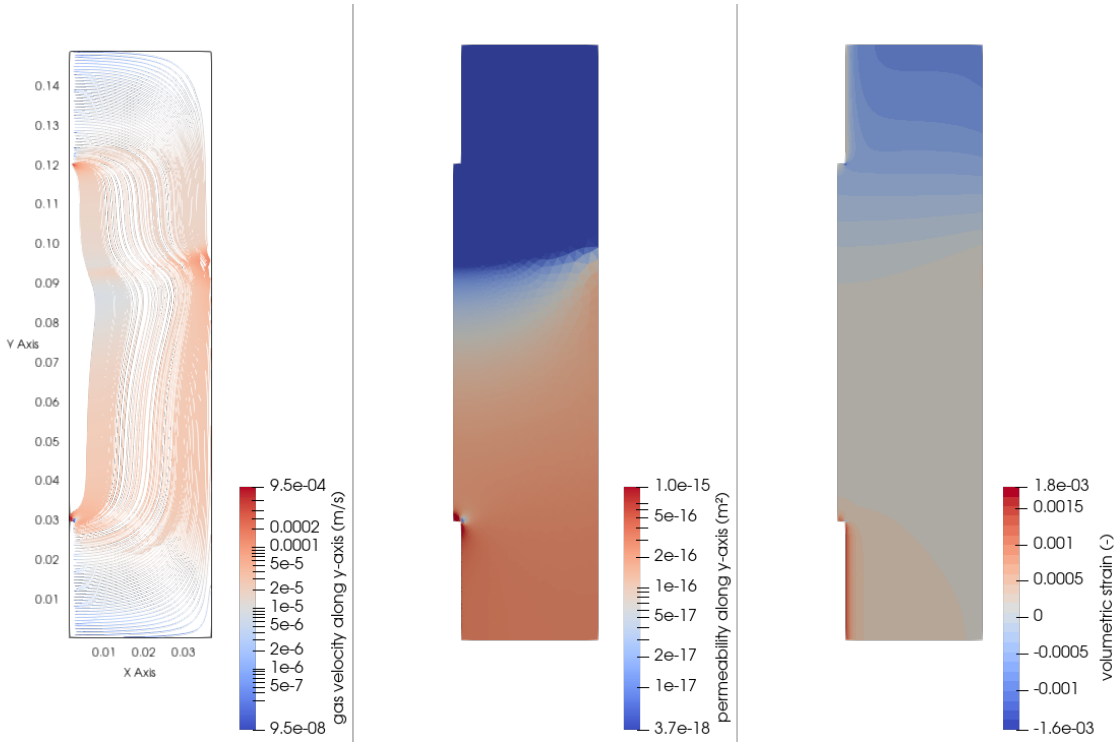

Figure 2.26: Gas velocity, permeability and volumetric strain distribution in the sample at the breakthrough event of the gas fracture test using the strain dependent permeability model.

to quantitatively predict the experimental results. It is also observed a clear dependency between the volumetric strains and the permeability when using the strain dependent permeability model and between the gas pressure and permeability when using the gas pressure dependent model.

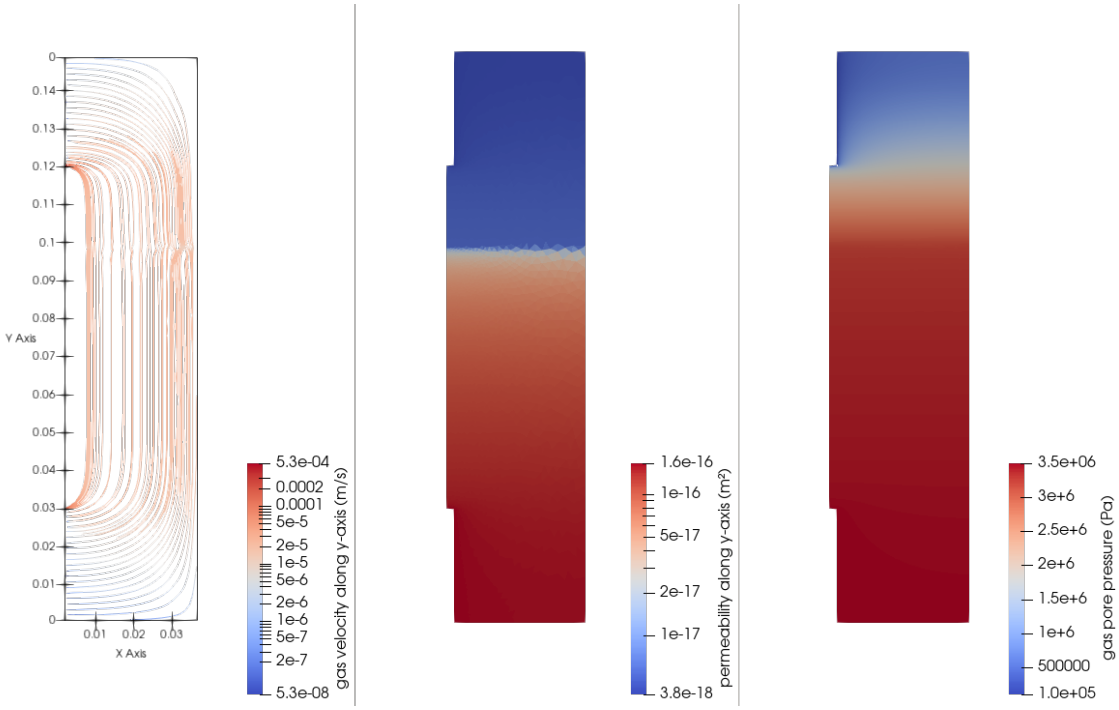

Figure 2.27: Gas velocity, permeability and volumetric strain distribution in the sample at the breakthrough event of the gas fracture test using the gas pressure dependent permeability model.

In summary, on can conclude that the use of permeability models can help to simulate the gas transport mechanism of dilatancy controlled gas flow and gas flow through tensile fractures following the Paul Marschall concept presented in Figure 1.1. The modelling of the IfG experiment showing a great agreement between numerical and experimental results validates this modelling approach. The main advantage of using permeability models relies in their applicability in repository scale continuum based models that are usually used for performance assessment of repository systems. This was the focus of the work in Task 4 of WP GAS. With this approach, the gas transport can be easily included in such assessment simulations. From the four models developed and tested in this study, the embedded fracture model was even able to predict discrete pathways where the gas transport occurs as it is observed experimentally.

2.1.9. Key learning points

New knowledge acquired

The TH2M model class of OGS-6 enables an investigation of different gas transport processes introduced in Fig. 1.1. The work performed in Task 3 and also in Task 2 aims on a validation of this code development, but also on an increased understanding of relevant effects in laboratory and in-situ experiments focusing on gas transport. This knowledge is a fundamental basis for the safety assessment on repository scale as it has been in the focus of the work in Task 4. One main outcome of Task 3 is on statements regarding the expected barrier integrity of a potential repository. The work in this task therefore essentially relates to the visco-capillary flow of gas and water phase, the so called "two-phase flow". In this context, the impact of gas pressure and deformation on the transport processes has been investigated by using and validating different permeability models. Comparison of numerical results with measurements indicates the applicability of the chosen model approach and the presented model set-ups to determine homogeneous two-phase flow effects on the laboratory scale.

Impact of acquired knowledge

The validation of the numerical TH2M modelling approach by several laboratory experiments highlights its applicability. The comparison of the modelling with the experimental results shows a very good agreement regarding the evolution of gas pressure, saturation and displacements. The implemented TH2M model enables the investigation of gas transport mechanisms like diffusion, advection considering two-phase flow and including the impact of changing material parameters, as the permeability.

Remaining knowledge gaps

The validation of modelling results against experiments has been performed on few laboratory scale experiments. The validation effort should be pursued by modelling other laboratory experiments realised under different boundary conditions and has to be extended to the in-situ scale. This would also be an essential basis for the safety assessment on the repository scale. The homogenized model set-up as used in sections 2.1.5, 2.1.6 and 2.1.8 does not represent the appearance of dilatancy controlled pathways as it would be possible with the phase field approach amongst others. Furthermore, initial material heterogeneities, which are generally to be expected in claystone and especially in the near field of excavations, have not been taken into account. Dealing with such heterogeneities is numerically demanding and must be based on a good database regarding local conditions. As a matter of fact, the use of more complex methods could be enhanced focusing on a general understanding. However, the use of these methods on repository scale should be considered carefully, also against the background of the good results of the simplified approaches used here.

Recommendations for the future

Gas transport in a potential repository system is based on various physical mechanisms such as diffusion and advection in combination with two-phase flow in dilatancy controlled pathways. Numerical modelling of these mechanisms is a valuable tool in safety analysis. The formulation of constitutive equations and the development of suitable numerical methods are essential for this. Herefore, a comprehensive physical understanding and a suitable mathematical formulation is required. The applicability of the models should be further tested by validation against laboratory and in situ scale experiments. The resulting understanding of the processes is an essential basis for the safety assessment on repository scale.

.

Uni Liège

2.2. University of Liège (Subtask 3.2)

2.2.1. Introduction

Based on experimental evidences, we define a constitutive model able to describe and predict the self-sealing in clayey rocks. In this context, the most relevant experimental works are summarized in (Bock et al., 2010). At the laboratory scale, it was observed that the main mechanisms responsible for the self-sealing are the swelling of clay minerals, the consolidation and creep (Bernier et al., 2007a). The process is therefore strictly related to the main properties of the potential host rock.

Concerning the Callovo-Oxfordian Claystone (COx), experimental campaigns were conducted both at the repository scale (de La Vaissière et al., 2015) and on laboratory samples (Davy et al., 2007), (Zhang, 2013), (Giot et al., 2019), (Di Donna et al., 2022), (Wang et al., 2022a), (Zhang and Talandier, 2023). It was observed that the mineralogical composition is crucial in the self-sealing process (Bock et al., 2010), (Delay et al., 2007), (Mayor et al., 2007): samples taken from the carbonate-rich unit (USC) have a more limited self-sealing capacity compared to the clay-rich unit (U.A.). Therefore, the swelling of clay minerals plays a major role in the recovery of hydraulic properties. Conversely, the presence of a high carbonate content prevents water from penetrating the sample and swelling the clay minerals. Moreover, it has been shown that swelling of clay minerals begins in the areas around the fracture and then progressively spreads throughout the sample (Bock et al., 2010). More specifically, a fracture results in an initial equivalent permeability of several orders of magnitude greater than in the intact clay. Then, during hydration and water uptake by the sample, some secondary cracks can be generated around the main one, defining a weak and disturbed zone characterized by low density compared to the intact material (Figure 2.28). Here, the re-saturation by water is relatively fast, inducing a quite rapid swelling of clay minerals, leading in turn to a rapid fracture closure and, thus, a rapid reduction in permeability (Di Donna et al., 2022; Wang et al., 2022a).

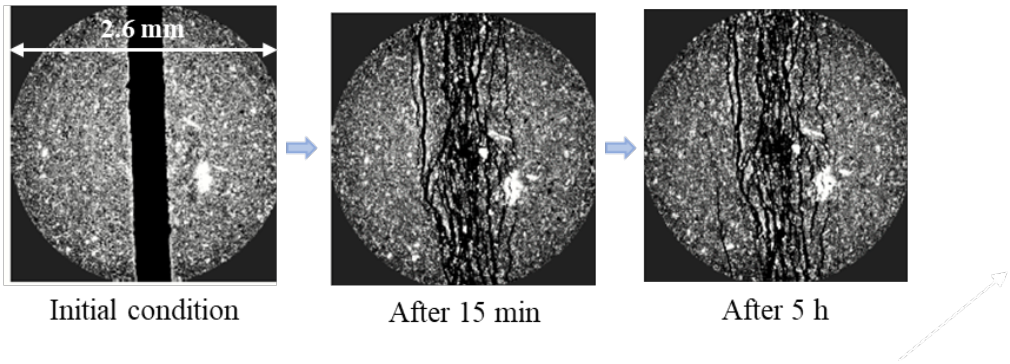

Figure 2.28: X-ray images of a fractured Callovo – Oxfordian cylindrical sample (horizontal sections) at different time steps of a hydration test from the beginning (left) to the end (right) of the test (Di Donna et al., 2022)

Finally, swelling involves clay minerals far from the fracture, the process becomes slower and slower until it stabilizes. This phenomenon has been observed by several experimental campaigns, as summarized in Figure 2.29 in terms of the temporal evolution of water permeability k_w.

Despite the large amount of experiments, limited attempts were made to model this phenomenon numerically. A numerical approach in this field is necessary to describe and understand the hydro-mechanical behavior of the fracture, and to predict the self-sealing process in the long term. Wang and co-authors (Wang et al., 2022c) proposed an elastoplastic damage model to describe self-sealing both at the sample scale and at the scale of the CDZ (Compression Damage Zone) experiment performed in ANDRA's URL. This model successfully describes the self-sealing of fractured unsaturated claystone; however, it does

not define a constitutive model for the fracture. To this aim, we defined a 2D constitutive model able to describe the sealing capacity of the COx claystone, accounting the clay swelling around the fracture as well as the role of its initial size. The main phenomenological aspects involved during the self-sealing are call back. Then, the finite element code LAGAMINE is used to validate the model against laboratory tests under pseudo-oedometric conditions. In the proposed model, the anisotropy of the material, but also the chemical properties of the saturation water are not considered. They both deserve to be implemented in future extensions of the model. Moreover, in a first version it is defined in 2D, describing a vertical section of a sample. This simplification is justified because the selected laboratory tests are carried out on cylindrical samples with a planar fracture. Then, a validation with a 3D model is also executed. This 3D version should be properly improved for further studies at the repository scale.

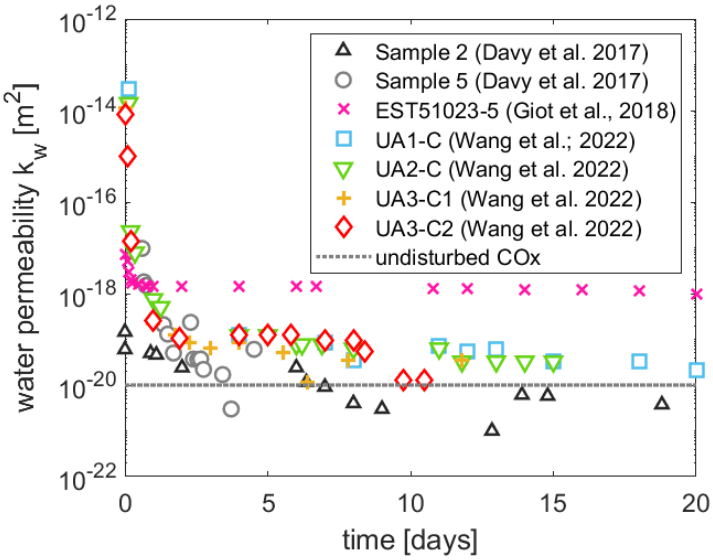

Figure 2.29: Temporal evolution of water permeability k_w observed experimentally during hydration tests

2.2.2. Conceptual model

2.2.2.1. Experimental evidences of self-sealing

As already said, when saturation starts, it first involves the clay minerals close to the fracture, which swell and tend to close the discontinuity quickly. This aspect was deeply investigated experimentally by (Di Donna et al., 2022) and is displayed in Figure 2.30a (images W1-W6), where displacements concentrate around the fracture lips, and their sign is consistent with the fracture closure (Figure 2.30b). Then the saturation progressively involves the whole sample (Figure 2.30a); W7-W10) until a final condition in which the swelling is prevented at the outer borders constrain.

The rapid swelling in the proximity of the fracture is associated with the generation of parallel micro-cracks around the main one (Figure 2.31a).

This fracture network defines a damaged zone and contributes to the recovery of the hydraulic properties. Moreover, it was observed that the size of this fractured zone is related to the initial size of the discontinuity: the smaller the initial fracture aperture, the smaller the space available for deformation, and the smaller the fractured area is. To further investigate self-sealing, Figure 2.31 allows the measurement of the thickness of the damaged zone (i.e., the zone including the main fracture and sub-fractured sides). Then, subtracting the size of the main discontinuity (already measured in (Di Donna et al., 2022)) gives the thickness of the damaged sides. Finally, for practical reasons, a symmetrical micro-cracks network is assumed, such that

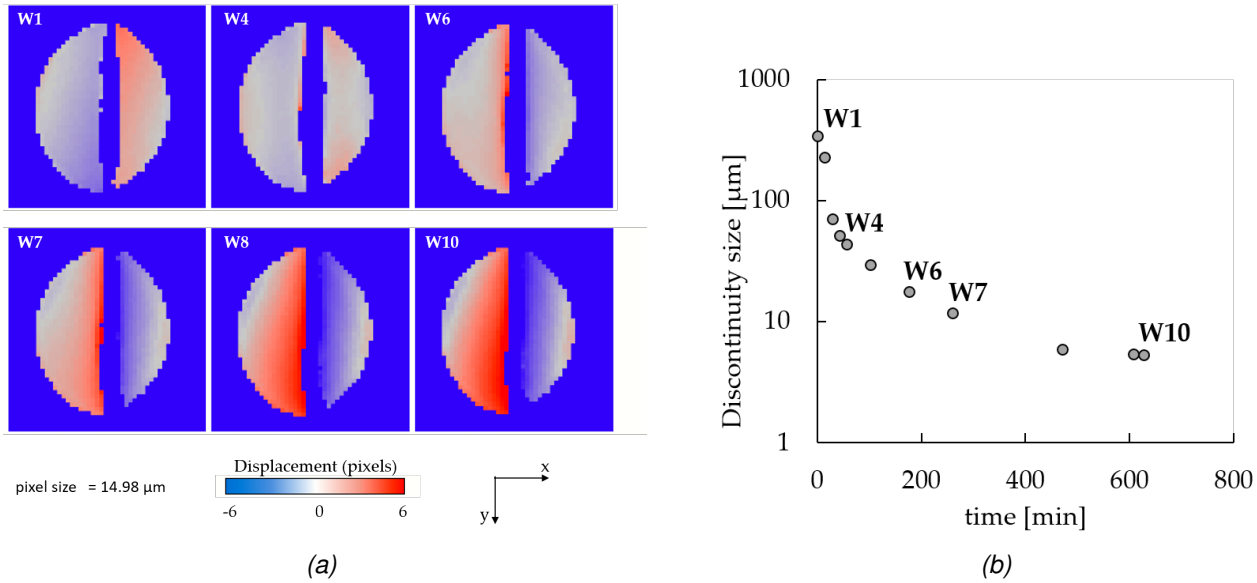

Figure 2.30: (a) X Displacement fields resulted from DVC for a cylindrical sample (n. 8182) of diameter 8 mm, averaged over the sample height for different time lapses; (b) Evolution of the discontinuity size with time (Di Donna et al., 2022)

the thickness computed previously can be divided by 2 to obtain the thickness of each damaged side at the beginning of hydration h_{ini}. This thickness is plotted against the initial size of the fracture d_{ini} in Figure 2.31b, for each hydration test of Figure 2.31a. Finally, results can be fitted by an empirical power law type that can be assumed representative of COx samples with planar fracture. This relationship is consistent with experimental evidence since the sample sides remain intact ($h_{ini} \rightarrow 0$) if the initial fracture is sufficiently small ($d_{ini} \rightarrow 0$).

2.2.2.2. Definition of the interface element

The modeling of the self sealing requires the definiton of both the intact material and the fracture. The former can be defined in the framework of the continuum mechanics and is assumed as a linear elastic material, while the fracture zone is modeled using a zero-thickness interface element (Charlier and Cescotto, 1988),(Day and Potts, 1994), (Goodman et al., 1968). This interface element is widely used in modeling joints and rock discontinuities since it is suitable for large deformations without re-meshing. It has also been used to model the interface between two different media (Cerfontaine et al., 2015), (Habraken and Cescotto, 1998). The contact zone is discretized through field nodes and is only activated in the case of contact. An accurate description of this type of contact element is provided by (Cerfontaine et al., 2015) for a 3D problem, while a 2D schematization is given in Figure 2.32a. The zero-thickness element is discretized by the three-node method, i.e., the interface element includes the inner of the discontinuity (index F) and the two adjacent sides (indexed Γ^2 and Γ^2) allowing the modeling of the fluid flow propagation along and through the discontinuity (f_l and f_{ti} in Figure 2.32b).In this study, each node of the two sides (i.e., nodes 1-6) carries 3 degrees of freedom (the displacements u_x and u_y in the horizontal and vertical direction, respectively, and the pore water pressure p_w). Each inner node (i.e., nodes 1'-3') is fixed in terms of displacement and thus carries only the pore water pressure degree of freedom. This is a strong simplification of the reality since the gas pressure is kept constant at environmental condition. This choice is justified by the fact that the propagation of gas inside the fracture is out of the scope of this study.

The three-nodes discretization allows a homogenous field of pressure across the interface while there is a transversal drop of pressure between the two sides of the fracture (Cerfontaine et al., 2015). The fracture opening d in Figure 2.32b is measured as the distance between the nodes of the side Γ^1 and those of

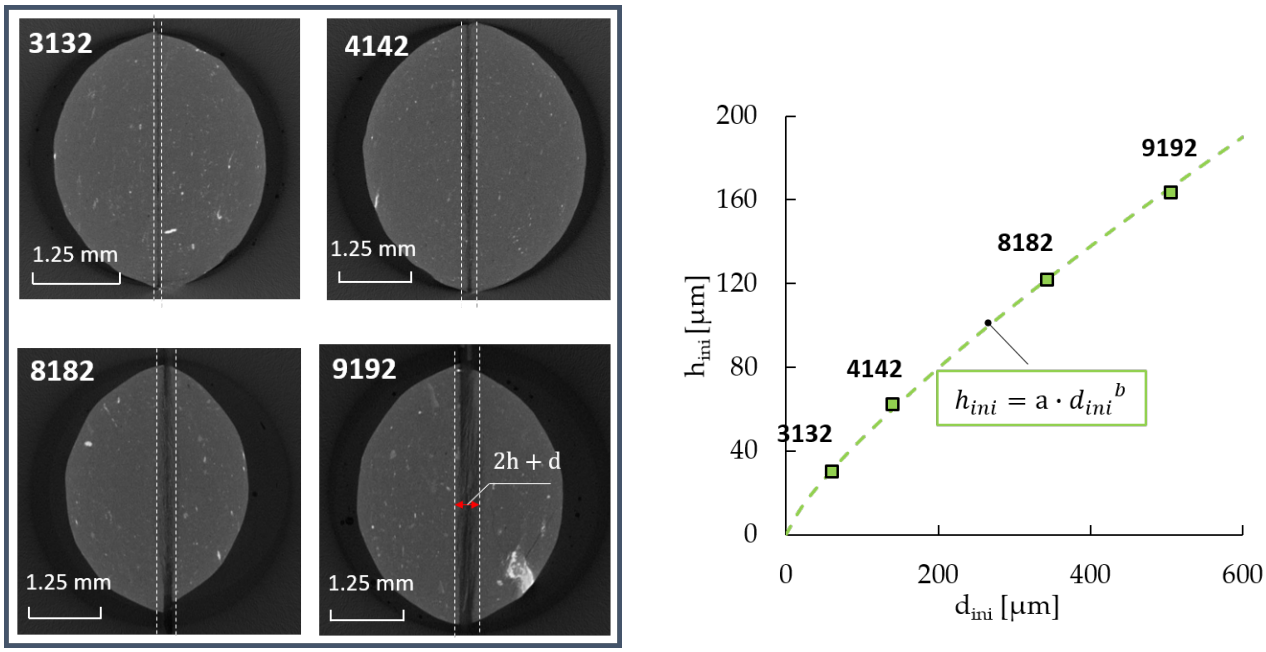

(a) (b)

Figure 2.31: (a) X-ray images after a few minutes of hydration, middle slice (Di Donna et al., 2022) with the definition of the interface zone in the middle of the section (white dashed line) including the fracture and the damaged sides; (b) Definition of the initial extension of the damaged sides ($h_{1,ini} = h_{2,ini} = h_{ini}$) *in relation with the initial size of the fracture* d_{ini} *fitted by a power law type* ($a = 1.2019$; $b = 0.7914$; $R^2 = 0.9989$)

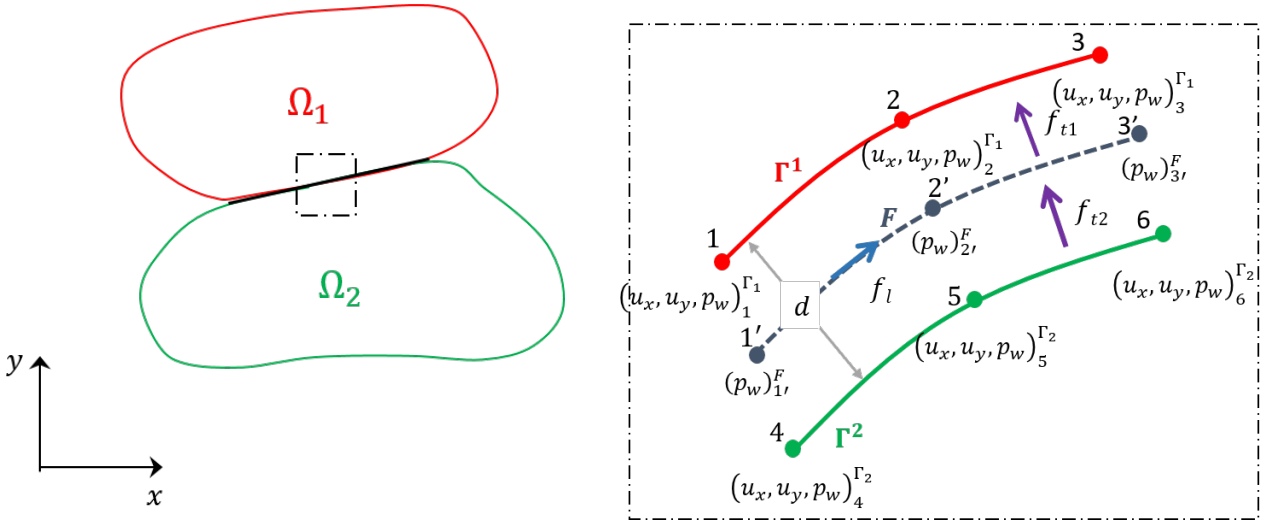

(a) (b)

Figure 2.32: a) Contact between two continuum deformable solids Ω_1 *and* Ω_2*; (b) Definition of the parabolic three-node discretization of an interface element where* Γ^1 *and* Γ^2 *are the side of the interface (nodes 1-6),* F *is the inner of the interface (nodes 1'-3' obtained as the projection of nodes 1-3 of the side* Γ^1*)*

$\Gamma^2$and is computed through a segment-to-segment discretization (Fischer and Wriggers, 2006; Bandis et al., 1983; Gens et al., 1990) as described in (Cerfontaine et al., 2015)).

2.2.2.3. The hydro-mechanical formulation for the fracture

The mechanical problem

The fracture mechanical behavior is defined in terms of variation of the contact pressure with the fracture closure V (or the hydraulic aperture d). When two perfectly smooth continuum elements are not in contact, the closure V takes positive values. If the two parts come into contact, their contact pressure increases while the distance V between them cancels (yellow curve in Figure 2.33). Nevertheless, the two counterparts are never perfectly smooth, but some roughness on contact area exists. Since it is not possible to model all the asperity by finite elements, the two adjacent surfaces are assumed to be perfectly smooth, and the average distance between them defines the fracture closure V. In the particular case of rock joints, a non-linear contact law accounting for the role of the asperities in contact was experimentally observed (Goodman et al., 1968; Plesha, 1995; Gentier et al., 1996; Bart et al., 2004; Salehnia et al., 2017). Among the others, a recent formulation to describe the non-linear mechanical behavior of the fracture was proposed by Bart (Bart et al., 2004; Guiducci et al., 2003) and is represented in Figure 2.31 in blue in terms of effective normal pressure p'_N. In the incremental form it writes:

$$\Delta p'_N = -\frac{\tilde{K}_N}{(1+\frac{V}{D_0})^{\gamma}}\Delta V \tag{2.16}$$

D_0 defines the asymptotic mechanical closure of the fracture in absolute value, $\tilde{K}_N$ is the stiffness coefficient defining the initial slope of the curve (for small values of $\Delta p'_N$) and the exponent γ is a correction factor taken equal to 2 to represent the rock fracture behavior. This coefficient generally varies between 2 and 6 (Plesha, 1995).

If two bodies initially not in contact get closer and closer, their asperities begin to touch and deform, with large displacement for low applied stress. This behavior is described through the initial slope $\tilde{K}_N$ defining a linear relationship between the normal contact pressure and the closure. Then, the applied stress progressively induces smaller and smaller deformations since the fracture is closing more and more, and the number of asperities in contact increases. At this stage, the interpenetration of the two counterparts is related to the contact and deformation of asperities. The pressure-closure relationship is no more linear and is defined by the normal stiffness:

$$K_N = \frac{\tilde{K}_N}{(1+\frac{V}{D_0})^{\gamma}} \tag{2.17}$$

It depends on the mechanical properties of the rock, the physical properties of the filling material (if any), and the configuration of the asperities (i.e., the number, surface, and relative position). In this study, it should be intended as a penalty parameter introduced to ensure the constraint of normal contact allowing the two contacting surfaces to interpenetrate each other to simulate the contact between asperities. It should be high enough to avoid artificial overlap between the two counterparts keeping in mind that too large values can ill-condition the problem. Finally, the fracture behavior can be compared with the intact rock for a given load applied. This occurrence explains the asymptote D_0 corresponding to the maximum mechanical closure of the fracture.

From Figure 2.33, the hydraulic opening d and closure V are related to each other by the relationship:

$$\|D_0\| = \|d\| + \|V\| = \|d_{ini}\| + \|V_{ini}\| \tag{2.18}$$

The index –ini indicates the initial values at the beginning of the test. Knowing the initial hydraulic aperture d_{ini}, the slope $\tilde{K}_N$ and the normal contact stress p'_N at the beginning of the test, D_0 is computed by coupling Eq. 2.18 with:

$$V_{ini} = D_0\left[\sqrt[1-\gamma]{\frac{1-\gamma}{D_0\tilde{K}_N}p'_{N,ini}+1}-1\right] \tag{2.19}$$

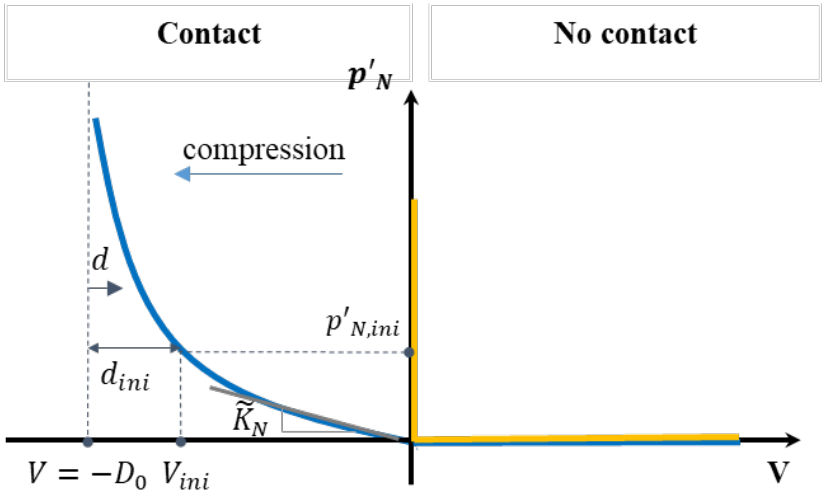

Figure 2.33: Interface normal behavior in terms of fault closure V *– effective normal contact pressure* $\Delta p'_N$ *in the ideal case of a smooth interface (in yellow) and the real one of a rough interface (in blue). The values* V_{ini}, d_{ini} *and* $p'_{N,ini}$ *indicate respectively the closure, hydraulic aperture and the contact pressure at the beginning of the test*

The opening d is always positive, while the closure V can be either positive (no contact) or negative (contact). Finally, the following statements apply:

- If there is no contact, the hydraulic closure V is zero, while the hydraulic opening d is equal to the mechanical asymptotic closure D_0 ($p'_N = 0 \rightarrow V = 0; d = D_0$);
- If the contact pressure reaches large values, then the hydraulic closure V reaches mechanical asymptotic closure D_0, while the hydraulic opening d becomes null ($p'_N = \infty \rightarrow V = D_0; d = 0$).

The fluid flow problem

The three-node discretization introduced above allows the description of the fluid flow (e.g., water in this particular case study) considering as a variable the pore water pressure inside the interface and on the two sides in contact. In this way, it is possible to calculate the longitudinal flow along the discontinuity and the transverse flow inside the interface (see Figure 2.32b).

The liquid water flow along the discontinuity is described by Darcy's equation:

$$q_l = -\frac{k_{r,w}^{(F)} k_w^{(F)}}{\mu_w} \Delta p_w^{(F)} \tag{2.20}$$

The index (F) stays for the fracture, μ_w is the water dynamic viscosity, $\Delta p_w^{(F)}$ is the gradient of pore water pressure, $k_{r,w}^{(F)}$ and $k_w^{(F)}$ are the relative and intrinsic permeability of the fracture. Since the fracture saturates quickly during water injection, the relative value $k_{r,w}^{(F)}$ is set to the unit value, hence the permeability is defined by the intrinsic value k_w^F that varies with the fracture opening.

The transversal flow, i.e., the flow through the two adjacent surfaces is defined as a function of the transversal permeability of the fractured material and the difference in pressure between the discontinuity and its

two counterparts. According to Figure 2.32b, the two transverse flow are:

$$\begin{aligned} f_w^{t1} &= \rho_w T_w^1 t_{r,w}^1 \left(p_w^{(F)} - p_w^{(\Gamma_1)} \right) \\ f_w^{t2} &= \rho_w T_w^2 t_{r,w}^2 \left(p_w^{(\Gamma_2)} - p_w^{(F)} \right) \end{aligned} \tag{2.21}$$

The transmissivity coefficient is defined as the product between the intrinsic and the relative value, i.e., T_w^i and $t_{r,w}^i$, respectively. They depend on the fluid and rock properties and should be adequately calibrated. The intrinsic transmissivity coefficient T_w^i is a constant of the material and must take into account the transfer between the fluid in the fracture and the two counterparts. When liquid water is considered, the transfer is faster than with vapour water because, in the latter case, some mass exchanges must occur at the wall of the counterparts. The relative value $t_{r,w}^i$ is a dimensionless parameter function of the degree of saturation, accounting for the water transmissivity in a two-phase flow (e.g., the water permeability in an unsaturated medium). Since this case study deals with the contact between two continuums of the same material, the same coefficients are assumed for the two adjacent parts 1 and 2:

$$\begin{aligned} T_w^1 &= T_w^2 = T_w \\ t_{r,w}^1 &= t_{r,w}^2 = t_{r,w} \end{aligned} \tag{2.22}$$

Water retention curve

The unsaturated behavior of a material is described by its water retention curve. In this case, since the two damaged sides are very narrow, they are assumed to follow the same flow equations and retention curve as the intact material, defined hereafter. To the authors' knowledge, there are no experimental investigations on the retention properties of the discontinuities. In this study, they are represented by the Van Genutchen relation (Van Genuchten, 1980):

$$S_w^{(F)} = \left[1 + \left(\frac{s^{(F)}}{p_a^{(F)}} \right)^{m^{(F)}} \right]^{\frac{1}{m^{(F)}} - 1} \tag{2.23}$$

Where S_w^F is the degree of saturation; $s^{(F)}$ (i.e.: $p_g^{(F)} - p_w^{(F)}$) is the suction; $p_a^{(F)}$ and $m^{(F)}$ are, respectively, the air entry pressure and the shape coefficient of the curve. More specifically, the air entry pressure is the suction value at which pore water starts to displace from the initially saturated condition. Therefore, the higher the fracture opening d and the smaller should be the threshold $p_a^{(F)}$. The Laplace equation accounts for this aspect:

$$p_a^{(F)} = \frac{2\sigma}{d} \tag{2.24}$$

Where σ is the water tension surface $\sigma = 0.073 \mathrm{N/m}$. As already said, in this study, the fracture is initially unsaturated and should rapidly become saturated during the hydration phase. This behavior can be considered by choosing a relatively high value for the shape coefficient $m^{(F)}$ in Eq. 2.23 (compared to the one referring to the intact material), bearing in mind that too large values can cause numerical convergence issues.

The relative transmissivity coefficient $t_{r,w}$ is related to the degree of saturation through the Van Genutchen equation (Van Genuchten, 1980):

$$t_{r,w} = \sqrt{S_w^{(F)}} \left[1 - \left(1 - S_w^{(F)\,1/n^{(F)}} \right)^{n^{(F)}} \right]^2 \tag{2.25}$$

The shape coefficient $n^{(F)}$ is related to the shape coefficient $m^{(F)}$ of the fracture retention curve defined in Eq. 2.23: $n^{(F)} = 1/m^{(F)} - 1$. In saturated conditions, the relative transmissivity assumes the unit value while

it assumes values lower than one in the unsaturated case, thus reducing the total transmissivity coefficient during drying. This aspect is consistent with the fact that the gas propagates more slowly than water. The main hydraulic parameters for the interface zone are synthesized in Table 2.5. As explained in the dedicated section, the transmissivity coefficient T_w is properly calibrated running numerical simulations both in vapor and water injection.

Table 2.5: Hydraulic parameters for the interface element

Parameters	Symbol [unit]	Value
Porosity	ϕ [%]	100
Tortuosity	τ [-]	1.00
Van Genutchen coefficient	$m^{(F)}$ [-]	1.67
Van Genutchen coefficient	$n^{(F)}$ [-]	0.401
Intrinsic transmissivity (water)	T_w [m $\times$ (Pa $\times$ s)$^{-1}$]	Calibrated
Intrinsic transmissivity (vapor)	T_w [m $\times$ (Pa $\times$ s)$^{-1}$]	Calibrated

The hydro-mechanical coupling

The hydraulic and mechanical formulations are coupled through the Terzaghi's effective stress principle under unsaturated conditions (Nuth and Laloui, 2008). On the other side, the flow properties of the fracture are strongly dependent on its aperture by the mean of the cubic law, defining the fluid flow proportional to the cubic of the fracture opening d. By schematizing the fracture as two flat surfaces separated by a distance equal to the opening d and characterized by a unit thickness w (Figure 2.34), Poiseuille's law defines the fluid flow rate Q as:

$$Q = \frac{wd^3}{12\mu_w}\frac{p_w^{out} - p_w^{in}}{L} \tag{2.26}$$

where p_w^{in} and p_w^{out} are respectively the inlet and the outlet pressure, and L is the fracture length.

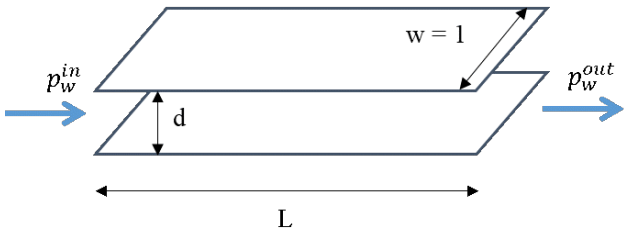

Figure 2.34: Simplification of the fracture as two parallel plates with the definition of the inlet and outlet pressure (p_w^{in} and p_w^{out}, respectively)

Then, the Darcy equation writes:

$$Q = \frac{k_w^{(F)} A}{\mu_w}\frac{p_w^{out} - p_w^{in}}{L} \tag{2.27}$$

WhereA = dw is the area of the cross-section. Combining the Eq. 2.26 and Eq. 2.27:

$$k_w^{(F)} = \frac{d^2}{12} \tag{2.28}$$

This equation is the expression of the cubic law correlating the water permeability of the fracture to its opening. Eq. 2.28 simplifies the reality as it does not consider roughness when assessing permeability. It has, however, been validated by several studies (Tsang and Witherspoon, 1981; Oron and Berkowitz, 1998). In particular, roughness can be considered by referring to the hydraulic opening instead of the mechanical opening (Olsson and Barton, 2001).

The calculation of the hydraulic opening d during the re-saturation process requires further investigation. As reminded before, the hydration of the fracture induces some micro-cracks around it, defining a damaged zone able to swell quickly, favoring the hydraulic closure of the fracture. The thickness of this zone depends, for the same material, on the initial thickness of the fracture. Hence, since the area around the discontinuity contributes to self-sealing, it must be considered when describing the interface constitutive behavior. The modeling of these damaged sides requires further numerical effort. Nevertheless, since they are narrow enough compared to the sample sizes (about the same order of magnitude as the initial fracture opening), they do not need to be explicitly meshed. This evidence allows us to implement them directly in the interface element with considerable numerical simplification, as illustrated in Figure 2.35.

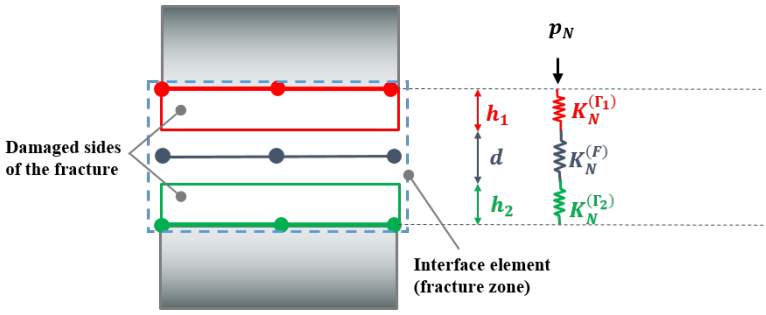

Figure 2.35: Sketch of the interface element accounting for the damaged area around the main fracture

This aspect is simulated numerically by including two deformable zones into the interface element: the stiffness of the two sides, Γ_1 and Γ_2, are $K_N^{(\Gamma_1)}$ and $K_N^{(\Gamma_2)}$ respectively, while inside the interface, the stiffness is computed as defined in Eq. 2.17. Since the thickness of these damaged boundaries is relatively small, isotropic behavior is assumed whereby the stiffness moduli are derived from the modified Cam Clay model (Roscoe and Burland, 1968) and normalized by their initial thickness, i.e. $h_{1,ini}$ and $h_{2,ini}$ respectively:

$$\begin{aligned} K_N^{(\Gamma_1)} &= \frac{1}{h_{1,ini}} \left(\frac{1 + e_{ini}}{\kappa_{el}^{(\Gamma_1)}} p_{N,ini}^{\prime(\Gamma_1)} \right) \\ K_N^{(\Gamma_2)} &= \frac{1}{h_{2,ini}} \left(\frac{1 + e_{ini}}{\kappa_{el}^{(\Gamma_2)}} p_{N,ini}^{\prime(\Gamma_2)} \right) \end{aligned} \tag{2.29}$$

where e_{ini} is the initial void ratio, $p_{N,ini}^{\prime(\Gamma_1)}$ and $p_{N,ini}^{\prime(\Gamma_2)}$ are the reference effective mean pressures (assumed equal to the respective values at the beginning of the test) and $\kappa_{el}^{(\Gamma_1)}$ and $\kappa_{el}^{(\Gamma_2)}$ are the elastic coefficients, which should be calibrated numerically.

For the equilibrium, the total pressure is the same across the whole system and, therefore, in the interface element, the same increment of total normal stress Δp_N is applied:

$$\Delta p_N^{(\Gamma_1)} = \Delta p_N^{(\Gamma_2)} = \Delta p_N^{(F)} = \Delta p_N \tag{2.30}$$

By applying the Terzaghi effective stress principle, the equilibrium of the system can be written as:

$$\begin{aligned} \Delta p_N &= \Delta p_N^{\prime(\Gamma_1)} + S_w^{(\Gamma_1)} \Delta p_w^{(\Gamma_1)} + (1 - S_w^{(\Gamma_1)}) \Delta p_g^{(\Gamma_1)} \\ \Delta p_N &= \Delta p_N^{\prime(\Gamma_2)} + S_w^{(\Gamma_2)} \Delta p_w^{(\Gamma_1)} + (1 - S_w^{(\Gamma_2)}) \Delta p_g^{(\Gamma_2)} \\ \Delta p_N &= \Delta p_N^{\prime(F)} + S_w^{(F)} \Delta p_w^{(F)} + (1 - S_w^{(F)}) \Delta p_g^{(F)} \end{aligned} \tag{2.31}$$

In the following, we will omit the terms $1 - S_w^{(\Gamma_1)}$ since the gas pressure is kept constant at environmental conditions. The variation of effective normal pressure $\Delta p_N'$ is obtained assuming an elastic constitutive

behavior for the whole interface element (i.e., inner fracture + damaged sides). In particular, the increment of the effective normal pressure inside the interface ($\Delta p_N'^{(F)}$) can be related to the increment of the fault opening Δd, as well as the increment of the effective normal stress on the two sides Γ_1 and Γ_2 can be related to their swelling Δh_1 and Δh_2 respectively:

$$\begin{aligned} \Delta p_N'^{(\Gamma_1)} &= -K_N^{(\Gamma_1)} \Delta h_1 \\ \Delta p_N'^{(\Gamma_2)} &= -K_N^{(\Gamma_2)} \Delta h_2 \\ \Delta p_N'^{(F)} &= -K_N^{(F)} \Delta d \end{aligned} \tag{2.32}$$

The negative sign indicates that the effective normal pressure is assumed positive in compression. Finally, substituting Eqs. 2.32 in Eqs. 2.31, it is possible to find the amount of swelling of the fracture sides (Δh_1 and Δh_2) and the increment of the hydraulic opening Δd:

$$\begin{aligned} \Delta h_1 &= \frac{K_N^{(\Gamma_2)} K_N^{(F)} \Delta h_{TOT} - K_N^{(F)} \left(S_w^{(\Gamma_1)} \Delta p_w^{(\Gamma_1)} - S_w^{(\Gamma_2)} \Delta p_w^{(\Gamma_2)} \right) - K_N^{(\Gamma_2)} \left(S_w^{(\Gamma_1)} \Delta p_w^{(\Gamma_1)} - S_w^{(F)} \Delta p_w^{(F)} \right)}{K_N^{(\Gamma_2)} K_N^{(\Gamma_1)} + K_N^{(F)} K_N^{(\Gamma_1)} + K_N^{(F)} K_N^{(\Gamma_2)}} \\ \Delta h_2 &= \frac{K_N^{(\Gamma_1)} K_N^{(F)} \Delta h_{TOT} - K_N^{(\Gamma_1)} \left(S_w^{(\Gamma_2)} \Delta p_w^{(\Gamma_2)} - S_w^{(F)} \Delta p_w^{(F)} \right) - K_N^{(F)} \left(S_w^{(\Gamma_2)} \Delta p_w^{(\Gamma_2)} - S_w^{(\Gamma_1)} \Delta p_w^{(\Gamma_1)} \right)}{K_N^{(\Gamma_2)} K_N^{(\Gamma_1)} + K_N^{(F)} K_N^{(\Gamma_1)} + K_N^{(F)} K_N^{(\Gamma_2)}} \\ \Delta d &= \frac{K_N^{(\Gamma_1)} K_N^{(\Gamma_2)} \Delta h_{TOT} - K_N^{(\Gamma_1)} \left(S_w^{(F)} \Delta p_w^{(F)} - S_w^{(\Gamma_2)} \Delta p_w^{(\Gamma_2)} \right) - K_N^{(\Gamma_2)} \left(S_w^{(F)} \Delta p_w^{(F)} - S_w^{(\Gamma_1)} \Delta p_w^{(\Gamma_1)} \right)}{K_N^{(\Gamma_2)} K_N^{(\Gamma_1)} + K_N^{(F)} K_N^{(\Gamma_1)} + K_N^{(F)} K_N^{(\Gamma_2)}} \end{aligned} \tag{2.33}$$

When the two fracture sides have an infinite bulk modulus ($K_N^{(\Gamma_1)} = K_N^{(\Gamma_2)} \to \infty$: i.e., a null elastic coefficient or a null thickness, as defined in Eq. 2.19), the constitutive mechanical laws defined in Eqs. 2.32 reduces to the form defined in Eq. 2.16 where $\Delta V = \Delta d$. Considering that the two claystone elements respond to the same constitutive behavior, the same material properties are assumed at the two disturbed zones around the fracture. They have the same initial thickness that can be computed as a function of the initial fracture aperture d as in Figure 2.31b (i.e., $h_{1,ini} = h_{2,ini} = h_{ini}$) and the same elastic coefficients ($\kappa_{el}^{(\Gamma_1)} = \kappa_{el}^{(\Gamma_2)} = \kappa_{el}$) that should be adequately calibrated. Together with the penalty factor $\tilde{K}_N^{(F)}$, they are properties of the material concerned independently from the test, the initial, and the boundary conditions. It is important that the ratio between the stiffness of the two disturbed zones and the penalty $\tilde{K}_N^{(F)}$ ensures the rapid hydraulic closure observed experimentally during wetting.

2.2.2.4. The hydro-mechanical formulation for the intact material

The intact claystone is described as an isotropic linear elastic material. However, during the preparation of small-size samples, the material can be disturbed. In this case, a lower Young modulus than the intact one should be considered. The main mechanical parameters of the Callovo Oxfordian claystone have been provided by several experimental campaigns and are synthesized in Table 2.6.

Table 2.6: Mechanical parameters of Callovo-Oxfordian argillite (from (Charlier et al., 2013b))

Parameters	Symbol [unit]	Value
Dry density	ρ_d [g/cm^3]	2.21-2.34
Grain density	ρ_s [g/cm^3]	2.71
Young's modulus	E [MPa]	4000
Poisson's coefficient	ν [-]	0.3

As for the interface, the hydraulic behavior is described by the Darcy's equation. The hydraulic parameters are based on previous studies describing the water retention curve and the relation between the relative

permeability and the saturation degree through the Van Genuthchen equation (Armand et al., 2017), as shown in Figure 2.36.

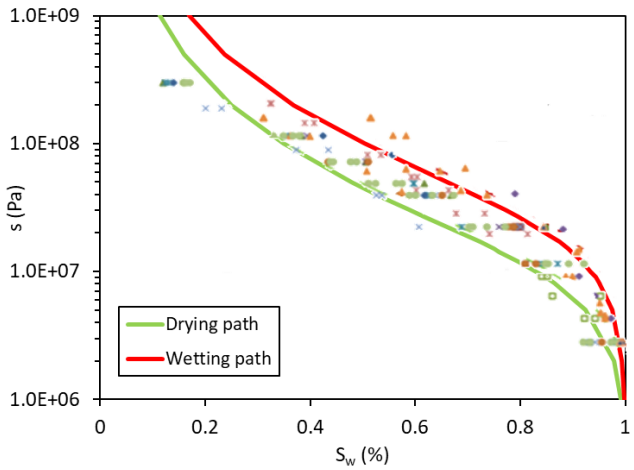

Figure 2.36: Water retention curve for Callovo-Oxfordian claystone (Armand et al., 2017)

As for the fracture, the water flow through the claystone depends on its hydraulic permeability that varies, in unsaturated conditions, with the degree of saturation. Similarly to the relative transmissivity coefficient defined in Eq. 2.25, the van Genuchten formulation defines the relative permeability as a function of the degree of saturation for the intact claystone:

$$k_{r,w} = \sqrt{S_w}\left[1 - \left(1 - S_w^{1/n}\right)^n\right]^2 \tag{2.34}$$

The hydraulic parameters for the Callovo-Oxfordian claystone are listed in Table 2.7. For the sake of simplicity, the hysteretic behavior of the retention curve in Figure 2.36 is not considered in the modeling and only the wetting curve is considered. Moreover, the model is defined in isotropic conditions. For the test described hereafter, the fracture is vertical and oriented parallel to the bedding plane; thus, only vertical permeability is accounted for in the numerical model.

Table 2.7: Hydraulic parameters for the Callovo-Oxfordian claystone (Armand et al., 2017; Charlier et al., 2013b; Levasseur et al., 2021)

Parameters	Symbol [unit]	Value
Horizontal saturated water permeability	$k_{w,H}^{sat}$ [m^2]	3.40×10^{-20}
Vertical saturated water permeability	$k_{w,V}^{sat}$ [m^2]	1.33×10^{-20}
Porosity	ϕ [%]	15-18
Water content	w [%]	3-7
Tortuosity	τ [−]	0.25
Air entry value	p_a [MPa]	12
Van Genutchen coefficient	m [−]	1.49
Van Genutchen coefficient	n [−]	0.329

2.2.3. Numerical model

The hydro-mechanical modeling of fractured COx samples is performed in 2D plane strain conditions by using the in-house finite element code LAGAMINE (Charlier, 1987a),(Collin, 2003a). Thus allows to

implement and couple the hydraulic and mechanical behaviour as well as contact element. The validation of the interface model requires the calibration of its parameters and the comparison with some laboratory tests. The following hydraulic paths are selected for this purpose:

- Wetting test (Wang et al., 2022a): water is injected into the fracture starting from the initial unsaturated condition;
- water vapor - wetting – drying test [-(Di Donna et al., 2022): the sample is firstly saturated by water vapor and then by liquid water, and finally, it is dried by injecting dry air;
- Drying–wetting test (Di Donna et al., 2022): the sample is firstly dried and then re-saturated by injecting liquid water

All the experimental tests used for calibration and validation were conducted on cylindrical samples artificially fractured, as illustrated in Figure 2.37a. The sample was contained in a rigid shell to prevent lateral deformation. To assess only the effect of re-saturation on the hydraulic recovery, no confining pressure was imposed. The sample fracture is oriented parallel to the bedding plane. Since the modeling was carried out in 2 dimensions, only a vertical slice of the sample was considered, as illustrated in Figure 2.37a, meaning that the anisotropy of the material is not taken into account. The geometry, mesh, and boundary conditions are schematized in Figure 2.37b.

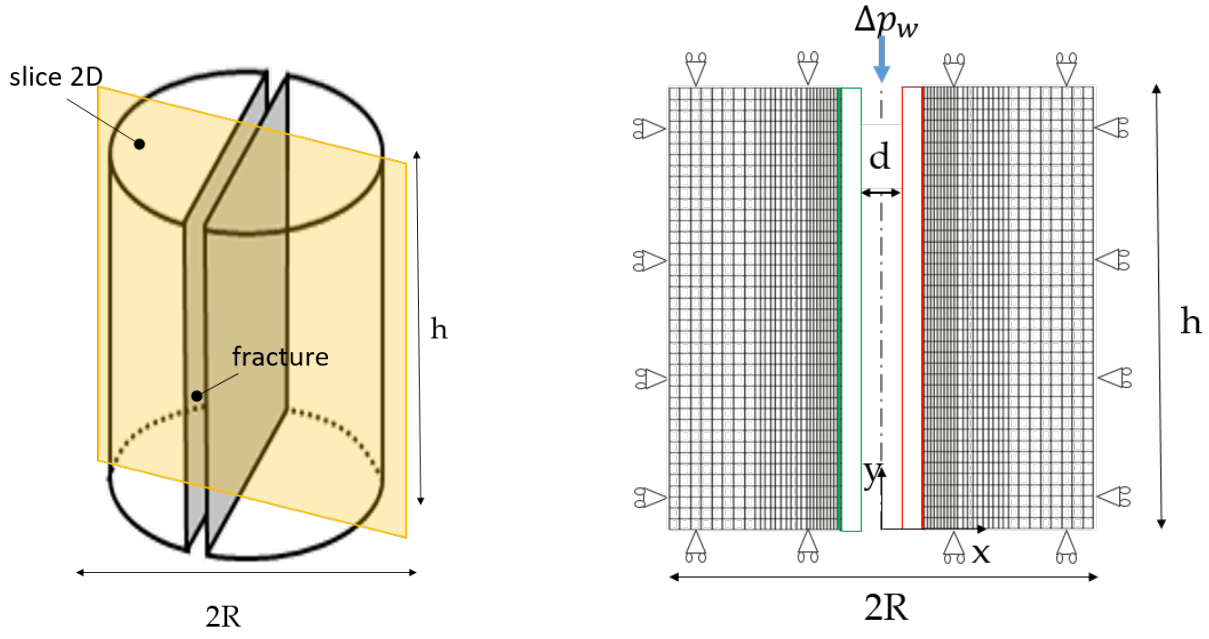

Figure 2.37: Construction of the model: (a) Sketch of a cylindrical sample prepared and fractured artificially, the vertical slice (in light yellow) is used for the 2D model construction; (b) 2D model with the definition of mesh, boundary conditions, and water injection Δp_w (the dimensions of the damaged elements and the aperture of the fracture are out of scale for schematizing purposes)

The sample dimensions and the initial thickness of the discontinuity are defined in the following subsections for each test. In all cases, the displacements normal to the external boundaries are fixed.

The two counterparts of the fracture are free to move, allowing swelling or contraction during the test. Then water is injected from one extremity of the fracture controlling the pressure while the other is set to

environmental conditions (p_w = 0.1MPa). Depending on the test, the water pressure applied can be either positive or negative. Depending on the clay transmissivity, water can flow across the interface, permeate the fractured walls, and eventually saturate/de-saturate the entire system, generating a new equilibrium condition. The intrinsic transmissivity coefficient needs to be calibrated, while the other main hydraulic parameters of the fracture are listed in Table 2.5. Moreover, the calibration also involves the mechanical parameters of the fracture, i.e., the coefficient $\tilde{K}_N$ of the discontinuity and the elastic coefficient κ_{el} of the two disturbed sides. The hydro-mechanical properties of the bulk material are defined in Table 2.6 and Table 2.7.

2.2.4. Results

2.2.4.1. Wetting test

Four samples with diameter 2R = 37mm and height h = 40mm collected from the U.A. were prepared and then fractured using the Brazilian splitting test. Sample preparation and experiments are described in (Wang et al., 2022a), whose basic information is recalled in Table 2.8.

Table 2.8: Data on Callovo-Oxfordian samples used for the wetting test (from (Wang et al., 2022a))

Sample	Core number	Depth [m]	Geological unit	Sat. degree [%]	Initial aperture [μm]
UA1-C	EST 57903	-490	UA	86.8	21.58
UA2-C	EST 58128	-490	UA	85.5	17.14
UA3-C1	EST 58145	-490	UA	84.3	16.02
UA3-C2	EST 58145	-490	UA	84.3	14.26

All samples are extracted from the same core and differ slightly from each other regarding the initial degree of saturation and initial fracture aperture. Synthetic water with specific mineralogical composition was prepared in the laboratory and then injected into the fracture, reaching the value of 0.5MPa. Then, the drainage valve was closed, allowing the whole sample to be re-saturated. Since the injection duration is unknown, it is assumed in the following that the desired water pressure is reached in 3 hours, after which the fracture becomes saturated, and water begins to flow through the system. This choice is justified because, at least numerically, the injection duration does not affect the results.

Calibration of the hydro-mechanical parameters during wetting

In the following, the test UA2-C is described in detail to understand the physical meaning of the unknown parameters and how to use them to fit the experiments. As defined in Table 2.8, the initial fracture aperture for the test UA2-C is d_{ini} = 21.58μm. The corresponding thickness of the damaged sides is h_{ini} = 11.4μm (see Fig.2.31b). A sensitivity analysis is performed to calibrate the penalty parameter $\tilde{K}_N$ in Eq. 2.17 and the elastic coefficients κ_{el} in Eq. 2.29. In addition, the intrinsic transmissivity T_w controlling the transversal flow (Eqs. 2.21-2.22) should be defined. The values used for this sensitivity analysis are listed in Table 2.9.

Table 2.9: Parameters used for the sensitivity analysis during the wetting test UA2-C

Parameter	Symbol [unit]	Value
Elastic coefficients for the damaged sides	κ_{el} [-]	$[0; 0.55; 1.10; 2.20]$
Stiffness parameter	$\tilde{K}_N$ [MPa/m]	$[100; 400; 1000; 4000]$
Intrinsic transmissivity	T_w [m $\times$ (Pa $\times$ s)$^{-1}$)]	$[10^{-14}; 10^{-15}; 10^{-16}]$

Figure 2.38 shows the profile of water pressure p_w, effective normal pressure p'_n, and hydraulic opening d in

the y-direction (i.e., along the fracture) when $\tilde{K}_N$ = 400MPa/m, κ_{el} = 2.20, and the absolute transmissivity is $T_w = 10^{-15}\text{m} \times (\text{Pa} \times \text{s})^{-1}$. Three main phases can be observed:

1. $t \leq 3h$, injection phase: the pore water pressure increases along the whole fracture (y-direction) as shown in Figure 2.38a; this corresponds to a slight reduction of the effective normal pressure (Figure 2.38b) and a slight increase of the fracture opening (Figure 2.38c); therefore this first part of the test is dominated by the resaturation of the fracture.

2. $3h < t \leq 4\text{days}$, self-sealing phase: once the defined values of pore water pressure are reached on the top and the bottom of the fracture ($t = 3h$), a transient process is observed (Figure 2.39). Water begins to flow transversely, firstly saturating the damaged area and then the rest of the sample. The two counterparts begin to swell, leading, by equilibrium, to the increase of the effective normal pressure within the fracture (Figure 2.38b) and consequently reducing its opening (Figure 2.38c). The variation in effective normal pressure p'_n and opening d along the fracture becomes more and more negligible until reaching a uniform trend along the y-direction after about 12 hours.

3. $t > 4\text{days}$, stabilization. The pore water pressure reaches stationarity, as illustrated in Figure 2.39. This result is consistent with Figure 2.38 since, after 4 days, there is no significant temporal change in terms of effective pressure and fracture opening.

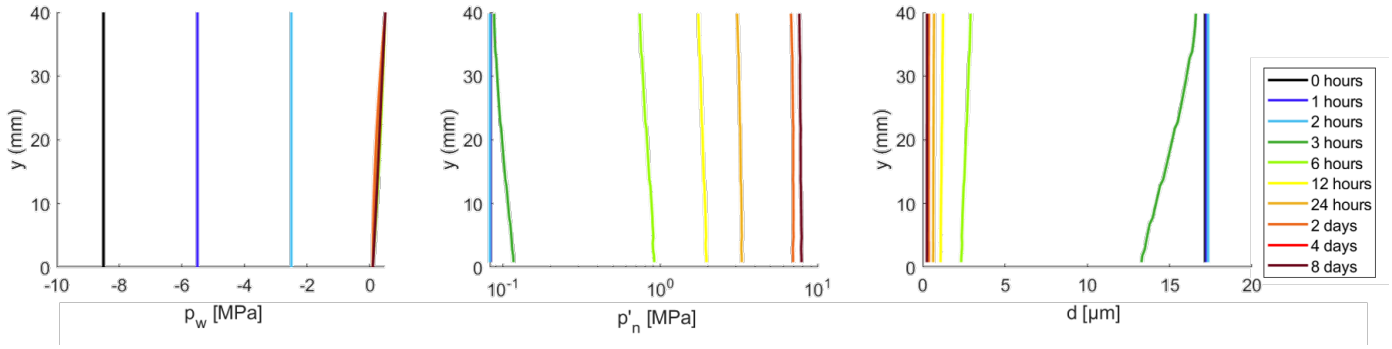

(a) (b) (c)

Figure 2.38: Profiles of the main hydro-mechanical features obtained numerically along the fault opening for the UA2-C test ($\tilde{K}_N$ = 400MPa/m, κ_{el} = 2.20 and $T_w = 10^{-15}\text{m} \times (\text{Pa} \times \text{s})^{-1}$: (a) pore water pressure; (b) effective normal pressure; (c) fault opening (the legend is on the right for the three graphs)

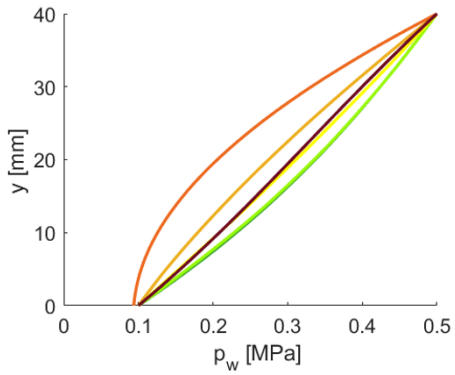

Figure 2.39: Pore water pressure along the fault opening after the injection phase

Several numerical tests were carried out to quantify the effect of the elastic coefficient κ_{el} of the damaged sides on self-sealing. The main results are plotted in Figure 2.40a in terms of the temporal evolution of the equivalent aperture. The figure also compares the numerical results with experiments. The initial opening (for $t \leq 3h$) is negligible compared to the following closure. Then, once the fracture saturates, it starts to close with time. This self-sealing process is not linear as it is rapid at the beginning, becoming slower and slower until stabilization at a constant final value (for $t = 4days$). These results are also consistent, at least qualitatively, with the trend observed experimentally (Giot et al., 2019; Wang et al., 2022a; Di Donna et al., 2022; Wang et al., 2022b; Zhang et al., 2020). Moreover, the increase in the elastic coefficient κ_{el} reduces the stiffness of the damaged sides (see Eq. 2.29), thus increases their swelling and the closure of the fracture giving results comparable to experiments. An equivalent effect is obtained by varying the penalty coefficient $\tilde{K}_N$, as illustrated in Figure 2.40b: the increase of the penalty coefficient increases the rigidity of the fracture, thus reducing its ability to seal. Considering the hydraulic properties, as already mentioned, the swelling of the rock depends on the ability of water to flow through it from the fracture; therefore, the transmissivity coefficient plays a predominant role, which is illustrated in Figure 2.40c. It defines the rapidity of the hydraulic closure process: when $T_w = 10^{-16} m \times (Pa \times s)^{-1}$, the water flow is relatively slow, while $T_w \geq 10^{-15} m \times (Pa \times s)^{-1}$ self-sealing is quick. In particular, $T_w = 10^{-14} m \times (Pa \times s)^{-1}$ gives a rapid reduction of the equivalent aperture that does not match experiments. The combination of parameters fitting better the experimental results is given by $\tilde{K}_N = 400 MPa/m$; $\kappa_{el} = 2.20$ and $T_w = 10^{-15} m \times (Pa \times s)^{-1}$.

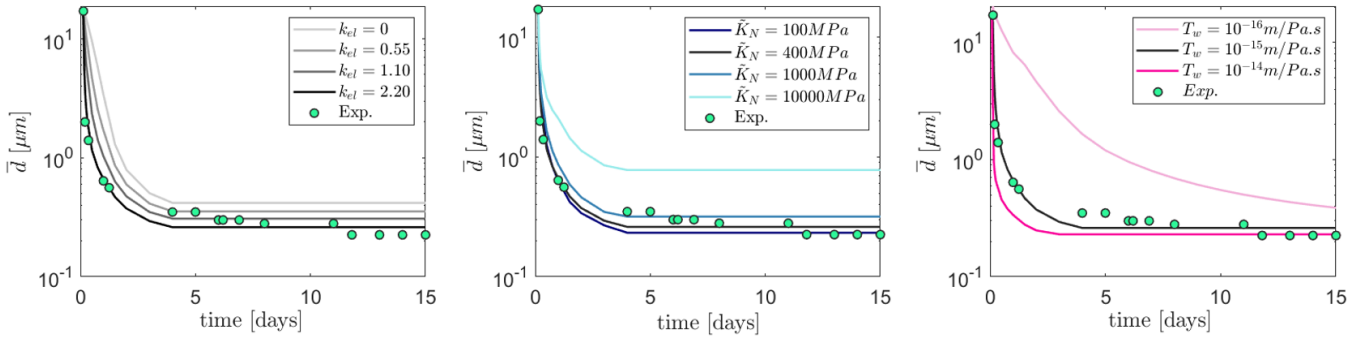

(a) *(b)* *(c)*

Figure 2.40: Calibration of the hydromechanical parameters and comparison with the experimental test UA2-C: (a) effect of the elastic coefficient κ_{el} ($\tilde{K}_N = 400 MPa/m$ and $T_w = 10^{-15} m \times (Pa \times s)^{-1}$); (b) effect of the stiffness coefficient $\tilde{K}_N$ ($\kappa_{el} = 2.20$ and $T_w = 10^{-15} m \times (Pa \times s)^{-1}$); (c) effect of the absolute tramsissvity T_w ($\kappa_{el} = 2.20$ and $\tilde{K}_N = 400 MPa/m$); the experimental data have been published in (Wang et al., 2022a)

Wetting tests results

The previously illustrated procedure is now adapted to the other samples of Table 2.8, and results are plotted in Figure 2.41 regarding the temporal evolution of mean hydraulic opening compared with the experimental results. Based on the calibration performed in the previous Section, the following set of parameters is chosen: $\tilde{K}_N = 400 MPa/m$; $\kappa_{el} = 2.20$ and $T_w = 2 \times 10^{-15} m \times (Pa \times s)^{-1}$, i.e., the same mechanical parameters used to obtain results in Figure 2.38, while the intrinsic transmissivity T_w was slightly increased to find the best match for all the tests. As illustrated in Figure 2.41, such parameters can fit the hydration tests successfully and reproduce self-sealing in the Callovo-Oxfordian claystone. It can be observed that the larger the initial fracture size, the smaller the sealing effect obtained.

A better understanding of the phenomena is achieved by observing the evolution of the water permeability with time. The equivalent fracture water permeability $\bar{k}_w^{(F)}$ is obtained by applying the cubic law in Eq.

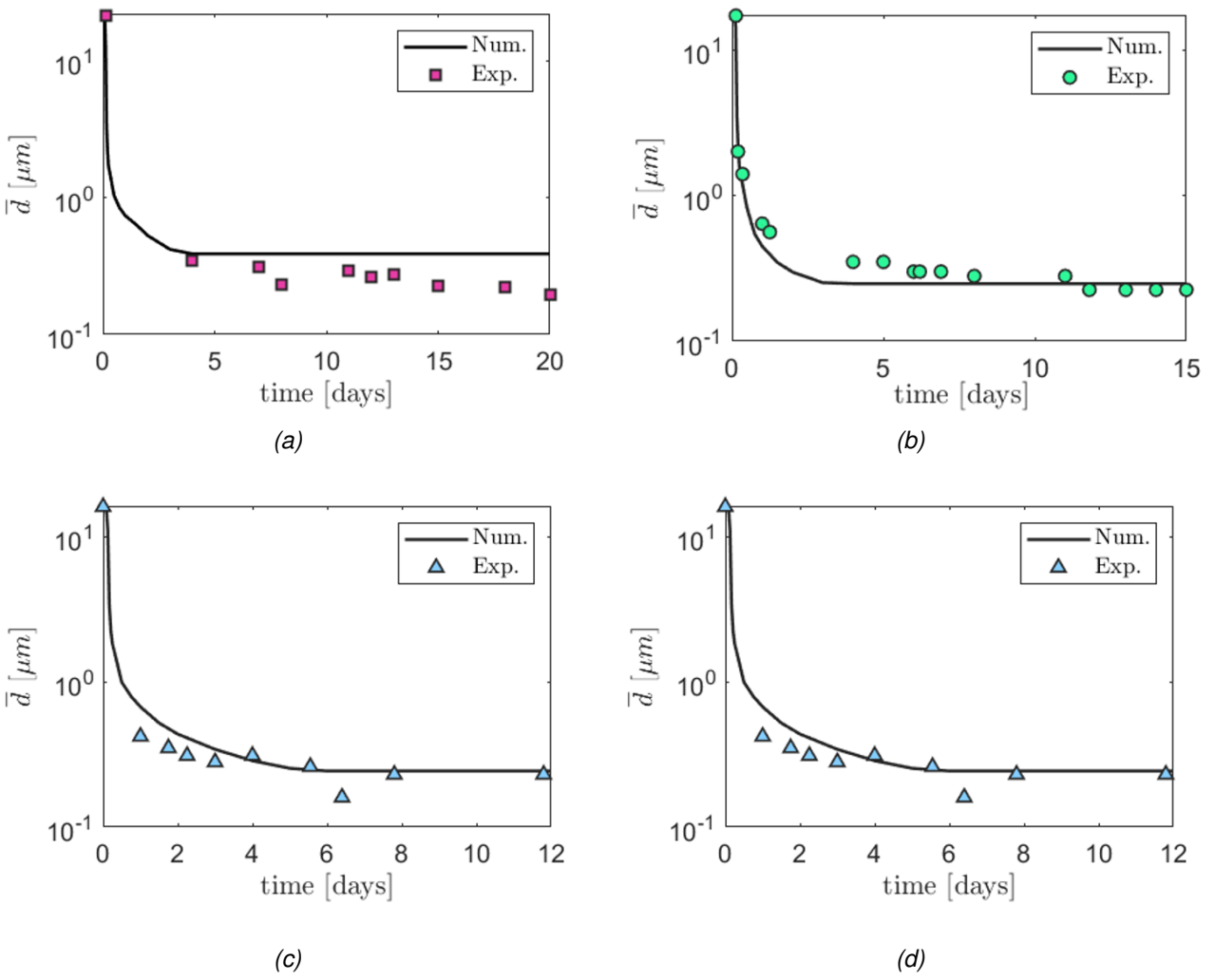

Figure 2.41: Temporal evolution of the average fracture opening during the wetting test, comparison between numerical and experimental results obtained by (Wang et al., 2022a): (a) Test UA1-C; (b) Test UA2-C; (c) Test UA3-C1; (d) Test UA3-C2

2.28 to the equivalent fracture opening $\bar{d}$. However, it is generally more helpful to define the equivalent permeability for the entire sample cross-section, which is calculated as follows:

$$k_{w,eq} = \frac{A^{(\Omega 1)} k_{w1} + A^{(\Omega 2)} k_{w2} + A^{(F)} \bar{k}_w^{(F)}}{A^{(\Omega 1)} + A^{(\Omega 2)} + A^{(F)}} \tag{2.35}$$

where $A^{(\Omega 1)}$ and $A^{(\Omega 2)}$ are the surfaces of the two bulk elements,k_{w1} and k_{w2} the respective permeabilities, $A^{(F)}$ is the surface of the fracture and A_{tot} is the surface of the whole sample. Results are illustrated in Figure 2.42. A good agreement between numerical and experimental results is also obtained in terms of equivalent permeability. It can be observed that the permeability of the intact material k = 1.33 $\times 10^{-20}$ m⁄s, gray dot line in Figure 2.42) is approached after the self-sealing process.

2.2.4.2. Vapor - Wetting - Drying test

Another experimental campaign has been carried out by Di Donna and co-authors, as detailed in (Di Donna et al., 2019) and (Di Donna et al., 2022). Cylindrical samples 8mm in diameter and 20mm in height were prepared and artificially fractured, as sketched in Figure 2.37. The experimental setup consists in

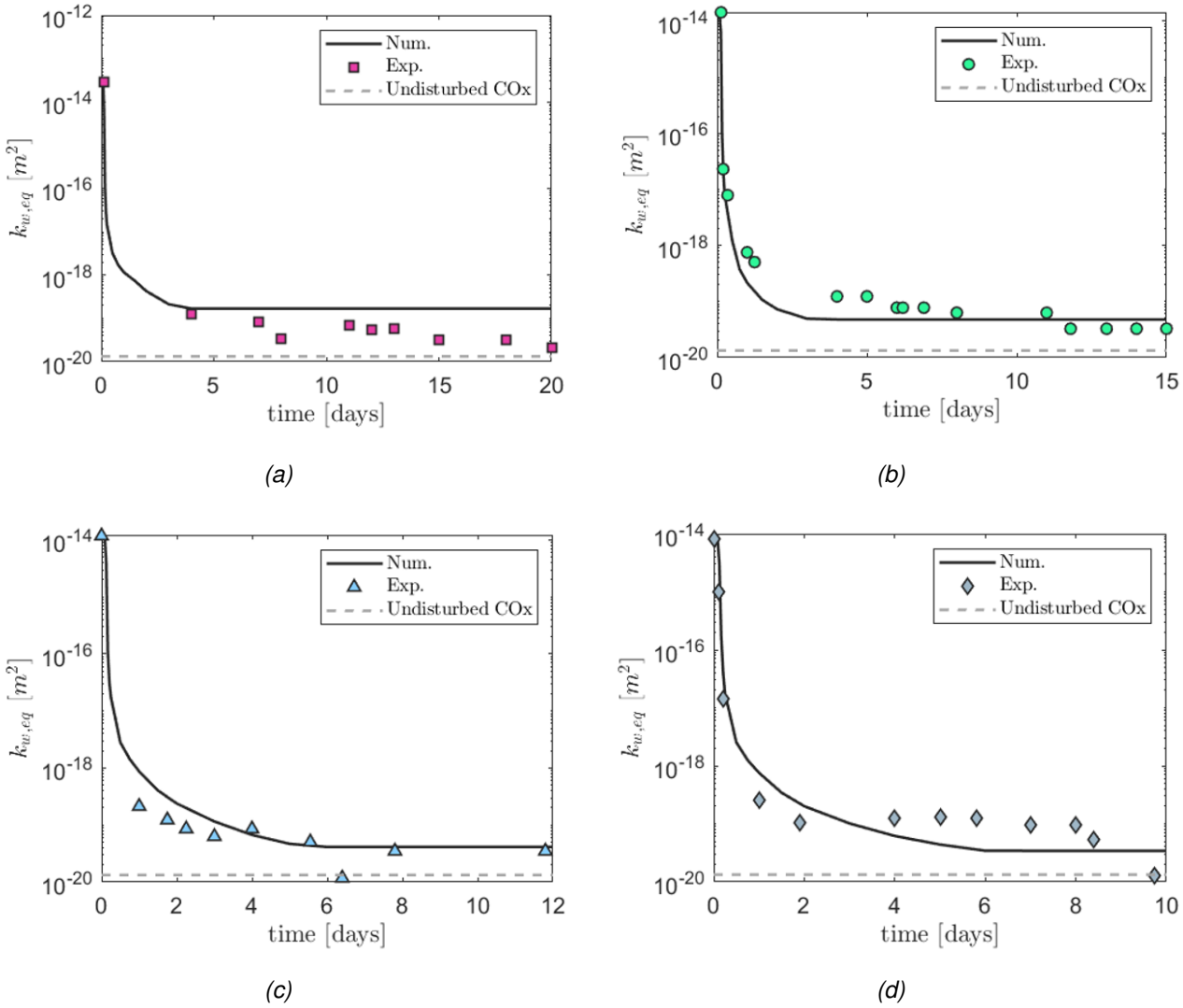

Figure 2.42: Temporal evolution of the average equivalent permeability during the wetting test, comparison between numerical and experimental results obtained by (Wang et al., 2022a): (a) Test UA1-C; (b) Test UA2-C; (c) Test UA3-C1; (d) Test UA3-C2

connecting the sample to a circuit that includes a pump and a reservoir. The sample defined in Table 2.10 was first saturated and then de-saturated. The saturation phase consists of injecting water vapor reaching relative humidity (RH $\simeq$ 100%) and then liquid water, while desaturation occurs by injecting dry air (RH $<$ 20%). A sensor monitors the relative humidity and temperature inside the reservoir.

Table 2.10: Main feature of the wetting-drying test (from (Di Donna et al., 2022))

Sample	Core number	Depth [m]	Geological Unit [-]	Water content [%]	Suction [MPa]	Initial aperture [μm]
3132	EST 53644	-490	UA	6.2	14.3	75

Hydro-mechanical parameters

Due to its small size (8 millimeters in diameter), the sample is assumed to become slightly damaged during its preparation. Therefore, the Young modulus of the material is assumed to be 20 times lower than the one

corresponding to the intact material. Concerning the flow properties, vapor injection causes no significant effect on hydraulic closure for the duration of the experimental test (Di Donna et al., 2022). Although the fracture becomes completely saturated, the vapor cannot quickly saturate the two adjacent clay elements as well. This evidence means that, contrary to what happens when liquid water is injected, the generation of secondary fractures on the sides of the main one is not clearly visible, and the swelling of clay minerals is minimal. However, the sample preparation and the creation of the main fracture, as well as the resaturation phase necessary to restore the sample to its in-situ condition (before starting the test), can induce some secondary cracks. This circumstance is considered in the model by accounting for a small thickness for the damaged sides (h = 2μm). Then water is injected into the fracture generating a well-defined weak zone around it, as illustrated previously in Fig. 2.31 (h = 32μm). The presence of a disturbed zone around the fracture also controls the subsequent drying phase. The stiffness parameters for the interface element are assumed to be equal to those defined in the previous case independently from the fluid injected (i.e., they are properties of the material: $\tilde{K}_N = 400\text{MPa}/\text{m}$; $\kappa_{el} = 2.20$). Concerning the hydraulic parameters, a low transmissivity coefficient T_w is used to model the vapor phase to account for the fact that the closure by saturation by the vapor is slower than the one achieved by injecting liquid water. Here the intrinsic transmissivity is set to $T_w = 8 \times 10^{-18}\text{m} \times (\text{Pa} \times \text{s})^{-1}$, while it is set to $2 \times 10^{-15}\text{m} \times (\text{Pa} \times \text{s})^{-1}$ for the water and drying phases (the same value is used in previous wetting cases). For practical reasons, the gas supply phase is simulated by injecting air at very low relative humidity; therefore, the same intrinsic transmissivity value is used in wetting and drying. However, relative transmissivity (Eq. 2.25) plays a fundamental role during drying since it considerably reduces the total transmissivity coefficient to values close to the transmissivity used during the vapor injection.

Results

The experimental and numerical evolution of the average fracture opening with time is plotted in Figure 2.43a. The three main stages of the test (i.e., vapor, water, and air) are visible both experimentally and numerically. The vapor phase lasted about two days. An initial opening is observed experimentally that might indicate that the vapor phase is still not equilibrated (Di Donna et al., 2022). Numerically, no initial opening is observed. Then, once saturation is achieved (relative humidity RH = 1 in Figure 2.43a), the fracture starts to close slowly. The wetting phase is consistent with the tests discussed in the previous Section: the closure of the fracture is quite rapid at the beginning and then becomes slower and slower. Both experimentally and numerically, no effect is observed at the beginning of the drying phase, whereas a rapid increase in the hydraulic opening is observed experimentally after about four days. Numerically the process starts slightly later. However, the final opening value achieved in the model is comparable with the one obtained from the test. The mismatch between numerical and experimental results during the drying phase can be due to the assumption made in the numerical model (e.g., the drying is simulated by injecting water at negative pressure).

Since the permeability was not measured experimentally, the comparison can only be performed regarding fracture opening. However, the cubic law allows the computation of the fracture permeability, from which it is possible to estimate the equivalent permeability for the whole sample, as defined in Eq. 2.35. Results are illustrated in Figure 2.43b. During the wetting phase, the equivalent permeability reaches the value $k_{w,eq} = 8 \times 10^{-18}\text{m}^2$ that is still larger than the value of the undisturbed rock and those computed in Figure 2.42. This result can be related to the size of the fracture that is larger in this test than in the previous case study; in fact, it was observed that the larger the fracture opening, the smaller the sealing effect. The hydraulic closure/opening of the fracture is driven by the swelling/contraction of the clay minerals from the lips of the fracture itself towards the sample boundaries.

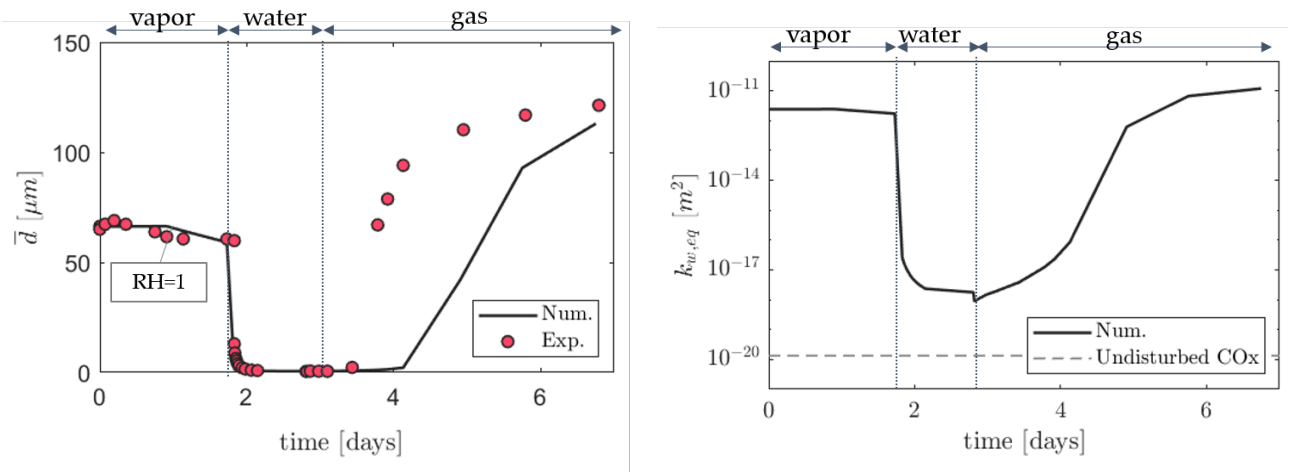

(a) *(b)*

Figure 2.43: Temporal evolution of the average fault opening during test 3132, the experimental results refer to (Di Donna et al., 2022); (b) equivalent water permeability during test 3132

2.2.4.3. Drying - Wetting test

In the experimental campaign published in (Di Donna et al., 2022) and introduced in Section 2.2.2, other tests were carried out by injecting first some dry air and then re-saturating with liquid water. The test selected in this study is the n. 8182, extracted from the same core of the test n. 3132 described in Table 2.10. Therefore, it has the same initial features as the previous one, except for the initial fracture size, which is 285 µm for the present case study. As for the test n. 3132, due to its small size, the Young modulus is reduced due to the preparation induced damage (E = 200MPa) with respect to the one of the undisturbed material.

Hydro-mechanical parameters

If the sample is firstly de-saturated, the drying does not induce any visible damage around the discontinuity, at least for the duration of the considered experimental test. Then, the hydration generates a well-defined damaged area around the fracture.

Through the power law in Figure 2.31b, it is possible to compute the thickness of the damaged sides during hydration (h = 122μm). The same mechanical and hydraulic parameters defined in Sections 2.2.4.1-2.2.4.2 are used for this numerical test.

Results

The experimental and numerical variations of the fracture opening with time are displayed in Figure 2.44a. Numerically, the aperture varies almost linearly with time. The hydration phase generates secondary cracks around the primary discontinuity that favor the hydraulic closure of the fracture: the opening $\bar{d}$ decreases very quickly at first and then more and more slowly, in line with what was discussed above in Sections 2.2.4.1-2.2.4.2. The same trend is observed numerically. The final equivalent water permeability reached (Figure 2.44b) is a few orders of magnitude higher than the permeability of the intact material.

Although the temporal evolution of the opening during drying does not follow the same behavior observed experimentally, there is a good match at the end of this phase. This aspect is confirmed by observing the displacement field in Figure 2.45 corresponding to point P1 in Figure 2.44. Afterward, almost at

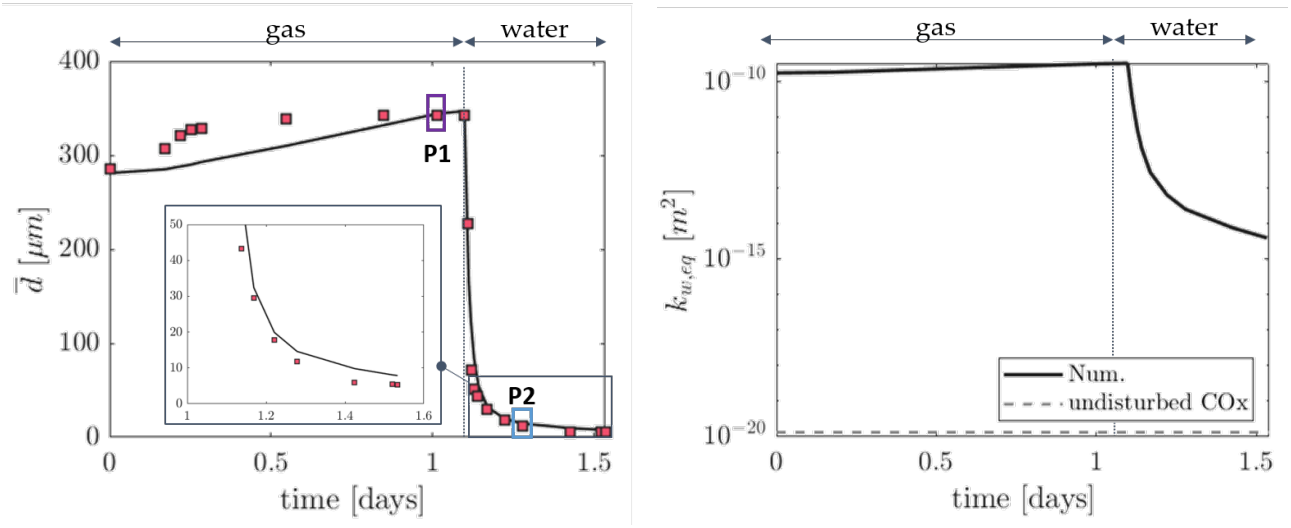

(a) (b)

Figure 2.44: Temporal evolution of the average fault opening during test 818, the experimental results refer to (Di Donna et al., 2022); (b) equivalent water permeability during test 8182

the end of the re-saturation process (point P2 in Figure 2.44), a good match between numerical and experimental displacement is observed in the whole section of the sample. The large displacements computed numerically close to the fracture (light blue zone in Figure 2.45) are related to the damage generated around it, as already observed in Figure 2.31.

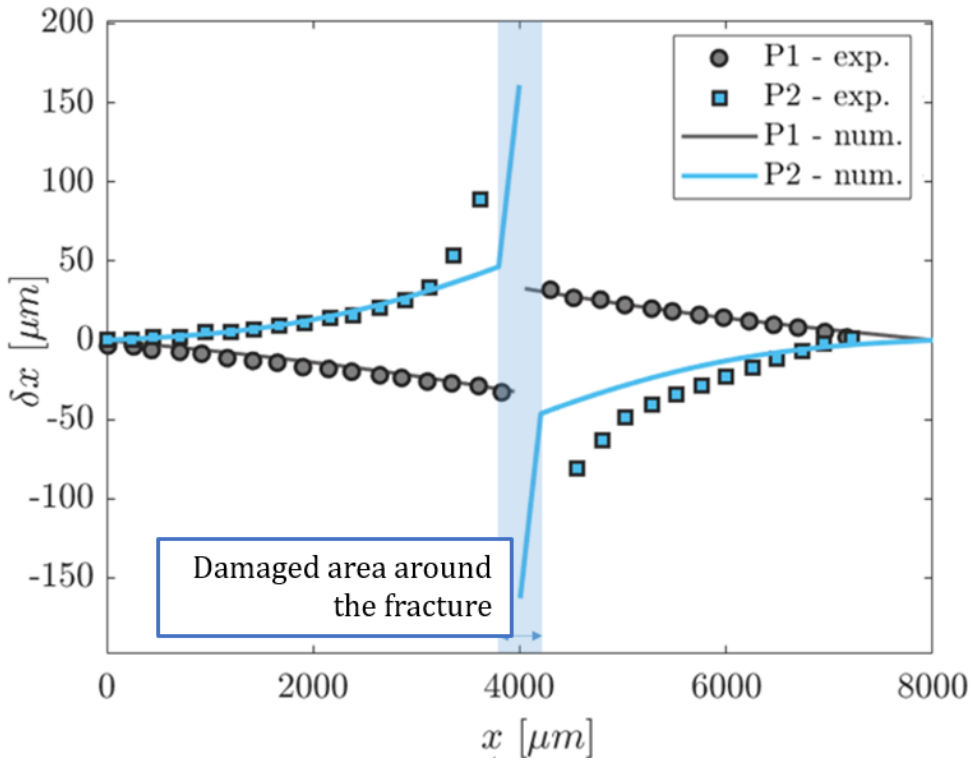

Figure 2.45: Gradient of displacements for a section in the middle of the sample and along the x-direction of dry air (point P1 in Fig. 2.44) and water (point P2 in Fig. 2.44)

2.2.5. Partial conclusions

The saturation phase generates micro-cracks around the fracture, defining a low-density and fairly compressible zone, which is even more evident the greater the initial size of the fracture. Thanks to the clay transmissivity, the water injected can permeate the clay, first involving the damaged zone and then the rest of the sample. This process is clearly demonstrated by both numerical and experimental results. However, the bigger the initial crack, the lower the recovery.

Fig. 2.46 shows the final fracture aperture d_f against the initial one d_{ini}. It is fairly straightforward to see that the model is capable of reproducing the self-sealing well for a low initial aperture d_{ini}. However, the 3132 and 8182 tests, corresponding to high initial aperture value, are more complex, as they include a vapor and gas injection phase in addition to the saturation phase with water. These phases were reproduced numerically by controlling the water pressure in the fracture and without taking into account the real nature and the chemical composition of the fluid injected, thus could explain the slight offset from the experimental results. The fracture closure dramatically reduces the water permeability, reaching values close to the intact material.

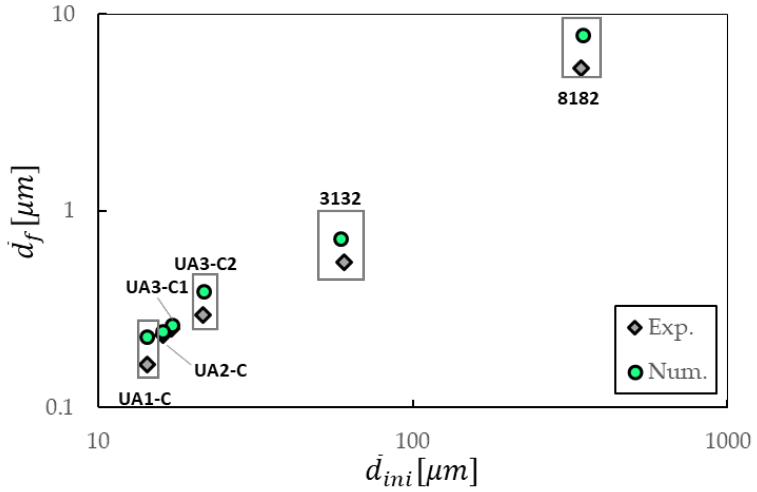

Figure 2.46: Variation of the averaged final fracture d_f *as a function of the initial value* d_{ini}

2.2.6. Introduction to the 3D model

The 2D model was then extended in 3D, as schematised in Figure 2.47 The model is validated performing firstly the same wetting tests described in Section 2.2.4.1, then, a further analysis was done in order to validate the 3D model against tests conducted by (Zhang and Talandier, 2023) on COx, where the hydraulic closure of the fracture is correlated to an imposed confining pressure.

The same hydromechanical laws defined in 2D apply for the 3D case, as well as the same sets of parameters. For the sake of simplicity, in a first moment the 3D sample is schematized as a cubic domain characterized by an equivalent cross section equal to the sample area. This simplification is necessary in order to avoid, at least initially,the introduction of complex boundary conditions that would require considerable numerical effort. In a second step, the model could be further enriched to represent *in-situ* conditions.

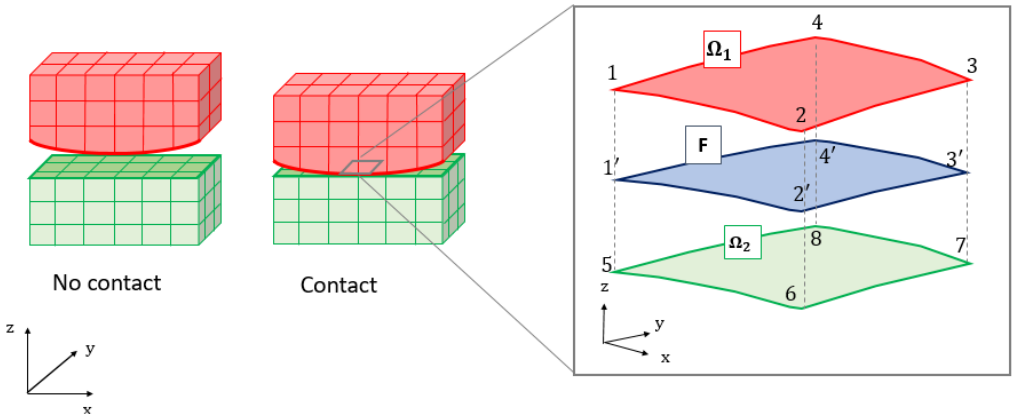

Figure 2.47: Sketch of the 3D model with the definition of the contact element

2.2.6.1. Wetting tests

The same tests defined in Section 2.2.4.1 are then conducted in 3D. As introduced before, the geometry of the sample was adapted to a simple hexaedric domain, as illustrated in Figure 2.48.

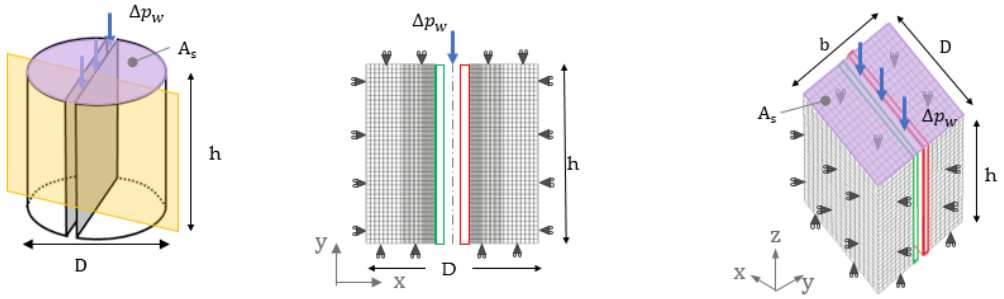

Figure 2.48: Sketch of the cylindrical sample (left) with the definition of the vertical slice represented in 2D (in yellow) and the equivalent cross section A_s (in pink) used for the 3D model; definition of the 2D model (centre) and the 3D (right)

The dimension b of the cross-section of the 3D model is defined through the relation:

$$A_s = \frac{\pi D^2}{4} = bD \tag{2.36}$$

where D is the length of the fracture, which is preserved in the 3D model.

The comparison between experimental, numerical 2D and numerical 3D results is provided in Figure 2.49 in terms of equivalent permeability. The 2D and 3D curves do not overlap perfectly but there is a small difference between them, which can be related to the different size of the cross section defined in the two models. Moreover, as the initial aperture decreases, the difference between 2D and 3D results increases. It should be reminder that the same mechanical parameters defined for the 2D model are used in 3D.

2.2.7. Wetting + hydrostatic test

To complete the validation of the model; another kind of experiments is considered. In this section we refer to test performed by (Zhang and Talandier, 2023) on COx cylindrical samples characterized by h = 100mm

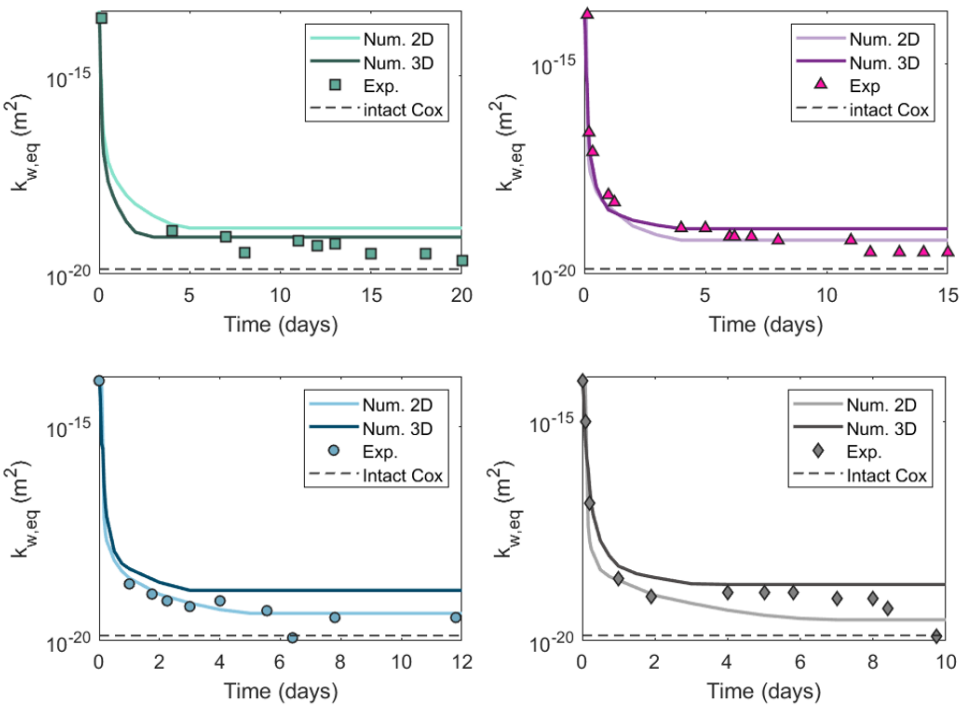

Figure 2.49: Comparison between experiments performed by (Wang et al., 2022a), 2D and 3D results for the tests: UA1C (top-left); UA2C (top-right); UA3C1 (bottom-left); UA3C2 (bottom-right)

and D = 50mm. In this case, the water injection is combined to increments of confining pressure. The main geometry and boundary conditions are defined in Figure 2.50. The step sequence of water pressure

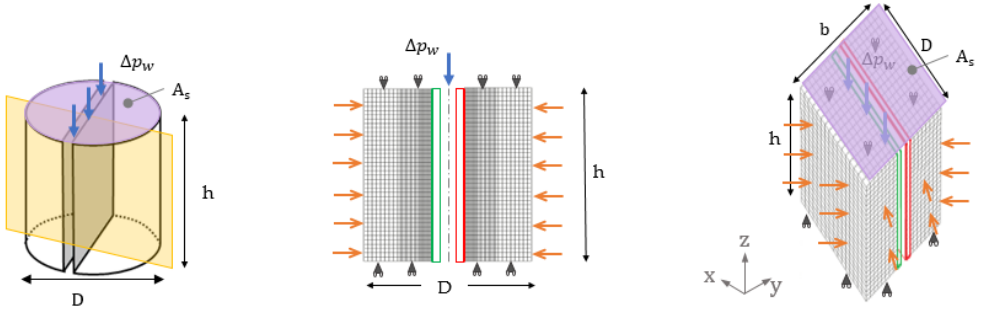

Figure 2.50: Sketch of the cylindrical sample (left) with the definition of the vertical slice represented in 2D (in yellow) and the equivalent cross section A_s (in pink) used for the 3D model; definition of the 2D model (centre) and the 3D (right)

p_w and confining pressure σ_c imposed in the test is illustrated in the figure 2.51.

Results are illustrated in Figure 2.52 in terms of temporal evolution of water permeability and variation of water permeability with the effective pressure σ_{eff}. An important reduction in permeability is initially observed numerically, but there are no experimental data at this stage. Later on, the numerical trend matches the experimental one. It can be seen that the reduction in permeability is this time strongly correlated to the increase in confining pressure, which leads to an increase in effective pressure and thus a reduction in the hydraulic opening of the fracture

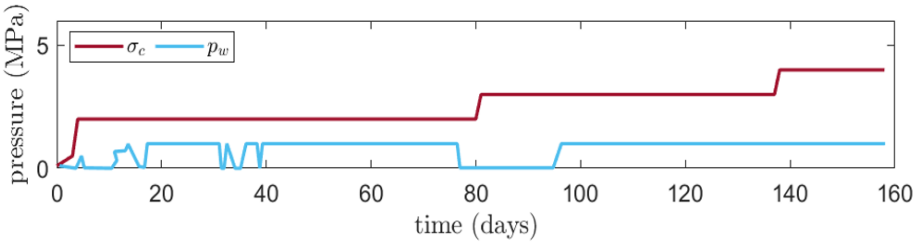

Figure 2.51: Application of water pressure p_w and confining pressure σ_c during the test performed by (Zhang and Talandier, 2023) in the UA COx sample

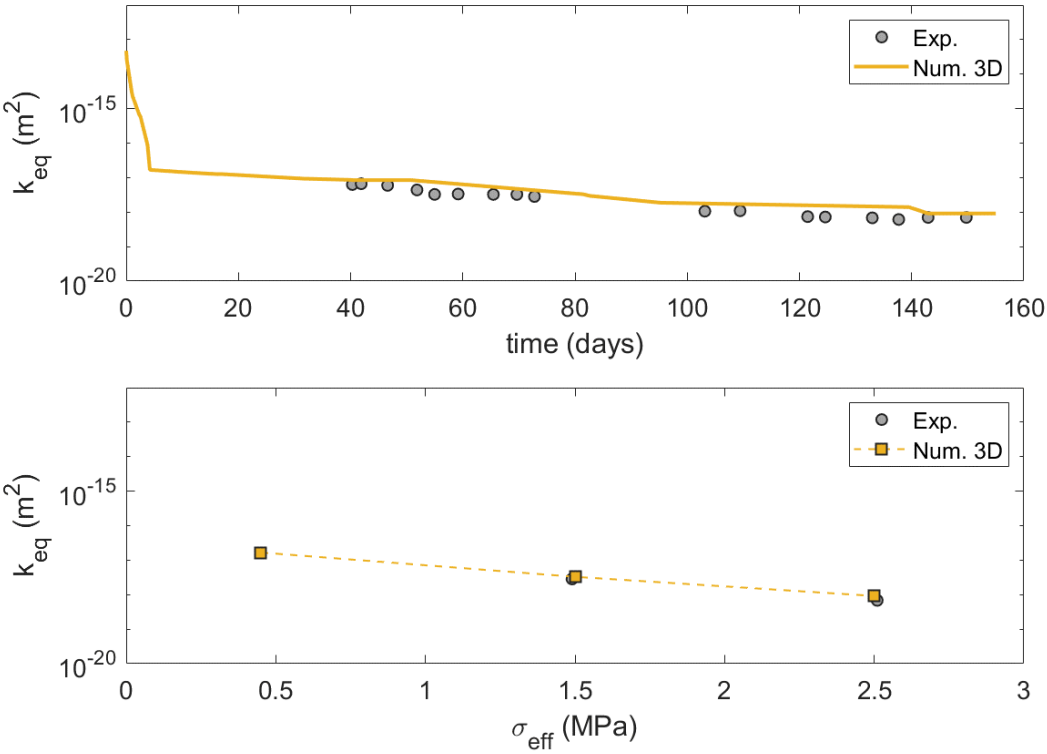

Figure 2.52: Comparison between the experimental test performed by (Zhang and Talandier, 2023) in the UA COx sample and the 3D numerical test in terms of: temporal evolution of water permeability (top); variation of water permeability with confining pressure (bottom)

2.2.8. Summary

The numerical model, together with the calibration of the mechanical and hydraulic parameters, is able to well reproduce the self-sealing of clay materials at the scale of laboratory tests in terms of fracture closure and water permeability. The latter is assumed to be related to the fracture opening through the cubic law. Both experimentally and numerically, once the fracture is saturated, the recovery takes place first quickly thanks to the swelling of clay minerals close to the fracture where some microcracks generate, defining preferential paths for the water migration, and then slowly until stabilization is reached. Here the permeability reaches a value close to the intact material. Recovery is generally successfully achieved for a small initial opening of the fracture. The recovery obtained by vapor saturation is negligible, but it is thought to be related to the short duration of the considered experiments. In this sense, it might be interesting to carry out longer tests. The drying phase leads to different results depending on whether it

follows or precedes hydration: in the first case, hydration leads to a clearly visible cracked area around the fracture which can contract during drying, favoring hydraulic opening, while in the second case, a slight opening is observed since the secondary cracks are absent or not visible at the beginning of the test and are not generated by the drying. This behavior is considered in the numerical modeling, and the results agree with the experiments. However, for the test n. 3132, the experimental results are not so well reproduced in terms of the fracture opening rate. As mentioned, this difference can be caused by the assumption in gas injection modeling. Moreover, the undisturbed material is assumed elastic, which simplifies the reality strongly. It is worth recalling that this study is focused on the self-sealing of the fracture and, thus, on the recovery of hydraulic properties during the hydration phase. The vapor and gas injection phases have been simplified since the gas pressure is kept constant to the environmental value. Moreover, additional experimental tests are necessary to further investigate the fluid exchanges during these phases. Nevertheless, horizontal displacements are uniform along the vertical direction, which is consistent with what was observed experimentally. To further validate the model, the interface constitutive equations can be employed to test other materials and ultimately to predict self-sealing at a large scale (i.e., in-situ experiments). Moreover, the model does not account for any material anisotropy, which can play an important role in self-sealing. The 3D model illustrated, although it requires further development, is of twofold interest: on the one hand, it has shown how, due to the particular symmetry conditions, the tests illustrated in this study can be represented in 2D, thus avoiding unnecessary time consumption for 3D. On the other hand, by validating the 2D and experimental results, this 3D model is proven to be a good starting point for a better representation and prediction of self-sealing at the repository scale.

2.2.9. Key learning points

New knowledge acquired

The model proposed is able to describe the self-sealing in the Callovo Oxfordian Claystone though an hydro-mechanical constitutive model based on some physical observation of the process. In particular, the model accounts the presence of a low-density and fairly compressible zone around the fracture, which is more evident the greater the initial size of the fracture. The sensitivity analysis shows that the self-sealing occurs even without considering these damaged sides, however, the process is slower and results do not match experiments properly. Moreover, the choice of integrate them into the interface elements avoid their re-meshing, with a considerable simplification of the problem. Thanks to the clay transmissivity, the water injected can permeate the clay, first involving the damaged zone and then the rest of the sample. However, the bigger the initial the crack, the lower the recovery.

The 3D model shows the effect of the confining pressure on the fracture closing (and reduction of water permeability), giving promising results for further studies.

Impact of acquired knowledge

The model is able to represent the self-sealing at the laboratory scale. A good match with experiments is obtained modeling different tests coming from different experimental campaigns by simply calibrates some parameters that should be considered as intrinsic proprieties of the materials. In this sense, it can be extended to other potential host rocks. It represent also a valid starting point for the prediction of the self-sealing at the scale of the repository.

Remaining knowledge gaps

Other host rock (e.g. the Boom Clay) can be modelled by the constitutive laws described in this study. Moreover, as already said, the 3D numerical model should be better defined. For example, it can be improved in terms of definition of the geometry of the problem and boundary conditions. It can be useful also

to represent the self sealing process around the gallery. Moreover, other aspects such as the chemistry of the water and the material anisotropy are not included in the model but can be considered for further studies.

Recommendations for the future

It would be interesting to collect all the necessary information before running numerical tests. For example, to model the self-sealing in Boom clay, it would be necessary to have access to the initial fracture opening and degree of saturation for wetting tests run in pseudo-oedometric conditions.

2.3. University of Liège (Subtask 3.3)

2.3.1. Introduction

Within the scope of Task 3 of the WP GAS, the primary objective of the work performed at the University of Liège is to contribute to conceptualise the gas transport processes taking place in the post-closure phase of a disposal system, in order to evaluate achievements by the application of modelling tools on *in situ* experiments.

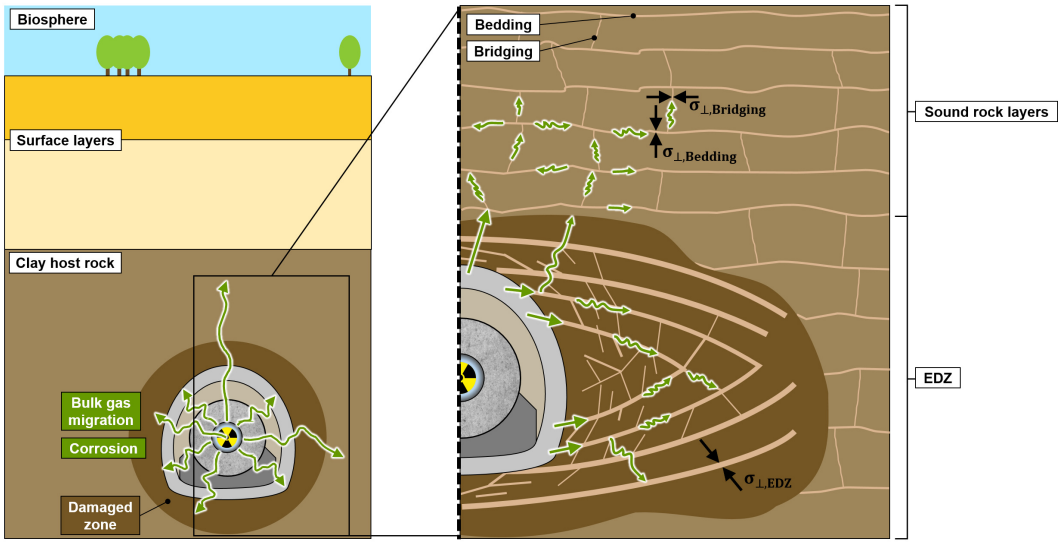

Figure 2.53: Conceptual scheme of a deep geological repository (a) focusing on the gas generation process with (b) the potential expected gas transport modes in the EDZ and the sound host rock.

These objectives have stimulated the development of novel and robust numerical models that can realistically simulate the gas transport mechanisms in low permeable clay rocks as well as the accompanied HM processes Corman (2024). Two distinct zones of the repository system have been more specifically identified in Figure 2.53, dividing the task into two sub-objectives:

- In the excavation damaged zone (EDZ), the gas migration is supposed to be governed by the hydraulic properties modification induced by the fracturation following the storage drifts excavation (Tsang et al., 2005; Armand et al., 2014). A first contribution aims thus at extending the second gradient method to two-phase flow hydro-mechanically coupled conditions in order to simultaneously capture the multi-physics interactions related to gas transfers and the development of fractures. This work is summarised in the present MS228 report, more details can be found in (Corman et al., 2022).
- In the sound clay rock, the gas migration is supposed to be governed by the rock structure at a micro-level (Harrington et al., 2012; Gonzalez-Blanco et al., 2016a). A second contribution aims thus at building a multi-scale model which captures the micro-scale effects on the macroscopic gas flow, by embedding the description of the microstructure constituents, like the pore network and the separation planes, on a representative element volume (REV) Corman et al. (2024). This work is part of Task 2, and has been summarised in MS228 report.

The simulations are carried out with the Lagamine Finite Element code, which is a non-linear finite element tool initially elaborated at the University of Liège, which has been constantly evolving with time since the

1980s (Charlier, 1987b; Habraken, 1989), supported by successive doctoral research and developments. The code has been primarily developed in two different fields namely the behaviour of metals and geomechanics. The latter more specifically explores multiple facets of the geomechanical environment, which requires Chemo-Thermo-Hydro-Mechanical coupled models. Accordingly, the code compiles both highly coupled constitutive laws based on elasto-plastic, elasto-visco-plastic frameworks, second gradient models (Collin et al., 2006) or on a multi-scale approach on the one hand, and coupled finite elements (Gerard et al., 2008a) (monolithic approach) dedicated to the modelling of multiphase or multiphysical problems (Collin et al., 2002b) on the other hand. This way, the Lagamine software constitutes an advanced numerical tool to tackle civil engineering problems involving soil-structure interactions (Cerfontaine et al., 2015) or soils and rocks mechanics problems, with specific applications to the modelling of nuclear waste disposal, slope stability, reservoir engineering.

2.3.2. Conceptual model

The development of a second gradient H^2M model (standing for two-phase flow hydro-mechanical model) has been stimulated in order to simultaneously capture the multi-physics couplings related to gas transfers in partially saturated clay formations and the strain localisation aspects associated with the creation of the EDZ. More specifically, this model pays special attention to the modelling of HM couplings prone to occur in the EDZ and susceptible to affect the kinetics of gas transfers.

Basic features

In the presented developments, the material is treated as a porous medium commonly considered as the superposition of several continua, relying on the mixture theory (Coussy and Ulm, 1995): an assembly of grains forming the solid matrix and voids between the grains filled by a combination of fluids (Figure 2.54). In particular, a binary fluid mixture is considered, which includes a liquid and a gaseous phase. Each of these phases corresponds to a combination of two species, namely the liquid phase is composed of liquid water and dissolved Hydrogen while the gaseous phase is an ideal mixture of dry Hydrogen and water vapour. In the proposed formulation, it is also assumed that the mineral species and the solid phase coincide, and that solid and fluid phases are immiscible.

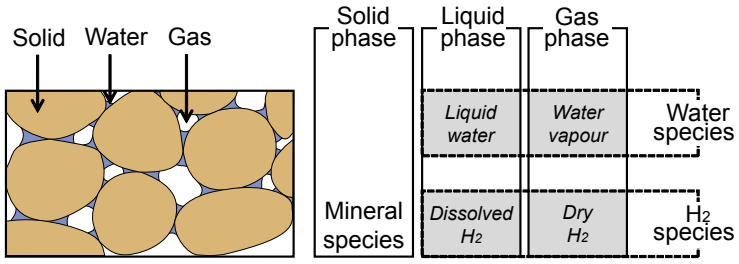

Figure 2.54: (a) Unsaturated triphasic porous medium and (b) definition of phases and species.

Taking a look at the process of underground gallery excavation, it appears that the development of macroscopic fractures is caused by by the formation and propagation of a failure plane that is in fact a zone of localised shear deformations. In particular, *in situ* observations in clay host rock for deep geological disposals attest to the development of extention and shear fractures around the galleries, leading to the creation of an Excavation Damaged Zone in the near field. From these observations, it is then necessary to provide modelling techniques capable of numerically reproducing damage as strain localisation in shear band mode. From a numerical point of view, the use of classical FE methods to predict strain localisa-

tion upon softening leads to a mathematically ill-posed boundary value problem in the post-localisation regime suffering of a dependency to the mesh size and orientation as widely reported in the literature (Pietruszczak and Mróz, 1981; De Borst and Mühlhaus, 1992; Zervos et al., 2001) and illustrated in Figure 2.55a. Instead, a regularisation techniques of second gradient type is implemented to introduce an internal length into the model in order to avoid the pathological mesh dependency, and control the shear band width no matter the mesh size, as illustrated in Figure 2.55b.

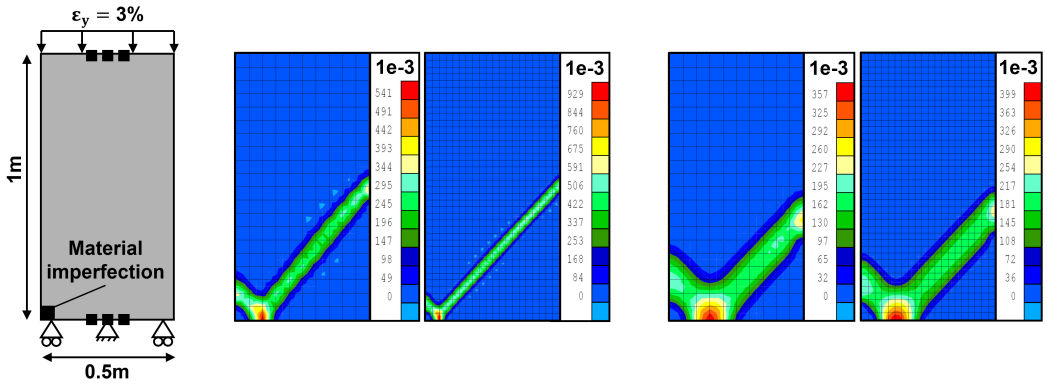

(a) Classical finite element method *(b) Regulation technique*

Figure 2.55: Modelling of a plane strain compression test with two distinct meshes of 10×20 *and* 20×40 *elements: total deviatoric strain using (a) a classical finite element method and (b) a regularisation technique of second gradient type.*

Balance equations

In the proposed developments, the local second gradient model is extended from a biphasic to a multiphasic medium (solid particles, gas and water), with a view of taking variable gas pressure into account (H^2M). Then, starting from the balance equations of the multiphasic problem in classical poromechanics, a microkinematic gradient field ν_{ij} is introduced in the framework of microstructure continuum theory in order to describe strain and rotation at the microscale, under the assumption of no relative deformation of the microstructure ($\nu_{ij} = F_{ij}$ and $\nu^*_{ij} = F^*_{ij}$). Moreover, when dealing with the second gradient theory in multiphasic context, the hypothesis of no pore fluids influence at microscale such that fluids pressure variations do not generate any microkinematic gradients generally holds (Ehlers and Volk, 1998). It means that the second gradient effects are only taken into account for the solid phase.

Consequently, the general form of the local momentum balance equation including both macro and micro quantities reads:

$$\frac{\partial \sigma_{ij}}{\partial x_j} - \underbrace{\frac{\partial^2 \Sigma_{ijk}}{\partial x_j \partial x_k}}_{\text{microstructure effects}} + \rho g_i = 0 \tag{2.37}$$

where Σ_{ijk} is the double stress dual of h^*_{ijk}, which needs an additional constitutive law introducing the internal length scale, $h^*_{ijk} = \frac{\partial \nu^*_{ij}}{\partial x_k}$ is the virtual micro second gradient. Developing the mixture homogenised density in this equation gives:

$$\rho = \rho_s(1-\phi) + \rho_w S_{r_w}\phi + \rho_g(1-S_{r_g})\phi \tag{2.38}$$

where $\phi = \frac{\Omega_v}{\Omega}$ is the porosity with Ω the current volume of a given mass of skeleton and Ω_v the corresponding porous volume, ρ_s is the solid grain density, ρ_w is the water density, ρ_g is the gas density, and S_{r_w} is the water degree of saturation.

Following the particular hypothesis that second gradient effects are only assumed for the solid phase (Ehlers and Volk, 1998), the water mass balance equation and gas mass balance equation of classical poromechanics are thus conserved and respectively read for a unit porous medium ($\Omega = 1$):

$$\underbrace{\frac{\partial f_{w,i}}{\partial x_i} + \dot{M}_w}_{\text{Liquid water}} + \underbrace{\frac{\partial f_{v,i}}{\partial x_i} + \dot{M}_v}_{\text{Water vapour}} - Q_w = 0 \tag{2.39}$$

$$\underbrace{\frac{\partial f_{g,i}}{\partial x_i} + \dot{M}_g}_{\text{Dry gas}} + \underbrace{\frac{\partial f_{dg,i}}{\partial x_i} + \dot{M}_{dg}}_{\text{Dissolved gas}} - Q_g = 0 \tag{2.40}$$

where $f_{w,i}$ and $f_{v,i}$ are the mass flows of liquid water and water vapour, $f_{g,i}$ and $f_{dg,i}$ are the mass flows of dry gas and dissolved gas, Q_w is the water source/sink term, Q_g is the gas source/sink term, M_w and M_v are the masses of liquid water and water vapour respectively, and M_g and M_{dg} are the masses of dry gas and dissolved gas respectively. The fluid masses inside a porous material volume Ω are respectively equal to:

$$M_w = \rho_w \phi S_{r_w} \Omega \quad \text{and} \quad M_v = \rho_v \phi (1 - S_{r_w}) \Omega \tag{2.41}$$

$$M_{H_2} = \rho_g \phi (1 - S_{r_w}) \Omega \quad \text{and} \quad M_{dg} = \rho_{dg} \phi S_{r_w} \Omega \tag{2.42}$$

Solid and fluids phases behaviour

The fluid mass balance equations (2.39) and (2.40) involve mass fluxes of water and gas which must be related to the main variables fields of the hydromechanical problem. The description of these different fluid flows is introduced by means of a two-phase flow transfer model.

The mass flows in both liquid and gas phases are a combination of advective and non-advective fluxes, that is to say the advection of each phase (phase movement), and the diffusion of the components within each phase (motion of species within phases). The different mass fluxes of liquid water, water vapour, dry gas and dissolved gas are respectively expressed as:

$$f_{w,i} = \rho_w q_{l,i} \tag{2.43}$$

$$f_{v,i} = \rho_v q_{g,i} + i_{v,i} \tag{2.44}$$

$$f_{g,i} = \rho_g q_{g,i} + i_{g,i} \tag{2.45}$$

$$f_{dg,i} = \rho_{dg} q_{l,i} + i_{dg,i} \tag{2.46}$$

where ρ_w, ρ_v, ρ_g and ρ_{dg} are the densities of liquid water, water vapour, dry gas and dissolved gas respectively, $q_{l,i}$ and $q_{g,i}$ are the advective fluxes respectively of the liquid and the gaseous phases, $i_{v,i}$, $i_{g,i}$ and $i_{dg,i}$ are the diffusive fluxes respectively for the water vapour, the dry gas, and the dissolved gas.

The advection of both liquid and gas phases is described by the generalisation of Darcy's law (Darcy, 1856) to unsaturated cases, which reads:

$$q_{l,i} = q_{w,i} = -\frac{k_w}{\mu_w}\left(\frac{\partial p_w}{\partial x_j} + \rho_w g_j\right) \tag{2.47}$$

$$q_{g,i} = -\frac{k_g}{\mu_g}\left(\frac{\partial p_g}{\partial x_j} + \rho_g g_j\right) \tag{2.48}$$

where k_w and k_g are the water and gas permeabilities of the partially saturated medium, commonly formulated as $k_w = k_{ij}^{int} k_{r_w}(S_{r_w})$ and $k_g = k_{ij}^{int} k_{r_g}(S_{r_w})$ respectively, and μ_w and μ_g are the dynamic viscosities

of liquid water and an *ideal mixture* of dry air and water vapour respectively, the latter being dependent on the dynamic viscosity of each component of the mixture as (Pollock, 1986):

$$\mu_g = \frac{1}{\frac{\rho_g}{\rho_g \mu_g} + \frac{\rho_v}{\rho_g \mu_v}} \tag{2.49}$$

where μ_g and μ_v are the dry gas and water vapour dynamic viscosities.

The diffusion of the components within each phase is governed by Fick's law (Fick, 1855), which reads:

$$i_{v,i} = -D^*_{v/g} \rho_g \frac{\partial}{\partial x_i}\left(\frac{\rho_v}{\rho_g}\right) = -i_{g,i} \tag{2.50}$$

$$i_{dg,i} = -D^*_{dg/w} \rho_w \frac{\partial}{\partial x_i}\left(\frac{\rho_{dg}}{\rho_w}\right) \tag{2.51}$$

where $D^*_{v/g}$ and $D^*_{dg/w}$ are the effective diffusion coefficients respectively in the gaseous mixture (dry gas - water vapour) and for the dissolved gas in liquid water, which are directly related to the porous volume of the material, its structure and its water content and can be decomposed as (Philip and de Vries, 1957):

$$D^*_{v/g} = \phi(1 - S_{r_w})\bar{\tau} D_{v/g} \tag{2.52}$$

$$D^*_{dg/w} = \phi S_{r_w} \bar{\tau} D_{dg/w} \tag{2.53}$$

where ϕ is the porosity, S_{r_w} and $(1 - S_{r_w})$ are the liquid and gas degrees of saturation respectively, with the product $\phi(1 - S_{r_w})$ stipulating that vapour diffusion takes place through the gas phase of the porous medium for a contribution of the total porosity to the vapour diffusion, and $\bar{\tau}$ is the tortuosity of the porous medium.

The fluid phase behaviour is characterised by compressible fluids which implies variation of liquid density. The isotropic compressibility of water is assumed to respect the following relationship (Lewis and Schrefler, 1998), which predicts an increase in water density as a function of water pressure:

$$\frac{\dot{\rho}_w}{\rho_w} = \frac{\dot{p}_w}{\chi_w} \tag{2.54}$$

where χ_w is the water compressibility.

This equation can be linearised to be implemented in a finite element code, thus expressing the liquid water density ρ_w in isothermal conditions as a function of the pore water pressure p_w according to:

$$\rho_w = \rho_{w,0}\left(1 + \frac{p_w - p_{w,0}}{\chi_w}\right) \tag{2.55}$$

where $\rho_{w,0}$ and $p_{w,0}$ are the initial values of water density and pore water pressure.

For the gaseous mixture of dry gas and water vapour, the ideal gas law is assumed (Clapeyron's equation (Clapeyron, 1834) and Dalton's law (Dalton, 1802)). The classical state equation of ideal gas applied to the considered gas mixture is used to write the gas densities as:

$$\rho_g = \rho_\alpha + \rho_v \quad \text{and} \quad p_g = p_\alpha + p_v \tag{2.56}$$

where p_α and p_v are the partial pressures of the gas species α and water vapour respectively, and ρ_α and ρ_v are the densities of the gas species α and water vapour which respectively reads:

$$\rho_\alpha = \frac{m_\alpha}{RT} p_\alpha \quad \text{and} \quad \rho_v = \frac{m_v}{RT} p_v \tag{2.57}$$

where R is the universal gas constant (= 8.3143 $J/mol \cdot K$), T is the absolute temperature in Kelvin, and m_α and m_v are the molar masses of the dry gas species α and the water vapour.

Advanced hydro-mechanical couplings

Advanced hydro-mechanical couplings are added to the second gradient hydro-mechanical model in partial saturation, in order to reproduce the preferential propagation of gas within the excavation damage zone. The primary motivation behind these developments arises from experimental evidences that gas transport is mainly governed by the hydraulic properties modifications induced by fracturation (Tsang et al., 2005; Armand et al., 2014). Knowing that the flow transfer properties are not homogeneous in the fractured zone, the basic idea consists in enriching the model with appropriate hydro-mechanical couplings that are established from a dependence with the deformations and are able to cause intense changes in the transfer properties inside the shear bands. More specifically, multiphysical interactions between pathways aperture and hydraulic properties, namely the permeability and the gas entry pressure are introduced.

On the one hand, the impact of fracturing on the flow transfer characteristics is captured by a strain-dependent isotropic evolution of the hydraulic permeability tensor based on a power (cubic) formulation (Pardoen, 2015):

$$k_{w,ij} = k_{w,ij,0}\left(1 + \beta_{per}\langle YI - YI^{thr}\rangle \hat{\varepsilon}^{3}_{eq}\right) \tag{2.58}$$

where $k_{w,ij,0}$ is the initial intrinsic water permeability tensor, β_{per} is an evolution parameter, $\langle\rangle$ are the Macaulay brackets, $\hat{\varepsilon}^{p}_{eq}$ is taken as the Von Mises' equivalent deviatoric plastic strain to consider the plastic deformation in the permeability evolution, which rate form reads:

$$\dot{\hat{\varepsilon}}^{p}_{eq} = \sqrt{\frac{2}{3}\dot{\hat{\varepsilon}}^{p}_{ij}\dot{\hat{\varepsilon}}^{p}_{ij}} \tag{2.59}$$

where $\dot{\hat{\varepsilon}}^{p}_{eq}$ is the deviatoric part of the plastic strain rate tensor:

$$\dot{\hat{\varepsilon}}^{p}_{ij} = \dot{\varepsilon}^{p}_{ij} - \frac{\dot{\varepsilon}^{p}_{kk}}{3}\delta_{ij} \tag{2.60}$$

and YI and YI^{thr} are respectively the yield index and a threshold value below which the intrinsic permeability variation is not considered. The yield index is defined as the reduced second deviatoric stress invariant:

$$YI = \frac{II_{\hat{\sigma}'}}{II^{p}_{\hat{\sigma}'}} \tag{2.61}$$

with $YI < 1$ if the current state of the material is elastic and $YI = 1$ if it is plastic (on the yield surface). In addition, it is to mention that fracture closure or material sealing/healing under elastic unloading, leading to permeability decrease in the fracture zone is not treated in the present work. permeability increases are thus assumed irreversible, which is implemented by keeping only the maximal estimation of permeability between the current and the last computed values, for every iterative step of the FE resolution process.

On the other hand, the second enhanced HM coupling that is introduced in the model deals with evolution of the water retention curve with strains and reproduces the effect of the modification of the pore network morphology on the water retention of the material (Olivella and Alonso, 2008b). Practically, the evolution of the parameter P_r, standing for the gas entry value in van Genuchten's model is correlated to the permeability evolution, and so to the deformations:

$$P_r = P_{r,0}\frac{\sqrt[3]{k_{ij,0}}}{\sqrt[3]{k_{ij}}} \tag{2.62}$$

where P_r is the van Genuchten's parameter for the current gas entry pressure, $P_{r,0}$ is the van Genuchten's parameter for the initial value of gas entry pressure, k_{ij} is the current permeability, $k_{ij,0}$ is the initial permeability.

This expression of the gas entry pressure is then integrated in the retention curve formulation. It follows that the minimal capillary force needed to desaturate the material pores is lowered by the damage process, leading to an amplification of the desaturation of the medium for a given capillary pressure.

2.3.3. Modelling small-scale MEGAS experiment

The numerical model is first applied to two field-scale gas injection experiments are carried out. The gas injection testing in question are the set of E4 and E5 experiments, conducted in Boom Clay using Helium, as part of the MEGAS EC project. This experimental design is translated into a numerical model which requires several ingredients that are listed below.

2.3.3.1. Modelling design

Geometries

The geometry of the E4 experiment corresponds to a 60 mm diameter piezometer that is numerically replicated for a specific cross-section located at the level of the injection filter No.6 using a 2D plane strain hydro-mechanical model, as sketched in Figure 2.56a. Similarly, the geometry of the E5 experiment corresponds to a 89 mm diameter piezometer that is numerically replicated for a specific cross-section located at the level of the injection filter No.9[6] using a 2D plane strain hydro-mechanical model. Infinitely rigid contact elements are employed to reproduce the casing of the piezometers, having a radius of respectively 0.03 m and 0.0445 m in the E4 and E5 configurations. A schematic representation of the numerical models involving the mesh and the different boundary conditions is illustrated in Figure 2.56.

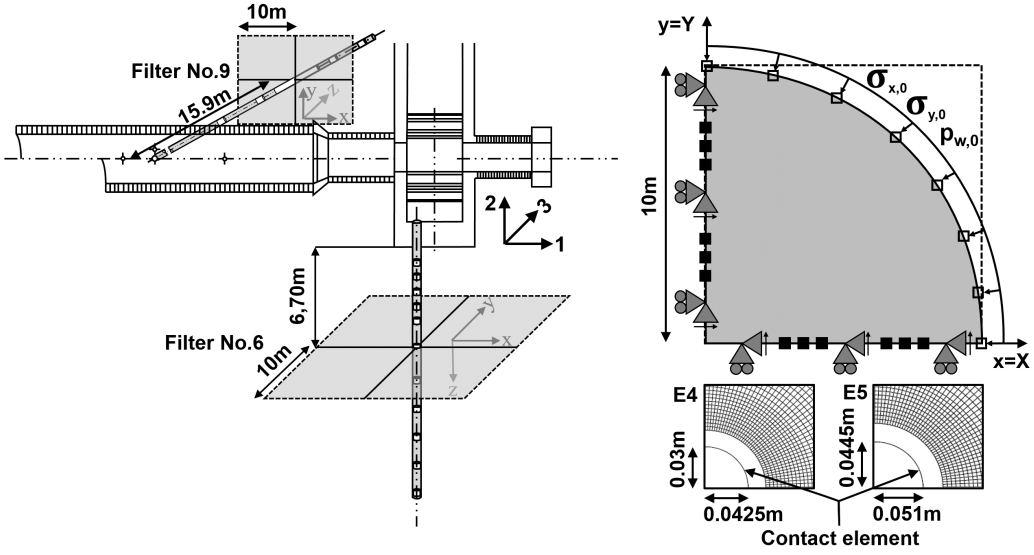

(a) (b)

Figure 2.56: (a) Location of the studied cross-sections in the E4 and E5 configurations. (b) Geometry and boundary conditions of the 2D plane strain models with a zoom on the refined zone of the mesh.

Initial conditions

At the level of the URL, the Boom Clay is assumed to be saturated and the total vertical stress and pore water pressure are respectively 4.5 MPa and 2.2 MPa, defining a vertical effective stress of 2.3 MPa (Bernier et al., 2007b). The Boom Clay presents an *in situ* stresses anisotropy, with an earth pressure coefficient at rest K_0 ranging from 0.8 to 1, and is also characterised by complex phenomena such as hardening/softening processes, and a strong anisotropy of the mechanical properties induced by the clay structure which displays horizontal bedding planes with alternating clay and silt layers.

[6] At about 15.70 m away from the main tunnel of the URL.

Considering a study section at the level of the injection filters No.6 (E4) and No.9 (E5) respectively, the initial conditions in the Boom Clay for the respective orientations of the piezometers are defined as:

$$\text{E4: } \sigma'_{x,0} = \sigma'_1 = 1.84 \text{ MPa}, \quad \sigma'_{y,0} = \sigma'_3 = 1.84 \text{ MPa}, \quad \sigma'_{z,0} = \sigma'_2 = 2.3 \text{ MPa}, \quad p_{w,0} = 2.2 \text{ MPa} \tag{2.63}$$

$$\text{E5: } \sigma'_{x,0} = \sigma'_1 = 1.84 \text{ MPa}, \quad \sigma'_{y,0} = \sigma'_2 = 2.3 \text{ MPa}, \quad \sigma'_{z,0} = \sigma'_3 = 1.84 \text{ MPa}, \quad p_{w,0} = 2.2 \text{ MPa} \tag{2.64}$$

where $\sigma'_{x,0}$, $\sigma'_{y,0}$, and $\sigma'_{z,0}$ are respectively the horizontal, vertical and out-of-plane (initial) effective stresses in the local coordinate system, and $p_{w,0}$ is the initial pore water pressure. In this configuration, the coefficient of earth pressure at rest K_0 takes a value of 0.8. In addition, the initial gas pressure is set to the atmospheric pressure of $p_{g,0} = 101325$ Pa, while the temperature is maintained constant at $T_0 = 20°C$ throughout the simulations.

Boundary conditions evolution

The drilling of the piezometer boreholes is performed with the convergence-confinement method which is an approximation method for tunnelling that allows transforming a whole 3D study of tunnel excavation into a 2D analysis in plane strain state, based on an identical gallery convergence assumption (Bernaud and Rousset, 1992). The effect of the excavation front progress is taken into account by applying a fictive pressure σ_r^Γ on the borehole wall that depends on the vicinity of the excavation front to the studied borehole section through a deconfinement rate ζ (Figure 2.57a):

$$\sigma_r^\Gamma = (1 - \zeta)\sigma_{r,0} \tag{2.65}$$

where σ_r^Γ is the total radial stress, $\sigma_{r,0}$ is the initial mechanical pressure on the borehole wall that corresponds to the initial stress in the material, and ζ is the deconfinement rate ranging from 0 to 1.

In the present work, a rate of 1 m/h is considered for both E4 and E5 *in situ* experiments, implying that the excavation front crosses the studied section after $\sim$ 6h42min and $\sim$ 10h36min, and that the excavation is fully completed after $\sim$ 6h48min and $\sim$ 10h42min in the E4 and E5 configurations respectively. The evolution of the deconfinement rates with time are detailed in Figure 2.57b, top and bottom, for E4 and E5 separately.

The pore water pressure at the borehole wall p_w^Γ is also affected during the excavation phase and starts to decrease quickly and linearly from its initial value towards the atmospheric pressure when the deconfinement starts. A pore water pressure rate ζ_w can thus be defined in the same manner as for the total radial stress:

$$p_w^\Gamma = (1 - \zeta_w)p_{w,0} \tag{2.66}$$

where p_w^Γ is the pore water pressure at gallery wall, $p_{w,0}$ is the initial water pressure on the borehole wall, and ζ_w is the deconfinement rate ranging from 0 to 1.

In addition, this stress imposition is also conditioned by the support of the borehole, namely the casing of the piezometer itself. Practically, the borehole wall is supposed to stop converging once the contact with the support, namely the steel casing of the inserted piezometer (modelled by an interface element and assumed to be in infinitely rigid) is reached. This first step is simulated during 24 hours.

After the excavation of the borehole, and the convergence of the circumferential wall to the casing of the piezometer, the system is supposed to be impervious. From this time, a period of pore water pressures stabilisation initiates since there is no more drainage of these water pressure through the excavated profile. It is numerically simulated by considering an impervious inner wall of the borehole as updated boundary condition. This second phase ranges from 1 day to 1 year.

After the excavation of the borehole and a one-year phase of water pressure re-establishment, a last phase of gas migration is considered. It is simulated by imposing a variation of the gas pressures at the interface

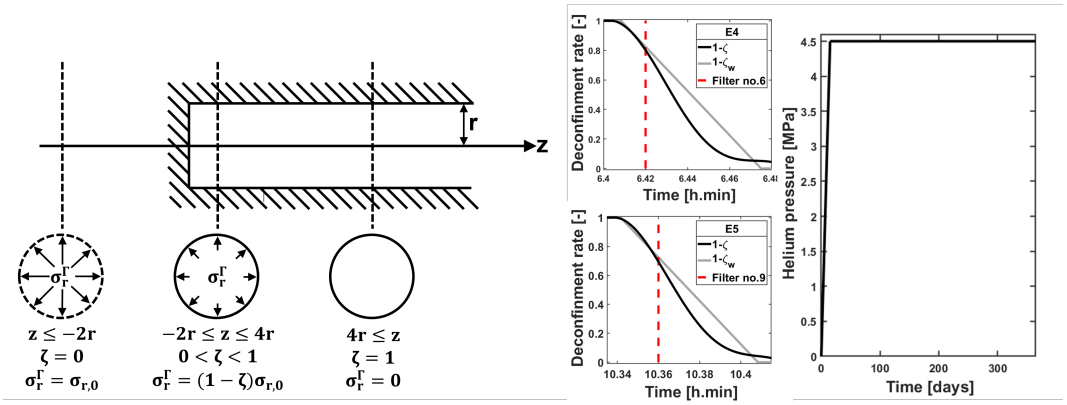

(a) (b) (c)

Figure 2.57: (a) Theory of deconfinement rate during tunnel excavation. (b) Applied deconfinement curves for the total radial stress and for the pore water pressure during E4 and E5 boreholes excavation. (c) Profile of gas pressures during Helium injection.

between the outer face of the E4 (or E5) piezometer and the rock according to the profile given in Figure 2.57c, while keeping the rest of the boundary conditions similar to those imposed during the previous phase. In practise, gas starts to be injected in the system in the form of Helium pressure change, starting from the atmospheric pressure at 0.101325 MPa to a peak of gas pressure at around 4.5 MPa. This last step is simulated for one additional year, during which the pressure ramp is imposed for one hour and then the maximum pressure is maintained constant for the rest of the year.

Mechanical model

An elasto-plastic internal friction model with cross-anisotropy and horizontal isotropic bedding planes is considered for the mechanical behaviour of the Boom Clay, which can be decomposed into an elastic and a plastic components.

The linear elastic behaviour of the rock is based on the classical Hooke's law, where the elastic compliance tensor is expressed as a function of only two parameters (ν and E or G and K) for an isotropic material which is the case in the E4 orientation. However, the Boom Clay is also characterised by a strong anisotropy of its mechanical properties between the directions parallel and perpendicular to the bedding planes as it is the case of the E5 orientation. Switching to such a configuration increases the total number of required parameters to five for a cross-anisotropic materials, such as the Boom Clay formation (Chen et al., 2011).

The elasto-plastic behaviour of the Boom Clay is characterised by an internal friction model with a non-associated plasticity and a Van Eekelen yield surface (Van Eekelen, 1980) (under soil mechanics convention with positive compressive stress). Furthermore, the model allows isotropic hardening or softening of the cohesion and of the friction angles upon loading. Further details about the elasto-plastic model are available in (Pardoen, 2015). The elasto-plastic geomechanical parameters used in the mechanical law of the Boom Clay for the E4 and E5 modelling are taken from (Ortiz et al., 1997; François, 2014) and reported in Tables 2.11 and 2.12 respectively.

Second gradient mechanical model

In the context of microstructure media, the second gradient mechanical model gives an additional constitutive stress-strain relation between the kinematics and the stress at microscale. Based on reference works (Mindlin, 1965), it is an isotropic linear elastic law which relates the double stress to the rate of micro second gradient, and depends on one constitutive elastic parameter D in its simplified version proposed by (Matsushima et al., 2002). This elastic modulus symbolises the physical microstructure of the material and is directly related to the internal length scale introduced to regularise the problem and which is suitable for shear band width (Chambon et al., 1998).

The value of this modulus has been selected on the basis of the results of specific numerical modelling of biaxial compression tests, and reported in Tables 2.11 and 2.12.

Hydraulic model

The hydraulic model used for the Boom Clay is based on the water-gas seepage and water diffusion constitutive law for partially saturated porous media. The transfer of the liquid phase (water and gas) by advection is thus defined by the generalised Darcy's law introduced in Equations (2.47) and (2.48).

Note that in the present simulations, the hydraulic permeabilities are isotropic in the horizontal plane considered for the E4 experiment, while there exists a ratio of about 2 between the components of the intrinsic permeability in the direction parallel and perpendicular to the bedding planes in the vertical plane defined for the E5 experiment, *i.e.* $k_{w\parallel}/k_{w\perp} = 2$.

The material retention behaviour is represented by a retention curve of van Genuchten's type (van Genuchten, 1980) , linking the capillary pressure to the degree of water saturation (Figure 2.58b):

$$S_{r_w} = S_{r_w,res} + (S_{r,max} - S_{r_w,res}) \left(1 + \left(\frac{s}{P_r}\right)^{\mathcal{N}}\right)^{\frac{1}{\mathcal{N}}-1} \tag{2.67}$$

where $P_r = 12.5$ MPa is the parameter of gas entry pressure taken as a mean value between those proposed in (Prime et al., 2016; Gonzalez-Blanco et al., 2016a), $S_{r,max} = 1$ and $S_{r_w,res} = 0.2$ are the maximum and residual degrees of water saturation, s is the suction, and $\mathcal{N} = \frac{1}{1-\mathcal{F}} = 2.5$ is a model parameter, fitted to obtain a good agreement with the experimental data in Figure 2.58b.

Moreover, the Mualem - van Genuchten's model (Mualem, 1976) is used to express the water relative permeability, while the cubic law is adopted to describe the gas relative permeability:

$$k_{r_w} = \sqrt{S_{r_w}} \left(1 - \left(1 - S_{r_w}^{\frac{1}{\mathcal{M}}}\right)^{\mathcal{M}}\right)^2 \quad \text{and} \quad k_{r_g} = (1 - S_e)^{\mathcal{L}} \tag{2.68}$$

where $S_e = \frac{S_{r_w} - S_{r_w,res}}{1 - S_{r_w,res} - S_{r_g,res}}$, with S_{r_w} the degree of water saturation, $S_{r_w,res}$ the residual degree of water saturation, $S_{r_g,res}$ the residual degree of gas saturation, and $\mathcal{M} = 1.1$ and $\mathcal{L} = 3$ are model parameters, is a model parameter, fitted to obtain a good agreement with the experimental data in Figure 2.58a.

All the parameters governing the hydraulic behaviour of Boom Clay are collected from the literature (Ortiz et al., 1997; Prime et al., 2016; Gonzalez-Blanco et al., 2016a), and summarized in Table 2.11 and Table 2.12, for the E4 and E5 configurations respectively. More specifically, the value of the parameter β_{per} which controls the permeability evolution is established from the results of the numerical modelling of biaxial compression tests, in such a way as to obtain a variation of only one order of magnitude of the value of the permeability.

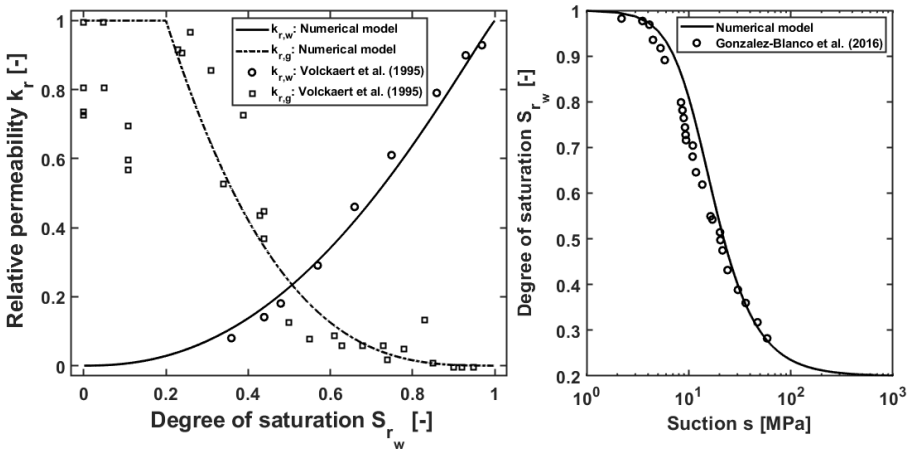

(a) *(b)*

Figure 2.58: Hydraulic model for E4 and E5 numerical simulations: (a) experimental data for relative permeability in Boom Clay (Volckaert et al., 1995a) together with model fitting, (b) experimental data for water retention curve in Boom Clay, (Gonzalez-Blanco et al., 2016a) and van Genuchten's numerical fitting.

Interface model

Two-dimensional interface elements having their own mechanical and flow constitutive laws are employed to model the rigid supports of the E4 and E5 boreholes.

The mechanical contact behaviour of the interface elements can be established based on the Coulomb's yield criterion. Since the two sides of the interface never match perfectly, the global behaviour of this zone is characterised by a normal contact constraint and a tangential contact constraint. Given that the regularisation of the contact condition is mathematically enforced via a penalty method, a linear elastic relation is assumed between the variations of stresses and gap function, which yields:

$$\begin{bmatrix} \dot{p}_N \\ \dot{\tau}_T \end{bmatrix} = \begin{bmatrix} K_N & 0 \\ 0 & K_T \end{bmatrix} \begin{bmatrix} \dot{g}_N \\ \dot{g}_T \end{bmatrix} \tag{2.69}$$

where the normal contact constraint p_N is the component related to the interpenetration of the two bodies in the contact zone, and the tangential contact constraint τ_T describes the shear behaviour of the interface.

In case of sticking, there is no relative tangential displacement of the two faces of the contact zone in the plane of the interface, developing a non-zero shear stress. In case of sliding, a relative tangential displacement occurs and the shear stress is limited by a Coulomb's criterion:

$$\tau_{max} = \mu p'_N \tag{2.70}$$

where μ is the Coulomb's friction coefficient.

To fully characterize the hydro-mechanical behaviour of the contact elements, fluid flows through ($f_{w,N}$) and along ($f_{w,L}$) the interface are also considered since these zones constitute a preferential path for the groundwater. The transversal fluid flow includes flows from the surrounding rock mass to the inside of the interface and a second one from the inside to the foundation, while the longitudinal flow is given by the well-known Darcy's equation:

$$f_{w,N} = \rho_w \, T_w \, \Delta p_w \quad \text{and} \quad f_{w,L} = -\rho_w \, \frac{k_l}{\mu_w} \, \nabla p_w \, + \, \rho_w g \nabla z \tag{2.71}$$

where T_w is the transmissivity. Pratically, the longitudinal and transverse transmissivities are set to zero in order to symbolise the impervious feature of the casing.

Further details about the contact element are available in (Cerfontaine et al., 2015). All the parameters of the contact laws are reported in Table 2.11 and Table 2.12 for the E4 and E5 configurations respectively.

Table 2.11: Set of Boom Clay parameters used in the E4 configuration. .

	Parameter	Symbol	Value	Unit
Geomechanical	Young's elastic modulus	E	300	[MPa]
	Poisson's ratio	ν	0.125	[–]
	Shear modulus	G	133	[MPa]
	Initial cohesion	c_i	300	[kPa]
	Final cohesion	c_f	100	[kPa]
	Cohesion softening parameter	B_c	0.01	[–]
	Initial friction angle	φ_i	5	[°]
	Final friction angle	φ_f	18	[°]
	Friction angle hardening parameter	B_φ	0.01	[–]
	Dilatancy angle	ψ	0	[°]
	Solid grain density	ρ_s	2650	[kg/m^3]
Microstructure	Second gradient elastic modulus	D	1.0	[kN]
Hydraulic	Initial porosity	n	0.39	[–]
	Intrinsic permeability	k	4.6×10^{-19}	[m^2]
	Water density	ρ_w	1000	[kg/m^3]
	Gas density (He)	ρ_g	0.1663	[kg/m^3]
	Water dynamic viscosity	μ_w	0.001	[Pa.s]
	Gas dynamic viscosity (He)	μ_g	2.0×10^{-6}	[Pa.s]
	Water compressibility	χ_w^{-1}	5×10^{-10}	[Pa^{-1}]
	Henry coefficient (He)	H_i	0.0091	[–]
	Gas entry pressure (1st coeff. of S_{r_w})	P_r	12.5	[MPa]
	Parameter (2nd coeff. of S_{r_w})	$\mathcal{N}$	2.5	[–]
	Parameter (1st coeff. of k_{r_w})	$\mathcal{M}$	1.1	[–]
	Parameter (1st coeff. of k_{r_g})	$\mathcal{K}$	3	[–]
	Max. degree of water saturation	$S_{r,max}$	1	[–]
	Residual degree of water saturation	$S_{r_w,res}$	0.2	[–]
	Evolution parameter	β_{per}	1×10^4	[–]
	Tortuosity	τ	0.6	[–]
Contact	Friction coefficient	μ	0.5	[–]
	Normal penalty coefficient	K_N	5×10^9	[Pa/m]
	Tangential penalty coefficient	K_T	5×10^9	[Pa/m]
	Transmissivity	T_w	0.0	[m/Pa/s]

Table 2.12: Set of Boom Clay parameters used in the E5 configuration.

	Parameter	Symbol	Value	Unit
Geomechanical	Parallel Young's modulus	$E_{\parallel}$	400	[MPa]
	Perpendicular Young's modulus	$E_{\perp}$	200	[MPa]
	Poisson's ratio	$\nu_{\parallel\parallel}$	0.125	[−]
	Poisson's ratio	$\nu_{\parallel\perp}$	0.125	[−]
	Poisson's ratio	$\nu_{\perp\parallel}$	0.0625	[−]
	Shear modulus	$G_{\parallel\perp} = G_{\perp\parallel}$	178	[MPa]
	Shear modulus	$G_{\parallel\parallel}$	178	[MPa]
	Solid grain density	ρ_s	2650	[kg/m^3]
	Initial cohesion	c_i	255 (0°)	[kPa]
			240 (45°)	[kPa]
			330 (90°)	[kPa]
	Ratio of cohesion softening	ξ_c	3	[−]
	Cohesion softening parameter	B_c	0.01	[−]
	Cohesion softening shifting	dec_c	0	[−]
	Initial compressive friction angle	$\varphi_{c,0}$	5	[°]
	Final compressive friction angle	$\varphi_{c,f}$	18	[°]
	Friction angle hardening parameter	B_φ	0.01	[−]
	Friction angle hardening shifting	dec_φ	0	[−]
	Dilatancy angle	ψ_c	0	[°]
Microstructure	Second gradient elastic modulus	D	1.0	[kN]
Hydraulic	Initial porosity	n	0.39	[−]
	Initial parallel intrinsic permeability	$k_{w,\parallel,0}$	4×10^{-20}	[m^2]
	Initial perp. intrinsic permeability	$k_{w,\perp,0}$	1.33×10^{-20}	[m^2]
	Water density	ρ_w	1000	[kg/m^3]
	Gas density (He)	ρ_g	0.1663	[kg/m^3]
	Water dynamic viscosity	μ_w	0.001	[Pa.s]
	Gas dynamic viscosity (He)	μ_g	2.0×10^{-5}	[Pa.s]
	Water compressibility	χ_w^{-1}	5×10^{-10}	[Pa^{-1}]
	Henry coefficient (He)	H_i	0.0091	[−]
	Gas entry pressure (1st coeff. of S_{r_w})	P_r	12.5	[MPa]
	Parameter (2nd coeff. of S_{r_w})	$\mathcal{N}$	2.5	[−]
	Parameter (1st coeff. of k_{r_w})	$\mathcal{M}$	1.1	[−]
	Parameter (1st coeff. of k_{r_g})	$\mathcal{K}$	3	[−]
	Max. degree of water saturation	$S_{r,max}$	1	[−]
	Residual degree of water saturation	$S_{r_w,res}$	0.2	[−]
	Evolution parameter	β_{per}	1×10^4	[−]
	Tortuosity	τ	0.6	[−]
Contact	Friction coefficient	μ	0.5	[−]
	Normal penalty coefficient	K_N	5×10^9	[Pa/m]
	Tangential penalty coefficient	K_T	5×10^9	[Pa/m]
	Transmissivity	T_w	0.0	[m/Pa/s]

2.3.3.2. Results

The first performed simulation focuses on the development of the EDZ following the drilling process of the different boreholes. The main purpose is to characterise the extent of fractures induced by rock deconfinement during the excavation phase. These fractures are reproduced by shear banding. The creation and evolution of the fractured zone can be observed through the development of shear strain localisation. The numerical results are presented in terms of the Von Mises' equivalent deviatoric total strain (total deviatoric strain), the plastic zone, i.e. the plastic loading integration points (red squares), and the deviatoric strain increment, which represents the band activity by the end of the excavation process, in Figure 2.59.

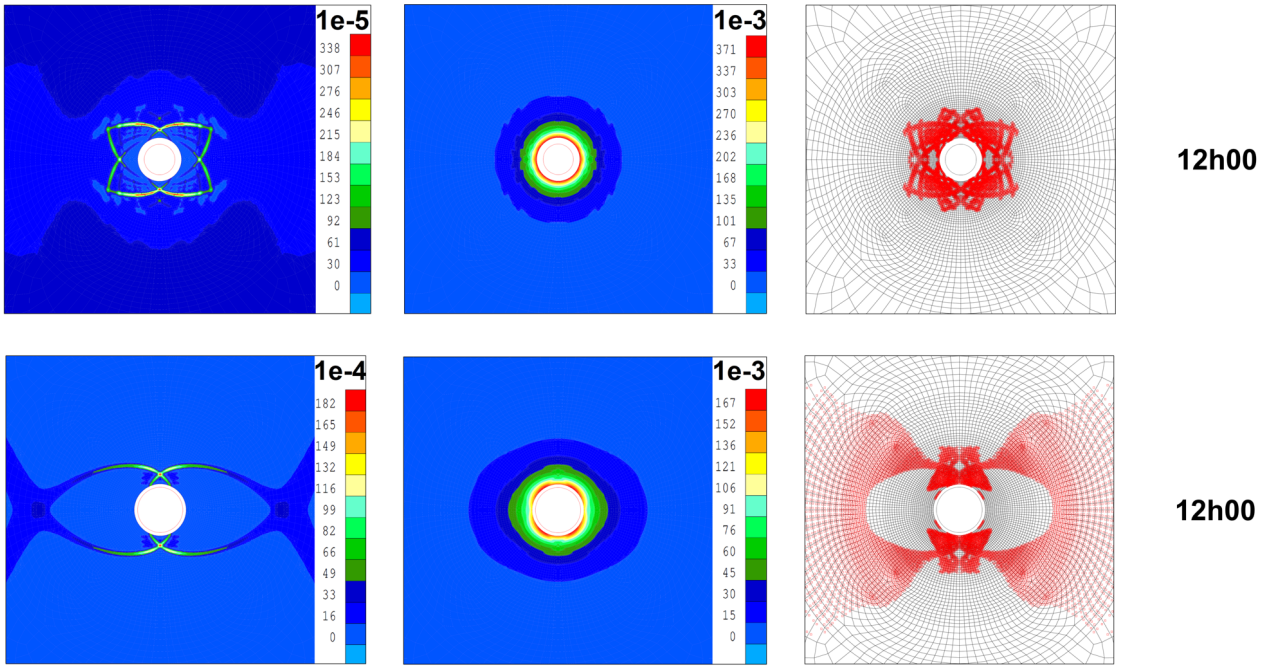

Figure 2.59: Development of shear bands at the end of the drilling process of the E4 borehole: (a) deviatoric strain increment, (b) total deviatoric strain and (c) plastic loading points.

In both cases, the modelling exhibits a symmetric shear band pattern, whose onset and shape can be attributed to the anisotropy of the material and of the initial stress state. Therefore, the shear banding zone is more concentrated all around the borehole in the E4 configuration presenting an isotropic stress state, while it develops preferentially in the direction of the minor principal stress, *i.e.* horizontal, in the E5 configuration with an anisotropic stress state. By the end of the drilling process, the plastic zone has expanded over about 0.015 m to 0.020 m in the horizontal and vertical directions. Yet, compared to the case of an unsupported excavation process, the installation of the piezometer has the consequences of limiting additional convergence of the borehole wall, thus limiting the points in plastic charge in the surrounding rock mass and inhibiting any further development of localisation.

Gas transfers in the form of Helium are simulated over the long term, according to the evolution profile given in Figure 2.57c. In Figures 2.60a and 2.60b (solid lines), gas pressure profiles are displayed along the horizontal section of the domain, highlighting the progressive propagation of Helium over a thin zone of about 1m across the rock mass. Once the maximum gas pressure of about 4.5 MPa is reached at the piezometer wall, a slight desaturation of a few percent associated to this peak of Helium pressure can be

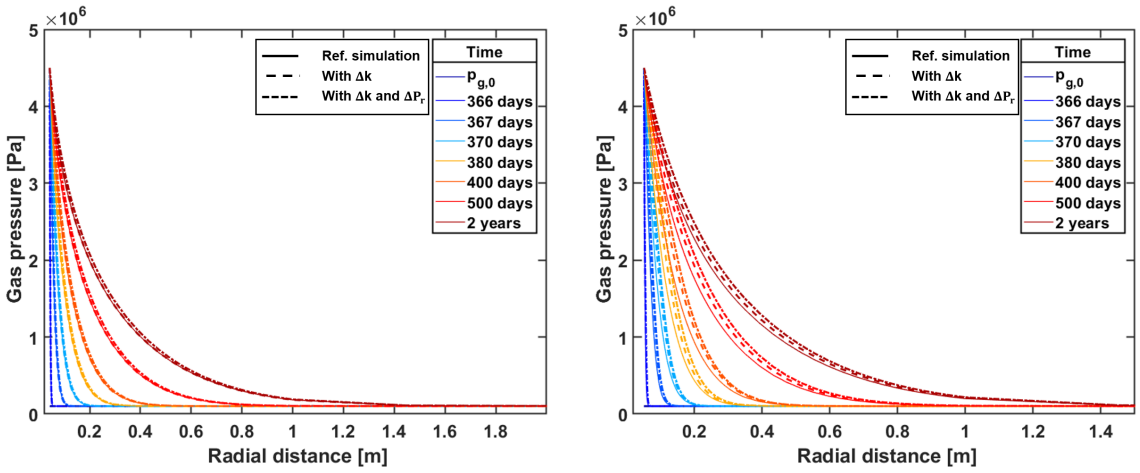

(a) E4 (b) E5

Figure 2.60: Evolution of gas (Helium) pressures as a function of the radial distance for different time steps for the (a) E4 and (b) E5 configurations: reference case (solid line), evolution of the permeability (dashed line) and of the retention curve (dash-dotted line) with strain.

observed in both configurations. These desaturation profiles can be put into perspective with the dissolved and total Hydrogen flows profiles displayed in Figures 2.63a and 2.63c respectively. Close to the injection zone, it appears that dissolved gas in the water phase is not sufficient enough to ensure transfers of Helium in the Boom Clay under the largest gas production sequences. This quantity of dissolved Helium is indeed physically limited by Henry's law, which leads to the creation of a gaseous phase, and the desaturation of the rock over a certain radial distance. Since total Helium fluxes decrease with the radial distance, dissolved Helium becomes predominant again at the transition between saturated and partially saturated zones.

To materialise the influence of the HM couplings, the variations in parallel (solid line) and perpendicular (dashed line) intrinsic water permeabilities around the boreholes are presented during the drilling process in Figures 2.61b (E4) and 2.62b (E5) respectively, and put into perspective with the creation of the plastic zone in Figures 2.61a (E4) and 2.62a (E5). Including a strain-dependent evolution of the intrinsic permeability in the simulation gives rise to additional hydro-mechanical couplings slightly interfering with the initiation of localisation, while leading to the same extent of the EDZ. Permeability variations are well visible in the part of the damaged zone which is the closest to the boreholes wall, and more particularly inside the strain localisation discontinuities where an increase of one order of magnitude (E4) or a bit less (E5) is obtained. This slight discrepancy directly results from the more important convergence of the E4 borehole, with respect to the E5 one.

From these observations, it follows that Helium tends to enter the damaged zone more easily, which is reflected by a slight horizontal offset of the dashed lines in Figures 2.60a (E4) and 2.60b (E5). The analysis of the Helium fluxes shown in Figures 2.63e (E4) and 2.63g (E5) reveals that for the largest amount of Helium, a distinct gas phase appears which desaturates the rock mass in the vicinity of the piezometers as displayed in Figures 2.63f (E4) and 2.63h (E5).

Next to the increase in the hydraulic permeability with strain, the evolution of the water retention curve with strain is also considered in order to obtain a more faithful representation of the influence of the EDZ on the hydraulic kinetics. The variations of the entry pressure parameter for the Helium P_r in the horizontal (solid line) and vertical (dashed line) directions during the drilling process is given in Figures 2.61c (E4) and 2.62c (E5). These results attest of a global drop in P_r in the EDZ, correlated to the evolution of intrinsic

permeability previously observed, which means that the minimum capillary pressure required to desaturate the rock mass is lowered by the cracking process. As for the evolution of the intrinsic permeability displayed in Figures 2.61b (E4) and 2.61b (E5), the influence of shear bands on P_r is also clearly visible.

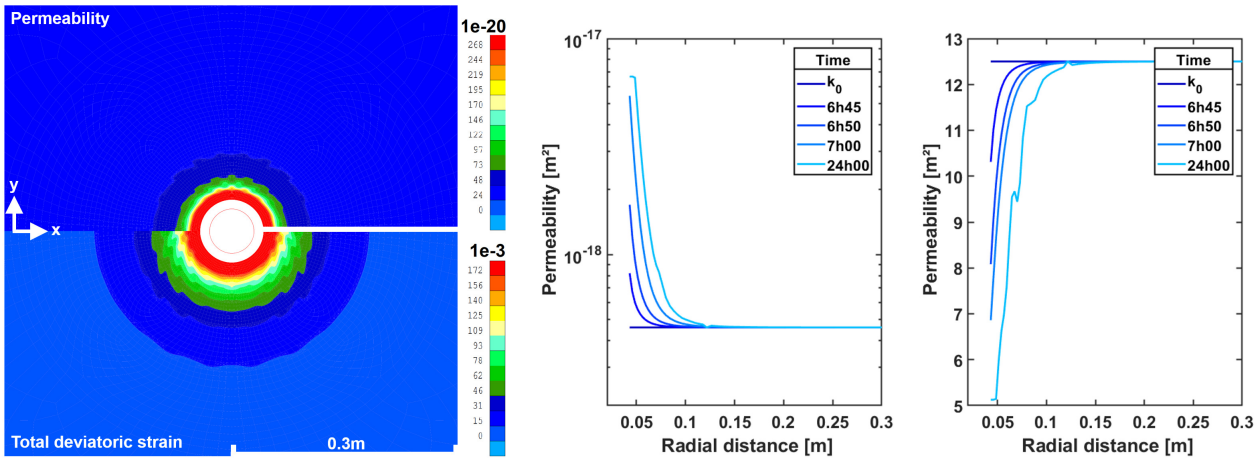

(a) (b) (c)

Figure 2.61: E4 configuration: (a) evolution of the intrinsic permeability in relation to the development of the plastic zone by the end of the drilling stage. Variations of (b) intrinsic permeability and (c) entry pressure as a function of the radial distance for different time steps.

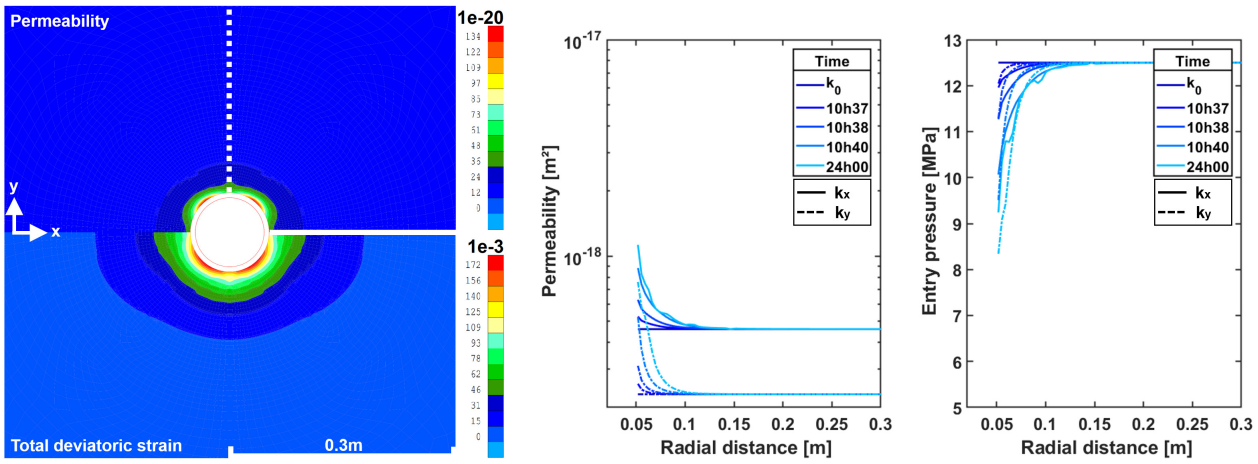

(a) (b) (c)

Figure 2.62: E5 configuration: (a) evolution of the intrinsic permeability in relation to the development of the plastic zone by the end of the drilling stage. Variations of (b) parallel (solid line) and perpendicular (dashed line) intrinsic permeability and (c) entry pressure as a function of the radial distance for different time steps.

Regarding the gas migration phase, it emerges from the horizontal offset of the dash-dotted lines in Figures 2.60a and 2.60b that the evolution of the retention curve with the deformations has a clear effect on the Helium migrations. The reduction of the gas entry pressure in the EDZ facilitates even more the penetration of gas into the Boom Clay. Once the Helium pressure reaches the maximum value set at 4.5 MPa, gas progresses in the form of a front through the zone affected by a reduction of the gas entry value. The distinct gas phase that emerges when the largest amounts of Helium are released is clearly discernible in

Figures 2.63i (E4) and 2.63k (E5). In the EDZ, Helium is no longer dissolved in water but is almost only transferred in the gaseous state, which contributes to a more rapid and important decrease in the degree of water saturation around the boreholes than in the previous simulations, as reported in Figures 2.63j (E4) and 2.63l (E5).

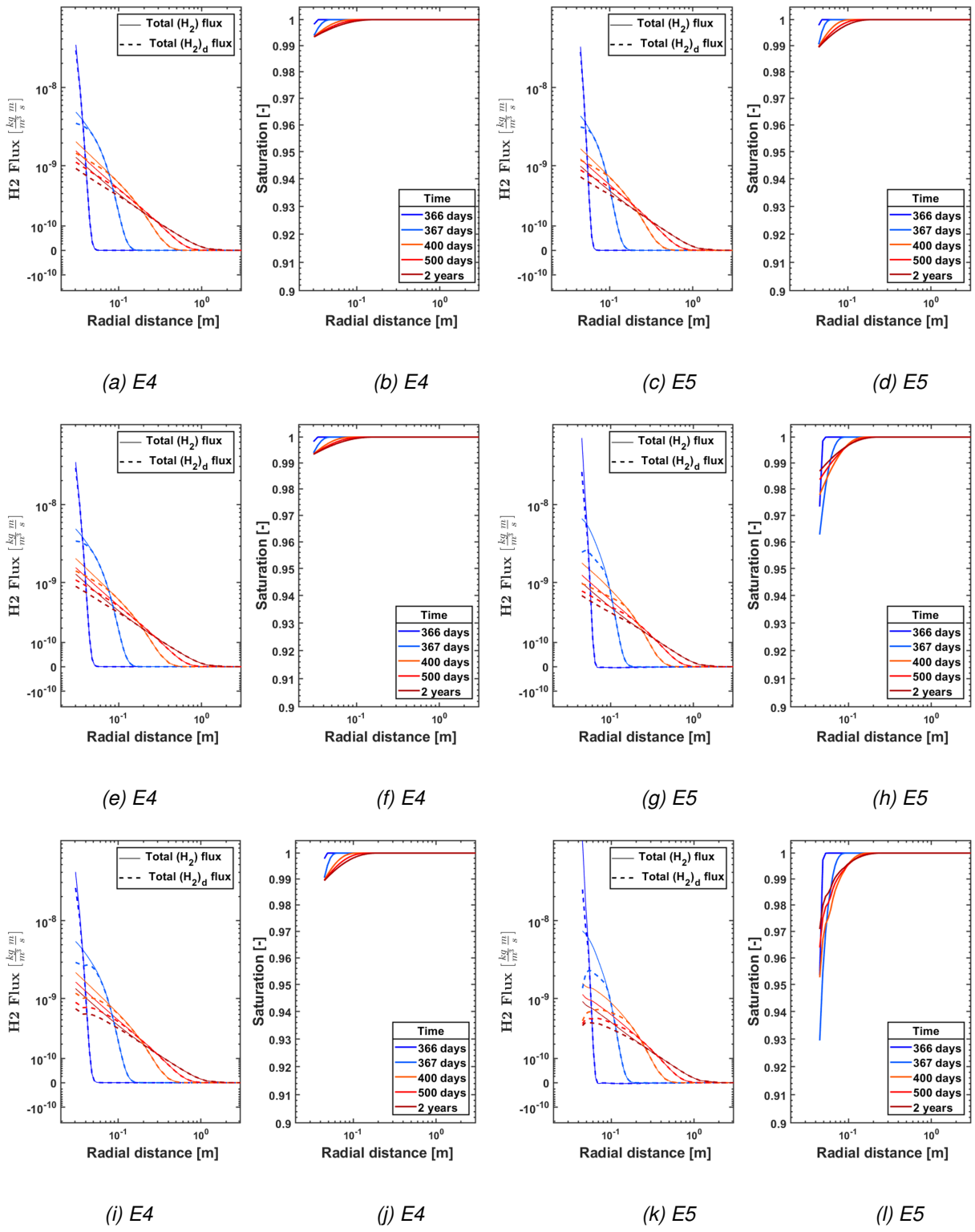

(a) E4 (b) E4 (c) E5 (d) E5

(e) E4 (f) E4 (g) E5 (h) E5

(i) E4 (j) E4 (k) E5 (l) E5

Figure 2.63: Comparison between dissolved Helium and total Helium flux (log scale along the Y-axis (Webber, 2013)), and corresponding saturation profiles as a function of the radial distance for different time steps for the E4 and E5 configurations: (a)-(d) reference case, (e)-(h) evolution of the permeability with strain and (i)-(l) evolution of the retention curve with strain.

2.3.4. Modelling large-scale MAVL storage drift

After the field-scale scale study, the numerical model is secondly applied to a large-scale storage gallery set up in the Callovo-Oxfordian claystone. The practical design of such a drift is translated into a numerical model which requires several ingredients that are listed below.

2.3.4.1. Modelling design

Geometry

MAVL galleries are made up of several hundred metres in length, 10.4 m in excavated diameter, and of concrete structural support ensuring stability, and are drilled in the low-permeable Callovo-Oxfordian claystone. It is worth noted that the support structure is modelled as a continuous shell, without considering the joints between the segments. This gives a final usable circular cross-section with a radius of R = 4.35 m, as presented in Figure 2.64b.

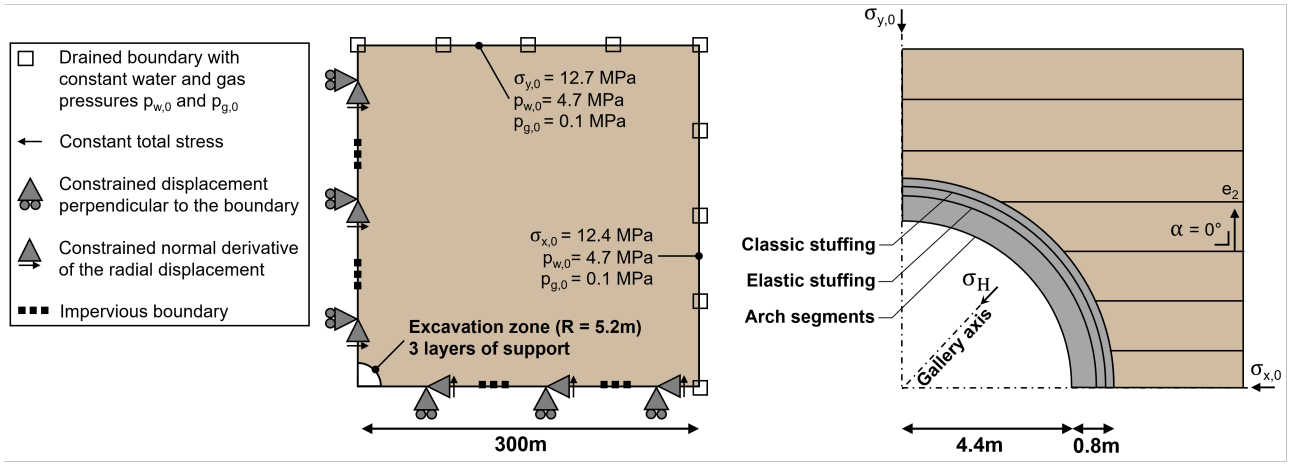

(a) (b)

Figure 2.64: (a) Geometry and boundary conditions of the 2D plane strain model. (b) Zoom on the refined support zone, with stress state and bedding plane orientation.

In the treated problem, the HM modelling of the tunnel is performed in two-dimensional plane strain state. A schematic representation of the numerical model involving the mesh and the different boundary conditions is illustrated in Figure 2.64a. The geometry extension covers a domain of 300 m $\times$ 300 m in the horizontal and vertical directions, establishing two far field boundary conditions, and integrates a more refined discretisation close to the tunnel.

Initial conditions

The MAVL configuration is oriented parallel to the major *in situ* principal stress. It is known that the level of the Meuse/Haute-Marne URL is characterised by an anisotropic stress regime, with a major principal stress in the horizontal direction, a vertical stress more or less equal to the minor principal horizontal stress and a homogeneous water pressure (Wileveau et al., 2007), such that:

$$\sigma_{x,0} = 12.4\ \mathrm{MPa},\quad \sigma_{y,0} = 12.7\ \mathrm{MPa},\quad \sigma_{z,0} = \sigma_H = 16.1\ \mathrm{MPa},\quad p_{w,0} = 4.7\ \mathrm{MPa} \tag{2.72}$$

where $\sigma_{x,0}$ is the minor horizontal principal total stress, $\sigma_{y,0}$ is the vertical principal total stress and $\sigma_{z,0}$ corresponds to the major horizontal principal total stress, while $p_{w,0}$ is the initial pore water pressure.

In addition, the initial gas pressure is set to the atmospheric pressure of $p_{g,0} = 101325$Pa, while the temperature is maintained constant at $T_0 = 20°$C throughout the simulations.

Boundary condition evolution

The drilling of the tunnel is performed with the convergence-confinement method, introduced in Figure 2.57a and expressed by Equations (2.65) and (2.66).

An excavation rate of 18 m per day is considered here, implying that the excavation front crosses the studied section after about 10 hours and that the excavation is fully completed after about 24 hours. The evolution of the deconfinement rate with time is detailed in Figure 2.65a where the origin of the time axis corresponds to the moment when the studied section starts to be influenced by excavation of the previous sections of the tunnel. Pore water pressure at drift wall p_w^Γ is also affected during the excavation phase and starts to decrease quickly and linearly from its initial value towards the atmospheric pressure when the deconfinement starts. In addition, the stress imposition at the gallery wall is also conditioned by the support structure. Practically, the three layers of support are supposed to be applied simultaneously at 96% deconfining as depicted in Figure 2.65a.

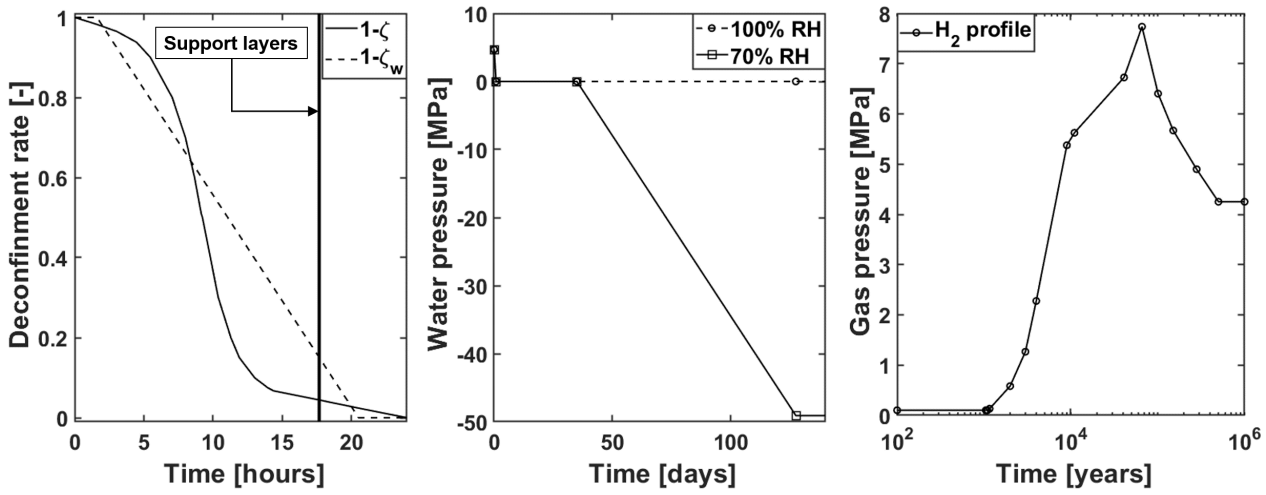

(a) (b) (c)

Figure 2.65: (a) Applied deconfinement curves for the total stress and for the pore water pressure during drift excavation. (b) Profile of pore water pressures during ventilation. (c) Profile of gas pressures during Hydrogen injection.

So far, there is no ventilation inside the gallery which means that the air is fully saturated with water vapour. This maximum concentration corresponds to air with 100% of Relative Humidity (RH) according to Kelvin's law:

$$RH = \frac{p_v}{p_v^0} = \frac{\rho_v}{\rho_v^0} = exp\left(\frac{-p_c M_v}{\rho_w RT}\right) \tag{2.73}$$

where p_v is the partial pressure of water vapour, p_v^0 is the pressure of saturated water vapour, and ρ_v^0 is the saturated vapour concentration, M_v is the molar mass of water vapour, R = 8.314 $[\mathrm{J/molK}]$ is the gas constant and T = 298.15 $[\mathrm{K}]$ is the absolute temperature.

Afterwards, the drift is ventilated during the operation phase in order to regulate the temperature according to workers needs. The ventilation imposes a RH of about 70% which modifies the hydraulic boundary condition at the drift wall by reducing the pore water pressure from 0.1 MPa to -49.1 MPa. This process is initiated 35 days after the excavation starts, the RH is progressively decreased during a period of 3 months

to reach the planned value of P_w after 125 days as exposed in Figure 2.65b. Ventilation is then maintained constant in the tunnel during an exploitation period of about 100 years.

Finally, after the 100-year phase of ventilation, the storage gallery is supposed to be entirely filled with waste packages, properly sealed and closed. From this time, the system becomes impervious to water and a period of pore water pressures stabilisation initiates since there is no more drainage imposed by the ventilation of the drift. Subsequently, gas starts to be generated in the form of hydrogen and is simulated by imposing a variation of gas pressures at the intrados of the support structure according to the H_2-profile given in Figure 2.65c (Talandier, 2005). This last phase ranges from 100 years to a million years, with peak value of gas pressures reached around 66000 years.

Mechanical model

An elasto-visco-plastic model with cross-anisotropy and horizontal isotropic bedding planes is considered for the mechanical behaviour of the rock, which can be decomposed into an elastic, a plastic and a viscous component.

The linear elastic behaviour of the rock is based on the classical Hooke's law. For cross-anisotropic materials such as the COx formation, the behaviour remains isotropic in the parallel bedding planes which requires 5 independent parameters to express the elastic compliance tensor (Amadei, 1983).

The elasto-plastic behaviour of the COx claystone is characterised by an internal friction model with a non-associated plasticity and a Van Eekelen yield surface (Van Eekelen, 1980) (under soil mechanics convention with positive compressive stress). Furthermore, the model allows isotropic hardening or softening of the cohesion and of the friction angles upon loading. The elasto-plastic geomechanical parameters used in the mechanical law of the Cox claystone, reported in Table 2.13 are taken from (Argilaga et al., 2019) after (Pardoen and Collin, 2017) where calibration is realised based on experimental data.

Viscoplasticity is also taken into account to reproduce the creep deformations characterising the long term behaviour of the claystone (Shao et al., 2003). A single viscoplastic flow mechanism decoupled from elastoplasticity is considered. A complete description of this viscoplastic model is available in (Jia et al., 2008; Zhou et al., 2008) and details about its implementation in the gallery excavation can be found in (Pardoen and Collin, 2017). The viscoplastic parameters of the COx claystone, detailed in Table 2.14, are taken from (Argilaga et al., 2019), after (Pardoen and Collin, 2017) and calibrated against laboratory tests.

Second gradient mechanical model

The second gradient mechanical model gives an additional constitutive stress-strain relation between the kinematics and the stress at microscale, which depends on one constitutive elastic parameter D in its simplified version proposed by (Matsushima et al., 2002). The value of this modulus selected to suitably regularise the problem is reported in Table 2.13.

Hydraulic model

In the hydraulic model used for the COx claystone, the transfer of the liquid phase (water and gas) by advection in an unsaturated porous medium is defined by the generalised Darcy's law (Darcy, 1856), with an anisotropic tensor of intrinsic permeability of the material k_{ij}^{int} , defined by two components $k_{||}$ and $k_{\perp}$ respectively parallel and perpendicular to the isotropic planes:

$$k_{w,ij} = \begin{bmatrix} k_{w||} & 0 & 0 \\ 0 & k_{w\perp} & 0 \\ 0 & 0 & k_{w||} \end{bmatrix} \tag{2.74}$$

The material retention behaviour is represented by a retention curve of van Genuchten's type (van Genuchten, 1980) introduced in Equation (2.67), linking the capillary pressure to the degree of water saturation (Figure 2.66a):

$$S_{r_w} = S_{r_w,res} + (S_{r,max} - S_{r_w,res}) \left(1 + \left(\frac{s}{P_r}\right)^{\mathcal{N}}\right)^{\frac{1}{\mathcal{N}}-1} \tag{2.75}$$

where P_r = 15 MPa is the parameter of gas entry pressure taken from (Gerard et al., 2014; Pardoen, 2015), $S_{r,max}$ = 1 and $S_{r_w,res}$ = 0.01 are the maximum and residual degrees of water saturation, s is the suction, and $\mathcal{N} = \frac{1}{1-\mathcal{F}}$ = 1.49 is a model parameter, fitted to obtain a good agreement with the experimental data.

Moreover, the Mualem - van Genuchten's model (Mualem, 1976) introduced in Equation (2.68) is used to express the water relative permeability in Figure 2.66b, and the cubic law is adopted to describe the gas relative permeability in Figure 2.66c:

$$k_{r_w} = \sqrt{S_{r_w}} \left(1 - \left(1 - S_{r_w}^{\frac{1}{\mathcal{M}}}\right)^{\mathcal{M}}\right)^2 \quad \text{and} \quad k_{r_g} = (1 - S_e)^{\mathcal{L}} \tag{2.76}$$

where $S_e = \frac{S_{r_w} - S_{r_w,res}}{1 - S_{r_w,res} - S_{r_g,res}}$, with S_{r_w} the degree of water saturation, $S_{r_w,res}$ the residual degree of water saturation, $S_{r_g,res}$ the residual degree of gas saturation, and $\mathcal{M}$ = 0.33 and $\mathcal{L}$ = 3 are model parameters, fitted to obtain a good agreement with the experimental data.

The hydraulic parameters of the COx claystone, reported in Table 2.15, are taken from (Pardoen and Collin, 2017), after (Charlier et al., 2013a) where a synthesis of the claystone parameters is detailed. The calibration is obtained from laboratory experiments and results, available in the literature.

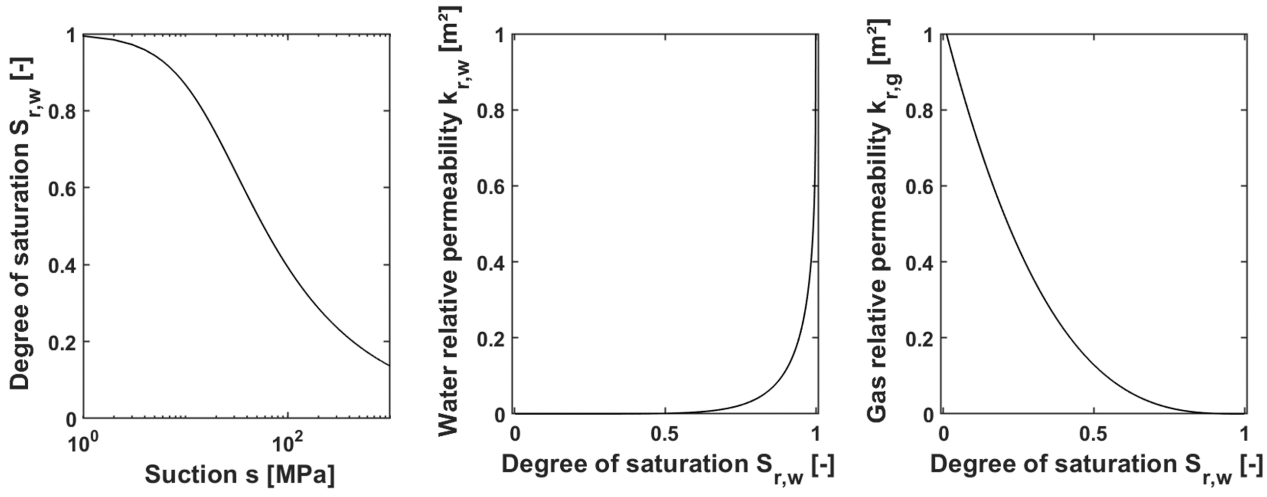

(a) (b) (c)

Figure 2.66: Definition of (a) water retention curve, (b) water relative permeability and (c) gas relative permeability.

Support behaviour

Practically, the classic and compressible stuffing layers of the support structure have a thickness of 0.15 m and 0.2 m respectively while the arch segments are 0.5 m thick. The concrete arch segments and the classic stuffing layer are characterised by an elastoplastic mechanical behaviour while the compressible stuffing layer is assumed to have a linear elastic behaviour. The mechanical parameters of the support layers are retrieved from (Andra, 2016; Gerard et al., 2008b) and gathered in the first part of Table 2.16.

Hydraulically, the same model as for the COx claystone is used for the support structure, without considering any evolution of hydraulic properties with strain. The specific hydraulic parameters assigned to each layer of the support are gathered in the second part of Table 2.16.

Table 2.13: Set of COx elasto-plastic mechanical parameters.

	Parameter	Symbol	Value	Unit
Geomechanical	Parallel Young's modulus	$E_{\parallel}$	5	[GPa]
	Perpendicular Young's modulus	$E_{\perp}$	4	[GPa]
	Poisson's ratio	$\nu_{\parallel\parallel}$	0.24	[−]
	Poisson's ratio	$\nu_{\parallel\perp}$	0.325	[−]
	Poisson's ratio	$\nu_{\perp\parallel}$	0.26	[−]
	Shear modulus	$G_{\parallel\perp} = G_{\perp\parallel}$	1.63	[GPa]
	Shear modulus	$G_{\parallel\parallel}$	2.016	[GPa]
	Parallel Biot's coefficient	$b_{\parallel}$	0.6	[−]
	Perpendicular Biot's coefficient	$b_{\perp}$	0.64	[−]
	Solid grain density	ρ_s	2750	[kg/m^3]
	Initial cohesion	c_i	4.1 (0°)	[MPa]
	Cohesion parameter	A_{11}	0.117	[−]
	Cohesion parameter	b_1	14.236	[−]
	Ratio of cohesion softening	ξ_c	5	[−]
	Cohesion softening parameter	B_c	0.003	[−]
	Initial compressive friction angle	$\varphi_{c,0}$	10	[°]
	Final compressive friction angle	$\varphi_{c,f}$	23	[°]
	Initial extensive friction angle	$\varphi_{e,0}$	7	[°]
	Final extensive friction angle	$\varphi_{e,f}$	23	[°]
	Friction angle hardening parameter	B_{φ}	0.001	[−]
	Dilatancy angles	$\psi_c = \psi_e$	0.5	[°]
Microstructure	Second gradient elastic modulus	D	14.016	[kN]

Table 2.14: Set of COx viscoplastic mechanical parameters.

	Parameter	Symbol	Value	Unit
Viscoplastic	Uniaxial compressive strength	R_c	21	[MPa]
	Internal friction coefficient	A^{vp}	2.62	[−]
	Cohesion coefficient	C^{vp}	0.03	[−]
	Viscoplastic potential parameter	β^{vp}	1.1	[−]
	Initial threshold for the VP flow	α_0^{vp}	0.142	[−]
	Reference fluidity	γ_0	700	[s^{-1}]
	Temperature parameter	γ_1	57×10^3	[J/mol]
	Creep curve shape parameter	$\mathcal{N}$	5.0	[−]
	VP hardening function parameter	B^{vp}	7.5×10^{-2}	[−]

Table 2.15: Set of COx hydraulic parameters.

	Parameter	Symbol	Value	Unit
Hydraulic	Initial porosity	n	0.173	[−]
	Initial parallel intrinsic permeability	$k_{w,\parallel,0}$	4×10^{-20}	[m^2]
	Initial perp. intrinsic permeability	$k_{w,\perp,0}$	1.33×10^{-20}	[m^2]
	Water density	ρ_w	1000	[kg/m^3]
	H2 density	ρ_{H2}	0.0794	[kg/m^3]
	Water dynamic viscosity	μ_w	0.001	[Pa.s]
	H2 dynamic viscosity	μ_{H2}	9×10^{-6}	[Pa.s]
	Water compressibility	χ_w^{-1}	5×10^{-10}	[Pa^{-1}]
	H2 Henry coefficient	H_i	0.0193	[−]
	Air entry pressure (1^{st} coeff. of S_r^w)	P_r	15	[MPa]
	Parameter (2^{nd} coeff. of S_r^w)	$\mathcal{F}$	1.49	[−]
	Parameter (1^{st} coeff. of $k_{r,w}$)	$\mathcal{M}$	0.32886	[−]
	Max. degree of water saturation	S_{max}	1	[−]
	Residual degree of water saturation	S_{res}	0.01	[−]
	Evolution parameter	β_{perm}	10^{10}	[−]
	Permeability variation threshold	ε_{eq}^{thr}	0.01	[−]
	Tortuosity	τ	0.25	[−]

Table 2.16: Set of parameters used in the different constitutive laws of the sustaining structure: classic stuffing, compressible stuffing and arch segments.

	Parameter	Symbol	Value	Unit
Classic Stuffing	Elastic Young's modulus	E	17.5	[GPa]
	Poisson'ratio	ν	0.25	[−]
	Friction angle	φ	30	[°]
	Cohesion	c	2.94	[MPa]
	Density	ρ	2300	$[\frac{kg}{m^3}]$
Compressible stuffing	Elastic Young's modulus	E	0.1	[GPa]
	Poisson's ratio	ν	0.0	[−]
	Density	ρ	2300	$[\frac{kg}{m^3}]$
Arch segments	Elastic Young's modulus	E	39	[GPa]
	Poisson's ratio	ν	0.2	[−]
	Friction angle	φ	38	[°]
	Cohesion	c	14.6	[MPa]
	Density	ρ	2650	$[\frac{kg}{m^3}]$
Compressible Stuffing	Initial porosity	n	0.25	[−]
	Initial parallel intrinsic permeability	$k_{w,\parallel,0}$	10^{-15}	[m^2]
	Initial perp. intrinsic permeability	$k_{w,\perp,0}$	10^{-15}	[m^2]
	Air entry pressure (1st coeff. of S_r^w)	P_r	1	[MPa]
	Parameter (2nd coeff. of S_r^w)	$\mathcal{G}$	1.54	[−]
	Parameter (1st coeff. of $k_{r,w}$)	$\mathcal{F}$	0.3507	[−]
	Max. degree of water saturation	S_{max}	1	[−]
	Residual degree of water saturation	S_{res}	0.01	[−]
	Tortuosity	τ	0.25	[−]
Compressible Stuffing	Initial porosity	n	0.5	[−]
	Initial parallel intrinsic permeability	$k_{w,\parallel,0}$	10^{-10}	[m^2]
	Initial perp. intrinsic permeability	$k_{w,\perp,0}$	10^{-10}	[m^2]
	Air entry pressure (1st coeff. of S_r^w)	P_r	0.2	[MPa]
	Parameter (2nd coeff. of S_r^w)	$\mathcal{G}$	1.54	[−]
	Parameter (1st coeff. of $k_{r,w}$)	$\mathcal{F}$	0.3507	[−]
	Max. degree of water saturation	S_{max}	1	[−]
	Residual degree of water saturation	S_{res}	0.01	[−]
	Tortuosity	τ	0.25	[−]
Arch Segments	Initial porosity	n	0.15	[−]
	Initial parallel intrinsic permeability	$k_{w,\parallel,0}$	10^{-18}	[m^2]
	Initial perp. intrinsic permeability	$k_{w,\perp,0}$	10^{-18}	[m^2]
	Air entry pressure (1st coeff. of S_r^w)	P_r	5	[MPa]
	Parameter (2nd coeff. of S_r^w)	$\mathcal{G}$	1.54	[−]
	Parameter (1st coeff. of $k_{r,w}$)	$\mathcal{F}$	0.3507	[−]
	Max. degree of water saturation	S_{max}	1	[−]
	Residual degree of water saturation	S_{res}	0.01	[−]
	Tortuosity	τ	0.25	[−]

2.3.4.2. Results

To emphasize the effect of the EDZ on gas migrations, three modelling cases are investigated. In the first reference simulation, the development of the EDZ is supposed to induce no alteration of the hydraulic properties in this zone. In the two subsequent simulations, the enhanced couplings between fluids transfers (water and gas) and the mechanical behaviour of the fractured zone are progressively activated. First, a strain-dependent evolution of the material intrinsic permeability is envisaged, subsequently enriched by the modification of the water retention property with the deformation.

Reference case

The first performed simulation focuses on the development of the EDZ following the drilling process. The main purpose is to characterise the extent of fractures induced by rock deconfinement during the excavation phase. These fractures are reproduced by shear banding and no modification of the hydraulic properties in the damaged zone is taken into account in this preliminary simulation. The creation and evolution of the fractured zone can then be observed through the evolution of the shear strain localisation. The numerical results are presented in terms of Von Mises' equivalent deviatoric total strain (total deviatoric strain), the plastic zone, i.e. the plastic loading integration points (red squares), and the deviatoric strain increment by the end of the excavation in Figure 2.67. The onset and shape of this strain localisation zone can be attributed to the anisotropy of the material as well as of the initial stress state (Pardoen, 2015). Since this initial stress state is not perfectly isotropic, the plastic zone appears to extent preferentially in the direction of the minor principal stress, namely horizontally. By the end of the excavation process, the plastic zone has expanded over 7 m in the horizontal direction and 5m in the vertical direction. The installation of the support has the consequences of limiting the points in plastic charge and inhibiting any further development of localisation.

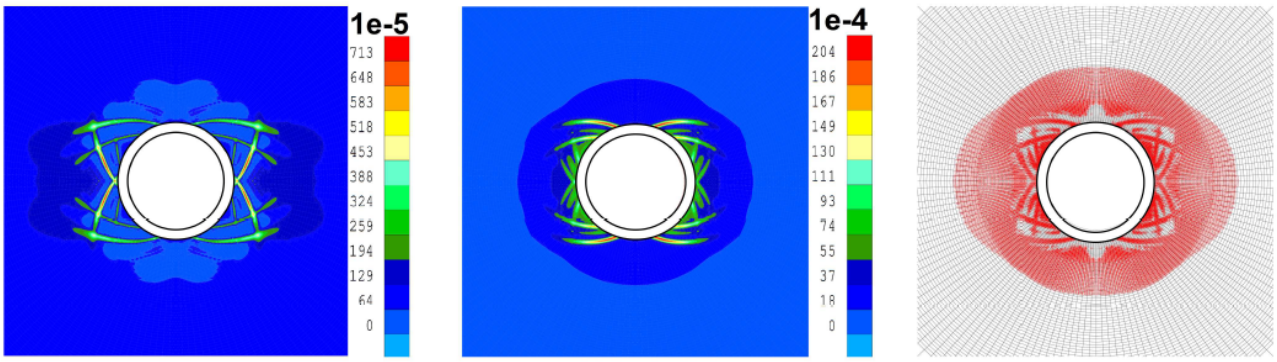

(a) *(b)* *(c)*

Figure 2.67: Development of shear bands at the end of the excavation process: (a) deviatoric strain increment, (b) total deviatoric strain and (c) plastic loading points.

The focus is then on gas transfers in the form of Hydrogen that take place in the long-term part of the simulation, according to the evolution profile given in Figure 2.65. In Figure 2.68a, gas pressure profiles are displayed along the horizontal section of the domain, highlighting the progressive propagation of Hydrogen across the rock mass. The temporal evolution of gas pressures in the zone adjacent to the drift wall is presented in Figure 2.68b. By referring to the time evolution of water pressure (Figure 2.65), it comes out that the release of Hydrogen materialized by an increase in gas pressure starts after a period of approximately 1000 years when the pore water pressure has almost recovered the initial value of 4.7 MPa. No water overpressure is observed subsequently as a result of this rise in gas pressure.

A maximum gas pressure of about 7.5 MPa is reached at the drift wall after a period of around 60000 years, and a desaturation of a few percent is associated to this peak of Hydrogen pressure. Desaturation profiles in the rock mass are illustrated in Figure 2.69b and put into perspective with the dissolved and total Hydrogen flows profiles displayed in Figure 2.69a in log scale. Close to the injection zone, it appears that dissolved gas in the water phase is not sufficient enough to ensure transfers of Hydrogen in the claystone rock under the largest Hydrogen production sequences. This quantity of dissolved Hydrogen is indeed physically limited by Henry's law, which leads to the creation of a gaseous phase, and to the desaturation of argillite over a certain radial distance. Since total Hydrogen fluxes decrease with the radial distance, dissolved hydrogen becomes predominant again at the transition between saturated and partially saturated zones.

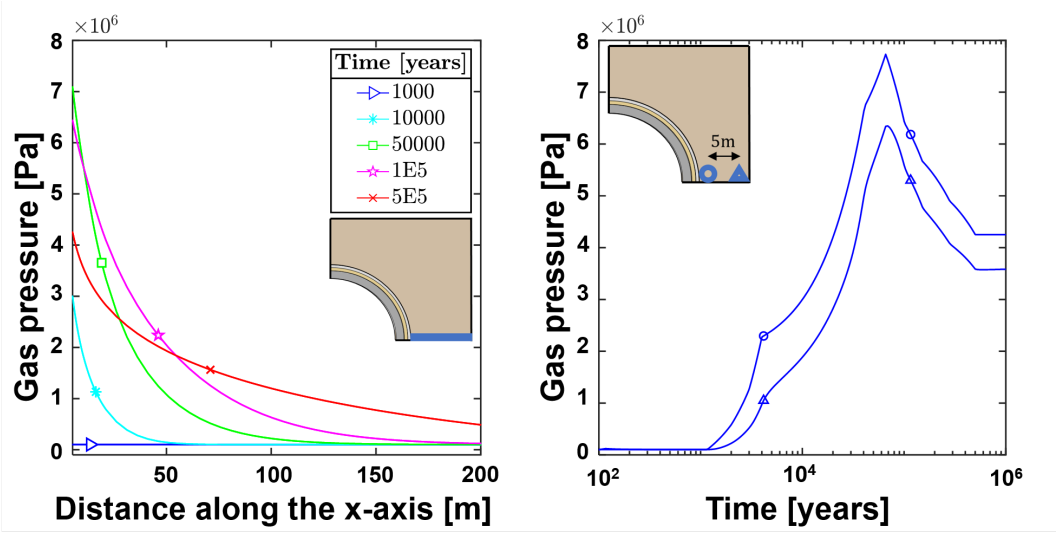

(a) (b)

Figure 2.68: Evolution of gas (Hydrogen) pressures (a) over the domain and (b) with time.

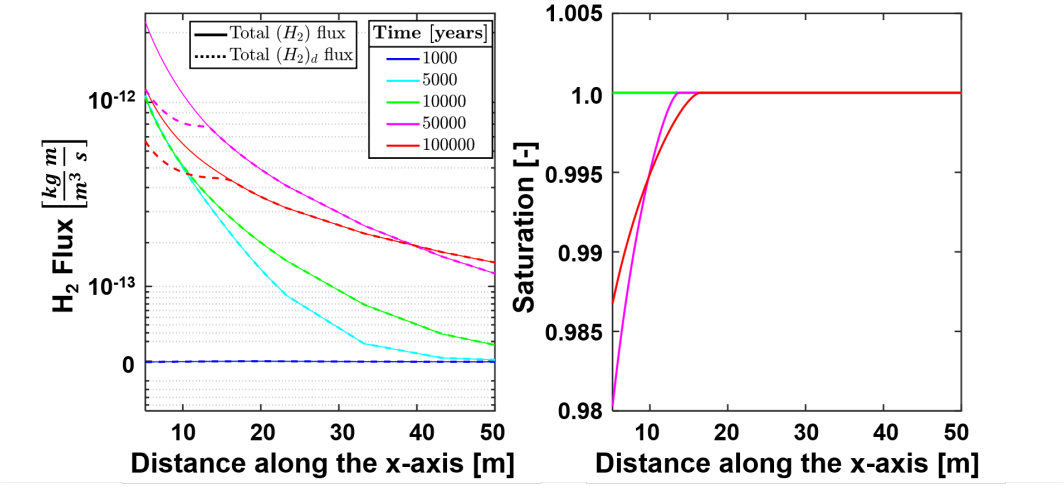

(a) (b)

Figure 2.69: (a) Comparison between dissolved Hydrogen and total Hydrogen flux (log scale along Y-axis) and (b) corresponding saturation profiles.

Evolution of the intrinsic permeability with the deformations

In this second part of the simulations, an advanced coupled hydro-mechanical behaviour of the EDZ is considered in order to end up with a more accurate representation of the phenomena related to gas migration. The impact of fracturing on the flow transfer characteristics is addressed by relating the intrinsic permeability evolution with the mechanical deformations according to expression (2.58).

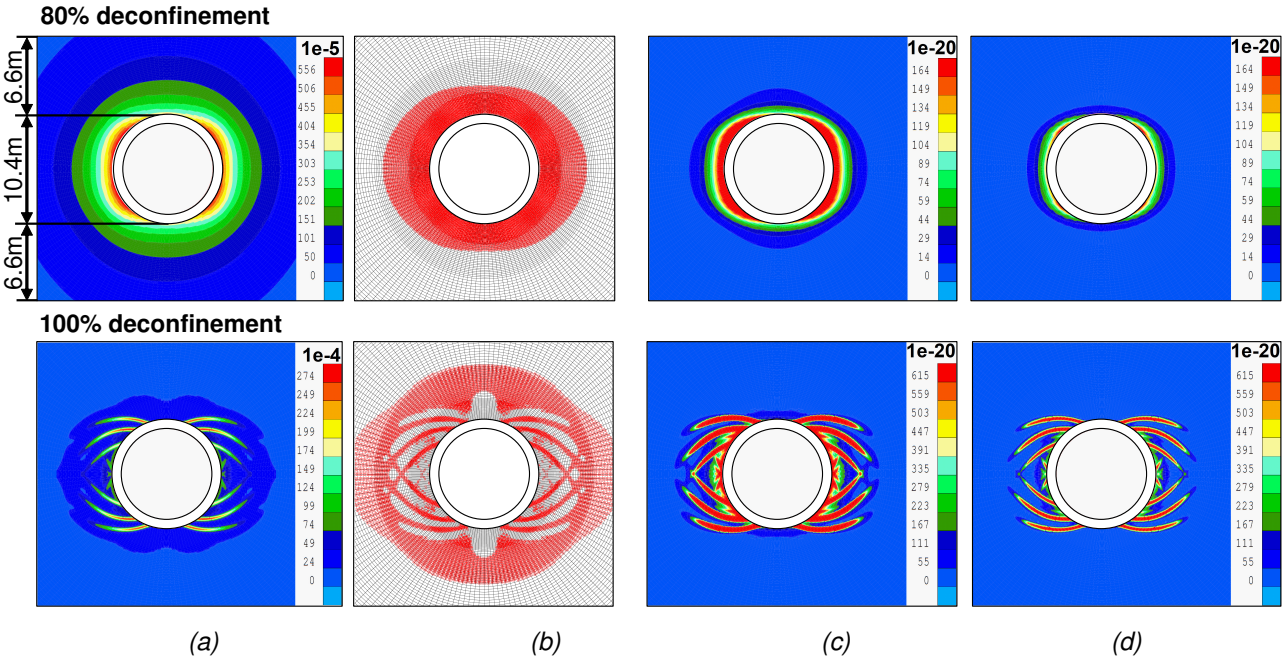

Figure 2.70: Development of shear bands and evolution of water permeability at the end of excavation: (a) total deviatoric strain, (b) plastic loading points, and intrinsic water permeability in the (c) horizontal and (d) vertical directions.

The variations in (parallel and perpendicular) intrinsic water permeabilities around the drift are presented at the end of the excavation process in Figures 2.70c and 2.70d respectively, and put into perspective with the creation of the plastic zone in Figures 2.70a and 2.70b. Compared to the results obtained for the reference case in Figure 2.67, minor differences are noticed in the overall development of the plastic zone. Including a strain-dependent evolution of the intrinsic permeability in the simulation gives rise to additional hydro-mechanical couplings slightly interfering with the initiation of localisation bands, that tend to grow preferentially in the horizontal direction. However, the total extent of the EDZ remains all in all identical. Permeability variations are well visible in the part of this damaged zone which is the closest to the drift wall, and more particularly inside the strain localisation discontinuities where a significant increase of several orders of magnitude is obtained.

A closer look at the distribution of the parallel intrinsic permeability provided in Figure 2.71 confirms a global permeability increase of about two orders of magnitude between the initial and final states of excavation, with permeability peaks along the diagonal and horizontal profiles because of the presence of shear bands in these directions. It is worth noting that a symmetrical evolution of the perpendicular intrinsic permeability would be obtained since the strain-dependent isotropic expression (2.58) conserves the initial directions of anisotropy and the imposed permeability ratio $\frac{k_{w,\parallel}}{k_{w,\perp}} = 3$.

With respect to the gas migration phase, the re-establishement of the pore water pressures is also made more progressive, extending the period necessary for the resaturation of the claystone. As a consequence, pore water pressure in the EDZ has not fully returned to its initial state prior to the beginning of gas injection

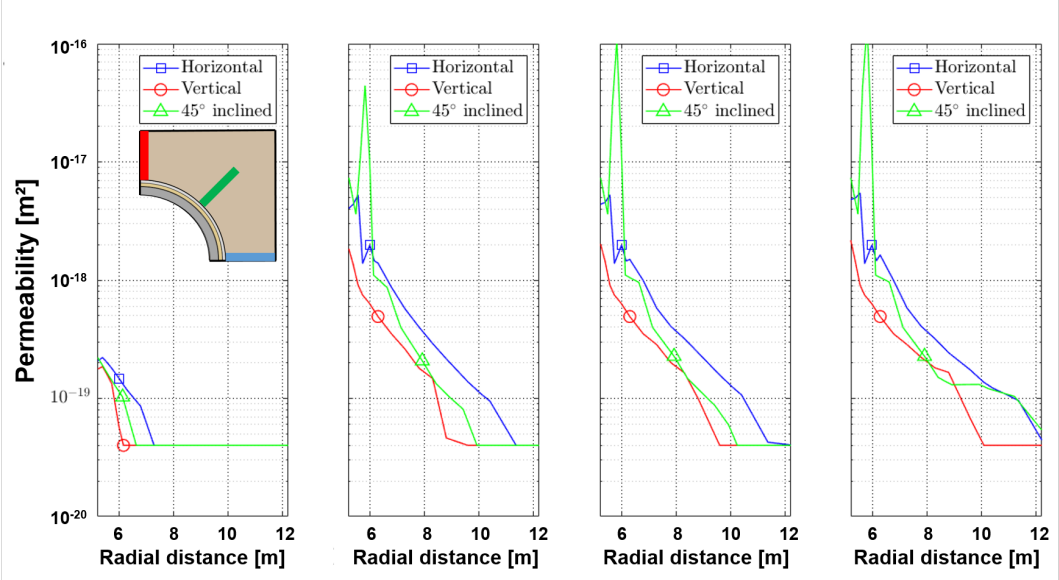

(a) 10h15 (65%) (b) 11h20 (80%) (c) 1 day (100%) (d) 100 years (100%)

Figure 2.71: Variation of parallel intrinsic permeability $k_{w,||}$ as a function of the radial distance for different time steps.

(Figure **??**). From these first observations, it follows that Hydrogen tends to enter the first meters of the rock mass more easily, which is highlighted by a slight horizontal offset of the curves in Figure 2.72a and by a rise in the maximum gas pressure reached beyond the EDZ in Figure 2.72b. As in the reference case, the analysis of the Hydrogen fluxes shown in Figure 2.73 reveals that for the largest amount of Hydrogen, a distinct gas phase appears which desaturates the argillite in the vicinity of the support. The maps of gas pressures in Figure 2.74 corroborate these aspects and show that Hydrogen propagates more efficiently in the EDZ. More specifically, preferential flow paths corresponding to the localised shear bands seem to initiate around the drift due to the high increase in permeability within these discontinuities where the deformation is concentrated.

Evolution of the retention curve with the deformations

Next to the increase in the hydraulic permeability with strain, an additional HM mechanism is considered in order to obtain a more faithful representation of the influence of the EDZ on the hydraulic kinetics. This second advanced HM coupling concerns the evolution of the water retention curve with strain (Olivella and Alonso, 2008b). This feature is integrated into the model thanks to the expression (2.62).

The evolution of the entry pressure parameter for the Hydrogen P_r is given in Figures 2.75 by the end of the excavation and ventilation phases. These results attest of a global drop in P_r in the EDZ, correlated to the evolution of intrinsic permeability previously observed. As for the evolution of the intrinsic permeability displayed in Figure 2.71, the influence of shear bands on P_r is also clearly visible.

Regarding the gas migration phase, it comes out that the pore water pressure has almost returned to its initial value, reestablishing a fully saturated state in the EDZ, prior to the beginning of gas injection. The evolution of the retention curve with the deformations has a clear influence on the Hydrogen migrations. The reduction of Hydrogen entry pressure in the EDZ facilitates even more the penetration of gas into the claystone. Once the Hydrogen pressure reaches and exceeds the water pressure set at 4.7 MPa (in the time window between 3×10^4 and 3×10^5 years), gas progresses in the form of a front through the zone affected by a reduction of the gas entry value (Figure 2.76a). The maximum gas pressure reached

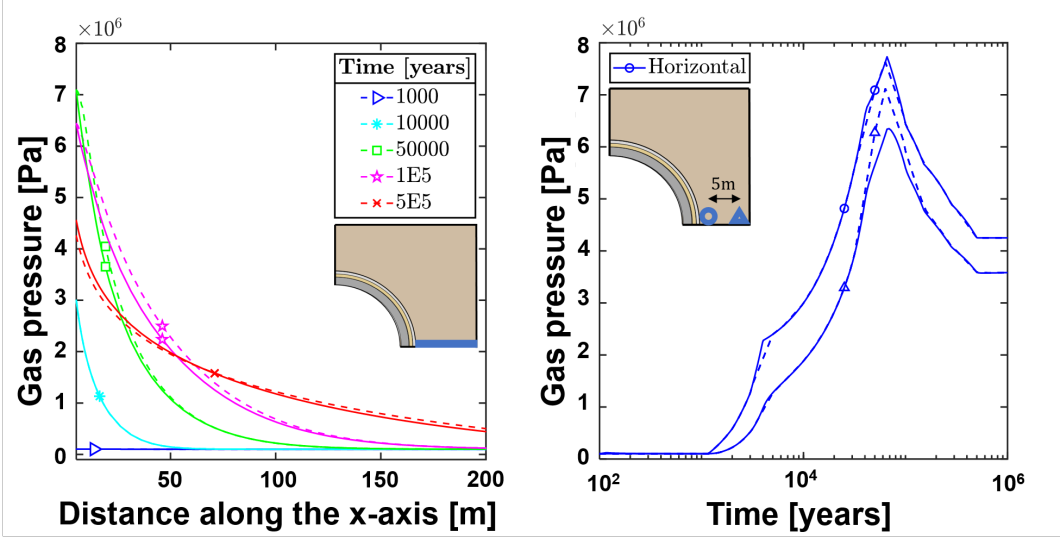

(a) (b)

Figure 2.72: Evolution of gas (Hydrogen) pressures (a) over the domain and (b) over time, considering a permeability evolution with strain.

at the limit of the EDZ is then drastically increased as shown in Figure 2.76b. The distinct gas phase that emerges when the largest amounts of Hydrogen are released is clearly discernible in Figure 2.77a. In the EDZ, Hydrogen is no longer dissolved in water but is almost only transferred in the gaseous state, which contributes to a more rapid and important decrease in the degree of water saturation around the drift than in the previous simulations, as reported in Figure 2.77b. All these observations can be further supported with the maps of gas pressures in the vicinity of the drift presented in Figure 2.74. The first foreseeable point that can be raised is that Hydrogen propagates easier and faster in that zone compared to the reference case. Moreover, since the cracking process in the EDZ amplifies the desaturation, one can notice a uniform and rapid increase in gas pressure across the whole EDZ.

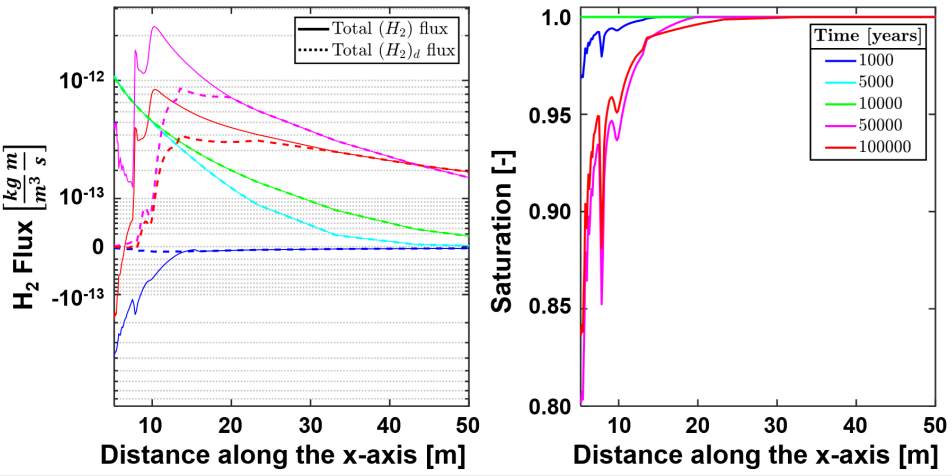

(a) (b)

Figure 2.73: (a) Comparison between dissolved Hydrogen and total Hydrogen flux (log scale along Y-axis Webber (2013)) and (b) corresponding saturation profiles, considering permeability evolution with strain.

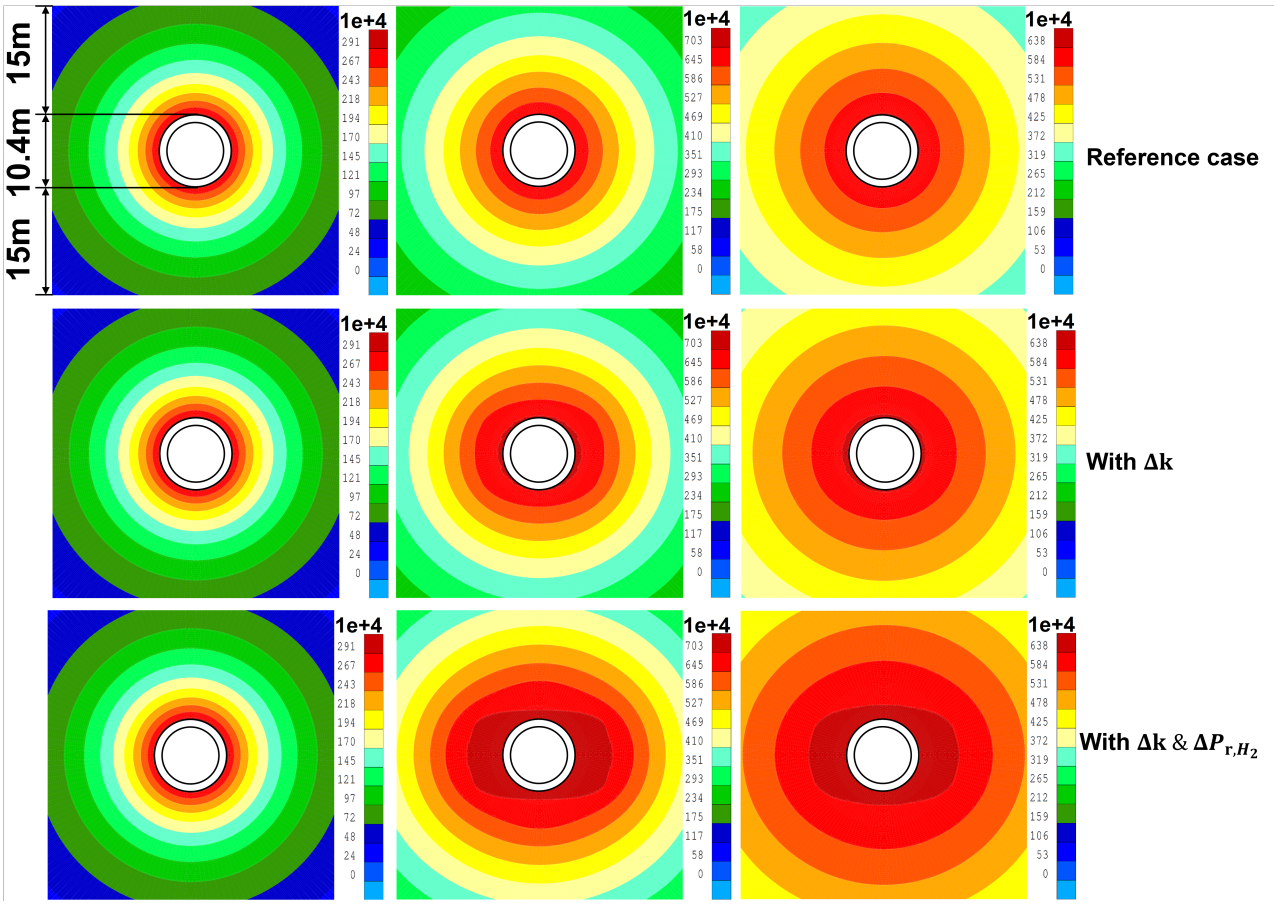

(a) 10 000 years (b) 50 000 years (c) 100 000 years

Figure 2.74: Evolution of gas (Hydrogen) pressure in the vicinity of the gallery wall, for the reference case and considering the HM couplings.

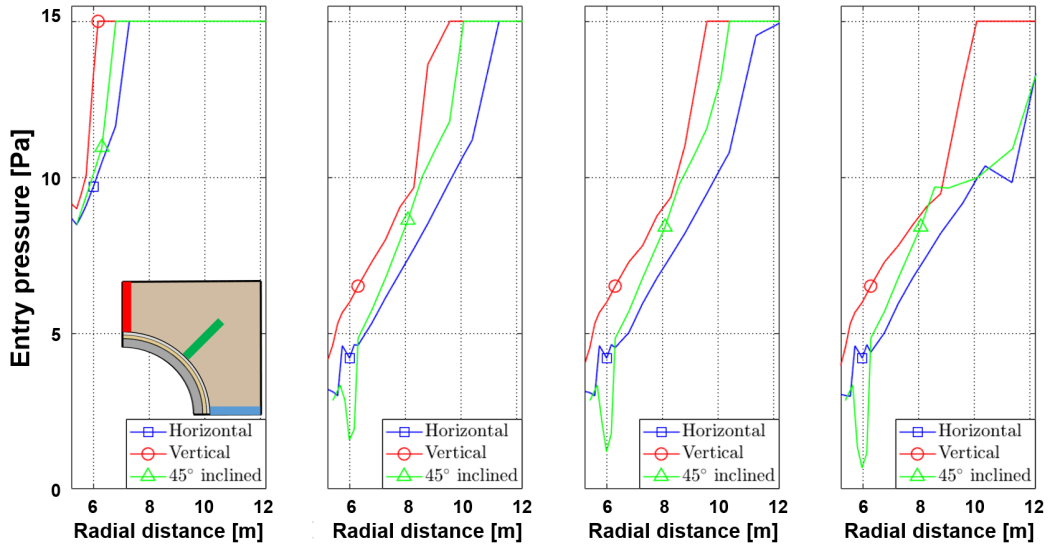

(a) 10h15 (65%) (b) 11h20 (80%) (c) 1 day (100%) (d) 100 years (100%)

Figure 2.75: Variation of gas (Hydrogen) entry pressure P_r as a function of the radial distance for different time steps.

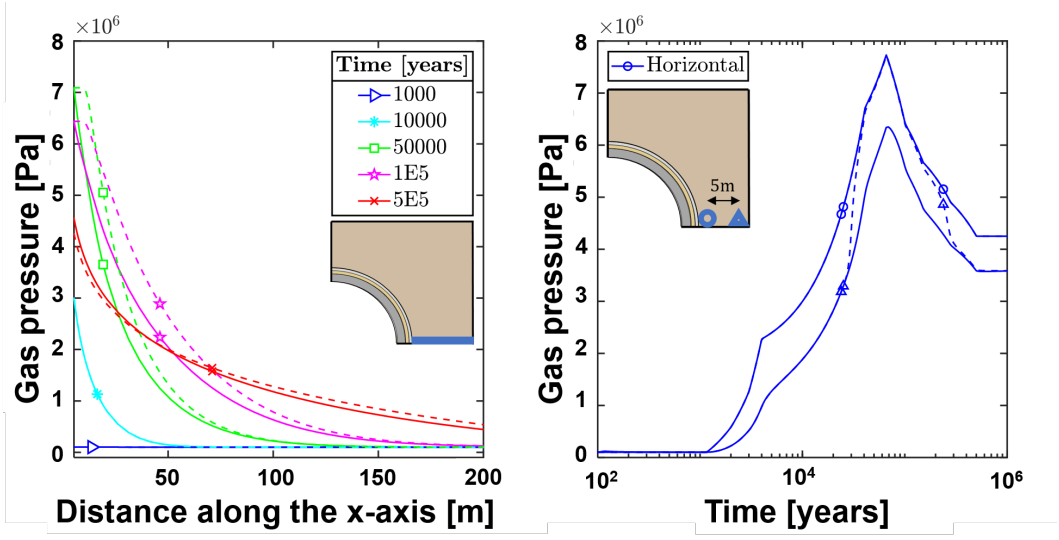

(a) (b)

Figure 2.76: Evolution of gas (Hydrogen) pressures (a) over the domain and (b) over time, considering an evolution of the retention curve with strain.

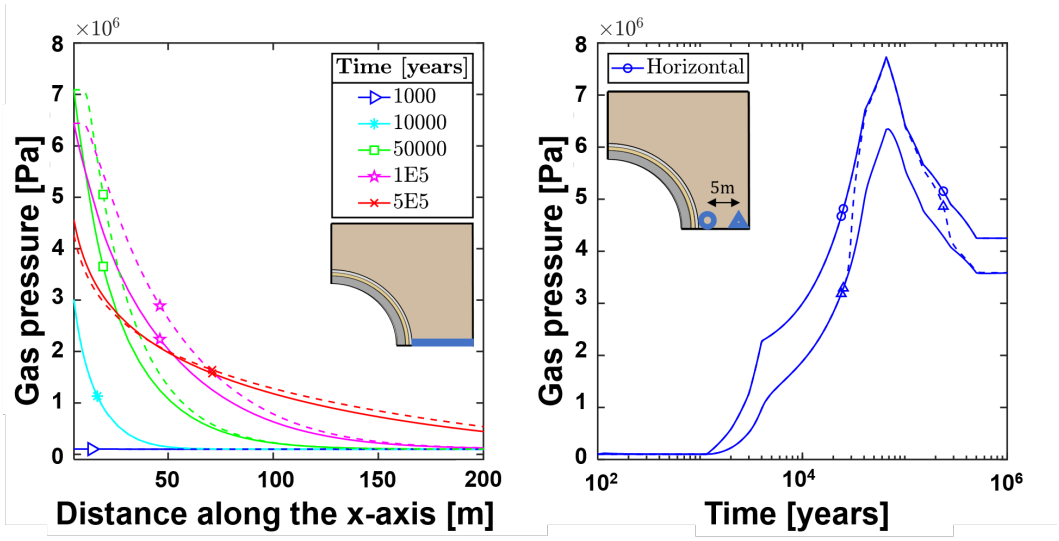

(a) (b)

Figure 2.77: (a) Comparison between dissolved Hydrogen and total Hydrogen flux (log scale along Y-axis (Webber, 2013)) and (b) corresponding saturation profiles, considering an evolution of the retention curve with strain.

2.3.5. Summary

The work presented by the University of Liège with respect to Task 3 is devoted to the numerical analysis of gas migrations in clay materials and their specific interaction with damaged rock (Corman, 2024). To that end, a second gradient two-phase flow hydro-mechanical (H^2M) model has been implemented. On the one hand, this model integrates the second gradient theory to properly reproduce the fractures around underground structures with strain localisation in shear band mode. On the other hand, the model incorporates the features of an extended two-phase flow transfer approach in order to deal with the mechanisms inherent to gas migrations. On top of that, specific coupled effects of the mechanical deformations on fluids transport properties like the intrinsic permeability and the retention behaviour have been taken into account, to better apprehend the impact of the excavation damaged zone on gas transport.

After a brief description of the equations implemented in the finite element code, the model has been first applied to a field-scale application dealing with gas injections tests in the Boom Clay. Subsequently, it has been applied to a large-scale case study, dealing with the MAVL storage drift drilled in the Callovo-Oxfordian claystone envisaged for deep geological disposal in France. Complete constitutive hydro-mechanical models have been employed to reproduce the behaviour of these low-permeable rocks. The emphasis of these simulations is on the non-negligible impact of the hydro-mechanical couplings inherent to the EDZ on gas migration (Corman et al., 2022). And so, by introducing the two HM effects in the numerical modelling, which couple the permeability and the retention property of the rock to the damage process, the model has shown capabilities of reproducing a rapid propagation of Hydrogen in the form of a gaseous front across the EDZ, that tends to attenuate deeper in the undisturbed rock mass.

2.3.6. Key learning points

New knowledge acquired

Developing a second gradient H^2M model offers the possibility of reproducing the mechanisms inherent to gas propagation in the EDZ of a clayey rock, by accurately replicating the development of damage with the second gradient approach and strongly coupling the mechanical deformations to the transfer properties. These advanced HM interactions are required to ensure a rapid gas invasion of the EDZ by the gas. Otherwise, it has been noticed that the fast mechanism of gas transport by visco-capillary two-phase flow is supplanted by the diffusion of dissolved gas in the liquid phase, which is a much slower mechanism.

Impact of the acquired knowledge

The performed numerical analysis is in line with the current state of knowledge of gas impact at repository scale. Indeed, it is accepted that the diffusion of dissolved gas in water-saturated clay is certain to occur but with a limited capacity of gas transfer. In parallel, it is also expected that visco-capillary two-phase flow of water and gas will be mainly located within the EDZ and its discontinuities. Since the developed numerical tool is able to replicate these two mechanisms of gas flow from a storage gallery to a clayey host rock with an EDZ (Figures 2.78a and 2.78b respectively), it should therefore help converging to more realistic and accurate predictions of the long-term integrity of the geological barrier.

Remaining knowledge gaps

Numerical models play an important role in the assessment of long-term repository safety, as they allow *e.g.* for parameter identification based on experiments, for fundamental process understanding and for prediction of repository evolution in the future. Although the advanced HM models proposed in this work have shown the ability to qualitatively reproduce the experimental response, they however still fail being

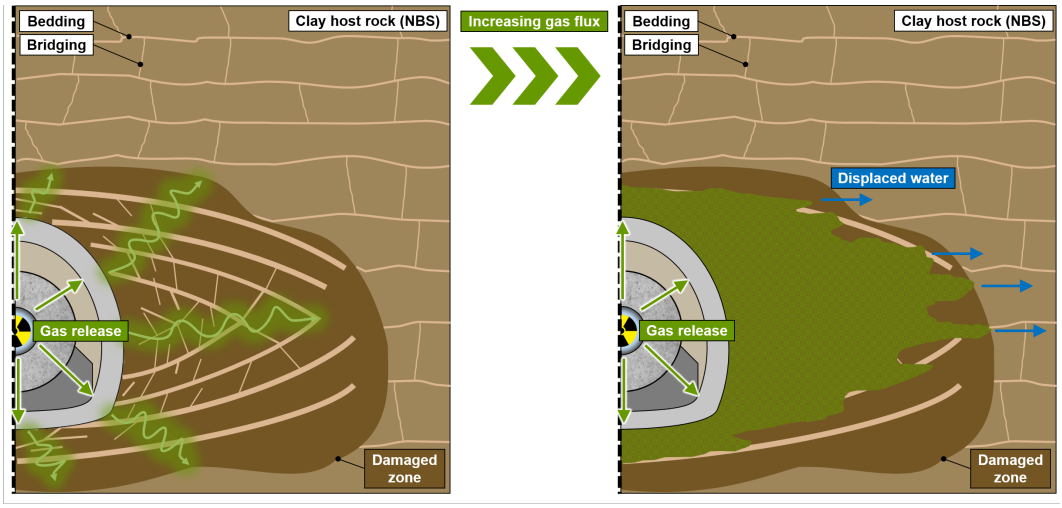

(a) (b)

Figure 2.78: Schematic representation of expected gas flow regimes in the EDZ of a water-saturated clayey host rock (not at scale): (a) Advection and diffusion of dissolved gas, (b) Visco-capillary two-phase flow. Inspired from Levasseur et al. (2024).

predictive, as some model parameters are tuned in order to mimic the data, which is another shortcoming to tackle.

Other uncertainties also remain in the simulations and are reflected in the ranges adopted for the values of the leading parameters, namely permeability and gas entry pressure, in the visco-capillary two-phase flow model (Corman et al., 2022).

The proposed approach is also based on a continuous description of the fractures in the material, instigated from strain localisation in shear band mode. Overall, such a description correctly reproduce the shape of the EDZ, but even if shearing is the predominant fracture mechanism in clay materials, the fracturing pattern could still be improved by considering other types of fractures that have been experimentally detected in the EDZ. For instance, the representation of the EDZ could be refined with a large number of thinner bands and tensile fractures, which would require other rupture mechanisms in the modelling strategy. Adapting the structure of the EDZ towards a more representative configuration would also affect the hydraulic aspects governing the gas transport mechanisms in that zone. For the strain localisation approach, one way to proceed could be to link the rock transfer properties with the tensile strain in the normal direction to the shear bands. Furthermore, the self-sealing capacity of the rock after gas transport is another mechanism that could be integrated into the conceptual model to capture the closure and sealing of these fractures in the EDZ over time.

Recommendations for the future

Since the problems relating to gas migrations in rocks are characterised by a multi-directional propagation, extending the modelling developments to 3D framework is possible way of perspective of the present work.

It must also be kept in mind that the numerical modelling of physical processes in the Earth science field also involves inherent uncertainties, arising from the variable nature of geological properties and the simplification of the conceptual models. Rather than using a strictly deterministic model where the output relies on a single set of parameters values and initial conditions, introducing ranges of values in the form of probability distributions for each parameter of the material and applying a stochastic approach would be

appropriate to upgrade the multi-scale model.

To go further and gain a unified and comprehensive vision of gas transport processes in the clay host rock surrounding a storage cell, integrating the second gradient H^2M model developed for gas transport processes in the EDZ, with a model capable of reproducing the gas migrations in sound rock layers (Corman et al., 2024) in one single simulation of gas release from the system would be beneficial. Nonetheless, such a modelling task would be restricted to a process-level investigation in the close vicinity of the storage drift because of the high computational costs of both approaches. Building an efficient and exhaustive model that describe the complex physical processes involved in the gas transport modes at the scale of the repository is indeed still missing at present.

Finally, the second gradient H^2M model that has been elaborated to study the impact of the damaged on gas transport processes could be extended to other coupled processes prone to occur in the context of a deep geological repository. In particular, it could involve the short-term thermal effects (Song et al., 2023) in order to study how the generated heat could induce water overpressures and affect the favourable properties of the clay host rock, especially its transport characteristics. Since clayey materials exhibit a strong capacity for self-sealing of discontinuities after sustaining mechanical perturbations, the transfer properties of the undisturbed rock could be restored over time in the EDZ. Accounting for such a mechanism in the modelling could have an influence the very long-term behaviour of the geological barrier subjected to an uninterrupted gas production.

.

TU Delft

2.4. Lagamine (TU Delft)

2.4.1. Introduction

The TU Delft team aims to develop a numerical model capable of reproducing, within a unified framework, the four gas transport mechanisms in initially saturated clays: i) diffusion and advection of dissolved gas, ii) visco-capillary two-phase flow, iii) dilatancy controlled gas flow, and iv) gas fracturing. This model will enable the investigation of the factors controlling the onset of each mechanism and the interaction between these mechanisms.

To select an appropriate modelling approach, a literature review on experimental characterisation of gas transport mechanisms in water-saturated clays and on existing numerical models to simulate this process has been performed. Based on this review, the available numerical tools and the researchers' experience, it was decided to develop a coupled Pneumo-Hydro-Mechanical (PHM) Finite Element (FE) model within the FE code LAGAMINE. Taking advantage of existing capabilities for simulating coupled PHM processes in continuum porous media, new developments were implemented to consider discrete fracturing processes via the use of zero-thickness interface elements. For this purpose, the governing equations and FE discretisation of a new type of PHM interface element have been developed and implemented in LAGAMINE, including a set of new mechanical and flow constitutive laws.

In the following sections 2.4.2, 2.4.3 and 2.4.4, the background of the proposed modelling approach and the adopted governing equations are described in detail. Section 2.4.5 summarises the FE formulation and the numerical implementation of the model. For further details on the model as well as benchmark examples refer to Liaudat et al. (2023). Finally, the proposed model is used to analyse two different gas migration experiments on Boom clay performed by the BGS (Section 2.4.6) and CIMNE (Section 2.4.7).

2.4.2. Modelling Approach

The gas migration in water saturated clay is modelled in 2D assuming isothermal conditions and using a Pneumo-Hydro-Mechanical (PHM) formulation discretised with FEM. In the proposed modelling approach, continuum elements are used to represent the mechanical and flow processes in the bulk clay material, while zero-thickness interface elements are used to represent existing or induced discontinuities (cracks). The interface elements are introduced a priori in between the continuum elements, thereby providing a set of potential propagation paths for cracks (Figure 2.79). The constitutive laws of the interface elements are such that, as long as they remain closed, they do not have any significant effect on the overall hydro-mechanical response of the modelled clay sample. However, when a certain mechanical threshold is reached (e.g. the tensile strength) and the interface element starts to open, localised mechanical and flow processes are triggered. Similar approaches can be found in the literature for modelling hydraulic fracturing of rocks Carrier and Granet (2012); Nguyen et al. (2017); Cordero et al. (2019a,b) and concrete cracking due to chemo-mechanical processes Idiart et al. (2011a,b); Liaudat et al. (2020). In addition, interface elements can be used to represent interfaces between different materials (e.g. the contact between a clay sample and steel cells used in lab tests) or existing discontinuities (e.g. bedding planes).

This approach has the conceptual advantage of treating the continuum and discontinuities as two separate (though connected) sub-domains within the clay material. In that way, different (though consistent) mechanical and flow constitutive laws can be used for the continuum porous medium and for the induced cracks or pre-existent discontinuities, allowing a more realistic representation of the effect of discontinuities in the clay material. As a negative counterpart, cracks can only develop at the pre-established lines where the interface elements have been inserted. This is a discretisation of a continuum problem. In reality, the potential cracking paths for a given boundary value problem are infinite, such that the propagation of cracks will form the pattern that requires exactly the minimum mechanical work. In contrast, with the proposed

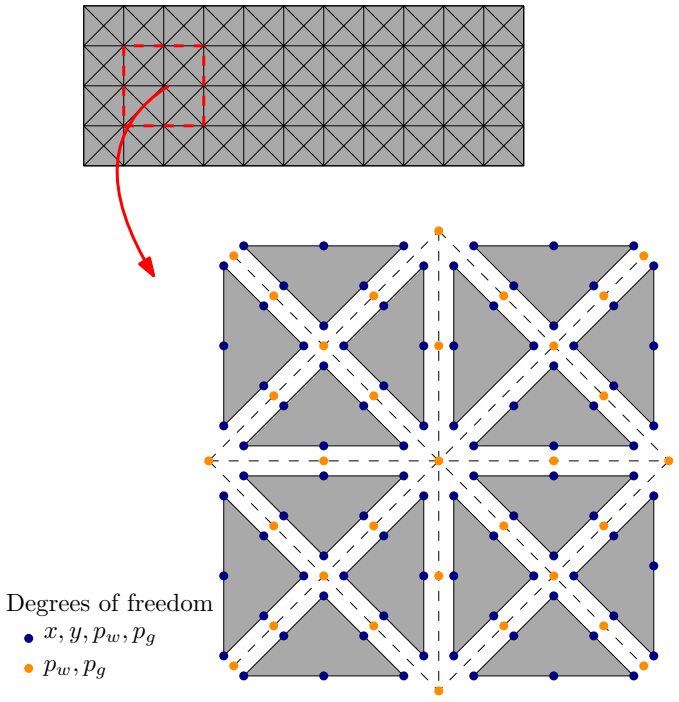

Figure 2.79: Introduction of zero-thickness interface elements in a conventional FE mesh. Adapted from Cordero et al. (2019a).

modelling approach the cracking pattern will be the one that requires the least mechanical work among the set of potential patterns provided by the adopted FE mesh with interface elements. This pattern is not necessarily the one requiring the minimum minimorum mechanical work for the boundary value problem considered, but it will be the closest among the available options. In that way, the refinement of the FE mesh makes it possible to approximate the actual cracking pattern more closely, and, therefore, the proposed modelling approach is mesh convergent. Nonetheless, previous studies of cracking processes with this approach, though considering cement-based materials, suggested that the macroscopic response is not significantly influenced by the precise location of the cracks as long as the initial layout of interfaces is 'reasonable', i.e., it includes all major potential cracking paths without excessive tortuosity Carol et al. (2001); Garello (1999); López et al. (2008). In any case, a post-process analysis of the evolution of the stress state in the continuum elements and a mesh sensitivity analysis must be always conducted to assess the suitability of the proposed mesh and propose a new discretisation, if needed.

The interface elements adopted for this model are of the triple-node type (Figure 2.79). The top and bottom face nodes, which are shared with the adjacent continuum elements, have four degrees of freedom (x, y coordinates, liquid phase pressure p_w, and gas phase pressure p_g), while inner nodes have only two (p_w and p_g). (Interface elements of the double-node type are those which only have nodes on the top and bottom faces.) The insertion of these elements in conventional FE meshes is performed with a separate programme which has been developed adapting the algorithm proposed by Nguyen (2014).

The flow problem is treated in the typical theoretical framework for isothermal two-phase flow in porous media, considering two chemical species (water and gas) and two fluid phases (liquid and gas phases). The liquid phase includes both liquid water and dissolved gas species, while the gas phase only comprises gas species, i.e. water vapour is not considered. The mechanical problem is treated with an updated Lagrangian formulation, i.e. geometric non-linearity is taken into account. Finite strain theory is considered for the continuum elements, though small tangential relative displacements are assumed for the discontinuities. In the latter, a node-to-node discretisation of the contact area is used. In a first approach, simple

constitutive laws are considered for both types of elements. The continuum medium is assumed to behave linear-elastically, while a simple bilinear elasto-damage law is used for the discontinuities, which is formulated in terms of relative displacements rather than strains. Note that the use of a cohesive-type constitutive relation to represent fracture leads to an automatic regularisation from the viewpoint of objectivity of the mechanical (fracture) problem with mesh refinement Carol et al. (2001), which is a significant advantage of the proposed modelling approach. In establishing the equilibrium equation, quasi-static conditions are assumed, i.e., dynamic forces are neglected. Since the model will be mainly used to simulate injection tests in samples of a few centimetres, body (gravity) forces are neglected.

The coupling between the mechanical and the flow formulations occurs in both directions. On one hand, the fluid phase pressures and the saturation degree are introduced in the mechanical equilibrium equation through the principle of effective stress. On the other hand, the flow properties (gas-entry value, storage capacity, longitudinal transmissivity and diffusivity) vary dramatically, governed largely by the mechanical aperture of the discontinuity. To deal with these strong couplings, a monolithic (fully coupled) numerical implementation is used.

The continuum medium part of the model follows the formulation proposed by Collin et al. (2002a) and Gerard et al. (2008a), without introducing significant changes. In contrast, for modelling the discontinuities a new triple-node PHM interface element has been developed using a node-to-node discretisation of the contact problem. The new interface element borrows concepts from previous works by Segura and Carol Segura and Carol (2004, 2008a,b), who developed a double-node HM interface element with node-to-node contact discretisation, and by Cerfontaine et al. Cerfontaine et al. (2015) and Dieudonné et al. Dieudonné et al. (2015), who developed a triple-node PHM interface element with segment-to-segment contact discretisation. Although the new interface element is presented in 2D, the formulation developed is valid and readily extensible to 3D.

In the segment-to-segment contact discretisation, the zones at each side of the discontinuity that are going to interact with each other are not defined a priori and may change during the simulation. For that reason, elements with segment-to-segment contact discretisation are able to model large relative displacements properly, although at the expense of a high computational cost. In contrast, in the node-to-node contact discretisation, the interacting zones at each side are defined a priori and are assumed to remain the same during the simulation. This assumption leads to a much lower computational cost, although restricting the applicability of this kind of element to problems with small tangential relative displacements. A brief review on contact discretisation methods can be found in Cerfontaine et al. (2015).

Note that the systematic use of interface elements all over the mesh, as illustrated in Figure 2.79, has the disadvantage of significantly increasing the number of degrees of freedom in comparison with standard continuum analysis. For the 2D analyses presented in this paper this increase of the computational cost can be afford, but 3D analysis would require a remedy. For instance, Pandolfi and Ortiz (1998) proposed a procedure based on calculation of inter-element forces to duplicate nodes and insert interface elements as needed.

2.4.3. PHM governing equations for the continuum porous medium

Mechanical problem

After neglecting the body forces, the linear momentum balance equation of the continuum porous medium reads as follows:

$$\nabla \cdot \boldsymbol{\sigma} = \mathbf{0} \tag{2.77}$$

where $\boldsymbol{\sigma}$ [Pa] is the Cauchy's total stress tensor. The sign convention of continuum mechanics (i.e. tensile stress is positive) is used in this paper.

The constitutive behaviour of the continuum porous medium is formulated in terms of the effective stress tensor $\boldsymbol{\sigma}'$ and its conjugate strain tensor ε. The material is assumed isotropic and linear elastic, with parameters E [Pa] (Young's modulus) and ν (Poisson's coefficient). The effective stress results from considering the effect of the pore fluid pressures acting on the solid grains of the porous medium via the following expressions:

$$\boldsymbol{\sigma}' = \boldsymbol{\sigma} + \mathbf{b}\mathbf{p_s}\mathbf{I} \tag{2.78}$$

$$p_s = S_w p_w + S_g p_g \tag{2.79}$$

where b is the Biot's coefficient, **I** is the identity tensor, and p_s [Pa] is the effective pore pressure, and p_π [Pa] and S_π [m^3/m^3] are the pressure and pore saturation degree of the fluid phase π (π = w for the liquid phase and π = g for the gas phase), respectively. The liquid saturation degree is obtained as a function solely of the capillary pressure ($p_c = p_g - p_w$), as it is described below. Since the pore space is assumed to be fully saturated with the liquid and gas phases, $S_g = 1 - S_w$.

Flow problem

Mass balance

The mass balance equations of gas and water species in a REV of porous medium are given by:

$$\frac{\partial}{\partial \mathbf{t}}\left(\mathbf{n}\mathbf{S_w}\rho_{\mathbf{ww}}\right) + \nabla \cdot \mathbf{q_w} = 0 \tag{2.80}$$

$$\frac{\partial}{\partial \mathbf{t}}\left(\mathbf{n}\mathbf{S_w}\rho_{\mathbf{gw}} + \mathbf{n}\mathbf{S_g}\rho_{\mathbf{gg}}\right) + \nabla \cdot \mathbf{q_g} = 0 \tag{2.81}$$

where n is the porosity, $\rho_{\varsigma\pi}$ [kg/m^3] is the mass concentration of ς species in the fluid phase π, and $\mathbf{q}_\varsigma$ [$kg/(m^2\,s)$] is the average mass flow vector of the ς species. Note that w and g subindexes (in Italic type) are used to denote the liquid and gas phases, while w and g subindexes (in Roman type) are used to denote water and gas species. The storage terms in Eqs. (2.80) and (2.81) couple the mechanical and the flow formulations via the porosity rate, which is obtained with the following expression:

$$\frac{\partial n}{\partial t} = (n - b)\left(C_s \frac{\partial p_s}{\partial t} + \frac{\partial \varepsilon_v}{\partial t}\right) \tag{2.82}$$

where C_s [1/Pa] is the compressibility (the inverse of the bulk modulus) of the solid grains, and $\varepsilon_v = \mathrm{tr}(\varepsilon)$ is the volumetric strain of the porous medium.

Equations of state

Only one species is considered in the gas phase, so the density of the gas phase and the density of gas species in the gas phase are the same, i.e. $\rho_{gg} = \rho_g$. Then, assuming ideal gas behaviour, the density of the gas phase is obtained as follows:

$$\rho_g = \frac{M_g}{RT} p_g \tag{2.83}$$

where M_g [kg/mol] is the molar weight of the gas species, R = 8.314 [$(m^3Pa)/(Kmol)$] is the gas constant, T [K] is the system temperature.

The mass of gas species dissolved per a unit volume of liquid phase (ρ_{gw} [kg/m^3]) is obtained, assuming local equilibrium, with the following Henry's law equation:

$$\rho_{gw} = H\rho_g \tag{2.84}$$

where H is the dimensionless Henry solubility constant for the gas species in liquid water. It is assumed that the dissolved gas has a negligible effect on the density of the liquid phase, and therefore, it is considered that $\rho_{ww} = \rho_w$.

The liquid phase density is assumed to depend linearly on the liquid phase pressure according to the following expression:

$$\rho_w = \rho_{w,o}\left[1 + C_w\left(p_w - p_{w,o}\right)\right] \tag{2.85}$$

where $\rho_{w,o}$ [kg/m^3] and C_w [1/Pa] are the water density and compressibility, respectively, at the reference pressure $p_{w,o}$.

Mass flows

The mass flow vectors in Eqs. (2.80) and (2.81) can be expanded as follows:

$$\mathbf{q}_w = \rho_{ww}\mathbf{v}_w \tag{2.86}$$

$$\mathbf{q}_g = \rho_{gw}\mathbf{v}_w + \rho_{gg}\mathbf{v}_g + \mathbf{i}_{gw} \tag{2.87}$$

where $\mathbf{v}_\pi$ [m/s] is the average (Darcy) velocity of the fluid phase π, and $\mathbf{i}_{gw}$ [kg/(m^{2}s)] is the average diffusive flow of gas species dissolved in the pore water.

The average fluid phase velocities are obtained with the following two-phase generalisation of Darcy's law:

$$v_\pi = -\frac{k_{\pi,r}}{\mu_\pi}\mathrm{k}\nabla p_\pi \quad \text{for } \pi = w, g \tag{2.88}$$

where k [m^2] is the intrinsic permeability tensor of the porous medium, μ_π [Pa s] is the dynamic viscosity of the fluid phase π, and $k_{\pi,r}$ is the dimensionless relative permeability coefficient, which ranges between 0 and 1 as a function solely of S_π.

The average diffusive flow vector of gas species in the pore water is obtained with following generalisation of Fick's law for an unsaturated porous medium:

$$\mathbf{i}_{gw} = -nS_w\tau D_{gw}\rho_w\nabla\left(\frac{\rho_{gw}}{\rho_w}\right) \tag{2.89}$$

where D_{gw} [m^2/s] is the diffusion coefficient of the gas species in bulk water, and τ is a dimensionless coefficient accounting for the effect of the tortuosity of the pore space.

Liquid retention and relative permeability

The retention behaviour of the continuum porous medium has been chosen, for simplicity, to be represented with the standard van Genuchten's model:

$$S_w\left(p_c\right) = \left(1 - S_{wr}\right)\left[1 + \left(\frac{\langle p_c - p_{ev}\rangle}{p_b}\right)\frac{1}{1-\lambda}\right]^{-\lambda} + S_{wr} \tag{2.90}$$

where S_{wr} is the residual degree of saturation, p_{ev} [Pa] is the gas-entry value, and p_b [Pa] and λ are a parameters that controls the shape of the curve.

The relative permeability coefficients for the liquid and gas phases are considered to be functions of the effective degree of saturation (S_e) according to the following power laws:

$$k_{w,r} = S_e^{n_w}; \quad k_{g,r} = \left(1 - S_e\right)^{n_g} \tag{2.91}$$

where n_w and n_g are dimensionless material parameters and

$$S_e = \frac{S_w - S_{wr}}{1 - S_{wr}} \tag{2.92}$$

2.4.4. PHM governing equations for the discontinuities

Mechanical problem

The equilibrium condition for a discontinuity is posed for a local basis with direction normal normal ($\mathbf{e_n}$) and tangential ($\mathbf{e_l}$) to the discontinuity mid-plane, as follows:

$$\frac{\partial \boldsymbol{\sigma}}{\partial l} = \mathbf{0} \tag{2.93}$$

where $\boldsymbol{\sigma} = \begin{bmatrix}\sigma_n & \sigma_l\end{bmatrix}^T$ is the total stress on the discontinuity mid-plane, with components normal (σ_n) and tangential (σ_l) to the discontinuity mid-plane (Figure 2.80).

The constitutive behaviour is formulated in terms of the effective stress $\boldsymbol{\sigma}' = \begin{bmatrix}\sigma'_n & \sigma_l\end{bmatrix}^T$ and the conjugate relative displacement $\mathbf{r} = \begin{bmatrix}r_n & r_l\end{bmatrix}^T$ (Figure 2.80). The effective stress is defined as follows:

$$\boldsymbol{\sigma}' = \boldsymbol{\sigma} + \mathbf{m} p_s \tag{2.94}$$

where p_s [Pa] is the effective fluid pressure at the discontinuity mid-plane, and $\mathbf{m} = \begin{bmatrix}1 & 0\end{bmatrix}^T$.

The effective fluid pressure is obtained as a function of the saturation degree and the fluid phase pressures with the same expression as for the continuum porous medium (Eq. (2.79)). However, here the liquid saturation degree is obtained not only as a function of the capillary pressure, but also of the normal separation (r_n), as it is discussed below. As for the continuum medium, the discontinuity is assumed to be fully saturated with the liquid and gas phases, i.e. $S_g = 1 - S_w$.

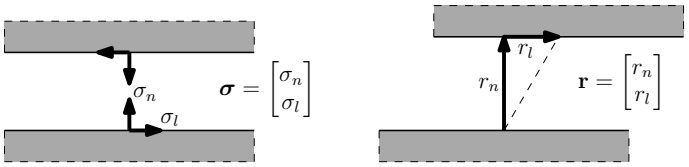

Figure 2.80: Definition of stress and conjugate relative displacement variables for a discontinuity.

In principle, the solid domains at both sides of the discontinuity cannot overlap each other, i.e. the normal relative displacement (r_n) cannot be negative. This strict condition, which would be very demanding for the numerical resolution of the problem, is relaxed by authorising a small interpenetration of the solids in contact using the penalty method. The interpenetration is limited in the constitutive law (see below the formulation of the constitutive law) by assigning a very high normal stiffness for $r_n < 0$.

Constitutive law

The mechanical constitutive behaviour of the discontinuity is modelled using the elasto-damage law proposed by Mi et al. Mi et al. (1998), combined with a Newtonian damper for the normal direction. The response of the elasto-damage law for pure normal (Mode I) and pure shear (Mode II) loading is schematically depicted in Figure 2.81. Three parameters characterise each of these constitutive curves: the maximum tensile/shear strength (σ_{n0}, σ_{l0}), the normal/tangential 'cracking' separation (r_{n0}, r_{l0}) and the normal/tangential debonding separation (r_{nc}, r_{lc}). The dashed lines in Figure 2.81a and b indicate the unloading-reloading path after reaching relative displacements r_n^* and r_l^*, respectively.

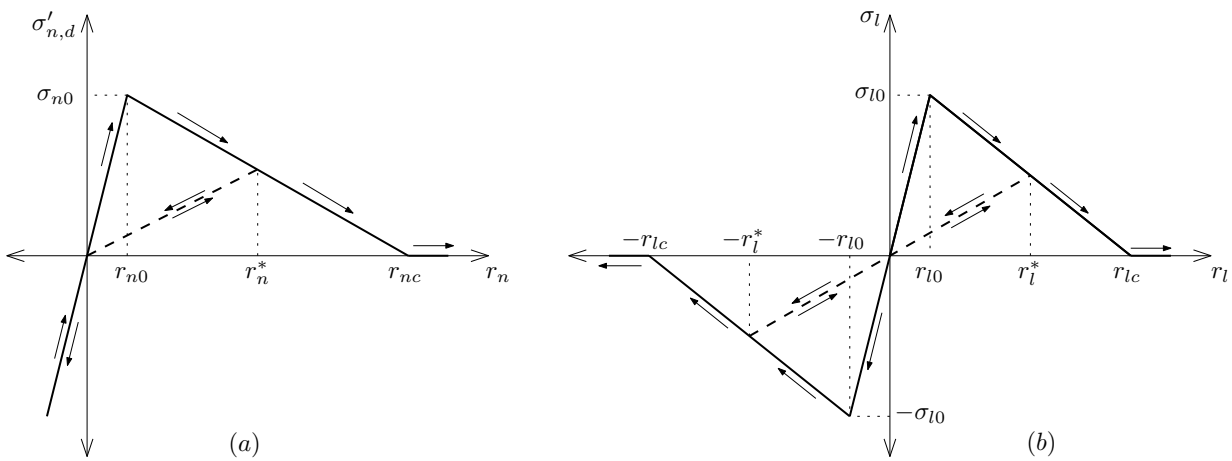

Figure 2.81: Constitutive relationships for (a) pure normal loading and (b) pure tangential loading.

In the general (mixed mode) loading condition, normal and tangential stresses are obtained with the following expressions:

$$\sigma'_{n,d} = \begin{cases} (1-D)\,K_n r_n & \text{if } r_n \geq 0 \\ K_n r_n & \text{if } r_n < 0 \end{cases} \tag{2.95}$$

$$\sigma_l = (1-D)\,K_l r_l \tag{2.96}$$

where $K_n = \sigma_{n0}/r_{n0}$ and $K_l = \sigma_{l0}/r_{l0}$ are the initial (very high) normal and tangential stiffness, respectively. In the context of this paper, these coefficients should be interpreted as penalty coefficients that must be set to values as high as possible without causing numerical problems, in order to reduce the artificial compliance introduced by the interface elements to negligible values.

Equations (2.95) and (2.96) are coupled through the damage variable D. The damage variable, which ranges between 0 and 1, accounts for the material softening when the normal and/or the tangential separation goes beyond the cracking separation, and it is obtained from the following expressions:

$$D = \min\left(\frac{\bar{\omega}}{1+\bar{\omega}}\frac{1}{\eta}, 1\right) \tag{2.97}$$

$$\bar{\omega} = \max(\omega) \tag{2.98}$$

$$\omega = \left\langle \left[\left(\frac{\langle r_n \rangle}{r_{n0}}\right)^{\beta} + \left(\frac{|r_l|}{r_{l0}}\right)^{\beta} \right]^{1/\beta} - 1 \right\rangle \tag{2.99}$$

$$\eta = 1 - \frac{r_{n0}}{r_{nc}} = 1 - \frac{r_{l0}}{r_{lc}} \tag{2.100}$$

where ω is a positive scalar that accounts for the mechanical degradation of the discontinuity for a given combination of normal and tangential separations, β is a material parameter that characterises the mixed mode damage and which will generally assume values between 1 and 2 (in this paper $\beta = 1$), $\bar{\omega}$ is a history variable that stores the maximum value reached by ω in the loading history, and $\langle \bullet \rangle = \left(\bullet + |\bullet|\right)/2$ is the Macaulay bracket. The restriction to the material parameter ratios r_{n0}/r_{nc} and r_{l0}/r_{lc} established in Eq. (2.100) guarantees that the tensile and shear strength are exhausted simultaneously.

Note in Eq.(2.95) that, under compression loading, the constitutive response is always determined by the (very high) initial stiffness K_n, regardless the damage state of the discontinuity. In that way, the possible overlapping of the solid domains at both sides of the discontinuity under compressive loads is kept small (i.e. the penalty method). Moreover, according to Eq. (2.100), no damage is induced by negative normal separations.

Finally, the effective stress in the normal direction is obtained by adding a viscous component as follows:

$$\sigma'_n = \sigma'_{n,d} + \sigma'_{n,v} \quad \text{with } \sigma'_{n,v} = \zeta \frac{\partial r_n}{\partial t} \tag{2.101}$$

where ζ [Pa s/m] is the viscosity. The viscous term is included to address numerical instabilities that may develop under certain conditions Liaudat et al. (2023).

Flow problem

The formulation of the flow problem is derived by considering a discontinuity of width w [m] surrounded by the continuum porous medium, and a local orthogonal coordinate system defined by the directions tangent ($\mathbf{e_l}$) and normal ($\mathbf{e_n}$) to the discontinuity (Figure 2.82). Flow of the water and gas species may occur both in the longitudinal and in the transversal directions to the discontinuity. For the sake of simplicity, it is assumed that the longitudinal flows depend on the gas and liquid phase pressures at the centre (mid-plane) of the discontinuity width w. Consistently, the remaining parameters/variables of the discontinuity are also computed at the mid-plane, but assumed to be valid across the discontinuity width.

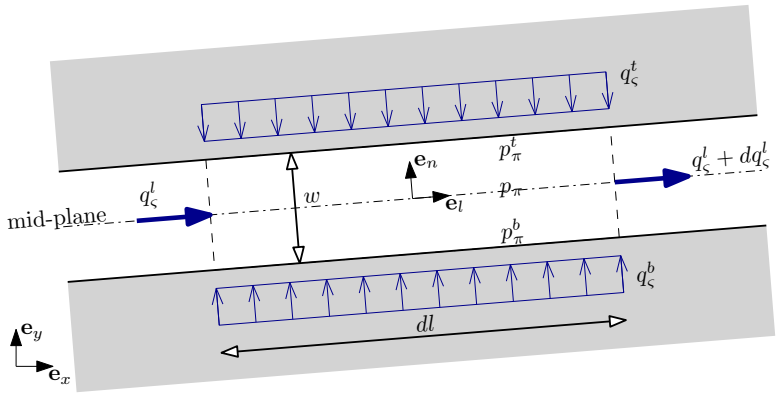

Figure 2.82: Flow problem definition for a 2D discontinuity, for fluid phases π = w, g and chemical species ς = w, g.

Mass balance

The mass balance of gas and water species is enforced in a differential volume of discontinuity wdl as follows:

$$\frac{\partial}{\partial t}\left(wS_w\rho_{ww}\right) + \frac{\partial q_w^l}{\partial l} - q_w^b - q_w^t = 0 \tag{2.102}$$

$$\frac{\partial}{\partial t}\left(wS_g\rho_{gg} + wS_w\rho_{gw}\right) + \frac{\partial q_g^l}{\partial l} - q_g^b - q_g^t = 0 \tag{2.103}$$

where q_ς^l [kg/(m s)] is the longitudinal mass flow of species ς, and q_ς^b and q_ς^t [kg/(m^2 s)] are the normal mass flows incoming to the discontinuity from the surrounding continuum medium. The densities $\rho_{\varsigma\pi}$ [kg/m^3] are evaluated using the same equations of state as for the continuum medium (see above). The liquid saturation degree is obtained as a function of the capillary pressure and the normal aperture (r_n), as it is described below. Note that in Eqs. (2.102) and (2.103) the change of the storage capacity due to the possible change of the discontinuity length has been neglected.

The discontinuity width will evolve with r_n as follows:

$$w = \langle r_n \rangle + w_0 \tag{2.104}$$

where w_0 [m] makes it possible to assign an initial storage volume to the discontinuity even if it is mechanically closed.

The mass flows of gas species may be expanded as follows:

$$\begin{aligned} q_g^l &= \rho_g v_g^l + \rho_{gw} v_w^l + i_{gw}^l \\ q_g^b &= \rho_g v_g^b + \rho_{gw} v_w^b + i_{gw}^b \\ q_g^t &= \rho_g v_g^t + \rho_{gw} v_w^t + i_{gw}^t \end{aligned} \tag{2.105}$$

where v_π^l [m^2/s], v_π^t [m/s] and v_π^b [m/s] are the longitudinal and transversal volumetric flows (top and bottom) of phase π, and i_{gw}^l [$kg/(m\,s)$], i_{gw}^b [$kg/(m^2\,s)$] and i_{gw}^t [$kg/(m^2\,s)$] are the longitudinal and normal diffusion fluxes of gas species dissolved in the liquid phase.

Similarly, the mass flows of water species are expanded as follows:

$$q_w^l = \rho_w v_w^l; \qquad q_w^b = \rho_w v_w^b; \qquad q_w^t = \rho_w v_w^t; \tag{2.106}$$

Volumetric fluid phase flows

The longitudinal volumetric fluid phase flows in Eqs. (2.105) and (2.106) are obtained from the following generalised Darcy's law:

$$v_\pi^l = -\frac{k_{\pi,r}}{\mu_\pi} t^l \frac{\partial p_\pi}{\partial l} \tag{2.107}$$

where $k_{\pi,r}$ and μ_π [Pa s] are the relative permeability and the dynamic viscosity of the fluid phase π, respectively, and t^l [m^3] is the longitudinal hydraulic coefficient.

Similarly, the transversal volumetric flows are assumed to be proportional to the transversal pressure drops $\check{p}_\pi^b$ and $\check{p}_\pi^t$ between the discontinuity boundaries and the mid-plane, namely:

$$v_\pi^b = -\frac{k_{\pi,r}}{\mu_\pi} k^b \check{p}_\pi^b \quad \text{for } \pi = w, g \tag{2.108}$$

$$v_\pi^t = -\frac{k_{\pi,r}}{\mu_\pi} k^t \check{p}_\pi^t \quad \text{for } \pi = w, g \tag{2.109}$$

where k^b and k^t [m] are the transversal hydraulic coefficients. The transversal pressure drops are defined as follows:

$$\check{p}_\pi^b = p_\pi - p_\pi^b; \qquad \check{p}_\pi^t = p_\pi - p_\pi^t \tag{2.110}$$

where p_π^b, p_π, and p_π^t [Pa] are the fluid phase pressures at the bottom side, mid-plane and top side of the discontinuity, respectively. With this definition, the transversal flows obtained with Eqs. (2.108) and (2.109) are positive when they go into the discontinuity, regardless of whether they enter through the top or the bottom face.

The hydraulic coefficients t^l, k^b and k^t are considered to be determined by the geometric characteristics of the discontinuity. In this sense, they play the role of the intrinsic permeability in the formulation for the continuum porous medium. The longitudinal coefficient is estimated as a function of the discontinuity normal aperture with the following expression:

$$t^l = \frac{\langle r_n \rangle^3}{12} + t_0^l \tag{2.111}$$

where the first term is given by the Hagen-Poiseuille equation for laminar flow between two parallel plates, and t_0^l makes it possible to assign an initial longitudinal transmissivity to the discontinuity even if it is closed from the mechanical point of view. In contrast, the transversal coefficients k^b and k^t are deemed constant parameters.

Diffusion of gas in the liquid phase

The longitudinal diffusive flow of gas species dissolved in the liquid phase, i_{gw}^l [kg/(m s)], is obtained with the following generalised Fick's law:

$$i_{gw}^l = -S_w D_{gw} d^l \rho_w \frac{\partial}{\partial l}\left(\frac{\rho_{gw}}{\rho_w}\right) \tag{2.112}$$

where D_{gw} [m^2/s] is the diffusion coefficient of the gas species in bulk water, and d_l [m] is a coefficient that accounts for the effect of the discontinuity geometry on the the diffusive flux (analogous to the product of porosity and tortuosity in the continuum medium formulation). The coefficient d^l is obtained as a linear function of the normal aperture as follows:

$$d^l = \langle r_n \rangle + d_0^l \tag{2.113}$$

where d_0^l makes it possible to assign an initial longitudinal diffusivity to the discontinuity even if it is closed from the mechanical point of view. This expression is based on the assumption that diffusion occurs along a clean channel of width $\langle r_n \rangle$ configured by the two faces of the discontinuity.

Considering Henry's law (Eq. (2.84)) and expanding the derivative, Eq. (2.112) can be rewritten in terms of the longitudinal gradients of gas and liquid pressures as follows:

$$i_{gw}^l = -S_w d^l D_{gw}\left(H\frac{\partial \rho_g}{\partial p_g}\frac{\partial p_g}{\partial l} - \frac{\rho_{gw}}{\rho_w}\frac{\partial \rho_w}{\partial p_w}\frac{\partial p_g}{\partial l}\right) \tag{2.114}$$

In addition to the longitudinal diffusive flux, normal fluxes i_{gw}^b and i_{gw}^t [kg/(m^2 s)] from the bottom and top sides of the discontinuity, respectively, are considered. These fluxes are obtained as follows:

$$i_{gw}^b = -S_w D_{gw} \tau^b \left(\rho_{gw} - \rho_{gw}^b\right) \tag{2.115}$$

$$i_{gw}^t = -S_w D_{gw} \tau^t \left(\rho_{gw} - \rho_{gw}^t\right) \tag{2.116}$$

where ρ_{gw}^b, ρ_{gw} and ρ_{gw}^t represent the mass concentration of gas species in the liquid phase at the bottom side, the mid-plane and the top side of the discontinuity, respectively, and τ^b and τ^t [1/m] are constant coefficients that account for the effect of the discontinuity geometry in the effective transversal diffusivities. These expressions are obtained under the assumption that the liquid phase density is constant across the discontinuity. As for the transversal fluid flows, the transversal diffusive flows are positive when they go into the discontinuity.

Finally, considering Henry's law (Eq. (2.84)) and assuming that the gas has an ideal behaviour, Eqs. (2.115) and (2.116) can be rewritten in terms of the normal gas pressure jumps (Eqs. (2.108) and (2.109)) as follows:

$$i_{gw}^b = -S_w D_{gw} \tau^b H \frac{\partial \rho_g}{\partial p_g} \breve{p}_g^b \tag{2.117}$$

$$i_{gw}^t = -S_w D_{gw} \tau^t H \frac{\partial \rho_g}{\partial p_g} \breve{p}_g^t \tag{2.118}$$

Liquid retention and relative permeability

Similarly to the continuum medium, the liquid retention of the discontinuity is also modelled with a van Genuchten curve. However, the assumption made for the continuum medium that the curve parameters will remain constant since the expected variation of the pore space is small is revised for discontinuities, where the 'pore' space filled with the fluid phases will vary dramatically with the normal aperture. In order to introduce this effect, Eq. (2.90) is rewritten in terms of functions $\bar{p}_b(r_n)$ and $\bar{S}_{wr}(r_n)$ instead of constant parameters p_b and S_{wr}, i.e.

$$S_w(p_c, r_n) = \left(1 - \bar{S}_{wr}\right)\left[1 + \left(\frac{\langle p_c - \bar{p}_{ev}\rangle}{\bar{p}_b}\right)\frac{1}{1-\lambda}\right]^{-\lambda} + \bar{S}_{wr} \tag{2.119}$$

Note that the parameter λ is still deemed a constant parameter.

In order to obtain functions $\bar{p}_{ev}(r_n)$, $\bar{p}_b(r_n)$ and $\bar{S}_{wr}(r_n)$, two possible states of the discontinuity are considered: closed, when $r_n \leq 0$, and open, when $r_n > 0$. As stated in above, one of the premises of the proposed modelling approach is that the interface elements representing potential cracking paths must not have any significant effect in the overall behaviour of the modelled material, as long as they remain closed. In other words, in closed state, the retention curve of the discontinuity must be the same as the one for the continuum medium. This implies that for $r_n \leq 0$, $\bar{p}_b = p_b$ and $\bar{S}_{wr} = S_{wr}$. In contrast, in the open state, the parameter $\bar{p}_b$, which is linked to the gas-entry value, and the parameter $\bar{S}_{wr}$, which accounts for the fraction of the discontinuity volume occupied by immobile (residual) liquid, is expected to decrease for increasing r_n.

In order to derive $\bar{p}_b(r_n)$ in the open state, first consider the Laplace equation to estimate the gas-entry value of the porous medium:

$$p_{ev} = T_s\left(\frac{1}{R_1} + \frac{1}{R_2}\right) \tag{2.120}$$

where T_s [N/m] is the liquid-gas interfacial tension, and R_1 and R_2 [m] are the curvature radii of the gas-liquid interface. Assuming that $R_1 = R_2 = d/2$, a characteristic pore size of the porous medium can be obtained as $d = 4T_s/p_{ev}$. Likewise, the gas-entry value of an open discontinuity ($\bar{p}_{ev}$) is approximated with the same Laplace's equation, but with $1/R_1 = 0$ and $R_2 = d/4 + \bar{r}/2$, i.e.

$$\bar{p}_{ev} = \frac{2T_s}{d/2 + \bar{r}} = \frac{d}{d + 2\bar{r}}p_{ev} \tag{2.121}$$

where $\bar{r}$ [m] represents the effective aperture of the discontinuity. In a strict sense, $\bar{r}$ should be the positive part of r_n. However, in order to prevent numerical problems, $\bar{r}$ is obtained as follows:

$$\bar{r}(r_n) = \langle r_n\rangle - \alpha\left[1 - \exp\left(\frac{-\langle r_n\rangle}{\alpha}\right)\right] \tag{2.122}$$

where the third term gives C^1 continuity to the function $\bar{r}(r_n)$ and makes it possible to smooth the transition between closed ($r_n \leq 0$) and open ($r_n > 0$) states by increasing the positive parameter α. Then, by assuming that $\bar{p}_b$ will evolve in proportion to $\bar{p}_{ev}$, the first expression sought is obtained:

$$\bar{p}_b = \frac{d}{d + 2\bar{r}}p_b \tag{2.123}$$

The second expression sought ($\bar{S}_{wr}$) is obtained by assigning an initial volume of immobile liquid phase to the discontinuity in closed state, and assuming that this volume will not grow nor decrease if the normal aperture becomes positive. Considering the pore volume associated to the closed discontinuity is nd,

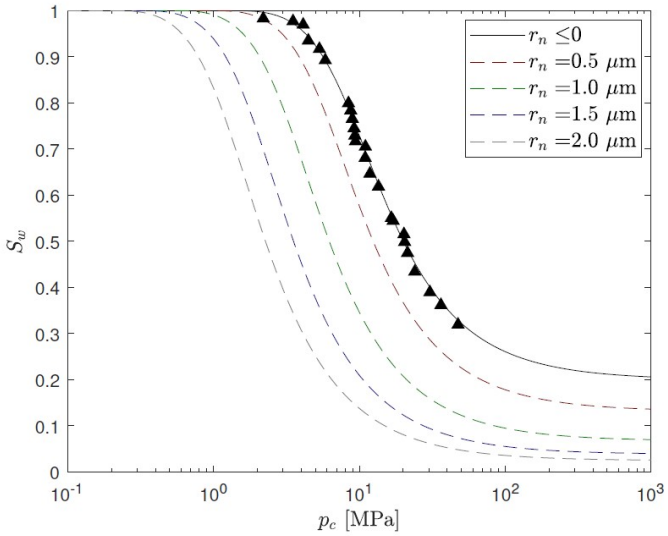

Figure 2.83: Liquid retention curves for discontinuities in Boom clay with different normal aperture. The solid line corresponds to the bulk porous medium or a closed discontinuity ($r_n \leq 0$), while dashed lines correspond to discontinuities with increasing aperture ($r_n > 0$). Markers indicate experimental psychrometer measurements of intact Boom clay from Gonzalez-Blanco et al. (2016a).

where n is the porosity of the porous medium and d is the above defined characteristic pore size, the volume of immobile liquid phase is estimated as $S_{wr} nd$. Then, considering the updated 'pore' volume of the discontinuity will be $nd + \bar{r}$, the residual saturation degree of the discontinuity will evolve as follows:

$$\bar{S}_{wr} = \frac{nd}{nd + \bar{r}} S_{wr} \tag{2.124}$$

Finally, the relative permeabilities are obtained with the same expressions used for the continuum medium (Eq. (2.91)), but introducing in the expression of the effective saturation the effect of the normal aperture in the residual saturation as obtained from Eq. (2.124), i.e.

$$S_e = \frac{S_w - \bar{S}_{wr}}{1 - \bar{S}_{wr}} \tag{2.125}$$

The proposed retention and relative permeability functions are illustrated in Figure 2.83 and Figure 2.84, respectively, which show their evolution for increasing values of r_n. The parameters used were $n = 0.39$, $p_{ev} = 1.5\,\text{MPa}$, $p_b = 7.5\,\text{MPa}$, $S_{wr} = 0.20$, $\lambda = 0.50$, $\alpha = 3{,}000\,\text{nm}$, $n_w = 1.5$, and $n_g = 3.0$. These parameters were calibrated for $r_n = 0$ with experimental data from bulk Boom clay Gonzalez-Blanco et al. (2016a); Volckaert et al. (1995b). A standard value of $T_s = 72.7\,\text{mN/m}$ corresponding to an air-water interface at $20\,^\circ\text{C}$ is adopted Vargaftik et al. (1983).

2.4.5. Finite Element implementation

The model outlined in the previous sections has been implemented in the FE code LAGAMINE. The porous medium equations have been discretised with a large strain element type, which is described in detail in Collin et al. (2002a). This element has five degrees of freedom at each node (x and y coordinates, liquid pressure, gas pressure and temperature), though the temperature is fixed for the model proposed in this paper. The implementation of this element in LAGAMINE allows the use of shape functions of different order to interpolate the nodal displacements and pore pressures, in order to comply with the Ladyzhenskaya-Babuška-Brezzi stability condition Arnold (1990); Brezzi and Bathe (1990). However, in the simulations performed for this paper the same parabolic shape functions has been used to interpolate displacements and fluid pressures, without observing spurious pressure oscillations or sub-optimal convergence behaviour. The nodal fluxes and forces are obtained after writing the integral forms of Eqs. (2.77),

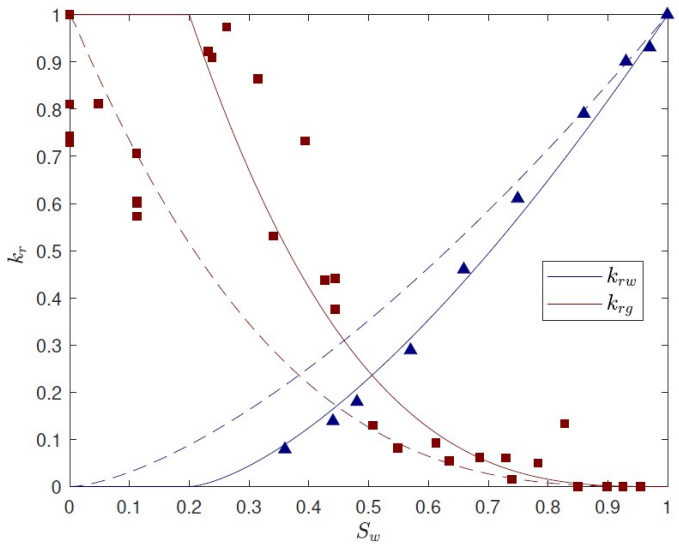

Figure 2.84: Relative permeability functions for discontinuities in Boom Clay. Solid lines correspond to the bulk porous medium or a closed discontinuity ($r_n \leq 0$), while dashed lines correspond to a discontinuity with a large aperture ($r_n = 10\,\mu m$). Markers indicate experimental data from Volckaert et al. (1995b) for intact Boom Clay only.

(2.80) and (2.81), and applying the Principle of Virtual Work (Collin, 2003b). To increase the numerical stability, nodal water and gas flows, and the corresponding stiffness sub-matrices are always computed in the initial configuration. The so-called tangential stiffness matrix of the coupled element is monolithic, including all the coupling terms and second order effects due to geometry variation (Collin, 2003b).

For the discontinuity equations, a new triple-node zero-thickness interface element has been formulated and implemented in LAGAMINE. The node numbering and nodal degrees of freedom are shown in Figure 2.85 for a quadratic element. Note that the outer nodes (labelled t and b) are considered for both the mechanical and the flow problems, while the inner nodes (labelled m) are only considered for the flow problem. The FE formulation of the mechanical problem is developed with an updated Lagrangian approach and with a node-to-node discretisation of the contact area, by adapting the formulation outlined in Lequesne (2009) for purely mechanical double-node interface elements. In contrast to small displacement formulations where the normal and tangential components of the relative displacements and stresses are obtained with regard to the original configuration, in the proposed update Lagrangian approach the position of the mechanical mid-plane, on which the local basis is defined, is updated in each loading increment. For this reason, the proposed element is suitable for problems in which the interface nodes experience large displacements and rotations, although with small relative displacement between opposite nodes of the same interface because of the node-to-node discretisation of the contact area.

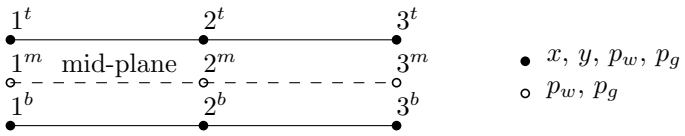

Figure 2.85: Element node numbering and nodal degrees of freedom.

The flow part of the FE formulation has been developed by adapting the coupled HM (single phase) formulation for double-node interface elements proposed in Segura and Carol Segura and Carol (2004, 2008b). In double-node element formulations, the pressure inside the discontinuity is not considered as an independent degree of freedom but assumed to be the average between the pressure at the bottom and top faces. In Liaudat et al. (2023), it is demonstrated that the accuracy of this assumption depends

mainly on the longitudinal fluid pressure profiles and the current values of the longitudinal and transversal hydraulic/diffusion coefficients, which in turn depends on the discontinuity mechanical aperture and the capillary pressure. It is concluded from this analysis, that the error introduced by the average pressure assumption used for double-node elements cannot be estimated a priori. Therefore, developing a triple-node element was preferred to be on the safe side, although at the expense of increasing the computational cost of the model. Moreover, triple-node elements outperform double-node ones in that they allow the user to hydraulically disconnect the continuum medium at one or both sides of the element from the discontinuity channel, just by nullifying the corresponding transversal hydraulic coefficients. In that way, triple-node elements are particularly well-suited for modelling hydraulic interfaces between a permeable medium and an impervious one, e.g. the interface between a clay sample and a metallic testing device. As with the continuum elements, in the proposed interface element the fluid pressure gradients are always computed in the initial configuration.

More comprehensive details of the formulation of the new interface element can be found in Liaudat et al. (2023).

Finally, after assemblage of the continuum and interface element nodal forces and mass fluxes, the mechanical equilibrium and mass balance with the imposed external forces/fluxes is enforced at the end of each time increment, i.e. adopting a backward Euler time integration scheme, using the standard Newton-Raphson Method.

The implementation in LAGAMINE of the new interface element and the corresponding constitutive laws has been systematically verified in simple benchmark problems with analytical solutions. A thorough verification of the continuum part of the model can be found in Collin (2003b).

2.4.6. BGS gas fracturing test on Boom Clay

This section analyses an experiment conducted by the British Geological Survey (BGS) as part of Task 3 within this work package. First, the main aspects of the experiment are summarised. Secondly, the preconditioning of the clay specimen is modelled to assess the influence of the loading history on the conditions at beginning of the gas injection test. Finally, using the state values estimated in the first set of simulations, the gas injection test is simulated, including the development of gas fractures.

2.4.6.1. The experiment

The experiment uses a newly designed apparatus known as the Fracture Visualisation Rig (FVR) (Wiseall et al., 2015, 2019) (see Figure 2.86). The FVR comprises a 110 mm diameter, 50 mm thick fused silica glass window securely held in place by a 230 mm diameter steel collar. This collar, in turn, is secured to a 250 mm diameter steel plate with twelve bolts.

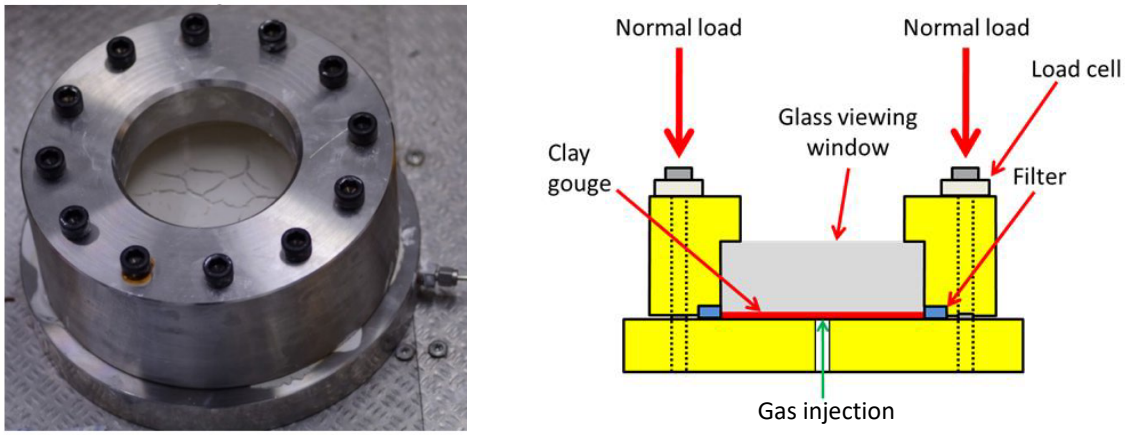

Figure 2.86: BGS Fracture Visualisation Rig (FVR) Wiseall et al. (2015, 2019).

To conduct the experiment, a clay specimen is prepared as a paste in a thin layer between the lower steel platen and the glass window. A porous plastic filter, opened to the atmosphere, holds the clay in place laterally. By tightening the bolts, a vertical load is applied to the clay paste prior to gas injection. The loads applied by three of the twelve bolts are monitored using doughnut load cells positioned between the bolt head and the collar.

Once the desired load level is achieved, gas is injected into the clay paste at the centre of the lower platen at a constant volumetric rate. Gas injection is performed using a high-precision syringe pump connected to a gas-water interface vessel. The formation of gas pathways is continuously monitored by a camera that captures images of the clay specimen through the glass at regular time intervals.

The specific test considered here was performed using Boom clay powder from HADES laboratory, mixed with synthetic pore solution to give a gravimetric water content of 60%. The amount of clay paste placed in the device has not been reported. However, the thickness of the consolidated clay specimen after the test was found to be approximately 1 mm. Helium gas was injected with a volumetric rate of $25\,\mathrm{mL/h}$. At the beginning of gas injection, the gas volume at the gas-water vessel was approximately $50\,\mathrm{mL}$ at a pressure of $0.5\,\mathrm{MPa}$. The vertical consolidation stress just before the the gas injection was approximately $3.4\,\mathrm{MPa}$. This stress level was achieved in a few hours before the gas injection. However, the specific loading path followed was not recorded. As it will be discussed in the following section, this may represent a limitation for the interpretation of the results.

Figure 2.87 shows the time evolution of the gas injection pressure and the average vertical stress, as well

as the cracking pattern approximately at the peak injection pressure. Before the start of the gas injection, a sharp variation of the vertical stress due to the last tightening of the bolts can be appreciated. Previous loading steps has not been recorded. Note that after this last vertical loading increment, the vertical stress underwent a relaxation process as the excess pore pressure induced by the load increment dissipated.

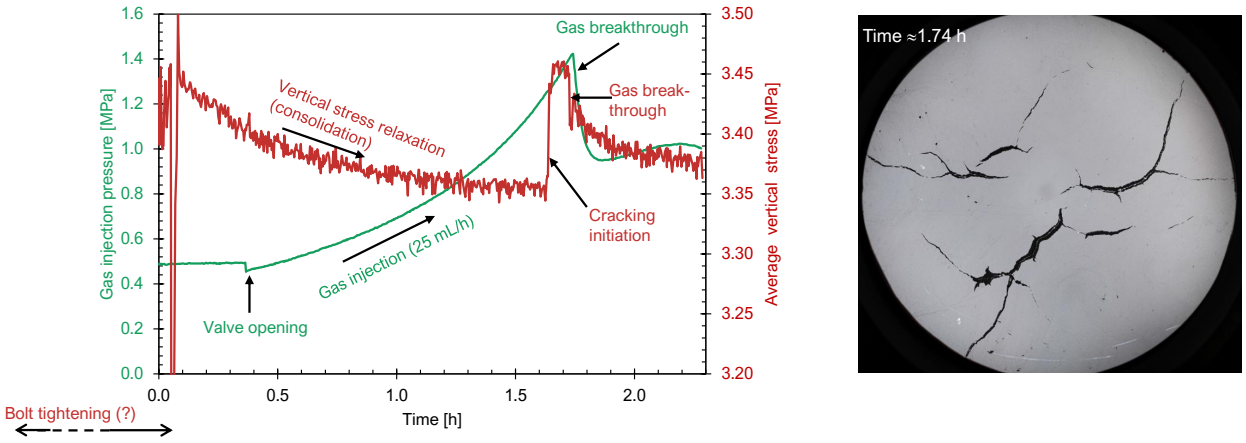

Figure 2.87: BGS gas fracturing test on Boom clay. Left, time evolution of the gas injection pressure and the average vertical stress. Right, cracking pattern at the peak gas pressure.

The initiation of the gas cracking and the subsequent gas breakthrough, when the cracks connected the injection point with the perimeter filter, are indicated in the plot. The cracking initiation is distinguished by a sudden increase in the average vertical stress. The gas breakthrough, in contrast, is appreciated in the synchronous gas pressure and vertical stress drops about 15 minutes later. Subsequently, the system approaches a quasi-steady state before the gas injection stopped.

2.4.6.2. Modelling of specimen conditioning

Figure 2.88 illustrates the axisymmetric FE mesh and boundary conditions used to model the preconditioning of the clay specimen. Three continuum domains are considered: Boom clay paste, sight glass, and a linear elastic block introduced to represent the combined compliance of the steel collar and bolts. Zero-thickness interface elements with segment-to-segment contact representation Cerfontaine et al. (2015) are placed between these domains to allow tangential sliding. The mechanical parameters of the interface elements are such that they offer no resistance to tangential sliding. The initial thickness of the clay paste was calibrated to render a thickness of approximately 1 mm at the end of the preconditioning.

Mechanical boundary conditions prohibit vertical displacements at the bottom boundary and horizontal displacements at the right boundary of the clay domain. The effect of tightening the bolts is simulated as a vertical displacement imposed on top of the equivalent spring. Water flow is only considered in the clay domain, with natural boundary conditions (no flux) at the bottom side, and water pressure fixed to 0.1 MPa at the right side, representing the ring filter connected to the atmosphere.

The fused silica glass and the equivalent spring are assumed to be linear elastic, with the parameters given in Table 2.17. The Young's modulus of the equivalent spring was calculated to render the same stiffness to vertical displacements as the 12 steel bolts of the FVR. The Poisson's ratio is irrelevant since there is no restraint to lateral deformation. The parameters of the glass were retrieved from commercial fused silica data sheets.

The Barcelona Basic Model (BBM) was used as mechanical constitutive law for Boom clay, with the parameters given in Table 2.17. Since the clay remains fully saturated, suction-related parameters are omitted. The elastoplastic volumetric compressibility ($\lambda(0)$) was calculated from the empirical expression for the In-

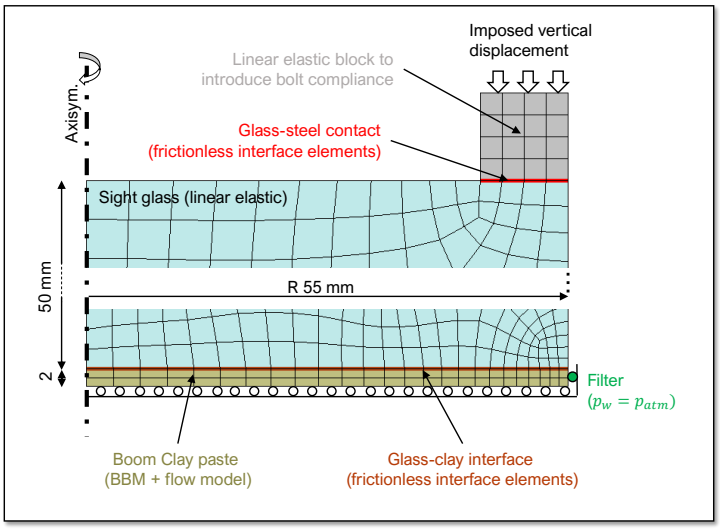

Figure 2.88: Finite Element mesh and boundary conditions for modelling clay consolidation in the FVR.

trinsic Compression Line proposed by Burland (1990), with the parameters calibrated by Deng et al. (2011) for Boom clay. The initial void ratio was obtained from the reported gravimetric water content, assuming full saturation and a solid density of 2.67. The remaining parameters were taken from Gonzalez-Blanco et al. (2016a).

The variation of intrinsic permeability with porosity was introduced via the following function of the Kozeny-Carman type available in Lagamine:

$$k = k_0 \frac{(1 - n_0)^M}{n_0^N} \frac{n^N}{(1 - n)^M} \tag{2.126}$$

where k_0 is the intrinsic permeability for a reference porosity n_0, and M and N are fitting parameters. The parameters of this function, given in Table 2.17, were adjusted to match the empirical permeability–porosity relationship proposed for mudstones by Yang and Aplin (2010), assuming a 40% clay content.

In order to explore the effect of the vertical loading history on the consolidation of the specimen, five simulations were conducted imposing the same vertical displacement in different time lapses, between 7.5 h to 120 h (Figure 2.89a). The time evolution of the total vertical reaction for the different loading rates is given in Figure 2.89b. All five reaction curves show a peak value at the end of the loading ramp due to the development of pore-water excess pressure. Subsequently, this excess pressure dissipates as water flows out radially through the filter, and the total reaction converges to a steady state value. Notably, the steady state vertical reaction is practically the same regardless the loading rate.

In contrast, the radial profiles of porosity and effective stress (Figure 2.89c–e) show significant dependence on the loading rate. In all cases, the consolidation of the specimen is not uniform, with lower dry density at the centre in comparison with the perimeter. However, this radial variation increases with the loading rate.

It shall be noted, that the vertical loading in the real experiment was performed in less than 7.5 h. However, the FE code was unable to successfully simulate faster loading rates. This is because, for such faster loading rates, liquefaction conditions are developed at the centre of the specimen, which cannot been properly handled by the model. Nonetheless, this local liquefaction can be expected to lead to even less uniform consolidation profiles.

Table 2.17: Relevant parameters used in the simulations of the initial conditioning.

Parameter	Symbol	Value
Fused silica glass – Linear elasticity		
Young's modulus	E	73.0 GPa
Poisson ratio	ν	0.33
Equivalent spring – Linear elasticity		
Young's modulus	E	12.3 GPa
Poisson ratio	ν	0.00
Boom clay paste – Barcelona Basic Model (BBM)		
Elastic compressibility against mean stress changes	κ	0.020
Poisson ratio	ν	0.33
Elastoplastic volumetric compressibility	$\lambda(0)$	0.19
Slope of the critical state line	M	0.73
Parameter for the plastic potential	α	0.33
Initial pre-consolidation stress for saturated conditions	p_0^*	0.01 MPa
Initial void ratio	e_0	1.60
Boom clay paste – Kozeny-Karman model		
Reference intrinsic permeability	k_0	5.8×10^{-19} m^2
Reference porosity	n_0	0.33
Exponents	n	5.5
	m	6.0

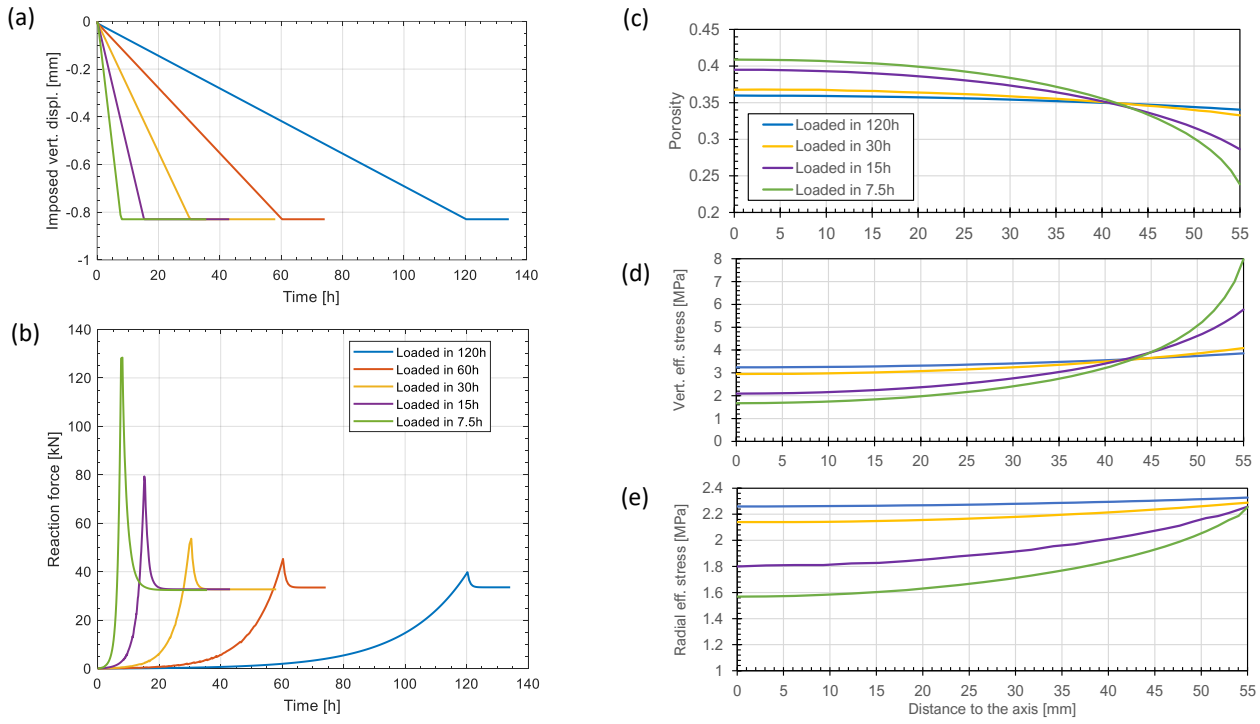

Figure 2.89: Vertical loading simulations: (a) imposed vertical displacement; (b) total vertical reaction; (c) radial profiles of porosity; (d, e) radial profiles of effective vertical and horizontal stress.

2.4.6.3. Modelling of gas fracturing

Figure 2.90 depicts the FE mesh and boundary conditions employed for modelling the gas injection tests using the FVR. Two continuum domain can be distinguished: the bulk Boom clay (sheon in brown), and the perimeter filter (shown in grey). The interface between these two materials is represented by zero-thickness interface elements, indicated by the thick blue line. In addition, interface elements have been

introduced along a vertical line (marked with a thick red line) within the clay specimen to provide a cracking path.

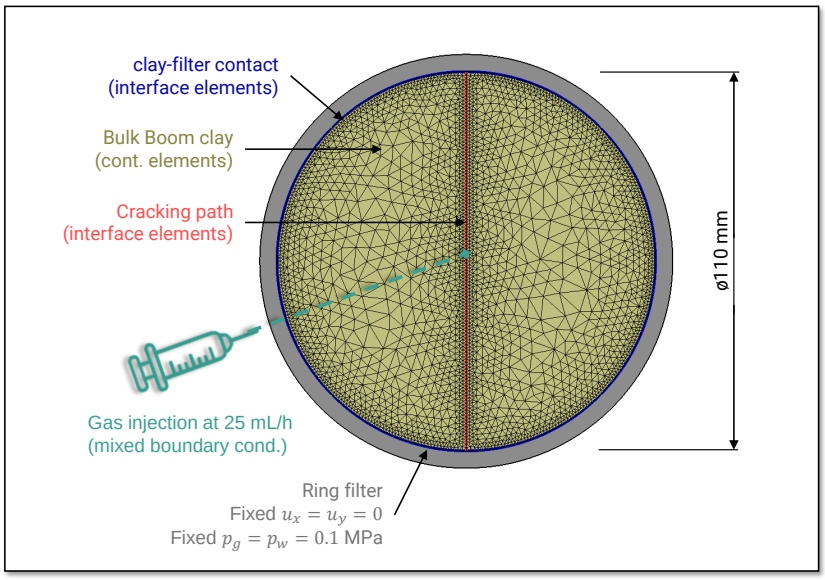

Figure 2.90: Finite Element mesh and boundary conditions for modelling gas injection in the FVR.

It is assumed that the FVR has high vertical stiffness and minimal tangential interaction with the clay, allowing for the consideration of plane strain conditions. Moreover, the adopted out-of-plane thickness is 1 mm.

The mechanical and flow constraints applied to the clay specimen by the ring filter are simulated using conventional Dirichlet boundary conditions. In particular, all nodes of the model ring filter have their displacements constrained, and both liquid and gas pressures are fixed at atmospheric levels. Gas injection is simulated by imposing a nodal gas flux at the central mid-plane node of the interface element at the specimen centre.

Since in the experiment, gas injection was controlled using a volumetric rate, the conventional Neumann boundary condition for imposing nodal mass fluxes was not suitable for modelling it. Therefore, it was necessary to implement in LAGAMINE a new mixed boundary condition to prescribe constant gas volumetric fluxes. This mixed boundary condition is defined as follows:

$$F_g(t) = \beta \left[V_g(t) \frac{\partial p_g}{\partial t} - r p_g \right] \tag{2.127}$$

$$V_g(t) = V_g(0) - \int_0^t r \, dt \tag{2.128}$$

Here, V_g[m^3] is the updated volume of gas in the injection system, r [m^3/s] represents the imposed volumetric rate, $\beta = \frac{M_g}{RT}$ [kg/(m^3 Pa)] denotes the gas compressibility, p_g [Pa] is the updated gas pressure at the injection node, and $F_g(t)$ [kg/s] stands for the updated nodal mass flux of gas species, to be assembled in the global "force" vector of the FE code. The initial volume of gas in the gas injection system considered in the simulations was V(0) = 54.5 mL. This value was calibrated to match the initial evolution of gas injection pressure observed in the experiments and closely aligns with the estimated value of 50 mL before the experiment.

The parameters considered for fluid phases/species are as follows: system temperature T = 293.15 K, gas molar mass M_g = 0.004 kg/mol, Henry's constant H = 9.668 $\times$ 10^{-3} Sander (2015), gas diffusivity in

bulk water $D_{gw} = 6.71 \times 10^{-9}\,m^2/s$, water reference density $\rho_{w,o} = 998\,kg/m^3$, water reference pressure $p_{w,o} = 0.1\,MPa$, water compressibility $C_w = 3.33 \times 10^{-10}\,1/Pa$, water viscosity $\mu_w = 8.9 \times 10^{-4}\,Pa\,s$ Haynes (2014), and gas viscosity $\mu_g = 1.96 \times 10^{-5}\,Pa \cdot s$ Haynes (2014). For the bulk clay the following material parameters are assumed: Young's modulus $E = 300\,MPa$, Poisson's coefficient $\nu = 0.30$, porosity $n = 0.39$, Biot's coefficient $b = 1.0$, intrinsic permeability $k = 3 \times 10^{-19}\,m^2$, and tortuousity $\tau = 0.164$. The same set of parameters is assumed for both the clay-filter and clay-clay interface elements. Namely: initial transport properties: $w_0 = t_0^l = d_0^l = 0$; transversal diffusion coefficients: $\tau^b = \tau^t = 1 \times 10^3\,1/m$; transversal hydraulic coefficients: $k^b = k^t = 1 \times 10^{-6}\,m$; mechanical law: $\sigma_{n0} = \sigma_{l0} = 1.0\,Pa$, $r_{n0} = r_{l0} = 1.0 \times 10^{-14}\,m$, $r_{nc} = r_{lc} = 1.0 \times 10^{-5}\,m$. The liquid retention and relative permeability parameters of the continuum and interface elements are the same as given in Section 2.4.5 for Figure 2.83 and Figure 2.84.

Figure 2.91 summarises the results obtained with the model in terms of the gas pressure at the injection locus, the average vertical stress vertical stress, the total gas mass outflow through the ring filter, and the cumulative gas mass in the (cracked) clay specimen. The black lines in Figure 2.91a and b correspond to the experimental results.

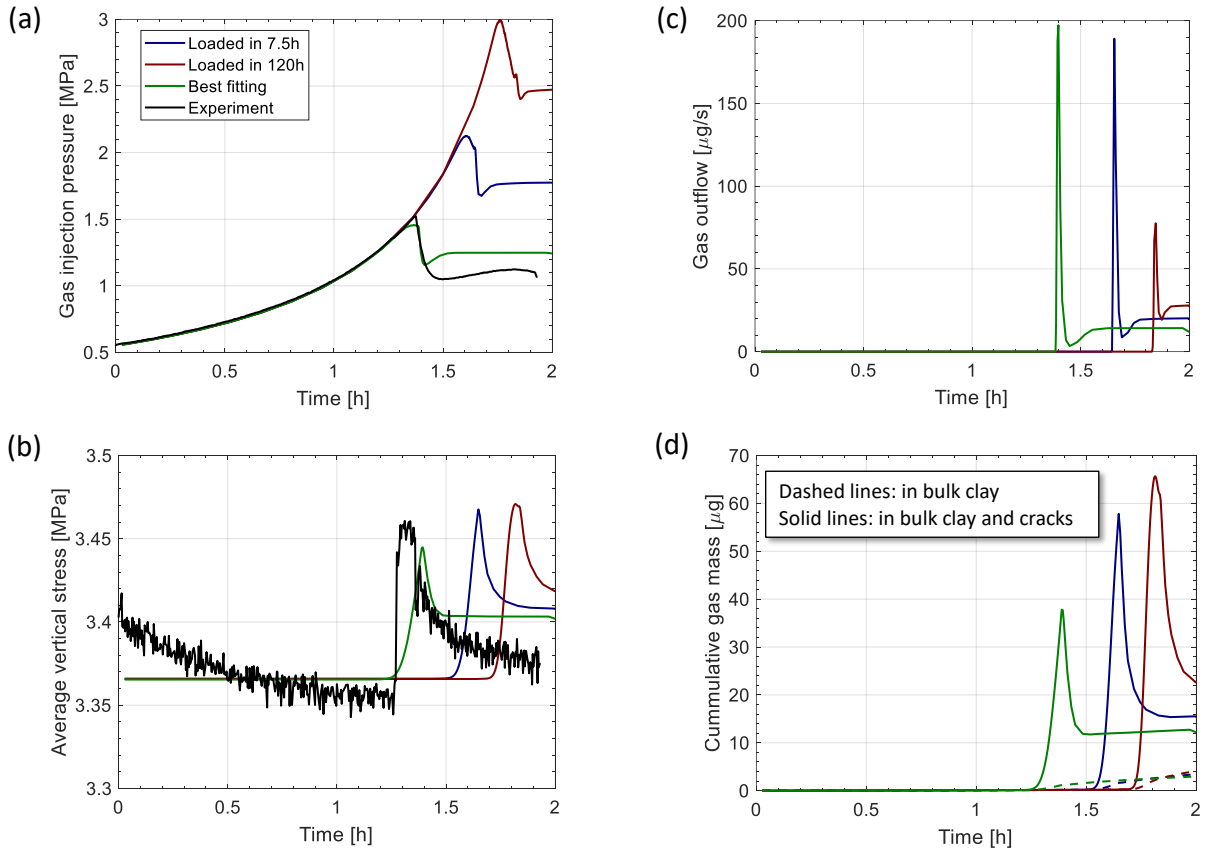

Figure 2.91: Gas fracturing simulations: (a) gas injection pressure, (b) average vertical stress, (c) total gas mass outflow, (d) cumulative gas mass in the clay specimen.

Three cases were simulated considering different initial stress conditions in the specimen plane. The blue and red curves were obtained considering initial in-plane effective stresses of 1.57 MPa and 2.26 MPa, respectively. These stress levels were obtained at the centre of specimen in the vertical loading simulations performed in Section 2.4.6.2, for the cases with the fastest and slowest loading rate, respectively. For the third simulation (green curves), the initial effective stress was reduced to 1.15 MPa to best fit the experimental gas injection pressure curve (Figure 2.91a). In all cases the initial gas and liquid pore pressure in the domain was 1 atm.

The average vertical stress $\bar{\sigma}_z$ (Figure 2.91b) and the cumulative gas mass $\mathcal{M}_g$ (Figure 2.91d) in the modelled clay specimen are obtained with the following expressions:

$$\bar{\sigma}_z = \frac{4}{\pi D_G^2}\left[\sum_{e=1}^{N_c}\int_{\Omega_c}\left(bp_s + \sigma_z'\right)dxdy + \sum_{j=1}^{N_j}\int_{\Gamma_j} p_s\,\langle r_n\rangle dl\right] \tag{2.129}$$

$$\mathcal{M}_g = \sum_{c=1}^{N_c}\int_{\Omega_c} n\left[S_w\rho_{gw} + (1-S_w)\,\rho_{gg}\right] edxdy + \sum_{j=1}^{N_j}\int_{\Gamma_j} w\left[S_w\rho_{gw} + (1-S_w)\,\rho_{gg}\right] edl \tag{2.130}$$

where D_G and e are the diameter and the out-of-plane thickness of clay specimen, respectively, σ_z' is the out-of-plane effective stress, and N_c and N_j are the total numbers of continuum and interface elements in the specimen, respectively. For the definition of other variables, refer to Section 2.4.5.

The three simulations exhibit qualitatively similar time evolution, albeit with significant quantitative disparities. Prior to the onset of cracking, gas pressure accumulates at the injection site, producing none to little mechanical effect. The established gas pressure gradient leads, in all cases, to the flow of dissolved gas into the bulk clay. Additionally, in the cases where the gas cracking pressure exceeds the gas-entry value (vertical loading at 7.5 and 120 hours), the clay experiences slight desaturation, accompanied by a modest advective flux. The gas mass migrating into the bulk clay is so minimal that it does not significantly impact the evolution of gas injection pressure. The pressure closely adheres to the theoretical compressibility curve for the gas within the injection system, perfectly aligning with the experimental curve (Figure 2.91a).

When the gas injection pressure is high enough to develop tensile strains, a crack starts to propagate at the injection locus. The initiation of cracking is scarcely discernible in the injection pressure curves but becomes evident through the increase in average vertical stress and cumulative gas mass within the clay domain (Figure 2.91b and d). Fitting the experimental results (green curves) necessitates the consideration of an in-plane initial stress lower than what was estimated for a vertical loading in 7.5 h. According to the results presented in Section 2.4.6.2, this suggests that the vertical loading in the actual experiment was conducted in less than 7.5 hours, aligning with the information in the available experimental report.

As the injection continues, the crack propagates further in the upward and downward directions. This is accompanied by accumulation of gas in the clay specimen (Figure 2.91d). The majority of this gas mass accumulates within the crack, but there is also a growing quantity of gas accumulating in the bulk clay (as depicted by the dashed lines in Figure 2.91d). The latter is primarily attributed to the transversal migration of gas from the crack into the bulk clay as dissolved gas. In the cases representing specimens vertically loaded in 7.5 and 120 hours, a gas phase is also observed within a slightly desaturated zone adjacent to the crack.

Eventually, the crack reaches the ring filter simultaneously at both ends of the cracking path. At this point, two direct pathways for gas advection are established, connecting the injection site to atmospheric pressure. This is evident in the sudden surge in gas outflow, the reduction in injection pressure, and the peak values of average vertical stress and accumulated gas mass (Figure 2.91). Notably, in the cases representing specimens vertically loaded in 7.5 and 120 hours, the injection pressure peaks occur before the gas break-through due to the surpassing of the gas-entry value, resulting in the development of two-phase flow in the bulk clay.

Following the gas break-through, the crack partially seals, and the injection pressure begins to recover, approaching a quasi-steady state before the test conclusion (Figure 2.91a). Note that the equilibrium gas injection pressure at this stage is determined by the in-plane stress level at the beginning of the test.

2.4.6.4. Concluding remarks

A gas fracturing test performed by the BGS on reconstituted Boom clay has been analysed using numerical models, in two differentiated stages.

In the first stage, the initial consolidation of the Boom clay paste in the FVR as the bolts are tighten has been modelled, considering a detailed representation of the testing device. From this initial analysis, the following conclusions are drawn:

- The consolidation of the clay paste within the FVR is not uniform in the radial direction due to the development of a pore-water pressure gradient between the centre of the specimen and the perimeter filter.
- This non-uniform consolidation is reflected in non-uniform radial profiles of effective stress, porosity, and associated state variables, even after the excess pore-water pressure has dissipated.
- The non-uniformity of the consolidation increases with the vertical loading rate. Moreover, for high loading rates, local liquefaction at the centre of the specimen can be expected.
- The average vertical stress is not a sufficient indicator of the specimen state. Very different states can be obtained for the same average vertical stress, depending on the applied loading rate.

In the second stage, a different model was constructed to simulate the gas fracturing test. This model was used with different initial stress conditions based on the numerical results obtained in the the first stage. From this second analysis, the following aspects are highlighted:

- The novel mixed boundary condition implemented allows for an inexpensive and accurate representation of the gas injection system.
- Despite the simplifying assumption of a single straight cracking path, the model can qualitatively replicate the gas injection pressure and average vertical stress signatures.
- The loading rate applied to condition the specimen determines the onset and evolution of the gas fracturing process.
- Future work will focus on matching the experimental cracking pattern by providing multiple potential cracking paths. This might also require consideration of a random field of material parameters and stochastic analysis.
- Further refinement of the model should address the mechanical interaction between the clay and the device due to tangential sliding as the cracks open.

2.4.7. CIMNE air injection test on Boom Clay

This section analyses a series of experiments conducted by Gonzalez-Blanco (2017). First, the main aspects of the experiments are summarised. Secondly, the geometry, initial and boundary conditions, and model parameters are described. Finally, the modelling results are presented.

2.4.7.1. The experiments

The experiments consist in gas injection tests performed under oedometer conditions on natural Boom clay (Gonzalez-Blanco, 2017). As shown in Figure 2.92, the oedometer cell is equipped with four automatic

pressure/volume controllers, namely one for gas injection at the bottom boundary and two for water injection for the bottom and top boundaries. A hydraulic vertical piston is used to apply the vertical stress, and an external linear variable differential transformer (LVDT) is used to measure the vertical displacement.

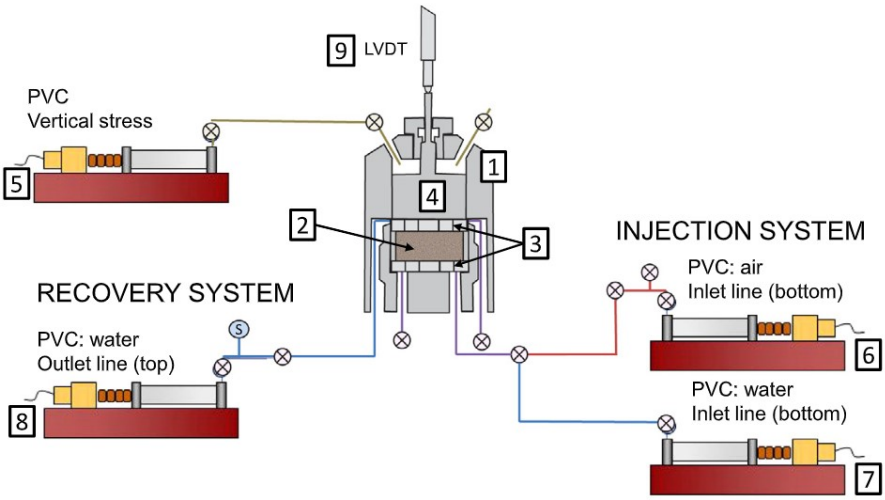

Figure 2.92: Scheme of the experimental set-up: (1) oedometer cell, (2) sample, (3) coarse porous concentric rings, (4) axial loading piston, (5) pressure/volume controller for vertical stress, (6) air pressure/volume controller, (7) and (8) water pressure/volume controllers, (9) LVDT, (10) acquisition system Gonzalez-Blanco (2017).

The test protocols are outlined in Figure 2.93. The first two stages aim at pre-conditioning the sample and determining the hydraulic conductivity. Then, the clay sample is consolidated to a total vertical load of 6 MPa. After replacing water by gas in the bottom filter, gas injection is performed in step 5 by imposing a constant injection volume rate of either 2 ml/min (slow injection) or 100 ml/min (fast injection). The injection stage finishes once the recorded injection pressure reaches 4 MPa. It is followed by a shut-off stage. Finally, the applied injection pressure and load are removed from the sample in the unloading stage. More details are provided in Gonzalez-Blanco (2017).

The experiments are performed with bedding planes either parallel or perpendicular to the direction of gas flow. Both conditions of fast and slow injection are considered. The evolution of fluid pressure at the top and bottom boundaries, the axial deformation, and the outflow volume of gas and water, are recorded during the experiments. Typically, the experimental results show that the outflow volume of gas and water at the top boundary remains low at the beginning, but increases sharply at a certain time during the shut-off stage, indicating a 'breakthrough' phenomenon. This 'breakthrough' occurs earlier in the case of fast injection than in the case of slow injection. The axial strain becomes larger (negative for expansion) due to gas-induced expansion of the sample, and the sample expands more significantly with fast injection rate. The experimental data show that the soil samples with bedding planes normal to the direction of gas flow undergoes higher expansion than the samples with bedding planes parallel to the direction of flow, while the 'breakthrough' occurs earlier in the samples with bedding planes parallel to the direction of flow.

2.4.7.2. Modelling of gas injection

Geometry

Two 2D plane-strain models of the gas injection tests (Figure 2.94) are constructed to simulate the relevant pneumo-hydro-mechanical processes: one is for the case of gas flow parallel to the bedding, referred as 'parallel gas flow' here, while the other is for gas flow perpendicular to the bedding, referred as 'perpendicular gas flow'. In both cases, the soil sample is 50 mm in width and 20 mm in height. Upstream and

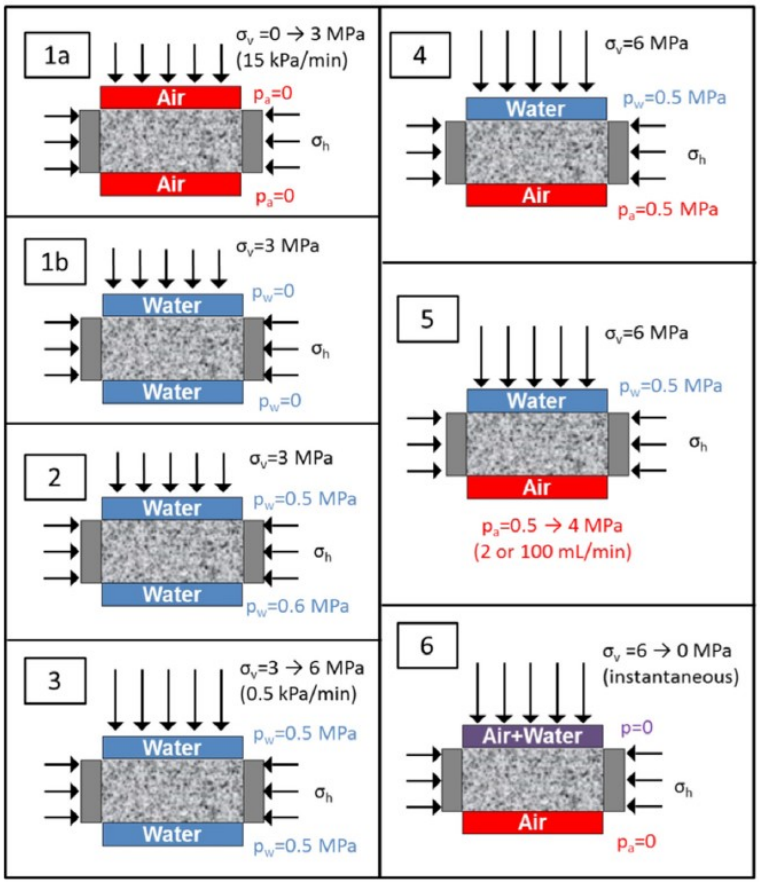

Figure 2.93: Test protocols followed: (1) pre-conditioning path: (a) undrained loading and (b) contact with synthetic Boom clay water, (2) water permeability determination, (3) drained loading, (4) fast replacement of water by air at the bottom cap, (5) air injection and dissipation stages, and (6) undrained unloading Gonzalez-Blanco (2017).

downstream reservoirs are also included in the model to represent the pistons, tube lines and porous disc filter. Very high permeability (10^{-10} m^2) and very low air entry value (0.001 MPa) are assigned to these reservoirs[7]. The volume of the two reservoirs is assigned according to Gonzalez-Blanco et al. (2016b). Interface elements, indicated by yellow lines in Figure 2.94, are used to represent the effects of bedding planes. There are also interface elements representing the interfaces between the soil sample and the testing device, at the bottom, top and lateral contacts. Note that all degrees of freedom of the confining walls are fixed to simulate the oedometric condition.

Initial and boundary conditions

Steps 4 to 6 of the experimental protocol (Figure 2.93) are modelled in the present analysis. Accordingly, the end of Step 3 serves as initial conditions for the model. A total vertical load (σ_v), set to 6.1 MPa, is applied at the top of the sample (downstream reservoir), while the initial water and gas pressures[8] in the sample (and reservoirs) are equal to 0.6 MPa and 0.1 MPa, respectively. Accordingly, the initial vertical effective stress in the sample is equal to 5.5 MPa. The initial horizontal effective stress σ_{x0} is calculated using the coefficient of earth pressure at rest k_0 = 0.84 according to Gonzalez-Blanco et al. (2016b).

The model starts with the simulation of the replacement of water by air in the bottom reservoir, and the

[7]Note that the all mechanical degrees of freedom of the reservoirs are fixed throughout the simulations.
[8]Note that the pressures used in the analysis is the absolute pressures.

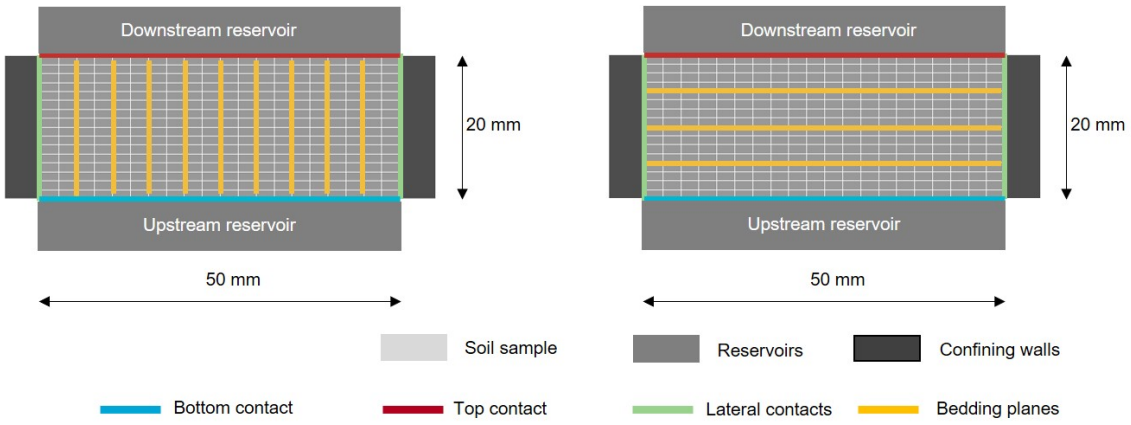

Figure 2.94: Geometry and finite element mesh for gas injection (a) parallel to the bedding planes and (b) perpendicular to the bedding planes.

increase of gas pressure to 0.6 MPa at the upstream reservoir. The gas injection is simulated by imposing gas pressure at the bottom boundary of the upstream reservoir following the recorded data in the test, while the back-pressure is set to a constant value of 0.6 MPa. Both fast (100 ml/min) and slow injection rates (4 ml/min) are considered in the model. Finally, the shut-off stage is simulated by changing the boundary condition at the bottom of the upstream reservoir from a fixed pressure to a no flux condition. The simulation of the unloading stage (step 6) is described in section 2.4.7.3.

Model parameters

With the geometry, initial and boundary conditions described above, 4 types of simulations were performed using a same set of parameters. The investigated cases are listed in Table 2.18. Each case is assigned a label, with 'P' for 'Parallel', 'N' for 'Normal' (i.e., 'Perpendicular'), 'F' for 'Fast', 'S' for 'Slow. Heterogeneity and hydro-mechanical anisotropy are considered throughout the interface elements.

Table 2.18: List of cases

Label	Bedding direction	Injection rate	Descriptions
PF	Parallel	Fast	Heterogeneity and hydro-mechanical anisotropy introduced by the interface elements
NF	Perpendicular	Fast	
PS	Parallel	Slow	
NS	Perpendicular	Slow	

The Barcelona Basic Model (BBM) is used to represent the mechanical behaviour of Boom clay. Its parameters are given in Table 2.19. The mechanical parameters were calibrated against the experimental data of the compression test, and more details are described below. Table 2.20 presents the hydraulic parameters used in the two phase-flow model. With the exception of the parameters used in the water retention model, other hydraulic parameters are taken from the case of 'perpendicular gas flow' in Gonzalez-Blanco (2017). The intrinsic permeability used for the continuum elements is considered to be isotropic, and permeability anisotropy of the samples is represented via the interface elements. The parameters used in the retention curve (as shown in Eq. 2.90) are calibrated against the experimental data from Gonzalez-Blanco (2017), and the calibration result is shown in Figure 2.83.

Table 2.19: Mechanical parameters used in BBM for the continuum elements

Definition parameter	Symbol	Value
Elastic behaviour		
Elastic compressibility against mean stress changes	κ_0	0.005
Volumetric compressibility against suction changes	κ_{s0}	0.002
Poisson ratio	ν	0.33
Plastic and shear strength behaviour		
Elastoplastic volumetric compressibility	$\lambda(0)$	0.1
Parameter defining LC yield curve	r	0.95
Parameter defining LC yield curve	β	4 MPa^{-1}
Parameter defining cohesion increase with suction	k	0.01
Reference stress	P_c	0.1 MPa
Friction angle	φ	19°
Cohesion in saturated conditions	c(0)	0.02 MPa
Initial state		
Initial preconsolidation stress for saturated conditions	p_0^*	5.1 MPa
Coefficient of earth pressure at rest	K_0	0.84
Initial porosity	ϕ	0.363
Solid specific mass	ρ_s	2,700 kg m^{-3}

Table 2.20: Hydraulic parameters used for the continuum elements

Definition parameter	Symbol	Value
Two phase flow model		
Isotropic intrinsic permeability	k_{in}	1.6×10^{-19} m^2
Soil porosity	n	0.363
Soil tortuosity	τ	0.25
Liquid dynamic viscosity	μ_w	0.001 Pa s
Liquid compressibility coefficient	$1/\chi_w$	5×10^{-10} Pa^{-1}
Air dynamic viscosity	μ_g	1.825×10^{-5} Pa s
Air density	ρ_g	1.204 kg m^{-3}
Henry coefficient	H	0.0234
Retention curve and relative permeability		
Initial bubbling pressure	$p_{b,0}$	7.5 MPa
Shape parameter	m	0.5
Initial air entry value	$P_{ev,0}$	1.5 MPa
Maximum saturation degree	S_{max}	1.0
Residual saturation degree	$S_{r,res}$	0.2
Parameter for liquid permeability	n_w	1.48
Parameter for gas permeability	n_g	2.8

The hydraulic and mechanical parameters for the interface elements are shown in Table 2.21. For all the interface elements, the initial discontinuity width (w_0) and the initial longitudinal diffusivity (d_0^l) are set to zero, while the transversal hydraulic coefficients (k^b; k^t) and the coefficients reflecting the transversal diffusivity (τ^b; τ^t) are assigned very high values, ensuring that initially the interface elements have no

effect on the hydraulic properties of the continuum elements. The initial longitudinal transmissivity (t_0^l) for the interfaces representing the bedding planes is equal to $1.3 \times 10^{-21}\,m^3$, so that the overall intrinsic permeability of the element groups (continuum elements with interface elements) in the direction parallel to the bedding can be calculated as $4.2 \times 10^{-19}\,m^2$ using:

$$k_{in}^t = k_{in} + \frac{t_0^l}{a} \tag{2.131}$$

where k_{in} is the intrinsic permeability of the continuum elements, k_{in}^t is the overall intrinsic permeability of the element groups in direction of parallel to the bedding, and a is the separation of the bedding planes. In contrast, the overall intrinsic permeability of the element groups in the direction perpendicular to the bedding remains $1.6 \times 10^{-19}\,m^2$, as specified in Table 2.20. The values of the overall intrinsic permeability for both cases of parallel and perpendicular gas flow are consistent with the measured values on the clay sample with n initial porosity of 0.363 Gonzalez-Blanco (2017).

The mechanical parameters for the interfaces are taken from Liaudat et al. (2023) for Boom clay. Accordingly, the maximum tensile strength (σ_{n0}), the normal 'cracking' and debonding separation ($r_{n0}; r_{nc}$), the maximum shear strength (σ_{l0}), the tangential 'cracking' and debonding separation ($r_{l0}; r_{lc}$), except that the normal 'cracking' separation (r_{n0}) for the bedding planes are set according to calibration of the compression test.

The value of r_{n0} for the interfaces representing the bedding in both the cases of parallel and perpendicular gas flow (Figure 2.94) is equal to $1.5 \times 10^{-6}\,m$, so that the stiffness of the above mentioned interfaces becomes $\sigma_{n0}/r_{n0} = 1.0 \times 10^{11}\,N\,m^{-3}$. This value of r_{n0} is calibrated using the experimental data of the compression test adapted from Gonzalez-Blanco (2017), as shown in Figure 2.95. The compression test is performed for both cases of parallel and perpendicular gas flow with three stages: unsaturated loading, water saturation, and saturated loading. Since the gas injection is performed after the saturation of soil, only the data during the stage of water drained loading is used for calibration. Originally the data shown in Gonzalez-Blanco (2017) is plotted with the vertical stress applying on the top of the soil sample (σ_v) versus the vertical strain of the soil sample (ε_v), while in Figure 2.95 the vertical strain is converted to the average porosity of the soil sample ($\bar{\phi}$). With the parameters mentioned above, the compression test is simulated for the stage of water drained loading by assigning the initial stress and porosity corresponding to the end of the water saturation stage, and then increasing the vertical load (σ_v) from 3 MPa to 9 MPa. In Figure 2.95, the blue line is for the modelling results, while the orange circle is for the experimental data. When σ_v is less than the preconsolidation stress of 5.1 MPa, as shown in Table 2.19, the material is in elastic condition and $\bar{\phi}$ decreases slightly with σ_v, and when σ_v is larger than 5.1 MPa, plastic deformation occurs and thus $\bar{\phi}$ decreases more rapidly with σ_v. Generally, the slope of the modelling results fit very well with the experimental data when $\sigma_v < 6.0$ MPa. Since the vertical load is always smaller than 6.0 MPa in the gas injection test, the calibrated parameters shown above ($r_{n0} = 1.5 \times 10^{-6}\,m$) satisfy the requirements for representing the anisotropic stiffness of the material.

The normal 'cracking' separations (r_{n0}) for the interface elements representing the contacts between the soil sample and the experiment devices are assigned very low value, and thus there is almost no compressibility of the interface elements, ensuring that the interface elements having no effects on the overall compressibility of the continuum elements.

Finally, in addition to the parameters described above, a lower value of P_b (= 1.0 MPa) is considered arbitrarily in some interface elements to represent the effects of weaknesses ('flaws'), as shown by the thick grey line in Figure 2.96. A 'flaw' is defined as an area with local reduction of the air entry value. Introducing the 'flaw' arbitrarily in the model is a first towards representing the effects of heterogeneity.

Modelling results

Table 2.21: Hydro-mechanical parameters for the interface elements

	Bedding planes	Bottom contact	Top contact	Left contact	Right contact
w_0 [m]	0.0	0.0	0.0	0.0	0.0
t_0^l [m^3]	1.3×10^{-21}	0.0	0.0	0.0	0.0
k^b [m]	1.0×10^{-6}	1.0×10^{-6}	1.0×10^{-6}	1.0×10^{-6}	0.0
k^t [m]	1.0×10^{-6}	1.0×10^{-6}	1.0×10^{-6}	0.0	1.0×10^{-6}
d_0^l [m]	0.0	0.0	0.0	0.0	0.0
τ^b [m^{-1}]	1.0×10^{3}	1.0×10^{3}	1.0×10^{3}	1.0×10^{3}	0.0
τ^t [m^{-1}]	1.0×10^{3}	1.0×10^{3}	1.0×10^{3}	0.0	1.0×10^{3}
σ_{n0} [Pa]	1.5×10^{5}	1.5×10^{4}	1.5×10^{4}	1.5×10^{4}	1.5×10^{4}
r_{n0} [m]	1.5×10^{-6}	1.5×10^{-10}	1.5×10^{-10}	1.5×10^{-10}	1.5×10^{-10}
r_{nc} [m]	1.5×10^{-4}	1.5×10^{-5}	1.5×10^{-5}	1.5×10^{-5}	1.5×10^{-5}
σ_{l0} [Pa]	2.0×10^{6}	2.0×10^{3}	2.0×10^{3}	2.0×10^{3}	2.0×10^{3}
r_{l0} [m]	2.0×10^{-8}	2.0×10^{-11}	2.0×10^{-11}	2.0×10^{-11}	2.0×10^{-11}
r_{lc} [m]	2.0×10^{-3}	2.0×10^{-4}	2.0×10^{-4}	2.0×10^{-4}	2.0×10^{-4}

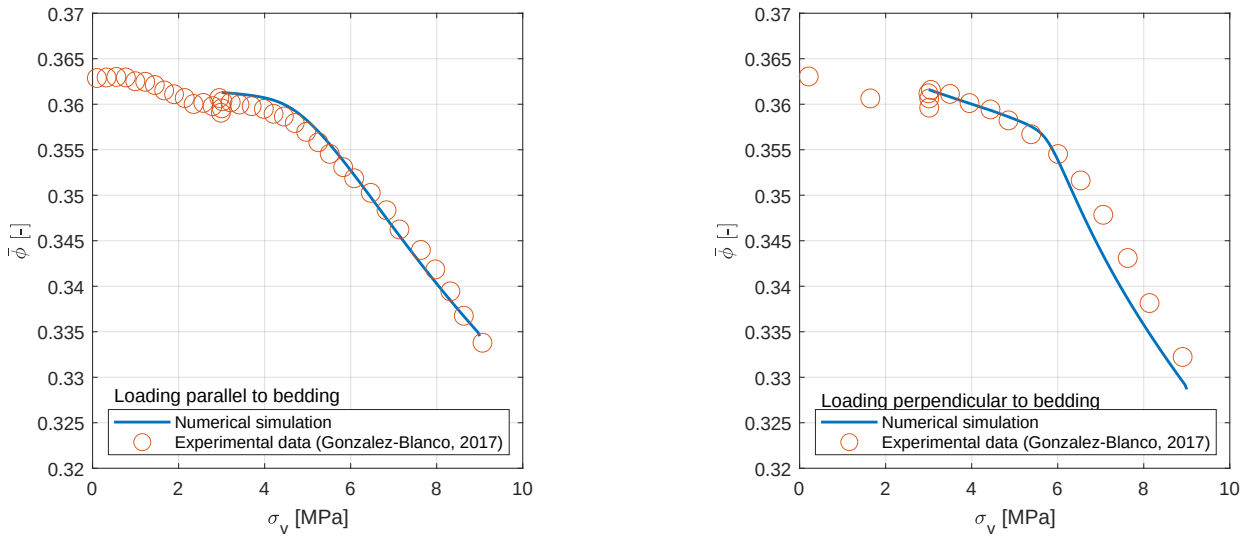

(a) Parallel gas flow *(b) Perpendicular gas flow*

Figure 2.95: Calibration of mechanical anisotropy based on compression test Gonzalez-Blanco (2017)

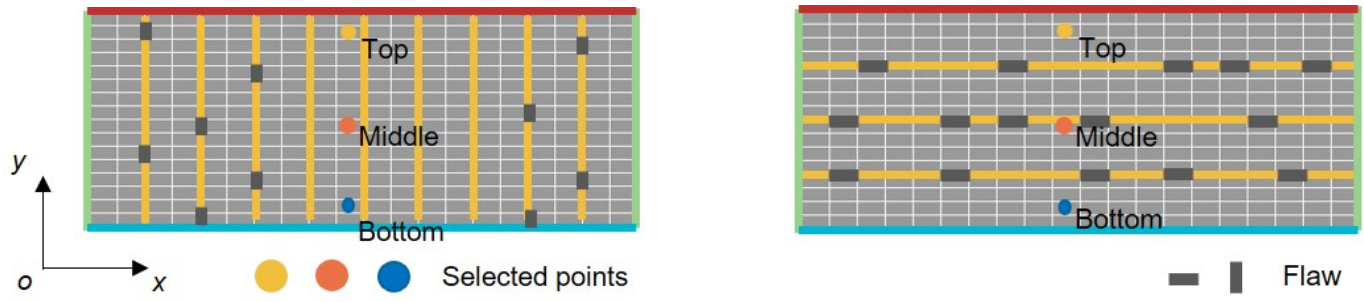

(a) Parallel gas flow *(b) Perpendicular gas flow*

Figure 2.96: Geometry and FE mesh of the soil sample

Figure 2.97 presents the evolution of the outflow volume (of the liquid and gas phases), axial strain and pressures at the sample boundaries in the case of fast injection. In this figure, the blue solid line corre-

sponds to the case of parallel gas flow (PF), while the red dash line is for the case of perpendicular gas flow (NF). Three key points, represented in blue, orange, and yellow, and located at the bottom, middle, and top of the sample (Figure 2.96) are selected to further analyse the results. Figure 2.98 shows the evolution of some key variables in three selected points. The key variables presented include gas pressure (p_g), saturation degree (S_w), vertical deformation (ε_{yy}), and horizontal deformation (ε_{xx}).

As shown in Figure 2.97, the outflow volume in 'PF' increases slightly faster than in 'NF', which is consistent with experimental observation. On the other hand, no significant gas breakthrough is observed. This can be explained by Figure 2.98, which shows that the saturation degree in both cases remain close to one during the simulation. Even though the dissolved gas can exsolve when it reaches the downstream reservoir, the outflow volume of the gas phase is not significant, since no large amount of gas phase is transported through the soil sample.

Figure 2.97 further shows an expansion of the sample as a result of gas invasion. This volumetric strain is associated to the development of gas pressure (Figure 2.98) in the soil, which overcomes the air entry value of 1.5 MPa and causes a decrease of the effective stress (positive for compression), eventually leading to expansive deformation of the soil. The results show that the soil expansion is larger in 'NF' than that in 'PF', which is consistent with the experimental observation Gonzalez-Blanco (2017). During gas injection, the vertical strain (ε_{yy}) in continuum elements (Figure 2.98) increases almost as much between 'PF' and 'NF'. However, in 'NF' the interfaces representing the bedding decompress due to build up of gas pressure, and this will cause expansion of the soil sample in the vertical direction. In contrast, in 'PF' the interfaces are compressed horizontally. This is linked to the fact that the horizontal displacement is constrained in the oedometeric conditions, and thus the horizontal expansion of continuum elements (see ε_{xx}) leads to compression of the bedding, which has no contribution to the soil expansion. Since 'breakthrough' does not occur in the model, the gas pressure accumulates in the soil without dissipation. Therefore, the soil expansion keeps increasing without reduction.

The results shown in Figure 2.99 and Figure 2.100 correspond to the case of slow injection rate. Similarly, the blue line represents the case of parallel gas flow (PS) and the red line is for the perpendicular gas flow (NS). Figure 2.99 shows the results of typical PHM responses and Figure 2.100 shows the evolution of some key variables in three selected points. The evolution of the results and the behind mechanism are similar to that described in the case of fast injection rate.

2.4.7.3. Modelling of cracking upon unloading

Following the shut-off stage of protocol step 5 (Figure 2.93), this section simulates the unloading stage of the experiment in protocol step 6. The boundary condition is applied following the experimental operation. First, all the fluid pressures on the boundaries of both the upstream and downstream reservoirs, as well as the vertical loading, are reduced simultaneously to the atmosphere pressure in 100 s. Then, to reproduce the process that the sample is taken out from the oedometric cell and ring, the horizontal degrees of freedom of the confining wall is released (Figure 2.94) and the gas pressure at the boundaries between the soil sample and the confining wall is set to atmosphere pressure (0.1 MPa). Only the condition of fast injection rate is considered in the present report, as the condition of slow injection rate is similar.

Figure 2.101 presents the evolution of the gas pressure field in the deformed configuration. Note that, for the sake of representation, the deformation of the mesh is magnified eight times. The results shown here are for the time at 0, 100, and 120 minuntes after unloading. The left figures correspond to the case of parallel gas flow (PF), while the right figures are for the case of perpendicular gas flow (NF). The figures show that the soil sample expands vertically and horizontally in both cases of 'PF' and 'NF'. Although the gas pressure dissipates gradually during the unloading process, gas-induced fractures occur and evolve due to removal of the confining pressure. The result demonstrates that gas-induced fractures could be

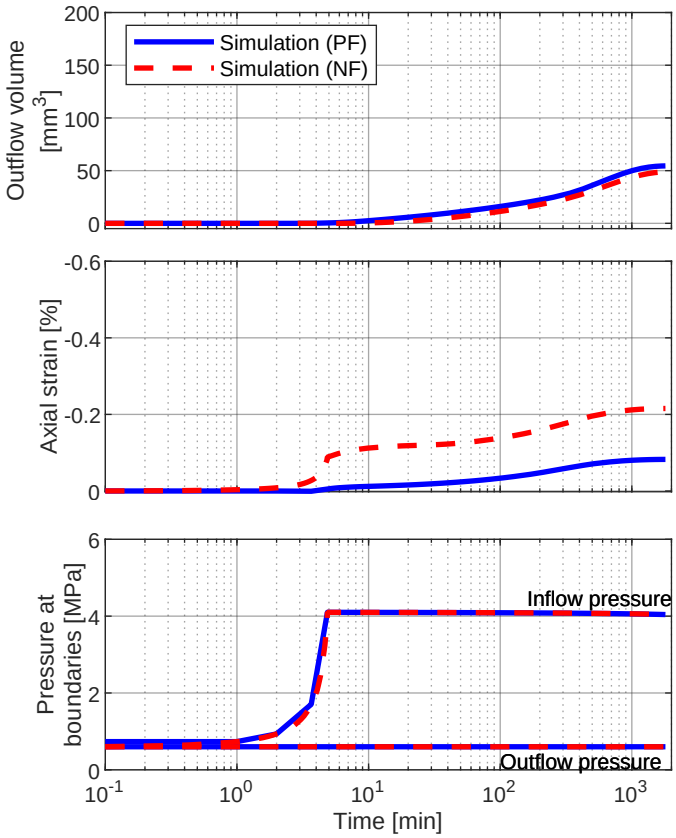

Figure 2.97: Typical PHM responses for the case of fast injection rate: parallel gas flow (PF), perpendicular gas flow (NF)

produced during the unloading stage of the experiment.

2.4.7.4. Concluding remarks

Gas injection test similar to those performed by Gonzalez-Blanco (2017) on natural Boom clay have been modelled, simulating the gas injection and unloading stages. The following conclusions are drawn from the modelling results:

- The anisotropy of stiffness and hydraulic conductivity can be satisfactorily represented by combining continuum elements and zero-thickness interface elements with suitable constitutive laws and parameters.
- By considering a constant permeability and arbitrary heterogeneities of the air entry value, the model does not predict gas breakthrough.
- The numerical results show that gas-induced fractures could be produced during the (fast) unloading stage of the experiment.

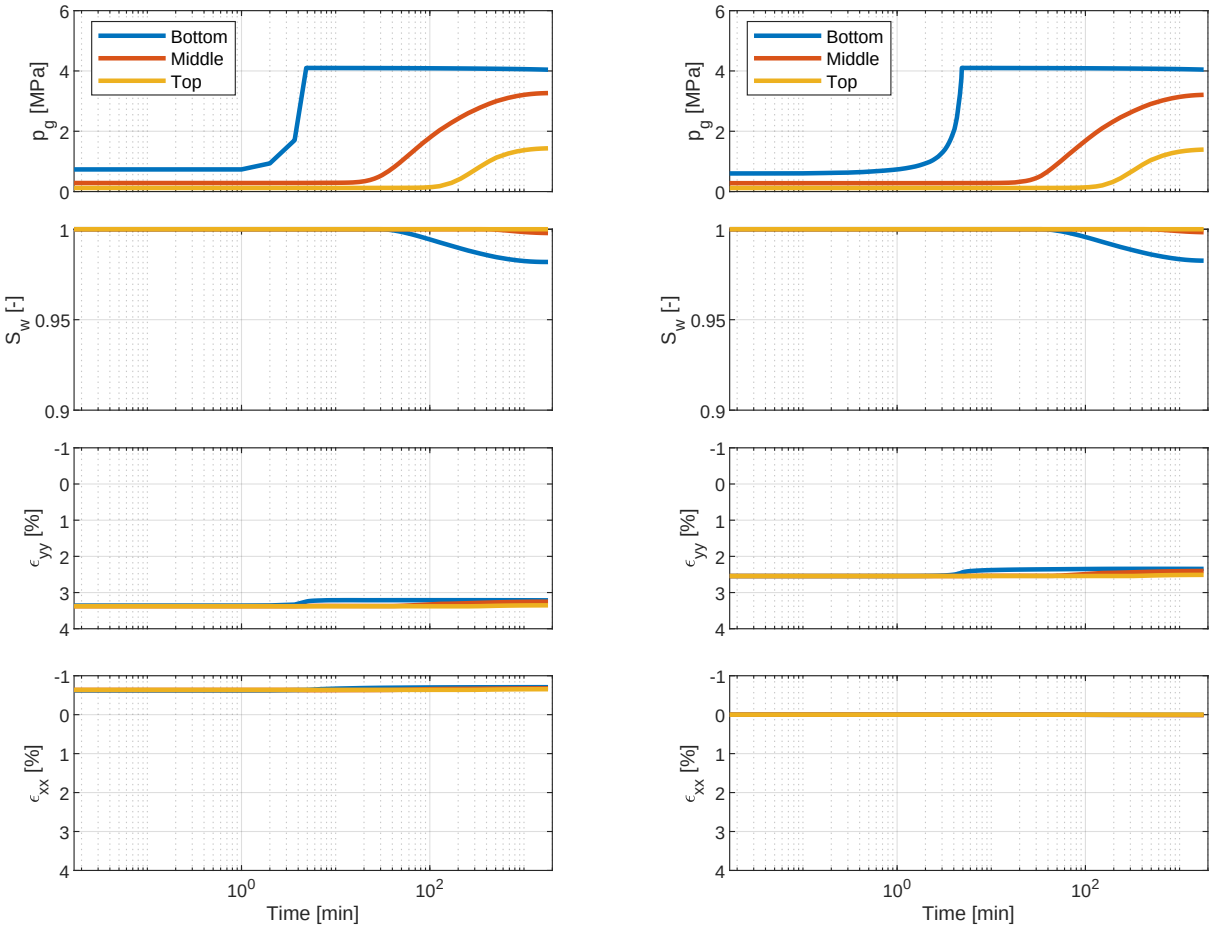

Figure 2.98: Key variables at selected points for the case of fast injection rate: parallel gas flow (PF for the left), perpendicular gas flow (NF for the right)

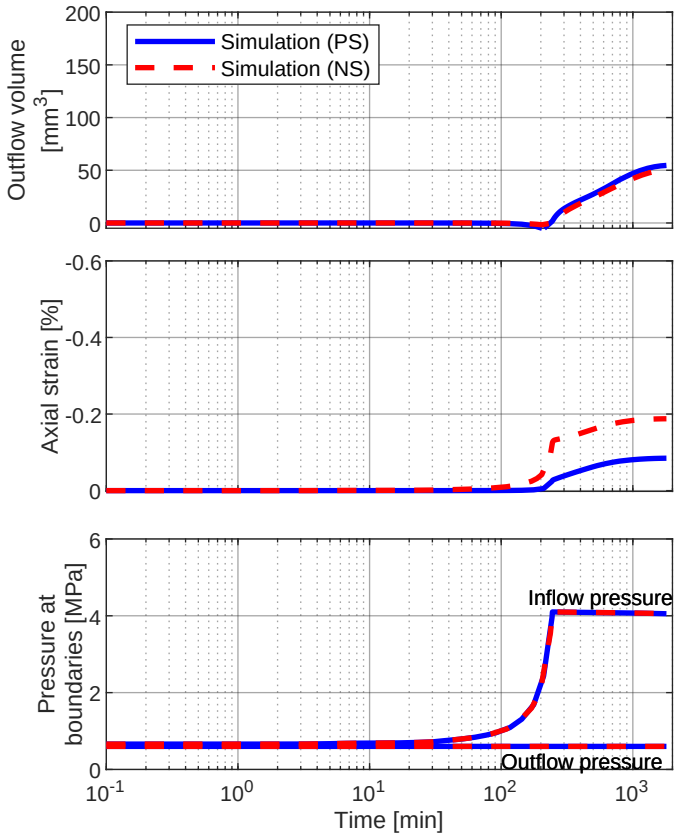

Figure 2.99: Typical PHM responses for the case of slow injection rate: parallel gas flow (PS), perpendicular gas flow (NS)

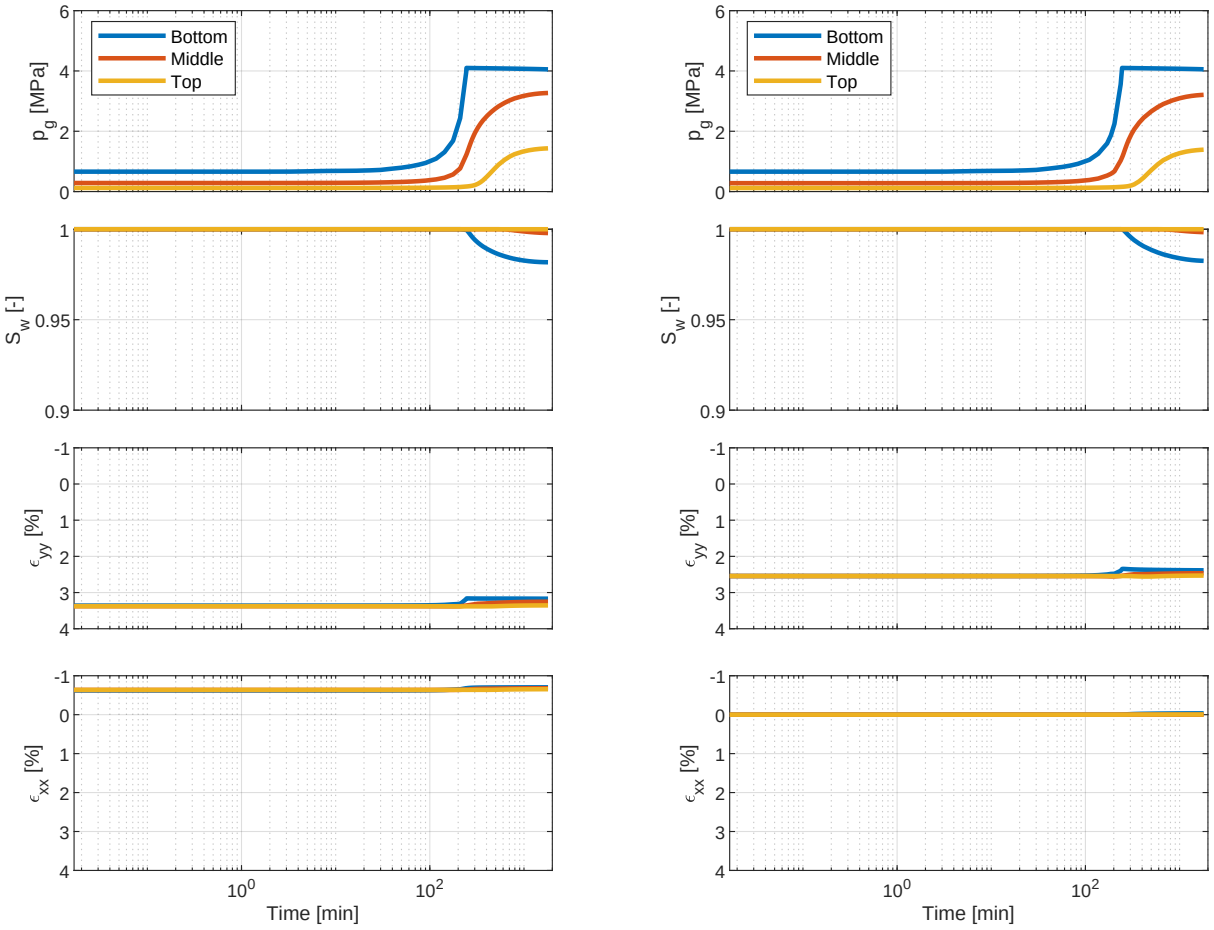

Figure 2.100: Key variables at selected points for the case of slow injection rate: parallel gas flow (PS for the left), perpendicular gas flow (NS for the right)

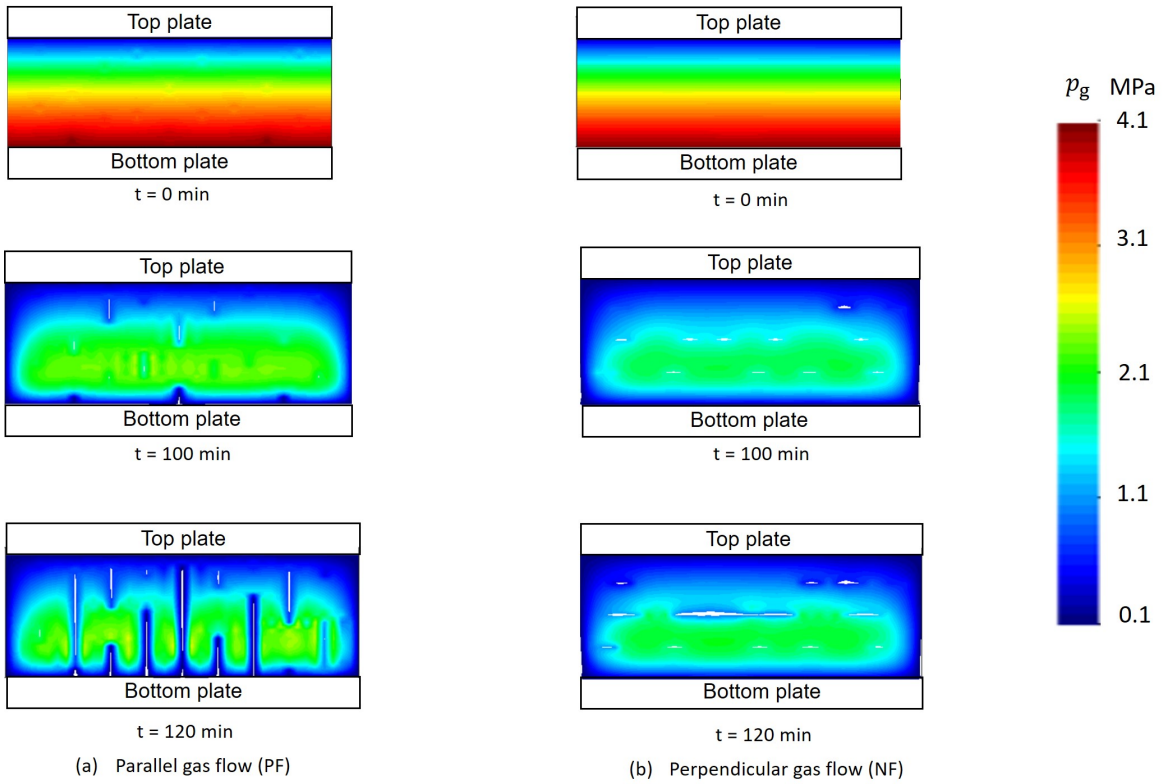

Figure 2.101: Crack evolution in the unloading stages (deformation factor = 8)

2.4.8. Key learning points

New knowledge acquired

We are now able to model, within a single modelling framework, gas flow through the bulk material as well as existing or induced discontinuities. As compared to previously available tools, we explicitly model the coupled pneumo-hydro-mechanical behaviour of discontinuities in saturated clays, so that we are able to simulate the initiation and propagation of cracks due to the build-up of gas pressure.

Impact of acquired knowledge

The explicit representation of discontinuities (e.g. fractures, joints, faults, material interfaces, etc.) will allow a more detailed study of the effect of these features in the overall pneumo-hydro-mechanical behaviour of the clay barriers. Moreover, we are now able to investigate the interactions between the gas transport processes in the continuum medium (diffusion and advection, two-phase flow, dilatancy controlled gas flow) with the gas fracturing process.

Remaining knowledge gaps

There is still uncertainty on the fluid transport and retention properties of clay discontinuities in general, and, particularly, on the effect of the discontinuity aperture on these properties.

Recommendations for the future

Further developments are still necessary to allow a quantitative validation of the model, e.g. implementation of the pathway dilation mechanism, introduction of variability/heterogeneity of the material properties, and extension to 3D. Moreover, in order to reduce the computational cost of the proposed modelling approach, a new numerical strategy would be advantageous to introduce (or activate previously introduced) interface elements only where/when they are needed to represent the formation of cracks.

.

UPC

2.5. Two-phase flow model coupled with mechanical deformations within the FE code CODE_BRIGHT (UPC)

Executive Summary

The safest long-term management solution for high-activity radioactive waste is known as geological disposal. Many countries (e.g. Canada, Finland, France, Switzerland, Sweden, UK and USA) have chosen to dispose of all or part of their spent nuclear fuel in facilities constructed at an appropriate depth in stable geological formations. Bentonite based materials have been proposed as engineered barrier system around the canister because of their high retention capacity, high swelling ability and low permeability (Toprak et al., 2020) (Toprak et al., 2020).

In the repository gas will be generated by several mechanisms, such as the anaerobic corrosion of metals, the microbial degradation of organic wastes and the radiolysis of water, which generate hydrogen, oxygen, methane and carbon dioxide. In the case of the engineer barriers, gas transport could take place mainly through preferential pathways, like the joints between compacted bentonite blocks, interfaces between different components or along the interface between host rock and buffer material. After the complete saturation of the barrier, gas generated will increase up to a locally defined threshold or breakthrough pressure, from which gas flow will take place through temporary pathways. Once breakthrough pressure is reached, preferential pathways will be created. The size of these pathways would depend on gas local pressure and structural clay restrictions. These pathways would close once gas pressure decrease below a certain value, known as residual pressure. Meanwhile, gas pressure will increase again at the interface up to a new threshold pressure. Therefore, the gas generated will be transported outwards in a cyclic manner, regulated by the opening and closure of pathways, which will depend on the pressure reached (Gutiérrez Rodrigo, 2019).

In order to investigate gas migration from bentonite barrier (FEBEX bentonite) and gas pathway development along the barrier; hydro-mechanical simulations of breakthrough tests on FEBEX material (Gutiérrez Rodrigo, 2019) have been performed.

2.5.1. Model introduction

Gas diffusion, two-phase flow and two-phase flow coupled with mechanical effects are some of mechanisms for gas transport that may lead to generation of apertures (small fractures) in the porous medium. Due to low permeability of EBS components, the air entry pressure is higher. Therefore, a higher capillary pressure is needed for the desaturation of clay based material during gas injection.

Under a certain rate of gas generation, the gas pressure may increase and once reaching values of BT, gas fracture processes will begin. Alternatively, through gas generation, gas may flow through existing discontinuities (Olivella et al., 1994). In order to take into account fracture opening and/or fracture formation because of gas generation a proper mechanical model is required.

In this work, a standard two-phase flow model has been used to simulate gas breakthrough tests on FEBEX material. The flow model is coupled to mechanical deformation. During gas injection, gas flow pathways develops (Figure 2.102). It is a continuous model where apertures have cubic law for permeability (Olivella and Alonso, 2008a).Generated gas is transported in a cyclic manner, regulated by the opening and closure of pathways.

Permeability increases during gas injection because of aperture of the fractures and reduces during closure of these apertures. Basic features of the model such as permeability coupled to mechanical behaviour

evolution of intrinsic permeability according to deformation rate (Olivella and Alonso, 2008a) and its impact on pathway development are shown in Figure 2.102. Hydro-mechanical models' equations and parameters are summarized from Table 2.22 to Table 2.25. Equations for the advective and dissolved non-advective gas flow can be found in details in (Olivella and Alonso, 2008a) and Olivella et al., 1994 (Olivella et al., 1994).

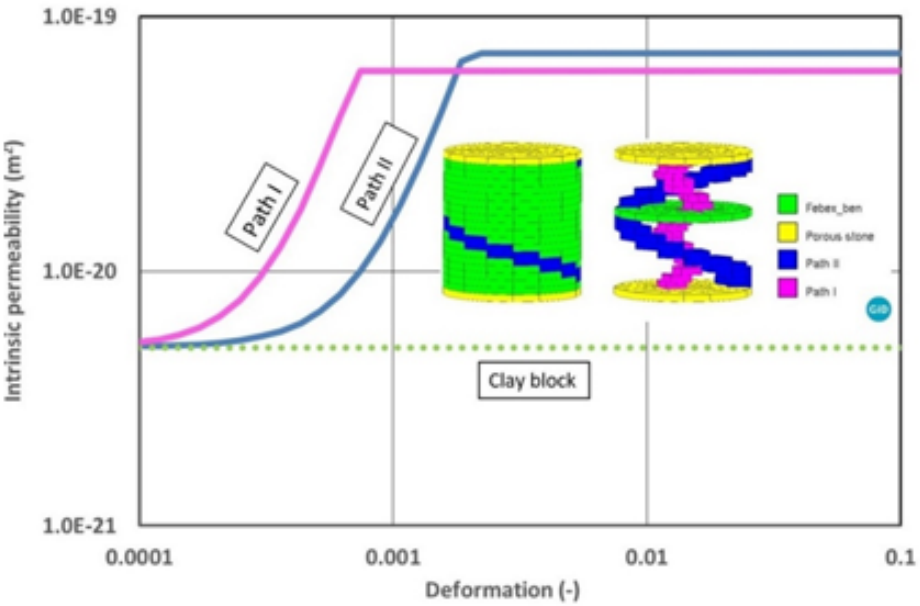

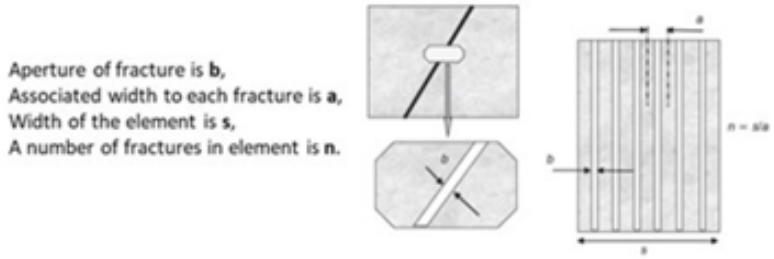

$$k_{\text{int}} = k_{\text{matrix}} + k_{\text{fractures}}$$

$$k_{\text{fractures}} = \frac{b^3}{12a}, \quad b = b_0 + \langle \varepsilon - \varepsilon_0 \rangle a \leq b_{\max}$$

Figure 2.102: Relationship between intrinsic permeability and deformation in the Model. Cubic law for permeability used for preferential paths.

Laws	Parameter	Units	Symbol	Equations
Van Genuchten retention curve	Capillary pressure parameter (in P(ϕ)) Shape parameter in $\lambda(\phi)$ Maximum saturation	(MPa) (–) (–)	P_0 λ_0 S_{ls}	$S_l = \left(1 + \left(\frac{p_g - p_l}{P}\right)^{\frac{1}{1-\lambda}}\right)^{-\lambda}$
Advective Darcy flux	Reference intrinsic permeability Reference porosity Initial porosity	(m^2) (–) (–)	k_0 ϕ_0 ψ	$\mathbf{q}_l = -\frac{\mathbf{k}k_{rl}}{\mu_l}(\nabla p_l + \rho_l g \nabla z)$ $\mathbf{k} = \mathbf{k}_0 \frac{\psi^3}{(1-\psi)^2}\frac{(1-\psi_0)^2}{\psi_0^3}$
Gas relative permeability	Gas relative permeability – constant Gas relative permeability – power Maximum gas saturation – power	(–) (–) (–)	A λ S_{gs}	$k_{rl} = AS_{eg}^{\lambda}$ $S_{eg} = \frac{S_g - S_{rg}}{S_{gs} - S_{rg}}$
Cubic law for permeability	Initial aperture to calculate a variable aperture Spacing of the fractures: Reference strain to calculate aperture variations Maximum aperture. Upper bound of aperture.	(m) (m) (–) (m)	b_0 a ε_0 b_{max}	$b = b_0 + \Delta b$ $k = k_{max} + \frac{b^3}{12a}$ $\Delta b = a\Delta\varepsilon = a(\varepsilon - \varepsilon_0)$ for $\varepsilon > \varepsilon_0$

Table 2.22: Constitutive equations for hydraulic laws used in the model

Equation	Parameter	Units	Symbol	FEBEX	Path I	Path II
Van Genuchten retention curve	Capillary pressure parameter (in P(ϕ)) Shape parameter in $\lambda(\phi)$ Maximum saturation	(MPa) (–) (–)	P_0 λ_0 Sls	20 0.18 1	20 0.18 1	20 0.18 1
Advective Darcy flux	Reference intrinsic permeability Reference porosity Initial porosity	(m^2) (–) (–)	k_0 ϕ_0 ψ	5×10^{-21} 0.33 0.33	5×10^{-21} 0.33 0.33	5×10^{-21} 0.33 0.33
Gas relative permeability	Gas relative permeability – constant Gas relative permeability – power Maximum gas saturation – power	(–) (–) (–)	A λ Sgs	100 3 1	100 3 1	100 3 1
Cubic law for permeability	Initial aperture to calculate a variable aperture Spacing of the fractures: Reference strain to calculate aperture variations Maximum aperture. Upper bound of aperture.	(m) (m) (–) (m)	b_0 a ε_0 b_{max}	– – – –	1×10^{-9} 1×10^{-5} 1×10^{-6} 2×10^{-8}	1×10^{-9} 4×10^{-5} 1×10^{-6} 3×10^{-8}
Diffusive Fick flux	Tortuosity coefficient	(–)	τ	0.8	0.8	0.8

Table 2.23: Hydraulic parameters of materials.

Most of the mechanical model (BBM) parameters have been derived from Alonso et al. (1990) and Gens et al. (2009). Back analyses of a swelling pressure test on FEBEX material has been performed in order to calibrate some of BBM parameters listed in Table 2.25. More details about FEBEX material can be found in (Enresa,2000) (Enresa, 2000) and (Enresa,2006) (Enresa, 2006).

Calibration of gas permeability is shown in Figure 2.103 . Water retention curve, LC curve and *s*-p_{eff}-*q* path for the clay are shown in Figure 2.104. Sensitivity analyses have been performed on these parameters in Chapter 3.

2.5.2. Initial Calculations

GID as a CAD system and Code_Bright as a Finite Element Method (FEM) program have been used in order to simulate gas breakthrough test (Gutiérrez Rodrigo, 2019) (laboratory scale – Figure 2.105) on FEBEX bentonite material.

Parameters	Units	Symbol	Equations
Parameters for elastic volumetric compressibility against mean net stress change	(–)	κ_{i0}	$d\varepsilon_v^e = \frac{\kappa_i(s)}{1+e}\frac{dp'}{p'} + \frac{\kappa_s(p',s)}{1+e}\frac{ds}{s+0.1}$
Parameters for elastic volumetric compressibility against suction change	(–)	κ_{s0}	
Minimum bulk modulus Poisson ratio	(MPa) (–)	K_{min} ν	$K = \frac{1+e}{\kappa}p'$, $G = \frac{3K(1-2\nu)}{2(1+\nu)}$
Slope of void ratio – mean net stress curve at zero suction	(–)	$\lambda(0)$	$p_0 = p^c\left(\frac{p_0^*(T)}{p^c}\right)^{\frac{\lambda(0)-\kappa_{i0}}{\lambda(s)-\kappa_{i0}}}$
Parameters for the slope void ratio mean net stress at variable suction	(–) (MPa^{-1})	r β	$\lambda(s) = \lambda(0)\left[(1-r)\exp(-\beta s) + r\right]$
Parameter for increase of tensile strength due to suction	(–)	k	$p_s = p_{s0} + ks\ \exp(-\rho\Delta T)$
Tensile strength in saturated conditions Reference pressure for the p_0 function Critical state line Non-associativity parameter	(MPa) (MPa) (–) (–)	p_{s0} p_c M α	$G = q^2 - \alpha M^2\left(p' + p_s\right)\left(p_0 - p'\right)$
Initial void ratio Pre-consolidation mean stress for saturated soil	(–) (MPa)	ε_0 $p*_0$	$dp_0^* = \frac{1+e}{\lambda(0)-\kappa_{i0}}p_0^* d\varepsilon_v^p$

Table 2.24: Constitutive equations for mechanical law used in the model.

Parameters	Units	Symbol	FEBEX
Parameters for elastic volumetric compressibility against mean net stress change	(–)	κ_{i0}	0.04
Parameters for elastic volumetric compressibility against suction change	(–)	κ_{s0}	0.03
Minimum bulk modulus	(MPa)	K_{min}	10
Poisson ratio	(–)	ν	0.4
Slope of void ratio – mean net stress curve at zero suction	(–)	$\lambda(0)$	0.15
Parameters for the slope void ratio mean net stress at variable suction	(–)	r	0.925
	(MPa^{-1})	β	0.1
Parameter for decrease of tensile strength due to temperature	($°C^{-1}$)	ρ	0.2
Parameter for increase of tensile strength due to suction	(–)	k	0.1
Tensile strength in saturated conditions	(MPa)	p_{s0}	0.1
Reference pressure for the p_0 function	(MPa)	p_c	0.5
Critical state line	(–)	M	1
Non-associativity parameter	(–)	α	0.53
Initial void ratio	(–)	ε_0	0.66
Pre-consolidation mean stress for saturated soil	(MPa)	$p*_0$	12

Table 2.25: Mechanical parameters for materials.

Model A and Model B correspond to arbitrary realization of heterogeneity assuming some preferential paths (A and B) and some random heterogeneous zones (B). In the future, more realizations should be done to analyse the response depending on the distribution of properties.

The sample (FEBEX bentonite) diameter is 38 mm and initial height of the sample is 20 mm. Initial saturation degree of the material is 81% which corresponds to initial water content of 15.3%. The test has been performed under constant volume.

The model has a 3D full geometry where porous stones have been simulate as separate materials. The geometry has structured mesh and the number of hexahedra elements is 960. There are 1197 nodes.

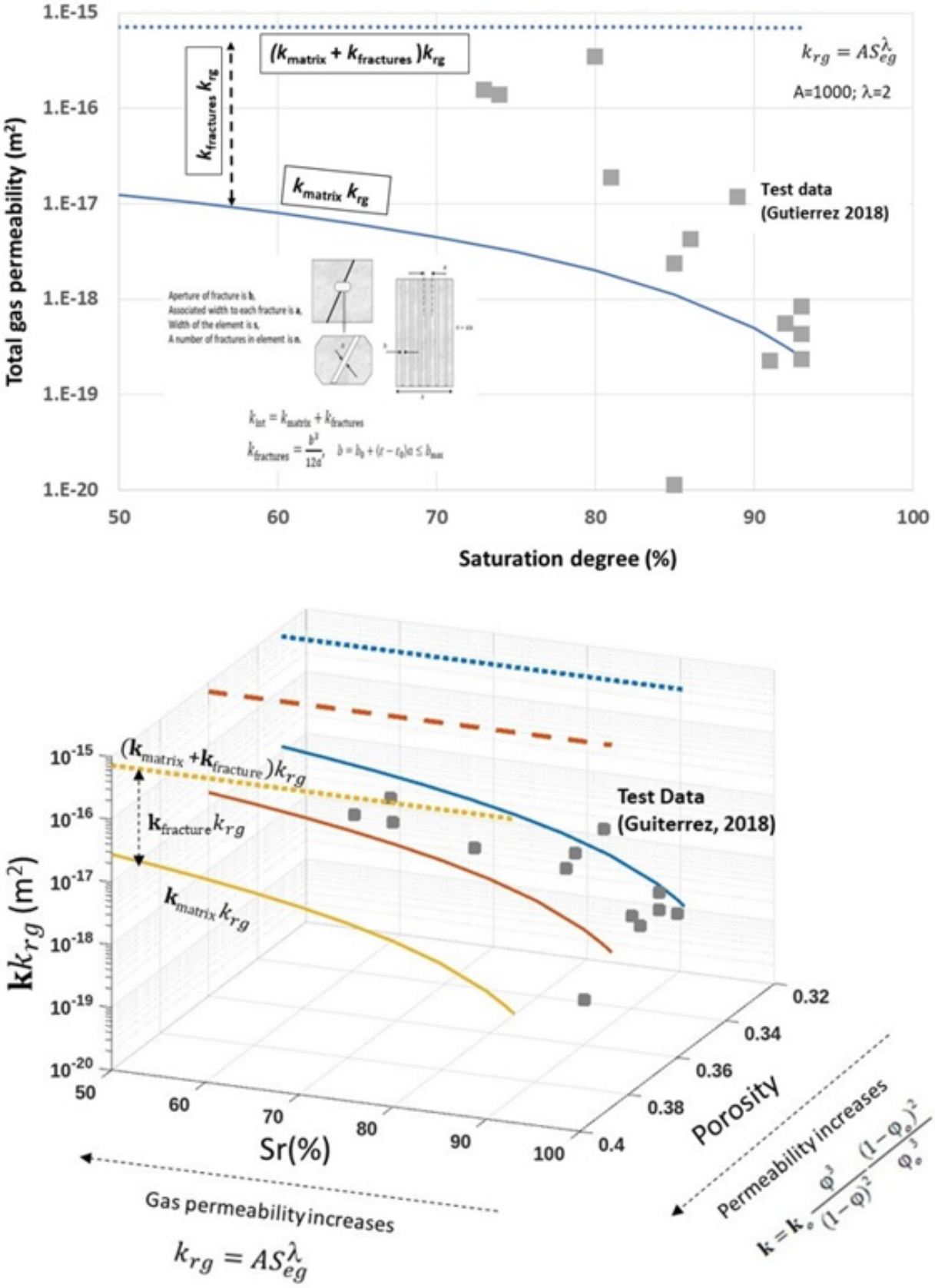

Figure 2.103: Calibration of total gas permeability parameters.

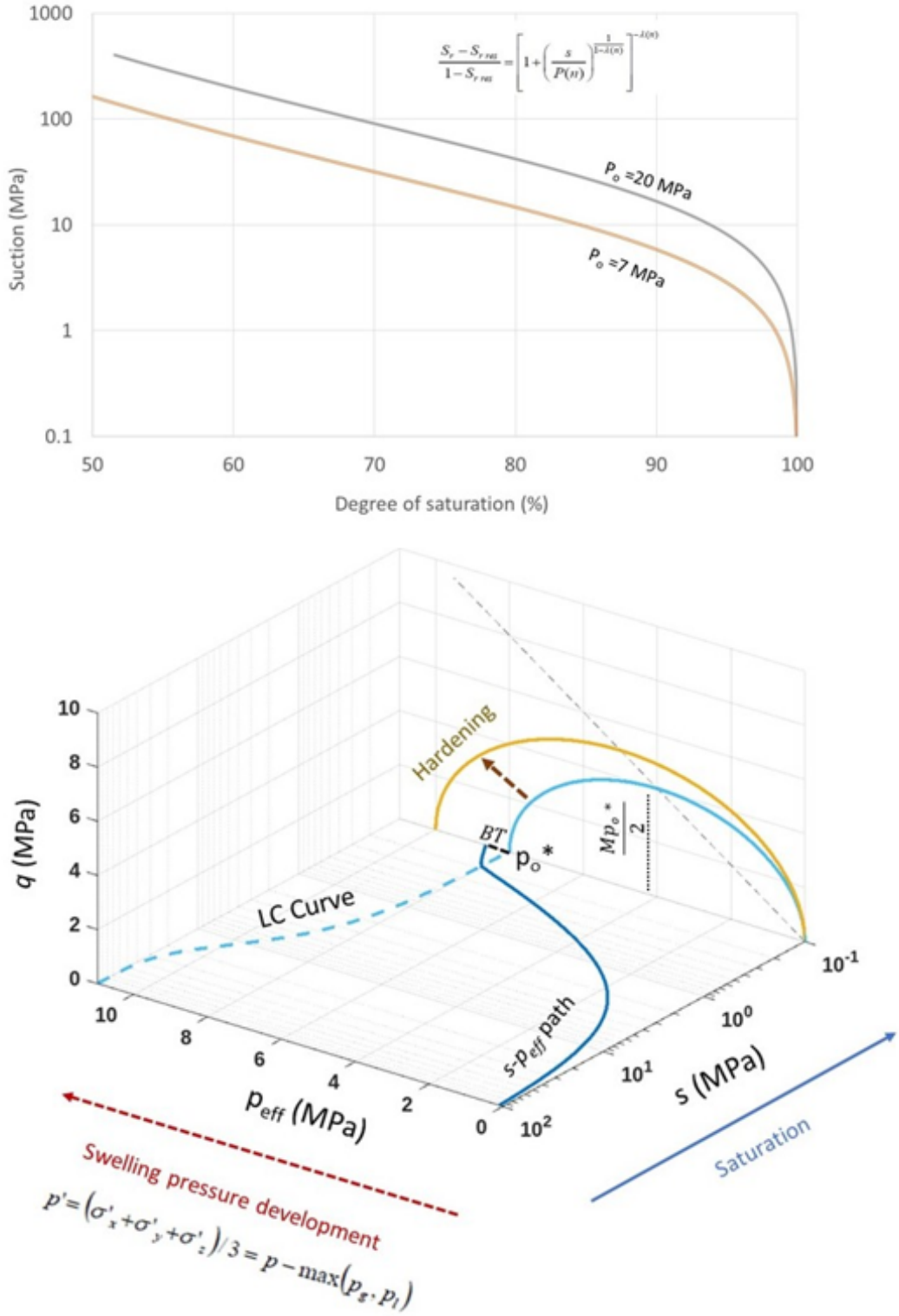

Figure 2.104: Water retention curve (above) and calibration of mechanical parameters (BBM) of the clay. LC curve and p_{eff}-q-s path (below).

The injector system have been introduced to the model as a boundary condition. Prescribed gas pressure has been applied from one end of the sample in the model. Boundary conditions have been shown in Figure 2.106). The model calibration has been performed by means of comparison of back pressures.

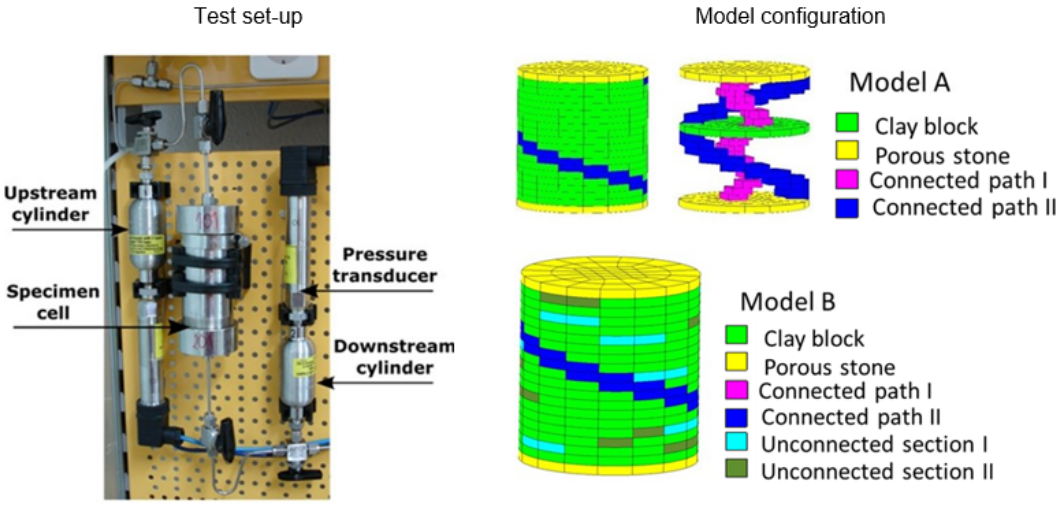

Figure 2.105: Test set-up and models (A and B) presentation (Gutiérrez Rodrigo, 2019). Model A and Model B correspond to arbitrary realization of heterogeneity assuming some preferential paths (A and B) and some random heterogeneous zones (B). In the future, more realizations should be done to analyse the response depending on the distribution of properties.

Hydraulic boundary conditions, together with time stepping and prescribed gas pressure on the upper and lower boundaries are depicted in Figure 2.106. The sample has been saturated during 60 days. After reaching the full saturation, gas injection takes place till breakthrough pressure. When the second breakthrough happens, the gas pressure source is closed. There is no water supply from lower or upper part of the sample during gas injection steps. There is no water or gas injection from lower part during gas injection steps. Lower part remains under initial conditions following to saturation (no gas or water injection).

Total inflow from upper boundary where the gas injection takes place and corresponding accumulated gas volume in the model are shown in Figure 2.107. At the end of first breakthrough, both in the test and in the model; total injected volume of gas is around 0.29 cm^3.

Hydro-mechanical parameters used for materials are listed in Table 2.26 and Table 2.27. Cubic law (Olivella and Alonso, 2008) has been used to simulate preferential paths as a permeability model (Figure 2.102 and Figure 2.103). The global intrinsic permeability is defined as sum of material matrix and internal fracture permeabilities. Cubic law parameters are calibrated by means of back-analyses. Barcelona Basic Model (BBM) (Alonso et al., 1990) has been used as the mechanical model for FEBEX. Porous stones are simulated as separate materials and have elastic parameters.

2.5.3. Model A

Figure 2.108 shows distribution of preferential paths in Model A. Two connected pathways have been incorporated to the geometry in a random manner. Model A corresponds to arbitrary realization of heterogeneity assuming some preferential paths. In the future, more realizations should be done to analyse the response depending on the distribution of properties.

Comparison of back pressure data and Model A results during Phase 2 and Phase 4 is summarised in Table 2.26. In Phase 4, a bigger back pressure has been succeeded. Figure 2.109 shows gas pressure development in the test (Phase 2 and Phase 4) and in the model. The response of back pressure in the Model A is similar to Phase 4. In the numerical model, back pressure develops in a more gradual way

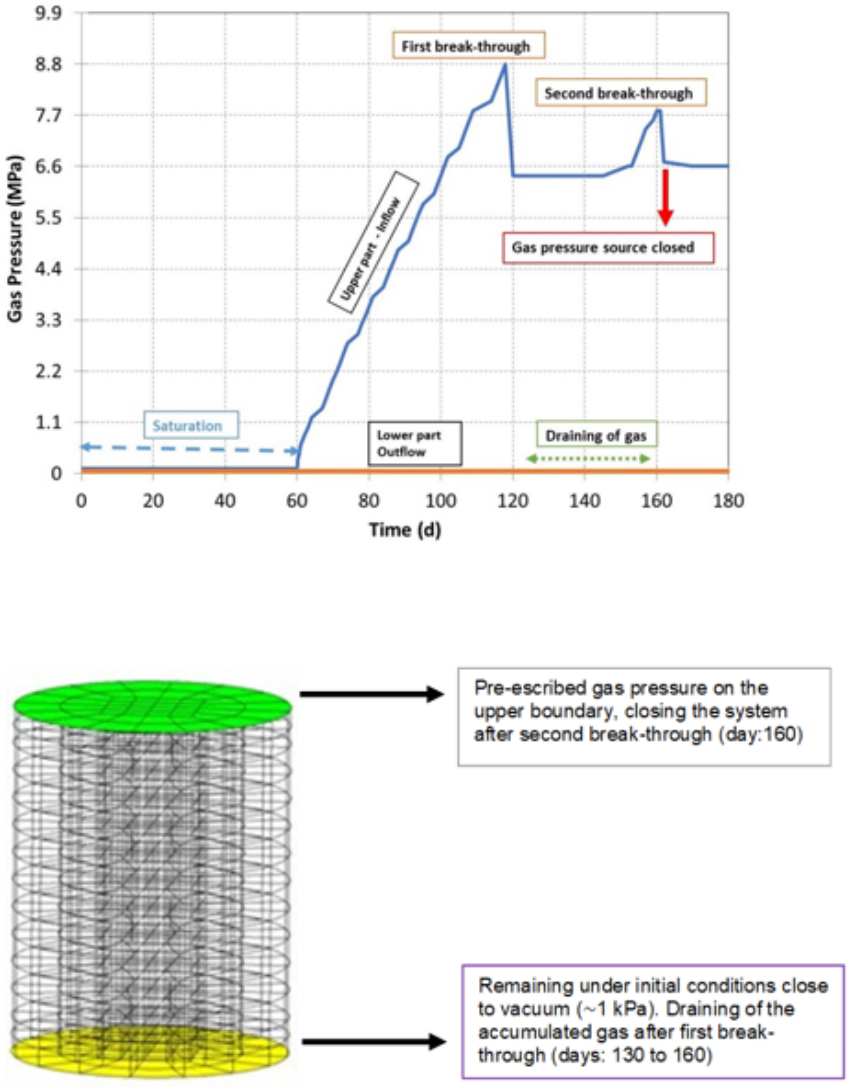

Figure 2.106: Gas pressure on the boundaries during gas injection steps.

compare to the test.

Figure 2.110 shows gas pressure distributions in 30, 58 (first BT), 90 (second BT) and 137 days later the gas injection initiation. Gas pressure evolution on the upper and lower part of the sample is also shown in Figure 2.110. First BT has occurred on 8.6 MPa and 4.4 MPa of back pressure has been achieved. Second BT has occurred in 7.6 MPa and 3.3 MPa of back pressure has been succeeded.

Figure 2.111 shows distribution of gas diffusion and gas advective flux in 30, 58 (first BT), 90 (second BT) and 137 days later the gas injection initiation. Gas advective fluxes through preferential pathways can be clearly seen during second BT (90 days).

Figure 2.112 shows mean total stresses distributions in 30, 58 (first BT), 90 (second BT) and 137 days later the gas injection initiation. In the Figure 2.112, mean total stress evolution in upper part of the sample is also shown. FEBEX bentonite was initially unsaturated. During the saturation period, swelling pressures have been developed. The total pressure reaches 8.9 MPa at the end of saturation process. After the saturation, water has been drained from the filters and gas injection test has re-started. Mean total stresses has reached to 8.6 MPa at the end of first BT. After first BT, residual gas has been drained from lower

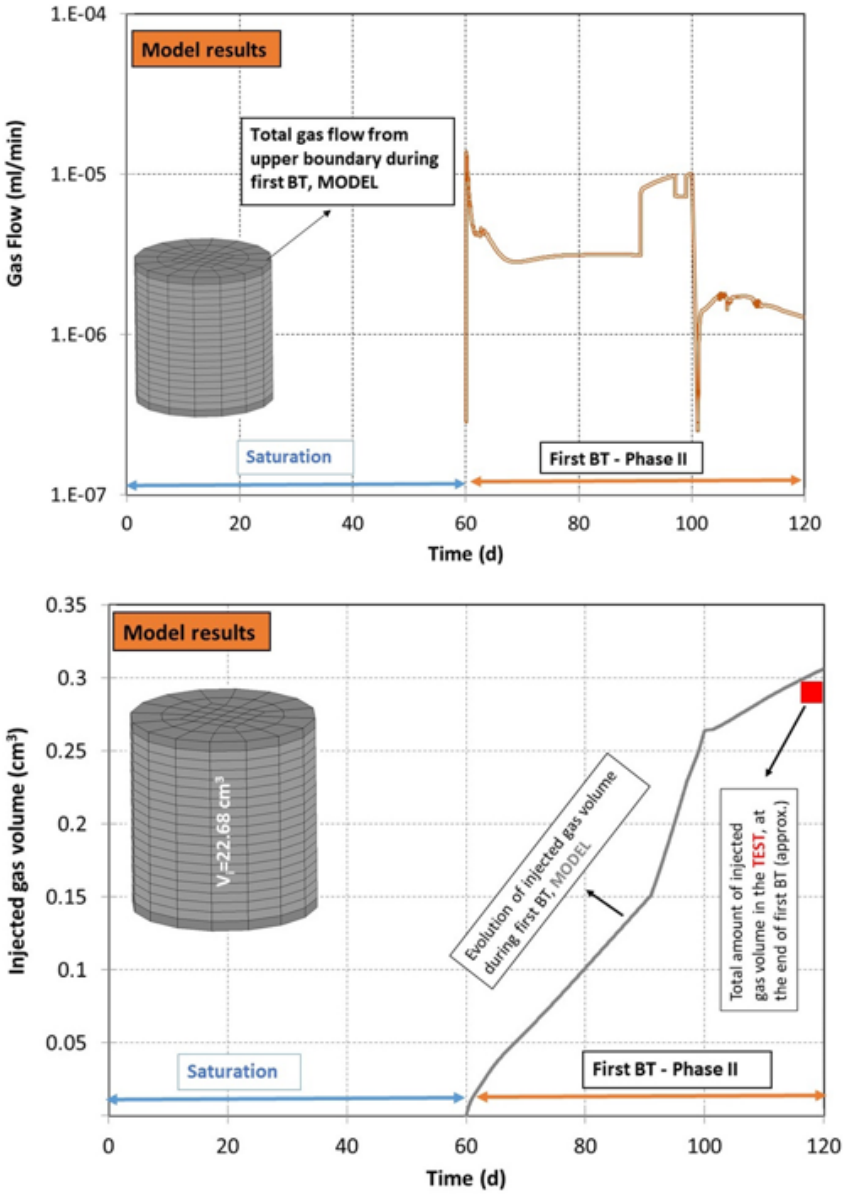

Figure 2.107: Total gas flow from upper boundary and corresponding accumulated injected gas volume in the Model A and in the Test.

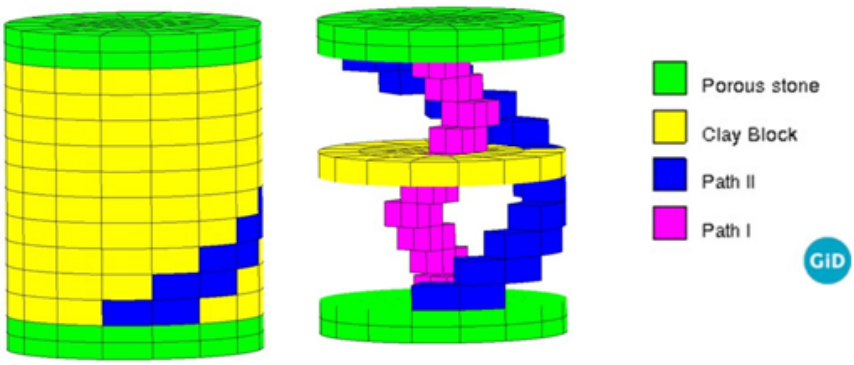

Figure 2.108: Materials considered in the model (A).

part of the sample and finally second BT test has started. The model is capable to simulate swelling pressure development during hydration; gas pressure development during gas injection test including draining process of water and gas under the same 3D configuration.

Table 2.26: Comparison of back pressure data and model results (Model A).

Breakthrough sequence	Back pressure (MPa)		
	Phase II	Phase IV	Model A
First BT	2.2	3.5	4.4
Second BT	1.7	3.4	3.3

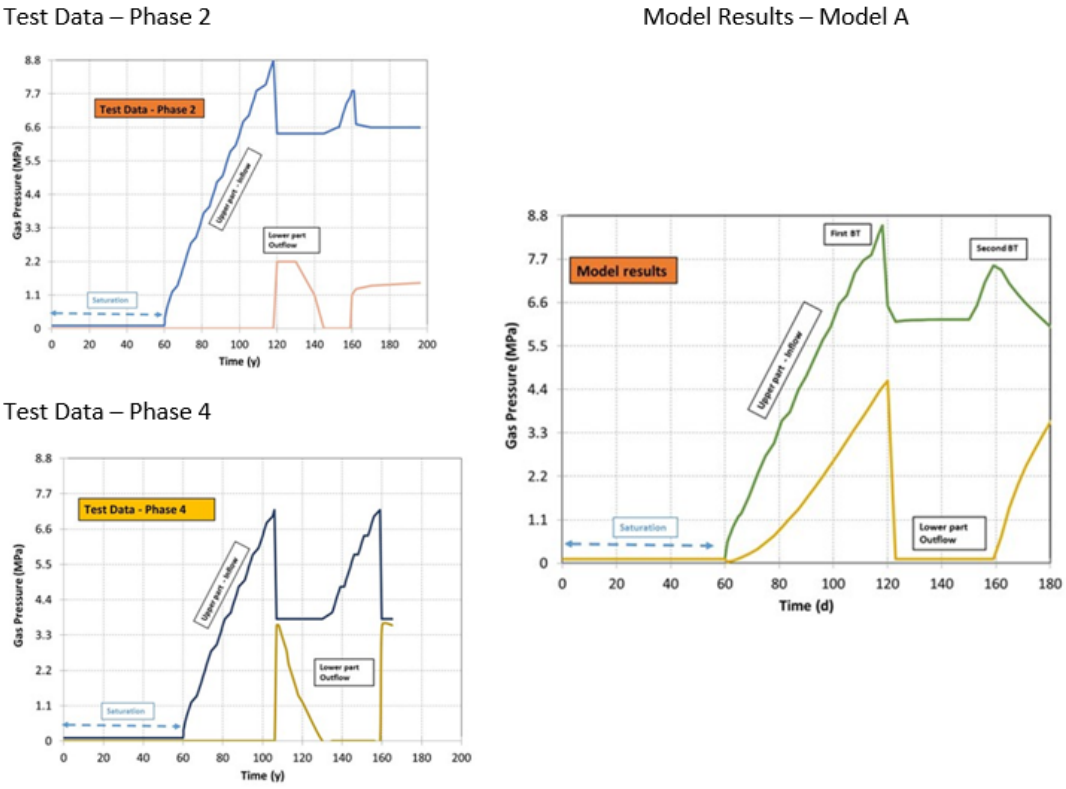

Figure 2.109: Gas pressure development in the tests and in the numerical simulation. (Model A)

2.5.4. Model B

Model B has been generated by means of incorporation of two unconnected sections into Model A geometry. Unconnected section I and unconnected section II has the same parameter set as Path I and Path II, respectively. As there are two unconnected sections in Model B, it is more heterogenous than Model A. Figure 2.113 shows distribution of connected paths and unconnected sections in Model B.

Model A and Model B correspond to arbitrary realizations of heterogeneity assuming some preferential paths (A and B) and some random heterogeneous zones (B). In the future, more realizations should be done to analyse the response depending on the distribution of properties.

Figure 2.114 shows gas pressure development in the test (Phase 2 and Phase 4) and in the Model B. Response of back pressure in the Model B is similar to Phase 4. In the numerical model, back pressure develops in a more gradual way compare to the test.

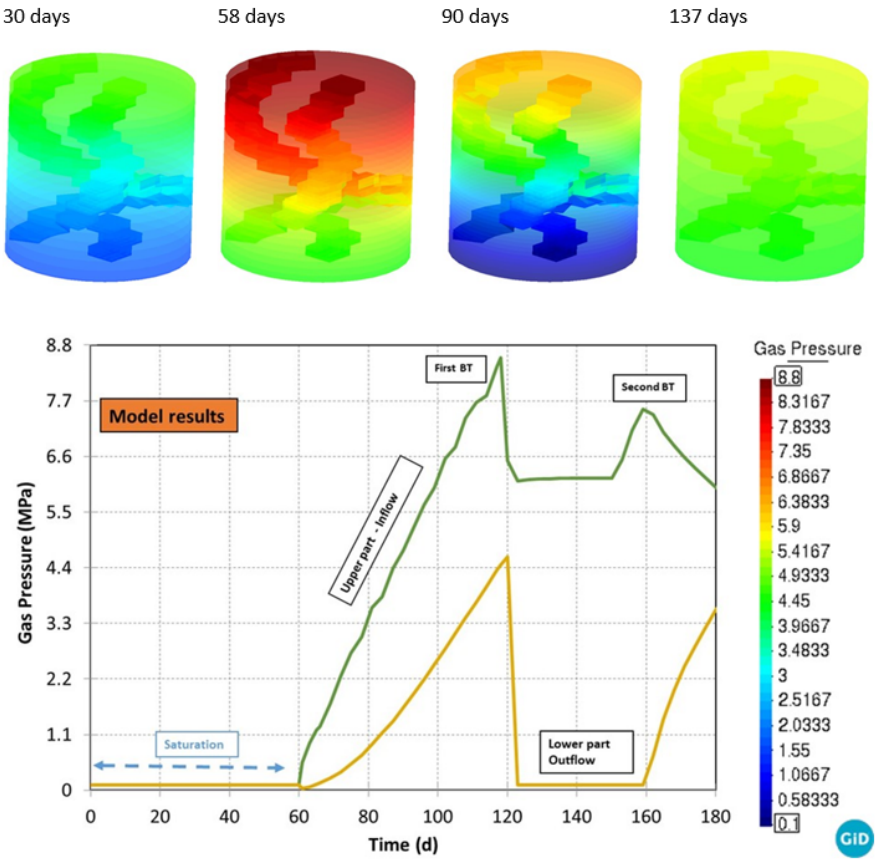

Figure 2.110: Gas pressure distributions in 30, 58 (first BT), 90 (second BT) and 137 days later the gas injection initiation. Gas pressure evolution on the upper and lower part of the sample. (Model A)

Figure 2.115 shows permeability evolution on the upper parts of the sections and distribution (during second BT) in Model B. As the pathways and unconnected sections have cubic law, intrinsic permeability increases during the aperture of these pathways. After the first breakthrough, intrinsic permeability of pathways stabilizes. Once the gas injection re-starts (second BT), pathways are activated and intrinsic permeability starts increasing again. After second BT, gas injection stops and intrinsic permeability of pathways decreases because of closure of fractures.

Figure 2.116 shows distribution of gas advective fluxes in 15, 30, 45 and 60 days in Model B. Gas advective fluxes have been concentrated on preferential pathways. Figure 2.117 shows comparison of gas diffusion (plus gas dispersion), gas advection and gas pressure at 60 days later injection. Diffusion is active in all model domain because it is non advective flux and there is no need of apertures and/or desaturation for gas diffusion. Additionally, gas diffusion is more dominant where gas advection is less relevant. Gas advection shows the preferential path formation.

2.5.5. Extended Models A and B

Model A_Extended and Model B_Extended correspond to time prolonged models that simulate all phases of the test. A summary of the phases and comparison of time stepping of the models are given in Table 2.27. After Phase II, the sample was dismantled and re-saturated. Following to re-saturation, gas injection was performed till first BT in Phase IV. The first BT pressure in Phase IV was 7.1 MPa resulting 3.5 MPa of back pressure. The second BT pressure in Phase IV was 6.6 MPa resulting 3.4 MPa of back pressure. compared to Phase II, gas BT pressures are lower but back pressures are higher. Mean value of gas BT pressure for the whole processes is 7.6 MPa and back pressure is around 3 MPa. There are differences

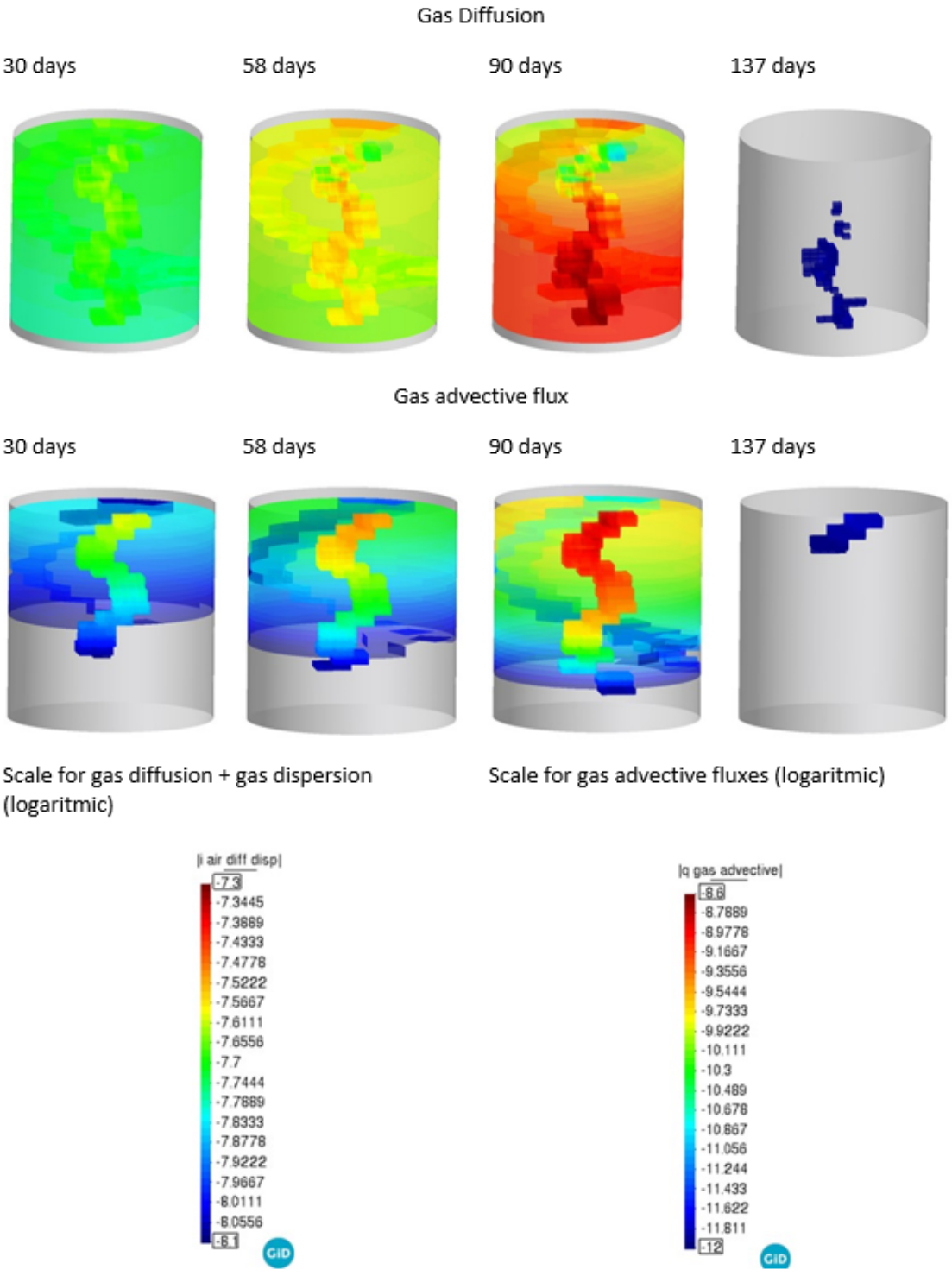

Figure 2.111: Distribution of gas diffusion and gas advective flux in 30, 58 (first BT), 90 (second BT) and 137 days later the gas injection initiation. (Model A)

between Phase II and Phase IV in terms of gas BT and back pressures because of changes in porosity-permeability and material structure during the whole process.

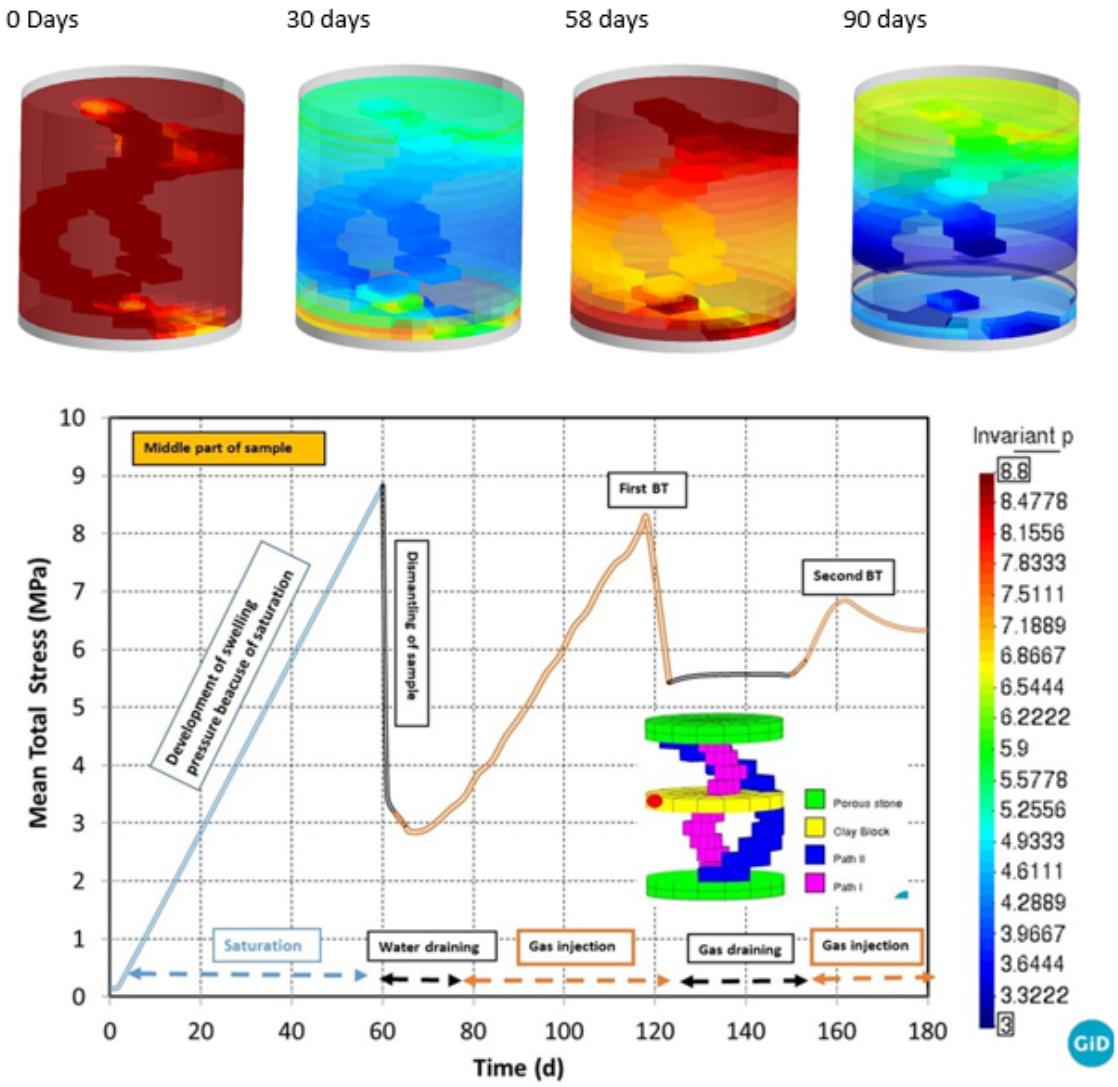

Figure 2.112: Mean total stresses distributions in 30,58 (first BT), 90 (second BT) and 137 days later the gas injection initiation. Mean total stress evolution on the middle part of the sample. (Model A)

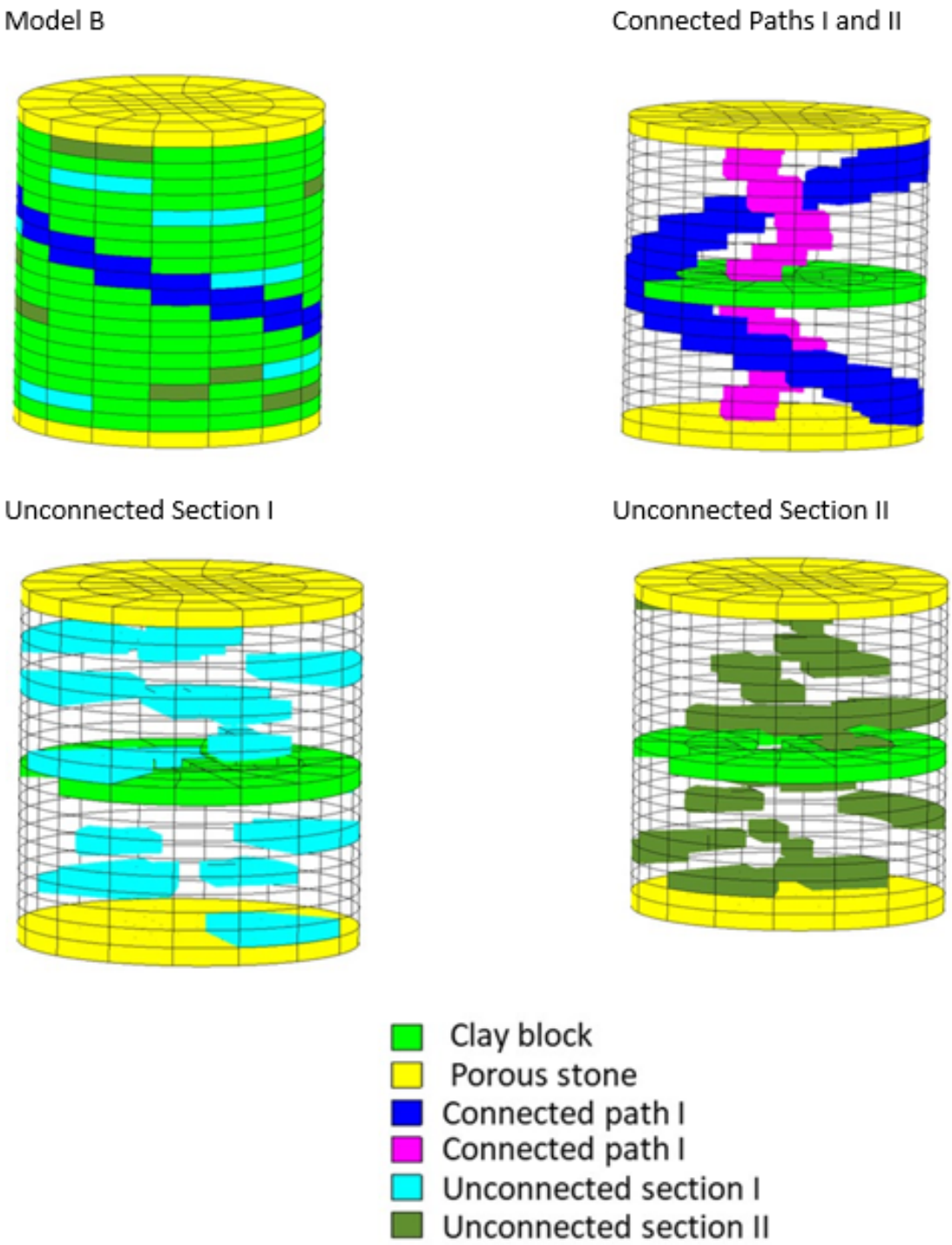

Figure 2.113: Distribution of materials in Model A.

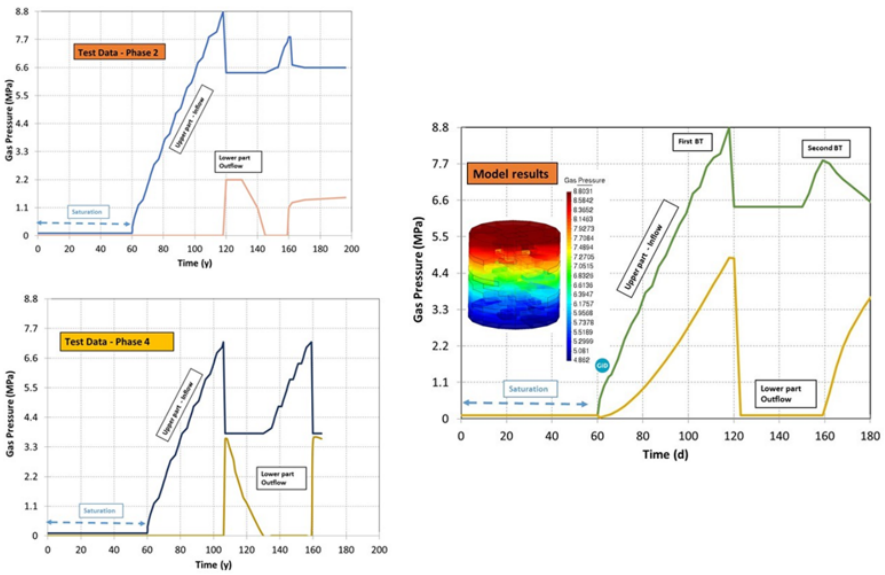

Figure 2.114: Gas pressure development in the tests and in the numerical simulation. (Model B)

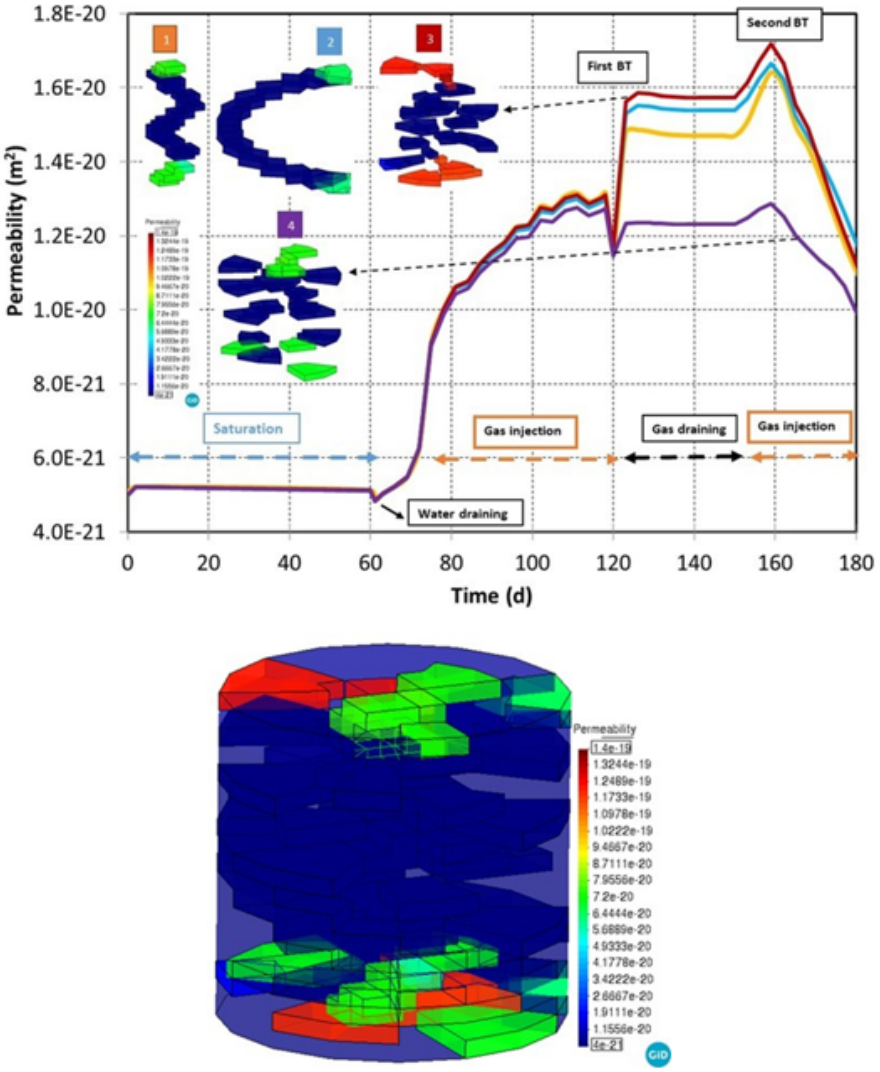

Figure 2.115: Permeability evolution on upper part of the sections and distribution (during second BT) for Model B.

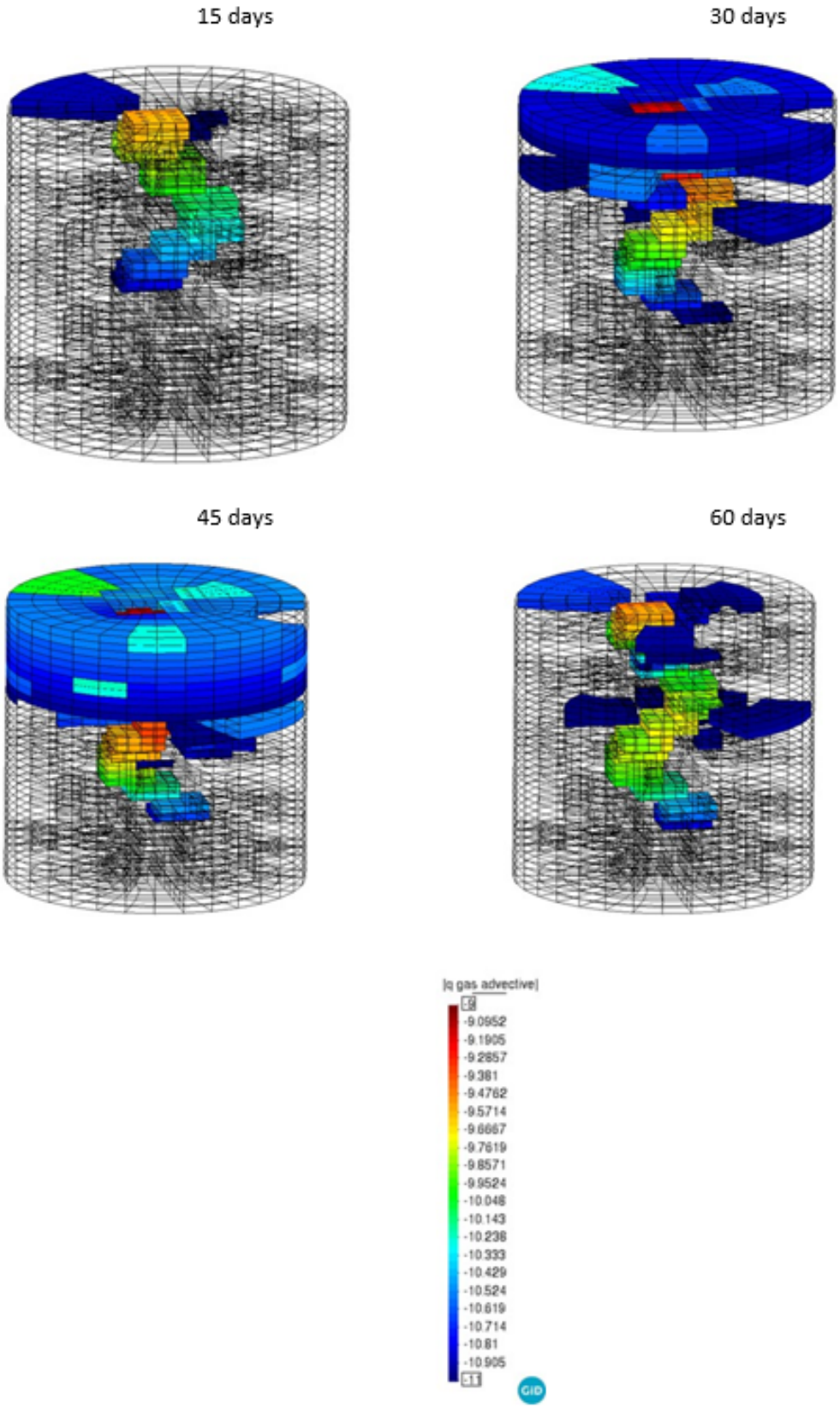

Figure 2.116: Distribution of gas advective fluxes (logarithmic scale) at 15, 30, 45 and 60 days for Model B.

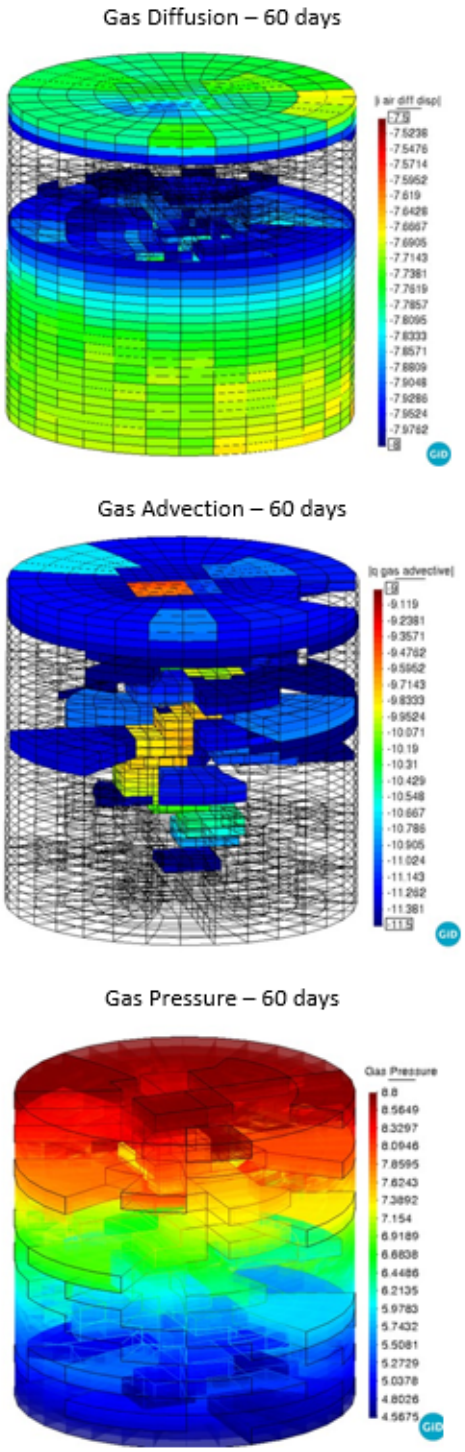

Figure 2.117: Distribution of gas diffusion (plus dispersion), gas advection and gas pressure at 60 days (Model B).

Table 2.27: Comparison of Model A, Model B and Model A_Extended.

Steps of breakthrough tests	Description	Duration (d)	Model A Model B	Model A_Extended Model B_Extended
Phase I	Saturation of the sample	60	+	+
Phase II	Gas injection - first breakthrough pressure	60	+	+
	Gas injection - second breakthrough pressure	80	+	+
Phase III	Dismantling of the sample and re-saturation	60	-	+
Phase IV	Gas injection - first breakthrough pressure	50	-	+
	Gas injection - second breakthrough pressure	50	-	+

Comparison of back pressures in the test and in the models are summarized in **Table 2.28**. Models prediction of back pressures at Phase IV is better than Phase II.

Table 2.28: Comparison of back pressure data and model results (Model A_Extended and Model B_Extended).

Breakthrough sequence	Back pressure (MPa) Test		Model A_Extended		Model B_Extended	
	Phase II	Phase IV	Phase II	Phase IV	Phase II	Phase IV
First BT	2.2	3.5	4.5	3.5	4.5	3.6
Second BT	1.7	3.4	4.5	3	4.6	3

Figure 2.118 shows gas pressure distributions in 120 (Phase II - first BT), 160 (Phase II - second BT), 310 (Phase IV - first BT) and 365 days (Phase IV - second BT). Gas pressure evolution on the upper and lower part of the model domain is also shown in Figure 2.118. In Model A_Extended and in Model B_Extended, back pressure value in Phase IV (first BT) is around 3.5 MPa which is consistent with the test data. Model A_Extended slightly overestimates back pressure in Phase II.

Figure 2.119 and Figure 2.120 shows evolution of total mass fluxes. There are three gas fluxes in the system which are gas advective fluxes (acting on preferential pathways and causing de-saturation because of water replaced by gas), dissolved advective fluxes (flux of dissolved gas into liquid phase) and non-advective fluxes (gas diffusion + dispersion). The sum of these three fluxes gives the total mass fluxes. As shown in Figure 2.119 and Figure 2.120, on the upper part where gas injection takes place; the dominant flux is gas advective flux. However, in central area of the model domain gas diffusion (dissolved non-advective flux) is more significant.

2.5.6. Sensitivity Analyses

In this Chapter, sensitivity analyses are described. The aim of the sensitivity analyses is to improve model capabilities and deal with the data uncertainties. Sensitivity analyses represent alternative material models, geomechanic model parameters and/or initial and boundary conditions. Sensitivity analyses shall remain within the scope set for the reference model in order to maintain modelling consistency. In this

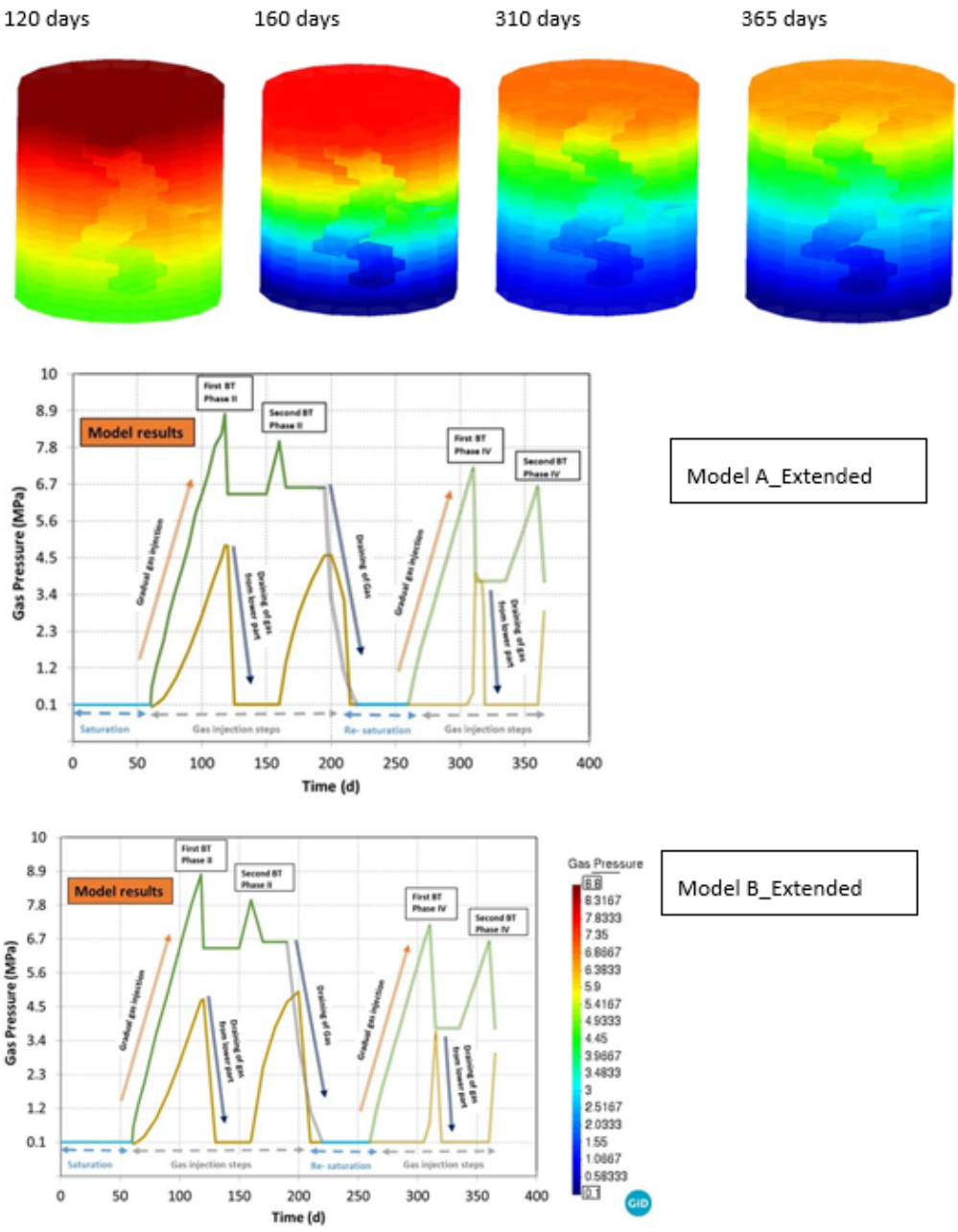

Figure 2.118: Gas pressure distributions in 120 (Phase II - first BT), 160 (Phase II - second BT) and 310 (Phase IV - first BT), 365 (Phase IV - second BT). Gas pressure evolution upper and lower part of the sample (Model A_Extended and Model B_Extended).

study, Model A has been selected as a reference model in order to develop further sensitivity analyses. Beside Model A_Extended, two more models have been prepared in order to check impact of time step (adding more phases of the test), number of nodes-elements and hydro-mechanical model parameters (gas relative permeability parameters, water retention curve parameters, pressure of pre-consolidation and heterogeneous porosity distribution) on the model response. These models are summarized in Table 2.29.

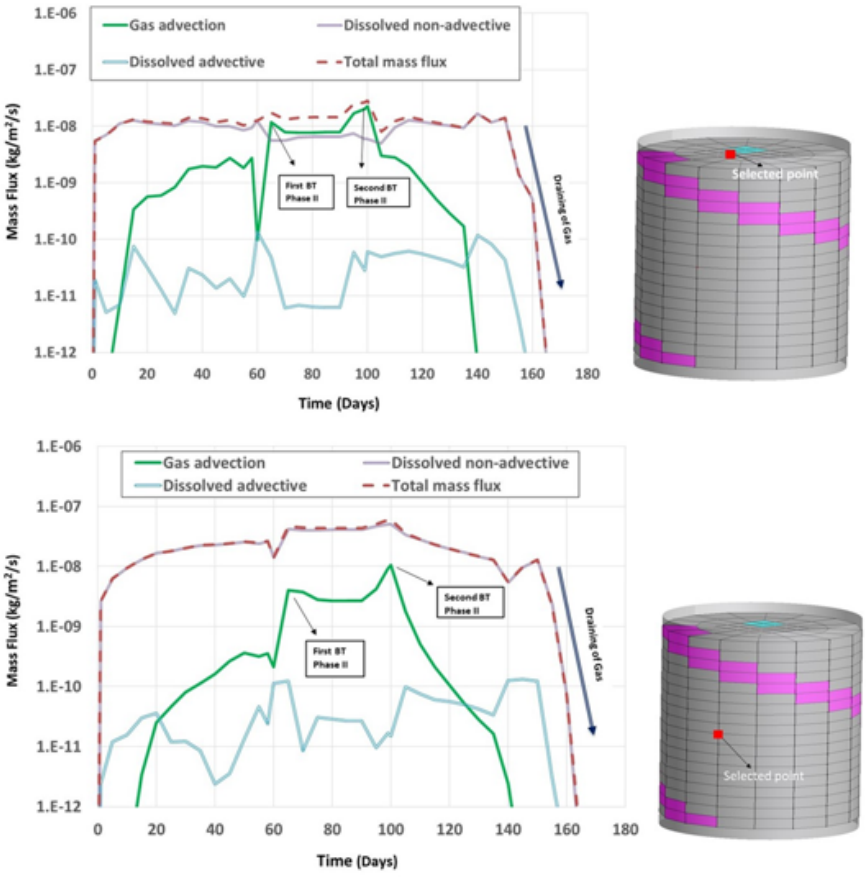

Figure 2.119: Evolution of mass fluxes till Phase III at selected points for Model A_Extended.

Table 2.29: Sensitivity analyses plan

Concept	Observation	Model
Time step	Phase III (re-saturation) and Phase IV (secondary gas injection steps) have been incorporated to Model A.	Model A_Extended (described in Chapter 2)
Hydro-mechanic	Initial heterogenous distribution of porosity has been incorporated to Model A.	Model A_Extended_1
Hydraulic	Gas relative permeability parameters have been modified. Total gas permeability has been increased. Gas entry pressure has been decreased. P_0 (WRC) has been decreased to 7 MPa from 20 MPa. (Figure 2.104, Chapter 1).	Model A_Extended_2
Mechanic	Pressure of pre-consolidation of the clay has been decreased to 8 MPa from 12 MPa (Figure 2.104, Chapter 1). Plasticity has been targeted as the Gas BT pressure was 8.8 MPa.	Model A_Extended_2

Table 2.29: Sensitivity analyses plan

Concept	Observation	Model
Computational	Number of nodes and elements have been increased in order to simulate better heterogeneity of the system.	Model A_Extended_1

Model A_Extended is a prolongation of Model A under the same geometrical configuration (connected paths). Phase III (dismantling of the sample and re-saturation) followed by Phase IV (gas injection steps) have been incorporated to Model A_Extended as discussed in Chapter 2. Figure 2.121 shows initial porosity distribution and describes main differences between the models.

Distribution of gas advective fluxes during the first BT (58 days later gas injection) are shown in Figure 2.122. Gas advective fluxes are mainly concentrated on preferential pathways. Permeability increases on these paths during gas injection because of apertures (cubic law for permeability). In Model A_Extended_2, gas permeability is the highest. Therefore, gas advection flux is the biggest in this model.

Distribution of gas diffusion (plus dispersion) during the first BT (58 days later gas injection) are shown in Figure 2.123. Gas diffusion is less relevant where the gas advection is more significant. While gas advection fluxes are mainly intensified on preferential pathways, gas diffusion is active in whole domain. For the gas diffusion there is no need of neither desaturation nor gas flow pathways development. Gas diffusion is mainly controlled by the porosity.

In Model A_Extended_1, initial distribution of porosity is heterogeneous. Consequently, distribution of gas advection fluxes and gas diffusion is relatively more heterogeneous in Model A_Extended_1 compare to other two models.

Figure 2.124 and Figure 2.125 shows evolution of total mass fluxes. There are three fluxes in the system which are gas advective fluxes, dissolved advective fluxes (dissolved gas into liquid phase) and non-advective fluxes (diffusion + dispersion). The sum of these three fluxes gives total mass fluxes as discussed in Chapter 2.

A node close to gas injection source has been selected in order to compare total fluxes in these three models. Gas advection is dominant in this selected point. Gas advection is more active in Model A_Extended_2 compare to other models because of higher gas permeability. As shown in Figure 2.125, total mass fluxes are bigger in Model A_Extended_2. There is no significant differences between Model A_Extended and Model A_Extended_1 during the first and second BT in terms of total mass fluxes. In the model, prescribed gas pressure has been applied from the upper part of the model domain. In three models, the prescribed pressures are same. However, there have been more total gas fluxes in Model A_Extended_2 because of higher permeability (both liquid and gas) and lower gas entry pressure.

Distribution of permeability during the first BT (58 days later gas injection) for three models are shown in Figure 2.126. In the preferential pathways, the permeability is higher compare to other sections in all three models. Model A_Extended_2 is more permeable than the other two models.

Distribution of liquid saturation degree during the first BT (58 days later gas injection) for three models are shown in Figure 2.127. Evolution of permeability and degree of saturation are shown in Figure 2.128. The sample was initially unsaturated. During the hydration period, it reaches the full saturation. Once the gas injection started, liquid replaced by the gas because of gas advective fluxes. Therefore, de-saturated zones

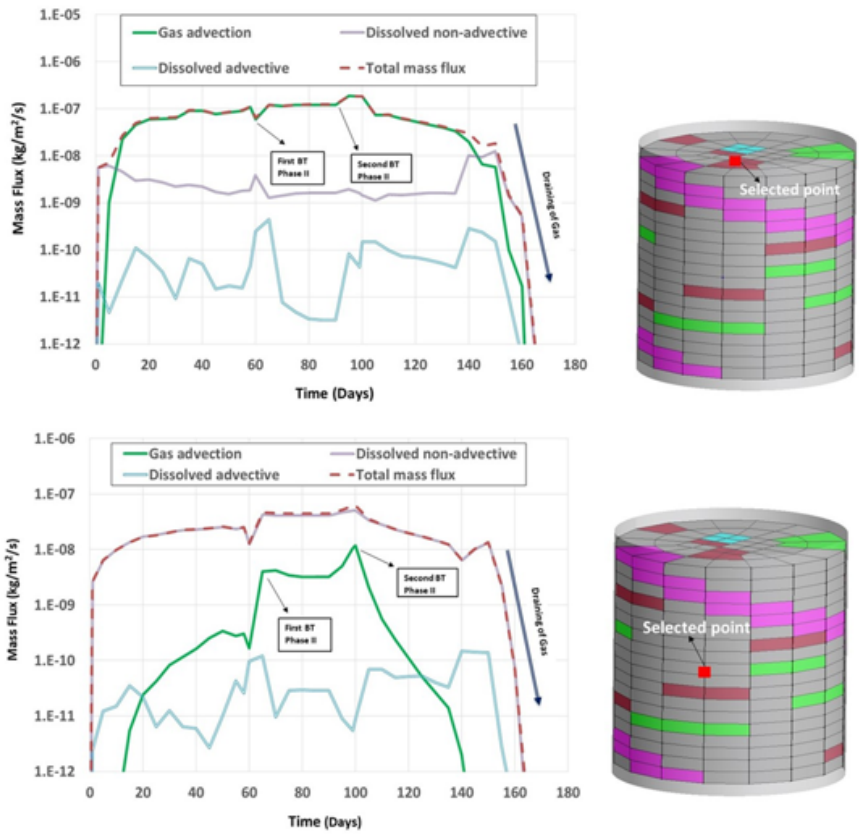

Figure 2.120: Evolution of mass fluxes till Phase III for Model B_Extended.

correspond to gas advective fluxes and show the preferential gas flow pathways. Similarly, permeability increases where the gas advective fluxes are significant. Hence both distribution of de-saturated zones and increased permeabilities indicate possible gas flow pathways.

Initial permeability (Figure 2.128) in Model A_Extended and Model A_Extended_1 is not same because of heterogenous distribution of porosity in Model A_Extended_1. In Model A_Extended_2, initial liquid permeability is one order bigger than the other two models. Permeability increases during gas injection and decreases during draining of gas in all three models.

Although Model A_Extended_2 is more permeable, it has a lower P_0 (water retention curve) value. Therefore, during gas breakthrough the de-saturation has been more significant (Figure 2.128) in Model A_Extended_2. However, re-saturation because of gas draining is faster in Model A_Extended_2 as it is more permeable.

Distribution of gas pressure during the first BT (58 days later gas injection) for three models are shown in Figure 2.129. Back pressures are around 4.6 MPa in Model A_Extended and Model A_Extended_1. Gas pressure distribution is relatively heterogeneous in Model A_Extended_1 because of initial heterogeneous distribution of porosity. In Model A_Extended_2, the highest back pressure has been succeeded as the total gas permeability was bigger in this model. The back pressure reaches to 8.4 MPa at the end of 58 days later gas injection initiation in Model A_Extended_2, which is significantly bigger than the test data.

Distribution of mean total stresses during the first BT (58 days later gas injection) for three models are shown in Figure 2.130. In Model A_Extended_2, the mean total stresses are bigger than the other two models at the end of 58 days of gas injection (first BT).

Evolution of gas pressure on the top (close to gas injection source) and the bottom (back pressure) to-

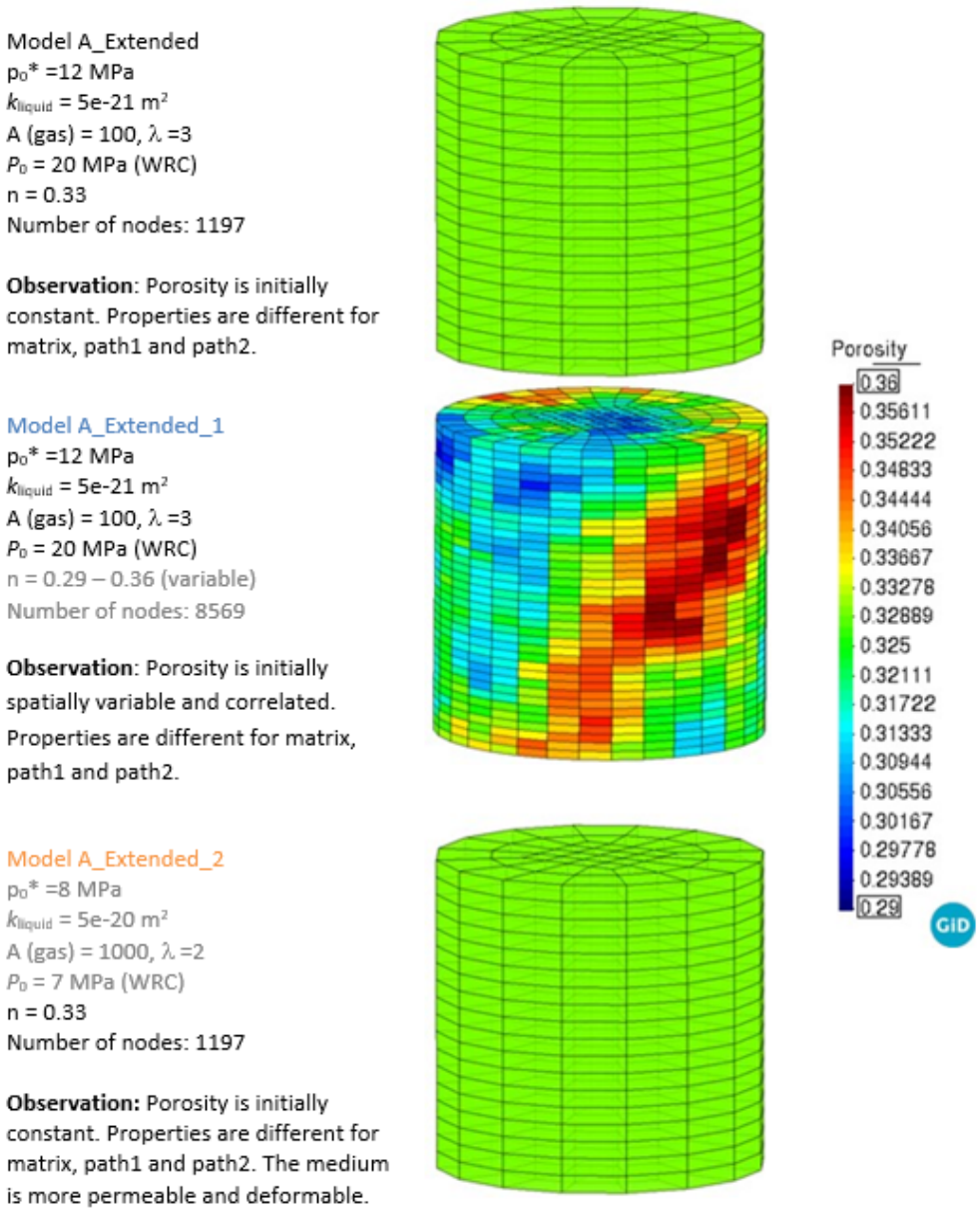

Figure 2.121: Distribution of initial porosity in three models.

gether with evolution of mean total stresses on central area are shown in Figure 2.131. In Phase II, back pressures were around 2.3 MPa and in Phase IV it was 3.5 MPa in the test. Model A_Extended and Model A_Extended_1 can predict adequately back pressures in Phase IV and slightly overestimate back pressures in Phase II. However, Model A_Extended_2 overestimates significantly back pressures in Phase II as it has a bigger permeability and lower gas entry pressure compare to other two models.

As shown Figure 2.131, developed mean total stresses during hydration (swelling pressure plus liquid pressure) in Model A_Extended_2 are lower compare to other two models. As preconsolidation pressure is lower in Model A_Extended_2, there has been less swelling pressure development during saturation phase. However, mean total stresses in Model A_Extended_2 are higher compare to other models during gas injection. As Model A_Extended_2 is more permeable, there is more gas pressure development on the selected point (central area) leading to higher mean total stresses. During the gas withdrawal from the lower part (draining of gas), the pressure dissipation is more significant in Model A_Extended_2 compare to other two models as it is more permeable.

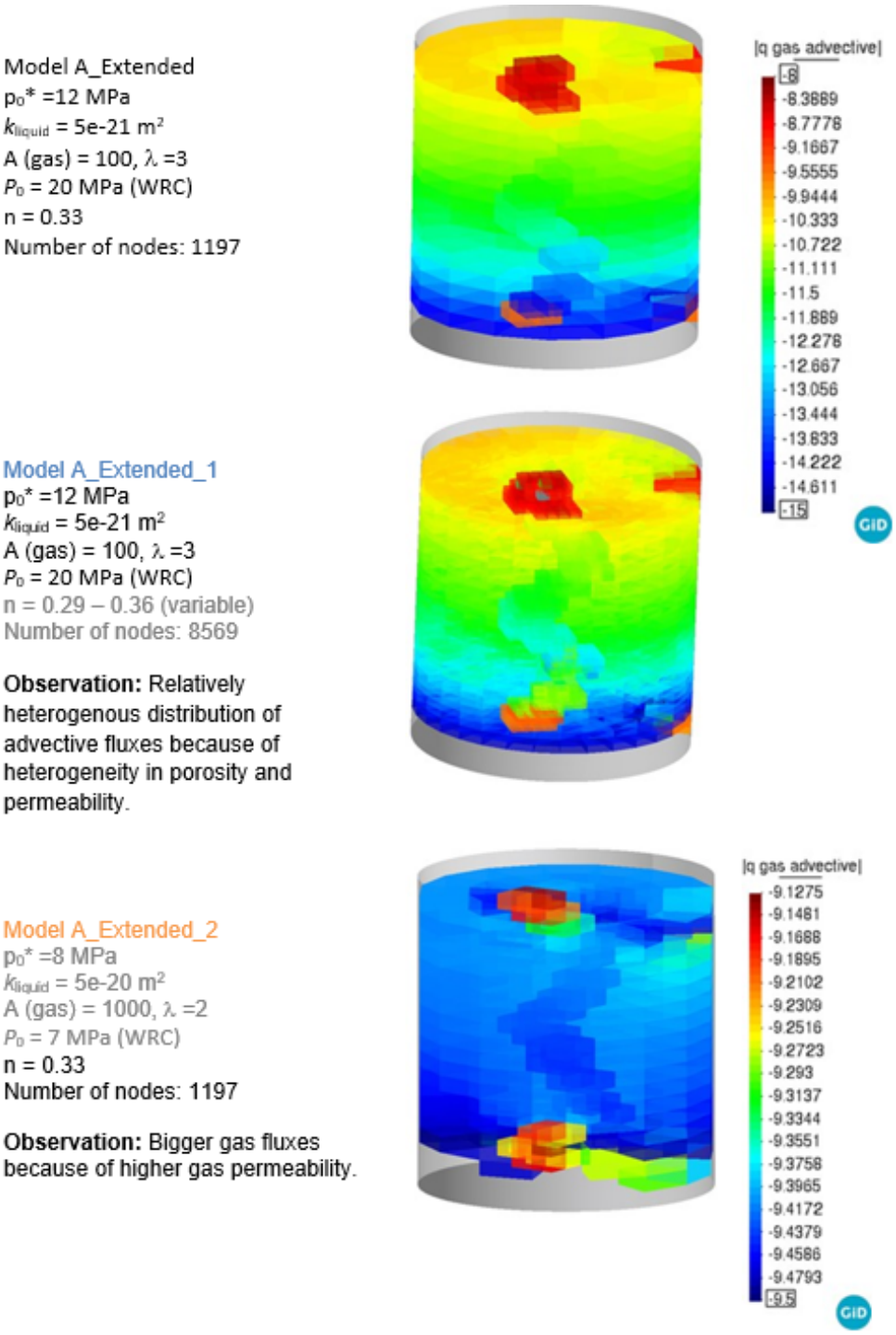

Figure 2.122: Distribution of gas advective fluxes (logarithmic scale) in three models during first breakthrough (58 days later gas injection).

Distribution of preconsolidation pressures during the first BT (58 days later gas injection) for three models are shown in Figure 2.132. In Model A_Extended_2, preconsolidation pressure has been considered as 8 MPa which is lower than the maximum gas BT pressure (8.8 MPa). Therefore, plasticity has been observed in this model. In Model A_Extended and Model A_Extended_1 preconsolidation pressure has been set as 12 MPa. Therefore, these two models are in elastic regime.

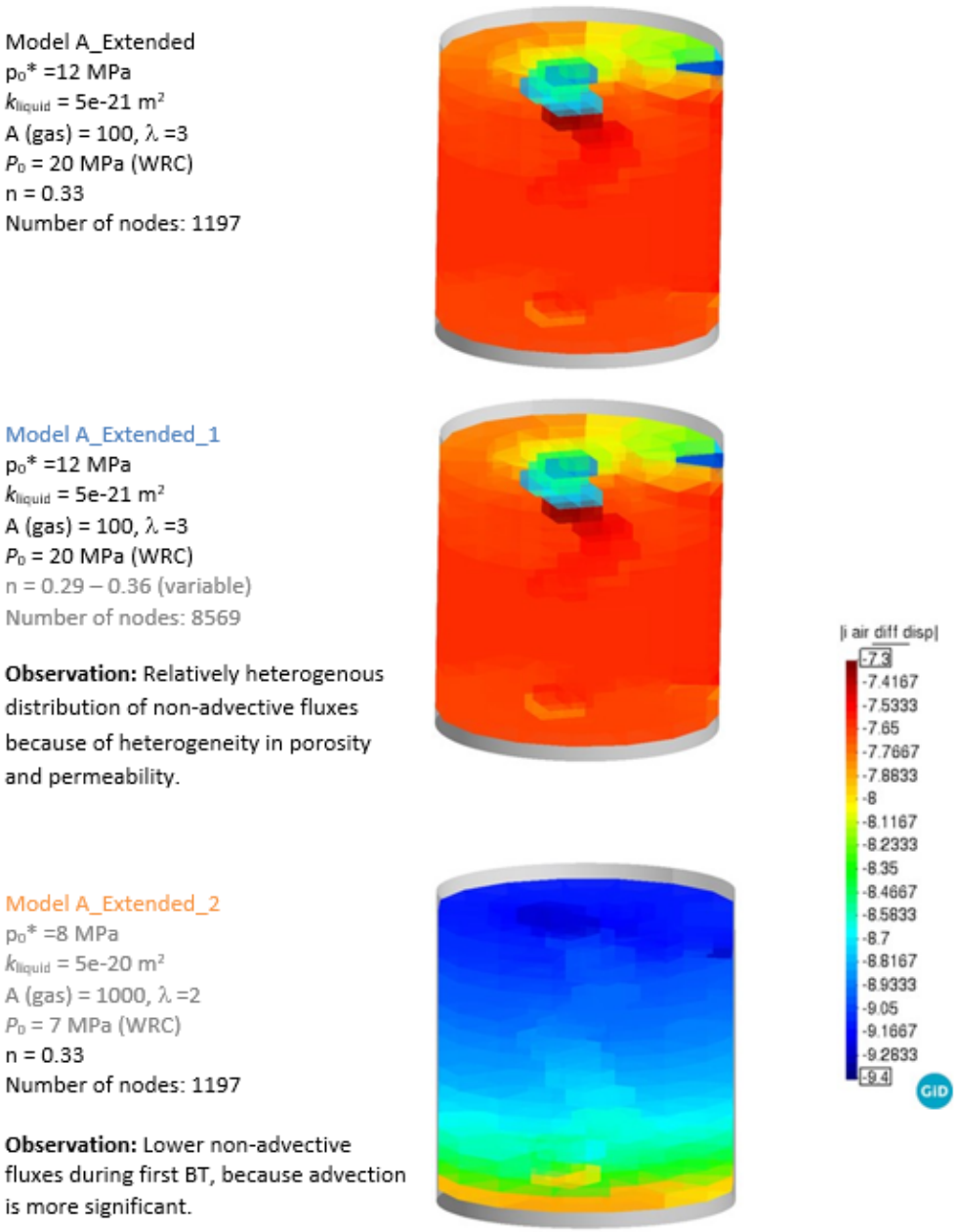

Figure 2.123: Distribution of gas diffusion plus dispersion (logarithmic scale) in three models during first breakthrough (58 days later gas injection).

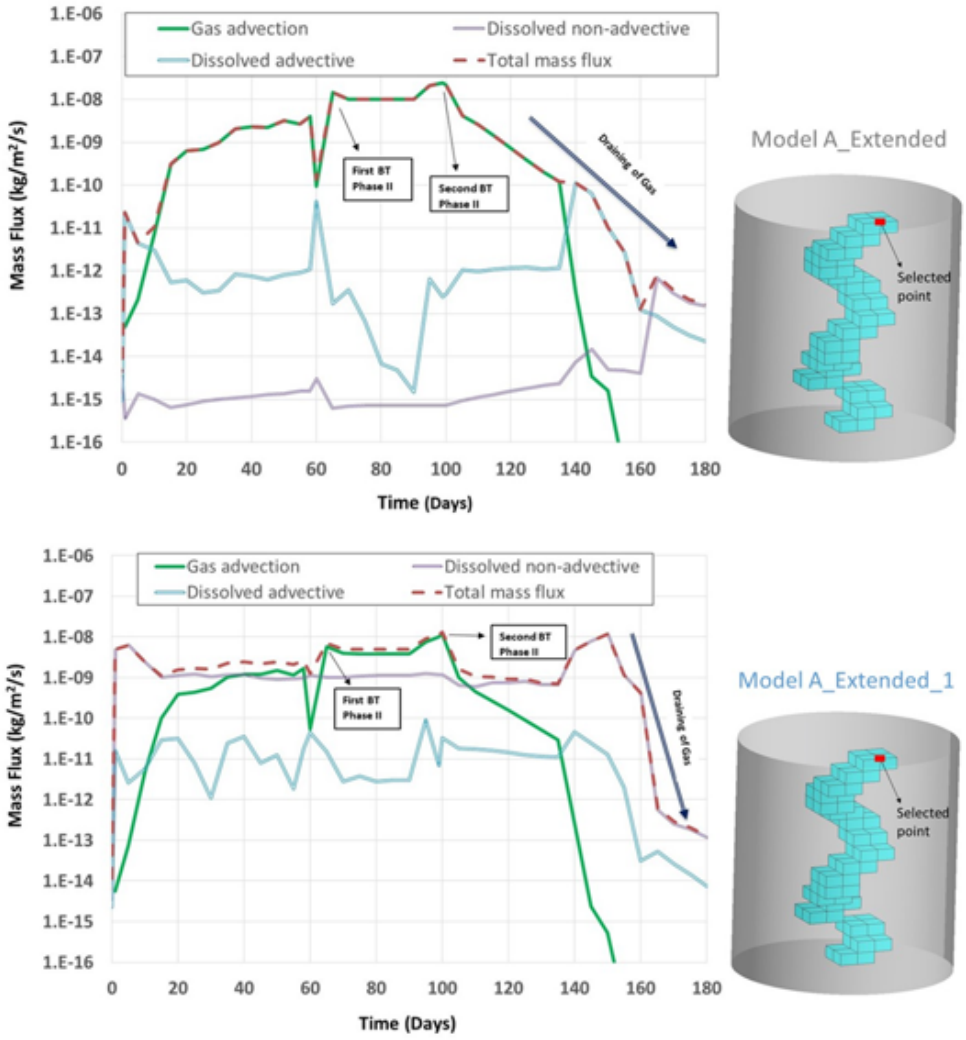

Figure 2.124: Mass fluxes at selected points in Model A_Extended (above) and Model A_Extended_1 (below).

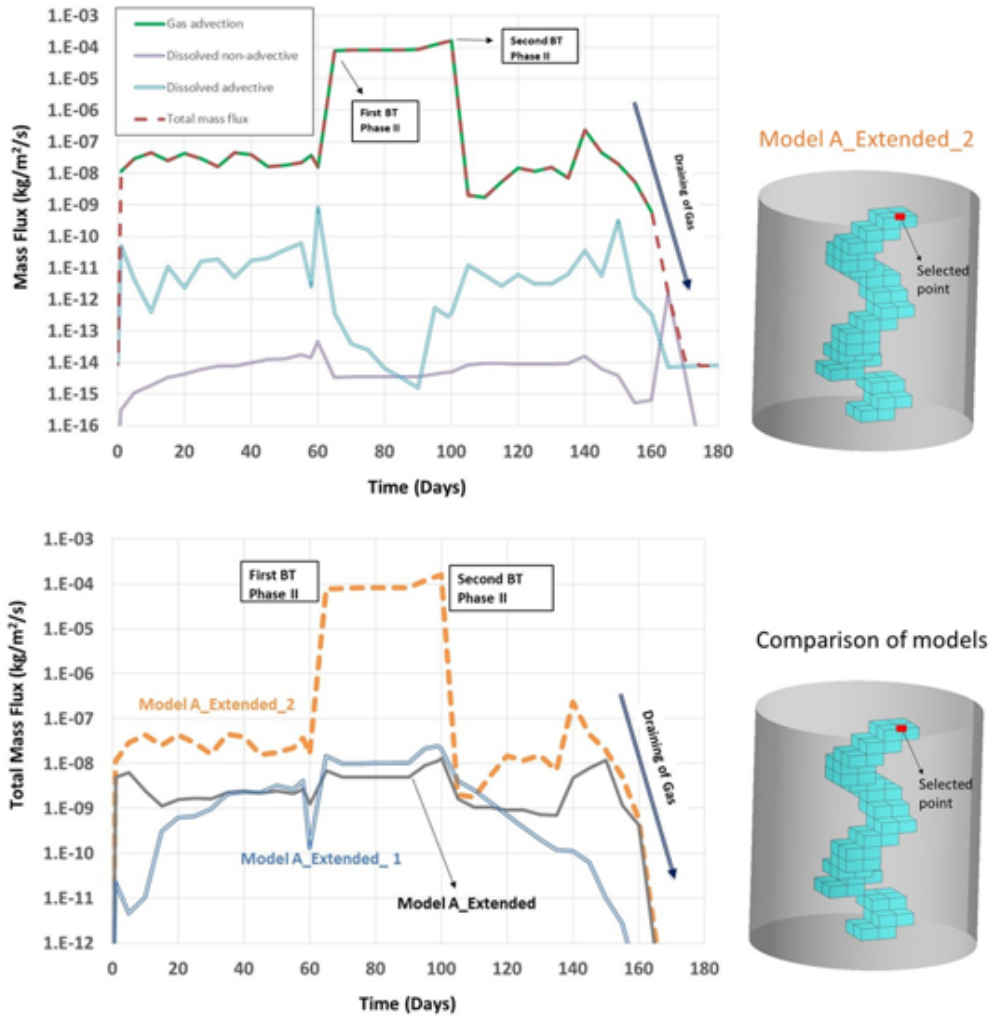

Figure 2.125: Mass fluxes in Model A_Extended_2 (above) and comparison of total mass fluxes for the different models (below).

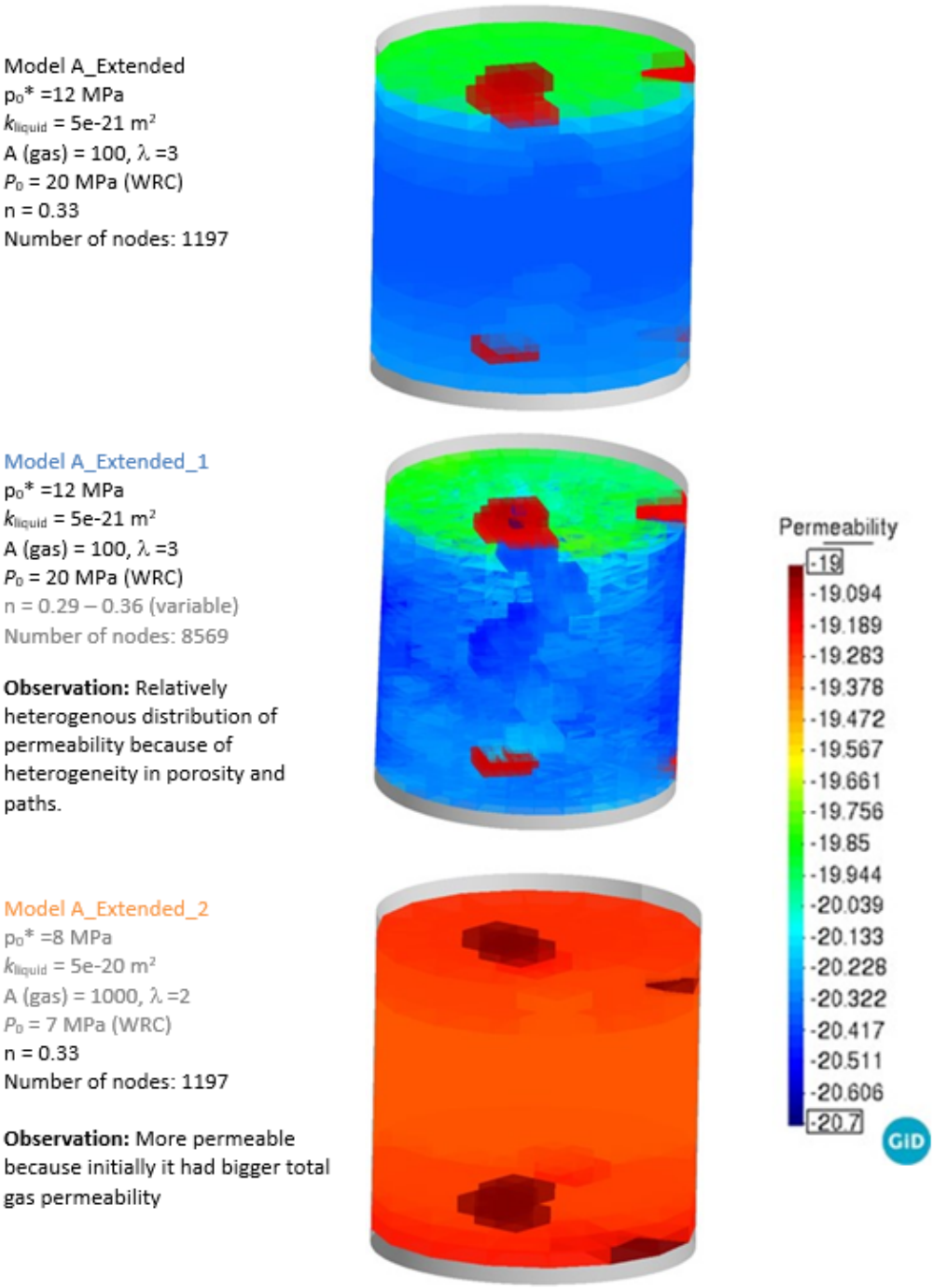

Figure 2.126: Distribution of permeability (logarithmic scale) in three models during first breakthrough (58 days later gas injection).

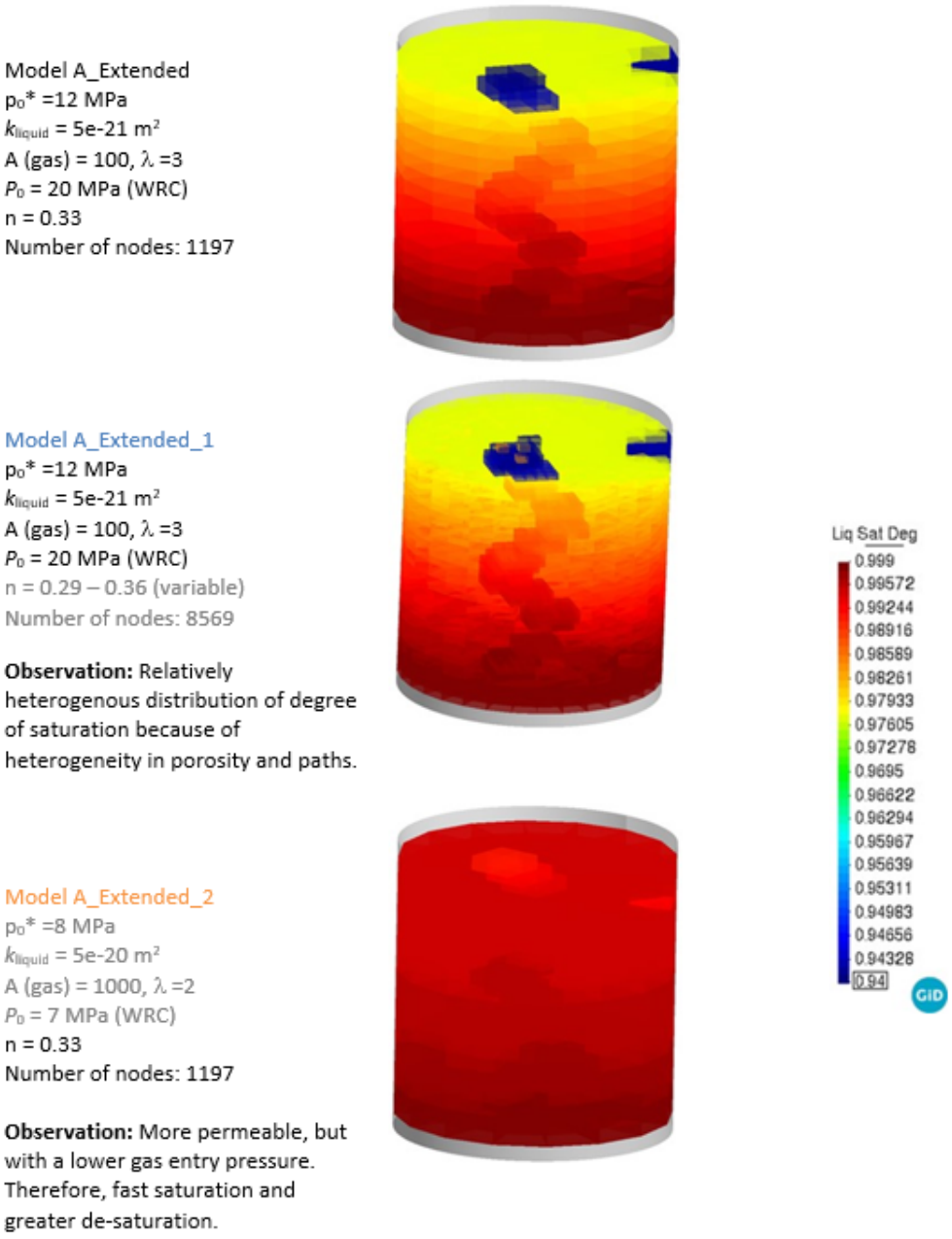

Figure 2.127: Distribution of liquid saturation degree in three models during first breakthrough (58 days later gas injection).

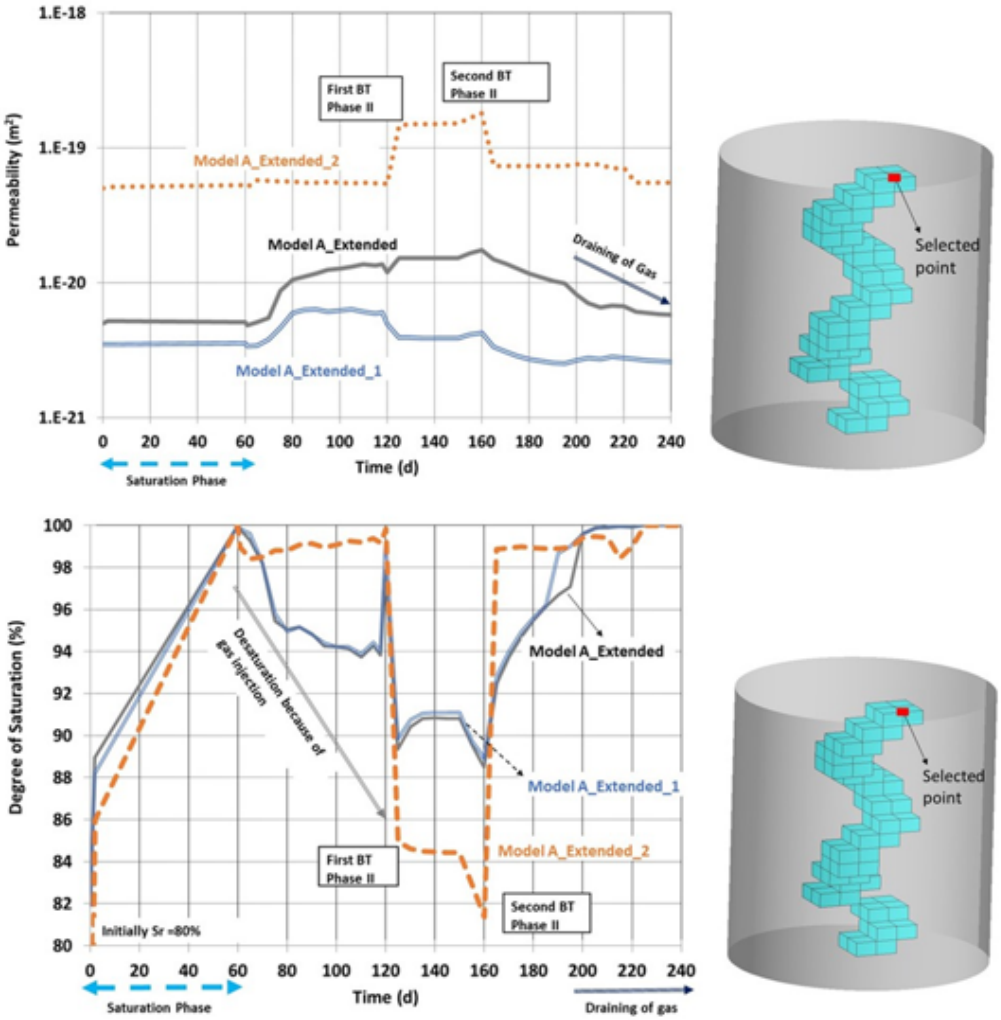

Figure 2.128: Comparison of permeability and degree of saturation evolutions in the models.

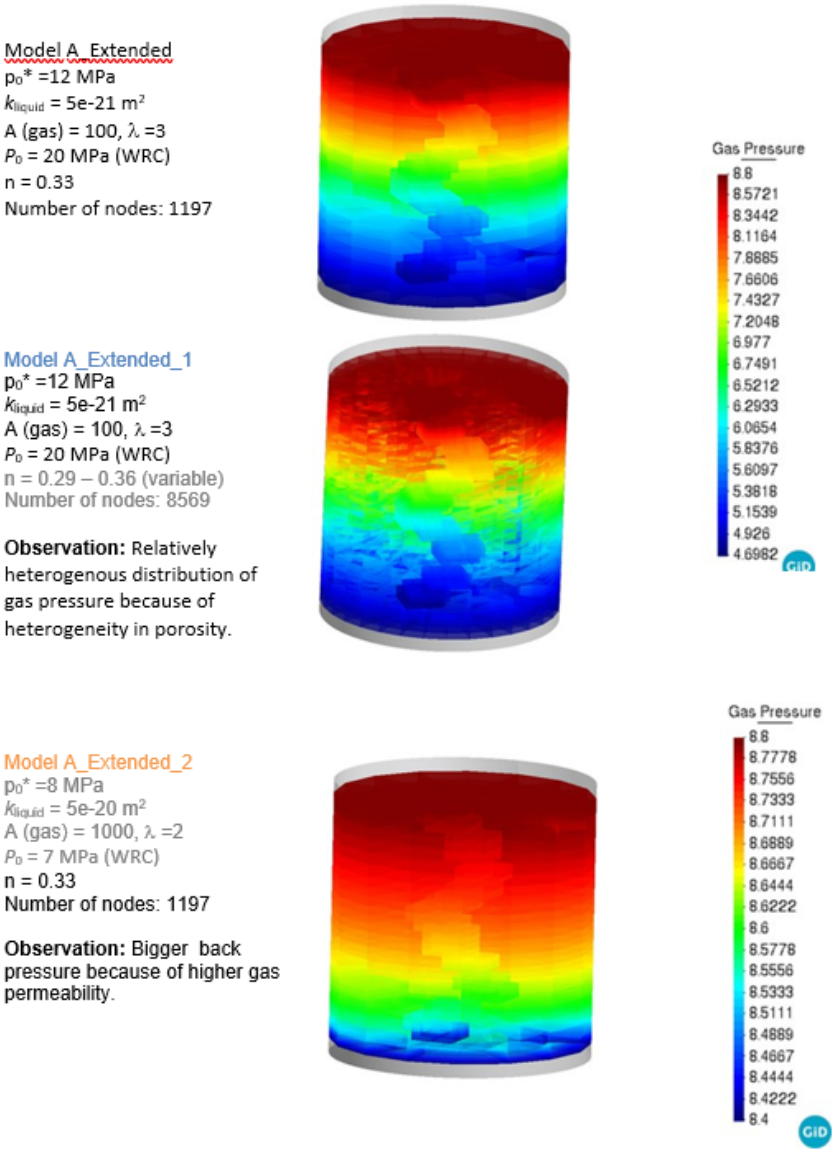

Figure 2.129: Distribution of gas pressure in three models during first breakthrough (58 days later gas injection).

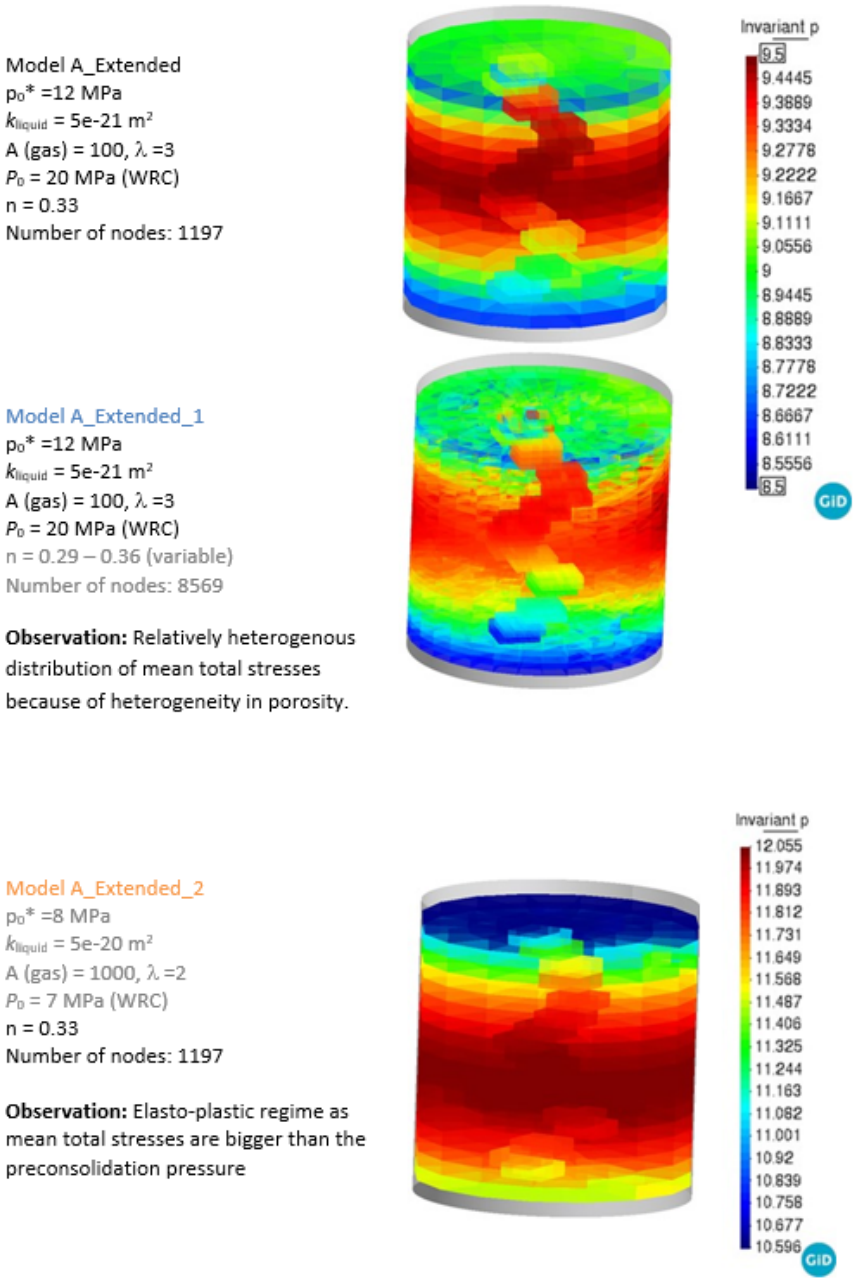

Figure 2.130: Distribution of mean total stresses in three models during first breakthrough (58 days later gas injection).

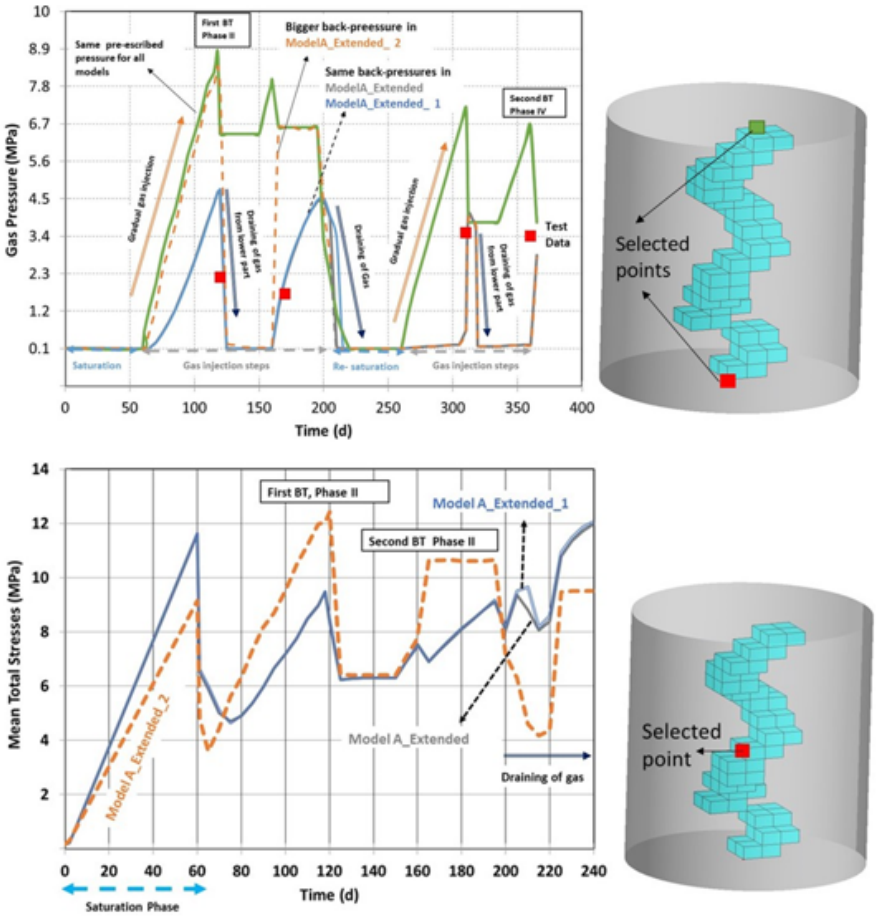

Figure 2.131: Comparison of gas pressure (above) and mean total stresses (below) in the models.

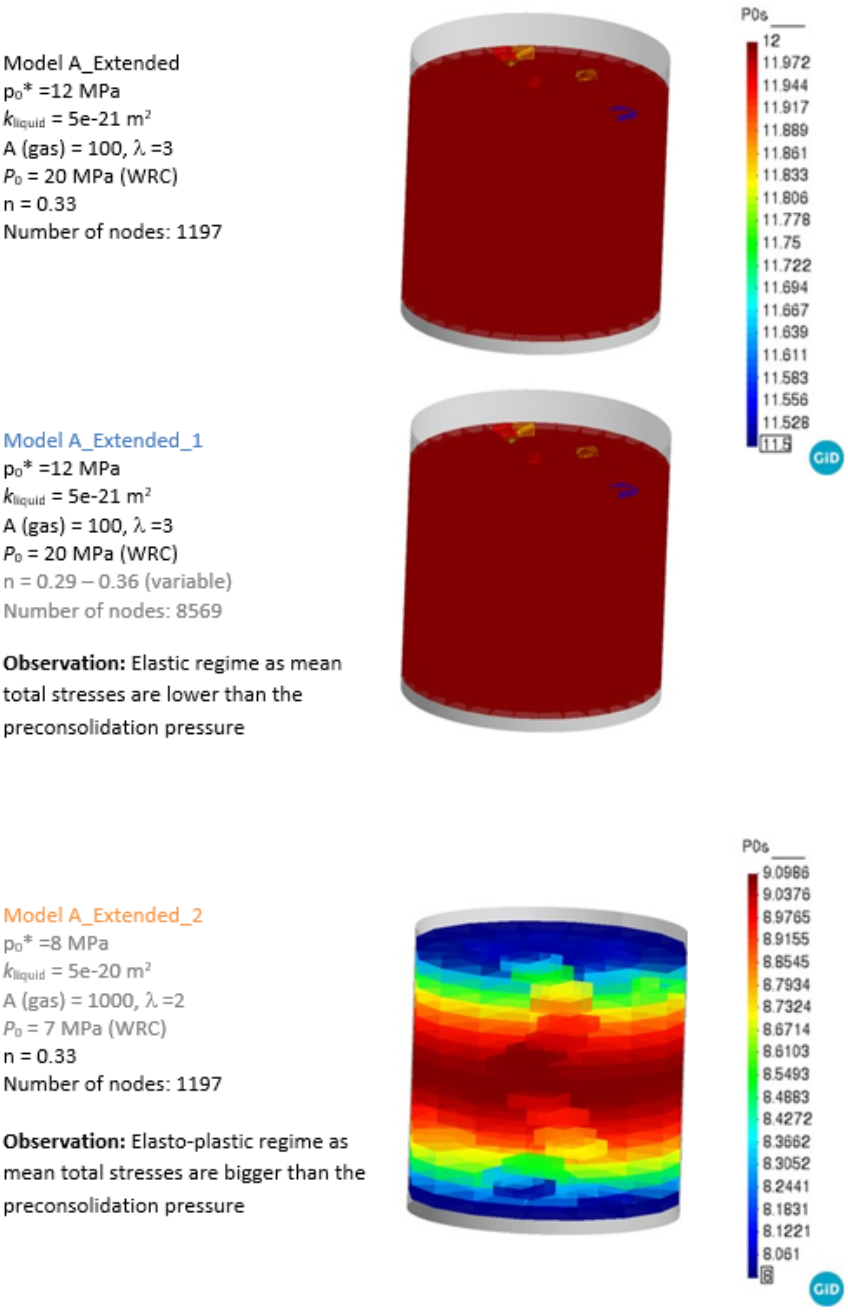

Figure 2.132: Distribution of pressure of pre-consolidation in three models during first breakthrough (58 days later gas injection).

2.5.7. Summary

In order to investigate gas transport process in bentonite barrier (FEBEX bentonite) and gas pathway development along the barrier; hydro-mechanical simulation of a breakthrough test (Gutierrez, 2018) has been performed. The objective of the modelling work was to simulate all phases of the test under proper boundary conditions, material model options and geometrical configuration.

BBM has been selected as a geo-mechanical model for the clay (FEBEX). In order to simulate increase in permeability during gas injection, cubic law for permeability has been used as a hydro-mechanical model for the gas flow pathways.

A full 3D geometry with different heterogeneity configurations (connected and unconnected paths), including porous stones, has been developed for the purpose of simulation of the test. One of the aims of the test was to simulate all processes (saturation, draining, gas injection, dismantling, etc.) taking place in the test.

A sensitivity analyses plan has been followed in order to improve model response and deal with test robustness and uncertainties. Table 2.30 summarizes objective, challenges, solutions and achievements of the modelling work.

Table 2.30: Summary, challenges and progress of the modelling work

Objective	• To investigate gas transport mechanism in FEBEX (initially unsaturated) material.
Challenges Limitations	• Mechanical Model : Using BBM in a 3D model with complex boundary conditions. • Boundary Conditions: Water/gas exchange procedure. Saturation and gas injection steps under the same 3D model. • Hydraulic Model: Verification and validation of heterogenous zones, preferential pathways and cubic law parameters.
Solutions Suggestions	• Preparation of a continues and layered geometry with structured mesh • Gradual gas injection and draining on the boundaries. • Follow a sensitivity analysis plan.
Sensitivity analyses	• Geometrical : Connected (Model A) and unconnected paths (Model B). • Time stepping : Prolongation of the test, including dismantling of the sample and re-saturation followed by new gas injection steps (Model A_Extended, Model B_Extended). • Hydro-mechanical model parameters: Variation of gas permeability, gas entry pressure; initial variable porosity and preconsolidation pressure (Model A_Extended_1 and Model A_Extended_2) • Computational: Refine of meshing, increasing number of elements (Model A_Extended_1)

Table 2.30: Summary, challenges and progress of the modelling work

Objective	• To investigate gas transport mechanism in FEBEX (initially unsaturated) material.
Achievements Progress	• HM Model**:** 3D modelling of a gas BT test on FEBEX with BBM and cubic law for permeability. • Full process: Saturation, draining, water/gas exchange, gas injection and gas/water exchange processes under the same 3D model. • Improvement of model response especially for Phase IV.

2.5.8. Key learning points

New knowledge acquired

It has been shown the possibility of modelling of gas breakthrough test with all experimental steps (saturation, gas injection, draining of gas, re-saturation and second gas injection) under a 3D full geometry by using complex hydro-mechanical models (cubic law for permeability and BBM as a mechanical model). The methodology can be applied to model other experiments and using other realizations of the heterogeneity field (based on imaging techniques for observation of real heterogeneity).

Impact of acquired knowledge

The model with heterogeneous zones (connected paths and/or unconnected paths) has been generated for a laboratory scale test. The model can be considered as a reference case and can be served to model in-situ and full scale gas injection tests under 3D geometries with complex hydro-mechanical models. The methodology used to generate heterogeneous zones and pathways can be used for upscaling.

Remaining knowledge gaps

The model is capable to predict test results. However, it considers arbitrarily random distribution of permeability zones (corresponding to realizations). By providing a better instrumentation and sensor data, imaging techniques, transparent walls, etc; permeability and porosity zones can be defined better.

Regarding material properties, it can also be interesting to incorporate double structure models (BExM) and geochemistry. In this way macro-porosity can play a key role on gas migration, and chemistry can have an influence on swelling capacity of the clay components.

Recommendations for the future

In this work, it was not possible to localize heterogeneous permeability fields as the sample was small and the instrumentation was limited. For this kind of tests, a better instrumentation is recommended. Also it is very important to collect realistic distributions of density or porosity for real samples before and after testing them.

There are two levels of heterogeneity observed during gas injection test. The first level of heterogeneity is associated with the variation of dry density (porosity) during the hydration. Gas BT pressures are associated with the final dry density (swelling pressure varies according to dry density) prior to gas injection

rather than the initial dry density. Therefore, hydration step shall be integrated in the modelling in order to improve the model predictions. The second level of heterogeneity is related to gas effective permeability. In intact clay (no advection of free gas), gas permeability and WRC is porosity dependent. In contrast, gas permeability and WRC is strain dependent in dilatant pathways. The magnitude of the apertures in dilatant pathways is variable. Therefore, at least two different gas flow pathways with different aperture characteristics shall be integrated into model. An elasto-plastic model such as BBM is required not only to reproduce development of swelling pressures during hydration part but also to simulate possible irreversible strains induced by gas injection under the heterogenous model configuration.

References

Alonso EE, Gens A and Josa A (1990) A constitutive model for partially saturated soils. Géotechnique 40(3): 405-430. 1990. pp. 405-430.

Enresa (2000) FEBEX Project. Full-scale engineered barriers experiment for a deep geological repository for high level radioactive waste in crystalline host rock. Enresa, Madrid, Spain. Final report, 1/2000.

Enresa (2006) Full-scale engineered barriers experiment. Enresa. Madrid. Spain. Updated final report 1994-2004. Technical publication 05-0/2006.

Gens A, Sánchez M and Guimaraes LN et al. (2009) A full-scale in situ heating test for high-level nuclear waste disposal: observations, analysis and interpretation. s.l.: Géotechnique, 59(4): 377-399, 2009. pp. 377-399.

Olivella S, Carrera J, Gens A & Alonso EE (1994) Nonisothermal multiphase flow of brine and gas through saline media. Barcelona, Spain. Transport in Porous Media, 1994. 271–293.

Olivella S. And E.E. Alonso, Gas flow through clay barriers, 2008, Geotechnique 58, No. 3, 157–176 [doi: 10.1680/geot.2008.58.3.157]

Gutiérrez Vanesa Transporte de gas en materiales de barrera, PhD dissertation, 2018.

Toprak E, Olivella S and Pintado X, (2020) Modelling engineered barriers for spent nuclear fuel repository using a double-structure model for pellets. Environmental Geotechnics, [doi: 10.1680/jenge.17.00086.

.

IC2MP (CNRS, University of Poitiers)

2.6. Barrier integrity - IC2MP (CNRS, University of Poitiers)

2.6.1. Introduction

2.6.1.1. Conceptual model

Consider a domain $\Omega = \Omega_i \cup \Omega_s \subset \mathbb{R}^n$ ($n \in \{2, 3\}$) entirely or partially cut by a discontinuity Γ such as $\Gamma = \Omega_i \cap \Omega_s$. The upper portion of the domain above the discontinuity is Ω_s, and its lower portion is Ω_i. The outward normals to the domain boundary $\partial\Omega$ and the discontinuity surface are respectively n and n_c.

We decompose:

- the domain boundary into $\partial\Omega = \Gamma_u \cup \Gamma_t \cup \Gamma_p \cup \Gamma_F$, where Neumann and Dirichlet boundary conditions are respectively imposed on Γ_u (M), $\Gamma_p = \Gamma_p^\ell \cup \Gamma_p^g$ (H) and Γ_t (M), $\Gamma_F = \Gamma_F^\ell \cup \Gamma_F^g$ (H).
- the discontinuity into $\Gamma = \Gamma_i \cup \Gamma_s \cup \Gamma_f$, where Γ_i and Γ_s are respectively the upper and lower surfaces of the discontinuity. Cohesive efforts may exert on Γ_i and Γ_s, while hydrodynamical efforts take place on $\Gamma_f = \Gamma_f^\ell \cup \Gamma_f^g$ due to fluid injection.

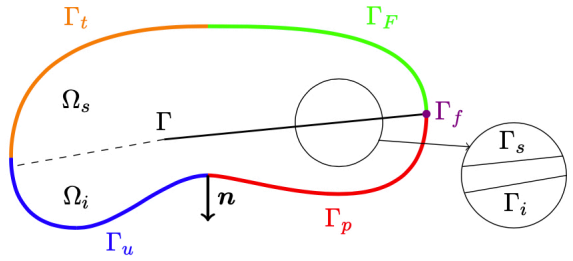

Figure 2.133: Domain decomposition.

Assumptions Consider a fractured porous medium composed of two separate entities: the solid matrix and the porous network. The latter is filled by at most two constituents; two phases at most for each constituent. To be more precise, the porous medium is filled by a liquid and a gas (*i.e.,* the two constituents), but phase changes may occur for each constituent. In other words, the liquid component is turned into the gas mixture as vapor, while the dry gas component may be found itself dissolved in the liquid phase.

What's more, we assume tangential flow along the fracture surface. For instance, fluid and gas exchanges may establish themselves between the fracture and the surrounding porous medium (cf. Figure 2.135). Eventually, phase changes may occur during exchange phenomena.

In Code_Aster, five constitutive models are implemented for the unsaturated porous medium (cf. Granet (2023)). Features of these constitutive models are summarized in Figure 2.134.

The most general constitutive model, namely `LIQU_AD_GAZ_VAPE`, is the focus of the present document. As a matter of fact, two phases (each composed of two constituents) are considered: the liquid phase (*e.g.,* composed of liquid water and dissolved dihydrogen) and the gas phase (*e.g.,* composed of dry dihydrogen and water vapor). However, `LIQU_VAPE_GAZ` and `LIQU_AD_GAZ` can readily be obtained from the aforementioned constitutive model by canceling out terms related to the dissolved gas and the vapor respectively. To finish, both constitutive models `LIQU_GAZ_ATM` and `LIQU_GAZ` are derived in previous study with XFEM in Faivre and Giot (2018).

Const. Law	Liquid	Gas (Dry)	Steam	Gas (Diss.)	Phase Changes	Comment
LIQU_GAZ_ATM	X	X			0	Gas at atmospheric pressure
LIQU_VAPE_GAZ	X	X	X		1	
LIQU_AD_GAZ_VAPE	X	X	X	X	2	
LIQU_AD_GAZ	X	X		X	1	
LIQU_GAZ	X	X			0	

Figure 2.134: Constitutive models available in Code_Aster for the unsaturated porous medium.

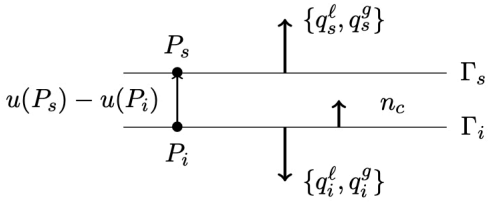

Figure 2.135: Conventions adopted.

At each fracture wall, fluid exchanges are conceptualized by means of two distinct quantities (units: $kg.m^{-2}.s^{-1}$), two per each phase. Especially, consider the couple (q_i^ℓ, q_i^g) only defined along the lower surface Γ_i, while (q_s^ℓ, q_s^g) only exists along the upper surface Γ_s.

As shown in Figure 2.135, fluid exchanges are oriented from Γ_i and Γ_s toward both the lower and the upper parts of the bulk.

Two pressure fields, namely p_ℓ (liquid) and p_g (gas), are introduced for each phase in order to characterize the bulk hydrodynamical behavior. Especially, according to Dalton's law of partial pressure, the total gas pressure p_g is assumed to be the sum of partial pressures of each gas component of the ideal gas mixture. Let p_w denote the liquid pressure, p_{vp} the (partial) vapor pressure, p_{as} the (partial) pressure of the dry gas component and p_{ad} the pressure of the dissolved gas component. Then it reads:

$$p_\ell = p_w + p_{ad} \qquad p_g = p_{as} + p_{vp}$$

However, these four pressure fields are not independent from one another. Indeed, the Henry's law states the pressure of the dissolved gas is proportional to the partial pressure of the dry gas (granted the latter behaves as an ideal gas). The same applies for both, the liquid pressure and the vapor pressure, via the liquid-vapor equilibrium. In other words, there is only one independent pressure field per constituent. As a matter of fact, we arbitrarily choose the following set of independent pressure fields: the total pressure of the gas phase p_g and the capillary pressure p_c. By definition, the capillary pressure states:

$$\begin{aligned} p_c &= p_g - p_\ell \\ &= p_g - p_w - p_{ad} \end{aligned}$$

For the sake of consistency, we introduce two additional pressure fields, respectively associated with the liquid phase p_ℓ^f and the gas phase p_g^f for the fracture. Similarly to the bulk's formulation, each pressure fields read:

$$p_\ell^f = p_w^f + p_{ad}^f \qquad p_g^f = p_{as}^f + p_{vp}^f$$

Hence, the capillary pressure exerting at each fracture wall holds:

$$\begin{aligned} p_c^f &= p_g^f - p_\ell^f \\ &= p_g^f - p_w^f - p_{ad}^f \end{aligned}$$

The displacement field in the bulk is u. If P_s is a point on Γ_s, P_i a point on Γ_i and n_c the outward normal to Γ_i, the displacement jump is defined as (positive or null: debonding; negative: interpenetration):

$$[\boldsymbol{u}] \cdot \boldsymbol{n_c} = (\boldsymbol{u}(P_s) - \boldsymbol{u}(P_i)) \cdot \boldsymbol{n_c} \geqslant 0$$

To finish, we assume:

- the Biot's effective stress assumption. Then, $\boldsymbol{\sigma}$ is the total stress tensor in the bulk, whereas t_c is the total cohesive stress tensor that exerts in the fracture process zone;
- infinitesimal strains;
- all variables are isotropic;
- all gas components behave ideally;
- ideal gas mixtures of nonreacting gases;
- constituents are supposed pure;
- and equilibrium between phases.

Boundary conditions The set of boundary conditions prescribed on $\partial\Omega$ are:

- $p_c = p_{c_0}$ on Γ_p^ℓ (prescribed capillary pressure);
- $p_g = p_{g_0}$ on Γ_p^g (prescribed gas pressure);
- $\left(\mathbf{M_w} + \mathbf{M_{vp}}\right) \cdot \mathbf{n} = \mathbf{M_{ext}^\ell}$ on Γ_F^ℓ (prescribed flux for the liquid constituent);
- $(\mathbf{M_{as}} + \mathbf{M_{ad}}) \cdot \mathbf{n} = \mathbf{M_{ext}^g}$ on Γ_F^g (prescribed flux for the gas constituent);

Let $W_w = W_w(x)$, $\mathbf{W_{vp}} = \mathbf{W_{vp}}(\mathbf{x})$, $\mathbf{W_{as}} = \mathbf{W_{as}}(\mathbf{x})$ and $\mathbf{W_{ad}} = \mathbf{W_{ad}}(\mathbf{x})$, where $x = (x, y, z)$. In the following, the borehole is shrunk to a point in 2D (*i.e.,* intersection of the normal level-set with the edge of the surface element where the injection is implemented) and to a line in 3D (*i.e.,* intersection of the normal level-set with the face of the volume element where the injection is implemented). As a matter of fact, the boundary condition associated with the injection of a liquid and/or a gas reads:

- $\left(\mathbf{W_w} + \mathbf{W_{vp}}\right) \cdot \mathbf{n_c} = \mathbf{W_{ext}^\ell} \delta_\mathbf{d}\left(\mathbf{x} - \mathbf{x_f^\ell}\right)$ on Γ_f^ℓ (prescribed flux for the liquid constituent);
- $(\mathbf{W_{as}} + \mathbf{W_{ad}}) \cdot \mathbf{n_c} = \mathbf{W_{ext}^g} \delta_\mathbf{d}\left(\mathbf{x} - \mathbf{x_f^g}\right)$ on Γ_f^g (prescribed flux for the gaseous constituent);

The delta-function δ_d refers to the Dirac function and $x_f^\ell = \left(x_f^\ell, y_f^\ell, z_f^\ell\right)$ the coordinates of the injection point where the liquid is injected and $x_f^g = \left(x_f^g, y_f^g, z_f^g\right)$ those where the gas is injected.

Mechanical equilibrium for the bulk The mechanical equilibrium for the bulk can be written using the definition of the potential energy of the system (see Section 2.6.1.2). Especially, the strain tensor is decomposed as the sum of its deviatoric and spheric parts:

$$\varepsilon(\boldsymbol{u}) = \boldsymbol{e}(\boldsymbol{u}) + \frac{\varepsilon_v(\boldsymbol{u})}{3}\boldsymbol{\delta} \tag{2.132}$$

where $\varepsilon_v(u) = \mathrm{Tr}(\varepsilon(u))$ is the volumetric strain, and $\boldsymbol{\delta}$ the identity matrix.

- $\boldsymbol{\sigma} = \boldsymbol{\sigma'} - b\left(p_g - S_{lq}p_c\right)$ **[Id]** where S_{lq} is the porous medium saturation ratio, and b the Biot's coefficient;
- r^h the homogenized density such as $r^h = r_0^h + m_w + m_g$. Then, r_0 is the homogenized density taken at the initial configuration, m_w and m_g are respectively the volumetric mass transfert ratios for the liquid and the gas;
- $r^h F$ are the body forces acting on the volume Ω. In practice, they are interpreted as the gravity effects.

This decomposition allows to introduce an auxiliary field π_h, interpreted as the hydrostatic pressure (or spheric part of the stress tensor), which is related to the volumetric strain as follows:

$$\pi_h = -K_0\varepsilon_v(\boldsymbol{u}) \tag{2.133}$$

where $K_0 = \dfrac{E}{3(1-2\nu)}$ is the drained bulk's modulus

On the first hand, this incompressibility condition allows to circumscribe locking effects observed with the finite element formulation when the (near-)incompressibility limit is reached Naylor (1974); Legrain et al. (2008). On the other hand, it renders possible to lump the mass matrix in the XFEM with traditional lumping techniques because all discretized fields live in the same function space (see mass balance equations, Eq. (**??**) and Eq. (**??**)). Indeed, the mass matrix (for the bulk) is no longer a function of the volumetric strain, but the hydrostatic pressure instead.

Mechanical equilibrium for the fracture Similarly to the saturated porous medium, the dynamics of the fracture is conceptualized using a cohesive zone model. As a matter of fact, the fracture is decomposed into three distinct zones (see Figure 2.136):

- zone 1: the fracture walls reached complete separation. This zone is traction-free, meaning the total cohesive stress is equal to $-\left(p_g^f - S_{lq}^f p_c^f\right)n_c$ on Γ_i and $\left(p_g^f - S_{lq}^f p_c^f\right)n_c$ on Γ_s. Only tangential flows participate in the fracture dynamics. It is worth mentioning that failure is reached and is irreversible. This regime of the cohesive stress is reached beyond the threshold $w_n > w_c$, where $w_c = \dfrac{2G_c}{\sigma_c}$;
- zone 2 also known as Fracture Process Zone is located beyond the physical crack front. Cohesive traction forces exert on each fracture wall in order to prevent complete separation. The total cohesive stress increases gradually as $\mathbf{t_c} = \mathbf{t_c'} - \left(\mathbf{p_g^f} - \mathbf{S_{lq}^f p_c^f}\right)\mathbf{n_c}$ until reaching a maximum stress (or critical

stress σ_c) at the fictitious crack front. Then, it reduces to the in-situ stress observed in the adherent zone.;

- zone 3: the walls of the fracture are in perfect adherence with no interpenetration. It is assimilated to any potential propagation surface (bifurcation may occur).

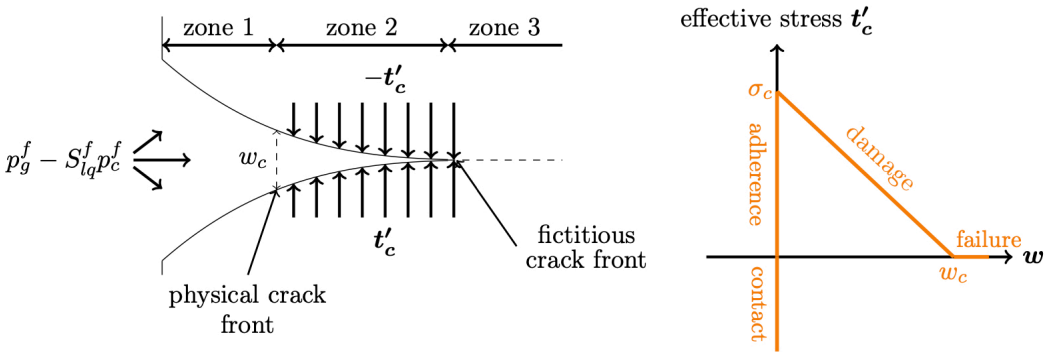

Figure 2.136: Representation of a cohesive zone model with tangential flow (left) and chart of the evolution of the effective cohesive stress (right).

Overview of the MORTAR constitutive law Ferte et al. (2015) Consider the definition of the energy surface density:

$$\Pi(\boldsymbol{w}, \boldsymbol{\lambda}) = \psi(\boldsymbol{\lambda} + r\boldsymbol{w}) - \frac{\boldsymbol{\lambda} \cdot \boldsymbol{\lambda}}{2r} \tag{2.134}$$

where ψ is a differentiable function and r the augmentation ratio.

From the definition of the energy surface density Eq. (2.134), the total cohesive stress as well as the interface law are retrieved and read:

$$\boldsymbol{t}'_c(\boldsymbol{\lambda} + r\boldsymbol{w}) = \frac{\partial \Pi}{\partial \boldsymbol{w}} = r\frac{\partial \psi}{\partial(\boldsymbol{\lambda} + r\boldsymbol{w})} \tag{2.135}$$

$$\frac{\partial \Pi}{\partial \boldsymbol{\lambda}} = \frac{1}{r}\left(\boldsymbol{t}'_c(\boldsymbol{\lambda} + r\boldsymbol{w}) - \boldsymbol{\lambda}\right) = \boldsymbol{0} \tag{2.136}$$

It is worth mentioning both Eq. (2.135) and Eq. (2.136) are defined upon the effective cohesive stress. What's more, Eq. (2.136) simply states (*i.e.,* interface law):

$$\boldsymbol{\lambda} = \boldsymbol{t}'_c(\boldsymbol{\lambda} + r\boldsymbol{w}) \tag{2.137}$$

Consider the following augmented equivalent traction and a threshold function φ satisfying both conditions:

$$(\boldsymbol{\lambda} + r\boldsymbol{w})_{eq} = \sqrt{\langle \lambda_n + rw_n \rangle_+^2 + (\boldsymbol{\lambda}_\tau + r\boldsymbol{w}_\tau)^2}$$

$$\varphi\left((\boldsymbol{\lambda}+r\boldsymbol{w})_{eq}\right)=\frac{(\boldsymbol{\lambda}+r\boldsymbol{w})_{eq}-\sigma_c}{rw_c-\sigma_c}$$

where $\langle\lambda_n+rw_n\rangle_+$ refers to the positive part of λ_n+rw_n, σ_c the critical effective stress and w_c the critical displacement jump (see Figure 2.136 (right)).

A dimensionless parameter α is then introduced in order to characterize the different regimes of the cohesive law. Especially, α verifies:

$$\begin{cases}\varphi\left((\boldsymbol{\lambda}+rw)_{eq}\right)-\alpha\leqslant 0\\ \dot{\alpha}\geqslant 0\\ \dot{\alpha}\left(\varphi\left((\boldsymbol{\lambda}+rw)_{eq}\right)-\alpha\right)=0\end{cases}\tag{2.138}$$

Then, $\alpha\in[0,1]$, with the limit range of values $\alpha\leqslant 0$ (perfect adherence) and $\alpha\geqslant 1$ (full debonding). For intermediate range of values (supposedly, the material is under loading conditions), the following holds:

$$\begin{cases}\alpha=\varphi\left((\boldsymbol{\lambda}+rw)_{eq}\right)\\ \psi\left(\lambda_n+rw_n,\boldsymbol{\lambda}_\tau+rw_\tau\right)=2G_c\left(1-\dfrac{\sigma_c}{rw_c}\right)\alpha\left(1-\dfrac{\alpha}{2}\right)+\dfrac{1}{2r}\langle\lambda_n+rw_n\rangle_-^2\end{cases}\tag{2.139}$$

Finally, let $t_{c,eq}$ denote the equivalent traction as follows:

$$t_{c,eq}=\sqrt{\langle t_{c,n}\rangle_+^2+\boldsymbol{t}_{c,\tau}^2}\tag{2.140}$$

Then, from Eq. (2.135) and Eq. (2.139), the equivalent traction may be rewritten as:

$$t_{c,eq}=(1-T_d)\,(\lambda+rw)_{eq}\tag{2.141}$$

where T_d is the damage tensor and its expression is (linear softening):

$$T_d=\frac{\alpha}{\left(1-\dfrac{\sigma_c}{rw_c}\right)\alpha+\dfrac{\sigma_c}{rw_c}}$$

Finally, each component of the total cohesive stress is identified term-by-term:

$$\begin{aligned}t'_{c,n}&=(1-T_d)\,\langle\lambda_n+rw_n\rangle_++\langle\lambda_n+rw_n\rangle_-\\ \boldsymbol{t}'_{c,\tau}&=(1-T_d)\,(\boldsymbol{\lambda}_\tau+r\boldsymbol{w}_\tau)\end{aligned}\tag{2.142}$$

Hydrodynamical equilibrium: mass balance equations for the bulk Consider an unsaturated porous medium filled up with two constituents, two phases per each constituent at most. Then, for each of them, the mass balance equation is:

$$\frac{\partial m_w}{\partial t} + \frac{\partial m_{vp}}{\partial t} + Div\left(\boldsymbol{M_w} + \boldsymbol{M_{vp}}\right) = -(Q_i^\ell + Q_s^\ell) \tag{2.143}$$

$$\frac{\partial m_{as}}{\partial t} + \frac{\partial m_{ad}}{\partial t} + Div\left(\boldsymbol{M_{as}} + \boldsymbol{M_{ad}}\right) = -(Q_i^g + Q_s^g) \tag{2.144}$$

where:

- m_w, m_{vp}, m_{as} and m_{ad} are respectively the mass (per unit volume) of each constituent, in $kg.m^{-3}$;
- M_w , $\mathbf{M_{vp}}$, $\mathbf{M_{as}}$ and $\mathbf{M_{ad}}$ are the flux for each constituent, in $kg.m^{-2}.s^{-1}$.
- $Q_i^\ell, Q_s^\ell, Q_i^g, Q_s^g$ are source terms interpreted as fluid exchanges between the fracture and the bulk. As seen later, these quantities are strictly equivalent to $q_i^\ell, q_s^\ell, q_i^g, q_s^g$. Mathematically, they refer to different multiplier living in different function spaces. This distinction is made in order to avoid spurious oscillations of $q_i^\ell, q_s^\ell, q_i^g, q_s^g$ along the fracture path.

Especially, the mass (per unit volume) can be written as (respectively for the liquid, the vapor, the dry gas and the dissolved gas):

$$m_w = \rho_w \varphi \left(1 - \frac{\pi_h}{K_0}\right) S_{lq} \tag{2.145}$$

$$m_{ad} = \rho_{ad} \varphi \left(1 - \frac{\pi_h}{K_0}\right) S_{lq} \tag{2.146}$$

$$m_{vp} = \rho_{vp} \varphi \left(1 - \frac{\pi_h}{K_0}\right) (1 - S_{lq}) \tag{2.147}$$

$$m_{as} = \rho_{as} \varphi \left(1 - \frac{\pi_h}{K_0}\right) (1 - S_{lq}) \tag{2.148}$$

where S_{lq} is the liquid saturation (*i.e.,* $S_{lq} \in [0, 1]$).

What's more, using the Darcy's law as well as the first Fick's law, the flux for each constituent are of the form:

$$\boldsymbol{M_w} = \rho_w \lambda_\ell^H \left(-\boldsymbol{\nabla} p_\ell + (\rho_w + \rho_{ad})\, \boldsymbol{F}\right) \tag{2.149}$$

$$\boldsymbol{M_{ad}} = \rho_{ad} \lambda_\ell^H \left(-\boldsymbol{\nabla} p_\ell + (\rho_w + \rho_{ad})\, \boldsymbol{F}\right) - F_{ad} \boldsymbol{\nabla} \rho_{ad} \tag{2.150}$$

$$\boldsymbol{M_{vp}} = \rho_{vp} \lambda_g^H \left(-\boldsymbol{\nabla} p_g + \left(\rho_{as} + \rho_{vp}\right) \boldsymbol{F}\right) - \rho_{vp} \left(1 - C_{vp}\right) F_{vp} \boldsymbol{\nabla} C_{vp} \tag{2.151}$$

$$\boldsymbol{M_{as}} = \rho_{as}\lambda_g^H\left(-\boldsymbol{\nabla} p_g + \left(\rho_{as} + \rho_{vp}\right)\boldsymbol{F}\right) + \rho_{as}C_{vp}F_{vp}\boldsymbol{\nabla} C_{vp} \tag{2.152}$$

where $\lambda_\ell^{\mathrm{H}} = \lambda_\ell^{\mathrm{H}}\left(\pi_{\mathrm{h}}, \mathrm{p_c}, \mathrm{p_g}\right)$ and $\lambda_{\mathrm{g}}^{\mathrm{H}} = \lambda_{\mathrm{g}}^{\mathrm{H}}\left(\pi_{\mathrm{h}}, \mathrm{p_c}, \mathrm{p_g}\right)$ are respectively the hydraulic conductivity for the liquid and the gas phases.

These quantities are expressed with respect to the intrinsic permeability of the porous medium $\mathrm{K}^{\mathrm{int}} = \mathrm{K}^{\mathrm{int}}(\varphi)$, the relative permeability to the liquid $\mathrm{k}_\ell^{\mathrm{rel}} = \mathrm{k}_\ell^{\mathrm{rel}}\left(\mathrm{S_{lq}}\right)$ (respectively the relative permeability to the gas $\mathrm{k}_{\mathrm{g}}^{\mathrm{rel}} = \mathrm{k}_{\mathrm{g}}^{\mathrm{rel}}\left(\mathrm{S_{lq}}, \mathrm{p_g}\right)$) and the viscosity of the phase at stake $\mu_{\mathrm{w}} = \mu_{\mathrm{w}}(\mathrm{T})$ or $\mu_{\mathrm{g}} = \mu_{\mathrm{g}}(\mathrm{T})$. Then, it leads to the following:

$$\lambda_\ell^H = \frac{K^{int}k_\ell^{rel}}{\mu_w}, \quad \lambda_g^H = \frac{K^{int}k_g^{rel}}{\mu_g}$$

One can notice three additional quantities related to the diffusion of constituents within phases:

$$C_{vp} = \frac{p_{vp}}{p_g}, \quad F_{vp} = \frac{D_{vp}}{C_{vp}\left(1 - C_{vp}\right)}, \quad F_{ad} = D_{ad}$$

where $\mathrm{C_{vp}}$ is the concentration of vapor within the gas phase, $\mathrm{D_{vp}}$ the Fick's diffusion coefficient of the gas phase and $\mathrm{D_{ad}}$ the Fick's diffusion coefficient of the liquid phase.

Hydrodynamical equilibrium: mass balance equations for the fracture Similarly to the porous medium, the fracture may be filled up with two constituents, two phases per each constituent at most. Then, the mass balance equation for each of them is:

$$\frac{\partial w_w}{\partial t} + \frac{\partial w_{vp}}{\partial t} + Div\left(\boldsymbol{W_w} + \boldsymbol{W_{vp}}\right) = q_i^\ell + q_s^\ell \tag{2.153}$$

$$\frac{\partial w_{as}}{\partial t} + \frac{\partial w_{ad}}{\partial t} + Div\left(\boldsymbol{W_{as}} + \boldsymbol{W_{ad}}\right) = q_i^g + q_s^g \tag{2.154}$$

The formulation of these two conservation equations accounts for a source term related to fluid exchanges between the fracture and the porous medium (*i.e.,* summation of the set of multipliers $\mathrm{q_i^x}$ and $\mathrm{q_s^x}$ ($\mathrm{x} = \{\ell; \mathrm{g}\}$)).

In the following, $\mathrm{w_n}$ refers to the local displacement jump in the normal direction to the fracture surface. For numerical stability purposes (*i.e.,* in order to lump the mass matrix), the present formulation depends upon the local projection w of the global displacement jump $\mathbf{[u]}$ onto the discontinuity surface Γ, rather than $\mathbf{[u]}$ as it was first introduced in Faivre et al. (2016) and Paul et al. (2018).

First, the mass (per unit surface, in $\mathrm{kg.m^{-2}}$) for each constituent is:

$$w_w = \rho_w^f S_{lq}^f w_n \tag{2.155}$$

$$w_{ad} = \rho^f_{ad} S^f_{lq} w_n \tag{2.156}$$

$$w_{as} = \rho^f_{as}(1 - S^f_{lq}) w_n \tag{2.157}$$

$$w_{vp} = \rho^f_{vp}(1 - S^f_{lq}) w_n \tag{2.158}$$

Second, the tangential flux along the fracture surface are expressed in terms of a Cubic Law and the First Fick's law:

$$\boldsymbol{W_w} = -\rho^f_w \alpha^f_\ell \nabla p^f_\ell \tag{2.159}$$

$$\boldsymbol{W_{ad}} = -\rho^f_{ad} \alpha^f_\ell \nabla p^f_\ell - F^f_{ad} \nabla \rho^f_{ad} \tag{2.160}$$

$$\boldsymbol{W_{vp}} = -\rho^f_{vp} \alpha^f_g \nabla p^f_g - \rho^f_{vp} \left(1 - C^f_{vp}\right) F^f_{vp} \nabla C^f_{vp} \tag{2.161}$$

$$\boldsymbol{W_{as}} = -\rho^f_{as} \alpha^f_g \nabla p^f_g + \rho^f_{as} C^f_{vp} F^f_{vp} \nabla C^f_{vp} \tag{2.162}$$

$(\mathbf{W_w}, \mathbf{W_{ad}})$ and $(\mathbf{W_{as}}, \mathbf{W_{vp}})$ are respectively defined upon $\alpha^f_\ell = \alpha^f_\ell\left(w_n, p^f_c\right)$ and $\alpha^f_g = \alpha^f_g\left(w_n, p^f_c, p^f_g\right)$ that read:

$$\alpha^f_\ell = \frac{\kappa^{rel}_\ell w_n^3}{12\mu_w}, \quad \alpha^f_g = \frac{\kappa^{rel}_g w_n^3}{12\mu_g}$$

Based upon the expression of the bulk's hydraulic conductivity, two different relative permeabilities $\kappa^{rel}_\ell = \kappa^{rel}_\ell\left(S^f_{lq}\right)$ and $\kappa^{rel}_g = \kappa^{rel}_g\left(S^f_{lq}, p^f_g\right)$ are associated to the liquid phase and the gas phase.

As for the bulk, one can notice three additional quantities related to the diffusion of constituents within phases along the fracture:

$$C^f_{vp} = \frac{p^f_{vp}}{p^f_g}, \quad F^f_{vp} = \frac{D^f_{vp}}{C^f_{vp}\left(1 - C^f_{vp}\right)}, \quad F^f_{ad} = D^f_{ad}$$

where C^f_{vp} is the concentration of the vapor component within the gas phase, D^f_{vp} the Fick's diffusion coefficient for the gas phase and D^f_{ad} the Fick's diffusion coefficient for the liquid phase.

Continuity of the pressure fields Due to the presence of the fracture, the capillary pressure and the gas pressure (*i.e.,* p_c and p_g) are discontinuous across the fracture surface. On the contrary, both pressure fields (*i.e.,* p_c^f and p_g^f) defined along the fracture path are continuous. Hence, the continuity must be satisfied at each fracture wall. As shown later (see Section 2.6.1.2), the continuity condition across the fracture is ensured through a projection of the capillary pressure p_c (as well as the gas pressure p_g) onto the fracture surface. To do so, the use of an augmented Lagrangian formulation is proposed.

Evaluation of the saturation: the Mualem-Van-Genuchten's model A relationship between the saturation (for both the porous medium and the fracture) must be provided (alongside their first derivative with respect to the capillary pressure). In doing so, we consider the Mualem-Van Genuchten's model (or a cubic variant). It is worth mentioning that any relationship established in the lab, between the capillary pressure and the saturation, would be acceptable. However, we specifically choose to refer to the Mualem-Van Genuchten's model in the present document.

In the following, we assume the relationship $S_{lq} = S_{lq}(p_c)$ applies for both the fracture and the porous medium.

As a matter of fact, the saturation is expressed with respect to the capillary pressure as follows:

$$S_{lq} = S_{wr} + \frac{1 - S_{wr}}{(1 + \beta^n)^m} \tag{2.163}$$

where S_{wr} is the residual water content, $\beta = \frac{p_c}{p_r}, (\beta > 0)$ the air entry suction, $n > 1$ is a measure of the pore-size distribution and $m = 1 - \frac{1}{n}$.

Then, the relative permeability to the liquid constituent and to the gas mixture are respectively:

$$k_w^{rel} = \sqrt{S_{we}} \left(1 - \left(1 - S_{we}^{lim}\right)^m\right)^2 \tag{2.164}$$

$$k_g^{rel} = \sqrt{1 - S_{we}} \left(1 - S_{we}^{lim}\right)^{2m} \tag{2.165}$$

where $S_{we} = \frac{1}{(1 + \beta^n)^m}$, and S_{we}^{lim} is evaluated for both limit cases $S_{lq} = 1$ and $S_{lq} = 0$.

2.6.1.2. Numerical model

Function spaces The definition of the function space for the displacement field u (for the domain Ω) is:

$$U = \{\boldsymbol{u} \in \left(L^2(\Omega)\right)^n, \boldsymbol{u}_{|\Omega_i} \in \left(W^{1,2}(\Omega_i)\right)^n \text{ and } \boldsymbol{u}_{|\Omega_s} \in \left(W^{1,2}(\Omega_s)\right)^n\}$$

where $n = \{2, 3\}$ is the dimension of the problem. $L^2(\Omega)$ is the Hilbert space of square-integrable functions, and $W^{1,2}\left(\Omega_{i,s}\right) \subset L^2(\Omega)$ is the Sobolev space of functions that are differentiable up to the first order.

Supposedly, the displacement field may be discontinuous across the discontinuity surface. As a matter of fact we introduce $u_{|\Omega_i}$ as the restriction of the displacement field u to the subdomain Ω_i as well as $u_{|\Omega_s}$ the restriction of the displacement field u to the subdomain Ω_s.

Due to the presence of the discontinuity, we need to introduce a trace operator for each subdomain Ω_i and Ω_s whose boundary matches the fracture walls. In other words, it will help us projecting the behavior of the bulk onto the discontinuity surface. Then, consider the definition of the following trace operators for the displacement field:

$$\begin{aligned} \mathcal{T}_i : \left(W^{1,2}(\Omega_i)\right)^n &\mapsto \left(L^2(\Gamma)\right)^n \\ u_{|\Omega_i} &\mapsto \mathcal{T}_i\left(u_{|\Omega_i}\right) \end{aligned} \tag{2.166}$$

$$\begin{aligned} \mathcal{T}_s : \left(W^{1,2}(\Omega_s)\right)^n &\mapsto \left(L^2(\Gamma)\right)^n \\ u_{|\Omega_s} &\mapsto \mathcal{T}_s\left(u_{|\Omega_s}\right) \end{aligned} \tag{2.167}$$

Similarly the definition of the function space for the capillary pressure field p_c, the gas pressure field p_g and the hydrostatic pressure field p_h (for the domain Ω) is:

$$P = \{p \in L^2(\Omega), p_{|\Omega_i} \in W^{1,2}(\Omega_i) \text{ and } p_{|\Omega_s} \in W^{1,2}(\Omega_s)\}$$

Similarly, $p_{|\Omega_i}$ is the restriction of the pressure field p to the subdomain Ω_i as well as $p_{|\Omega_s}$ the restriction of the pressure field p to the subdomain Ω_s.

The same applies to the pressure fields:

$$\begin{aligned} T_i : W^{1,2}(\Omega_i) &\mapsto L^2(\Gamma) \\ p_{|\Omega_i} &\mapsto T_i\left(p_{|\Omega_i}\right) \end{aligned} \tag{2.168}$$

$$\begin{aligned} T_s : W^{1,2}(\Omega_s) &\mapsto L^2(\Gamma) \\ p_{|\Omega_s} &\mapsto T_s\left(p_{|\Omega_s}\right) \end{aligned} \tag{2.169}$$

The definition of the function space of the Lagrange multipliers $\boldsymbol{\lambda}$, w and $\boldsymbol{\mu}$ (along the discontinuity Γ) is:

$$\Pi = \left(L^2(\Gamma)\right)^n$$

The definition of the function space of the Lagrange multipliers q_i^ℓ, q_s^ℓ, Q_i^ℓ, Q_s^ℓ, π_i^c, π_s^c, q_i^g, q_s^g, Q_i^g, Q_s^g, π_i^g, π_s^g (along the discontinuity Γ) is:

$$\Lambda = L^2(\Gamma)$$

To finish the definition of the function space for the capillary pressure p_c^f and the gas pressure p_g^f (along the discontinuity Γ) is:

$$Q = W^{1,2}(\Gamma)$$

In practice, we choose Λ instead of Q. Indeed, the degree-of-freedoms associated to the pressure fields along the fracture path are involved in equality relationships, the same way as the set of Lagrange multipliers mentioned above, to avoid spurious oscillations of the numerical solution (for more details about the selection algorithm, refer to Ferte et al. (2015)).

The discretization of the domain Ω leads to the subdomain $\Omega_h \subset \Omega$ and as well as for the discontinuity Γ we get $\Gamma_h \subset \Gamma$. Similarly, we define: $U_h \subset U$, $P_h \subset P$, $\Lambda_h \subset \Lambda$, $\Pi_h \subset \Pi$ and $Q_h \subset Q$.

As seen later, a lumping technique is used on mass matrix entries as recommended by Celia et al. (1990) in order to scrap oscillatory behavior of certain fields (*e.g.* capillary pressure, gas pressure, effective cohesive stress and so on and so forth) when near to a high rate of change range of values. What's more, authors like Chen and Thomée (1985) demonstrated that lumping of the mass matrix entries is equivalent to using an inner product $(.,.)_h$ that approximates the conventional inner product in $L^2(\Gamma_h)$ or $L^2(\Omega_h)$. This inner product is particularly suited to parabolic equations like the mass balance equation in the bulk, as well as in the fracture.

Weak formulation of the mechanical problem First, consider the expression of the total potential energy:

$$\begin{aligned} E_p(u,\pi_h,\boldsymbol{\lambda},w) &= \frac{1}{2}\int_{\Omega_h} e(u) : \mathbb{C} : e(u)\, d\Omega_h - \int_{\Omega_h} b\left(p_g - S_{lq}p_c\right)\varepsilon_v(u)\, d\Omega_h \\ &- \frac{1}{2}\int_{\Omega_h}\frac{\pi_h^2}{K_0} d\Omega_h - \int_{\Omega_h}\pi_h\varepsilon_v(u)\, d\Omega_h - \int_{\Gamma_{t_h}} t\cdot u^* d\Gamma_{t_h} - \int_{\Omega_h} r^h F u^* d\Omega_h \\ &+ \int_{\Gamma_h}\Pi(w,\boldsymbol{\lambda})\, d\Gamma_h - \left(\left(p_g^f - S_{lq}^f p_c^f\right)n_c, w\right)_h \end{aligned} \tag{2.170}$$

- r^h is the homogenized density such as $r^h = r_0^h + m_w + m_{as} + m_{ad} + m_{vp}$. Let r_0 be the homogenized density taken at the initial configuration, and m_w, m_{as}, m_{vp} and m_{ad} respectively the mass of liquid, the mass of dry air, the mass of vapor as well as the mass of dissolved air;
- $r^h F$ are the body forces acting on the volume Ω. In practice, they are interpreted as the gravity effects.

Using the definition of the trace operator (Eq. (2.166) and Eq. (2.167)) on each subdomain of Ω, the displacement jump (cf. Section 2.6.1.1) can be rewritten as follows:

$$[\![\boldsymbol{u}]\!] = \mathcal{T}_s\left(\boldsymbol{u}_{|\Omega_s}\right) - \mathcal{T}_i\left(\boldsymbol{u}_{|\Omega_i}\right)$$

The weak formulation of the mechanical equilibrium is retrieved using an augmented Lagrangian formulation:

$$\mathcal{L}(u,\pi_h,w,\boldsymbol{\lambda},\boldsymbol{\mu}) = E_p(u,\pi_h,\boldsymbol{\lambda},w) + \int_{\Gamma_h}\boldsymbol{\mu}\cdot([\![u]\!] - w)\, d\Gamma_h \tag{2.171}$$

Especially, a saddle point of the augmented Lagrangian $(u,,\pi_h,\boldsymbol{\lambda},w,\boldsymbol{\mu})$ is a solution to the minimization of the total potential energy E_p. As a matter of fact, we can write the following set of optimality conditions of the augmented Lagrangian $\mathcal{L}$:

$$\underset{\boldsymbol{w}=[\boldsymbol{u}]}{\arg\min}\, \mathcal{L}\left(\boldsymbol{u}^*, \pi_h^*, \boldsymbol{w}^*, \boldsymbol{\lambda}^*, \boldsymbol{\mu}^*\right) \Leftrightarrow \begin{cases} \forall \mathbf{u^*} \in \mathbf{U_h} & \dfrac{\partial \mathcal{L}}{\partial \mathbf{u^*}} = \mathbf{0} \\ \forall \pi_h^* \in P_h & \dfrac{\partial \mathcal{L}}{\partial \pi_h^*} = 0 \\ \forall \mathbf{w^*} \in \mathbf{\Pi_h} & \dfrac{\partial \mathcal{L}}{\partial \mathbf{w^*}} = \mathbf{0} \\ \forall \boldsymbol{\lambda}^* \in \mathbf{\Pi_h} & \dfrac{\partial \mathcal{L}}{\partial \boldsymbol{\lambda}^*} = \mathbf{0} \\ \forall \boldsymbol{\mu}^* \in \mathbf{\Pi_h} & \dfrac{\partial \mathcal{L}}{\partial \boldsymbol{\mu}^*} = \mathbf{0} \end{cases} \tag{2.172}$$

Find $(u, \pi_h, w, \boldsymbol{\lambda}, \boldsymbol{\mu}) \in U_h \times P_h \times \Pi_h \times \Pi_h \times \Pi_h$ such as:

- Mechanical equilibrium:

$$\begin{aligned} \forall u^* \in U_h \qquad & \int_{\Omega_h} e(u) : \mathbb{C} : e\left(u^*\right) d\Omega_h - \int_{\Omega_h} b\left(p_g - S_{lq} p_c\right) \varepsilon_v\left(u^*\right) d\Omega_h - \int_{\Omega_h} \pi_h \varepsilon_v\left(u^*\right) d\Omega_h \\ - & \int_{\Gamma_{t_h}} t \cdot u^* d\Gamma_{t_h} + \int_{\Gamma_h} \boldsymbol{\mu} \cdot \left[u^*\right] d\Gamma_h - \int_{\Omega_h} r F u^* d\Omega_h = 0 \end{aligned} \tag{2.173}$$

- Incompressibility condition:

$$\forall \pi_h^* \in P_h \quad - \int_{\Omega_h} \left(\frac{\pi_h}{K_0} + \varepsilon_v(\boldsymbol{u}) \right) \pi_h^* d\Omega_h = 0 \tag{2.174}$$

- Projection of the displacement jump onto the reduced approximation space Π_h:

$$\forall \boldsymbol{\mu}^* \in \Pi_h \quad \int_{\Gamma_h} \boldsymbol{\mu}^* \cdot (\boldsymbol{[u]} - \boldsymbol{w})\, d\Gamma_h = 0 \tag{2.175}$$

- Expression of the total cohesive stress:

$$\forall \boldsymbol{w}^* \in \Pi_h \quad - \int_{\Gamma_h} \boldsymbol{\mu} \cdot \boldsymbol{w}^* d\Gamma_h + \left(\boldsymbol{w}^*, \boldsymbol{t_c'}(\boldsymbol{\lambda} + r\boldsymbol{w})\right)_h + \left(\boldsymbol{w}^*, -\left(p_g^f - S_{lq}^f p_c^f\right) \boldsymbol{n_c}\right)_h = 0 \tag{2.176}$$

- Interface law (local expression of the effective cohesive stress):

$$\forall \boldsymbol{\lambda}^* \in \Pi_h \quad \left(\boldsymbol{\lambda}^*, -\frac{\boldsymbol{\lambda} - \boldsymbol{t_c'}(\boldsymbol{\lambda} + r\boldsymbol{w})}{r}\right)_h = 0 \tag{2.177}$$

Weak formulation of the hydrodynamical problem **Augmented Lagrangian** Similarly to Section 2.6.1.2, the following augmented Lagrangian formulation is introduced (for the liquid constituent):

$$\begin{aligned} \mathcal{H}\left(p_c, p_c^f, q_i^\ell, q_s^\ell, \pi_i^c, \pi_s^c, Q_i^\ell, Q_s^\ell\right) &= W_1(p_c) + W_2\left(p_c^f\right) + \left(q_i^\ell, \pi_i^c - p_c^f\right)_h + \left(q_s^\ell, \pi_s^c - p_c^f\right)_h \\ &+ \int_{\Gamma_h} Q_i^\ell \left(T_i\left(p_{c_{|\Omega_i}}\right) - \pi_i^c\right) d\Gamma_h + \int_{\Gamma_h} Q_s^\ell \left(T_s\left(p_{c_{|\Omega_s}}\right) - \pi_s^c\right) d\Gamma_h \end{aligned}$$

The following minimization problem under both equality constraints $T_i\left(p_{c_{|\Omega_i}}\right) = \pi_i^c$, $T_s\left(p_{c_{|\Omega_s}}\right) = \pi_s^c$ gives the set of optimality conditions of the augmented Lagrangian $\mathcal{H}$

$$\underset{\substack{T_i\left(p_{c_{|\Omega_i}}\right)=\pi_i^c \\ T_s\left(p_{c_{|\Omega_s}}\right)=\pi_s^c}}{\arg\min} \quad \mathcal{H}\left(p_c^*, p_c^{f*}, q_i^{\ell*}, q_s^{\ell*}, \pi_i^{c*}, \pi_s^{c*}, Q_i^{\ell*}, Q_s^{\ell*}\right) \Leftrightarrow \begin{cases} \forall p_c^* \in P_h & \dfrac{\partial \mathcal{H}}{\partial p_c^*} = 0 \\ \forall p_c^{f*} \in Q_h & \dfrac{\partial \mathcal{H}}{\partial p_c^{f*}} = 0 \\ \forall q_i^{\ell*} \in \Lambda_h & \dfrac{\partial \mathcal{H}}{\partial q_i^{\ell*}} = 0 \\ \forall q_s^{\ell*} \in \Lambda_h & \dfrac{\partial \mathcal{H}}{\partial q_s^{\ell*}} = 0 \\ \forall \pi_i^{c*} \in \Lambda_h & \dfrac{\partial \mathcal{H}}{\partial \pi_i^{c*}} = 0 \\ \forall \pi_s^{c*} \in \Lambda_h & \dfrac{\partial \mathcal{H}}{\partial \pi_s^{c*}} = 0 \\ \forall Q_i^{\ell*} \in \Lambda_h & \dfrac{\partial \mathcal{H}}{\partial Q_i^{\ell*}} = 0 \\ \forall Q_s^{\ell*} \in \Lambda_h & \dfrac{\partial \mathcal{H}}{\partial Q_s^{\ell*}} = 0 \end{cases} \tag{2.178}$$

As well as for the gaseous constituent:

$$\begin{aligned} \mathcal{G}\left(p_g, p_g^f, q_i^g, q_s^g, \pi_i^g, \pi_s^g, Q_i^g, Q_s^g\right) &= G_1\left(p_g\right) + G_2\left(p_g^f\right) + \left(q_i^g, \pi_i^g - p_g^f\right)_h + \left(q_s^g, \pi_s^g - p_g^f\right)_h \\ &+ \int_{\Gamma_h} Q_i^g\left(T_i\left(p_{g_{|\Omega_i}}\right) - \pi_i^g\right) d\Gamma_h + \int_{\Gamma_h} Q_s^g\left(T_s\left(p_{g_{|\Omega_s}}\right) - \pi_s^g\right) d\Gamma_h \end{aligned}$$

and under the following equality constraints $T_i\left(p_{g_{|\Omega_i}}\right) = \pi_i^g$ and $T_s\left(p_{g_{|\Omega_s}}\right) = \pi_s^g$:

$$\underset{\substack{T_i\left(p_{g_{|\Omega_i}}\right)=\pi_i^g \\ T_s\left(p_{g_{|\Omega_s}}\right)=\pi_s^g}}{\arg\min} \quad \mathcal{G}\left(p_g^*, p_g^{f*}, q_i^{g*}, q_s^{g*}, \pi_i^{g*}, \pi_s^{g*}, Q_i^{g*}, Q_s^{g*}\right) \Leftrightarrow \begin{cases} \forall p_g^* \in P_h & \dfrac{\partial \mathcal{G}}{\partial p_g^*} = 0 \\ \forall p_g^{f*} \in Q_h & \dfrac{\partial \mathcal{G}}{\partial p_g^{f*}} = 0 \\ \forall q_i^{g*} \in \Lambda_h & \dfrac{\partial \mathcal{G}}{\partial q_i^{g*}} = 0 \\ \forall q_s^{g*} \in \Lambda_h & \dfrac{\partial \mathcal{G}}{\partial q_s^{g*}} = 0 \\ \forall \pi_i^{g*} \in \Lambda_h & \dfrac{\partial \mathcal{G}}{\partial \pi_i^{g*}} = 0 \\ \forall \pi_s^{g*} \in \Lambda_h & \dfrac{\partial \mathcal{G}}{\partial \pi_s^{g*}} = 0 \\ \forall Q_i^{g*} \in \Lambda_h & \dfrac{\partial \mathcal{G}}{\partial Q_i^{g*}} = 0 \\ \forall Q_s^{g*} \in \Lambda_h & \dfrac{\partial \mathcal{G}}{\partial Q_s^{g*}} = 0 \end{cases} \tag{2.179}$$

The first two optimality conditions (for both the liquid and gaseous constituents) are discretized in time using a θ-scheme (for both the fracture and the bulk). The coupled problem is solved using:

- an explicit scheme when $\theta = 0$;
- a Cranck-Nicholson's method when $\theta = 0.5$;
- or an implicit scheme when $\theta = 1$.

In order to ensure the unconditional stability of the numerical solution, an implicit scheme is considered when $0.5 < \theta \leqslant 1$. To finish, a variable provided with the superscript (n) is taken at the current time step, while a variable provided with the superscript $(n-1)$ is taken at the previous time step. The time step increment is $\Delta t = t^{(n)} - t^{(n-1)}$.

Liquid constituent

Find $\left(p_c, Q_i^\ell, Q_s^\ell, \pi_i^c, \pi_i^c, q_i^\ell, q_s^\ell, p_c^f\right) \in P_h \times \Lambda_h \times \Lambda_h \times \Lambda_h \times \Lambda_h \times \Lambda_h \times \Lambda_h \times Q_h$ such as:

- Mass balance equation (bulk):
  $\forall p_c^* \in P_h$

$$\begin{aligned}
&\left(p_c^*, -\frac{m_w^{(n)} - m_w^{(n-1)}}{\Delta t}\right)_h + \left(p_c^*, -\frac{m_{vp}^{(n)} - m_{vp}^{(n-1)}}{\Delta t}\right)_h + \theta \int_{\Omega_h} M_w^{(n)} \cdot \boldsymbol{\nabla} p_c^* d\Omega_h \\
+ \quad & (1-\theta) \int_{\Omega_h} M_w^{(n-1)} \cdot \boldsymbol{\nabla} p_c^* d\Omega_h + \theta \int_{\Omega_h} M_{vp}^{(n)} \cdot \boldsymbol{\nabla} p_c^* d\Omega_h + (1-\theta) \int_{\Omega_h} M_{vp}^{(n-1)} \cdot \boldsymbol{\nabla} p_c^* d\Omega_h \\
= \quad & \int_{\Gamma_{F_h}^\ell} M_{ext}^\ell p_c^* d\Gamma_{F_h}^\ell - \theta \int_{\Gamma_h} Q_i^{\ell(n)} T_i\left(p_{c_{|\Omega_i}}^*\right) d\Gamma_h - (1-\theta) \int_{\Gamma_h} Q_i^{\ell(n-1)} T_i\left(p_{c_{|\Omega_i}}^*\right) d\Gamma_h \\
- \quad & \theta \int_{\Gamma_h} Q_s^{\ell(n)} T_s\left(p_{c_{|\Omega_s}}^*\right) d\Gamma_h - (1-\theta) \int_{\Gamma_h} Q_s^{\ell(n-1)} T_s\left(p_{c_{|\Omega_s}}^*\right) d\Gamma_h
\end{aligned} \tag{2.180}$$

- Projection of the trace of the capillary pressure onto the reduced approximation space Λ_h:

$$\forall Q_i^{\ell*} \in \Lambda_h \quad \int_{\Gamma_h} \left(T_i\left(p_{c_{|\Omega_i}}\right) - \pi_i^c\right) Q_i^{\ell*} d\Gamma_h = 0 \tag{2.181}$$

$$\forall Q_s^{\ell*} \in \Lambda_h \quad \int_{\Gamma_h} \left(T_s\left(p_{c_{|\Omega_s}}\right) - \pi_s^c\right) Q_s^{\ell*} d\Gamma_h = 0 \tag{2.182}$$

- Expression of the rate of flow:

$$\forall \pi_i^{c*} \in \Lambda_h \quad \left(\pi_i^{c*}, q_i^\ell\right)_h - \int_{\Gamma_h} Q_i^\ell \pi_i^{c*} d\Gamma_h = 0 \tag{2.183}$$

$$\forall \pi_s^{c*} \in \Lambda_h \quad \left(\pi_s^{c*}, q_s^\ell\right)_h - \int_{\Gamma_h} Q_s^\ell \pi_s^{c*} d\Gamma_h = 0 \tag{2.184}$$

- Interface law (continuity of the capillary pressure):

$$\forall q_i^{\ell*} \in \Lambda_h \quad \left(q_i^{\ell*}, \pi_i^c - p_c^f\right)_h = 0 \tag{2.185}$$

$$\forall q_s^{\ell*} \in \Lambda_h \quad \left(q_s^{\ell*}, \pi_s^c - p_c^f\right)_h = 0 \tag{2.186}$$

- Mass balance equation (fracture):
  $\forall p_c^{f*} \in Q_h$

$$\begin{aligned}
&\left(p_c^{f*}, -\frac{w_w^{(n)} - w_w^{(n-1)}}{\Delta t}\right)_h + \left(p_c^{f*}, -\frac{w_{vp}^{(n)} - w_{vp}^{(n-1)}}{\Delta t}\right)_h + \theta \int_{\Gamma_h} W_w^{(n)} \cdot \nabla p_c^{f*} d\Gamma_h \\
+ \quad & (1-\theta) \int_{\Gamma_h} W_w^{(n-1)} \cdot \nabla p_c^{f*} d\Gamma_h + \theta \int_{\Gamma_h} W_{vp}^{(n)} \cdot \nabla p_c^{f*} d\Gamma_h + (1-\theta) \int_{\Gamma_h} W_{vp}^{(n-1)} \cdot \nabla p_c^{f*} d\Gamma_h \\
= \quad & \int_{\Gamma_{f_h}^{\ell}} W_{ext}^{\ell} \delta_d \left(x - x_f^{\ell}\right) p_c^{f*} d\Gamma_{f_h}^{\ell} + \theta \left(p_c^{f*}, q_i^{\ell(n)}\right)_h + (1-\theta) \left(p_c^{f*}, q_i^{\ell(n-1)}\right)_h \\
+ \quad & \theta \left(p_c^{f*}, q_s^{\ell(n)}\right)_h + (1-\theta) \left(p_c^{f*}, q_s^{\ell(n-1)}\right)_h
\end{aligned} \tag{2.187}$$

Gas constituent

Find $\left(p_g, Q_i^g, Q_s^g, \pi_i^g, \pi_i^g, q_i^g, q_s^g, p_g^f\right) \in P_h \times \Lambda_h \times \Lambda_h \times \Lambda_h \times \Lambda_h \times \Lambda_h \times \Lambda_h \times Q_h$ such as:

- Mass balance equation (bulk):
  $\forall p_g^* \in P_h$

$$\begin{aligned}
&\left(p_g^*, -\frac{m_{as}^{(n)} - m_{as}^{(n-1)}}{\Delta t}\right)_h + \left(p_g^*, -\frac{m_{ad}^{(n)} - m_{ad}^{(n-1)}}{\Delta t}\right)_h + \theta \int_{\Omega_h} M_{as}^{(n)} \cdot \nabla p_g^* d\Omega_h \\
+ \quad & (1-\theta) \int_{\Omega_h} M_{as}^{(n-1)} \cdot \nabla p_g^* d\Omega_h + \theta \int_{\Omega_h} M_{ad}^{(n)} \cdot \nabla p_g^* d\Omega_h + (1-\theta) \int_{\Omega_h} M_{ad}^{(n-1)} \cdot \nabla p_g^* d\Omega_h \\
= \quad & \int_{\Gamma_{F_h}^g} M_{ext}^g p_g^* d\Gamma_{F_h}^g - \theta \int_{\Gamma_h} Q_i^{g(n)} T_i \left(p_{g_{|\Omega_i}}^*\right) d\Gamma_h - (1-\theta) \int_{\Gamma_h} Q_i^{g(n-1)} T_i \left(p_{g_{|\Omega_i}}^*\right) d\Gamma_h \\
- \quad & \theta \int_{\Gamma_h} Q_s^{g(n)} T_s \left(p_{g_{|\Omega_s}}^*\right) d\Gamma_h - (1-\theta) \int_{\Gamma_h} Q_s^{g(n-1)} T_s \left(p_{g_{|\Omega_s}}^*\right) d\Gamma_h
\end{aligned} \tag{2.188}$$

- Projection of the trace of the gas pressure onto the reduced approximation space Λ_h:

$$\forall Q_i^{g*} \in \Lambda_h \quad \int_{\Gamma_h} \left(T_i \left(p_{g_{|\Omega_i}}\right) - \pi_i^g\right) Q_i^{g*} d\Gamma_h = 0 \tag{2.189}$$

$$\forall Q_s^{g*} \in \Lambda_h \quad \int_{\Gamma_h} \left(T_s \left(p_{g_{|\Omega_s}}\right) - \pi_s^g\right) Q_s^{g*} d\Gamma_h = 0 \tag{2.190}$$

- Expression of the rate of flow:

$$\forall \pi_i^{g*} \in \Lambda_h \quad \left(\pi_i^{g*}, q_i^g\right)_h - \int_{\Gamma_h} Q_i^g \pi_i^{g*} d\Gamma_h = 0 \tag{2.191}$$

$$\forall \pi_s^{g*} \in \Lambda_h \quad \left(\pi_s^{g*}, q_s^g\right)_h - \int_{\Gamma_h} Q_s^g \pi_s^{g*} d\Gamma_h = 0 \tag{2.192}$$

- Interface law (continuity of the gas pressure):

$$\forall q_i^{g*} \in \Lambda_h \quad \left(q_i^{g*}, \pi_i^g - p_g^f\right)_h = 0 \tag{2.193}$$

$$\forall q_s^{g*} \in \Lambda_h \quad \left(q_s^{g*}, \pi_s^g - p_g^f\right)_h = 0 \tag{2.194}$$

- Mass balance equation (fracture):
  $\forall p_g^{f*} \in Q_h$

$$\begin{aligned}
&\left(p_g^{f*}, -\frac{w_{as}^{(n)} - w_{as}^{(n-1)}}{\Delta t}\right)_h + \left(p_g^{f*}, -\frac{w_{ad}^{(n)} - w_{ad}^{(n-1)}}{\Delta t}\right)_h + \theta \int_{\Gamma_h} W_{as}^{(n)} \cdot \nabla p_g^{f*} d\Gamma_h \\
+ \quad & (1-\theta) \int_{\Gamma_h} W_{as}^{(n-1)} \cdot \nabla p_g^{f*} d\Gamma_h + \theta \int_{\Gamma_h} W_{ad}^{(n)} \cdot \nabla p_g^{f*} d\Gamma_h + (1-\theta) \int_{\Gamma_h} W_{ad}^{(n-1)} \cdot \nabla p_g^{f*} d\Gamma_h \\
= \quad & \int_{\Gamma_{f_h}^g} W_{ext}^g \delta_d \left(x - x_f^g\right) p_g^{f*} d\Gamma_{f_h}^g + \theta \left(p_g^{f*}, q_i^{g(n)}\right)_h + (1-\theta) \left(p_g^{f*}, q_i^{g(n-1)}\right)_h \\
+ \quad & \theta \left(p_g^{f*}, q_s^{g(n)}\right)_h + (1-\theta) \left(p_g^{f*}, q_s^{g(n-1)}\right)_h
\end{aligned} \tag{2.195}$$

Extended finite element formulation Degree-of-freedom and discretization

Fields related to the bulk material must be discontinuous due to the presence of the discontinuity, whereas all fields defined along the fracture surface must be continuous.

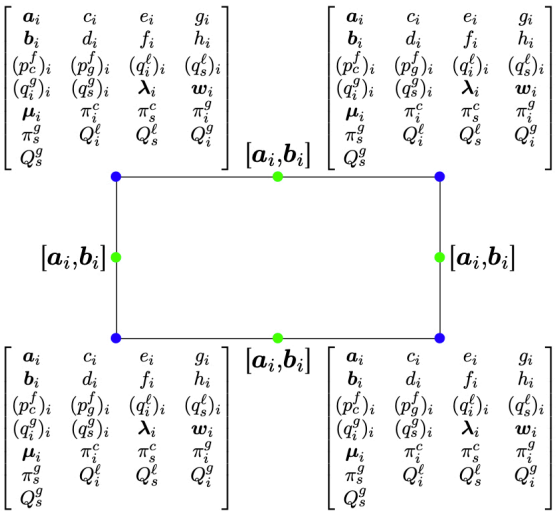

Figure 2.137: Sketch of a HHM-XFEM quadratic element.

On the first hand, the approximation to the displacement field (Eq. (2.196)) as well as to the hydrostatic pressure (Eq. (2.199)) are considered as strong discontinuities, meaning the primal field and its gradient are discontinuous across the fracture's surface. On the contrary, both approximations of the capillary pressure (Eq. (2.197)) and the gas pressure (Eq. (2.198)) are treated as weak discontinuities. Mathematically speaking, these two are strong discontinuities. Supposedly, both pressure fields (and their respective gradients) are discontinuous across the fracture surface. However, the continuity of both pressure fields is enforced on the upper and lower walls of the fracture using projection operators, as described in Section 2.6.1.2.

$$\boldsymbol{u}(\boldsymbol{x}) = \sum_{i \in I} \boldsymbol{a}_i \varphi_i(\boldsymbol{x}) + \sum_{j \in J} \boldsymbol{b}_j \varphi_j(\boldsymbol{x}) H_j(\boldsymbol{x}), \quad \boldsymbol{u} \in U_h \subset U \tag{2.196}$$

$$p_c(\boldsymbol{x}) = \sum_{i \in I_s} c_i \psi_i(\boldsymbol{x}) + \sum_{j \in J_s} d_j \psi_j(\boldsymbol{x}) H_j(\boldsymbol{x}), \quad p_c \in P_h \subset P \tag{2.197}$$

$$p_g(\boldsymbol{x}) = \sum_{i \in I_s} e_i \psi_i(\boldsymbol{x}) + \sum_{j \in J_s} f_j \psi_j(\boldsymbol{x}) H_j(\boldsymbol{x}), \quad p_g \in P_h \subset P \tag{2.198}$$

$$\pi_h(\boldsymbol{x}) = \sum_{i \in I_s} g_i \psi_i(\boldsymbol{x}) + \sum_{j \in J_s} h_j \psi_j(\boldsymbol{x}) H_j(\boldsymbol{x}), \quad \pi_h \in P_h \subset P \tag{2.199}$$

The fracture surface is materialized by a set of two level-sets: the normal level-set lsn and the tangential level-set lst. The former represents the fracture surface, while the latter is used in order to detect and actualize the fictitious crack front (see Figure 2.136) during the propagation procedure.

In order to fulfill the *inf-sup* condition (*i.e.,* avoid spurious oscillations of the numerical solution), the quadratic base functions $(\varphi_i)_{i \in I}$ are used to approximate the displacement field. All pressure fields are approximated by means of the following linear base functions $(\psi_i)_{i \in I_s}$.

The base functions $(\varphi_j H_j)_{j \in J}$ (or $(\psi_j H_j)_{j \in J_s}$), first introduced by Fries (2008), are considered in order to reduce ill-conditioned matrix phenomena as proven in Ndeffo et al. (2017). The closed-form expression for the shift-enrichment function H_j at node $j \in J$ (or $j \in J_s$) is given by:

$$H_j(\boldsymbol{x}) = H(\boldsymbol{x}) - H(\boldsymbol{x_j}) \tag{2.200}$$

where x_j is the position of node j, H is the generalized Heaviside function such as:

$$H(x) = \begin{cases} -1 & \text{if } x < 0 \\ +1 & \text{if } x > 0 \end{cases}$$

The approximation to the fields related to the fracture follows the same guideline. Basically, the dimension of the multipliers's approximation space must be smaller than the dimension of the displacement field's approximation space. To do so, a selection procedure is performed in order to assign equality relationships between Lagrange multipliers amid a set of element edges cut but the normal level-set lsn (for more information, the reader may refer to Ferte et al. (2015); Faivre et al. (2016); Paul et al. (2018)). Particularly, this selection procedure implies the use of a modified version of the base functions $(\psi_i)_{i \in I_s}$ to the approximation of the Lagrange multipliers.

As shown in Figure 2.138, for a given quadratic element, if a vertex is not connected to any edges intersected by the normal level-set lsn (*i.e.,* in this example, i = 2), the value of the linear shape function $\psi_{i=2}$ is assigned to zero. However, to fulfill the partition of the unity principle, the nodal value of $\psi_{i=2}$ at node i = 2 is equally dispatched among the set of vertex connected to intersected edges. In this example, the modified shape function $\widetilde{\psi}_i$ is:

$$\begin{cases} \widetilde{\psi}_i = \psi_i + \dfrac{\psi_2}{3} & i \in \{1, 3, 4\} \\ \widetilde{\psi}_2 = 0 \end{cases} \tag{2.201}$$

The set of Lagrange multipliers (in $\Lambda_h \subset \Lambda$) is then approximated as follows:

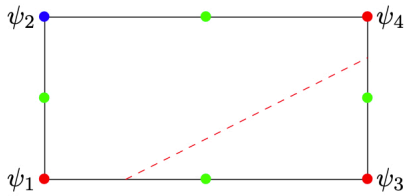

Figure 2.138: Modified shape functions for the Lagrange multiplier interpolation.

$$p_c^f(\boldsymbol{x}) = \sum_{k\in K}\left(p_c^f\right)_k \widetilde{\psi}_k(\boldsymbol{x}), \qquad p_g^f(\boldsymbol{x}) = \sum_{k\in K}\left(p_g^f\right)_k \widetilde{\psi}_k(\boldsymbol{x}) \tag{2.202}$$

$$\pi_i^c(\boldsymbol{x}) = \sum_{k\in K}\left(\pi_i^c\right)_k \widetilde{\psi}_k(\boldsymbol{x}), \qquad \pi_s^c(\boldsymbol{x}) = \sum_{k\in K}\left(\pi_s^c\right)_k \widetilde{\psi}_k(\boldsymbol{x}) \tag{2.203}$$

$$\pi_i^g(\boldsymbol{x}) = \sum_{k\in K}\left(\pi_i^g\right)_k \widetilde{\psi}_k(\boldsymbol{x}), \qquad \pi_s^g(\boldsymbol{x}) = \sum_{k\in K}\left(\pi_s^g\right)_k \widetilde{\psi}_k(\boldsymbol{x}) \tag{2.204}$$

$$Q_i^\ell(\boldsymbol{x}) = \sum_{k\in K}\left(Q_i^\ell\right)_k \widetilde{\psi}_k(\boldsymbol{x}), \qquad Q_s^\ell(\boldsymbol{x}) = \sum_{k\in K}\left(Q_s^\ell\right)_k \widetilde{\psi}_k(\boldsymbol{x}) \tag{2.205}$$

$$Q_i^g(\boldsymbol{x}) = \sum_{k\in K}\left(Q_i^g\right)_k \widetilde{\psi}_k(\boldsymbol{x}), \qquad Q_s^g(\boldsymbol{x}) = \sum_{k\in K}\left(Q_s^g\right)_k \widetilde{\psi}_k(\boldsymbol{x}) \tag{2.206}$$

$$q_i^\ell(\boldsymbol{x}) = \sum_{k\in K}\left(q_i^\ell\right)_k \widetilde{\psi}_k(\boldsymbol{x}), \qquad q_s^\ell(\boldsymbol{x}) = \sum_{k\in K}\left(q_s^\ell\right)_k \widetilde{\psi}_k(\boldsymbol{x}) \tag{2.207}$$

$$q_i^g(\boldsymbol{x}) = \sum_{k\in K}\left(q_i^g\right)_k \widetilde{\psi}_k(\boldsymbol{x}), \qquad q_s^g(\boldsymbol{x}) = \sum_{k\in K}\left(q_s^g\right)_k \widetilde{\psi}_k(\boldsymbol{x}) \tag{2.208}$$

$$\boldsymbol{\lambda}(\boldsymbol{x}) = \sum_{i\in K}\boldsymbol{\lambda}_i\widetilde{\psi}_i(\boldsymbol{x}), \quad \boldsymbol{w}(\boldsymbol{x}) = \sum_{i\in K}\boldsymbol{w}_i\widetilde{\psi}_i(\boldsymbol{x}), \quad \boldsymbol{\mu}(\boldsymbol{x}) = \sum_{i\in K}\boldsymbol{\mu}_i\widetilde{\psi}_i(\boldsymbol{x}) \tag{2.209}$$

Before jumping into the discretization of the linearized matrix system, we provide a sketch of a HHM_XFEM element (pictured in Figure 2.137). It is worth mentioning that quadrangular elements as well as triangular elements are available in 2D (for the propagation of a fracture along a predefined path). However, for the propagation of a fracture along a non-predefined path, only quadrangular element are made available (for symmetry and stability purposes).

2.6.2. Results

2.6.2.1. Simulation of the injection of a gas into the Callovo-Oxfordian clayey: Experimental setting and material parameters

Consider a sample of rock of height h = 10mm and width ℓ = 5mm. The sample is entirely cut by a fracture in x = 0. The initial capillary pressure as well as the gas pressure exerting inside the sample are

respectively $p_c\,(x, y, 0) = p_c^0 = 4\text{MPa}$ and $p_g\,(x, y, 0) = 1\text{atm}$. The Mualem-Van Genuchten's model provides a relationship between the capillary pressure and the saturation, so the saturation of the rock sample is initially taken at about 96% (see Figure 2.141 (left)).

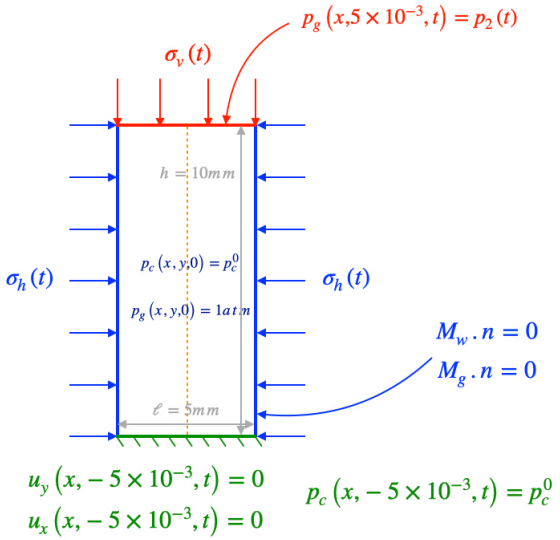

Figure 2.139: Triaxial shear test and boundary conditions

At the bottom of the rock sample, displacements are prevented in all directions and the capillary pressure p_c^0 is imposed at the initial capillary pressure and kept constant the whole time. In Figure 2.140, the loading history applied to the rock sample is represented.

First of all, the rock sample is brought to a hydrostatic state by applying the following time-depend stress on the left, right and top sides:

$$\sigma_h\,(t) = \begin{cases} \dfrac{5t}{t_0} \text{ if } 0 \leqslant t \leqslant t_0 \\ 5 \quad \text{if } t > t_0 \end{cases}$$

where $t_0 = 3600\text{s}$.

Then, after an hour, a deviator is applied on top of the rock sample. Similarly, it follows:

$$\sigma_v\,(t) = \begin{cases} \dfrac{5t}{t_0} & \text{if } 0 \leqslant t \leqslant t_0 \\ \dfrac{8\,(t - t_0)}{t_1 - t_0} + 5 \text{ if } t_0 < t \leqslant t_1 \\ 8 & \text{if } t > t_1 \end{cases}$$

where $t_1 = 7200\text{s}$.

To finish, when the desired stress state is reached, a time-dependent gas pressure is imposed at the top of the column and is:

$$p_2(t) = \begin{cases} 0 & \text{if } 0 \leqslant t \leqslant t_1 \\ \dfrac{11.5\,(t - t_1)}{t_2 - t_1} & \text{if } t_1 < t \leqslant t_2 \\ 11.5 & \text{if } t > t_2 \end{cases}$$

The simulation of the triaxial shear test depicted in this section runs from t = 0 to t = 48 hrs.

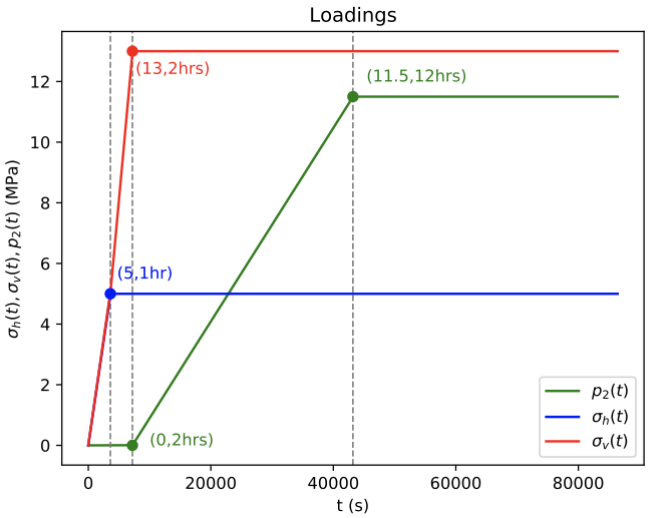

Figure 2.140: Loading history

Material parameters are summarized in Table 2.31. In the following, the denomination (MVG) stands for a parameter of the Mualem-Van Genuchten's model.

Table 2.31: Material parameters for the Callovo-Oxfordian rock sample.

Viscosity of the liquid	μ	10^{-3} Pa.s
Viscosity of the gas	μ_g	1.8×10^{-5}Pa.s
Liquid compressibility	$\frac{1}{K_w}$	5×10^{-10}Pa^{-1}
Density of the liquid	ρ	1 kg.m^{-3}
Molecular weight of the gas	M_g^{ol}	2×10^{-3}g.mol^{-1}
Young's Modulus	E	4.5 GPa
Poisson's ratio	ν	0.3
Biot coefficient	b	0.85
Permeability	K^{int}	5.097×10^{-21}m^2
Critical stress	σ_c	2 MPa
Cohesive energy	G_c	120 Pa.m
Augmented ratio	r	100 Pa.m^{-1}
Porosity	ϕ	0.15
Pore-size distribution ratio (MVG)	n	1.49
Residual water content (MVG)	S_{wr}	0.01
Residual capillary pressure (MVG)	p_r	14.7 MPa

In Figure 2.141 (left) and (right) are respectively depicted the evolution of the saturation with respect to the capillary pressure (given by the Mualem-Van Genuchten's model) as well as the evolution of the effective cohesive stress with respect to the vertical opening of the fracture (given by the cohesive constitutive model described in Section 2.6.1.1). Each regime of the cohesive law are tagged along the profile of the effective cohesive stress t_c'. Particularly, the critical opening is reached for $w_c = 1.2 \times 10^{-4}$m. Beyond this

point, all fracture energy has been dissipated and the walls of the fracture reached complete separation. This process is irreversible.

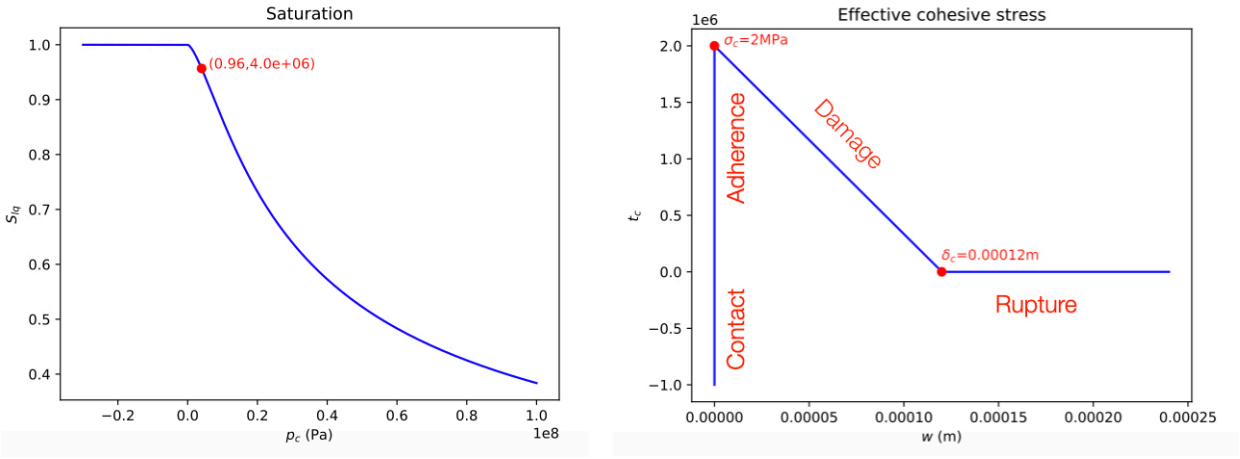

Figure 2.141: Evolution of the saturation with respect to the capillary pressure (left); evolution of the effective stress with respect to the vertical opening (right).

2.6.2.2. Interpretation

In the following, on each profile involving the physical time, three different sections of the rock sample are represented. The blue-dotted, green-dotted and orange-dotted lines represent respectively the evolution of a field at the points $(x = 0, y = -0.005)$ (bottom of the column), $(x = 0, y = 0.005)$ (top of the column), $(x = 0, y = 0)$ (middle of the column) with respect to t.

In order to interpret the effects of gas injection throughout the rock sample, let's start analyzing the profiles of the evolution of the effective cohesive stress (see Figure 2.142).

At the beginning of the loading phase (hydrostatic + deviator), the evolution of the cohesive stress with respect to time is clearly in the contact regime all along the fracture path. The compressive state induced by the external loadings leads the sample to contract (see Figures 2.147). This induce a collapsing effect on the porous matrix that generates a slight increase in liquid saturation above this initial saturation threshold (see Figure 2.144 (bottom right)).

Then, as soon as the injection of the gas starts off, the green-dotted and orange-dotted lines seems to evolve from the contact regime to the adherence regime (the transition is marked by a compressive stress state in the former and a tensile stress state in the latter). The sample expands in the vertical direction as can be seen in Figure 2.147. At some point (about $t = 44820$s), the effective cohesive stress reaches $t_c' = \sigma_c$ and evolves now in the damage regime of the cohesive law.

Indeed at $t = 44820$s, in Figure 2.143 (top left), the profile of the evolution of the horizontal displacement along the fracture path shows the fracture opening is no longer equal to zero. It is really interesting to observe that, contrariwise to the general believe, we do not observe that the fracture is reactivated at the injection point but in the mid-section region. In other words, we observe the propagation of a double-tipped fracture, until the tip near to the top region vanishes, while the tip near to the bottom continues its course toward the bottom of the sample.

This peculiar observation can be correlated to the vertical distribution of the fluid inside the rock sample. As the gas injection goes on, the gas diffuses into the porous medium and pushes the liquid away from the top of the column. This statement can be supported by the profiles of the evolution of the saturation

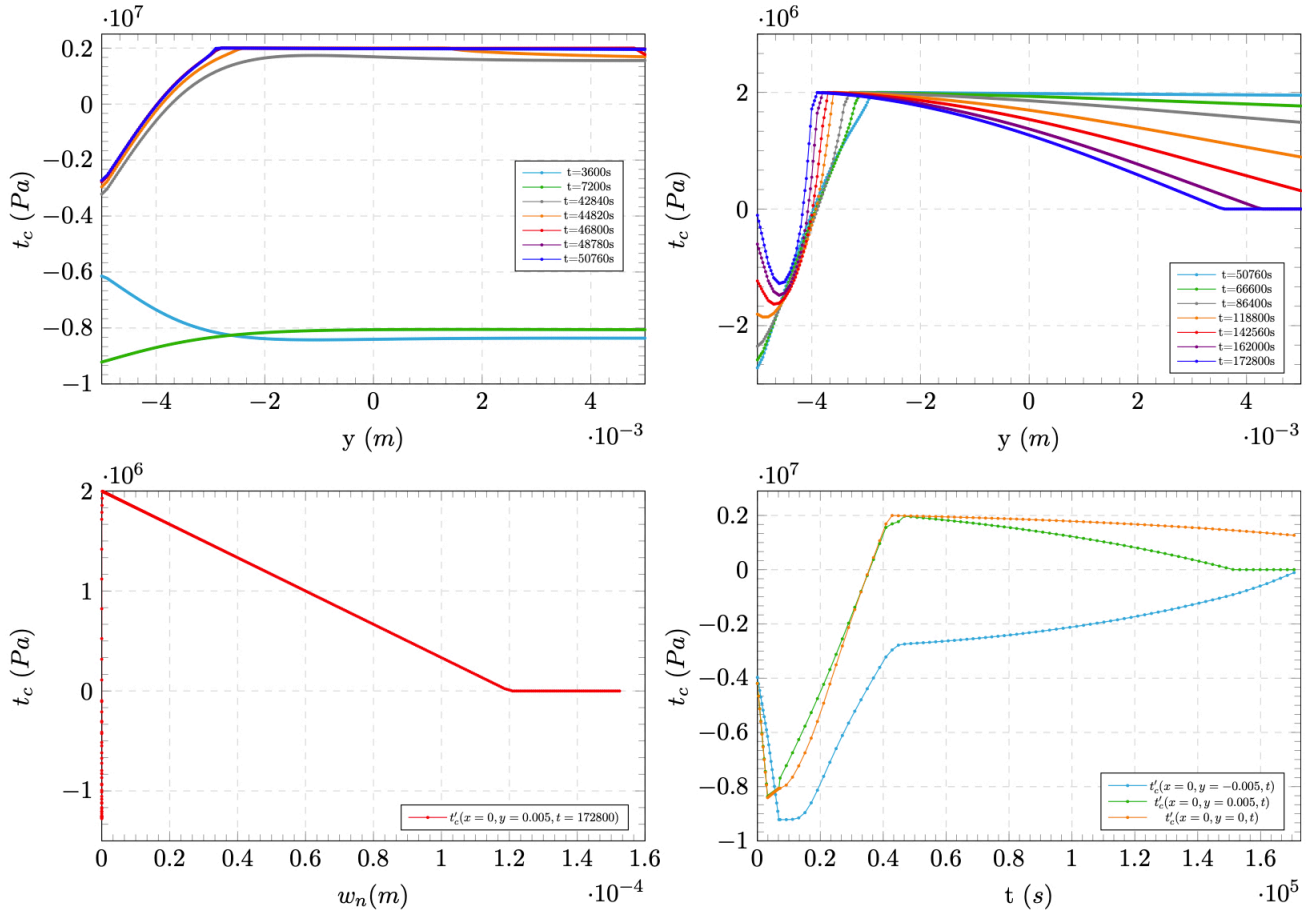

Figure 2.142: Evolution of the effective cohesive stress along the fracture path.

along the fracture surface (see Figure 2.144) and the profiles of the evolution of the fluid pressure along the fracture path (see Figure 2.145). At the top of the column, past the consolidation phase of the sample (*i.e.,* $t > t_1$), the liquid saturation plummets until the curve records a slight upright turn.

As the gas is injected into the sample, the fluid accumulates in the the lower section of the sample and, in the mean time, participates in inducing a poro-elastic effect that favors the transition from the contact regime (*i.e.,* compressive state) to adherence and damage regimes (*i.e.,* tensile stress state). Then, as the reactivation of the fracture begins, the liquid is sucked up inside the fracture (*i.e.,* increase of the fluid saturation mentioned above) and pushes its way toward the top of the column. As a result, the fracture propagates faster in the region near the top of the column. What's more, the fluid pressure as well as the gas pressure are uniform inside the fracture at any given time step, which suggests most of the energy is dissipated through fracturing the solid matrix. Viscous effects seem negligible in this example. One should notice that the fracture keeps on propagating toward the bottom of the column at a much slower pace because the gas hasn't diffused yet in this area, and therefore, hasn't generated a sufficient poro-elastic effect that participates in transitioning into the damage regime.

Eventually, the rupture regime (beyond w_c) is reached in the region near the top of the sample as of $t = 162000$s (see Figure 2.142 (top right) and (bottom right)). Additionally, at this time step, several sections of the fracture path are in different regimes. For example, if $y \in [0.0043, 0.005]$: rupture, if $y \in [-0.0038, 0.0043]$: damage, if $y \in [-0.004075, -0.0038]$: adherence, if $y \in [-0.005, -0.004075]$: contact. An other way to picture the evolution of the injection point is to plot the evolution of the effective cohesive stress with respect to the normal opening (see Figure 2.142 (bottom left)). As a matter of fact,

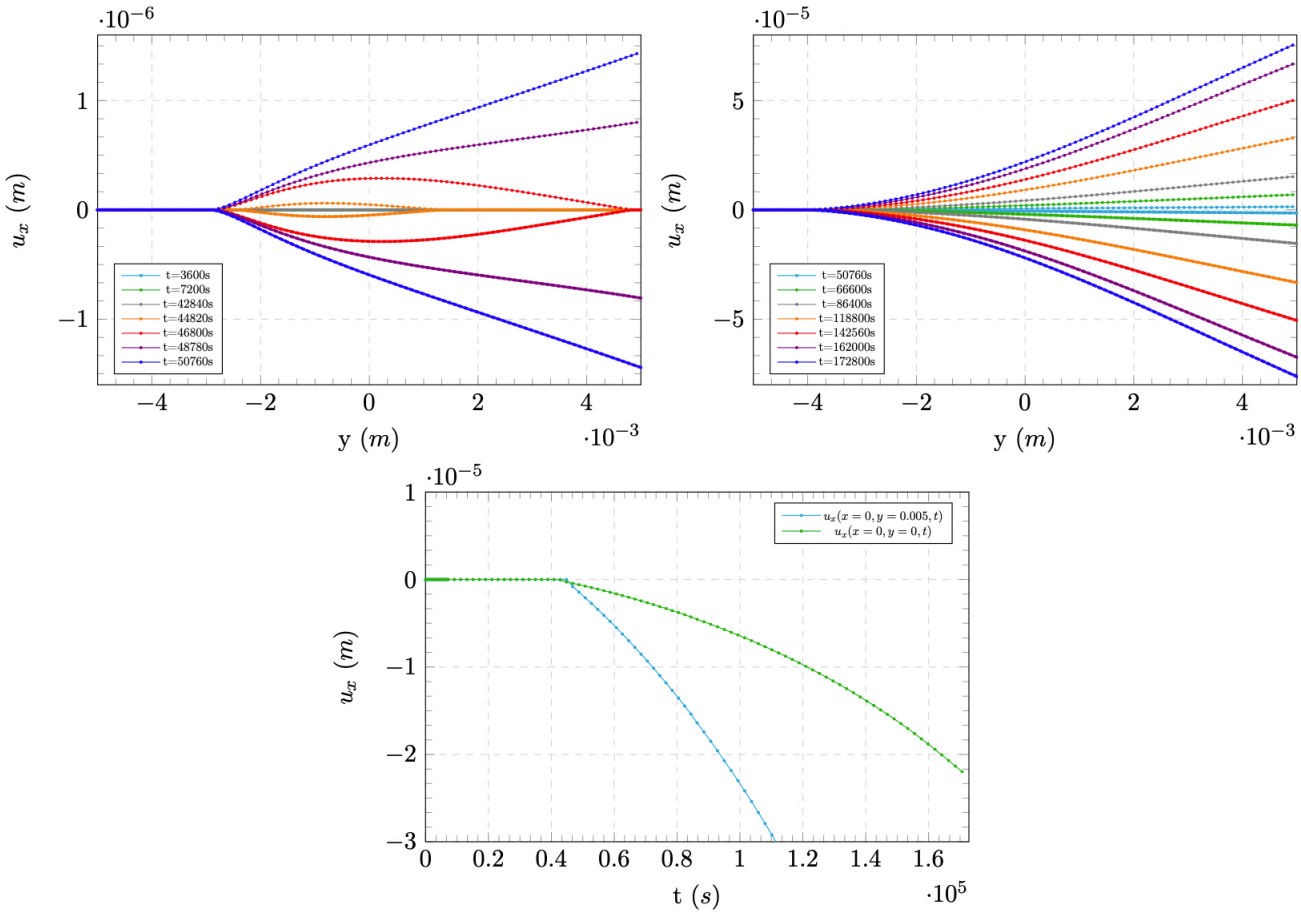

Figure 2.143: Fracture opening along the direction normal to the fracture surface.

all regimes of the cohesive law are retrieve and the numerical profile matches exactly the theoretical path predicated by the cohesive constitutive law (see Figure 2.141 (right) and Section 2.6.1.1).

2.6.3. Summary

The present work is the continuation of previous contributions developed by the same authors (Faivre et al. (2016), Paul et al. (2018)) to implement a fully coupled two-phase flow numerical model in the eXtended Finite Element Method (XFEM). This method was first introduced to assess the propagation of a discontinuity without the need for remeshing Belytschko and Black (1999). Several publications followed up and combined the XFEM and thermo-hydromechanical models all together (for example Khoei et al. (2012)). In our case, an augmented Lagrangian formulation is considered that involves a series of projection equations. To properly describe the mechanical behavior of the interface, the displacement jump as well as the total cohesive stress are projected onto a carefully designed function space (Ferte et al., 2015) associated with a specific inner product equivalent to lumped mass methods (Chen and Thomée, 1985). The dynamics of the fluid-driven fracture is then described by a non-regularized cohesive law. Hence, no dependency upon regularization parameters is introduced, that usually leads to spurious oscillations if not carefully calibrated. Similarly, both diffusion equations, for the bulk and the fracture, are connected to each other using a second augmented Lagrangian formulation. This allows to enforce the continuity of the pressure fields by a series of projections onto the same function space as for the mechanical fields. Additionally, the use of this inner product, that is particularly suited for parabolic equations, allows to lump the mass matrix of both diffusion equations canceling out abnormal behaviors near high-gradient range areas. Additionally, a mixed formulation (Legrain et al., 2008) was introduced so the mass matrix is only

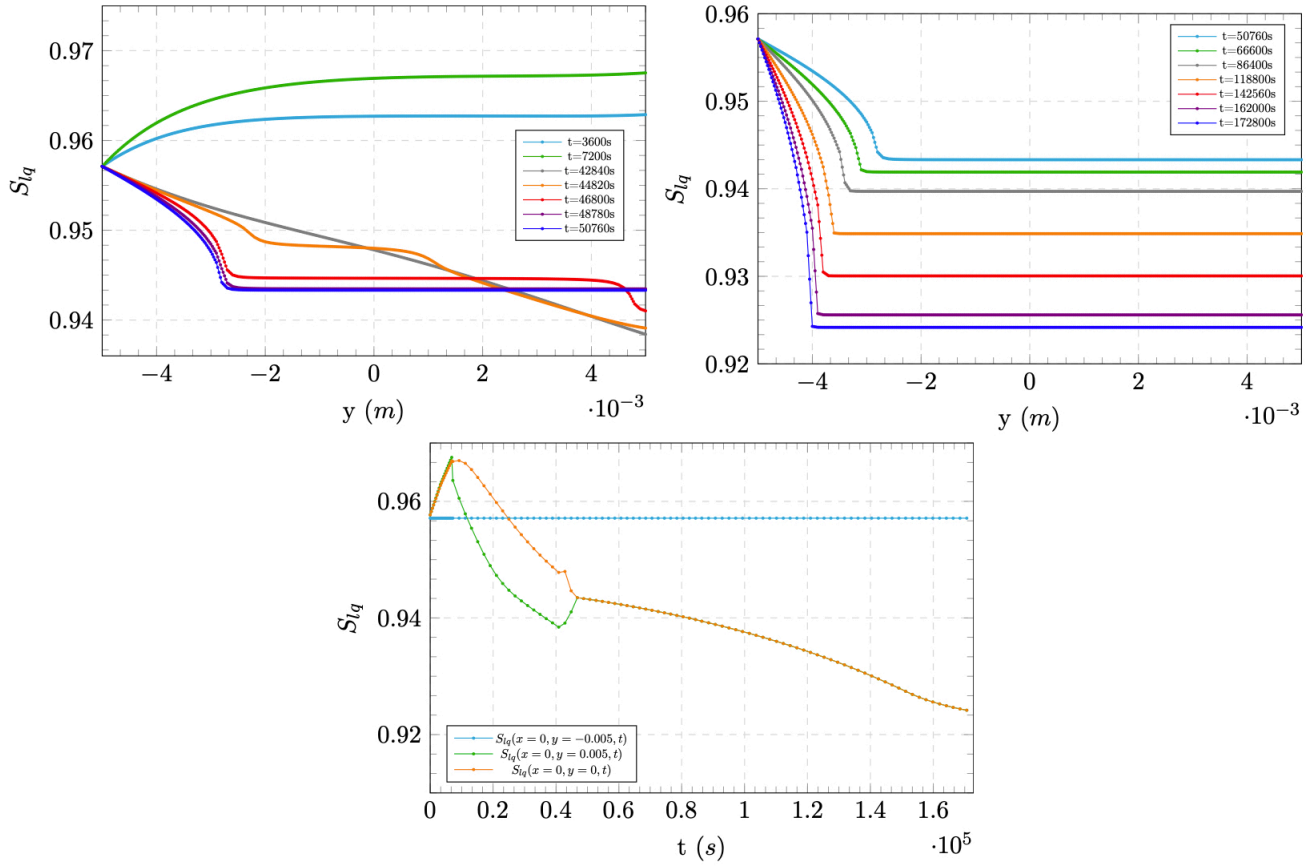

Figure 2.144: Evolution of the liquid saturation along the fracture path.

defined upon linear fields that live in the same function space, which is a requirement of the inner product mentioned above. What's more, our numerical model is now able to simulate the propagation of a fracture for the three-phase porous medium case. The fluid in the crack may be either a gas or a liquid. A capillary pressure/saturation relationship is provided using a Mualem-Van-Genuchten model. Eventually, an interesting feature of the HHM-XFEM model is its ability to simulate the propagation of a discontinuity, along which internal gas pressure falls into the range of atmospheric conditions. In this work, we showcase a triaxial test on a sample of Callovo-Oxfordian clay rock under undrained conditions. Especially, we want to simulate the injection of a gas into a fractured sample. Comparison is made with fracture reactivation driven by water injection. Our goal is to quantify the effects of the gas injection on the dynamics of the fracture. This work is carried out in the framework of the GAS Work Package of EURAD project.

2.6.4. Key learning points

New knowledge acquired

In past contributions, the present XFEM model was applied to simulating the propagation in saturated conditions (Faivre et al. (2016), Paul et al. (2018)). However, we stumbled upon numerical results that showed spurious oscillations. The following methodology proved to be successful to stabilize the HHM-XFEM model:

- Introduction of a mixed formulation (Legrain et al., 2008), in order to project the spheric part of the strain tensor onto the same function space as the fluid pressure/gas pressure defined in the bulk

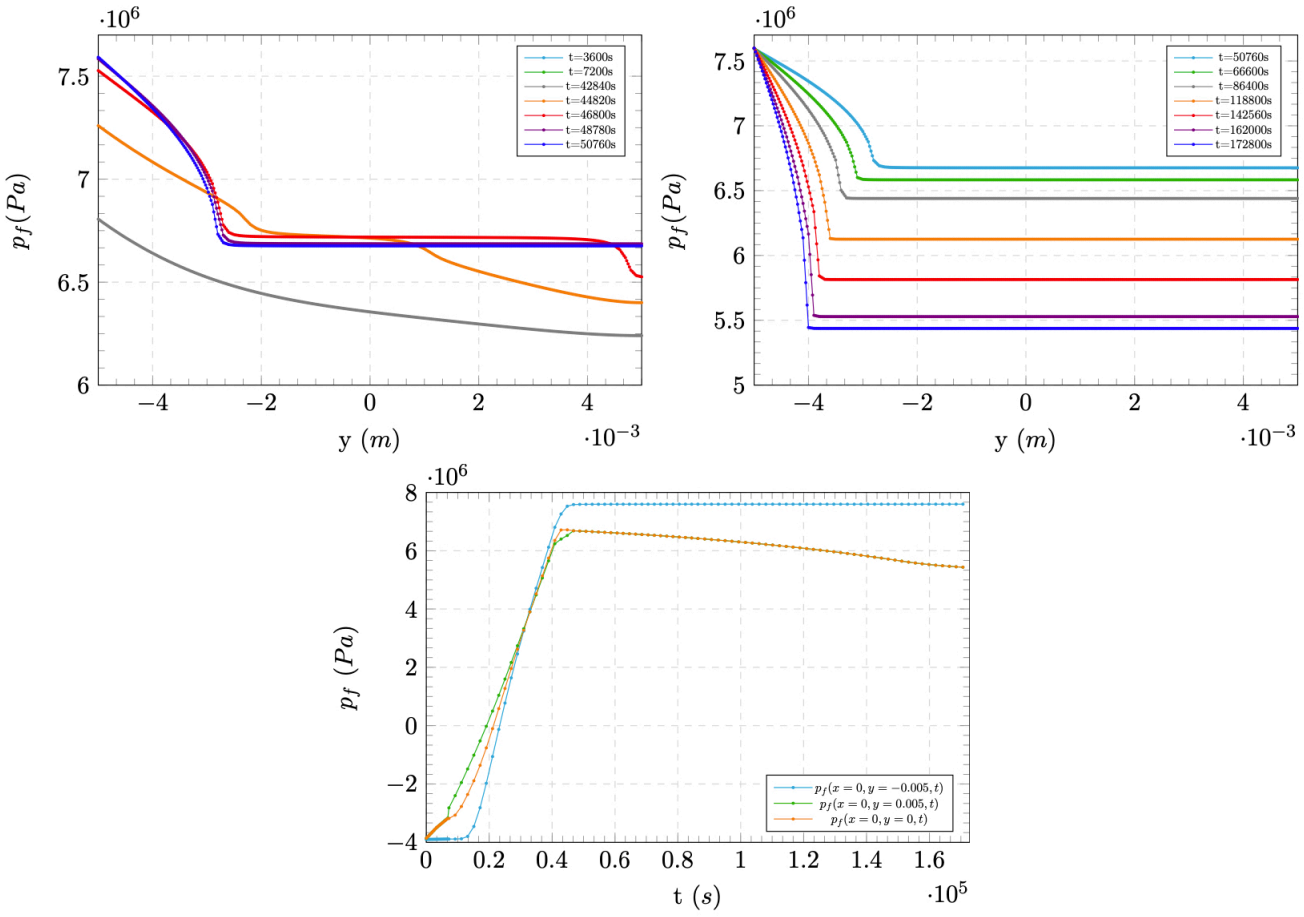

Figure 2.145: Evolution of the fluid pressure along the fracture path.

(because the fluid is supposed compressible):

$$-\int_{\Omega_h}\left(\frac{p_h}{K_0}-\varepsilon_v\left(\boldsymbol{u}\right)\right)d\Omega_h=0. \tag{2.210}$$

- Previous bullet point allows to lump the mass matrix. Conventional techniques do not apply because of the discontinuity. It is first lumped using the Hansbo enrichment base functions and the inner product $(.,.)_h$ (Chen and Thomée, 1985) that approximates the standard inner product in L^2. A transformation matrix (Areias and Belytschko, 2006) is then used to represent this enrichment in the standard XFEM base;
- Introduction of an augmented Lagrangian (Ferte et al., 2015) to project the trace of the fluid/gas pressure (bulk) onto the discontinuity (i.e., field living in the same function space) to use conventional lumping techniques aiming at stabilizing the flux in the normal direction to the fracture surface;
- and regularization of the diffusion equation in the tip region (i.e., becomes singular) using a minimal opening w_f.

Impact of the acquired knowledge

The model developed should allow to simulate gas circulation and crack propagation due to gas migration in initially sound material. Lots of numerical issues were encountered and almost completely fixed with

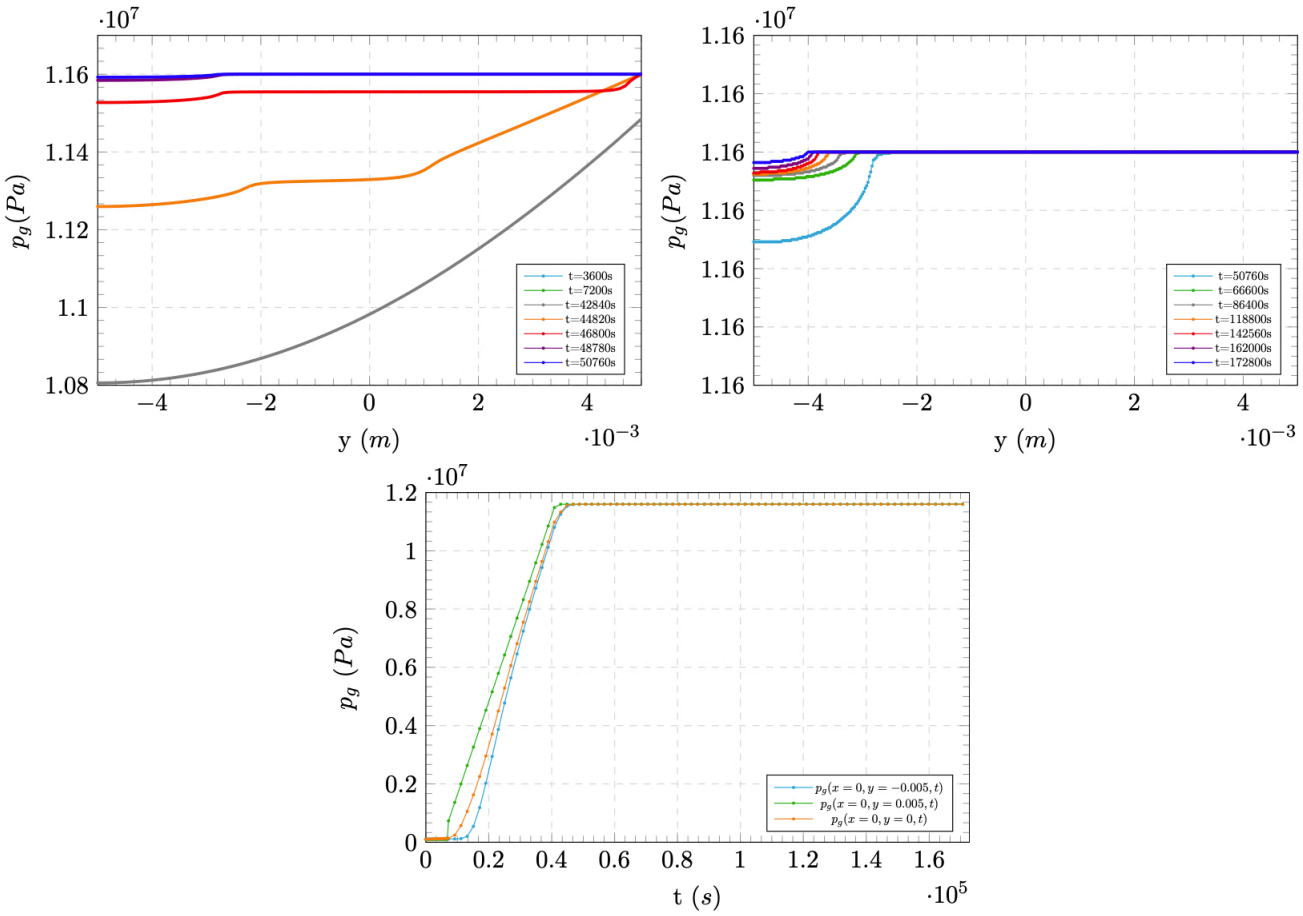

Figure 2.146: Evolution of the gas pressure along the fracture path.

specific numerical technics. Gas injection tests consist in a complex physics resulting in a lot of degrees of freedom in the model, inducing time and machine consuming calculations.

Recommendations for the future

Not applicable.

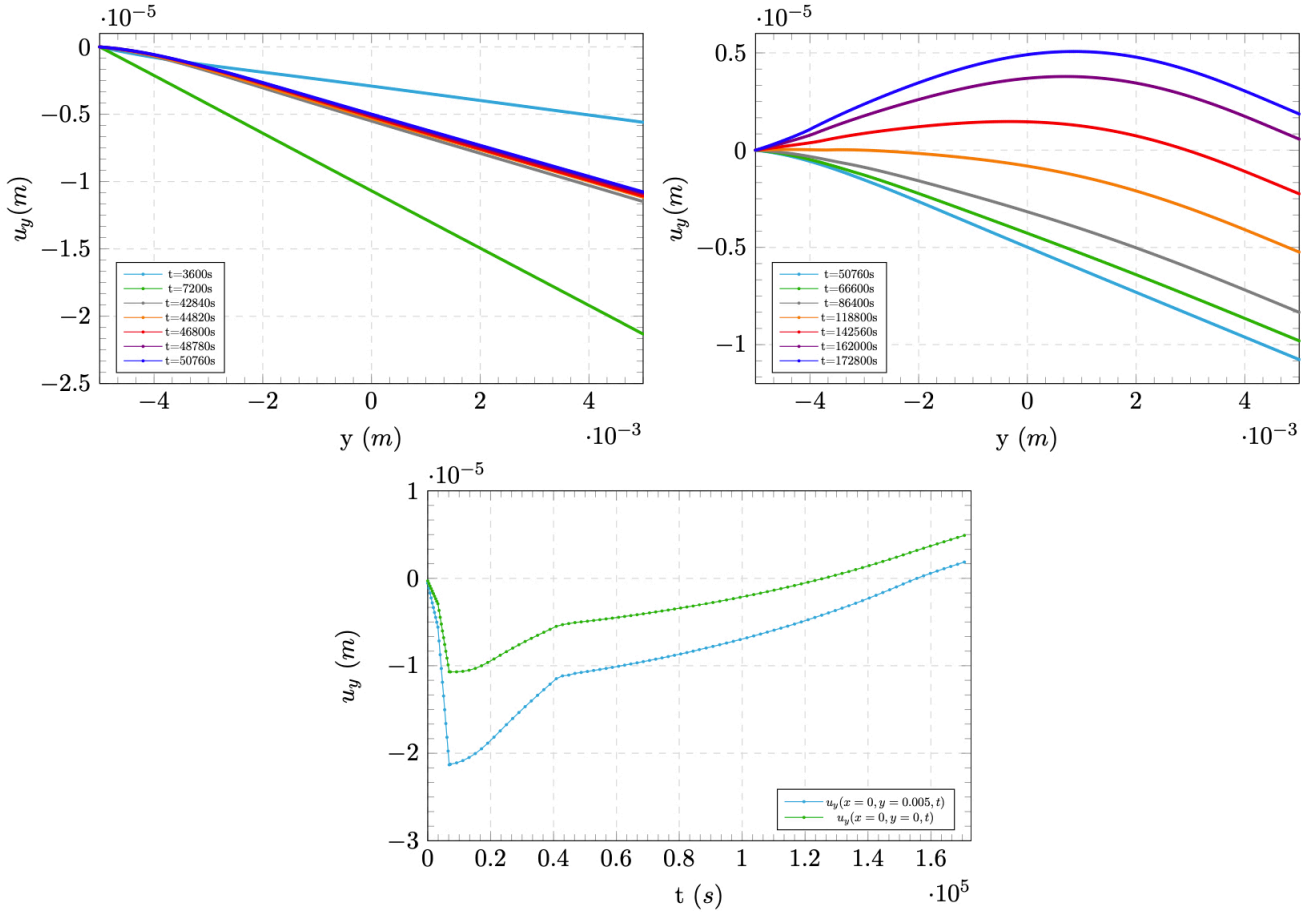

Figure 2.147: Vertical displacement in the vertical direction along the fracture path.

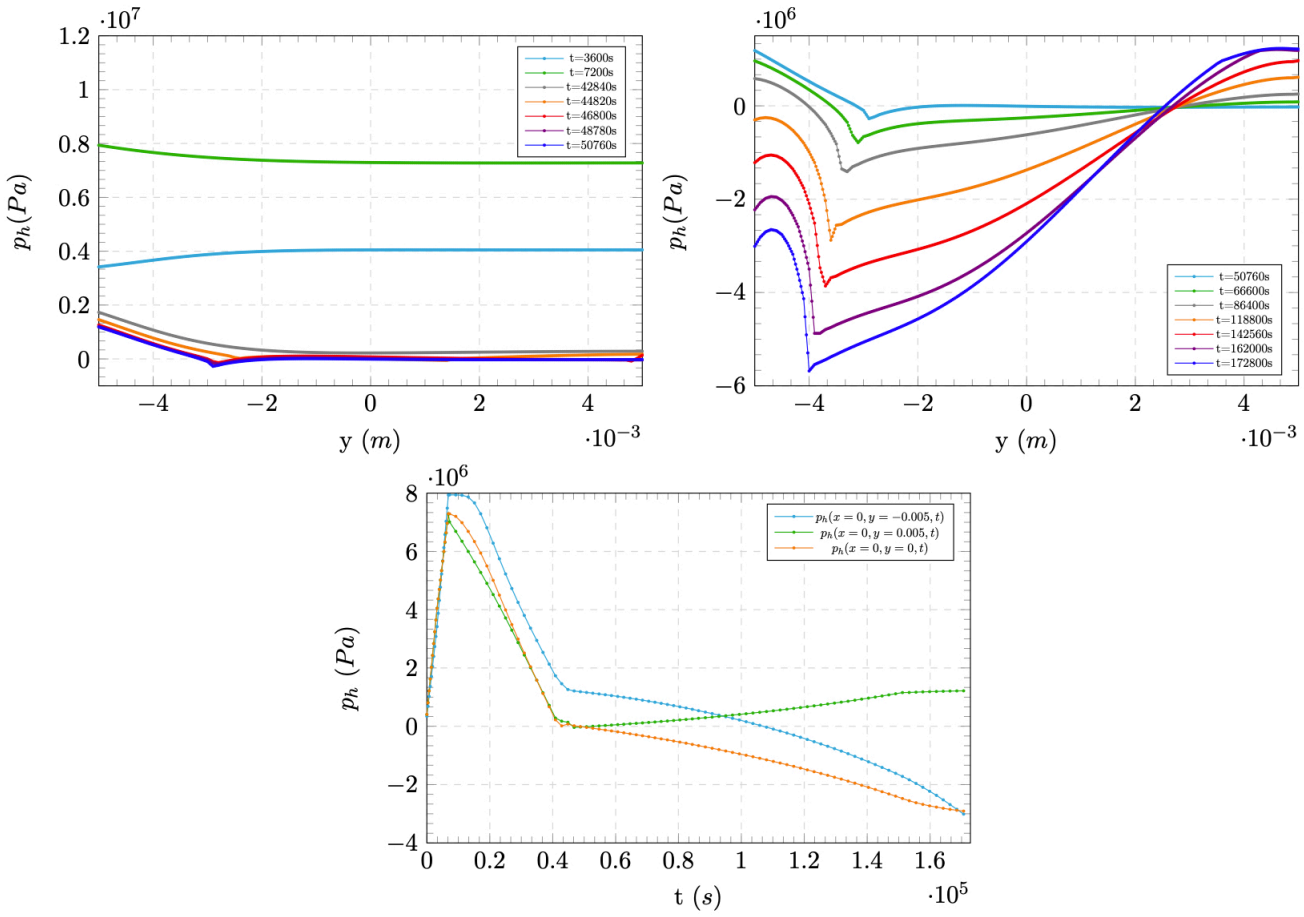

Figure 2.148: Evolution of the hydrostatic pressure along the fracture path.

.

EDF

2.7. Numerical modelling of experimental triaxial gas injection tests on Callovo-Oxfordian samples (EDF)

2.7.1. Introduction

EDF's work for task 3.3 is dedicated to the modeling of experimental tests provided by GeoRessource (CNRS-U. Lorraine) on intact COx samples. These experimental tests performed within sub-task 3.1 (see corresponding section) are triaxial compression tests under confining pressure, with gas injection and measurement of permeability. The aim of these experiments is to study the impact of damage-induced cracks on the gas transfer within clay host rocks. The goal of EDF's work is first to model the induced damage of COx at the same time as gas injection and second to model the coupling with gas transfer i.e. to provide analysis of gas propagation and interactions with cracking in claystone. For the considered triaxial experimental tests, damage is not produced by gas injection, but gas transfer is affected by it. It is worth noting that the initial proposal of EDF included also to model mechanical damage provided by gas injection itself. For this purpose, experimental tests were envisaged in task 2.2 (tests also conducted for self-sealing study) but these complex experiments couldn't be completed in time for this project, hence not allowing to perform this additional work

To simulate these triaxial experimental tests, a continuous macroscopic hydro-mechanical model is used. This model has been developed for many years by EDF in Code_Aster software within a two-phase flow poromechanical formalism (THM modulus of Code_Aster). Code_Aster is an open-source Finite Element software developed by EDF R&D (www.code_aster.org). The model used in this work will be finely described in the subsequent sections.

Several triaxial experimental tests with gas injection have been carried out by GeoRessource with both orientations (parallel or perpendicular to bedding). As described in the experimental part of this report, different techniques have been tested to resaturate the sample (with or without confinement, with liquid injection or in a bell jar at imposed hygrometry) but all of them have produced important damage. For these reasons, tests without a preliminary resaturation stage have also been provided, even if this material is far away from the saturated one. Considering this, a preliminary computation was done by EDF on the damaged saturated sample in order to check that the classical parameters used for intact COx have to be adapted and to set up main lines of the modeling. In a second step a modeling of the unsaturated sample was established. Even if the material is not representative of the in-situ COx, these computations allow the development of a methodology to study gas volume evolution linked to mechanical comportment. It also allows to understand coupling processes. For both cases (with or without resaturation), only tests made on samples parallel to bedding will be modeled.

2.7.2. Conceptual model

2.7.2.1. Generalities

A continuous macroscopic fully-coupled hydro-mechanical model is used for all calculations detailed in this section. This model is based on the classical Biot porous media approach with a formulation in total stresses /effective stresses (respectively σ and σ') such as:

$$d\sigma = d\sigma^{'} - b\mathbf{I}d\pi$$

With b the Biot coefficient and π the hydraulic stress.

For unsaturated porous media, this formulation is written as a combination of gas pressure P_g, capillary pressure P_c, and liquid saturation S_l (Coussy et al., 2004):

$$d\pi = dP_g - S_l dP_c$$

The model is fully coupled and is based on equilibrium on total stress for the mechanical part and mass conservation for hydraulic part. Classical two-phase flow model is applied for the hydraulic part and is detailed in sec. 2.7.2.2.

Several constitutive mechanical laws could be applied to describe the relationship between effective stress and displacement. For this study a viscoplastic law dedicated to geomaterials called “LKR” (Raude et al., 2016; Cuvilliez et al., 2017) is used. Main features of this law are presented in section 2.7.2.3. To avoid localization phenomena due to softening and mesh dependencies, a regularization technique based on volumic second gradient deformation is also used (Fernandes et al., 2008).

For all the following, the material is assumed to be a continuous medium and the hypothesis of small strains and transformations is made.

2.7.2.2. Mechanical law

From several years, EDF has developed a specific viscoplastic law dedicated to geomaterials with different degrees of complexity. This law called LKR (for Laigle, Kleine and Raude) is fully detailed in (Raude et al., 2016; Cuvilliez et al., 2017). An anisotropic version of this law has been developed more recently (Djouadi et al., 2020) but is not relevant for the current work (modeled triaxial tests are performed on a sample parallel to bedding). This model represents two physical mechanisms: the first describes the instantaneous deviatoric behaviour of geomaterials and the second, viscoplastic mechanism, reflects the effect of time on the deviatoric behaviour of rock.

The instantaneous deviatoric behaviour of the rock is usually characterized by extension and unconfined compression triaxial tests. The conceptual framework retained for the development of the elasto-plastic mechanism is mainly based on the analysis of behaviour in triaxial compression. The response of geo-materials to this kind of compression breaks up into two phases. For relatively weak deformations, the resistance of a sample increases with its axial deformation. This phase, qualified as pre-peak, ends when the material reaches its maximum resistance. Beyond this peak, resistance decreases until reaching a residual value. The evolution of a material between its resistances of peak and residual is described as post-peak. The effect of time on the deviatoric behaviour is characterized by triaxial compression or creep tests at various loading rates.

The main features of this constitutive model could be summarized as follows:

- A generalized Hoek-Brown criterion is used as plasticity surfaces.
- The elastoplastic part of the model, related to instantaneous behaviour, is described by strain hard-ening, followed by strain softening.
- The overstress concept of Perzyna describes the viscoplastic part of the model that is related to the delayed behaviour.
- A specific non-associated flow rule allows to take into account the evolution of the dilatancy with respect to the stress state.

- A coupling between instantaneous and delayed mechanisms is accounted for.

The strain tensor εcould be decomposed in elastic strain ε_e, plastic strain ε_p and viscoplastic strain ε_{vp}tensor.

All details of this model are given in the code_aster documentation available online (https://code-aster.org /V2/doc/default/en/man_r/r7/r7.01.40.pdf).

The LKR model depends on many parameters that are usually determined from triaxial compression tests and creep tests at different temperatures and confining pressures. As a first approach, parameters retained for the intact COx are the ones previously used by EDF; and determined with several experimental tests according to Figure 2.149.

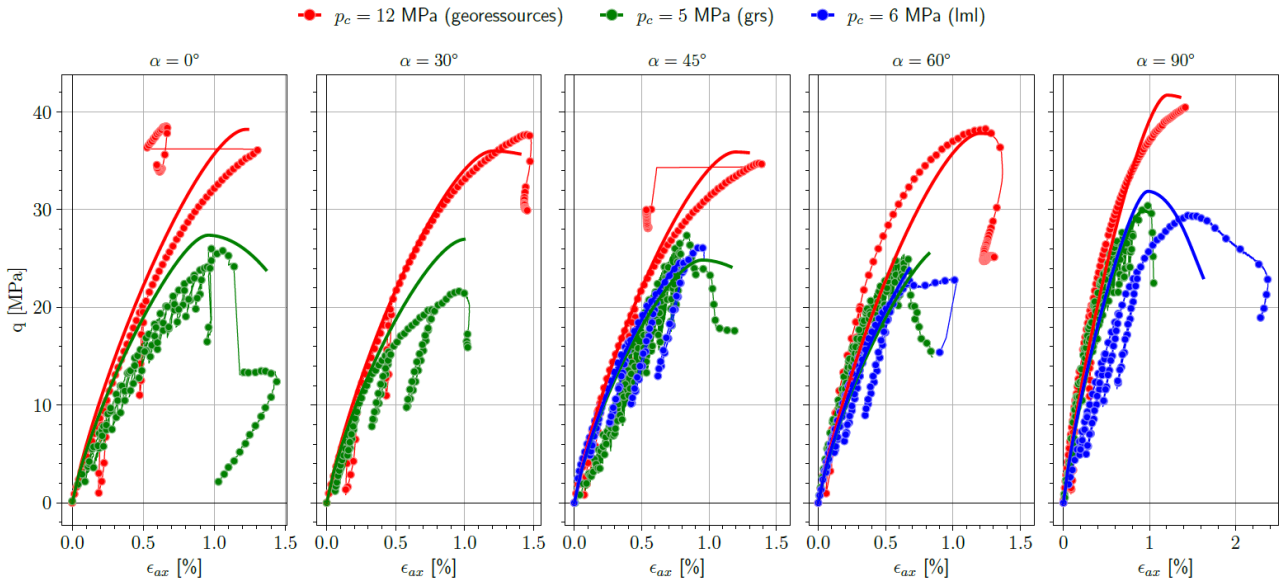

Figure 2.149: Triaxial tests on intact COx modelled by LKR law

The experimental tests which are modelled in the following are performed on samples parallel to bedding with a confinement pressure of 12 MPa. Consequently, we will use the parameters corresponding to the red curve and α=0 in the Figure 2.149. For all modelings, temperature is supposed to be constant (and equal to ambient temperature). Parameters are given in Table 2.32 for specific LKR parameters and in Table 2.33 for elastic ones. These parameters are also used in HITEC (see deliverable D7.6).

These parameters will be considered as “reference parameters”. In section 1.4, sensitivity analyses will focus on applying several young modulus E and mean compressive strengths σ_c (in grey).

Table 2.32: LKR Parameters (reference)

Parameter	Description	Value	Unit
β, γ	Shape parameters of the plasticity criterion in the deviatoric plane	1,5 ; 0,85	-
$\widehat{\sigma_c}$	Mean compressive strength	12,5	MPa
$m^0_{[0]}$	Slope of the initial elasticity threshold	0,1	-
$m^0_{[1]}$	Slope of the maximal strength threshold	8	-

Table 2.32: LKR Parameters (reference)

Parameter	Description	Value	Unit
V_1	Parameter for the pre-peak strain hardening kinetic	1,89	-
$\xi^0_{[1]}$	Value of the strain-hardening variable on the maximal strength threshold	6,3 10^{-3}	-
V_2	Parameter for the post-peak strain hardening kinetic	1,85	-
$\xi^0_{[2]}$	Value of the strain-hardening variable on the intermediate threshold	2.10^{-2}	-
$a_{[2]}$	Curvature of the intermediate threshold	0,7	-
q^0_i	Intersection of maximal strength intermediate and residual threshold	59,5	-
$r^x_{[2]}$	Axial strain-stress relation at different temperatures and confining pressure	0	-
A_v, η_v	Parameters for the creep kinetic	9,34 10^{-14} ; 1,86	s^{-1},-
f_p	Creep parameter	0,1	-
$\xi^0_{[5]}$	Parameter for the ampltitude of delayed strain	2,71 10^{-3}	-
ρ_1 , ρ_2 , ρ_3	Parameters for the amplitude of volumetric strains	1 ; 0,14 ; 1,1	-

Table 2.33: LKR Parameters (reference

Parameter	Description	Value	Unit
E	Young Modulus	5000	MPa
ν	Poisson coefficient	0,35	-

2.7.2.3. Two-phase flow model

A standard two-phase flow model is used in the calculations. In the following, the 2 components (N_2 and H_20) are denoted by upper index c. These 2 components could exist in 2 phases (liquid and gas), denoted by lower index p. In the following, vapor is neglected; hence water does not exist in a gaseous phase. Gaseous phase (g) is therefore composed only of nitrogen, liquid phase (l) is composed of water and dissolved nitrogen.

Mass conservation reads for component c(c = N_2 or H_20):

$$\dot{m}_c + \nabla \cdot (F_l^c + F_g^c)$$

where m_c (resp. F_l^c , F_g^c) designates mass inflow (resp. liquid, gaseous flux) of component c. For each phase p, hydraulic fluxes obey to Darcy's law:

$$F_p = -\frac{f_p K.\mathbf{I}.k_r^p(S_l)}{\mu_p}\nabla p_p$$

k_r^p stands for relative permeability and μ_p for dynamic viscosity of phase p. As the material is isotropic, K.**I** stands for intrinsic permeability tensor. As it is well known that "intrinsic permeability" notion is questionable, factor f_p is introduced to distinguish "intrinsic" gas and water permeability. In the general case $f_l = f_g = 1$ but most of the time $f_g \gg 1$ has to be considered. This will be studied in section 2.7.4.

As it is the initial objective of this work, evolution of intrinsic permeability will be studied. Several relationships could have be investigated according to different parameters (porosity, gas pressure, deformation, etc.). As done in (Mahjoub et al., 2018), we propose to investigate here a relation between permeability and volumic plastic deformation such as:

$$K\left(\varepsilon_p\right) = K^0.\left(1 + \kappa\left\langle\varepsilon^p\right\rangle^\gamma\right) \text{ if } \varepsilon^p > 0$$

$K\left(\varepsilon_p\right) = K^0$ if $\varepsilon^p \leq 0$

κ and γ are parameters that will be fitted on experimental tests.

Diffusion in liquid phase obeys to Fick's law:

$$\frac{F_l^{H_2O}}{\rho_l^{H_2O}} + \frac{F_l^{N_2}}{\rho_l^{N_2}} = -D_l \nabla \rho_l^{N_2}$$

where D_l stands for Fick diffusion coefficient in liquid phase. In the sequel, we will express D_l as a linear function of saturation and porosity such that:

$$D_l = S_l.\phi.D_{N2}^w$$

with D_{N2}^w the diffusion coefficient of nitrogen into water.

An important coupling is due to variation of porosity given by a classical Eulerian representation:

$$d\phi = (b - \phi)\left(d\varepsilon_v + \frac{S_g dp_g + S_l dp_l}{K_S}\right)$$

With ε_v is volumic strain and K_S the compressibility of the skeleton.

Nitrogen N_2 obeys to perfect gas law:

$$p_g = p_g^{N_2} = \frac{\rho_g^{N_2}}{} RT$$

Where we introduce $\rho_g^{N_2}$ the gas density, $M_{N_2}^{ol}$ the nitrogen molar mass, R the perfect gas constant and T the temperature. Water is slightly compressible; hence we have the relation:

$$\frac{d\rho_l}{\rho_l} = \frac{dp_l}{K_l}$$

where coefficient K_l denotes water compressibility. Nitrogen dissolution obeys to Henry's law

$$\frac{\rho_l^{H_2}}{M_{N_2}^{ol}} = \frac{p_g^{H_2}}{K_H}$$

where K_H designates Henry's constant.

Liquid pressure $p_l = p_l^{H_2O} + p_l^{H_2}$ and gas pressure $p_g = p_g^{H_2}$ are related by capillary pressure $p_c = p_g - p_l$. p_c is related to water saturation S_l by Van-Genuchten relation. We use a classical Van-Genuchten relationship including entry pressure such as:

$$S_e = \frac{1}{\left(1 + \left(\frac{Pc-Pe}{p_r}\right)^n\right)^m}, \ if \ S_e \leq 1 - \varepsilon$$

$$S_e = \frac{S_l - S_{lr}}{1 - S_{lr}} \quad , \quad m = 1 - 1/n \text{ and } \alpha = 1/P_r$$

where S_{lr} the residual saturation, S_e the effective saturation, p_r an n Van-Genuchten parameters such as: $m = 1 - 1/n$. ε is a numerical parameter that is taken equal to 0,001.

When $S_e = 1 - \epsilon$, the forgoing relation is completed by an hyperbolic function in order that S tends to 1 when Pc tends to $-\infty$:

$$S_e = 1 - \frac{a}{b - Pc'}$$

The numbers a and b are computed so that the function remains C1 when $S_e = 1 - \varepsilon$.

It means that when capillary pressure is negative (or lower than an entry pressure if there is one), capillary pressure corresponds to the opposite of liquid pressure (ignoring a small solved hydrogen pressure, see section 1.3.1).

According to Mualem Van-Genuchten model, relative permeabilities are the following:

$$k_r^l(S_l) = \sqrt{S_e}\left(1 - \left(1 - {S_e}^{1/m}\right)^m\right)^2$$

$$k_r^g(S_l) = \sqrt{1 - S_e}\left(1 - {S_e}^{\frac{1}{m}}\right)^{2m}$$

In the following table, we indicate the parameters that are used for all simulations. Specific parameters (used for sensitive analysis or depending on the modeling test) will be indicated in the appropriated section.

Table 2.34: Parameters used for the simulations

$M^{ol}_{N_2}$ (kg.m^{-3})	0,028
Nitrogen diffusion in water D^{w}_{N2}(m^2.s^{-1})	2.10^{-9}
Liquid Viscosity μ_l (Pa.s)	10^{-3}
Gas Viscosity μ_g (Pa.s)	1,7 10^{-5}
Initial liquid density ρ_l (kg/ m^3)	1000
Inverse of liquid compressibility $1/K_l$ (Pa)	5 10^{-10}
Biot coefficient	0,9
Henry coefficient (Pa.m^3.mol^{-1})	126847

2.7.3. Numerical model

2.7.3.1. Software and general descriptions

For all simulations made by EDF in this task, Code_Aster is used. Code_Aster is an open source software (www.code_aster.org) developed mainly by the mechanical analysis department (ERMES, ElectRo – MEchanics Studies) of EDF's research and development. **Code_Aster** is a solver, based on the theory of the mechanics of the continuous media, which uses the method of the finite elements to solve different types of mechanical, thermal, acoustic, seismic, etc. problems. It is a general software used for simulations in mechanics and calculation of structures. Besides the standard functions of classical simulation softwares in thermomechanics, Code_Aster considers many laws of behavior, finite elements, types of loadings. Its modelling, algorithms and solvers are constantly under enhanced to improve and complete them (1,200,000 lines of code, 200 operators function). The Code_Aster quality criteria, which are governing the development and distribution of the code, are based on a regularly audited quality framework of reference meeting the requirements set by the French Nuclear Structures Safety Authority. These criteria constitute the Code_Aster Software Quality Plan and are defined in the code Administration Manual. Moreover, the theoretical foundations of Code_Aster models are documented in the Reference Manuals. A porous media modulus dedicated to thermo-hydro-mechanical modelling has been developed for over 25 years including formulation in total/effective stresses, constitutive laws in kit form. The model described in the previous section is included in this modulus and is fully detailed in[9].

As temperature is considered constant in this work (see previous section), we use the "HHM" model corresponding to two-phase flow coupled with mechanic. The treatment of gas appearance is included in the choice of principal numerical unknowns: $\left(p_c, \chi_l^{N_2}\right)$with:

$$\chi_l^{N_2} = \frac{K_H \rho_l^{N_2}}{M^{ol}_{N_2}}$$

Thanks to Henry's law, $\chi_l^{N_2} = p_g$ for an under-saturated media. For a saturated one, $\chi_l^{N_2}$ is a function of nitrogen concentration in liquid, and capillary pressure correspond to $P_c = \chi_l^{N_2} - P_l$.

For the HHM model, the main unknowns (degrees of freedom) are:

- Displacements (dx, dy,dz)

[9]https://code-aster.org/V2/doc/default/en/man_r/r7/r7.01.11.pdf

- Capillary pressure p_c
- "Gas pressure" $\chi_l^{N_2}$

The problem is solved with finite elements with linear interpolation functions for pressures and bilinear interpolation functions for displacements. To ensure maximum principle and prevent oscillations in case of an hydraulic shock, we use a method of "selective" mass matrix lumping. The selective method consists in separating integration points: on the vertex for the transient terms (lumping) and on the Gauss point for diffusion terms to avoid deteriorated results for those terms.

Time discretization is fully implicit and a non-linear system is solved, by a classical Newton method.

Due to the softening character of rock, regularization techniques are required in order to avoid mesh dependency. For that an improved model based on volumetric second gradient deformation is used (Fernandes et al., 2008; Cuvilliez et al., 2017).

2.7.3.2. Geometry

Experimental test made by GeoRessource are fully described in the MS229 report. We just recall that the hydro-mechanical experiments are performed on cylindrical samples in a triaxial compression cell with measurement of gas permeability. The samples have more or less a diameter of 20 mm and are 40 mm high.

Given the numerous unknowns concerning the triaxial cell (especially the different volumes of the cell apparatus) and for reasons of simplification, only the sample is modelled here. Despite a simple axisymetric geometry is sufficient to represent the geometry, a 3D model representing half the sample is used in order to apply the second gradient model. Indeed, it is considered that localization shear bands have no real meaning in 2D and the model exists only in 3D for the moment.

The mesh is composed of 25788 tetrahedrons and 5526 triangles and is represented Figure 2.150.

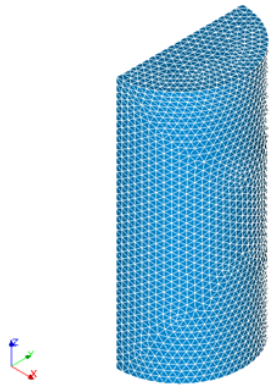

Figure 2.150: Mesh of the sample modelled in Code_Aster

2.7.3.3. Initial conditions and boundary conditions for the test performed on sample EST-66423-6

This test is composed of 3 steps: the sample is first resaturated, injecting water on both sides of the sample with a pressure of 1 MPa under confining conditions of 12 MPa. Then, the breakthrough pressure is sought with several steps of gas injection of 1 MPa until reaching this beakthrough. Last, the "real test"

– and final step - begins: a deviatoric confinement is applied on the sample and at the same time a gas pressure is applied.

For this test, gas breakthrough is obtained with gas pressure Pg = 8MPa. For the triaxial test a bigger pressure is applied: 9 MPa.

Due to the complexity of the different steps, only the final step (deviatoric stress) will be modelled here. Nevertheless, a preliminary step of 1h is modelled in order to represent a first gas transfer after the resaturation step and facilitate the convergence. This time of 1h is arbitrary and we confirmed that it doesn't have influence on the following.

Step 0 (-1h -> 0)

We consider that the sample is initially saturated with a liquid pressure equal to 1MPa (due to the previous step). With the model unknowns (Pc, Pg = $\chi_l^{N_2}$) it is equivalent to consider a very small initial "gas" pressure corresponding to solved Nitrogen and a capillary pressure corresponding to the opposite of liquid pressure (see 1.3.1). A gas pressure of 9 MPa is imposed at the bottom of the sample while an atmospheric pressure is applied at the top. Nothing is applied for the capillary pressure which corresponds to a liquid flow equal to zero. This boundary condition (which will also be applied in the next step) could be questionable but seems to be the more relevant in this case. Indeed, imposing a capillary pressure would be equivalent to imposing a saturation which is not consistent with the test. An isotropic confinement of 12 MPa is first applied. This boundary and initial conditions are summarized Figure 2.151.

We also consider that porosity is little affected by the confinement and the resaturation step and is taken equal to 0.2.

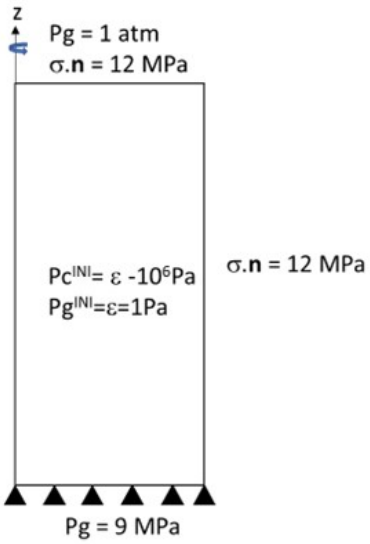

Figure 2.151: Initial and Boundary conditions applied to the sample for step 0

Step 1 (0 -> 55 000)

In this main phase, a deviatoric loading is applied and the gas pressure is imposed at the bottom of the sample while an atmospheric pressure is applied at the top. As in the previous step (step 0), nothing is applied for the capillary pressure.

The test is controlled by displacement: to increase the deviatoric stress, vertical displacement is increased

with a speed of $40x10^{-6}$ mm/s until a variation of 5 MPa is obtained since the last step. When this increment is reached, a step of 2 hours with constant displacement is applied; then the displacement is increased again with the same conditions until failure of the sample, as shown in Figure 2.152. Boundary conditions are summarized Figure 2.153.

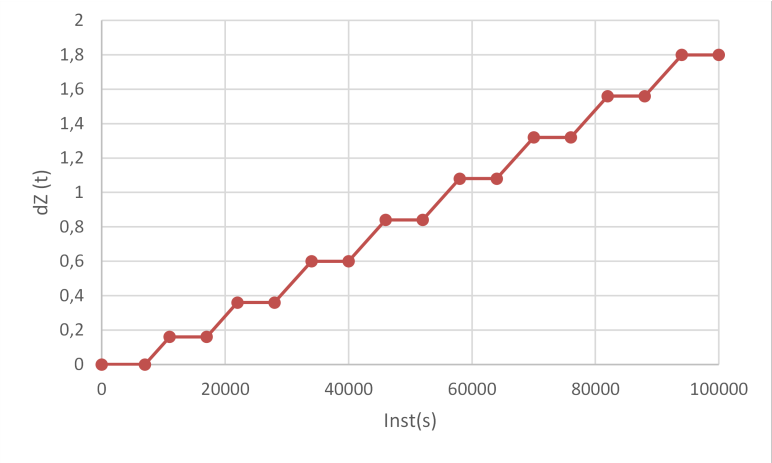

Figure 2.152: Vertical loading applied to the sample (EST-66423-6)

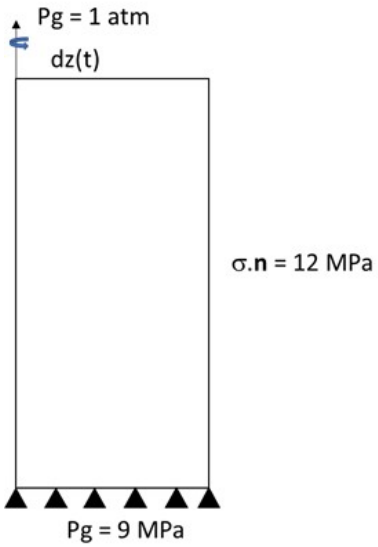

Figure 2.153: Boundary conditions applied to sample for step 1

2.7.3.4. Initial and boundary conditions for the test performed on sample EST-66721 MO1

All the samples which have been primarily resaturated have been highly damaged during this stage (see GeoRessource section in report MS229) which makes the tests difficult to exploit. This includes this present test but also those made in a bell jar without confinement. To counteract this issue, the same tests without resaturation have been performed. Even if the samples are far away from saturated intact COx, it allows to consider an intact rock and to study main tendencies.

Information concerning initial state of this sample has been given by GeoRessource such as:

- Water content in the sample w=6%
- Initial sample porosity $\phi^0 = 0,164$

- Mass of the sample = 29,37 g
- Dry density of the sample ρ_s= 2692,8 kg.m^{-3}

Water content is defined as the ratio between mass of the water in the sample and dry sample, such as:

$$w = \frac{\phi.\rho_l.S_l}{(1-\phi).\rho_s}$$

Applying the previous equation, an initial saturation corresponding to 0,82 is obtained (smaller than 0.9 is very low for COx).

We apply the same steps as in sec. 2.7.3.3 with these new parameters and loadings (Gas pressure of 8 MPa and mechanical loading given Figure 2.155). All these conditions are summarized in Figure 6, Figure 2.155 and Figure 2.156. Capillary pressure is a function of saturation and depends on Van Genuchten parameters that will be given in the section 2.7.4.

Step 0 (-1h -> 0)

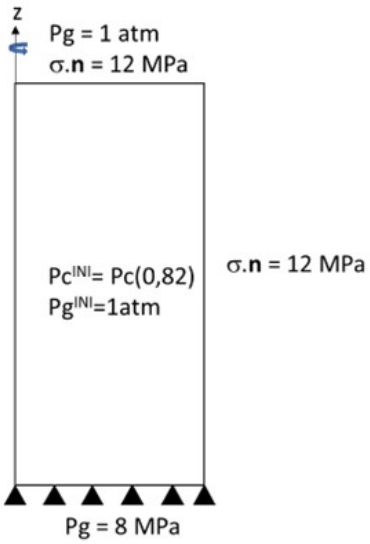

Figure 2.154: Initial and Boundary conditions applied to the sample 66721 for step 0

Step 1 (0 -> 53 000)

2.7.4. Results

2.7.4.1. Modeling of test EST-66423-6

Main experimental results Applying vertical loadings defined in Figure 2.152 on the resaturated sample, the deviatoric stresses, given in Figure 2.157, are obtained (blue curve). We recall that the deviatoric stress is the difference between the vertical total stress and the total lateral stress (i.e. 12 MPa). The injected gas volume is represented in orange.

It is obvious that this deviatoric stresses curve is quite far away from the classical response of intact Callovo-Oxfordian. As shown for example on Figure 2.149, the failure is expected around 37 MPa instead

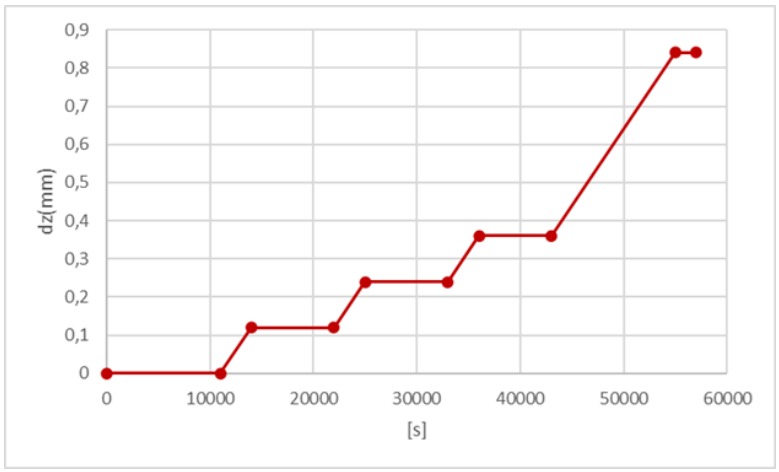

Figure 2.155: Vertical loading for step1 (EST 66721)

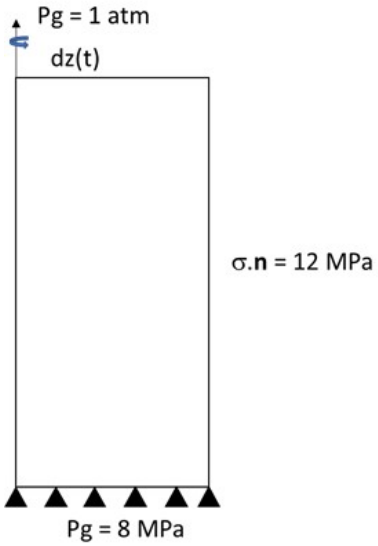

Figure 2.156: Boundary conditions applied to the sample 66721 for step 1

of 20 MPa on the experimental results. This failure is logically accompanied by an abrupt rise of the gas volume which is injected to insure the pressure of 8 MPa in the reservoir. It means that this sample is initially damaged.

Modeling of EST 66423-6 with reference parameters For this computation, all the parameters defined previously are used. Transfer parameters are indicated in Table 2.35. The entry pressure is very small since the sample is damaged. Intrinsic permeability is supposed to be constant. $S(P_c)$ and relative permeabilities corresponding to these parameters are drawn respectively in Figure 2.158 and Figure 2.159.

Table 2.35: Transfer parameters for EST-66423

Parameter	
Intrinsic permeability K (m^2)	5.10^{-21} ($=K^0$)
Gas factor.f_g (-)	1
Van Genuchten « n » (-)	1,7

Table 2.35: Transfer parameters for EST-66423

Parameter	
Van-Genuchten « Pr » (MPa)	17
Gas entry pressure « Pe » (MPa)	1,2
Residual water saturation “Slr” (-)	0

The deviatoric stress evolution is given in Figure 2.164 and compared to experimental results (for detailed experimental results, see corresponding section of Georessource). As expected, the deviatoric stress evolution obtained with reference parameters shows that failure of the sample is obtained around 34 MPa ; a value much higher than the 20 MPa obtained experimentally.

To complete these results, profiles along the sample are plotted for several times on Figure 2.161, Figure 2.162 and Figure 2.163 for gas pressure, liquid saturation and capillary pressure, respectively. Logically the sample will desaturate on the side of injection. After 40 000 s, all the sample is partially desaturated (between 0,94 and 0,99). It is worth noting that the decrease of deviatoric stress we observe on the first step (i.e. before 7000 s) is due to the imposed gas pressure. After an initial state with a liquid pressure of 1MPa (corresponding to a capillary pressure inverse to that value), gas injection creates a gradient of pressure which will generate change in capillary pressure and thus in hydraulic stress $\mathrm{d}\pi$. This will involve a small decrease for vertical total stresses.

To evaluate the part of the damage coming from gas injection, the same modelling as previously detailed is done with a gas pressure of 1 MPa instead of 9 MPa. The comparison of the results of these 2 calculations is shown on Figure 2.164. As expected, the small decrease of deviatoric stress observed before 7000 s disappears (no more important hydraulic stress $\mathrm{d}\pi$, see previously). The failure of the clay is observed at around 37 MPa as expected (see triaxial tests without pressure on Figure 2.149). The gas pressure of 9 MPa (with a Biot coefficient equal to 0.9) has an impact of an order of magnitude of 5 MPa on the deviatoric stress. It is not enough to explain that the experimental failure is observed around 20 MPa.

As observed by the experimental teams, the sample has been highly fractured during the resaturation phase. Consequently, this test is difficult to exploit. Nevertheless, mechanical fitting of this test is proposed in the next section.

Calibration of mechanical parameters In order to fit the mechanical model parameters and confirm the fact that the sample is highly damaged, a sensitive analysis is done, changing first the Young modulus (which is predominant for the first steps of deviatoric stress, when the behaviour remains elastic) and then the mean compressive strength σ_c. Results are showed on Figure 2.165.

The best fitting is observed with E = 1,5 GPa (instead of 6 MPa) and $\sigma_c$between 5 and 6 MPa (instead of 12 MPa). These parameters are far away from the ones of an intact COx. It confirms numerically what is observed experimentally: the sample is highly damaged, probably by saturation stage. To complete these results, isovalues of volumetric and viscoplastic deformations are given on Figure 2.166 for several times. These deformations become larger than zero starting from 22000s, which means the sample begins to plastify. Localization shear bands also appear at this time.

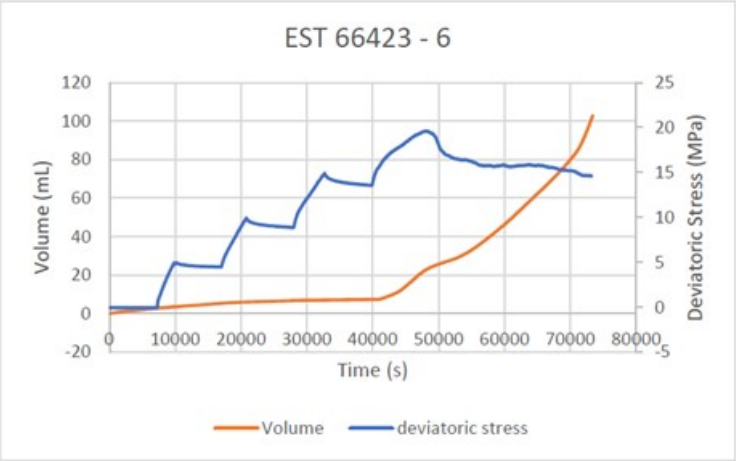

Figure 2.157: Experimental results for EST 66423-6: deviatoric stress and gas volume

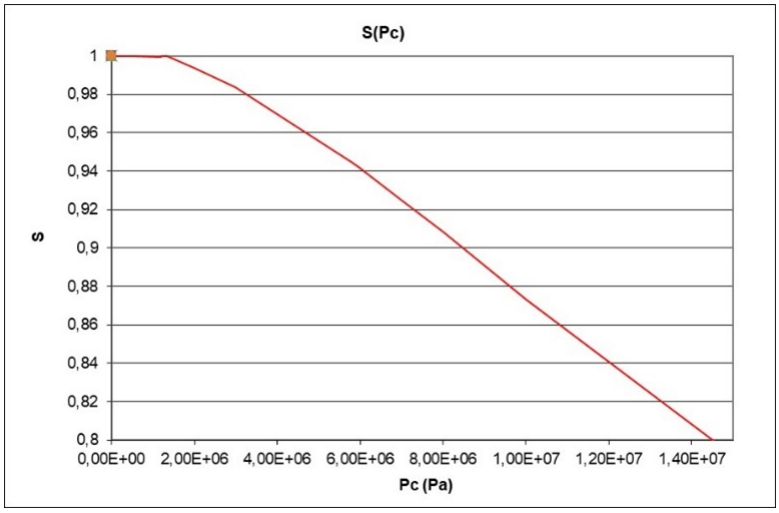

Figure 2.158: S(Pc) with chosen parameters

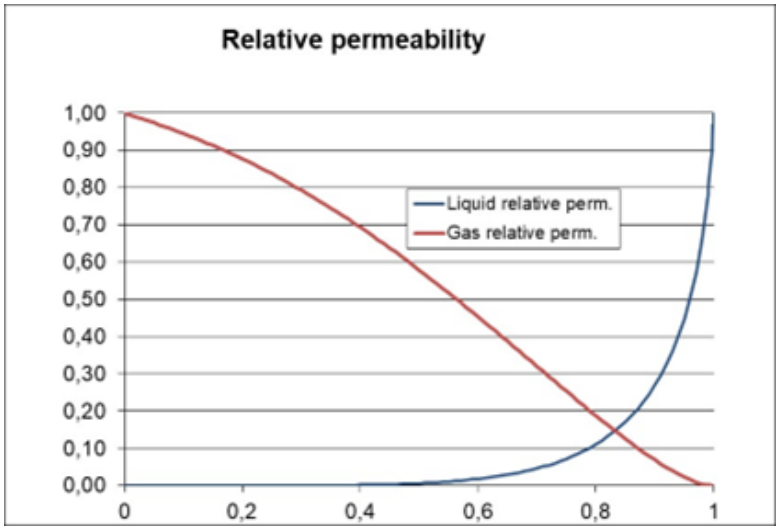

Figure 2.159: Relative permeabilities with chosen parameters

	Plastic volumetric deformation	Viscoplastic volumetric deformation
	Plastic volumetric deformation	Viscoplastic volumetric deformation
17 000 s	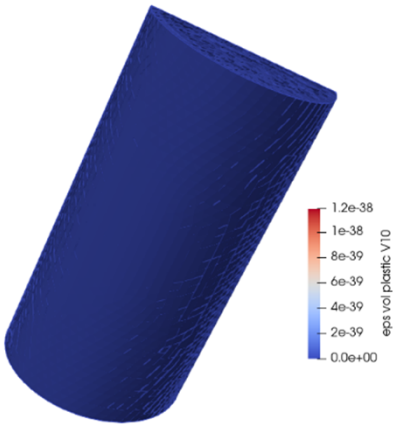	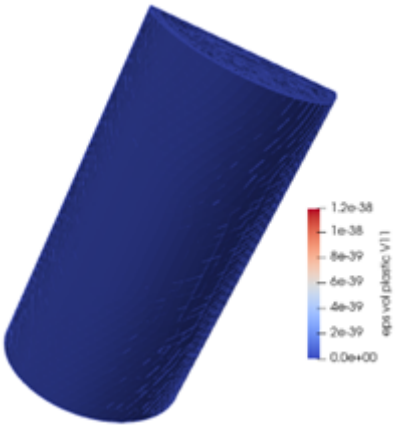
22 000 s	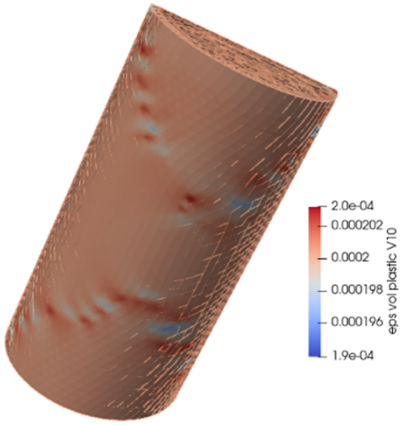	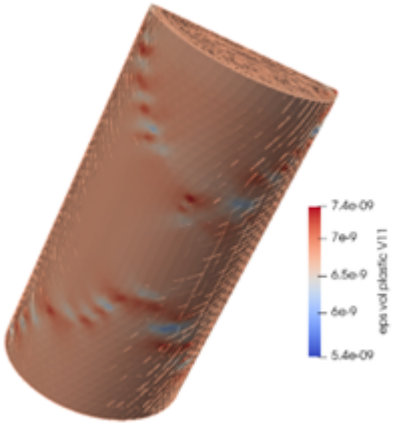
28 000 s	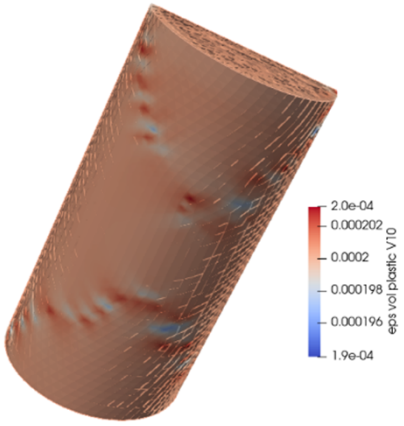	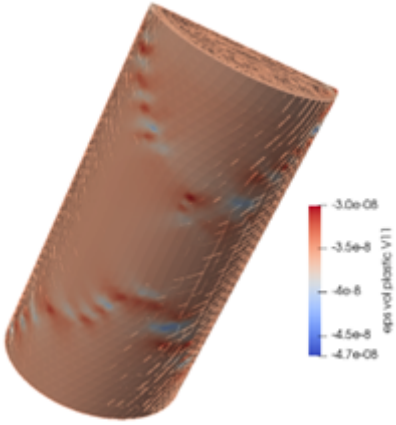

	Plastic volumetric deformation	Viscoplastic volumetric deformation
40 000 s	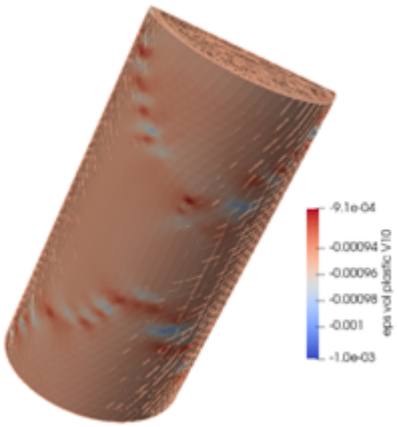	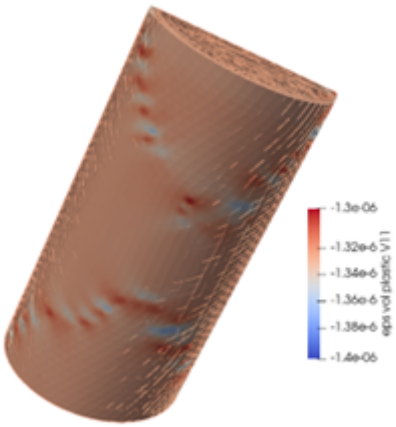

To complete this study, computations - with E = 1,5 GPa and σ_c = 6 MPa - are run again with a sensitivity analysis on 2 points:

- First, the Mualem gas relative permeability is replaced by a cubic law such as $k_r^g(S_l) = (1 - S_l)^3$, we also consider that entry pressure is zero. We call this study VGC (compared to VGM for the previous one).
- The time of step 0 is reduced to 60s (instead of 1h) in order to verify that this time doesn't influence the calculation results.

The results are shown in Figure 2.167 and confirm the weak influence of gas relative permeability and step 0 on mechanical responses.

Conclusion for this test As indicated in the experimental report MS229, sample EST-66423 has been highly damaged, probably during the resaturation stage. This happens to all the samples which have been resaturated before gas injection. Nevertheless, in order to check our methodology, we model this test with the model described in chapter 1.3 of the present document. With the usual parameters used for intact COx, the mechanical response is far away from the experimental results – as expected. Young modulus and compressive strength used in the calculations need to be significantly decreased to reproduce roughly the deviatoric evolution. Consequently, this sample is very different from intact COx and it doesn't make sense to further study this test. Finally, the work has been finally focussed on a test performed on unsaturated sample. This experimental test has been conducted successfully.

2.7.4.2. Modeling of test EST-66721 MO1

Main experimental result We remind the reader that the description of test EST-66721 MO1 // is provided in appropriated section as the previous one.

We focus first on experimental results. The vertical loading applied for this test is given in Figure 2.155. This loading is directly applied on a sample naturally desaturated. The resulting deviatoric stresses are given on Figure 2.168 on the blue curve. The red curve in this figure gives the injected nitrogen volume needed to ensure that gas pressure remains equal to 8 MPa in the reservoir. This experimental result

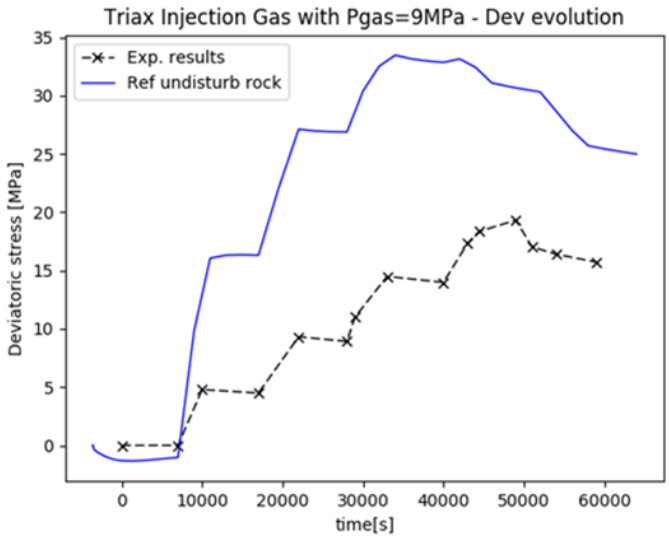

Figure 2.160: Numerical results obtained with reference parameters for EST-66423 and comparison with experimental results

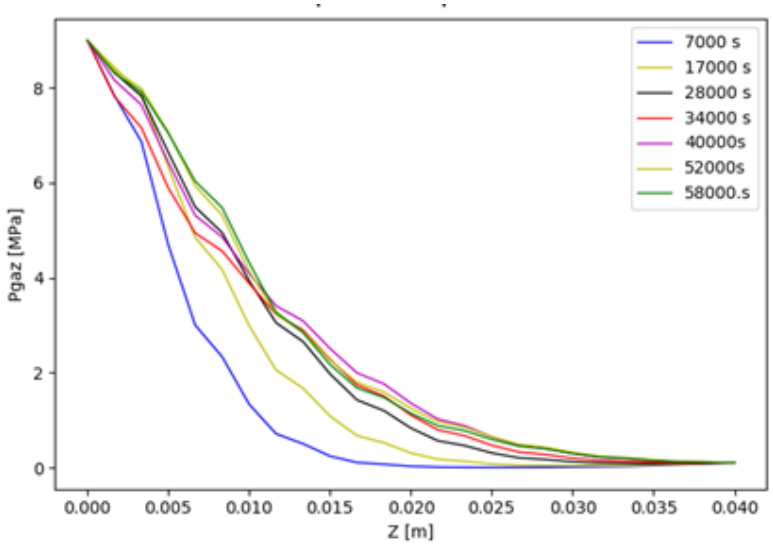

Figure 2.161: Gas profiles at different times obtained with reference parameters

indicates that failure happens before 30 MPa (at around 55 000 s). Increase of the gas volume happens a little bit later. Figure 21 indicates with blue circles the corresponding gas permeability (around 5.10^{-18} m^2 after failure, between 10^{-19} m^2 and 10^{-20} m^2).

This experimental response is not perfectly clear, and it appears that the behaviour is heckled after the 3rd steps (i.e. after 43000 s) and a change of slope in deviatoric stress is observed (actually the curve is “rounded”).

Experimental observations indicate that the sample doesn’t look damaged before the gas injection phase. This behaviour, with a lower peak compared to those observed and measured on intact COx (see Figure 1), is probably due to the partially desaturated state of the sample which is quite important (w = 6%).

In the following we try to reproduce numerically the main tendencies of this experimental test, even if this sample is very different from a saturated one. The goal is also to reproduce the gas injection linked

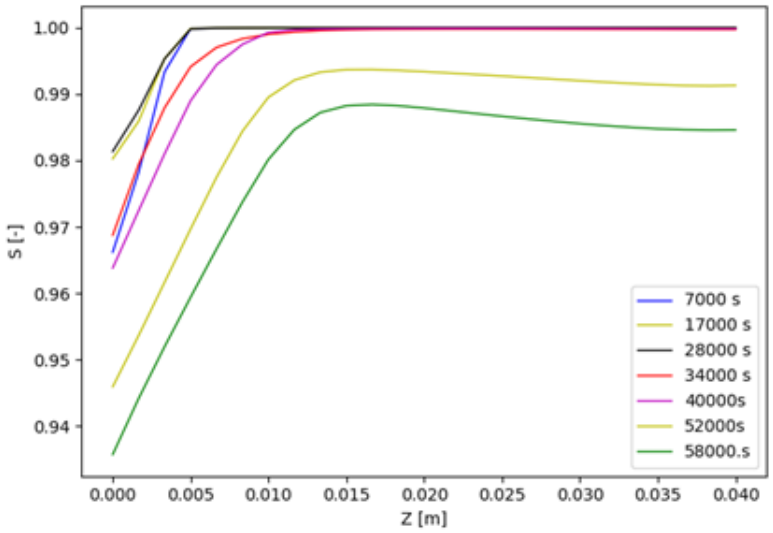

Figure 2.162: Saturation profiles at different times obtained with reference parameters

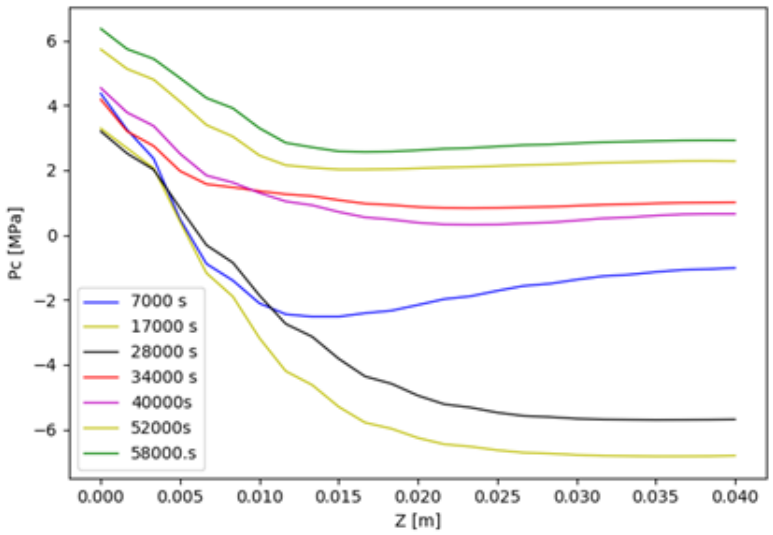

Figure 2.163: Capillary pressure profiles at different times obtained with reference parameters

to permeability evolution. The same methodology as for sample EST-66423 is applied: we first used the reference mechanical parameters defined in Table 2.32 and then try to fit the experimental curves. Sensitivity analyses are then be done on permeability. Finally, the hydraulic response is studied.

Mechanical response with the "reference parameters" model For this computation, all the parameters defined previously are used (see Table 2.32 and Table 2.34). Nevertheless, an intrinsic permeability smaller than previously is used for numerical reasons. A sensitivity study is therefore done in the following. Since the initial saturation is equal to 0.82, the initial corresponding capillary pressure is equal to 13 MPa.

Table 2.37: Transfer parameters for EST-66721

Parameter	
Intrinsic permeability K (m^2)	10^{-21} (cte= K^0)
Gas factor.f_g (-)	1

Table 2.37: Transfer parameters for EST-66721

Parameter	
Van Genuchten « n » (-)	1,7
Van-Genuchten « Pr » (MPa)	17
Gas entry pressure « Pe » (MPa)	1,2
Residual water saturation “Slr” (-)	0

Deviatoric stress evolution is given Figure 2.170 and compared to experimental results. The red line corresponds to the reference test (initial saturation equal to 0.82 and permeability of $10^{-21}m^2$).

As expected, deviatoric stresses obtained by calculation with reference parameters are much higher than for experimental results. This is due to the fact that the sample is highly desaturated and very different from the saturated one (as for the tests detailed in Figure 2.149). For this computation, convergence is not possible after t= 45000s and the slope becomes already very steep after 43000 s which indicates numerical problems around the time of failure appearance.

We add on this figure in sky blue color results for the same computation with an intrinsic permeability K^0 equal to $10^{-20}m^2$ instead of $10^{-21}m^2$. The impact of this modification impact is quite small (around 1 MPa). For this permeability, convergence is not possible after 43000 s. We add also a dark blue curve corresponding to the same test with an initial saturation equal to 0.9 which seems physically more reasonable than 0.82. The impact is also quite small.

Calibration of mechanical parameters As previously detailed, mechanical parameters (Young modulus and mean compressive strength σ_c) are recalibrated in order to fit the mechanical response. Results are showed on Figure 2.171.

The best fitting is obtained with E = 2 GPa (instead of 6 MPa) and σ_c= 6 MPa (instead of 12 MPa). **These parameters will be kept for all following computations.** Corresponding volumetric plastic and viscoelastic deformation are shown for several times in Figure 2.172. Plastic and viscoelastic deformation appears between 22000 and 25000 s and their value increases until 43000 s. Localization bands appear clearly. Before 22 000 s, the material remains elastic. At 45000s, deformations become negative which is not a physical result anymore (model seems out of convergence).

	Plastic volumetric deformation	Viscoplastic volumetric deformation
22 000 s	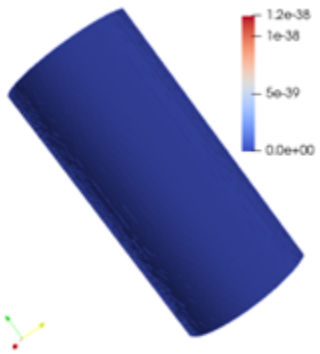	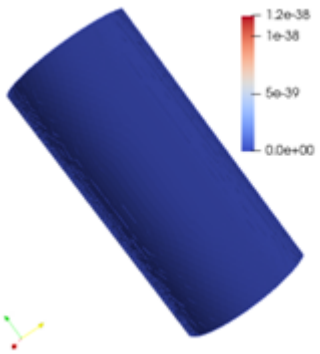

	Plastic volumetric deformation	Viscoplastic volumetric deformation
25 000 s	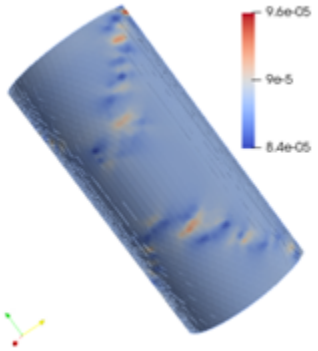	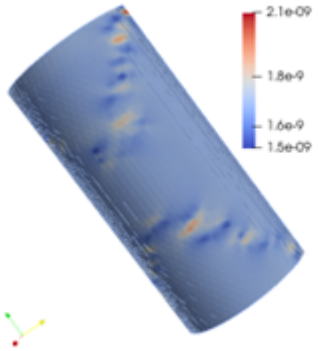
36 000 s	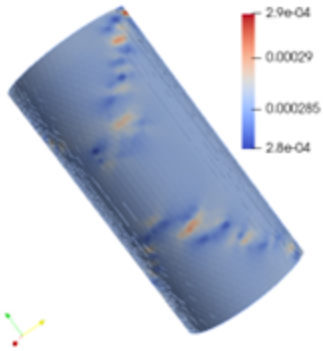	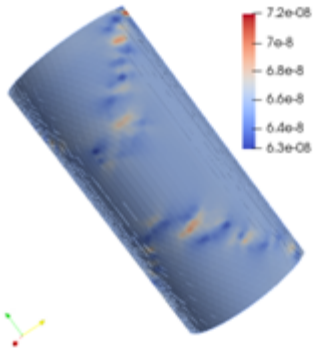
43 000 s	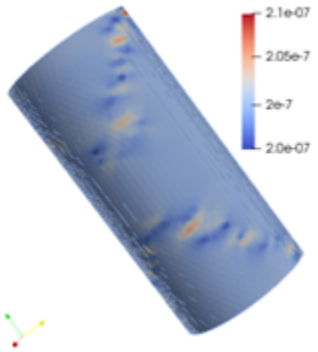	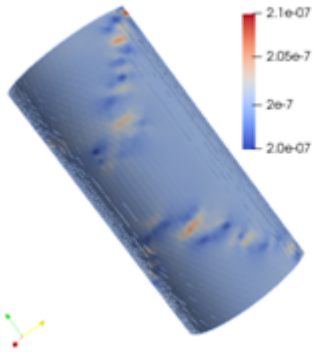
45 000 s	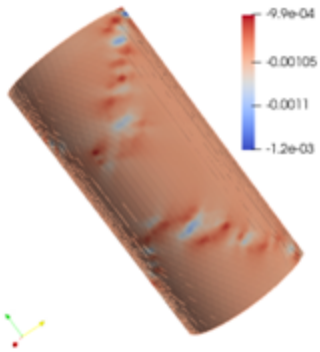	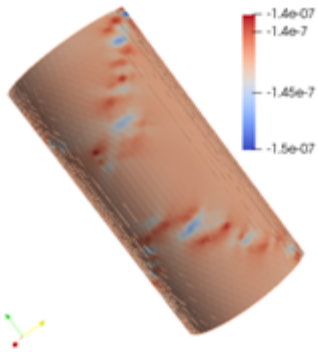

Finally, the impact of gas pressure injection is highlighted on Figure 2.173, comparing the previous results

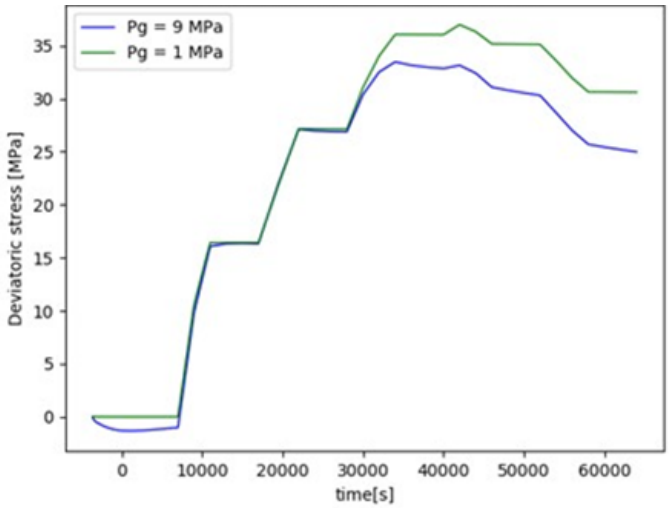

Figure 2.164: Numerical results obtained with reference parameters: impact of injected gas

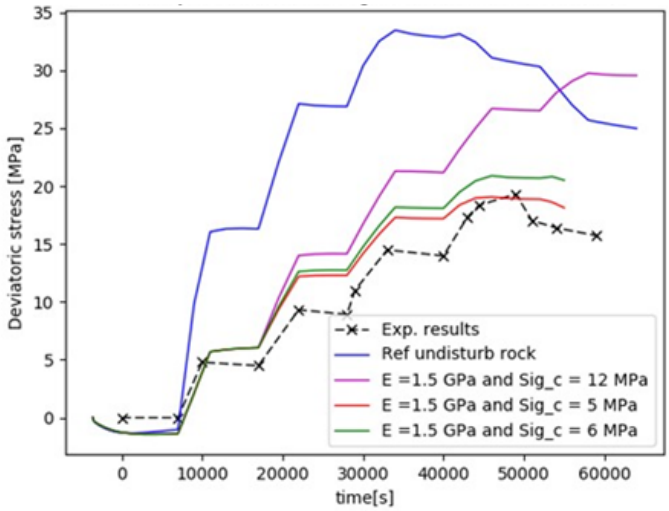

Figure 2.165: Calibration of the mechanical calculations results for EST-66323

Figure 2.166: Isovalue of volumetric deformation (for E = 1,5 GPa and σ_c = 6 MPa)

(in red) with the results of a modelling with a gas injected at a pressure of 0,1 MPa (green). These stresses with a small pressure of injected gas are logically higher than those obtained with 8 MPa.

Impact of permeability on mechanical response of the sample Using the mechanical parameters fixed in the previous section (E = 2. GPa and σ_c= 6 MPa), impact of permeability is studied in this section. The impact of f_g previously equal to 1 is studied but also the relationship $K\left(\varepsilon_p\right) = K^0.\left(1 + \kappa \left\langle \varepsilon^p \right\rangle^\gamma\right)$ if $\varepsilon^p > 0$ as indicated in section 1.2.3.

4 cases are studied:

- Case 1: $K^0 = 10^{-21}$ m^2; κ =0; f_g = 1 (“new” reference case)
- Case 2: $K^0 = 10^{-21}$ m^2; $\kappa = 10^{12}$; f_g = 1

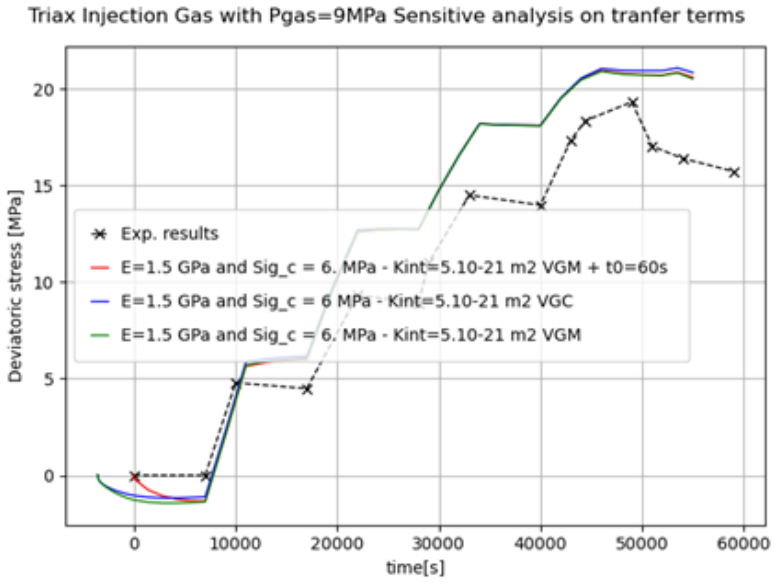

Figure 2.167: Sensitivity analysis on deviatoric stress

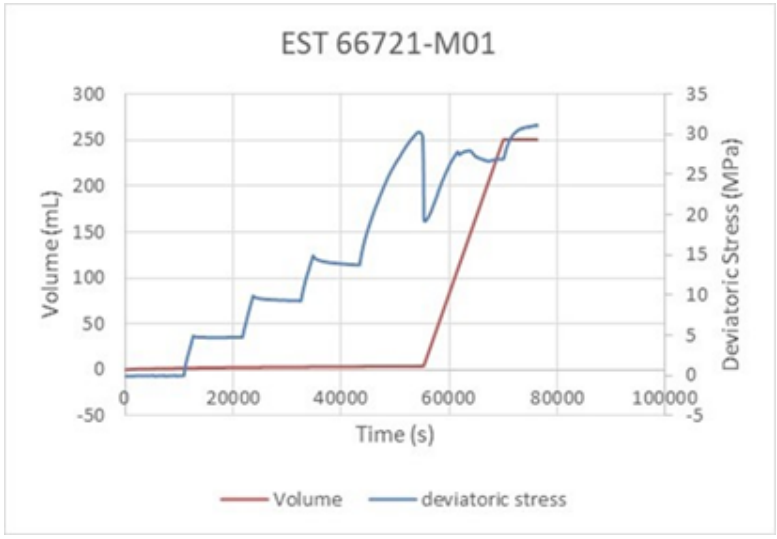

Figure 2.168: Experimental results for EST 66721 MO1: deviatoric stress and gas volume

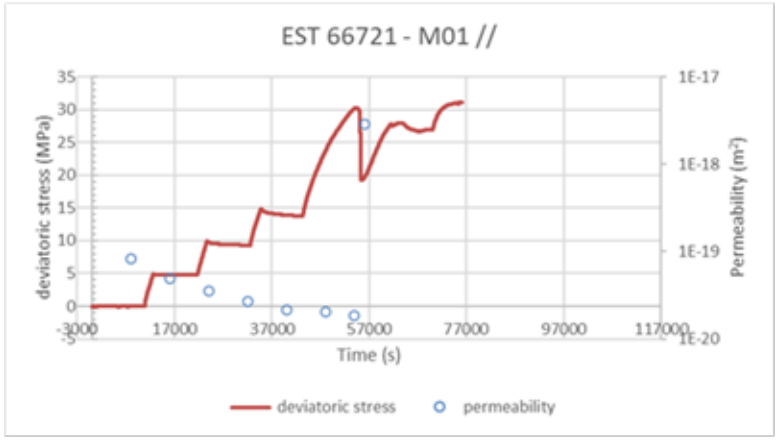

Figure 2.169: Experimental results for EST 66721 MO1: deviatoric stress and gas permeability

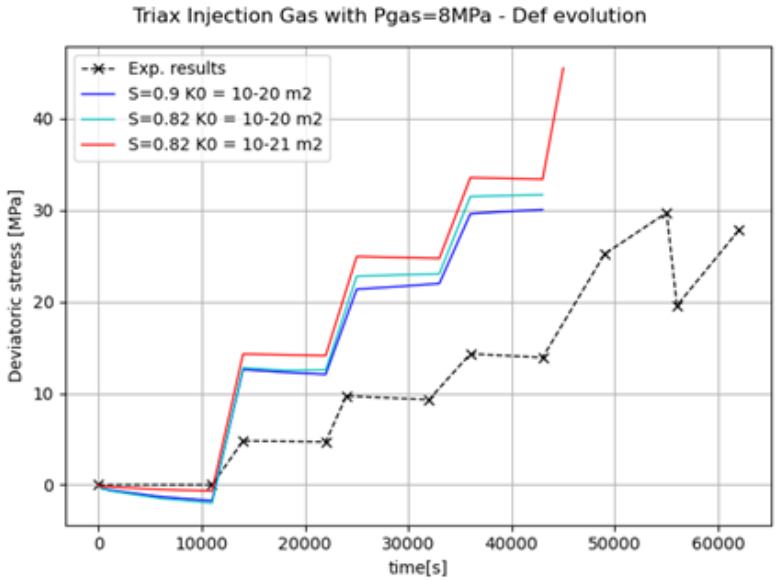

Figure 2.170: Numerical results obtained with different initial saturations and intrinsic permeability ; comparison with experimental results obtained on for sample EST-66721

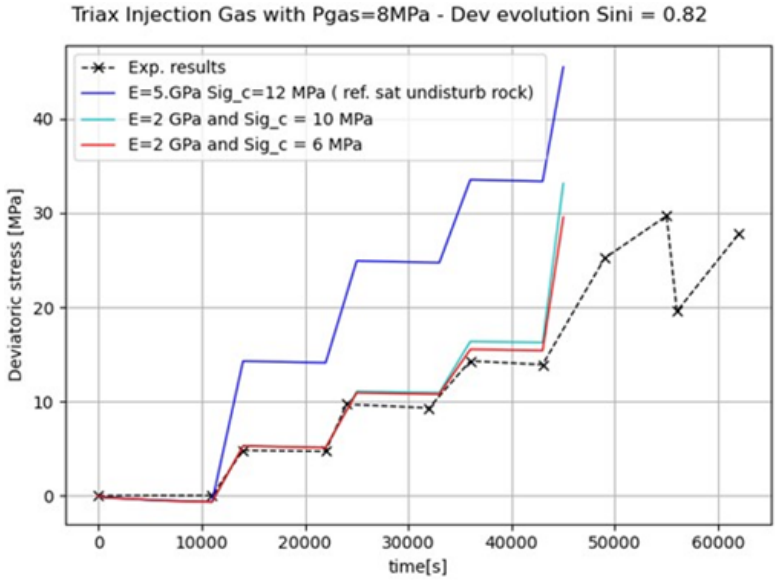

Figure 2.171: Calibration of the mechanical results for EST-66721

Figure 2.172: Isovalues of volumetric deformation for EST-66721 (E = 2 GPa and σ_c = 6 MPa)

- Case 3: $K^0 = 10^{-21}$ m^2; $\kappa = 10^{12}$; $f_g = 100$
- Case 4: $K^0 = 5.10^{-21}$ m^2; $\kappa = 10^{12}$; $f_g = 100$

For all cases $\gamma = 3$.

Corresponding results are shown in Figure 2.174. Logically case 1 and 2 give the same results when the material remains plastic (after 22000 s given Figure 2.172), and only a weak difference appears after 35 000s. Impact is minor on mechanical results. Regarding Case 3 and 4 (which are very close to one another), a significant impact appears at the beginning of the simulation. Speed up of gas transfer due to

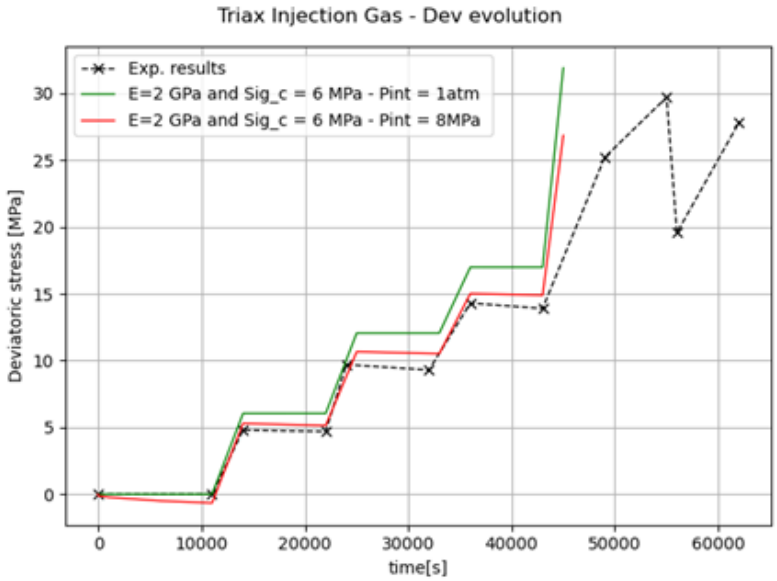

Figure 2.173: Impact of pressure injection on deviatoric stress

higher permeability has an impact and is probably due to hydraulic stress $d\pi$ provided by capillary and gas pressures. This will involve a small decrease for vertical total stress (as seen in 1.4.1.2). After this period, results become progressively similar.

Globally, permeability has only a minor impact on the mechanical response.

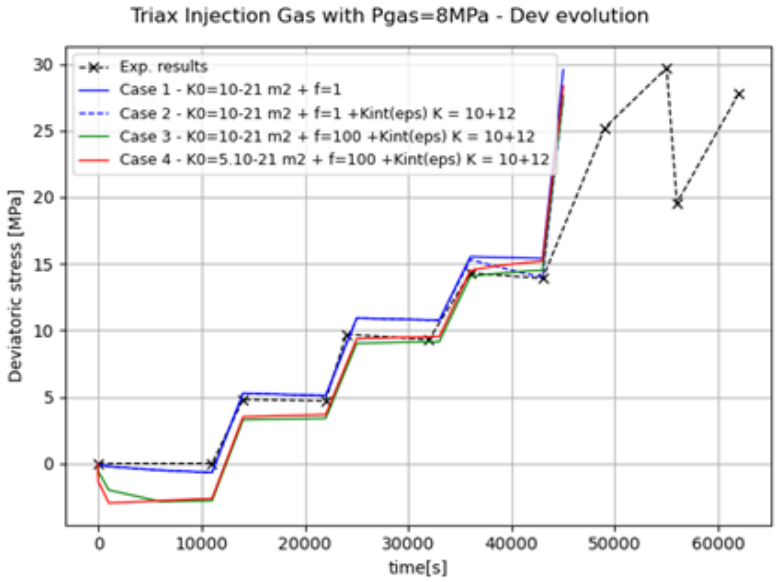

Figure 2.174: Impact of permeability

Hydraulic results analysis As explained at the beginning of this chapter, one of the objectives of this work is to reproduce the permeability evolution with cracking. To do that, the proposal is to model the volume of injected nitrogen which is necessary to maintain a pressure of 8 MPa at the bottom of the sample (see red curve on Figure 2.168).

Considering Dirichlet boundary conditions of the model (see Figure 2.156) we propose to post-treat the Nitrogen flow $F_l^{N_2} + F_g^{N_2}$ (kg.m^{-2}.s^{-1}) obtained by simulation at the bottom of the sample and to integrate

this flow in time in order to obtain the volume such as:

$$V(t) = \int_0^t \frac{S}{\rho_{N_2}} \left(F_l^{N_2} + F_g^{N_2} \right) dt$$

With V(t) the Volume of injected Nitrogen, S the surface of the bottom of the sample (i.e. 3,1 10^{-4} m^2) and ρ_{N_2} the Nitrogen density which is computed by ideal gas law for a pressure of 8 MPa (pressure imposed in the reservoir of injection) such as:

$\rho_{N_2} = \frac{p_g}{RT} M_{N_2}^{ol} = 92$ kg.m^{-3}

Considering the same 4 cases than those in Figure 2.174, volume evolution V(t) is presented in Figure 2.175. Figure 2.176 shows the corresponding "intrinsic gas permeabilities" which correspond to $f_g.K.\left(1 + \kappa \left\langle \varepsilon^p \right\rangle^\gamma\right)$. Given that gas permeability should also include relative permeability (see Figure 2.182 or Figure 2.183), this value is shown Figure 2.177.

With $f_g = 1$; gas volume is logically much smaller than for $f_g = 100$. Necessity to take $f_g = 100$ is physically more realistic and is a well-known result. Regarding Case 3 and Case 4, gas volume increases progressively until t $\approx$ 33 000 s and, after a change of slope, increases abruptly. This corresponds to a failure. Actually, this evolution represents the permeability evolution, itself linked to plastic deformation trends. As seen in Figure 2.172, plastic deformation becomes negative after 4300 s which is probably not physical. At this state, the model restores the permeability to its initial value. Nevertheless, this last step should not be considered. Considering experimental results shown in Figure 2.168, the change of slop happens later after the probable failure (observed around 55 MPa) which is difficult to explain. Nevertheless main tendencies of the test are well reproduced by the model.

To complete these results and to focus on gas transfer inside the sample, we compile profiles along the sample for different variables. Figure 2.178 and Figure 2.179 show respectively gas pressure profiles at several times for case 2 and 3 (which differ by the value of f_g.). It is coherent that for $f_g = 1$, permanent state is not reached. For $f_g = 100$, gas pressure is quickly stabilized, which confirms that $f_g = 100$ must be retained. Figure 2.180 and Figure 2.181 shows liquid saturation profiles for these same times and cases. Finally, Figure 2.182 and Figure 2.183 show gas relative permeabilities which are a decreasing function of the saturation. Saturation profiles are consistent with gas pressure: for $f_g = 1$, saturations are not stabilized whereas in the case of $f_g = 100$ there are constant along the sample as expect at the top of the sample where an effect of boundary condition is observed (only gas can escape, and water is "concentrated" in this part). Nevertheless, and whatever the case, saturation remains between 0,82 and 0,88 (it is recalled that initial saturation is equal to 0,82). This case is physically very different from the saturated one: indeed, for a sample initially saturated, the Nitrogen moves essentially by diffusion in the sample (it is essentially dissolved in the liquid) and saturation remains close to 1 (see Figure 2.162). To the contrary, for this case, gas is expressed and advective transport is important (saturation far away from 1 and gas relative permeabilities much higher than 0).

In order to reproduce by calculation the same order of magnitude for the volume than in experimental results, an additional study is done on **parameter** κ. For subsequent computations, all parameters are the same: E **= 2. GPa and** σ_c**= 6 MPa** f_g **= 100;** K^0**=** 10^{-21} m^2

Volume and permeabilities are presented respectively Figure 2.184 and Figure 2.185. It is obvious that playing with this parameter allows to capture the same order of magnitude as the one of experimental volume evolution (increase about 250 mL). Looking at volume evolution, κ between 10^{13} and 5.10^{13} seems reasonable, corresponding to a permeability $f_g.K.\left(1 + \kappa \left\langle \varepsilon^p \right\rangle^\gamma\right)$. between 2.10^{-17} and 10^{-16}m^2. Taking into

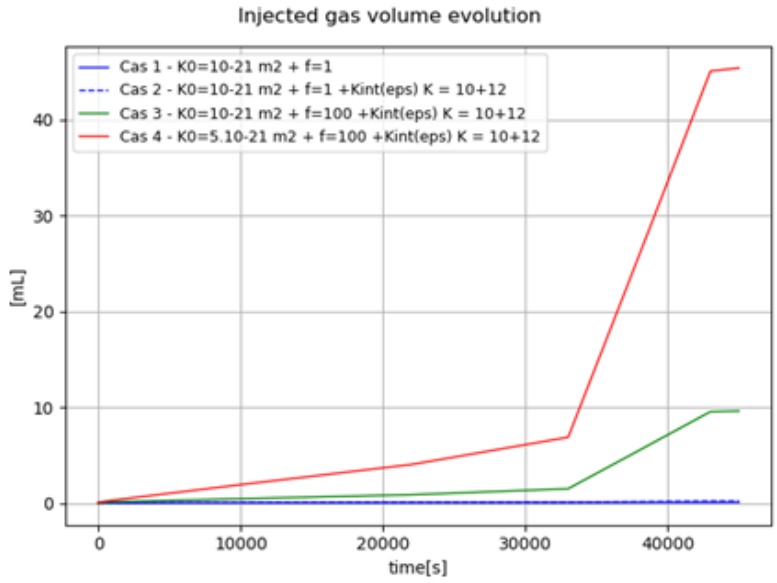

Figure 2.175: Nitrogen volume evolution

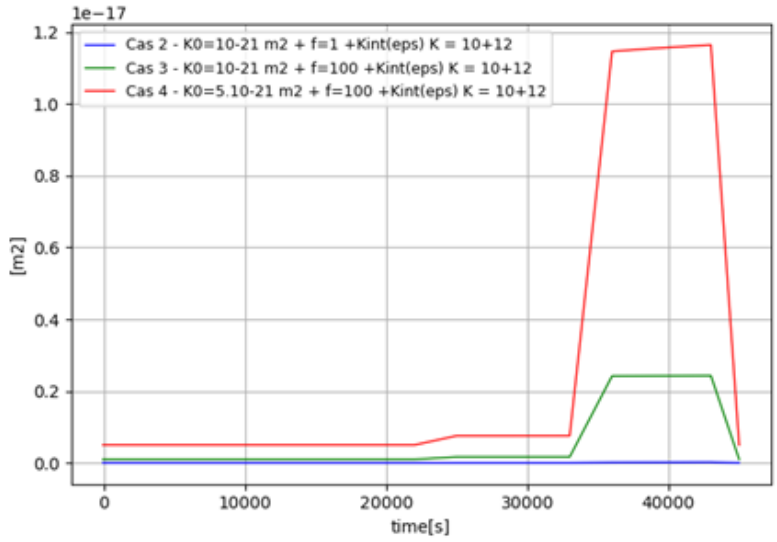

Figure 2.176: Intrinsic Gas Permeability evolution

account relative permeability, Figure 2.186 shows that gas permeability is between 2.10^{-18} and $10^{-17}m^2$ which is consistent with the experimental measurement (around 5.10^{-18} m^2, see Figure 2.169). It is worth noting that the order of magnitude of κ is consistent with (Mahjoub 2018) which is an interesting result.

Nevertheless, these results should be treated with caution: a lot of other parameters could be influent (initial permeability for example but also Van Genuchten parameters) and it seems difficult to use this method as a predictive one. Moreover, the experimental result is ambiguous: it is difficult to understand the “post peak” behaviour and when failure exactly appears. More experimental tests are necessary on sample with the same orientation to confirm this approach.

More than access to quantitative data, the important result of this work is the ability to capture main tendencies.

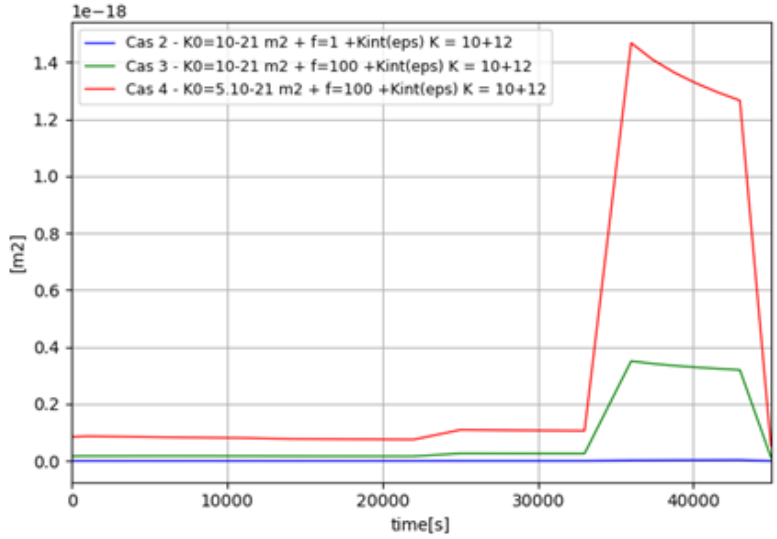

Figure 2.177: Gas Permeability evolution

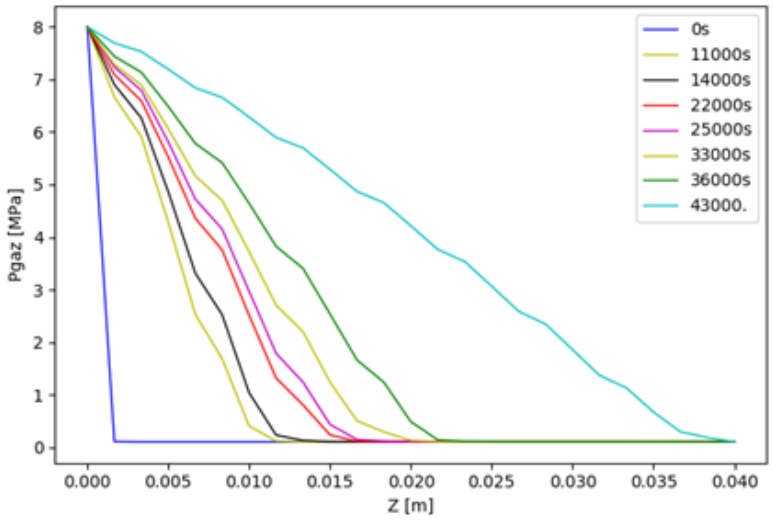

Figure 2.178: Gas pressure profile (case 2 – fg = 1)

2.7.5. Summary

The initial proposal of EDF for task 3.3 was to simulate experimental tests of gas injection on Callovo-Oxfordian samples, with a hydro-mechanical model implemented in Code_Aster. The goal was to analyse gas propagation and its interaction with cracking. The initial idea was to model on one hand mechanical damage provided by gas injection (with experimental tests realized in task 2.2) and on the other hand gas injection with damage provided by a mechanical loading (with experimental tests performed by Georessource in task 3.1). However, due to delays and difficulties in experimental tests; only the second part of the work has been performed.

The work performed by EDF for task 3.3 therefore covers the modeling of experimental tests provided by GeoRessource (CNRS-U. Lorraine) on initially intact COx samples. These tests, done within sub-task 3.1 (see corresponding section) are triaxial compression tests under confining pressure with gas injection and measurement of permeability. The aim of these experiments is to study the impact of damage-induced cracks on gas transfer within clay host rocks. Aim of EDF's work is first to properly model the induced damage of COx at the same time at which gas injection takes place and then, when relevant, to study the

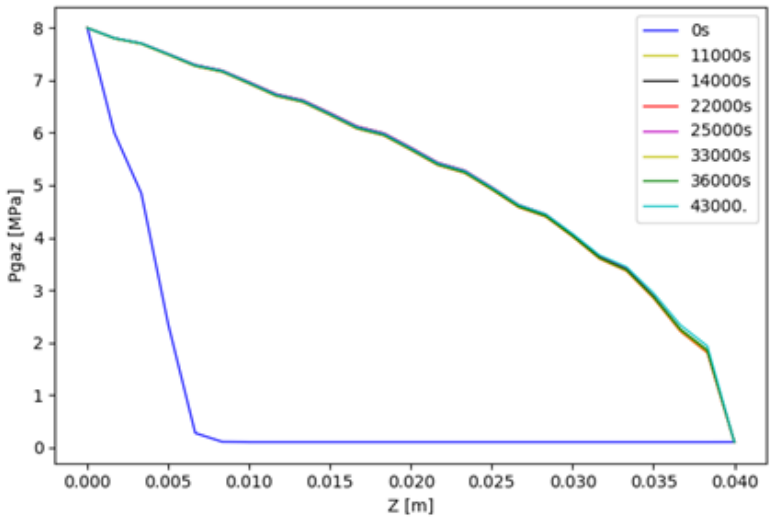

Figure 2.179: Gas pressure profile (case 3 – fg = 100)

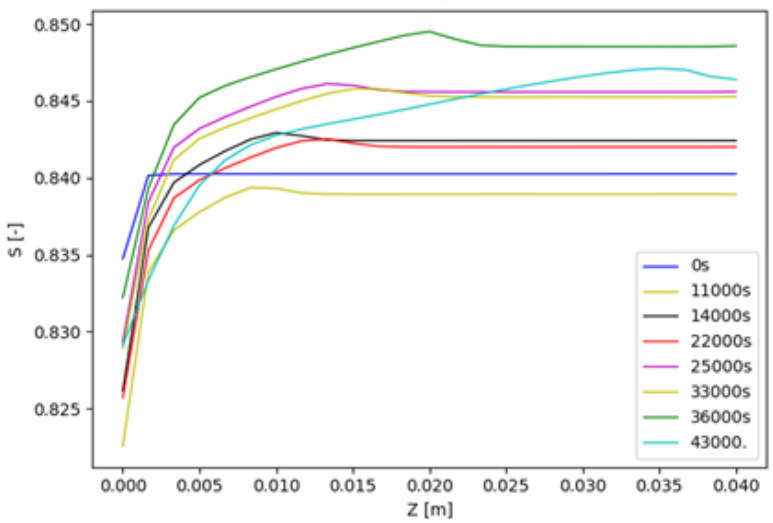

Figure 2.180: Saturation profile (case 2 – fg = 1)

evolution of permeability ie the link between gas injection and damage or deformation.

Several experimental tests have been performed with both orientations (parallel and perpendicular to bedding). As described in the experimental part of this report, different techniques have been tested to resaturate the sample (with or without confinement, with liquid injection or in a bell jar at imposed hygrometry) but all of them have produced important damage. For these reasons, tests without resaturation have also been provided, even if this material is far away from the saturated state. This test provides more consistent results because samples are initially intact.

In the end, 2 tests are modelized: the first one on a saturated sample (test EST-66423) despite this test being highly damaged and another one for unsaturated one (test EST-66721). Even if the tests are notrepresentative of the in-situ COx, these computations allow to develop a methodology of computation and to better understand coupling processes.

For both cases and for time reasons, only samples parallel to bedding were modeled.

To model these experiments, a continuous macroscopic hydro-mechanical model is used. This model

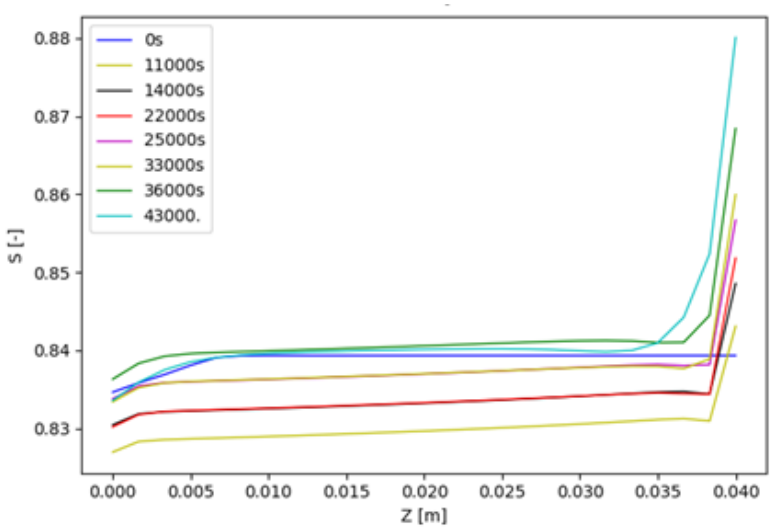

Figure 2.181: Saturation profile (case 3 – fg = 100)

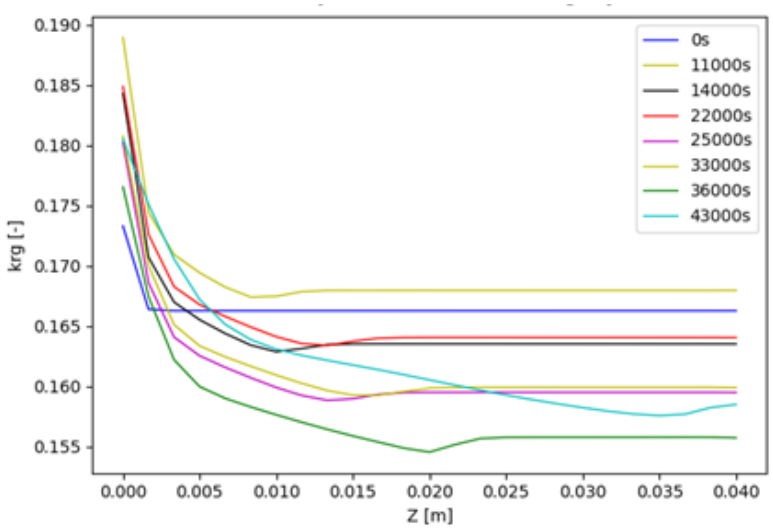

Figure 2.182: Gas relative permeability profile (case 2 – fg = 1)

is based on a classical fully coupled hydro-mechanical model developed in EDF's software Code_Aster. It includes a classical two-phase flow model considering diffusion/advection phenomena. This model is coupled to a mechanical viscoplastic constitutive law called 'LKR model'. This law has been fitted on previous tests done on intact COx for several confinement pressures. To avoid localization phenomena due to softening and mesh dependencies, a regularization technique based on a volumetric second gradient deformation is used. In Code_Aster, this approach requires a 3D model. For this reason, a 3D mesh is used to model half of the sample. Finally, to study the evolution of permeability, a relationship between permeability and plastic deformation has been developed and fitted for test EST-66721.

It is worth noting that coupling a two-phase flow model with a complex viscoplastic law is complex from a numerical point of view and is rare, to the best of our knowledge. Indeed, huge non linearities and singularities are expected and these kinds of simulations are really challenging.

Based on the previous assumptions, calculational results were obtained on the 2 aforementioned samples.

Results obtained for EST-66423-6

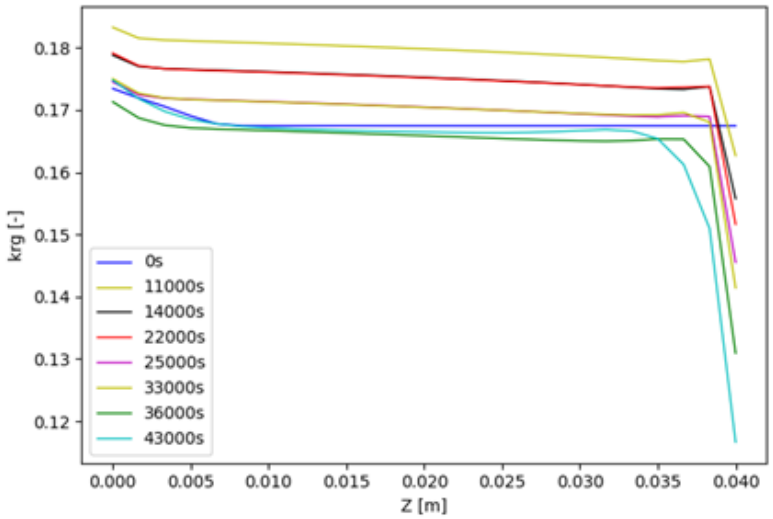

Figure 2.183: Gas relative permeability profile (case 3 – fg = 100)

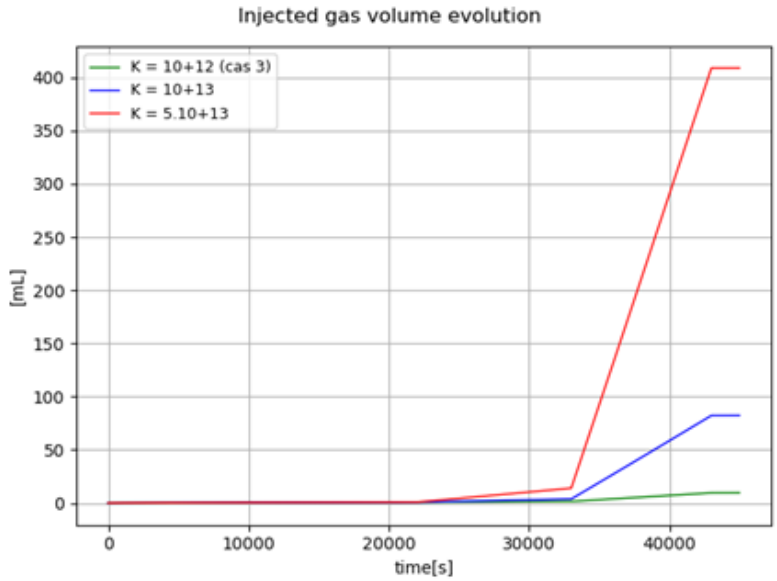

Figure 2.184: Volume evolution; impact of κ

This experimental test is first composed of a resaturation step under confinement (12 MPa). After that a deviatoric stress is applied simultaneously as the Nitrogen is injected. The observation is that results are quite far away from the classical response of intact Callovo-Oxfordian. The failure obtained by the calculation is normally expected around 37 MPa instead of 20 MPa on the experimental results.

The model allows to reproduce the global tendencies before and after the deviatoric peak. As expected, using the classical parameters of intact COx, the computed deviatoric stresses show that failure is obtained around 34 MPa, ie much higher than the 20 MPa measured. The impact of gas pressure is also studied: results show that it has a rather minor effect on peak value. Young modulus and compressive strength need to be significantly decreased to reproduce roughly the deviatoric evolution. The sample has probably been highly damaged during the resaturation stage and it is difficult to further exploit the experimental test.

Our work has finally been focused on a test performed with an unsaturated sample which has been conducted successfully.

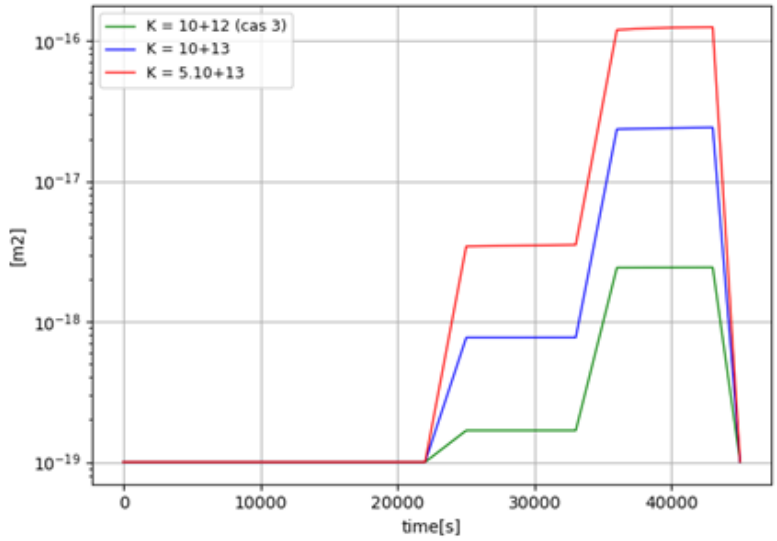

Figure 2.185: Intrinsic gas Permeability evolution; impact of κ

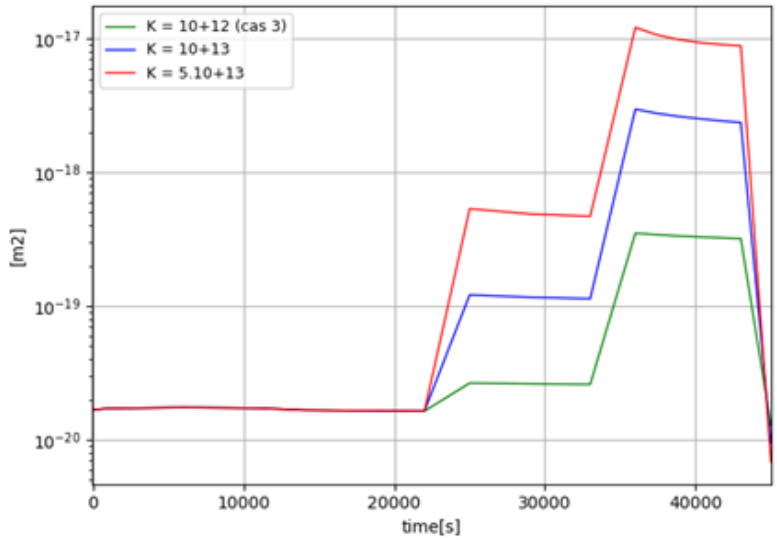

Figure 2.186: Gas Permeability evolution; impact of κ

Results obtained for EST-66721

Contrary to the previous test, deviatoric stress is directly applied on the sample in its current state. Information is given by the experimental team's report on a very desaturated sample with a water content of 6%. On the other hand, mechanical response seems to be more consistent. Failure is nevertheless difficult to capture experimentally (a complex behaviour after 45000 s is observed, with a sudden round of the curve, then a decrease which could correspond to a potential failure but also by an increase of the nitrogen volume obtained later).

In the work performed by EDF, the mechanical response is first analysed and mechanical parameters (Young modulus E and mean compressive strength σ_c) are recalibrated in Code_Aster. The best fitting is obtained with E = 2 GPa (instead of 6 MPa for intact COx) and σ_c= 6 MPa (instead of 12 MPa for intact COx). Due to the unsaturated state of the sample, it is logical that different parameters from those corresponding to a saturated sample are required. Calculations show that plastic and viscoplastic deformations increase with time and localization bands appear. However, numerical convergence is not possible after

45000 s of simulated time, corresponding more or less to the appearance of the failure (strong change of the slope in the mechanical response). The impact of gas permeability and initial saturation state has also been studied and calculational results show a minor impact of these parameters on the mechanical response.

Additionnaly, a hydraulic response has been studied with computation of an injected Nitrogen volume. For these calculations Nitrogen flows provided by the experiment are exploited. Main tendencies are well reproduced by calcualtion, and the use of appropriated parameters in the relationship between plastic deformation and permeability allows to obtain about the same order of magnitude for volume and permeability both in the calculation and the experiment. Nevertheless, these results should be treated with caution: indeed, a lot of parameters are needed and this kind of modelization cannot be reasonably predictive. This is even more the case for an unsaturated state. This work should be completed with several additional experimental tests on each direction and ideally on an intact saturated sample to be quantitatively conclusive.

More than the quantitative data obtained through this work, the important result of the simulations is the ability to capture main tendencies. The coupling between two-phase flow and viscoplastic modesl as well as the use of a permeability relationship has been successful, at least until the stress peak.

One of the initial goals of this work was also to perform a comparison with a discrete approach, for example with the model developed by IC2MP Poitier. For time reasons, this work could not be completed on time. The current work could be a good basis for future comparisons with this team (possibility to represent the fracture propagation with discrete approach).

2.7.6. Key learning points

New knowledge acquired through this work

This work has highlighted the ability of a classical continuum macroscopic model of Code_Aster (two-phase flow coupled to a viscoplastic constitutive law called LKR) to reproduce the main tendencies of a triaxial test with gas injection. Although this is a proven approach for a mechanical test *without* gas, coupling *with* gas seemed more complex for numerical and physical reasons. Even if the work has been performed on a desaturated COx sample (and not a saturated intact COx which is quite different), the methodology has been successfully set up.

Modeling of a simple geometry (only the sample is meshed) and treatment of the flow seems sufficient to capture the gas volume evolution. Moreover, a simple relationship between permeability and deformation allows to fit the volume and permeability evolution.

It shows also numerical difficulties when all mechanisms are activated (viscoplasticity, high desaturation involving high nonlinearities) and the necessity to develop even more robust models to obtain convergence after the failure peak. Especially for the mechanical part, development of a model simpler than LKR, keeping the main mechanisms and within a mathematically rigorous formalism, would be required.

Impact of acquired knowledge

At the beginning of the EURAD Program the ambition was to study both the damage due to gas injection and the gas transfer modified by a mechanical loading. Due to notable delays in experimental tests (these tests are very difficult to manage) only the second part has been performed at the time we write this report. A methodology has been successfully put in place which could be reused with other laboratories experiments. Some results of this work are also available to make comparisons in the future with results

obtained via discrete approaches provided by other teams (which was one of the goals for this work, but could not be performed due to delays).

Remaining knowledge gaps

Even if this approach allows to reproduce the main tendencies of gas transfer and couplings with mechanical loadings, number of parameters need to be treated with caution. A simple law (for example for permeabilities) allows to reduce the amount of parameters to be treated with care, but it seems unreasonable to use this kind of laws to be predictive of the behaviour of the samples. A lot of experiments with different size of samples and different loadings would indeed be necessary to comfort the chosen approach, from a quantitative point of view. Due to the long time required to resaturation of the sample, carrying out so many tests is very difficult.

The study of damage due to gas injection remains also a key point which still needs to be further investigated in the future. For this purpose, a damage mechanical model needs to be used instead of viscoelasticity model for example.

Finally, a comparison to a discrete approach would be very beneficial.

Recommendations for the future

For future works, the relationship / communication between modelers and experimental teams should be maintained and reinforced with periodic meeting - when it is necessary - to confirm or infirm common hypothesis. Several teams working on the same experimental tests should be of course preferred even it is not always possible.

References

Coussy, O., Dangla, P., Lassabatere, T., and Baroghel-Bouny, V. (2003). The equivalent pore pressure and the swelling and shrinkage of cement-based materials. Mater. Struct. *37*, 15–20.

Cuvilliez S., Djouadi I. and Raude S. (2017). An elastoviscoplastic constitutive model for geomaterials: Application to hydromechanical modelling of claystone response to drift excavation. Computers and Geotechnics 85, 321–340.

Djouadi I., Giot R., S Raude, Cuvilliez S., Laigle F. (2020) Integration of Transverse Isotropy in the Instantaneous Behaviour of Geomaterials with Application to Numerical Modelling of Underground Structures - Geotechnical and Geological Engineering 38, 4917-4938.

Fernandes R, Chavant C, Chambon R. A simplified second gradient model for dilatant materials: theory and numerical implementation. Int J Solids Struct 2008;45(20):5289–307.

Mahjoub M., Rouabhi A., Tijani M., Granet S., M'Jahad S. and Talandier J. (2018). Numerical Study of Callovo-Oxfordian Argillite Expansion due to Gas Injection. International Journal of Geomechanics 18.

Raude S., Laigle F., Giot R. and Fernandes R. (2016). A unified thermoplastic/viscoplastic constitutive model for geomaterials. Acta Geotechnica 11 (4), 849–869.

3. Synthesis

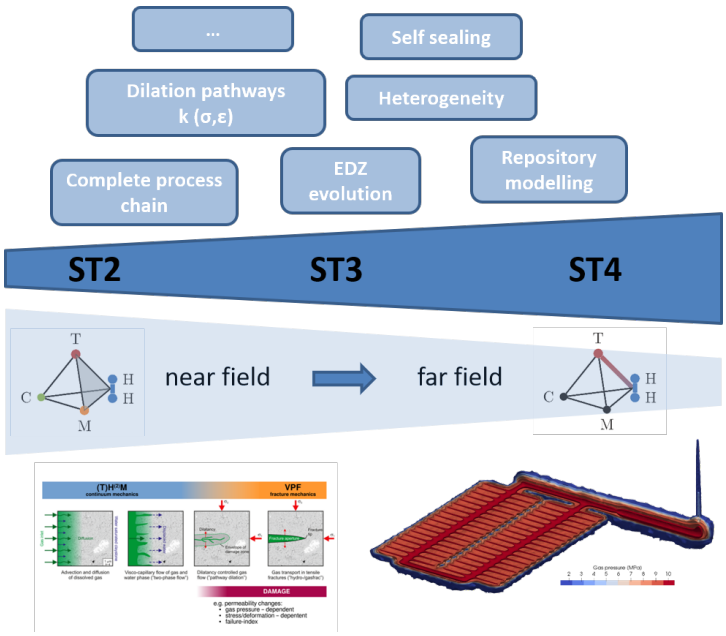

Figure 3.1: Modelling foci of WP GAS and upscaling concept

Fig. 3.1 depicts the modeling foci of WP GAS and the corresponding classification of the SubTasks (ST) in the scale concept. ST2 is focused on smaller-scale processes such as diffusion and the advective gas flow in the immediate vicinity of the gas sources (see Deliverable D6.7). The topic of ST3 is barrier integrity, focusing primarily on the pneumo-hydro-mechanical interactions between gas pressure and possible damage to the barrier as well as possible self-sealing when the gas pressure decreases again (Deliverable D6.8 - Part 1). The technical focal points, dilatancy (sec. 3), influence of heterogeneities (sec. 3), self-sealing (sec. 3), are briefly summarized below (boxes in the Fig. 3.1 top). Furthermore, the relationship between model complexity and scales is outlined in the Fig. 3.1 (center). While the full process coupling (TH2M)[1] including the nonlinear material behavior (complex constitutive material laws for the solid phase and the porous medium) can be mapped on the small-scale simplified models (TH2) are initially used for modeling complete storage systems. This has to do with the extensive computational effort of large-scale TH2M models, but also with the lack of understanding of coupled processes on a larger scale due to uncertainty in parameterization.[2] Process complexity (TH2M >> THM >> TH2) is symbolized by the tetrahedron icons below the SubTasks.[3] With the improved understanding of the fundamental processes based on the systematic analysis of the experiments in WP GAS (MODEX, Fig. 3.1 bottom left and sec. 1) and the consideration of EDZ evolution (sec. 3), important foundations for the modeling of SMA repositories ST4 have been created (Fig. 3.1 bottom right).

Process chain

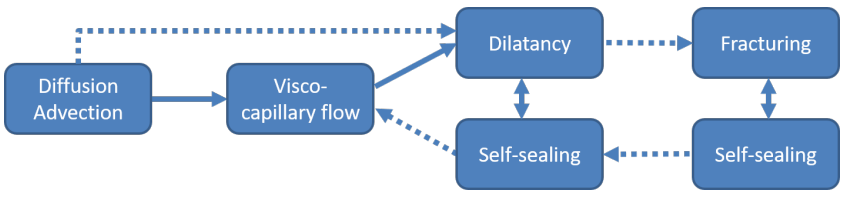

Figure 3.2: Sketch of the process chain, see Fig. 1.1

The modelling approach in WP GAS is based on the process chain in clay-rich barrier material (Figs. 3.2 and 1.1). This includes the transition from diffusion and advection up to damage processes, which occurs

[1] WP GAS focuses on isothermal processes, while WP HITEC considers non-isothermal processes. The models used in WP GAS can account for non-isothermal processes and are also used in WP HITEC. See also sec. 3

[2] Fully coupled monolithic TH2M models at full repository scale remain computationally challenging and not yet feasible. This remains a conceptual and computational task for future research.

[3] The modeling advance in EURAD GAS includes that three different model types can be used, TH2M, THM, TH2, at different scales and dominated processes.

as gas pressures increaes. Self-sealing is also taken into account when pressure decreases. The critical conditions for fracture nucleation and propagation are considered to prevent loss of barrier integrity. Rather than analysing individual experiments, model developments and benchmarking were also carried out along the entire process chain. To this end, EURAD GAS has established a strong link between modelling and experimental teams (MODEX, Fig. 1.2).

While experimental work often focuses on individual processes, WP GAS has resulted in several codes capable of modelling processes across various scales (sec. 2.1.3, 2.4) and materials (different clays and bentonites), thus filling an important gap in the overall view of barrier systems. In the following most important WP GAS model developments have been listed concerning the process chain and code implementations:

- CODE_ASTER: Coupling of two-phase flow model (liquid and gas phases) with elasto-viscoplastic mechanical law with second gradient. Development of couplings between permeability and plastic deformation.
- CODE_BRIGHT: 3D heterogeneous, coupled HM-G, BBM + cubic law for permeability, comprehensive protocol of hydration intervals and gas injection intervals, Toprak et al. (2023)
- LAGAMINE (ULiege): Extension of the second gradient method to two-phase flow hydro-mechanically coupled conditions including strong couplings between transfer properties and the deformations (Corman et al., 2022). Development of a hydro-mechanical interface constitutive model to reproduce the self-sealing process in an artificially fractured sample (Quacquarelli et al., 2024).
- LAGAMINE (TU Delft): Development of a pneumo-hydro-mechanical (PHM) framework to model gas-induced crack initiation and propagation in clays (Liaudat et al., 2023).
- OpenGeoSys (OGS-6): Development of a monolithic thermo-hydro-(two-phase-flow)-mechanical TH2M model (Grunwald et al., 2022) and fracture mechanics based on phase-field method (Mollaali et al., 2023) and various applications to laboratory and field experiments.

Dilatancy

One of the outcomes of the FORGE EC project was that the capillary two-phase flow alone was not sufficient to explain the gas transport in clay materials. Dilatancy controlled path flow has been identified as a major transport mechanism in clay (Shaw, 2013). The mechanism of dilatancy-controlled gas flow arises when gas pressure triggers localized consolidation or creates microfractures. This process effectively amplifies the local porosity, resulting in a marked increase in permeability and a decrease in the gas-entry pressure value (Cuss et al., 2014a). In Tasks 2 and 3 of WP GAS, the modelling of dilatancy controlled path flows was investigated by introducing permeability models that affect the gas transport in clay materials. Different permeability models describing permeability by pore gas pressure and by deformation were developed and implemented in the open source finite element code OpenGeoSys 6 (OGS 6) (Bilke et al., 2019; Lehmann et al., 2024). To validate these models, the modelling of a gas injection test in Opalinus clay performed by Popp et al. (2007) from Institut für Gebirgsmechanik (IfG) has been carried out. In this test, a reversible dilatant behavior of the clay sample upon gas injection was provoked. The modelling of this test in OpenGeoSys under single- and two-phase-flow conditions using the developed permeability models shows a good agreement with experimental results with best results obtained when the permeability is coupled with the mechanical strains. Based on the obtained results, it can be concluded that the dilatant controlled gas transport can be predicted numerically through the introduction of permeability models that depend on the mechanical strains induced by the gas pressure in the clay material.

Further numerical investigations were conducted in order to understand the occurrence of viscous-capillary flow in low permeable clays. For this purpose, we referred to an experiment conducted at EPFL by Minardi (2018). This experiment explored the hydro-mechanical behaviour of water-saturated samples during gas injection at varying gas pressures. The results of this experiment evidence that the sample showed a reversible behavior during the experiment. Minardi (2018) interpreted this finding as evidence of viscous-capillary flow as the predominant gas transport mechanism in this experiment. Our numerical analysis aimed to verify this conclusion as it is apparently in contradiction with the findings from the FORGE project.

The experiment proceeded in two stages. First, the sample underwent resaturation. Subsequent to achieving water saturation, a water pressure gradient was applied across the sample. Upon reaching a steady state, hydraulic conductivity was calculated following Darcy's law. After the first stage, the upstream water pressure was halted, and gas (air) was injected. Concurrently, the downstream water pressure was reduced and then held steady. Both radial and axial stresses remained constant during this gas injection period.

Our simulation outcomes, using the numerical process model in OpenGeoSys developed by Grunwald et al. (2022) that accounts for the viscous-capillary flow, align well with the experimental data. The model indicates that only water contributes to the outflow volume, as no gas outflow is discernible at the model's downstream end. Further numerical examinations of the saturation evolution within the sample have shown that the sample remained saturated during the experiment. It results from these observations that the gas did not penetrate into the pores of the clay sample. From the modelling perspective, one can conclude that the viscous-capillary flow was not the dominant gas transport mechanism in this experiment. This confirms the conclusions of the FORGE EC project stating that no experimental evidences of two-phase flow could be identified in experiments on low permeability porous media such as clays and bentonite close to saturation with water (Shaw, 2013). Thus, the dilatancy controlled path flow can be seen as the predominant gas transport mechanism in clays at gas pressures below the gas fracturing level. More investigations that are experimental are necessary to examine the conditions of under which viscous-capillary flow occurs in low permeable clay materials.

The activation and prevalence of the different gas transport mechanisms depend on several factors, including the hydraulic and mechanical properties of the clay, the gas pressure at the injection locus and the hydro-mechanical state of the material. A new pneumo-hydro-mechanical (PHM) modelling framework for crack initiation and propagation has been developed and implemented in LAGAMINE (Liaudat et al., 2023). The modelling approach uses continuum elements to represent the mechanical and flow processes in the bulk clay material and zero-thickness interface elements to represent existing or induced discontinuities (cracks). Thereby, gas flow through the bulk material (through diffusion and advection of dissolved gas, and two-phase flow) as well as existing or induced discontinuities can be modelled within a single modelling framework. The developed framework enables the investigation of the factors controlling the onset of each gas transfer mechanism and the interaction between these mechanisms.

The H2M model with a viscoplastic law (LKR) and second gradient has also been applied to triaxial tests with gas injection on COx clays (EDF, GeoRessources, see section 2.7). A straightforward relationship between permeability and deformation allows the fitting of permeability evolution due to deviatoric stress. Main tendencies observed in such a test with gas injection are well-reproduced depending on the initial state of the sample. The second-gradient H2M model for gas transport in EDZ and surrounding intact rock has been successfully applied to MEGAS and MAVL experiments in Boom and COx clays, respectively (Corman et al., 2022; Corman, 2024).

A limited number in-situ experiments in clay host rocks at larger scales can be reproduced by two-phase flow models. Consequently, the presented conclusions must be consolidated through further experiments. In particular, there is currently no evidence that the predominance of dilatancy versus two-phase flow is

also valid for EBS containing clay and a significant percentage of sand.

Heterogeneity

There are two levels of heterogeneity observed during gas injection test. The first level is associated with the variation of dry density (porosity) during the hydration. Gas breakthrough pressures are associated with the final dry density (while swelling pressure varies according to dry density) prior to gas injection rather than the initial dry density. Consequently, hydration step is integrated in the modelling in order to improve the model predictions. The second level of heterogeneity is related to gas effective permeability. In intact clay (without advection of free gas), gas permeability and water retention curves are porosity dependent. In contrast, gas permeability and water retention curves are strain dependent in dilatant pathways. The magnitude of the apertures in dilatant pathways is variable. Therefore, at least two different gas flow pathways with different aperture characteristics are integrated into the model. An elasto-plastic model such as the Barcelona Basic Model (BBM) is required not only to reproduce the development of swelling pressures during the hydration part but also to simulate possible irreversible strains induced by gas injection under the heterogeneous model configuration.

Self-sealing

During excavation, an excavated damaged zone (EDZ) is created, where the hydro-mechanical properties of the host rock are modified. The EDZ is characterized by a network of shear and tension fractures, where the permeability increases. However, after circulation of water within the fracture, it is observed both at the laboratory scale and in situ that the initial permeability is progressively recovered. The underlying process is the self-sealing of the fracture zones. A hydro-mechanical model for an interface element was developed: it encompasses two low-density and fairly compressible zones around the fracture. They are integrated into the interface elements to avoid their re-meshing, with a considerable simplification of the problem. Thanks to the clay transmissivity, the water injected can permeate the clay, first involving the damaged zone and then the rest of the sample. This model is able to reproduce the evolution of crack opening during wetting and drying tests on artificially fractured COx samples as well as the influence of the confining pressure on the self-sealing process. The upscaling of such an approach from the laboratory scale to the gallery one remains an open question.

EDZ evolution

An important aspect that goes along with the creation of an EDZ in clay host formations is the modification of the hydro-mechanical properties, which has a non-negligible impact on gas transport processes. The numerical modelling should therefore not only reproduce fracture development inherent to the EDZ but also integrate strong interactions coupling the flow and transfer properties (e.g. intrinsic permeability, retention curve) to the mechanical behavior. In this way, the model demonstrates an ability to replicate the transition between gas transport modes with increasing gas pressures in line with the current state of knowledge in the damaged zone. First, a slow background process of gas transport by diffusion is certain to occur but with a limited capacity of gas transfer. For larger gas production sequences, the activation of a two-phase flow mechanism in the discontinuities leads to a faster propagation of gas through the entire EDZ in the form of a gaseous front. The transition between these two modes of gas transport is all the more operating as the EDZ is active and the transfer properties are affected. Yet, some uncertainties remain in the ranges of variation of the key flow parameters that govern the two-phase flow model.

EURAD links and collaboration

Networking within EURAD and beyond plays an important role in the European Joint Programme on Radioactive Waste Management. There are close links between the EURAD work packages ACED, DONUT, GAS, and HITEC concerning the modeling platforms which are jointly shared between the WPs with different foci (Figure 3.3).

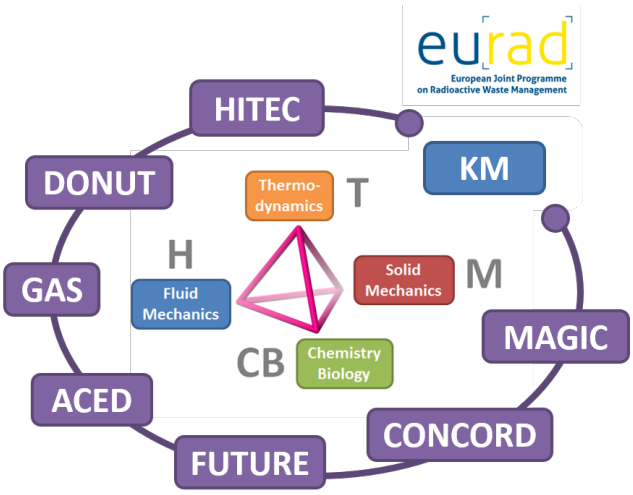

Figure 3.3: Networking within EURAD

In order to exemplify findings from EURAD modelling work packages we list main subjects of the selected work packages here, which will be illustrated with selected results in the presentation:

- ACED is dealing with reactive transport processes and related LILW and HLW evolution (e.g. Claret et al. (2022); Montenegro et al. (2023)),
- CONCORD is focusing on canister corrosion in clayey environments considering microbiological activity and irradiation effects (e.g. Altmaier et al. (2022)),
- DONUT is dealing with fundamental model development for reactive transport (Claret et al., 2022) and thermo-hydro-mechanical coupled processes, computational efficiency (HPC) as well as appropriate benchmarking concepts of machine learning and non-isothermal multiphase reactive transport (Prasianakis et al., 2020). As an example, we present the variational phase field method for THM fracture processes (Yoshioka et al., 2022), which is also directly connected to Task G of DECOVALEX 2023 (Mollaali et al., 2023),
- FUTURE is investigating the radionuclide transport and retention to provide the basis for the sorption and diffusion databases used in the safety assessment of deep geological repositories;
- GAS is dealing with gas transport through multi-barrier system and evaluating barrier integrity aspects in various clay rock environments (Levasseur et al., 2022),
- HITEC is additionally including thermal processes, e.g. for preventing thermo-mechanical damage (Levasseur et al., 2022),
- MAGIC is developing chemo-bio-mechanical coupled models for the evolution of massive concrete infrastructure (Claret et al., 2022),
- and KM (Knowledge Management): State-of-Knowledge, Guidance and Training and Mobility.

Collaboration within EURAD and beyond on modelling activities is schematically illustrated in Fig. 3.3, where model development (DONUT) as well as model validation and application come together (e.g. ACED, CONCORD, FUTURE, GAS, HITEC, MAGIC, KM). Various work packages have organized joint workshops and training activities to foster collaboration across different institutions and train young generations. Process modelling will also form an important basis for digital twin concepts, e.g. to exploit the synergies of digitalisation and as a communication tool in radioactive waste management (Kolditz et al., 2023; Jacques et al., 2023).

In addition, WP GAS has strong links to external initiatives such as BenVaSim (see section 2.1.4.2) and DECOVALEX (section 2.1.4.3) for mutual benefits. Other related activities have been the iCROSS and GeomInt projects Kolditz et al. (2021). Some demonstration examples as resulted added value of EURAD networking and beyond are illustrated in Fig. 3.4.

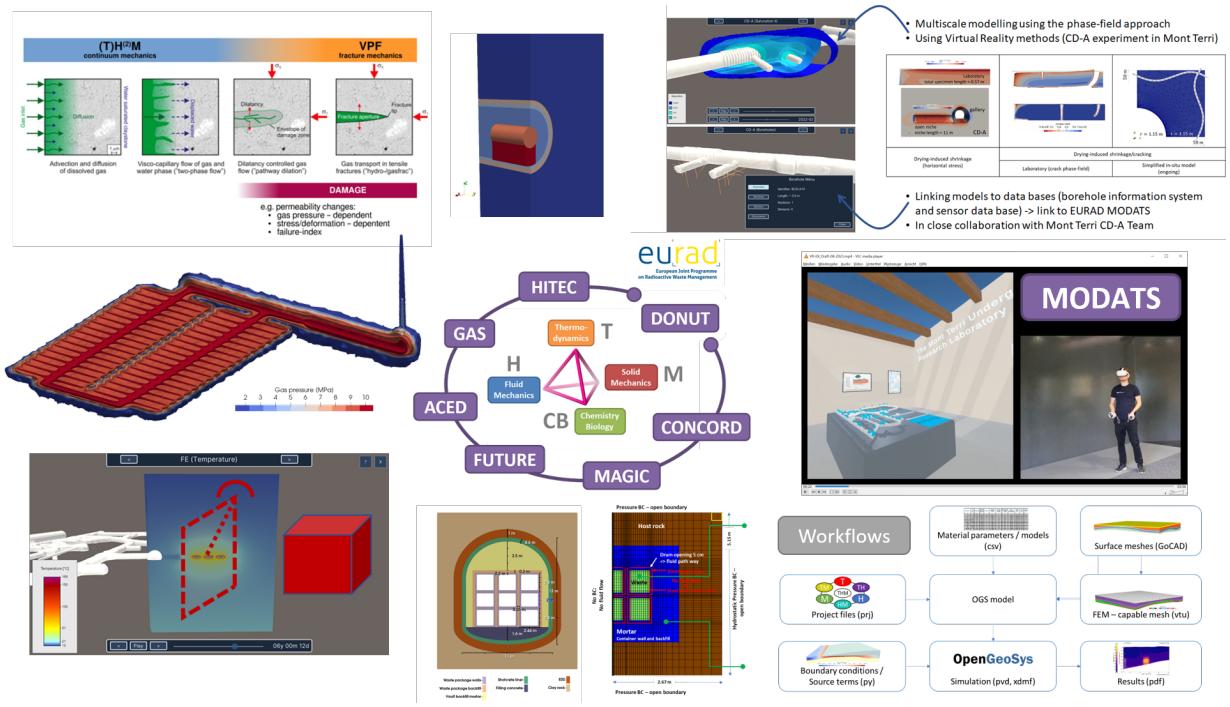

Figure 3.4: Some demonstration examples for EURAD networking (presented at the DECOVALEX 2023 final workshop)

Publications

To summarise the modelling results, we refer to the extensive body of literature on WP GAS contributions. Furthermore, a significant number of experiments on WP GAS have been successfully analysed (refer to Figure 1.1). Here are most important publications:

- Development of hierarchical TH2M models in OpenGeoSys (OGS6) (Grunwald et al., 2022, 2023)
- Benchmarking hierarchical TH2M models of OGS6 and experimental analyses (Pitz et al., 2023a,c)
- Development of path dilation approaches (H2M processes) and experimental analyses (Radeisen et al., 2023b,a; Tamayo-Mas et al., 2024)
- 3D HM modelling of gas injection tests under heterogeneous model configuration (Toprak et al., 2023, Toprak and Olivella, 2023).
- Modelling of gas injection tests in clay barriers, laboratory to field-scale Workshop of CODE_BRIGHT users, Barcelona 2023
- Development of a second gradient H2M model in LAGAMINE (Corman et al., 2022; Corman, 2024)
- Numerical modeling of self-sealing in fractured clayey materials (Quacquarelli et al., 2024)
- Development of a pneumo-hydro-mechanical (PHM) framework to model gas-induced crack initiation and propagation in LAGAMINE (Liaudat et al., 2023).

Bibliography

Alonso, E., Gens, A., and Josa, A. (1990). A constitutive model for partially saturated soils. *Geotechnique*, 40(3):405 – 430. Cited by: 2248; All Open Access, Green Open Access.

Alonso, E. E., Olivella, S., and Arnedo, D. (2006). Mechanisms of gas transport in clay barriers. *J. Iber. Geol.*, 32(2):175–196.

Altmaier, M., Bertrand, J., Churakov, S., and Diomidis, N. (2022). Long-term radionuclide retention in the near field: collaborative r&d studies within eurad focusing on container optimisation, mobility, mechanisms and monitoring. *EPJ Nuclear Sciences and Technologies*, 8. Cited by: 0; All Open Access, Gold Open Access, Green Open Access.

Amadei, B. (1983). *Rock anisotropy and the theory of stress measurements*. Springer-Verlag. Lecture Notes in Engineering Series., New-York, The United States.

Andra (2016). Analyse de l'interaction (thermo-)hydro-mécanique des alvéoles MAVL - Approche milieu continu. Technical report, Agence natioanle pour la gestion des déchets radioactifs, Châtenay-Malabry, France.

Areias, P. and Belytschko, T. (2006). A comment on the article "a finite element method for simulation of strong and weak discontinuities in solid mechanics" by a. hansbo and p. hansbo [comput. methods appl. mech. engrg. 193 (2004) 3523–3540]. *Comput. Methods Appl. Mech. Engrg.*, 195:1275–1276.

Argilaga, A., Collin, F., Lacarrière, L., Charlier, R., Armand, G., and Cerfontaine, B. (2019). Modelling of Short-Term Interactions Between Concrete Support and the Excavated Damage Zone Around Galleries Drilled in Callovo–Oxfordian Claystone. *International Journal of Civil Engineering*, 17(1).

Armand, G., Conil, N., Talandier, J., and Seyedi, D. M. (2017). Fundamental aspects of the hydromechanical behaviour of callovo-oxfordian claystone: from experimental studies to model calibration and validation. *Computers and Geotechnics*, 85:277–286.

Armand, G., Leveau, F., Nussbaum, C., de La Vaissiere, R., Noiret, A., Jaeggi, D., Landrein, P., and Righini, C. (2014). Geometry and properties of the excavation-induced fractures at the Meuse/Haute-Marne URL drifts. *Rock Mechanics and Rock Engineering*, 47(1):21–41.

Arnold, D. N. (1990). Mixed finite element methods for elliptic problems. *Computer methods in applied mechanics and engineering*, 82(1-3):281–300.

Bandis, S., Lumsden, A., and Barton, N. (1983). Fundamentals of rock joint deformation. In *International Journal of Rock Mechanics and Mining Sciences & Geomechanics Abstracts*, volume 20, pages 249–268. Elsevier.

Bart, M., Shao, J., Lydzba, D., and Haji-Sotoudeh, M. (2004). Coupled hydromechanical modeling of rock fractures under normal stress. *Canadian geotechnical journal*, 41(4):686–697.

Belytschko, T. and Black, T. (1999). Elastic crack growth in finite elements with minimal remeshing. *Int. J. Numer. Methods Engrg.*, 45:601–620.

Bernaud, D. and Rousset, G. (1992). La « nouvelle méthode implicite » pour l'étude du dimensionnement des tunnels. *Revue Française de Géotechnique*, 60:5–26.

Bernier, F., Li, X., Bastiaens, W., Ortiz, L., Van Geet, M., and Wouters, L. (2007a). Selfrac: fractures and self-healing within the excavation disturbed zone in clays. final report. *EURIDICE Rep.*

Bernier, F., Li, X.-L., and Bastiaens, W. (2007b). Twenty-five years' geotechnical observation and testing in the Tertiary Boom Clay format. *Géotechnique*, 57(2):229–237.

Bilke, L., Flemisch, B., Kalbacher, T., Kolditz, O., Helmig, R., and Nagel, T. (2019). Development of Open-Source Porous Media Simulators: Principles and Experiences. *Transport in Porous Media*, 130(1):337–361. cited By 5.

Blecha, C., Raith, F., Scheuermann, G., Nagel, T., Kolditz, O., and Maßmann, J. (2019). Analysis of coupled thermo-hydro-mechanical simulations of a generic nuclear waste repository in clay rock using fiber surfaces. *IEEE Pacific Visualization Symposium*, 2019-April:189–201. cited By 0.

Bock, H., Dehandschutter, B., Martin, C. D., Mazurek, M., de Haller, A., Skoczylas, F., and Davy, C. (2010). Self-sealing of fractures in argillaceous formations in the context of geological disposal of radioactive waste. *NEA*. https://www.oecd-nea.org/jcms/pl_14208.

Brezzi, F. and Bathe, K.-J. (1990). A discourse on the stability conditions for mixed finite element formulations. *Computer methods in applied mechanics and engineering*, 82(1-3):27–57.

Burland, J. B. (1990). On the compressibility and shear strength of natural clays. *Geotechnique*, 40(3):329–378.

Cajuhi, T., Haghighat, N., Maßmann, J., Mollaali, M., Sattari, A., Ziaei-Rad, V., Ziefle, G., Nagel, T., Wuttke, F., and Yoshioka, K. (2023). Hydro-mechanical effects and cracking in opalinus clay. *GeomInt—Discontinuities in Geosystems From Lab to Field Scale*.

Carol, I., López, C. M., and Roa, O. (2001). Micromechanical analysis of quasi-brittle materials using fracture-based interface elements. *International Journal for Numerical Methods in Engineering*, 52(1-2):193–215.

Carrier, B. and Granet, S. (2012). Numerical modeling of hydraulic fracture problem in permeable medium using cohesive zone model. *Engineering Fracture Mechanics*, 79:312–328.

Celia, M., Bouloutas, E. T., and Zabra, R. L. (1990). A general mass-conservative numerical solution for the unsaturated flow equation. *Water Resources Research*, 26:1483–1496.

Cerfontaine, B., Dieudonné, A. C., Radu, J. P., Collin, F., and Charlier, R. (2015). 3D zero-thickness coupled interface finite element: Formulation and application. *Computers and Geotechnics*, 69:124–140.

Chambon, R., Caillerie, D., and El Hassan, N. (1998). One-dimensional localisation studied with a second grade model. *European Journal of Mechanics, A/Solids*, 17(4):637–656.

Charlier, R. (1987a). *Approche unifiée de quelques problèmes non linéaires de mécanique des milieux continus par la méthode des éléments finis: (grandes déformations des métaux et des sols, contact unilatéral de solides, conduction thermique et écoulements en milieu poreux)*. Collection des publications de la Faculté des Sciences Appliquées.

Charlier, R. (1987b). *Approche unifiée de quelques problèmes non linéaires de mécanique des milieux continus par la méthode des éléments finis (grandes déformations des métaux et des sols, contact unilatéral de solides, conduction thermique et écoulements en milieux poreux)*. PhD thesis, Faculty of Applied Sciences, University of Liège, Belgium.

Charlier, R. and Cescotto, S. (1988). Modélisation du phénomène de contact unilatéral avec frottement dans un contexte de grandes déformations. *Journal de Mécanique Théorique et Appliquée*, 7(Suppl. 1).

Charlier, R., Collin, F., Pardoen, B., Talandier, J., Radu, J. P., and Gerard, P. (2013a). An unsaturated hydro-mechanical modelling of two in-situ experiments in Callovo-Oxfordian argillite. *Engineering Geology*, 165:46–63.

Charlier, R., Collin, F., Pardoen, B., Talandier, J., Radu, J.-P., and Gerard, P. (2013b). An unsaturated hydro-mechanical modelling of two in-situ experiments in callovo-oxfordian argillite. *Engineering geology*, 165:46–63.

Chen, C. M. and Thomée, V. (1985). The lumped mass finite element method for a parabolic problem. *The Journal of the Australian Mathematical Society. Series B. Applied Mathematics*, 26(3):329–354.

Chen, G. J., Sillen, X., Verstricht, J., and Li, X. L. (2011). ATLAS III in situ heating test in boom clay: Field data, observation and interpretation. *Computers and Geotechnics*, 38(5):683–696.

Chukwudozie, C., Bourdin, B., and Yoshioka, K. (2019). A variational phase-field model for hydraulic fracturing in porous media. *Computer Methods in Applied Mechanics and Engineering*, 347:957–982. cited By 27.

Clapeyron, E. (1834). Mémoire sur la Puissance Motrice de la Chaleur. *Journal de l'École polytechnique*, 23:153–191.

Claret, F., Dauzeres, A., Jacques, D., Sellin, P., Cochepin, B., De Windt, L., Garibay-Rodriguez, J., Govaerts, J., Leupin, O., Mon Lopez, A., Montenegro, L., Montoya, V., Prasianakis, N. I., Samper, J., and Talandier, J. (2022). Modelling of the long-term evolution and performance of engineered barrier system. *EPJ Nuclear Sciences and Technologies*, 8. Cited by: 6; All Open Access, Gold Open Access, Green Open Access.

Collin, F. (2003a). Couplages thermo-hydro-mécaniques dans les sols et les roches tendres partiellement saturés.

Collin, F. (2003b). *Couplages thermo-hydro-mécaniques dans les sols et les roches tendres partiellement saturés*. Phd thesis, Faculty of Applied Sciences, University of Liège, Belgium.

Collin, F., Chambon, R., and Charlier, R. (2006). A finite element method for poro mechanical modelling of geotechnical problems using local second gradient models. *International Journal for Numerical Methods in Engineering*, 65(11):1749–1772.

Collin, F., Li, X., Radu, J., and Charlier, R. (2002a). Thermo-hydro-mechanical coupling in clay barriers. *Engineering Geology*, 64(2-3):179–193. cited By 94 [5].

Collin, F., Li, X. L., Radu, J. P., and Charlier, R. (2002b). Thermo-hydro-mechanical coupling in clay barriers. *Engineering Geology*, 64:179–193.

Cordero, J. A. R., Sanchez, E. C. M., and Roehl, D. (2019a). Hydromechanical modeling of unrestricted crack propagation in fractured formations using intrinsic cohesive zone model. *Engineering Fracture Mechanics*, 221:106655.

Cordero, J. A. R., Sanchez, E. C. M., Roehl, D., and Pereira, L. C. (2019b). Hydro-mechanical modeling of hydraulic fracture propagation and its interactions with frictional natural fractures. *Computers and Geotechnics*, 111:290–300.

Corman, G. (2024). *Hydro-mechanical modelling of gas transport processes in clay host rocks in the context of a nuclear waste repository*. Phd thesis, Faculty of Applied Sciences, University of Liège, Belgium.

Corman, G., Gonzalez-Blanco, L., Levasseur, S., and Collin, F. (2024). Hydro-mechanical modelling of gas transport processes in clay materials using a multi-scale approach. *Computers and Geotechnics*, Under review.

Corman, G., Vu, M. N., and Collin, F. (2022). Numerical investigation of the couplings between strain localisation processes and gas migrations in clay materials. *International Journal of Solids and Structures*, 256(June):111974.

Coussy, O., Dangla, P., Lassabatère, T., and Baroghel-Bouny, V. (2004). The equivalent pore pressure and the swelling and shrinkage of cement-based materials. *Materials and Structures/Materiaux et Constructions*, 37(1):15 – 20. Cited by: 121.

Coussy, O. and Ulm, F. (1995). *Mechanics of Porous Continua*. John Wiley & Sons, Ltd, New-York, The United States.

Cuss, R., Harrington, J., Graham, C., and Noy, D. (2014a). Observations of pore pressure in clay-rich materials; implications for the concept of effective stress applied to unconventional hydrocarbons. volume 59, page 59 – 66. Cited by: 7; All Open Access, Bronze Open Access, Green Open Access.

Cuss, R. J., Harrington, J. F., Noy, D. J., Graham, C. C., and Sellin, P. (2014b). Evidence of localised gas propagation pathways in a field-scale bentonite engineered barrier system; results from three gas injection tests in the large scale gas injection test (Lasgit). *Applied Clay Science*, 102:81–92.

Cuvilliez, S., Djouadi, I., Raude, S., and Fernandes, R. (2017). An elastoviscoplastic constitutive model for geomaterials: Application to hydromechanical modelling of claystone response to drift excavation. *Computers and Geotechnics*, 85:321 – 340. Cited by: 14.

Dalton, J. (1802). Essay IV. On the expansion of elastic fluids by heat. *Memoirs of the Literary and Philosophical Society of Manchester*, 5(2):595–602.

Darcy, H. (1856). *Les fontaines publiques de la ville de Dijon*. Librairie des Corps Impériaux des Ponts et Chaussées et des Mines, Paris, France.

Davy, C. A., Skoczylas, F., Barnichon, J.-D., and Lebon, P. (2007). Permeability of macro-cracked argillite under confinement: gas and water testing. *Physics and Chemistry of the Earth, Parts A/B/C*, 32(8-14):667–680.

Day, R. and Potts, D. (1994). Zero thickness interface elements—numerical stability and application. *International Journal for numerical and analytical methods in geomechanics*, 18(10):689–708.

De Borst, R. and Mühlhaus, H.-B. (1992). Gradient-Dependent Plasticity: Formulation and Algorithmic Aspects. *International Journal for Numerical Methods in Engineering*, 35(3):521–539.

de La Vaissière, R., Armand, G., and Talandier, J. (2015). Gas and water flow in an excavation-induced fracture network around an underground drift: a case study for a radioactive waste repository in clay rock. *Journal of Hydrology*, 521:141–156.

Delay, J., Vinsot, A., Krieguer, J.-M., Rebours, H., and Armand, G. (2007). Making of the underground scientific experimental programme at the meuse/haute-marne underground research laboratory, north eastern france. *Physics and Chemistry of the Earth, Parts A/B/C*, 32(1):2–18.

Deng, Y. F., Tang, A. M., Cui, Y. J., Nguyen, X. P., Li, X. L., and Wouters, L. (2011). Laboratory hydro-mechanical characterisation of Boom Clay at Essen and Mol. *Physics and Chemistry of the Earth, Parts A/B/C*, 36:1878–1890.

Di Donna, A., Charrier, P., Dijkstra, J., Andò, E., and Bésuelle, P. (2022). The contribution of swelling to self-sealing of claystone studied through x-ray tomography. *Physics and Chemistry of the Earth, Parts A/B/C*, 127:103191.

Di Donna, A., Charrier, P., Salager, S., and Bésuelle, P. (2019). Self-sealing capacity of argillite samples. In *7th International Symposium on Deformation Characteristics of Geomaterials*.

Dieudonné, A.-C., Cerfontaine, B., Collin, F., and Charlier, R. (2015). Hydromechanical modelling of shaft sealing for CO2 storage. *Engineering geology*, 193:97–105.

Djouadi, I., Giot, R., Raude, S., Cuvilliez, S., Laigle, F., and Fernandes, R. (2020). Integration of transverse isotropy in the instantaneous behaviour of geomaterials with application to numerical modelling of underground structures. *Geotechnical and Geological Engineering*, 38(5):4917 – 4938. Cited by: 1.

Ehlers, W. and Volk, W. (1998). On theoretical and numerical methods in the theory of porous media based on polar and non-polar elasto-plastic solid materials. *Int J Solids Struct*, 35(34-35):4597–4617.

Enresa (2000). FEBEX Project. Full-scale engineered barriers experiment for a deep geological repository for high level radioactive waste in crystalline host rock, Final report, 1/2000. Technical report, Enresa, Madrid, Spain.

Enresa (2006). Full-scale engineered barriers experiment. Enresa. Madrid. Spain. Updated final report 1994-2004. Technical publication 05-0/2006. Technical report, Enresa, Madrid, Spain.

Faivre, M. and Giot, R. (2018). Development and implementation of the hhm_xfem model.

Faivre, M., Paul, B., Golfier, F., Giot, R., Massin, P., and Colombo, D. (2016). 2d coupled hm-xfem modeling with cohesive zone model and applications to fluid-driven fracture network. *Engineering Fracture Mechanics*, 159:115–143.

Fernandes, R., Chavant, C., and Chambon, R. (2008). A simplified second gradient model for dilatant materials: Theory and numerical implementation. *International Journal of Solids and Structures*, 45(20):5289 – 5307. Cited by: 28.

Ferte, G., Massin, P., and Moes, N. (2015). 3d crack propagation with cohesive elements in the extended finite element method. *Computer Methods in Applied Mechanics and Engineering*, 300:347–374.

Fick, A. (1855). Über Diffusion [Translated: On liquid diffusion]. *Poggendorff's Annalen der Physik und Chemie*, 170(1):59–86.

Fischer, K. A. and Wriggers, P. (2006). Mortar based frictional contact formulation for higher order interpolations using the moving friction cone. *Computer methods in applied mechanics and engineering*, 195(37-40):5020–5036.

François, B. (2014). Hollow Cylinder Tests on Boom Clay : Modelling of Strain Localization in the Anisotropic Excavation Damaged Zone. *Rock Mech Rock Eng*, 47:71–86.

Fries, T.-P. (2008). A corrected xfem approximation without problems in blending elements. *International Journal for Numerical Methods in Engineering*, 75(5):503– 532.

Garello, C. M. L. (1999). *Análisis microestructural de la fractura del hormigón utilizando elementos finitos tipo junta. Aplicación a diferentes hormigones*. PhD thesis, Universitat Politècnica de Catalunya (UPC).

Gens, A., Carol, I., and Alonso, E. (1990). A constitutive model for rock joints formulation and numerical implementation. *Computers and Geotechnics*, 9(1-2):3–20.

Gens, A., Sánchez, M., Guimarães, L., Alonso, E., Lloret, A., Olivella, S., Villar, M., and Huertas, F. (2009). A full-scale in situ heating test for high-level nuclear waste disposal: Observations, analysis and interpretation. *Geotechnique*, 59(4):377–399. cited By 180.

Gentier, S., Petitjean, C., Riss, J., and Archambault, G. (1996). Hydromechanical behavior of a natural joint under shearing. In *ARMA North America Rock Mechanics Symposium*, pages ARMA–96. ARMA.

Gerard, P., Charlier, R., Chambon, R., and Collin, F. (2008a). Influence of evaporation and seepage on the convergence of a ventilated cavity. *Water Resources Research*, 44(7). cited By 27 [4].

Gerard, P., Charlier, R., Su, K., Duveau, G., Giot, R., Chavant, C., and Collin, F. (2008b). Numerical modelling of coupled mechanics and gas tansfer around radioactive waste in long-term storage. *Journal of Theoretical and Applied Mechanics*, 38:25–44.

Gerard, P., Harrington, J., Charlier, R., and Collin, F. (2014). Modelling of localised gas preferential pathways in claystone. *International Journal of Rock Mechanics and Mining Sciences*, 67:104–114.

Giot, R., Auvray, C., and Talandier, J. (2019). Self-sealing of claystone under x-ray nanotomography. *Geological Society, London, Special Publications*, 482(1):213–223.

Gonzalez-Blanco, L. (2017). Gas migration in deep argillaceous formations: Boom clay and indurated clays.

Gonzalez-Blanco, L., Romero, E., Jommi, C., Li, X., and Sillen, X. (2016a). Gas migration in a Cenozoic clay: Experimental results and numerical modelling. *Geomechanics for Energy and the Environment*, 6:81–100.

Gonzalez-Blanco, L., Romero, E., Jommi, C., Li, X., and Sillen, X. (2016b). Gas migration in a cenozoic clay: Experimental results and numerical modelling. *Geomechanics for Energy and the Environment*, 6:81–100.

Goodman, R. E., Taylor, R. L., and Brekke, T. L. (1968). A model for the mechanics of jointed rock. *Journal of the soil mechanics and foundations division*, 94(3):637–659.

Granet, S. (2023). Modèles de comportement thhm. *Documentation Code_Aster [R7.01.11]*.

Grunwald, N., Lehmann, C., Maßmann, J., Naumov, D., Kolditz, O., and Nagel, T. (2022). Non-isothermal two-phase flow in deformable porous media: systematic open-source implementation and verification procedure. *Geomechanics and Geophysics for Geo-Energy and Geo-Resources*, 8(3). cited By 2.

Grunwald, N., Nagel, T., Pitz, M., and Kolditz, O. (2023). Extended analysis of benchmarks for gas phase appearance in low-permeable rocks. *Geomechanics and Geophysics for Geo-Energy and Geo-Resources*, 9(1):170.

Guiducci, C., Collin, F., Radu, J.-P., Pellegrino, A., and Charlier, R. (2003). Numerical modeling of hydro-mechanical fracture behavior. In *ISRM Congress*, pages ISRM–10CONGRESS. ISRM.

Gutiérrez Rodrigo, V. (2019). *Transporte de gas en materiales de barrera*. PhD thesis, Universidad Complutense de Madrid, Facultad de Ciencias Geológicas, Departamento de Geodinámica.

Habraken, A. (1989). *Contribution à la modélisation du formage des métaux par la méthode des éléments finis*. PhD thesis, University of Liège.

Habraken, A. and Cescotto, S. (1998). Contact between deformable solids: the fully coupled approach. *Mathematical and Computer modelling*, 28(4-8):153–169.

Harrington, J. F., Milodowski, A. E., Graham, C. C., Rushton, J. C., and Cuss, R. J. (2012). Evidence for gas-induced pathways in clay using a nanoparticle injection technique. *Mineralogical Magazine*, 76(8):3327–3336.

Haynes, W. (2014). *CRC Handbook of Chemistry and Physics*. CRC Handbook of Chemistry and Physics. CRC Press, 95 edition.

Huang, Y., Shao, H., Wieland, E., Kolditz, O., and Kosakowski, G. (2018). A new approach to coupled two-phase reactive transport simulation for long-term degradation of concrete. *Construction and Building Materials*, 190:805–829. cited By 6.

Idiart, A. E., López, C. M., and Carol, I. (2011a). Chemo-mechanical analysis of concrete cracking and degradation due to external sulfate attack: A meso-scale model. *Cement and Concrete Composites*, 33(3):411–423.

Idiart, A. E., López, C. M., and Carol, I. (2011b). Modeling of drying shrinkage of concrete specimens at the meso-level. *Materials and structures*, 44:415–435.

Jacques, D., Kolditz, O., Szőke, I., Churakov, S. V., García, D., Laloy, E., Montoya, V., Prasianakis, N. I., and Samper, J. (2023). Digitalization and digital twins in long term management of radioactive waste. In *Proceedings of ASME 2023 International Conference on Environmental Remediation and Radioactive Waste Management, ICEM 2023*. Cited by: 0.

Jia, Y., Bian, H. B., Duveau, G., Su, K., and Shao, J. F. (2008). Hydromechanical modelling of shaft excavation in Meuse/Haute-Marne laboratory. *Physics and Chemistry of the Earth*, 33(SUPPL. 1):422–435.

Khoei, A., Moallemi, S., and Haghighat, E. (2012). Thermo-hydro-mechanical modelling of impermeable discontinuity in saturated porous media with X-FEM technique. *Engineering Fracture Mechanics*, 96:701–723.

Kolditz, O., Bauer, S., Bilke, L., Böttcher, N., Delfs, J., Fischer, T., Görke, U., Kalbacher, T., Kosakowski, G., McDermott, C., Park, C., Radu, F., Rink, K., Shao, H., Shao, H., Sun, F., Sun, Y., Singh, A., Taron, J., Walther, M., Wang, W., Watanabe, N., Wu, Y., Xie, M., Xu, W., and Zehner, B. (2012). OpenGeoSys: An open-source initiative for numerical simulation of thermo-hydro-mechanical/chemical (THM/C) processes in porous media. *Environmental Earth Sciences*, 67(2):589–599. cited By 297.

Kolditz, O., Görke, U.-J., Konietzky, H., Maßmann, J., Nest, M., Steeb, H., Wuttke, F., and Nagel, T. (2021). GeomInt – Mechnanical Integrity of Host Rocks. In *Terrestrial Environmental Sciences*, page 277. Springer, Heidelberg.

Kolditz, O., Yoshioka, K., Cajuhi, T., Günther, R.-M., Steeb, H., Wuttke, F., and Nagel, T. (2023). GeomInt - Discontinuities in Geosystems From Lab to Field Scale. In *SpringerBriefs in Earth System Sciences*, page 120. Springer, Heidelberg.

Labuz, J. and Zang, A. (2012). Mohr–Coulomb failure criterion. *Rock Mechanics and Rock Engineering*, 45(6):975–979.

Legrain, G., Moes, N., and Huerta, A. (2008). Stability of incompressible formulations enriched with x-fem. *Computer Methods in Applied Mechanics and Engineering*, 197(21-24):1835–1849.

Lehmann, C., Bilke, L., Buchwald, J., Graebling, N., Grunwald, N., Heinze, J., Meisel, T., Lu, R., Naumov, D., Rink, K., Özgür Sen, O., Selzer, P., Shao, H., Wang, W., Zill, F., Nagel, T., and Kolditz, O. (2024). Openworkflow—development of an open-source synthesis-platform for safety investigations in the site selection process. *Grundwasser*, 29(1):31–47.

Lepillier, B., Yoshioka, K., Parisio, F., Bakker, R., and Bruhn, D. (2020). Variational Phase-Field Modeling of Hydraulic Fracture Interaction With Natural Fractures and Application to Enhanced Geothermal Systems. *Journal of Geophysical Research: Solid Earth*, 125(7). cited By 2.

Lequesne, C. (2009). Modeling of fracture in heavy steel welded beam-to-column connection submitted to cyclic loading by finite elements.

Levasseur, S., Collin, F., Daniels, K., Dymitrowska, M., Harrington, J., Jacops, E., Kolditz, O., Marschall, P., Norris, S., Sillen, X., et al. (2021). Initial state of the art on gas transport in clayey materials. *Deliverable D6*, 1.

Levasseur, S., Collin, F., Daniels, K., Dymitrowska, M., Harrington, J., Jacops, E., Kolditz, O., Marschall, P., Norris, S., Sillen, X., Talandier, J., Truche, L., and Wendling, J. (2024). State of the Art on Gas Transport in Clayey Materials II. Deliverable D6.2 of HORIZON 2020 project EURAD, Work Package Gas. EC Grant agreement no: 847593. Technical report, European commission.

Levasseur, S., Sillen, X., Marschall, P., Wendling, J., Olin, M., Grgic, D., and Svoboda, J. (2022). Euradwaste'22 paper - host rocks and thmc processes in dgr: Eurad gas and hitec: mechanistic understanding of gas and heat transport in clay-based materials for radioactive waste geological disposal. *EPJ Nuclear Sciences and Technologies*, 8. Cited by: 3; All Open Access, Gold Open Access, Green Open Access.

Lewis, R. and Schrefler, B. (1998). The Finite Element Method in the Static and Dynamic Deformation and Consolidation of Porous Media. Second Edition. *Communications in Numerical Methods in Engineering*, 34.

Liaudat, J., Carol, I., and López, C. M. (2020). Model for alkali-silica reaction expansions in concrete using zero-thickness chemo-mechanical interface elements. *International Journal of Solids and Structures*, 207:145–177.

Liaudat, J., Dieudonné, A.-c., and Vardon, P. J. (2023). Modelling gas fracturing in saturated clay samples using triple-node zero-thickness interface elements. *Computers and Geotechnics*, 154:105128.

Lu, R., Nagel, T., Shao, H., Kolditz, O., and Shao, H. (2018). Modeling of Dissolution-Induced Permeability Evolution of a Granite Fracture Under Crustal Conditions. *Journal of Geophysical Research: Solid Earth*, 123(7):5609–5627. cited By 3.

Lux, K.-H. and Rutenberg, M. (2018). Vorprojekt - Internationales Benchmarking zur Verifizierung und Validierung von TH2M-Simulatoren insbesondere im Hinblick auf fluiddynamische Prozesse in Endlagersystemen (BenVaSim) : Abschlussbericht zum BMWi-Forschungsvorhaben : Zeitraum: 01.07.2016-30.04.2017. Technical report, Lehrstuhl für Deponietechnik und Geomechanik, Technische Universität Clausthal, Clausthal-Zellerfeld. in German.

Lux, K.-H., Rutenberg, M., Feierabend, J., Czaikowski, O., Friedenberg, L., Maßmann, J., Pitz, M., Sentís, M. L., Graupner, B. J., Hansmann, J., Hotzel, S., Kock, I., Rutqvist, J., Hu, M., and Rinaldi, A. P. (2021). Synthesis report. BenVaSim – International Benchmarking for Verification and Validation of TH2M Simulators with Special Consideration of Fluid Dynamical Processes in Radioactive Waste Repository Systems. Technical report, Technische Universität Clausthal.

López, C. M., Carol, I., and Aguado, A. (2008). Meso-structural study of concrete fracture using interface elements. I: numerical model and tensile behavior. *Materials and structures*, 41:583–599.

Mahjoub, M., Rouabhi, A., Tijani, M., Granet, S., M'Jahad, S., and Talandier, J. (2018). Numerical Study of Callovo-Oxfordian Argillite Expansion due to Gas Injection. . *International Journal of Geomechanics*, 18.

Marschall, P., Horseman, S., and Gimmi, T. (2005a). Characterisation of gas transport properties of the opalinus clay, a potential host rock formation for radioactive waste disposal. *Oil & gas science and technology*, 60(1):121–139.

Marschall, P., Horseman, S., and Gimmi, T. (2005b). Characterisation of gas transport properties of the Opalinus Clay, a potential host rock formation for radioactive waste disposal. *Oil and Gas Science and Technology*, 60(1):121–139. cited By 173.

Matsushima, T., Chambon, R., and Caillerie, D. (2002). Large strain finite element analysis of a local second gradient model: application to localisation. *International Journal for Numerical Methods in Engineering*, 54(4):499–521.

Mayor, J.-C., García-Siñeriz, J., Alonso, E., Alheid, H.-J., and Blümbling, P. (2007). Engineered barrier emplacement experiment in opalinus clay for the disposal of radioactive waste in underground repositories. *Rep. Swiss Geol. Surv.*, 1:115–180.

Mi, Y., Crisfield, M. A., Davies, G., and Hellweg, H.-B. (1998). Progressive delamination using interface elements. *Journal of Composite Materials*, 32:1246–1272.

Miao, X.-Y., Kolditz, O., and Nagel, T. (2019). Modelling thermal performance degradation of high and low-temperature solid thermal energy storage due to cracking processes using a phase-field approach. *Energy Conversion and Management*, 180:977–989. cited By 3.

Minardi, A. (2018). Hydro-mechanical characterization of gas shales and Opalinus Clay shale in partially saturated conditions. Technical report, IIC, Lausanne.

Mindlin, R. D. (1965). Second gradient of strain and surface-tension in linear elasticity. *International Journal of Solids and Structures*, 1(4):417–438.

Mollaali, M., Kolditz, O., Hu, M., Park, C.-H., Park, J.-W., McDermott, C. I., Chittenden, N., Bond, A., Yoon, J. S., Zhou, J., Pan, P.-Z., Liu, H., Hou, W., Lei, H., Zhang, L., Nagel, T., Barsch, M., Wang, W., Nguyen, S., Kwon, S., Lee, C., and Yoshioka, K. (2023). Comparative verification of hydro-mechanical fracture behavior: Task g of international research project decovalex–2023. *International Journal of Rock Mechanics and Mining Sciences*, 170. Cited by: 2; All Open Access, Green Open Access.

Montenegro, L., Samper, J., Mon, A., De Windt, L., Samper, A.-C., and García, E. (2023). A non-isothermal reactive transport model of the long-term geochemical evolution at the disposal cell scale in a hlw repository in granite. *Applied Clay Science*, 242. Cited by: 1; All Open Access, Green Open Access, Hybrid Gold Open Access.

Mualem, J. (1976). A new model for predicting the hydraulic conductivity of unsaturated porous media. *Water Resources Research*, 12(3):513–522.

Naylor, D. (1974). Stress in nearly incompressible materials for finite elements with application to the calculation of excess pore pressure. *Int. J. Numer. Methods Engrg*, 8:443–460.

Ndeffo, M., Massin, P., Moës, M., Martin, A., and Gopalakrishnan, S. (2017). On the construction of approximation space to model discontinuities and cracks with linear and quadratic extended finite elements. *Advanced Modeling and Simulation in Engineering Sciences*, 4:1–51.

Nguyen, V. P. (2014). An open source program to generate zero-thickness cohesive interface elements. *Advances in Engineering Software*, 74:27–39.

Nguyen, V. P., Lian, H., Rabczuk, T., and Bordas, S. (2017). Modelling hydraulic fractures in porous media using flow cohesive interface elements. *Engineering Geology*, 225:68–82.

Nuth, M. and Laloui, L. (2008). Effective stress concept in unsaturated soils: Clarification and validation of a unified framework. *International journal for numerical and analytical methods in Geomechanics*, 32(7):771–801.

Olivella, S. and Alonso, E. (2008a). Gas flow through clay barriers. *Geotechnique*, 58(3):157–176. cited By 106.

Olivella, S. and Alonso, E. (2008b). Gas flow through clay barriers . *Géotechnique*, 58(3):157–176.

Olivella, S. and Alonso, E. E. (2008c). Gas flow through clay barriers. *Géotechnique*, 58(3):157–176.

Olivella, S., Carrera, J., Gens, A., and Alonso, E. (1994). Nonisothermal multiphase flow of brine and gas through saline media. *Transport in Porous Media*, 15(3):271–293. cited By 312.

Olsson, R. and Barton, N. (2001). An improved model for hydromechanical coupling during shearing of rock joints. *International journal of rock mechanics and mining sciences*, 38(3):317–329.

Oron, A. P. and Berkowitz, B. (1998). Flow in rock fractures: The local cubic law assumption reexamined. *Water Resources Research*, 34(11):2811–2825.

Ortiz, L., Volckaert, G., De Cannière, P., Put, M., Sen, M., Horseman, S.T., Harrington, J., Impey, M., and Einchcomb, S. (1997). MEGAS: modelling and experiments on GAS migration in repository host rocks. Final report phase 2. Technical report, Eur. Comm., [Rep.] EUR 17453 EN.

Pandolfi, A. and Ortiz, M. (1998). Solid modeling aspects of three-dimensional fragmentation. *Engineering with Computers*, 14(4):287–308.

Pardoen, B. (2015). *Hydro-mechanical analysis of the fracturing induced by the excavation of nuclear waste repository galleries using shear banding*. PhD thesis, University of Liège.

Pardoen, B. and Collin, F. (2017). Modelling the influence of strain localisation and viscosity on the behaviour of underground drifts drilled in claystone. *Computers and Geotechnics*, 85:351–367.

Parisio, F., Naumov, D., Kolditz, O., and Nagel, T. (2018). Material forces: An insight into configurational mechanics. *Mechanics Research Communications*, 93:114–118. cited By 3.

Parisio, F., Tarokh, A., Makhnenko, R., Naumov, D., Miao, X.-Y., Kolditz, O., and Nagel, T. (2019a). Experimental characterization and numerical modelling of fracture processes in granite. *International Journal of Solids and Structures*, 163:102–116. cited By 4.

Parisio, F., Vilarrasa, V., Wang, W., Kolditz, O., and Nagel, T. (2019b). The risks of long-term re-injection in supercritical geothermal systems. *Nature Communications*, 10(1). cited By 1.

Parisio, F., Vinciguerra, S., Kolditz, O., and Nagel, T. (2019c). The brittle-ductile transition in active volcanoes. *Scientific Reports*, 9(1). cited By 4.

Paul, B., Faivre, M., Massin, P., Giot, R., Colombo, D., Golfier, F., and Martin, A. (2018). 3d coupled hm-xfem modeling with cohesive zone model and applications to non planar hydraulic fracture propagation and multiple hydraulic fracture interference. *Computer Methods in Applied Mechanics and Engineering*, 324:321–353.

Philip, J. R. and de Vries, D. A. (1957). Moisture movement in porous materials under temperature gradients. *Eos, Trans Amer Geophys Union*, 38(2):222–232.

Pietruszczak, S. and Mróz, Z. (1981). Finite element analysis of deformation of strain-softening materials. *International Journal for Numerical Methods in Engineering*, 17(3):327–334.

Pitz, M., Grunwald, N., Graupner, B., Kurgyis, K., Radeisen, E., Maßmann, J., Ziefle, G., Thiedau, J., and Nagel, T. (2023a). Benchmarking a new th2m implementation in ogs-6 with regard to processes relevant for nuclear waste disposal. *Environmental Earth Sciences*, 82(13). Cited by: 4; All Open Access, Green Open Access, Hybrid Gold Open Access.

Pitz, M., Grunwald, N., Graupner, B., Radeisen, E., Maßmann, J., Ziefle, G., Thiedau, J., and Nagel, T. (2023b). Benchmarking a new TH2M implementation in OGS-6 with regard to processes relevant for nuclear waste disposal. *Environmental Earth Sciences*. under review.

Pitz, M., Kaiser, S., Grunwald, N., Kumar, V., Buchwald, J., Wang, W., Naumov, D., Chaudhry, A. A., Maßmann, J., Thiedau, J., Kolditz, O., and Nagel, T. (2023c). Non-isothermal consolidation: A systematic evaluation of two implementations based on multiphase and richards equations. *International Journal of Rock Mechanics and Mining Sciences*, 170. Cited by: 3; All Open Access, Hybrid Gold Open Access.

Plesha, M. E. (1995). Rock joints: theory, constitutive equations. In *Studies in applied mechanics*, volume 42, pages 375–393. Elsevier.

Pollock, D. (1986). Simulation of fluid flow and energy transport processes associated with high-level radioactive waste disposal in unsaturated alluvium. *Water Resources Research*, 22(5):765–775.

Popp, T., Wiedemann, M., Böhnel, H., and Minkley, W. (2007). Untersuchungen zur Barriereintegrität im Hinblick auf das Ein-Endlager-Konzept. Technical report, Institut für Gebirgsmechanik GmbH, Leipzig.

Prasianakis, N. I., Haller, R., Mahrous, M., Poonoosamy, J., Pfingsten, W., and Churakov, S. V. (2020). Neural network based process coupling and parameter upscaling in reactive transport simulations. *Geochimica et Cosmochimica Acta*, 291:126 – 143. Cited by: 28.

Prime, N., Levasseur, S., Miny, L., Charlier, R., Léonard, A., and Collin, F. (2016). Drying-induced shrinkage of boom clay: An experimental investigation. *Canadian Geotechnical Journal*, 53(3):396–409.

Quacquarelli, A., Talandier, J., Di Donna, A., and Collin, F. (2024). Numerical modeling of self-sealing in fractured clayey materials. *Acta Geotechnica*. Accepted for publication.

Radeisen, E., Shao, H., Hesser, J., Kolditz, O., Xu, W., and Wang, W. (2023a). Simulation of dilatancy-controlled gas migration processes in saturated bentonite using a coupled multiphase flow and elastoplastic h2m model. *Journal of Rock Mechanics and Geotechnical Engineering*, 15(4):803 – 813. Cited by: 5; All Open Access, Gold Open Access.

Radeisen, E., Shao, H., Pitz, M., Hesser, J., and Wang, W. (2023b). Derivation of heterogeneous material distributions and their sensitivity to hm-coupled two-phase flow models exemplified with the lasgit experiment. *Environmental Earth Sciences*, 82(14). Cited by: 1; All Open Access, Hybrid Gold Open Access.

Raude, S., Laigle, F., Giot, R., and Fernandes, R. (2016). A unified thermoplastic/viscoplastic constitutive model for geomaterials. *Acta Geotechnica*, 11(4):849–869.

Roscoe, K. and Burland, J. B. (1968). On the generalized stress-strain behaviour of wet clay.

Salehnia, F., Sillen, X., Li, X., and Charlier, R. (2017). Numerical simulation of a discontinuous gallery lining's behavior, and its interaction with rock. *International Journal for Numerical and Analytical Methods in Geomechanics*, 41(15):1569–1589.

Sander, R. (2015). Compilation of Henry's law constants (version 4.0) for water as solvent. *Atmospheric Chemistry and Physics*, 15(8):4399–4981.

Segura, J. and Carol, I. (2004). On zero-thickness interface elements for diffusion problems. *International journal for numerical and analytical methods in geomechanics*, 28(9):947–962.

Segura, J. M. and Carol, I. (2008a). Coupled HM analysis using zero-thickness interface elements with double nodes. Part I: Theoretical model. *International Journal for Numerical and Analytical Methods in Geomechanics*, 32(18):2083–2101.

Segura, J. M. and Carol, I. (2008b). Coupled HM analysis using zero-thickness interface elements with double nodes—Part II: Verification and application. *International Journal for Numerical and Analytical Methods in Geomechanics*, 32(18):2103–2123.

Shao, H., Hesser, J., Kolditz, O., and Wang, W. (2019). Hydraulic characterisation of clay rock under consideration of coupled THM properties. *Environmental Science and Engineering*, pages 33–40. cited By 0.

Shao, J. F., Zhu, Q. Z., and Su, K. (2003). Modeling of creep in rock materials in terms of material degradation. *Computers and Geotechnics*, 30(7):549–555.

Shaw, R. E. (2013). Gas Generation and Migration, International Symposium and Workshop. In *Conference Book*. cited By 0.

Song, H., Corman, G., and Collin, F. (2023). Thermal Impact on the Excavation Damage Zone Around a Supported Drift Using the 2nd Gradient Model. *Rock Mechanics and Rock Engineering*, (0123456789).

Talandier, J. (2005). La production et le transfert de gaz dans un stockage et dans la couche du Callovo-Oxfordien - Lien avec le transitoire hydraulique - Site de Meuse / Haute-Marne. Rapport Andra n° C.NT.ASCM.03.0042. Technical report, Andra.

Tamayo-Mas, E., Harrington, J., Damians, I., Olivella, S., Radeisen, E., Rutqvist, J., and Wang, Y. (2024). Advective gas flow in bentonite: Development and comparison of enhanced multi-phase numerical approaches. *Geomechanics for Energy and the Environment*, 37. Cited by: 0.

Toprak, E., Olivella, S., and Pintado, X. (2020). Modelling engineered barriers for spent nuclear fuel repository using a double-structure model for pellets. *Environmental Geotechnics*, 7(1):72–94. cited By 10.

Tsang, C., Bernier, F., and Davies, C. (2005). Geohydromechanical processes in the Excavation Damaged Zone in crystalline rock, rock salt, and indurated and plastic clays - In the context of radioactive waste disposal. *International Journal of Rock Mechanics and Mining Sciences*, 42(1):109–125.

Tsang, Y. W. and Witherspoon, P. (1981). Hydromechanical behavior of a deformable rock fracture subject to normal stress. *Journal of Geophysical Research: Solid Earth*, 86(B10):9287–9298.

Van Eekelen, H. A. M. (1980). Isotropic yield surfaces in three dimensions for use in soil mechanics. *International Journal for Numerical and Analytical Methods in Geomechanics*, 4(1):89–101.

van Genuchten, M. (1980). Predicting the hydraulic conductivity of unsaturated soils. *Soil. Sci. Soc. Am. J*, 44(5):892–898.

Van Genuchten, M. T. (1980). A closed-form equation for predicting the hydraulic conductivity of unsaturated soils. *Soil science society of America journal*, 44(5):892–898.

Vargaftik, N., Volkov, B., and Voljak, L. (1983). International tables of the surface tension of water. *Journal of Physical and Chemical Reference Data*, 12(3):817–820.

Volckaert, G., Ortiz, L., Canniere, P. D., Put, M., Horseman, S. T., Harrington, J. F., Fioravante, V., and Impey, M. (1995a). MEGAS: modelling and experiments on GAS migration in repository host rocks. Final report phase 1. Technical report, Eur. Comm., [Rep.] EUR 16235 EN.

Volckaert, G., Ortiz, L., Canniere, P. D., Put, M., Horseman, S. T., Harrington, J. F., Fioravante, V., and Impey, M. (1995b). MEGAS: modelling and experiments on GAS migration in repository host rocks. Final report phase 1. Technical report, SCK-CEN.

Wang, C., Talandier, J., and Skoczylas, F. (2022a). Swelling and fluid transport of re-sealed callovo–oxfordian claystone. *Rock Mechanics and Rock Engineering*, pages 1–16.

Wang, H., Cui, Y.-J., Vu, M. N., Talandier, J., and Conil, N. (2022b). Fracture effect on the hydro-mechanical behaviour of callovo-oxfordian claystone. *Engineering Geology*, 303:106674.

Wang, H., de La Vaissière, R., Vu, M.-N., La Borderie, C., and Gallipoli, D. (2022c). Numerical modelling and in-situ experiment for self-sealing of the induced fracture network of drift into the callovo-oxfordian claystone during a hydration process. *Computers and Geotechnics*, 141:104487.

Wang, W., Shao, H., Nagel, T., and Kolditz, O. (2020). Analysis of coupled thermal-hydro-mechanical processes during small scale in-situ heater experiment in Callovo-Oxfordian clay rock introducing a failure-index permeability model. *International Journal of Rock Mechanics and Mining Sciences*, revised manuscript under review.

Wang, W., Shao, H., Nagel, T., and Kolditz, O. (2021). Analysis of coupled thermal-hydro-mechanical processes during small scale in situ heater experiment in Callovo-Oxfordian clay rock introducing a failure-index permeability model. *International Journal of Rock Mechanics and Mining Sciences*.

Webber, J. B. W. (2013). A bi-symmetric log transformation for wide-range data. *Measurement Science and Technology*, 24(2).

Wileveau, Y., Cornet, F. H., Desroches, J., and Blumling, P. (2007). Complete in situ stress determination in an argillite sedimentary formation. *Physics and Chemistry of the Earth*, 32(8-14):866–878.

Wiseall, A. C., Cuss, R., and Hough, E. (2019). Visualising hydraulic fractures in bedded and fractured shales: A series of analogue experiments. *5th International Conference on Fault and Top Seals 2019*, (September 2019):1–5.

Wiseall, A. C., Cuss, R. J., Graham, C. C., and Harrington, J. F. (2015). The visualization of flow paths in experimental studies of clay-rich materials. *Mineralogical Magazine*, 79(6):1335–1342.

Witherspoon, P. A., Wang, J. S. Y., Iwai, K., and Gale, J. E. (1980). Validity of cubic law for fluid flow in a deformable rock fracture. *Water Resour. Res.*, 16(6):1016–1024.

Xu, W., Shao, H., Hesser, J., Wang, W., Schuster, K., and Kolditz, O. (2013a). Coupled multiphase flow and elasto-plastic modelling of in-situ gas injection experiments in saturated claystone (Mont Terri Rock Laboratory). *Engineering Geology*, 157:55–68. cited By 21.

Xu, W., Shao, H., Marschall, P., Hesser, J., and Kolditz, O. (2013b). Analysis of flow path around the sealing section HG-A experiment in the Mont Terri Rock Laboratory. *Environmental Earth Sciences*, 70(7):3363–3380. cited By 14.

Yang, Y. and Aplin, A. C. (2010). A permeability-porosity relationship for mudstones. *Marine and Petroleum Geology*, 27(8):1692–1697.

Yoshioka, K., Parisio, F., Naumov, D., Lu, R., Kolditz, O., and Nagel, T. (2019). Comparative verification of discrete and smeared numerical approaches for the simulation of hydraulic fracturing. *GEM - International Journal on Geomathematics*, 10(1). cited By 12.

Yoshioka, K., Sattari, A., Nest, M., Günther, R.-M., Wuttke, F., Fischer, T., and Nagel, T. (2022). Numerical models of pressure-driven fluid percolation in rock salt: nucleation and propagation of flow pathways under variable stress conditions. *Environmental Earth Sciences*, 81(5). Cited by: 4; All Open Access, Hybrid Gold Open Access.

Zervos, A., Papanastasiou, P., and Vardoulakis, I. (2001). A finite element displacement formulation for gradient elastoplasticity. *International Journal for Numerical Methods in Engineering*, 50(6):1369–1388.

Zhang, C.-L. (2013). Sealing of fractures in claystone. *Journal of Rock Mechanics and Geotechnical Engineering*, 5(3):214–220.

Zhang, C.-L. and Talandier, J. (2023). Self-sealing of fractures in indurated claystones measured by water and gas flow. *Journal of Rock Mechanics and Geotechnical Engineering*, 15(1):227–238.

Zhang, F., Cui, Y.-J., Conil, N., and Talandier, J. (2020). Assessment of swelling pressure determination methods with intact callovo-oxfordian claystone. *Rock Mechanics and Rock Engineering*, 53:1879–1888.

Zhang, N. and Nagel, T. (2020). Error-controlled implicit time integration of elasto-visco-plastic constitutive models for rock salt. *International Journal for Numerical and Analytical Methods in Geomechanics*, 44(8):1109–1127. cited By 0.

Zhou, H., Jia, Y., and Shao, J. F. (2008). A unified elastic–plastic and viscoplastic damage model for quasi-brittle rocks. *International Journal of Rock Mechanics and Mining Sciences*, 45(8):1237–1251.

Zill, F., Lüdeling, C., Kolditz, O., and Nagel, T. (2021). Hydro-mechanical continuum modelling of fluid percolation through rock salt. *International Journal of Rock Mechanics and Mining Sciences*, 147:104879.